

A 3D visualization of a turbulent flow field, likely a wake or a jet, rendered in a color gradient from purple to yellow. The flow is overlaid on a grid of streamlines. The background is a gradient from orange to blue.

Markus Raffel · Christian E. Willert
Fulvio Scarano · Christian J. Kähler
Steven T. Wereley · Jürgen Kompenhans

Particle Image Velocimetry

A Practical Guide

Third Edition

 Springer

Particle Image Velocimetry


Markus Raffel · Christian E. Willert
Fulvio Scarano · Christian J. Kähler
Steven T. Wereley · Jürgen Kompenhans


Particle Image Velocimetry


A Practical Guide


Third Edition


 Springer


Markus Raffel 
Institut für Aerodynamik und
Strömungstechnik
Deutsches Zentrum für Luft- und Raumfahrt
e.V. (DLR)
Göttingen
Germany

Christian E. Willert 
Institut für Antriebstechnik
Deutsches Zentrum für Luft- und Raumfahrt
e.V. (DLR)
Köln
Germany

Fulvio Scarano 
Department of Aerospace Engineering
Delft University of Technology
Delft
The Netherlands

Christian J. Kähler 
Institut für Strömungsmechanik und
Aerodynamik
Universität der Bundeswehr München
Neubiberg
Germany

Steven T. Wereley 
Department of Mechanical Engineering,
Birck Nanotech Center
Purdue University
West Lafayette
USA

Jürgen Kompenhans 
Institut für Aerodynamik und
Strömungstechnik
Deutsches Zentrum für Luft- und Raumfahrt
e.V. (DLR)
Göttingen
Germany

ISBN 978-3-319-68851-0 ISBN 978-3-319-68852-7 (eBook)
<https://doi.org/10.1007/978-3-319-68852-7>

Library of Congress Control Number: 2017954491

1st and 2nd editions: © Springer-Verlag Berlin Heidelberg 1998, 2007

3rd edition: © Springer International Publishing AG, part of Springer Nature 2018

This work is subject to copyright. All rights are reserved by the Publisher, whether the whole or part of the material is concerned, specifically the rights of translation, reprinting, reuse of illustrations, recitation, broadcasting, reproduction on microfilms or in any other physical way, and transmission or information storage and retrieval, electronic adaptation, computer software, or by similar or dissimilar methodology now known or hereafter developed.

The use of general descriptive names, registered names, trademarks, service marks, etc. in this publication does not imply, even in the absence of a specific statement, that such names are exempt from the relevant protective laws and regulations and therefore free for general use.

The publisher, the authors and the editors are safe to assume that the advice and information in this book are believed to be true and accurate at the date of publication. Neither the publisher nor the authors or the editors give a warranty, express or implied, with respect to the material contained herein or for any errors or omissions that may have been made. The publisher remains neutral with regard to jurisdictional claims in published maps and institutional affiliations.

The cover image visualizes the flow around a cube by presenting 3D velocity vectors in a plane together with isosurfaces of the Q-criterion, see Sect. 18.3.

Printed on acid-free paper

This Springer imprint is published by the registered company Springer International Publishing AG part of Springer Nature
The registered company address is: Gewerbestrasse 11, 6330 Cham, Switzerland

Preface to the Third Edition

Particle image velocimetry (PIV) is a measurement technique that allows for capturing velocity fields in fractions of a second. Its development started in the 1980s of the last century based on earlier work in the field of laser speckle photography. When the first edition of this book was prepared by MARKUS RAFFEL, CHRISTIAN WILLERT, and JÜRGEN KOMPENHANS in 1998, the PIV technique had emerged from laboratories to applications in fundamental and industrial research, in parallel to the transition from photographic to video recording techniques.

The early progress made with the PIV technique might best be characterized by the experience gained during aerodynamic research of the authors at DLR (DEUTSCHES ZENTRUM FÜR LUFT- UND RAUMFAHRT) at that time. The first applications of PIV outside the laboratory, in wind tunnels, as performed in the mid 1980s were characterized by the following timescales: Time required to set up the system and to obtain well-focused photographic PIV recordings was 2–3 days, time required to process the film was 0.5–1 day, and time required to evaluate a single photographic PIV recording by means of optical evaluation methods was 24–48 h. Later, in 1998, with electronic cameras and computers, it was possible to verify the image focus online, to capture several recordings per second, and to evaluate a digital recording within seconds. During a typical measurement campaign, about 100 GB of raw data could easily be collected.

The time from 1998 to 2007, when the second edition of this book has been published, was characterized by a rapid development of hard- and software for the PIV technique. Improved cameras, lasers, optics, and advanced evaluation techniques led to a further significant increase in performance and offered the possibility of high-speed and three-component measurements. The use of the PIV technique in micro-flows, which proved to be very successful, required dedicated hard- and software. Thus, STEVEN T. WERELEY, with his knowledge in 2D micro-PIV, joined the group of authors for the second edition.

Since 2007, the PIV technique has undergone further progress, in particular toward high-speed measurements and volumetric techniques capable of capturing all three components of the velocity vectors within a volume of the flow field instantaneously. Issues such as accuracy and reliability of the PIV data, comparison

of experimental PIV data with results of numerical calculations, and parallel application of PIV with other measurement techniques, as for density, surface pressure and surface deformation, sound pressure, temperature, etc., have become of increasing importance. Being well-known experts in these areas FULVIO SCARANO and CHRISTIAN J. KÄHLER joined the group of authors for this third edition. Due to their valuable contributions, a major expansion of this book became possible. The recent developments of PIV and LPT (Lagrangian particle tracking) related to 3D and time-resolved measurements have mainly found their impact in the chapters *Techniques for 3D-PIV* and chapters 11 to 18 (*Examples of Application*), and those related to accuracy and reliability in the chapter *PIV Uncertainty and Measurement Accuracy* of this book. In addition, the chapter on micro-PIV was significantly extended taking the advances of 3D flow analysis techniques into account.

To characterize the present state of development of the PIV technique, it should be noted that it is now possible to capture the 3D flow field from a volume of $50 \times 50 \times 10 \text{ mm}^3$ with a spatial resolution of less than a millimeter and a temporal resolution on the order of 10,000 frames/sec in air. The recent developments have expanded the measurement volume up to $200 \times 200 \times 500 \text{ mm}^3$ in low-speed wind tunnels. Raw images can be acquired at rates exceeding 10 GB/s yielding 3D and time-resolved vector fields with more than 100,000 vectors per snapshot for a typical measurement (e.g., for validation of numerical results). Data collected during a single measurement campaign may range up to several terabytes.

Given the extreme versatility of PIV, the range of possible applications has drastically increased over the last three decades. PIV is nowadays used in very different areas from aerodynamics to biology, from fundamental turbulence research to applications in the space station, from combustion to two-phase flows and in microfluidic devices. Due to this wide range of possible applications of PIV, the number of research groups employing this technique world wide has increased from a handful at the beginning of the 1980s to several thousands today.

These developments have led to standards for PIV systems commercially available in different configurations, which cover the most important areas of applications and allow the use of the PIV technique also for non-experts in a much easier way than it was possible thirty years ago. However, due to the variety of different applications of PIV and the large number of different possibilities to illuminate, to record, and to evaluate, many different custom-built technical modifications of the PIV technique (and thus of the standard PIV systems) have been developed, which need to be known and well understood not only by the developer, but also by the PIV end user.

Rather than to provide a highly detailed and complete description of all aspects of the PIV technique, with proper reference to all original work, the intention of this book is to present, in a more general context, mainly those aspects of the PIV technique, which are relevant to today's end users and their applications. This objective is supported by the experience gained by all authors during collaboration with their co-workers for more than three decades on the development of PIV and a large number of the most different applications of PIV. Major test campaigns

utilizing the PIV technique have often been jointly carried out in international and interdisciplinary cooperation, together with PIV developers, staff of large-scale research facilities, and end users, being scientists, engineers, technicians, students, project managers, etc.

The target audience of this book is similar to that of the annual course on particle image velocimetry held since 1993 at the DLR CENTER in GÖTTINGEN. In this regard, the material presented in this book also takes into account the feedback from the hundreds of participants of these courses along the past years.

Due to the experience of the authors, this Practical Guide to PIV provides in a condensed form most of the information relevant for planning, performing, and optimizing experiments employing the PIV technique. It is mainly intended for engineers, scientists, and students, who already have some basic knowledge of fluid mechanics and non-intrusive optical measurement techniques.

For many researchers and engineers, who are planning to utilize PIV for their special industrial or scientific applications, PIV is first and foremost an attractive tool with unique features, which they expect helping them to gain new insights in problems of fluid mechanics. Therefore, becoming a PIV specialist before starting one's investigation may not be of high priority to them, but some of the basic concepts of PIV must be well understood before performing the experiment. A good understanding of the basics is not only required to set up and optimize a given PIV experiment, but also to interpret the velocity data and all derived quantities in a proper manner. Our hope is that this book will serve this purpose by providing an easy transfer of the know-how gathered by the authors to the readers. As with all publications, the amount of information covered in this book is limited, unfortunately rendering completeness impossible. Many of the concepts underlying the PIV technique can only be covered in a condensed manner, and the reader will be provided with relevant references for further reading on the respective subjects, typically textbooks or journal grade publications.

Starting from the present edition, additional material will be available to the reader in digital form. The *Digital Content*, which is available at a dedicated Web site: www.pivbook.org, expands the available information also by means of example images, and results that can be inspected with more detail than in the regular book.

The *Digital Content* is provided to the readers of this book on a voluntary basis without any responsibilities of the authors or the publisher.

Organization of the Book

The book starts with a brief introduction to the basic principles of PIV and describes the main milestones along the development of the PIV technique, discussing some of the problems and technical constraints to be kept in mind.

Next, the different topics will be described in more detail. Firstly, the background of the most important physical principles will be provided. In the following,

the mathematical background of statistical PIV evaluation is given. With this knowledge, the path has been prepared for the understanding of the recording and evaluation methods applied in PIV. Measurement noise and accuracy need to be optimized to achieve high-quality raw data, which shall be postprocessed for further analysis. Furthermore, the present state of the technical development of the methods that access all three components of the velocity vector in a *plane*, such as stereo PIV, and in a *volume*, such as tomographic PIV and Lagrangian particle tracking (LPT), will be described. A special chapter is devoted to the application of PIV to micro-fluids. The statements made on the scientific and technical features of the PIV technique will be underlined by presenting examples of application of PIV to cases relevant to fluid mechanics from micro-fluidics to large-scale aerodynamics. Many ideas about problems associated with special applications of PIV and their solution can be found in the chapters on applications, to which many PIV experts worldwide contributed with their expertise gained in the most different areas of flow research. In the final chapter, related techniques allowing to measure the deformation of an object or the density within a flow will be presented, which make use of evaluation methods related to the PIV technique.

Like the PIV technique, the process of publication of a book has also undergone a transition process from the analog (print version) to the digital (eBook, Web site) world. Storage of the working version of the book in the cloud allowed shared access and joint work of the authors at the different parts of the book.

For the first time, additional *Digital Content (DC)* will be made available through a dedicated Web site pivbook.org/digital-content/index.html. PIV being a technique working with images and image sequences, this allows to make available such material to the readers in a digital format at much higher resolution than possible in print. Some material (e.g., movies) even cannot be provided in print. In addition, some of the material can be used by the readers for own testing or verification of the performance of PIV evaluation software under development. But also, in particular for beginners, examples for best practice and bad practice (which should be avoided) are given.

The Web site containing the *Digital Content* also allows to present text, examples of application, and reference lists of the first two editions of this book, which are still scientifically valid but no longer up-to-date, and as such not of direct interest for the PIV user in the present days. This will help keeping the Practical Guide as focused to the immediate needs of a user of the PIV technique as possible, but provide links to further background information if reasonable. After publication of this book the *Digital Content* will allow to inform about updates and errata.

Within the text, we will directly link to the relevant examples, exercises, and applications using labels such as $DC_{n_{chapter},m_{element}}$. Readers of the electronic version of this book just need to follow the link, appearing when the pointer (mouse cursor) is moved over the $DC_{n,m}$ label. Readers of the print version of this book need to open the Web site pivbook.org/digital-content/index.html and to use the search function of the Web site to access the respective Digital Content by giving the input $DC_{n,m}$, for example, use the label $DC_{1,5}$ to find the fifth entry in the first chapter (*Introduction*) of the *Digital Content*. It is envisaged to extend the *Digital*

Content over time. The first page of each chapter contains a link to the *Digital Content* in order to keep track with modifications made after the publication of this edition.

In addition, the electronic version of this book also links to sections, figures, or references within the book, if the pointer is moved over their respective icons, such as numbers or names within the text. Similar links may lead to external Web sites. Authors and publisher do not take any responsibility for the contents of such Web sites.

Getting Started

One objective of this book is to help the readers avoid beginners' errors and bring them to a position to obtain results of high quality when employing PIV right from the beginning of their work. We recommend to start reading the introduction and the introductory remarks of each technical chapter first. For a deeper treatment of the fundamentals, we have included a list of book recommendations in Appendix A of this book.

For those, already working in the field of PIV, the technical chapters of this book may serve as a guide. Each chapter provides references to further publications containing more details. Those readers, who need to develop and set up a PIV system for their special scientific problem, should study the applications described in this book, which are intended as a starting point describing various technical problems and solutions found by others, for similar scientific investigations. The additional material found in the *Digital Content* can be used to compare the quality of PIV recordings obtained in own experiments with those typically required for publication of results in scientific journals.

About the Authors

Markus Raffel received his degree in Mechanical Engineering in 1990, from the University of Karlsruhe, his doctorate in Engineering in 1993, from the University of Hannover, and his lecturer qualification (Habilitation) from the Clausthal University of Technology, in 2001. He started working on PIV at the German Aerospace Center (DLR) in 1991, with emphasis on the development of PIV recording techniques in high-speed flows. In this process, he applied the method to a number of aerodynamic problems mainly in the context of rotorcraft investigations. Markus Raffel additionally works on the development of other flow metrology like the background-oriented schlieren technique and the differential infrared thermography. He is Professor at the University of Hannover and head of the Department of Helicopters at DLR's Institute of Aerodynamics and Flow Technology in Göttingen.

Christian E. Willert received his Bachelor of Science in Applied Science from the University of California at San Diego (UCSD) in 1987. Subsequent graduate work in experimental fluid mechanics at UCSD leads to the development of several non-intrusive measurement techniques for application in water (particle tracing, 3-D particle tracking, digital PIV). After receiving his Ph.D. in Engineering Sciences in 1992, he assumed postdoctoral positions first at the Institute for Nonlinear Science (INLS) at UCSD, then at the Graduate Aerospace Laboratories at the California Institute of Technology (Caltech). In 1994, he joined DLR Göttingen's measurement sciences group as part of an exchange program between Caltech and DLR. Since 1997, he has been working in the development and application of planar velocimetry techniques (PIV and doppler global velocimetry (DGV)) at the Institute of Propulsion Technology of DLR and now is heading the Department of Engine Measurement Techniques there.

Fulvio Scarano graduated in Aerospace Engineering at University of Naples "Federico II" (1996), obtained the Ph.D. in 2000 (von Karman Institute, Theodore von Karman prize), and joined TU Delft at the faculty of Aerospace Engineering in the Aerodynamics Section in the same year. Since 2008, he is full professor of Aerodynamics and acts as head of section since 2010. Director of Aerospace Engineering Graduate School (2012). Currently, he is director of the AWEP department (Aerodynamics, Wind Energy, Flight Performance and propulsion). He is recipient of Marie-Curie grant (1999), Dutch Science Foundation VIDI grant (2005), and the European Research Council grant (ERC, 2009). He is European project coordinator (AFDAR, Advanced Flow Diagnostics for Aeronautical Research, 2010–2013). He has promoted and supervised more than 20 PhDs. The research interests cover the development of particle image velocimetry (PIV) and its applications to high-speed aerodynamics in the supersonic and hypersonic regime. Notable developments are the image deformation technique, tomographic PIV for 3D flow velocity measurements, and its use to quantitatively determine pressure fluctuations and acoustic emissions in wind tunnel experiments. Recent works deal with the combination of PIV data with CFD techniques, extension of PIV to large-scale wind tunnel experiments, and applications ranging from sport aerodynamics to ground vehicles, from aircraft to rocket aerodynamics. Author of more than 200 publications delivered more than 20 keynote lectures worldwide. He acts as editorial board member of many international conferences and journals, Measurement Science and Technology and Experiments in Fluids, among others.

Christian J. Kähler received his Physics Diploma Degree from the Clausthal University of Technology in 1997, his Ph.D. in Physics from the Georg-August University of Göttingen in 2004, and his Habilitation from the Technical University in Brunswick in 2008. From 1996 to 2001, Dr. Kähler worked at the German Aerospace Center (DLR) in Göttingen (Dr. Kompenhans), during which he had research stays at the University of Illinois at Urbana Champaign in 1996 (Prof. Adrian) and at Caltech in 1998 (Prof. Gharib). From 2001 to 2008, he was the head of the research group on Flow Control and Measuring Techniques at the Technical University Brunswick (Prof. Radespiel). He then became Professor for Fluid Dynamics and was appointed director of the Institute of Fluid Mechanics and

Aerodynamics of the Universität der Bundeswehr München in 2008. In 2012, he was offered an Einstein professorship for Aerodynamics at the Technical University of Berlin (declined) and in 2017, the Technical University Darmstadt offered him to become head of the chair of Fluid Mechanics (declined). His research covers a broad range of topics involving the development of optical measurement techniques on the micro- and macroscale in order to further investigate complex phenomena in micro-fluidics and turbulent flows at subsonic, transonic, and supersonic conditions. He is an associate editor of *Experiments in Fluids* (Springer Nature), an editorial advisory board member of *Flow, Turbulence and Combustion* (Springer Nature), editorial board member of *Theoretical & Applied Mechanics Letters* (Elsevier), and a steering committee member and organizer of the International PIV Challenge (2001 Göttingen, 2003 Busan, 2005 Pasadena, 2014 Lisbon).

Steven T. Wereley received both his Bachelor of Arts in Physics from Lawrence University at Appleton, Wisconsin, and his Bachelor of Science in Mechanical Engineering from Washington University at St. Louis in 1990. He received his Master of Science and Ph.D. degrees from Northwestern University in Evanston, Illinois, in 1992 and 1997, respectively. Subsequently, he spent two years at the Mechanical and Environmental Engineering Department at the University of California in Santa Barbara developing particle image velocimetry algorithms for micro-domain investigations. Since 1999, he has been a Professor at Purdue University in the School of Mechanical Engineering—as an Assistant Professor from 1999 to 2005 and an Associate Professor since then. Professor Wereley’s research is largely concerned with micro-particle image velocimetry techniques and micro-electromechanical systems with applications in biophysics and bioengineering.

Jürgen Kompenhans received his doctoral degree in physics in 1976, from the Georg-August University of Göttingen. From 1977 to 2011, he worked for the German Aerospace Center (DLR) in Göttingen, Germany, mainly developing and applying non-intrusive measurement techniques for aerodynamic research, starting with the PIV technique back in 1985. Since 2001, he has been head of the Department of Experimental Methods of DLR’s Institute of Aerodynamics and Flow Technology in Göttingen. Within this department, image-based methods such as pressure sensitive paint, temperature sensitive paint, particle image velocimetry, model deformation measurement techniques, density measurement techniques, acoustic field measurement techniques etc., are developed for application as mobile systems in large industrial wind tunnels. As coordinator of several European networks, he has contributed to promote and to disseminate the use of image-based measurement techniques for industrial research. At present, his interest is focused on contributing to the development of flow meters as well as of components required for the use of the PIV technique.

Acknowledgements

During the past decades, a large number of colleagues have contributed to our successful work on development and use of PIV, which helped us essentially to prepare the third edition of this book: technicians, students, and scientists. Among these, we especially want to acknowledge the contributions of Klaus Hinsch, Hans Höfer, and Hugues Richard who helped us developing our knowledge in the early years. Being a colleague and friend of most of the authors, Andreas Schröder contributed to their success since more than two decades until today. Andreas Schröder together with Daniel Schanz, Sebastian Gesemann and Matteo Novara contributed the major part of the text about the Lagrangian particle tracking technique, like the description of the Shake-the-Box method, which constitutes a novel access to particle dynamics.

In particular we would like to thank Johannes Braukmann (DLR) for his support, dedicated work and ideas how to organize the interaction with the many contributors during the long process of writing this book. Without him being the focal point of the cooperation between the authors, this third edition would not have been possible. We would also like to thank Annika Köhne (DLR) who supported Johannes during this process. We are very grateful to Holger Frahnert for the design and functionality of the Digital Content Web site.

The authors would also like to thank André Bauknecht for his contribution to the Related Techniques chapter and Sven Scharnowski for the many stimulating discussions about uncertainty quantification and his support during the writing of this section. In addition, the support of Thomas Fuchs during the writing of the 2D and 3D-PTV sections is also greatly recognized as well as the contribution by Rainer Hain. Furthermore, the careful proofreading of Chap. 6 by Andrea Sciacchitano is greatly appreciated. Christian Kähler would also like to recognize the productive interactions and discussions with Christian Cierpka during his postdoc period at Christian Kähler's institute, which was essential for the writing of the 2D-PTV and volumetric micro-PIV sections. We would also like to thank Dr. Gerhard Holst (PCO GmbH, Kelheim), who edited the text on CMOS and CCD cameras.

The third edition is, even more than the first two, based on the supplementary work of many scientists. We are very much indebted to a great number of researchers worldwide who have provided contributions on special topics related to the PIV technique, which allowed covering a broad field of applications. These contributions shall be acknowledged next, giving the name of the author and institute where the research has been performed.

Contributions to the application chapters (chapters 11 to 18) of the third edition have been provided by:

- | | |
|-----------------|--|
| J. Agocs | Institute of Aerodynamics and Flow Technology
German Aerospace Center
Bunsenstrasse 10, 37073 Göttingen, Germany |
| D. Baczynzalski | Institute of Fluid Mechanics and Aerodynamics
Universität der Bundeswehr München
Werner-Heisenberg-Weg 39, 85577 Neubiberg,
Germany |

- S.J. Beresh Sandia National Laboratories
New Mexico, P.O. Box 5800, Albuquerque, NM 87185,
USA
- C. Böhm ZARM
University of Bremen
Am Fallturm, 28359 Bremen, Germany
- J. Bosbach Institute of Aerodynamics and Flow Technology
German Aerospace Center
Bunsenstrasse 10, 37073 Göttingen, Germany
- C. Cierpka Institute of Thermodynamics and Fluid Mechanics
Department of Mechanical Engineering
Technische Universität Ilmenau
Max-Planck-Ring 14, 98693 Ilmenau, Germany
- N.K. Depuru-Mohan Department of Engineering
University of Cambridge
Homerton College Hills Road
Cambridge CB2 8PH, UK
- U. Dirksheide LaVision GmbH
Anna-Vandenhoeck-Ring 19, 37081 Göttingen,
Germany
- D. Favier Laboratoire d'Aérodynamique et de
Biomécanique du Mouvement
Centre national de la recherche scientifique (CNRS)
163 Avenue de Luminy, CP 918
13288 Marseille Cedex 09, France
- R. Geisler Institute of Aerodynamics and Flow Technology
German Aerospace Center
Bunsenstrasse 10, 37073 Göttingen, Germany
- S. Gesemann Institute of Aerodynamics and Flow Technology
German Aerospace Center
Bunsenstrasse 10, 37073 Göttingen, Germany
- S. Ghaemi Department of Mechanical Engineering
University of Alberta
116 Street and 85 Avenue, Edmonton, AB, Canada
- M. Gharib Aeronautics and Bioengineering
California Institute of Technology
1200 East California Boulevard, 205-45
Pasadena CA 91125, USA

- E. Göttlich
Institute for Thermal Turbomachinery
and Machine Dynamics
Technical University of Graz
Inffeldgasse 25A, 8010 Graz, Austria
- J.T. Heineck
Experimental Physics Branch
NASA Ames Research Center
Moffet Field, CA 94035, USA
- A. Henning
Institute of Aerodynamics and Flow Technology
German Aerospace Center
Bunsenstrasse 10, 37073 Göttingen, Germany
- M. Herr
Institute of Aerodynamics and Flow Technology
German Aerospace Center
Lilienthalplatz 7, 38108 Braunschweig, Germany
- F. Huhn
Institute of Aerodynamics and Flow Technology
German Aerospace Center
Bunsenstrasse 10, 37073 Göttingen, Germany
- R.A. Humble
Department of Aerospace Engineering
Texas A and M University
College Station, United States
- K. Kindler
Institute of Aerodynamics and Flow Technology
German Aerospace Center
Bunsenstrasse 10, 37073 Göttingen, Germany
- J. Klinger
Institute of Propulsion Technology
German Aerospace Center
Linder Höhe, 51147 Köln, Germany
- R. Konrath
Institute of Aerodynamics and Flow Technology
German Aerospace Center
Bunsenstrasse 10, 37073 Göttingen, Germany
- M. Kotsonis
Department of Aerospace Engineering
Delft University of Technology
Kluyverweg 1, 2629 HS, Delft, The Netherlands
- C. Jux
Department of Aerospace Engineering
Delft University of Technology
Kluyverweg 1, 2629 HS, Delft, The Netherlands
- H. Lang
Institute for Thermal Turbomachinery
and Machine Dynamics
Technical University of Graz
Inffeldgasse 25, 8010 Graz, Austria

- T. Lauke
Institute of Aerodynamics and Flow Technology
German Aerospace Center
Lilienthalplatz 7, 38108 Braunschweig, Germany
- P. Manovski
Aerodynamics & Aeroelasticity Aerospace Division
Defence Science & Technology Group
Blg 11, 506 Lorimer St, Fishermans Bend, VIC 3207,
Australia
- C.D. Meinhart
Dept. of Mechanical and Environmental Engineering
University of California - Santa Barbara
Santa Barbara, CA 93106, USA
- K. Mulleners
Institute of Aerodynamics and Flow Technology
German Aerospace Center
Bunsenstr  e 10, 37073 G  ttingen, Germany
- M. Novara
Institute of Aerodynamics and Flow Technology
German Aerospace Center
Bunsenstr  e 10, 37073 G  ttingen, Germany
- M. Percin
Department of Aerospace Engineering
Delft University of Technology
Kluyverweg 1, 2629 HS, Delft, The Netherlands
- C. Poelma
Faculty Mechanical, Maritime and Materials Engineering
Delft University of Technology
Leeghwaterstraat 21, 2628 CA, Delft, The Netherlands
- D. Ragni
Department of Aerospace Engineering
Delft University of Technology
Kluyverweg 1, 2629 HS, Delft, The Netherlands
- N. Reuther
Institute of Fluid Mechanics and Aerodynamics
Universit  t der Bundeswehr M  nchen
Werner-Heisenberg-Weg 39, 85577 Neubiberg,
Germany
- H. Richard[†]
Institute of Aerodynamics and Flow Technology
German Aerospace Center
Bunsenstr  e 10, 37073 G  ttingen, Germany
- C. Rondot
Laboratoire d'A  rodynamique et de
Biom  canique du Mouvement
Centre national de la recherche scientifique (CNRS)
163 Avenue de Luminy, CP 918
13288 Marseille Cedex 09, France

- M. Rossi
Institute of Fluidmechanics and Aerodynamics
Universität der Bundeswehr München
Werner-Heisenberg-Weg 39, 85577 Neubiberg,
Germany
- D. Schanz
Institute of Aerodynamics and Flow Technology
German Aerospace Center
Bunsenstrasse 10, 37073 Göttingen, Germany
- E.T. Schairer
Experimental Physics Branch
NASA Ames Research Center
Moffet Field, CA 94035, USA
- D. Schmeling
Institute of Aerodynamics and Flow Technology
German Aerospace Center
Bunsenstrasse 10, 37073 Göttingen, Germany
- F. Schrijer
Department of Aerospace Engineering
Delft University of Technology
Kluyverweg 1, 2629 HS, Delft, The Netherlands
- A. Schröder
Institute of Aerodynamics and Flow Technology
German Aerospace Center
Bunsenstrasse 10, 37073 Göttingen, Germany
- M. Schroll
Institute of Propulsion Technology
German Aerospace Center
Linder Höhe, 51147 Köln, Germany
- A. Sciacchitano
Department of Aerospace Engineering
Delft University of Technology
Kluyverweg 1, 2629 HS, Delft, The Netherlands
- Y. Shah
Department of Aerospace Engineering
Delft University of Technology
Kluyverweg 1, 2629 HS, Delft, The Netherlands
- W. Terra
Department of Aerospace Engineering
Delft University of Technology
Kluyverweg 1, 2629 HS, Delft, The Netherlands
- R. van de Meerendonk
Department of Aerospace Engineering
Delft University of Technology
Kluyverweg 1, 2629 HS, Delft, The Netherlands
- B.G. van der Wall
Institute of Flight Systems
German Aerospace Center
Lilienthalplatz 7, 38108 Braunschweig, Germany

- B.W. van Oudheusden Department of Aerospace Engineering
 Delft University of Technology
 Kluyverweg 1, 2629 HS, Delft, The Netherlands
- D. Violato Department of Aerospace Engineering
 Delft University of Technology
 Kluyverweg 1, 2629 HS, Delft, The Netherlands
- M. Voges Institute of Propulsion Technology
 German Aerospace Center
 Linder Höhe, 51147 Köln, Germany
- C. Wagner Institute of Aerodynamics and Flow Technology
 German Aerospace Center
 Bunsenstraße 10, 37073 Göttingen, Germany
- S. M. Walker Experimental Physics Branch
 NASA Ames Research Center
 Moffet Field, CA 94035, USA
- J. Woisetschläger Institute for Thermal Turbomachinery
 and Machine Dynamics
 Technical University of Graz
 Inffeldgasse 25, 8010 Graz, Austria
- M. Yoda George W. Woodruff School of Mechanical Engineering
 Georgia Institute of Technology
 771 Ferst Drive, Atlanta, Georgia 30332-0405, USA

Last but not least, we are deeply indebted to all friends and colleagues of the worldwide PIV community who helped us to better understand the different aspects of the PIV technique by their work, their publications, and conference contributions, and by personal discussions.

Göttingen, Germany
 June 2017

Markus Raffel
 Christian E. Willert
 Fulvio Scarano
 Christian J. Kähler
 Steven T. Wereley
 Jürgen Kompenhans

Contents

1	Introduction	1
1.1	Historical Background	1
1.2	Principles of Measuring Velocities	6
1.3	Principle of Particle Image Velocimetry (PIV)	8
1.4	Development of PIV During the Last Decades	15
1.4.1	Early Development of PIV	15
1.4.2	PIV Today	16
1.4.3	Major Technological Milestones of PIV	17
1.4.4	PIV for Fundamental Research in Turbulent Flows	20
1.4.5	PIV for Industrial Research in Large Test Facilities	26
	References	29
2	Physical and Technical Background	33
2.1	Tracer Particles	33
2.1.1	Fluid Mechanical Properties	33
2.1.2	Neutrally Buoyant Particles	37
2.1.3	Effect of Centrifugal Forces	38
2.1.4	Brownian Motion	40
2.1.5	Light Scattering Behavior	42
2.1.6	Effective Size of Polydisperse Particles	46
2.2	Particle Generation and Supply	49
2.2.1	Seeding of Liquids	49
2.2.2	Seeding of Gases	51
2.2.3	Seeding Distribution in Wind Tunnels	59
2.3	Light Sources	60
2.3.1	Lasers	60
2.3.2	Features and Components of PIV Lasers	66

2.3.3	Light Emitting Diodes	73
2.3.4	White Light Sources	77
2.4	Light Delivery	77
2.4.1	Light Sheet Optics	77
2.4.2	Fiber Based Illumination	80
2.4.3	Illumination of Small Volumes	81
2.4.4	Illumination of Large Volumes	83
2.5	Imaging of Small Particles	84
2.5.1	Diffraction Limited Imaging	84
2.5.2	Lens Aberrations	88
2.5.3	Perspective Projection	91
2.5.4	Basics of Microscopic Imaging	93
2.5.5	In-Plane Spatial Resolution of Microscopic Imaging	95
2.5.6	Microscopes Typically Used in Micro-PIV	96
2.5.7	Confocal Microscopic Imaging	99
2.6	Sensor Technology for Digital Image Recording	99
2.6.1	Characteristics of CCD Sensors	100
2.6.2	Characteristics of CMOS Sensors	101
2.6.3	Sources of Noise	104
2.6.4	Spectral Characteristics	105
2.6.5	Linearity and Dynamic Range	106
	References	107
3	Recording Techniques for PIV	113
3.1	Digital Cameras for PIV	115
3.1.1	Full-Frame CCD	116
3.1.2	Frame Transfer CCD	118
3.1.3	Interline Transfer CCD	119
3.1.4	CMOS Imaging Sensors	121
3.1.5	High-Speed Cameras	123
3.2	Single Frame/Multi-exposure Recording	125
3.2.1	Image Shifting	125
	References	126
4	Mathematical Background of Statistical PIV Evaluation	129
4.1	Particle Image Locations	129
4.2	Image Intensity Field	131
4.3	Mean Value, Auto-correlation and Variance of a Single Exposure Recording	133
4.4	Cross-Correlation of a Pair of Two Singly Exposed Recordings	136

- 4.5 Correlation of a Doubly Exposed Recording 138
- 4.6 Expected Value of Displacement Correlation 141
- References 143
- 5 Image Evaluation Methods for PIV 145**
 - 5.1 Correlation and Fourier Transform 146
 - 5.1.1 Correlation 146
 - 5.1.2 Optical Fourier Transform 147
 - 5.1.3 Digital Fourier Transform 149
 - 5.2 Overview of PIV Evaluation Methods 149
 - 5.3 PIV Evaluation 150
 - 5.3.1 Discrete Spatial Correlation in PIV Evaluation 151
 - 5.3.2 Correlation Signal Enhancement 158
 - 5.3.3 Evaluation of Doubly Exposed PIV Images 167
 - 5.3.4 Advanced Digital Interrogation Techniques 169
 - 5.3.5 Cross-Correlation Peak Detection 182
 - 5.3.6 Interrogation Techniques for PIV Time-Series 187
 - 5.4 Particle Tracking Velocimetry 189
 - 5.4.1 Particle Image Detection and Position Estimation 190
 - 5.4.2 Particle Pairing and Displacement Estimation 192
 - 5.4.3 Spatial Resolution 192
 - 5.4.4 Performance of Particle Tracking 193
 - 5.4.5 Multi-frame Particle Tracking 196
 - References 196
- 6 PIV Uncertainty and Measurement Accuracy 203**
 - 6.1 Common PIV Measurement Error Contributions 203
 - 6.1.1 Measurement Error Due to Invalid Measurements 206
 - 6.1.2 Relative Uncertainty, Dynamic Velocity Range
and Dynamic Spatial Range 208
 - 6.1.3 Measurement Error 209
 - 6.1.4 Error Propagation 211
 - 6.2 PIV Measurement Error Estimation 214
 - 6.2.1 Synthetic Particle Image Generation 216
 - 6.2.2 Optimization of Particle Image Diameter 218
 - 6.2.3 Peak Locking 219
 - 6.2.4 Optimization of Particle Image Density 224
 - 6.2.5 Effect of Background Noise 225
 - 6.2.6 Effect of Particle Image Shift 227
 - 6.2.7 Effect of Out-of-Plane Motion 228
 - 6.2.8 Effect of Displacement Gradients 229
 - 6.2.9 Effect of Streamline Curvature 231

- 6.3 Optimization of PIV Uncertainty 232
- 6.4 Multi-camera Systems 235
- References 238
- 7 Post-processing of PIV Data 243**
 - 7.1 Data Validation 244
 - 7.1.1 Vector Difference Test 249
 - 7.1.2 Median Test 249
 - 7.1.3 Normalized Median Test 249
 - 7.1.4 Z-Score Test 251
 - 7.1.5 Global Histogram Operator 251
 - 7.1.6 Other Validation Filters 253
 - 7.1.7 Implementation of Data Validation Algorithms 255
 - 7.2 Replacement Schemes 256
 - 7.3 Data Assimilation Techniques 256
 - 7.3.1 Error Minimization 257
 - 7.3.2 Enhancing Temporal Resolution 257
 - 7.3.3 Enhancing Spatial Resolution 259
 - 7.4 Vector Field Operators 259
 - 7.5 Estimation of Differential Quantities 260
 - 7.5.1 Standard Differentiation Schemes 262
 - 7.5.2 Alternative Differentiation Schemes 265
 - 7.5.3 Uncertainties and Errors in Differential Estimation 269
 - 7.6 Estimation of Integral Quantities 271
 - 7.6.1 Path Integrals – Circulation 271
 - 7.6.2 Path Integrals – Mass Flow 272
 - 7.6.3 Area Integrals 273
 - 7.6.4 Pressure and Forces from PIV Data 275
 - 7.7 Vortex Detection 279
 - References 280
- 8 Stereoscopic PIV 285**
 - 8.1 Implementation of Stereoscopic PIV 286
 - 8.1.1 Reconstruction Geometry 287
 - 8.1.2 Stereo Viewing Calibration 290
 - 8.1.3 Camera Calibration 292
 - 8.1.4 Disparity Correction 296
 - 8.1.5 Stereo-PIV in Liquids 301
 - 8.1.6 General Recommendations for Stereo PIV 305
 - References 305
- 9 Techniques for 3D-PIV 309**
 - 9.1 Three-Component PIV Measurements in a Volume 309
 - 9.2 Tomographic PIV 312

9.2.1	General Features	312
9.2.2	3D Object Reconstruction	323
9.2.3	3D Motion Analysis	333
9.2.4	4D-PIV Analysis	335
9.2.5	Media Gallery	335
9.3	Volumetric Particle Tracking Velocimetry	335
9.3.1	Overview of PTV Measurement Techniques	336
9.4	Shake-The-Box Lagrangian Particle Tracking	341
9.4.1	Iterative Particle Reconstruction	342
9.4.2	Calibration of Optical Transfer Function	344
9.4.3	Shake-The-Box Algorithm	347
9.4.4	Shake-The-Box for multi-pulse systems: 3D Lagrangian particle tracking in high speed flows	351
9.4.5	Fitting Particle Positions Along the Trajectory	353
9.4.6	Data Assimilation for Interpolation to Cartesian Mesh	354
	References	358
10	Micro-PIV	367
10.1	Introduction	367
10.1.1	Microfluidics Background	367
10.1.2	Microfluidic Diagnostics	369
10.2	Typical Implementation of 2D Planar μ PIV	370
10.3	2D Planar Micro-PIV Development	372
10.4	Imaging of Volume-Illuminated Small Particles in μ PIV	374
10.4.1	Three-Dimensional Diffraction Pattern	374
10.4.2	Depth of Field	376
10.4.3	Depth of Correlation	377
10.4.4	Particle Visibility	381
10.5	3D Micro-PIV	384
10.5.1	Overview	384
10.5.2	Epi-Fluorescence Scanning Microscopy	386
10.6	Multi Camera Approaches	387
10.6.1	(Scanning) Stereoscopic Imaging	387
10.6.2	Tomographic Imaging	388
10.7	Single Camera Approaches	390
10.7.1	Confocal Scanning Microscopy	390
10.7.2	Techniques Based on Out-of-Focus Imaging Without Aperture	392
10.7.3	Defocused Imaging with Aperture (Three-Pinhole Technique)	393
10.7.4	Imaging Based on Aberrations (Astigmatism)	397
10.7.5	General Defocusing Particle Tracking (GDPT)	402
	References	403

- 11 Applications: Boundary Layers** 413
 - 11.1 Boundary Layer Instabilities 413
 - 11.2 Near Wall Turbulent Boundary Layer 416
 - 11.3 Boundary Layer Characterization 419
 - 11.4 Turbulent Boundary Layer Analysis by Means of Large-Scale PIV and Long-Range μ PTV 424
 - 11.5 Shock Wave/Turbulent Boundary Layer Interaction 430
 - References 434

- 12 Applications: Transonic Flows** 439
 - 12.1 Cascade Blade with Cooling Air Ejection 439
 - 12.2 Transonic Flow Above an Airfoil 442
 - 12.3 Transonic Flow Around a Fan Blade 444
 - 12.4 Stereo PIV Applied to a Transonic Turbine 449
 - 12.5 PIV Applied to a Transonic Centrifugal Compressor 454
 - 12.6 Transonic Buffeting Measurements on a 1:60 Scale Ariane 5 Launcher Using High Speed PIV 461
 - 12.7 Supersonic PIV Measurements on a Space Shuttle Model 466
 - 12.8 PIV in a High-Speed Wind Tunnel 469
 - References 474

- 13 Applications: Helicopter Aerodynamics** 477
 - 13.1 Rotor Flow Investigation 477
 - 13.2 Wind Tunnel Measurements of Rotor Blade Vortices 478
 - 13.3 Measurement of Rotor Blade Vortices in Hover 481
 - 13.3.1 The Experimental Setup 482
 - 13.3.2 Evaluation and Analysis 483
 - 13.3.3 Conclusions 487
 - 13.4 Flow Diagnostics of Dynamic Stall on a Pitching Airfoil 488
 - 13.5 Investigation of Laminar Separation Bubble on Helicopter Blades 493
 - References 497

- 14 Applications: Aeroacoustic and Pressure Measurements** 501
 - 14.1 PIV Applied to Aeroacoustics 501
 - 14.2 PIV in Trailing-Edge Noise Estimation 505
 - 14.3 A High-Speed PIV Study on Trailing-Edge Noise Sources 508
 - 14.4 Three-Dimensional Vortex and Pressure Dynamics of Revolving Wings 512
 - 14.5 PIV-Based Pressure and Load Determination in Transonic Aircraft Propellers 516
 - References 520

- 15 Applications: Flows at Different Temperatures** 523
 - 15.1 Study of Thermal Convection and Couette Flows 523
 - 15.2 Combined PIT/PIV of Air Flows Using Thermochromic
Liquid Crystals 528
 - 15.3 PIV for Characterisation of Plasma Actuators 532
 - 15.4 PIV in Reacting Flows 536
 - 15.5 Flow Field Measurements Above Wing of High-Lift Aircraft
Configuration at High Reynolds Number 541
 - References 544
- 16 Applications: Micro PIV** 547
 - 16.1 Flow in a Microchannel 547
 - 16.1.1 Analytical Solution to Channel Flow 547
 - 16.1.2 Experimental Measurements 549
 - 16.2 Flow in an Electrothermal Micro-Vortex 551
 - 16.3 Proper Orthogonal Reconstruction of 3D Micro PIV Data 555
 - 16.4 Hybrid Experimental-Numerical Technique for 3D
Reconstruction 556
 - 16.5 Particle Velocimetry Using Evanescent-Wave Illumination
for Near-Wall Flows 558
 - 16.6 Measurements of the Flow around a Growing Hydrogen
Bubble Using Long-Range μ PIV and Shadowgraphy 565
 - 16.7 In Vivo Blood Flow Measurements Using Micro-PIV 571
 - 16.8 Reconstruction of Fluid Interfaces using 3D Astigmatic
Particle Tracking Velocimetry 574
 - References 580
- 17 Applications: Stereo PIV and Multiplane Stereo PIV** 585
 - 17.1 Stereo PIV Applied to a Vortex Ring Flow 585
 - 17.2 Multiplane Stereo PIV 590
 - References 596
- 18 Applications: Volumetric Flow Measurements** 597
 - 18.1 Vorticity Dynamics of Jets with Tomographic PIV 597
 - 18.2 Near-Wall Turbulence Characterization in a Turbulent
Boundary Layer Using Shake-The-Box 600
 - 18.3 Large-Scale Volumetric Flow Measurement of a Thermal
Plume Using Lagrangian Particle Tracking
(Shake-The-Box). 606
 - 18.4 Lagrangian Particle Tracking in a Large-Scale Impinging
Jet Using Shake-The-Box 610
 - 18.5 3D Lagrangian Particle Tracking of a High-Subsonic
Jet Using Four-Pulse Shake-The-Box 616

- 18.6 Flow over a Full-Scale Cyclist Model by Tomographic PTV . . . 623
- References 629
- 19 Related Techniques 633**
- 19.1 Deformation Measurement by Digital Image Correlation (DIC) 634
 - 19.1.1 Deformation Measurement in a High-Pressure Facility 635
- 19.2 Background-Oriented Schlieren Technique (BOS) 638
 - 19.2.1 Introduction 638
 - 19.2.2 Principle of the BOS Technique 638
 - 19.2.3 Application of the BOS to Compressible Vortices 641
 - 19.2.4 Conclusions 647
- References 648
- Appendix A: Suggested Text Books 651**
- Appendix B: Mathematical Appendix 655**
- Appendix C: List of Symbols and Acronyms 657**
- Index 665**

Chapter 1

Introduction

1.1 Historical Background

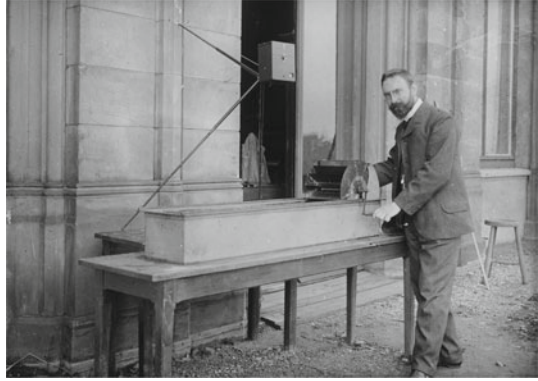
Human beings are extremely interested in the observation of nature, as this was and still is of utmost importance for their survival. Human senses are especially well adapted to recognize moving objects as in many cases they promise food, sometimes they mean eventual danger. One can easily imagine how the observation of moving objects has stimulated first simple experiments with set-ups and tools easily available in nature. Today the same primitive behavior becomes obvious, when small children throw little pieces of wood down from a bridge in a river and observe them floating downstream. Even this simple experimental arrangement allows them to make a rough estimate of the velocity of the running water and to detect structures in the flow such as swirls, wakes behind obstacles in the river, water shoots, etc.

However, with such experimental tools only *qualitative* statements can be made. The first necessary step beyond pure *qualitative visualization* was the ability to be able *to record* the observed flow patterns. For example, it is reported that prehistoric people, such as the JOMON people, used structures resembling KÁRMÁN vortices to decorate their pottery already more than 4500 years ago [DC1.2]. 500 years ago LEONARDO DA VINCI, being an artist with excellent skills and an educated observer of nature at the same time, created very detailed drawings of vortices within a water flow by careful observation. Thus, he could share his perception of the flow structures with others [DC1.3].

The major breakthrough at *qualitative flow visualization* was made in the late 19th century, early 20th century, when it became possible to store still pictures or even movies of flows by means of *photographic recording techniques*. Now results of flow visualization could easily be exchanged and discussed in the scientific community. For instance LUDWIG MACH used smoke (consisting of tiny particles not being possible to be resolved by the human eye) to visualize streamlines [32]. Noteworthy are the efforts of both ÉTIENNE- JULES MAREY and FRIEDRICH AHLBORN visualizing

An overview of the Digital Content to this chapter can be found at [DC1.1].

Fig. 1.1 LUDWIG PRANDTL in front of his water channel for flow visualization in 1904 [47]



turbulence in air and water using specifically designed flumes and wind tunnels along with photography [6, 33, 34, 37] (comprehensive reviews are given in [21–23]). In particular AHLBORN describes both surface flow visualization using particles on the water surface, such as aluminum powder or lycopodium seeds, as well as sub-surface visualization using particles in a water tunnel with illumination through a narrow slit window, effectively making use of a light sheet illumination ([5], see Sect. 2.4.1). The application of flash illumination, triggered on events appearing in the flow, if necessary, allowed investigating fast and transient flow phenomena. Thus, *qualitative flow visualization* became an important tool to explore flow phenomena of fundamental as well as of industrial interest.

A well known promoter and user of such visualization methods was LUDWIG PRANDTL, one of the most prominent representatives of fluid mechanics in the first half of the 19th century, who designed and utilized flow visualization techniques in a water channel to study aspects of unsteady separated flows behind wings and other objects closely following visualization procedures originally developed by AHLBORN [5].

Figure 1.1 shows PRANDTL in 1904 in front of his water channel, driving the flow manually by rotating a paddle wheel [47]. The tunnel comprises an upper and lower section separated by a horizontal wall. The water recirculates from the upper open channel, where the flow may be observed, back through the lower closed duct. Two-dimensional models such as cylinders, prisms and wings can be easily mounted vertically in the upper channel, thereby extending above the level of the water surface. The box camera above the channel most likely was used to acquire single frame time-lapse photographs already at the turn of the past century. For details about the experimental set-up see [DC1.4].

The flow is visualized by distributing a suspension of micaceous iron ore (“Eisenglimmer”) particles on the surface of the water, accentuating e.g. vortices by the glossy appearance of lamellae locally oriented in the same direction. PRANDTL studied the structures of the flow in steady as well as unsteady flow (at the onset of flow) with this arrangement [38].

Fig. 1.2 Separated flow behind wing profile, visualized with modern equipment in a replica of LUDWIG PRANDTL's water channel. The image shows the superposition of two sequentially acquired images in order to resemble a photographic recording of 1904

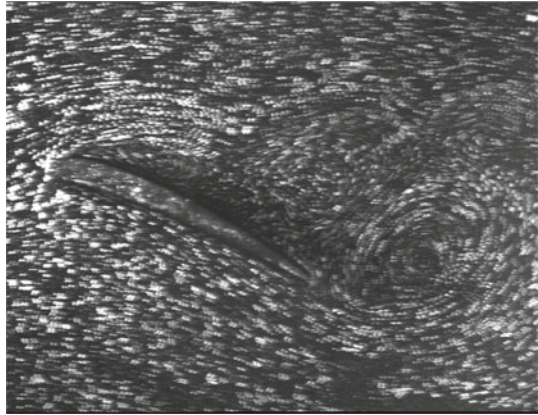
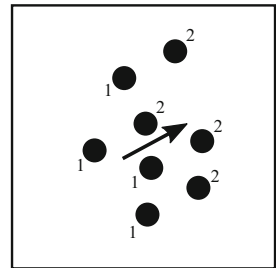


Fig. 1.3 Position of tracers at two different instants of time, t_1 and t_2 , with time of illumination of tracers shorter than time interval between t_1 and t_2 , *particle images*



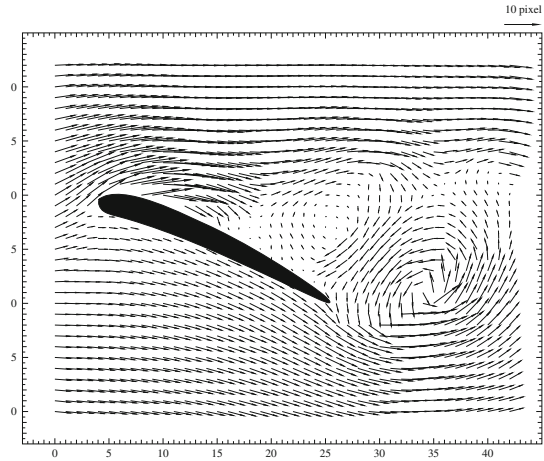
Being able to change a number of parameters of the experiment (model, angle of incidence, flow velocity,...) PRANDTL gained insight into many basic features of unsteady flow phenomena. However, at that time only photographic recording of the flow field made visible by the tracers was possible. No quantitative data about such unsteady flow phenomena could be obtained at that time.

Today, a century after PRANDTL's experiments, it is easily possible also to extract quantitative information about the instantaneous flow velocity field exactly from the same kind of images as were available to PRANDTL in 1904. This is illustrated in Fig. 1.2. A replica of PRANDTL's water channel together with a flash lamp for illumination and a video camera have been employed to obtain visualization of the flow by means of aluminum particles distributed uniformly on the water surface. As in PRANDTL's original photographs the tracer particles are clearly detectable.

In this experiment the surface of the fluid was illuminated *twice* within a short time interval by the flash lamp placed above the water surface, to capture the location of each tracer particle at each of the two illuminations. Now, simply said, it is possible to determine the local flow velocity from the local displacement of the tracer particles and the time interval between the two illuminations. The sketch shown in Fig. 1.3 exemplifies this principle.

Automatic evaluation of this recording by sophisticated methods, which will be described later in Chap. 5, results in a vector map of the instantaneous velocity field

Fig. 1.4 Vector map of instantaneous velocity field corresponding to Fig. 1.2



shown in Fig. 1.4. This illustrates, that the basic principles underlying the *quantitative* visualization technique *Particle Image Velocimetry* (PIV) have already been known for a long time. It should be noted, that the important feature common to both, PRANDTL's experiments and the PIV technique, is, that clearly distinguishable tracer particles have been used for visualization and not unstructured tracer material such as smoke. While in PIV the motion of an ensemble of tracer particles is evaluated to determine the local velocity vector, the possibility to detect individual particles and to track them over a known time interval is possible as well. This approach is called Particle Tracking Velocimetry (PTV) or Lagrangian Particle Tracking (LPT), offering further information about the flow field but velocity.

Even more, probably some of the oldest *time-resolved* image sequences, which today can be quantitatively evaluated using PIV methods were acquired by PRANDTL and his colleagues O. TIETJENS and W. MÜLLER using flow visualization methods as described in [61]. By the late 1920s PRANDTL and his colleagues began recording visualizations of unsteady free surface flows created inside different water channels. The visualization was achieved by means of small particles (aluminum powder, ferrous mica or lycopodium powder) scattered on the surface following a method originally developed by Ahlborn in HAMBURG [5], created inside facilities such as the flume shown in Fig. 1.1.

Mainly intended for instructional purposes to illustrate the process of flow separation, the films were recorded with a film camera at 20 frames per second either in a laboratory-stationary frame or while moving with a surface-piercing object like an airfoil or cylinder. Contrary to the frequently used time integrated single recordings which resulted in *particle streak images* (see e.g. [6, 38] and Fig. 1.5), the time resolved recordings of small tracers allowed for instance the clear observation of upstream flow inside separation bubbles, a subject of considerable dispute at the time as manifested by a lengthy discussion between PRANDTL, AHLBORN and other

Fig. 1.5 Position of tracers during time interval from t_1 to t_2 with continuous illumination/recording, *particle streak images*

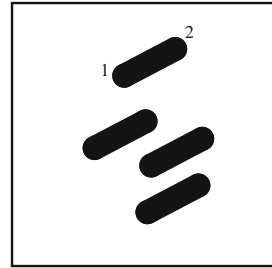
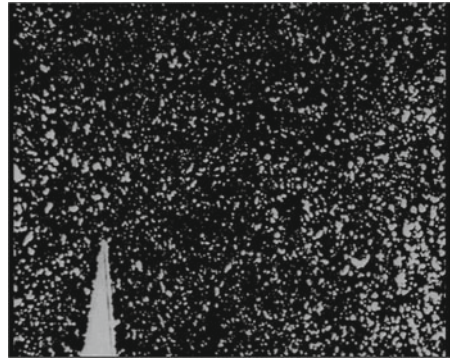


Fig. 1.6 Snap shot of flow field, as captured by PRANDTL with tracer particles behind a wedge [41]



scientists following a presentation by AHLBORN [7] at the 1927 congress of the Wissenschaftliche Gesellschaft für Luftfahrt (WGL) in Wiesbaden, Germany.

In 2009 the original visualization films of PRANDTL and his co-workers, which had been acquired in the period from 1927 to 1933 [39, 40], were made available in the form of a Digital Video Disk (DVD) [41] by the Institut für wissenschaftlichen Film (IWF, Institute for Scientific Film) in Göttingen. Today, the movies are available online at the Technische Informationsbibliothek (TIB) Hannover, for links see [39, 49]. A single exemplary frame of the acquired movies is provided in Fig. 1.6 showing a snap shot of the flow field behind a wedge at sudden on-set of flow. Remarkable about these images is the very homogeneous particle distribution and the practical absence of particle image streaking, that would make it difficult to discern the nature of the flow from a single image. In effect, the images exhibit the recommended particle image density and distribution for PIV – a subject that will be addressed in further detail in Chap. 5.

Given the time series of surface flow visualization (see Fig. 1.7) it is a simple and elucidating exercise to use today's computer based PIV algorithms to extract the displacement and corresponding velocity and vorticity fields. Exemplary results are provided in Fig. 1.8, showing the main and secondary vortices behind a wedge at sudden on-set of flow. The digitized images have a spatial resolution of 720×576 pixel (PAL video format) and could be reliably sampled at a resolution of 16×16 pixel yielding 45×36 discrete vectors. Movies of the vorticity fields very nicely illustrate

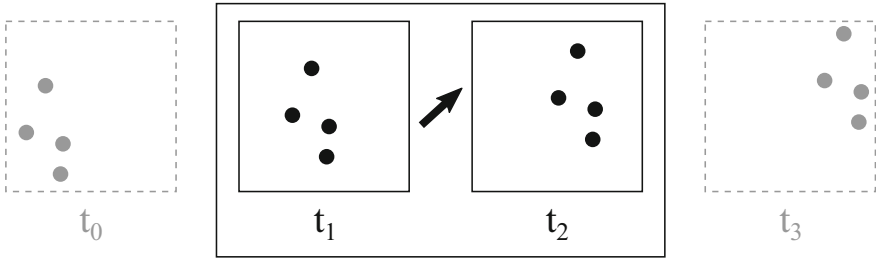
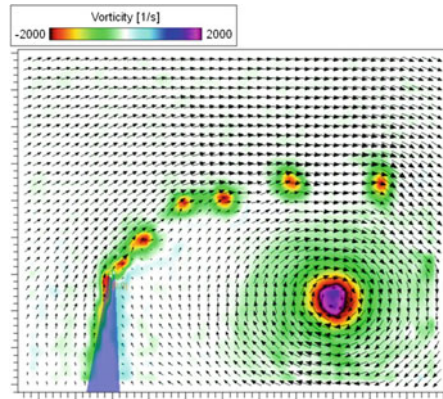


Fig. 1.7 Position of tracers at two different frames at two consecutive instants of time, t_1 and t_2 , taken out of a sequence of continuously recorded images

Fig. 1.8 Snap shot of velocity and vorticity field behind a wedge at sudden on-set of flow corresponding to Fig. 1.6



unsteady shedding, vortex formation and transition effects. Additional information about PRANDTL's qualitative visualization of unsteady flows around objects, such as spheres, wings, wedges etc. can be found at [DC1.5], a compilation of short sequences of such movies, evaluated with today's PIV evaluation methods, is available at [68].

These examples underline, that the scientific and technical progress achieved in the recent decades in lasers, digital imaging and computer techniques was prerequisite to further develop methods for *qualitative* flow visualization to such a stage that they can be employed for *quantitative* measurement of complex instantaneous velocity fields.

1.2 Principles of Measuring Velocities

In order to determine the velocity of an object, *distance* and *time* need to be measured, either the distance traveled during a given time or the time needed to travel a given

distance. To determine the velocity of a flow is not that easy, as gases as well as pure liquids do not contain moving objects that reveal the velocity of the fluid.

Thus, many measurement techniques have been developed, determining the flow velocity indirectly by measuring other quantities as velocity, such as:

- pressure (pressure probes),
- rotational speed (wind anemometer),
- heat transfer (hot film, hot wire).

In these cases the velocity of the flow is finally derived through well-established relations of physics.

The advantage of the indirect measurement techniques is that they are easy to use and cheap. Their disadvantage is that they may disturb the flow or fluid properties, leading to measurement errors, and that they deliver results only at a single location. In order to obtain information about the velocity *field*, the probe needs to be traversed through the flow field. As the process of traversing requires some time, only averaged data can be obtained. Therefore, the structure of an unsteady flow field (snapshot) cannot be obtained by such methods.

In order to overcome such difficulties optical measurement techniques have been developed, which allow placing their sensors outside of the flow and to capture images of the whole flow field of interest. In general, these techniques are quite complex and the costs for the needed equipment are high. Those optical measurement techniques, which have found wider use, need *tracer particles* that follow the flow motion faithfully without disturbing the flow or the fluid properties. By measuring their position in time, the velocity of the flow can be measured indirectly.

The most important optical measurement techniques for flow velocity exploit:

- the *Doppler effect*, relating the speed of the moving tracer particles to the frequency shift of the light scattered from the tracer particles (Laser Doppler Velocimeter (LDV), point-wise measurement, and Doppler Global Velocimeter (DGV), planar measurement),
- the *travelling time* of tracer particles between two light barriers (Laser Two Focus (L2F), point-wise measurement),
- the *displacement* of tracer particles between two instants of time (Particle Image Velocimetry (PIV), focusing on ensembles of tracer particles, and Particle Tracking Velocimetry (PTV), focusing on single tracer particles, planar and volumetric measurement).

For a detailed discussion of the properties of flow measurement techniques in general the reader is referred to works such as the *Springer Handbook of Experimental Fluid Mechanics* [62].

1.3 Principle of Particle Image Velocimetry (PIV)

In the following, the basic features of the Particle Image Velocimetry (PIV) measurement technique will be described briefly.^{1,2}

The experimental set-up of a PIV system typically consists of several subsystems.

- **Seeding:** In most applications tracer particles have to be added to the flow.
- **Illumination:** These tracer particles have to be illuminated in a plane or volume of the flow at least twice within a short and known time interval.
- **Recording:** The light scattered by the tracer particles has to be recorded either on two separate frames or on a sequence of frames of a camera.
- **Calibration:** In order to determine the relation between the particle image displacement in the image plane and the tracer particle displacement in the flow, a calibration is required.
- **Evaluation:** The displacement of the particle images between the light pulses has to be determined through evaluation of the PIV recordings.
- **Post-Processing:** In order to detect and remove invalid measurements and to extract complex flow quantities of interest, sophisticated post-processing is required.

Figure 1.9 briefly sketches a typical set-up for PIV recording of *two velocity components* within the flow field in a *plane* in a wind tunnel (2C-2D PIV). Small

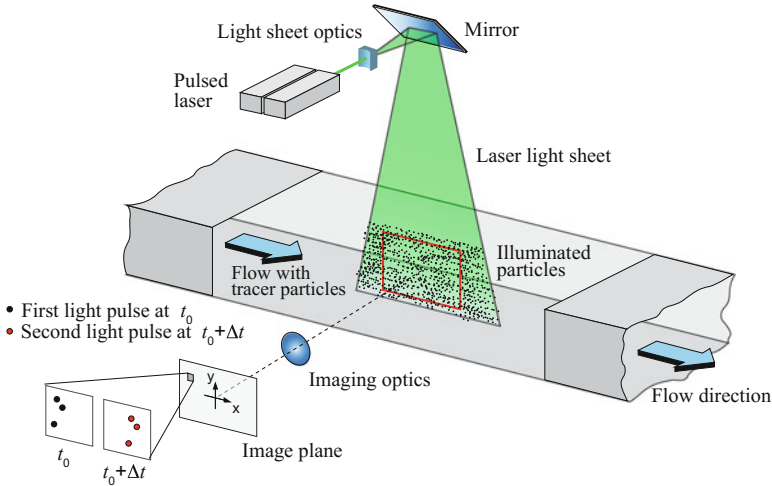


Fig. 1.9 Experimental arrangement for planar 2C-2D PIV in a wind tunnel

¹In earlier years other names such as *laser speckle velocimetry*, *particle image displacement velocimetry* etc. have been used as well.

²*Particle Tracking Velocimetry (PTV)* focuses on single tracer particles (instead of ensembles of tracer particles) and thus requires different evaluation methods as PIV. However, most considerations for the experimental set-up are similar to those for the PIV technique.

tracer particles are added to the flow at a location where the flow of interest will not be disturbed. The plane of interest within the flow is illuminated twice by means of a *laser light sheet*. The *time delay* between pulses must be chosen with respect to the flow *velocity* and the *magnification* at imaging. For simplicity it is assumed that the tracer particles move with local flow velocity between the two illuminations. The light scattered by the tracer particles is recorded *via a high quality lens* on two separate frames of a dedicated *cross-correlation digital camera*. The output of the digital sensor is transferred to the memory of a computer.

For *evaluation* the digital PIV recording is divided in small subareas called “interrogation areas”. The local displacement vector for the images of the tracer particles of the first and second illumination is determined for each interrogation area by means of statistical methods (*cross-correlation*). The projection of the vector of the local flow velocity into the plane of the light sheet (two-component velocity vector) is computed taking into account the time delay between the two illuminations and the *calibration* of the imaging system.

The evaluation is repeated for all interrogation areas of the PIV recording. With modern digital cameras (several thousand sensor elements per line and more) it is possible to capture more than 100 PIV recordings per minute. High-speed recording with dedicated sensors even allows for acquisition in the kHz-range. The time required for evaluation of one digital PIV recording with several thousand instantaneous velocity vectors (depending on the size of the recording, the interrogation area and processing algorithm) is of the order of a second with standard computers. If data is required at even faster rates for online monitoring of the flow, dedicated software algorithms which perform evaluations of reduced precision within fractions of a second are commercially available.

In principle, more complex PIV set-ups such as stereo PIV (which just requires adding a second camera, viewing at a different angle), volumetric PIV, high-speed PIV, or set-ups, no longer in use such as photographic recording, make and made use of similar arrangements of the illumination, imaging, and recording equipment.

In order to facilitate the understanding of certain technical solutions described later on, some general aspects of the PIV technique will be briefly discussed next. In particular, this concerns aspects, which need to be considered during the planning of the experiment, during the set-up and during the recording of the PIV images. Mistakes made during these phases of an investigation usually cannot be recovered during the later evaluation or analysis of the data.

Non-intrusive velocity measurement. In contrast to techniques for the measurement of flow velocities employing probes such as pressure tubes or hot wires, the PIV technique being an optical technique works non-intrusively. This allows the application of PIV even in high-speed flows with shocks or in laminar boundary layers close to the wall, where the flow may be disturbed by the presence of the probes.

Indirect velocity measurement. In the same way as with laser Doppler velocimetry or L2F the PIV technique measures the velocity of a fluid element indirectly by means of the measurement of the velocity of tracer particles within the flow, which – in most applications – need to be added to the flow before the experiment starts. In particle laden flows particles are already present in the flow. In such a case it will be

possible to measure the velocity of the particles themselves as well as the velocity of the fluid (to be additionally seeded with small tracer particles).

Whole field technique. PIV is a technique which allows to record images of large parts of flow fields in a variety of applications in gaseous and liquid media and to extract the velocity information out of these images. This feature is unique to the PIV technique. Aside from *Doppler Global Velocimetry* (DGV), also known as *Planar Doppler Velocimetry* [13, 35, 46, 49], which is a technique particularly appropriate for medium to high-speed air flows, and *Molecular Tagging Velocimetry* (MTV) [30] all other techniques for velocity measurements only allow the measurement of the velocity of the flow at a single point, however in most cases with a high temporal resolution. The spatial resolution of PIV is large, whereas the temporal resolution (frame rate of recording PIV images) is limited due to current technological restrictions. These features must be kept in mind, in particular when comparing results obtained by PIV with those obtained with traditional techniques. Instantaneous image capture and high spatial resolution of PIV allow the detection of spatial structures even in unsteady flow fields.

Distribution of tracer particles in the flow. At *qualitative* flow visualization certain areas of the flow are made visible by marking a stream tube in the flow with tracer particles (smoke, dye). According to the location of the seeding device the tracers will be entrained in specific areas of the flow (boundary layers, wakes behind models, etc.). The structure and the temporal evolution of these structures can be studied by means of *qualitative* flow visualization. For PIV the situation is different: a homogeneous distribution of medium density is desired for high quality PIV recordings in order to obtain optimal *quantitative* evaluation. *No structures of the flow field can be detected on a PIV recording of high quality.*

Density of tracer particle images. Qualitatively three different types of *image density* can be distinguished [2], which is illustrated in Fig. 1.10. In the case of low image density (Fig. 1.10a), the images of individual particles can be detected and images corresponding to the same particle originating from different illuminations can be identified. Low image density requires tracking methods for evaluation.

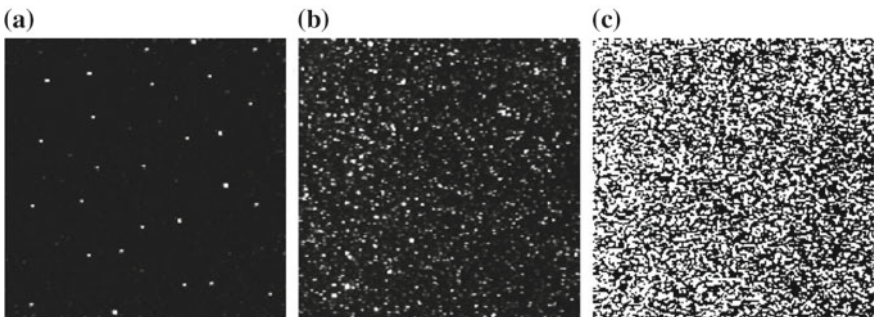


Fig. 1.10 The three modes of particle image density: **a** low (PTV), **b** medium (PIV), and **c** high image density (LSV)

Therefore, this situation is referred to as *Particle Tracking Velocimetry* (PTV). In the case of medium image density (Fig. 1.10b), the images of individual particles can be detected as well. However, it is no longer possible to identify matching images of the same tracer particle by visual inspection of the recordings unambiguously. Medium image density is required to apply the standard statistical PIV evaluation techniques. In the case of high image density (Fig. 1.10c), it is not even possible to detect individual images as they overlap in most cases and form speckles. This situation is called “*Laser Speckle Velocimetry*” (LSV), a term which has been used at the beginning of the nineteen-eighties for the medium image density case as well, as the (optical) evaluation techniques were quite similar for both situations.

Velocity lag. The need to employ tracer particles for the measurement of the flow velocity requires the user to check carefully for each experiment, whether the particles will faithfully follow the motion of the fluid elements, at least to that extent required by the objectives of the investigations and the desired accuracy. In case of macroscopic flows smaller particles will follow the flow better. In case weak and strong velocity gradients are present in the same observation field, a compromise has to be found, e.g. opting for a large observation field (requiring bigger tracer particles when utilizing the same light source) does not allow to resolve the velocity close to the area of strong velocity gradients correctly.

Illumination. For applications in gas flows a high power light source for illumination of the tiny tracer particles is required in order to well expose the video sensor by scattered light. In principle, the need to utilize larger particles because of their better light scattering efficiency is in contradiction to the demand to have as small particles as possible in order to follow the flow faithfully. In most applications a compromise has to be found. In water flows bigger particles can be utilized, which scatter more light than the particles of a diameter of $1\ \mu\text{m}$, which are usually used in air flows. Light sources of considerably lower peak power, such as shuttered continuous (CW) lasers, high power LEDs, and flash lamps can be used here. This means that experimental requirements (and costs) are more relaxed for PIV applications in water than in air. One criterion for selecting light sources for PIV is that they must allow to illuminate the observation area homogeneously, which means that the profile of the beam of a pulse laser to be expanded to the light sheet should be of Gaussian or top-hat shape as close as possible, without holes or gaps. If two light pulses are generated by different sources (laser oscillators) and fed through the same light sheet optics, it must be verified that they really illuminate exactly the same part of the observation area (or volume), as otherwise no matching pairs of images of the tracer particles will be found.

Ambient conditions. Optical set-ups need to be robust against ambient conditions such as noise, vibrations, background illumination etc. To minimize the effect of vibrations usually individual solutions have to be found. Sometimes it is reasonable to fix light sheet optics and recording camera on the same mechanical support, sometimes it is better to mount optics and camera at the wall of the test facility. While vibrating illumination optics and cameras will deteriorate the quality of the PIV recordings, the changes of the position of objects under investigation, such as wind tunnel models, due to vibrations can be adjusted during evaluation, if they are

known at time of recording. If ambient light cannot be avoided, which often will lead to undesired background illumination in the second frame of a cross correlation camera, filters tuned to the wavelength of the laser light source should be used.

Health and Safety. In particular, if pulse laser or high power LEDs are used, special attention has to be paid observing the respective laser safety regulations [DC1.6]. Health issues with regard to the seeding material need to be addressed [DC1.7]. Pollution of the laboratory or test facility by the tracer particles as required for standard PIV systems must be avoided. At minimum all national standards and legal requirements must be met. It is recommended to check international standards possibly demanding higher protection levels for comparison as well.

Duration of illumination pulse. The duration of the illumination light pulse must be short enough to “freeze” the motion of the particles during the pulse exposure in order to avoid blurring of the particle images (no streaks, compare the tracer images sketched in Fig. 1.3 with those sketched in Fig. 1.5).

Time delay between illumination pulses. The time delay between the illumination pulses must be long enough to be able to determine the displacement between the images of the tracer particles with sufficient resolution and short enough to avoid too many particles with an out-of-plane velocity component leaving the light sheet between subsequent illuminations.

Repetition rate. For standard PIV double pulse Nd:YAG lasers with two oscillators the time delay between the illumination pulses can be very short (in the order of microseconds), whereas due to restrictions of technology, the time between consecutive PIV recordings is in the order 0.05–0.1 s (10–20 Hz). Dedicated high-speed lasers allow recording frequencies of 1–100 kHz, mostly associated with loss in pulse energy, result in smaller observation areas. However, depending on the time scale of the flow phenomena, such systems may allow temporally resolved measurements.

Number of illuminations per recording. In principle one has to distinguish whether, due to the time scale of the experiment and illumination/recording technology, it will be possible to store images of the tracer particles on different frames for each illumination (see Fig. 1.7) or whether all particle images due to the different illuminations must be stored on a single frame (see Fig. 1.3). Not being able to store the images of the tracer particles on a separate frame for each illumination constituted a major problem at the early use of PIV with photo-graphic recording (*ambiguity* of sign of direction of velocity vector, particles sketched in Fig. 1.3 could have moved in opposite direction as well). This problem has been solved when cross-correlation video cameras became available. For cases, where a very short time delay between the illumination pulses is necessary (e.g. high speed flows) methods have been developed using two cameras, each triggering on one illumination pulse, or (in air) using differently polarized light for each illumination of the tracer particles and cameras with matching polarization filters to distinguish between the two illuminations.

Averaging. In particular when comparing with the results obtained with other measurement techniques, with the results of numerical calculations, or if statistical quantities are looked for, time averaged data are of interest even for unsteady flow fields. The number of PIV recordings required to obtain converged averaged data needs to be found as compromise between the time needed to take the recordings

(which is quite short with PIV) and the time during which the external conditions of the experiment can be kept constant.

Optimizing PIV recordings for evaluation. Besides the parameters mentioned above other parameters such as size of particle images (required for optimal working of evaluation algorithms), size of interrogation area, number of particle images within the interrogation area (required to obtain the desired accuracy), and the number of interrogation areas within the PIV recording (determining the number of velocity vectors achievable) etc. need to be optimized for each experiment prior to the final recording of PIV images. These parameters and, in addition, the fact, whether the lens of the camera is well focused on the tracer particles within the illuminated observation area have to be checked as *on-line monitoring* of the raw data during the measurement.

Objects within the flow. Glare may be present in the vicinity of objects within the flow, such as wind tunnel models, due to reflections of the light hitting the surface of the model. CCD sensors will be over-exposed and no images of tracer particles can be detected within this region. The experimental set-up needs to be optimized e.g. by changing the angle of the incident light or by covering the model surface with special fluorescent paint and blocking the fluorescent light with narrow-bandwidth interference filters tuned to the frequency of the illuminating laser light. Such filters can also be used, if it is not possible to suppress ambient light or if the flow field within flames shall be investigated.

Triggering. Many light sources used for PIV, such as standard double pulse Nd:YAG lasers operate with a given repetition rate. Triggering such lasers, including their flash lamps and Pockels cells (see Sect. 2.3.2), and the recording cameras relative to external (random or repetitive) events is possible employing appropriate hard- and software. Solutions found are usually application dependent (for examples see Chaps. 11 to 18 on applications).

Number of components of the velocity vector. With planar illumination of the flow field and just a single camera, as sketched in Fig. 1.9 only two (in-plane) components of the velocity vector can be determined in standard two-component PIV (2C PIV). The today mostly used technique to extract the third component of the velocity vector is to add a second camera for observation of the light sheet in stereo configuration (see Sect. 8.1). Less used are techniques such as dual-plane PIV and holographic recording [19, 20], which itself is three-dimensional. These techniques would be labeled 3C PIV. All methods mentioned above work in planar domains of the flow field (2D PIV).

Extension of the observation volume. Chapter 9 will explain the tomographic PIV, 3D-PTV and Shake-The-Box techniques, which can be used to access the volume of the flow. In case of snapshots of the flow velocity field in the volume, one would label these techniques 3C-3D PIV, in case of temporally resolved flow fields they would be labeled *time-resolved* 3C-3D PIV. These 3D methods, which have been developed in the past few years, have proven to be superior to those techniques having been in use already for a number of years, such as holographic techniques [48]. Other methods, such as establishing several parallel light sheets in a volume [18] or scanning a volume in a temporal sequence [9, 10] would be referred to as 2.5D PIV.

Temporal resolution. Standard PIV systems allow to record with high spatial resolution, but at relative low repetition rates. However, the recent development of dedicated high-speed lasers and high-speed cameras allows time resolved measurements of most liquid and low-speed aerodynamic flows. The term *time-resolved PIV* should only be used, if the relevant features of the flow field are temporally well resolved. Otherwise the term *high-speed PIV* should be used.

Spatial resolution. The size of the interrogation areas during evaluation must be small enough for the velocity gradients inside the flow area interrogated not to have significant influence on the results. Furthermore, for a given sensor size it determines the number of independent velocity vectors and therefore the maximum spatial resolution of the velocity map, which can be obtained at a given spatial resolution of the sensor employed for recording. But also the bandwidth of scales that can be resolved depend critically on the spatial resolution and the size of the field of view (FOV). Besides buying sensors with a higher number of pixel, a higher bandwidth can also be achieved by using several cameras adjacent to each other for observation. Sometimes it is also advisable to combine cameras with different magnification, allowing a higher flexibility while obtaining an overview and focusing on details of the flow field at the same time.

Temporal versus spatial resolution. Usually a compromise between spatial and temporal resolution has to be found, depending on the objectives of the respective investigation and the available technology. It should be kept in mind, that the technical limitations, which determine such a compromise, will change over time due to the fast technical progress being made with the development of light sources and cameras.

Evaluation methods. Simply said, the *PIV technique* works with ensembles of images of the tracer particles and statistical (correlation methods) for evaluation, whereas the *PTV technique* works with single, identifiable images of tracer particles and tracking methods for evaluation. The PIV technique delivers the results on a regular grid, whereas PTV delivers the results on an irregular grid. During the early development phase both methods have been used. Later, due to the robustness of the correlation methods, the fast evaluation offered by them, and the customer friendly availability of the results on a regular grid, the PIV method became the most widely used technique. Recently things seem to change, as powerful lasers, sensitive cameras and increasing computer power, highly accurate calibration methods, and new evaluation algorithms lead to high quality particle images that can be reliably and accurately tracked. Consequently, PTV is becoming more popular as it has a number of advantages compared to PIV.

Upgrade of PIV system. Due to the modularity of the components of PIV systems, it is possible to start research using PIV with a simple 2C-2D system and to expand it in different steps to a full 3C-3D system, depending on the particular requirements, available budget and experience with PIV. Some considerations related to the foresighted planning of the possible future use and upgrade of a PIV system with increasing complexity of requirements are given at [DC1.8].

Repeatability of evaluation. In PIV the full information about the flow velocity field (except the time delay between pulses and magnification (calibration) at imaging) is stored at time of recording before any data reduction has been

performed. This allows to reduce the time needed for the PIV measurement (which necessarily will require the expensive PIV equipment and the possibly expensive test facilities) to a minimum. The more time consuming evaluation and post-processing of the PIV recordings can be performed separately later on in the laboratory with dedicated computer systems. Moreover, this unique feature of the PIV technique results in the interesting possibility that PIV recordings can easily be exchanged for evaluation and post-processing with others employing different techniques. Any information about the flow velocity field, already completely contained in the PIV recording, can be exploited later on with different methods in quite a different way from that for which it had originally been planned without the need to repeat the experiment. The evaluation of PRANDTL's movies as described in Sect. 1.1 may serve as striking example.

In this section many aspects of the PIV technique have been described briefly to support a general understanding of its features and how to consider them during the experiment. Most of these aspects, in particular those related to evaluation and post-processing, will be discussed in detail later in this book. However, already from what has been said, it becomes quite obvious that PIV is a fascinating technique offering new insights in fluid mechanics, especially in unsteady flows, as it allows for capturing the whole velocity fields instantaneously, even in a volume. In combination with other measurement techniques for pressure, temperature or deformation a detailed analysis of complex unsteady flows is possible nowadays for fundamental and applied flow research, but also for comparison with the results of high fidelity numerical calculations and their validation.

1.4 Development of PIV During the Last Decades

1.4.1 *Early Development of PIV*

The development of particle image velocimetry during the past 30 years is characterized by the fact that analog recording and evaluation techniques have been replaced by digital techniques. Though these analog methods have widely contributed to the success of the PIV technique in its initial stage of development, these techniques will only be discussed as far as they support the understanding of the present state of the art of PIV.

A number of sources describing the basic principles of PIV in the context of its historical development are readily available. Thus, for further information the reader is referred to the SPIE Milestone Series 99, edited by IAN GRANT in 1994 [14]. This volume comprises more than 70 original papers, first published between 1932 and 1993. The majority of them originate from the eighties, including contributions describing the roots of modern PIV, such as laser speckle velocimetry, initiated by the pioneering work of T.D. DUDDERAR and P.G. SIMPKINS [12], R. GROUSSON and S. MALLICK [16], and D.B. BARKER and M.E. FOURNEY [8], the early work

of ROLAND MEYNART [36], the development of low and high image density PIV, optical correlation techniques, etc. Review articles by WERNER LAUTERBORN and Alfred VOGEL (1984) [31] and by RONALD J. ADRIAN (1986, 1991) [1, 2], some of which are also reprinted in the Milestone Series on PIV [14], demonstrate the fast development and compilation of know-how about PIV within a decade.

PIV seen from the side of optics is described in the chapter “Particle Image Velocimetry” written by KLAUS HINSCH in 1993 [17], included in a book on “Speckle metrology” [55]. This contribution is especially useful for the understanding of the optical aspects of PIV. It includes 104 references to other literature on PIV.

At that time a strong competition with respect to the better performance of optical and digital methods in the evaluation of PIV recordings took place. Details of the theoretical fundamentals of digital particle velocimetry can be found in the Ph.D. thesis *Digital particle image velocimetry – Theory and practice* published also in 1993 by JERRY WESTERWEEL [64]. This book includes more than 100 references.

A review paper “Particle image velocimetry: a review” by Grant appeared in 1997 [15] and gives a summary of different implementations of PIV illumination, recording and evaluation techniques at that time. Many of those are not covered in this book. The paper includes 188 references.

As indicated, all four publications mentioned previously include a detailed bibliography of the literature on PIV, which the reader should refer to if further details are required on special aspects of PIV exceeding the framework of this book. Furthermore, a bibliography on PIV with nearly 1200 references dating from 1917 till 1995 was compiled by ADRIAN [3].

Another comprehensive source of information on PIV development and early applications is provided through the VON KARMAN INSTITUTE which has offered a number of lecture series and associated monographs dedicated to PIV since 1991 [11, 43–45, 51].

The large number of references listed in the early review articles demonstrate the successful development of the Particle Image Velocimetry technique, which gave rise to the fact that PIV is nowadays a well accepted tool for the investigation of velocity fields in many different areas.

“Historical” content of the first (1998) and second (2007) edition of this book, mostly related to analog recording and evaluation techniques and thus no longer contained in this third edition, can be found at the Historical Background section of the DC at pivbook.org/digital-content/historical-background/index.html.

1.4.2 PIV Today

After initial impetus from the side of optical research the development of PIV has been primarily driven by the demands of fluid mechanics and aerodynamics for the investigation of air and water flows. The progress made has brought PIV to a state that it is now routinely applied in aerodynamic research and related fields. However, new

areas of application outside of fluid mechanics and aerodynamics are continuously reported.

This means that a number of special implementations of the PIV technique had to be developed for such different applications as, for example, in biology or turbomachinery. The dissemination of the PIV technique to the most different applications can be illustrated by the results achieved by the joint project work performed by a large partnership from universities, research organizations, small enterprises and industry made possible with funding from the European Commission [54, 56, 60].

PIV being used in many different areas nowadays, results of current research activities employing PIV are widely spread in a large number of international journals, which cannot be listed here. Journals, in particular those providing a platform to communicate new developments of PIV and innovative applications, are, amongst others, the journals of *Experiments in Fluids*, link.springer.com/journal/348 and *Measurement Science and Technology*, iopscience.iop.org/journal/0957-0233.

Similar as for journals also for international conferences, just a few of those shall be listed, where a significant number of new developments and applications of the PIV technique are presented, such as the *Lisbon International Symposium*, lisbonsimposia.org (including access to the proceedings of previous symposia), the *International Symposium on Particle Image Velocimetry*, www.ispiv2017.org and the *International Symposium on Flow Visualization*, www.ethz.ch/isfv18.

The *International PIV Challenge*, <http://pivchallenge.org> presents links to the results of several international comparisons of PIV evaluation methods as well as the provided test images, which can be downloaded for own further analysis [26, 57–59].

Finally, reference shall be made to the book *Particle Image Velocimetry* [4] by RONALD. J. ADRIAN and JERRY WESTERWEEL, which provides a comprehensive and consolidated overview over the concept of PIV. In particular the theoretical aspects of the fundamental principles of PIV are treated in-depth – to a much larger extent than is possible in this book focusing on the practical aspects of application of PIV.

Nevertheless, even today a nearly complete and nearly stable picture of the general technical aspects of PIV can best be given if looking at the demands of applications in fluid mechanics or aerodynamics. Most of the technical problems in the application of PIV encountered in these special fields appear in other PIV applications as well. Many of the basic considerations can easily be transferred to other applications.

1.4.3 Major Technological Milestones of PIV

Earlier in this section some references to papers describing the general historical development of PIV have been given. In a practical guide more devoted to the technical aspects of PIV it might be of even greater interest to outline the development of PIV towards its applicability in complex flows in terms of the achievement of major technical milestones.

The understanding of some of the technical restrictions in the application of PIV in the past and their conquest may be useful for new users of the PIV technique, in order to assess the discussion in some older publications sometimes dealing with – nowadays – “strange” looking efforts to solve technical problems which no longer exist today.

The selection of these milestones was done according to the technical progress in the past as experienced by the authors in their own work. Thus, the choice is a subjective one.

Feasibility of modern PIV. The feasibility of employing the particle image velocimetry technique for the measurement of flow velocity fields in water and even in air was demonstrated in the early eighties at the VON KARMAN INSTITUTE in Brussels, mainly by MEYNART [11, 36]. At that time the evaluation methods were based on the developments made in the field of speckle interferometry (see references in [14]).

Reliable high power light sources for application in air. The use of double oscillator Nd:YAG lasers (two resonators; frequency doubled, to achieve a wavelength of $\lambda = 532$ nm in visible light) allowed for the first time the illumination of a plane in the flow with laser pulses of the same, constant energy at any time delay between the two pulses as required by the experiment at repetition rates of the order of 10 Hz [29]. Alignment of the light sheet optics and image acquisition was thus facilitated considerably. These lasers are (after 30 years) still the most common PIV light sources.

Ambiguity removal. Especially with photographic recording it was not possible in most cases to store the images of the tracer particles due to first and second illumination on two different recordings. Thus, without further information it was not possible to determine the temporal sequence of the images of the tracer particles and hence the sign of the displacement (velocity) vector. Methods to remove this ambiguity had to be developed (see references in [14]). The most widely used technique was image shifting. By enabling the investigation of complex, unsteady 3D flow fields, this development contributed considerably to the increasing interest in PIV. Modern cameras store the particle images of different illuminations on different frames making image shifting dispensable.

Generation and distribution of tracer particles in the flow. The development of powerful aerosol generators and the know-how to distribute tracer particles of a well defined size within the flow homogeneously improved the particle image density and the quality of the PIV recordings considerably.

Computer hardware. The improvement of computer hardware with respect to processor speed and larger memory still continues according to Moore’s law. Difficult only a decade ago, the handling and processing of numerous mega-pixel sized PIV images has become trivial on today’s personal computers. Processing of these images is possible in fractions of a second. Tomographic evaluation of volumetric multi-camera recordings can be performed on parallel CPU or GPU computers within minutes.

Improved peak detection. The impact of digital PIV was initially affected by the limited size and resolution of the digital sensors as compared to that of photographic

recording. The use of sub-pixel peak position estimation by means of the Gaussian function allowed for the determination of the displacement with drastically improved accuracy [67]. Thus, smaller interrogation windows could be utilized, leading to an increase of spatial resolution (number of vectors) in digital PIV.

Cross-correlation video camera. Today progressive CCD cameras allow users to store a pair of images of the tracer particles on separate frames for each illumination with inter-framing times of less than $1 \mu\text{s}$ [63]. This feature immediately solves the problem of ambiguity removal even for high-speed flows. Sensor sizes in excess of 25 million pixel with superior signal-to-noise ratio together with the application of cross-correlation methods yield velocity vector fields that in the past were reserved to medium format photographic film. Active cooling of the sensor furthermore reduces camera noise which increases the camera's sensitivity and dynamic range. Thus less laser power is necessary to capture a similar sized flow field.

High-speed CMOS camera. Another technical improvement for PIV applications was the development of CMOS sensors with the active pixel sensor (APS) technology in which, in addition to the photodiode, a readout amplifier is incorporated into each pixel. This converts the charge accumulated by the photodiode into a voltage which is amplified inside the pixel and then transferred in sequential rows and columns to further signal processing circuits. This, together with highly parallel readout electronics storage devices, allows for the recording and handling of up to a several thousand frames per second at acceptable noise levels. An additional advantage of most CMOS sensors is their ability to record images of high contrast without blooming.

High-repetition rate Nd:YAG and Nd:YLF lasers. The introduction of high-speed CMOS cameras has generated a need for laser light sources that can operate at correspondingly high frame rates in the kilohertz range. As a consequence thereof, diode pumped lasers were adapted to high-speed PIV. These lasers were originally developed for materials processing and as pump sources for more complex scientific lasers. Specialized, high repetition rate, double oscillator lasers, designed specifically for high speed PIV were recently introduced. Such laser systems allow very short pulse separation times, while having acceptable beam profiles and stability. This allows high frame rate PIV experiments to be designed for a wide range of air and water flow velocities.

Microscopic PIV recording. During the past 15 years, significant progress has been made in the development and application of micron-resolution Particle Image Velocimetry (μPIV). Developments of the technique have extended typical spatial resolutions of PIV from the order of 1 mm to the order of $1 \mu\text{m}$. These advances have been obtained as a result of novel improvements in instrument hardware and post-processing software. The utility of μPIV has been demonstrated by applying it to flows in microchannels, micronozzles, BioMEMS, and flow around cells. While the technique was initially developed for micro-scale velocity measurements, it has been extended to measure wall positions with tens of nanometers resolution, the deformation of hydrogels, micro-particle thermometry and infrared-PIV. In the past decade sophisticated 3D-PTV techniques have been developed that allow for a volumetric analysis even in micro systems. By using functional particles it is also possible to

measure simultaneously the 3D velocity field along with the 3D temperature field for instance.

Adaptive evaluation algorithms. Standard evaluation algorithms provide reliable velocity vectors. However, their accuracy is limited due to the loss of particle image pairs in complex flow regions. As a straight forward approach to tackle this problem, the second interrogation window can be displaced with respect to the window in the first image or different window sizes can be used in combination with a direct correlation scheme [27]. More sophisticated algorithms evaluate the image repeatedly, first with larger interrogation windows in order to find the local mean displacements, then with smaller windows and increasingly higher spatial resolution. Many PIV algorithms additionally use the displacement information of a previous pass in order to determine the actual deformation of the interrogation volume between the illuminations and deform the secondly recorded images accordingly [50].

Improved calibration algorithms. The reconstruction of 3-component and/or 3-dimensional flow fields requires prior knowledge of the mapping function between image planes and physical space. Highly accurate stereoscopic measurements, but especially tomographically evaluated multi-camera measurements or 3D-PTV recordings, require an increased precision of calibration. This can be practically achieved by a-posteriori correction of the calibration mapping function – the so called disparity correction [66] or self calibration technique [65].

Volumetric 3C-3D PIV. The adaptation of computer tomography algorithms rendered possible the analysis of multi-camera recordings from volumetric domains. This also allowed for the inclusion of the temporal domain for an effective way to avoid ghost particles that frequently hampers the analysis of 3D data by the classical evaluation schemes of computer tomography. Expanding the knowledge used for 3D particle position analysis by fluid mechanical assumptions like Kolmogorov time scales and maximum expected acceleration values – as in the Shake-The-Box scheme – is another ongoing and promising activity.

Theoretical understanding of PIV. At the beginning of the development of PIV the understanding of the technique was a more intuitive one. Progress was often made just by trial and error. In the past three decades the theoretical understanding of the basic principles of the PIV technique has been improved considerably. Such theoretical considerations as well as simulations of the recording and evaluation process give useful information on many parameters important for the layout of an experiment utilizing PIV.

The following two sections will demonstrate the application of PIV for fundamental and industrial research in an exemplary manner.

1.4.4 PIV for Fundamental Research in Turbulent Flows

This description of the application of PIV in turbulent flows will be taken to demonstrate the increase in quality of data and information obtainable through the progress achieved at the development of PIV.

Standard measurement techniques such as hot-wire or LDV allow to extract the flow velocity at a single point within the flow with adequate temporal resolution. In order to be able to extract information about the spatial organization of the flow, statistical methods based on field data collected at thousands of points simultaneously are required.

Figure 1.11 shows the evaluation of an early photographic PIV recording taken in the mid-eighties in a wind tunnel with laminar flow, but with a grid of mesh size of 25 mm and a rod size of 5 mm upstream of the observation area to generate turbulence [28]. Even without being able to apply image shifting at that time the vortical structures generated by the grid can be clearly observed.

Such results encouraged the use of PIV in wall boundary layers, where a huge amount of theoretical, analytical, numerical and experimental data was available to assess the results of investigations of flow structures in a boundary layer (see sketch in Fig. 1.12) as obtained with PIV.

Figure 1.13 shows the instantaneous flow velocity field in main flow direction of a turbulent boundary layer taken with the photographic PIV method in 1995 [24]. The particle images due to both illuminations had to be stored on the same photographic plate and auto-correlation methods had to be employed for evaluation. The observation area had a size of $110 \times 60 \text{ mm}^2$. The photographic plate had a spatial resolution of 3.600×2.400 lines. The temporal resolution was one frame per second ($f_r = 1 \text{ Hz}$). The instantaneous turbulent structures could be well resolved in the plane under observation with the equipment available at that time.

The development of digital PIV allowed recording the images of the tracer particles on two different frames for both illuminations (see Fig. 1.14). At the bottom of the picture the reflection of the light sheet at the wall can be seen. Figure 1.15 shows a superposition of both frames, thus artificially creating doublets of images of the tracer particles to demonstrate the recording situation as had been the case for the photographic PIV method.

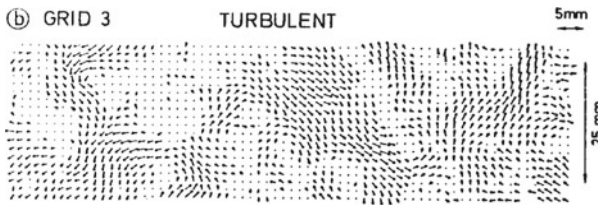
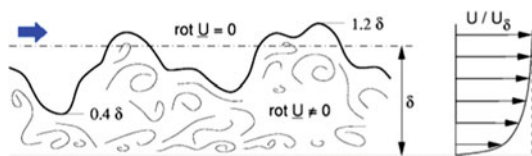


Fig. 1.11 Instantaneous turbulent flow velocity field behind grid in a wind tunnel with laminar flow, $U = 10 \text{ m/s}$, $T_{\text{turb}} = 1.1\%$

Fig. 1.12 Sketch of turbulent boundary layer structure and mean velocity profile



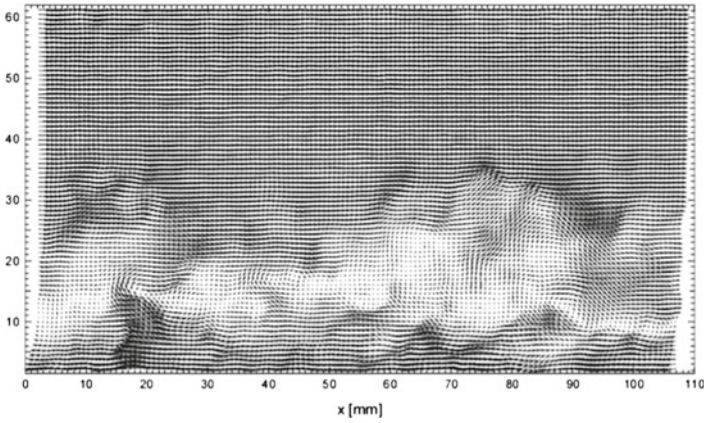


Fig. 1.13 Instantaneous flow velocity field of turbulent boundary layer, $U = 20$ m/s, the average flow velocity of the instantaneous velocity field has been subtracted (from [24])

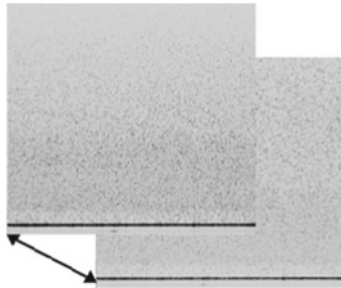


Fig. 1.14 Images of tracer particles within two frames of a PIV recording, taken within an interval of $30 \mu\text{s}$ in a turbulent boundary layer

Figure 1.16 shows the instantaneous flow velocity field of a turbulent boundary layer, now recorded with a CCD camera with a spatial resolution of 1024×1024 pixel [24]. The observation area had a size of $30 \times 30 \text{ mm}^2$. The comparison with Fig. 1.13 shows that this area is much smaller than for the photographic plate, as in 1995 only CCD cameras with lower sensitivity than that of photographic film have been available for recording. However, the use of the CCD camera allowed to take 10 PIV recordings per second. Thus, mean velocity profiles (Fig. 1.17) could be determined along with the Reynolds stresses for instance.

At this point of development of the PIV technique it was possible to capture instantaneous two component velocity fields in a plane of the flow (2C-2D PIV) with a repetition rate of 10 recordings per second. This allowed not only to reveal the instantaneous structures of the turbulent boundary layer in a plane, but also to determine averaged velocity profiles and to calculate statistical data and to compare them with experimental results obtained with single location sensor and theoretical results.

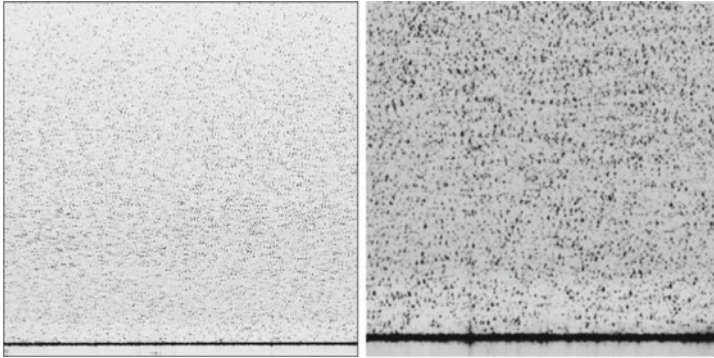


Fig. 1.15 Superposition of frames of Fig. 1.14, simulating the recording situation as had been the case for photographic PIV with doublets of images of the tracer particles. Right: detail of lower right corner

Fig. 1.16 Instantaneous flow velocity field of turbulent boundary layer, $U = 10$ m/s, the average flow velocity of the instantaneous velocity field has been subtracted to display the turbulent flow structures (from [24])

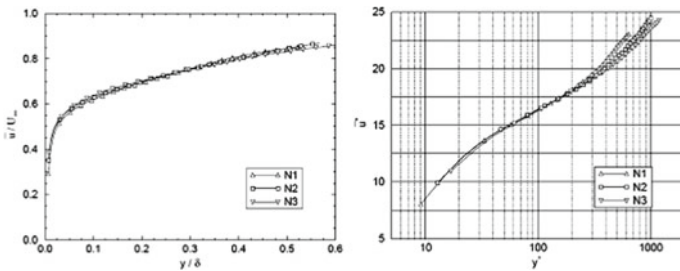
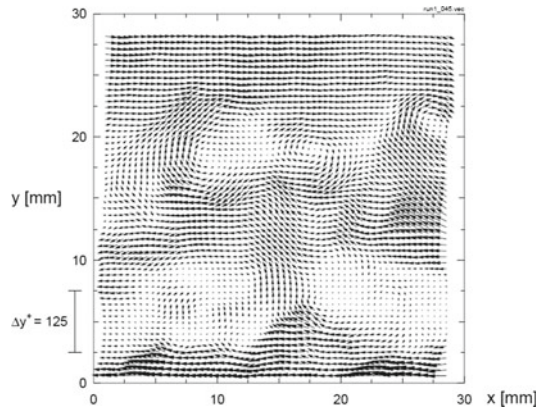


Fig. 1.17 Mean velocity profile in outer (left) and inner variables (right), Laminar Flow Wind Tunnel, at 10, 15, and 20 m/s, (see [24] for details)

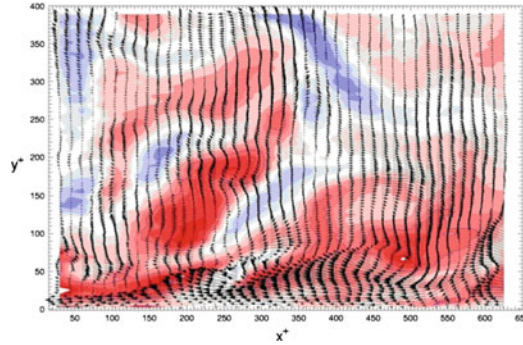


Fig. 1.18 Instantaneous flow velocity field of turbulent boundary layer, $U = 3$ m/s, the mean velocity profile has been subtracted to display the turbulent velocity fluctuations, the out-of-plane velocity component is color coded. (A colored version of the figure can be found at [\[DC1.9\]](#))

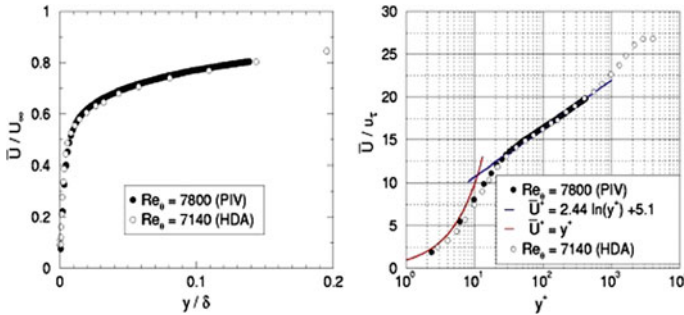
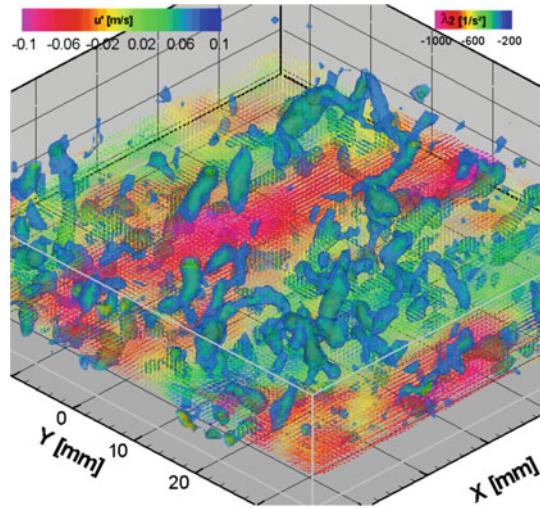


Fig. 1.19 Mean velocity profile in outer (left) and inner variables (right) measured at LML in Lille at 3 m/s with digital stereoscopic PIV and comparison with hot-wire (HDA) results, (see [\[25\]](#) for details)

The consequent next step has been to expand the experimental set-up for a stereo configuration of the cameras to obtain the third (out-of-plane) velocity component as well (3C-2D PIV). Such measurements [\[25\]](#) have been performed in 2004. The CCD sensor had a resolution of 1280×1024 pixel. Due to the higher light sensitivity of the cameras it was possible to expand the observation area to 80×52 mm² (see [Fig. 1.18](#)). PIV recordings could be obtained with a rate of six recordings per second. [Figure 1.19](#) shows a comparison of results for mean velocity profile and inner variables, obtained with PIV and hot-wire.

For many following years stereoscopic PIV was the method of choice to study the structures in turbulent boundary layer flows. However, stereoscopic PIV providing access to all three velocity components in a plane, still allowed only planar cuts through the instantaneous structures in the wall boundary.

Fig. 1.20 Instantaneous velocity vector volume (TOMO PIV) with swirl strength within the turbulent boundary layer flow at $Re_\theta = 2460$, (see [52] for details) (A colored version of the figure can be found at [DC1.10])

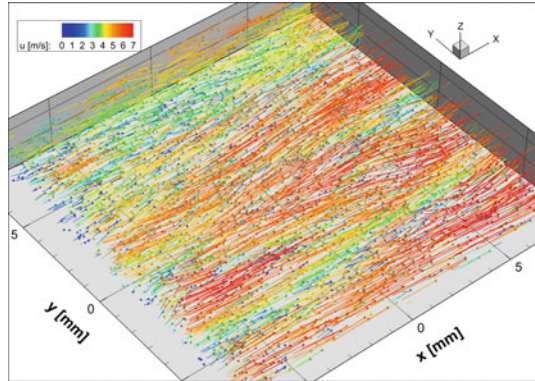


The final break through enabling to really *see* the instantaneous structures within the turbulent boundary layer was achieved by the development of tomographic PIV (3C-3D PIV). Multi-camera high speed PIV systems (sensors with a spatial resolution of 1000×1000 pixel and a temporal resolution exceeding $f_r = 1000$ Hz) now allowed obtaining results not only in a volume of the flow but even (*time-resolved* 3C-3D PIV). Figure 1.20 shows that now the instantaneous three dimensional flow structures within the boundary layer clearly become visible [52]. The size of the observation volume is $63 \times 68 \times 15$ mm³, filled with more than 200.000 instantaneous three-component velocity vectors.

In recent years the Shake-The-Box (STB) method, which uses sophisticated dense Lagrangian particle tracking algorithms for evaluation, has been developed for volumetric flow analysis. The STB method uses the temporal information inherent in the time series of particle images in order to predict and correct (“shake”) 3D particle positions iteratively along found trajectories. This approach allows for an accurate reconstruction of particle trajectories from which velocity and acceleration (material derivative) data can be derived analytically using an optimized temporal fit function. Figure 1.21 shows the tracks of 5600 tracer particles recorded within the near-wall region $y^+ < 32$ of a turbulent boundary layer obtained with STB (see [53] and Application 18.2 for details). In order to achieve a recording rate of $f_r = 15.873$ Hz the spatial resolution of the high speed cameras had to be reduced to 528×420 pixel resulting in an observation volume of $16 \times 1.5 \times 16$ mm³. The total measuring time of 14.49 s allowed to analyze 230.000 time steps providing e.g. converged one- and two-point statistics in bins of sizes down to 0.08 viscous units.

The last two examples demonstrated the extension of the PIV technique from a planar technique to the investigation of (small) volumes in the boundary layer with a (limited) temporal resolution of a few kHz. Recently the planar PIV technique has also been extended to high temporal resolution and applied in boundary layers in

Fig. 1.21 Instantaneous velocity vector volume (LPT with STB) within the turbulent boundary layer flow, flow velocity color coded, (see [53] and Sect. 18.2 for details; a colored version of the figure can be found at [DC1.11])



order to obtain statistically converged turbulence data, thereby accepting a limited field of view in streamwise direction. Section 11.3 describes how experimental data, such as velocity profile and variances, skewness and flatness agree with DNS.

This brief discussion of the remarkable development and increasing capability of the PIV technique to reveal three-dimensional structures in complex flow fields, taking turbulent boundary layers as example, illustrates why PIV is of high interest for fundamental research in fluid mechanics.

1.4.5 PIV for Industrial Research in Large Test Facilities

The use of PIV in large scale industrial test facilities poses different and more severe problems as its use for fundamental research. Nevertheless, it is quite obvious that the use of the PIV technique also is very attractive in modern aerodynamics, because it helps to understand unsteady flow phenomena as, for example, in separated flows over models at high angle of incidence, vortices behind airplanes or vortices behind propellers or rotors. PIV enables spatially resolved measurements of such instantaneous flow velocity fields within a very short time and allows the detection of large and small scale spatial structures in the flow velocity field. Another need of modern aerodynamics is that the increasing number and increasing quality of numerical calculations of flow fields require adequate experimental data for validation of the numerical codes in order to decide whether the physics of the problem has been modeled correctly.

Towards this purpose carefully designed experiments have to be performed in close cooperation with those scientists doing the numerical calculations. The experimental data of the flow field must possess high resolution in time and space in order to be able to compare them with high density numerical data fields. The PIV technique is an appropriate experimental tool for this task, especially if information about the instantaneous velocity field is required. Mostly such investigations

for industrial projects have to be performed in large test facilities. When applying PIV at fundamental research, in order to obtain high quality results, the experimental environment usually can be tailored to meet the requirements of the PIV technique. This is completely different for application in an industrial environment, where the test facility usually cannot be adapted for the needs of optical measurement techniques. Moreover, industrial test facilities usually are very large and its use is very expensive. Of course, the end user of PIV results from industrial tests wants to obtain results of similar quality as achievable at fundamental research in a laboratory. In the following, some of the features which have to be developed for a PIV system to be applied in an industrial wind tunnel shall be discussed.

A PIV system for the investigation of air flows in wind tunnels must be serviceable in low-speed flows (e.g. flow velocities of less than 1 m/s in boundary layers) as well as in high-speed flows (flow velocities up to 600 m/s in supersonic flows with shocks). Flow fields over solid, moving or deforming models have to be investigated. The application of the PIV technique in large, industrial wind tunnels poses a number of special problems: installation of the seeding equipment, minimizing contamination of the wind tunnel, limited optical access, large observation area, long distances between the observation area and the light source and the recording cameras, restricted time for the measurement, and high operational costs of the wind tunnel. The description of the demands as given above leads to the definition of requirements which should be fulfilled when PIV is applied in an industrial wind tunnel. First of all, a high spatial resolution of the data field is necessary in order to resolve large scale as well as small scale structures in the flow with high accuracy. This condition directly influences the choice of the recording equipment. A second important condition is that a high density of experimental data is required for a meaningful comparison with the results of numerical calculations. Thus, the tracer particle image density (i.e. number of particle images per interrogation area) must be high. A powerful seeding generator (high concentration of tracer particles in the measuring volume in the flow even at high flow velocities) is needed for this purpose. As the flow velocity is measured indirectly by means of the measurement of the velocity of tracer particles added to the flow, the particles must follow the flow faithfully. This requires the use of very small tracer particles. However, small particles scatter very little light. This fact results in a third important condition for the application of PIV in aerodynamics: a powerful pulse laser is required for the illumination of the flow field.

However, there are more than these PIV specific demands. In case of moving (rotors, blades) or vibrating (models at high incidence or investigations of the aeroelasticity of a model) objects, the position of the model and its deformation have to be measured simultaneously. The triggering of the PIV system has to be performed in such a way that data at the desired phase angle of rotating objects will be obtained. The data obtained with PIV has to be merged with the data obtained by the wind tunnel data acquisition system. Beginning and end of data acquisition of PIV has to be synchronized with the wind tunnel acquisition system. Due to the high operational costs of the test facility and the large distances within the facility all important parameters must be remotely controlled. The measurements, usually performed far from the laboratory, require a careful preparation of the experiment. Sometimes a mock-

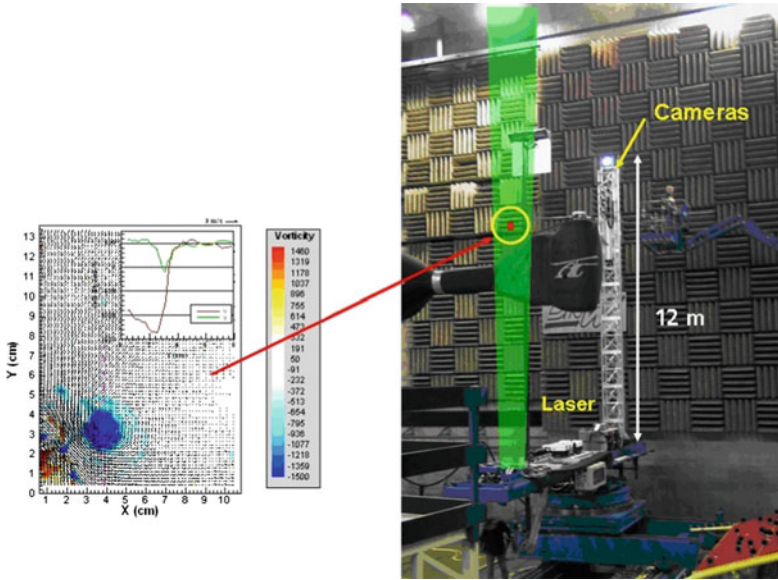


Fig. 1.22 PIV set-up for investigation of helicopter blade tip vortex in the open test section of the DNW-LLF wind tunnel ($8\text{ m} \times 6\text{ m}$) and instantaneous flow field of tip vortices ($100\text{ mm} \times 120\text{ mm}$) (see [42] for details)

up of the set-up to be used in the wind tunnel has to be built to check the optical access for example. Increasingly, this can be done by implementing a numerical mock-up nowadays. The investigation of the tip vortices of a helicopter blade in the open test section of the DNW-LLF wind tunnel (see Fig. 1.22) shall illustrate the problems of large distances and the triggering of illumination and recording in order to obtain the quite small instantaneous flow field of the tip vortex.

Beside the high effort required to get sufficiently contrasted, sharp images of sub-micron particles over the large observation and illumination distances, the PIV evaluation had also to be adapted to compensate for the motion of the camera and laser supports. In contrast to more controlled laboratory applications, stereoscopic PIV recordings in large industrial facilities require a sophisticated calibration scheme and a refinement of the dewarping process. When strong velocity gradients are present, as is the case with the blade-tip vortices to be measured here, a very small misalignment (on the order of a millimeter) will lead to severe errors during the reconstruction of the out-of-plane velocity component. For the large dimensions of the camera support (see Fig. 1.22) small misalignments could not be avoided. Therefore, special evaluation techniques were developed to compensate the unwanted misalignments. All serious misalignments caused by translation, rotation or deformation (magnification change of one image) were found and corrected by a re-computation of the dewarping coefficients. This relatively easy elimination of the residual-alignment errors was possible only, because the dewarping was performed prior to the cross-correlation

of the images. More details of the camera calibration techniques and the disparity correction described can be found in [42] and Sect. 8.1.

After having discussed the most important aspects of PIV in a simplified manner in this introduction to support the general understanding, they will be treated in-depth in the following main chapters of this book.

References

1. Adrian, R.J.: Multi-point optical measurements of simultaneous vectors in unsteady flow - a review. *Int. J. Heat Fluid Flow* **7**(2), 127–145 (1986). DOI 10.1016/0142-727X(86)90062-7. URL [https://dx.doi.org/10.1016/0142-727X\(86\)90062-7](https://dx.doi.org/10.1016/0142-727X(86)90062-7)
2. Adrian, R.J.: Particle-imaging techniques for experimental fluid mechanics. *Ann. Rev. Fluid Mech.* **23**(1), 261–304 (1991). DOI 10.1146/annurev.fl.23.010191.001401. URL <https://dx.doi.org/10.1146/annurev.fl.23.010191.001401>
3. Adrian, R.J.: Bibliography of particle image velocimetry using imaging methods: 1917 – 1995. Technical report, Arizona State University, Tempe (Az) (2011). Reprint: DLR-Mitteilung 2011-01
4. Adrian, R.J., Westerweel, J.: Particle Image Velocimetry. Cambridge Aerospace Series. Cambridge University Press, Cambridge (2011). URL <http://www.cambridge.org/de/academic/subjects/engineering/thermal-fluids-engineering/particle-image-velocimetry>
5. Ahlborn, F.: Über den Mechanismus des hydrodynamischen Widerstandes, Abhandlungen aus dem Gebiete der Naturwissenschaften, vol. 17. L. Friederichsen & Co, Hamburg (1902)
6. Ahlborn, F.: Über den Mechanismus des Widerstandes flüssiger Medien. *Physikalische Zeitschrift* **3**(6), 120–124 (1902)
7. Ahlborn, F.: Die Ablösungstheorie der Grenzschichten und die Wirbelbildung. *Jahrbuch der wissenschaftlichen Gesellschaft für Luftfahrt e.V. (WGL)* pp. 171–177 (1927)
8. Barker, D.B., Fournay, M.E.: Measuring fluid velocities with speckle patterns. *Opt. Lett.* **1**(4), 135–137 (1977). DOI 10.1364/OL.1.000135. URL <https://dx.doi.org/10.1364/OL.1.000135>
9. Brücker, C.: 3-D PIV via spatial correlation in a color-coded light-sheet. *Exper. Fluids* **21**(4), 312–314 (1996). DOI 10.1007/BF00190682. URL <https://dx.doi.org/10.1007/BF00190682>
10. Brücker, C.: Spatial correlation analysis for 3-D scanning PIV: simulation and application of dual-color light-sheet scanning. In: 8th International Symposium on the Applications of Laser Techniques to Fluid Mechanics, Lisbon (Portugal) (1996)
11. Buchlin, J.M. (ed.): Digital Image Processing in Fluid Dynamics. von Karman Institute for Fluid Dynamics Lecture Series, VKI LS 1984-03. Von Karman Institute, Rhode-Saint-Genèse, Belgium (1984). URL <https://store.vki.ac.be/digital-image-processing-in-fluid-dynamics-200.html>
12. Dudderar, T.D., Simpkins, P.G.: Laser speckle photography in a fluid medium. *Nature* **270**, 45–47 (1977). DOI 10.1038/270045a0. URL <https://dx.doi.org/10.1038/270045a0>
13. Elliott, G.S., Beutner, T.J.: Molecular filter based planar Doppler velocimetry. *Progr. Aerosp. Sci.* **35**(8), 799–845 (1999). DOI 10.1016/S0376-0421(99)00008-1. URL [https://dx.doi.org/10.1016/S0376-0421\(99\)00008-1](https://dx.doi.org/10.1016/S0376-0421(99)00008-1)
14. Grant, I.: Selected Papers on Particle Image Velocimetry. SPIE Milestone Series, vol. MS99. SPIE Optical Engineering Press (1994). URL http://spie.org/Publications/Book/172964?&origin_id=x649&sort=PubDateASC&start_at=73
15. Grant, I.: Particle image velocimetry: a review. *Proc. Inst. Mech. Eng. Part C J. Mech. Eng. Sci.* **211**(1), 55–76 (1997). DOI 10.1243/0954406971521665. URL <https://dx.doi.org/10.1243/0954406971521665>

16. Grousson, R., Mallick, S.: Study of flow pattern in a fluid by scattered laser light. *Appl. Opt.* **16**(9), 2334–2336 (1977). DOI 10.1364/AO.16.002334. URL <https://dx.doi.org/10.1364/AO.16.002334>
17. Hinsch, K.D.: Particle image velocimetry. In: Sirohi, R. (ed.) *Speckle Metrology*, pp. 235–324. Marcel Dekker, New York (1993)
18. Hinsch, K.D.: Three-dimensional particle velocimetry. *Meas. Sci. Technol.* **6**(6), 742 (1995). DOI 10.1088/0957-0233/6/6/012. URL <https://dx.doi.org/10.1088/0957-0233/6/6/012>
19. Hinsch, K.D.: Holographic particle image velocimetry. *Meas. Sci. Technol.* **13**(7), R61 (2002). DOI 10.1088/0957-0233/13/7/201. URL <https://dx.doi.org/10.1088/0957-0233/13/7/201>
20. Hinsch, K.D., Hinrichs, H.: Three-dimensional particle velocimetry. In: T. Dracos (ed.) *Three-Dimensional Velocity and Vorticity Measuring and Image Analysis Techniques*. ERCOFTAC Series, vol. 4, pp. 129–152. Springer, Netherlands (1996). DOI 10.1007/978-94-015-8727-3_6. URL https://dx.doi.org/10.1007/978-94-015-8727-3_6
21. Hinterwaldner, I.: Parallel lines as tools for making turbulence visible. *Representations* **124**(1), 1–42 (2013). DOI 10.1525/rep.2013.124.1.1. URL <https://dx.doi.org/10.1525/rep.2013.124.1.1>
22. Hinterwaldner, I.: Model building with wind and water: Friedrich Ahlborn’s photo-optical flow analysis. *Stud. Hist. Philos. Sci. Part A* **49**, 1–17 (2015). DOI 10.1016/j.shpsa.2014.10.003. URL <https://dx.doi.org/10.1016/j.shpsa.2014.10.003>
23. Hoffmann, C.: Superpositions: Ludwig Mach and Étienne-Jules Marey’s studies in streamline photography. *Stud. Hist. Philos. Sci. Part A* **44**(1), 1–11 (2013). DOI 10.1016/j.shpsa.2012.08.002. URL <https://dx.doi.org/10.1016/j.shpsa.2012.08.002>
24. Kähler, C.J.: Ortsaufgelöste Geschwindigkeitsmessungen in einer turbulenten Grenzschicht. Technical report, DLR, Göttingen, Germany (1997). DLR-FB-1997-32
25. Kähler, C.J.: The significance of coherent flow structures for the turbulent mixing in wall-bounded flows. Ph.D. thesis, Georg-August-University zu Göttingen (Germany) (2004). <http://hdl.handle.net/11858/00-1735-0000-0006-B4C8-8>. DLR-FB-2004-24
26. Kähler, C.J., Astarita, T., Vlachos, P.P., Sakakibara, J., Hain, R., Discetti, S., La Foy, R., Cierpka, C.: Main results of the 4th international PIV challenge. *Exper. Fluids* **57**(6), 97 (2016). DOI 10.1007/s00348-016-2173-1. URL <http://dx.doi.org/10.1007/s00348-016-2173-1>
27. Keane, R.D., Adrian, R.J.: Theory of cross-correlation analysis of PIV images. *Appl. Sci. Res.* **49**(3), 191–215 (1992). DOI 10.1007/BF00384623. URL <https://dx.doi.org/10.1007/BF00384623>
28. Kompenhans, J., Hoecker, R.: Investigation of turbulent flows by means of particle image velocimetry. In: *Proceedings of the Fifth International Symposium on Flow Visualization*, Prague, p. 6 (1989)
29. Kompenhans, J., Reichmuth, J.: Particle imaging velocimetry in a low turbulent wind tunnel and other flow facilities. In: *AGARD Conference on Advanced Instrumentation for Aero Engine Components*, 19–23 May, Philadelphia (USA), vol. 399, pp. 35 (1–13) (1986)
30. Koochesfahani, M.M., Cohn, R.K., Gendrich, C.P., Nocera, D.G.: Molecular tagging diagnostics for the study of kinematics and mixing in liquid-phase flows. In: R.J. Adrian, D. Durao, F. Durst, M. Heitor, M. Maeda, J.H. Whitelaw (eds.) *Developments in Laser Techniques in Fluid Mechanics*, pp. 125–134. Springer, New York (1997). URL http://www.egr.msu.edu/tmual/Papers_PDF/1996_MTV_Review-Springer-Chapter.pdf
31. Lauterborn, W., Vogel, A.: Modern optical techniques in fluid mechanics. *Ann. Rev. Fluid Mech.* **16**(1), 223–244 (1984). DOI 10.1146/annurev.fl.16.010184.001255. URL <https://dx.doi.org/10.1146/annurev.fl.16.010184.001255>
32. Mach, L.: Über die Sichtbarmachung von Luftstromlinien. *Zeitschrift für Luftschiffahrt und Physik der Atmosphäre* **15**(6), 129–139 (1896)
33. Marey, E.J.: Le mouvement des liquides étudié par la chronophotographie. *Comptes Rendus Hebdomadaires des Séances de l’Académie des Sciences* **117**, 913–924 (1893)
34. Marey, E.J.: Les mouvement de l’air étudiés par la chronophotographie. *La Nature* **49**, 252–254 (1901)

35. Meyers, J.F., Komine, H.: Doppler global velocimetry: a new way to look at velocity. In: ASME Fourth International Conference on Laser Anemometry (August 3–9, 1991), vol. 1, pp. 289–296 (1991). URL <https://ntrs.nasa.gov/archive/nasa/casi.ntrs.nasa.gov/20040161444.pdf>
36. Meynard, R.: *Mémoire de champs de vitesse d'écoulements fluides par analyse de suites d'images obtenues par diffusion d'un feuillet lumineux*. Ph.D. thesis, Faculté des Sciences Appliquées, Université Libre de Bruxelles (1983). URL <https://www.vki.ac.be/index.php/departments/ea-department-other-menu-68/25-years-of-piv>
37. Noguès, F.: *Recherches expérimentales de Marey sur le mouvement dans l'air et dans l'eau*. Publications scientifiques et techniques du Ministère de l'Air. Gauthier-Villars, Paris (1933)
38. Prandtl, L.: Über Flüssigkeitsbewegung bei sehr kleiner Reibung. In: *Verhandlungen des III. Internationalen Mathematiker-Kongresses, Heidelberg (1904)*, pp. 484–491. Teubner, Leipzig (1905). DOI 10.1007/978-3-662-11836-8_43. URL https://dx.doi.org/10.1007/978-3-662-11836-8_43. Reprint
39. Prandtl, L.: *Entstehung von Wirbeln bei Wasserströmungen I. - Entstehung von Wirbeln und künstliche Beeinflussung der Wirbelbildung*. Reichsstelle für den Unterrichtsfilm, Berlin, Germany (1927–1933). DOI 10.3203/IWF/C-1. URL <https://doi.org/10.3203/IWF/C-1>
40. Prandtl, L.: *Entstehung von Wirbeln bei Wasserströmungen II. - Anwendungen auf die Strömung durch Krümmer, Hohlräume und Verzweigungsstücke*. Reichsstelle für den Unterrichtsfilm, Berlin, Germany (1932–1933). DOI 10.3203/IWF/C-2. URL <https://doi.org/10.3203/IWF/C-2>
41. Prandtl, L.: *Entstehung von Wirbeln bei Wasserströmungen*. IWF Wissen und Medien gGmbH, DVD, Göttingen, Germany (2009)
42. Raffel, M., Richard, H., Ehrenfried, K., van der Wall, B.G., Burley, C., Beaumier, P., McAlister, K., Pengel, K.: Recording and evaluation methods of PIV investigations on a helicopter rotor model. *Exper. Fluids* **36**(1), 146–156 (2004). DOI 10.1007/s00348-003-0689-7. URL <http://dx.doi.org/10.1007/s00348-003-0689-7>
43. Riethmuller, M. (ed.): *Particle Image Velocimetry*. von Karman Institute for Fluid Dynamics. Lecture Series, VKI LS 1996-03. Von Karman Institute, Rhode-Saint-Genèse, Belgium (1996)
44. Riethmuller, M. (ed.): *Particle Image Velocimetry and Associated Techniques*. von Karman Institute for Fluid Dynamics Lecture Series, VKI LS 2000-01. Von Karman Institute, Rhode-Saint-Genèse, Belgium (2000)
45. Riethmuller, M., Scarano, F. (eds.): *Advanced measuring techniques for supersonic flows*. von Karman Institute for Fluid Dynamics Lecture Series, VKI LS 2005-01. Von Karman Institute, Rhode-Saint-Genèse, Belgium (2005). URL <https://store.vki.ac.be/lecture-series-monographs/measurement-techniques/advanced-measuring-techniques-for-supersonic-flows.html>
46. Roehle, I.: Three-dimensional Doppler global velocimetry in the flow of a fuel spray nozzle and in the wake region of a car. *Flow Meas. Instrum.* **7**(3–4), 287–294 (1996). DOI 10.1016/S0955-5986(97)00011-3. URL [https://dx.doi.org/10.1016/S0955-5986\(97\)00011-3](https://dx.doi.org/10.1016/S0955-5986(97)00011-3)
47. Rotta, J.: *Die Aerodynamische Versuchsanstalt in Göttingen, ein Werk Ludwig Prandtls*. Vandenhoeck & Ruprecht, Göttingen, Germany (1990)
48. Royer, H., Stanislas, M.: Stereoscopic and holographic approaches to get the third velocity component in PIV. *Particle Image Velocimetry*. von Karman Institute for Fluid Dynamics Lecture Series 1996–03, pp. II–156. Von Karman Institute, Rhode-Saint-Genèse, Belgium (1996)
49. Samimy, M., Wernet, M.P.: Review of planar multiple-component velocimetry in high-speed flows. *AIAA J.* **38**(4), 553–574 (2000). DOI 10.2514/2.1004. URL <https://dx.doi.org/10.2514/2.1004>
50. Scarano, F.: Iterative image deformation methods in PIV. *Meas. Sci. Technol.* **13**(1), R1 (2002). DOI 10.1088/0957-0233/13/1/201. URL <https://dx.doi.org/10.1088/0957-0233/13/1/201>
51. Scarano, F., Riethmuller, M. (eds.): *Recent advances in particle image velocimetry*. von Karman Institute for Fluid Dynamics Lecture Series, VKI LS 2009-01. Von Karman Institute, Rhode-Saint-Genèse, Belgium (2009). URL <https://store.vki.ac.be/lecture-series-monographs/measurement-techniques/recent-advances-in-particle-image-velocimetry.html>

52. Schröder, A., Geisler, R., Staack, K., Elsinga, G.E., Scarano, F., Wieneke, B., Henning, A., Poelma, C., Westerweel, J.: Eulerian and Lagrangian views of a turbulent boundary layer flow using time-resolved tomographic PIV. *Exper. Fluids* **50**(4), 1071–1091 (2011). DOI 10.1007/s00348-010-1014-x. URL <https://dx.doi.org/10.1007/s00348-010-1014-x>
53. Schröder, A., Schanz, D., Geisler, R., Gesemann, S., Willert, C.E.: Near-wall turbulence characterization using 4D-PTV “Shake-The-Box”. In: 11th International Symposium on Particle Image Velocimetry - PIV2015. Santa Barbara (CA), USA (2015)
54. Schröder, A., Willert, C.E. (eds.): *Particle Image Velocimetry: New Developments and Recent Applications*. Topics in Applied Physics, vol. 112. Springer, Berlin (2008). DOI 10.1007/978-3-540-73528-1. URL <https://dx.doi.org/10.1007/978-3-540-73528-1>
55. Sirohi, R.S.: *Speckle metrology*. In: *Optical Science and Engineering*, vol. 38. Taylor and Francis (1993)
56. Stanislas, M., Kompenhans, J., Westerweel, J.: *Particle Image Velocimetry: Progress Towards Industrial Application*. Fluid Mechanics and Its Applications. Springer, Netherlands (2000). DOI 10.1007/978-94-017-2543-9. URL <https://dx.doi.org/10.1007/978-94-017-2543-9>
57. Stanislas, M., Okamoto, K., Kähler, C.J.: Main results of the First International PIV Challenge. *Meas. Sci. Technol.* **14**(10), R63 (2003). DOI 10.1088/0957-0233/14/10/201. URL <http://stacks.iop.org/0957-0233/14/i=10/a=201>
58. Stanislas, M., Okamoto, K., Kähler, C.J., Westerweel, J.: Main results of the Second International PIV Challenge. *Exper. Fluids* **39**(2), 170–191 (2005). DOI 10.1007/s00348-005-0951-2. URL <http://dx.doi.org/10.1007/s00348-005-0951-2>
59. Stanislas, M., Okamoto, K., Kähler, C.J., Westerweel, J., Scarano, F.: Main results of the third international PIV challenge. *Exper. Fluids* **45**(1), 27–71 (2008). DOI 10.1007/s00348-008-0462-z. URL <http://dx.doi.org/10.1007/s00348-008-0462-z>
60. Stanislas, M., Westerweel, J., Kompenhans, J.: *Particle Image Velocimetry: Recent Improvements: Proceedings of the EUROPIV 2 Workshop held in Zaragoza, Spain, March 31 – April 1, 2003*. Springer, Berlin (2004). DOI 10.1007/978-3-642-18795-7. <https://dx.doi.org/10.1007/978-3-642-18795-7>
61. Tietjens, O.: *Hydro- und Aeromechanik – nach Vorlesungen von L. Prandtl*, vol. 2. Julius Springer, Berlin (1931)
62. Tropea, C., Yarin, A.L., Foss, J.F.: *Springer Handbook of Experimental Fluid Mechanics*. Springer, Berlin (2007). DOI 10.1007/978-3-540-30299-5. URL <https://dx.doi.org/10.1007/978-3-540-30299-5>
63. Vogt, A., Baumann, P., Kompenhans, J., Gharib, M.: Investigations of a wing tip vortex in air by means of DPIV. In: *Advanced Measurement and Ground Testing Conference*, New Orleans, LA, 17–20 June. American Institute of Aeronautics and Astronautics (1996). DOI 10.2514/6.1996-2254. URL <https://dx.doi.org/10.2514/6.1996-2254>
64. Westerweel, J.: *Digital particle image velocimetry: Theory and application*. Ph.D. thesis, Mechanical Maritime and Materials Engineering, Delft University of Technology (1993). URL <http://repository.tudelft.nl/islandora/object/uuid:85455914-6629-4421-8c77-27cc44e771ed/datastream/OBJ/download>
65. Wieneke, B.: Stereo-PIV using self-calibration on particle images. *Exper. Fluids* **39**(2), 267–280 (2005). DOI 10.1007/s00348-005-0962-z. URL <https://dx.doi.org/10.1007/s00348-005-0962-z>
66. Willert, C.E.: Assessment of camera models for use in planar velocimetry calibration. *Exper. Fluids* **41**(1), 135–143 (2006). DOI 10.1007/s00348-006-0165-2. URL <https://dx.doi.org/10.1007/s00348-006-0165-2>
67. Willert, C.E., Gharib, M.: Digital particle image velocimetry. *Exper. Fluids* **10**(4), 181–193 (1991). DOI 10.1007/BF00190388. URL <https://dx.doi.org/10.1007/BF00190388>
68. Willert, C.E., Kompenhans, J.: *Particle Image Velocimetry (PIV) analysis of Ludwig Prandtl’s historic flow visualisation films*. Deutsches Zentrum für Luft- und Raumfahrt (DLR), Technische Informationsbibliothek (TIB), Hannover, Germany (2010). DOI 10.5446/12719. URL <https://doi.org/10.5446/12719>

Chapter 2

Physical and Technical Background

2.1 Tracer Particles

It is clear from the principle of PIV that this technique – in contrast to hot wire or pressure probe techniques – is based on the direct determination of the two fundamental dimensions of the velocity: length and time. On the other hand, the measurement technique is indirect as it determines the velocity of tracer particles instead of the velocity of the fluid. Therefore, the interaction of the particles and the surrounding fluid has to be examined in order to avoid significant discrepancies between fluid and particle motion. Moreover, the technique is based on imaging. Therefore, the optical properties of the seeding particles play an equally important role for the selection of suitable tracers.

2.1.1 Fluid Mechanical Properties

A primary source of error is the influence of gravitational forces on the velocity of the tracer particles, if the densities of the fluid ρ and the tracer particles ρ_p do not match. Even though it can be neglected in many practical situations, we will derive the gravitationally induced velocity \mathbf{U}_g from STOKES' drag law to introduce the particle's behavior under acceleration. Therefore, we assume spherical particles in a viscous fluid at a very low Reynolds number. This yields:

$$\mathbf{U}_g = d_p^2 \frac{(\rho_p - \rho)}{18\mu} \mathbf{g} \tag{2.1}$$

where \mathbf{g} is the acceleration due to gravity, μ the dynamic viscosity of the fluid and d_p is the diameter of the particle. The equation implies that sedimentation of particles

An overview of the Digital Content to this chapter can be found at [\[DC2.1\]](#).

can be avoided if the density of the fluid and particles is identical (neutral buoyancy). The latter is easily achieved in liquid flows. In gas flows, the density of the particles is typically much higher than that of the fluid. Therefore, the particle diameter must be chosen sufficiently small in order to minimize the settling velocity of the particles. A known exception is that of soap bubbles filled with lighter-than-air gas (typically helium), where the neutral buoyancy condition can be obtained balancing the weight of the soap film with the volume of the helium filled bubble.

In analogy to Eq.(2.1), we can derive an estimate for the velocity lag \mathbf{U}_s of a particle in a continuously accelerating fluid:

$$\mathbf{U}_s = \mathbf{U}_p - \mathbf{U} = d_p^2 \frac{(\rho_p - \rho)}{18\mu} \mathbf{a} \quad (2.2)$$

where \mathbf{U}_p and \mathbf{U} denote the particle and surrounding fluid velocity respectively, where ρ_p is the particle density. In case of a sudden deceleration the step response of \mathbf{U}_p typically follows an exponential law. If the density of the particle is much greater than the fluid density:

$$\mathbf{U}_p(t) = \mathbf{U} \left[1 - \exp\left(-\frac{t}{\tau_s}\right) \right] \quad (2.3)$$

with the response time τ_p given by:

$$\tau_p = d_p^2 \frac{\rho_p}{18\mu}. \quad (2.4)$$

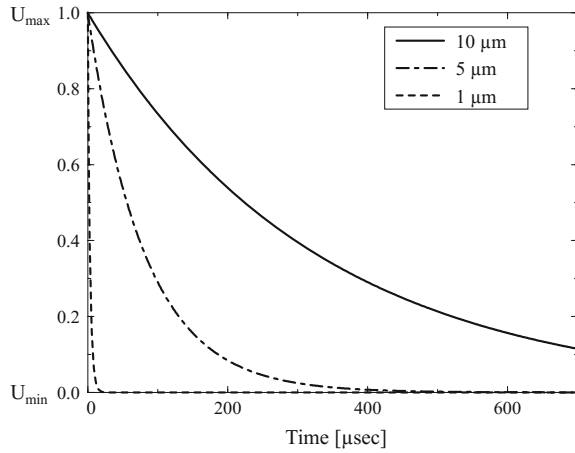
If the fluid acceleration is not constant or Stokes drag does not apply (e.g. for larger particles or at higher flow velocities), the solution is no longer a simple exponential decay of the particle velocity. This is due to the equations of the particle motion becoming non-linear and more difficult to solve. Nevertheless, τ_p remains a convenient measure for the tendency of particles to attain velocity equilibrium with the fluid. The result of Eq. (2.3) is illustrated in Fig. 2.1, where the response time of particles with different diameters is shown for a step-wise deceleration in an air flow.

Knowing the response time of a particle tracer is not sufficient to determine if it will follow the flow with enough fidelity. For this purpose the particle Stokes number is introduced:

$$\text{Stk} = \frac{\tau_p}{\tau_f} \quad (2.5)$$

where τ_f stands for the characteristic time scale in the flow. The latter refers to velocity fluctuations along the particle trajectory. A value of the Stokes number below 10^{-1} yields an acceptable flow tracing accuracy [54]. The value of τ_f is often inferred from dimensional analysis as a ratio between a length scale and a characteristic velocity. For instance in turbulent boundary layers τ_f may be taken as the ratio of boundary layer thickness and free stream velocity; in vortex dominated flows, as the ratio between vortex diameter and swirling velocity.

Fig. 2.1 Theoretical time response of oil particles with different diameters in air after an instantaneous flow deceleration



When applying PIV to liquid flows (e.g. water), particles matching the fluid density are commonly used tracers. A list is given in Tables 2.3 and 2.4. In air flows, particles with the same overall density as the air can be generated using liquid bubbles filled by a gas lighter than air (e.g. helium-filled soap bubbles, HFBS) [4]. However, the use of helium-filled soap bubbles is limited to low-speed aerodynamics [57]. Early applications of PIV have already demonstrated that more difficulties arise in providing high quality seeding in gas flows compared to applications in liquid flows [6, 24, 27, 47, 65]. The problems are similar to those faced by Laser Doppler Velocimetry, but amplified by the demand of a homogeneous particle concentration that has to be established at all times.

From Eq. (2.2) and Fig. 2.1 it can be seen that, due to the difference in density between the fluid and the tracer particles, the diameter of the particles should be very small in order to ensure good tracking of the fluid motion. On the other hand, the particle diameter should not be too small, as the scattered light will also become very small, as will be shown in Sect. 2.1.5. It is therefore obvious that a compromise has to be found. This problem is discussed extensively in the literature [28, 31, 42–44]. The most commonly used seeding particles for PIV investigations of gaseous flows are listed in Table 2.4. For most applications in aerodynamics, oil or DEHS (di-ethyl-hexyl-sebacate) droplets are generated with systems based on the Laskin nozzle (see Fig. 2.16), with a mean droplet diameter close to 1 μm. For open-return wind tunnels smoke generators are also frequently employed. Finally, in confined facilities, such as blow-down wind tunnels for high-speed flows or combustion, solid particles (e.g. SiO₂ and TiO₂) are commonly used.

The response time for different seeding materials used in aerodynamics are summarized in Table 2.1. According to RAGNI et al. [52] the DEHS droplets show a time response of 2 μs. For the solid particles, the relaxation time ranges from 0.4–3.7 μs. Titanium and silicon dioxide particles in the crystal size range 12–50 nm had an improved time response when dehydrated. The shortest time response is obtained by

Table 2.1 Time response of seeding materials and typical data dispersion

ID material	Seeder	Mean τ_p (μs)		$\sigma(\tau_p)$ (μs)	
		Stored (τ_H)	De-hydrated (τ_{Dh})	Stored	De-hydrated
DEHS	A	1.92–2.02	–	0.40–0.38	–
SiO2R104	C	2.49	2.21	0.22	0.17
SiO2R972	C	2.64	2.29	0.19	0.28
TiO214	C	3.25	3.71	0.12	0.12
TiO230	C	2.56	2.20	0.11	0.07
TiO250	C	2.77	2.09	0.18	0.09
TiO250	C _F	–	0.56	–	0.10
SiO2R104	C _F	–	0.37	–	0.10
TiO250	F _L	–	1.36	–	0.05
TiO250	F _H	–	1.67	–	0.08
TiO2170	C	2.50	3.13	0.13	0.19
TiO2240	C	2.52	2.64	0.09	0.15
TiO2550	C	2.43	2.78	0.07	0.22
Al2O3	PG	–	0.18	–	–

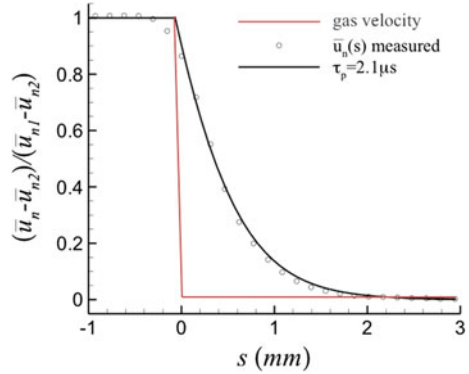
Table after RAGNI et al. [52] - C cyclone, CF cyclone with 1 μm filter, A atomizer, F fluidized bed dispersion, L/H low/high mass flow rate, PG plasma generator (data from GHAEMI et al. [17])

using the cyclone generator with dehydrated particles combined with a 1 μm particle filter. This yields a relaxation time response of 0.56 μs for the 50 nm crystal size TiO₂ particles and 0.36 μs for the SiO₂ with a 16 nm crystal size. Specific techniques that use nano-particles [9, 17] have led to minimum response time as low as 0.2 μs using fractal aggregates of Al₂O₃.

For liquid particles, it is well known from Laser Doppler Velocimetry (LDV) measurements in gas flows that the size and the distribution of the tracer particles may change during the travel from the aerosol generator to the test section, where the measurements take place. It is therefore recommended to inspect the particles' properties and the velocity lag directly from the observation area [6, 27, 33, 52]. The result of one examination of this problem is presented in Fig. 2.2.

The flow velocity along a line perpendicular to a stationary oblique shock wave is measured with PIV in a supersonic wind tunnel at Mach 2. The total velocity is approximately 500 m/s, whereas the component normal to the shock is 330 m/s before the shock and 220 m/s after it. The TiO₂ particles with a mean diameter of 0.5 μm reach the flow velocity after the shock within a distance of 2 mm. The real extent of the shock is less than 1 μm , beyond the spatial and temporal resolution associated with the interrogation areas and the time separation between pulses (≈ 0.5 mm, ≈ 1 μs). A calculation of the velocity lag of particles with a diameter of 0.5 μm and a relative weight of $4 \cdot 10^3$ kg/m³ yields a similar velocity distribution along the shock normal direction as measured with PIV (compare circles and solid line in Fig. 2.2).

Fig. 2.2 Comparison between PIV measurements (circles) and theoretical prediction (solid black line) of particle velocity for Titanium dioxide tracers of $0.5 \mu\text{m}$ diameter across a stationary oblique shock wave. Result for the change of shock normal velocity component



It is pointless to utilize tracer particles with a diameter much smaller than $1 \mu\text{m}$ considering that the PIV evaluation averages the velocity within the interrogation area and during the time separation between pulses. Smaller tracer particles would only be necessary if a higher spatial resolution in the vicinity of the shock is required.

2.1.2 Neutrally Buoyant Particles

When the density of tracers approaches that of the fluid they are immersed in, the expression of the time response in the Stokes regime reads as:

$$\tau_p = \frac{d_p^2 \Delta\rho}{18\mu} \quad (2.6)$$

In this case $\Delta\rho$ can be made several orders of magnitude smaller than the particle density. In air flows, for instance, a density difference below 0.1 kg/m^3 can be easily obtained with Helium filled soap bubbles (HFSB), compared to the value of 10^3 kg/m^3 typical of oil droplets. This condition allows to relax the constraint on particle size, which can be chosen orders of magnitude larger with little detriment to their time response and tracing fidelity. Recent work on sub-millimeter HFSB tracers [57] has assessed their time response. The shock wave test is unsuited for these tracers as they are mostly utilized in low speed flows. The flow ahead of a circular cylinder produces a constant deceleration along the stagnation streamline. The measurement of tracers deceleration and of the velocity slip allows to estimate the time response of these tracers:

$$\tau_p = \left| (U_{bubble} - U) / \left(U \frac{dU}{dx} \right) \right| \quad (2.7)$$

Particles of approximately 0.3 mm respond to velocity fluctuations within a time scale of 10–50 μs depending on their closeness to the neutral buoyancy condition [57]. Approaching neutral buoyancy in water flows is easily obtained using materials as heavy as water (e.g. polyamide, hollow glass spheres). The tracking fidelity in water flows is more easily achieved considering its higher viscosity and the fact that experiments are typically conducted at lower speed compared to air flows. As a result, larger tracers can be employed (10–100 microns) maintaining a good tracing fidelity.

2.1.3 Effect of Centrifugal Forces

Even when the particle slip can be neglected for the purpose of velocity measurements, the integrated effect of particle drift can lead to undesired inhomogeneity of the tracers spatial distribution. This is particularly evident in the case of streamwise vortices (Fig. 2.3-top left), strong vortices in high speed flows (Fig. 2.3-top right) and for laminar boundary layers (Fig. 2.4). In a stationary vortex [64] the bias error of the velocity measurement due to the particle lag may be negligible, with respect to the other sources of error. However, the particle density in the center of the vortex may attain too low values to perform a reliable analysis of their motion. In PIV experiments with supersonic and hypersonic wind tunnels [56], typically operated at low

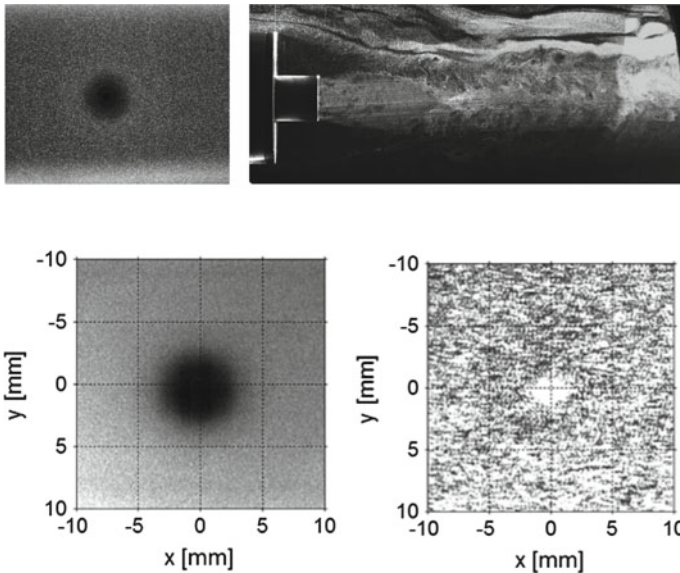


Fig. 2.3 Particles distribution inside a strong vortex seeded with oil droplets (top left, [64]); behind a rocket model seeded with TiO_2 particles (top right, [50]). Time-averaged particles distribution inside a delta-wing vortex seeded with fog droplets (bottom-left) and HFSB (bottom right, [8])

pressure, the loss of seeding over separated regions is a typical problem (Fig. 2.3-top right). In this case, the seeding particles concentration follows the thermodynamic density of the flow and additionally, they hardly penetrate shear layers where the turbulent mixing is inhibited by compressibility effects.

Another relevant example is the laminar flow development around airfoils. Due to the combined effect of a strong centrifugal force around the airfoil leading edge and the effects of flow shear, an outward movement of the particles is induced, perpendicular to the curved streamlines. While the measurement error due to the velocity lag is usually negligible as the cross-flow component of the particle is relatively small compared to the component along the streamline, the loss of seeding instead compromises the measurement in the region close to the wall. The flow around the *leading* edge of a tailplane is illustrated in Fig. 2.4 for different values of the free stream velocity and varying the size of the particle tracers. Right behind the strongest curvature a laminar separation bubble occurs on the lower side of the airfoil. Particles with a diameter of $1\ \mu\text{m}$ are not present in the separation bubble (Fig. 2.4-top), whereas particles with $0.25\ \mu\text{m}$ diameter are detected inside the separated region at $U = 30\ \text{m/s}$ (Fig. 2.4-middle). At a higher velocity even the latter particles do not

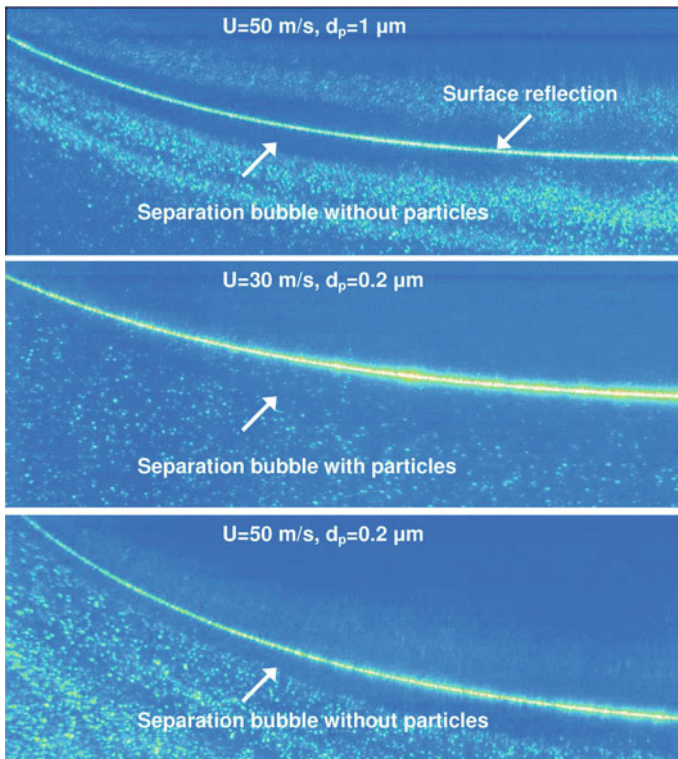


Fig. 2.4 Particle image concentration in the separated region for different free-stream velocities U and diameter of the tracer particles d_p (flow direction from left to right) [30]

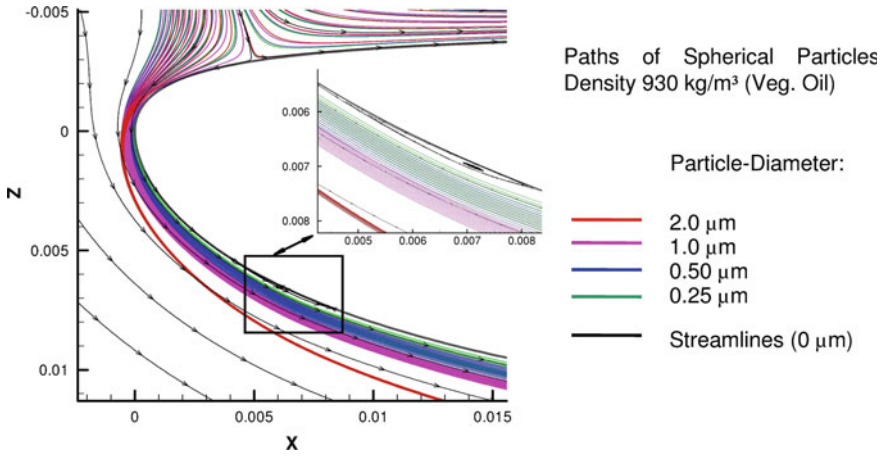


Fig. 2.5 Particle path around the airfoil nose in dependence on the size of the particle [30]

persist in the wall region of the laminar boundary layer and in the separation bubble (Fig. 2.4-bottom and Fig. 2.5).

The use of neutrally buoyant or lighter-than-air particles is a possible approach to solve the problem of tracers depletion in the core of vortices. The application of HFSB in a delta-wing vortex shows that these tracers persist (or even accumulate, Fig. 2.3-bottom right) in the vortex core due to their weight distribution from lighter-than-air to heavier-than-air [8]. The same tracers, instead, cannot solve the problem in vicinity of solid walls as the bubbles collapse when entering in contact with the solid wall.

2.1.4 Brownian Motion

When seed particles smaller than one micrometer are used for the analysis of liquid flows, the collective effect of collisions between the particles and a moderate number of fluid molecules is unbalanced, preventing the particle from following the flow to some degree. This phenomenon, commonly called *Brownian motion*, has two potential implications for μ PIV: one is to cause an error in the measurement of the flow *velocity*; the other is to cause an uncertainty in the *location* of the flow tracing particles. In order to fully consider the effect of Brownian motion, it is first necessary to establish how particles suspended in micro-scale flows behave.

Flow/Particle Dynamics. In stark contrast to many macroscale fluid mechanics experiments, the hydrodynamic size of a particle (a measure of its ability to follow the flow based on the ratio of inertial to drag forces) is usually not a concern in microfluidic applications because of the large surface to volume ratios at small length scales. As described in Sect. 2.1.1, a simple model for the response time of a

particle subjected to a step change in local fluid velocity can be used to gauge particle behavior. The latter is based on a simple first-order inertial response to a constant flow acceleration (assuming Stokes flow for the particle drag).

Considering typical μ PIV experimental parameters of 300 nm-diameter polystyrene latex spheres immersed in water, the particle response time would be 10^{-9} s. This response time is much smaller than the time scales of any realistic liquid or low-speed gas flow field.

In the case of high-speed gas flows, the particle response time may be an important consideration when designing a system for microflow measurements. For example, a 400 nm particle seeded into an air micronozzle that expands from sonic at the throat to Mach 2 over a 1 mm distance may experience a particle-to-gas relative flow velocity of more than 5% (assuming a constant acceleration and a stagnation temperature of 300 K). Particle response to flow through a normal shock would be significantly worse. Another consideration in gas microchannels is the breakdown of the no-slip and continuum assumption as the particle Knudsen number Kn_p , defined as the ratio of the mean free path of the gas to the particle diameter, approaches (and exceeds) one. For the case of the slip-flow regime ($10^{-3} < \text{Kn}_p < 0.1$), it is possible to use corrections to the Stokes drag relation to quantify particle dynamics [2]. For example, a correction offered by MELLING [42] suggests the following relation for the particle response time.

$$\tau_p = (1 + 2.76\text{Kn}_p) \frac{d_p^2 \rho_p}{18\mu} \quad (2.8)$$

Particle velocity fluctuations induced by Brownian effects. The effect of the Brownian motion on the accuracy of flow measurements in μ PIV has been investigated in the past years [55]. An in-depth consideration of the phenomenon of Brownian motion is necessary to completely explain its effects in μ PIV. Brownian motion is the random thermal motion of a particle suspended in a fluid [51]. The motion results from collisions between fluid molecules and suspended microparticles. The velocity spectrum of a particle due to the Brownian motion includes contributions at frequencies too high to be fully resolved and is commonly modeled as Gaussian white noise [67]. A quantity more readily characterized is the particle's average displacement after many velocity fluctuations. For time intervals Δt much larger than the particle inertial response time, the dynamics of Brownian displacement are independent of inertial parameters such as particle and fluid density, and the mean square distance of diffusion is proportional to $D\Delta t$, where D is the diffusion coefficient of the particle. For a spherical particle subject to Stokes drag law, the diffusion coefficient D was first given by EINSTEIN [14] as:

$$D = \frac{KT_a}{3\pi\mu d_p} \quad (2.9)$$

where d_p is the particle diameter, K is Boltzmann's constant, T_a is the absolute temperature of the fluid, and μ is the dynamic viscosity of the fluid. The random

Brownian displacements cause particle trajectories to fluctuate about the deterministic pathlines of the fluid flow. In the assumption of steady flow regime over the time of measurement and that the local velocity gradient is small, the imaged Brownian particle motion can be considered a fluctuation about a streamline that passes through the particle's initial location. An ideal, non-Brownian (i.e., deterministic) particle following a particular streamline for a time period Δt exhibits a displacement of:

$$\Delta X = U \Delta t$$

where U is the X component of the time-averaged, local fluid velocity. The relative error, ε_X incurred as a result of imaging the Brownian particle displacements in a two-dimensional measurement of the x component of particle velocity, is given as:

$$\varepsilon_X = \frac{\sigma_X}{\Delta X} = \frac{1}{U} \sqrt{\frac{2D}{\Delta t}} \quad (2.10)$$

This Brownian error establishes a lower limit on the measurement time interval Δt since, for shorter times, the measurements are dominated by uncorrelated Brownian motion. These quantities (ratios of the root mean square (rms) fluctuation-to-average velocity) describe the relative magnitudes of the Brownian motion and will be referred to here as Brownian intensities.

Particle Position Error. In addition to the flow velocity measurement error associated with particle displacement measurements, the Brownian motion incurred during the exposure time t_{exp} may also be important in determining the particle location, especially for slow flows with long exposures and small tracer particles. For example, a 50 nm particle in water at room temperature will have a displacement uncertainty of $\varepsilon_{\text{rms}} = 300$ nm if imaged with a 10 ms exposure time. For this particle image, the Brownian displacements projected into the image plane during the time of exposure are on the order of the image size estimated by Eq. (2.8) (given the best available far-field, visual optics with a numerical aperture of 1.4). This random displacement during image exposure can increase the uncertainty associated with estimating the particle location. For low velocity gradients, the centroid of this particle image is an estimate of the average location of the particle during the exposure. This particle location uncertainty is typically negligible for exposure times where the typical Brownian displacement in the image plane is small compared to the particle image diameter or a value of the diffusion time $d_p^2/(4DM^2)$ much less than the exposure time. For the experimental parameters mentioned above, $d_p^2/(4DM^2)$ is 300 ms and the exposure time is 5ns for a typical Nd:YAG laser.

2.1.5 Light Scattering Behavior

In this section, some of the most important characteristics of light scattered by tracer particles will be summarized. Since the obtained particle image intensity and there-

fore the contrast of the PIV recordings is directly proportional to the scattered light power, it is often more effective and economical to increase the image intensity by properly choosing the scattering particles than by increasing the laser power. In general, the light scattered by small particles is a function of the particle's size, shape, orientation and the ratio of the refractive indices of the particles and the surrounding medium. Furthermore, the light scattering also depends on polarization and observation angle. For spherical particles with diameters d_p larger than the wavelength of the incident light λ , Mie's scattering theory can be applied. A detailed description and discussion is given in the literature [26]. According to MELLING [43], a convenient measure of the (spatially integrated) light scattering capability is the scattering cross section C_s , defined as the ratio of the total scattered power P_s to the laser intensity I_0 incident on the particle:

$$C_s = \frac{P_s}{I_0} .$$

Figure 2.6 shows the variation of C_s as a function of the ratio of the particle diameter d_p to the wavelength of the incident light λ , for spherical particles with a refractive index $n=1.6$ surrounded by air. For aerodynamic investigations typical particle diameters are $d_p = 1 \mu\text{m}$ and the typical wavelength used for illumination is $\lambda = 532 \text{ nm}$. The steep slope for $d_p/\lambda < 1$ in Fig. 2.6 corresponds to the Rayleigh-scattering regime and the scattering cross section for values $d_p/\lambda > 1$ corresponds to the Mie-scattering regime.

Table 2.2 compares approximate values for the scattering cross section for different oil particles in air in more detail. These examples indicate clearly the enormous difference between the light scattering cross sections of particles of diameter $0.5 \mu\text{m} - 1.0 \mu\text{m}$ which are typical seeds for PIV experiments in air. Due to the strong reduction of light scattering of particles in the Rayleigh regime ($d_p < 0.5 \mu\text{m}$) a proportional increase of laser energy is required to sufficiently expose the detector. This has to be kept in mind when discussing the effective particle diameters, especially

Fig. 2.6 Light scattering cross section as a function of the particle size d_p [43]

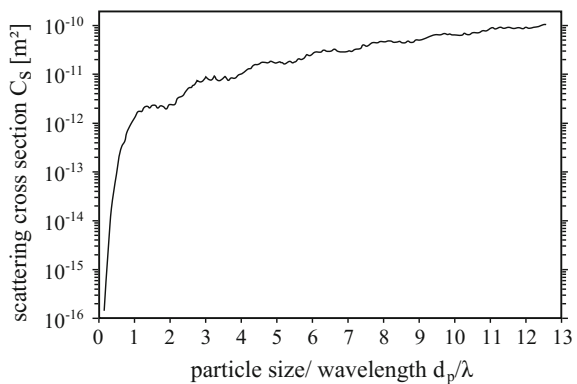


Table 2.2 Approximate scattering cross section for different oil particles in air

Particle diameter d_p (μm)	Scattering cross section CS [m^2]
1.0	$\approx 10^{-12}$
0.5	$\approx 10^{-12}$
0.2	$\approx 10^{-13}$
0.125	$\approx 10^{-14}$

Fig. 2.7 Light scattering by a $1 \mu\text{m}$ oil particle in air

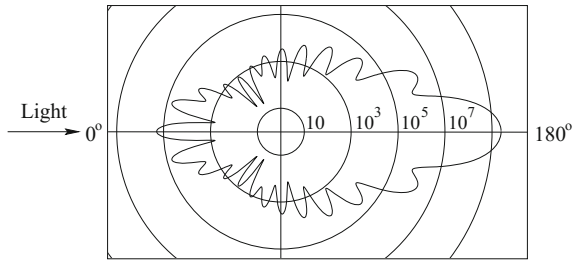
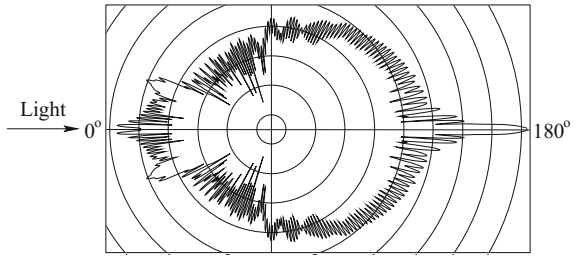


Fig. 2.8 Light scattering by a $10 \mu\text{m}$ oil particle in air. Intensity scales as in Fig. 2.7



for the seeding of gaseous flows, and will be further discussed in the following section.

Figures 2.7 and 2.8 show the polar distribution of the scattered light intensity for oil particles of different diameters in air with a wavelength λ of 532 nm according to Mie’s theory. The intensity scales are displayed in logarithmic scale plotted so that the intensity for neighboring circles differ by a factor of 100. The Mie scattering can be characterized by the normalized diameter, q , defined by:

$$q = \frac{\pi d_p}{\lambda} .$$

If q is larger than unity, approximately q local maxima appear in the angular distribution over the range from 0° to 180° . For increasing q the ratio of forward to backward scattering intensity will increase rapidly.

In case of stereoscopic or 3D PIV, the camera arrangement can be done in forward configuration to maximize the signal. However, in case of 2C2D PIV the recording must be performed at 90° to avoid perspective errors and uncertainties due to

unfocused particle images as a result of the limited depth of focus of the imaging system, see Sect. 6.1. In general, the light scattered paraxially (i.e. at 0° or 180°) from a linearly polarized incident wave is linearly polarized in the same direction and the scattering efficiency is independent of polarization. In contrast, the scattering efficiency for most other observation angles strongly depends on the polarization of the incident light. Furthermore, for observation angles in the range from 0° to 180° , the polarization direction can be partially turned. This is particularly important if polarization-based image separation is applied. Therefore, such a technique only works reliably for certain particles, for example $1\ \mu\text{m}$ diameter oil particles in air.

Besides the clear tendency of the scattered light intensity to increase with increasing particle diameter, Figs. 2.7 and 2.8 make clear that the function of the light intensity versus particle diameter is characterized by rapid oscillations, if only one certain observation angle is taken into account. Consequently, particle images of high intensity do not necessarily mean that the particle is located at the center of the measurement volume. Hence, relating the out-of-plane particle displacement in a light sheet with known intensity profile by the variation of the image intensity is usually not feasible. When averaging over a range of observation angles, which is determined by the observation distance and the recording lens aperture, the intensity curve is smoothed considerably reducing the influence of the effects discussed above. The average intensity roughly increases with q^2 and the scattering efficiency strongly depends on the ratio of the refractive index of the particles to that of the fluid. Since the refractive index of water is considerably larger than that of air, the scattering of particles in air is at least one order of magnitude more powerful compared to particles of the same size in water. Therefore, much larger particles have to be used for water flow experiments, which can mostly be accepted since the density matching of particles and fluid is usually quite good, which reduces the velocity lag. Thus tracer particles used for PIV experiments in water typically have particle diameters in the range between $10\ \mu\text{m}$ and $30\ \mu\text{m}$. In Figs. 2.9, 2.10 and 2.11, the normalized scattered intensity of different diameter glass particles in water according to the Mie theory are shown at $\lambda = 532\ \text{nm}$.

It can be seen from all Mie scattering diagrams that the light is not blocked by the small particles, but spreads in all directions. Therefore, for a large number of particles inside the light sheet, massive multiscattering will occur. In such a case the light imaged by the recording lens is not only due to direct illumination, but

Fig. 2.9 Light scattering by a $1\ \mu\text{m}$ glass particle in water

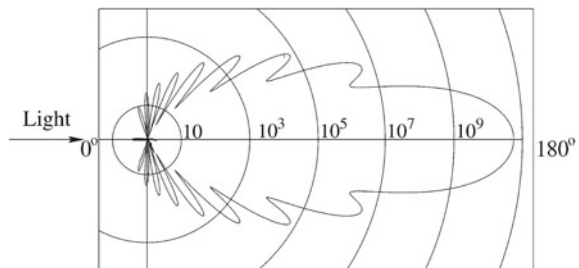


Fig. 2.10 Light scattering by a $10\ \mu\text{m}$ glass particle in water. Intensity scales as in Fig. 2.9

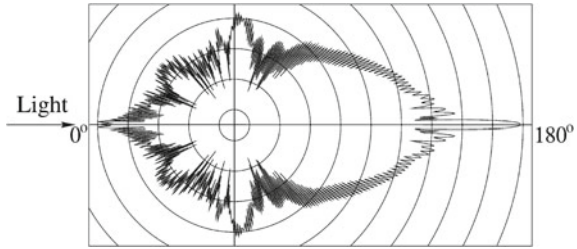
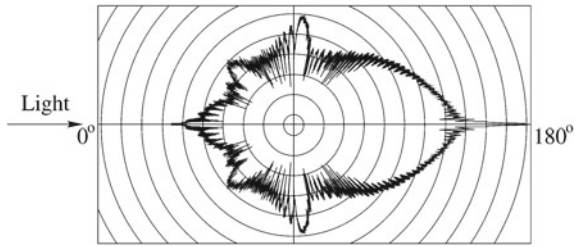


Fig. 2.11 Light scattering by a $30\ \mu\text{m}$ glass particle in water. Intensity scales as in Fig. 2.9



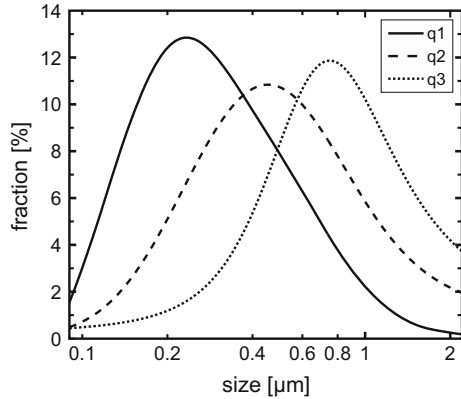
also due to portions of light scattered by many particles. In the case of heavily seeded flows, this considerably increases the intensity of individual particle images, because the intensity of light directly received from the particle – at 90° to the incident illumination – is orders of magnitude smaller than that received via multi-scattering, which involves much stronger forward scattering.

One interesting consequence is that not only larger particles can be used to increase the scattering efficiency but also a larger particle density. However, two problems limit this effect from being intensively used. First, the background noise and therefore the noise on the recordings will increase significantly. Second, if polydisperse particles (i.e. particles of different sizes) are used, it is not certain whether the number of visible particles has been increased by simply increasing the number of very large particles. Since images of larger particles dominate the results of PIV evaluation in such a case, estimating the effective particle size and the corresponding velocity lag will be affected by large uncertainties.

2.1.6 Effective Size of Polydisperse Particles

Interpreting results of size measurements of polydisperse particles requires an understanding of the measurement technique used and of the way in which the results are presented. Results can be depicted in various ways: some authors report only the size indicated by the peak of the frequency distribution, while others provide more details of different particle size distributions. In PIV literature the peak sizes are most frequently reported. However, their relevance is questionable. This - but also the char-

Fig. 2.12 Three representations of a Laskin nozzle atomized DEHS particle size distribution; solid line: distribution of length (q_1), dashed line: distribution of area (q_2), dotted line: distribution of volume (q_3)

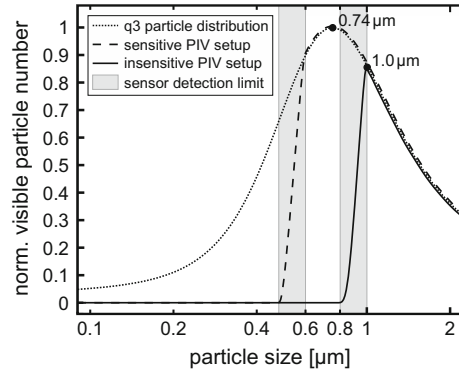


acteristics of the different weighted size distribution diagrams - will be discussed in more detail in the following.

The peak of the frequency distribution identifies the particle size most commonly found in the distribution as measured by the particle size analyzer. It can be quite different from the particle size most commonly imaged by the PIV-system, because of the different optical designs of both systems. The values also vary depending on whether the measured frequency distribution is weighed by volume, surface or is just the number of the particles. Figure 2.12 for example depicts three representations of the same size distribution of DEHS particles atomized by Laskin nozzles: the number frequency (or distribution of length), the surface frequency (or distribution of area) and the volume frequency (or distribution of volume). It can be seen that peak values of the three representations (q_1 , q_2 , q_3) of the same polydisperse particle sample differ vastly. Most of the literature found on PIV particles showing the volume distribution report a peak at approximately $1 \mu\text{m}$ or slightly below. Articles dealing with applications sometimes state that the particles are approximately $1 \mu\text{m}$ without mentioning, if this is the peak value, the median, or the mean value and what type of frequency distribution is considered. Very low values indicate the use of the peak of the number frequency instead of for example the volume frequency. The most adequate representation for PIV from a theoretical viewpoint is the distribution of area, as the visibility of the relevant larger particles increases with the scattering cross section according to the Mie-scattering theory as described earlier. However, the distribution of volume frequently delivers more realistic values as it emphasizes the large particles even more. The justification for why that can be important is given in the following.

To a different extent the three types of weighted frequency distributions do neglect the important issue that the visible particle size of a polydisperse distribution depends on the optical setup and electronic configuration of the camera used for PIV imaging. Closing the aperture of the imaging lens can, for example, increase the velocity lag of the imaged particles, because smaller particles become undetectable. Similar effects are observed for a variation of the noise and sensitivity of the camera and the intensity

Fig. 2.13 Effective (q_3) particle size distributions for identical particles recorded with different PIV setups



of the laser illumination, which differs largely along and across the light sheet. Figure 2.13 depicts a computation of the volume weighted particle size distribution (q_3) (dashed line in Fig. 2.12) and its variation due to different sensor detection limits. This effect will become even larger when comparing (q_1) and (q_2) peak values with realistic values of limited systems. The corresponding curves and their peak positions depicted in Fig. 2.13 illustrate the shift of the particles' characteristic size when recording with PIV systems of different sensitivities.

We can therefore conclude three simple, but frequently neglected facts:

- Firstly, particles with small mean diameters can be used only if the optical sensitivity (laser power and camera sensitivity) is such to be able to record images of these small particles (scattering performance drops drastically with decreasing particle diameters as mentioned above).
- Secondly, larger particles dominate the PIV signal and in turn the measurement fidelity. The reduction of larger particles is therefore at least as important as the generation of small particles, when the velocity lag needs to be reduced.
- Thirdly, a quantification of the measurement error due to velocity lag of poly-dispersed particles cannot be determined easily with a calculation based on the particles most frequent size, but requires a more complex procedure, for instance based on in situ measurements with the same particles and optical settings.

The light scattered by larger tracers like helium filled soap bubbles has the main advantage of being several orders of magnitude more intense than that of micron droplets. Recent experiments report a factor 10^4 for HFSB tracers of $300\ \mu\text{m}$ compared to one micron fog droplets. Nevertheless, other effects need to be considered: the particle is imaged through two reflection points (glare points), symmetrically offset from the center of the bubble. This effect creates an ambiguity regarding the exact position of the particle. In large-scale experiments, however, the distance between glare points may fall below the imaging diffraction limit, which mitigates the above problem.

2.2 Particle Generation and Supply

The challenges faced when generating and supplying particles to flows differ largely depending on the fluid medium and the test facilities used. In some cases adequate particles can just be purchased and for example stirred into the liquid under investigation, in other cases powerful particle generators and dedicated equipment for particle supply have to be used. The aim for all PIV measurements is to have a maximum number of particle images equally distributed over the whole area of interest. Areas with too many particle images that cannot be identified separately anymore, will lead to the same gaps in the evaluated velocity field as areas with an insufficient number of particle images. The strobe illumination typically used for PIV emphasizes potential inhomogeneities in seeding density and therefore increases the effort required for adequate particle supply.

2.2.1 Seeding of Liquids

Descriptions of seeding particles and their characteristics have been given in many scientific publications. In contrast to that, little information can be found in the literature on how to practically supply the particles into the flow under investigation. For some cases, the seeding can easily be realized or is already and naturally present in the flow field. The use of natural seeding is sometimes acceptable, if enough visible particles with sufficient following behavior are naturally present to act as tracers for PIV. In almost all other cases it is required to add tracers to achieve sufficient image contrast and to control the particle size. For most liquid flows, seeding can easily be done by suspending solid particles into the fluid and mixing them to ensure a homogeneous distribution.

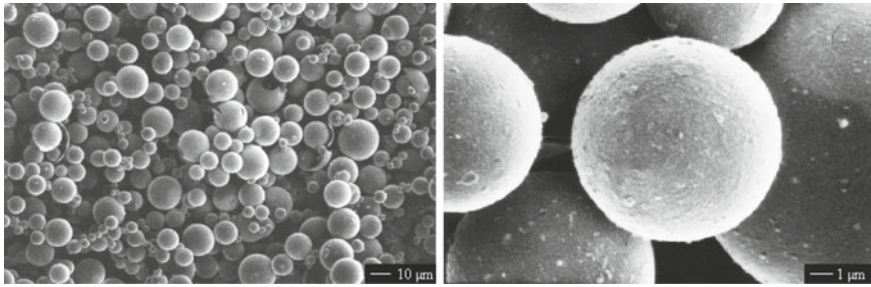
A number of different particles which can be used for flow visualization, LDV, and PIV are listed in Table 2.3 for liquid and in Table 2.4 for gas flows. For experiments in oil and water flows, hollow coated glass spheres of approximately 10 μm diameter work very well, as shown in Fig. 2.14 for two different magnifications. They offer good scattering efficiency and the velocity lag is small enough for many applications.

Table 2.3 Seeding materials for liquid flows

Type	Material	Mean diameter in μm
Solid	Polystyrene	10–100
	Aluminum flakes	2–7
	Hollow glass spheres	10–100
	Granules for synthetic coatings	10–500
Liquid	Different oils	50–500
Gaseous	Oxygen bubbles	50–1000

Table 2.4 Seeding materials for gas flows

Type	Material	Mean diameter in μm
Solid	Polystyrene	0.5–10
	Alumina Al_2O_3	0.2–5
	Titania TiO_2	0.1–5
	Glass micro-spheres	0.2–3
	Glass micro-balloons	30–100
	Granules for synthetic coatings	10–50
	Diocetylphthalate	1–10
	Smoke	< 1
Liquid	Different oils	0.5–3
	Different propylene glycols	0.5–1.5
	Glycerine-water mixture	0.5–2.0
	Di-ethyl-hexyl-sebacate (DEHS)	0.5–1.5
	Helium-filled soap bubbles	200–3000

**Fig. 2.14** Micrographs of silver coated hollow glass spheres: $\times 500$ and $\times 5000$

From a practical standpoint, particles slightly lighter (few percent) than the liquid will tend to accumulate on the upper edge of the facility (sometimes a free surface). In case of large water tanks or water channels, this gives an advantage in terms of cleaning procedures. Another approach is to use particles that slowly sink and will deposit on the bottom floor of the facility.

Tracer particles small compared to λ . When decreasing the size of the observation field and increasing the optical resolution of the investigation for examples by microscopic recording, the tracer particle diameters obviously have to be decreased as well. In the Rayleigh scattering regime, where the particle diameter d_p is much smaller than the wavelength of light, $d_p \ll \lambda$, the amount of light scattered by a particle varies as d_p^6 [3]. Since the diameter of the flow-tracing particles must be small to ensure that the flow being measured is not disturbed, they must frequently be of the order of 50–100 nm. Their diameters are then 1/10–1/5 of the wavelength of green light, $\lambda_{\text{green}} = 532 \text{ nm}$, and are therefore approaching the Rayleigh scattering

criteria. This places significant constraints on the image recording optics, making it extremely difficult to record particle images with sufficiently high illumination intensity.

One solution to this imaging problem is to use epi-fluorescence imaging to record light emitted from fluorescently-coated particles. This method requires a wavelength-specific long-pass filter being part of the recording optics in order to remove the background light, leaving only the light fluoresced by the particles. This technique has frequently and successfully been used in liquid flows to record images of 200 to 300 nm-diameter fluorescent particles [41].

2.2.2 *Seeding of Gases*

In gas flows, the increased difference in density between the gaseous bulk fluid and the particles can result in a significant velocity lag. Health considerations are also more important since the experimentalists may inhale seeded air, for example in wind tunnels with open test sections. Theatrical fog commonly used is not easy to handle because its liquid droplets tend to evaporate and thereby change size rather quickly. Solid particles are difficult to disperse and tend to agglomerate. The particles often must be injected into the flow close to the location where the gaseous medium enters the test section. The injection has to be done without disturbing the flow, but in a way and at a location that ensures homogeneous distribution of the tracers. Since the existing turbulence in many test set-ups is not strong enough to distribute the particles sufficiently, the particles have to be supplied to a large number of locations in the flow field simultaneously. Distributors, like rakes consisting of many small pipes with a large number of tiny holes, are often used. Therefore, particles which can be transported inside small pipes are required.

A number of techniques are used to generate and supply particles for seeding gas flows [28, 31, 32, 42–44]. Dry powders can be dispersed in fluidized beds or by air jets. Liquids can be evaporated and afterwards precipitated in condensation generators, or liquid droplets can directly be generated in atomizers. Atomizers can also be used to disperse solid particles suspended in evaporating liquids [69, 70], or to generate tiny droplets of high vapor pressure liquids (e.g. oil) that have been mixed with low vapor pressure liquids (e.g. alcohol) which evaporate prior to entry in the test section. Condensation and smoke generators are frequently used for flow visualization and LDV in wind tunnels.

While fluorescently-labeled particles are well-suited for micro-PIV studies in liquid flows, they are not readily applicable to most gaseous flows for several reasons. Commercially available fluorescently-labeled particles are generally available as aqueous suspensions. A few manufacturers offer dry fluorescent particles, but with larger diameters, $>7\ \mu\text{m}$. In principle, the particle-laden aqueous suspensions can be dried, and the particles subsequently suspended in a gas flow, but this often proves to be problematic because the electrical surface charge that the particles easily acquire causes them to stick to walls and windows of the facilities and to each

Fig. 2.15 Oil seeding generator

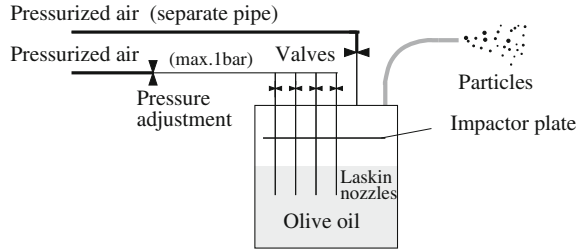
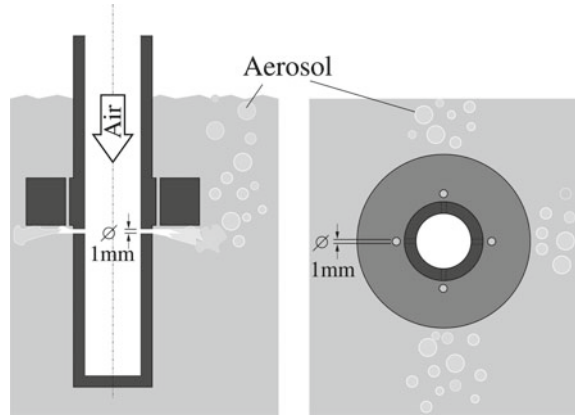


Fig. 2.16 Sketch of a Laskin nozzle



other. Furthermore, the emission decay time of many fluorescent molecules is on the order of several nanoseconds, which may cause streaking of the particle images for high-speed flows.

Droplet seeding of air flows. For most of the PIV measurements in air flows, Laskin nozzle generators supplied with oil have been used. These particles can offer the advantage of being less harmful than most solid particles, staying in air at rest for hours and not changing in size significantly under various conditions. In recirculating wind tunnels, they can be used for a global seeding of the complete tunnel volume or for a local seeding of a stream tube by a seeding rake with a few hundred tiny holes. Technical descriptions of those atomizers are given below.

A typical aerosol generator consists of a closed cylindrical container with two air inlets and one aerosol outlet (Fig. 2.15). The present example features four air supply pipes – mounted at the top – which dip into vegetable oil or DEHS (Di-ethyl-hexyl-sebacate) inside the container. They are connected to one air inlet by a tube and each one has a valve. The pipes are closed at their lower ends (see detail in Fig. 2.16). Four Laskin nozzles, 1 mm in diameter, are equally spaced on the circumference of each pipe [13]. Experience shows that the manufacturing of Laskin nozzles require high precision engineering and good control of form and position tolerances as well as the avoidance of burr at the edge of the small holes. Nozzles produced with less care produce particle sizes that vary strongly with pressure levels and may even result in

flow reversal in the vertical liquid holes [31]. A horizontal circular impactor plate is placed inside the container as shown in Fig. 2.15, so that a small gap of about 2 mm is formed between the impactor plate and the inner wall of the container. The second air inlet and the aerosol outlet are connected directly to the top part of the container. Two gauges measure the pressure on the inlet of the nozzles and inside the container, respectively. Compressed air with 0.5–1 bar overpressure with respect to the outlet pressure is applied to the Laskin nozzles and creates air bubbles within the liquid. Due to the shear stress induced by the tiny air jets, small droplets are generated and carried inside the bubbles towards the oil surface where they are released by the bursting bubbles. Big particles are retained by the impactor plate; small particles escape through the gap and reach the aerosol outlet. The number of particles can be controlled by the four valves at the nozzle inlets. The particle concentration can be decreased by an additional air supply via the second air inlet.

The mean size of the particles generally depends on the type of liquids being atomized, but is only slightly dependent on the operating pressure of the nozzles and other parameters as shown in detail in [31]. Vegetable oils and DEHS are the most commonly used liquids, since vegetable oil droplets are believed to be less harmful than many other particles and DEHS offers the advantage to evaporate in the long term. However, any kind of seeding particles which are toxic or cannot be dissolved in water should not be inhaled. This is the reason why mixtures of propylene glycols and glycerin atomized with dedicated pneumatic particle generators become more common (Fig. 2.17). Adequate results can be obtained when calibrated nozzles are used (Fig. 2.18). This leads to narrow size distributions at pressure levels between 0.5 bar and 1.5 bar. Figure 2.19 depicts the particle size distributions (volume frequency q_3) for a propylene glycol mixtures and DEHS atomized with calibrated nozzles at 1.0 bar overpressure. Seeding fluids from propylene glycol in food grade quality are commercially available. They can be mixed with water in order to reduce the effective droplet size (Fig. 2.18).

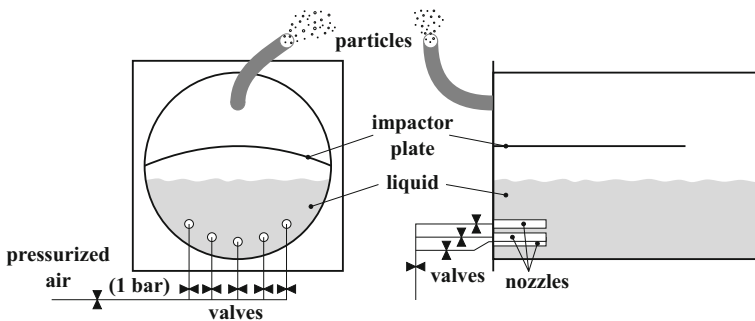


Fig. 2.17 Seeding generator designed for various liquids (glycol, glycerin, DEHS)

Fig. 2.18 Sketch of calibrated nozzles (CN) for various liquids

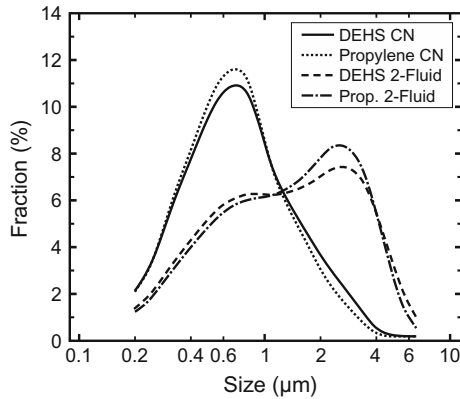
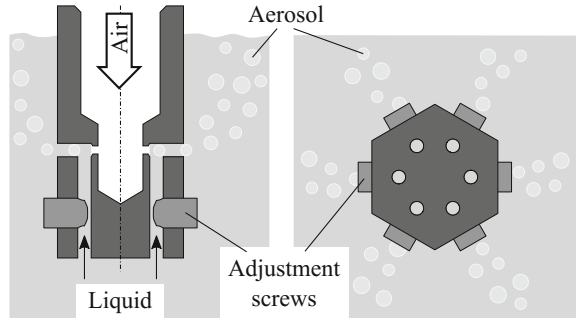


Fig. 2.19 Particle size distributions (q_3) for a PIV seeding liquid from a propylene glycol mixture (PIVLight) and DEHS atomized with a calibrate nozzle at 1.0 bar (left) and a 2-fluid nozzle at 1.4 bar (right)

Atomizers with a combination of two-fluid nozzles have been developed that offer the advantage of generating larger particles and to allow a variation of particle sizes under certain pressure conditions (Fig. 2.20). The same flow field can then, for example, either be recorded at a high spatial resolution with a small field of view with small particles or with lower spatial resolution with large particles. The larger droplets used in the latter case require longer distances to adapt to fluid flow variations, but offer the advantage of giving enough scattering performance for larger fields of view.

Powder-based seeding of air flows. In cases where the stability of the seeding material cannot be guaranteed due to increased temperatures or reactive environments, droplet-based seeding is no longer feasible. In these cases, seeding based on solids must be used. Metal oxide powders are especially well suited for this purpose due to their inertness, high melting point, and rather low cost. Tables 2.4 lists titanium

Fig. 2.20 Sketch of a two-fluid nozzle generator for larger particles (CTS1000 from Seika Digital Imaging [DC2.2])

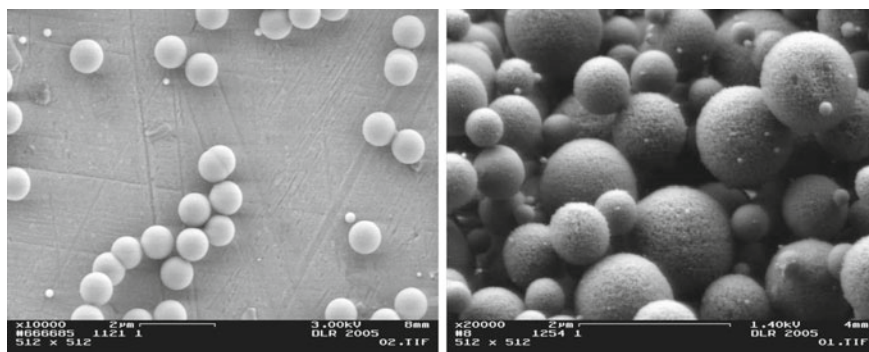
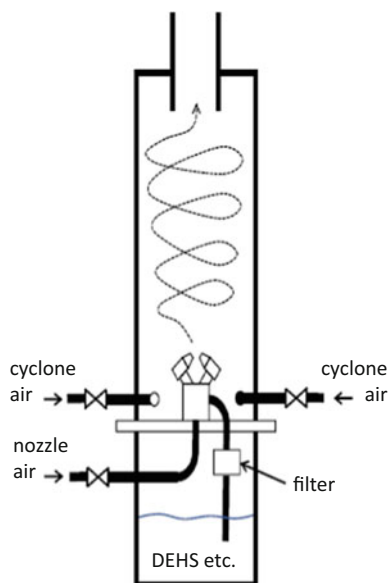


Fig. 2.21 Micrographs of 800 nm mono-disperse SiO_2 spheres (left), porous SiO_2 spheres (right)

dioxide, alumina, and silica powders, with corresponding micrographs shown in Figs. 2.21 and 2.22.

A controlled dispersion of these powders is more challenging than for liquid materials, as the powders have a strong tendency to form agglomerates, especially for small grain sizes in the sub-micron range. The seeding device, therefore, has to either break up the agglomerates or remove them from the aerosol prior to delivery into the facility such as through the use of a cyclone separator [60, 66].

Another approach to de-agglomerate the bulk seed material was originally proposed by WERNET & WERNET [69] and recently updated [70]: the inter-particle forces responsible for the agglomeration can directly be influenced by controlling the acid-

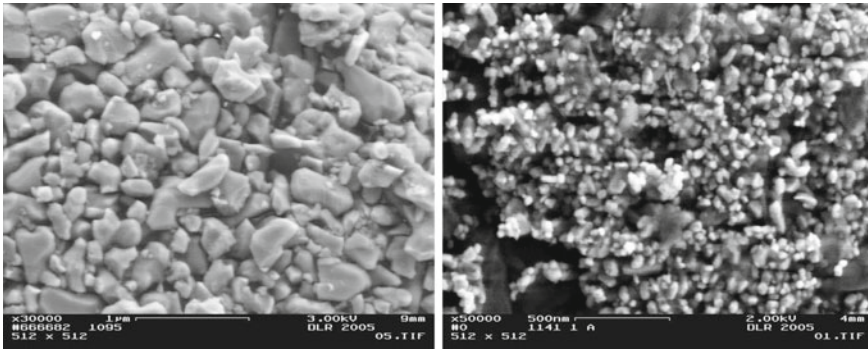


Fig. 2.22 Left: Ground Al_2O_3 powder for seeding reactive flows [72], right: TiO_2 powder for seeding supersonic flows [60]

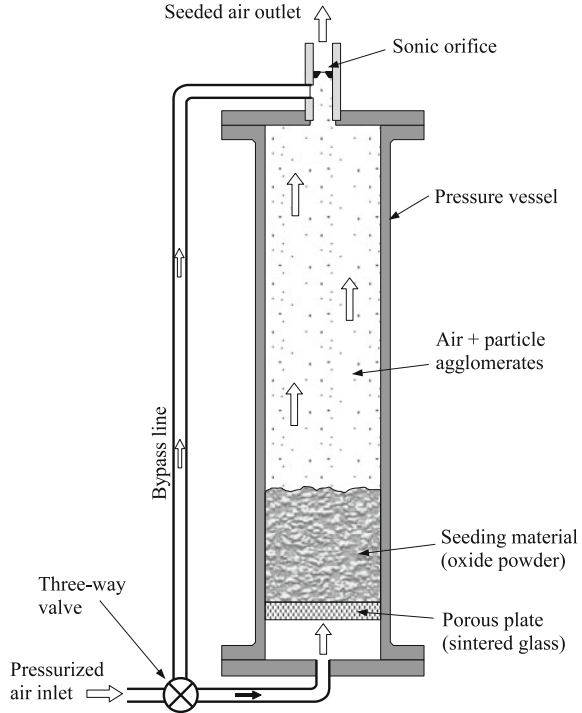
ity of liquid suspensions of the seed material. They suggest the use of alumina/water or alumina/ethanol dispersions with a pH value of 1 which can be dispersed using liquid atomization. The solid seed material remains after evaporation of the carrier liquid.

Depending on the relative mass-flow rates between seeded and unseeded flows, the use of liquid-particle suspensions is not always feasible especially when the flow is disturbed due to evaporation cooling and/or changes in the reactive chemistry. In this case, the aerosol has to be created directly from the dry powder. A common approach is to aerate the powder inside a vertical tube from below resulting in a fluidized bed. The flow rate through the seeder is chosen just large enough to fluidize the bed of particles carrying smaller particles into the region above the bed (known as *freeboard*) towards the exit orifice and from there into the facility under investigation. Figure 2.23 shows a simple fluidized bed seeding device for use in elevated pressure applications [71, 72]. This generator has two noteworthy features: the strong shear flow present in a sonic orifice at the exit serves to break up larger agglomerates. The size of this orifice is chosen to ensure sufficient flow rate to aerate the powder. The second feature is a switchable by-pass line which maintains constant mass flow rates into a test facility even when no seeding is required.

The following recommendations are given for the successful operation of fluidized bed seeders:

- The seeding powder should be kept dry, preferably by heating the material to remove excess moisture before filling the seeding device. Dry air or nitrogen should be used to operate the seeder.
- Short supply lines between seeder and facility should be used to prevent the formation of agglomerates. If possible, additional carrier air should be used to reduce the relative seeding concentrations.
- Frequent agitation of the seeding system reduces the chance of channel formation within the fluidized bed. A shaker motor attached to the seeding vessel is sufficient.

Fig. 2.23 Fluidized bed seeding device for high pressure applications



- The mechanical interaction of the seed material with small brass spheres (100 – 500 μm) added to the fluidized bed also helps to break up agglomerates. This configuration is referred to as *two-phase fluidized bed*.

Soap bubble seeding for air flows. The finite scattering efficiency of any tracer particle is usually the limiting factor when increasing the field of view (FOV) in a PIV measurement. Oil droplets with diameters of $d = 1 \mu\text{m}$ for example restrict the FOV to areas around $500 \times 400 \text{ mm}^2$ when standard Nd:YAG lasers with pulse energies of up to 300 mJ are used.

One possibility to overcome this limitation is to use larger tracer particles. Here, however, the mass of the particles is critical, since for PIV ideally neutrally buoyant particles are required. Soap bubble generators can provide neutrally buoyant particles with dimensions from 0.2 mm up to several millimeters (Fig. 2.24). They generate helium-filled soap bubbles, in which a helium filling of the particles compensates for the weight of the soap layer. Different possibilities to generate such bubbles are discussed in detail in [38]. An orifice type nozzle, as depicted in Fig. 2.25, can be used to generate smaller bubbles with only 0.1–0.3 mm diameter. Miniaturized generators have been recently developed based on the same principle as that depicted in Fig. 2.26, which can more easily be installed on seeding rakes inside wind tunnels.

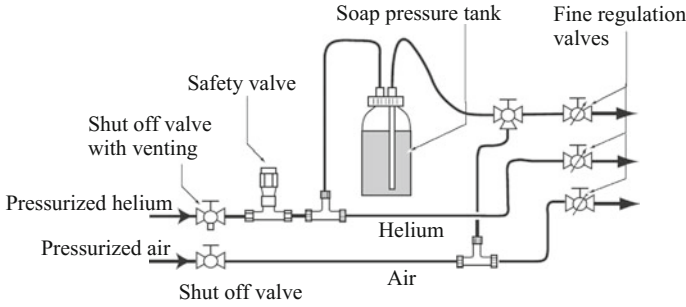
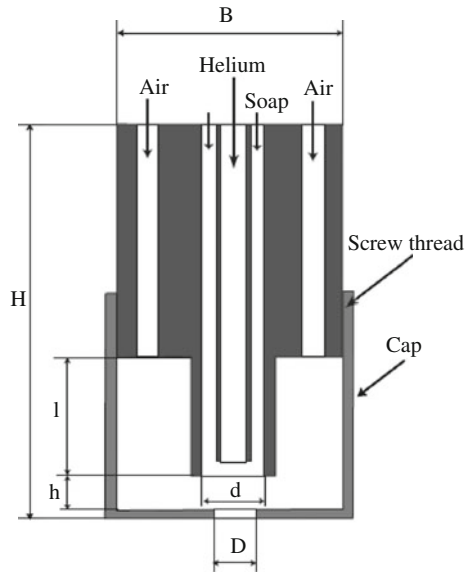


Fig. 2.24 Scheme of the air, helium, and soap supply for a bubble generator [38]

Fig. 2.25 Schematic drawing of an orifice type nozzle for the generation of *He*-filled soap bubbles [38]. Approximate dimensions: $B = 15\text{ mm}$; $H = 40\text{ mm}$; $l = 12\text{ mm}$; $h = 1.5\text{ mm}$; $d = 3\text{ mm}$; $D = 0.8\text{ mm}$



Gaseous helium is blown through a central pipe, which is mounted coaxially into a second pipe where the flow of bubble fluid solution (BFS) is driven at a predefined flow rate. Air flow surrounds the soap film released from the inner ducts and transports it through a small orifice where bubbles regularly detach. A schematic illustration is given in Fig. 2.26. A sketch of the complete HFSB- system is shown in Fig. 2.27.

The generation of neutrally buoyant bubbles relies on a proper adjustment of helium pressure, air-pressure, BFS flow rate, and the distance between nozzle cap and tubes, h (see Fig. 2.25). The BFS typically consists of a mixture of water, glycerin, and soap. Experiments with HFSB in wind tunnels have shown that sub-millimeter bubbles can respond to variations in the flow velocity with a time response in order of $10\ \mu\text{s}$ [57].

Fig. 2.26 Schematic principle of helium filled soap bubbles formation from a miniature generator

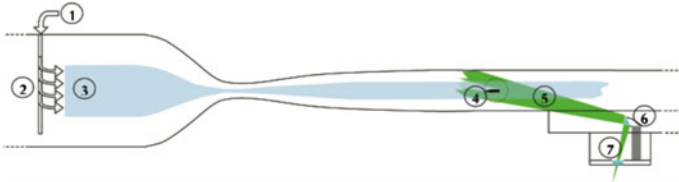
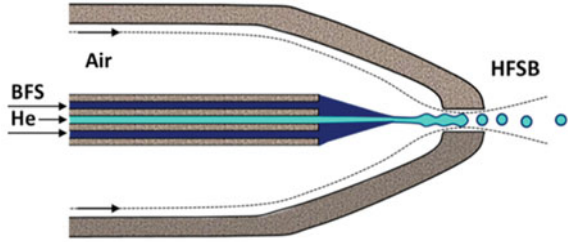


Fig. 2.27 Schematic of the seeding distribution in a blow-down supersonic wind tunnel [58]

HFSB have been used for PIV measurements of low speed convective flows for very large observation areas [4] and for large-volume measurements with tomographic PIV [34]. More recently, low-speed wind tunnel measurements with tomographic PIV have been reported by [57, 59].

2.2.3 Seeding Distribution in Wind Tunnels

Uniform seeding concentration in the flow region of interest is a necessary condition for the reliable analysis of the particles image motion. Several approaches can be followed to introduce the tracers. The approach is much dependent upon the type of flow facility. A brief discussion is given here for the category of wind tunnels.

Closed-Loop (Göttingen Type) Aerodynamic Wind Tunnels

The most common approach in these wind tunnels is that of inserting the seeding tracers downstream of the test section, generally at the position of the diffuser. This approach is simple to implement and it minimizes the aerodynamic interference of the seeding device with the air stream in the test section. Once the desired seeding

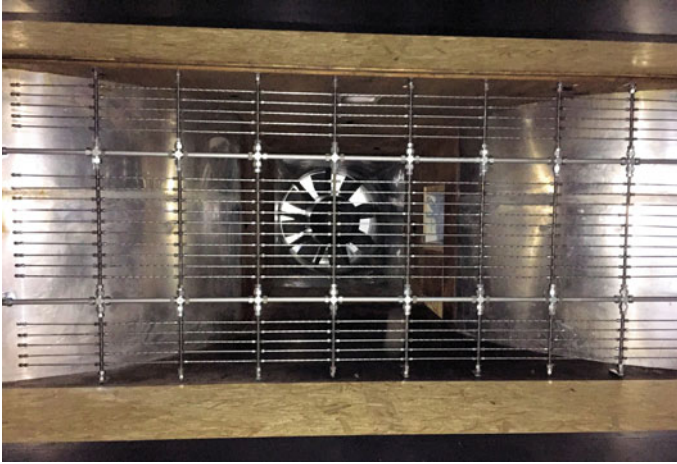


Fig. 2.28 Seeding particle distribution by a rake in the 2 m × 5 m settling chamber of an Eiffel type (open circuit) wind tunnel

concentration is reached it is sufficient to supply particles at lower rate to compensate the amount that evaporates. In this working regime the entire wind tunnel stream is seeded uniformly as a result of mixing by the fan and the turbulence in the circuit.

Open-Loop (Eiffel Type) Aerodynamic Wind Tunnels

For wind tunnels driven by a fan before settling chamber, the seeding is typically inserted upstream of the fan for better homogeneity. In case the flow is driven by a fan downstream of the test section the seeding can be inserted at the settling chamber, resulting in local seeding with less homogeneous distribution (Fig. 2.28).

Blow-Down High-Speed Wind Tunnels

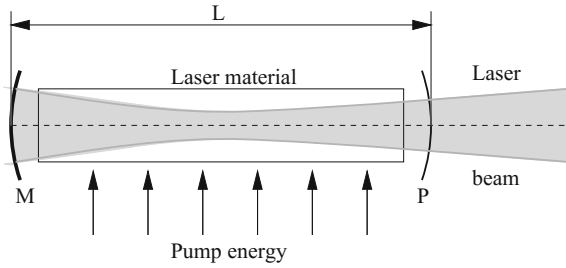
For high-speed flows the wind tunnel is often driven by a compressed air vessel, connected to the wind tunnel Laval nozzle. The seeding can be distributed with a seeding rake from the settling chamber where the flow is at low speed. Only a part of the stream is seeded (local seeding) and the level of tracers homogeneity is usually lower than for low-speed wind tunnels (Fig. 2.27).

2.3 Light Sources

2.3.1 Lasers

Lasers are widely used in PIV, because of their ability to emit monochromatic light with high energy density, which can easily be bundled into thin light sheets for

Fig. 2.29 Schematic diagram of a laser



illuminating and recording the tracer particles without chromatic aberrations. In Fig. 2.29 a typical configuration of a laser with its three main components is shown.

The laser material consists of an atomic or molecular gas, semiconductor or solid material.

The pump source excites the laser material by the introduction of electromagnetic or chemical energy.

The mirror arrangement, i.e., the resonator allows an oscillation within the laser material.

In the following we will describe the principle of gas lasers and give an overview of the lasers used in PIV.

It is well known from quantum mechanics that each atom can be brought into various energy states by three elementary kinds of interaction with electromagnetic radiation. This can be illustrated in an energy level diagram, as shown in Fig. 2.30 for a hypothetical atom with only two possible energy states. An *excited* atom at level E_2 usually drops back to the state E_1 after a very short, but not exactly defined period of time and emits the energy $E_2 - E_1 = h\nu$ in the form of a randomly directed photon (h and ν are Planck’s constant and the frequency respectively). This process is called *spontaneous emission* and shown in Fig. 2.30 (center).

However, if, on the other hand, a photon with “appropriate” frequency ν impinges on an atom, two effects are possible. Either – in the case of *absorption* – an atom in the state E_1 can receive the energy $h\nu$, that is it becomes *raised* to E_2 (Fig. 2.30, left); or the incident photon can stimulate an atom in the excited E_2 state into a specific,

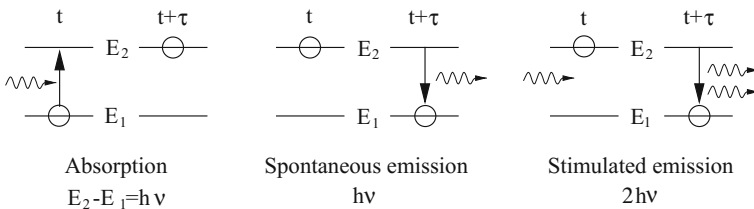


Fig. 2.30 Elementary kinds of interactions between atoms and electromagnetic radiation

non-spontaneous, transition to E_1 . Then, in addition to the incident photon, a second one is emitted in phase with the former. The impinging wave therefore is coherently amplified (*stimulated emission*, Fig. 2.30, right).

For large numbers of atoms, one of the two processes – absorption or stimulated emission – predominates. In case of population density inversion, i.e., $N_2 > N_1$ (number of atoms in excited state greater than number of atoms in ground state), stimulated emission predominates, otherwise, $N_1 > N_2$, absorption is favored.

However, in a system which consists of only two energy states, as described so far, no population inversion can be achieved, because when the number of atoms N_2 in level E_2 equals the number N_1 in level E_1 , absorption and stimulated emission are equally likely and the material will become transparent at the frequency $\nu = (E_2 - E_1)/h$. In other words, the number of transitions from the upper level E_2 to the lower level E_1 and vice versa are on average the same. Hence, at least three energy levels of the laser medium are essential to achieve population inversion. However, a three level system is not very efficient because a fraction of more than 50% of the atoms of the system had to be excited in order to amplify an impinging photon. This means that the energy needed for the excitation of this fraction is lost for the amplification. In the case of a four level laser the lower laser level E_2 does not coincide with the basic level E_1 and therefore remains unoccupied at room temperature. In this way it is easier to achieve the population inversion and a four level laser requires substantially less pumping power. This is illustrated in Fig. 2.31. If for instance state E_4 is achieved by optical pumping at frequency ν according to $h\nu = E_4 - E_1$, then a rapid non-radiative transition to the upper laser level E_3 occurs. The atoms remain in this metastable state E_3 for a relatively long interim period before they drop down to the unoccupied lower laser level E_2 .

Since the laser requiring stimulated emission can only operate if a *population inversion* is forced to take place ($N_2 > N_1$), external energy has to be transferred to the laser material because atoms usually exist in their ground state. This is achieved

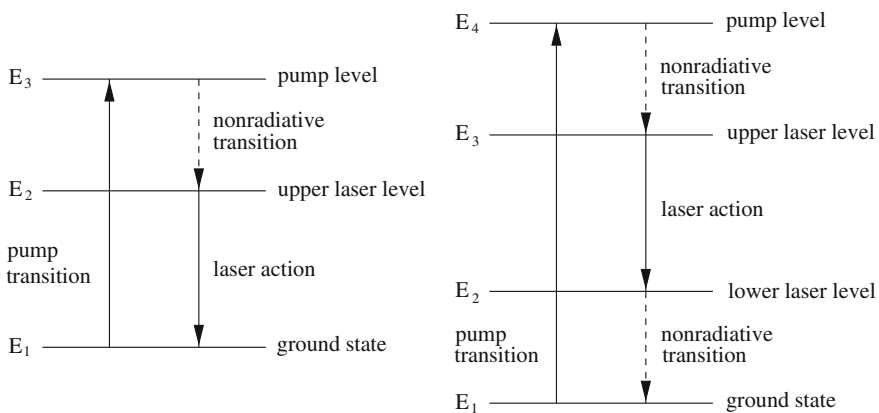


Fig. 2.31 Level diagrams of three (left) and four (right) level lasers

by different pump mechanisms depending on the kind of laser material. Solid laser materials are generally pumped by electromagnetic radiation, semiconductor lasers by electronic current, and gas lasers by collision of the atoms or molecules with electrons and ions.

As a consequence of population inversion through energy transfer by the pump mechanism spontaneous emission occurs in all directions which causes excitation of further neighboring atoms. This initiates a rapid increase of stimulated emission and therefore of radiation in a chain reaction.

In the case of a cylindrical shape of the laser material, the rapid increase of radiation occurs in a defined direction because the amplification increases with increasing length of the laser medium. Within an optical resonator (mirror arrangement) the laser material can be arranged to form an oscillator. The simplest way to achieve this is to place the material between two exactly aligned mirrors. In this case, a photon which impinges randomly on one of the mirror surfaces is reflected and amplified in the laser material again. This process will be repeated and generates an avalanche of light which increases exponentially with the number of reflections, finally resulting in a stationary process. In other words, standing waves are produced for a resonator length corresponding to the condition

$$L = \frac{m\lambda}{2n} \quad (2.11)$$

where n is the refractive index, m an integer number, and L the resonator length. Since the frequency ν according to the transition $\nu h = E_2 - E_1$ does not correspond to exactly one wavelength, but rather to a spectrum of a certain band width $\Delta\nu$ depending on the transition time τ of the process, these conditions can be fulfilled by different wavelengths λ or frequencies ν and the resonator can oscillate in many axial modes with distinct frequencies.

Consecutive modes are separated by a constant difference $\Delta\nu = c/(2Ln)$, wherein c is the speed of light. Moreover, the cross-section of the laser beam can be divided into several ranges oscillating out of phase with intermediate node lines, that is, different transverse modes can be sustained as well (see Fig. 2.32). Their occurrence depends on the resonator design and alignment. The lowest order transverse mode TEM₀₀ (TEM = transverse electric mode; index = node in X - and Y -direction) is most commonly used, because it produces a beam with uniform phase and a Gaussian intensity distribution along the beam cross-section.

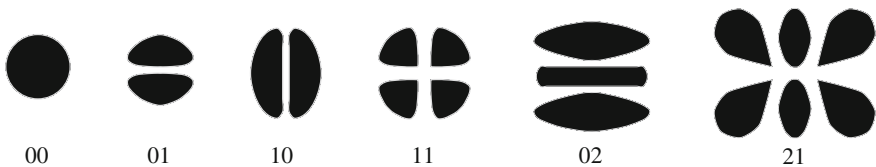


Fig. 2.32 Examples of different transverse modes

There are various types of resonators with different mirror curvatures. The confocal resonator, shown in Fig. 2.29, is particularly stable and easy to adjust. Hemispherical resonators use one planar and one concave mirror, and critical resonators use two planar mirrors. Critical resonators offer the advantage of having no beam waist inside the laser rod and therefore using its whole volume for amplification. However, they are sensitive for thermal lens effects and misalignment.

As mentioned above, different pumping mechanisms exist. In gas lasers, which are usually used for continuous operations (CW = continuous wave), free electrons are accelerated by an electrical field resulting in an excitation of the gaseous medium. The plasma tube in which the excitation takes place is closed by Brewster windows (plates tilted at the polarization angle). Therefore, these lasers emit linearly polarized light. In the case of optically pumped solid-state lasers, the light of the rod-shaped flash lamp is concentrated on the laser rod by a cylindrical mirror with an elliptical cross-section. In lasers, which basically consist of luminescence diodes, two polished, parallel surfaces work as resonator mirrors. The laser light perpendicular to the p-n junction is more divergent due to the lower aperture width.

Some of the popular lasers for PIV are briefly described below in order to provide an overview of the abilities and limitations of the different systems.

Argon-ion lasers (Ar^+ lasers $\lambda = 514, 488 \text{ nm}$) are gas lasers, similar to the He-Ne lasers described above. In argon lasers, very high currents have to be achieved for ionization and excitation. This is technologically much more complicated compared to He-Ne lasers. Typically the efficiency of these lasers is of the order of a tenth of a percent. Large versions of these lasers can supply over 100 W in the blue-green range and 60 W in the near ultraviolet range. Emission is produced at several wavelengths through the use of broadband laser mirrors. Individual wavelengths can be selected by means of Brewster prisms in the laser resonator. The individual wavelengths can be adjusted by rotating the prism. The most important wavelengths are 514.5 and 488.0 nm (green and blue). Nearly all conventional inert gas ion lasers supply TEM_{00} . Despite the extreme load on the tubes resulting from the high currents, product lives of several thousand operating hours can be achieved. Since argon lasers are frequently used for LDV measurements, they are often found in fluid mechanics laboratories. In PIV they can easily be used for low-speed water investigations.

Semiconductor lasers offer the advantage of being very compact. The laser material is typically 1 cm long and has a diameter of the order of 1 mm. The total efficiency of commercial diode laser pumped Nd:YAG and Nd:YLF systems is around 7%. Since heating is considerably reduced, these types of pumped lasers supply a very good beam quality of over 100 mW in the TEM_{00} mode during continuous operations. Diode lasers are of interest for PIV because of two reasons: The high efficiency allows the production of Nd:YLF lasers with high average and peak power needed for high-speed applications. Due to their ability to generate beams with excellent quality, semiconductor lasers can also be used as seed lasers for an improvement of the coherence length of flash lamp pumped Nd:YAG lasers for use in holographic PIV. A particularly interesting variant is the combination of a diode-pumped laser oscillator and a flash lamp pumped amplifier. Together with other optical components,

like vacuum-pinholes and phase-conjugated mirrors, this concept offers very good beam properties, but at the same time, its initial purchase costs are high.

Neodym-YAG lasers (Nd:YAG lasers $\lambda = 1064$ nm, infrared, and $\lambda = 532$ nm, and green) are the most important solid-state laser for PIV in which the beam is generated by Nd^{3+} ions. The Nd^{3+} ion can be incorporated into various host materials. For laser applications, YAG crystals (yttrium-aluminum-garnet) are commonly used. Nd:YAG lasers have a high amplification and good mechanical and thermal properties. Excitation is achieved by optical pumping in broad energy bands and non-radiative transitions into the upper laser level.

Solid-state lasers can be pumped with white light as a result of the arrangement of the atoms which form a lattice. The periodic arrangement leads to energy bands formed by the upper energy levels of the single atoms. Therefore, the upper energy levels of the system are not discrete as in the case of single atoms, but are continuous.

As already mentioned, the Nd:YAG laser is a four-level system which has the advantage of a comparably low threshold to start the stimulated emission. At standard operating temperatures, the Nd:YAG laser only emits the strongest wavelength, 1064 nm. In the relaxation mode the population inversion takes place as soon as the threshold is reached, with this threshold value depending on the design of the laser cavity. In this way, many successive laser pulses can be obtained during the pump pulse of the flash lamp. By including a quality switch (Q-switch) inside the cavity the laser can be operated in a triggered mode. The Q-switch has the effect of altering the resonance characteristics of the optical cavity. If the Q-switch is operated, allowing the cavity to resonate at the most energetic point during the flash lamp cycle, a very powerful laser pulse, the giant pulse, can be achieved. Q-switches normally consist of a polarizer and a Pockels cell (modifying the direction of polarization), which together change the quality of the optical resonator depending on the Pockels cell voltage. The Q-switched mode of operation is usually used in PIV. Although Q-switches can be used to generate more than one giant pulse out of a single resonator, PIV lasers are mostly designed as double oscillator systems (two resonators). This enables the user to adjust the separation time between the two illuminations of the tracer particles independently of the pulse strength. The beam of Q-switch lasers is linearly polarized. For PIV, and many other applications, the fundamental wavelength of 1064 nm is frequency-doubled using special crystals. Details of these KD*P crystals are provided in the next section. After separation of the frequency-doubled portion, approximately one third of the original light energy is available at 532 nm. Nd:YAG lasers are usually driven in a repetitive mode. Since the optical properties of the laser cavity change with changing temperature, good and constant beam properties will only be obtained at nominal repetition rates and flash lamp voltage. Due to thermal lensing, the beam quality which is very often poor compared to those of other laser types, decreases significantly when, for example, single pulses are used. This is not that critical for confocal and telescopic resonator arrangements but very important for modern critical resonator systems. The coherence length of pulsed Nd:YAG lasers is normally of the order of only a few centimeters. For holographic recording, lasers with a narrow spectral bandwidth have to be used. This is

usually done by injection from a smaller semiconductor laser into the cavity by a partially reflecting mirror. Then, the laser pulse builds up from this small seeding pulse of narrow bandwidth, resulting in coherence lengths of 1 or 2 m. However, very precise laser timing and temperature control for the primary cooling circuit are required for this purpose.

Neodym-YLF lasers (Nd:YLF lasers $\lambda = 1053$ nm and $\lambda = 526$ nm) are used for an increasing number of applications, including high-speed PIV techniques, which require a reliable high average-power laser source that enables efficient frequency conversion to visible wavelengths. For this and other applications, several variants of the diode-pumped solid state lasers have been developed, and of these, the Nd:YLF (neodymium: yttrium lithium fluoride) laser produces the highest pulse energy and average power, with repetition rates up to approximately 10 kHz. They can be operated at different fundamental wavelengths. The fundamental wavelength most frequently used in PIV is $\lambda = 1053$ nm, which is turned into the visible range at $\lambda = 526$ nm by frequency doublers in a similar way as in case of the Nd:YAG lasers. A fundamental wavelength of $\lambda = 1047$ nm can be obtained by rotating a polarizer inside the resonator. However, the advantage of using the $\lambda = 1053$ nm wavelength is its ability of an amplification by neodym-phosphate glass.

2.3.2 Features and Components of PIV Lasers

Commercially available Nd:YAG laser rods are up to 150 mm long and have diameters up to 10 mm. Typically pulse energies of 400 mJ or more can be achieved with a single oscillator. For high pulse energies, more than one flash lamp and critical resonators with plane mirror surfaces have to be used. However, for such configurations the beam profile tends to be very poor: hot spots and different ring modes can often be found. In order to improve the beam profile, output mirrors with a reflectivity that varies with the radius are frequently used. However, even with these mirrors the beam profile is sometimes very poor, even though it is specified to be 80% Gaussian in the near and 95% Gaussian in the far field. Two laser systems of the same manufacturer often have different beam properties depending on the laser rod properties and the alignment of the laser. Since a good beam profile is essential for PIV (see Chap. 4) it must be specified not only in the near and in the far field – as most manufacturers do – but also in the mid-field at a distance of 2–10 m from the laser. If two or more laser beams are combined for PIV measurements, it is most important that all lasers have a similar intensity distribution, so that the amplitude, width and shape match. The exact profile is much less important. However, the minimum and maximum energy inside the beam profile is relevant in order to ensure a hole-free intensity distribution without hot spots.

In Fig. 2.33, the intensity profiles across the light sheet thickness measured at five different distances from the laser are shown. The light sheet optics used for this experiment are shown in Fig. 2.48. The peak value of the distribution has been

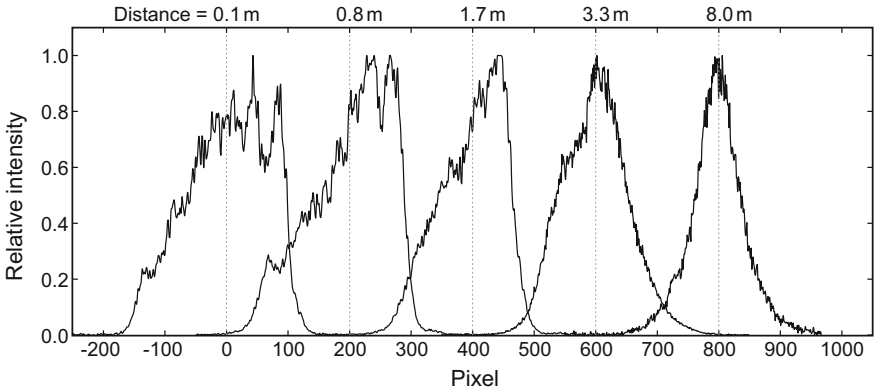


Fig. 2.33 Evolution of the light sheet profile with increasing distance from the laser

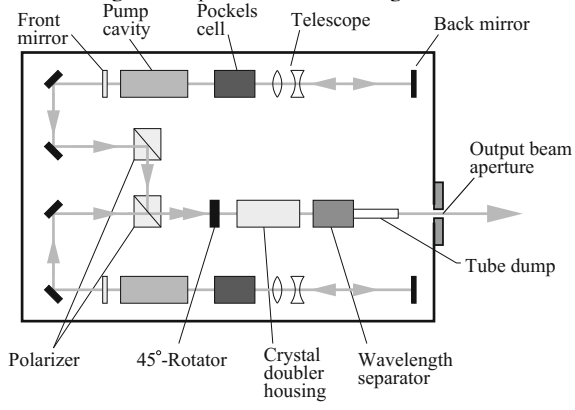


Fig. 2.34 Double oscillator laser system with telescopic resonators

adjusted close to full scale for each position (0.1, 0.8, 1.7, 3.3, 8.0m). It can be seen that the thickness of the light sheet varies slowly with the distance from the laser. A certain asymmetry is visible at every position but seems to disappear at 8 m. When assessing these light sheet profiles it has to be taken into account that the loss of correlation during the evaluation of PIV recordings is strongly influenced by the light sheet intensity distribution at recording (see Chap.4). If a light sheet intensity profile has a significant local minimum, the light next to it will be lost in most situations, because a very small flow velocity component in the lateral direction would displace particles from bright towards dark areas and would therefore lead to only one illumination of the tracer particles. For flow fields without any significant out-of-plane velocity component the light sheet can be focused more precisely and a better, more Gaussian-like, intensity profile will be obtained across the light sheet.

In Table 2.5, some critical parameters are listed which should be specified when assessing a double oscillator Nd:YAG laser. The laser system and all the specifications

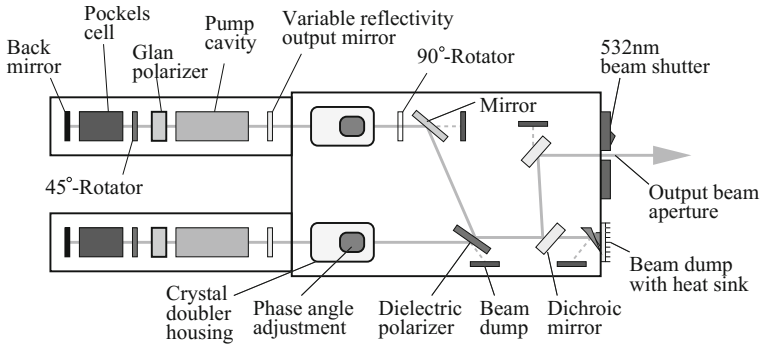


Fig. 2.35 Double oscillator laser system with critical resonators. The beam alignment behind the frequency doubling leads to two polarization directions of the laser beams. (typically one laser beam horizontally and the other beam vertically polarized)

are made with respect to a wavelength of 532 nm and a repetition rate of 10 Hz of the two pulses, unless otherwise stated. All trigger signals of the laser should be TTL compatible.

In Fig. 2.34 a laser with a telescopic resonator is shown. It offers only 2×70 mJ pulse energy but has the advantage of a good and stable beam profile. Based on the authors' experience it can be said that the beam profile of this laser has been stable during more than 30 years of application.

In Fig. 2.35 a laser system with critical resonators is shown. These systems typically have 150–450 mJ per pulse. The disadvantages of critical resonators have already been described above. In general it has to be mentioned that beam properties very much depend on manufacturers' know-how and the tuning of each individual laser.

In the following section a short description of essential Nd:YAG and Nd:YLF laser components is given.

The *flash lamp pumping chamber* contains the laser crystal rod and a linear flash lamp which are sealed into their respective mountings with O-rings. These two components are surrounded by ceramic reflectors which provide efficient optical pumping of the laser rod. Glass filter plates absorb the ultraviolet radiation from the flash lamp. Flash lamp pumped Nd:YAG lasers are still the most common for conventional PIV applications where high pulse energies at moderate repetition rates are required. Diode-pumped lasers, on the other hand, offer better stability and higher reliability than flash lamp pumped laser systems.

The *diode pumping chambers* can be divided into two major categories: end pumping and side pumping configurations. End pumped designs offer the advantage of reaching best quality by reshaping an astigmatic diode-laser beam into a beam with a circular symmetry. Their disadvantage is the greater complexity and the fact that they cannot easily be scaled to high average-power output. Main advantages of the side pumped configurations are simplicity, reliability and physical and thermal tolerance. Most modern high-speed lasers used for PIV contain side pumped designs

Table 2.5 Properties and specifications of modern Nd:YAG PIV-laser systems

Repetition rate ^a	10 Hz
Pulse energy for each of two pulses	320 mJ
Roundness at 8 m from laser output ^b	75%
Roundness at 0.5 m from laser output ^c	75%
Spatial intensity distribution at 8 m from laser output ^d	<0.2
Spatial intensity distribution at 0.5 m from laser output ^d	<0.2
Linewidth	1.4 cm ⁻¹
Power drift over 8 hours ^e	<5%
Energy stability ^f	<5%
Beam pointing stability ^g	100 μrad
Deviation from collinearity of laser beams	<0.1 mm/m
Beam diameter at laser output	9 mm
Divergence ^h	0.5 mrad
Jitter between two following laser pulses	2 nm
Delay between two laser pulses	0–10 ms
Resolution	5 ps
Working temperatures	15–35°C
Cooling water ⁱ	10–25°C
Power requirements	220–240 V, 50 Hz

^aAnd integral fractions of 10 Hz, eg. 5, 2.5 Hz etc

^bRatio between two perpendicular axis (major and minor axis)

^cIf laser beam is elliptical, major axis of both oscillators must be parallel

^d $|I_{\max} - I_{\min}|/|(I_{\max} + I_{\min})|$, with I being the peak intensity in the spatial distribution limited by the diameter at half maximum for both oscillators

^eWithout readjustment of phase-matching for ambient temperatures of $18^\circ\text{C} < T < 35^\circ\text{C}$

^fShot to shot, peak to peak, 100% of shots

^gRMS, on 200 alternating pulses at the focal plane of a 2 m lens

^hFull angle on 200 pulses at e^{-2} of the peak, 85% of total energy

ⁱSecondary circuit, 10 l/min pressure, 1.5–3 bar

which are producing high average power and good beam quality needed for the efficient generation of the green wavelengths at $\lambda = 526$ nm.

The *output mirror* has a plane surface in most cases with a partially reflecting coating facing into the cavity. The opposite plane surface has an antireflection coating. In some cases, the output mirror has a curved surface with a variable reflectivity coating decreasing from the center to the edges.

The *back mirror* has a highly reflective surface facing towards the cavity. Usually, this mirror has a slightly curved surface.

The decay of energy inside a resonator can be described by introducing a quality factor or Q-factor. This factor can be changed with the help of the *Q-Switch*. The Q-switch normally consists of a polarizer plate, a temperature stabilized Pockels cell crystal and a beam path correcting prism. It is driven by high voltages and is used to release the energy stored in the laser rod in a giant pulse by rapidly changing the

resonance conditions. Its principle is as follows: during the beginning of the flash lamp pulse the (voltage dependent) birefringence of the Pockels cell makes it act as a quarterwave plate. The polarization of the light that passes the polarizer is rotated by 90° on its way through the crystal towards the mirror and back towards the polarizer. The reflected light is then rejected by the polarizer. Therefore, no laser oscillation and no light amplification will take place. When the energy stored in the laser rod reaches a maximum the Pockels cell voltage is altered and the polarization of passing light will no longer be changed. As a result, the laser oscillation begins immediately and the energy stored is extracted in a pulse of only a few nanoseconds duration. Since the birefringence of the Pockels cell is also temperature dependent, the Pockels cell is generally temperature stabilized.

An intra-cavity *telescope* can be used to avoid high order modes within the cavity. It also compensates for thermal lensing effects inside the laser rod.

A *second harmonic generator* (SHG) is a nonlinear crystal used for the frequency doubling of the Nd:YAG laser emission. Simply speaking, it converts infrared light of a wavelength of 1064 nm into visible green light of 532 nm. The process of frequency doubling takes place only when the crystal is oriented such that the direction of propagation of the pump beam is at a specific angle to the crystal axis. This condition is known as phase matching. Therefore, the crystal can usually be angle tuned by the user. Since the refractive index and therefore the actual phase matching changes with temperature, the crystal has to be temperature stabilized to ensure stable conversion efficiencies. As most crystals used are hygroscopic the heating of the crystals should not be switched off in order to protect its surface from moisture. The crystal most commonly used is called KD*P. It can be cut in two different orientations (Type I or Type II) and has to be chosen depending on the final configuration of the laser. For Type I crystals, the incident laser light has to be linearly, typically vertically or horizontally, polarized. The frequency doubled light emerges with a polarization which is orthogonal to that of the pump radiation. This type of doubler is used for PIV laser systems with two polarization directions as, for example, shown in Fig. 2.35. In order to generate green light of identical polarization one Type II crystal is generally used. Therefore, the infrared laser light must have two polarization components. The second harmonic will then have one polarization direction parallel to one of both original components depending on the orientation of the crystal. In order to provide two components of the incident laser light, its linear polarization is turned by an angle of 45° using a polarization rotator.

A *polarization rotator* is a crystal which continuously rotates the polarization angle of linearly polarized light as it propagates through it. The rate of rotation is dependent on the material, its thickness and the wavelength. A 45° rotator will be used when a Type II doubling crystal is used. A 90° rotator might be used in front of the beam combination optics, if two oscillators of identical orientation are used (see Fig. 2.35).

A *prism harmonic separator* can be used to separate the second harmonic wave by deflecting it into an energy dump. Two energy dumps are provided; one for the fundamental and one for the third harmonic wave. These separators are most efficient when used with only one polarization direction, as the reflection losses at the prism surfaces are lower for one polarization (see Fig. 2.34).

Fig. 2.36 Double oscillator high-speed PIV laser system with intra cavity doubler

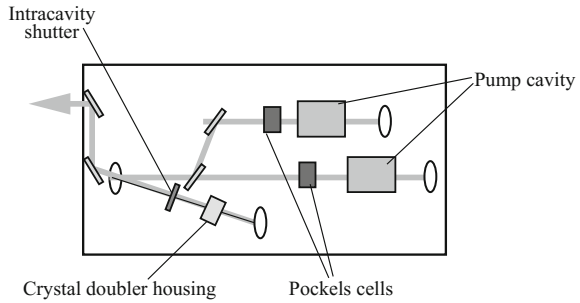
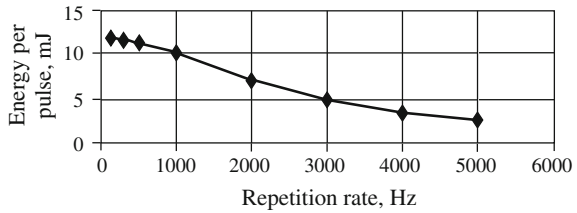


Fig. 2.37 Pulse energy versus repetition rate of a double oscillator high-speed PIV laser system



A *dichroic mirror* has maximum reflectivity for one given wavelength. The fundamental and any unwanted harmonic waves pass through such a mirror and can therefore be steered into an external energy dump.

The time delay between the trigger signals of the flash lamp and the Pockels cells can be varied resulting in a varying intensity of the green laser pulse. The value for optimum pulse energy is depending on the specific laser design and is typically in the order of 200 μ s.

Figure 2.36 shows the sophisticated optical layout of a modern high-speed PIV laser system, in which the two infrared beams are combined. This principle is patent pending by one of the leading PIV laser manufactures and offers an effective mechanism, the intra-cavity doubling. The working principle is as follows: Both infrared beams are reflected by the output mirror that is coated to reflect infrared and transmit green laser light. Both infrared beams are reflected back towards the second harmonic generator (SHG) by this same output mirror. They pass through the second harmonic generator. The beams are then reflected by a back mirror through the second harmonic generator again and then are transmitted through the output mirror out of the laser head. Therefore, the beams are always co-linear since they are combined within the combined resonators. This doubling mechanism provides a high conversion from infrared to green. The two separate cavities produce two pulses with the same pulse width given by identical resonator lengths.

The properties and specifications of a high-speed Nd:YLF PIV-laser system are listed in Table 2.6. Pulse width and pulse energies vary with the chosen repetition rate. Typical values of pulse energy and pulse width are shown in Figs. 2.37 and 2.38 respectively.

Table 2.6 Properties and specifications of a high-speed Nd:YLF PIV-laser system

Repetition rate ^a	0.01–10 kHz
Pulse energy for each of two pulses	15–3 mJ
Roundness at 4 m from laser output ^b	75%
Roundness at 0.5 m from laser output ^c	75%
Spatial intensity distribution at 4 m from laser output ^d	<0.2
Spatial intensity distribution at 0.5 m from laser output ^d	<0.2
Pulse width at 1 kHz	<180 ns
Power drift over 8 hours	<5%
Energy stability ^e	<1%
Deviation from co-linearity of laser beams	<0.1 mm/m
Beam diameter at laser output	2 mm
Divergence ^f	<3 mrad
Spatial mode	multi-mode, $M^2 < 6$
Cooling water	10–25 °C

^aRepetition rate per cavity

^bRatio between two perpendicular axis (major and minor axis)

^cIf laser beam is elliptical, major axis of both oscillators is parallel

^d $|(I_{max} - I_{min})|/|(I_{max} + I_{min})|$, with I being the peak intensity in the spatial distribution limited by the diameter at half maximum for both oscillators

^eRMS after 10 minutes warm up at 2 kHz

^fFull angle at e^{-2} of the peak, 85% of total energy

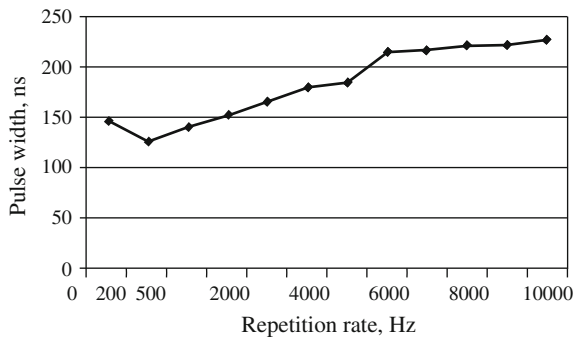


Fig. 2.38 Pulse width versus repetition rate of a modern double oscillator high-speed PIV laser system

2.3.3 Light Emitting Diodes

In recent years light emitting diodes (LEDs) have undergone significant progress regarding their output power and efficiency such that they now find uses in a multitude of areas in particular in the area of lighting. The underlying theory of operation including the effect of electroluminescence will not be covered here and the interested reader is referred to textbooks on photonics [53]. In the following, we will focus on the characteristics of LEDs in the context of particle based flow velocimetry.

Compared to lasers, LEDs have a significantly wider spectral width of up to tens of nanometers (see Fig. 2.39) with a correspondingly short coherence length of $\mathcal{O}(10\mu\text{m})$. In consequence speckle effects are practically non-existent for LEDs. Furthermore the directional emission characteristic or radiation pattern is nearly Lambertian. This means that the emitted light is directly proportional to the cosine of the angle between the direction of the emitted light and the normal to the emitter surface according to Fig. 2.40. This property on the one hand reduces handling risks as the uncollimated light is not directly focused within the eye as with laser sources. On the other hand the finite size of the emitter coupled with the large spreading angle of the light makes it difficult to collimate the light, for instance to generate a thin light sheet suitable for PIV. However, it should be noted that modern high power LEDs require maintaining similar safety measures as pulse lasers.

The spreading of light from a finite area is referred to as etendue and describes the light (or flux) gathering capability of an optical system in a purely geometrical sense. Its dimensions are area A times solid angle Ω . The collected power is the product of the radiance of the source and the etendue. Important in this context is the property that – ignoring losses due to light scatter and absorption – etendue is conserved throughout an optical system, a so-called Lagrangian invariant, that is, $A_1\Omega_1 = A_2\Omega_2 = \text{const}$. This property has important implications regarding the collimation of light (see Fig. 2.41). For instance, if the light emitting area of an

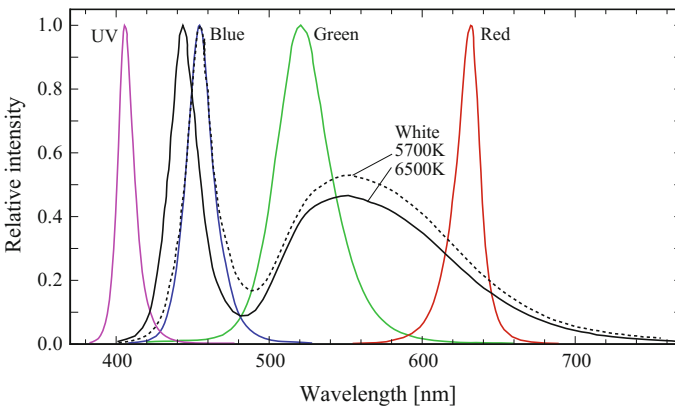


Fig. 2.39 Spectral intensity versus wavelength for various monochrome LEDs and white LEDs

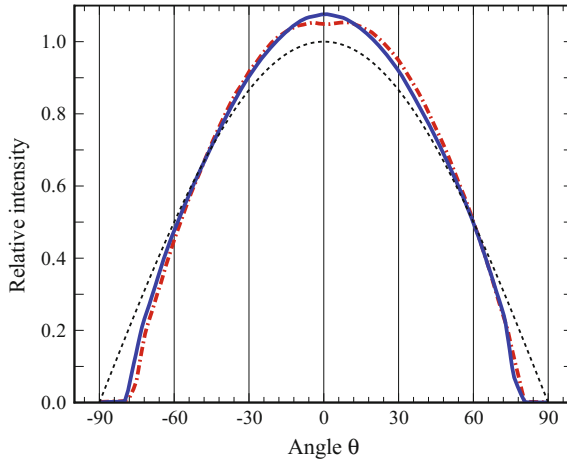


Fig. 2.40 Radiation pattern of a blue (—) and red (- · - ·) LED without collimating optics in comparison to a true Lambertian emitter (- - -, cosine-law)

LED with a given numerical aperture is focussed onto a smaller area the numerical aperture increases proportionally. Hence a light sheet will have a very short waist quickly diverging on either side.

Similarly the coupling of LED light into a fiber is ultimately limited by the finite area of the emitter coupled with its emission cone. As the fiber itself has a limited acceptance angle (i.e. numerical aperture, NA) only the light within the acceptance cone is coupled into the fiber (see Fig. 2.42). Focussing the LED light into a smaller spot will not increase the amount of light coupled into the fiber because an increasing amount of rays will exceed the acceptance angle of the fiber. Similarly an optical taper can also not concentrate the light into a smaller area without significant losses owing to the conservation of etendue throughout the optical system.

Another interesting characteristic of LED's is that the light emission per unit time can be increased by increasing the drive current (Fig. 2.43). The light emission from an LED is roughly proportional to the drive current allowing it to be overdriven beyond the manufacturer's specifications, provided that the junction temperature within the LED does not exceed the damage threshold. In this regard Fig. 2.44 indicates that the light output can be increased by a factor of three by increasing the drive current by approximately fourfold. This however is only possible when the pulses are sufficiently short to prevent its damage, here $\tau_p = 5 \mu s$.

In comparison to laser systems the construction of pulsed LED illumination sources is considerably simpler with the required components being readily available. Figure 2.45 shows a simplified circuit to illustrate the pulsed operation of LED. Aside from the LED itself two components are the main actors for its pulsed operation, a capacitor with high charge capacity (and low internal resistance) and a MOSFET transistor as a quick acting switch. In the off-state the capacitor is charged to a fixed voltage by an external power supply. Using a driver unit the MOSFET transistor can

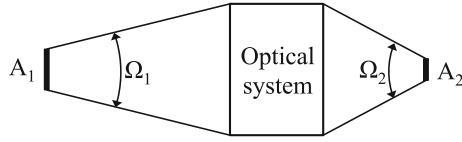


Fig. 2.41 Etendue, the product of illuminated or luminous area and solid angle, is preserved through an optical system

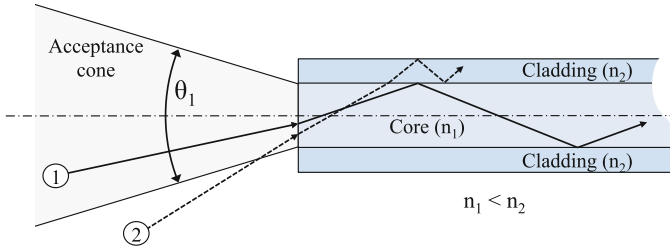


Fig. 2.42 Simplified model of fiber optic illustrating the acceptance cone. Only light ray 1 is propagated through fiber

Fig. 2.43 Response of LED to input drive current of $0.5 \mu\text{s}$ duration

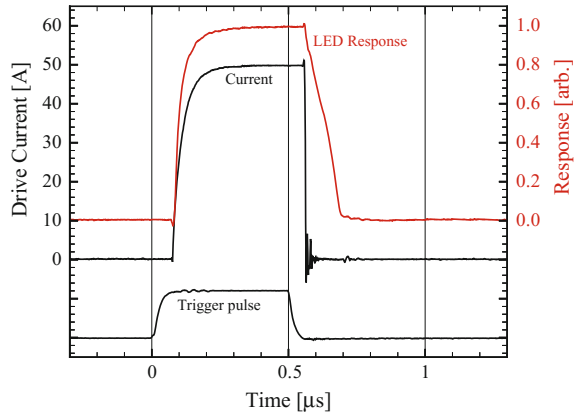


Fig. 2.44 LED light emission versus drive current for a green high-power LED operated with $5\ \mu\text{s}$ pulses at 1 kHz. Line at 36 A indicates manufacturer's recommended operation at 240 Hz with 50% duty cycle (from [7])

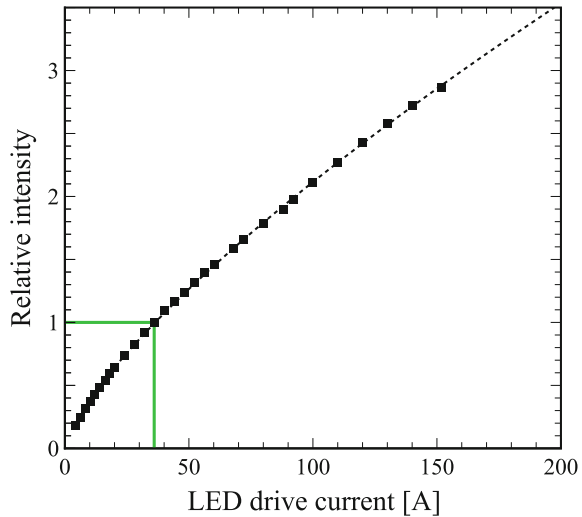
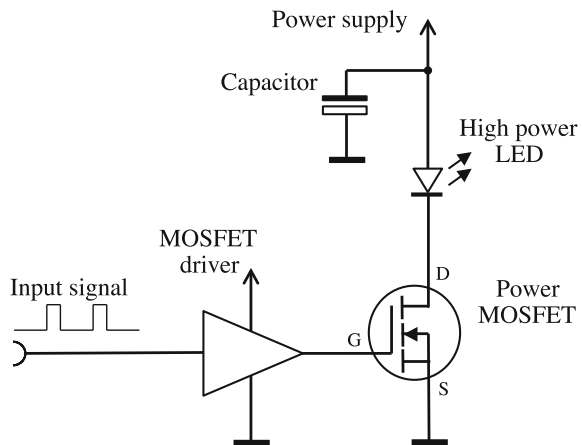


Fig. 2.45 Simplified drive circuit for pulsed LED operation



be rapidly switched to the on-state thereby draining the charge from the capacitor with the current flowing through the LED causing it to emit light. The reader is referred to [7, 73] for further details on actual circuit implementations.

The following summarizes some of the advantages and disadvantages of LEDs in the context of flow visualization:

- + simple operation, robust
- + easy to pulse (lag-free)
- + no noticeable speckle (due to broad spectral emission)
- + reduced risk (non-collimated light, lower operating voltages), therefore suitable for educational purposes (depending on power of LED)
- difficult to collimate (into light sheet or fiber transmission)
- shorter pulses tend to provide lower pulse energy

2.3.4 *White Light Sources*

Even though most PIV investigations are performed using laser light sheets, white light sources might also be used. Due to the finite extension of these sources and since white light cannot be collimated as well as monochromatic light, they clearly have some disadvantages. On the other hand, the spectral output of sources like Xenon lamps is well suited for use with CCD cameras because of their similar spectral sensitivity. Systems are commercially available which can easily be triggered and offer a repetition rate that matches the video rate. Two flash lamps can be linked by optical fiber bundles in order to achieve short pulse separation times. If the outputs of the fibers are arranged in line, the generation of a light sheet is considerably simplified.

An attractive alternative to discharge flash lamps is provided by white-light LEDs that are increasingly finding widespread uses in general lighting applications replacing less efficient incandescent light sources. Regarding its electrical properties the white-light LED is no different to its monochromatic counterparts and can be operated in a pulsed mode in the same manner as described before. The emission spectrum of commonly available white LEDs is plotted in Fig. 2.39 and shows two distinct maxima, one sharp peak in the blue and a broader peak with a maximum in the yellow. The reason lies in the fact that the “white-light” LEDs actually are phosphor coated blue LEDs. The phosphor down-converts the blue light to a yellowish light such that, in combination with the blue light, it is perceived as white light. In some cases this bi-modal emission spectrum may not be desired, for instance for liquid crystal thermometry [12]. In such cases, the combination of several different-colored LEDs should be considered, in particular, if matched to the color filters of a color camera.

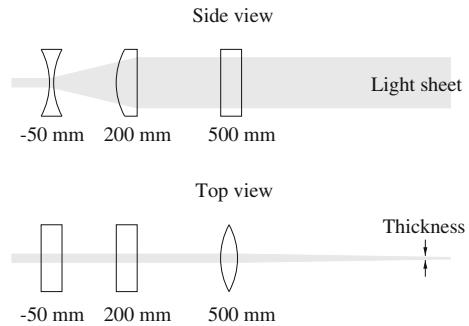
The main advantage of these white light sources is – aside from reduced cost – that their application is not hampered by laser safety rules.

2.4 Light Delivery

2.4.1 *Light Sheet Optics*

This section treats the optics for the illumination of the particles by a thin light sheet. Therefore, we describe three different lens configurations which are frequently used. For a more detailed analysis or the design of complex optical systems ray tracing programs can be used, but this is beyond the scope of the book. Rules for the calculation of the light sheet intensity distribution are not given herein. The reason for this is that geometric optics rules are already sufficient for a general layout of the chosen lens configuration. They do not require a special description and can readily be found in any book on optics [23]. On the other hand, more sophisticated calculations based on Gaussian optics usually require some assumptions, which are

Fig. 2.46 Light sheet optics using three cylindrical lenses (one of them with negative focal length)



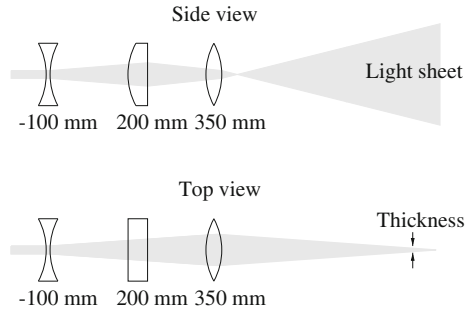
valid only for exceptional cases. Computer programs can be used in order to predict further parameters such as the light sheet thickness at the beam waist where the theoretical (geometrical) thickness is zero, but their description is beyond the scope of this book.

The essential element for the generation of a light sheet is a cylindrical lens. When using lasers with a sufficiently small beam diameter and divergence – like for example argon-ion lasers – one cylindrical lens can be sufficient to generate a light sheet of appropriate shape. For other light sources – like for example Nd:YAG lasers – a combination of different lenses is usually required in order to generate thin light sheets of high intensity. At least one additional lens has then to be used for focusing the light to an appropriate thickness. Such a configuration is shown in Fig. 2.46, where also a third cylindrical lens has been added in order to generate a light sheet of constant height.

The reason why a diverging lens has been used first is that focal points and lines should be avoided for high power pulse lasers, as otherwise the air close to the focal point will be ionized. Focal lines usually do not ionize the air but dust particles might be burnt if the area in the vicinity of the line is not covered or evacuated. In both cases acoustic radiation will occur and the beam properties will change significantly. For the light sheet shown in Fig. 2.46, the position of its minimum thickness is given by the beam divergence of the light source and the focal length of the cylindrical lens on the right hand side, for example at a distance of 500 mm from the last lens for the conditions illustrated in Fig. 2.46.

The combination of a cylindrical lens together with two spherical lenses acting as a telescope makes the system more versatile. This is shown in Fig. 2.47 where spherical lenses have been used, because they are in general easier to manufacture, especially if short focal length lenses are required. The height of the light sheet shown in Fig. 2.47 is mainly given by the focal length of the cylindrical lens in the middle. A diverging lens – negative focal length – could also be used, however, since the focal line has a relatively large extension this configuration can therefore also be used for pulsed lasers without risking plasma ignition. The adaptation of the light sheet height has to be done by replacing the cylindrical lens with a cylindrical lens

Fig. 2.47 Light sheet optics using two spherical lenses (one of them with negative focal length) and one cylindrical lens



of a different focal length. The adjustment of the thickness can easily be done by shifting the spherical lenses with respect to each other.

The use of spherical lenses in general does not allow light sheet height and thickness to be changed independently. This can be done by the configuration shown in Fig. 2.48. Additionally this setup allows for the generation of light sheets which are thinner than the beam diameter at every location. It therefore enables the generation of light sheets which are already thin shortly behind the last lens. With this arrangement the thickness can be held constantly small. However, the energy per unit area of such a configuration is high. Therefore, the critical region close to the focal line has to be covered in order to avoid reflections by dust or seeding particles. Using a diverging cylindrical lens first would solve those problems, but the combination shown in Fig. 2.48 has the advantage of imaging the beam profile from a certain position in front of the lens to the observation area while keeping its properties constant.

Simple geometric considerations can be used for these lens combinations to determine from which position the laser beam has been imaged and, if the development of the beam profile of the laser is known, this information can be used to optimize the light sheet intensity distribution, see Fig. 2.33 on page 67. The evolution of a light sheet profile generated by a lens configuration similar to that shown in Fig. 2.48 has been shown as a function of the distance from the laser. For lasers with a critical beam profile this can improve the valid data yield, because the light sheet intensity distribution especially in the out-of-plane direction is essential for the quality of the measurement (see Chap. 4).

A few general rules should also be given here. Uncoated lens surfaces in air exhibit a slight reflectivity of $[(n - 1)/(n + 1)]^2$. Since this value is of the order of 4% for common lens surfaces (and therefore more than 7% per lens) the losses due to the reflection could be accepted in some cases. However, these reflections can cause damage, if they are focused close to other optical components. This can either be avoided by the proper orientation of the lenses as illustrated in Fig. 2.49 or by an appropriate lens coating. Configuration c and d depicted in Fig. 2.49 reduce the risk of unwanted reflections and will also minimize aberrations. For other configurations it is advised to tilt the lens slightly in order to avoid reflections on to other lenses or towards the laser or even into the resonator.

Fig. 2.48 Light sheet optics using three cylindrical lenses

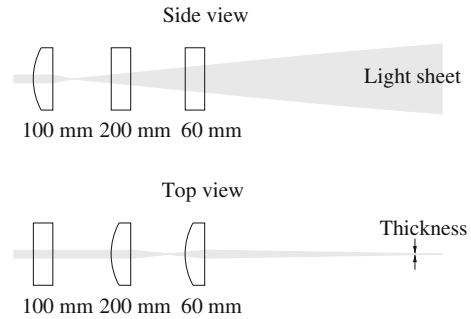
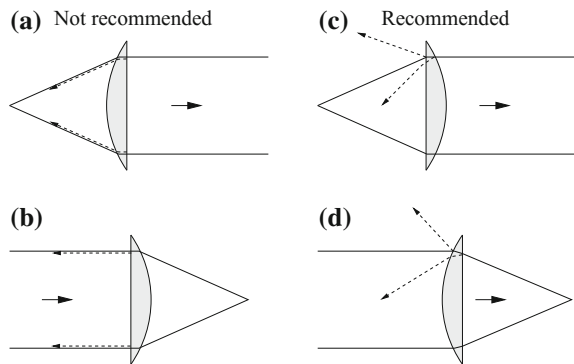


Fig. 2.49 General considerations on the orientation of lenses inside the light sheet optics



2.4.2 Fiber Based Illumination

Fiber optics in principle offer an attractive alternative to conventional free space transmittal of light, in particular for the delivery of high energy laser light. For instance the movement of the measurement plane is much simpler; critical areas are restricted to the laser and the light sheet optics. However the delivery of short, high power laser pulses through fibers is not trivial. Once collimated, the high energy density of the laser pulse quickly reaches the damage threshold of most optical fibers, such that only limited amounts of energy can be transmitted. Small surface imperfections lead to damage to the end face and self-focussing induced by local index-of-refraction changes of the pulse-heated fiber causes internal damage, typically several millimeters into the fiber. While considerable energies can be transmitted in the infrared (e.g. for use in laser based surface treatment), most fibers exhibit increasing attenuation at reduced wavelengths in the visible range and beyond leading to increased heating and nonlinear effects. Also suitable fibers for the transmission of high energy pulsed light have large diameters in the 100–500 μm range such that the emitted light exhibits a significant amount of speckle; any modal properties of the laser are not preserved.

One solution is to transmit higher energy levels through a fiber based system is to use tapered fibers, fiber bundles (array of fibers), longer pulse lengths, larger fiber diameters, diffractive optical elements (DOE) or combinations thereof [22]. For

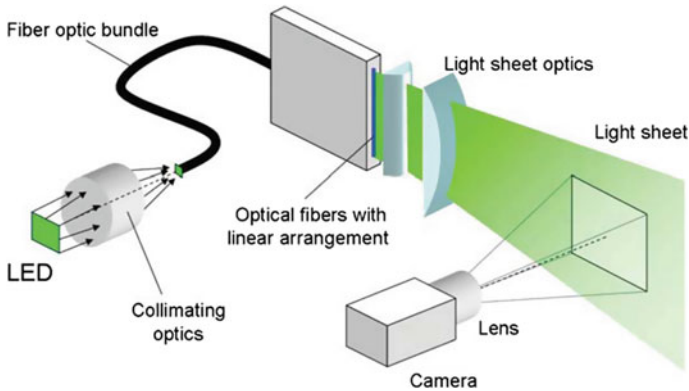


Fig. 2.50 LED-based light sheet illumination using a fiber optic line-light assembly [73]

instance some high-speed lasers have pulse lengths of several hundred nanoseconds and can be provided with fiber optic beam delivery at energy levels in the range of 1–10 mJ at 1–10 kHz [25].

The other use of fibers is to (re)collimate the light of incoherent light sources such as discharge lamps or light emitting diodes (LED). For instance WILLERT et al. [73] demonstrated that a single LED can illuminate particles in a side-scatter arrangement which is commonly used in planar PIV. They performed experiments using the LED light bundled into a light sheet by means of a fiber optic illumination system, also known as line light. As illustrated in Fig. 2.50 the entry side of the fiber bundle is round (3 mm diameter) while the fibers at the distal end are arranged along a straight line (0.3 mm thickness). A light sheet can then be formed by projecting this line into the area under investigation using a short focal length cylindrical lens. The light sheet's waist thickness depends on the width of the line, the focal length of the lens and the numerical aperture of the fibers. While a short focal length makes the light sheet thinner, the length of the waist will also shorten which reduces the useful (near uniform thickness) area of the light sheet.

2.4.3 Illumination of Small Volumes

Whereas most conventional PIV investigations utilize light sheet illumination, they are typically not a practical source of illumination for micro-flows, due to a lack of optical access along with significant diffraction in light sheet forming optics. Consequently, the flow must be volume illuminated, leaving two choices for the visualization of the seed particles – with an optical system whose depth of field exceeds the depth of the flow being measured or with an optical system whose depth of field is small compared to that of the flow. Both of these techniques have been used in various implementations of μ PIV. CUMMINGS [11] uses a large depth of field

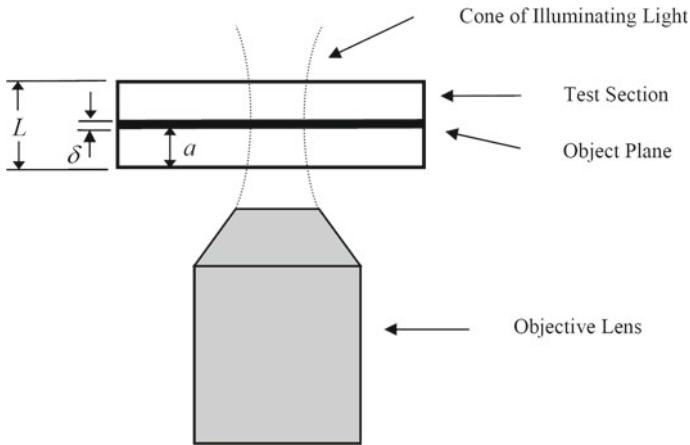


Fig. 2.51 Schematic showing the geometry for volume illumination particle image velocimetry. The particles carried by the flow are illuminated by light coming out of the objective lens (i.e. upward)

imaging system to explore electrokinetic and pressure-driven flows. The advantage of the large depth of field optical system is that all particles in the field of view of the optical system are well-focused and contribute to the velocity measurement comparably. The disadvantage of this scheme is that all knowledge of the depth of each particle is lost, resulting in velocity fields that are completely depth-averaged. For example in a pressure-driven flow where the velocity profile is expected to be parabolic with depth, the fast moving particles near the center of the channel will be focused at the same time as the slow moving particles near the wall. The measured velocity will be a weighted-average of the velocities of all the particles imaged. CUMMINGS [11] addresses this problem with advanced processing techniques that will not be covered here.

The second choice of imaging systems is one whose depth of field is smaller than that of the flow domain, as shown in Fig. 2.51. The optical system will then sharply focus those particles that are within the depth of field δ of the imaging system while the remaining particles will be unfocused – to greater or lesser degrees – and contribute to the background noise level. Since the optical system is being used to define thickness of the measurement domain, it is important to characterize exactly how thick the depth of field, or more appropriately, the *depth of correlation* Z_{corr} , is. The distinction between depth of field and depth of correlation is an important although subtle one. The depth of field refers to distance a point source of light may be displaced from the focal plane and still produce an acceptably focused image whereas the depth of correlation refers to how far from the focal plane a particle will contribute significantly to the correlation function. The depth of correlation can be calculated starting from the basic principles of how small particles are imaged [40, 68].

2.4.4 Illumination of Large Volumes

Recent literature reports a number of PIV applications involving LED clusters as light sources [5, 10, 15, 20, 36, 48]. In these applications the LEDs were frequently overdriven operated in an in-line imaging arrangement or relied on large particles to achieve sufficient light scattering. Such an array was developed by KÜHN et al. [34] for the investigation of large scale flows in aircraft cabins. Each LED was equipped with a collimating optic consisting of a concave mirror. This resulted in an opening angle of approximately $6^\circ - 10^\circ$. Figure 2.52 follows this concept with each LED capable of delivering a luminous flux in excess of 1200lm in continuous operation. Due to the associated generation of heat by the multitude of LEDs the array is mounted on a fan-cooled heat sink.

Volumetric illumination can also be performed by a multi-pass system as shown in Fig. 2.53 with limited laser power. It favorably consists of two opposing mirrors in order to obtain multiple reflections of the light beam along the measurement volume. The laser beam passes through a beam expander and collimating optics and is then directed towards the measurement region. Two coated and highly reflective dielectric mirrors are installed on opposite sides of the measurement region. The collimated laser beam is directed almost normal to one mirror. The distance between

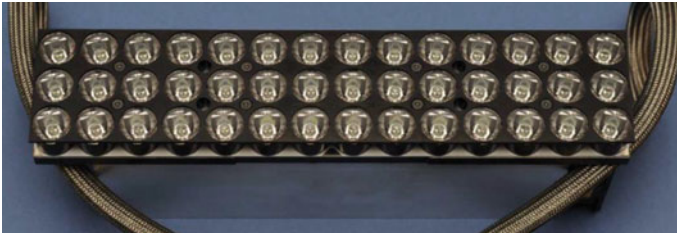
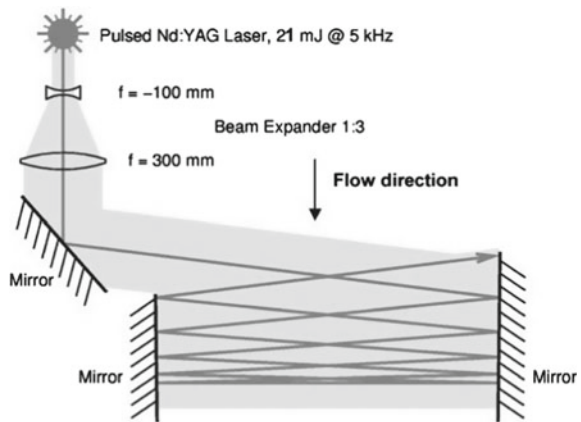


Fig. 2.52 LED-array comprising 3×14 LEDs with collimating optics mounted on a heat sink

Fig. 2.53 Optical path of the laser beam along with the spherical lenses and the mirrors for multi-pass light amplification [61]



two subsequent beams decreases toward the lower side of the mirrors. The intensity of the laser beam also reduces due to optical losses such as beam divergence, scattering by the particles and reflection loss along the transmission path. According to GHAEMI et al. [16] an amplification factor of 7 and 5 times is achieved in comparison to the single pass and the double-pass configurations, respectively. A further advantage of these multiple pass illumination systems is that cameras may observe the scattered light from particles in the more favorable forward scattering direction from multiple viewing directions.

2.5 Imaging of Small Particles

2.5.1 Diffraction Limited Imaging

This section provides a description of diffraction limited imaging, which is an effect of practical significance in optical instrumentation, and of particular interest for PIV recording. In the following we will restrict our description of imaging by considering only one-dimensional functions.

If plane light waves impinge on an opaque screen containing a circular aperture they generate a far-field diffraction pattern on a distant observing screen. By using a lens – for example an objective in a camera – the far field pattern can be imaged on an image sensor. However, the image of a distant point source (e.g. a small scattering particle inside the light sheet) does not appear as a point in the image plane but forms a diffraction pattern even if it is imaged by a perfectly aberration-free lens [23]. The central peak of the intensity distribution is called Airy disk, and the rings around the maximum are called Airy rings.

It can be shown that the intensity of the Airy pattern represents the Fourier transform of the aperture's transmissivity distribution [19, 35]. Taking into account the scaling theorem of the Fourier transform, it becomes clear that small aperture diameters correspond to large Airy disks and large apertures to small disks as can be seen in Fig. 2.54.

The Airy function represents the impulse response – the so-called point spread function – of an aberration-free lens. It is equivalent to the square of the first order Bessel function. Therefore, the first dark ring, which defines the extension of the Airy disk, corresponds to the first zero of the first order Bessel function shown as a line plot through the center of the pattern in Fig. 2.55. We will now determine the diameter of the Airy disk d_{diff} , because it represents the smallest particle image that can be obtained for a given imaging configuration (see Fig. 2.55).

The value of the radius of the ring and therefore of the Airy disk for a given aperture diameter D_a and wavelength λ is:

$$\frac{I(x)}{I_{\text{max}}} = 0 \quad \Rightarrow \quad \frac{d_{\text{diff}}}{2x_0} = 1.22$$

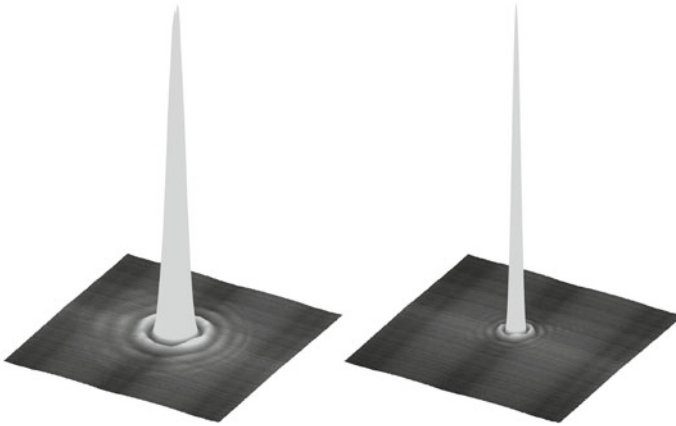
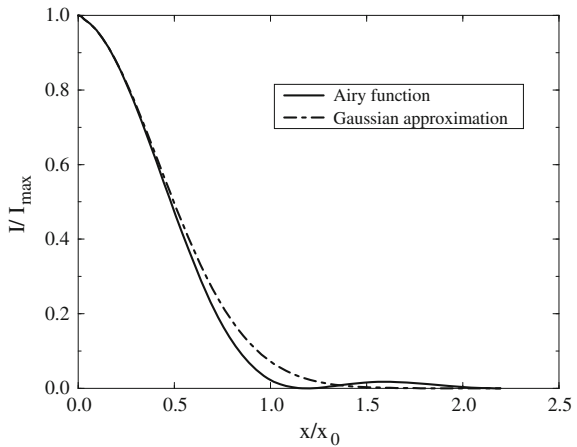


Fig. 2.54 Airy patterns for both a small (50 μm, left hand side) and large (100 μm, right hand side) aperture diameter. A helium-neon laser was used to create the pinhole intensity profile. The intensity is normalized by the maximum intensity for both the contour levels and the z-axes

Fig. 2.55 Normalized intensity distribution of the Airy pattern and its approximation by a Gaussian bell curve



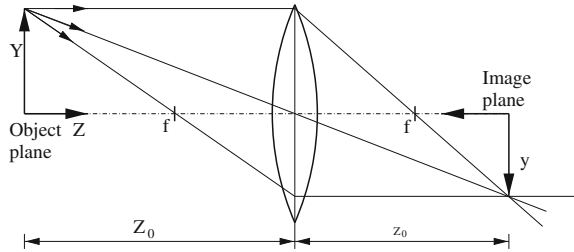
with

$$x_0 = \frac{\lambda}{D_a} .$$

If we consider imaging of objects in air – the same media on both sides of the imaging lens – the focus criterion is given by (see Fig. 2.56):

$$\frac{1}{z_0} + \frac{1}{Z_0} = \frac{1}{f} \tag{2.12}$$

Fig. 2.56 Geometric image reconstruction



where z_0 is the distance between the image plane and lens and Z_0 the distance between the lens and the object plane. Together with the definition of the magnification factor

$$M = \frac{z_0}{Z_0}$$

the following formula for the diffraction limited minimum image diameter can be obtained:

$$d_{\text{diff}} = 2.44 f_{\#}(M + 1) \lambda \quad (2.13)$$

where $f_{\#}$ is the f-number of the lens, defined as the ratio between the focal length f and the aperture diameter D_a [19]. In PIV, this minimum image diameter d_{diff} will only be obtained when recording small particles – of the order of a few microns – at small magnifications. For larger particles and/or larger magnifications, the influence of geometric imaging becomes more and more dominant. The image of a finite-diameter particle is given by the convolution of the point spread function with the geometric image of the particle. If lens aberrations can be neglected and the point spread function can be approximated by the Airy function, the following formula can be used for an estimate of the particle image diameter [1]:

$$d_{\tau} = \sqrt{(Md_p)^2 + d_{\text{diff}}^2} . \quad (2.14)$$

When the size of the particle's geometric image Md_p is considerably smaller than d_{diff} , this expression is dominated by diffraction effects and reaches a constant value of d_{diff} . It is dominated by the geometric image size for geometric image sizes considerably larger than d_{diff} where $d_{\tau} \approx Md_p$.

In practice the point spread function is often approximated by a normalized Gaussian curve also shown in Fig. 2.55 and defined by:

$$\frac{I(x)}{I_{\text{max}}} = \exp\left(-\frac{x^2}{2\sigma^2}\right) \quad (2.15)$$

where the parameter σ must be set to $\sigma = f_{\#}(1 + M)\lambda\sqrt{2}/\pi$, in order to approximate diffraction limited imaging. This approximation is particularly useful because it

allows a considerable simplification of the mathematics encountered in the derivation of modulation transfer functions, which also includes other kinds of optical aberrations of the imaging lens as will be described later.

In practice there are two good reasons for optimizing the particle image diameter:

First, an analysis of PIV evaluation shows that the error in velocity measurements strongly depends on the particle image diameter (see e.g. Sect. 6.2.2). For most practical situations, the error is minimized by minimizing both the particle image diameter d_τ and the uncertainty in locating the image centroid or correlation peak centroid respectively.

Second, sharp and small particle images are particularly essential in order to obtain a high particle image intensity I_{\max} , since at constant light energy scattered by the tracer particle the light energy per sensor area increases quadratically with decreasing image areas ($I_{\max} \sim 1/d_\tau^2$).

Equation (2.14) shows that for the range of particle diameters greater than the wavelength of the scattered light, where Mie's theory applies ($d_p \gg \lambda$), the diffraction limit becomes less important and the image diameter increases nearly linearly with increasing particle diameter. Since the average energy of the scattered light increases with $(d_p/\lambda)^2$ for particles with a diameter greater than the wavelength, the image intensity becomes independent of the particle diameter, as both the scattered light and the image area increase with d_p^2 .

A point in the object plane generates a sharp image at only one defined position in the image space, where the rays transmitted by different parts of the lens intersect (see Fig. 2.57). This point of intersection and therefore of best focusing can be calculated according to Eq. (2.12). If the distance between the lens and the image sensor is not perfectly adjusted, the geometric image is blurred and its diameter can also be determined by geometric optics. This blur of images due to misalignment of the lens does not depend on diffraction or lens aberrations. However, the minimum image diameter d_{diff} which can be obtained due to diffraction is commonly used also to define the acceptable diameter of the geometric image (Δd_g in Fig. 2.57). Therefore, the particle image diameter obtained by Eq. (2.14) can be used to estimate the depth of field for typical macroscopic PIV recordings δ_Z using the following approximation [63]:

$$\delta_Z = 2 f_{\#} d_{\text{diff}} (M + 1) / M^2 . \quad (2.16)$$

Some theoretical values for the diffraction limited imaging of small particles ($d_p \approx 1 \mu\text{m}$) are shown in Table 2.7 (calculated with a wavelength of $\lambda = 532 \text{ nm}$ and a magnification of $M = 1/4$). It can be seen that a large aperture diameter (small f-number) is needed to collect sufficient light from each individual particle within the light sheet, and to get sharp particle images, because – as already shown in Fig. 2.54 – the size of the diffraction pattern decreases with increasing the aperture diameter. Unfortunately, a large aperture diameter yields a small focal depth which is a significant problem when imaging small tracer particles. Since lens aberrations become more and more important for a large aperture, they will be considered next.

Table 2.7 Theoretical values of f-number, image diameter and depth of focus for diffraction limited imaging of small particles ($\lambda = 532 \text{ nm}$, $M = 1/4$, $d_p = 1 \mu\text{m}$)

$f\# = f/D_a$	$d_r [\mu\text{m}]$	$\delta z [\text{mm}]$
2.8	4.7	0.5
4.0	6.6	1.1
5.6	9.1	2.0
8.0	13.0	4.2
11	17.8	7.8
16	26.0	16.6
22	35.7	31.4

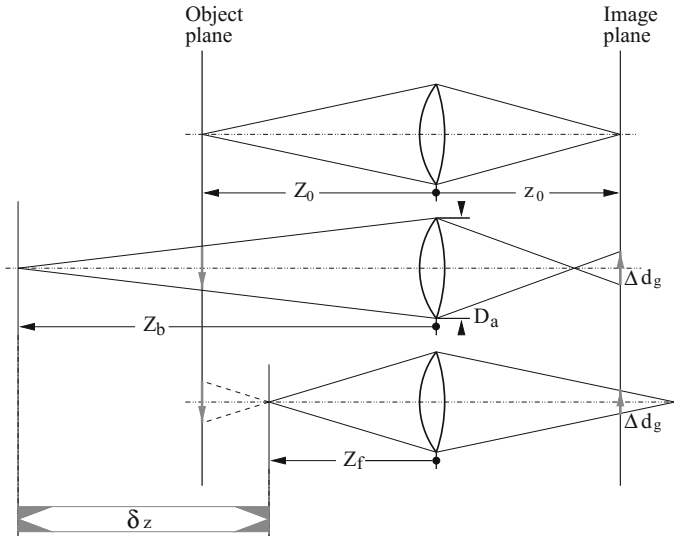
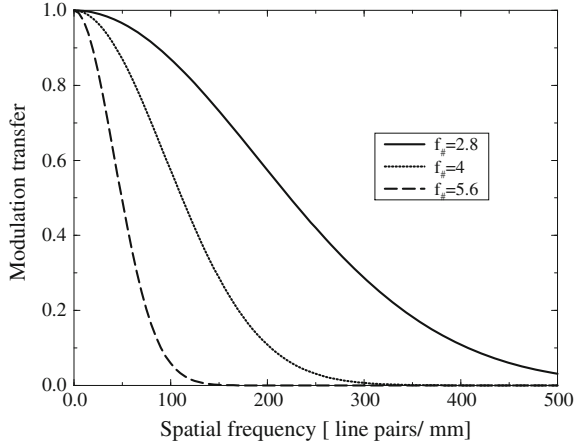


Fig. 2.57 Depth of focus for an acceptable diameter of the geometric image sketch for both extremal positions of out-of-focus imaging

2.5.2 Lens Aberrations

In analogy to linear system analysis the performance of an optical system can be described by its impulse response – the point spread function – or by the highest spatial frequency that can be transferred with sufficient contrast. This upper frequency – the resolution limit – can be obtained by the reciprocal value of the characteristic width of the impulse response. According to this, the physical dimension is the reciprocal of a length; typically it is interpreted as the number of line pairs per millimeter (lps/mm) that can be resolved. The traditional means of determining the quality of a lens was to evaluate its limit of resolution according to the RAYLEIGH criterion: two point sources were said to be “barely resolved” when the center of one Airy disk falls on the first minimum of the Airy pattern of the other point source. This means that the theoretical resolution limit ρ_m is the reciprocal value of the radius of the Airy

Fig. 2.58 Image modulation versus spatial frequency for a hypothetical lens systems without spherical aberrations at three different f-numbers (Gaussian approximations)



disk [23]:

$$\rho_m = \frac{2}{d_{\text{diff}}} = \frac{1}{1.22 f_{\#}(M + 1)\lambda} \tag{2.17}$$

Another useful parameter in evaluating the performance of an optical system is the contrast or image modulation Mod defined by the following equation:

$$\text{Mod} = \frac{I_{\text{max}} - I_{\text{min}}}{I_{\text{max}} + I_{\text{min}}} \tag{2.18}$$

The measurement of the ratio of image modulation for varying spatial frequencies yields the modulation transfer function (MTF). The modulation transfer function has become a widely used means of specifying the performance of lens systems and photographic films.

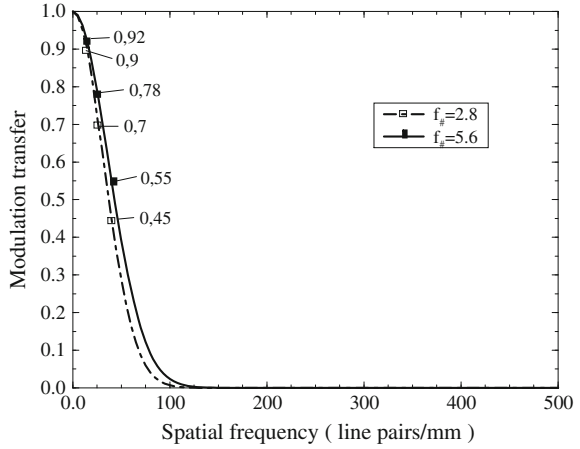
In practice, an approximation of the MTF can be obtained by an inverse Fourier transformation of the point spread function. The Gaussian approximation given by Eq. (2.15) and shown in Fig. 2.55 greatly simplifies this transformation. In the following we continue to simplify the description of imaging by considering only one-dimensional functions. The Fourier transformation FT of a one-dimensional Gaussian function is given by:

$$\sigma\sqrt{2\pi} \exp(-2\pi^2\sigma^2r^2) \xleftrightarrow{\text{FT}} \frac{1}{\sigma\sqrt{2\pi}} \exp\left(-\frac{x^2}{2\sigma}\right) \tag{2.19}$$

where σ determines the width of the Gaussian curve and r represents the variable for the spatial frequency.

Figure 2.58 shows a plot of image modulation Mod versus spatial frequency for three apertures of a hypothetical lens system without spherical aberration as obtained by the inverse transformation of the Gaussian approximation of the Airy function. As

Fig. 2.59 Modulation transfer data of a high quality 100 mm lens for two different f-numbers at three spatial frequencies each and a Gaussian fit through the data measured at the highest frequency



already shown in Table 2.7, the minimum image diameter decreases with decreasing f-numbers. As a consequence, high spatial frequencies can only be recorded at small f-numbers and, for a given spatial frequency r , small f-numbers yield better contrast compared to large f-numbers. Although the shape of these curves of the image modulation Mod as a function of the spatial frequencies only roughly approximates the shape of MTFs of real lens systems, the qualitative behavior can clearly be seen.

However, taking lens aberrations into account results in major changes of the MTFs, especially when using small f-numbers. This can be seen in Fig. 2.59 where the measured values of a high quality 100 mm lens are presented together with a Gaussian curve fitted to the value measured at the highest frequency. These values of the modulation transfer are often given in the data sheets of a lens system for different f-numbers and magnifications. From experience these values can be used for a rough estimation of the image diameters to be expected, regardless of the fact that they were originally measured using white light and therefore consider also chromatic aberrations, which do not have to be taken into account for monochromatic laser light. According to the previous discussion, we assume that the MTF can be described by the inverse Fourier transform of the Gaussian approximation of the normalized image intensity distribution $I(x)/I_{\max}$, which can be written in normalized form as:

$$\tilde{M}_{TF} = \exp(-2\pi^2\sigma^2r^2) . \tag{2.20}$$

Taking a characteristic value r' for the spatial frequency ($r' \approx d_\tau$) and the corresponding MTF value \tilde{M}_{TF} into account, Eq. (2.15) can be used in order to determine σ and therefore a function through this point in the MTF (e.g. $\tilde{M}_{TF}(r') = 0.55$ at $r' = 40$ line pairs/mm from Fig. 2.59):

$$\sigma = \sqrt{-\frac{\ln[\tilde{M}_{TF}(r')]}{2\pi^2r'^2}} . \tag{2.21}$$

Now, Eq. (2.15) can be used to approximate the normalized intensity distribution of the image. In contrast to the Bessel function the Gaussian approximation has no zero-crossings (see Fig. 2.55). An image diameter can therefore not be determined by taking the x -value of the first zero. This requires some kind of threshold level. In digital PIV a certain threshold is normally used because of electronic background noise. In the following we assume that the lower 20% of the intensity of an image will not be used for evaluation. This assumption and Eq. (2.15) yield the following formula for the radius of an image of a circular object:

$$x' = \sqrt{-2\sigma^2 \ln 0.2} \quad (2.22)$$

When substituting Eq. (2.21) we obtain an approximation of the image diameter d' that corresponds to a circular object which has an extension $(2r')^{-1}$:

$$d' \approx 0.8 \sqrt{-\frac{\ln [\tilde{M}_{\text{TF}}(r')]}{r'^2}}. \quad (2.23)$$

For the estimation of the image diameters of smaller objects the same approximation as in Eq. (2.14) can be used to obtain:

$$d_\tau \approx \sqrt{-0.64 \frac{\ln [\tilde{M}_{\text{TF}}(r')]}{r'^2} - \left(\frac{M}{2r'}\right)^2}. \quad (2.24)$$

The use of a MTF is a practical approach to describe the performance of optical systems. Since the underlying optical processes are much more complex, the description would be more complete when considering also the relative phase shift. However, phase shifts in optical systems occur only off axis and are of less interest than the MTF [23]. For many practical applications, the MTF of a complex optical system can be assumed to be simply the product of the MTFs of the individual components. The image diameter estimated by Eq. (2.24) is approximately 20 μm ($M = 1/4$, $f_\# = 2.8$) and is in good correspondence with image diameters found during experiments.

2.5.3 Perspective Projection

Figure 2.56 explained the imaging of objects from the *object plane* to the *image plane*. However, in most case the particle in the flow will not just move in a plane parallel to the light sheet, but will also have a velocity component perpendicular to the light sheet plane. In order to fully explain the influence of the velocity component perpendicular to the light sheet on the location of the image points in the coordinate system x, y, z (Fig. 2.60), the imaging through the lens must be taken into account. Ideal imaging

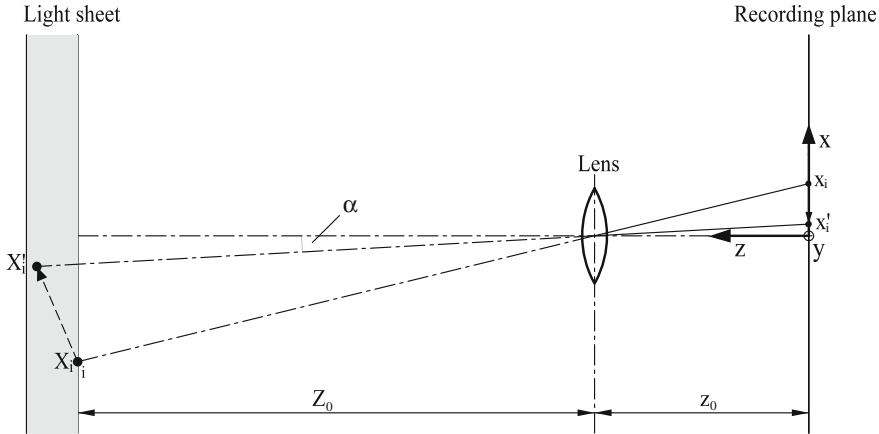


Fig. 2.60 Imaging of a particle within the light sheet on the recording plane

conditions are assumed for this calculation. Image distortions resulting from non-ideal lenses could be taken into account by means of an extended model which is beyond the scope of this book (see [18]). The underlying perspective projection can either be modeled by defining a homogeneous coordinate system in a more general way or in this simple case by trigonometric considerations (see Fig. 2.60).

\mathbf{D} defines the particle displacement between the two light pulses by its components D_X, D_Y, D_Z in the object plane (light sheet). The following relation between the location of corresponding images in the image plane (sensor) due to the recording of a particle at position \mathbf{x}_i and \mathbf{x}'_i is obtained (Fig. 2.61):

$$\tan(\alpha) = \frac{x'_i}{z_0} \tag{2.25}$$

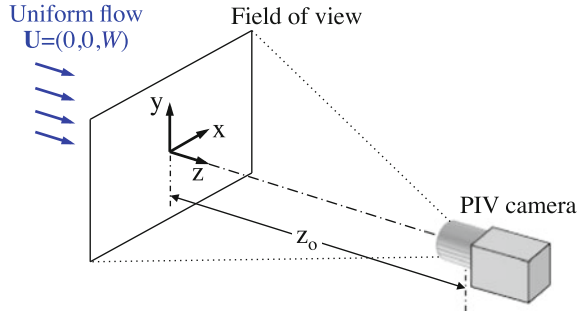
The image displacement $\mathbf{d} = \mathbf{x}'_i - \mathbf{x}_i$ corresponding to a certain particle displacement \mathbf{D} can be obtained:

$$x'_i - x_i = -M(D_X + D_Z x'_i/z_0) \tag{2.26}$$

$$y'_i - y_i = -M(D_Y + D_Z y'_i/z_0) . \tag{2.27}$$

Assuming a particle displacement only in the X , and Y directions ($D_Z \approx 0$) would simplify Eqs. (2.26) and (2.27) considerably. Then, the in-plane particle displacement could easily be determined by multiplying the image displacement by $(-M)$. In this particular case, the only uncertainty of the velocity measurement would be introduced by the uncertainty in determining the image displacement and the geometric parameters. However, in practical cases a flow field is never strictly two-dimensional over the whole observation field. Moreover, conventional PIV, which was – at the

Fig. 2.61 3D representation of the coordinate system, the observation field and a generic uniform flow aligned with the viewing axis of the PIV camera



beginning – developed for measurements of flow fields with weak out-of-plane components only, has been adapted also for use in highly three-dimensional flows over the last decade. It can be seen in Eqs. (2.26) and (2.27), that a particle displacement in the Z -direction influences the particle image displacement, especially for large magnitudes of X'_i and Y'_i at the edges of the observation field [37, 62]. This effect introduces an uncertainty in measuring the in-plane velocity components, because it cannot be separated from the in-plane components. This uncertainty will turn into a systematic error if it is assumed that PIV determines just the in-plane components even for larger viewing angles (see Sect. 6.1).

One way to reduce this error is to increase the camera standoff distance Z_0 thereby reducing the viewing angles towards the edge of the field of view (see Sect. 6.4). However, the only way to completely avoid this error is – in particular for highly three-dimensional flows – to measure all three components of the velocity vectors, for example by means of stereoscopic techniques (see Sect. 8.1).

2.5.4 Basics of Microscopic Imaging

To date, micron-resolution PIV is of increasing interest because of growing applications in biomicrofluidics and microfluidics in general. Both are increasingly popular and spreading fields of research since the beginning of the century. The principles of microscopic imaging are considerably different from imaging through camera lenses. These differences will be discussed here.

Microscopes usually consist of two magnifying stages, the objective lens and the eyepiece lens (sometimes referred to as the ocular). The objective lens is composed of potentially many simple lenses that together form the intermediate image of the object under investigation. In modern microscopes the space between the objective lens and the eyepiece lenses is called infinity space. A point source at the focal plane is transformed to parallel rays after passing through the objective lens. The virtue of this approach is that any number of planar elements, e.g. color filters, neutral density filters, beam splitters, may be inserted into this space without changing the imaging focal characteristics of the microscope. The infinity-corrected image then passes

through the eyepiece where it is further magnified and focused to form an image the user can see with the eyes. The total magnification of a microscope is given by the product of the individual magnifications of the objective and eyepiece [29].

The *numerical aperture* of a microscope objective determines the ability to gather light and resolve fine details at a certain object distance. However, the total resolution of a microscope system additionally depends on the numerical aperture of the substage condenser.

A *microscope objective* is the most important component of an optical microscope since it determines the image quality. Standard bright-field objectives are the most common for investigations utilizing traditional illumination techniques. More complex methods frequently require a detector close to the rear focal plane. Plan apochromat or fluorite objectives with a high numerical aperture allow for the investigation of thinly cut fixed tissues adhered to glass substrates and usually produce high-resolution images. However, attempts to image details at micrometer distances from the cover glass in a fluid often suffer from severe spherical aberration. The use of water instead of oil reduces these aberration problems. Most microscope objectives are designed to be used with a cover glass. Thicknesses of 0.17 mm are satisfactory when the objective numerical aperture is 0.4 or less. However, when using a higher numerical aperture, cover glass thickness variations of only a few micrometers result in dramatic image degradation due to aberration, which grows with increasing cover glass thickness. Specially designed objective lenses featuring correction collars that allow the adjustment of the central lens group position to coincide with fluctuations in cover glass thickness can be used in order to compensate for this source of error.

In modern wide-field fluorescence microscopy and laser scanning confocal microscopy (described in Sect. 2.5.7), the collection and measurement of secondary emission gathered by the objective can be accomplished by photomultipliers, photodiodes and CCD or CMOS sensors.

In analogy to the imaging of conventional objective lenses described in Sect. 2.5.2, microscopes might typically suffer from five common aberrations: spherical, chromatic, curvature of field, comatic and astigmatic. In stereoscopic microscopy geometrical distortion has to be considered additionally. All optical microscopes, including conventional wide-field microscopes and confocal microscopes (Sect. 2.5.7) are limited in the resolution that can be achieved. As described in Sect. 2.5.1, in a perfect optical system, resolution and therefore contrast is limited by numerical aperture of the optical components and by the wavelength of the light. In a real fluorescence microscope, contrast is determined by the dynamic range of the signal, optical aberrations of the imaging system, number of photons collected from the fluorophore (if fluorescence is used) and the number of picture elements (pixel) per unit area.

The *eyepieces* in combination with microscope objectives further magnifies the intermediate image. Literature usually distinguishes two types of eyepieces depending on the lens and aperture diaphragm arrangement: the negative eyepieces with an internal aperture diaphragm and positive eyepieces with an aperture diaphragm below the lenses of the eyepiece. The eyepiece is usually designed to work together with objectives to eliminate chromatic aberration.

The *substage condenser* gathers light from the microscope light source and concentrates it into a cone of light that illuminates the object with uniform intensity over the entire field of view. The performance of the condenser is one of the most important factors in obtaining high quality images in the microscope.

The object illumination is one of the critical aspects in optical microscopy. In conventional microscopy the illumination is performed by a white light source and a condenser, which is a lens arrangement generating uniform illumination of the object. There are many ways to arrange the illumination depending on the properties of the samples being observed. Commonly, microscopes are used to observe thin, transparent samples. Consequently transmission mode is frequently used. In micro-PIV the systems being imaged often only have one direction of optical access. Consequently, reflection and fluorescence modes are often used. Regardless of the imaging mode used, image brightness is governed by the illumination light intensity and the numerical aperture. The brightness of the microscope illumination is determined by the square of the condenser working numerical aperture, whereas the brightness of the image is proportional to the square of the objective numerical aperture. One caveat to this brightness discussion in the case of fluorescent imaging is that once the illumination brightness is sufficiently high that all the fluorophores on a particle are excited, the particle brightness cannot be increased except by increasing the exposure time, allowing more fluorophore excitement and emission cycles.

In reflected light microscopy oblique or epi-illumination (illumination from above) is utilized for the study of objects that are opaque, including semiconductors, ceramics, metals, polymers and many others. Beside reflection, fluorescence can be used in order to emit light from parts of the object for imaging. The lasers commonly employed in micro PIV need larger pulse widths compared to PIV applications where scattered light is recorded. More details on modern microscopy can be found in [29].

2.5.5 *In-Plane Spatial Resolution of Microscopic Imaging*

For infinity-corrected microscope objective lenses, MEINHART & WERELEY [39] showed that

$$f_{\#} = \frac{1}{2} \left[\left(\frac{n}{NA} \right)^2 - 1 \right]^{\frac{1}{2}}. \quad (2.28)$$

The numerical aperture is defined as $NA \equiv n \sin \theta$, where n is the index of refraction of the recording medium and θ is the half-angle subtended by the aperture of the recording lens. Numerical aperture is a more convenient expression to use in microscopy because of the different immersion media used. In photography, generally air is the only immersion medium used and hence $f_{\#}$ is sufficient. To avoid confusion when reading the μ PIV literature, it must be noted here that Eq. (2.28) reduces to

$$f_{\#} \approx \frac{1}{2NA} \tag{2.29}$$

for the immersion medium being air ($n_{\text{air}} \approx 1.0$) and small numerical apertures. This is a small angle approximation that is accurate to within 10% for $NA \leq 0.25$ but approaches 100% error for $NA \geq 1.2$ [39]. This approximation is used, for example, by [49, 55]. Combining Eqs. (2.13) and (2.28) yields the expression

$$d_{\text{diff}} = 1.22M\lambda \left[\left(\frac{n}{NA} \right)^2 - 1 \right]^{\frac{1}{2}} \tag{2.30}$$

for the diffraction-limited spot size in terms of the numerical aperture directly. As mentioned above, the actual recorded image can be estimated as the convolution of the point-spread function with the geometric image (see Eq. (2.14)).

2.5.6 Microscopes Typically Used in Micro-PIV

The most common microscope objective lenses range from diffraction-limited oil-immersion lenses with $M = 60$, $NA = 1.4$ to low magnification air-immersion lenses with $M = 10$, $NA = 0.1$. Table 2.8 gives effective particle diameters recorded through a circular aperture and then projected back into the flow, d_{τ}/M . Using conventional microscope optics, particle image resolutions of $d_{\tau}/M \sim 0.3 \mu\text{m}$ can be obtained using oil-immersion lenses with numerical apertures of $NA = 1.4$ and particle diameters $d_p < 0.2 \mu\text{m}$. For particle diameters $d_p > 0.3 \mu\text{m}$, the geometric component of the image decreases the resolution of the particle image. The low magnification air-immersion lens with $M = 10$, $NA = 0.25$ is diffraction-limited for particle diameters $d_p < 1.0 \mu\text{m}$. (see right column in Table 2.8)

Table 2.8 Effective particle image diameters when projected back into the flow, d_{τ}/M (μm) [68]

M	60	40	40	20	10
NA	1.40	0.75	0.60	0.50	0.25
n	1.515	1.00	1.00	1.00	1.00
d_p (μm)	Eff. particle image dia. d_{τ}/M (μm)				
0.01	0.29	0.62	0.93	1.24	2.91
0.10	0.30	0.63	0.94	1.25	2.91
0.20	0.35	0.65	0.95	1.26	2.92
0.30	0.42	0.69	0.98	1.28	2.93
0.50	0.58	0.79	1.06	1.34	2.95
0.70	0.76	0.93	1.17	1.43	2.99
1.00	1.04	1.18	1.37	1.59	3.08
3.00	3.01	3.06	3.14	3.25	4.18

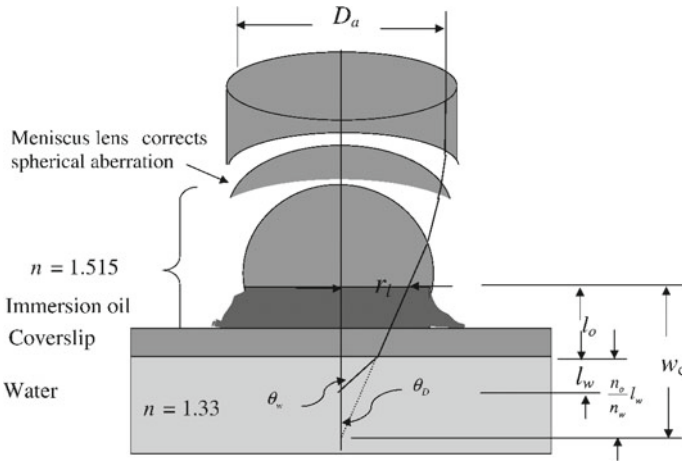


Fig. 2.62 Geometry of a high numerical aperture oil-immersion lens, immersion oil, coverslip, and water as the working fluid. A point source of light emanating from a depth in the water, l_w , appears to be at a distance w_d from the lens entrance. After [39]

Effective numerical aperture. In experiments where the highest possible spatial resolution is desired, researchers often choose high numerical aperture oil-immersion lenses. These lenses are quite complicated and designed to conduct as much light as possible out of a sample (see Fig. 2.62) by not allowing the light to pass into a medium with a refractive index as low as that of air ($n_{\text{air}} \approx 1.0$). When the index of refraction of the working fluid is lower than that of the immersion medium, the effective numerical aperture that an objective lens can deliver is decreased from that specified by the manufacturer because of total internal reflection. MEINHART & WERELEY [39] have analyzed this numerical aperture reduction through a ray tracing procedure.

As a specific example, assume that a $60\times$ magnification, numerical aperture $NA_D = 1.4$ oil-immersion lens optimized for use with a $170 \mu\text{m}$ coverslip and a maximum working distance w_d of $200 \mu\text{m}$ is used with immersion oil having an index of refraction n_o matching that of the coverslip and a working fluid (water) with a lower refractive index (n_w). This is a common situation in μPIV and is described by MEINHART & WERELEY [41], among many others. The following analysis is not restricted to these specific parameters and is easily generalizable to any arbitrary immersion medium and working fluid as long as the immersion medium refractive index exceeds that of the working fluid.

Using a complicated ray-tracing procedure, MEINHART & WERELEY [39] derived an implicit expression relating the depth into the flow at which the focal plane is located, called the imaging depth l_w , to the effective numerical aperture NA_{eff} . The expression is

Fig. 2.63 Effective numerical aperture of an oil-immersion lens imaging into water as a function of the dimensionless imaging depth, after [39]

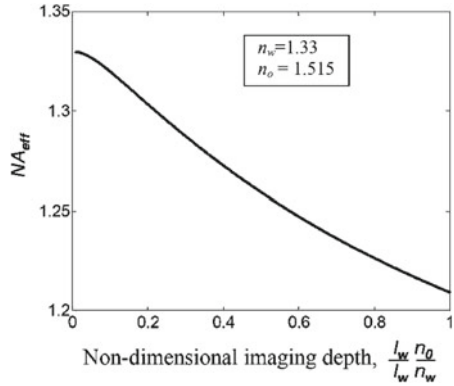


Table 2.9 Estimates of the diffraction-limited spot size d_{diff} for various imaging media as a function of imaging depth l_w [39]

Imaging depth l_w	Imaging medium	NA_{eff}	d_{diff} (μm)
All Depths	Oil	1.40	18.8
0 μm (min)	Water	1.33	24.8
200 μm (max)	Water	1.21	34.2

$$\frac{w_d}{\left[\left(\frac{n_o}{NA_D}\right) - 1\right]^{\frac{1}{2}}} = \frac{l_w}{\left[\left(\frac{n_w}{NA_{\text{eff}}}\right) - 1\right]^{\frac{1}{2}}} + \frac{w_d - \frac{n_o}{n_w} l_w}{\left[\left(\frac{n_o}{NA_{\text{eff}}}\right) - 1\right]^{\frac{1}{2}}} \tag{2.31}$$

where n_o and n_w are the refractive indices of the oil and water and w_d is the lens's working distance. Since no closed-form analytical solution is possible for Eq. (2.31), it is solved numerically for the imaging depth l_w in terms of NA_{eff} . Figure 2.63 shows the numerical solution of Eq. (2.31) using $n_o = 1.515$ and $n_w = 1.33$. When imaging at the coverslip boundary, i.e. only slightly into the water, the effective numerical aperture is approximately equal to the refractive index of the water, 1.33. The effective numerical aperture decreases with increasing imaging depth. At the maximum imaging depth the effective numerical aperture is reduced to approximately 1.21. The effective numerical aperture and the diffraction-limited spot size are given as a function of the imaging medium and imaging depth in Table 2.9. The refractive index change at the water/glass interface significantly reduces the effective numerical aperture of lens, even when the focal plane is right at the surface of the glass. This in turn increases the diffraction-limited spot size which reduces the spatial resolution of the μPIV technique.

In experiments where the working fluid is water, a similar diffraction-limited spot size can be achieved using a $NA = 1.0$ water-immersion lens, $d_{\text{diff}} = 39.8 \mu\text{m}$, compared to an oil-immersion lens, which may only achieve an effective numerical aperture, $NA_{\text{eff}} \approx 1.21$ where $d_{\text{diff}} = 34.2 \mu\text{m}$. A water-immersion lens with $NA_D = 1.2$ will exhibit better performance than the oil-immersion lens, having $d_{\text{diff}} = 21.7$

μm . Further, water-immersion lenses are designed to image into water and will produce superior images to the oil immersion lens when being used to image a water flow.

2.5.7 Confocal Microscopic Imaging

The laser scanning confocal microscope (LSCM) techniques offer some advantages over conventional optical microscopy. This kind of microscopes feature a controllable depth of field, the elimination of image degrading out-of-focus information and have the ability to image serial optical sections of relatively thick objects. Its basic concept has been developed by MARVIN MINSKY and was patented in 1957 [45, 46]. As described earlier, in a conventional wide-field microscope, the object is illuminated mostly by a white light source. In contrast to that, the method of image formation in a laser confocal microscope is fundamentally different. Illumination is achieved by a scanning laser beam through the object. In its classical form, the light of this beam is focused by the objective lens and the sequences of points of light from the object are detected by a photomultiplier tube through a pinhole. The output is built into an image and displayed by the computer. Digital image processing methods applied to sequences of images allow the representation image series of different depth and three-dimensional representation of specimens, as well as the time-sequence presentation of 3D data as four-dimensional imaging. The reflected light within the object can as well be used for imaging as fluorescence. The latest generation of confocal instruments has tunable filters for the control of excitation wavelength ranges and intensity. They allow the control of the intensity on a pixel-by-pixel basis while maintaining a high scanning rate.

2.6 Sensor Technology for Digital Image Recording

Sensors for digital recording are subject to a continuous rapid development. However, the potential uses of sensors introduced in the future should be assessable given a basic understanding of the interdependence between current sensor architecture and their possible application to PIV. Since the optical and electronic characteristics of sensors have a direct influence on the technical possibilities in PIV recording and the accompanying error sources, this section will be devoted to describing the operation and characteristics of these electronic sensors. There is a variety of electronic image sensors available today, but only solid state sensors will be described here. The most common are charge coupled devices, or CCD, and CMOS devices. Over the past two decades, the CCD has found the most widespread use. However, the rapid development of chip technology in the early 90s of the last century allowed the manufacturing of CMOS sensors with an improved signal-to-noise ratio and resolution. Since a couple of years they are more and more frequently used for

digital photography, machine vision and, last but not least, for high-speed PIV. Their potential application to PIV recording will be described in Sect. 3.1. A performance comparison of CCD- and CMOS-based PIV cameras can be found in [21].

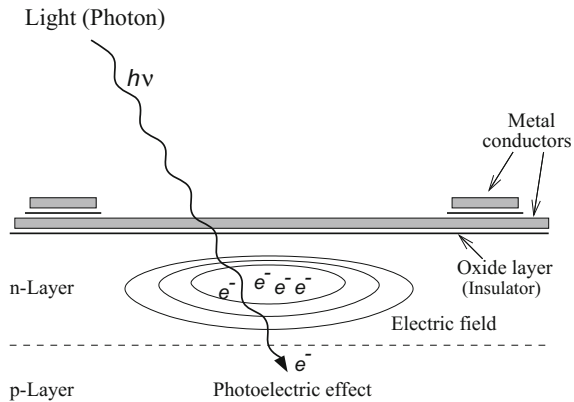
2.6.1 Characteristics of CCD Sensors

In general a CCD is an electronic sensor that can convert light (i.e. photons) into electric charge (i.e. electrons). Speaking of a CCD sensor, we generally refer to an array of many individual CCDs, either in the form of a line (e.g. in a line scan camera), or arranged in a rectangular array (of course other specialized forms also exist). The individual CCD element in the sensor is called a pixel. Its size is generally of the order of $10 \times 10 \mu\text{m}^2$, or 100 pixel/mm.

The operation of these pixel is best described by referring to the schematic cross-section shown in Fig. 2.64. The CCD is built on a semiconducting substrate, typically silicon, with metal conductors on the surface, an insulating oxide layer, an n-layer (anode) and a p-layer (cathode) below that. A small voltage applied between the metal conductors and the p-layer generates an electric field within the semiconductor. The local minimum in the electric field that is formed below the center of the pixel is associated with a lack of electrons and is known as a potential well. In essence the potential well is equivalent to a capacitor allowing it to store charge, that is, electrons. When a photon of proper wavelength enters the p-n junction of the semiconductor an electron-hole pair is generated. In physics this effect is known as the inner photoelectric effect. While the *hole*, considered as a carrier of positive charge, is absorbed in the p-layer, the generated electron (or charge) migrates along the gradient of the electric field toward its minimum (i.e. potential well) where it is stored. Electrons continue to accumulate for the duration of the pixel's exposure to light. However, the pixel's storage capacity is limited, described by its fullwell capacity which is measured in electrons per pixel. Typical CCD sensors have a fullwell capacity of the order of 10 000 to 100 000 electrons per pixel. When this number is exceeded during exposure (overexposure) the additional electrons migrate to the neighboring pixel which leads to image blooming. This effect is significantly reduced through specialized antiblooming architectures incorporated in modern CCD sensors: the overflowing charge is captured by conductors as it migrates toward the neighboring CCD cells.

Another characteristic of a pixel is its fill factor or aperture which is defined as the ratio of its optically sensitive area and its entire area. This value can reach 100% for special, scientific-grade, back-illuminated sensors or may be as low as 15% for complex interline-transfer sensors which will be described in a later section. The primary reason for the limited aperture of most pixel is the presence of opaque areas on the surface of the sensors, either metal conductors used to form the potential wells and facilitate the transport of the accumulated charge to the readout port(s), or areas which are masked off to locally store charge before it is read out. Two methods exist for improving the fill factor: back-thinning is a costly process which

Fig. 2.64 Simplified model of a (CCD) pixel



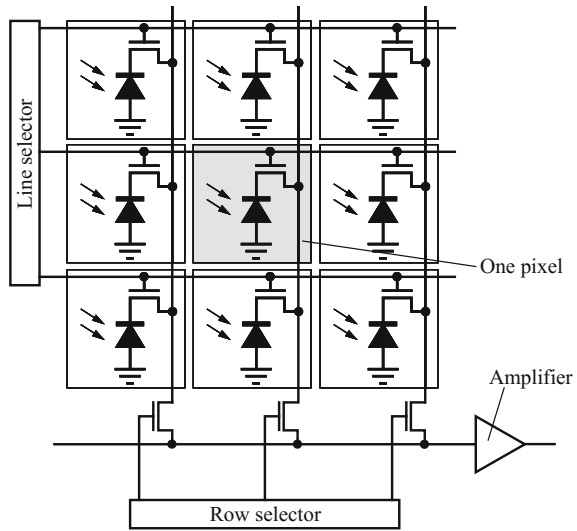
removes the back of the substrate to a few tens of microns such that the sensor may be exposed from the back. Back-thinned CCDs are custom built and are frequently applied in astronomy and spectroscopy. Also the process cannot be applied to all CCD architectures because opaque regions are frequently needed to temporarily store collected charge. An alternative and more economical approach to enhance the fill factor is to deposit an array of microlenses on to the sensor allowing each pixel to collect more of the incoming light. The light sensitivity of each pixel, as well of CCD as of CMOS sensors, may then be improved up to a factor of three.

2.6.2 Characteristics of CMOS Sensors

In most of the CMOS sensors the underlying electro-optical principle of each pixel is the photodiode as described in Sect. 2.6.1. Their main advantage compared to other techniques like photogates or phototransistors is their high sensitivity and relatively low noise. But in contrast to CCD pixel, the photodiodes in CMOS sensors can be controlled separately by MOS-FET transistors. Since the beginning of the new century, the CMOS technology has drastically improved, and offers some interesting advantages with respect to CCD technology. The breakthrough on the high-speed sensor market came with the progress in lithography that allowed the very large scale integration (VLSI) technique to be applied for CMOS sensors. Their specific architecture allows the combination of the electro-optical process with further electronic processing of the signal directly on chip.

The fundamental principle of a CMOS sensor is shown in Fig. 2.65. Each individual pixel contains an electronic circuit. This active pixel architecture together with the individual access to each pixel offer some major advantages and allows to integrate fundamental camera function like amplification, non-linear signal transformations and AD-conversion on chip. Furthermore, the number of pixel to be active can be chosen by the definition of a sub-domain, the region of interest (ROI). This allows to

Fig. 2.65 Simplified model of a CMOS sensor

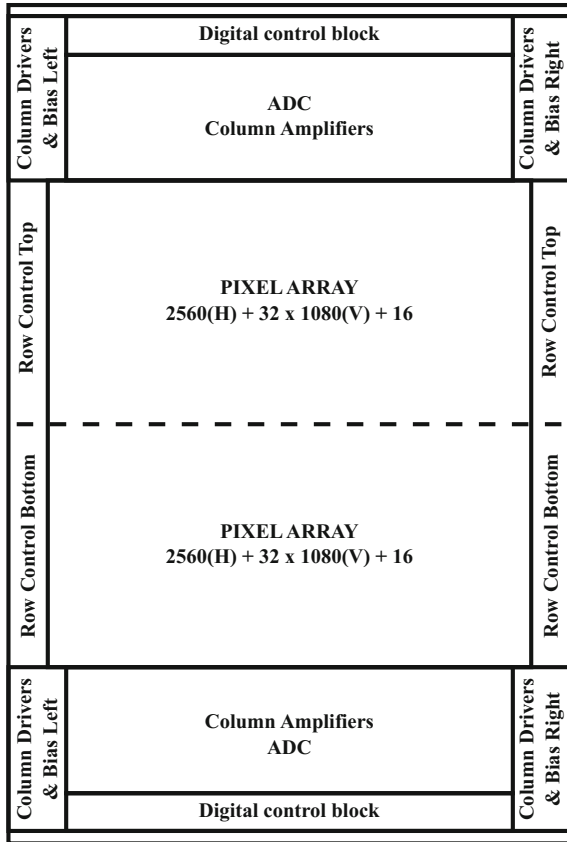


come to higher framing rates in trade of image resolution. The major drawback that still hinders the CMOS sensors to completely replace CCDs are the capacities of the relatively long electrical lines for each row and column. This leads to a significant electronic noise since the noise of the MOSFET transistors used for readout increases with the capacitance connected to their gate. This yields especially for larger sensors which are usually needed for PIV applications. The way out of this problem is the active pixel sensor (APS) which contains a separate electronic amplifier for each pixel.

2.6.2.1 Scientific CMOS Sensors

In 2009 a new type of CMOS image sensor was presented as a result of a common development of a consortium of three companies: Fairchild Imaging (nowadays belonging to BAE), Andor Technology and PCO. At the time the partners decided to call the CMOS image sensor a scientific CMOS or “sCMOS” image sensor (see Fig. 2.66) to make clear from the very beginning, that the performance data of this new type of image sensor, are very different from the usual standard CMOS image sensors. The combination of high sensitivity, low readout noise, high frame rate, high resolution and high dynamic range did not exist before, not even within the commonly used cooled CCD and emCCD cameras, which were applied in microscopy. The sensor was designed specifically to feature low readout noise which allows to discriminate even weak signals from the background and is a prerequisite for the imaging of low light signals. In other image sensors such as emCCDs (electron multiplication charge coupled devices) this is achieved by an amplification prior to the readout process. Thereby the signal-to-noise increases. In sCMOS the readout noise

Fig. 2.66 Typical sCMOS sensor layout



is extremely low. Since the values are the result of averaging calculations and a fit of a model to the intensity data (Gaussian with RMS or median) it introduces fractional intensity counts which are not so obvious as fractions of noise electrons are not physically possible. Considering a median readout noise value of 0.9 electrons implies that more than 50% of the pixel over a given time either have one noise electron or none in the recorded images. The smaller the average value is the larger the amount of images where the corresponding pixel has no noise electron. A second effect of such a low noise is its beneficial influence on the intra-scene dynamic (often used as dynamic of the image sensor or camera) of the image sensor, describing the darkest and brightest information within one image, which can be detected. Simply speaking, the smaller the noise the larger the resulting dynamic range. Furthermore the sCMOS sensors feature an excellent quantum efficiency between 60–80%, which is only outperformed by back-illuminated image sensors, but it is more than sufficient for most of the relevant PIV applications. This property opens the door for large field of view PIV applications or PIV measurements with low power and thus low cost light sources. Maybe one of the main advantages of sCMOS image sensors is

the highly parallel readout process which allows for high frame rates of up to 100 images/s (frames/s) at full resolution of 2560×2160 pixel. If the area of interest is reduced, this specific sensor can reach frame rates of up to 1000 frame/s and more allowing rapid averaging of image data. Averaging can be reduced to a couple of seconds compared to a couple of minutes. As a consequence, if high frame rates are important for an application the exposure or shutter time is decreased, which in turn reduces the influence of the dark current and increases the requirement for more light. Independent of the image sensor this also increases the data load requirements for the storage system. The dynamic range refers to the intra-scene dynamic or often named just dynamic of the sCMOS image sensors, typically in a range of 1: 25000 up to 1: 33000. It is determined by the full-well capacity of the image sensor (describing the maximum amount of charge carriers each pixel can collect before it starts to overflow) divided by the smallest signal that can be discriminated which is the readout noise.

In terms resolution of typically 5.5 or 4.2 megapixel the sCMOS cameras are rather unimpressive compared to today's consumer digital cameras and are of similar magnitude as the currently available larger interline transfer CCD-based PIV camera sensors. With $6.5 \mu\text{m}$ their pixel size is considerably larger than the consumer grade image sensors allowing for a much higher full-well capacity and with it higher dynamic range.

2.6.3 Sources of Noise

As with any electronic device, the digital image sensors are subject to electronic noise. For many electronic imaging applications the issue of noise only plays a secondary role in that it corrupts the visual perception of the image. In the case of PIV, the light scattered from small particles is ideally captured on an otherwise black background. Due to the limited light scattering efficiency of the tiny tracer particles, the recorded signal will sometimes only barely exceed the background noise level of the sensor as the observation area and observation distance is increased.

A major source of this noise is due to thermal effects which also generate electron-hole pairs that cannot be separated from those generated by the photoelectric effect: as a result weak particle images can no longer be distinguished from noise. For CCDs the production rate of the electron-hole pairs is constant at a given temperature and exposure. This dark current or dark count can be accounted for by subtracting a constant bias voltage at the output of the charge-to-voltage converter. However, the dark current has a tendency to fluctuate over time giving rise to noise, better known as dark current noise or dark noise which also increases with temperature and has a value of approximately the square root of the dark current. The rate of generation doubles for every $6-7^\circ\text{C}$ increase in temperature, which is the primary motivation for the use of cooled sensors in scientific imaging. Cryogenically cooled CCD sensors as applied in astronomy may generate less than one electron per second in each pixel.

Another source of noise is read noise or shot noise which is a direct consequence of the charge-to-voltage conversion during the readout sequence. In general, the read noise increases with the readout frequency which is why many scientific applications require *slow-scan* cameras. Under standard operating conditions a normal CCD camera will have a noise level of several hundred electrons generated in each pixel for the period of integration (1/25 or 1/30 s). A careful optimization of the conversion electronics, a reduced readout frequency as well as cooling of the sensor may limit the read noise to a few electrons RMS per pixel. Up to now the prohibitive cost of these specialized cameras has made their use for PIV recording unfeasible. Nevertheless cameras based on Peltier-cooled (i.e. electrically cooled) CCD sensors are increasingly used for PIV applications.

Images from cameras which have multiple amplifiers like the later described active pixel CMOS cameras and high-speed CCD cameras usually contain fixed pattern noise (FPN). Fixed pattern noise includes the formerly described shot noise and dark current noise. In CMOS sensors additionally spike noise appears and contributes to the FPN. Spike noise is a switching noise occurring on the video line via the drain to gate capacitance of the MOSFET transistor when an address pulse is input. A large fraction of this noise is constant and can therefore be subtracted from each pixel value before PIV evaluation (flat-field correction).

2.6.4 Spectral Characteristics

Similar to photographic film, the digital sensor has a sensitivity and spectral response. A pixel's sensitivity or quantum efficiency, QE, is defined as the ratio between the number of generated and collected photoelectrons and the number of incident photons per pixel and is most commonly measured in collected charge over light intensity $Cb/(J \cdot \text{cm}^2)$. Alternatively, units of current, $I = Q/\Delta t$, over incident power, $P = E/(\Delta t \cdot \text{Area})$, are used: $A/(W \cdot \text{cm}^2)$. To a large extent this value depends on the pixel's architecture, that is, its aperture (i.e. fill factor), material and thickness of the optically sensitive area. Due to the width and position of the frequency-dependent band-gap of silicon, the sensor's substrate material, photons of different frequencies will penetrate the sensor differently resulting in a wavelength dependent quantum efficiency of the sensor. Examples for the spectral response of several sensors are given in Fig. 2.67.

To reduce the susceptibility to infrared light, many commercially available CCD and CMOS cameras come equipped with an infrared filter in front of the sensor. Other filters may also be used to match the spectral characteristics to that of the human eye, which matches to the requirements of PIV, if a green light source is used for illumination.

The responsivity of a sensor element expresses the ratio of useful signal voltage to exposure for a given illumination. This quantity depends on both the quantum efficiency and the on-chip charge-to-voltage conversion.

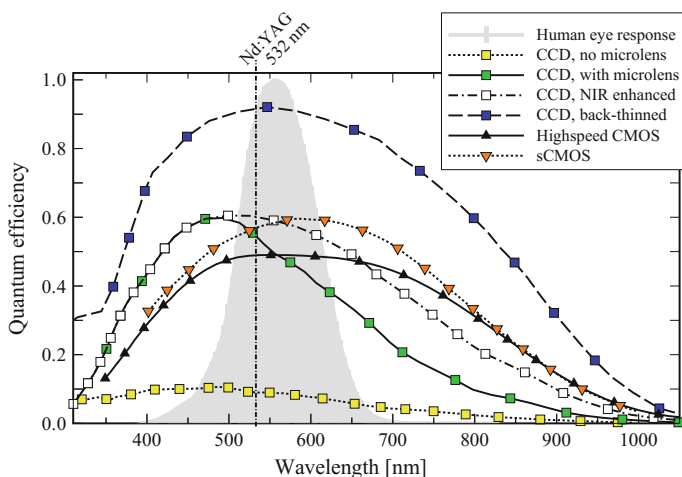


Fig. 2.67 Quantum efficiencies for various CCD and CMOS sensors. The vertical line indicates the wavelength of the most commonly used laser for PIV. Gray shaded area represents the luminous efficiency function of the human eye. Quantum efficiencies obtained from manufacturers' data sheets: Kodak KAI-4020, Sony ICX285AL, e2v CCD201-20, PCO AG Dimax-S4, Andor neo sCMOS

2.6.5 Linearity and Dynamic Range

Since each electron captured in the potential well adds linearly to the cumulative collected charge, the output signal voltage for the individual pixel is practically directly proportional to the collected charge. Nonlinearities of CCD images are usually due to overexposure or poorly designed output amplifiers. In contrast to CCDs, CMOS sensors allow for a non-linear amplification and conversion of the signals on chip. However, for most of the cameras used for PIV, the signal is linearly amplified and encoded. With adequate design, linearities with deviations of less than 1% are possible. Linearity is of importance in PIV recording when small particle images are to be located with accuracies below half a pixel. Any nonlinear behavior during recording jeopardizes the capability of measuring the particle image displacement in the sub-pixel regime.¹ Especially if the particles themselves are to be located and tracked as in PTV, a linear dependency between recorded signal and scattered light is of importance.

The sensors' dynamic range is defined as the ratio between the full-well capacity and the dark current noise. The sensors' dynamic range is defined as the ratio between the full-well capacity and the total readout noise. Since the dark current noise is temperature dependent, the dynamic range of a CCD increases as the temperature

¹A commonly used expression signifying a length scale below the spatial resolution limit of a digital image, i.e. a pixel, is called sub-pixel. For instance the intensity distribution of a particle image may be used to estimate its position with *sub-pixel* accuracy.

is lowered. Standard video sensors operating at room temperature typically have a dynamic range of 100–200 gray levels which exceeds that of human perception. Once digitized the useful signal is 7–8 bits in depth. With additional cooling and careful camera design a dynamic range exceeding 65 000 gray levels (16 bits/pixel) is possible. For the application of electronic imaging in digital PIV recording a dynamic range of 6–8 bits allows the use of small interrogation windows (32^2 pixel) with a reasonable measurement uncertainty of less than 0.1 pixel (see Sect. 6.1). For a detailed comparison of various electronic imaging cameras the reader is referred to HAIN et al. [21].

References

1. Adrian, R.J., Yao, C.S.: Pulsed laser technique application to liquid and gaseous flows and the scattering power of seed materials. *Appl. Opt.* **24**(1), 44–52 (1985). DOI 10.1364/AO.24.000044. URL <http://ao.osa.org/abstract.cfm?URI=ao-24-1-44>
2. Beskok, A., Karniadakis, G., Trimmer, W.: Rarefaction and compressibility effects in gas microflows. *ASME. J. Fluids Eng.* **118**(3), 448–456 (1996). DOI 10.1115/1.2817779. URL <http://fluidsengineering.asmedigitalcollection.asme.org/article.aspx?articleid=1428203>
3. Born, M., Wolf, E.: *Principles of Optics*, 7th edn. Cambridge University Press, Cambridge (1999). URL <https://www.cambridge.org/de/academic/subjects/physics/optics-optoelectronics-and-photonics/principles-optics-electromagnetic-theory-propagation-interference-and-diffraction-light-7th-edition>
4. Bosbach, J., Kühn, M., Wagner, C.: Large scale particle image velocimetry with helium filled soap bubbles. *Exper. Fluids* **46**(3), 539–547 (2009). DOI 10.1007/s00348-008-0579-0. URL <http://dx.doi.org/10.1007/s00348-008-0579-0>
5. Bröder, D., Sommerfeld, M.: Planar shadow image velocimetry for the analysis of the hydrodynamics in bubbly flows. *Meas. Sci. Technol.* **18**(8), 2513 (2007). DOI 10.1088/0957-0233/18/8/028. URL <http://stacks.iop.org/0957-0233/18/i=8/a=028>
6. Bryanston-Cross, P.J., Epstein, A.: The application of sub-micron particle visualisation for PIV (particle image velocimetry) at transonic and supersonic speeds. *Progr. Aerosp. Sci.* **27**(3), 237–265 (1990). DOI 10.1016/0376-0421(90)90008-8. URL <http://www.sciencedirect.com/science/article/pii/0376042190900088>
7. Buchmann, N.A., Willert, C.E., Soria, J.: Pulsed, high-power LED illumination for tomographic particle image velocimetry. *Exper. Fluids* **53**(5), 1545–1560 (2012). DOI 10.1007/s00348-012-1374-5. URL <http://dx.doi.org/10.1007/s00348-012-1374-5>
8. Caridi, G.C.A., Sciacchitano, A., Scarano, F.: Helium-filled soap bubbles for vortex core velocimetry. *Exper. Fluids* **58**, 130 (2017). DOI 10.1007/s00348-017-2415-x. URL <https://doi.org/10.1007/s00348-017-2415-x>
9. Chen, F., Liu, H., Rong, Z.: Development and application of nanoparticle tracers for PIV in supersonic and hypersonic flows. In: 50th AIAA Aerospace Sciences Meeting including the New Horizons Forum and Aerospace Exposition, AIAA (2012). DOI 10.2514/6.2012-36. URL <https://doi.org/10.2514/6.2012-36>
10. Chételat, O., Kim, K.C.: Miniature particle image velocimetry system with LED in-line illumination. *Meas. Sci. Technol.* **13**(7), 1006 (2002). DOI 10.1088/0957-0233/13/7/306. URL <http://stacks.iop.org/0957-0233/13/i=7/a=306>
11. Cummings, E.B.: An image processing and optimal nonlinear filtering technique for particle image velocimetry of microflows. *Exper. Fluids* **29**(1), S042–S050 (2000). DOI 10.1007/s003480070006. URL <http://dx.doi.org/10.1007/s003480070006>

12. Dabiri, D.: Digital particle image thermometry/velocimetry: a review. *Exper. Fluids* **46**(2), 191–241 (2009). DOI 10.1007/s00348-008-0590-5. URL <http://dx.doi.org/10.1007/s00348-008-0590-5>
13. Echols, W.H., Young, J.A.: Studies of portable air-operated aerosol generators. Technical report, NRL Report 5929, Naval Research Laboratory, Washington D.C (1963)
14. Einstein, A.: On the movement of small particles suspended in a stationary liquid demanded by the molecular-kinetic theory of heat. *Annalen der Physik (Leipzig)* **17**, 549–560 (1905). DOI 10.1002/andp.19053220806. URL <http://dx.doi.org/10.1002/andp.19053220806>
15. Estevadeordal, J., Goss, L.: PIV with LED: Particle shadow velocimetry (PSV). In: 43rd AIAA Aerospace Sciences Meeting and Exhibit, Reno, NV (USA), pp. 12,355–12,364 (2005). DOI 10.2514/6.2005-5009. URL <http://dx.doi.org/10.2514/6.2005-5009>
16. Ghaemi, S., Scarano, F.: Multi-pass light amplification for tomographic particle image velocimetry applications. *Meas. Sci. Technol.* **21**(12), 127,002 (2010). DOI 10.1088/0957-0233/21/12/127002. URL <http://stacks.iop.org/0957-0233/21/i=12/a=127002>
17. Ghaemi, S., Schmidt-Ott, A., Scarano, F.: Nanostructured tracers for laser-based diagnostics in high-speed flows. *Meas. Sci. Technol.* **21**(10), 105,403 (2010). DOI 10.1088/0957-0233/21/10/105403. URL <https://doi.org/10.1088/0957-0233/21/10/105403>
18. Gonzalez, R.C., Woods, R.E.: *Digital Image Processing*, 4th edn. Pearson (2018). URL http://www.imageprocessingplace.com/DIP-4E/dip4e_main_page.htm
19. Goodman, J.W.: *Introduction to Fourier Optics*, 4th edn. Macmillan Learning (2017). URL <http://www.macmillanlearning.com/Catalog/product/introductiontofourieroptics-fourthedition-goodman>
20. Hagsäter, S.M., Westergaard, C.H., Bruus, H., Kutter, J.P.: Investigations on LED illumination for micro-PIV including a novel front-lit configuration. *Exper. Fluids* **44**(2), 211–219 (2008). DOI 10.1007/s00348-007-0394-z. URL <http://dx.doi.org/10.1007/s00348-007-0394-z>
21. Hain, R., Kähler, C.J., Tropea, C.: Comparison of CCD, CMOS and intensified cameras. *Exper. Fluids* **42**(3), 403–411 (2007). DOI 10.1007/s00348-006-0247-1. URL <http://dx.doi.org/10.1007/s00348-006-0247-1>
22. Hand, D.P., Entwistle, J.D., Maier, R.R.J., Kuhn, A., Greated, C.A., Jones, J.D.C.: Fibre optic beam delivery system for high peak power laser PIV illumination. *Meas. Sci. Technol.* **10**(3), 239 (1999). URL <http://stacks.iop.org/0957-0233/10/i=3/a=021>
23. Hecht, E., Zajac, A.: *Optics*. Addison-Wesley Pub. Company, Massachusetts (2001)
24. Höcker, R., Kompenhans, J.: Application of particle image velocimetry to transonic flows. In: Adrian, R.J., Durao, D., Durst, F., Maeda, M., Whitelaw, J.H. (eds.) *Applications of Laser Techniques to Fluid Mechanics: 5th International Symposium Lisbon, Portugal, 9–12 July, 1990*, pp. 416–434. Springer, New York (1991)
25. Hsu, P.S., Roy, S., Jiang, N., Gord, J.R.: Large-aperture, tapered fiber-coupled, 10-kHz particle-image velocimetry. *Opt. Express* **21**(3), 3617–3626 (2013). DOI 10.1364/OE.21.003617. URL <http://www.opticsexpress.org/abstract.cfm?URI=oe-21-3-3617>
26. van de Hulst, H.C.: *Light Scattering by Small Particles*. Wiley, Inc., New York (republished 1981 by Dover Publications, New York) (1957)
27. Humphreys, W., Bartram, S., Blackshire, J.: A survey of particle image velocimetry applications in langley aerospace facilities. In: 31st Aerospace Sciences Meeting, January 11–14, Reno, NV. American Institute of Aeronautics and Astronautics (1993). DOI 10.2514/6.1993-411. URL <http://dx.doi.org/10.2514/6.1993-411>
28. Hunter, W.W., Nichols, C.E.: Wind tunnel seeding systems for laser velocimeters. In: NASA Workshop, 19–20 March, NASA Langley Research Center, vol. NASA-CP-2393. NASA (1985). URL <http://ntrs.nasa.gov/search.jsp?R=19860001970>
29. Inoué, S., Spring, K.R.: *Video Microscopy: The Fundamentals*. Language of Science, 2nd edn. Springer, New York (1997)
30. Kähler, C.J.: High Resolution Measurements by Long-range Micro-PIV. VKI Lecture Series: Recent Advances in Particle Image Velocimetry (2009). URL <https://store.vki.ac.be/lecture-series-monographs/measurement-techniques/recent-advances-in-particle-image-velocimetry.html>

31. Kähler, C.J., Sammler, B., Kompenhans, J.: Generation and control of tracer particles for optical flow investigations in air. *Exper. Fluids* **33**(6), 736–742 (2002). DOI 10.1007/s00348-002-0492-x. URL <http://dx.doi.org/10.1007/s00348-002-0492-x>
32. Kähler, C.J., Sammler, B., Kompenhans, J.: Generation and control of tracer particles for optical flow investigations in air. In: M. Stanislas, J. Westerweel, J. Kompenhans (eds.) *Particle Image Velocimetry: Recent Improvements*, pp. 417–426. Springer, Berlin (2004). DOI 10.1007/978-3-642-18795-7_30. URL http://dx.doi.org/10.1007/978-3-642-18795-7_30
33. Kompenhans, J., Raffel, M.: Application of PIV technique to transonic flows in a blow-down wind tunnel. In: S.S. Cha, J.D. Trolinger (eds.) *Optical Techniques in Fluid, Thermal, and Combustion Flow*, San Diego, CA, United States, vol. 2005, pp. 425–436 (1993). DOI 10.1117/12.163727. URL <http://dx.doi.org/10.1117/12.163727>
34. Kühn, M., Ehrenfried, K., Bosbach, J., Wagner, C.: Large-scale tomographic particle image velocimetry using helium-filled soap bubbles. *Exper. Fluids* **50**(4), 929–948 (2011). DOI 10.1007/s00348-010-0947-4. URL <http://dx.doi.org/10.1007/s00348-010-0947-4>
35. Lauterborn, W., Kurz, T.: *Coherent Optics - Fundamentals and Applications*, 2nd edn. Springer, Berlin (2003). DOI 10.1007/978-3-662-05273-0. URL <https://dx.doi.org/10.1007/978-3-662-05273-0>
36. Lindken, R., Merzkirch, W.: A novel PIV technique for measurements in multiphase flows and its application to two-phase bubbly flows. *Exper. Fluids* **33**(6), 814–825 (2002). DOI 10.1007/s00348-002-0500-1. URL <http://dx.doi.org/10.1007/s00348-002-0500-1>
37. Lourenço, L.M.: Some comments on particle image displacement velocimetry. In: *Particle Image Displacement Velocimetry*, von Karman Lecture Series 1988-06. Von Karman Institute, Rhode-Saint-Genèse, Belgium (1988)
38. Machacek, M.: A quantitative visualization tool for large wind tunnel experiments. Ph.D. thesis, ETH Zürich (2003)
39. Meinhart, C.D., Wereley, S.T.: The theory of diffraction-limited resolution in microparticle image velocimetry. *Meas. Sci. Technol.* **14**(7), 1047 (2003). DOI 10.1088/0957-0233/14/7/320. URL <http://stacks.iop.org/0957-0233/14/i=7/a=320>
40. Meinhart, C.D., Wereley, S.T., Gray, M.H.B.: Volume illumination for two-dimensional particle image velocimetry. *Meas. Sci. Technol.* **11**(6), 809 (2000). DOI 10.1088/0957-0233/11/6/326. URL <http://stacks.iop.org/0957-0233/11/i=6/a=326>
41. Meinhart, C.D., Wereley, S.T., Santiago, J.G.: PIV measurements of a microchannel flow. *Exper. Fluids* **27**(5), 414–419 (1999). DOI 10.1007/s003480050366. URL <http://dx.doi.org/10.1007/s003480050366>
42. Melling, A.: Seeding gas flows for laser anemometry. In: *AGARD Conference on Advanced Instrumentation for Aero Engine Components*, 19–23 May, Philadelphia (USA), AGARD-CP 399-8 (1986)
43. Melling, A.: Tracer particles and seeding for particle image velocimetry. *Meas. Sci. Technol.* **8**(12), 1406 (1997). DOI 10.1088/0957-0233/8/12/005. URL <http://stacks.iop.org/0957-0233/8/i=12/a=005>
44. Meyers, J.: Generation of particles and seeding. In: *Laser Velocimetry*, von Karman Institute for Fluid Dynamics Lecture Series 1991-08, vol. 8. Von Karman Institute, Rhode-Saint-Genèse, Belgium (1991)
45. Minsky, M.: Microscopy apparatus (1961). US Patent 3,013,467
46. Minsky, M.: Memoir on inventing the confocal scanning microscope. *Scanning* **10**(4), 128–138 (1988). DOI 10.1002/sca.4950100403. URL <http://dx.doi.org/10.1002/sca.4950100403>
47. Molezzi, M.J., Dutton, J.C.: Application of particle image velocimetry in high-speed separated flows. *AIAA J.* **31**(3), 438–446 (1993). DOI 10.2514/3.113490. URL <http://arc.aiaa.org/doi/abs/10.2514/3.11349>
48. Nogueira, S., Sousa, R.G., Pinto, A.M.F.R., Riethmuller, M.L., Campos, J.B.L.M.: Simultaneous PIV and pulsed shadow technique in slug flow: a solution for optical problems. *Exper. Fluids* **35**(6), 598–609 (2003). DOI 10.1007/s00348-003-0708-8. URL <http://dx.doi.org/10.1007/s00348-003-0708-8>

49. Olsen, M.G., Adrian, R.J.: Out-of-focus effects on particle image visibility and correlation in microscopic particle image velocimetry. *Exper. Fluids* **29**(1), S166–S174 (2000). DOI 10.1007/s003480070018. URL <http://dx.doi.org/10.1007/s003480070018>
50. van Oudheusden, B.W., Scarano, F.: PIV Investigation of Supersonic Base-Flow–Plume Interaction, pp. 465–474. Springer, Berlin (2008). DOI 10.1007/978-3-540-73528-1_25. URL http://dx.doi.org/10.1007/978-3-540-73528-1_25
51. Probst, R.: *Physicochemical Hydrodynamics: An Introduction*, 2nd edn. Wiley (2003). URL <http://eu.wiley.com/WileyCDA/WileyTitle/productCd-0471458309.html>
52. Ragni, D., Schrijer, F., van Oudheusden, B.W., Scarano, F.: Particle tracer response across shocks measured by PIV. *Exper. Fluids* **50**(1), 53–64 (2011). DOI 10.1007/s00348-010-0892-2. URL <http://dx.doi.org/10.1007/s00348-010-0892-2>
53. Saleh, B.E.A., Teich, M.C.: *Fundamentals of Photonics. Pure and Applied Physics*, 2nd edn. Wiley, Inc. (2007). DOI 10.1002/0471213748. URL <http://dx.doi.org/10.1002/0471213748>
54. Samimy, M., Lele, S.K.: Motion of particles with inertia in a compressible free shear layer. *Phys. Fluids A* **3**(8), 1915–1923 (1991). DOI 10.1063/1.857921. URL <http://scitation.aip.org/content/aip/journal/pofa/3/8/10.1063/1.857921>
55. Santiago, J.G., Wereley, S.T., Meinhart, C.D., Beebe, D.J., Adrian, R.J.: A particle image velocimetry system for microfluidics. *Exper. Fluids* **25**(4), 316–319 (1998). DOI 10.1007/s003480050235. URL <http://dx.doi.org/10.1007/s003480050235>
56. Scarano, F.: Overview of PIV in Supersonic Flows, pp. 445–463. Springer, Berlin (2008). DOI 10.1007/978-3-540-73528-1_24. URL http://dx.doi.org/10.1007/978-3-540-73528-1_24
57. Scarano, F., Ghaemi, S., Caridi, G.C.A., Bosbach, J., Dierksheide, U., Sciacchitano, A.: On the use of helium-filled soap bubbles for large-scale tomographic PIV in wind tunnel experiments. *Exper. Fluids* **56**(2), 42 (2015). DOI 10.1007/s00348-015-1909-7. URL <http://dx.doi.org/10.1007/s00348-015-1909-7>
58. Scarano, F., van Oudheusden, B.W.: Planar velocity measurements of a two-dimensional compressible wake. *Exper. Fluids* **34**(3), 430–441 (2003). DOI 10.1007/s00348-002-0581-x. URL <http://dx.doi.org/10.1007/s00348-002-0581-x>
59. Schneiders, J.F.G., Caridi, G.C.A., Sciacchitano, A., Scarano, F.: Large-scale volumetric pressure from tomographic PTV with HFSB tracers. *Exper. Fluids* **57**(11), 164 (2016). DOI 10.1007/s00348-016-2258-x. URL <https://doi.org/10.1007/s00348-016-2258-x>
60. Schrijer, F.F.J., Scarano, F., van Oudheusden, B.W.: Application of PIV in a Mach 7 double-ramp flow. *Exper. Fluids* **41**(2), 353–363 (2006). DOI 10.1007/s00348-006-0140-y. URL <http://dx.doi.org/10.1007/s00348-006-0140-y>
61. Schröder, A., Geisler, R., Elsinga, G.E., Scarano, F., Dierksheide, U.: Investigation of a turbulent spot and a tripped turbulent boundary layer flow using time-resolved tomographic PIV. *Exper. Fluids* **44**(2), 305–316 (2008). DOI 10.1007/s00348-007-0403-2. URL <http://dx.doi.org/10.1007/s00348-007-0403-2>
62. Sinha, S.K.: Improving the accuracy and resolution of particle image or laser speckle velocimetry. *Exper. Fluids* **6**(1), 67–68 (1988). DOI 10.1007/BF00226137. URL <http://dx.doi.org/10.1007/BF00226137>
63. Solf, K.D.: *Fotografie: Grundlagen, Technik, Praxis. Fischer-Handbücher. 6034. Fischer-Taschenbuch-Verlag* (1978)
64. Stanislas, M., Okamoto, K., Kähler, C.J.: Main results of the first international PIV challenge. *Meas. Sci. Technol.* **14**(10), R63 (2003). DOI 10.1088/0957-0233/14/10/201. URL <http://stacks.iop.org/0957-0233/14/i=10/a=201>
65. Towers, C.E., Bryanston-Cross, P.J., Judge, T.R.: Application of particle image velocimetry to large-scale transonic wind tunnels. *Opt. Laser Technol.* **23**, 289–295 (1991). DOI 10.1016/0030-3992(91)90007-B. URL adsabs.harvard.edu/abs/1991OptLT.23.289T
66. Urban, W.D., Mungal, M.G.: Planar velocity measurements in compressible mixing layers. *J. Fluid Mech.* **431**, 189–222 (2001). DOI 10.1017/S0022112000003177. URL http://journals.cambridge.org/article_S0022112000003177
67. Van Kampen, N.G.: *Stochastic Processes in Physics and Chemistry*, 3rd edn. Elsevier Science, North-Holland Personal Library (2011)

68. Wereley, S.T., Meinhart, C.D.: Micron-resolution particle image velocimetry. In: K.S. Breuer (ed.) *Microscale Diagnostic Techniques*, pp. 51–112. Springer, Berlin (2005). DOI 10.1007/3-540-26449-3_2. URL http://dx.doi.org/10.1007/3-540-26449-3_2
69. Wernet, J.H., Wernet, M.P.: Stabilized alumina/ethanol colloidal dispersion for seeding high temperature air flows. In: *ASME Symposium on Laser Anemometry: Advances and Applications*, 19–23 June, Lake Tahoe, Nevada (USA) (1994). URL <https://ntrs.nasa.gov/search.jsp?R=19940028477>
70. Wernet, M.P., Hadley, J.A.: A high temperature seeding technique for particle image velocimetry. *Meas. Sci. Technol.* **27**(12), 125.201 (2016). DOI 10.1088/0957-0233/27/12/125201. URL <http://stacks.iop.org/0957-0233/27/i=12/a=125201>
71. Willert, C.E., Hassa, C., Stockhausen, G., Jarius, M., Voges, M., Klinner, J.: Combined PIV and DGV applied to a pressurized gas turbine combustion facility. *Meas. Sci. Technol.* **17**(7), 1670 (2006). DOI 10.1088/0957-0233/17/7/005. URL <http://stacks.iop.org/0957-0233/17/i=7/a=005>
72. Willert, C.E., Jarius, M.: Planar flow field measurements in atmospheric and pressurized combustion chambers. *Exper. Fluids* **33**(6), 931–939 (2002). DOI 10.1007/s00348-002-0515-7. URL <http://dx.doi.org/10.1007/s00348-002-0515-7>
73. Willert, C.E., Stasicki, B., Klinner, J., Moessner, S.: Pulsed operation of high-power light emitting diodes for imaging flow velocimetry. *Meas. Sci. Technol.* **21**(7), 075402 (2010). DOI 10.1088/0957-0233/21/7/075402. URL <http://dx.doi.org/10.1088/0957-0233/21/7/075402>

Chapter 3

Recording Techniques for PIV

The PIV recording modes can be classified into two main categories: (1) methods which capture the images of the illuminated particles at multiple times onto a single frame and (2) methods which provide a single image of the illuminated particle distribution for each time of illumination. These branches are referred to as *single-frame/double-exposure* or *single-frame/multi-exposure* PIV (Fig. 3.1) and *double-frame/single-exposure* or *multi-frame/single-exposure* PIV (Fig. 3.2), respectively [2].

The principal distinction between the two categories is that, without additional effort, the single frame approaches do not retain any information on the temporal order of the illumination pulses. Consequently, a directional ambiguity in the recovered displacement vector exists. This necessitated the introduction of a wide variety of schemes to account for the directional ambiguity, if the flow direction is not known, such as displacement biasing, the so-called image shifting (i.e. using a rotating mirror or birefringent crystal), pulse tagging or color coding¹ [1, 3, 5–8].

In contrast, multi-frame/single-exposure PIV recording inherently preserves the temporal order of the particle images and hence is the method of choice if the technological requirements can be met. Also in terms of evaluation this approach yields more reliable results as the unique detection of the correlation peak maximum becomes possible even for tiny particle image displacements and displacements larger than the interrogation window size.

Historically single-frame/multi-exposure PIV recording was first utilized in conjunction with photography (For details see [DC3.2]). Today double-frame/single-exposure or multi-frame/single-exposure PIV recording is used predominantly as modern camera technology allows for the acquisition of images in rapid succession.

An overview of the Digital Content to this chapter can be found at [DC3.1].

¹Strictly speaking color coding is a form of *multi-frame/single-exposure* PIV: the color recordings can be separated into different color channels containing single exposed particle images.

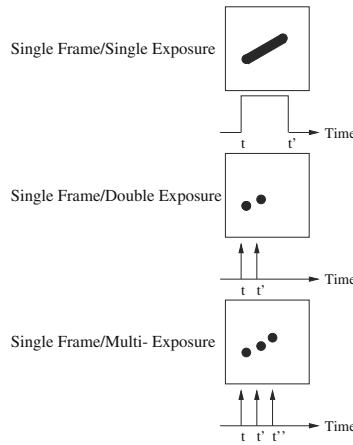


Fig. 3.1 Single frame techniques

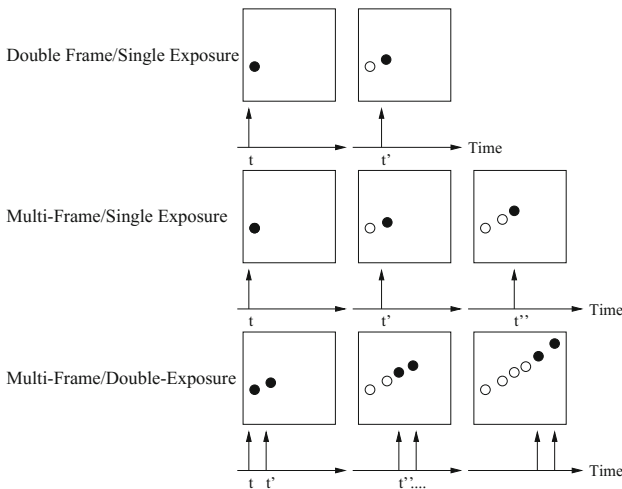


Fig. 3.2 Multiple frame techniques (open circles indicate the particles' positions in previous frames)

A variety of different sophisticated ideas related to the design of PIV systems has been reported in the literature over the past decades. Some of the respective implementations are catered to solve the demands of a specific application and may not be suitable for another application. It is clear that a decision on which method is optimal, cannot be made without taking the individual needs of each application into account. Due to the large scope of possible PIV implementations a complete coverage is beyond the scope of this book. Therefore both the PIV recording techniques described in this chapter and the PIV evaluation approaches, described in Chap. 5, are not complete and not necessarily the best, but presently the most commonly used.

In summary it can be stated for all PIV investigations that the design of an experimental PIV setup must be based on the priority of the following constrains:

- Desired spatial and/or temporal resolution,
- required accuracy of velocity measurements,
- components that are already available in the laboratory or can be obtained for the experiment.

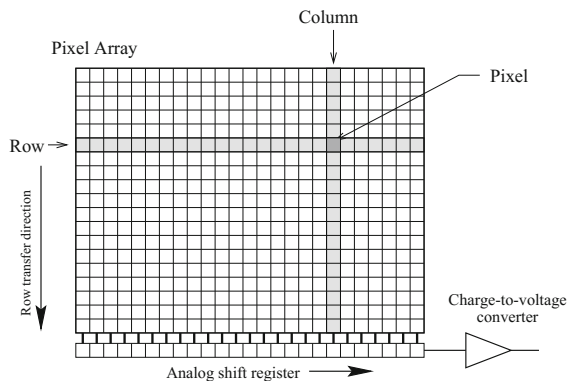
Depending on the choice of priority an appropriate system for recording can be configured. However, it must be kept in mind that not every requirement can be fulfilled, which is mainly due to technical limitations such as the available laser power, pulse repetition rates, camera frame rate, etc. Additional opportunities and constraints will be imposed by the available PIV evaluation methods.

3.1 Digital Cameras for PIV

The following section describes CCD and CMOS based digital camera which over the past decades have become the work horses for nearly all technical and scientific PIV applications that required only moderate or no temporal resolution. Flash lamp pumped double oscillator Nd:YAG-lasers offer high pulse energies and repetition rates that matched with the frame rates of most of the commercially available CCD cameras. The CCD cameras used for PIV offer two important advantages, one being increased spatial resolution, the second the electronic architecture that permits two PIV recordings, temporally spaced by microseconds or even nanoseconds, to be recorded by the same camera (see Sect. 3.1.3). Therefore, the architecture of CCD sensors will be described in the following. More recently, CMOS technology based cameras which are capable of much higher read-out rates than CCDs have become available and will be described in Sect. 3.1.4.

Figure 3.3 schematically describes the layout of a typical CCD sensor. The individual pixel are typically grouped into a rectangular array to form a light sensitive

Fig. 3.3 Typical CCD sensor geometry



area (linear, circular or hexagonal formats also exist). It should be pointed out that, in contrast to most CMOS sensors, the array has to be read out sequentially in a two-step process: after exposing the sensor the accumulated charge (i.e. electrons) is shifted vertically, one row at a time, into a masked (optically blind) analog shift register on the lower edge of the sensor's active area. Each row in the analog shift register is then clocked, pixel-by-pixel, through a charge-to-voltage converter and thereby provides one voltage for each pixel. Depending on the employed image transmission format the read-out of the sensor can either be sequential (also known as *progressive scan*) or interlaced, in which first all odd rows are read out before the even rows are accessed. Since the progressive scan approach preserves the image integrity, it is more useful for PIV recording as well as for other imaging applications such as machine vision.

In the following four sections we will concentrate on the operation of the various types of CCD sensors and how these may be utilized in PIV recording. Section 3.1.4 deals with the recently developed active pixel CMOS sensors, which became the state of the art design of sensors used for high-speed PIV. Section 3.1.5 describes camera types that can be used for high-speed recording.

3.1.1 Full-Frame CCD

The full-frame CCD sensor represents the CCD in its classical form (Fig. 3.3): a photosensitive area of a pixel that is first exposed to light and then read out sequentially (progressive scan) on a row-by-row basis without separating the image into two separate interlaced fields such as in several common video standards. This sensor has been in use in scientific imaging such as astronomy, spectroscopy and remote sensing ever since its introduction in the 1960s. It is characterized by large fill factors which can even reach 100% for special back-thinned, back-illuminated sensors.² With adequate cooling and slow read-out speeds, imaging at very low noise levels with high dynamic range (up to 16 bits) is possible. These sensors are available as very large arrays with pixel counts exceeding tens of millions.

The use of these sensors does however have some major drawbacks. To achieve the low read-out noise and high dynamic range, the pixel read-out rate has to be kept low. Even at standard video characteristics the data rate is limited to 10–20 MHz which results in a decreasing frame rate as the number of pixel increases. Frame rates of less than 1 Hz are not uncommon for larger sensors. For this reason multiple read-out ports are sometimes used, which brings about the problem of calibrating the respective charge-to-voltage converters with respect to one another. Another drawback is that the sensor stays active during read-out. Unless a shutter is placed

²In case of a back-illuminated CCD, the photo-active parts are illuminated from “behind” through the silicon-substrate. Therefore, the back of the device is thinned down to $O[10] \mu\text{m}$ and coated to avoid reflections.

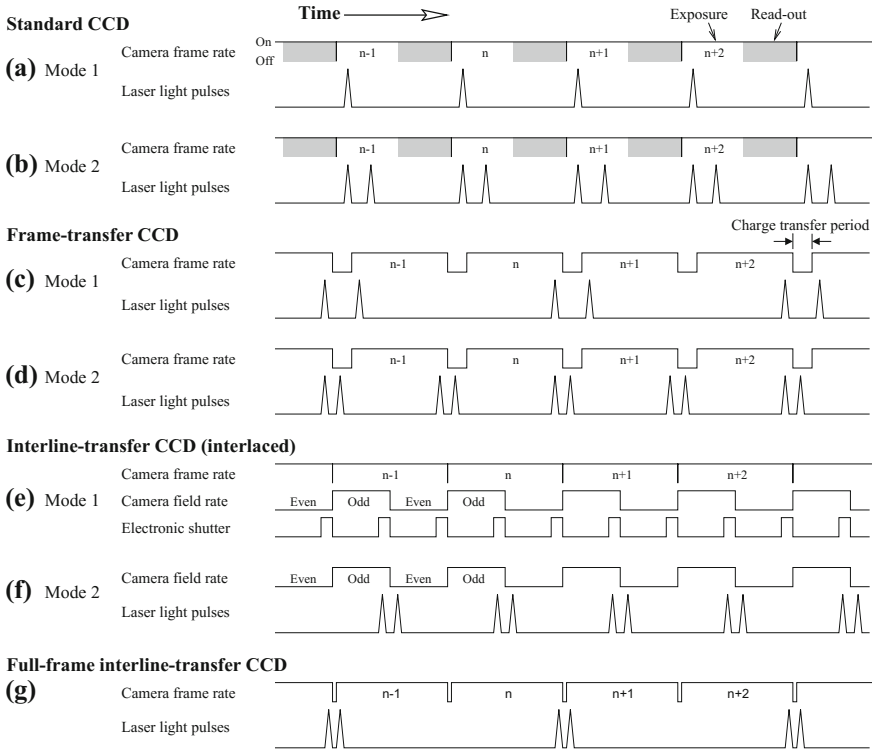


Fig. 3.4 Timing diagrams for PIV recording based on various types of CCD sensors

in front of it, light falling on to the sensor will also be captured resulting in a vertical smear in the final image.

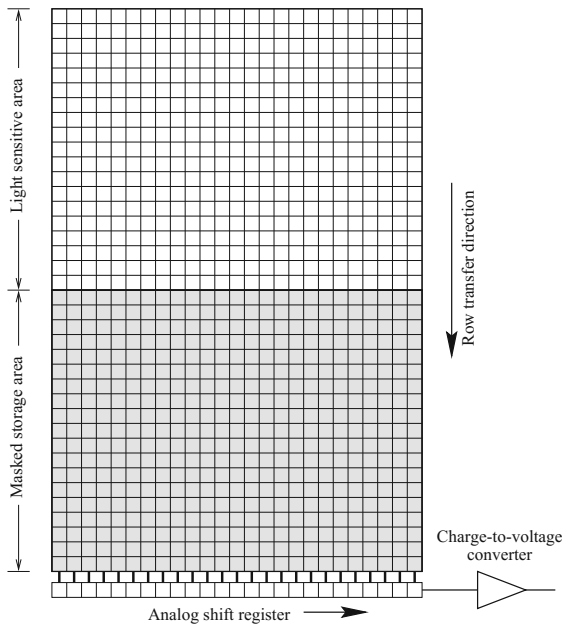
Because of its high spatial resolution, the full-frame sensor can be used as a direct replacement of photographic film. These sensors are frequently incorporated into 35 mm SLR camera bodies. As for their use in PIV, single images containing multiple exposed particle images ($n_{exp} \geq 2$) can be recorded analogous to the photographic method. The same ambiguity removal schemes as in photographic PIV recording (rotating mirror, birefringent crystal) can be employed (For details see [DC3.3]). If the flow under investigation is sufficiently slow in comparison to the frame rate of a camera based on this sensor, then single exposed PIV recordings can be obtained. In this case the ambiguity removal schemes are not needed. The timing charts given in Fig. 3.4a, b summarize how the particle illumination pulses have to be placed to produce single exposed or multiple exposed PIV images.

3.1.2 Frame Transfer CCD

The pixel architecture of the frame-transfer CCD sensor (Fig. 3.5) is essentially equivalent to that of the full-frame CCD sensor with the difference that the lower half of its rows are masked off and cannot be exposed by incoming light. Once exposed, the rows of accumulated charge are rapidly shifted down into the masked-off area at rates as fast as $\Delta t_{\text{row-shift}} = 1 \mu\text{s}$ per row. The entire image can thereby be shielded from further exposure within $0.5 < \Delta t_{\text{transfer}} < 1 \text{ ms}$ depending on the vertical clocking speed and vertical image size. However, the sensor does stay active during the vertical transfer time such that vertical smear is possible. Charge stored within the masked area prior to the shift is lost however. Once the shift has been completed, the sequential read-out is equivalent to that of a full-frame CCD (Sec. 3.1.3).

The frame-transfer CCD sensor offers two application possibilities in PIV recording. The fast transfer of the accumulated charge into the storage area allows two single exposed PIV images to be captured at a time delay, Δt , slightly longer than the transfer time, for example $\Delta t \geq \Delta t_{\text{transfer}}$. To achieve this, the illumination pulses are placed such that the first pulse occurs immediately before the frame-transfer event (i.e. on frame n), while the second pulse occurs immediately thereafter (i.e. on frame $n + 1$, see Fig. 3.4c). This placement of the illumination pulses with respect to the CCD sensor's periodic exposure cycles is sometimes referred to as *frame straddling*. At standard video resolution and a field of view of 200 mm the measurement of flow velocities up to the order of 5 m/s is possible. In this case the PIV frame rate is half the camera frame rate.

Fig. 3.5 Frame transfer CCD sensor layout



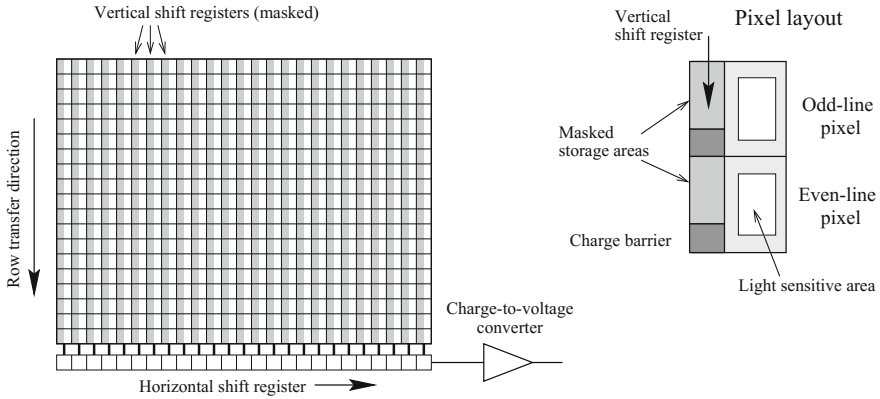


Fig. 3.6 Progressive scan, interline-transfer CCD layout

The frame-transfer CCD sensor can alternatively be used to impose an image shift in order to remove the displacement bias associated with single-frame double-exposure PIV recording. This is achieved by placing the first illumination pulse just prior to the start or at the beginning of the vertical transfer period (Fig. 3.4d). The second light pulse is placed such that it occurs while the collected charge of the first exposure is transferred into the masked area. For example, at a transfer rate of $\Delta t_{\text{row-shift}} = 1 \mu\text{s}$ per row, a pulse delay of $\Delta t = 10 \mu\text{s}$ would produce a maximum of 10 pixel image shifts. In this mode of operation the PIV frame rate is equal to the camera’s frame rate.

3.1.3 Interline Transfer CCD

Compared to the *classical* CCD sensor and the frame transfer CCD, the interline CCD has an important feature that makes it particularly suitable for PIV: each pixel is associated with its own storage cell, in effect, a blind-folded pixel, that allows the intermediate storage of accumulated photo-electrons. The storage pixel are located in-between the pixel rows – hence its name ‘interline’ (Fig. 3.6, right side). The transfer of accumulated charge to the storage cell can be accomplished in the sub-microsecond range which effectively allows the capture of two separate images in a similarly short time interval.

Originally this sensor is a derivative of the field-based, interline-transfer CCD in which each storage cell was shared by two row-neighboring active pixel – a relic of the interlaced-based transmission of video signals dating back to the early days of television. The interline-transfer CCD was introduced in the first half of the 1990’s and cameras based on these progressive scan sensors rapidly gained popularity in the field of machine vision as they removed all the artifacts associated with interlaced

video imaging. The electronic shutter can be applied to the entire image rather than to one of its fields as for previously available interline-transfer CCDs. Asynchronous triggering allows the capture of an image pair a short time after receiving the trigger, an approach first documented by LOURENÇO [9], who convinced a major camera manufacturer to add this capability to their cameras directly catering to the PIV market.

One major drawback of these sensors is their reduced fill factor due to the additional storage sites next to each light-sensitive area. Here additional microlenses on the face of the sensor improve their light gathering capability by increasing the effective fill factor from about 10% to up to 60%. Improving the light gathering capability by back-thinning the sensor is not possible as the additional storage sites would no longer be shielded from incoming light and would act as regular pixel.

The fast transfer of the entire exposed image into the adjoining storage sites within a few hundred nanoseconds in conjunction with higher resolution formats, in a departure from the standard video resolutions available up to then, has extended the application of single-exposure double-frame PIV images into the transonic flow velocity regime. Utilizing the frame straddling approach, the maximum PIV image frame rate is half the camera's frame rate allowing laser pulse separations below $1 \mu\text{s}$ [12, 13]. As these cameras also frequently have asynchronous reset possibilities, they are the most suitable CCD system for PIV imaging and have become the de-facto standard for single-exposure/dual-frame PIV.

A timing diagram showing the synchronization between the camera and a double-pulse laser system for PIV recording is given in Fig. 3.7. Here an important feature of the cameras operation can be observed: Whereas the first frame, associated with the first laser pulse, is exposed for a very short time (microseconds), the second frame is exposed for an extended period of time corresponding to the readout time

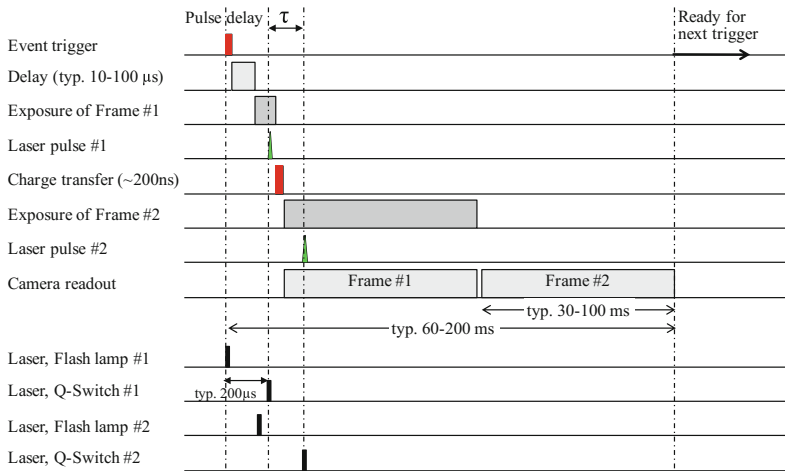


Fig. 3.7 Timing diagram for dual-frame PIV image capture with interline transfer CCD showing synchronization with double cavity pulsed Nd:YAG laser

of the first recording from the sensor. In most PIV applications this is effect has no implications on the PIV measurements themselves. In bright environments (e.g. daylight conditions) the long exposure of the second frame can lead to its saturation. In these cases a narrow bandwidth laser line filter generally is sufficient to suppress the unwanted signal from the recording. However, under extreme conditions (e.g. highly luminous flames) the stray signal cannot be sufficiently attenuated and requires alternative approaches to PIV image recording (see e.g. Chap. 11).

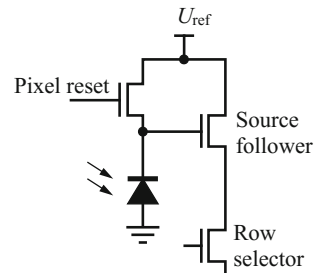
3.1.4 CMOS Imaging Sensors

The most relevant CMOS sensors for PIV applications are based on the active pixel sensor (APS) technology in which, in addition to the photodiode, a readout amplifier is incorporated into each pixel. This converts the charge accumulated by the photodiode into a voltage which is amplified inside the pixel and then transferred in sequential rows and columns to further signal processing circuits as described in Sect. 2.6.2. As can be seen in Fig. 3.8 each pixel contains a photodiode, a triad of transistors that converts accumulated electron charge to a measurable voltage, resets the photodiode and transfers the voltage to a vertical column bus. In addition to that, some CMOS sensors contain shutter transistors for each pixel. The amplifier transistor represents the input device of what is generally termed a source follower. It converts the charge generated by the photodiode into a voltage that is output to the column bus. The reset transistor controls integration time, and a row-select transistor connects the pixel output to the column bus for readout.

During the operation of the sensor, first the reset transistor is initialized in order to drain the charge from the photosensitive region. Then, the integration period begins and the electrons from the photo diode are stored in the potential well lying beneath the surface. After the integration period, the row-select transistor connects the amplifier transistor in the selected pixel to its load to form a source follower and thus converts the charge of the photo-diode into a voltage on the column bus. The cyclic repetition of this process to read out every row thereby forms the image.

One problem that frequently occurs when recording PIV images close to model surfaces with CCD cameras is blooming (see Sect. 2.6.1). In this case, the high intensity of the light scattered from the surface leads to a migration of electrons

Fig. 3.8 APS-CMOS pixel layout with integrated amplifier (source follower)



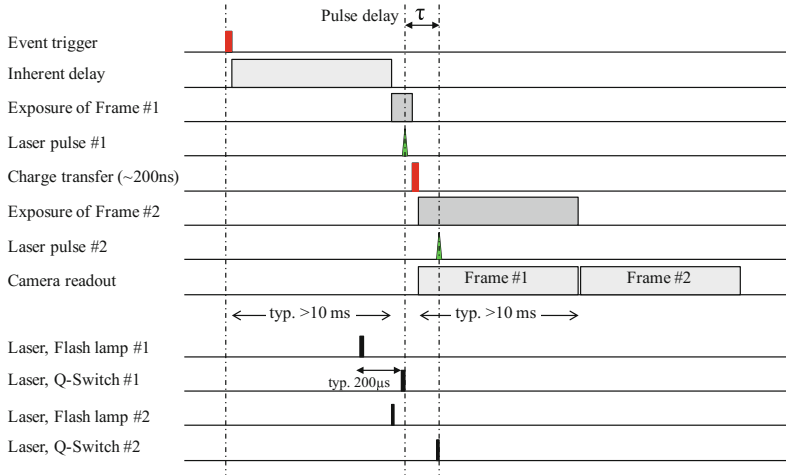


Fig. 3.9 Timing diagram for dual-frame PIV image capture with a sCMOS image sensor showing synchronization with double cavity pulsed Nd:YAG laser

to neighboring pixel, that makes the recording of particle images in those areas impossible. If too much light impinges on the pixel of some CMOS image sensors, it can cause an increase of the reference level. This in turn causes negative intensity values that appear as “black spots” in the bright areas due to the subtraction of signal and reference. However, one of the main advantages of most CMOS sensors is their ability to record images with high contrast without a migration of electrons to neighboring sensor areas.

The recent introduction of the scientific CMOS sensor (sCMOS, see Sect. 2.6.2.1) nowadays offers CMOS imaging quality comparable to that of CCD’s. While active cooling reduces sensor noise to a minimum the general architecture of CMOS-based sensors permits a pixel read-out rate in excess of 200 MHz. However, similar to the interline transfer CCD described in Sect. 3.1.3, the sCMOS sensor stays active during the image read-out phase. In addition, image capture with the sCMOS sensor requires a reference-image to be acquired preceding the capture of the actual image. This reference image accounts for the time-varying noise signature and is internally subtracted from the acquired image(pair). For PIV image acquisition the camera therefore needs to be triggered considerably in advance — typically 1 frame period — of the actual PIV image acquisition. A timing diagram illustrating the synchronization between sCMOS camera and dual-cavity pulse laser is shown in Fig. 3.9. Ongoing developments suggest that this intrinsic delay prior to double-image acquisition will be reduced in the future.

3.1.5 High-Speed Cameras

In Sect. 3.1 the different types of CCD and CMOS sensors were introduced. These sensors, especially the full-frame interline-transfer CCD, is chosen for most of the conventional PIV applications with moderate frame rates. However, special developments based on the CCD technology can also be used for high-speed PIV.

High frame rates, together with the relatively high spatial resolution needed for most PIV applications result in large amount of data that has to be transferred from the chip into the storage. This requires high clock speeds and, as a consequence thereof, a high bandwidth of the read out electronics. The high bandwidth of the sensor increases the noise while the efficiency decreases. Those problems resulted in sensor designs, in which the sensor is divided into smaller segments, which are read out in parallel. The required read out speed could therefore be reduced by the number of separate channels [11]. In addition to that, most of the CCD based high-speed cameras contain a so-called split-frame storage into which half of the image is read-out from the top of the chip and the other half from the bottom. Other variants make use of quadrant-wise readout schemes. In spite of all the efforts to increase the combined pixel readout rates by parallel transfer and storage, the rates are considerably higher in comparison to conventional cameras and the read out electronics need to be carefully optimized with respect to noise. Today's commercially available high-speed CCD cameras offer frame rates in the order of 1000 frames/s at moderate resolutions (1024×1024 pixel).

The introduction of CMOS based imaging brought forward a number of advantages in comparison to CCD, in particular the capability of much higher read-out rates. Thus the most advanced high-speed cameras suited for PIV are based on multi-tap CMOS sensors. The parallel structure of the CMOS sensor, which has been described previously, allows for more readout channels than were available with CCDs. CMOS cameras used for high-speed PIV application frequently have a significant number of parallel readout channels. For the same clock speed CMOS cameras offer higher pixel rates, since CMOS pixels can be read out with one clock pulse, while CCDs typically require two to four clock pulses per pixel read out. In contrast to most CCD sensors, high-speed CMOS sensors have electronic shuttering integrated in each pixel or cluster of pixels. As already mentioned, CMOS sensors are less prone to blooming. While saturation effects can occur also on CMOS sensors (the over-exposed pixel turn black), high scene luminosity does not affect the image in the way image blooming affects CCD sensors where saturated pixel tend to spread into neighboring pixel.

Windowing, the formerly described technique to read smaller sub windows of the CMOS sensor array, is a feature that allows to produce higher frame rates at reduced image resolutions. This feature is available in most of the high-speed CMOS cameras and is frequently used for high-speed PIV recording, since it allows for using the very high repetition rates of most high-speed lasers. Some CMOS cameras allow an extremely flexible read-out of the sensor. They may have hundreds of selectable resolutions, helping the user to obtain the desired resolution at maximum performance. Advanced CMOS-sensor designs use fewer components per pixel than earlier designs

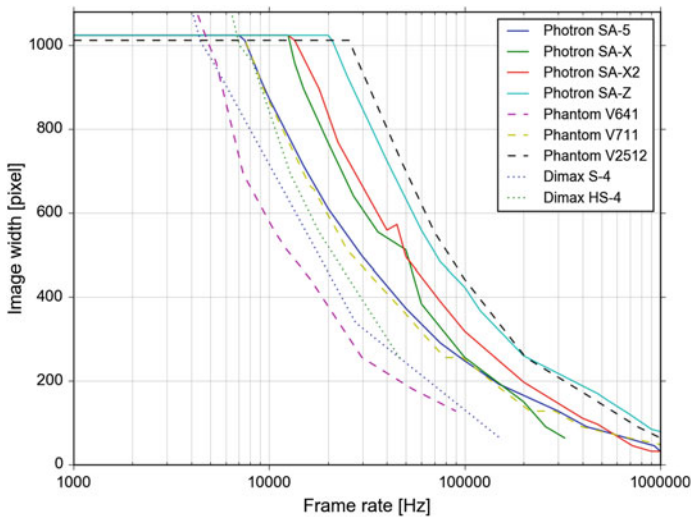


Fig. 3.10 Frame rate of high-speed cameras with respect to image size

and take advantage of smaller size of the components. This leads to a better light sensitivity than that of most CCD based high-speed cameras. Additionally, the image quality of new CMOS high-speed cameras has significantly been improved. The fact that some leading manufactures of digital SLR cameras nowadays offer CMOS sensors in their products, leads to the assumption that this trend is continuing. Some of the established manufacturers have in fact announced the discontinuation of CCD production in the coming years in favor of the CMOS architecture.

Today's commercially available high-speed CMOS cameras offer frame rates exceeding several thousand frames per second at full mega-pixel resolution at read out rates up to 25 Giga-pixel per second. At reduced resolutions even higher frame rates can be achieved. In order to deal with the enormous amount of data that can be recorded within seconds, the cameras feature on-board memory of up to 100 Giga-bytes where data are stored temporarily prior to transfer to the computer. Figure 3.10 illustrates that the frame rate of the high-speed cameras does not increase proportional to the reduction of the utilized sensor size; halving the active area does not necessarily double the camera's framing rate. This can be attributed to the block-wise parallel readout structure of the CMOS sensor that works most efficiently when the entire sensor array is being accessed. This effect must be considered for PIV measurements beyond the current 10 kHz range. Furthermore, most of the currently available high-speed cameras have pixel sizes of $20\ \mu\text{m}$ or more which can introduce pixel-locking artifacts due to spatially under-sampled particle images, that is, particles are imaged below the optimal size of 2 pixel.

3.2 Single Frame/Multi-exposure Recording

When using single frame cameras for PIV recording, two or more exposures of the same particles are stored on a single recording. Therefore, the sign of the direction of the particle motion within each interrogation window cannot be determined uniquely, since there is no way to decide which image is due to the first and which is due to the second illumination pulse. Although, for many applications the sign of the velocity vector can be derived from a priori knowledge of the flow, other cases involving flow reversals, such as in separated flows, require a technique by which the sign of the displacement can be determined correctly.

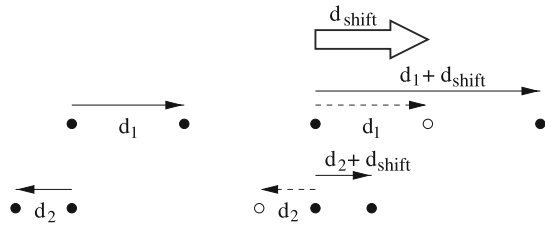
3.2.1 Image Shifting

The most common method to remove the directional ambiguity of the velocity measurement from single frame PIV recordings is the image shifting technique as described by various authors [1, 4, 8]. Image shifting enforces a constant additional displacement on the image of all tracer particles at the time of their second illumination. In contrast to other methods for ambiguity removal, which require a special, or at least a specially adapted, method of evaluation, image shifting leaves the proven evaluation process employing statistical methods unchanged.

Figure 3.11 explains the removal of directional ambiguity of two tracer particles by means of image shifting, one of which is moving to the right and the other one is moving to the left (flow reversal). Introducing an additional image shift, d_{shift} , to the flow-induced displacements of the particle images d_1 and d_2 , the situation changes. By a selection of the additional image shift, d_{shift} , in such a manner that it is always greater than the maximum value of the reverse-flow component (i.e. d_2), it is guaranteed that the tracer images of the second exposure are always located in the “positive” direction with respect to the location of the first exposure (Fig. 3.11). The elimination of the directional ambiguity does not depend on the direction within the observation plane where the shift takes place if the maximum of the corresponding reverse-flow component is predicted accordingly. Thus, an unambiguous determination of the sign of the displacement vector is established. The value and correct sign for the displacement vectors d_1 and d_2 will be obtained by subtracting the “artificial” contribution d_{shift} after the extraction of the displacement vectors for the PIV recording.

As already mentioned in Chap. 4 the application of the cross-correlation technique for two subareas of a single frame/multi-exposure recording instead of performing an auto-correlation on a single sub-area, increases the flexibility of the PIV system. This evaluation approach cannot remove the directional ambiguity of the velocity vectors or handle situations where the image displacements are of the order of the particle image diameter. However, the pulse separation time can be adapted in a wider range, because the size of the two interrogation windows and their displacement can be adapted later on during evaluation. The most widely used experimental technique

Fig. 3.11 Elimination of the ambiguity of direction of the displacement vector as observed in the recording plane



for image shifting involves the use of a rotating mirror over which the observation area within the flow is imaged. The magnitude of the additional displacement of the images of the tracer particles depends on the angular speed of the mirror, the distance between the light sheet plane and the mirror, the magnification of the imaging system and the time delay between the two illumination pulses [8]. In the early years of PIV when photographic cameras have been used, image shifting was the key for a versatile recording setup. Besides resolving the directional ambiguity, image shifting is required in order to optimize the recording for later auto-correlation evaluation. More details on the different aspects of image shifting were described by RAFFEL & KOMPENHANS [10] (For details see [DC3.4]).

References

1. Adrian, R.J.: Image shifting technique to resolve directional ambiguity in double-pulsed velocimetry. *Appl. Opt.* **25**(21), 3855–3858 (1986). DOI 10.1364/AO.25.003855. URL <http://ao.osa.org/abstract.cfm?URI=ao-25-21-3855>
2. Adrian, R.J.: Particle-imaging techniques for experimental fluid mechanics. *Annu. Rev. Fluid Mech.* **23**(1), 261–304 (1991). DOI 10.1146/annurev.fl.23.010191.001401. URL <https://dx.doi.org/10.1146/annurev.fl.23.010191.001401>
3. Bertuccioli, L., Gopalan, S., Katz, J.: Image shifting for PIV using birefringent and ferroelectric liquid crystals. *Exp. Fluids* **21**(5), 341–346 (1996). DOI 10.1007/BF00189054. URL <http://dx.doi.org/10.1007/BF00189054>
4. Gauthier, V., Riethmuller, M.L.: Application of PIDV to complex flows: Resolution of the directional ambiguity. In: *Particle Image Displacement Velocimetry*, von Karman Institute for Fluid Dynamics Lecture Series 1988-06. Von Karman Institute, Rhode-Saint-Genève, Belgium (1988)
5. Goss, L.P., Post, M.E., Trump, D.D., Sarka, B.: Two-color particle velocimetry. In: *ICALEO 1989*, vol. 68, pp. 101–111. Laser Institute of America (1989). DOI 10.1117/12.35014. URL <http://dx.doi.org/10.1117/12.35014>
6. Grant, I., Liu, A.: Directional ambiguity resolution in particle image velocimetry by pulse tagging. *Exp. Fluids* **10**(2–3), 71–76 (1990). DOI 10.1007/BF00215013. URL <http://dx.doi.org/10.1007/BF00215013>
7. Landreth, C.C., Adrian, R.J.: Electrooptical image shifting for particle image velocimetry. *Appl. Opt.* **27**(20), 4216–4220 (1988). DOI 10.1364/AO.27.004216. URL <http://ao.osa.org/abstract.cfm?URI=ao-27-20-4216>
8. Landreth, C.C., Adrian, R.J., Yao, C.S.: Double pulsed particle image velocimeter with directional resolution for complex flows. *Exp. Fluids* **6**(2), 119–128 (2004). DOI 10.1007/BF00196463. URL <http://dx.doi.org/10.1007/BF00196463>

9. Lourenço, L.M., Gogineni, S.P., LaSalle, R.T.: On-line particle-image velocimeter: an integrated approach. *Appl. Opt.* **33**(13), 2465–2470 (1994). DOI 10.1364/AO.33.002465. URL <http://ao.osa.org/abstract.cfm?URI=ao-33-13-2465>
10. Raffel, M., Kompenhans, J.: Theoretical and experimental aspects of image-shifting by means of a rotating mirror system for particle image velocimetry. *Meas. Sci. Technol.* **6**(6), 795 (1995). DOI 10.1088/0957-0233/6/6/016. URL <http://stacks.iop.org/0957-0233/6/i=6/a=016>
11. Turko, B.T., Yates, G.J., King, N.S.P.: Processing of multiport CCD video signals at very high frame rates. In: Cha, S.S., Trolinger, J.D. (eds.) *Optical Techniques in Fluid, Thermal, and Combustion Flow*, San Diego, CA, United States, vol. 2549, pp. 11–15 (1995). DOI 10.1117/12.218305. URL <http://dx.doi.org/10.1117/12.218305>
12. Vogt, A., Baumann, P., Kompenhans, J., Gharib, M.: Investigations of a wing tip vortex in air by means of DPIV. In: *Advanced Measurement and Ground Testing Conference*, New Orleans, LA, 17-20 June. American Institute of Aeronautics and Astronautics (1996). DOI 10.2514/6.1996-2254. URL <https://dx.doi.org/10.2514/6.1996-2254>
13. Willert, C.E., Raffel, M., Stasicki, B., Kompenhans, J.: High-speed digital video camera systems and related software for application of PIV in wind tunnel flows. In: *8th Intern. Symp. on Laser Techniques to Fluid Mechanics*, Lisbon, Portugal, 8–11 July (1996)

Chapter 4

Mathematical Background of Statistical PIV Evaluation

The first detailed mathematical description of statistical PIV evaluation has been given by ADRIAN [1]. This early work from 1988 concentrated on auto-correlation methods and was later expanded to cross-correlation analysis [6]. A complete and careful mathematical description of digital PIV has been given by WESTERWEEL [10, 11]. ADRIAN & WESTERWEEL [2] published the most complete book on Particle Image Velocimetry in 2011. The characteristics and limitations of the statistical PIV evaluation have been described therein in great detail.

In this chapter, a simplified mathematical model of the recording and subsequent statistical evaluation of PIV images will be presented. For this purpose the two-dimensional spatial estimator for the correlation will be referred to as the *correlation*. First, we analyze the cross-correlation of two frames of singly exposed recordings. Then we expand the theory for the evaluation of doubly exposed recordings.

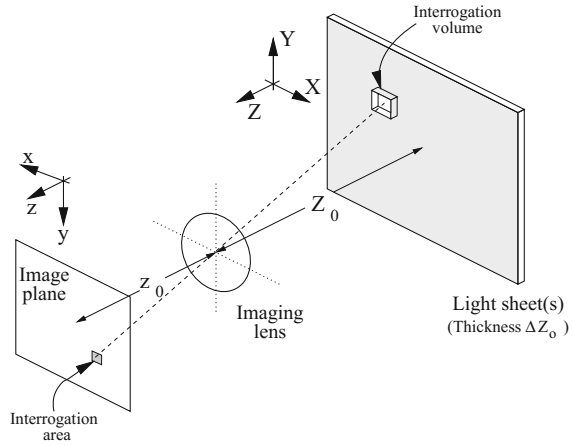
4.1 Particle Image Locations

Typically, PIV recordings are subdivided into interrogation areas during evaluation. These areas are called interrogation windows.¹ Due to reasons stated afterwards, for cross-correlation analysis those interrogation areas need not necessarily be located at the same position of the PIV recording. Their geometrical back-projection into the light sheet will be referred to as interrogation volumes in the following (see Fig. 4.1). Two interrogation volumes used for statistical evaluation together define

An overview of the Digital Content to this chapter can be found at[DC4.1]

¹The local sample of a PIV image from which a velocity vector is determined is referred to as the interrogation window. Its size determines to what degree the recovered velocity field is spatially smoothed.

Fig. 4.1 Schematic representation of geometric imaging



the measurement volume. Now, a single exposure recording is considered. It consists of a random distribution of particle images, which correspond to the following pattern of N tracer particles inside the flow:

$$\Gamma = \begin{pmatrix} X_1 \\ X_2 \\ \vdots \\ X_N \end{pmatrix} \quad \text{with} \quad X_i = \begin{pmatrix} X_i \\ Y_i \\ Z_i \end{pmatrix}$$

being the position of a tracer particle in a $3N$ -dimensional space. Γ describes the state of the ensemble at a given time t . X_i is the position vector of the particle i at time t . For more details about the mathematical description of the tracer ensemble, see [2, 10, 11]. The lower case letters refer to the coordinates in the image plane (Fig. 4.1) such that

$$\mathbf{x} = \begin{pmatrix} x \\ y \end{pmatrix}$$

is the image position vector in this plane.

In the remainder of this section we will assume that the particle position and the image position are related by a constant magnification factor M for simplicity, such that:

$$X_i = x_i/M \quad \text{and} \quad Y_i = y_i/M .$$

As already described in Sect. 2.5.3, a more complex model of imaging geometry has to be used to take the effect of perspective projection into account.

4.2 Image Intensity Field

In this section a mathematical representation of the intensity distribution in the image plane is given. It is assumed that the image can best be described by a convolution of the geometric image and the impulse response of the imaging system, the point spread function [3]. For infinite small particles and perfectly aberration-free, well focused lenses the amplitude of the point spread function can mathematically be described by the square of the first order Bessel function also known as Airy function (see Sect. 2.5).

A more complex model of imaging has to include imperfections of lenses and imaging sensors. For lenses an estimation of the main effects besides diffraction can be obtained by analyzing their modulation transfer functions (MTF's) (see Sect. 2.5.2). For CCD sensors, a careful analysis requires more complex models which have not yet been described in the PIV literature sufficiently. The description of digital imaging of very small objects is especially important, because the systematic arrangement of sensor elements can cause significant bias errors in statistical particle image displacement estimation (q.v. peak locking; in Sect. 6.1).

In the following analysis we assume the point spread function of the imaging lens $\tau(\mathbf{x})$ to be Gaussian versus x and y (see Appendix B.2), which is a common practice in literature and a good approximation for the point spread function of real lens systems [1, 10]. The convolution product of $\tau(\mathbf{x})$ with the geometric image of the tracer particle at the position \mathbf{x}_i therefore describes the image of a single particle located at position \mathbf{X}_i . Furthermore, we restrict the analysis to infinitely small geometric particle images which would be the case for small particles imaged at small magnifications. Therefore, we use the Dirac delta-function shifted to position \mathbf{x}_i to describe the geometric part of the particle image. As schematically illustrated in Fig. 4.2, the image intensity field of a single exposure may be expressed by:

$$I = I(\mathbf{x}, \Gamma) = \tau(\mathbf{x}) * \sum_{i=1}^N V_0(\mathbf{X}_i) \delta(\mathbf{x} - \mathbf{x}_i) \tag{4.1}$$

where $V_0(\mathbf{X}_i)$ is the transfer function giving the light energy of the image of an individual particle i inside the interrogation volume V_I and its conversion into an

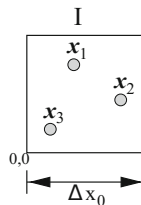


Fig. 4.2 Example of an intensity field I (single exposure)

electronic signal.² $\tau(\mathbf{x})$ is considered to be identical for every particle position. The visibility of a particle depends on many parameters as for example the scattering properties of the particle, the light intensity at the particle position, the sensitivity of the recording optics and the sensor at the corresponding image position. However, we adopt that the particles at every position have the same scattering properties and the recording optics and media have a constant sensitivity over the image plane.

In many situations different weight is assigned to different locations inside the interrogation area by a multiplication of the recorded image intensity with weight kernels. Further on, we presume that Z is the viewing direction, the light intensity inside the interrogation volume is only a function of Z and the image intensity finally analyzed depends on X and Y only due to the weight function. Therefore, $V_0(\mathbf{X})$ just describes the shape, extension and location of the actual interrogation volume:

$$V_0(\mathbf{X}) = W_0(X, Y) I_0(Z) \quad (4.2)$$

where $I_0(Z)$ is the intensity profile of the laser light sheet in the Z direction and $W_0(X, Y)$ is the interrogation window function geometrically back-projected into the light sheet. This is mathematically not correct, because it does not consider the convolution with the point spread function. For rectangular interrogation windows this means that in our mathematical description we neglect the effects of partially cropped images at the edges of the interrogation area. However, we will use this simple model of the interrogation volumes in the flow, because it also simplifies the description of PIV evaluation:

$$I_0(Z) = I_Z \exp\left(-8 \frac{(Z - Z_0)^2}{\Delta Z_0^2}\right)$$

might be used to describe the Gaussian intensity profile of the laser light sheet, where ΔZ_0 is the thickness of the light sheet measured at the e^{-2} points and I_Z is the maximum intensity of the light sheet. $W_0(X, Y)$ can be described in a similar way if a Gaussian window function with a maximum weighting W_{XY} at position X_0, Y_0 has to be considered:

$$W_0(X, Y) = W_{XY} \exp\left(-8 \frac{(X - X_0)^2}{\Delta X_0^2} - 8 \frac{(Y - Y_0)^2}{\Delta Y_0^2}\right).$$

Since many pulsed lasers used for PIV have an intensity distribution which is closer to a top-hat function than to a Gaussian function and since digitized recordings are commonly interrogated with rectangular windows, $V_0(\mathbf{X})$ can also be defined as a rectangular box:

$$I_0(Z) = \begin{cases} I_Z & \text{if } |Z - Z_0| \leq \Delta Z_0/2 \\ 0 & \text{elsewhere} \end{cases} \quad (4.3)$$

²Strictly speaking Eq. (4.1) is valid only for incoherent light. For coherent light a term considering the interference of overlapping particle images has to be included [10]. In most practical situations the particle images do not overlap. Therefore, we use Eq. (4.1) also for coherent illumination.

$$W_0(X, Y) = \begin{cases} W_{XY} & \text{if } |X - X_0| \leq \Delta X_0/2 \text{ and } |Y - Y_0| \leq \Delta Y_0/2 \\ 0 & \text{elsewhere.} \end{cases} \quad (4.4)$$

The factor $I_0(Z_i)$ represents the amount of light received from the particle i inside the flow, and located at distance $|Z_i - Z_0|$ from the center plane of the laser light sheet. ΔZ_0 is the light sheet thickness and therefore the extension of the interrogation volume in the Z direction. $\Delta X_0 = \Delta x_0/M$ and $\Delta Y_0 = \Delta y_0/M$ are the extension of the interrogation volume in the X - and Y -direction respectively. With $\tau(\mathbf{x} - \mathbf{x}_i) = \tau(\mathbf{x}) * \delta(\mathbf{x} - \mathbf{x}_i)$ and the assumption that the particle images under consideration do not overlap, Eq. (4.1) can alternatively be written as:

$$I(\mathbf{x}, \boldsymbol{\Gamma}) = \sum_{i=1}^N V_0(\mathbf{X}_i) \tau(\mathbf{x} - \mathbf{x}_i) . \quad (\text{see Appendix B}) \quad (4.5)$$

This expression for the image intensity field will intensively be used in the following sections. Next we will illustrate different representations of the intensity field and their correlation by giving an example for the recording of three arbitrarily located particles.

4.3 Mean Value, Auto-correlation and Variance of a Single Exposure Recording

In this section we will determine spatial estimators for the mean value and the variance of the image intensity field, because these quantities will be used for the normalization of the cross-correlation. Furthermore, auto-correlation and auto-covariance of a single exposure intensity field will be introduced. The main equations used in the following are taken from PAPOULIS [7, 8]. The spatial average is defined as:

$$\langle I(\mathbf{x}, \boldsymbol{\Gamma}) \rangle = \frac{1}{a_1} \int_{a_1} I(\mathbf{x}, \boldsymbol{\Gamma}) d\mathbf{x}$$

where a_1 is the interrogation area. Employing Eq. (4.5) yields:

$$\langle I(\mathbf{x}, \boldsymbol{\Gamma}) \rangle = \frac{1}{a_1} \int_{a_1} \sum_{i=1}^N V_0(\mathbf{X}_i) \tau(\mathbf{x} - \mathbf{x}_i) d\mathbf{x} .$$

The mean value of the intensity field can be approximated by:

$$\mu_1 = \langle I(\mathbf{x}, \boldsymbol{\Gamma}) \rangle = \frac{1}{a_1} \sum_{i=1}^N V_0(\mathbf{X}_i) \int_{a_1} \tau(\mathbf{x} - \mathbf{x}_i) d\mathbf{x} .$$

We can now derive the auto-correlation of the single exposure intensity field in a similar way:

$$\begin{aligned} R_I(\mathbf{s}, \boldsymbol{\Gamma}) &= \langle I(\mathbf{x}, \boldsymbol{\Gamma}) I(\mathbf{x} + \mathbf{s}, \boldsymbol{\Gamma}) \rangle \\ &= \frac{1}{a_1} \int_{a_1} \sum_{i=1}^N V_0(\mathbf{X}_i) \tau(\mathbf{x} - \mathbf{x}_i) \sum_{j=1}^N V_0(\mathbf{X}_j) \tau(\mathbf{x} - \mathbf{x}_j + \mathbf{s}) d\mathbf{x} \end{aligned}$$

where \mathbf{s} is the separation vector in the correlation plane. By distinguishing the $i \neq j$ terms which represent the correlation of different particle images and therefore randomly distributed noise in the correlation plane, and the $i = j$ terms which represent the correlation of each particle image with itself, we come to the following representation:

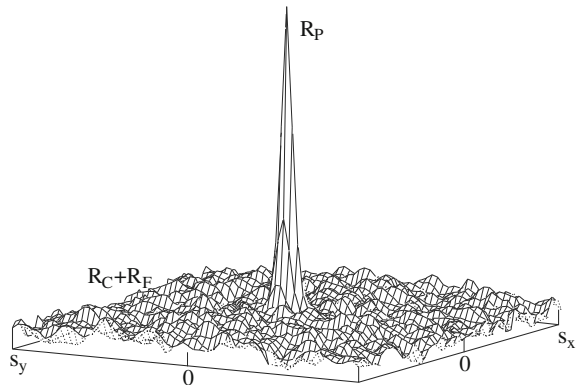
$$\begin{aligned} R_I(\mathbf{s}, \boldsymbol{\Gamma}) &= \frac{1}{a_1} \sum_{i \neq j}^N V_0(\mathbf{X}_i) V_0(\mathbf{X}_j) \int_{a_1} \tau(\mathbf{x} - \mathbf{x}_i) \tau(\mathbf{x} - \mathbf{x}_j + \mathbf{s}) d\mathbf{x} \\ &\quad + \frac{1}{a_1} \sum_{i=j}^N V_0^2(\mathbf{X}_i) \int_{a_1} \tau(\mathbf{x} - \mathbf{x}_i) \tau(\mathbf{x} - \mathbf{x}_j + \mathbf{s}) d\mathbf{x} . \end{aligned}$$

Following the decomposition proposed by ADRIAN, we can write:

$$R_I(\mathbf{s}, \boldsymbol{\Gamma}) = R_C(\mathbf{s}, \boldsymbol{\Gamma}) + R_F(\mathbf{s}, \boldsymbol{\Gamma}) + R_P(\mathbf{s}, \boldsymbol{\Gamma})$$

where $R_C(\mathbf{s}, \boldsymbol{\Gamma})$ is the convolution of the mean intensities of I and $R_F(\mathbf{s}, \boldsymbol{\Gamma})$ is the fluctuating noise component both resulting from the $i \neq j$ terms. $R_P(\mathbf{s}, \boldsymbol{\Gamma})$ finally is the self-correlation peak located at position $(0, 0)$ in the correlation plane. It results from the components that correspond to the correlation of each particle image with itself ($i = j$ terms). The auto-correlation of actual particle image data is provided in Fig. 4.3 and clearly shows a strong central self-correlation peak surrounded by a noise floor.

Fig. 4.3 Composition of peaks in the auto-correlation function. R_P depicts the self-correlation peak



We will now concentrate on this central peak in order to evaluate its features. For a Gaussian particle image intensity distribution

$$\tau(\mathbf{x}) = K \exp\left(-\frac{8|\mathbf{x}|^2}{d_\tau^2}\right)$$

it can be shown that the auto-correlation $R_\tau(s)$ is again a Gaussian function with a width that is $\sqrt{2}d_\tau$ (see Appendix B.3). Consequently $R_P(s, \Gamma)$ may be rewritten as follows:

$$R_P(s, \Gamma) = \sum_{i=1}^N V_0^2(\mathbf{X}_i) \exp\left(\frac{-8|s|^2}{(\sqrt{2}d_\tau)^2}\right) \frac{1}{a_1} \int_{a_1} \tau^2\left(\mathbf{x} - \mathbf{x}_i + \frac{s}{2}\right) d\mathbf{x} .$$

In the remainder of this book we will always use the representation:

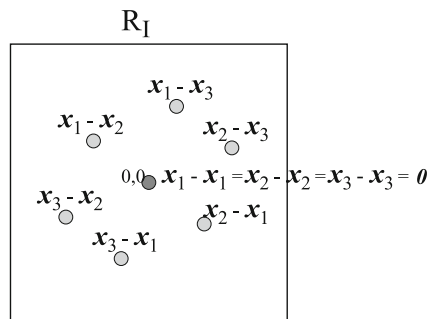
$$R_\tau(s) = \exp\left(\frac{-8|s|^2}{(\sqrt{2}d_\tau)^2}\right) \frac{1}{a_1} \int_{a_1} \tau^2\left(\mathbf{x} - \mathbf{x}_i + \frac{s}{2}\right) d\mathbf{x}$$

taking into account that its features are mainly the same also for non-Gaussian $\tau(\mathbf{x})$: the maximum of $R_\tau(s)$ is located at $|s| = 0$ and the characteristics of its shape is given by the particle images shape. Therefore, we will write R_P as

$$R_P(s, \Gamma) = R_\tau(s) \sum_{i=1}^N V_0^2(\mathbf{X}_i) .$$

In Fig. 4.4 the schematic of the auto-correlation of the example intensity field I is given. The correlation peaks (R_P and R_F) occur at locations which are given by the vectorial differences between particle image locations. Their strength is proportional to the number of all possible differences which result in that location. As three vectorial differences contribute to R_P , the peak of R_P is three times stronger in this example than the other peaks.

Fig. 4.4 Schematic representation of the auto-correlation of the intensity field I given in Fig. 4.2



For intensity fields with zero mean value the auto-correlation equals the auto-covariance. For nonzero mean values of the intensity field the auto-covariance $C_I(\mathbf{s})$ can be obtained by [8]:

$$C_I(\mathbf{s}) = R_I(\mathbf{s}) - \mu_I^2 .$$

An estimator of the variance of the intensity field can be obtained by:

$$\sigma_I^2 = C_I(\mathbf{0}, \Gamma) = R_I(\mathbf{0}, \Gamma) - \mu_I^2 = R_P(\mathbf{0}, \Gamma) - \mu_I^2 .$$

4.4 Cross-Correlation of a Pair of Two Singly Exposed Recordings

PIV recordings are evaluated by locally cross-correlating two frames of single exposures of the tracer ensemble whenever possible Sect. 3.1. The mathematical background of this technique will be described in the following.

In the remainder of this section, a constant displacement \mathbf{D} of all particles inside the interrogation volume is assumed, so that the particle locations during the second exposure at time $t' = t + \Delta t$ are given by:

$$\mathbf{X}_i' = \mathbf{X}_i + \mathbf{D} = \begin{pmatrix} X_i + D_X \\ Y_i + D_Y \\ Z_i + D_Z \end{pmatrix} .$$

Furthermore, we assume that the particle image displacements are given by:

$$\mathbf{d} = \begin{pmatrix} MD_X \\ MD_Y \end{pmatrix}$$

which is a simplification of the perspective projection that is valid only for particles located in the vicinity of the optical axis (see Sect. 2.5.3).

We come to the following representation of the image intensity field for the time of the second exposure (in analogy to Eq. (4.5)):

$$I'(\mathbf{x}, \Gamma) = \sum_{j=1}^N V_0'(\mathbf{X}_j + \mathbf{D}) \tau(\mathbf{x} - \mathbf{x}_j - \mathbf{d})$$

where $V_0'(\mathbf{X})$ defines the interrogation volume during the second exposure.

If we first consider identical light sheet and windowing characteristics, the cross-correlation function of the two interrogation areas can be written as:

$$R_{II}(\mathbf{s}, \Gamma, \mathbf{D}) = \frac{1}{a_I} \sum_{i,j} V_0(\mathbf{X}_i) V_0(\mathbf{X}_j + \mathbf{D}) \int_{a_I} \tau(\mathbf{x} - \mathbf{x}_i) \tau(\mathbf{x} - \mathbf{x}_j + \mathbf{s} - \mathbf{d}) d\mathbf{x}$$

where \mathbf{s} is the separation vector in the correlation plane. Analogous to the procedure used in the previous section we arrive at:

$$R_{II}(\mathbf{s}, \mathbf{\Gamma}, \mathbf{D}) = \sum_{i,j} V_0(\mathbf{X}_i) V_0(\mathbf{X}_j + \mathbf{D}) R_\tau(\mathbf{x}_i - \mathbf{x}_j + \mathbf{s} - \mathbf{d}) .$$

By distinguishing the $i \neq j$ terms which represent the correlation of different randomly distributed particles and therefore mainly noise in the correlation plane and the $i = j$ terms, which contain the displacement information desired, we obtain:

$$\begin{aligned} R_{II}(\mathbf{s}, \mathbf{\Gamma}, \mathbf{D}) &= \sum_{i \neq j} V_0(\mathbf{X}_i) V_0(\mathbf{X}_j + \mathbf{D}) R_\tau(\mathbf{x}_i - \mathbf{x}_j + \mathbf{s} - \mathbf{d}) \\ &\quad + R_\tau(\mathbf{s} - \mathbf{d}) \sum_{i=1}^N V_0(\mathbf{X}_i) V_0(\mathbf{X}_i + \mathbf{D}) . \end{aligned}$$

Again, we can decompose the correlation into three parts:

$$R_{II}(\mathbf{s}, \mathbf{\Gamma}, \mathbf{D}) = R_C(\mathbf{s}, \mathbf{\Gamma}, \mathbf{D}) + R_F(\mathbf{s}, \mathbf{\Gamma}, \mathbf{D}) + R_D(\mathbf{s}, \mathbf{\Gamma}, \mathbf{D})$$

where $R_D(\mathbf{s}, \mathbf{\Gamma}, \mathbf{D})$ represents the component of the cross-correlation function that corresponds to the correlation of images of particles obtained from the first exposure with images of identical particles obtained from the second exposure ($i = j$ terms):

$$R_D(\mathbf{s}, \mathbf{\Gamma}, \mathbf{D}) = R_\tau(\mathbf{s} - \mathbf{d}) \sum_{i=1}^N V_0(\mathbf{X}_i) V_0(\mathbf{X}_i + \mathbf{D}) . \quad (4.6)$$

Hence, for a given distribution of particles inside the flow, the displacement correlation peak reaches a maximum for $\mathbf{s} = \mathbf{d}$.

Therefore, as already anticipated, the location of this maximum yields the average in-plane displacement, and thus the U and V components of the velocity inside the flow.

In Fig. 4.5 the schematic of the cross-correlation of the example intensity fields I and I' displayed in Fig. 4.6 is given. Nearly the same correlation peaks occur as in the auto-correlation shown in Fig. 4.4, but at locations which are displaced by \mathbf{d} . The strength of R_p at position \mathbf{d} is two times stronger than that of the other peaks for this example, see Fig. 4.7. The reason is that correlations of \mathbf{x}'_2 do not appear here, because this image is located outside the interrogation window (see Fig. 4.6).

It can be seen from Eq. (4.6) that the displacement correlation is a function of the random variables $(\mathbf{X}_i)_{i=1 \dots N}$. Consequently it is a random variable itself and for different realizations at the same overall conditions we will obtain different qualities of the displacement estimation depending on the state of the tracer ensemble. In order to derive rules for a general optimization of the displacement estimation, we will determine the expected value of the displacement correlation in Sect. 4.6.

Fig. 4.5 Schematic representation of the cross-correlation of the intensity fields I and I' given in Fig. 4.6

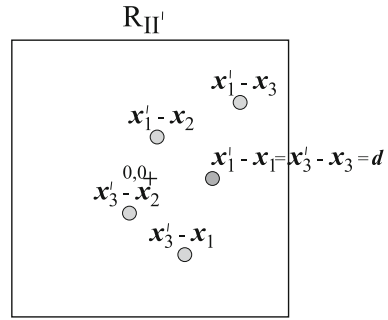


Fig. 4.6 The intensity field I recorded at time t and the intensity field I' recorded after a time delay of Δt at t'

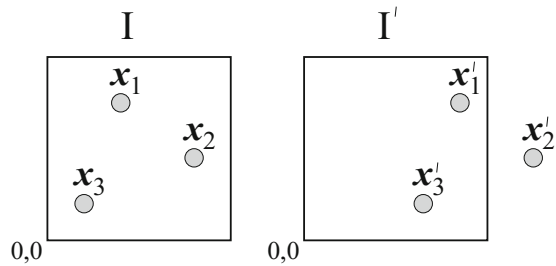
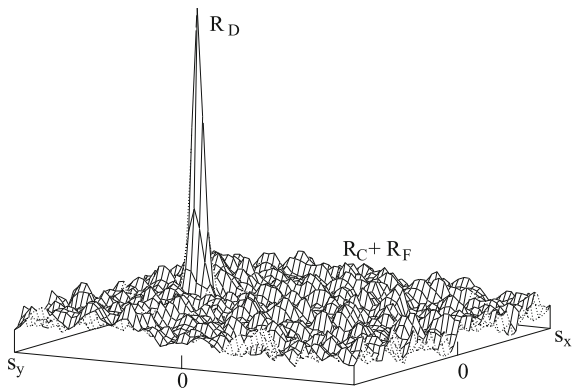


Fig. 4.7 Composition of peaks in the cross-correlation function. R_D corresponds to the correlation of images of identical particles at the two illuminations



4.5 Correlation of a Doubly Exposed Recording

In cases where the two illuminations of the tracer particle cannot be recorded on separate frames (see Sect. 3.2), the correlation function of doubly (or multiply) exposed recordings has to be determined. This correlation function can be derived by analogy to the correlation for single exposed recordings. Instead of cross-correlating I with I' , we will consider the correlation of the intensity field $I^+ = I + I'$ with itself. Assuming identical light sheets and windowing characteristics, the intensity field of both exposures I^+ can be written as:

$$\begin{aligned}
 I^+(\mathbf{x}, \Gamma) &= I(\mathbf{x}, \Gamma) + I'(\mathbf{x}, \Gamma) \\
 &= \sum_{i=1}^N (V_0(\mathbf{X}_i) \tau(\mathbf{x} - \mathbf{x}_i) + V_0(\mathbf{X}_i + \mathbf{D}) \tau(\mathbf{x} - \mathbf{x}_i - \mathbf{d})) .
 \end{aligned}$$

It can be shown that the auto-correlation of I^+ consists of four terms:

$$R_{I^+}(s, \Gamma, \mathbf{D}) = R_I(s, \Gamma) + R_{I'}(s, \Gamma) + R_{II}(s, \Gamma, \mathbf{D}) + R_{II}(-s, \Gamma, \mathbf{D}) .$$

It is therefore appropriate to decompose the estimator into the following terms:

$$\begin{aligned}
 R_{I^+}(s, \Gamma, \mathbf{D}) &= R_C(s, \Gamma, \mathbf{D}) + R_F(s, \Gamma, \mathbf{D}) + R_P(s, \Gamma) \\
 &\quad + R_{D^+}(s, \Gamma, \mathbf{D}) + R_{D^-}(s, \Gamma, \mathbf{D})
 \end{aligned} \tag{4.7}$$

where $R_C(s, \Gamma, \mathbf{D})$ is the convolution of the mean intensity of I^+ and $R_F(s, \Gamma, \mathbf{D})$ is the fluctuating noise component. $R_P(s, \Gamma)$ is the self-correlation peak located at the center of the correlation plane. It results from the components that correspond to the correlation of each particle image with itself. $R_{D^+}(s, \Gamma, \mathbf{D})$ and $R_{D^-}(s, \Gamma, \mathbf{D})$ represent the components of the correlation function which correspond to the correlation of images of particles obtained from the first exposure with that of images of identical particles obtained from the second exposure and vice versa (Figs. 4.8 and 4.9).

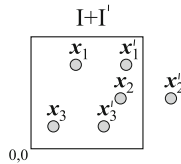
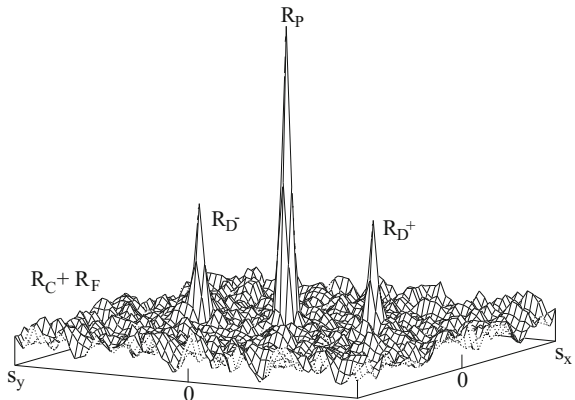


Fig. 4.8 The sum of the intensity fields I and I' (see Fig. 4.6) as obtained by a recording of the tracer ensemble at t and t' on the same frame

Fig. 4.9 Components of the auto-correlation function



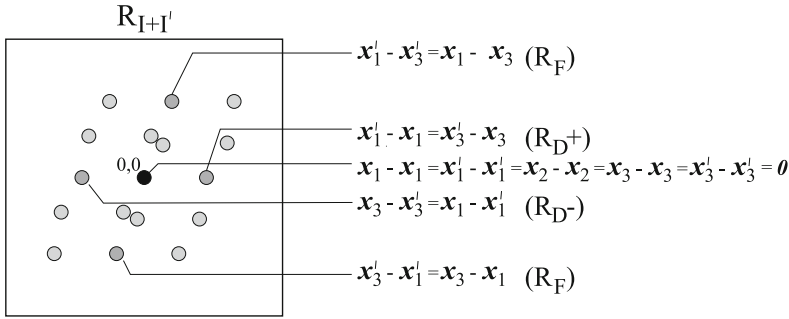


Fig. 4.10 Schematic representation of the auto-correlation of the intensity field $I + I'$ given in Fig. 4.8

When comparing the correlation of a doubly exposed recording with the correlation of a pair of two singly exposed recordings, the following statements can be made: R_{I+} is symmetric with respect to the center of the plane and thus to its central peak R_P . Two identical displacement peaks R_{D+} and R_{D-} appear, which are located symmetrically to center of the plane, and as a consequence the sign of the displacement cannot be determined. Therefore, the correlation of a doubly exposed recording is not conclusive if the displacement field of the whole recording is not unidirectional. Another problem appears if the field contains displacements close to zero, which would lead to an overlap between the displacement peaks with the central peak. As a consequence, these problems have to be solved during recording. Precautions have to be made so that the images of identical particles due to the different exposures do not overlap and the sign of their displacement is determined. If the flow field under investigation contains areas of reverse flow or of relative slow velocities image shifting has to be used (see Sect. 3.2). It can be seen from Fig. 4.10 that the correlation of doubly exposed recordings contains more than twice the number of randomly distributed noise peaks.

The example given in Fig. 4.10 shows that in situations for which the cross-correlation of single exposure yields good results, the correlation of doubly exposed recordings may contain noise peaks of similar strength as the displacement peak. Hence, the evaluation of doubly or multiply exposed recordings has to be performed with more particle image pairs in order to get the same performance as that of single exposure evaluation. This can be done by different methods: the seeding density and/or the number of exposures or the light sheet thickness can be increased. Besides other problems related to these methods their application is restricted due to the limited number of particle images that can be stored on the sensor without a significant overlap. Therefore, in most cases the size of the interrogation areas has to be increased compared to the evaluation of single exposures resulting in a lower spatial resolution of the measurement at the same sensor size. This explains why auto-correlation PIV based on single frame recordings today is only used in cases where the recording of double or multiple frames for later cross-correlation evaluation is not viable.

4.6 Expected Value of Displacement Correlation

In order to derive rules for a general optimization of the displacement estimation we will determine the expected value of the displacement correlation $E\{R_D\}$ for all realizations of \mathbf{F} . More concretely: we want to calculate the mean correlation function of all possible “patterns” that can be realized with N particles. From Eq. (4.6), it follows that

$$\begin{aligned} E\{R_D\} &= E \left\{ R_\tau(\mathbf{s} - \mathbf{d}) \sum_{i=1}^N V_0(\mathbf{X}_i) V_0(\mathbf{X}_i + \mathbf{D}) \right\} \\ &= R_\tau(\mathbf{s} - \mathbf{d}) E \left\{ \sum_{i=1}^N V_0(\mathbf{X}_i) V_0(\mathbf{X}_i + \mathbf{D}) \right\} \end{aligned}$$

Defining $f_1(\mathbf{X}) = V_0(\mathbf{X}) V_0(\mathbf{X} + \mathbf{D})$ yields:

$$E\{R_D\} = R_\tau(\mathbf{s} - \mathbf{d}) E \left\{ \sum_{i=1}^N f_1(\mathbf{X}_i) \right\}. \quad (4.8)$$

We prove in Appendix B.4 that:

$$E \left\{ \sum_{i=1}^N f_1(\mathbf{X}_i) \right\} = \frac{N}{V_F} \int_{V_F} f_1(\mathbf{X}) d\mathbf{X}$$

where $\int_{V_F} f_1(\mathbf{X}) d\mathbf{X}$ is the volume integral

$$\int \int \int f_1(X, Y, Z) dX dY dZ .$$

Thus:

$$E\{R_D\} = \frac{N}{V_F} R_\tau(\mathbf{s} - \mathbf{d}) \int_{V_F} f_1(\mathbf{X}) d\mathbf{X}. \quad (4.9)$$

Since we defined N to be the number of all particles of the ensemble, V_F has to be interpreted as the whole volume of fluid that has been seeded with particles. According to the above definition of $f_1(\mathbf{X})$ we can say in a more practical sense that the integration has to be performed over the volume which contained all particles that were inside the interrogation volumes during the first or second exposure. We can rewrite the integral over $f_1(\mathbf{X})$ as:

$$\begin{aligned}
\int_{V_F} f_l(\mathbf{X}) d\mathbf{X} &= \int I_0(Z) I_0(Z + D_Z) dZ \\
&\quad \times \int \int W_0(X, Y) W_0(X + D_X, Y + D_Y) dXdY \\
&= \int_{V_F} V_0^2(\mathbf{X}) d\mathbf{X} \cdot F_O(D_Z) F_I(D_X, D_Y)
\end{aligned}$$

with

$$F_I(D_X, D_Y) = \frac{\int \int W_0(X, Y) W_0(X + D_X, Y + D_Y) dXdY}{\int \int W_0^2(X, Y) dXdY} \quad (4.10)$$

and

$$F_O(D_Z) = \frac{\int I_0(Z) I_0(Z + D_Z) dZ}{\int I_0^2(Z) dZ} . \quad (4.11)$$

KEANE & ADRIAN [4–6] have defined F_I as a factor expressing the in-plane loss-of-pairs, and F_O as a factor expressing the out-of-plane loss-of-pairs. When no in-plane or out-of-plane loss-of-pairs are present the latter two are unity. Finally Eq.(4.9) yields:

$$E\{R_D(s, \mathbf{D})\} = C_R R_\tau(s - \mathbf{d}) F_O(D_Z) F_I(D_X, D_Y) \quad (4.12)$$

where the constant C_R is defined as:

$$C_R = \frac{N}{V_F} \int_{V_F} V_0^2(\mathbf{X}) d\mathbf{X} .$$

In 2D PIV the loss-of-correlation due to out-of-plane motion or light-sheet mismatch has two effects. First, it reduces the probability of detecting a valid vector see Sect. 6.1.1. Second, it increases the uncertainty measured in velocity fields, see Sect. 6.2.7. The validity of the original F_O definition by Kean and Adrian is limited to use with identical laser intensity profiles. As light sheets for the first and second illumination usually differ in width and shape, the proposed definition is of limited use in practice. To overcome this limitation, a new definition for F_O is proposed in [9] which covers the effect of light-sheets with different shapes and widths. The analysis shows that the new definition of F_O accurately predicts the loss-of-correlation for all tested light-sheet mismatches and agrees with the old definition for the ideal case involving identical light-sheets. Based on the new definition, F_O can be estimated reliably from the laser profiles in the case of zero out-of-plane motion. Furthermore,

the authors have demonstrated that the ratio of the cross-correlation function and the auto-correlation function provides F_O directly from PIV images. Thus, an online optimization of the PIV setup is easily possible for flows with out-of-plane motion.

References

1. Adrian, R.J.: Statistical properties of particle image velocimetry measurements in turbulent flow. In: 4th International Symposium on Laser Techniques to Fluid Mechanics, Lisbon, Portugal, 11–14 July (1988)
2. Adrian, R.J., Westerweel, J.: Particle Image Velocimetry. Cambridge Aerospace Series. Cambridge University Press, New York (2011). URL <http://www.cambridge.org/de/academic/subjects/engineering/thermal-fluids-engineering/particle-image-velocimetry>
3. Hecht, E., Zajac, A.: Optics. Addison-Wesley Pub. Company, Massachusetts (2001)
4. Keane, R.D., Adrian, R.J.: Optimization of particle image velocimeters. I. Double pulsed systems. Meas. Sci. Technol. **1**(11), 1202 (1990). DOI 10.1088/0957-0233/1/11/013. URL <http://stacks.iop.org/0957-0233/1/i=11/a=013>
5. Keane, R.D., Adrian, R.J.: Optimization of particle image velocimeters: II. Multiple pulsed systems. Meas. Sci. Technol. **2**(10), 963 (1991). DOI 10.1088/0957-0233/2/10/013. URL <http://stacks.iop.org/0957-0233/2/i=10/a=013>
6. Keane, R.D., Adrian, R.J.: Theory of cross-correlation analysis of PIV images. Appl. Sci. Res. **49**(3), 191–215 (1992). DOI 10.1007/BF00384623. URL <https://dx.doi.org/10.1007/BF00384623>
7. Papoulis, A.: Signal Analysis. McGraw-Hill Inc., New York (1981)
8. Papoulis, A., Pillai, S.U.: Probability, Random Variables, and Stochastic Processes. 4th edn. McGraw-Hill Education Ltd., New York (2002). URL <http://www.mhhe.com/engcs/electrical/papoulis/>
9. Scharnowski, S., Grayson, K., de Silva C., Hutchins, N., Marusic I., and Kähler, C.J.: Generalization of the PIV loss-of-correlation formula introduced by Keane and Adrian. Exp. Fluids **58** (2017). DOI 10.1007/s00348-017-2431-x. URL <https://doi.org/10.1007/s00348-017-2431-x>
10. Westerweel, J.: Digital particle image velocimetry: Theory and application. Ph.D. thesis, Mechanical Maritime and Materials Engineering, Delft University of Technology (1993). URL <http://repository.tudelft.nl/islandora/object/uuid:85455914-6629-4421-8c77-27cc44e771ed/datastream/OBJ/download>
11. Westerweel, J.: Fundamentals of digital particle image velocimetry. Meas. Sci. Technol. **8**(12), 1379 (1997). DOI 10.1088/0957-0233/8/12/002. URL <http://stacks.iop.org/0957-0233/8/i=12/a=002>

Chapter 5

Image Evaluation Methods for PIV

This chapter treats the fundamental techniques for the evaluation of PIV recordings. In order to extract the displacement information from a PIV recording some sort of interrogation scheme is required. Initially, this interrogation was performed manually on selected images with relatively sparse seeding which allowed the tracking of individual particles [2, 20]. With computers and image processing becoming more commonplace in the laboratory environment it became possible to automate the interrogation process of the particle track images [25, 27, 28, 98]. The application of tracking methods, that is to follow the images of an individual tracer particle from exposure to exposure, is best practicable in the low image density case, see Fig. 1.10a. The low image density case often appears in strongly three-dimensional high-speed flows (e.g. turbomachinery) where it is not possible to provide enough tracer particles or in two phase flows, where the transport of the particles themselves is investigated. Additionally, the Lagrangian motion of a fluid element can be determined by applying tracking methods [14, 19].

In principle, however, a high data density is desired on the PIV vector fields, especially if strong spatial flow variations need to be resolved or for the comparison of experimental data with the results of numerical calculations. This demand requires a medium concentration of the images of the tracer particles in the PIV recording. Medium image concentration is characterized by the fact that matching pairs of particle images – due to subsequent illuminations – cannot be detected by visual inspection of the PIV recordings, see Fig. 1.10b. Hence, statistical approaches, which will be described in the next sections, were developed. After a statistical evaluation has been performed first, tracking algorithms can be applied additionally in order to achieve sub-window spatial resolution of the measurement, which is known as *super resolution* PIV [45].

An overview of the Digital Content to this chapter can be found at [DC5.1].

Tracking algorithms have continuously been improved during the past decade. Today, particle tracking is an interesting alternative to statistical PIV evaluation methods as we will see in more detail in Sect. 5.4.

Comparisons between cross-correlation methods and particle tracking techniques together with an assessment of their performance have been performed in the framework of the *International PIV Challenge* [40, 88–90].

5.1 Correlation and Fourier Transform

5.1.1 Correlation

The main objective of the statistical evaluation of PIV recordings at medium image density is to determine the displacement between two patterns of randomly distributed particle images, which are stored as a 2D distribution of gray levels. Looking around in other areas of metrology (e.g. radars), it is common practice in signal analysis to determine, for example, the shift in time between two (nearly) identical time signals by means of correlation techniques. Details about the mathematical principles of the correlation technique, the basic relations for correlated and uncorrelated signals and the application of correlation techniques in the investigation of time signals can be found in many textbooks [8, 63, 64]. The theory of correlation is easily extended from the one dimensional (1D time signal) to the two- and three-dimensional (gray level spatial distribution) case. In Chap. 4 the use of auto- and cross-correlation techniques for statistical PIV evaluation has already been explained. Analogously to spectral time signal representations, for a 2D spatial signal $I(x, y)$ the power spectrum $|\hat{I}(r_x, r_y)|^2$ can be determined where r_x, r_y are spatial frequencies in orthogonal directions. The basic theorems for correlation and Fourier transform known from the theory of time signals are also valid for the 2D case (with appropriate modifications) [10].

For the calculation of the auto-correlation function two possibilities exist: either direct numerical calculation or indirectly (numerically or optically), using the Wiener-Khinchin theorem [8, 10]. This theorem states that the Fourier transform of the auto-correlation function R_1 and the power spectrum $|\hat{I}(r_x, r_y)|^2$ of an intensity field $I(x, y)$ are Fourier transforms of each other.

The direct numerical calculation is computationally more intensive and has barely been used for 2D PIV. It becomes a viable approach for recording with a sparse distribution of particles, such as encountered in 3D PIV see Sect. 9.3.

Figure 5.1 illustrates that the auto-correlation function can either be determined directly in the spatial domain (upper half of the figure) or indirectly by Fourier transform FT (left hand side), multiplication, that is the calculation of the squared modulus, in the frequency plane (lower half of the figure), and by inverse Fourier transform FT^{-1} (right hand side).

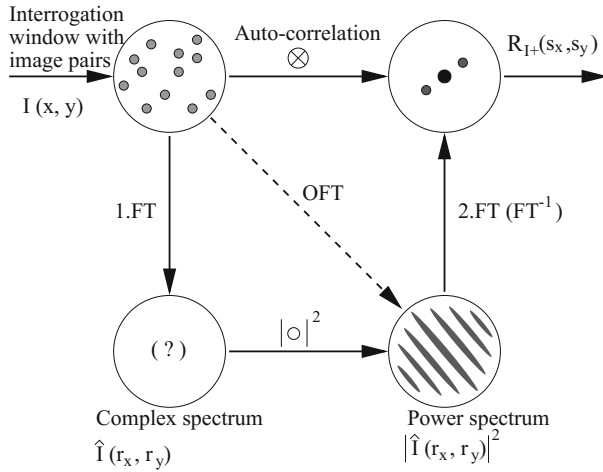


Fig. 5.1 Sketch of relation between 2D correlation function and spatial spectrum by means of the Wiener–Khinchin theorem. FT – Fourier transform, FT^{-1} – inverse Fourier transform, OFT – optical Fourier transform

5.1.2 Optical Fourier Transform

As already mentioned in Sect. 2.5 the far field diffraction pattern of an aperture transmissivity distribution is represented by its Fourier transform [26, 47, 68]. A lens can be used to transfer the image from the far field close to the aperture. For a mathematical derivation of this result some assumptions have to be made, which are described by the Fraunhofer approximation. These assumptions (large distance between object and image plane, phase factors) can be fulfilled in practical optical setups for Fourier transforms.

Figure 5.2 shows two different configurations for such optical Fourier processors. In the arrangement on the left hand side the object, which would consist of a transparency to be Fourier transformed (e.g. the photographic PIV recording), is placed in front of the so-called Fourier lens (at $-f$ usually). In the second setup (right hand side) the object is placed behind the lens. As derived in the book of GOODMAN [26] both arrangements differ only by the phase factors of the complex spectrum and a scale factor. Light sensors (photographic film as well as CCD sensors) are only sensitive to the light intensity. The intensity corresponds to the squared modulus of the complex distribution of the electromagnetic field; hence phase differences in the light wave cannot be detected. Therefore, both arrangements shown in Fig. 5.2 can be used for PIV evaluation. The result of the optical Fourier transform (OFT, dashed line in Fig. 5.1) is the power spectrum of the gray value distribution of the transparency.

In the following this will be illustrated for the case of a pair of two particle images. White (transparent) images of a tracer particle on a black (opaque) background

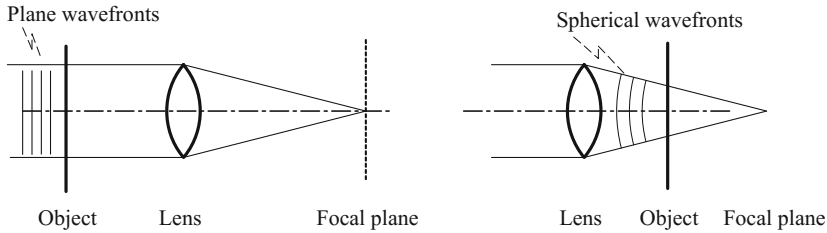


Fig. 5.2 Optical Fourier processor, different positions of object and Fourier lens

will form a double aperture on the photographic PIV recording. With good lens systems the diameter of an image of a tracer particle on the recording is of the order of 20 to 30 μm . The spacing between the two images of a tracer particle should be approximately 150–250 μm , in order to obtain optimum conditions for optical evaluation (compare Sect. 3.2). Figure 5.3 shows a cross-sectional cut through the diffraction pattern of a double aperture (parameters are similar to those of the PIV experiment). The figure at the left side shows several peaks of the light intensity distribution under an envelope. The envelope represents the diffraction pattern of a single aperture with the same diameter (i.e. the Airy pattern, see Sect. 2.5). The intensity distribution will extend in the 2D presentation in the vertical direction, thus forming a fringe pattern, that is the Young's fringes. The fringes are oriented normal to the direction of the displacement of the apertures (tracer images). The displacement between the fringes is inversely proportional to the displacement of the apertures (tracer images). If the distance between the apertures (tracer images) is decreased, the distance between the fringes will increase inversely. This is illustrated in the center of Fig. 5.3, where the distance between the two apertures is only half that of the example on the left side. It can be seen that the distance between the fringes is increased by a factor of two. The same inverse relation, which is due to the scaling theorem of the Fourier transform, is valid for the envelope of the diffraction pattern: if the diameter of the aperture (particle images) decreases, the extension of the Airy pattern will increase inversely (see Fig. 5.3, right side). As a consequence, more fringes can be detected in those fringe patterns which are generated by smaller apertures (particle images). This is one reason to explain why small and well focused particle images will increase the quality and detection probability in the evaluation of PIV recordings. Due to another property of the Fourier transform, that is the shift theorem, the characteristic shape of the intensity pattern does not change if the position of the particle image pairs is changed inside the interrogation spot. Increasing the number of particle image pairs also does not change the Young's fringe pattern significantly. Of course this is not true for the case of just two image pairs: two fringe systems of equal intensity will overlap, allowing no unambiguous evaluation.

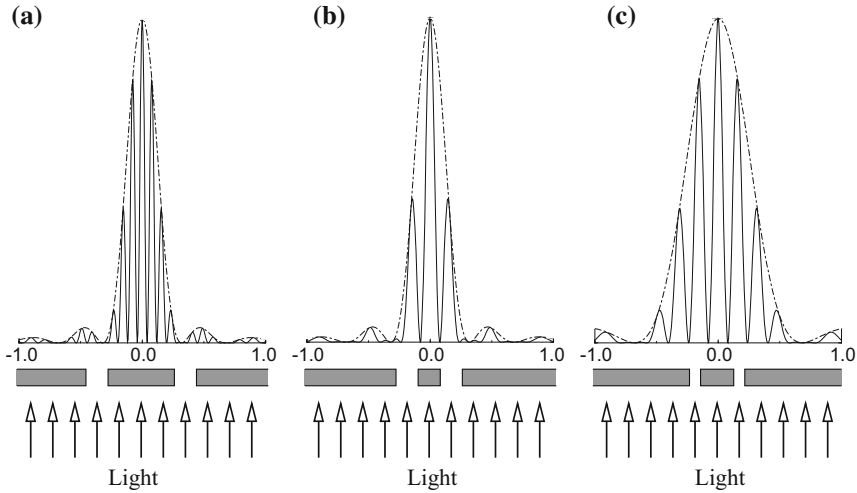


Fig. 5.3 Fraunhofer diffraction pattern of three different double apertures, from left to right, first the separation between the apertures has been decreased, then – on the right hand side – the diameter of the apertures has been decreased

5.1.3 Digital Fourier Transform

The digital Fourier transform is the basic tool of modern signal and image processing. A number of textbooks describe the details [8, 10, 36, 109]. The breakthrough of the digital Fourier transform is due to the development of fast digital computers and to the development of efficient algorithms for its calculation (Fast Fourier Transformation, FFT) [8, 10, 12, 109]. Those aspects of the digital Fourier transform relevant for the understanding of digital PIV evaluation will be described in Sect. 5.3.

5.2 Overview of PIV Evaluation Methods

In the following the different methods for the evaluation of PIV recordings by means of correlation and Fourier techniques will be summarized.

Figure 5.4 presents a flow chart of the fully digital auto-correlation method, which can be implemented in a straight-forward manner following the equations given in Chap. 4. The PIV recording is sampled with comparatively small interrogation windows (typically 30–250 samples in each direction). For each window the auto-correlation function is calculated and the position of the displacement peak in the correlation plane is determined. The calculation of the auto-correlation function is carried out either in the spatial domain (upper part of Fig. 5.1) or – in most cases – through the use of FFT algorithms.

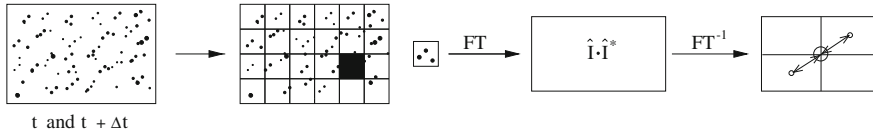


Fig. 5.4 Single frame/double exposure cross-correlation method flow chart

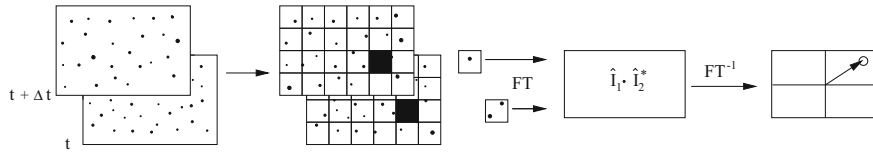


Fig. 5.5 Analysis of double frame/single exposure recordings: the digital cross-correlation method

If the PIV recording system allows the employment of the double frame/single exposure recording technique (see Fig. 3.2) the evaluation of the PIV recordings is performed by cross-correlation (Fig. 5.5). In this case, the cross-correlation between two interrogation windows sampled from the two recordings is calculated. As will be explained later in Sect. 5.3, it is advantageous to offset both these samples according to the mean displacement of the tracer particles between the two illuminations. This reduces the in-plane loss of correlation and therefore increases the correlation peak strength. The calculation of the cross-correlation function is generally computed numerically by means of efficient FFT algorithms.

Single frame/double exposure recordings may also be evaluated by a cross-correlation approach instead of auto-correlation by choosing interrogation windows slightly displaced with respect to each other in order to compensate for the in-plane displacement of particle images. Depending on the different parameters, auto-correlation peaks may also appear in the correlation plane in addition to the cross-correlation peak.

Computer memory and computation speed being limited in the beginning of the eighties, PIV work was strongly promoted by the existence of optical evaluation methods. The most widely used method was the Young's fringes method [DC5.2], which in fact is an optical-digital method, employing optical as well as digital Fourier transforms for the calculation of the correlation function.

In the next section the most commonly used and very flexible digital evaluation methods will be discussed in more detail.

5.3 PIV Evaluation

With the wide-spread introduction of digital imaging and improved computing capabilities the optical evaluation approaches used for the analysis of photographic PIV recordings quickly became obsolete. Initially a desktop slide scanner for the

digitization of the photographic recording replaced the complex opto-mechanical interrogation assemblies with computer-based interrogation algorithms. Then rapid advances in electronic imaging further allowed for a replacement of the rather cumbersome photographic recording process. In the following we describe the necessary steps in the fully digital analysis of PIV recordings using statistical methods. Initially, the focus is on the analysis of single exposed image pairs, that is single exposure/double frame PIV, by means of cross-correlation. The analysis of multiple exposure/single frame PIV recordings can be viewed as a special case of the former.

5.3.1 Discrete Spatial Correlation in PIV Evaluation

Before introducing the cross-correlation method in the evaluation of a PIV image, the task at hand should be defined from the point of view of linear signal or image processing. First of all let us assume we are given a pair of images containing particle images as recorded from a light sheet in a traditional PIV recording geometry. The particles are illuminated stroboscopically so that they do not produce streaks in the images. The second image is recorded a short time later during which the particles will have moved according to the underlying flow (for the time being ignoring effects such as particle lag, three-dimensional motion, etc.). Given this pair of images, the most we can hope for is to measure the straight-line displacement of the particle images since the curvature or acceleration information cannot be obtained from a single image pair. Further, the seeding density is too large and homogeneous that it is difficult to match up discrete particles. In some cases the spatial translation of groups of particles can be observed. The image pair can yield a field of linear displacement vectors where each vector is formed by analyzing the movement of localized groups of particles. In practice, this is accomplished by extracting small samples or interrogation windows and analyzing them statistically (Fig. 5.6).

From a signal (image) processing point of view, the first image may be considered the input to a system whose output produces the second image of the pair (Fig. 5.7). The system's transfer function, \mathbf{H} , converts the input image I to the output image I' and is comprised of the displacement function \mathbf{d} and an additive noise process, N . The function of interest is a shift by the vector \mathbf{d} as it is responsible for displacing the particle images from one image to the next. This function can be described, for instance, by a convolution with $\delta(\mathbf{x} - \mathbf{d})$. The additive noise process, N , in Fig. 5.7 models effects due to recording noise and three-dimensional flow among other things. If both \mathbf{d} and N are known, it should then be possible to use them as transfer functions for the input image I to produce the output image I' . With both images I and I' known the aim is to estimate the displacement field \mathbf{d} while excluding the effects of the noise process N . The fact that the signals (i.e. images) are not continuous – the dark background cannot provide any displacement information – makes it necessary to estimate the displacement function \mathbf{d} using a statistical approach based on localized interrogation windows (or samples).

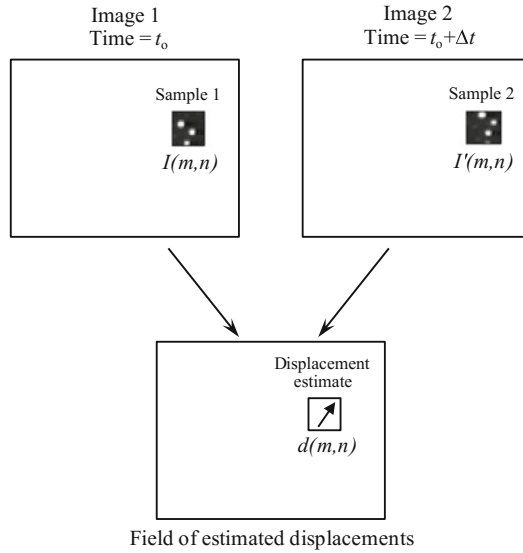


Fig. 5.6 Conceptual arrangement of frame-to-frame image sampling associated with double frame/single exposure Particle Image Velocimetry

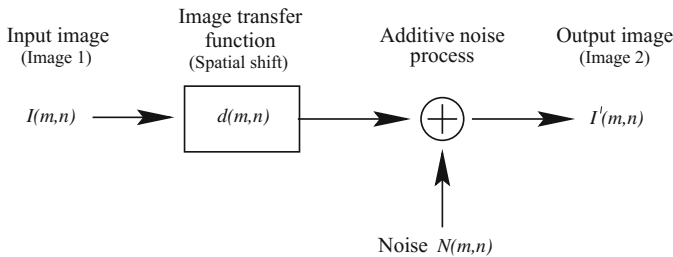


Fig. 5.7 Idealized linear digital signal processing model describing the functional relationship between two successively recorded particle image frames.

One possible scheme to recover the local displacement function would be to deconvolve the image pair. In principle this can be accomplished by dividing the respective Fourier transforms by each other. This method works when the noise in the signals is insignificant. However, the noise associated with realistic recording conditions quickly degrades the data yield. Also the signal peak is generally too sharp to allow for a reliable sub-pixel estimation of the displacement.

Rather than estimating the displacement function d analytically, the method of choice is to locally find the best match between the images in a statistical sense. This is accomplished through the use of the discrete cross-correlation function, whose integral formulation was already described in Sect. 4:

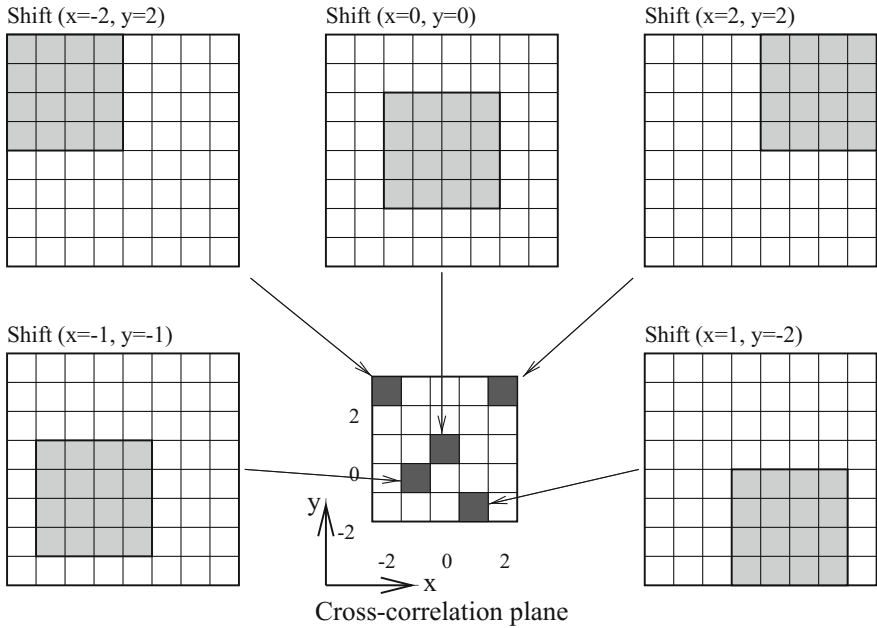


Fig. 5.8 Example of the formation of the correlation plane by direct cross-correlation: here a 4×4 pixel template is correlated with a larger 8×8 pixel sample to produce a 5×5 pixel correlation plane

$$R_{II}(x, y) = \sum_{i=-K}^K \sum_{j=-L}^L I(i, j)I'(i + x, j + y) . \tag{5.1}$$

The variables I and I' are the samples (e.g. intensity values) as extracted from the images where I' can be taken larger than the template I . Essentially the template I is linearly ‘shifted’ around in the sample I' without extending over edges of I' . For each choice of sample shift (x, y) , the sum of the products of all overlapping pixel intensities produces one cross-correlation value $R_{II}(x, y)$. By applying this operation for a range of shifts $(-M \leq x \leq +M, -N \leq y \leq +N)$, a correlation plane the size of $(2M + 1) \times (2N + 1)$ is formed. This is shown graphically in Fig. 5.8. For shift values at which the samples’ particle images align with each other, the sum of the products of pixel intensities will be larger than elsewhere, resulting in a high cross-correlation value R_{II} at this position (see also Fig. 5.9). Essentially the cross-correlation function statistically measures the degree of match between the two samples for a given shift. The highest value in the correlation plane can then be used as a direct estimate of the particle image displacement which will be discussed in detail in Sect. 5.3.5.

Upon examination of this direct implementation of the cross-correlation function two things are obvious: first, the number of multiplications per correlation value

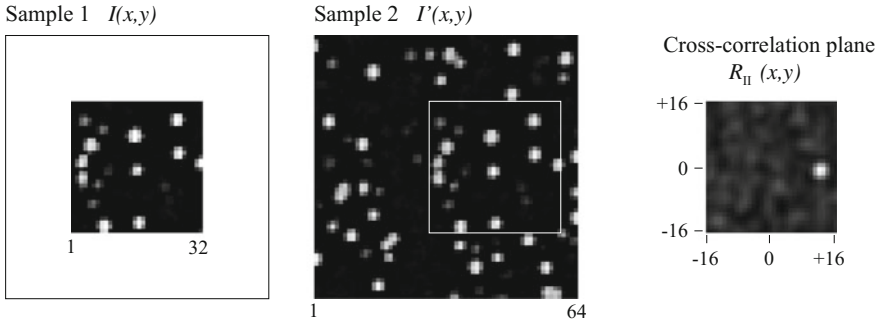


Fig. 5.9 The cross-correlation function R_{II} (right) as computed from real data by correlating a smaller template I (32×32 pixel) with a larger sample I' (64×64 pixel). The mean shift of the particle images is approximately 12 pixel to the right. The approximate location of best match of I within I' is indicated as a white rectangle

increases in proportion to the interrogation window (or sample) size, and second, the cross-correlation method inherently recovers linear shifts only. No rotations or deformations can be recovered by this first order method. Therefore, the cross-correlation between two particle image samples will only yield the displacement vector to first order, that is, the average linear shift of the particles within the interrogation window. This means that the interrogation window size should be chosen sufficiently small such that the higher-order effects can be neglected.

The *first* observation concerning the quadratic increase in multiplications with sample size imposes a quite substantial computational effort. In a typical PIV interrogation the sampling windows cover of the order of several thousand pixel while the dynamic range in the displacement may be as large as ± 10 to ± 20 pixel which would require up to one million multiplications and summations to form only one correlation plane. Clearly, taking into account that several thousand displacement vectors can be obtained from a single PIV recording, a more efficient means of computing the correlation function is required.

5.3.1.1 Frequency Domain Based Calculation of Correlation

The alternative to calculating the cross-correlation directly using Eq. (5.1) is to take advantage of the correlation theorem which states that the cross-correlation of two functions is equivalent to a complex conjugate multiplication of their Fourier transforms:

$$R_{II} \iff \hat{I} \cdot \hat{I}'^* \quad (5.2)$$

where \hat{I} and \hat{I}' are the Fourier transforms of the functions I and I' , respectively. In practice the Fourier transform is efficiently implemented for discrete data using the fast Fourier transform or FFT which reduces the computation from $O[N^2]$ operations

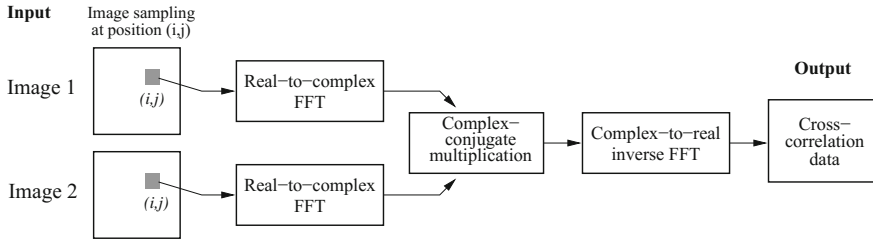


Fig. 5.10 Implementation of cross-correlation using fast Fourier transforms

to $O[N \log_2 N]$ operations [12, 36, 66]. The tedious two-dimensional correlation process of Eq. (5.1) can be reduced to computing two two-dimensional FFT's on equal sized samples of the image followed by a complex-conjugate multiplication of the resulting Fourier coefficients. These are then inversely Fourier transformed to produce the actual cross-correlation plane which has the same spatial dimensions, $N \times N$, as the two input samples. Compared to $O[N^4]$ for the direct computation of the two-dimensional correlation the process is reduced to $O[N^2 \log_2 N]$ operations. The computational efficiency of this implementation can be increased even further by observing the symmetry properties between real valued functions and their Fourier transform, namely the real part of the transform is symmetric: $\text{Re}(\hat{I}_i) = \text{Re}(\hat{I}_{-i})$, while the imaginary part is antisymmetric: $\text{Im}(\hat{I}_i) = -\text{Im}(\hat{I}_{-i})$. In practice two real-to-complex, two-dimensional FFTs and one complex-to-real inverse, two-dimensional FFT are needed, each of which require approximately half the computation time of standard FFTs (Fig. 5.10). A further increase in computation speed can of course be achieved by optimizing the FFT routines such as using lookup tables for the required data, reordering and weighting coefficients and/or fine tuning the machine level code [22, 23].

The use of two-dimensional FFT's for the computation of the cross-correlation plane has a number of properties whose effects have to be dealt with.

Fixed sample sizes: The FFT's computational efficiency is mainly derived by recursively implementing a symmetry property between the even and odd coefficients of the discrete Fourier transform (*the Danielson-Lanczos lemma* [12, 66]). The most common FFT implementation requires the input data to have a base-2 dimension (i.e. 16×16 pixel or 32×32 pixel samples). For reasons explained below it generally is not possible to simply pad a sample with zeroes to make it a base-2 sized sample.

Periodicity of data: By definition, the Fourier transform is an integral (or sum) over a domain extending from negative infinity to positive infinity. In practice however, the integrals (or sums) are computed over finite domains which is justified by assuming the data to be periodic, that is, the signal (i.e. image sample) continually repeats itself in all directions. While for spectral estimation there exist a variety of methods to deal with the associated artifacts, such as windowing, their use in the computation of the cross-correlation will introduce systematic errors or will even hide the correlation signal in noise.

One of these methods, zero padding, which entails extending the sample size to four times the original size by filling in zeroes, will perform poorly because the data (i.e. image sample) generally consists of a nonzero (noisy) background on which the signal (i.e. particle images) is overlaid. The edge discontinuity brought about in the zero padding process contaminates the spectra of the data with high frequency noise which in turn deteriorates the cross-correlation signal. The slightly more advanced technique of FFT data windowing removes the effects of the edge discontinuity, but leads to a nonuniform weighting of the data in the correlation plane and to a bias of the recovered displacement vector. The treatment of this systematic error is described in more detail below.

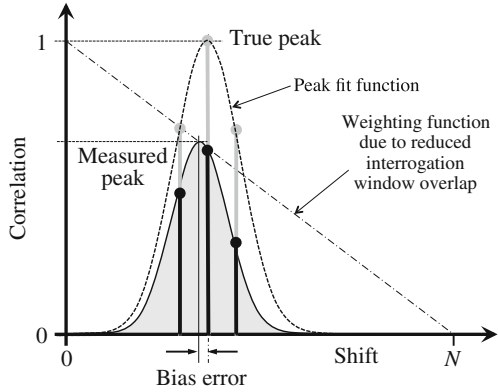
Aliasing: Since the input data sets to the FFT-based correlation algorithm are assumed to be periodic, the correlation data itself is also periodic. If the data of length N contains a signal (i.e. displacements) exceeding half the sample size $N/2$, then the correlation peak will be folded back into the correlation plane to appear on the opposite side. For a displacement $d_{x,true} > N/2$, the measured value will be $d_{x,meas.} = d_{x,true} - N$. In this case the sampling criterion (Nyquist-Shannon sampling theorem) has been violated causing the measurement to be *aliased*. The proper solution to this problem is to either increase the interrogation window size, or, if possible, reduce the laser pulse delay, Δt .

Displacement range limitation: As mentioned before the sample size N limits the maximum recoverable displacement range to $\pm N/2$. In practice however, the signal strength of the correlation peak will decrease with increasing displacements, due to the proportional decrease in possible particle matches. Earlier literature reports a value of $N/3$ to be an adequate limit for the recoverability of the displacement vector [107]. A more conservative, but widely adopted limit is $N/4$, sometimes referred to as the *one-quarter rule* [43]. However, by using iterative evaluation techniques with window-shifting techniques these requirements are only essential for the first pass and obsolete for all other passes as we will see later.

Bias error: Another side effect of the periodicity of the correlation data is that the correlation estimates are biased. With increasing shifts less data are actually correlated with each other since the periodically continued data of the correlation template makes no contribution to the actual correlation value. Values on the edge of the correlation plane are computed from only the overlapping half of the data and should be weighted accordingly. Unless the correlation values are weighted accordingly, the displacement estimate will be biased to a lower value (Fig. 5.11). This error decreases with increasing sample sizes. Larger particle images and along with it wider correlation peaks are associated with larger bias errors. The proper weighting function to account for this biasing effect will be described in Sect. 5.3.5.

If all of the above points are properly handled, an FFT-based interrogation algorithm as shown in Fig. 5.10 will reliably provide the necessary correlation data from which the displacement data can be retrieved. For the reasons given above, this implementation of the cross-correlation function is sometimes referred to as circular cross-correlation compared to the linear cross-correlation of Eq. (5.1).

Fig. 5.11 Bias error introduced in the calculation of the cross-correlation using FFTs



5.3.1.2 Calculation of the Correlation Coefficient

For a number of cases it may be useful to quantify the degree of correlation between the two image samples. The standard cross-correlation function Eq. (5.1) will yield different maximum correlation values for the same degree of matching because the function is not normalized. For instance, samples with many (or brighter) particle images will produce much higher correlation values than interrogation windows with fewer (or weaker) particle images. This makes a comparison of the degree of correlation between the individual interrogation windows impossible. The cross-correlation coefficient function normalizes the cross-correlation function Eq. (5.1) properly:

$$c_{II}(x, y) = \frac{C_{II}(x, y)}{\sqrt{\sigma_I(x, y)}\sqrt{\sigma_I'(x, y)}} \tag{5.3}$$

where

$$C_{II}(x, y) = \sum_{i=0}^M \sum_{j=0}^N [I(i, j) - \mu_I] [I'(i + x, j + y) - \mu_{I'}(x, y)] \tag{5.4}$$

$$\sigma_I(x, y) = \sum_{i=0}^M \sum_{j=0}^N [I(i, j) - \mu_I]^2 \tag{5.5}$$

$$\sigma_I'(x, y) = \sum_{i=0}^M \sum_{j=0}^N [I'(i, j) - \mu_{I'}(x, y)]^2 \tag{5.6}$$

The value μ_I is the average of the template and is computed only once while $\mu_{I'}(x, y)$ is the average of I' coincident with the template I at position (x, y) . It has to be computed for every position (x, y) . Equation (5.3) is considerably more difficult to implement using an FFT-based approach and is usually computed directly in the spatial domain. In spite of its computational complexity, the equation does permit the

samples to be of unequal size which can be very useful in matching up small groups of particles. Nevertheless a first order approximation to the proper normalization is possible if the interrogation windows are of equal size and are not zero-padded:

- Step 1:** Sample the images at the desired locations and compute the mean and standard deviations of each.
- Step 2:** Subtract the mean from each of the samples.
- Step 3:** Compute the cross-correlation function using 2D-FFTs as displayed in Fig. 5.10.
- Step 4:** Divide the cross-correlation values by the standard deviations of the original samples. Due to this normalization the resulting values will fall in the range $-1 \leq c_{II} \leq 1$.
- Step 5:** Proceed with the correlation peak detection taking into account all artifacts present in FFT-based cross-correlation.

5.3.2 Correlation Signal Enhancement

5.3.2.1 Image Pre-processing

The correlation signal is strongly affected by variations of the image intensity. The correlation peak is dominated by brighter particle images with weaker particle images having a reduced influence. Also the non-uniform illumination of particle image intensity, due to light-sheet non-uniformities or pulse-to-pulse variations, as well as irregular particle shape, out-of-plane motion, etc. introduce noise in the correlation plane. For this reason image enhancement prior to processing the image is oftentimes advantageous. The main goal of the applied filters is to enhance particle image contrast and to bring particle image intensities to a similar signal level such that all particle images have a similar contribution in the correlation function [85, 102, 108].

Among the image enhancement methods, *background subtraction* from the PIV recordings reduces the effects of laser flare and other stationary image features. This background image can either be recorded in the absence of seeding, or, if this is not possible, through computation of an average or minimum intensity image from a sufficiently large number of raw PIV recordings (at least 20 – 50). These images can also be used to extract areas to be masked.

A filter-based approach to image enhancement is to *high-pass filter* the images such that the background variations with low spatial frequency are removed leaving the particle images unaffected. In practice this is realized by calculating a low-passed version of the original image and subtracting it from the original. Here the filter kernel width should be larger than the diameter of the particle images: $k_{\text{smooth}} > d_{\tau}$.

Thresholding or *image binarization*, possibly in combination with prior high-pass filtering, results in images where all particles have the same intensity and thus have equal contribution to the correlation function. This binarization, however, is associated with an increase in the measurement uncertainty.

The application of a narrow-width, *low-pass filter* may be suitable to remove high-frequency noise (e.g. camera shot noise, pixel anomalies, digitization artifacts, etc.) from the images. It also results in widening of the correlation peaks, thus allowing a better performance of the sub-pixel peak fitting algorithm (see Sect. 6.2.2). In cases where images are under-sampled ($d_r < 2$) it reduces the so-called peak-locking effect, but also increases the measurement uncertainty.

Range clipping is another method of improving the data yield. The *intensity capping* technique [85], which was found to be both very effective and easy to implement, relies on setting intensities exceeding a certain threshold to the threshold value. Although optimal threshold values may vary with the image content, it may be calculated for the entire image from the grayscale median image intensity, I_{median} , and its standard deviation, σ_I : $I_{\text{clip}} = I_{\text{median}} + n\sigma_I$. The scaling factor n is user defined and generally positive in the range $0.5 < n < 2$.

A similar approach to intensity capping is to perform *dynamic histogram stretching* in which the intensity range of the output image is limited by upper and lower thresholds. These upper and lower thresholds are calculated from the image histograms by excluding a certain percentage of pixel from the either the upper or lower end of the histogram, respectively.

While the previous two methods provide contrast normalization in a global sense, the *min/max filter* approach suggested by WESTERWEEL [102] also adjusts to variations of image contrast throughout the image. The method relies on computing envelopes of the local minimum and maximum intensities using a given tile size. Each pixel intensity is then stretched (normalized) using the local values of the envelopes. In order not to affect the statistics of the image the tile size should be larger than the particle image diameter, yet small enough to eliminate spatial variations in the background [102]. Sizes of 7×7 to 15×15 are generally suitable.

A very robust method of image contrast enhancement capable of dealing with non-uniform image background intensity is to subtract an image based on the local mean and local standard deviation as proposed in [74]. First a Gaussian filtered version of the image $M_I(x, y)$ is subtracted from the original image $I(x, y)$ and then divided by an image of the local variance $\sigma_I(x, y)$:

$$I_{\text{out}}(x, y) = \frac{I(x, y) - M_I(x, y, \sigma_1)}{\sigma_I(x, y, \sigma_2)}.$$

where σ_1 and σ_2 are user defined kernel sizes for the Gaussian filter operations with typically $\sigma_1 < \sigma_2$.

Normalization by the time-average image intensity is also an effective technique to remove stationary background with time-varying intensity. By decomposing a given raw image sequence into its POD modes MENDEZ et al. [56] have shown that the PIV particle pattern can be recovered by filtering out few of the first POD modes and thus rejecting unwanted features such as wall-reflections, noise and non-uniform illumination.

When PIV time series are available, unwanted light reflections can be removed via a high pass filter in the frequency domain [83]. A robust approach to suppress background reflections is based on variants of local normalization method [55]. The specific problem of near-wall measurements contaminated by surface reflections requires dedicated approaches, including for instance the treatment of the solid object region as discussed in [111].

When applying any of the previously described contrast enhancement methods, it should be remembered that modifications of the image intensities may also affect the image statistics which in turn can result in increased measurement uncertainties. This has to be balanced against the increase in data yield. Selective application of contrast enhancing filters in areas of low data would be the logical consequence. Also it should be made clear that strong reflections near walls can only be alleviated through processing as long as the image is not overexposed (saturation) in these areas. Care should be taken to minimize these reflections while acquiring the PIV image data.

5.3.2.2 Phase-Only Correlation

Improvement of the correlation signal may be achieved through adequate filters applied in the spectral domain (Fig. 5.12). Since most PIV correlation implementations rely on FFT based processing, spectral filtering is easily accomplished with very little computational overhead. A processing technique proposed by WERNET [101] called symmetric phase only filtering (SPOF) is based on phase-only filtering techniques which are commonly found in optical correlator systems. SPOF has been shown to improve the signal-to-noise ratio in PIV cross-correlation. In practice these filters also normalize the contribution of all sampled particle images, thus providing contrast normalization. In addition the influence of wall reflections (streaks or lines) and other undesired artifacts can be reduced. According to [85] SPOF yields more accurate results in the presence of DC-background noise, but is not as well suited as the *intensity capping* technique in reducing the displacement bias influence of bright spots with high spatial frequencies.

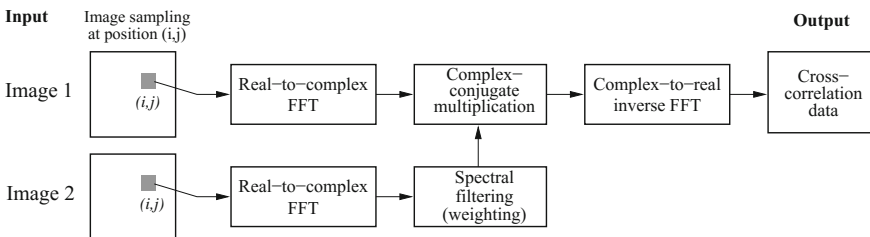


Fig. 5.12 Modification of the cross-correlation processor of Fig. 5.10 to more accurately represent the matched spatial filtering operation as proposed in [101]

5.3.2.3 Correlation-Based Correction

Another form of improving the signal-to-noise ratio in the correlation plane (e.g. displacement peak detection rate) was proposed by HART [32]. The technique involves the multiplication of at least two correlation planes calculated from samples located close-by, typically offset by one quarter to half the correlation sample width. Provided that the displacement gradient between the samples is not significant the multiplication of the correlation planes will enhance the main signal correlation peak while removing noise peaks that generally have a more random occurrence. Correlation plane averaging, that is summation of the of correlation planes instead of multiplication, is more robust when the number of combined correlation planes increases. The method, however, is less effective in removing spurious correlation peaks [53].

5.3.2.4 Ensemble Correlation Techniques

While the previous method is applied within a given PIV image pair, it can also be applied to a sequence of images. This PIV processing approach, also known as *ensemble correlation* or *correlation averaging*, was developed in the framework of micro-PIV applications in an effort to reduce the influence of Brownian motion that introduces significant noise in data obtained from a single PIV recording. Rather than obtaining displacement data for each individual image pair, the technique relies on averaging the correlation planes obtained from a sequence of images. With increasing frame counts a single correlation peak will accumulate for each correlation plane reflecting the mean displacement of the flow [42, 54, 104]. Although computationally very efficient, the main drawback of this approach is that all information pertaining to the unsteadiness of the flow is lost (e.g. no RMS values). Its use with conventional (macroscopic) PIV recording has been verified by the authors [38, 39]. Among the main benefits of this method are the fast calculation of the mean flow and the potentially high spatial resolution. Since this processing is very fast, it has potential as a quasi-online diagnostic tool. To demonstrate the effectiveness of the ensemble correlation technique, MEINHART et al. compared three different averaging algorithms applied to a series of images acquired from a steady flow through a microchannel [54]. The signal-to-noise ratio for measurements generated from a single pair of images was low due to an average of only 2.5 particle images in each 16×64 pixel interrogation window. As a result velocity measurements are noisy and approximately 20% appear to be erroneous. Three types of average are compared.

- *Image averaging*: a time average of the first exposure and second exposure image series are produced that are then correlated (Fig. 5.13). This approach is very efficient and effective when working with low image density (LID) recordings. A variant of this technique consists in producing a maximum image from a given series of recordings (image overlapping). An example is given in Fig. 5.14.

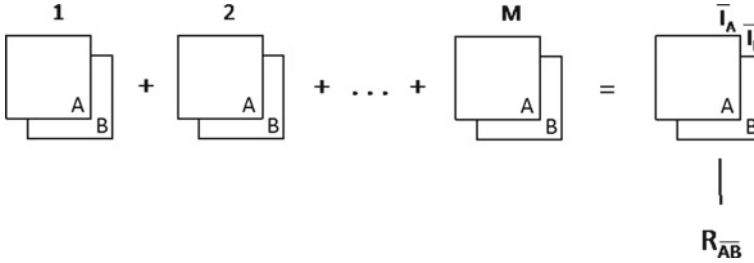


Fig. 5.13 Schematic diagram of cross-correlation from image average

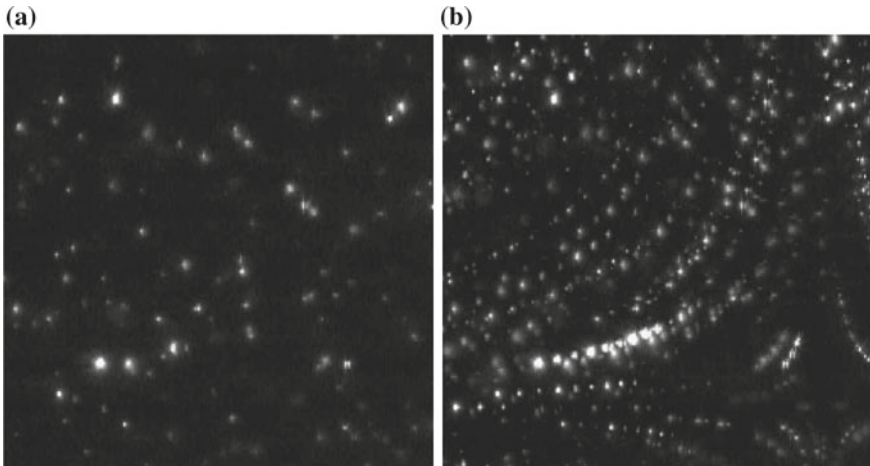


Fig. 5.14 Example of image overlapping: **a** one of the LID-PIV recordings; and **b** result of overlapping 9 LID-PIV recordings. Image size: 256×256 pixel [100]. Copyright 2002, AIAA. Reprinted with permission

Especially in μ PIV the low image density recordings are evaluated with particle-tracking algorithms, whereby the velocity vector is determined with only one particle, and hence the accuracy and reliability of the technique are limited. In addition, interpolation procedures are necessary to obtain velocity vectors on the desired regular grid from the randomly distributed particle-tracking data (Fig. 5.15), which brings additional uncertainties to the final results. The ensemble image permits to evaluate the flow at higher resolution than that allowed by cross-correlation analysis of the individual image pair. The underlying hypothesis for this approach is that the flow is stationary and laminar: condition often met in micro fluidics, but rarely applicable within macroscopic flows.

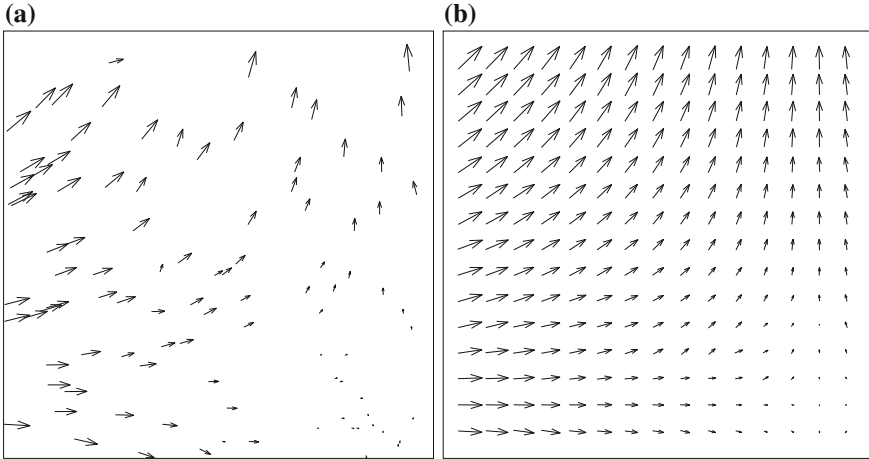


Fig. 5.15 Effect of image overlapping: **a** results for a single LID-PIV recording pair with a particle-tracking algorithm; and **b** results for the overlapped PIV recording pair with a correlation-based algorithm [100]. Copyright 2002, AIAA. Reprinted with permission

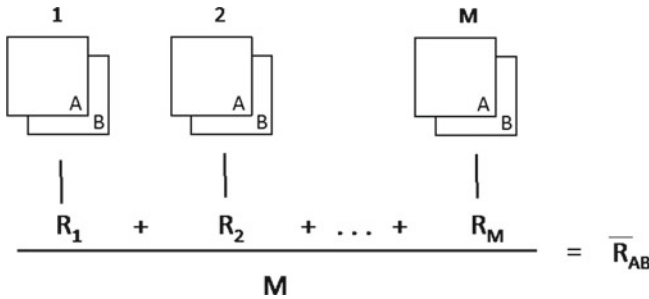


Fig. 5.16 Schematic description of ensemble-averaged cross-correlation

- *Correlation field averaging*: the correlation function from each image pair is calculated and averaged along the sequence of recordings. This method is computationally more demanding than the image averaging technique. The benefit is that it is effective both at low and high level of seeding density (Fig. 5.16).
- *Velocity vector averaging*: the velocity measurement is calculated for each image pair and then averaged along the sequence.

The performance comparison based on synthetic images is illustrated in Fig. 5.17. The fraction of valid mean velocity vectors is displayed as a function of the number of image pairs considered for the analysis. Clearly the combination of few recordings is very beneficial to the yield of valid vectors. The ensemble average correlation technique shows the fastest rise towards a totality of valid vectors. Averaging the

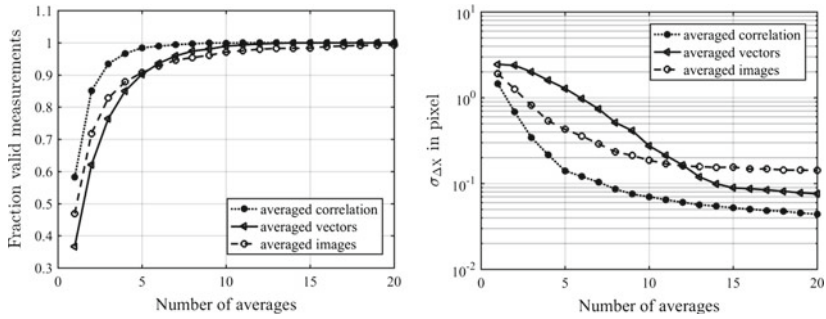


Fig. 5.17 Comparison of the three ensemble interrogation methods: Fraction of valid detected vectors (left) and the corresponding shift vector uncertainty (right)

velocity vectors gives a similar result, however with a slower convergence. Finally, averaging the images and then calculating the correlation shows in this case a similar trend. It shall be retained in mind that image averaging reaches an optimum and then the number of valid vectors will decline as a result of the drop of image contrast over long averages. The rms uncertainty of these three techniques indicates again that cross-correlation averaging is more accurate than vector averaging, followed by image averaging. An important advantage of correlation averaging and image averaging is that the interrogation window can be reduced when the number of recording is increased. Therefore correlation averaging and image averaging techniques offer a higher spatial resolution compared to vector averaging, where the interrogation window needs to contain a minimum number of pairs at each recording.

5.3.2.5 Single-Pixel Ensemble-Correlation

Following the discussion in Sect. 5.3.1 the discrete correlation can be performed between a small template (interrogation template or window) to be searched for in a larger template in the second exposure (search window). The limit case is that the interrogation template is represented by a single pixel. In this case the interrogation of a single pair of images cannot yield any reliable information as the multiplication of the search template by a single value is a replica of itself. When the operation is repeated for a larger number of recordings (typically 10^4 – 10^5), the ensemble correlation signal will emerge with a distinct peak and an acceptable signal-to-noise ratio.

This evaluation method was first applied by WESTERWEEL et al. [104] for stationary laminar flows in micro-fluidics and by BILLY et al. [9] for the analysis of periodic laminar flows. Later, the approach was extended by KÄHLER and co-workers for the analysis of macroscopic laminar, transitional, and turbulent flows [42], and for the analysis of compressible flows at large Mach numbers [38, 80]. Furthermore, the technique was extended for the analysis of stereoscopic PIV images by SCHOLZ

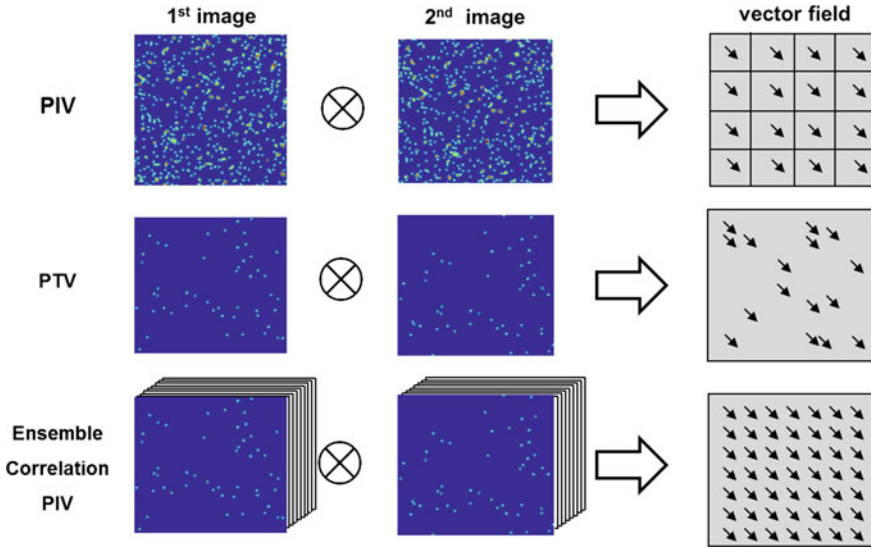


Fig. 5.18 Comparison of three evaluation techniques. Top: Spatial cross-correlation analysis yields instantaneous vector fields at high seeding concentrations by averaging the displacement of small particle image groups within interrogation windows. Middle: Particle tracking analysis provides instantaneous velocity information at particle image locations. This approach is best suited for low and moderate particle image concentrations. Bottom: Ensemble correlation analysis provides only mean flow fields and the mean intensity of the velocity fluctuations by averaging the correlation planes obtained in many independent measurements. This technique works at any seeding concentration but the higher the concentration the faster it converges

& KÄHLER [81]. The product of the pixel intensity and the intensity distribution in the second frame over a search region is the instantaneous contribution to forming the ensemble correlation signal. Applications of single pixel correlations both in micro-PIV and aerodynamic flows (combined with long-range microscopy) have demonstrated the ability to measure the time-averaged flow velocity at unprecedented spatial resolution (in the order of a micron or less). Further discussion is given in Chap. 10.

Figure 5.18 summarizes the input and output expected by applying the techniques described above. Figure 5.19 illustrates schematically the properties of the correlation signal resulting from single pair analysis, ensemble cross-correlation and single pixel ensemble correlation. The latter requires typically two to three order of magnitude more samples to achieve the same signal-to-noise ratio than ensemble correlation for instance when a window of 32×32 pixel is adopted. The position of the maximum in the ensemble correlation map captures only the mean velocity vector. It is possible to extract the velocity probability density function from the analysis of the shape of the correlation peak, if a sufficiently large number of PIV image pairs is available [1, 3, 38, 80, 87, 106].

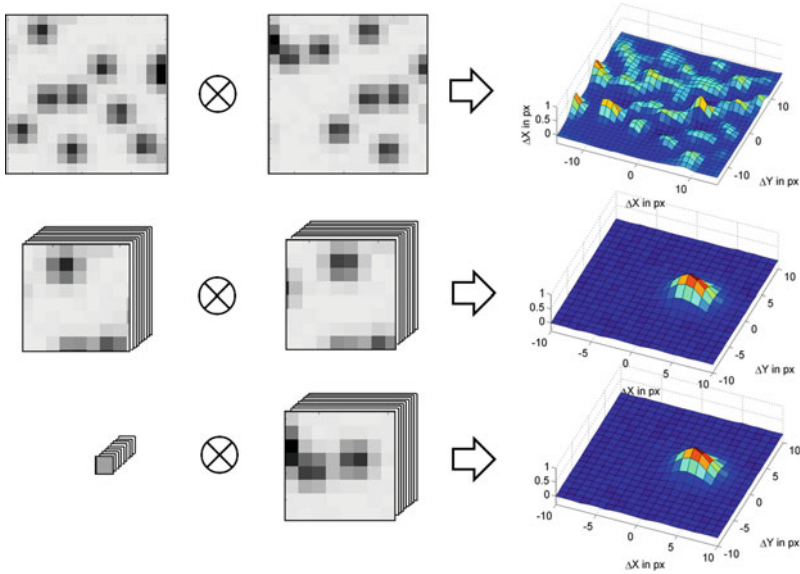


Fig. 5.19 Comparison of the spatial cross-correlation of an image pair (top), the ensemble-correlation of a sequence of image pairs with improved resolution (center), and the single-pixel ensemble-correlation (bottom)

The correlation function can be regarded as the convolution of the velocity probability density function (pdf) and the image auto-correlation function. De-convolving the correlation signal from the auto-correlation function gives an estimate of the velocity pdf and allows for the estimation of the Reynolds stresses at high spatial resolution, when the single-pixel ensemble correlation is used.

Figure 5.20 shows an example from experiments in a transonic backward-facing step flow where single-pixel correlation is used. The very steep velocity profile is better captured with the single-pixel analysis.

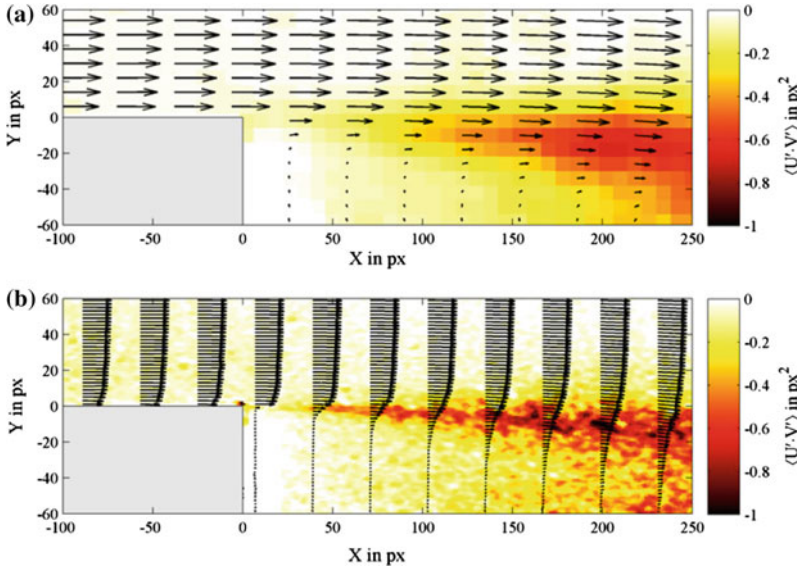


Fig. 5.20 Comparison of mean displacement field and Reynolds shear stress distribution of a transonic backward facing step flow computed from 10000 PIV double images: a) 16×16 pixel window correlation: every 4th vector in X -direction and each vector in Y -direction is shown. b) single-pixel ensemble correlation: every 32nd vector in X -direction and every 2nd vector in Y -direction is shown. The correlation peaks were averaged over 6×3 pixel. From SCHARNOWSKI et al. [80]

5.3.3 Evaluation of Doubly Exposed PIV Images

Although the current technology allows PIV recording in single exposure/multiple frame mode, in some experiments multiple exposed particle images may still be utilized. This is especially the case when photographic recording with high spatial resolution or digital SLR cameras are used. In the early days of PIV, optical techniques for extracting the displacement information from the photographs were utilized. However, desktop slide scanners also make it possible to digitize the photographic negatives and thus enable a purely digital evaluation. Analysis of double-exposed recordings also arises when frame separation no longer is possible for digital cameras, for instance, for the combination of very high-speed flows with high image magnification.

Essentially the same algorithms utilized in the digital evaluation of PIV image pairs described before can be used with minor modifications to extract the displacement field from multiple exposed recordings. The major difference between the evaluation modes arises from the fact that all information is contained on a single frame – in the trivial case a single sample is extracted from the image for the displacement estimation (Fig. 5.21, case I). From this sample, the auto-correlation function is computed by the same FFT method described earlier. In fact, the

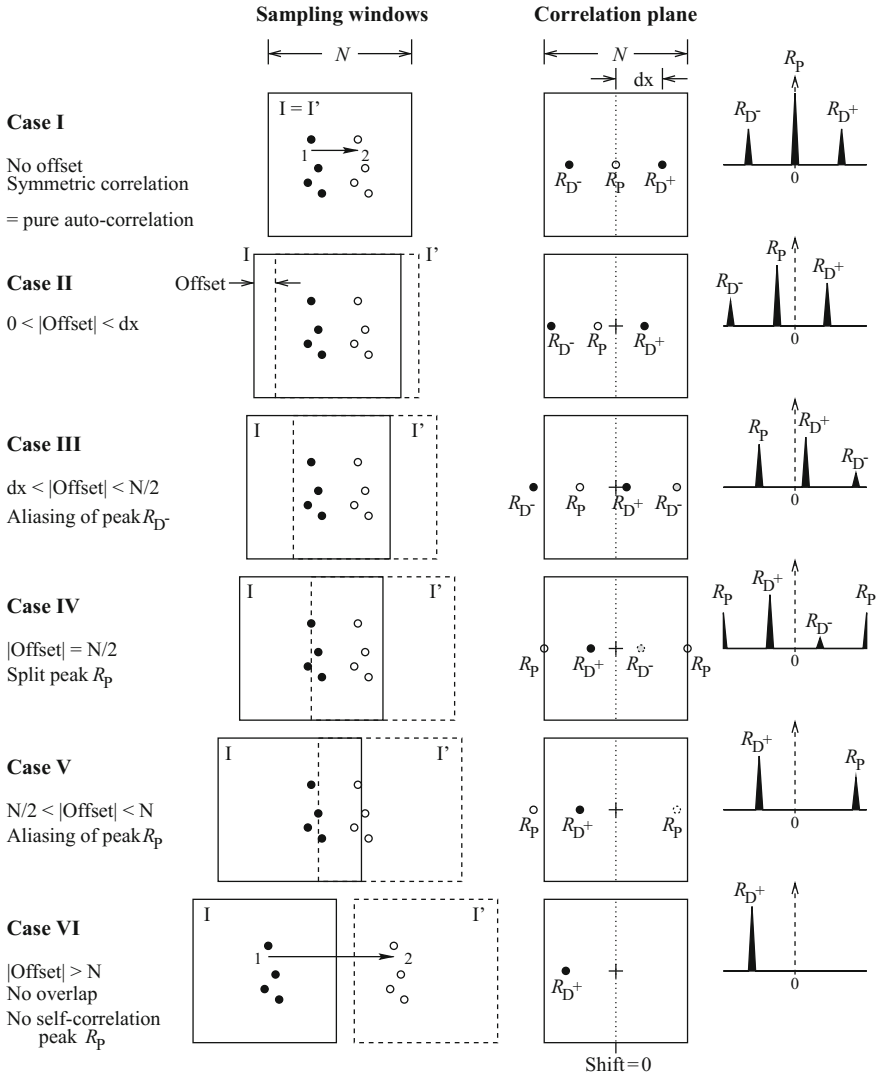


Fig. 5.21 The effect of interrogation window offset on the position of the correlation peaks using FFT based cross-correlation on double exposed images. R_{D^+} marks the displacement correlation peak of interest, R_p is the self-correlation peak. In this case a horizontal shift is assumed

auto-correlation can be considered as a special case of the cross-correlation where both samples are identical. Unlike the cross-correlation function computed from different samples the auto-correlation function will always have a self-correlation peak located at the origin (see also the mathematical description in Sect. 4.5). Located symmetrically around the origin, two peaks with less than one fourth the intensity

describe the mean displacement of the particle images in the interrogation area. The two peaks arise as a direct consequence of the directional ambiguity in the double (or multiple) exposed/single frame recording method.

To extract the displacement information in the auto-correlation function the peak detection algorithm has to ignore the self-correlation peak, R_p , located at the origin, and concentrate on the two displacement peaks, R_{D^+} and R_{D^-} . If a preferential displacement direction exists, either from the nature of the flow or through the application of displacement biasing methods (e.g. image shifting), then the general search area for the peak detection can be predefined. Alternatively a given number of peak locations can be saved from which the correct displacement information can be extracted using a global histogram operator (Sect. 7.15).

The digital evaluation of multiple exposed PIV recordings can be significantly improved by sampling the image at two positions which are offset with respect to each other according to the mean displacement vector. This offers the advantage of increasing the number of paired particle images while decreasing the number of unpaired particle images. This minimization of the in-plane loss-of-pairs increases the signal-to-noise ratio, and hence the detection of the principal displacement peak R_{D^+} . However, the interrogation window offset also shifts the location of the self-correlation peak, R_p , away from the origin as illustrated in Fig. 5.21 (Case II – Case V).

The use of FFTs for the calculation of the correlation plane introduces a few additional aliasing artifacts that have to be dealt with. As the offset of the interrogation window is increased, first the negative correlation peak, R_{D^-} , and then the self-correlation peak, R_p , will be aliased, that is, folded back into the correlation plane (Fig. 5.21 Case III – Case V). In practice, detection of the two strongest correlation peaks by the procedure described in Sect. 5.3.5.1 is generally sufficient to recover both the positive displacement peak, R_{D^+} , and the self-correlation, R_p . The algorithm can be designed to automatically detect the self-correlation peak because it generally falls within a one pixel radius of the interrogation window offset vector.

5.3.4 Advanced Digital Interrogation Techniques

The transition of PIV from the analog (photographic) recording to digital imaging along with improved computing resources prompted significant improvements of interrogation algorithms. The various schemes can roughly be categorized into five groups:

- single pass interrogation schemes such as presented in WILLERT & GHARIB [107]
- multiple pass interrogation schemes with integer sampling window offset [99, 103].
- coarse-to-fine interrogation schemes (resolution pyramid [33, 86, 105]) or (flow-)adaptive resolution schemes

- schemes relying on the deformation of the interrogation samples according to the local velocity gradient [76]
- super-resolution schemes and single particle tracking [7, 45, 91]

Especially the combination of the grid refining schemes in conjunction with image deformation have recently found widespread use as they combine significantly improved data yield with higher accuracy compared to first-order schemes (rigid offset of the interrogation sample). The following sections give brief overview of each of these schemes.

5.3.4.1 Multiple Pass Interrogation

The data yield in the interrogation process can be significantly increased by using a window offset equal to the local integer displacement in a second interrogation pass [103]. By offsetting the interrogation windows according to the mean displacement, the fraction of matched particle images to unmatched particle images is increased, thereby increasing the signal-to-noise ratio of the correlation peak (see Sect. 6.2.4). Also, the measurement noise or uncertainty in the displacement, ε , reduces significantly when the particle image displacement is less than half a pixel (i.e. $|d| < 0.5$ pixel) where it scales proportional to the displacement [103]. The interrogation window offset can be relatively easily implemented in an existing digital interrogation software for both single exposure/double frame PIV recordings or multiple exposure/single frame PIV recordings described in the previous section. The interrogation procedure could take the following form:

- Step 1:** Perform a standard digital interrogation with an interrogation window offset close to the mean displacement in the data.
- Step 2:** Scan the data for outliers using a predefined validation criterion as described in Sect. 7.1. Replace outlier data by interpolating from the valid neighbors.
- Step 3:** Use the displacement estimates to adjust the interrogation window offset locally to the nearest integer.
- Step 4:** Repeat the interrogation until the integer offset vectors converge to ± 1 pixel. Typically three passes are required.

The speed of this multiple pass interrogation can be increased significantly by comparing the new integer window offset to the previous value allowing unnecessary correlation calculations to be skipped. The data yield can be further increased by limiting the correlation peak search area in the last interrogation pass.

As pointed out by WERELEY & MEINHART [99] a symmetric offset of the interrogation samples with respect to the point of interrogation corresponds to a central difference interrogation which is second-order accurate in time in contrast to a simple forward differencing scheme that simply adds the offset to the interrogation point (see Fig. 5.22).

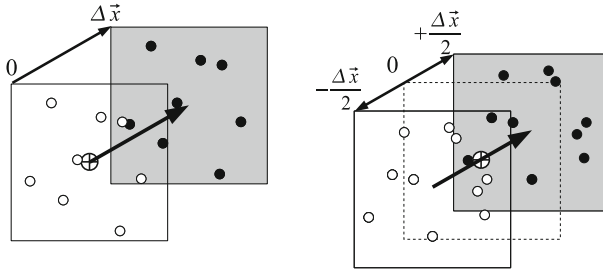


Fig. 5.22 Sampling window shift using a forward difference scheme (left) and central difference scheme, right (from [76])

5.3.4.2 Grid Refining Schemes

The multiple pass interrogation algorithm can be further improved by using a hierarchical approach in which the sampling grid is continually refined while the interrogation window size is reduced simultaneously. This procedure, originally introduced by SORIA [86] and WILLERT [105], has the added capability of successfully utilizing interrogation window sizes smaller than the particle image displacement. This permits the dynamic spatial range (DSR) to be increased by this procedure. This is especially useful in PIV recordings with both a high image density and a high dynamic range in the displacements. In such cases standard evaluation schemes cannot use small interrogation windows without losing the correlation signal due to the larger displacements (one-quarter rule, [44]). Instead the offset of the interrogation window at subsequent iterations allows to circumvent the above rule and obtain good correlation signal even for interrogation windows smaller than the particle image displacement. However, a hierarchical grid refinement algorithm is more difficult to implement than a standard interrogation algorithm. Such an algorithm may look as follows:

- Step 1:** Start with a large interrogation sample that is known to capture the full dynamic range of the displacements within the field of view by observing the one-quarter rule (p. 156).
- Step 2:** Perform a standard interrogation using windows that are large enough to obey the one-quarter rule.
- Step 3:** Scan for outliers and replace by interpolation. As the recovered displacements serve as estimates for the next higher resolution level, the outlier detection criterion should be more stringent than that for single-step analysis to prevent possible divergence of the new estimate from the true value [82].
- Step 4:** Project the estimated displacement data on to the next higher resolution level. Use this displacement data to offset the interrogation windows with respect to each other.

- Step 5:** Increment the resolution level (e.g. halving the size of the interrogation window) and repeat steps **1** through **4** until the actual image resolution is reached.
- Step 6:** Finally perform an interrogation at the desired interrogation window size and sampling distance (without outlier removal and smoothing). By limiting the search area for the correlation peak the final data yield may be further increased because spurious, potentially stronger correlation peaks can be excluded if they fall outside of the search domain.

In the final interrogation pass the window offset vectors have generally converged to ± 0.5 pixel of the measured displacement thereby guaranteeing that the PIV image was optimally evaluated. The choice for the final interrogation window size depends on the particle image density. Below a certain number of matched pairs in the interrogation area (typically $\mathcal{N}_I < 4$) the detection rate will decrease rapidly (see Chap. 9). Figure 5.23 shows the displacement data of each step of the grid and interrogation refinement.

The processing speed may be significantly increased by down-sampling the images during the coarser interrogation passes. This can be achieved by consolidating neighboring pixel by placing the sum of a block of $N \times N$ into a single pixel (pixel binning) [105]. This allows the use of smaller interrogation samples that are evaluated much faster. In fact, a constant size of the correlation kernel can be used regardless of the image resolution (e.g. a $4 \times$ down-sampled image interrogated by a 32×32 pixel sampling window corresponds to a 128×128 pixel sample at the initial image resolution).

5.3.4.3 Image Deformation Schemes

The particle image pattern displacement is measured by cross-correlation under the assumption that the motion of the particles image within the interrogation window is approximately uniform. In practice this condition is often violated as most flows of interest produce a velocity distribution with significant velocity gradients due to shear layers and vortices. In these cases the cross-correlation peak produced by image pairs with a different velocity becomes broader and it can split into multiple peaks due to large velocity differences across the window (Fig. 5.24).

As a result, the measurement of velocity in presence of large velocity gradient (e.g. in the core of a vortex, Fig. 5.23) is affected by larger uncertainty and suffers from a higher vector rejection rate. The window deformation technique is meant to compensate the in-plane velocity gradient and the peak broadening effect. Both can be largely reduced when the two PIV recordings are deformed according to an estimation of the velocity field. The technique can be implemented within the multi-grid method [86, 105] described before (see Sect. 5.3.4.2). The main advantage with respect to the multi-grid window shifting method is an increased robustness and accuracy over shear flows such as boundary layers, vortices and turbulent flows in general. The basic principle is illustrated in Fig. 5.25, where a continuous image deforma-

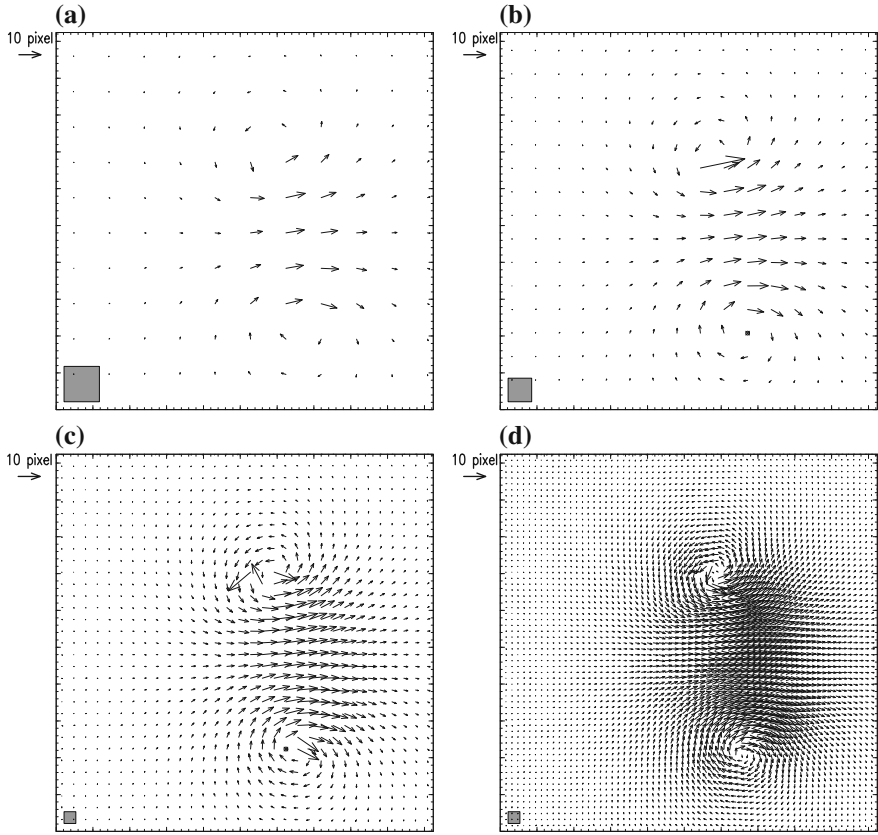


Fig. 5.23 Iteration steps used in a multiple pass, multi-grid interrogation process. The gray squares in the lower left of each data set indicate the size of the utilized interrogation window. In the first pass the original image was downsampled 3 times using pixel binning

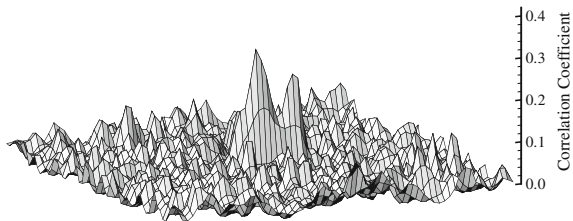


Fig. 5.24 Discrete spatial correlation map in a shear flow. Interrogation with 1-step correlation. The peak broadens and splits into several individual peaks

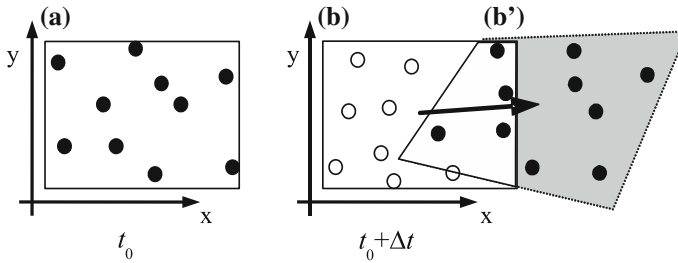


Fig. 5.25 Principle of the window deformation technique. Left: tracer pattern in the first exposure. Right: tracer pattern at the second exposure (solid circles represent the tracers correlated with the first exposure in the interrogation window). In grey deformed window according to the displacement distribution estimated from a previous interrogation

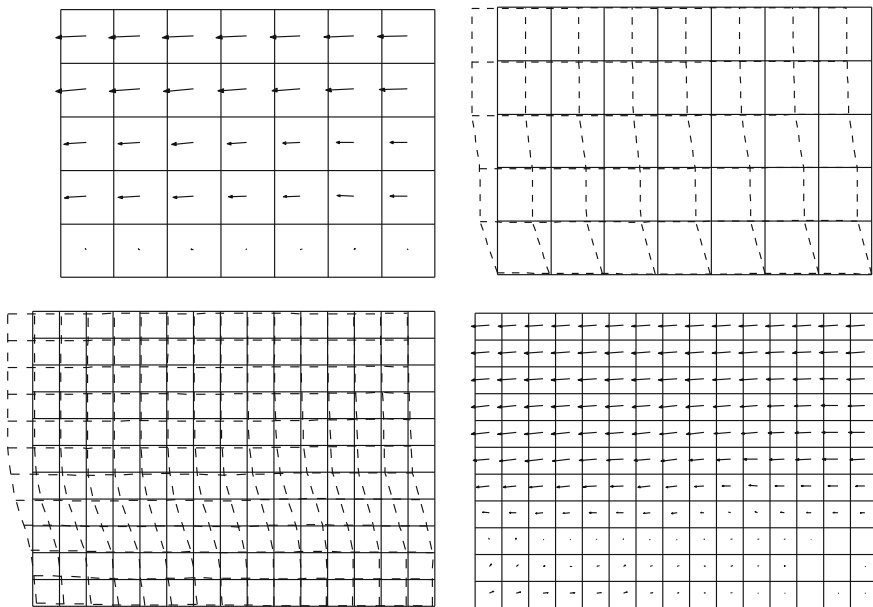


Fig. 5.26 Graphical scheme of the image deformation technique with one multi-grid step. Non-deformed interrogation windows as solid lines and deformed windows as dashed lines

tion progressively transforms the images towards two hypothetical recordings taken simultaneously at time $t + \Delta t/2$.

In analogy with the discrete window shift technique, this method is referred to as window deformation; however, the efficient implementation of the procedure is based on the deformation of the entire PIV recordings, which is sometimes referred to as image deformation (Fig. 5.26). The two approaches are therefore synonyms of the same concept. The image deformation technique can be summarized as follows:

- Step 1:** Standard digital interrogation with an interrogation window complying with the one quarter rule (p. 156)
- Step 2:** Low-pass filtering of the velocity vector field. A filter kernel equivalent to the window size is sufficient to smooth spurious fluctuations and suppress fluctuations at sub-window wavelength. Moving average filters or spatial regression with a 2nd order least squares regression are suitable choices [82].
- Step 3:** Deformation of the PIV recordings according to the filtered velocity vector field with a central difference scheme. The image resampling scheme influences the accuracy of the procedure [5]. For typical PIV images with particle image diameter of 2 to 3 pixel, high order schemes (cardinal interpolation, B-splines) yield better results than low order interpolators (bilinear interpolation) [95, 97].
- Step 4:** Further interrogation passes on the deformed images with an interrogation window reduced in size, yet containing at least 4 image pairs.
- Step 5:** Add the result of the correlation to the filtered velocity field.
- Step 6:** Scan the velocity vector field for outliers and replace these by interpolation.
- Step 7:** Repeat steps 2 to 6 two or three times. With each iteration the incremental change in the displacement field will decrease.

In analogy to the standard cross-correlation function given in Eq. (5.1) the equation used for the spatial cross-correlation for deformed images reads as follows:

$$R_{\Pi}(x, y) = \sum_{i=-K}^K \sum_{j=-L}^L \tilde{I}(i, j) \tilde{I}'(i+x, j+y) . \quad (5.7)$$

where $\tilde{I}(i, j)$ and $\tilde{I}'(i, j)$ are the image intensities reconstructed after deformation using the predicted deformation field $\Delta s(\mathbf{x})$ in a central difference scheme:

$$\tilde{I}(\mathbf{x}) = I\left(\mathbf{x} - \frac{\Delta s(\mathbf{x})}{2}\right) \quad (5.8)$$

$$\tilde{I}'(\mathbf{x}) = I'\left(\mathbf{x} + \frac{\Delta s(\mathbf{x})}{2}\right) \quad (5.9)$$

The deformation field $\Delta s(\mathbf{x})$ is a spatial distribution which generally is not uniform and therefore requires interpolation at each pixel in the image. Here a truncation of the Taylor series at the first order term is commonly sufficient for the reconstruction of the local displacement:

$$\Delta s_1(\mathbf{x}) = \Delta s(\mathbf{x}_0) + \nabla[\Delta s(\mathbf{x}_0)] \cdot (\mathbf{x} - \mathbf{x}_0) + \dots + \mathcal{O}(\mathbf{x} - \mathbf{x}_0)^2 \quad (5.10)$$

Here \mathbf{x}_0 denotes the position of the center of the interrogation window. Since the size of the interrogation window normally exceeds the spacing of the displacement vectors (overlap factor 50–75%) the displacement distribution within the window is

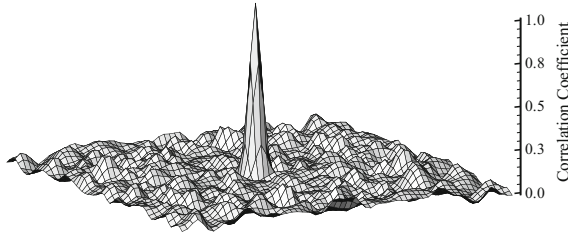


Fig. 5.27 Correlation map of a shear flow as in Fig. 5.24 with multi-step correlation and window deformation. A single peak can be clearly distinguished from the correlation noise with a correlation coefficient of 99.5% compared to 27.3% for the undeformed image

a piecewise linear function resulting in a higher order approximation of the velocity distribution within the window. Dedicated literature on the performance of velocity field interpolators indicates that B-splines are an optimal choice in terms of accuracy and computational cost [4].

When steps 2–6 are repeated a number of times, the distance between particle image pairs is minimized and $\tilde{I}(i, j)$ and $\tilde{I}'(i, j)$ tend to coincide except for out-of-plane particle motion and shot-to-shot image intensity variation. As a consequence, the correlation function returns a peak located at the center of the correlation plane.

The procedure has the additional benefits of yielding a more symmetrical correlation peak, approximately at the origin of the correlation plane, reducing uncertainties due to distorted peak shape or inaccurate peak reconstruction (see Figs. 5.27 and 5.28). Another advantage is that the spatial resolution is approximately doubled with respect to a rigid window interrogation [82], with the caveat of a selective amplification of wavelengths smaller than the interrogation window (see Fig. 5.29). The latter needs to be compensated for by low-pass filtering the intermediate result [82] (see Fig. 5.30).

5.3.4.4 Image Interpolation for PIV

Due to the continuously varying displacement field, the intensity of the deformed images needs to be resampled (e.g. by interpolation) at non-integer pixel locations, which increases the computational load of the technique. Depending on the choice of interpolator significant bias errors may be introduced as shown in Fig. 5.31. The data was obtained from synthetic images with constant particle image displacement using the Monte Carlo methods described in Sect. 6.2.1. Polynomial interpolation produces a significant bias error up to one fifth of a pixel and are not particularly suited for this purpose.

A review of the topic on the background of medical imaging along with a performance comparison is given by THÉVENAZ et al. [95]. They suggest the use of generalized interpolation with non-interpolating basis functions such as B-splines

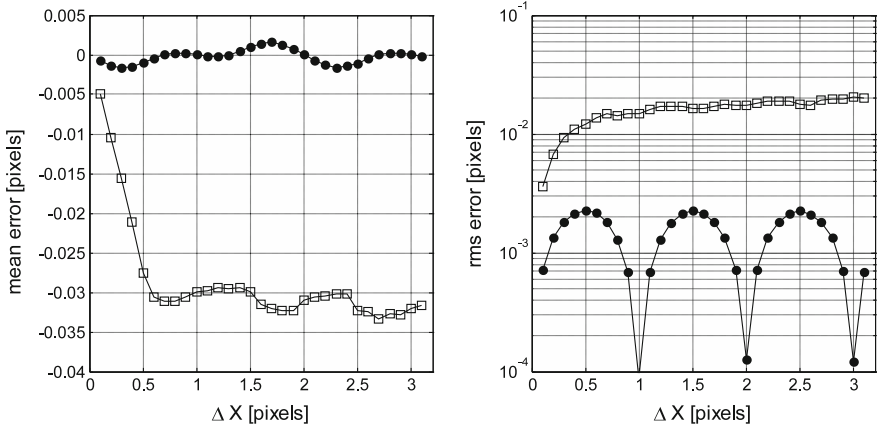
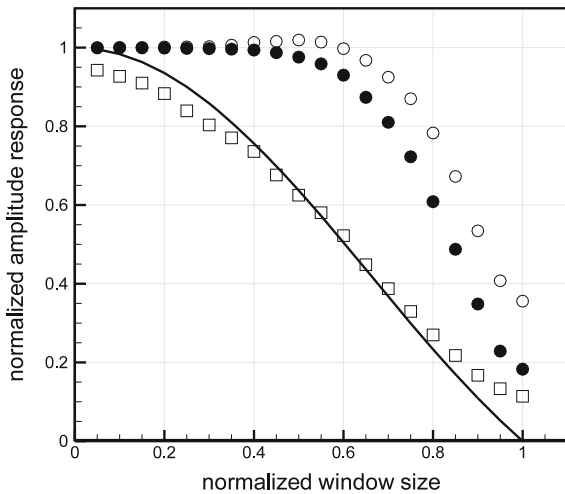


Fig. 5.28 Displacement error as a function of the particle image displacement (32×32 pixel window size). \square 1-step cross-correlation; \bullet window deformation

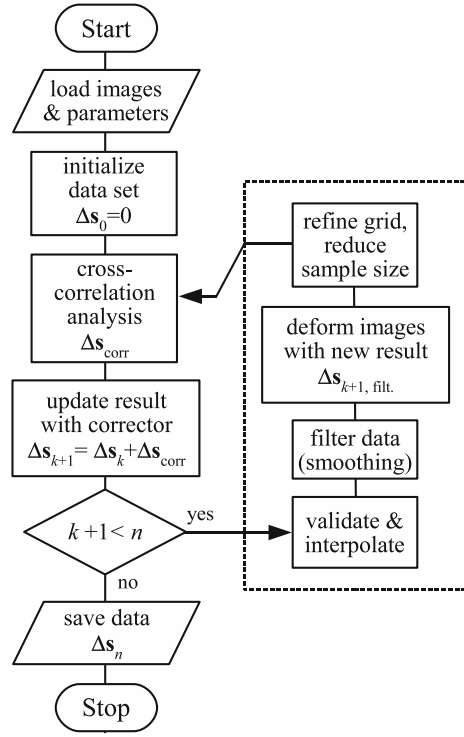
Fig. 5.29 Sine wave test: normalized amplitude response as a function of the normalized window size. Solid line: theoretical response (sinc); \square 1-step cross-correlation; \bullet window deformation with 2nd order least squares filter; \circ window deformation without filtering



or shifted bi-linear interpolation in favor of more commonly used polynomial or bandlimited sinc-based interpolation.

In contrast to many other imaging applications, a properly recorded PIV image generally contains almost discontinuous data with significant signal strength in the shortest wavelengths close to the sampling limit (i.e. strong intensity gradients). Because of this the image interpolator should primarily be capable of properly reconstructing these steep intensity gradients. A concise comparison of various advanced image interpolators for use in PIV image deformation is provided by ASTARITA & CARDONE [5]. In accordance to the findings reported by

Fig. 5.30 Block diagram of the iterative image deformation interrogation method with filtered predictor



THÉVENAZ et al. [95], they suggest the use of B-splines for an optimum balance between computational cost and performance. The bias error for B-splines of third and fifth order shown in Fig. 5.31 clearly supports this. If higher accuracy is required then sinc-based interpolation, such as Whittaker reconstruction [79], or FFT-based interpolation schemes [110] with a large number of points should be used. However, processing time may increase an order of magnitude.

5.3.4.5 Iterative PIV Interrogation and Its Stability

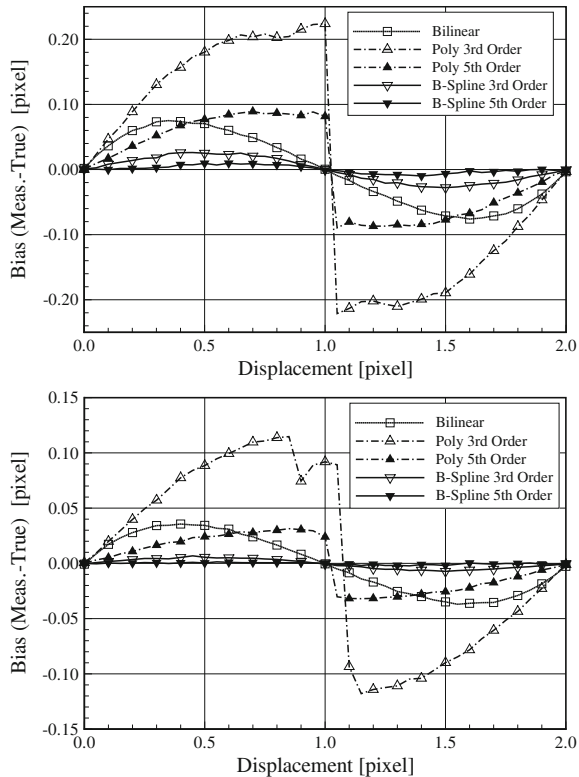
Multi-step analysis of PIV recordings can be seen as comprising of two procedures:

(1) Multi-grid analysis where the interrogation window size is progressively decreased. This process eliminates the one-quarter rule constraint and usually terminates when the required window size (the smallest) is applied.

(2) Iterative analysis at a fixed sampling rate (grid spacing) and spatial resolution (window size). This process further improves the accuracy of the image deformation and enhances the spatial resolution.

In essence the iterative analysis can be described by a predictor-corrector process governed by the following equation:

Fig. 5.31 Bias error in image deformation PIV processing for three image interpolation schemes. Particle image diameter: $d_\tau = 2.0$ (top), $d_\tau = 4.0$ (bottom)



$$\Delta s_{k+1}(\mathbf{x}) = \Delta s_k(\mathbf{x}) + \Delta s_{\text{corr}}(\mathbf{x}) \quad (5.11)$$

where Δs_{k+1} indicates the result of the evaluation at the k th iteration. The correction term Δs_{corr} can be viewed as a residual and is obtained by interrogating the deformed images as calculated by the central difference expression Eq. (5.8). The procedure can be repeated several times, however two to three iterations are already sufficient to achieve a converged result with most of the in-plane particle image motion compensated through the image deformation.

The iterative scheme introduced above appears very logical and its simplicity makes it straightforward to implement, which probably explains why it has been so broadly adopted in the PIV community [21, 35, 78, 79, 99]. However, when such iterative interrogation is performed without any spatial filtering of the velocity field, the process produces spurious oscillations of small amplitude that grow with the number iterations. The instability arises from the sign reversal in the sinc shape of the response function associated to the top-hat function of the interrogation window. For instance, taking two almost identical images except for artificial pixel noise, the displacement field measurement after some iterations begins to oscillate at a spatial wavelength $\lambda_{\text{unst}} \approx 2/3D_1$ and yields a wavy pattern [82].

The above result is consistent with the response function of a top-hat weighted interrogation window being $r_s = \sin(x/D_1)/(x/D_1)$. Therefore wavelengths in the range with negative values of the sinc function are systematically amplified. The iterative process requires stabilization by means of a low-pass filter applied to the updated result (Fig. 5.30), which damps the growth of fluctuations at wavelengths smaller than the window size. A moving average filter with a kernel size corresponding to that of the interrogation window is more than sufficient to stabilize the process.

However, filtering with a second order least-squares spatial regression allows to both maximize spatial resolution and minimize the noise. Other means of stabilization are based on interrogation window weighting techniques (e.g. Gaussian or LFC [58]). A numerical simulation using a sine-modulated shear flow shows that the single-pass cross-correlation amplitude modulation (empty squares in Fig. 5.29) follows closely that of a sinc function with a 10% cut-off occurring when the window size is about one-quarter the spatial wavelength ($D_1/\lambda = 0.25$). The iterative interrogation (full circles in Fig. 5.29) delays the cut off at $D_1/\lambda = 0.65$. This implies that with a window size of 32 pixel the single-step cross-correlation is only capable of accurately recovering fluctuations with a wavelength larger than 120 pixel. The minimum wavelength reduces to 50 pixel with the iterative deformation interrogation. The higher response of the iterative interrogation without filter (empty circles in Fig. 5.29) is only hypothetical because the process is unstable and the error is dominated by the amplified wavy fluctuations.

In conclusion the spatial resolution achieved with iterative deformation is about twice as high than that of the single-step or window-shift procedure. It should be retained in mind that the increase in resolution becomes only effective when the velocity field is sampled spatially at a higher rate, that is, increasing the overlap factor to 75% between adjacent windows instead of 50%. Otherwise, the error committed when evaluating for instance the velocity spatial derivatives is dominated by numerical truncation due to the large distance between neighboring vectors.

5.3.4.6 Adaptive Interrogation Techniques

The iterative multi-grid interrogation may help in increasing the spatial resolution by decreasing the final window size. However, in several cases the flow and the flow seeding distribution are not homogeneous over the observed domain. In this case, the optimization rules for interrogation can only be satisfied in an average sense and local non-optimal conditions may occur such as poor correlation signal or too low flow sampling rate. Moreover, the window filtering effect can be minimized when the flow exhibits variations along a preferential direction. For instance, in case of stationary interfaces an adaptive choice of the interrogation volume shape and orientation may contribute to achieve further improvements especially when dealing with shear layers [93] or shock waves [94]. The main rationale behind adaptive choice of the interrogation window is that, maintaining its overall size, one can reduce its length in one direction and compensate it enlarging the window in the orthogonal direction. The parameter governing this choice can be the velocity gradient or higher

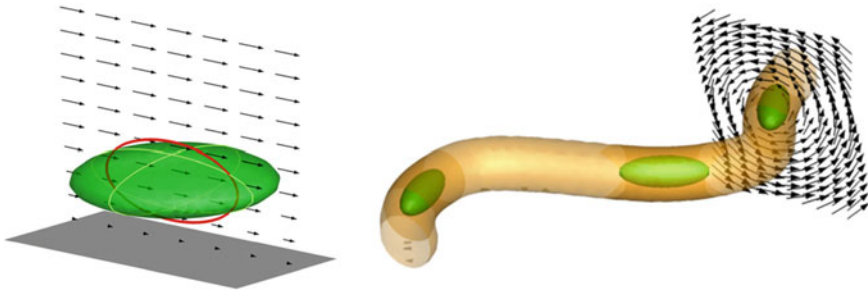


Fig. 5.32 Examples of adaptive shape and orientation of the interrogation window. A coin like shape is mostly useful to improve resolution in the wall-normal direction of a boundary layer. Cigar like shape improves the resolution in the core of a vortex

spatial derivative [77], but also more simply the direction of a solid surface nearby. Spatial adaptivity is particularly attractive for 3D PIV where the interrogation volume can be shaped as flat as a coin or elongated as a cigar depending on the velocity gradient topology [59] (Fig. 5.32).

5.3.4.7 Non-correlation-Based Interrogation Techniques

Other interrogation algorithms exist that do not rely on cross-correlation. Most work has been devoted to image motion estimation, also referred to as optical flow, which is a fundamental issue in low-level vision and has been the subject of substantial research for application in robot navigation, object tracking, image coding or structure reconstruction [6, 34]. These applications are commonly confronted with the problem of fragmented occlusion (i.e. looking through branches of a tree) or depth discontinuities in space, which are analogous to shocks within fluid flows.

Optical flow for the analysis of PIV images was first reported by QUENOT et al. who investigated a thermally driven flow of water [67]. Further implementations of optical flow adapted to the evaluation of PIV images have been reported by RUHNAU et al. [72, 73]. The potential of optical flow for achieving high spatial resolution and accurate results in high-gradient regions was demonstrated in the scope of the “International PIV-Challenge” [88–90]. One known deficiency of established optical flow techniques available in computer vision is their instability in the presence of out-of-plane motion of particles that is associated with a loss of image correspondence. Therefore additional constraints have to be implemented in the algorithms to successfully apply them to PIV recordings [72, 73]. The latter can potentially be resolved by the application of optical flow techniques to 3D experiments, which remains to date a topic of research.

The degree of image matching can be evaluated not only by intensity multiplication as in the case of cross-correlation, but also by calculating the difference between two patterns. The method of minimum quadratic differences (MQD) is based on

the difference between the reference and search template. The application to PIV has been investigated by GUI & MERZKIRCH [29, 30] among others. The method performs similar to cross-correlation analysis in terms of accuracy of displacement estimation. The potential advantage of the method is that the operation of difference can be more easily accelerated than the multiplication with dedicated microprocessors. One of the shortcomings of MQD is the higher sensitivity to variations in the illumination between the two exposures, which needs to be accounted for with intensity equalization.

The least-squares matching algorithm is based on MQD operations, but the function to be minimized is not defined in the physical space of spatial shift, but in that of the coefficients of affine transformations (shift, rotation, dilation, shear) [46]. The method is therefore also very well suited to the analysis of flows with a variety of length scales where the deformation in between the two recordings cannot be neglected.

Earlier work from TOKUMARU & DIMOTAKIS [96] presented the image correlation velocimetry (CIV), followed by a number of optimizations by FINCHAM & DELERCE [21] leading to an algorithm performing iterative window refinement, including the deformation, comparable to that based on cross-correlation.

5.3.5 *Cross-Correlation Peak Detection*

One of the most crucial, but not necessarily easily understood features of digital PIV evaluation, is that the position of the correlation peak can be estimated to subpixel accuracy. Estimation accuracies of the order of $1/10$ – $1/20$ th of a pixel are realistic for 32×32 pixel samples from 8-bit digital images. Simulation data such as those presented in Sect. 6.1 can be used to quantify the achievable accuracy for a given imaging setup.

Since the input data itself is discretized, the correlation values exist only for integral shifts. The highest correlation value would then permit the displacement to be determined only with an uncertainty of $\pm 1/2$ pixel. However, with the cross-correlation function being a statistical measure of best match, the correlation values themselves also contain useful information. For example, if an interrogation sample contains ten particle image pairs with slightly varying shift of 2.5 pixel on average, then from a statistical point of view, five particle image pairs will, for instance contribute to the correlation value associated with a shift of 2 pixel, while the other five will indicate a shift of 3 pixel. As a result, the correlation values for the 2 pixel and 3 pixel shifts will have the same value. An average of the two shifts will yield an estimated shift of 2.5 pixel. Although rather crude, the example illustrates that the information hidden in the correlation values can be effectively used to estimate the mean particle image shift within the interrogation window.

A variety of methods of estimating the location of the correlation peak have been utilized in the past. Centroiding, which is defined as the ratio between the first order moment and zeroth order moment, is frequently used, but requires a method of

defining the region that comprises the correlation peak. Generally, this is done by assigning a minimum threshold value separating the correlation peak signal from the background noise. The method works best with broad correlation peaks where many values contribute in the moment calculation. Nevertheless, separating the signal from the background noise is not always straightforward.

A more robust method is to fit the correlation data to some function. Especially for narrow correlation peaks, the approach of using only three adjoining values to estimate a component of displacement has become wide-spread. The most common of these three-point estimators are listed in Table 5.1, with the Gaussian peak fit most frequently implemented. The reasonable explanation for this is that the particle images themselves, if properly focused, describe Airy intensity functions which are approximated very well by a Gaussian intensity distribution (see Sect. 2.5.1). The correlation between two Gaussian functions can be shown also to result in a Gaussian function.

The three-point estimators typically work best for rather narrow correlation peaks formed from particle images in the 2–3 pixel diameter range. Simulations such as those shown in Fig. 6.12 indicate that for larger particle images the achievable measurement uncertainty increases which can be explained by the fact that, while the noise level on each correlation value stays nearly the same, the differences between the three adjoining correlation values become too small to provide a reliable shift estimate. In other words, the noise level becomes increasingly significant while the differences between the neighboring correlation values decrease. In this case, a centroiding approach may be more adequate since it makes use of more values around the peak than a three-point estimator. If in turn, when the particle images become too small ($d_\tau < 1.5$ pixel), the three-point estimators will also perform poorly, mainly because the values adjoining the peak are hidden in noise, see Chap. 6.

In the remainder we describe the use and implementation of the three-point estimators, which were used for almost all the data sets presented as examples in this book. The following procedure can be used to detect a correlation peak and obtain a subpixel accurate displacement estimate of its location:

- Step 1:** Scan the correlation plane $R = R_{II}$ for the maximum correlation value $R_{(i,j)}$ and store its integer coordinates (i, j) .
- Step 2:** Extract the adjoining four correlation values: $R_{(i-1,j)}$, $R_{(i+1,j)}$, $R_{(i,j-1)}$ and $R_{(i,j+1)}$.
- Step 3:** Use three points in each direction to apply the three point estimator, generally a Gaussian curve. The formulas for each function are given in Table 5.1.

Two alternative peak location estimators also deserve to be mentioned in this context as they provide even higher accuracy than the previously mentioned methods. First, the fit to a two-dimensional Gaussian, as introduced by RONNEBERGER et al. [70], is capable of using more than the immediate values neighboring the correlation maximum and also recovers the aspect ratio and skew of the correlation peak. Therefore, it is well suited in the position estimation of non-symmetric (e.g. elliptic) correlation peaks.

Table 5.1 Three-point estimators for determining the displacement from the correlation data at the subpixel level

Fitting function	Estimators
Peak centroid $f(x) = \frac{\text{first order moment}}{\text{zero order moment}}$	$x_0 = \frac{(i-1)R_{(i-1,j)} + iR_{(i,j)} + (i+1)R_{(i+1,j)}}{R_{(i-1,j)} + R_{(i,j)} + R_{(i+1,j)}}$ $y_0 = \frac{(j-1)R_{(i,j-1)} + jR_{(i,j)} + (j+1)R_{(i,j+1)}}{R_{(i,j-1)} + R_{(i,j)} + R_{(i,j+1)}}$
Parabolic peak fit $f(x) = Ax^2 + Bx + C$	$x_0 = i + \frac{R_{(i-1,j)} - R_{(i+1,j)}}{2R_{(i-1,j)} - 4R_{(i,j)} + 2R_{(i+1,j)}}$ $y_0 = j + \frac{R_{(i,j-1)} - R_{(i,j+1)}}{2R_{(i,j-1)} - 4R_{(i,j)} + 2R_{(i,j+1)}}$
Gaussian peak fit $f(x) = C \exp\left[\frac{-(x_0-x)^2}{k}\right]$	$x_0 = i + \frac{\ln R_{(i-1,j)} - \ln R_{(i+1,j)}}{2 \ln R_{(i-1,j)} - 4 \ln R_{(i,j)} + 2 \ln R_{(i+1,j)}}$ $y_0 = j + \frac{\ln R_{(i,j-1)} - \ln R_{(i,j+1)}}{2 \ln R_{(i,j-1)} - 4 \ln R_{(i,j)} + 2 \ln R_{(i,j+1)}}$

$$f(x, y) = I_0 \exp \left[\frac{-(x-x_0)^2}{(1/8)d_{\tau_x}^2} - \frac{(y-y_0)^2}{(1/8)d_{\tau_y}^2} - \frac{k_{xy}(x-x_0)(y-y_0)}{d_{\tau_x}d_{\tau_y}} \right] \quad (5.12)$$

The expression given in Eq. (5.12) contains a total of six coefficients that need to be solved for: d_{τ_x} and d_{τ_y} define the correlation peak widths along x and y respectively, while k_{xy} describes the peak's ellipticity. The correlation peak maximum is located at position coordinates x_0 and y_0 and has maximum peak height of I_0 . The solution of Eq. (5.12) can usually only be achieved by nonlinear regression methods, utilizing for instance a Levenberg-Marquardt least-squares minimization algorithm [66]. If only 3×3 points are used the coefficients in Eq. (5.12) can also be solved for explicitly in a least squares sense [57].

The second estimator is based on signal reconstruction theory and is often referred to as Whittaker or cardinal reconstruction [49, 69]. The underlying function is a superposition of shifted sinc functions whose zeroes coincide with the sample points. Values between the sample points (i.e. correlation values) are formed from the sum of the sinc functions. Since the reconstructed function is continuous, the position of the peak value between the sample points has to be determined iteratively using for instance Brent's method [66]. In principle all correlation values of the correlation plane could be used for the estimation, but in practice it suffices to perform one-dimensional fits on the row and column intersecting the maximum correlation value.

5.3.5.1 Multiple Peak Detection

To detect a given number of peaks, n , within the same correlation plane, a different search algorithm is necessary which sorts out only the highest peaks. In this case it is necessary to extract local maxima based on neighborhood analysis. This procedure is especially useful for correlation data obtained from single frame/multiple exposed PIV recordings. Also, multiple peak information is useful in cases where the strongest peak is associated with an outlier vector. An easily implemented recipe based on looking at the adjoining five or nine (3×3) correlation values is given here:

- Step 1:** Allocate a list to store the pixel coordinates and values of the n highest correlation peaks.
- Step 2:** Scan through the correlation plane and look for values which define a local maximum based on the local neighborhood, that is, the adjoining 4 or 8 correlation values.
- Step 3:** If a detected maximum can be placed into the list, reshuffle the list accordingly, such that the detected peaks are sorted in the order of intensity. Continue with **Step 2** until the scan through the correlation plane has been completed.
- Step 4:** Apply the desired three-point peak estimators of Table 5.1 for each of the detected n highest correlation peaks, thereby providing n displacement estimates.

5.3.5.2 Displacement Peak Estimation in FFT-Based Correlation Data

As already described in Sect. 5.3.1.1 the assumption of periodicity of both the data samples and resulting correlation plane brings in a variety of artifacts that need to be dealt with properly.

The most important of these is that the correlation plane, due to the method of calculation, does not contain unbiased correlation values, and results in the displacement to be biased to lower magnitudes (i.e. bias error, p. 156). This displacement bias can be determined easily by convolving the sampling weighting functions, generally unity for the size of the interrogation windows, with each other. For example, the circular cross-correlation between two equal sized uniformly weighted interrogation windows results in a triangular weighting distribution in the correlation plane. This is illustrated in Fig. 5.33 for the one-dimensional case.

The central correlation value will always have unity weight. For a shift value of $N/2$ only half the interrogation windows' data actually contribute to the correlation value such that it carries only a weight of $1/2$. When a three-point estimator is applied to the data, the correlation value closer to the origin is weighted more than the value further out and hence the magnitude of the estimated displacement will be too small. The solution to this problem is very straightforward: before applying the three-point estimator, the correlation values R_{II} have to be adjusted by dividing out the corresponding weighting factors. The weight factors can be obtained by

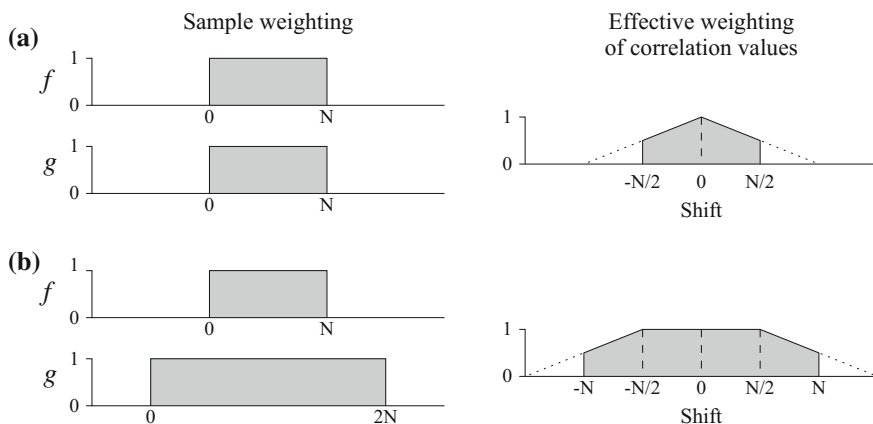


Fig. 5.33 Effective correlation value weighting in FFT-based ‘circular’ cross-correlation calculation: **a** for interrogation windows of equal size, and **b** for interrogation windows of unequal size (using zero-padding on signal f)

convolving the image sampling function with itself – generally a unity weight, rectangular function – as illustrated in Fig. 5.33a. In the case where the two interrogation windows are of unequal size a convolution between these two sampling functions will yield a weighting function with unity weighting near the center (Fig. 5.33b). The extension of the method to nonuniform interrogation windows is of course also possible.

On a related note it should be mentioned that many FFT implementations result in the output data to be shuffled. Often the DC-component is found at index (0) with increasing frequencies up to index $(N/2 - 1)$. The next index, $(N/2)$, is actually both the highest positive frequency and highest negative frequency. The following indices represent the negative frequencies in descending order such that index $(N - 1)$ is the lowest negative frequency component. By periodicity, the DC component reappears at index (N) . In order to achieve a frequency spectrum with the DC component in the middle, the entire data set has to be rotated by $(N/2)$ indices. As illustrated in Fig. 5.34 two-dimensional FFT-data has to be unfolded in a corresponding manner.

For correlation planes calculated by means of a two-dimensional FFT, the zero-shift value (i.e. origin) would initially appear in the lower left corner which would make a similar unfolding of the resulting (periodic) correlation data necessary. Without unfolding, negative displacement peaks will actually appear on the opposite side. However, a careful implementation of the peak finding algorithm allows proper peak detection and shift estimation without having to unscramble to the correlation plane first.

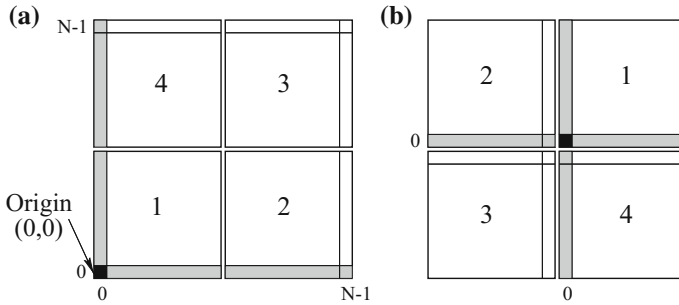


Fig. 5.34 Spatially folded output from a two-dimensional FFT routine (a) requires unfolding to place the origin back at the center of the correlation plane (b)

5.3.6 Interrogation Techniques for PIV Time-Series

The availability of high-speed PIV hardware (see Sect. 3.1.5) makes it possible to record several subsequent images with short time separation such that one can analyze the motion of the tracers over more than just two recordings. The interrogation of time-series takes advantage of two fundamental aspects: first, the time between exposures can locally varied, such to avoid the case of too small or too large displacement [31]; secondly, the availability of more time samples enables a time-accurate analysis that takes into account the time-varying behavior of the particles velocity [50]. Some techniques that have exploited these advantages are briefly described below.

Multi-frame cross-correlation: The time separation between images for cross correlation can be varied at choice for instance obtaining an almost constant displacement even for flows with large velocity variations, as outlined in Fig. 5.35. By this technique, the time separation between frames can be chosen freely, such that the particle image displacement remains within a favorable range (typically between 5 and 10 pixel) [31]. As a result, also regions at low velocity are represented with large enough displacement and the overall dynamic range of the technique is increased. The separation between frames needs to obey also additional constraints, most notably out-of-plane motion and in-plane velocity gradient [31].

Sliding Average cross-correlation: When multiple frames are used for cross-correlation the random error can be reduced if the correlation maps are combined (see Fig. 5.36). If constant time separation is applied, the method refers to sliding average correlation. Averaging several correlation maps has a beneficial effect similar to the correlation based correction method [32] or the ensemble correlation [75] with a significant increase of signal-to-noise ratio and a reduction of the random error component. A simple criterion to select the maximum number of frames is that the fluid motion during the overall time does not exceed the length of the interrogation window, otherwise spatio-temporal averaging effects will become significant.

Pyramid correlation algorithm: The beneficial aspects of multi-frame analysis and correlation averaging are combined in the pyramid correlation algorithm [84].

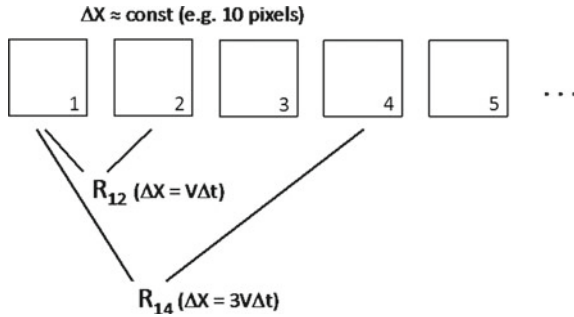


Fig. 5.35 Single-pair cross-correlation with multi-frame analysis. The particle image displacement is maintained constant varying the time separation Δt between frames. Velocity dynamic range is increased

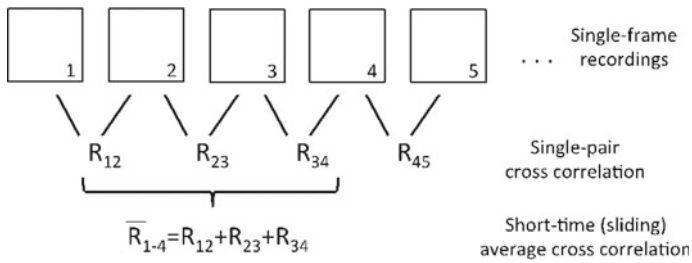


Fig. 5.36 Sliding average cross-correlation. The correlation map from successive pairs at fixed time separation Δt is averaged. Signal-to-noise ratio is increased

In this case, cross-correlation is evaluated between all possible pairs within a chosen group of subsequent frames. First, the correlation maps obtained at fixed time separation are averaged. Subsequently, the combination of correlation maps obtained at different heights of the pyramid (i.e. with different time separation) requires a rescaling (homothetic transformation) before being averaged again. As a result, the method offers an increased signal-to-noise ratio along with a higher dynamic range.

The above methods can be implemented making use of the image deformation technique after a first evaluation step is made to estimate the in-plane displacement and deformation field.

The **fluid trajectory correlation** (FTC) technique [50] is based on multi-frame analysis. The technique takes a short sequence of recordings. Cross-correlation is applied from a given frame (typically in the middle of the series) to the other frames. With an iterative procedure (predictor-corrector) the path of the fluid element corresponding to the tracers inside the window, is built with cross-correlation. This algorithm offers the advantage of a high velocity dynamic range, based on the longer time of the sequence. Since FTC is based on a Lagrangian cross-correlation approach, it allows a longer time kernel compared to the above techniques, based on a Eulerian

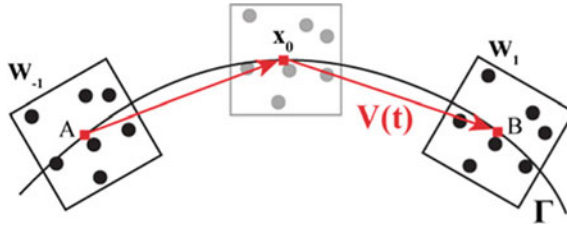


Fig. 5.37 Fluid trajectory correlation. The velocity along a finite interval of fluid path is estimated by cross correlation among the (time) center window and the preceding and successive recordings. The high-dynamic range results from the long kernel used and the lower truncation errors due to high-order trajectory modeling

(local) analysis scheme. As a result, the measurement precision error scales as $N^{-3/2}$ where N is the number of considered frames (Fig. 5.37).

A further improvement on this approach is given by the **fluid trajectory ensemble evaluation (FTEE)** [37] which realizes the objectives of FTC with a more robust ensemble cross-correlation based on the pyramid scheme.

5.4 Particle Tracking Velocimetry

The spatial resolution in PIV evaluation can be even further increased by eventually tracking the individual particle images, a procedure referred to as *super-resolution PIV* by KEANE et al. [44] who applied the technique to double-exposure images. A similar procedure was also implemented for image pairs by COWEN & MONI-SMITH [18] for the study of a flat plate turbulent boundary layer.

The working principle of PTV can be briefly by the following operations:

1. Detection of particle images from each recording. This is usually done by eliminating background intensity and analyzing the images in search of a local maximum.
2. Forming a vector of particle positions at each of the two time instants with sub-pixel accuracy. The same procedure as discussed above for the correlation peak fit is usually followed.
3. Pairing particle images corresponding to the same physical tracer. Here the most common criterion for a simple analysis is that the image pair with closest distance corresponds to the correct pair.

Although the above approach works on a pair of images it becomes generally much more reliable when working with image sequences, because the probability of spurious pairing over a sequence becomes much smaller than that for a single pair of images. PTV schemes applied to single image pairs can only rely on additional information and constraints such as the time regularity of particle image intensity.

Predictor-corrector schemes where a-priori knowledge of the velocity field is imposed to match particle images have been applied in numerous versions and they

can be used to make the technique more robust. The latter are often based on the availability of more robust PIV analysis for the large scale motions. While many implementations rely on detection and position estimation of particle images prior to matching, other schemes prefer to use cross-correlation of small samples (typ. 8×8 pixel) centered on the detected individual particle image. The existence of a matched pair is confirmed by applying the procedure in reverse by starting from the second particle image. The main advantage of the correlation-based approach is the increased robustness in presence of overlapping images, and thus more suited for high particle image density data.

The PTV analysis offers a number of advantages. First, the velocity information is obtained with higher spatial localization as a velocity vector pertains to a single particle image, which is significantly smaller than the interrogation window used for cross-correlation. The measurements are therefore not affected by bias errors due to spatial averaging [39]. Consequently, the technique is well suited to analyze flows with strong velocity gradient, such as for instance turbulent boundary layers. Second, PTV is less prone to bias errors in the case of inhomogeneous seeding distributions. This is important for near wall flow measurements for instance, as the seeding concentration drops towards the wall due to the Saffman effect (see Sect. 2.1.3).

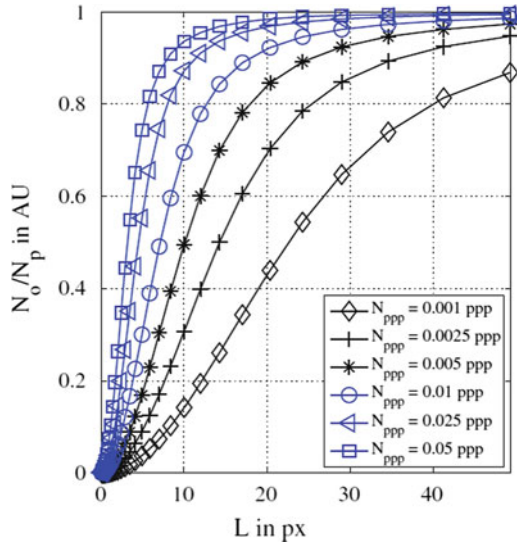
Finally, the spatial resolution of mean velocity distribution can be virtually achieve sub-pixel level. This is made possible by determining the particle location with sub-pixel precision. This holds true until the resolution becomes comparable to the particle image diameter. The final resolution of the measurement is ultimately determined by the diameter of the tracer particle and therefore flow structures smaller than the diameter cannot be resolved. However, the latter limit is only reached for high magnification imaging in microfluidics or by using a long-range microscope.

A final interesting feature of the PTV technique is that it can be applied for measurements at low seeding concentration, thereby reducing the contamination of the flow facilities due to excessive seeding. On the other hand, the analysis of particle images with PTV technique is notably less robust than that based on cross correlation due to the possibility of spurious pairing between particle images.

5.4.1 Particle Image Detection and Position Estimation

Generally, the particle tracking technique is well suited for accurate flow field measurements at any magnification, provided the seeding concentration is sufficiently low for a reliable particle image matching between subsequent frames. At high seeding concentrations two major sources of errors can occur. First, the likelihood of matching non-corresponding particle images increases. This problem can be solved by using sophisticated particle tracking approaches or by evaluating time resolved data. However, both strategies require sufficiently smooth flow variations in space or time, such that spatial homogeneity or temporal smoothness assumptions can be applied locally. Second, the random error increases, as the likelihood of overlap-

Fig. 5.38 Ratio of the number of overlapping particle images N_o versus the total number of particle images N_p for different particle image distances L and particle image concentrations N_{ppp} in particles per pixel (from CIERPKA et al. [16])



ping particle images arises with increasing particle image densities. This is caused by larger uncertainties in the particle image location determination, since the model used for the sub-pixel position estimation, normally a Gaussian intensity distribution, is not appropriate in case of overlapping particle image patterns [17]. Furthermore, the correct identification of two slightly overlapping particle images becomes increasingly difficult with increasing overlap between particle images. Finally, even if the positions of both overlapping particle images can be determined, the correct particle track identification becomes ambiguous, yielding larger uncertainties. MAAS [51] derived an expression connecting the number of individual particle images N_p with the number of overlapping particle images N_o for circular particle images that are randomly distributed on a sensor with size A .

$$N_o = (N_p - 1) + \frac{A}{A_{crit}} \cdot \left(\exp \frac{-(N_p - 1)A_{crit}}{A} - 1 \right) \tag{5.13}$$

A_{crit} is the critical area in which a particle image starts to overlap with the boundaries of another particle image. The boundaries of the particle images are defined to be at the radial location where the intensity has decreased to e^{-2} of the peak intensity value. Thus, the critical area is $A_{crit} = \pi D^2$, since particle images share the same boundary if the centers have a distance of D . If a critical particle image overlap of 50% corresponding to $L = D/2$ is assumed, the critical area reduces to $A_{crit} = \pi L^2$, with L being the distance of particle image centers that can be separated. Figure 5.38 illustrates the ratio of overlapping particle images as a function of L for different particle image densities N_{ppp} .

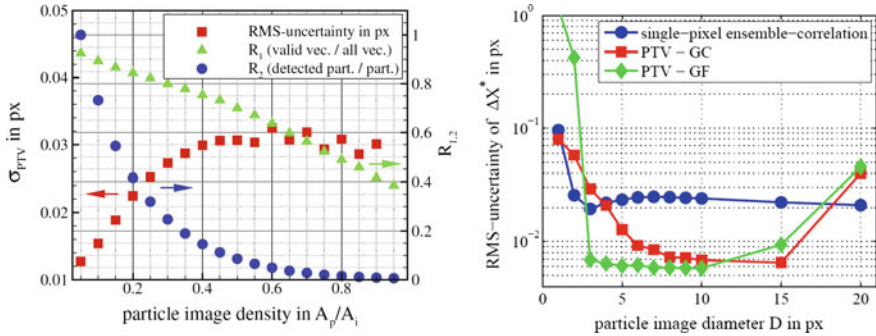


Fig. 5.39 Left, RMS-uncertainty and ratio of valid vectors to total vectors and detected particles to the number of generated particles for increasing particle image density ($D = 5$ pixel). Right: random error of the estimated displacement using PTV and single pixel ensemble-correlation (from KÄHLER et al. [40])

For particle image diameters of 2.5 pixel, this results in a fraction of about 20% overlapping particle images. At a diameter of 5 pixel, the overlap ratio would reach 80% for comparison. Compared to PIV processing, the particle image density can be reduced by a factor of 6–10 to get almost the same number of vectors. In this case, only 5% of the particle images overlap at a diameter of 2.5 pixel and 0.005 ppp. One can either accept these 5% as a loss of information by detecting and rejecting them or one can use special algorithms like the one of LEI et al. [48] that showed a reliable position determination for particle images that overlap up to 50% (see CIERPKA et al. [16] for details).

5.4.2 Particle Pairing and Displacement Estimation

The probability of correct particle pairing R_{12} (Fig. 5.39-left, right axis) decreases rapidly with the particle image density, whereas, the RMS uncertainty (left axis) achieves a stable value beyond an image density $A_p/A_i = 0.4$ [40]. The uncertainty of the displacement measurement for two different particle image detection methods is compared to single pixel ensemble correlation [40] showing that for high-quality imaging conditions, the uncertainty of the particle tracking is rather low and little dependent upon the particle image diameter as long as $D > 2$ pixel.

5.4.3 Spatial Resolution

One of the commonly adopted tests for spatial resolution is the step-response. Figure 5.40(left) shows that strong flow gradients can be nicely resolved using parti-

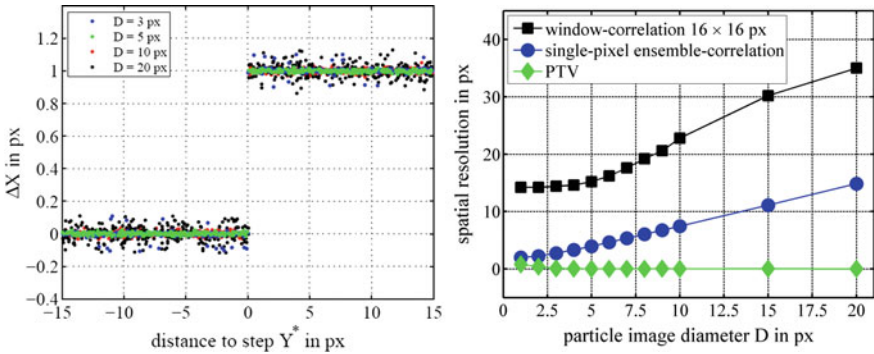


Fig. 5.40 Left, Response to a step-like displacement profile for different digital particle image sizes computed with PTV algorithms. Right, Step response width of the estimated displacement with respect to the digital particle image diameter (from KÄHLER et al. [40])

cle tracking even in case of large particle images, which are typical in microfluidics. Although the raising uncertainty with increasing particle image diameter is visible, bias errors due to spatial averaging do not exist, unlike for PIV methods. The right plot illustrates that correct measurements can be obtained over a large range of particle image diameters. In the case of single pixel ensemble-correlation the spatial resolution is limited by the size of the particle image and in case of spatial cross-correlation analysis by the size of the interrogation window.

It is evident that the precise determination of the particle image location is an important aspect of all PTV techniques. To achieve sub-pixel accuracy the discrete particle image distribution is typically approximated by a continuous Gaussian fit function, where the maximum denotes the particle image center precisely. This approach is well suited for macroscopic imaging. However, in microscopic domains with large magnifications different models might be more suitable [71]. A comparison of different center determination methods indicated that a Gaussian fit provides the best trade-off between accuracy and processing time. For a signal to noise ratio of $SNR = 10$, the center determination yielded an uncertainty of about 0.05 pixel [15]. Peak locking is largely avoided when the particle image diameter is larger than 2 pixel (see Sect. 6.3 for further details).

5.4.4 Performance of Particle Tracking

Once the positions of the particle images are determined, the challenge of identifying the correct partners in subsequent frames has to be solved. The most straightforward method to match corresponding particle images is a nearest neighbor PTV algorithm [52]. This algorithm is suited for very low particle image densities, since the particle displacements must be smaller than the inner distance between neighboring

particles. More elaborate approaches allow increasing the particle image densities and in turn the information density. These methods comprise artificial neural networks or relaxation methods that minimize a local or global cost function [65]. Alternatively, OKAMOTO et al. [61] presented a spring force model, where particle pairs were identified by searching for the smallest spring force calculated over particles in a certain neighborhood. Probabilistic approaches that take the motion of neighboring particles into account show a very high vector yield at larger particle image densities, however at the expense of spatial resolution as the motion of neighboring particles must be correlated. Another method to improve the detection of corresponding particle pairs is the use of a predictor for the displacement. A predictor can significantly decrease the search area in the second frame and thus improve the match probability of particles. In general, such predictors can be based on theoretically known velocity distributions or experimentally obtained PIV evaluations [13, 18, 45, 92]. BREVIS et al. [11] combined a PIV predictor with a relaxation PTV algorithm to further enhance the performance. However, in comparison with PIV, the gain in resolution is only minor and does not justify the effort in many cases. A fully PTV-based algorithm was presented by OHMI & LI [60], where a case sensitive search radius in the second frame is used to identify possibly matching particles. This is done for all particles detected reliably in the first frame. For each possible match, the algorithm updates the probabilities of similar neighbor vectors iteratively. The threshold for the common motion of the neighboring particles is another parameter that needs to be specified. To address this drawback, FUCHS et al. [24] introduced a robust and user-friendly tracking algorithm, where only the displacement limits need to be specified, while all other parameters do not require any adjustment.

For the identification of the correct displacement of a certain particle, the histograms of all possible displacements of the particle of interest and its neighbors lying within the specified displacement range are analyzed. The resulting displacement to the subsequent frame showing the lowest deviation from the maximum values of the histogram in each spatial direction is considered to be the most probable displacement for the particle of interest. The algorithm is computationally efficient, since it does not need to iteratively update probabilities.

Moreover, this non-iterative tracking method (NIT) is capable of yielding reliable tracking results for large particle image densities. Thus, the method is assessed by means of the analysis of the first image pair of the synthetic data set 301 ($ppp = 0.06$), provided by OKAMOTO et al. [62]. Figure 5.41 gives an overview of the displacement field of the using the NIT method and clearly only few outliers are yielded, even in regions where the displacements are significantly larger than the distance between the particles. A closer look on the tracking performance is given Table 5.2, comparing a nearest neighbor (NN) algorithm, the NIT algorithm, and the iterative tracking (IT) algorithm of OHMI & LI [60]. The nearest neighbor algorithm fails to provide reliable tracking results at this high particle image density, as it can only identify 868 out of 4042 actual tracks. Furthermore, the number of invalid and not detected tracks is large. Both, the IT and the NIT algorithm, show a good tracking performance with a large number of valid vectors (3846 and 3940, respectively) and only a low number of invalid and not detected tracks. Thus, the NIT algorithm comes close to

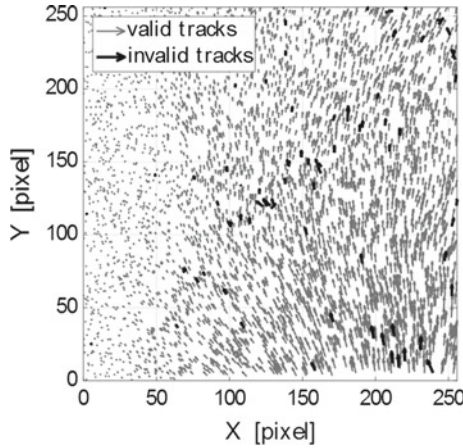
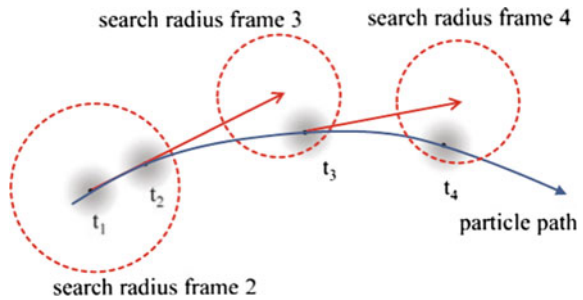


Fig. 5.41 Displacement field of the first image pair of the synthetic data set 301, provided by OKAMOTO et al. [62]. Using the non-iterative algorithm introduced by FUCHS et al. [24], the displacements can be determined reliably, even in regions where the displacements are significantly larger than distance between the particles (from FUCHS et al. [24])

Table 5.2 Tracking performance for the analysis of the first frame of the synthetic data set 301 (OKAMOTO et al. [62]). Comparison among nearest neighbor (NN), non-iterative (NIT) and iterative (IT) (OHMI & LI [60])

Tracks: 4042	NN	NIT	IT
Valid	868	3846	3940
Invalid	1840	91	50
Not detected	3174	196	102

Fig. 5.42 Schematic of the working principle of a four-frame method. The circles indicate the search area for the corresponding frames (from CIERPKA et al. [16])



the IT algorithm in terms of performance, while offering the advantage being less user dependent, which is an important feature for new and inexperienced users.

5.4.5 Multi-frame Particle Tracking

The accuracy and the robustness of double-frame methods are limited by the fact that only two recordings are available. Approaches to further enhance the precision in estimating the flow velocity are based on multi-pulse or multi-frame techniques, which rely upon the temporal smoothness of the particle trajectory and regularity of the image signal. Multi-pulse or multi-frame PTV techniques improve the probability for correct particle matching by tracking particles over more than two successive frames [16]. Furthermore, trajectory curvature can be accounted for considering curved particle path fitting the particle image positions (see Fig. 5.42). The same holds for tangential acceleration along the particle trajectory. The accurate determination of the local acceleration of the flow is important for unsteady flows and for pressure estimation from the velocity field (see Sect. 7.6.4).

In a multi-frame algorithm the displacement between the first two particle images can be reliably obtained making the time interval between frame one and two small enough (for instance 4–8 pixel). The estimated velocity vector is used as predictor to point to frame three and similarly towards frame four. The approach can be extended to more frames when the hardware allows recording longer sequences. The large observation time interval and thus large displacement yield a high dynamic velocity range.

References

1. Adrian, R.J.: Statistical properties of particle image velocimetry measurements in turbulent flow. In: 4th International Symposia on Laser Techniques to Fluid Mechanics, (Lisbon, Portugal, 11–14 July) (1988)
2. Agüí, J.C., Jiménez, J.: On the performance of particle tracking. *J. Fluid Mech.* **185**, 447–468 (1987). DOI 10.1017/S0022112087003252. URL http://journals.cambridge.org/article_S0022112087003252
3. Arnold, W., Hinsch, K.D., Mach, D.: Turbulence level measurement by speckle velocimetry. *Appl. Opt.* **25**(3), 330–331 (1986). DOI 10.1364/AO.25.000330. URL <http://ao.osa.org/abstract.cfm?URI=ao-25-3-330>
4. Astarita, T.: Analysis of velocity interpolation schemes for image deformation methods in PIV. *Exp. Fluids* **45**(2), 257–266 (2008). DOI 10.1007/s00348-008-0475-7. URL <http://dx.doi.org/10.1007/s00348-008-0475-7>
5. Astarita, T., Cardone, G.: Analysis of interpolation schemes for image deformation methods in PIV. *Exp. Fluids* **38**(2), 233–243 (2005). DOI 10.1007/s00348-004-0902-3. URL <http://dx.doi.org/10.1007/s00348-004-0902-3>
6. Barron, J.L., Fleet, D.J., Beauchemin, S.S.: Performance of optical flow techniques. *Int. J. Comput. Vis.* **12**(1), 43–77 (1994). DOI 10.1007/BF01420984. URL <http://dx.doi.org/10.1007/BF01420984>
7. Bastiaans, R.J.M., van der Plas, G.A.J., Kieft, R.N.: The performance of a new PTV algorithm applied in super-resolution PIV. *Exp. Fluids* **32**(3), 346–356 (2002). DOI 10.1007/s003480100363. URL <http://dx.doi.org/10.1007/s003480100363>
8. Bendat, J.S., Piersol, A.G.: *Random Data: Analysis and Measurement Procedures*, 4th edn. Wiley, New York (2012). DOI 10.1002/9781118032428. URL <http://dx.doi.org/10.1002/9781118032428>

9. Billy, F., David, L., Pineau, G.: Single pixel resolution correlation applied to unsteady flow measurements. *Meas. Sci. Technol.* **15**(6), 1039 (2004). DOI 10.1088/0957-0233/15/6/002. URL <http://stacks.iop.org/0957-0233/15/i=6/a=002>
10. Bracewell, R.N.: *The Fourier Transform and Its Applications*, 3rd edn. Electrical Engineering Series. McGraw Hill, New York (1999)
11. Brevis, W., Niño, Y., Jirka, G.H.: Integrating cross-correlation and relaxation algorithms for particle tracking velocimetry. *Exp. Fluids* **50**(1), 135–147 (2011). DOI 10.1007/s00348-010-0907-z. URL <http://dx.doi.org/10.1007/s00348-010-0907-z>
12. Brigham, E.O.: *The Fast Fourier Transform*. Prentice-Hall Signal Processing Series. Prentice-Hall, Englewood Cliffs (1974)
13. Cardwell, N.D., Vlachos, P.P., Thole, K.A.: A multi-parametric particle-pairing algorithm for particle tracking in single and multiphase flows. *Meas. Sci. Technol.* **22**(10), 105,406 (2011). DOI 10.1088/0957-0233/22/10/105406. URL <http://stacks.iop.org/0957-0233/22/i=10/a=105406>
14. Cenedese, A., Querzoli, G.: PIV for lagrangian scale evaluation in a convective boundary layer. In: Tanida, Y., Miyashiro, H. (eds.) *Flow Visualization VI*, pp. 863–867. Springer, Berlin (1992). DOI 10.1007/978-3-642-84824-7_155. URL http://dx.doi.org/10.1007/978-3-642-84824-7_155
15. Cierpka, C., Kähler, C.J.: Cross-correlation or tracking - comparison and discussion. In: 16th International Symposium on Applications of Laser Techniques to Fluid Mechanics Lisbon, Portugal, 09–12 July (2012). http://lctces.dem.ist.utl.pt/lxaser/lxaser2012/upload/299_paper_wupzup.pdf
16. Cierpka, C., Lütke, B., Kähler, C.J.: Higher order multi-frame particle tracking velocimetry. *Exp. Fluids* **54**(5), 1533 (2013). DOI 10.1007/s00348-013-1533-3. URL <http://dx.doi.org/10.1007/s00348-013-1533-3>
17. Cierpka, C., Scharnowski, S., Kähler, C.J.: Parallax correction for precise near-wall flow investigations using particle imaging. *Appl. Opt.* **52**(12), 2923–2931 (2013). DOI 10.1364/AO.52.002923. URL <http://dx.doi.org/10.1364/AO.52.002923>
18. Cowen, E.A., Monismith, S.G.: A hybrid digital particle tracking velocimetry technique. *Exp. Fluids* **22**(3), 199–211 (1997). DOI 10.1007/s003480050038. URL <http://dx.doi.org/10.1007/s003480050038>
19. Dracos, T.: Particle tracking in three-dimensional space. In: Dracos, T. (ed.) *Three-Dimensional Velocity and Vorticity Measuring and Image Analysis Techniques*. ERCOFTAC Series, vol. 4, pp. 209–227. Springer, Netherlands (1996). DOI 10.1007/978-94-015-8727-3_10. URL http://dx.doi.org/10.1007/978-94-015-8727-3_10
20. Dracos, T.: Particle tracking velocimetry (PTV). In: Dracos, T. (ed.) *Three-Dimensional Velocity and Vorticity Measuring and Image Analysis Techniques*. ERCOFTAC Series, vol. 4, pp. 155–160. Springer, Netherlands (1996). DOI 10.1007/978-94-015-8727-3_7. URL http://dx.doi.org/10.1007/978-94-015-8727-3_7
21. Fincham, A., Delerce, G.: Advanced optimization of correlation imaging velocimetry algorithms. *Exp. Fluids* **29**(1), S013–S022 (2000). DOI 10.1007/s003480070003. URL <http://dx.doi.org/10.1007/s003480070003>
22. Frigo, M., Johnson, S.G.: FFTW: an adaptive software architecture for the FFT. In: *Proceedings 1998 IEEE International Conference Acoustics Speech and Signal Processing*, vol. 3, pp. 1381–1384. IEEE (1998). DOI 10.1109/ICASSP.1998.681704. URL <http://dx.doi.org/10.1109/ICASSP.1998.681704>
23. Frigo, M., Johnson, S.G.: The design and implementation of FFTW3. *Proc. IEEE* **93**(2), 216–231 (2005). DOI 10.1109/JPROC.2004.840301. URL <http://dx.doi.org/10.1109/JPROC.2004.840301> (Special issue on “Program Generation, Optimization, and Platform Adaptation”)
24. Fuchs, T., Hain, R., Kähler, C.J.: Non-iterative double-frame 2D/3D particle tracking velocimetry. *Exp. Fluids* **58**(199). (2017). DOI 10.1007/s00348-017-2404-0. URL <http://dx.doi.org/10.1007/s00348-017-2404-0>

25. Gharib, M., Willert, C.E.: Particle tracing: revisited. In: Gad-el Hak, M. (ed.) *Advances in Fluid Mechanics Measurements*. Lecture Notes in Engineering, vol. 45, pp. 109–126. Springer, Berlin (1989). DOI 10.1007/978-3-642-83787-6_3. URL http://dx.doi.org/10.1007/978-3-642-83787-6_3
26. Goodman, J.W.: *Introduction to Fourier Optics*, 4th edn. Macmillan Learning (2017). <http://www.macmillanlearning.com/Catalog/product/introductiontofourieroptics-fourthedition-goodman>
27. Grant, I., Liu, A.: Method for the efficient incoherent analysis of particle image velocimetry images. *Appl. Opt.* **28**(10), 1745–1748 (1989). DOI 10.1364/AO.28.001745. URL <http://ao.osa.org/abstract.cfm?URI=ao-28-10-1745>
28. Guezennec, Y.G., Brodkey, R.S., Trigui, N., Kent, J.C.: Algorithms for fully automated three-dimensional particle tracking velocimetry. *Exp. Fluids* **17**(4), 209–219 (1994). DOI 10.1007/BF00203039. URL <http://dx.doi.org/10.1007/BF00203039>
29. Gui, L.C., Merzkirch, W.: A method of tracking ensembles of particle images. *Exp. Fluids* **21**(6), 465–468 (1996). DOI 10.1007/BF00189049. URL <http://dx.doi.org/10.1007/BF00189049>
30. Gui, L., Merzkirch, W.: Generating arbitrarily sized interrogation windows for correlation-based analysis of particle image velocimetry recordings. *Exp. Fluids* **24**(1), 66–69 (1998)
31. Hain, R., Kähler, C.J.: Fundamentals of multiframe particle image velocimetry (PIV). *Exp. Fluids* **42**(4), 575–587 (2007). DOI 10.1007/s00348-007-0266-6. URL <http://dx.doi.org/10.1007/s00348-007-0266-6>
32. Hart, D.P.: PIV error correction. *Exp. Fluids* **29**(1), 13–22 (2000). DOI 10.1007/s003480050421. URL <http://dx.doi.org/10.1007/s003480050421>
33. Hart, D.P.: Super-resolution PIV by recursive local-correlation. *J. Vis.* **3**(2), 187–194 (2000). DOI 10.1007/BF03182411. URL <http://dx.doi.org/10.1007/BF03182411>
34. Horn, B.K.P., Schunck, B.G.: Determining optical flow. *Artif. Intell.* **17**, 185–203 (1981). DOI 10.1016/0004-3702(81)90024-2. URL [http://dx.doi.org/10.1016/0004-3702\(81\)90024-2](http://dx.doi.org/10.1016/0004-3702(81)90024-2)
35. Huang, H.T., Fiedler, H.E., Wang, J.J.: Limitation and improvement of PIV, part II. Particle image distortion, a novel technique. *Exp. Fluids* **15**(4–5), 263–273 (1993). DOI 10.1007/BF00223404. URL <http://dx.doi.org/10.1007/BF00223404>
36. Jähne, B.: *Digital Image Processing and Image Formation*, 7th edn. Springer, Berlin (2018). <http://www.springer.com/us/book/9783642049491>
37. Jeon, Y.J., Chatellier, L., David, L.: Fluid trajectory evaluation based on an ensemble-averaged cross-correlation in time-resolved PIV. *Exp. Fluids* **55**(7), 1766 (2014). DOI 10.1007/s00348-014-1766-9. URL <http://dx.doi.org/10.1007/s00348-014-1766-9>
38. Kähler, C.J., Scholz, U.: Transonic jet analysis using long-distance micro-PIV. In: 12th International Symposium on Flow Visualization - ISFV 12, Göttingen, Germany (2006)
39. Kähler, C.J., Scholz, U., Ortmanns, J.: Wall-shear-stress and near-wall turbulence measurements up to single pixel resolution by means of long-distance micro-PIV. *Exp. Fluids* **41**(2), 327–341 (2006). DOI 10.1007/s00348-006-0167-0. URL <http://dx.doi.org/10.1007/s00348-006-0167-0>
40. Kähler, C.J., Scharnowski, S., Cierpka, C.: On the uncertainty of digital PIV and PTV near walls. *Exp. Fluids* **52**(6), 1641–1656 (2012). DOI 10.1007/s00348-012-1307-3. URL <http://dx.doi.org/10.1007/s00348-012-1307-3>
41. Kähler, C.J., Scharnowski, S., Cierpka, C.: On the resolution limit of digital particle image velocimetry. *Exp. Fluids* **52**(6), 1629–1639 (2012). DOI 10.1007/s00348-012-1280-x. URL <http://dx.doi.org/10.1007/s00348-012-1280-x>
42. Kähler, C.J., Astarita, T., Vlachos, P.P., Sakakibara, J., Hain, R., Discetti, S., La Foy, R., Cierpka, C.: Main results of the 4th International PIV Challenge. *Exp. Fluids* **57**(6), 97 (2016). DOI 10.1007/s00348-016-2173-1. URL <http://dx.doi.org/10.1007/s00348-016-2173-1>
43. Keane, R.D., Adrian, R.J.: Optimization of particle image velocimeters. I. double pulsed systems. *Meas. Sci. Technol.* **1**(11), 1202 (1990). DOI 10.1088/0957-0233/1/11/013. URL <http://stacks.iop.org/0957-0233/1/i=11/a=013>

44. Keane, R.D., Adrian, R.J.: Theory of cross-correlation analysis of PIV images. *Appl. Sci. Res.* **49**(3), 191–215 (1992). DOI 10.1007/BF00384623. URL <https://dx.doi.org/10.1007/BF00384623>
45. Keane, R.D., Adrian, R.J., Zhang, Y.: Super-resolution particle imaging velocimetry. *Meas. Sci. Technol.* **6**(6), 754 (1995). DOI 10.1088/0957-0233/6/6/013. URL <http://stacks.iop.org/0957-0233/6/i=6/a=013>
46. Kitzhofer, J., Westfeld, P., Pust, O., Nonn, T., Maas, H.G., Brücker, C.: Estimation of 3D deformation and rotation rate tensor from volumetric particle data via 3D least squares matching. In: 15th International Symposium on Applications of Laser Techniques to Fluid Mechanics Lisbon, Portugal, 05–08 July 2010 (2010). http://lctes.dem.ist.utl.pt/lxaser/lxaser2010/upload/1677_lfplgn_3.1.4.Full_1677.pdf
47. Lauterborn, W., Kurz, T.: *Coherent Optics - Fundamentals and Applications*, 2nd edn. Springer, Berlin (2003). DOI 10.1007/978-3-662-05273-0. URL <https://dx.doi.org/10.1007/978-3-662-05273-0>
48. Lei, Y.C., Tien, W.H., Duncan, J., Paul, M., Ponchaut, N., Mouton, C., Dabiri, D.: Rösigen, T., Hove, J.: A vision-based hybrid particle tracking velocimetry (PTV) technique using a modified cascade correlation peak-finding method. *Exp. Fluids* **53**(5), 1251–1268 (2012). DOI 10.1007/s00348-012-1357-6. URL <http://dx.doi.org/10.1007/s00348-012-1357-6>
49. Lourenco, L., Krothapalli, A.: On the accuracy of velocity and vorticity measurements with PIV. *Exp. Fluids* **18**(6), 421–428 (1995). DOI 10.1007/BF00208464. URL <http://dx.doi.org/10.1007/BF00208464>
50. Lynch, K., Scarano, F.: A high-order time-accurate interrogation method for time-resolved PIV. *Meas. Sci. Technol.* **24**(3), 16 (2013). DOI 10.1088/0957-0233/24/3/035305. URL <http://stacks.iop.org/0957-0233/24/i=3/a=035305>
51. Maas, H.G.: *Digitale Photogrammetrie in der dreidimensionalen Strömungsmesstechnik*. Ph.D. thesis, ETH Zürich (1992)
52. Malik, N.A., Dracos, T., Papantoniou, D.A.: Particle tracking velocimetry in three-dimensional flows. *Exp. Fluids* **15**(4), 279–294 (1993). DOI 10.1007/BF00223406. URL <http://dx.doi.org/10.1007/BF00223406>
53. Meinhart, C.D., Wereley, S.T.: Optimum particle size and correlation strategy for sub-micron spatial resolution. In: Joint International PIVNET II/ERCOFTAC Workshop on Micro PIV and Applications in Microsystems, 7–8 April, Delft (the Netherlands) (2005). <http://ahd.tudelft.nl/~mpiv/prog.html>
54. Meinhart, C.D., Wereley, S.T., Santiago, J.G.: A PIV algorithm for estimating time-averaged velocity fields. *J. Fluids Eng.* **122**(2), 285–289 (2000). DOI 10.1115/1.483256. URL <http://dx.doi.org/10.1115/1.483256>
55. Mejia-Alvarez, R., Christensen, K.T.: Robust suppression of background reflections in PIV images. *Meas. Sci. Technol.* **24**(2), 027,003 (2013). DOI 10.1088/0957-0233/24/2/027003. URL <http://stacks.iop.org/0957-0233/24/i=2/a=027003>
56. Mendez, M.A., Raiola, M., Masullo, A., Discetti, S., Ianiro, A., Theunissen, R., Buchlin, J.M.: POD-based background removal for particle image velocimetry. *Exp. Thermal Fluid Sci.* **80**, 181–192 (2017). DOI 10.1016/j.expthermflusci.2016.08.021. URL <http://www.sciencedirect.com/science/article/pii/S08941771716302266>
57. Nobach, H., Honkanen, M.: Two-dimensional gaussian regression for sub-pixel displacement estimation in particle image velocimetry or particle position estimation in particle tracking velocimetry. *Exp. Fluids* **38**(4), 511–515 (2005). DOI 10.1007/s00348-005-0942-3. <http://dx.doi.org/10.1007/s00348-005-0942-3>
58. Nogueira, J., Lecuona, A., Rodríguez, P.A.: Identification of a new source of peak locking, analysis and its removal in conventional and super-resolution piv techniques. *Exp. Fluids* **30**(3), 309–316 (2001). DOI 10.1007/s003480000179. URL <http://dx.doi.org/10.1007/s003480000179>
59. Novara, M., Ianiro, A., Scarano, F.: Adaptive interrogation for 3D-PIV. *Meas. Sci. Technol.* **24**, 024012 (2013). DOI 10.1088/0957-0233/24/2/024012. URL <http://dx.doi.org/10.1088/0957-0233/24/2/024012>

60. Ohmi, K., Li, H.Y.: Particle-tracking velocimetry with new algorithms. *Meas. Sci. Technol.* **11**(6), 603 (2000). DOI 10.1088/0957-0233/11/6/303. URL <http://stacks.iop.org/0957-0233/11/i=6/a=303>
61. Okamoto, K., Hassan, Y.A., Schmidl, W.D.: New tracking algorithm for particle image velocimetry. *Exp. Fluids* **19**(5), 342–347 (1995). DOI 10.1007/BF00203419. URL <http://dx.doi.org/10.1007/BF00203419>
62. Okamoto, K., Nishio, S., Saga, T., Kobayashi, T.: Standard images for particle-image velocimetry. *Meas. Sci. Technol.* **11**(6), 685 (2000). DOI 10.1088/0957-0233/11/6/311. URL <http://stacks.iop.org/0957-0233/11/i=6/a=311>
63. Papoulis, A.: *Signal Analysis*. McGraw-Hill Inc., New York (1981)
64. Papoulis, A., Pillai, S.U.: *Probability, Random Variables, and Stochastic Processes*, 4th edn. McGraw-Hill Education Ltd., New York (2002). <http://www.mhhe.com/engcs/electrical/papoulis/>
65. Pereira, F., Stüer, H., Graff, E.C., Gharib, M.: Two-frame 3D particle tracking. *Meas. Sci. Technol.* **17**(7), 1680 (2006). DOI 10.1088/0957-0233/17/7/006. URL <http://stacks.iop.org/0957-0233/17/i=7/a=006>
66. Press, W.H., Teukolsky, S.A., Vetterling, W.T., Flannery, B.P.: *Numerical Recipes: The Art of Scientific Computing*, 3rd edn. Cambridge University Press, New York (2007). <http://numerical.recipes/>
67. Quénot, G.M., Pakleza, J., Kowalewski, T.A.: Particle image velocimetry with optical flow. *Exp. Fluids* **25**(3), 177–189 (1998). DOI 10.1007/s003480050222. URL <http://dx.doi.org/10.1007/s003480050222>
68. Reynolds, G.O., DeVelis, J.B., Parrent, G.B., Thompson, B.J.: *The New Physical Optics Notebook: Tutorials In Fourier Optics*. Optical Engineering Press, Bellingham (1989). DOI 10.1117/3.2303. URL <http://dx.doi.org/10.1117/3.2303>
69. Roesgen, T.: Optimal subpixel interpolation in particle image velocimetry. *Exp. Fluids* **35**(3), 252–256 (2003). DOI 10.1007/s00348-003-0627-8. URL <http://dx.doi.org/10.1007/s00348-003-0627-8>
70. Ronneberger, O., Raffel, M., Kompenhans, J.: Advanced evaluation algorithms for standard and dual plane particle image velocimetry. In: *9th International Symposium on Applications of Lasers to Fluid Mechanics*, Lisbon (Portugal) (1998)
71. Rossi, M., Segura, R., Cierpka, C., Kähler, C.J.: On the effect of particle image intensity and image preprocessing on the depth of correlation in micro-PIV. *Exp. Fluids* **52**(4), 1063–1075 (2012). DOI 10.1007/s00348-011-1194-z. URL <http://dx.doi.org/10.1007/s00348-011-1194-z>
72. Ruhnau, P., Schnörr, C.: Optical Stokes flow estimation: an imaging-based control approach. *Exp. Fluids* **42**(1), 61–78 (2007). DOI 10.1007/s00348-006-0220-z. URL <http://dx.doi.org/10.1007/s00348-006-0220-z>
73. Ruhnau, P., Kohlberger, T., Schnörr, C., Nobach, H.: Variational optical flow estimation for particle image velocimetry. *Exp. Fluids* **38**(1), 21–32 (2005). DOI 10.1007/s00348-004-0880-5. URL <http://dx.doi.org/10.1007/s00348-004-0880-5>
74. Sage, D.: *Local normalization - filter to reduce the effect on a non-uniform illumination*. Technical Report, Biomedical Image Group, EPFL, Switzerland (2011). <http://bigwww.epfl.ch/sage/soft/localnormalization/>
75. Santiago, J.G., Wereley, S.T., Meinhart, C.D., Beebe, D.J., Adrian, R.J.: A particle image velocimetry system for microfluidics. *Exp. Fluids* **25**(4), 316–319 (1998). DOI 10.1007/s003480050235. URL <http://dx.doi.org/10.1007/s003480050235>
76. Scarano, F.: Iterative image deformation methods in PIV. *Meas. Sci. Technol.* **13**(1), R1 (2002). DOI 10.1088/0957-0233/13/1/201. URL <https://dx.doi.org/10.1088/0957-0233/13/1/201>
77. Scarano, F.: Theory of non-isotropic spatial resolution in PIV. *Exp. Fluids* **35**(3), 268–277 (2003). DOI 10.1007/s00348-003-0655-4. URL <http://dx.doi.org/10.1007/s00348-003-0655-4>
78. Scarano, F., Riethmüller, M.L.: Iterative multigrid approach in PIV image processing with discrete window offset. *Experiments in Fluids* **26**(6), 513–523 (1999). DOI 10.1007/s003480050318. URL <http://dx.doi.org/10.1007/s003480050318>

79. Scarano, F., Riethmuller, M.L.: Advances in iterative multigrid PIV image processing. *Exp. Fluids* **29**(1), S051–S060 (2000). DOI 10.1007/s003480070007. URL <http://dx.doi.org/10.1007/s003480070007>
80. Scharnowski, S., Hain, R., Kähler, C.J.: Reynolds stress estimation up to single-pixel resolution using PIV-measurements. *Exp. Fluids* **52**(4), 985–1002 (2012). DOI 10.1007/s00348-011-1184-1. URL <http://dx.doi.org/10.1007/s00348-011-1184-1>
81. Scholz, U., Kähler, C.J.: Dynamics of flow structures on heaving and pitching airfoils. In: 13th International Symposium on Applications of Laser Techniques to Fluid Mechanics, Lisbon, Portugal (2006). http://lctes.dem.ist.utl.pt/lxaser/lxaser2006/downloads/papers/40_4.pdf
82. Schrijer, F.F.J., Scarano, F.: Effect of predictor-corrector filtering on the stability and spatial resolution of iterative PIV interrogation. *Exp. Fluids* **45**(5), 927–941 (2008). DOI 10.1007/s00348-008-0511-7. URL <http://dx.doi.org/10.1007/s00348-008-0511-7>
83. Sciacchitano, A., Scarano, F.: Elimination of PIV light reflections via a temporal high pass filter. *Meas. Sci. Technol.* **25**(8), 084,009 (2014). DOI 10.1088/0957-0233/25/8/084009. URL <http://stacks.iop.org/0957-0233/25/i=8/a=084009>
84. Sciacchitano, A., Scarano, F., Wieneke, B.: Multi-frame pyramid correlation for time-resolved PIV. *Exp. Fluids* **53**(4), 1087–1105 (2012). DOI 10.1007/s00348-012-1345-x. URL <http://dx.doi.org/10.1007/s00348-012-1345-x>
85. Shavit, U., Lowe, R.J., Steinbuck, J.V.: Intensity capping: a simple method to improve cross-correlation PIV results. *Exp. Fluids* **42**(2), 225–240 (2007). DOI 10.1007/s00348-006-0233-7. URL <http://dx.doi.org/10.1007/s00348-006-0233-7>
86. Soria, J.: An investigation of the near wake of a circular cylinder using a video-based digital cross-correlation particle image velocimetry technique. *Exp. Thermal Fluid Sci.* **12**(2), 221–233 (1996). DOI 10.1016/0894-1777(95)00086-0. URL <http://www.sciencedirect.com/science/article/pii/0894177795000860>
87. Soria, J., Willert, C.E.: On measuring the joint probability density function of three-dimensional velocity components in turbulent flows. *Meas. Sci. Technol.* **23**(6), 065,301 (2012). DOI 10.1088/0957-0233/23/6/065301. URL <http://dx.doi.org/10.1088/0957-0233/23/6/065301>
88. Stanislas, M., Okamoto, K., Kähler, C.J.: Main results of the first international PIV challenge. *Meas. Sci. Technol.* **14**(10), R63 (2003). DOI 10.1088/0957-0233/14/10/201. URL <http://stacks.iop.org/0957-0233/14/i=10/a=201>
89. Stanislas, M., Okamoto, K., Kähler, C.J., Westerweel, J.: Main results of the second international PIV challenge. *Exp. Fluids* **39**(2), 170–191 (2005). DOI 10.1007/s00348-005-0951-2. URL <http://dx.doi.org/10.1007/s00348-005-0951-2>
90. Stanislas, M., Okamoto, K., Kähler, C.J., Westerweel, J., Scarano, F.: Main results of the third international PIV challenge. *Exp. Fluids* **45**(1), 27–71 (2008). DOI 10.1007/s00348-008-0462-z. URL <http://dx.doi.org/10.1007/s00348-008-0462-z>
91. Stitou, A., Riethmuller, M.L.: Extension of PIV to super resolution using PTV. *Meas. Sci. Technol.* **12**(9), 1398 (2001). DOI 10.1088/0957-0233/12/9/304. URL <http://stacks.iop.org/0957-0233/12/i=9/a=304>
92. Takehara, K., Adrian, R.J., Etoh, G.T., Christensen, K.T.: A kalman tracker for super-resolution PIV. *Exp. Fluids* **29**(1), S034–S041 (2000). DOI 10.1007/s003480070005. URL <http://dx.doi.org/10.1007/s003480070005>
93. Theunissen, R., Scarano, F., Riethmuller, M.L.: On improvement of PIV image interrogation near stationary interfaces. *Exp. Fluids* **45**(4), 557–572 (2008). DOI 10.1007/s00348-008-0481-9. URL <http://dx.doi.org/10.1007/s00348-008-0481-9>
94. Theunissen, R., Scarano, F., Riethmuller, M.L.: Spatially adaptive PIV interrogation based on data ensemble. *Exp. Fluids* **48**(5), 875–887 (2010). DOI 10.1007/s00348-009-0782-7. URL <http://dx.doi.org/10.1007/s00348-009-0782-7>
95. Thévenaz, P., Blu, T., Unser, M.: Interpolation revisited. *IEEE Trans. Med. Imaging* **19**(7), 739–758 (2000). DOI 10.1109/42.875199. URL <http://dx.doi.org/10.1109/42.875199>
96. Tokumaru, P.T., Dimotakis, P.E.: Image correlation velocimetry. *Exp. Fluids* **19**(1), 1–15 (1995). DOI 10.1007/BF00192228. URL <http://dx.doi.org/10.1007/BF00192228>

97. Unser, M.: Splines: a perfect fit for signal and image processing. *IEEE Signal Process. Mag.* **16**(6), 22–38 (1999). DOI 10.1109/79.799930. URL <http://dx.doi.org/10.1109/79.799930> (IEEE Signal Processing Society's 2000 magazine award)
98. Virant, M., Dracos, T.: Establishment of a videogrammetric PTV system. In: Dracos, T. (ed.) *Three-Dimensional Velocity and Vorticity Measuring and Image Analysis Techniques*. ERCOFTAC Series, vol. 4, pp. 229–254. Springer, Netherlands (1996). DOI 10.1007/978-94-015-8727-3_11. URL http://dx.doi.org/10.1007/978-94-015-8727-3_11
99. Wereley, S.T., Meinhart, C.D.: Second-order accurate particle image velocimetry. *Exp. Fluids* **31**(3), 258–268 (2001). DOI 10.1007/s003480100281. URL <http://dx.doi.org/10.1007/s003480100281>
100. Wereley, S.T., Gui, L., Meinhart, C.D.: Advanced algorithms for microscale particle image velocimetry. *AIAA J.* **40**(6), 1047–1055 (2002). DOI 10.2514/2.1786. URL <http://arc.aiaa.org/doi/abs/10.2514/2.1786>
101. Wernet, M.P.: Symmetric phase only filtering: a new paradigm for DPIV data processing. *Meas. Sci. Technology* **16**(3), 601 (2005). DOI 10.1088/0957-0233/16/3/001. URL <http://stacks.iop.org/0957-0233/16/i=3/a=001>
102. Westerweel, J.: Digital particle image velocimetry: theory and application. Ph.D. thesis, Mechanical Maritime and Materials Engineering, Delft University of Technology, 1993. <http://repository.tudelft.nl/islandora/object/uuid:85455914-6629-4421-8c77-27cc44e771ed/datastream/OBJ/download>
103. Westerweel, J., Dabiri, D., Gharib, M.: The effect of a discrete window offset on the accuracy of cross-correlation analysis of digital PIV recordings. *Exp. Fluids* **23**(1), 20–28 (1997). DOI 10.1007/s003480050082. URL <http://dx.doi.org/10.1007/s003480050082>
104. Westerweel, J., Geelhoed, P., Lindken, R.: Single-pixel resolution ensemble correlation for micro-PIV applications. *Exp. Fluids* **37**(3), 375–384 (2004). DOI 10.1007/s00348-004-0826-y. URL <http://dx.doi.org/10.1007/s00348-004-0826-y>
105. Willert, C.E.: Stereoscopic digital particle image velocimetry for application in wind-tunnel flows. *Meas. Sci. Technol.* **8**, 1465–1479 (1997). DOI 10.1088/0957-0233/8/12/010. URL <http://stacks.iop.org/0957-0233/8/i=12/a=010>
106. Willert, C.E.: Adaptive PIV processing based on ensemble correlation. In: *14th International Symposium on Applications of Laser Techniques to Fluid Mechanics*, Lisbon (Portugal) (2008). http://lces.dem.ist.utl.pt/lxaser/lxaser2008/papers/02.1_5.pdf
107. Willert, C.E., Gharib, M.: Digital particle image velocimetry. *Exp. Fluids* **10**(4), 181–193 (1991). DOI 10.1007/BF00190388. URL <https://dx.doi.org/10.1007/BF00190388>
108. Willert, C.E., Jarius, M.: Planar flow field measurements in atmospheric and pressurized combustion chambers. *Exp. Fluids* **33**(6), 931–939 (2002). DOI 10.1007/s00348-002-0515-7. URL <http://dx.doi.org/10.1007/s00348-002-0515-7>
109. Yaroslavsky, L.P.: Digital picture processing: an introduction. *Information Sciences*, vol. 9. Springer, Berlin (1985). DOI 10.1007/978-3-642-81929-2. URL <http://dx.doi.org/10.1007/978-3-642-81929-2>
110. Yaroslavsky, L.P.: Signal sinc-interpolation: A fast computer algorithm. *Bioimaging* **4**(4), 225–231 (1996). DOI 10.1002/1361-6374(199612)4:4<225::AID-BIO1>3.0.CO;2-G. URL [http://dx.doi.org/10.1002/1361-6374\(199612\)4:4<225::AID-BIO1>3.0.CO;2-G](http://dx.doi.org/10.1002/1361-6374(199612)4:4<225::AID-BIO1>3.0.CO;2-G)
111. Zhu, Y., Yuan, H., Zhang, C., Lee, C.: Image-preprocessing method for near-wall particle image velocimetry (PIV) image interrogation with very large in-plane displacement. *Meas. Sci. Technol.* **24**(12), 125,302 (2013). DOI 10.1088/0957-0233/24/12/125302. URL <http://stacks.iop.org/0957-0233/24/i=12/a=125302>

Chapter 6

PIV Uncertainty and Measurement Accuracy

6.1 Common PIV Measurement Error Contributions

The overall measurement error in PIV is a combination of a variety of aspects extending from the set-up and recording process all the way to the methods of evaluation. Therefore, errors are introduced in a variety of ways.

Errors due to installation and alignment must first be considered. For instance, if the light sheet plane is not properly aligned with respect to the desired flow direction, the projection of the velocity vector in the measurement plane is obtained and not the flow components of interest. Furthermore, if a significant flow component perpendicular to the light sheet exists, large perspective errors will be present whose magnitude rises with increasing distance from the optical axes of the lens, as illustrated in Fig. 6.1. These errors can be reduced by decreasing the observation angle α , which can be done by increasing the working distance d_0 or reducing the field of view by selecting a lens with longer focal length or cropping the PIV images. To fully compensate for this error, stereoscopic recording approaches are required as outlined in Sect. 8.1.

Also the calibration procedure frequently contributes an error if the measurement plane does not perfectly coincide with the plane selected for the calibration. Besides mechanical misalignment (parallel offset in Z direction or tilt between planes around the X and Y axis), this can easily happen if the calibration conditions are not identical with the measurement conditions. For instance, if the wind-tunnel is switched on after the calibration, the reduced static pressure in the test section may deform the windows of the facility slightly and this may alter the light sheet position. The same holds if the pressure and thus the density in the facility changes during the runtime causing the light sheet to refract at the air glass interface. These errors are minimized if the light has an incidence of 90° through the wind tunnel window. Furthermore, mirrors installed in the flow to direct the light sheet to the desired location might slightly change their orientation when the flow is turned on, which alters the propagation

An overview of the Digital Content to this chapter can be found at [DC6.1].

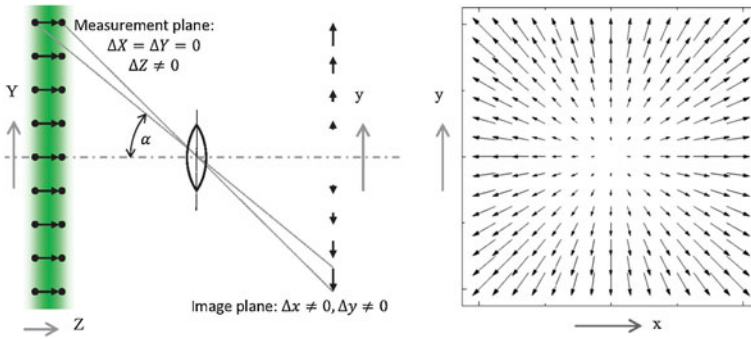


Fig. 6.1 Illustration of the perspective error for a constant out-of-plane particle displacement ($\Delta Z \neq 0$) and zero in-plane shift ($\Delta X = \Delta Y = 0$). A camera with the optical axis in $-Z$ direction will observe a particle image shift in x and y direction even if only motion in Z direction is present. The particle displacement is biased and the magnitude and direction depends on the observation angle α with respect to the optical axis

direction of the light sheet. In addition, it may be that the calibration target is not accurately manufactured leading to a wrong scaling factor for the conversion of pixel to meter. Another source of calibration error can occur if the light sheet is relatively thick and the observation distance short. In this case, the magnification can vary significantly across the light sheet thickness and the determination of the flow velocity becomes erroneous. This has to be considered in particular if high magnification measurements are performed with low observation distance.

Second, errors caused by the system components need to be considered. For example, if the pulse delay Δt of the light source deviates from the selected number on the control panel. This is in particular problematic if the pulse delay is in the nanosecond range because the time delay and the timing errors may have the same order of magnitude. Sometimes different cable lengths used to trigger the system components or changing the firing order of the laser oscillators may already cause a variation of the pulse separation if both oscillators of a double pulse laser are not perfectly identical. Using a fast diode to monitor the exact pulse delay with an oscilloscope is recommended for PIV measurements at large Mach numbers or large magnifications in microfluidics to detect and correct these timing errors. Optical elements between the particles and the sensor such as glass windows, filters or beam-splitter cubes may cause optical aberrations that affect the error of the peak detection if the particle images are not Gaussian like anymore. Image distortions can also be introduced by the imaging optics if the field of view is large and the observation distance small (non-Gaussian imaging conditions), see Fig. 6.2.

Image distortions on the other hand, as indicated in Fig. 6.3, may cause a slight direction error between the measured and real flow direction but also the magnitude might be incorrectly determined if the magnification factor varies across the image. Also, cameras affect the measurement error due to noise or hot (always maximum intensity value) and cold (always zero intensity value) pixel or if the light pulse is too

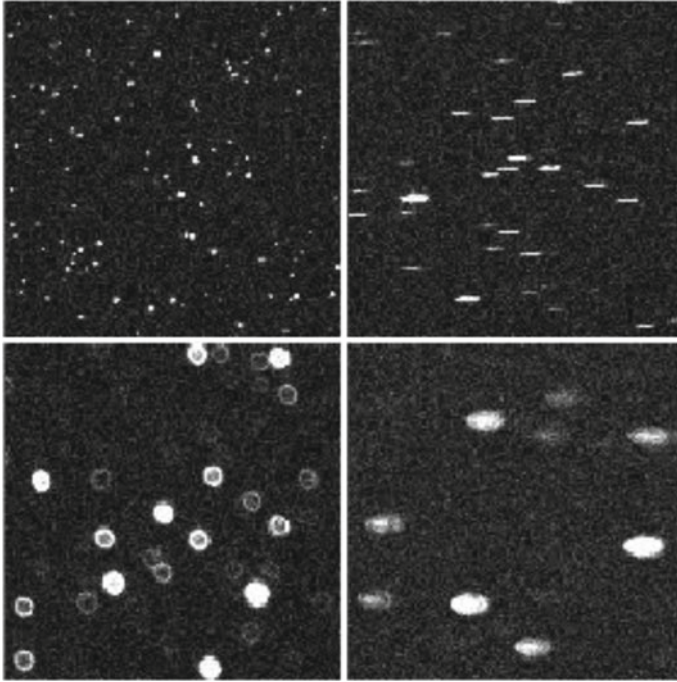


Fig. 6.2 Optical aberrations and out-of-focus imaging leads to non-Gaussian particle image distributions which do not resemble the assumption of the Gaussian peak-fit function for the sub-pixel displacement estimation. The upper left image shows the ideal imaging conditions (focused particle images without strong optical aberrations). The lower left image illustrates out-of-focus particle images and the right column reveals the effect of astigmatic aberrations superimposed on the focused and unfocused particle images

close to the frame transfer of the camera. In this case, a crosstalk can appear meaning that the images of the first frame are also visible on the second. Finally, if the collected data is compressed to reduce the needed storage capacity, this may contribute to an information loss that can affect the uncertainty of the image evaluation.

Third, errors due to the flow itself have to be considered. In particular, large flow gradients or strong velocity fluctuations in turbulent flows can cause measurement errors due to the particle slip but also density gradients due to shocks or strong vibrations can result in measurement errors that need to be considered. Furthermore, variations of the Reynolds and Mach number or the temperature, viscosity or density of the fluid during the experiment runtime may cause measurement errors. Finally, errors introduced by the evaluation techniques need to be considered. These specific errors will be analyzed in more detail in the following sections.

Reducing the error in an experiment requires training and experience but also prudence, preciseness and persistence of the user. It is always important but also worth to invest time to optimize experiments and measurement set-ups in order to

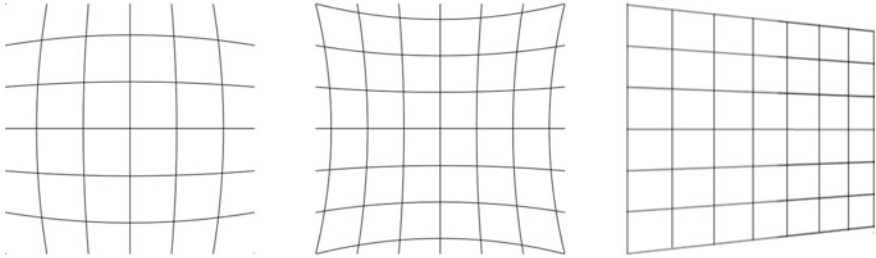


Fig. 6.3 Schematic of image distortions caused by non-Gaussian imaging. Left: barrel distortions. Center: pincushion distortions. Right: perspective distortion due to oblique viewing. The former two are typical if large digital sensors are combined with low quality lenses

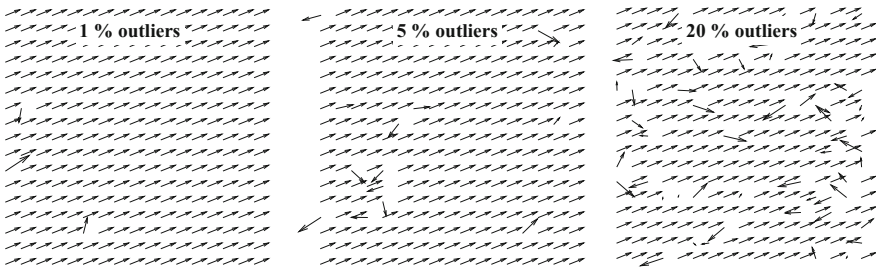


Fig. 6.4 Examples of vector fields with different amounts of invalid measurements

ensure that the desired flow information is captured in the recordings in the best possible way. This is of primary importance as no evaluation software will be able to recover the desired information if the information is not collected and stored in the recordings in a proper manner.

6.1.1 Measurement Error Due to Invalid Measurements

In the early days of PIV, the particle image recordings suffered from a low signal-to-noise ratio because of the low output energy of available lasers and the poor sensitivity of the recording media. The combination of inhomogeneous seeding distributions with strong model reflections or background patterns frequently resulted in large amounts of invalid vectors, as illustrated in Fig. 6.4 for different fractions of outliers.

Due to the outlier problem, the attention of the researchers was mainly directed towards the problem of invalid vector detection and removal [19, 21, 52]. The classical graph shown in Fig. 6.5 indicates the probability of valid measurements in dependency on the number of particle images within the interrogation window \mathcal{N}_I , the in-plane loss of pairs F_I and the out-of-plane loss of pairs F_O . F_I and F_O become

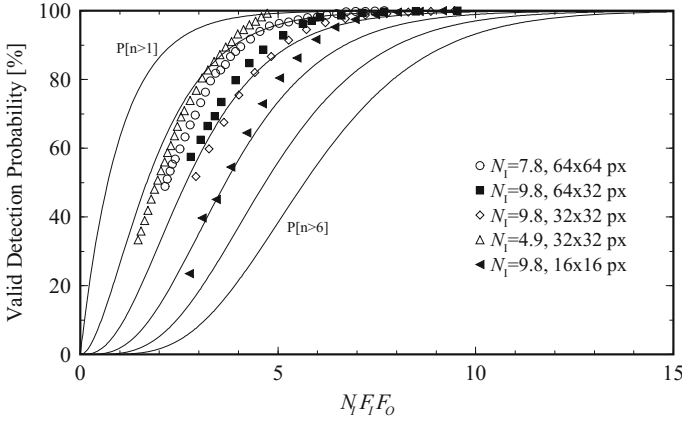


Fig. 6.5 Vector detection probability as a function of the product of number of particle images \mathcal{N}_I , in-plane loss of pairs F_I and out-of-plane loss of pairs F_O . The solid line represents the probability for having at least a given number of particle images in the interrogation spot (see also Fig. 4 in KEANE & ADRIAN [21])

zero per definition if the particle image displacement becomes larger than the interrogation window dimensions or the light sheet thickness according to:

$$F_I = \left(1 - \frac{|\Delta x|}{D_I}\right) \left(1 - \frac{|\Delta y|}{D_I}\right)$$

$$F_O = \left(1 - \frac{|\Delta z|}{\Delta z_0}\right)$$

The simulated results illustrate that the effective number of particle images N within the interrogation window, given by the product of the three factors,

$$N = \mathcal{N}_I \cdot F_I \cdot F_O \tag{6.1}$$

should be greater than or equal to 5 on average, to limit the amount of spurious measurements to a few percent. This makes their detection, elimination and replacement rather simple and reliable as discussed in Sect. 7.1 in detail.

If the effective number of particle images decreases, the valid detection probability decreases and more spurious vectors will appear. As a result, the detection and rejection of the outliers becomes more difficult. Moreover, the spurious vectors will contribute to the error of the velocity measurement if they are not properly filtered out and may even influence the interpretation of the results. Furthermore, if state-of-the-art iterative multi-grid interrogation algorithms are used and the outliers are not correctly detected and removed at early iterations (on the coarser grid), they will cause erroneous velocity evaluations in relatively large clusters of vectors (on the

finer grid). On the other hand, if valid vectors are rejected beside the invalid ones, the velocity measurement statistics might even be biased. For this reason the rejection of outliers without rejection of valid vectors is a very important procedure that needs to be done with care, see Sect. 7.1 for details.

6.1.2 *Relative Uncertainty, Dynamic Velocity Range and Dynamic Spatial Range*

Lower outlier probability can often be achieved by reducing the time interval between the illuminations, increasing the size of the interrogation windows or raising the seeding concentration according to Chap. 5. However, these adjustments may raise the measurement uncertainty of valid measurements as well. For instance, if the time interval between two illuminations is reduced, the dynamic range of the velocity measurement, defined in Eq. (6.2), decreases resulting in a larger relative measurement uncertainty, as $\sigma_{\Delta x}/\Delta x$ becomes larger. The numerator denotes the precision in determining the location of the correlation peak maximum and thus the precision in estimating the displacement of the particle image ensemble within an interrogation window. In case of $\sigma_{\Delta x} = 0.05$ pixel, which can be achieved from carefully aligned experiments [18, 47], a relative uncertainty of 1 % requires a particle image displacement of at least 5 pixel. As $\sigma_{\Delta x}$ is often larger than 0.05 pixel, a Δx of 10 pixel is frequently recommended in the literature. However, for precise measurements displacements up to 50 pixel and more are sometimes required. Consequently, the desired displacement depends on the specific scientific question that is intended to answer by means of PIV. In some experiments it might be difficult to achieve the desired error due to other constraints which will be outlined in the following sections. However, it is always important to maximize the dynamic velocity range DVR given by [1]

$$\text{DVR} = \frac{\Delta x_{\max}}{\sigma_{\Delta x}} = \frac{U_{\max}}{\sigma_U}. \quad (6.2)$$

On the other hand, if the size of the interrogation window is increased, the range of scales that can be resolved decreases as the smallest flow scales that can be resolved are determined by the size of the interrogation window. The range of scales or dynamic spatial range DSR is given by [1]

$$\text{DSR} = \frac{x_{\max}}{D_I} \quad (6.3)$$

with x_{\max} being the sensor size in pixel and D_I the size of the interrogation window. If the sensor measures 2560 pixel in length and the interrogation window 16 pixel the DSR is 160 and 250 for a sensor with 4000 pixel. This corresponds to a 250 mm long tape measure with a millimeter scale. This is a relatively small number for a

measurement technique that highlights the significance of large digital sensor sizes and high resolution image analysis methods. On the other hand, it has to be kept in mind that the power of PIV is its capability to provide multi-point data at thousands of points simultaneously and non-intrusive. To compensate for the loss of information on the small scales it might be an option to raise the magnification of the imaging system along with the seeding concentration, as

$$U_p = \frac{\Delta x}{M_0 \Delta t} \quad (6.4)$$

holds. In this case, the uncertainty can be decreased but on the cost of a reduced field of view. However, as the field of view determines the size of the largest flow scales that can be measured, this is not an option in many experiments. Therefore, it is obvious that a certain number of spurious vectors should be accepted to reduce the measurement uncertainty and to raise the range of scales that can be resolved. As long as the outliers appear randomly (no clusters of spurious vectors) they can be easily detected and rejected, so that the remaining vectors can be considered as valid vectors with a certain measurement error. The correct detection and removal of clusters of invalid vectors is still under investigation (see for instance [24]).

Today, powerful lasers, sensitive digital cameras and sophisticated image analysis and outlier detection techniques are available but also well-established methods to generate homogeneous seeding concentrations and to avoid model reflections as well as background patterns have been developed. Thanks to these achievements, the quality of PIV measurements has greatly improved since the first implementation of PIV and instead of invalid vector treatment the quantification of the uncertainty of valid vectors became of major interest in recent years. Fortunately, the measurement uncertainty will still continue to decrease due to the rise in power and quality of the technical components involved (laser, digital cameras, computer power). However, performing measurements with low uncertainty is still not a simple task as the uncertainty depends on many parameters which cannot be optimized independently. In the following sections the most important impact factors affecting the uncertainty of the measurement will be outlined. A fundamental knowledge about the main sensitivities is important to optimize real experiments but also to ensure that the quality of the data is sufficient to answer the desired fluid mechanical question or to validate numerical flow simulations or to prove theoretical model assumptions such as turbulence models.

6.1.3 Measurement Error

Every real measurement is subject to a finite measurement error. Thus any measured value can be decomposed into a true but unknown value and the measurement error δ_X which is as well unknown for each single measurement:

$$X_{\text{measured}} = X_{\text{true}} + \delta_X \quad (6.5)$$

Therefore, the value of both quantities can only be approximated and characterized in a statistical sense from a large number of independent measurements. Measurement errors are typically divided into two types: systematic errors and random errors. Systematic errors, also called bias errors, can be caused by incorrect calibration or incorrect operation of the measurement system, as already discussed at the beginning of this chapter. Systematic errors are typically constant and predictable if known. Thus, they can be compensated in principle if identified correctly. The magnitude of the systematic error ε of a measurement determines the *accuracy*.¹

The random error of a measurement is characterized by its non-predictable nature. Random errors can change in magnitude and sign for each single measurement. They have a zero mean value and are usually described by their standard deviation σ :

$$\sigma_x = \sqrt{\frac{1}{n-1} \sum_{i=1}^n (x_i - \langle x \rangle)^2} \quad (6.6)$$

The parameter x_i and $\langle x \rangle$ denote the individual measurements and the corresponding mean value, n is the number of samples and i the control variable. The standard deviation of the random error of a measurement determines the *precision*. Figure 6.6 illustrates the effect of random and bias errors on the distribution of two-dimensional measurements. It is important to realize that measurements can be precise (low random error) but inaccurate (large bias error) at the same time.

To determine systematic errors experimentally an independent measurement with higher accuracy is needed. In order to determine the standard deviation of the random error according to Eq. (6.6), a measurement must be repeated many times to ensure that the measured standard deviation converges towards its true value determined by the possible values of δ_X in Eq. (6.5). Therefore, the repeatability and stability of an experiment must be well balanced with the uncertainty of the measurement techniques applied.

It is important to note, that knowledge about the standard deviation of the random error is not sufficient to determine the actual error in a statistical sense and thus, the true value that can be estimated. This becomes evident when the experiment is repeated many times and the average value for the mean and standard deviation of all independent experiments are compared. To take this so called standard error into account, which results from the random nature of the mean and standard deviation as a consequence of the specific random sample (i.e. a non-random mean can only be calculated from an infinite number of samples) considered for the calculation of the quantities, the standard deviation is used to set a confidence interval around the measured value in which the true value can be expected with a certain probability.

¹Sometimes the term accuracy is also used to describe the actual closeness of the measurement to the true value. In this work accuracy is used to quantify only the systematic deviation between the measured value and the true value. An alternative term is the *trueness*.

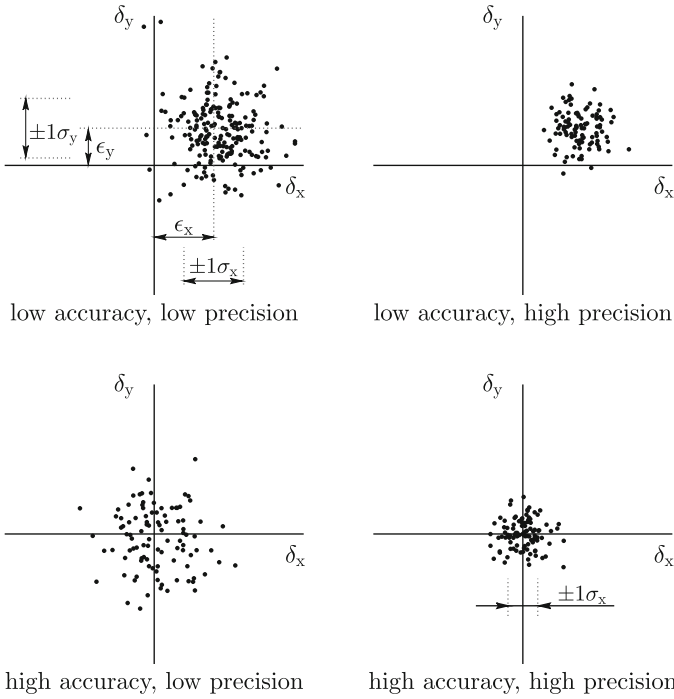


Fig. 6.6 Ensembles of two-dimensional measurement values for two levels of *accuracy* and *precision*. The scatter of the measurement points is due to random errors characterized by σ while the mean offset to the true value is the bias error ϵ

To make probability statements, the probability density function of the measurement distribution must be known. If the random error follows a Gaussian distribution, which is usually a good approximation in practice, the interval of $\pm 1\sigma$, $\pm 2\sigma$ or $\pm 3\sigma$ around the measured mean value contains the true value with a probability of 68.2, 95.4 or 99.7%, respectively. It is important to mention the confidence interval selected whenever an uncertainty is reported. If not stated differently, values for the uncertainty are given with a confidence interval of $\pm 1\sigma$ in this chapter, as sketched in Fig. 6.6.

6.1.4 Error Propagation

The quantification of uncertainties is of paramount importance if more complex quantities are derived from the PIV data sets as outlined in Chap. 7. Typical examples are Reynolds stresses or spatial correlations of the velocity fluctuations in case of turbulent flows or the wall-shear stress to characterize the friction or the vorticity in

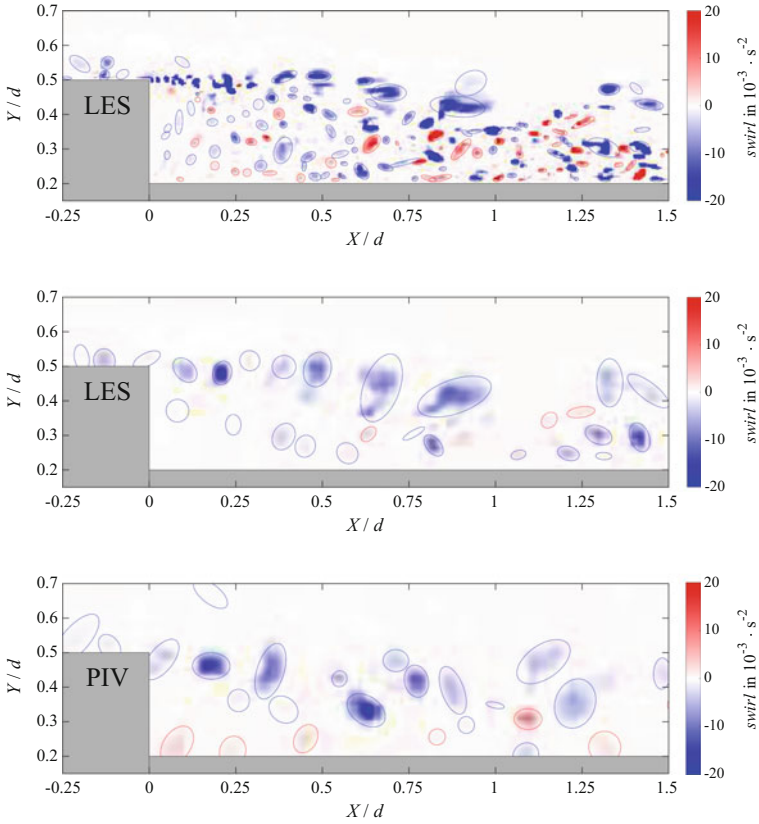


Fig. 6.7 Characteristic vortex distribution in the space launcher models wake for LES simulation (top), for an experimental PIV velocity field (bottom) and for artificially coarse LES matching the PIV resolution (middle) [40]

order to detect flow regions of significant shear or the vorticity or λ_2 criterion for the detection of vortices. In these cases error propagation methods need to be applied. To illustrate the significance Fig. 6.7 (top) shows the vortices detected in the solution of a Large Eddy Simulation (LES) behind a backward facing step by using the swirl criteria given by:

$$\text{swirl} = \max \left\{ 0; \left(\frac{\partial U}{\partial X} + \frac{\partial V}{\partial Y} \right)^2 - 4 \left(\frac{\partial U}{\partial X} \frac{\partial V}{\partial Y} - \frac{\partial U}{\partial Y} \frac{\partial V}{\partial X} \right) \right\} \cdot \text{sign} \left(\frac{\partial V}{\partial X} - \frac{\partial U}{\partial Y} \right)$$

The spatial resolution and precision of the LES simulation cannot be reached by means of PIV and in effect the measurement results are spatially low pass filtered due to the size of the interrogation window as shown in the bottom image. If the simulated

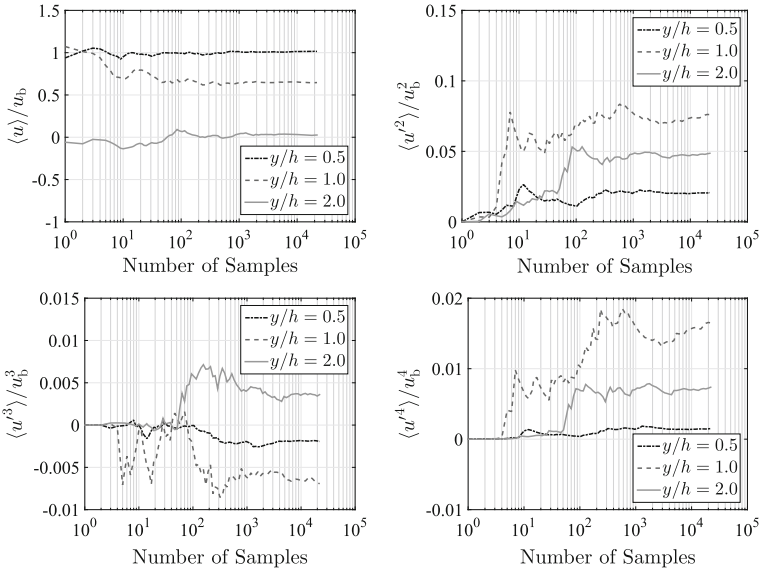


Fig. 6.8 Evolution of the mean value for the streamwise velocity (top left) and the other streamwise higher-order moments for three different wall-normal positions in a separated shear layer in a periodic hill flow [17]

results are filtered with a window corresponding to the size of the interrogation window, the results in the center image are obtained. These results (Fig. 6.7, middle) have comparable spatial resolution with the lower image but without superimposed measurement uncertainty due to the PIV evaluation approach. The comparison of the results indicates that the estimation of the correct flow information requires a high spatial resolution (small window size) and low measurement uncertainty (precise shift detection) at the same time to resolve the turbulent flow features correctly.

To obtain accurate and precise values of average flow quantities it is not only important to have a high spatial resolution and a low measurement error. In addition it is important to acquire enough independent velocity fields until convergence of the flow quantities is reached. Figure 6.8 shows the convergence of various quantities measured in a water channel with streamwise periodic hills [17]. It is evident that the convergence depends on the specific quantity but also on the flow state. In separated flow regions (dashed lines), which is of transient nature in this experiment, the convergence is very slow compared to flow regions with a uniform flow direction (solid lines).

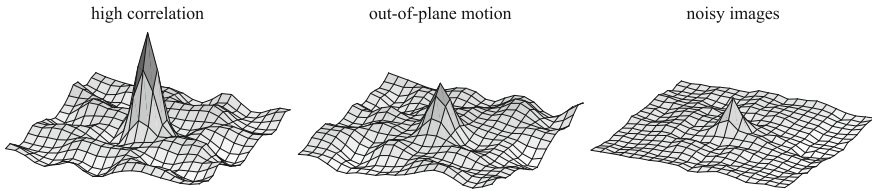


Fig. 6.9 Typical cross-correlation functions with high signal (left) and reduced signal due to out-of-plane motion (middle) and image noise (right)

6.2 PIV Measurement Error Estimation

Many parameters, including particle image size, intensity and density, turbulent fluctuations, velocity gradients, noise level and interrogation window size, affect the uncertainty. In the last years, different methods were developed to quantify the uncertainty of PIV velocity fields [2, 5, 16, 26, 41–43, 49, 54, 58, 59]. Two promising strategies have emerged: The first one is based on identifying all parameters that influence the measurement uncertainty and determining their effect on the overall uncertainty [49, 58]. This requires that all relevant parameters and sensitivities are known. The second approach reduces the parameter space by analyzing the correlation functions only. This is motivated by the fact that the correlation signal is a result of all parameters that contribute to the measurement uncertainty [2, 54]. Figure 6.9 illustrates the sensitivity of the correlation signal on the out-of-plane particle motion (center) and the image noise (right). Both approaches have demonstrated that error estimation for PIV is possible in principle. However, these methods must be individually calibrated for each evaluation software and the sensitivity for each parameter must be checked carefully which makes the uncertainty quantification a quite complex task.

The random and systematic errors in digital PIV evaluation can only be assessed if the displacement data is known. For instance, PIV recordings obtained from a static (quiescent) flow were used in determining the measurement uncertainty in the cross-correlation [55–57]. Although this approach is likely to provide the most realistic estimate for the measurement uncertainty, it only permits a limited study of how specific parameters, such as particle image diameter and background noise, influence the measurement precision. Furthermore, the results are often not transferable to other experimental configurations using different components. A second approach uses particles embedded in a transparent block mounted on a high precision translation stage in order to generate well known particle displacements [31]. This concept is also realistic in view of the technical components involved but the transparent acrylic block causes optical aberrations which raise the uncertainty of the measurements. Furthermore, particle parameter variations are limited due to the fact that they are embedded in the block.

Another approach to assessing the measurement uncertainty in PIV evaluation is based on numerical simulation which is a well accepted approach taken by a number

of researchers since the early days of PIV [2, 5, 6, 15, 16, 19–22, 26, 38, 39, 41, 43, 44, 49, 51, 54, 55, 58, 59]. By varying only a single parameter at a time, artificial particle image recordings of known content can be generated, evaluated and compared with the known result. Random positioning of particle images and a high number of simulations ($O[1000]$) per choice of parameters are crucial in providing reliable measurement precision estimates. The predictions of these Monte Carlo simulations can then be compared with theory or used to understand the effect of individual parameters on the PIV result in order to optimize the measurement setup.

The uncertainty estimation based on synthetic images offers three main advantages according to [15]: first, it gives full control of all parameters considered for the simulation (as opposed to experiments where many uncertainties exist such as local density, temperature, viscosity, flow velocity, particle properties, illumination power and pulse-to-pulse stability, local energy density in the light sheet, imaging optics, recording medium, and bias effects due to data transfer that are unknown or cannot be precisely controlled as it can be done with simulations). Second, the variation of single parameters is possible (which is often difficult to do in experiments because of the mutual dependence of the parameters like light intensity and signal-to-noise ratio, optical magnification and lens aberrations). Third, the range of the parameters can be increased beyond the experimentally accessible range (higher shear rates and turbulence levels, higher particle concentrations, etc.).

The major drawback of the synthetic image approach is that not all physical effects can be simulated properly because of a lack of physical knowledge and the fact that each experimental setup is unique. Besides, the assumed flows used to shift the particle images are often too simplistic (small range of scales, no out-of-plane motion, weak velocity gradients, only shift in one direction, no Brownian motion, etc.). Thus, the idealized assumptions and approximations that are used in simulations underestimate the true value of the uncertainty achievable in experiments. Sometimes this deviation can easily reach an order of magnitude if the idealized synthetic situation does not represent the real experiments. To keep the deviations small, the important physical effects must be considered, while the higher-order effects, which are below the resolution limit of the techniques, can be neglected. As this requires an a priori knowledge, experiments are always necessary to prove the main predictions and sensitivities of the simulations and to identify the differences of the simulation relative to the experiment.

In the following sections the methodology for Monte Carlo simulation in the assessment of the measurement uncertainty of PIV will be explained. A discussion about realistic synthetic PIV images is followed by a study of the sensitivity of the most important parameters on the uncertainty of the shift vector representing the displacement of the particle image ensemble (within the interrogation window) during the time interval Δt by the action of the flow. A solid understanding of the cause and sensitivities of the uncertainties is the key to optimize PIV setups and to perform reliable measurements.

6.2.1 Synthetic Particle Image Generation

The core of the Monte Carlo based measurement error analysis in digital PIV evaluation lies in the generation of appropriate particle image recordings. The particle image generator has to fulfil the requirement of providing artificial particle images with known characteristics: diameter, shape, spatial density and image depth, among others. In the majority of the simulations presented here, the individual particle images are described by a Gaussian intensity profile

$$I(x, y) = I_0 \exp \left[\frac{-(x - x_0)^2 - (y - y_0)^2}{(1/8) d_\tau^2} \right] \quad (6.7)$$

where the center of the particle image is located at (x_0, y_0) with a peak intensity of I_0 . This is a reasonable approximation as long as the particles are in focus. For out-of-focus particles, as shown in the lower left of Fig. 6.2, this approximation does not hold. The particle image diameter, d_τ , is defined by the e^{-2} intensity value of the Gaussian normal distribution which by definition contains 95% of the scattered light. When the particle image diameter is reduced to zero, the particle images will be represented as delta functions. The factor I_0 is a function of the particle's position, Z , within the light sheet, see Fig. 6.10. In order to account for a three-dimensional particle image distribution, the intensity of the particle images must be adapted to their Z -position according to the laser light-sheet intensity profile centered at $Z = 0$:

$$I_0(Z) = q \exp \left[-\frac{1}{\sqrt{2\pi}} \left| \frac{2Z^2}{\Delta Z_0^2} \right|^s \right] \quad (6.8)$$

where q denotes the efficiency with which the particles scatter the incident light, ΔZ_0 is the thickness of the light sheet at which the intensity drops to $(-1/\sqrt{2\pi}) \approx 0.67$ of the maximum intensity and s is a shape factor. For $s = 2$ the intensity profile is Gaussian, and for larger values it becomes closer to a top-hat profile, as sketched in

Fig. 6.10 Three-dimensional volume containing a light sheet and particles used in the generation of artificial particle images

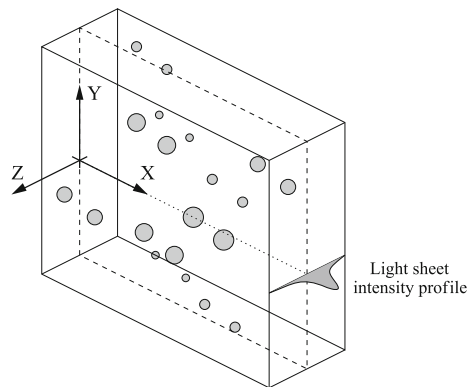


Fig. 6.11 Laser intensity profile according to Eq. (6.8) for different shape factors s

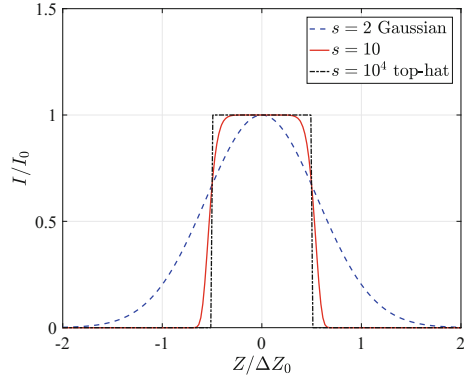


Fig. 6.11. Further on, it is assumed that the particle diameter is much smaller than the light sheet thickness, ΔZ_0 .

To generate a particle image, a random number generator specifies the particle's position (X_1, Y_1, Z_1) within a three-dimensional slab containing the light sheet (Fig. 6.10). The peak intensity $I_0(Z_1)$ is determined using Eq. (6.8). This value is then substituted into Eq. (6.7) for the calculation of the light captured by each pixel. Here the integration of Eq. (6.7) across each pixel can be greatly simplified by computing the product of the error functions (closed form integral of the Gaussian function) along both X and Y . To generate a displacement, a generic flow is often simulated by means of analytical (laminar) or numerical (turbulent) solutions of the conservation equations of fluid mechanics to move the particle location to a new position (X_2, Y_2, Z_2) for which a new particle image intensity distribution is calculated. More particles are added until a desired particle image density N_{ppp} is reached (ppp stands for particle images per pixel). The image is then quantized to the desired image depth (i.e. bits per pixel) and noise is added in some cases to simulate the sensor's shot noise for instance.

The next sections illustrate the effect of various important parameters on the random and bias error of the displacement measurements. The aim here is not to predict the measurement uncertainty or bias error for a specific set of parameters. Rather, the behavior of these errors with respect to the variation of a given parameter will clearly illustrate the sensitivity of uncertainties on individual parameters. This in turn will allow for the design and optimization of real experiments with minimized uncertainty.

If not stated differently each data point in the following simulations is based on 100 synthetic image pairs 512×512 pixel in size, each with a randomly chosen constant particle image displacement between -1 and $+1$ pixel independently for Δx and Δy . The maximum particle image intensity was set to 1000 counts for a particle image centered at a full pixel location. The default laser light sheet profile is the top-hat ($s = 10,000$). The particle image density was set to $1/64$ ppp.

A homogeneous background noise with a mean intensity and a standard deviation of 50 counts and 10 counts, respectively, was simulated.

The displacement vector estimation is based on a multiple-pass cross-correlation approach including iterative image deformation and Gaussian window-weighting if not stated differently, see Chap. 5 for details. These state-of-the-art evaluation techniques lead to the lowest errors which are of interest here. The uncertainty of the shift vector is estimated from the standard deviation of the displacement's x -component, given by Eq. (6.6).

6.2.2 Optimization of Particle Image Diameter

Figure 6.12 displays the variation of the random error as a function of the particle image diameter for digital PIV evaluation using a three-point Gaussian peak approximation. Three important consequences follow from this figure. First, the uncertainty decreases with increasing interrogation window size for a fixed N_{ppp} no matter which evaluation approach is applied. This is because the larger the number of particle images considered for the particle image displacement estimation the better the statistical convergence and the lower the effect of correlation noise in case of homogeneous displacements. Consequently, the seeding concentration, light sheet thickness and spatial resolution must be well selected to obtain accurate measurement results. This goes along with the requirements for avoiding spurious measurements according to Fig. 6.4. Second, it is important to realize that all graphs have a minimum

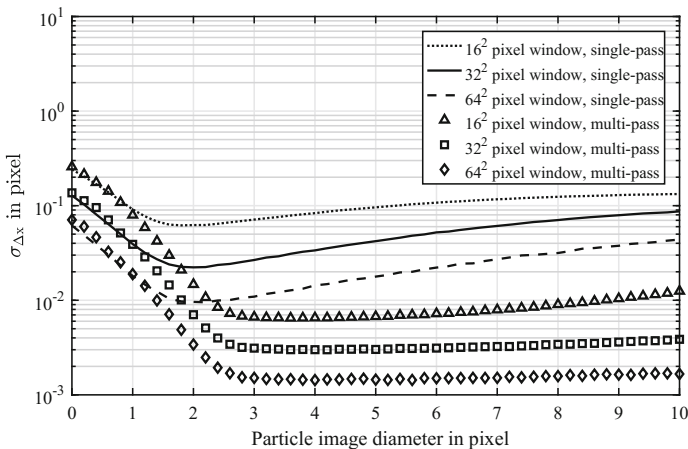


Fig. 6.12 Measurement uncertainty (random error) in digital cross-correlation PIV evaluation with respect to varying particle image diameters. The evaluation was performed for different interrogation window sizes using single-pass evaluation and multiple-pass evaluation with Gaussian window weighting and iterative image deformation based on bi-cubic intensity interpolation, respectively

and this implies an optimal particle image diameter for digital evaluation. Third, the optimal particle image diameter depends on the evaluation technique applied. For single-pass PIV evaluation this diameter is around 2 pixel and results in an uncertainty of 0.022 pixel for the selected simulation parameters and for the evaluation with a standard PIV software using an interrogation window size of 32^2 pixel, for instance. For multi-pass evaluation with iterative image deformation and Gaussian window weighting the uncertainty decreases to values as low as 0.003 pixel for the same window size. Furthermore, the optimum particle image diameter is shifted to larger values and covers a broader range, i.e. from 3 to 6 pixel. Based on these results it is obvious that state-of-the-art multi-pass evaluation techniques are superior in terms of measurement uncertainty compared to (fast) single-pass approaches. Advantageous is also the flat minimum which lowers the sensitivity of the uncertainty on the particle image diameter. However, it must be taken into account that the low uncertainty value following from the synthetic investigation can never be reached in any real experiment. The values are about an order of magnitude below realistic values according to the results obtained in the framework of the PIV-Challenge [18, 45–47]. However, the sensitivity of the uncertainty on the evaluation approach is covered correctly by this synthetic analysis.

For large particle image diameters the uncertainty raises as the variation of the particle image intensity around the maximum decreases and this makes the estimation of the location with the 3-point peak-fit more inaccurate. Peak-fitting routines with larger number of points would be able to compensate for this effect but on the cost of larger computational times [32]. This is important for microfluidic flow measurements because the particle image diameter raises with increasing magnification, see Chap. 10. The increasing uncertainty with decreasing particle image diameter on the other hand is due to the fact that the image is not properly sampled by the discrete pixel of the sensor and thus the 3-point peak-fit is not able to give good estimates of the true displacement. Small particle images are typical if the observation distance is large and the magnification of the imaging system is small as typical for aerodynamic investigations in large wind tunnels. In this case it might be an option to maximize the laser power and to slightly defocus the particle images in order to reach the optimal particle image size range according to Fig. 6.12.

6.2.3 Peak Locking

Figure 6.12 only shows the random part of the error of the estimated displacement vector averaged over particle image displacements between $-1 \leq \Delta x \leq 1$. A detailed analysis of the uncertainty with respect to the particle image displacement shows that the uncertainty is significantly lower for integral values and reaches a maximum in between the same. This effect is illustrated in the top part of Fig. 6.13 for both bi-linear and bi-cubic image interpolation techniques.

Besides the random error discussed above, a systematic error occurs for small particle images: the continuous intensity distribution of very small particle images

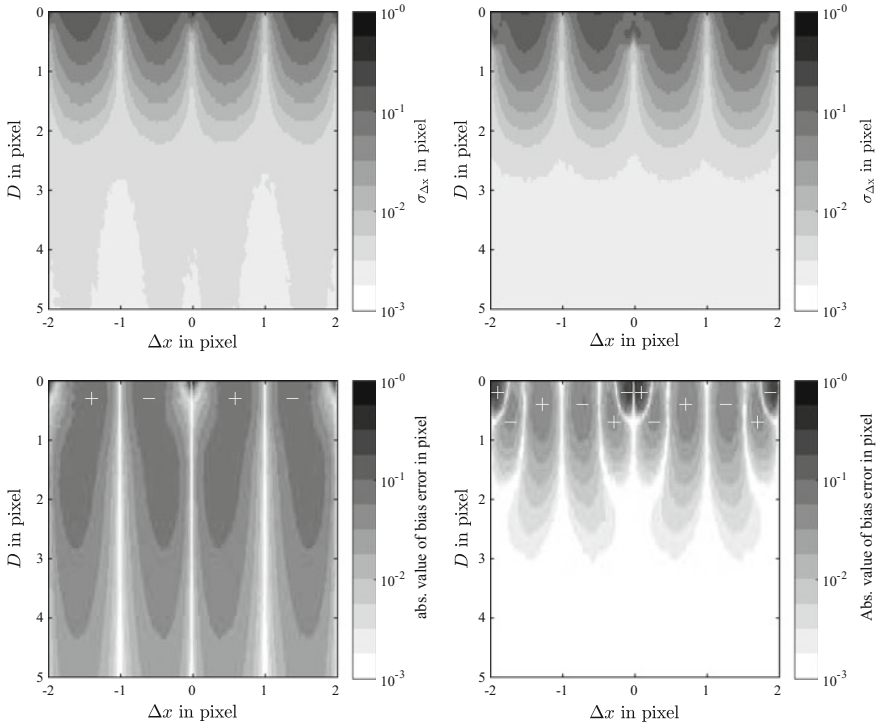


Fig. 6.13 Random error (top) and bias error (bottom) as function of the particle image displacement and the particle image diameter for bi-linear (left) and bi-cubic (right) intensity interpolation during image deformation. For the bias error the absolute value is color coded and the sign is indicated by “+” and “-”, respectively

is insufficiently sampled by the discretized digital camera sensor. Thus, if the low intensities of the pixel next to the one containing the maximum intensity of one particle image are in the order of the image noise level, the sub-pixel position is lost and cannot be reconstructed.

As a result of the discretization, the displacements tend to be biased towards integral values, as illustrated in Fig. 6.13, bottom; again for two image interpolation methods. While bi-linear interpolation (bottom left in the figure) results in a noticeable systematic deviation for a broad range of particle image sizes, the bi-cubic intensity interpolation limits this effect to very small particle images (bottom right in Fig. 6.13). However, for particle image diameters in the order of one pixel or less the bias error is still significant. Furthermore, the bi-cubic reconstruction results in a more complex pattern of the bias error for small particle images, as shown in Fig. 6.13 as well as in Fig. 6.14. It is important to note that the magnitude of the peak locking effect is very sensitive on the image interpolation approach, see [11]. However, in comparison to the case without image deformation a strong improvement takes place. This is because the manipulation of the image by means of image deformation tech-

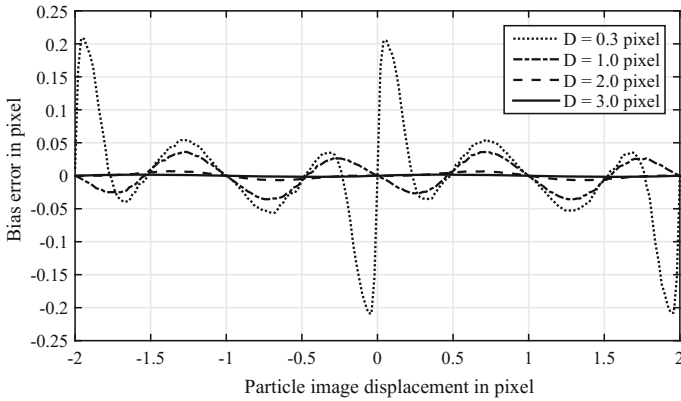


Fig. 6.14 Bias error due to “peak locking” for different particle image diameters

niques allows the maximum of the correlation peak to shift towards the correlation plane center. This leads to a symmetric correlation peak whose maximum can be estimated best by using the symmetric Gaussian fit function. This also explains why the random error is significantly lower in Fig. 6.12 for the multiple-pass evaluation with image deformation. The presence of this “peak-locking” or “pixel-locking” effect² can be detected by plotting a displacement histogram [9] such as given in Fig. 6.15, left. Such a distorted histogram can serve as a good indicator that the systematic errors (due to too small particle images) are larger than the random noise in the displacement estimates. However, a smooth histogram can also be present when the random noise is larger than the systematic error, so care must be taken with regard to misinterpreting the histogram data. If a PIV measurement can be repeated with different time delays and the data is converted into m/s all histograms should collapse if no peak-locking is present. In reality, significant differences can be observed as illustrated by NERGER et al. [27] or OVERMARS et al. [30] and others [3, 4, 7, 33]. Pixel-locking can be also detected in vector fields if the relative variation of the measured velocities is small and dominant vortical structures are present in the flow field. In this case the circular nature of vortices becomes more and more rectangular due to the peak-locking effect, as illustrated in Fig. 6.16. With increasing DVR (Eq. (6.2)) the influence of peak-locking on the data reduces.

In some cases the particle images are below one pixel but peak-locking is not visible by visual inspection of the histogram, individual vortices or average velocity profiles. In this case it is likely that the random noise of other error sources is too large to observe peak-locking.

To avoid significant bias errors due to peak locking it is important to have a particle image diameter of at least two pixel. Smaller sizes usually appear in the case of low

²The term peak-locking or pixel-locking is a frequently used term to describe a displacement bias error that has a periodic pattern on pixel intervals. Mostly it is caused by particle images that are too small.

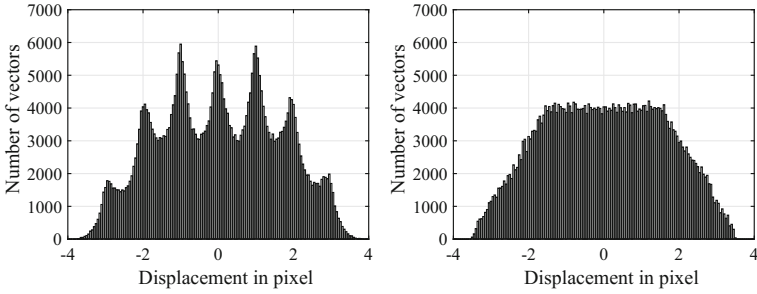


Fig. 6.15 Histograms of the estimated displacement for a particle image diameter of 1 pixel illustrating the “peak locking” associated with insufficient particle image size (left) and for a particle image size of 3 pixel (right). Histogram bin-width of 0.05 pixel

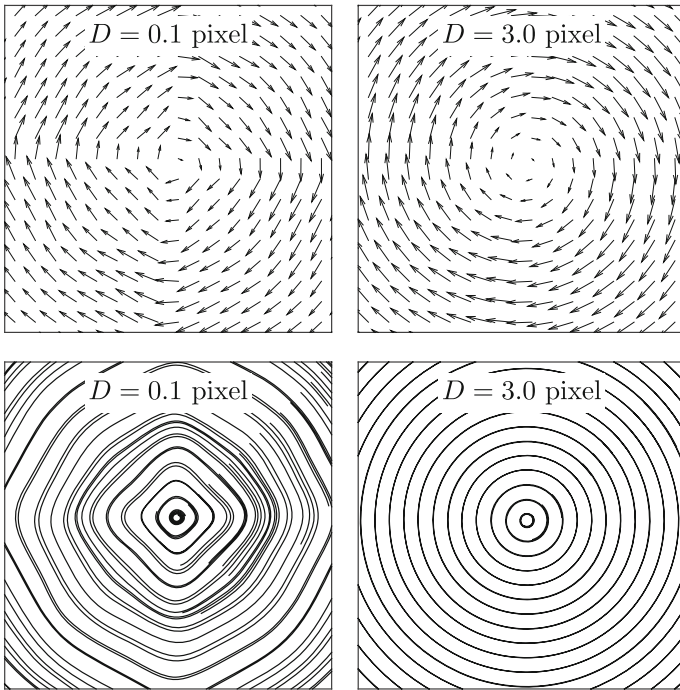


Fig. 6.16 The effect of pixel locking on vector field and stream lines of a synthetic Lamb-Oseen vortex for two particle image diameters. The maximum displacement is only 0.5 pixel

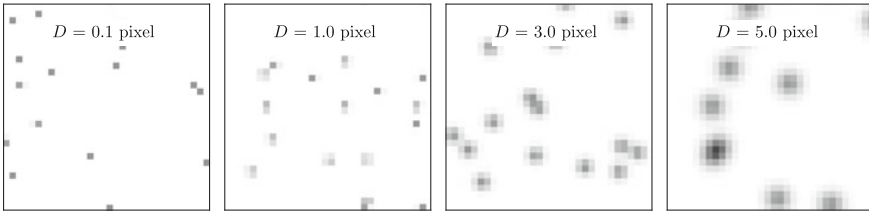


Fig. 6.17 Sample PIV images with increasing particle image diameters

optical magnification or for camera sensors with large pixel spacing, which is typical for some high-speed cameras. To increase the particle image size again, one could use a diffuser plate in front of the camera sensor [25] or slightly defocus the objective. The diffuser plate typically consists of two thin bi-refringent plates (e.g. calcite) with their dispersion direction rotated 90 deg with respect to each other. A dispersion of 0.5–1 pixel is generally sufficient to blur the single-pixel sized particle images to the optimal size of 2–3 pixel. Another approach is to close the lens aperture. However, when starting to close the aperture the particle image at first decreases due to the reduced spherical lens aberrations and only when the aperture is significantly closed does the particle image begin to increase due to diffraction. With both approaches the light intensity accumulated on the image sensor decreases, the visible effect in the image plane is usually opposite to the theoretical one unless the decay of intensity is compensated by raising the laser intensity. Since increasing the laser beam intensity is often not possible, decreasing the aperture size or introducing a diffuser plate in order to increase the particle image size is not always viable.

Based on this analysis it can be concluded that for particle images between 3 and 6 pixel in diameter the lowest uncertainty is achieved if iterative multi-pass evaluation procedures with 3-point peak-estimators are applied. However, with increasing particle image diameter, overlapping particle images become more likely. This promotes a deviation of the correlation peak from the Gaussian shape and makes the displacement estimation more uncertain as the Gaussian model does not match anymore to the correlation function. To avoid this effect the inner particle distance must be raised and this in turn requires the seeding density to be lowered. To maintain the number of particle images, the interrogation windows must be enlarged. Therefore, smaller particle images are preferred in terms of spatial resolution. Thus, the optimum particle image diameter which results in the best resolution and the lowest measurement error is around 3 pixel. Figure 6.17 shows example images with different particle image sizes.

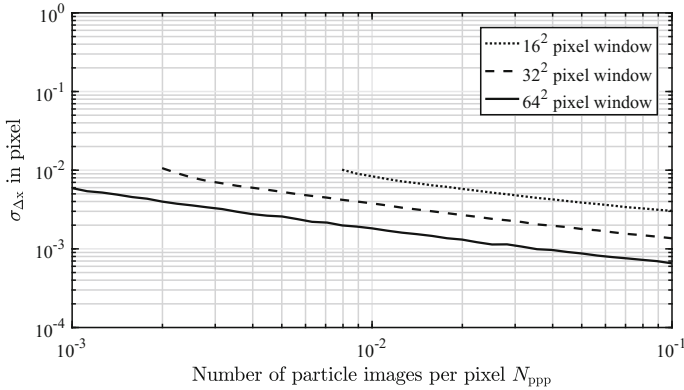


Fig. 6.18 Measurement uncertainty as a function of the particle image density for various interrogation window sizes

6.2.4 Optimization of Particle Image Density

The particle images are the information carriers within a PIV image. The probability of detecting a valid displacement is sufficiently high if the effective number of particle images reaches 5 for single exposure/double frame PIV according to Fig. 6.5. The number of image pairs captured in an interrogation window itself depends mainly on three factors, namely, the overall particle image density, N_{ppp} , the amount of in-plane displacement and the amount of out-of-plane displacement. KEANE & ADRIAN [19–21] have defined these three quantities as the effective particle image pair density within the interrogation window, N , a factor expressing the in-plane loss-of-pairs, F_I and a factor expressing the out-of-plane loss-of-pairs, F_O . When in-plane or out-of-plane loss-of-pairs is not present the latter two are unity. On the other hand, the larger the loss of information the more these factors approach zero. The product of the three quantities $\mathcal{N}_I F_I F_O$ expresses the mean effective number of particle image pairs in the interrogation window. Multi-pass evaluation with iterative image deformation compensates the in-plane loss of pairs, so that $F_I \rightarrow 1$.

If the effective number of particle images is further increased, the shift vector uncertainty can be reduced significantly, which can be explained by the simple fact that more particle image pairs increase the signal strength of the correlation peak with respect to correlation noise (recall that a white background noise with a standard deviation of 1% of the particle maximum image intensity was simulated).

\mathcal{N}_I can be controlled by the particle image density as well as by the interrogation window size. For a fixed seeding concentration the spatial resolution and the uncertainty are nearly proportional, as illustrated in Fig. 6.18. At $N_{ppp} = 0.01$, for example, the uncertainty is appr. 0.002 pixel for an interrogation window size of 64^2 pixel and increases to 0.004 and 0.008 for 32^2 pixel and 16^2 pixel windows, respectively (Fig. 6.19).

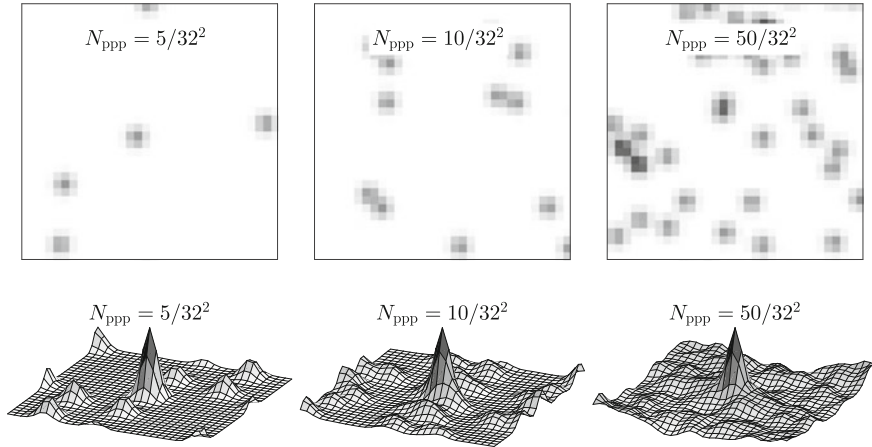


Fig. 6.19 Examples of synthetic PIV images (32^2 pixel) with constant particle image diameter $D = 3$ pixel and varying particle image density (top) and the corresponding correlation functions (bottom)

6.2.5 Effect of Background Noise

Figure 6.20 illustrates the increase of measurement uncertainty due to background noise caused by multiple scattered photons in densely seeded flows or by electron generation in digital sensors according to Sect. 2.6. In the following simulations, normal-distributed (white) noise at a specified fraction of the particle image maximum intensity I_0 was linearly added to each pixel. Moreover, the noise for a given pixel was completely uncorrelated with its neighbors or with its counterpart on a different image. However, these features are not always the case for actual image sensors. Figure 6.20 shows that a small noise level already has a strong effect on the shift vector uncertainty. Furthermore, it is interesting to note that without any image noise the curves from different particle image densities tend to collapse on a single uncertainty value, while with image noise added, the particle image density strongly affects the uncertainty. Consequently, noise minimization is important not only because of how image noise affects the shift vector uncertainty but also how it results in a loss-of-correlation. The magnitude of the loss-of-correlation depends on the noise level itself and the signal level [DC6.2]. A beneficial definition of the signal level of a PIV image is the intensity standard deviation of the noise-free image σ_A . Consequently, the signal-to-noise ratio SNR can be defined as [39]:

$$SNR = \frac{\sigma_A}{\sigma_n} = \frac{I_0}{2\sigma_n} \sqrt{N_{ppp} \cdot \left(\frac{\pi}{4} D^2 - 1\right)} \tag{6.9}$$

Thus, PIV images with higher particle image density also have a higher signal level. Often the ratio of maximum particle image intensity and noise level standard devi-

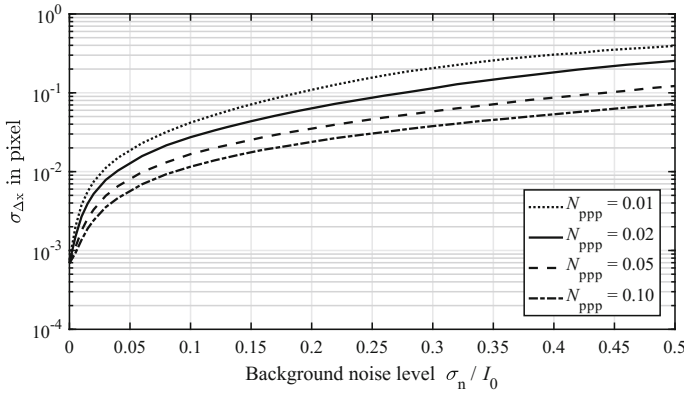


Fig. 6.20 Measurement uncertainty as a function of white background noise for various particle image densities

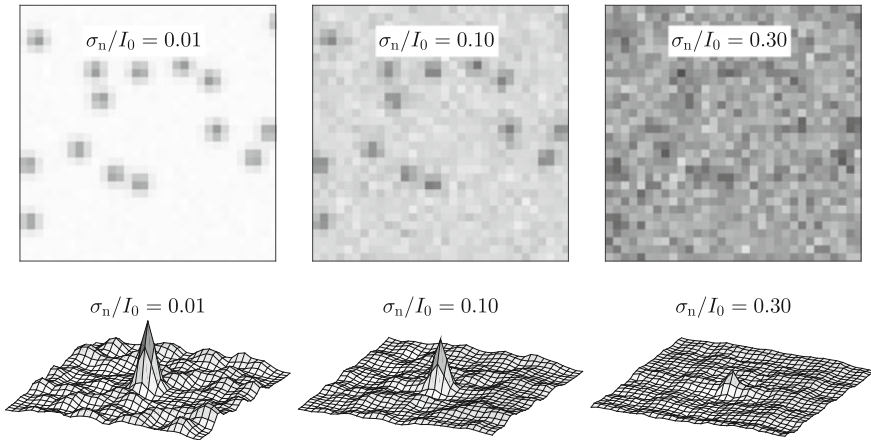


Fig. 6.21 Examples of synthetic PIV images with varying background noise level (top) and the corresponding correlation functions (bottom)

ation I_0/σ_n is used, but it is not a very useful quantity to characterize the SNR in cross-correlation based PIV because it does not include the effect of particle image density. Due to the loss-of-correlation caused by the image noise the effective number of particle images N within a correlation window depends on the product $\mathcal{N}_1 F_1 F_O F_\sigma$, where F_σ is the loss-of-correlation due to image noise [39]. Example images with different noise levels are shown in Fig. 6.21 together with the correlation functions to illustrate this effect.

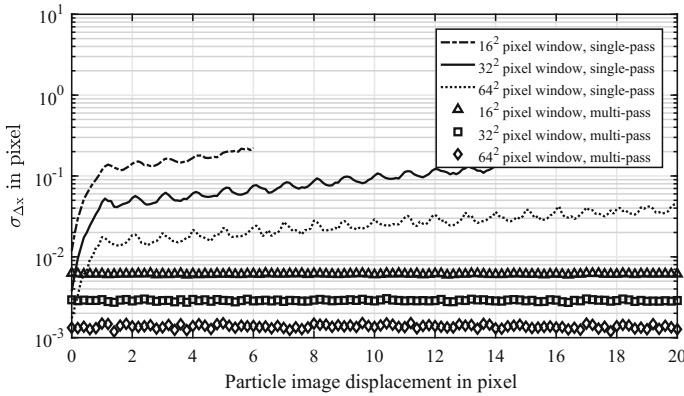


Fig. 6.22 Measurement uncertainty as a function of particle image displacement

6.2.6 Effect of Particle Image Shift

The particle image shift depends on the flow velocity, the optical magnification and the time delay between the laser pulses. Generally, a large shift is desired in order to obtain a small relative uncertainty and a large dynamic velocity range according to Eq. (6.2). In the case of single-pass evaluation, the maximum shift is ultimately limited by the window size and in order to ensure a sufficiently high probability in detecting a valid vector. The so called one-quarter rule [20] is a common guideline, which states that the maximum displacement of the particle images should be equal to or less than one quarter of the interrogation window extend in the direction of the particle image shift. With larger displacements the uncertainty increases for single pass interrogation without window shifting, as shown in Fig. 6.22.

In the case of multi-pass evaluation, the one-quarter-rule still applies but only for the first pass. Thereafter, the window size can be reduced iteratively to the limit given by the particle image density ($N > 5$) and F_1 will be always equal to one no matter how large the in-plane particle image displacement is (the largest displacement is limited by the sensor size of course). In principle particle image displacements which are even larger than the final window size can be measured as demonstrated in Fig. 6.22 for the 16^2 pixel evaluation. This even holds true if in-plane flow gradients exist because they can be compensated completely by using image deformation techniques [8, 29, 34, 35, 48] (see also Chap. 5). However, due to out-of-plane loss-of-pairs very large particle image displacement can be hardly achieved in many experiments. Figure 6.22 also shows that due to the image shifting technique the uncertainty becomes independent of the particle image displacement if no gradients and no out-of-plane motions are present. The effect of gradients and out-of-plane motion on the uncertainty is discussed in the next sections.

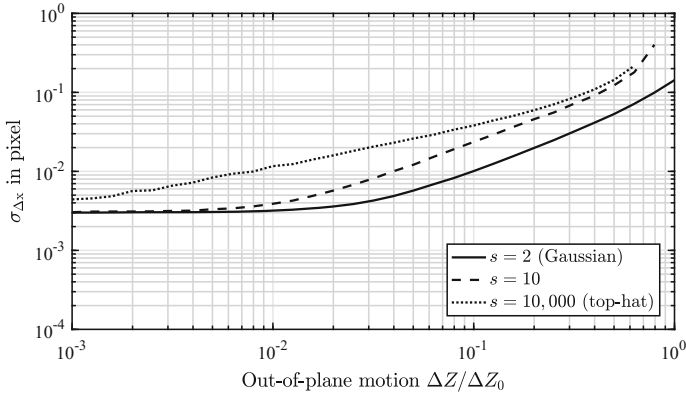


Fig. 6.23 Measurement uncertainty as a function of out-of-plane motion

6.2.7 Effect of Out-of-Plane Motion

Frequently, the PIV method is applied to investigate highly three-dimensional flows, in some cases even with the mean flow normal to the light sheet. Examples of these may be the study of wing-tip vortices or other structures aligned with the flow. In this arrangement, the out-of-plane loss of pairs is significant such that the correlation peak signal strength diminishes. As a result, the possibility of valid peak detection reduces and the uncertainty increases. In the case of non top-hat light sheet profiles the intensity of the particle images changes with their location in the light sheet and this can affect the uncertainty of the measurement as well [28]. Figure 6.23 shows the effect of out-of-plane motion on the uncertainty of the estimated shift vector for different light-sheet shapes. A top-hat profile is more sensitive to out-of-plane motion than a Gaussian, because particles that leave or enter the light sheet cause a sudden vanishing or appearing of the particle images those cannot be paired.

On the other hand, in the case of a smoothly varying light sheet intensity, like a Gaussian bell curve, the question of the actual light sheet thickness arises, because at low intensity the light scattered by the particles might not be sufficient to produce a signal of sufficient strength in the recording or it has a negligible contribution to the correlation signal. As the effective light sheet thickness determines the measurement volume over which the displacement is averaged in the out-of-plane direction and also partly for the in-plane direction in the case of stereoscopic measurements, its quantification is important [DC6.3].

Three methods exist to compensate for the loss-of-pairs due to out-of-plane motion. First, the pulse delay Δt between the recordings can be reduced which has the side effect of reducing the dynamic velocity range in the measurement according to Eq. (6.2). Second, the light sheet thickness can be increased to accommodate the out-of-plane motion for a given pulse delay such that less than one-quarter of the particles get lost in the out-of-plane direction between the two laser pulses (the

one-quarter rule also applies in out-of-plane direction). However, this is often not feasible because the energy density of the light sheet is reduced proportionally to the increased thickness and thus particle image signals will also decrease. This also increases the measurement volume in out-of-plane direction over which the velocity is averaged. Third, the mean out-of-plane flow component can be accommodated with a parallel offset of the light sheets between the illumination pulses in the direction of the flow [13]. This method works best when the mean out-of-plane flow component is nearly constant across the field of view. The best results can be achieved by combining all three of these approaches. Just as with the in-plane loss-of-pairs, the general guideline is to keep the out-of-plane loss-of-pairs small enough to still ensure the presence of a minimum number of particle image pairs within the interrogation window (typically $N > 5$) [36].

6.2.8 *Effect of Displacement Gradients*

PIV estimates the mean particle image displacement averaged over the interrogation window and weighted by the particle image intensities. Ideally all particle images within a window experience the same displacement. However, this is often not the case in real experiments. One common example is a boundary layer flow, sketched in Fig. 6.24: between the near-wall region and the outer region the mean velocity profile is strongly curved and the instantaneous velocity profiles may even show inflectional points. Consequently, the velocity changes within the interrogation window. For a constant in-plane gradient the deviations from the mean displacement cancel out and the mean displacement is estimated without a bias error in case of a homogeneous particle image distribution. Furthermore, multi-pass evaluation with iterative image deformation ensures that the correlation function is not stretched in flow direction. This leads to a constant shift vector uncertainty over a large range of in-plane gradients, as shown in Fig. 6.25. However, in the case of the strongly curved velocity profile, the gradient is not constant. The average shift of the particle images within a window is for a boundary layer flow generally higher than the one at the window's center, were the vector is located. As a result the velocity is generally overestimated for this kind of velocity profile.

Furthermore, for non-constant in-plane gradients the image deformation does not fully compensate for the different displacements within the interrogation window. This may result in stretched correlation peaks and increased uncertainty. This effect is also observed if out-of-plane flow gradients are present, like in case of wall-parallel measurement planes in a boundary layer flow. Here, the out-of-plane gradients cannot be compensated by image deformation because the individual particle images within the interrogation window experience different displacements depending on their out-of-plane position within the light-sheet. Figure 6.26 shows that the broadening of the correlation peak due to out-of-plane gradients significantly affects the measurement uncertainty. To reduce errors associated with out-of-plane gradients it is necessary to reduce the light sheet thickness. However, this will also reduce the particle image

Fig. 6.24 Overestimated velocity in the near-wall region of a boundary layer [15]

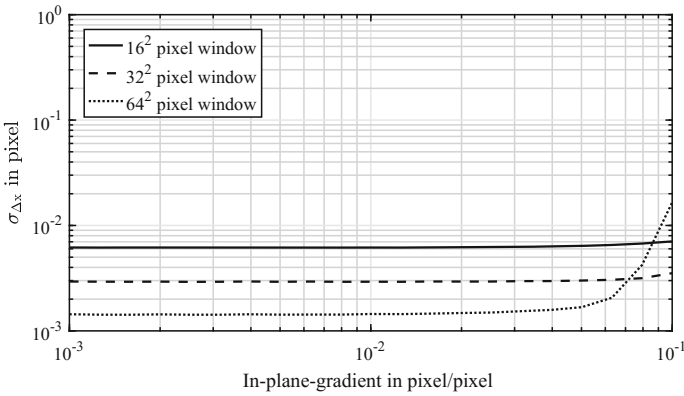
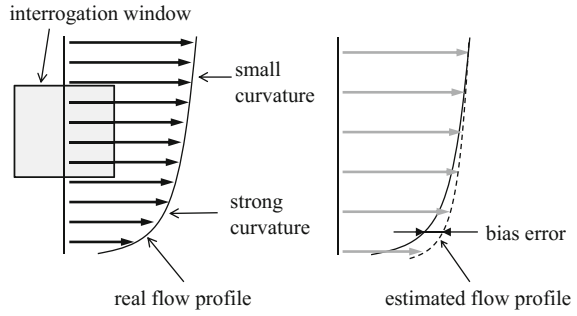


Fig. 6.25 Measurement uncertainty as a function of in-plane gradients for a particle image diameter of $D = 3.5$ pixel

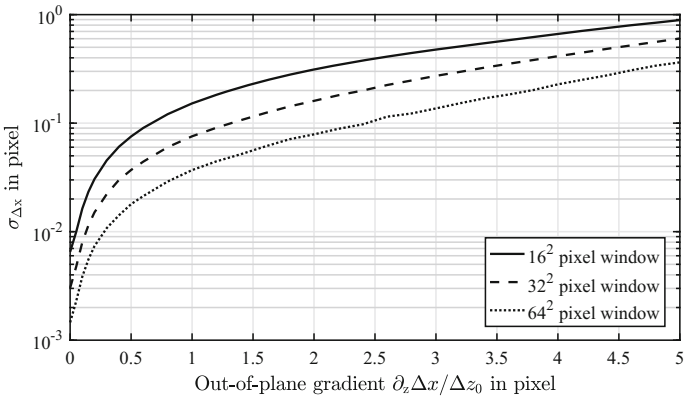


Fig. 6.26 Measurement uncertainty as a function of out-of-plane gradients for a particle image diameter of $D = 3.5$ pixel

density and needs to be compensated by increasing the interrogation window size or the seeding concentration. If this is not possible, because of gradient effects for instance or limitations of the seeding generators, particle tracking methods and/or volumetric measurements could help [15, 16]. To reduce errors associated with in-plane gradients the spatial resolution must be high enough to ensure nearly constant velocity within the interrogation windows.

6.2.9 Effect of Streamline Curvature

Another important point to consider, is that particles are usually assumed to follow a straight line between the two illuminations. However, in the case of strong gradients alternative paths, as shown in Fig. 6.27, are certainly possible. The first-order velocity vector is located at the start position of the particle group investigated (at time t). It can be seen from Fig. 6.28 that the orientation of this vector is biased in the case of a curved streamline.

With symmetric image deformation the shift vector is re-located to a position half way between the start point and the end point of a straight line. This corresponds to the velocity at said location at the time between the recordings ($t + \Delta t / 2$) with an accuracy of second order [50]. Thus, the flow direction is corrected for the case of a curved streamline. However, the shift vector magnitude is still slightly underestimated as the real path of the particle ensemble is longer than the assumed straight line.

The effects of streamline curvature can be compensated efficiently by applying multi-frame techniques, as discussed in Sect. 5.3.6. For highly resolved vector fields, where the distance of neighboring shift vectors is smaller than their length, the most likely path with constant curvature can be estimated from the first or the second order shift vector field and its gradient field, as discussed in [37] in detail. The condition regarding the shift vector density is for instance often fulfilled in the case of single-pixel ensemble correlation (Sect. 5.3.2.5). Figure 6.29 illustrates the estimated shift vector field of a Lamb-Oseen vortex for first-order and second-order accuracy as well as for curvature corrected vectors. A comparison of the simulated and the

Fig. 6.27 Estimated path and other possible paths between two particle locations [15]

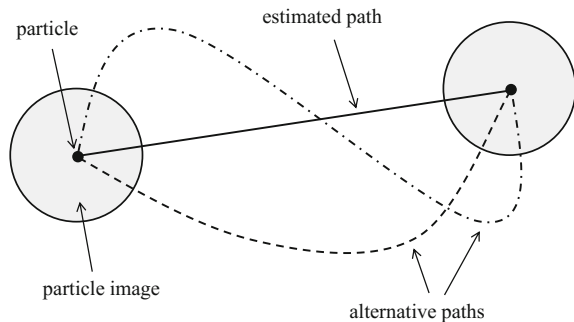


Fig. 6.28 Particle path estimated from the position of the particle image at time t and $t + \Delta t$ [37]

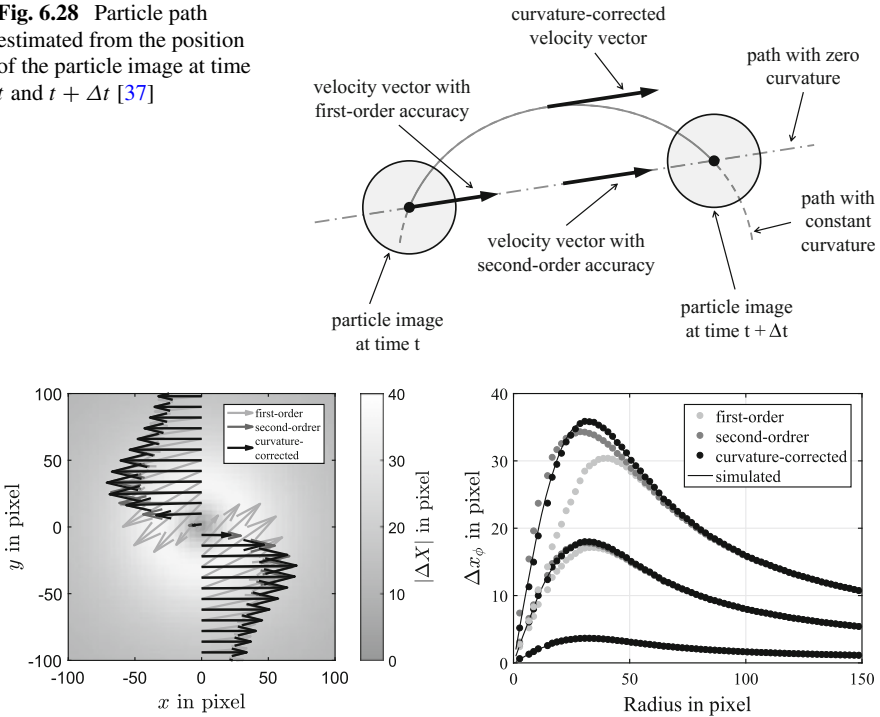


Fig. 6.29 Averaged curvature-corrected shift vector field along with vectors of first and second order accuracy (left) and estimated circumferential velocity component of a simulated Lamb-Oseen vortex (right) [37]

estimated circumferential velocity, right in the figure, shows that the bias error of the second order accurate vectors is negligible as long as the streamline radius is large compared to the vector length.

In order to avoid strong bias errors due to curved streamlines it is important to use a sufficiently high magnification to resolve this kind of gradient. Whereas the resolution in flow direction is determined by the time separation between the two PIV images.

6.3 Optimization of PIV Uncertainty

The quality of a PIV measurement is determined by the relative error of the estimated velocity, that is, the ratio of the measurement error and the absolute value of the measured particle shift. For a given magnification the particle shift is adjusted by the pulse delay between the successive light pulses. Besides technical limitations, some general effects have to be considered. According to the principle of PIV the

measured velocity is determined by the ratio of two components of the measured particle displacement between successive light pulses ΔX and ΔY respectively, and the pulse separation time Δt . Since the particle displacement – which is considered to be a function of Δt in the following – is determined by the particle image displacement with $\Delta x(\Delta t) = \Delta X(\Delta t)/M$ and $\Delta y(\Delta t) = \Delta Y(\Delta t)/M$ respectively, and the measured image displacements contain certain errors, δ_x , we can define the following equation for the locally measured velocity:

$$U = \frac{\Delta x(\Delta t)}{M \Delta t} + \frac{\delta_x}{M \Delta t} \quad (6.10)$$

Since the particle image displacement for a given recording configuration reduces linearly with the pulse separation time, the first term of the above equation stays constant for vanishing pulse separations:

$$\lim_{\Delta t \rightarrow 0} \frac{\Delta x(\Delta t)}{M \Delta t} = U \quad (6.11)$$

In contrast to that, the random part of the error contained in the measured image displacement will not be reduced below a certain limit by a reduction of the pulse separation. Therefore, the second term of Eq. (6.10) – which states that the measurement error is weighted with $1/\Delta t$ – increases rapidly with decreasing pulse separation:

$$\lim_{\Delta t \rightarrow 0} \frac{|\delta_x|}{M \Delta t} = \infty \quad (6.12)$$

From these considerations it can be seen that the uncertainty of PIV measurements can be reduced by increasing the separation time between the exposures at least within certain limits. On the one hand, Fig. 6.22 shows that the absolute uncertainty is rather independent of the particle image displacement for multi-pass evaluations and without any gradients or loss-of-pairs. On the other hand, the loss-of-pairs due to out-of-plane motion as well as the correlation peak broadening, in the case of gradients, increases the uncertainty in estimating the particle image shift [36]. Thus, one fraction of the uncertainty is constant and one is increasing with increasing Δt (or Δx). The total relative uncertainty is a combination of these two types and has a global minimum at a finite Δx for any non-zero out-of-plane motion or gradients.

In Fig. 6.30 the two aspects of the choice of Δt on the quality of the PIV results are shown: the dashed line represents the effect of the weighting of the constant part of the random error with Δt , the dotted line represents the influence of the increasing uncertainty due to loss-of-pairs and correlation peak broadening. The optimum Δx could therefore be found by determining the minimum of a relative uncertainty function, which is represented by the solid line.

However, the shape of curves has been chosen arbitrarily, since a general value for the uncertainty of a measurement is difficult to define. When using digital equipment, which allows immediate feedback during the measurement, the optimum can be

found interactively by slowly increasing the pulse separation until the number of obvious outliers within the vector map increases. However, the number of valid data points is only one measure of the measurement quality, and cannot be used to completely evaluate the quality of the obtained data.

Figure 6.31 illustrates on the left side a simple PIV setup for which Δt could be optimized. The flow downstream of a nozzle was evaluated in a slightly tilted plane to investigate the effect of out-of-plane motion. On the right side of the figure the relative uncertainty, computed from the ratio of the shift vectors standard deviation and the mean displacement, shows a clear minimum of around 0.3% between 20 and 40 pixel shifts [38].

It is important to note, that the investigated flow is homogeneous within the field of view. For a flow field with spatial varying velocities and gradients, an optimum Δt can only be found locally in general. According to our experience it is advisable to apply a quick-look evaluation during recording for the optimization of the experimental parameters, and also to store the original recordings in order to be able to optimize the evaluation after the experiment.

Fig. 6.30 Optimized relative uncertainty

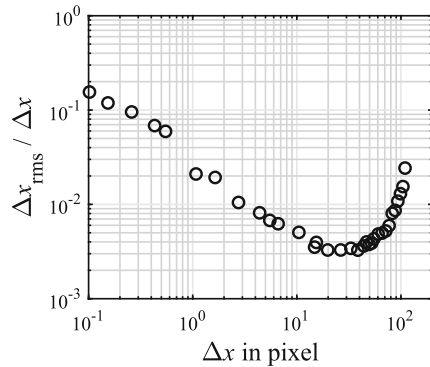
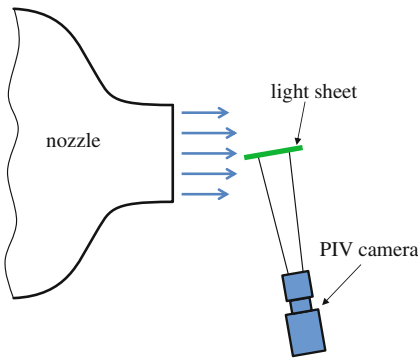
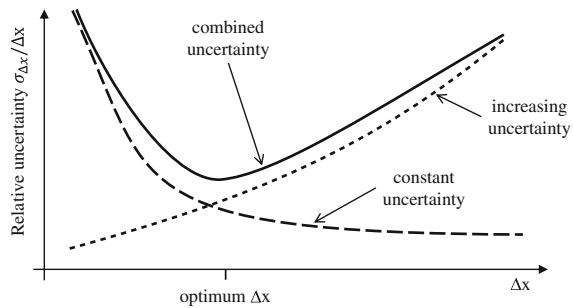


Fig. 6.31 Experimental example for an optimized displacement in the case of strong out-of-plane motion [38]

6.4 Multi-camera Systems

So far the analysis of classical two component planar PIV measurements was considered. However, to account for the perspective error outlined in Fig. 6.1 and in order to measure all three velocity components in a plane or even in a volume, two or more PIV cameras are required as discussed in Chaps. 8 and 9 in detail. In this case, the uncertainty of the reconstructed velocity field depends on the quality of all camera images. Therefore, all the statements made in the foregoing sections also apply for the analysis of stereoscopic images. However, as the results from two independent measurements are combined all errors become larger apart from the perspective error shown in Fig. 6.1. Furthermore, there are several additional errors that need to be considered for stereoscopic or multi-camera imaging. For the reconstruction of the out-of-plane component in the case of a stereoscopic setup, as sketched in Fig. 8.2 in Sect. 8.1, the in-plane displacements of both cameras are considered. If the uncertainty and the observation angle for both stereo cameras is $\sigma_{\Delta X}$ and α , respectively, the uncertainty of the out-of-plane component is given by [23]:

$$\sigma_{\Delta Z} = \frac{\sigma_{\Delta X}}{\tan \alpha} \quad (6.13)$$

Thus, the uncertainty increases with decreasing observation angle as illustrated in Fig. 6.32. For $\alpha = 45^\circ$ the uncertainty ratio becomes unity. For smaller observation angles the uncertainty of the third component becomes significantly larger than those of the in plane components. On the other hand, the larger the angle is the worse the in-plane resolution becomes. Additionally, the perspective error, discussed at the beginning of this chapter and in Chap. 2, increases with α . Often an observation angle of $\alpha = 45^\circ$ is selected (90° opening angle between both camera views) to ensure that the uncertainty is equal for all components. However, in some experiments not all components are equally relevant and therefore other observation angles might be more appropriate depending on the applications. It is recommended to use an opening angle between the cameras of 30 to 60° .

Aside from the proper opening angle between the observation cameras it is important that the flow information measured independently with multiple cameras is combined in a proper manner to avoid systematic errors. The main problem is the proper correspondence of information from each camera. This implies that the image points from all cameras must be precisely related to the corresponding object points to avoid the combination of velocity vectors from different flow regions so that the derived third velocity component is absent of perspective errors. It is evident that a mismatch between corresponding points leads to significant measurement errors in case of complex flows even if the mismatch is only a fraction of the interrogation window size, as indicated in Fig. 6.33. The correspondence problem is solved by means of a careful calibration. However, it is already mentioned that calibration errors can be easily introduced if the light sheet is slightly displaced during the experiment compared to the calibration conditions [10, 12, 53]. In this case the mismatch between corresponding points leads to significant errors as indicated in

Fig. 6.32 Uncertainty of the out-of-plane shift component normalized with the uncertainty of the in-plane component with respect to the observation angle for a stereo PIV setup

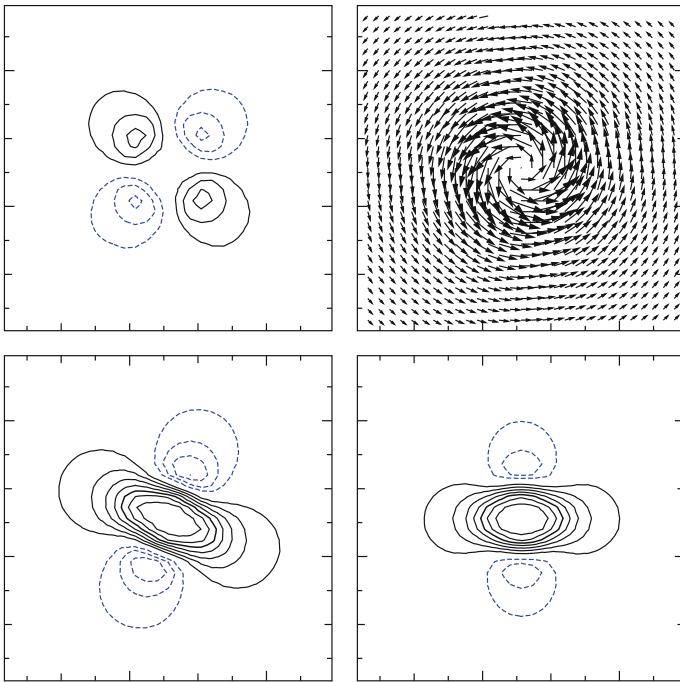
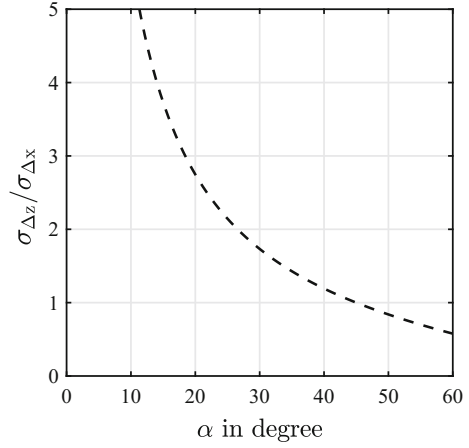


Fig. 6.33 Induced out-of-plane flow components (line plots) caused by misalignment between two cameras in a stereo configuration (reproduced from [10, 11]). The interrogation window size was 32 by 32 pixel and the mismatch 16 pixel

Table 6.1 Range of out-of-plane errors in a stereo configuration due to inter-camera misalignment (reproduced from [10, 11]) The size of the interrogation window is 32 by 32 pixel

In-plane shift [pixel]		Out-of-plane error [pixel]
$\Delta x = 8$	$\Delta y = 0$	$-0.520 \leq \delta_{\Delta Z} \leq 0.482$
$\Delta x = 16$	$\Delta y = 0$	$-0.688 \leq \delta_{\Delta Z} \leq 0.705$
$\Delta x = 32$	$\Delta y = 0$	$-1.049 \leq \delta_{\Delta Z} \leq 1.109$
$\Delta x = 8$	$\Delta y = 8$	$-0.576 \leq \delta_{\Delta Z} \leq 1.147$
$\Delta x = 16$	$\Delta y = 16$	$-0.824 \leq \delta_{\Delta Z} \leq 1.526$
$\Delta x = 32$	$\Delta y = 32$	$-1.120 \leq \delta_{\Delta Z} \leq 2.076$
$\Delta x = 0$	$\Delta y = 8$	$-0.486 \leq \delta_{\Delta Z} \leq 1.076$
$\Delta x = 0$	$\Delta y = 16$	$-0.602 \leq \delta_{\Delta Z} \leq 1.611$
$\Delta x = 0$	$\Delta y = 32$	$-0.969 \leq \delta_{\Delta Z} \leq 2.049$

Fig. 6.33 for a simple vertical flow without any out-of-plane motion. The upper right part in Fig. 6.33 shows the velocity field. For perfect conditions the out-of-plane component would be zero everywhere in the field. A small mismatch between the vector fields acquired with two independent cameras in a stereoscopic configuration introduces a systematic non-zero out-of-plane velocity component as indicated in the other three sub-figures of Fig. 6.33. The upper left one shows a mismatch with a pure x -component and the lower right the error due to a pure y displacement. The lower left sample image shows a combined shift in x - and y -direction. In the case of a 2D laminar flow it would be immediately clear by inspecting the out-of-plane velocity component that the out-of-plane motion is not physical. However, for turbulent flows with many superimposed vortices of different size, orientation and strength it would be impossible to detect the systematic errors by visual inspection. In the case of a statistical analysis of the measurements the error can be recognized, in particular, if a comparison with independent measurements takes place. Table 6.1 summarizes a range of the systematic out-of-plane error for different in-plane shifts. It can be observed that a mismatch of a fraction of the interrogation window size can already cause errors which are much larger than all errors discussed in the previous sections. The relative error can easily reach 20% and more, which is not acceptable in real experiments. Furthermore, it must be noted that also the in-plane components are biased due to this error according to the stereoscopic equations.

To compensate this error it is recommended to use the calibration image to deform the measured images so that the perspective distortion vanishes. Next a correlation can be performed between the left and right images recorded at the same time. As the particle image field should be almost identical the displacement field should be zero if the mismatch between the images is zero and the correspondence perfect. However, if any misalignment is present, the correlation between deformed images taken at the same instant of time will result in a displacement field which indicates the disparity between the independent measurements with a stereoscopic system. Now the information of the disparity map can be used to shift both fields with respect to each other such that the disparity vanishes after another cross-correlation. This approach was first applied in [14] and is further discussed in Sect. 8.1.4. As the

disparity map yields only information about the relative shift it is not known if only one or both camera views are affected. Therefore, this compensation of the mismatch results in velocity measurements with lower error but the position of the vector in physical space becomes more uncertain as long as the absolute direction of the shift is not known. However, the position error is usually not as significant as long as the flow gradients are weak (see e.g. [16]).

References

1. Adrian, R.J.: Dynamic ranges of velocity and spatial resolution of particle image velocimetry. *Meas. Sci. Technol.* **8**(12), 1393–1398 (1997). DOI 10.1088/0957-0233/8/12/003. URL <https://doi.org/10.1088/0957-0233/8/12/003>
2. Charonko, J.J., Vlachos, P.P.: Estimation of uncertainty bounds for individual particle image velocimetry measurements from cross-correlation peak ratio. *Meas. Sci. Technol.* **24**(6), 065301 (2013). DOI 10.1088/0957-0233/24/6/065301. URL <http://stacks.iop.org/0957-0233/24/i=6/a=065301>
3. Chen, J., Katz, J.: Elimination of peak-locking error in PIV analysis using the correlation mapping method. *Meas. Sci. Technol.* **16**(8), 1605 (2005). DOI 10.1088/0957-0233/16/8/010. URL <http://stacks.iop.org/0957-0233/16/i=8/a=010>
4. Christensen, K.T.: The influence of peak-locking errors on turbulence statistics computed from PIV ensembles. *Exp. Fluids* **36**(3), 484–497 (2004). DOI 10.1007/s00348-003-0754-2. URL <http://dx.doi.org/10.1007/s00348-003-0754-2>
5. Christensen, K.T., Scarano, F.: Uncertainty quantification in particle image velocimetry. *Meas. Sci. Technol.* **26**(7), 070201 (2015). DOI 10.1088/0957-0233/26/7/070201. URL <http://stacks.iop.org/0957-0233/26/i=7/a=070201>
6. Cowen, E.A., Monismith, S.G.: A hybrid digital particle tracking velocimetry technique. *Exp. Fluids* **22**(3), 199–211 (1997). DOI 10.1007/s003480050038. URL <http://dx.doi.org/10.1007/s003480050038>
7. Eckstein, A.C., Charonko, J., Vlachos, P.: Phase correlation processing for DPIV measurements. *Exp. Fluids* **45**(3), 485–500 (2008). DOI 10.1007/s00348-008-0492-6. URL <http://dx.doi.org/10.1007/s00348-008-0492-6>
8. Huang, H.T., Fiedler, H.E., Wang, J.J.: Limitation and improvement of PIV, Part II. Particle image distortion, a novel technique. *Exp. Fluids* **15**(4–5), 263–273 (1993). DOI 10.1007/BF00223404. URL <http://dx.doi.org/10.1007/BF00223404>
9. Kähler, C.J.: Ortsaufgelöste Geschwindigkeitsmessungen in einer turbulenten Grenzschicht. Technical report, DLR, Göttingen, Germany (1997). DLR-FB-1997-32
10. Kähler, C.J.: Multiplane stereo PIV - recording and evaluation methods. In: *EUROMECH 411: Application of PIV to Turbulence Measurements*, University of Rouen, France (2000)
11. Kähler, C.J.: The significance of coherent flow structures for the turbulent mixing in wall-bounded flows. Ph.D. thesis, Georg-August-University zu Göttingen, Germany (2004). URL <http://hdl.handle.net/11858/00-1735-0000-0006-B4C8-8.DLR-FB-2004-24>
12. Kähler, C.J., Kompenhans, J.: Multiple plane stereo PIV – technical realization and fluid-mechanical significance. In: *3rd International Workshop on PIV*, Santa Barbara, USA (1999)
13. Kähler, C.J., Kompenhans, J.: Fundamentals of multiple plane stereo particle image velocimetry. *Exp. Fluids* **29**(1), S070–S077 (2000). DOI 10.1007/s003480070009. URL <http://dx.doi.org/10.1007/s003480070009>
14. Kähler, C.J., Adrian, R.J., Willert, C.E.: Turbulent boundary layer investigations with conventional and stereoscopic particle image velocimetry. In: *9th International Symposium on Applications of Laser Techniques to Fluid Mechanics*, Lisbon, Portugal (1998)

15. Kähler, C.J., Scharnowski, S., Cierpka, C.: On the resolution limit of digital particle image velocimetry. *Exp. Fluids* **52**(6), 1629–1639 (2012). DOI 10.1007/s00348-012-1280-x. URL <http://dx.doi.org/10.1007/s00348-012-1280-x>
16. Kähler, C.J., Scharnowski, S., Cierpka, C.: On the uncertainty of digital PIV and PTV near walls. *Exp. Fluids* **52**(6), 1641–1656 (2012). DOI 10.1007/s00348-012-1307-3. URL <http://dx.doi.org/10.1007/s00348-012-1307-3>
17. Kähler, C.J., Scharnowski, S., Cierpka, C.: Highly resolved experimental results of the separated flow in a channel with streamwise periodic constrictions. *J. Fluid Mech.* **796**, 257–284 (2016). DOI 10.1017/jfm.2016.250. URL <http://dx.doi.org/10.1017/jfm.2016.250>
18. Kähler, C.J., Astarita, T., Vlachos, P.P., Sakakibara, J., Hain, R., Discetti, S., La Foy, R., Cierpka, C.: Main results of the 4th international PIV challenge. *Exp. Fluids* **57**(6), 97 (2016). DOI 10.1007/s00348-016-2173-1. URL <http://dx.doi.org/10.1007/s00348-016-2173-1>
19. Keane, R.D., Adrian, R.J.: Optimization of particle image velocimeters. I. Double pulsed systems. *Meas. Sci. Technol.* **1**(11), 1202 (1990). DOI 10.1088/0957-0233/1/11/a=013. URL <http://stacks.iop.org/0957-0233/1/i=11/a=013>
20. Keane, R.D., Adrian, R.J.: Optimization of particle image velocimeters: II. Multiple pulsed systems. *Meas. Sci. Technol.* **2**(10), 963 (1991). DOI 10.1088/0957-0233/2/10/013. URL <http://stacks.iop.org/0957-0233/2/i=10/a=013>
21. Keane, R.D., Adrian, R.J.: Theory of cross-correlation analysis of PIV images. *Appl. Sci. Res.* **49**(3), 191–215 (1992). DOI 10.1007/BF00384623. URL <https://dx.doi.org/10.1007/BF00384623>
22. Keane, R.D., Adrian, R.J., Zhang, Y.: Super-resolution particle imaging velocimetry. *Meas. Sci. Technol.* **6**(6), 754 (1995). DOI 10.1088/0957-0233/6/6/013. URL <http://stacks.iop.org/0957-0233/6/i=6/a=013>
23. Lawson, N.J., Wu, J.: Three-dimensional particle image velocimetry: experimental error analysis of a digital angular stereoscopic system. *Meas. Sci. Technol.* **8**(12), 1455 (1997). DOI 10.1088/0957-0233/8/12/009. URL <http://stacks.iop.org/0957-0233/8/i=12/a=009>
24. Masullo, A., Theunissen, R.: Adaptive vector validation in image velocimetry to minimise the influence of outlier clusters. *Exp. Fluids* **57**(3), 33 (2016). DOI 10.1007/s00348-015-2110-8. URL <http://dx.doi.org/10.1007/s00348-015-2110-8>
25. Michaelis, D., Neal, D.R., Wieneke, B.: Peak-locking reduction for particle image velocimetry. *Meas. Sci. Technol.* **27**(10), 104005 (2016). DOI 10.1088/0957-0233/27/10/104005. URL <http://stacks.iop.org/0957-0233/27/i=10/a=104005>
26. Neal, D.R., Sciacchitano, A., Smith, B.L., Scarano, F.: Collaborative framework for PIV uncertainty quantification: the experimental database. *Meas. Sci. Technol.* **26**(7), 074003 (2015). DOI 10.1088/0957-0233/26/7/074003. URL <http://stacks.iop.org/0957-0233/26/i=7/a=074003>
27. Nerger, D., Kähler, C.J., Radespiel, R.: Zeitaufgelöste PIV-Messungen an einem schwingenden SD7003-Profil bei $re = 6 \times 10^4$. *Lasermethoden in der Strömungsmechanik*, GALA eV, Braunschweig, Germany (2003). URL <http://www.gala-ev.org/images/Beitraege/Beitraege>
28. Nobach, H., Bodenschatz, E.: Limitations of accuracy in PIV due to individual variations of particle image intensities. *Exp. Fluids* **47**(1), 27–38 (2009). DOI 10.1007/s00348-009-0627-4. URL <http://dx.doi.org/10.1007/s00348-009-0627-4>
29. Nogueira, J., Lecuona, A., Rodriguez, P.: Local field correction PIV: on the increase of accuracy of digital PIV systems. *Exp. Fluids* **27**(2), 107–116 (1999). DOI 10.1007/s003480050335. URL <http://dx.doi.org/10.1007/s003480050335>
30. Overmars, E.F.J., Warncke, N.G.W., Poelma, C., Westerweel, J.: Bias errors in PIV: the pixel locking effect revisited. In: 15th International Symposium on Applications of Laser Techniques to Fluid Mechanics Lisbon, Portugal, 05–08 July 2010 (2010). URL http://ltces.dem.ist.utl.pt/lxaser/lxaser2010/upload/1787_ysdxtb_1.12.1.Full_1787.pdf
31. Ronneberger, O.: Measurement of all three velocity components with particle image velocimetry using a single camera and two parallel light sheets. Technical report, DLR, Göttingen, Germany (1998). URL <https://lmb.informatik.uni-freiburg.de/Publications/1998/Ron98/>. Diploma thesis, Universität Göttingen, Germany

32. Ronneberger, O., Raffel, M., Kompenhans, J.: Advanced evaluation algorithms for standard and dual plane particle image velocimetry. In: 9th International Symposium on Applications of Lasers to Fluid Mechanics, Lisbon, Portugal (1998)
33. Roth, G.I., Katz, J.: Five techniques for increasing the speed and accuracy of PIV interrogation. *Meas. Sci. Technol.* **12**(3), 238 (2001). DOI 10.1088/0957-0233/12/3/302. URL <http://stacks.iop.org/0957-0233/12/i=3/a=302>
34. Scarano, F.: Iterative image deformation methods in PIV. *Meas. Sci. Technol.* **13**(1), R1 (2002). DOI 10.1088/0957-0233/13/1/201. URL <https://dx.doi.org/10.1088/0957-0233/13/1/201>
35. Scarano, F., Riethmuller, M.L.: Advances in iterative multigrad PIV image processing. *Exp. Fluids* **29**(1), S051–S060 (2000). DOI 10.1007/s003480070007. URL <http://dx.doi.org/10.1007/s003480070007>
36. Scharnowski, S., Grayson, K., de Silva, C.M., Hutchins, N., Marusic, I., Kähler, C.J.: Generalization of the PIV loss-of-correlation formula introduced by Keane and Adrian, *Experiments in Fluids*, **58**(10), p.150 (2017). DOI 10.1007/s00348-017-2431-x. URL <https://doi.org/10.1007/s00348-017-2431-x>
37. Scharnowski, S., Kähler, C.J.: On the effect of curved streamlines on the accuracy of PIV vector fields. *Exp. Fluids* **54**(1), 1435 (2012). DOI 10.1007/s00348-012-1435-9. URL <http://dx.doi.org/10.1007/s00348-012-1435-9>
38. Scharnowski, S., Kähler, C.J.: Estimation and optimization of loss-of-pair uncertainties based on PIV correlation functions. *Exp. Fluids* **57**(2), 23 (2016). DOI 10.1007/s00348-015-2108-2. URL <http://dx.doi.org/10.1007/s00348-015-2108-2>
39. Scharnowski, S., Kähler, C.J.: On the loss-of-correlation due to PIV image noise. *Exp. Fluids* **57**(7), 119 (2016). DOI 10.1007/s00348-016-2203-z. URL <http://dx.doi.org/10.1007/s00348-016-2203-z>
40. Scharnowski, S., Statnikov, V., Meinke, M., Schröder, W., Kähler, C.J.: Combined experimental and numerical investigation of a transonic space launcher wake. In: EUCASS Proceedings Series - Advances in AeroSpace Sciences, Progress in Flight Physics, vol. 7, pp. 311–328 (2015). DOI 10.1051/eucass/201507311. URL <https://doi.org/10.1051/eucass/201507311>
41. Sciacchitano, A., Wieneke, B.: PIV uncertainty propagation. *Meas. Sci. Technol.* **27**(8), 084006 (2016). DOI 10.1088/0957-0233/27/8/084006. URL <http://stacks.iop.org/0957-0233/27/i=8/a=084006>
42. Sciacchitano, A., Scarano, F., Wieneke, B.: Multi-frame pyramid correlation for time-resolved PIV. *Exp. Fluids* **53**(4), 1087–1105 (2012). DOI 10.1007/s00348-012-1345-x. URL <http://dx.doi.org/10.1007/s00348-012-1345-x>
43. Sciacchitano, A., Wieneke, B., Scarano, F.: PIV uncertainty quantification by image matching. *Meas. Sci. Technol.* **24**(4), 045302 (2013). DOI 10.1088/0957-0233/24/4/045302. URL <http://stacks.iop.org/0957-0233/24/i=4/a=045302>
44. Sciacchitano, A., Neal, D.R., Smith, B.L., Warner, S.O., Vlachos, P.P., Wieneke, B., Scarano, F.: Collaborative framework for PIV uncertainty quantification: comparative assessment of methods. *Meas. Sci. Technol.* **26**(7), 074004 (2015). DOI 10.1088/0957-0233/26/7/074004. URL <http://stacks.iop.org/0957-0233/26/i=7/a=074004>
45. Stanislas, M., Okamoto, K., Kähler, C.J.: Main results of the first international PIV challenge. *Meas. Sci. Technol.* **14**(10), R63 (2003). DOI 10.1088/0957-0233/14/10/201. URL <http://stacks.iop.org/0957-0233/14/i=10/a=201>
46. Stanislas, M., Okamoto, K., Kähler, C.J., Westerweel, J.: Main results of the second international PIV challenge. *Exp. Fluids* **39**(2), 170–191 (2005). DOI 10.1007/s00348-005-0951-2. URL <http://dx.doi.org/10.1007/s00348-005-0951-2>
47. Stanislas, M., Okamoto, K., Kähler, C.J., Westerweel, J., Scarano, F.: Main results of the third international PIV challenge. *Exp. Fluids* **45**(1), 27–71 (2008). DOI 10.1007/s00348-008-0462-z. URL <http://dx.doi.org/10.1007/s00348-008-0462-z>
48. Sugii, Y., Nishio, S., Okuno, T., Okamoto, K.: A highly accurate iterative PIV technique using a gradient method. *Meas. Sci. Technol.* **11**(12), 1666 (2000). DOI 10.1088/0957-0233/11/12/303. URL <https://doi.org/10.1088/0957-0233/11/12/303>

49. Timmins, B.H., Wilson, B.W., Smith, B.L., Vlachos, P.P.: A method for automatic estimation of instantaneous local uncertainty in particle image velocimetry measurements. *Exp. Fluids* **53**(4), 1133–1147 (2012). DOI 10.1007/s00348-012-1341-1. URL <http://dx.doi.org/10.1007/s00348-012-1341-1>
50. Wereley, S.T., Meinhart, C.D.: Second-order accurate particle image velocimetry. *Exp. Fluids* **31**(3), 258–268 (2001). DOI 10.1007/s003480100281. URL <http://dx.doi.org/10.1007/s003480100281>
51. Westerweel, J.: Digital particle image velocimetry: theory and application. Ph.D. thesis, Mechanical Maritime and Materials Engineering, Delft University of Technology (1993). URL <http://repository.tudelft.nl/islandora/object/uuid:85455914-6629-4421-8c77-27cc44e771ed/datastream/OBJ/download>
52. Westerweel, J., Scarano, F.: Universal outlier detection for PIV data. *Exp. Fluids* **39**(6), 1096–1100 (2005). DOI 10.1007/s00348-005-0016-6. URL <http://dx.doi.org/10.1007/s00348-005-0016-6>
53. Wieneke, B.: Stereo-PIV using self-calibration on particle images. *Exp. Fluids* **39**(2), 267–280 (2005). DOI 10.1007/s00348-005-0962-z. URL <https://dx.doi.org/10.1007/s00348-005-0962-z>
54. Wieneke, B.: PIV uncertainty quantification from correlation statistics. *Meas. Sci. Technol.* **26**(7), 074002 (2015). DOI 10.1088/0957-0233/26/7/074002. URL <http://stacks.iop.org/0957-0233/26/i=7/a=074002>
55. Willert, C.E.: The fully digital evaluation of photographic PIV recordings. *Appl. Sci. Res.* **56** (2–3), 79–102 (1996). DOI 10.1007/BF02249375. URL <http://dx.doi.org/10.1007/BF02249375>
56. Willert, C.E., Gharib, M.: Digital particle image velocimetry. *Exp. Fluids* **10**(4), 181–193 (1991). DOI 10.1007/BF00190388. URL <https://dx.doi.org/10.1007/BF00190388>
57. Willert, C.E., Stasicki, B., Raffel, M., Kompenhans, J.: Digital video camera for application of particle image velocimetry in high-speed flows. In: S.S. Cha, J.D. Trolinger (eds.) *Optical Techniques in Fluid, Thermal, and Combustion Flow*, San Diego, CA, United States, vol. 2546, pp. 124–134 (1995). DOI 10.1117/12.221515. URL <http://dx.doi.org/10.1117/12.221515>
58. Wilson, B.M., Smith, B.L.: Uncertainty on PIV mean and fluctuating velocity due to bias and random errors. *Meas. Sci. Technol.* **24**(3), 035302 (2013). DOI 10.1088/0957-0233/24/3/035302. URL <http://stacks.iop.org/0957-0233/24/i=3/a=035302>
59. Xue, Z., Charonko, J.J., Vlachos, P.P.: Particle image pattern mutual information and uncertainty estimation for particle image velocimetry. *Meas. Sci. Technol.* **26**(7), 074001 (2015). DOI 10.1088/0957-0233/26/7/074001. URL <http://stacks.iop.org/0957-0233/26/i=7/a=074001>

Chapter 7

Post-processing of PIV Data

The recording and evaluation of PIV images has been described in the previous two chapters. Investigations employing the PIV technique usually result in a great number of images which must be further processed. If looking for statistical quantities the recorded data can easily amount to some gigabytes, which can be handled with today's computer hardware. The amount of data has always been increasing and even more data per investigation are to be expected in future. Thus, it is quite obvious that a fast, reliable and fully automatic post-processing of the PIV data is essential. Moreover, with the need to inspect large amount of data, extracting essential features of interest need to be based on objective and criteria and well established procedures.

In principle, post-processing of PIV data is characterized by the following steps:

Validation of the raw data. After automatic evaluation of the PIV recordings, a certain number of obviously incorrectly determined velocity vectors (outliers) can usually be found by visual inspection of the raw data. In order to detect these incorrect data, the raw flow field data have to be validated. For this purpose, special algorithms have to be developed, which must work automatically.

Replacement of incorrect data. For most post-processing algorithms (e.g. calculation of vector operators) it is required to have complete data fields on a Cartesian mesh as often the case for numerically obtained data. Such algorithms will not work if data gaps are present in the experimental set. Thus, the gaps need to be filled with an estimated value of the velocity. Criteria for a consistent and accurate vector replacement in the experimental data must be developed.

Data reduction. It is quite difficult to inspect several hundred or thousands velocity vector maps and to describe their fluid mechanical features. The task becomes even harder when dealing with three-dimensional data sets. Simple techniques like

An overview of the Digital Content to this chapter can be found at [\[DC7.1\]](#).

averaging (in order to extract the information about the mean flow and its fluctuations) are straightforward. However, when dealing with conditional sampling (e.g. phase averaging, in order to distinguish between periodic and non-periodic parts of the flow fluctuations) are of less straightforward formulation. Vector field operators (e.g. vorticity, divergence in order to detect structures in the flow) are also considered under the common denominator of data reduction. Furthermore, the evaluation of the structures dominating the dynamical behavior of unsteady flows requires the simplification of information by decomposition into modes. Proper orthogonal decomposition (POD, also known as principal component analysis, PCA) and dynamic mode decomposition (DMD) are the most followed approaches for the above purpose.

Data assimilation. In many cases, PIV experiments are conducted in flow regimes where the governing equations that relate to fundamental flow properties are known. A typical example is the principle of mass conservation, which translates into the divergence-free condition for the velocity in incompressible flows. Another example is the momentum equation, or its formulation in terms of vorticity dynamic equation. PIV data can be post-processed such to locally force it to obey these governing laws. Data assimilation of PIV data has fulfilled several purposes, from noise reduction, to the enhancement of spatial and temporal resolution. Potentially, this approach can also be used to fill measurement gaps or to extrapolate data from the measurement domain outwards.

Data display and animation. A number of software packages – commercial as well as in-house developed ones – are available for the graphical presentation of the PIV field data. It is also very important to support the easier understanding of a human observer of the main features of the flow field. This can be done by contour plotting, surface rendering, color coding, etc. Animation of the PIV data is very useful for better and more intuitive understanding of time series of PIV recordings or 3D data.

In the following sections those steps of post-processing with special requirements due to the PIV technique will be explained in greater detail.

7.1 Data Validation

The following describes some of the issues and methods relating to the validation of displacement data obtained in the PIV processing chain. Essentially all of today's PIV processing software perform data validation by default using a set of built-in robust schemes with default values that oftentimes lead to acceptable results. Robust data validation is also essential for the convergence of many of the advanced, multiple-pass, multi-scale PIV processing algorithms with the exact validation settings oftentimes buried deep inside the software algorithm.

In the following example the validation filters have been purposely turned off to demonstrate the nature of erroneous PIV data. Figure 7.1 shows the instantaneous turbulent flow field inside a channel of width 76 mm in a plane about 6 mm from the wall. The flow is from left to right and a mean convection velocity of 3 m/s has

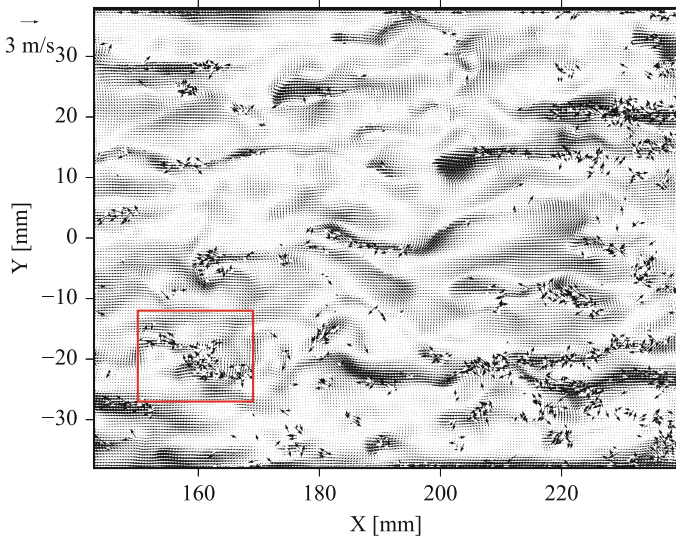


Fig. 7.1 Velocity vector map (raw data) of instantaneous flow field near the side wall of a square channel ($H = 76$ mm, $U_\infty = 3.5$ m/s, $\tau = 300$ μ s, $m = 26.1$ pixel/mm); a constant convection velocity of $U = 3.0$ m/s is subtracted

been subtracted in order to enhance details of the fluctuating flow field. Meandering structures, typically occurring in near-wall turbulent boundary layer are observed. Meanwhile “stray” or “spurious” vectors are also present throughout the measurement domain that do not match the surrounding areas. One such area, indicated by the rectangle, is enlarged in Fig. 7.2 for better visibility. When subjected to statistical evaluation, the velocity fluctuations due to physical flow process will be erroneously mixed with those given by the stray vectors. It is therefore of uppermost importance that the latter vectors are removed and replaced before further steps in the analysis are made.

Typical features of incorrect velocity vectors, some of which can be observed in Fig. 7.2, are that:

- their magnitude and direction differ considerably from their surrounding neighbors,
- in many cases they appear as isolated spurious vectors,
- they may also appear clustered in groups, sometimes pointing toward the same direction,
- they very often appear at the edges of the data field (near the surface of the model, at the edges of drop-out areas, at the edges of the illuminated area, in regions of increased out-of-plane motion or where a strong gradient is present).

From this description it can be concluded that it is most likely that during the evaluation procedure a correlation peak was detected which is due to noise or artifacts

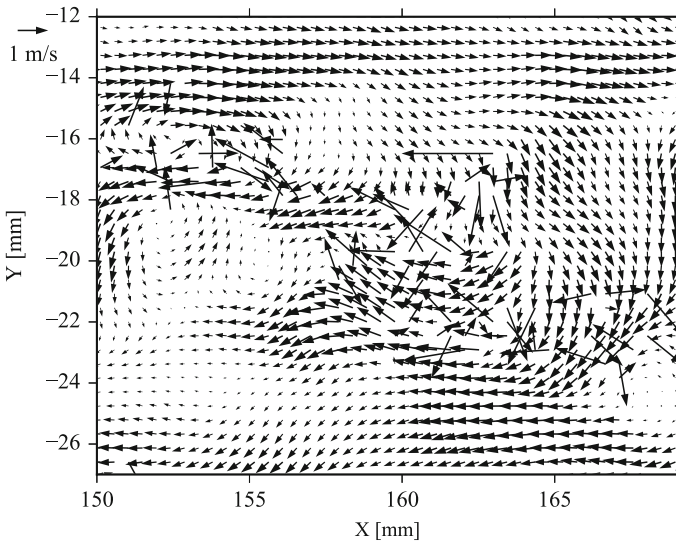


Fig. 7.2 Detail of Fig. 7.1 highlighting an area with increased number of erroneous vectors

(model surface, out-of-plane motion, noise of different sources, etc.) and not due to the correlation of properly matched image pairs. These questionable or spurious data points are frequently defined as *outliers*. In general an outlier may be defined as an observation (data point) which is very different from the rest of the data based on some measure.

Human perception is very efficient in detecting these outliers. For a small number of PIV recordings with few vectors, these erroneous velocity vectors may be treated interactively. This is no longer viable as both the number of vectors per data and the number of recordings increases. To illustrate: the data shown in Fig. 7.1 is one of 1000 recordings containing about 37,000 vectors each of which about 1% are outliers. However, for the further processing of the flow field data it is absolutely necessary to detect and exclude all such erroneous data. Clearly all subsequent operations, for instance involving differential operators and integration, applied to non-validated vector data would propagate these errors and could thus mask data of good quality, possibly even leading to misinterpretation of the data. This would affect differential operations for the estimation of the vorticity or divergence field or the calculation of differences between numerical and experimental flow field data. In contrast to this, the application of operations utilizing averaging processes over a great number of data, (e.g. mean value, variance, turbulence intensity, etc.) are less affected by a few incorrect data values, in part also because the erroneous data is often normally distributed such that its contribution cancels out in the statistics to a certain degree. It follows that all PIV data should generally be checked for erroneous data. Because of the great amount of data this can only be performed by means of an automatic

algorithm. Based on this a guiding principle for handling questionable data should be:

- The algorithm must ensure with a high level of confidence (99% or higher) that no questionable data are included in the final PIV data set.
- Any questionable data should be rejected, if the validation algorithm is inconclusive regarding the validity of the data.

As a consequence of the application of the validation algorithm, the number of PIV data obtained from a given recording will be reduced by a small percentage depending on the quality of the PIV recording and the type of flow to be investigated. Replacement of the detected outliers by means of interpolation or extrapolation should only be performed after completion of the data validation algorithm. It should be emphasized again that this procedure prevents information arising from incorrect data from being spread into areas with data of good quality. For the same reason no smoothing of the data should be carried out on data that has not been validated.

The challenge in data validation is to provide algorithms that strike a good balance between over-detection, that is the removal of valid data, and under-detection in which too many spurious vectors are accepted. The literature on this subject provides a large variety of validation algorithms for which a complete review is beyond the scope of this book. However, to date no general validation solution can be offered that will work for all PIV applications. Nonetheless, some degree of generalized validation is possible through the use of the normalized median filter proposed by WESTERWEEL

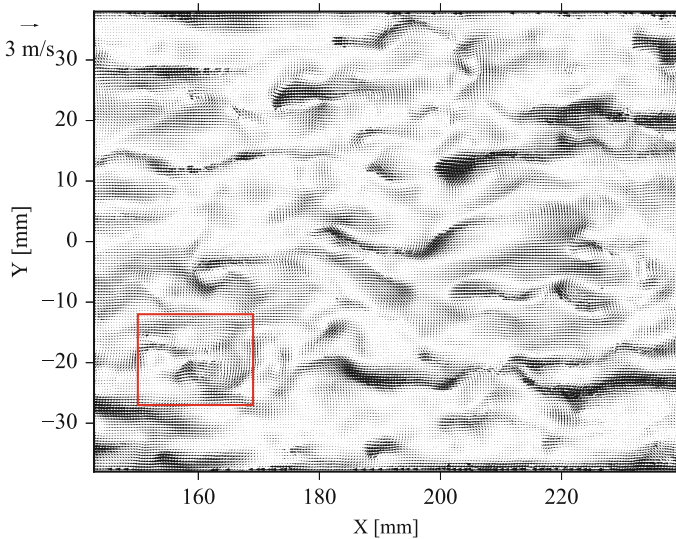


Fig. 7.3 Validated and interpolated velocity vector map of instantaneous flow field near the side wall of a square channel; a constant convection velocity of $U = 3.0$ m/s is subtracted

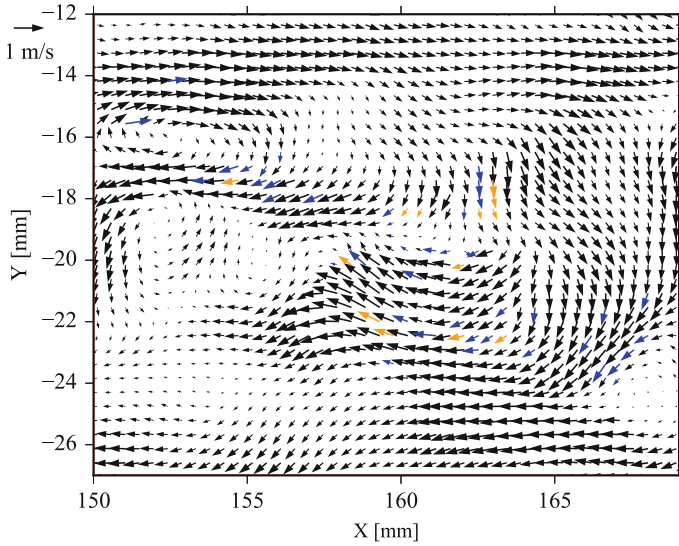
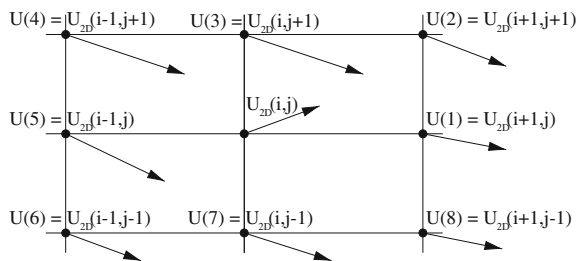


Fig. 7.4 Detail of validated data set indicated through rectangle in Fig. 7.3

& SCARANO [47] (see p. 250). Variable threshold approaches determine the detection threshold from filtered versions of the non-validated data set [17, 31]. Other validation approaches make use of a larger number of recordings to decompose a flow into its principal modes, for instance through proper value decomposition (POD), and use this information to detect outliers [11, 20]. Nowadays most PIV processing software use several validation algorithms in combination such that the overall detection rate is maximized. After completion of the validation procedure and interpolation of the gaps the previously noisy data set should appear as in Figs. 7.3 and 7.4.

Prior to describing a selection of validation algorithms some definitions are given in the following. The instantaneous velocity vector field (U, V) has been sampled (“interrogated”) at positions which form a regular grid in the flow field. In our case the grid, a part of which is shown in Fig. 7.5, consists of $I \times J$ grid points in the X and Y directions with constant distance $\Delta X_{\text{step}}, \Delta Y_{\text{step}}$ between neighboring grid points in both directions. The two-dimensional velocity vector at the position i, j ($i =$

Fig. 7.5 Sketch of data grid with notation of vectors



$1 \dots I, j = 1 \dots J$) is denoted $\mathbf{U}_{2D}(i, j)$. In the following discussion the relation between the central velocity vector $\mathbf{U}_{2D}(i, j)$ and one of its nearest neighbors $\mathbf{U}_{2D}(n)$ is considered. The nearest neighbors are labeled by n , ($n = 1, \dots, N$). Usually, N is chosen to be eight. The distance d between the central velocity vector $\mathbf{U}_{2D}(i, j)$ and its nearest neighbors $\mathbf{U}_{2D}(n)$ is either $\Delta X_{\text{step}}, \Delta Y_{\text{step}}$ or $(\Delta X_{\text{step}}^2 + \Delta Y_{\text{step}}^2)^{0.5}$, depending on its position on the grid. The magnitude of the vector difference between the central velocity vector $\mathbf{U}_{2D}(i, j)$ and $\mathbf{U}_{2D}(n)$ is $|\mathbf{U}_{\text{diff},n}| = |\mathbf{U}_{2D}(n) - \mathbf{U}_{2D}(i, j)|$.

7.1.1 Vector Difference Test

The gradient filter or vector difference filter computes the magnitude of the vector difference of a particular vector in question $\mathbf{U}_{2D}(i, j)$ to each of its four or eight neighbors $\mathbf{U}_{2D}(n)$:

$$|\mathbf{U}_{\text{diff},n}| = |\mathbf{U}_{2D}(n) - \mathbf{U}_{2D}(i, j)| < \varepsilon_{\text{thresh}} \quad \text{with} \quad \varepsilon_{\text{thresh}} > 0. \quad (7.1)$$

The basic idea is to count the number of instances for which the validation criterion $|\mathbf{U}_{\text{diff},n}| < \varepsilon_{\text{thresh}}$ is violated. A displacement vector can then be classified as questionable when it is ‘conflicting’ with at least half its neighbors. The test can be modified by applying it not only to the magnitude but also to the U and V components of the vector, or by utilizing a larger number of neighbors for comparison.

7.1.2 Median Test

PIV data validation by means of median filtering has been proposed by WESTERWEEL [45]. While median filtering is frequently utilized in image processing to remove spurious noise, it may also be used for the efficient treatment of spurious velocity vectors. Median filtering simply speaking means that all neighboring velocity vectors $\mathbf{U}_{2D}(n)$ are sorted linearly either with respect to the magnitude of the velocity vector, or their U and V components. The central value in this order (i.e. either the fourth or fifth of eight neighbors) is the median value. The velocity vector under inspection $\mathbf{U}_{2D}(i, j)$ is considered valid if

$$|\mathbf{U}_{2D}(\text{med}) - \mathbf{U}_{2D}(i, j)| < \varepsilon_{\text{thresh}}.$$

7.1.3 Normalized Median Test

A slight modification of the median test results in a very powerful validation scheme for spurious velocity vectors. WESTERWEEL & SCARANO [47] demonstrated that a

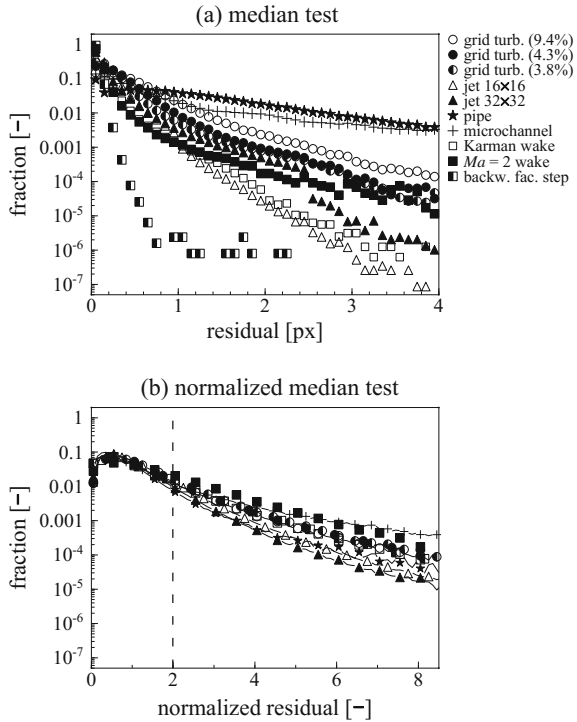
normalization of the standard median test given in Eq. (7.1.2) yields a rather universal probability density function for the residual such that a single threshold value can be applied to effectively detect spurious vectors. The normalization requires that the residual r_i , defined as: $r_i = |\mathbf{U}_i - \mathbf{U}_{\text{med}}|$ is first determined for each surrounding vector $\{\mathbf{U}_i | i = 1, \dots, 8\}$. Next the median of these eight residuals, r_{med} , is determined and used to normalize the standard median test as follows:

$$\frac{|\mathbf{U}_{2D}(\text{med}) - \mathbf{U}_{2D}(i, j)|}{r_{\text{med}} + \varepsilon_0} < \varepsilon_{\text{thresh}}$$

The additional term ε_0 is required to account for remaining fluctuations obtained from correlation analysis of otherwise quiescent or homogeneous flow. In practice this value should be set around 0.1–0.2 pixel, corresponding to the mean noise level of PIV data [46] (see also Sect. 6.1).

The efficiency of the normalized median test was demonstrated by WESTERWEEL & SCARANO [47] by applying it to a number of PIV experiments covering a wide range of Reynolds numbers. The probability density functions of both the standard and normalized median for these experiments is shown in Fig. 7.6. Integration of the histograms of the residual for the normalized median indicated that the 90-percentile occurs for $r_{\text{med}} \approx 2$. This meant that in all experiments investigated a single

Fig. 7.6 Histograms of the residuals using the conventional median (a) and the normalized median (b) for a wide variety of experimental data as presented by WESTERWEEL & SCARANO [47]



detection threshold labeled the largest 10% of residuals. The detection efficiency is less stringent for thresholds $r_{\text{med}} > 2$ and vice versa.

The universality of this detection scheme makes it especially well suited for iterative PIV interrogation schemes such as those presented in Sect. 5.3.4.2 and should be very suited for self-optimizing PIV algorithms. The method can be also extended for use with non-gridded data (e.g PTV data) using the distance of the neighboring points as a weighting factor [5].

7.1.4 Z-Score Test

Also known as Chauvenet's criterion, this validation filter operates globally and under the assumption that the data is normally distributed [34]. Given a set of N measurements u_1, \dots, u_N , the corresponding mean value μ_U and standard deviation σ_U , the data may be normalized with

$$Z_i = \frac{u_i - \mu_U}{\sigma_U} \quad (7.2)$$

with the mean $\mu_Z \equiv 0$. This normalization now lends itself for a validation based on the deviation of the value Z_i from zero in terms of the number of normal standard deviations. Choosing a threshold value Z_{thresh} a value u_i may be considered questionable if it does not satisfy the condition

$$|Z_i| < Z_{\text{thresh}} \quad (7.3)$$

In practice the threshold will have a value in the range of $Z_{\text{thresh}} = 3 \dots 5$. For normal distributed data the likelihood of values beyond a threshold $Z_{\text{thresh}} = 3$ is less than 0.3% such that, in principle, spurious vectors are very likely to be detected. For flow field data the test can be applied for each of the velocity components. However, due to the assumption that the data is normally distributed the performance of this filter depends on the nature of the flow field. For example, its application in homogenous turbulence is more suited than in a flow field containing regions of both uniform flow and turbulence (e.g. jet in cross-flow). Its suitability becomes increasingly questionable as the probability density function of the velocity departs from a normal distribution, as illustrated in the following example.

7.1.5 Global Histogram Operator

While the flow field shown in Fig. 7.1 has a certain degree of uniformity throughout the field of view, this is not necessarily always the case. Consider for instance the flow field shown in Fig. 7.7 for the transonic flow above a NACA0012 airfoil at a

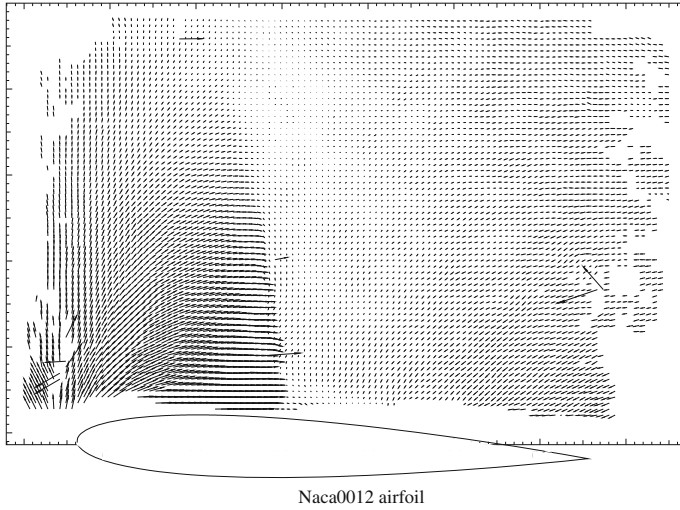
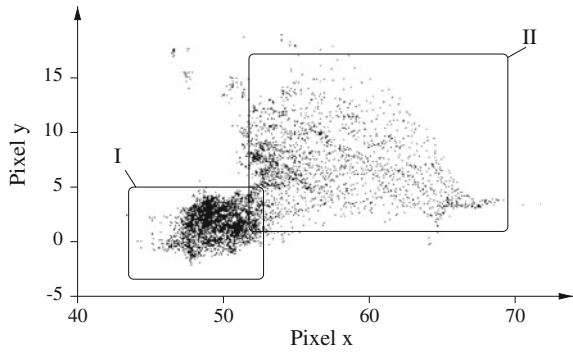


Fig. 7.7 Velocity vector map (raw data) of instantaneous flow field $(U - \bar{U}, V)$ above NACA 0012 airfoil ($Ma = 0.75, \alpha = 5^\circ, l_c = 20 \text{ cm}, \tau = 4 \mu\text{s}, \bar{U} = 344 \text{ m/s}$)

Fig. 7.8 Location of correlation peaks in the correlation plane. Rectangles indicate areas of plausible data, area (I) $Ma < 1$, (II) $Ma > 1$



free stream Mach number $Ma = 0.75$. The supersonic flow regime above the leading edge of the airfoil and the terminating shock with its strong velocity gradient can clearly be detected. Due to the velocity discontinuity across the shock some of the neighborhood-based validation filters may reject true measurement data in this area.

The data shown in Fig. 7.7 can also be presented in the form of two-dimensional histogram or joint probability distribution (PDF). In Fig. 7.8 each dot represents a single velocity vector or, equivalently, the position of the correlation peak in the correlation plane. Two separated areas of accumulated correlation peaks (velocity vectors) can be detected, one circular region (I) and a second region (II) with greater scattering of the peak's locations (i.e. of the velocity vectors). The area marked (I) is due to the subsonic part of the flow field, whereas the area (II) is due to the supersonic part of the flow field just above the leading edge of the airfoil. These areas could

be enclosed with suitable rectangular boxes or other enclosing areas such that all displacement peaks (velocity vectors) lying outside these regions will be marked and rejected. Most outliers due to noise in the correlation plane can be rejected by application of this simple algorithm.

Figure 7.8 also demonstrates that there may be situations with two or more areas in the correlation (or velocity) plane, where the peaks (or velocity vectors) accumulate, that is, the velocity data generally does not have a normal distribution. In the present case this is due to discontinuities in the flow field (i.e. shocks are embedded in the flow field). Summarizing, one can say that the global histogram operator employs physical arguments (upper and lower limit of possible flow velocities) to remove all data, which physically cannot exist in the flow field. Moreover, the inspection of the global velocity histogram gives useful information about the quality of the PIV evaluation (number of incorrect data due to noise, dynamic range of the flow field, maximum utilization of the optimal range for PIV evaluation by selecting the proper time delay between the light pulses for illumination, etc.).

7.1.6 Other Validation Filters

While fluid mechanical information can be used for validation, it is commonly only used indirectly by assuming that the investigated flow must observe a certain degree of continuity or coherency through the application of neighborhood operators. Another forms of data validation are possible through the use of redundant information that is available from time resolved, multi-frame PIV data [10] or from additional view points such as in stereo-PIV (see p. 289).

The following describes a few more validation methods which are of lesser importance for various reasons. Their performance in comparison to the previous methods is outlined in Table 7.1.

Dynamic Mean Value Operator

Many of the neighborhood based PIV validation schemes in the literature make use of mean value or difference tests by comparing each velocity vector individually with its immediate neighbors as described for the gradient filter on p. 249. However, the application of these tests has shown some problems if discontinuities (i.e. shocks) are present in the flow field. By incorporating the local variance the algorithm locally varies the threshold level ε for validation can thus deal with flows with strong velocity gradients.

Table 7.1 Various validation filters - outlier detection efficiency, number of required parameters and potential for self-optimization

Validation filter	Application	No. of params.	Detection efficiency	Automated optimization	Reference
Magnitude	Global	1	Poor	Simple	–
Range	Global	2–4	Medium	Simple	p. 252
Difference	Local	1	High	Possible	p. 249
Median	Local	1	High	Possible	p. 249
Normalized median	Local	1	High	Simple	p. 250
Z-score	Global	1	Medium	Simple	p. 250
Dynamic mean	Local	2	Medium	Difficult	p. 253
Minimum correlation	Global	1	Poor	Possible	p. 254
Correlation peak ratio	Global	1	Poor	Difficult	p. 254
Correlation SNR	Global	1	Poor	Simple	p. 254
3C residuals ^a	Global	1	High	Simple	p. 289

^aOnly for reconstructed stereo PIV data

The local mean vector μ_U is calculated from the $N = 8$ closest neighbors:

$$\mu_U(i, j) = \frac{1}{N} \sum_{n=1}^N U_{2D}(n) . \quad (7.4)$$

The averaged magnitude or variance σ_U^2 of the vector difference between the average vector μ_U and its 8 neighbors is also calculated:

$$\sigma_U^2(i, j) = \frac{1}{N} \sum_{n=1}^N (\mu_U(i, j) - U_{2D}(n))^2 . \quad (7.5)$$

The criterion for data validation is:

$$|\mu_U(i, j) - U_{2D}(i, j)| < \varepsilon_{\text{thresh}} \quad (7.6)$$

$$\varepsilon_{\text{thresh}} = C_1 + C_2 \sigma_U(i, j) \quad (7.7)$$

with $C_1, C_2 =$ constants which have to be determined once for a given experiment and can then be utilized for the whole series of PIV recordings.

Minimum Correlation Filter

As mentioned earlier, a low correlation coefficient is indicative of a strong loss a particle match and may have a variety of causes. Thus, a validation filter may be very helpful in detecting problematic areas in the field of view. However it is of lesser importance for the actual validation of PIV data, as low correlation values do not necessarily point to invalid displacement readings.

Peak Height Ratio Filter

In this case the correlation peak representative of the displacement reading is compared to the first noise peak in the correlation map. A low ratio of the peak heights may point to an inadequately seeded area and a higher likelihood that the measured displacement is questionable. In terms of validation it is less effective because mismatched areas may have high correlation coefficients especially when seeding levels are low.

Signal-to-Noise Filter

Here the signal-to-noise ratio in the correlation plane – defined as the quotient of correlation peak height with respect to the mean correlation level – is used to validate the data. However its use is questionable because mismatched particle images or stationary background features can also produce high levels of correlation.

POD-Based Validation

The use of proper orthogonal decomposition for the purpose of PIV data validation is based on the assumption that spurious vectors are not correlated with specific flow features. Therefore, their occurrence is mostly random. Once the dataset is decomposed in orthogonal modes, the highest in rank represent the dominant physical fluctuations of velocity. The energy in the lowest rank modes is mostly representative of random errors and spurious vectors. Decomposing the data set with POD and performing a low order reconstruction (based for instance on 95% of the total energy) is a robust technique to eliminate erroneous vectors and at the same time replacing them with a realistic estimate. The latter shall be solely regarded as an empirical criterion for reference. If the reconstruction is truncated too early, the result will underestimate the flow fluctuations. Conversely, including too many modes (late truncation) will not be effective in removing the spurious vectors. Recent studies have focused on determining a universal criterion for truncating the reconstruction such that the reliability (lowest number of outliers) [11] or the accuracy (lowest level of random error) [21] of the result is maximized.

7.1.7 Implementation of Data Validation Algorithms

Since there is no unique validation filter suitable for all applications, the common approach has been to apply a combination of several different filters in succession. By

adjusting the validation parameters individually for each filter, high data validation rates can be achieved even if the individual filters are not operating at their optimum. This strategy is especially attractive when processing larger data sets.

A successful validation procedure should be to collect as much a priori information about the flow field to be investigated as possible and to express this knowledge in the form of fluid mechanical or image processing operators. The first simple fluid mechanical operators were already introduced in the 1990s [4] and are nowadays quite far developed (see e.g. [3]).

7.2 Replacement Schemes

After having validated all PIV data it is possible to fill in missing data using, for instance, bilinear interpolation. According to WESTERWEEL [45] the probability that there is another spurious vector in the direct neighborhood of a spurious vector is given by a binominal distribution. For instance, if the data contains 5% spurious vectors, more than 80% of the data can be recovered by a straight bilinear interpolation from the four valid neighboring vectors (incidentally, the bilinear interpolation also fulfills continuity). The remaining missing data can be estimated by using some sort of weighted average of the surrounding data, such as the adaptive Gaussian window technique proposed by AGÜI & JIMÉNEZ [1].

Some post-processing methods also require smoothing of the data. The reason is that the experimental data is affected by noise in contrast to numerical data. A simple convolution of the data with a 2×2 , 3×3 or larger smoothing kernel (with equal weights) is generally sufficient for this purpose. By choosing the kernel size to have spatial dimensions smaller than the effective interrogation window size, additional lowpass filtering of the velocity field can be minimized. Median filtering is another effective means for spurious noise reduction.

High-quality PIV data typically exhibits less than 1% of spurious vectors under regular conditions and less than 5% in rather challenging experimental situations. Replacement schemes should therefore not be used thoughtlessly if the amount of spurious vectors is (locally) larger than that.

The low order reconstruction based on POD is an approach that simultaneously replaces spurious vectors and reduces the random errors. In principle, a single parameter needs to be chosen, which is the fraction of cumulative energy where truncating the modes used for reconstruction. In this respect, POD offers a rather simple solution to the problem of data validation and vector replacement.

7.3 Data Assimilation Techniques

There is an increased interest in connecting the growing capabilities of computer simulations to enhance measurement data and vice-versa. The techniques that aim

at performing these operations are considered under the category of data assimilation. The number of research articles in this area is growing, as data assimilation can be used in multiple directions, from stabilizing [32] to conditioning computer simulations towards a preferred solution [33].

7.3.1 Error Minimization

The discussion herein is limited to the simpler case of incompressible flows, where mass conservation is written in differential form as

$$\frac{\partial U}{\partial X} + \frac{\partial V}{\partial Y} + \frac{\partial W}{\partial Z} = 0 \quad (7.8)$$

PIV data from planar measurements cannot be easily treated with this equation because the out-of-plane term $\frac{\partial W}{\partial Z}$ cannot be accounted for. Instead, for three-dimensional data issued for instance by scanning PIV, holographic or tomographic PIV, imposing Eq. (7.8) can be used to reduce the amount of measurement noise [25].

7.3.2 Enhancing Temporal Resolution

Based on Eq. (7.9) in PIV data the time-advancing term can be estimated from the other terms on the right hand side. This approach leads to time advancing a PIV instantaneous velocity and vorticity field solely based on the existing data set. The main use of this approach is to estimate the temporal behavior of the flow even by measurements that do not capture the time scales at a rate dictated by Nyquist criterion. This technique is referred to as time-supersampling and it has shown the ability to reconstruct the velocity time history and spectrum from undersampled

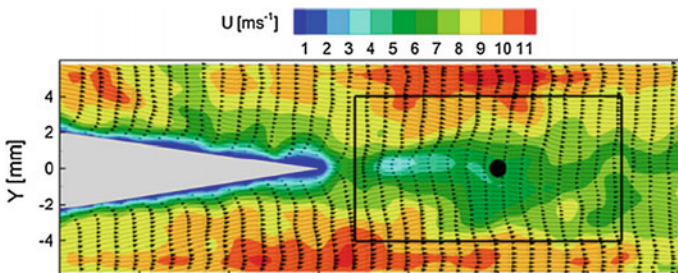


Fig. 7.9 Instantaneous velocity field at the trailing edge of a NACA0012 airfoil. The black circle indicates the point where the velocity time history is evaluated

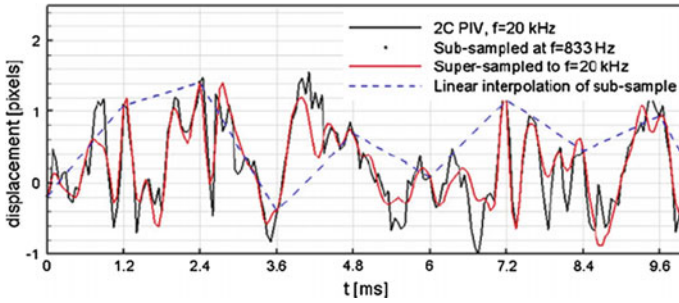
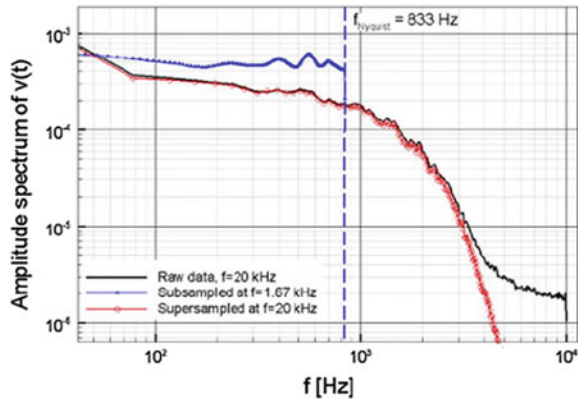


Fig. 7.10 Time history of vertical velocity component. Original measurements at 20 kHz (solid black line), samples extracted at 833 Hz (dots), super-sampled from 833 Hz to 20 kHz (solid red), linear interpolation of samples at 833 Hz (dashed blue) (A colored version of this figure can be found at [DC7.2].)

Fig. 7.11 Amplitude spectrum of vertical velocity fluctuations. Comparison between reference data at 20 kHz (black), subsampled at 1.67 kHz (blue) and super-sampled by advection (red). Nyquist limit for the subsampled data indicated in dashed blue line (A colored version of this figure can be found at [DC7.2].)



data [27]. The use of a simpler model such as local advection of velocity has proven useful for planar data where the full vorticity equation cannot be measured [23]. The velocity at a delayed time instant can be estimated from the velocity field with the assumption of frozen transport:

$$V(X, t + \Delta t) \approx V(X - V_{conv} \Delta t, t). \tag{7.9}$$

In the wake of an airfoil immersed in a stream at 14 m/s the velocity time history as well as its frequency spectrum, requiring a time resolution of 20 kHz according to Nyquist criterion, have been reconstructed from measurements at a sampling rate below 1 kHz (see Figs. 7.9, 7.10 and 7.11).

For three-dimensional data, the use of the vorticity equation has been proven of more general validity as it can reconstruct the time history and spectrum also for free shear flows with separation, where the frozen turbulence hypothesis does not hold [27].

7.3.3 Enhancing Spatial Resolution

The recent increase of interest in 3D PIV by means of Lagrangian particle tracking (e.g. Shake-The-Box [24]) has signaled the need to increase the spatial density of the velocity vectors for these intrinsically sparse measurements. Data assimilation techniques have proven a better ability than interpolators to “fill the empty space” between particle tracers. The most followed approach is that of minimizing a cost function obtained from the difference between the measured data and that obtained from a computer simulation.

A simple approach minimizes only the difference of the measured velocity, whereas, more constraints can be imposed if also the fluid acceleration [28] or the whole particle trajectory are known. Finding the optimum of the cost function in a computationally efficient manner makes use of adjoint techniques as demonstrated in recent works [26, 33].

7.4 Vector Field Operators

In many fluid mechanical applications the velocity information by itself is of secondary interest in the physical description, which is principally due to the lack of simultaneous pressure and density field measurements. In general the pressure, density and velocity fields are required to completely recover all terms in the Navier–Stokes equation:

$$\rho \frac{DU}{Dt} = -\nabla p + \mu \nabla^2 \mathbf{U} + \mathbf{F} \quad (7.10)$$

where \mathbf{F} represents the contribution of the body forces such as gravity. Efforts to obtain some of these field quantities in addition to the velocity field is subject of current research, which is partially realized by the application of several methods in parallel or through volume capturing methods such as tomographic PIV. Clearly, the task of obtaining all of these field quantities simultaneously is a remaining challenge. By itself, the planar velocity field obtained by PIV can already be used to estimate other fluid mechanically relevant quantities by means of differentiation or integration which will be outlined in the following.

Of the differential quantities the vorticity field is of special interest because this quantity, unlike the velocity, is independent of the frame of reference. In particular, if it is resolved temporally, the vorticity field can be much more useful in the study of flow phenomena than the velocity field by itself, especially in highly vortical flows such as turbulent boundary layers, wake vortices and complex vortical flows. For incompressible flows ($\nabla \cdot \mathbf{U} = 0$)¹ the Navier–Stokes equation can actually be rewritten in terms of the vorticity, that is the vorticity equation:

¹Incompressibility is a fairly stringent condition for Eq. (7.11). However, the pressure term vanishes and Eq. (7.11) holds, if $\nabla \rho \parallel \nabla p$, that is the fluid is barotropic.

$$\frac{\partial \boldsymbol{\omega}}{\partial t} + \mathbf{U} \cdot \nabla \boldsymbol{\omega} = \boldsymbol{\omega} \cdot \nabla \mathbf{U} + \nu \nabla^2 \boldsymbol{\omega} \quad (7.11)$$

which expresses the rate of change of vorticity of a fluid element (for simplicity, $\mathbf{F} = 0$). Although the pressure term has been eliminated from this expression, the estimation of the last term, $\nabla^2 \boldsymbol{\omega}$, is difficult from actual PIV data. Because of its frequent use in fluid mechanical descriptions, the estimation of vorticity from PIV data will serve as an example for the available differentiation schemes given in the following sections.

Integral quantities can also be obtained from the velocity field. The instantaneous velocity field obtained by PIV can also be integrated yielding either single values through path integrals or another field quantity such as the stream function. Analogous to the vorticity field, the circulation which is obtained through path integration is also of special interest in the study of vortex dynamics, mainly because it is also independent of the reference frame. Other PIV applications may require the calculation of mass flow rates in a control volume type of analysis. A crucial condition for the application of integral analysis is that the field of view allows for an appropriate choice of the integration path. The later sections of this chapter will be devoted to the aspects of integration.

7.5 Estimation of Differential Quantities

Before addressing the actual calculation schemes available for the differentiation of the velocity field data, it should be determined which terms can actually be calculated from the planar velocity field. Standard PIV data provide only the two components² of the three-dimensional vector field while more advanced PIV methods like stereoscopic PIV provide three-component velocity data. Unless several light sheet planes are recorded simultaneously, the classical 2C PIV implementation method can only provide a single plane of velocity data thereby excluding all possibilities of calculating gradients normal to the light sheet. In order to see which differential terms actually can be calculated, the full velocity gradient tensor or deformation tensor, $d\mathbf{U}/d\mathbf{X}$, will be given first:

$$\frac{d\mathbf{U}}{d\mathbf{X}} = \begin{bmatrix} \frac{\partial U}{\partial X} & \frac{\partial V}{\partial X} & \frac{\partial W}{\partial X} \\ \frac{\partial U}{\partial Y} & \frac{\partial V}{\partial Y} & \frac{\partial W}{\partial Y} \\ \frac{\partial U}{\partial Z} & \frac{\partial V}{\partial Z} & \frac{\partial W}{\partial Z} \end{bmatrix} \quad (7.12)$$

This deformation tensor can be decomposed into a symmetric part and an antisymmetric part:

²We ignore the fact that standard PIV only yields a two-dimensional projection of the three-dimensional vector.

$$\frac{d\mathbf{U}}{d\mathbf{X}} = \begin{bmatrix} \frac{\partial U}{\partial X} & \frac{1}{2} \left(\frac{\partial V}{\partial X} + \frac{\partial U}{\partial Y} \right) & \frac{1}{2} \left(\frac{\partial W}{\partial X} + \frac{\partial U}{\partial Z} \right) \\ \frac{1}{2} \left(\frac{\partial U}{\partial Y} + \frac{\partial V}{\partial X} \right) & \frac{\partial V}{\partial Y} & \frac{1}{2} \left(\frac{\partial W}{\partial Y} + \frac{\partial V}{\partial Z} \right) \\ \frac{1}{2} \left(\frac{\partial U}{\partial Z} + \frac{\partial W}{\partial X} \right) & \frac{1}{2} \left(\frac{\partial V}{\partial Z} + \frac{\partial W}{\partial Y} \right) & \frac{\partial W}{\partial Z} \end{bmatrix} + \begin{bmatrix} 0 & \frac{1}{2} \left(\frac{\partial V}{\partial X} - \frac{\partial U}{\partial Y} \right) & \frac{1}{2} \left(\frac{\partial W}{\partial X} - \frac{\partial U}{\partial Z} \right) \\ \frac{1}{2} \left(\frac{\partial U}{\partial Y} - \frac{\partial V}{\partial X} \right) & 0 & \frac{1}{2} \left(\frac{\partial W}{\partial Y} - \frac{\partial V}{\partial Z} \right) \\ \frac{1}{2} \left(\frac{\partial U}{\partial Z} - \frac{\partial W}{\partial X} \right) & \frac{1}{2} \left(\frac{\partial V}{\partial Z} - \frac{\partial W}{\partial Y} \right) & 0 \end{bmatrix} \quad (7.13)$$

A substitution of the strain and vorticity components yields:

$$\frac{d\mathbf{U}}{d\mathbf{X}} = \begin{bmatrix} \varepsilon_{XX} & \frac{1}{2}\varepsilon_{XY} & \frac{1}{2}\varepsilon_{XZ} \\ \frac{1}{2}\varepsilon_{YX} & \varepsilon_{YY} & \frac{1}{2}\varepsilon_{YZ} \\ \frac{1}{2}\varepsilon_{ZX} & \frac{1}{2}\varepsilon_{ZY} & \varepsilon_{ZZ} \end{bmatrix} + \begin{bmatrix} 0 & \frac{1}{2}\omega_Z & -\frac{1}{2}\omega_X \\ -\frac{1}{2}\omega_Z & 0 & \frac{1}{2}\omega_Y \\ -\frac{1}{2}\omega_X & \frac{1}{2}\omega_Y & 0 \end{bmatrix} \quad (7.14)$$

Thus the symmetric tensor represents the strain tensor with the elongational strains on the diagonal and the shearing strains on the off-diagonal, whereas the antisymmetric part contains only the vorticity components.

Given that conventional two-component PIV provides only the U and V velocity components and that this data can only be differentiated in the X and Y directions, only a few terms of the deformation tensor, $d\mathbf{U}/d\mathbf{X}$, can be estimated with PIV:

$$\omega_Z = \frac{\partial V}{\partial X} - \frac{\partial U}{\partial Y} \quad (7.15)$$

$$\varepsilon_{XY} = \frac{\partial U}{\partial Y} + \frac{\partial V}{\partial X} \quad (7.16)$$

$$\eta = \varepsilon_{XX} + \varepsilon_{YY} = \frac{\partial U}{\partial X} + \frac{\partial V}{\partial Y} \quad (7.17)$$

Therefore, only the vorticity component normal to the light sheet can be determined, along with the in-plane shearing and extensional strains. In this regard it is interesting to note that the additional availability of the third velocity component, W , by stereoscopic PIV methods, does not yield any additional strains or vorticity components.

Assuming incompressibility, that is, $\nabla \cdot \mathbf{U} = 0$, the sum of the in-plane extensional strains in Eq. (7.17) can be used to estimate the out-of-plane strain ε_{ZZ} :

$$\varepsilon_{ZZ} = \frac{\partial W}{\partial Z} = -\frac{\partial U}{\partial X} - \frac{\partial V}{\partial Y} = -\eta \quad (7.18)$$

However it should be kept in mind that the quantity η only indicates the presence of out-of-plane flow; it does not recover the out-of-plane velocity, W , which should be retrieved directly using stereo PIV for instance.

The multiplane stereo PIV technique (p. 560) can be used to estimate the full vorticity vector. The technique provides three-component velocity data at typically two slightly Z -displaced parallel planes, from which the out-of-plane differentials $\frac{\partial U_i}{\partial Z}$ can be estimated through central differences.

7.5.1 Standard Differentiation Schemes

Since PIV provides the velocity vector field sampled on a two-dimensional, evenly spaced grid, finite differencing has to be employed in the estimation of the spatial derivatives of the velocity gradient tensor, $d\mathbf{U}/d\mathbf{X}$. Moreover, each of the velocity data, U_i , is disturbed by noise, that is, a measurement uncertainty, ε_U . Although the error analysis used for the estimation of the uncertainty in the differentials assumes the measurement uncertainty of each quantity to be decoupled from its neighbors, this is not always the case. For instance, if the PIV image is oversampled, that is the interrogation interval (sample points) is smaller than the interrogation area dimensions ($\Delta X < \Delta X_0$ and/or $\Delta Y < \Delta Y_0$), the recovered velocity estimates are not independent because the neighboring interrogation areas partly sample the same particles. At low image densities, this problem worsens especially in regions of high displacement gradients (see also Fig. 6.25). For simplicity the differentiation schemes described in the next section assume the measurement uncertainties to be independent of their neighbors.

Table 7.2 First order differential operators for data spaced at uniform ΔX intervals along the X -axis

Operator	Implementation	Accuracy	Uncertainty
Forward difference	$\left(\frac{df}{dx}\right)_{i+1/2} \approx \frac{f_{i+1} - f_i}{\Delta X}$	$\mathcal{O}(\Delta X)$	$\approx 1.41 \frac{\varepsilon_U}{\Delta X}$
Backward difference	$\left(\frac{df}{dx}\right)_{i-1/2} \approx \frac{f_i - f_{i-1}}{\Delta X}$	$\mathcal{O}(\Delta X)$	$\approx 1.41 \frac{\varepsilon_U}{\Delta X}$
Central difference	$\left(\frac{df}{dx}\right)_i \approx \frac{f_{i+1} - f_{i-1}}{2\Delta X}$	$\mathcal{O}(\Delta X^2)$	$\approx 0.7 \frac{\varepsilon_U}{\Delta X}$
Richardson extrapol.	$\left(\frac{df}{dx}\right)_i \approx \frac{f_{i-2} - 8f_{i-1} + 8f_{i+1} - f_{i+2}}{12\Delta X}$	$\mathcal{O}(\Delta X^3)$	$\approx 0.95 \frac{\varepsilon_U}{\Delta X}$
Least squares	$\left(\frac{df}{dx}\right)_i \approx \frac{2f_{i+2} + f_{i+1} - f_{i-1} - 2f_{i-2}}{10\Delta X}$	$\mathcal{O}(\Delta X^2)$	$\approx 1.0 \frac{\varepsilon_U}{\Delta X}$

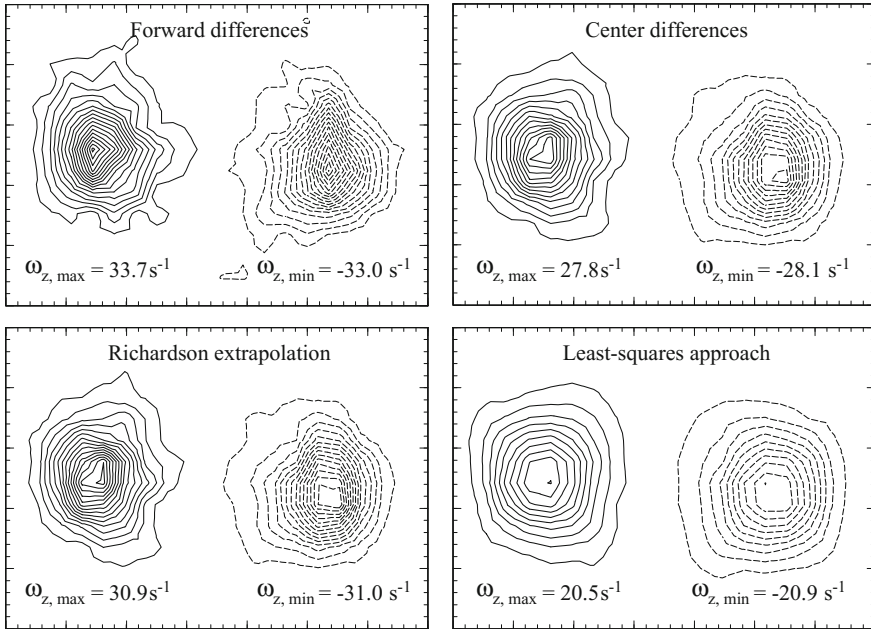


Fig. 7.12 Vorticity field estimates obtained from twice-oversampled PIV data, e.g. the interrogation window overlap is 50%. The vortex pair is known to be laminar and thus should have smooth vorticity contours

Table 7.2 lists a number of finite difference schemes to obtain estimates for the first derivative, df/dx , of a function $f(x)$ sampled at discrete locations $f_i = f(x_i)$. The “accuracy” in this table reflects the truncation error associated with derivation of each operator by means of Taylor series expansion. The actual uncertainty in the differential estimate due to the uncertainty in the velocity estimates ε_U can be obtained using standard error propagation methods assuming the individual data to be independent of each other.

The difference between the Richardson extrapolation scheme and the least squares approach is that the former is designed to minimize the truncation error while the latter attempts to reduce the effect of the random errors, that is, the measurement uncertainty, ε_U . The least squares approach therefore seems to be the most suitable method for PIV data. In particular, for oversampled velocity data where neighboring data are no longer uncorrelated, the Richardson extrapolation scheme along with the less sophisticated finite difference schemes will perform poorly with respect to the least-squares approach. On the other hand, the least-squares approach has a tendency to smooth the estimate of the differential because the outer data $f_{i\pm 2}$ are more weighted than the inner data $f_{i\pm 1}$.

The effect of oversampling on the estimation of the differential quantities is demonstrated in Fig. 7.12 for vorticity fields computed from the same velocity data at different mesh spacings. Since the data is taken from a laminar vortex pair, the vor-

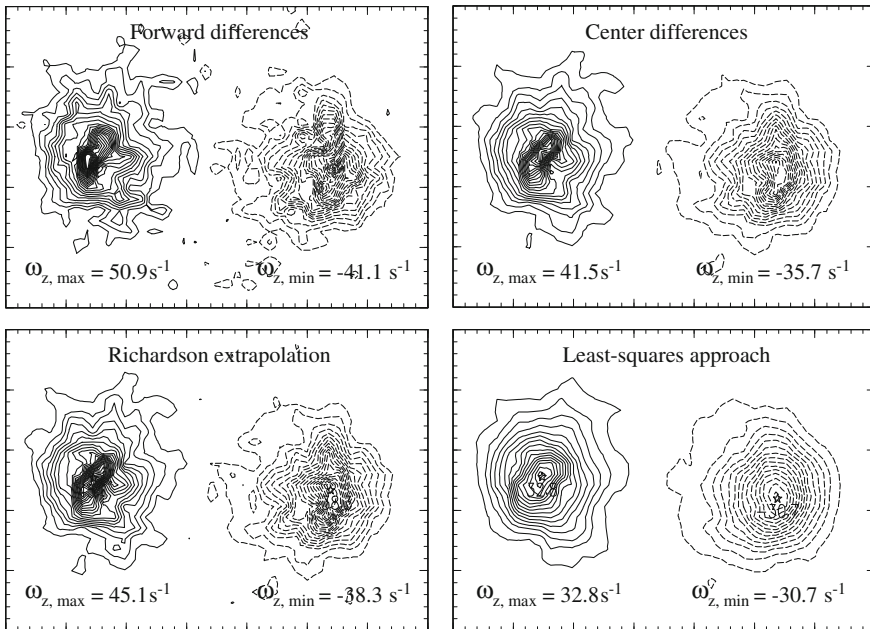


Fig. 7.13 Vorticity field estimates obtained from four times oversampled PIV data, e.g. the interrogation window overlap is 75%

ticity contours are expected to be smooth (data from [48]). For a 50% interrogation window overlap all schemes produce reasonable results since neighboring data are only weakly correlated. The estimate obtained from the forward difference scheme is the most noisy because the data entering in the formula are correlated (by 50% overlap) which is not the case for the center difference scheme.

By increasing the interrogation window overlap, such as in Fig. 7.13, much noisier vorticity fields are obtained which has two related causes: first the grid spacing, ΔX , ΔY , is reduced by a factor of two while the measurement uncertainty for the velocity, ε_U , stays the same. As a result the vorticity measurement uncertainty is doubled. Secondly, all or part of the data used in the differentiation scheme will be correlated because of the increased overlap. For instance velocity gradient induced bias errors will be similar in neighboring points which in turn results in a biased estimate of the vorticity. Thus, the estimation of differential quantities from the velocity field has to be optimized with respect to the grid spacing. A coarser grid not only yields less noisy estimates of the gradient quantity, but also results in a reduced spatial resolution.

The noise performance and frequency response of these as well as more advanced differentiation schemes have been investigated in further detail by FOUCAUT & STANISLAS [7], FOURAS & SORIA [8] and ETEBARI & VLACHOS [6]. In the following section, some alternative differentiation schemes are introduced.

7.5.2 Alternative Differentiation Schemes

The finite differencing formulae given in Table 7.2 have been derived for functions of one variable, that is, they are applied in one dimension at a time. Almost by definition, the velocity data obtained by PIV is provided on a two-dimensional grid which also holds for the differential quantities obtained from it. As a consequence, the use of one-dimensional finite difference schemes for the estimation of the two-dimensional differential field quantities seems inadequate. Using the estimation of the out-of-plane vorticity component, ω_z , as an example several alternative approaches to the problem of differential estimation will be given.

By definition the vorticity is related to the circulation by Stokes theorem

$$\Gamma = \oint \mathbf{U} \cdot d\mathbf{l} = \int (\nabla \times \mathbf{U}) \cdot d\mathbf{S} = \int \boldsymbol{\omega} \cdot d\mathbf{S} \tag{7.19}$$

where \mathbf{l} describes the path of integration around a surface S . The vorticity for a fluid element is found by reducing the surface S , and with it the path \mathbf{l} , to zero:

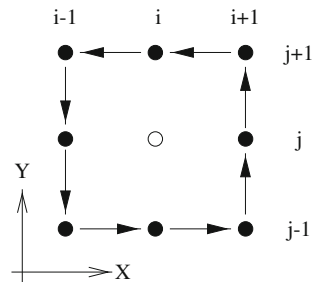
$$\hat{\mathbf{n}} \cdot \boldsymbol{\omega} = \hat{\mathbf{n}} \cdot \nabla \times \mathbf{U} = \lim_{S \rightarrow 0} \frac{1}{S} \oint \mathbf{U} \cdot d\mathbf{l} \tag{7.20}$$

where the unit vector $\hat{\mathbf{n}}$ is normal to the surface S . Stokes theorem can also be applied to the (X, Y) -gridded PIV velocity data:

$$(\bar{\omega}_z)_{i,j} = \frac{1}{A} \Gamma_{i,j} = \frac{1}{A} \oint_{l(X,Y)} (U, V) \cdot d\mathbf{l} \tag{7.21}$$

where $(\bar{\omega}_z)_{i,j}$ reflects the average vorticity within in the enclosed area. In practice Eq.(7.21) is implemented by choosing a small rectangular contour (Fig. 7.14, for instance two mesh points wide and two mesh points high) around which the circulation is calculated using a standard integration scheme such as the trapezoidal rule. The local circulation is then divided by the enclosed area to arrive at an average vorticity in this area. The following formula provides a vorticity estimate at point

Fig. 7.14 Contour for the circulation calculation used in the estimation of the vorticity at point (i, j)



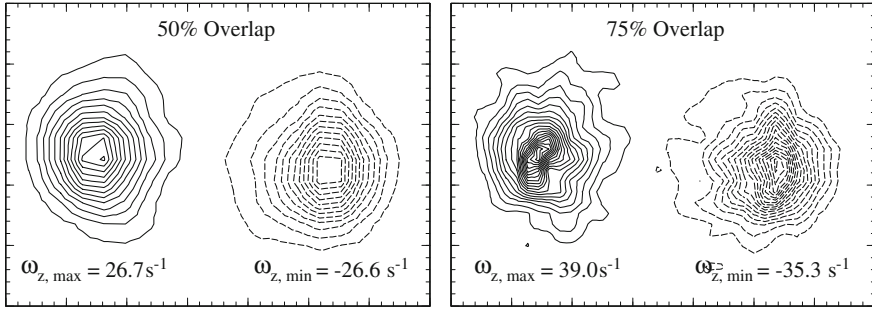


Fig. 7.15 Vorticity field estimates obtained from PIV velocity fields by the circulation method: (left) the velocity field is twice oversampled, (right) four times oversampled. The contours of this laminar vortex pair are known to be smooth such that the non-uniformities are due to measurement noise

(i, j) based on a circulation estimate around the neighboring eight points:

$$(\omega_z)_{i,j} \hat{=} \frac{\Gamma_{i,j}}{4\Delta X \Delta Y} \quad (7.22)$$

with

$$\begin{aligned} \Gamma_{i,j} = & \frac{1}{2} \Delta X (U_{i-1,j-1} + 2U_{i,j-1} + U_{i+1,j-1}) \\ & + \frac{1}{2} \Delta Y (V_{i+1,j-1} + 2V_{i+1,j} + V_{i+1,j+1}) \\ & - \frac{1}{2} \Delta X (U_{i+1,j+1} + 2U_{i,j+1} + U_{i-1,j+1}) \\ & - \frac{1}{2} \Delta Y (V_{i-1,j+1} + 2V_{i-1,j} + V_{i-1,j-1}) . \end{aligned} \quad (7.23)$$

Vorticity fields estimated by this expression are shown in Fig. 7.15. When compared to Figs. 7.12 and 7.13, this differentiation scheme clearly performs better, especially in the four-times oversampled data. The principle reason for this is that more data enter in each vorticity estimate. A closer inspection of Eq. (7.22) reveals that the expression is equivalent to applying the central difference scheme (Table 7.2) to a smoothed (3×3 kernel) velocity field [44]. While the vorticity estimation by one-dimensional finite differences (Table 7.2) requires only 4–8 velocity data values this expression utilizes 12 data values. The uncertainty in the vorticity estimate, assuming uncorrelated velocity data, then reduces to $\varepsilon_\omega \approx 0.61\varepsilon_U/\Delta X$ compared to $\varepsilon_\omega \approx \varepsilon_U/\Delta X$ for center differences or $\varepsilon_\omega \approx 1.34\varepsilon_U/\Delta X$ for the Richardson extrapolation method. Further effects due to data oversampling are not as significant as with some of the simpler one-dimensional differentiation schemes because no differences of directly adjoining data are used.

A similar approach may be used in the estimation of the shear strain and the out-of-plane strain.

$$\begin{aligned}
(\varepsilon_{xy})_{i,j} = \left(\frac{\partial U}{\partial Y} + \frac{\partial V}{\partial X} \right)_{i,j} \hat{=} & - \frac{U_{i-1,j-1} + 2U_{i,j-1} + U_{i+1,j-1}}{8\Delta Y} \\
& + \frac{U_{i+1,j+1} + 2U_{i,j+1} + U_{i-1,j+1}}{8\Delta Y} \\
& - \frac{V_{i-1,j+1} + 2V_{i-1,j} + V_{i-1,j-1}}{8\Delta X} \\
& + \frac{V_{i+1,j-1} + 2V_{i+1,j} + V_{i+1,j+1}}{8\Delta X} \quad (7.24)
\end{aligned}$$

$$\begin{aligned}
-(\varepsilon_{zz})_{i,j} = \left(\frac{\partial U}{\partial X} + \frac{\partial V}{\partial Y} \right)_{i,j} \hat{=} & \frac{V_{i-1,j-1} + 2V_{i,j-1} + V_{i+1,j-1}}{8\Delta Y} \\
& - \frac{V_{i+1,j+1} + 2V_{i,j+1} + V_{i-1,j+1}}{8\Delta Y} \\
& + \frac{U_{i+1,j-1} + 2U_{i+1,j} + U_{i+1,j+1}}{8\Delta X} \\
& - \frac{U_{i-1,j+1} + 2U_{i-1,j} + U_{i-1,j-1}}{8\Delta X} \quad (7.25)
\end{aligned}$$

For the out-of-plane or normal strain an analogy to the vorticity/circulation relation can be given: in place of the circulation the net flow across the boundaries of the contour is calculated. However, no such analogy exists for the shear strain, ε_{XY} . Figure 7.16 graphically illustrates the three differential estimation schemes described in this section.

Aside from the above mentioned techniques for differential estimation in PIV velocity data, the literature has suggested alternative methods. Earlier it was noted that the estimation uncertainty, ε_{Δ} , for the same differentiation scheme is directly proportional to the grid spacing (ΔX , ΔY), that is, $\varepsilon_{\Delta} \approx \varepsilon_U / \Delta X$. Once the interrogation window overlap exceeds 50%, the velocity data entering in the differentiation are increasingly correlated (i.e. biased) and cause the differential estimates to be biased. For these reasons LOURENÇO & KROTHAPALLI [15] suggested the use of an adaptive scheme for the computation of vorticity. The method is based on Richardson extrapolation and is aimed at minimizing the total error in the vorticity estimate by combining vorticity estimates at several different grid spacings. Even better results can be obtained by also including a least squares second order polynomial approximation in the differentiation scheme. The extension of this principally one-dimensional approach to differential estimation would certainly also be possible.

The task of differential estimation from velocity field data can also be studied from a two-dimensional signal processing point of view as suggested by NOGUEIRA et al. [17]. Linear filter theory is used to derive and optimize a variety of one- and

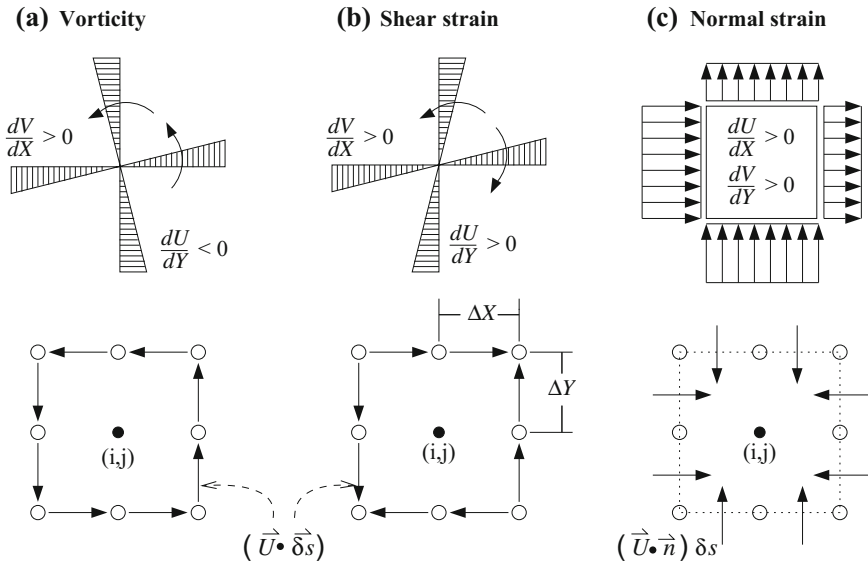


Fig. 7.16 Implementation of the three major differential quantities obtainable with planar PIV data. The deformation of the fluid element is given on top while the bottom shows the path of integration

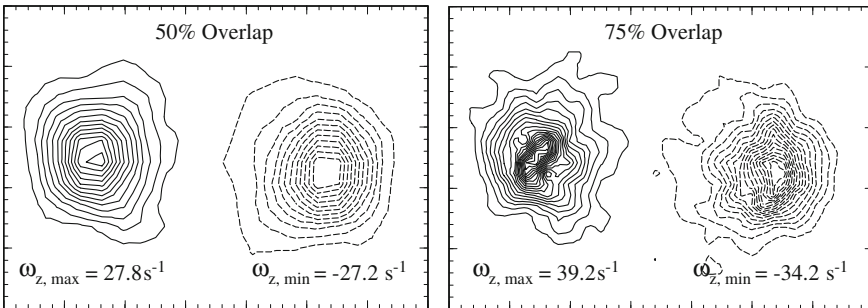


Fig. 7.17 Vorticity field estimates obtained from PIV velocity fields using a linear, two-dimensional filter: (left) the velocity field is twice-oversampled, (right) four times oversampled

two-dimensional differentiating filters whose performance is tested on noisy PIV data. Vorticity estimates from one such filter (f) are shown in Fig. 7.17. Compared to the circulation method Eq. (7.22) this differential filter is more susceptible to the side-effects of oversampling described before because it is designed to perform well at higher spatial frequencies.

7.5.3 Uncertainties and Errors in Differential Estimation

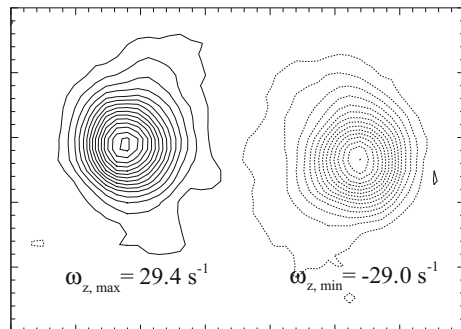
As already noted in the previous section a variety of factors enter in the uncertainty of a differential estimate.

Uncertainty in velocity: Each PIV velocity estimate $U_{i,j}$ is associated with a measurement uncertainty ε_U whose magnitude depends on a wide variety of aspects such as interrogation window size, particle image density, displacement gradients, etc. (see Sect. 6.1). Since differential estimates from the velocity data require the computation of local differences on neighboring data the noise increases inversely proportional to the local difference, $U_b - U_a$, as the spacing between the data $\Delta X = |X_a - X_b|$ is reduced. That is, the estimation uncertainty in the differential, ε_Δ , scales with $\varepsilon_U / \Delta X$.

Oversampled velocity data: It is common practice to oversample a PIV recording during interrogation at least twice in order to bring out small-scale features in the flow. Because of this oversampling, neighboring velocity data are estimated partially from the same particle images and therefore are correlated with each other. Because of this, neighboring data are likely to be biased to a similar degree, especially in regions containing high velocity gradients and/or low seeding densities. This localized velocity bias then causes the differential estimate to be biased as well. The oversampling effects can be observed very well by comparing Figs. 7.12 and 7.13.

The effect of oversampling is partially reduced through application of advanced processing schemes such as iterative image deformation techniques as introduced in Sect. 5.3.4.3. To illustrate this the vortex pair data shown in the previous section was processed by an image deforming algorithm at 75% overlap and differentiated using the circulation approach (Eq. (7.22)). In spite of the high oversampling the contours in Fig. 7.18 are smooth as expected from the laminar flow. In part this is a direct result of the smoothing applied during the intermediate processing steps of the processing algorithm. Nonetheless, the advanced processing algorithms are capable of providing nearly bias-free data where the choice of subsequent differentiation scheme is less critical.

Fig. 7.18 Vorticity estimate calculated from 75% overlapped PIV data using Eq. (7.22). Compared to the earlier examples an iterative image deformation PIV algorithm was first used to calculate the velocity data



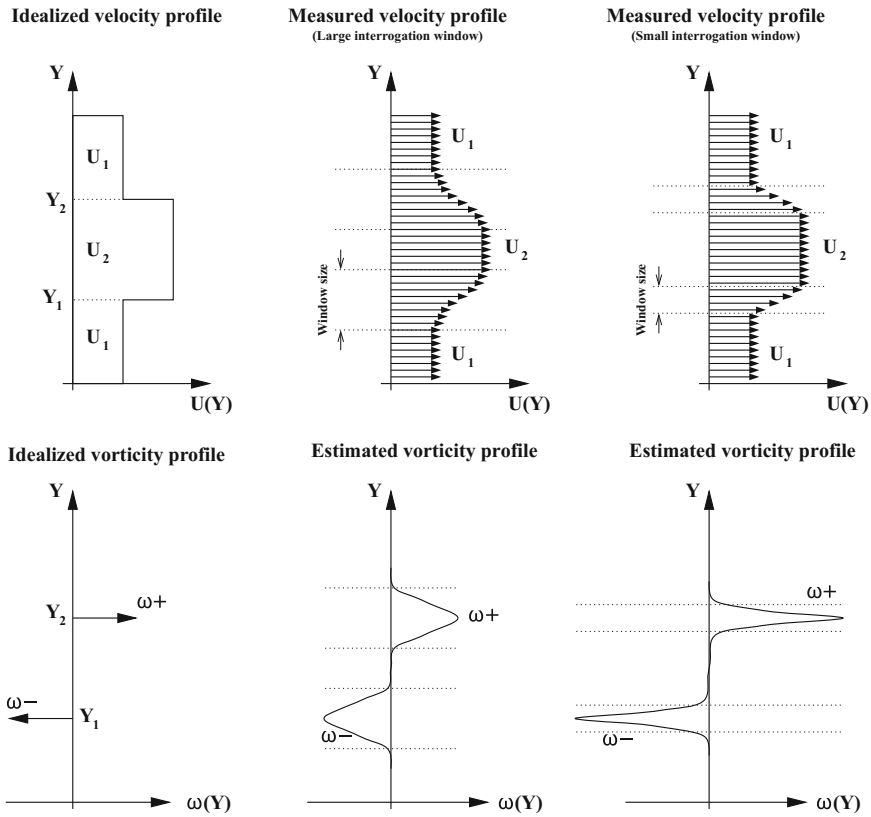


Fig. 7.19 Effect of spatial resolution on vorticity estimation

Interrogation window size: The size of the interrogation window in the object plane ($\Delta X_0 \times \Delta Y_0$) defines the spatial resolution in the recovered velocity data. The spatial resolution in the velocity field in turn limits the obtainable spatial resolution of the differential estimate. Depending on the utilized differentiation scheme the spatial resolution will be reduced to some degree due to smoothing effects. The effect of the interrogation window size on both the velocity as well as vorticity estimate is given in Fig. 7.19.

Curvature effects: The standard PIV method is only a first order approximation to the true particle image displacement. Since it generally relies on only two illumination pulses, effects due to acceleration and curvature are lost. In regions of rotating flow this straight line approximation underestimates the actual particle image displacement and thereby the local velocity. Differential estimates will then have a tendency to be biased to lower magnitudes as well. By reducing the illumination pulse delay, Δt , this effect can be reduced at the cost of increased noise in the differential estimate due to the velocity measurement uncertainty, ε_U , itself.

As pointed out by WERELEY & MEINHART [43] the symmetric offset of the interrogation windows during iterative processing provides second order accurate displacement estimates and thus reduces the effects of curvature because the displacement vector is attached to the midpoint between the offset samples.

7.6 Estimation of Integral Quantities

7.6.1 Path Integrals – Circulation

By definition, the vorticity integrated over an area A equals the circulation, Γ . Using Stokes theorem (Eq. (7.19)) this operation reduces to a line integral of the dot product between the local velocity vector, \mathbf{U} , and the incremental path element vector $d\mathbf{X}$ where the integration path is defined by the boundary, C , of the enclosed area A :

$$\Gamma = \int_A \omega \, dA \quad (7.26)$$

$$= \oint_C \mathbf{U} \cdot d\mathbf{X} \quad (7.27)$$

For two-component velocity data constrained to the XY plane with $\mathbf{U} = (U, V)$, the above equation reduces to:

$$\Gamma = \iint_{A(X,Y)} \omega_Z \, dX \, dY \quad (7.28)$$

$$= \oint_{C(X,Y)} \mathbf{U}(X, Y) \cdot d\mathbf{X} \quad (7.29)$$

$$= \oint_{C(X,Y)} U \, dX + V \, dY \quad (7.30)$$

Given the path of integration, the evaluation of Eq. (7.30) is straightforward using integration schemes such as the trapezoidal approximation or Simpson's rule. To determine the circulation of clearly defined, nearly round vortical structures, a circular integration path centered at the position of maximum vorticity is generally sufficient. By plotting the circulation with respect to integration path radius, an asymptotic convergence towards the value of the structure's circulation can be observed (provided no other vortices are included by the integration contour). This convergence coincides with a decay of vorticity away from the vortex core.

For more complex vortical structures the assignment of a reasonable integration path is not very simple. For vortical structures, the ideal integration path would be defined by a dividing stream line which separates it from other vortical structures. However, the computation of the required stream function from the unsteady velocity

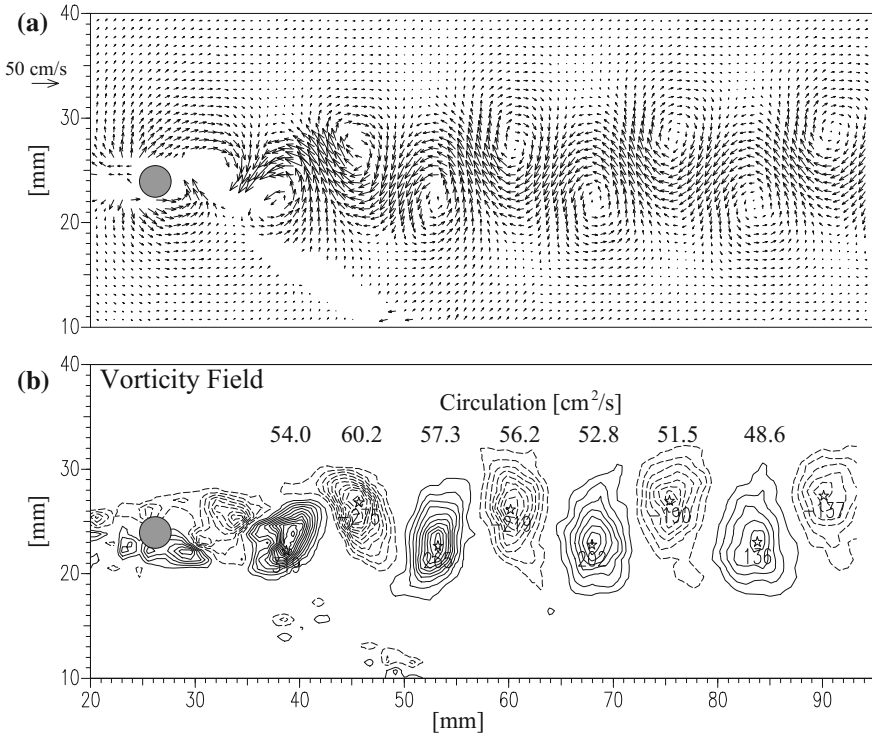


Fig. 7.20 The contours of the vorticity field are used as integration paths for the circulation whose magnitude is given above the individual vortices (data courtesy of SCHRÖDER [30])

data is nontrivial and often nonunique (see Sect. 7.6.3). Since the circulation actually is an area-integral of vorticity, an integration along a constant-vorticity contour near zero will evaluate to a value close to the vortex’s actual circulation. This approach was chosen, for instance, in the evaluation of the Karman vortex street data shown in Fig. 7.20. Although this approach is very robust, the difficulty often lies in retrieving the desired closed contour from the vorticity data. Once the contour is available, a bi-linear interpolation of the velocity on to the contour is sufficient for the evaluation of Eq. (7.30).

7.6.2 Path Integrals – Mass Flow

In some applications the rate mass or volume across a control surface, CS , is of interest and is expressed as a surface integral:

$$\dot{M} = \frac{dm}{dt} = \iint_{CS} \rho(\mathbf{U} \cdot \hat{\mathbf{n}}) dS \tag{7.31}$$

For two-dimensional data constrained to the XY plane, the surface reduces to a path integral similar to Eq. (7.30):

$$\dot{M}_{XY} = \frac{dm_{XY}}{dt} = \oint_C \rho(U dY - V dX) \tag{7.32}$$

The units of \dot{M}_{XY} are mass flow per unit depth and if $\rho \equiv 1$ then Eq. (7.32) represents a volume flow rate per unit depth. With regard to its numerical implementation, similar integration schemes as for the estimation of the circulation (Sect. 7.6.1) can be used.

In cases where three-dimensional velocity data is available in a plane, the actual mass (or volume) flow rate across this surface or portions thereof can be determined using an area integral:

$$\dot{M} = \iint_{A(X,Y)} W dX dY \tag{7.33}$$

where W is the velocity component normal to the light sheet. In this case the approximation of the integral is more complicated than for the previously described line integrals.

7.6.3 Area Integrals

The following integration schemes are based on the assumption that the integrand, that is, the flow field, is two-dimensional as well as incompressible. Further on, assuming the flow to be irrotational, potential theory relates the velocity field, $\mathbf{U} = (U(X, Y), V(X, Y))$, to the stream function, Ψ , and potential function, Φ :

$$U = \frac{\partial \Psi}{\partial Y} = \frac{\partial \Phi}{\partial X} \tag{7.34}$$

$$V = -\frac{\partial \Psi}{\partial X} = \frac{\partial \Phi}{\partial Y} \tag{7.35}$$

which can be integrated over the domain (i.e. XY plane) to:

$$\Psi = \int_Y U dY - \int_X V dX \tag{7.36}$$

$$\Phi = \int_X U dX + \int_Y V dY \tag{7.37}$$

Although these purely kinematic conditions will work reasonably well for the flows studied with PIV, the inherent problem is that, depending on the chosen frame of

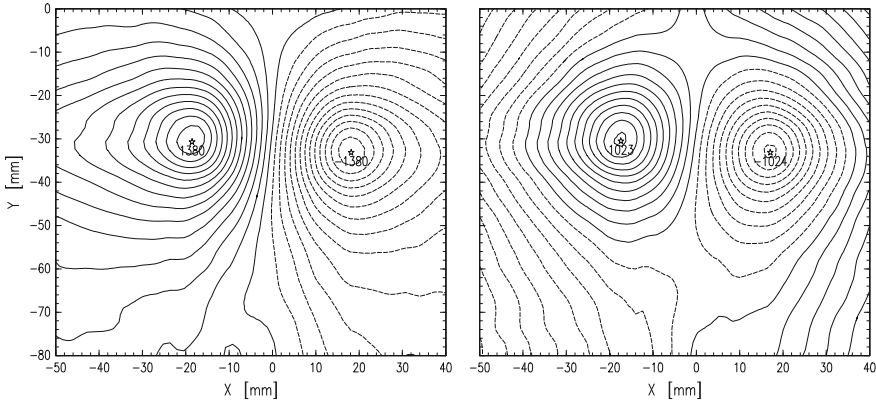


Fig. 7.21 Two-dimensional stream function computed from vortex pair velocity data in a laboratory-fixed reference frame (left) and in a reference frame moving 20 mm/s upward with the vortex pair (right)

reference, non-unique solutions to Ψ and Φ are obtained. This is due to the fact that Eqs. (7.36) and (7.37) are a simplification of the Poisson equation:

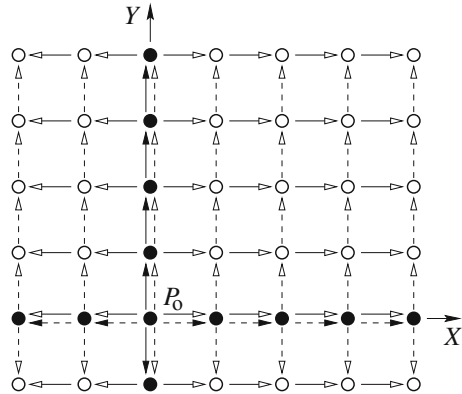
$$\nabla^2 \Psi = -\omega_z \quad (7.38)$$

to a Laplace equation, $\nabla^2 \Psi = 0$ using the condition of irrotationality (i.e. $\omega_z = 0$). The integration of Eq. (7.38) is rather difficult because the integrand can only be approximated from the velocity field data (see Sect. 7.5). Further, the boundary conditions along the edges of the field of view need to be defined prior to integrating Eq. (7.38).

Figure 7.21 shows the result of integrating Eq. (7.36) on an actual flow, a vortex pair, which can be assumed to be nearly two-dimensional, but not irrotational. Depending on the choice of the reference frame two entirely different results are obtained. For instance, if the vortex propagation speed is subtracted, the bounding streamline of the Kelvin oval, that is, the body of fluid moving with the vortex pair, can be approximated. This is not the case for streamlines computed in a laboratory-fixed reference frame (Fig. 7.21 left).

Since Eqs. (7.36) and (7.37) are path-independent integrals, the numerical integration of the velocity field can be freely chosen. In this case an integration scheme as presented by IMAICHI & OHMI [12] is used. The trapezoid approximation is used to integrate between two neighboring points. To start the integration a starting point, P_0 , is chosen, preferably near the middle of the velocity field since errors in the individual velocity data are propagated through integration. As illustrated in Fig. 7.22 there are two principal integration methods: a column-major integration or a row-major integration. In the first case, the integration proceeds in opposite horizontal directions away from the starting point, P_0 , producing new values of the integral for each node on the horizontal. These new estimates are then used as initial values for

Fig. 7.22 Integration routes used to integrate two-dimensional stream and potential functions as well as pressure. Two paths of integration follow either the dashed or solid arrows (after [12])



the integration in opposite directions along the vertical columns, producing estimates of the integral throughout the domain. A second estimate of the integral can then be obtained by reversing the order of the integration scheme, that is, by starting the integration off in opposite directions along the vertical line containing the starting point. The two results are then arithmetically averaged together.

Since the described integration scheme tends to propagate disturbances due to noisy or erroneous data “down-stream” of its occurrence, more sophisticated integration schemes, such as a multigrid approach, could be used. In this case the integral is first computed on highly smoothed and subsampled versions of the flow field and successively updated as the sampling mesh is refined.

7.6.4 Pressure and Forces from PIV Data

The feasibility of obtaining the flow pressure from PIV (or particle tracking) velocity data has been demonstrated abundantly over the recent years, notably for low speed conditions. This method provides an appealing approach to measure the flow field pressure in a non-intrusive way. Knowledge of the pressure and the way it acts in the flow field is of fundamental importance in several fluid-dynamic areas, such as aerodynamics, aero-acoustics, cavitation problems and fluid-structure interactions. Early applications of this method can be found in [2, 9, 12], while a recent overview has been provided in [37]. Its basic operating principle is that, in absence of body forces, the Navier-Stokes momentum equation relates the local pressure gradient to the flow acceleration and the viscous stress term (see also the application example in Sect. 15.3).

General Formulation for Unsteady Pressure Fluctuations

For incompressible flow (with constant density ρ and viscosity μ) the pressure gradient can be directly evaluated from the measured velocity field \mathbf{U} :

$$\nabla p = -\rho \frac{D\mathbf{U}}{Dt} + \mu \nabla^2 \mathbf{U} = -\rho \left(\frac{\partial \mathbf{U}}{\partial t} + (\mathbf{U} \cdot \nabla) \mathbf{U} \right) + \mu \nabla^2 \mathbf{U} \quad (7.39)$$

Note that although the viscous term can also be evaluated and maintained in this formulation for completeness, several studies (e.g. [37, 39]) have confirmed that its contribution to the pressure computation is negligible in the majority of cases, which justifies that it is commonly omitted from the analysis. Hence, the pressure gradient is dominated by the flow material acceleration term.

The nature of the flow configuration under consideration dictates the type of PIV data required for the method implementation: planar PIV data may be sufficient for a nearly two-dimensional laminar flow, but volumetric velocity data are required for turbulent flows, notably three-dimensional. Similarly, if instantaneous pressure is to be determined in case of an unsteady flow, the flow material acceleration term in Eq. (7.39) involves the evaluation of the temporal development of the flow field, which would require high-speed (time-resolved) PIV measurements to be performed.

The first step in the pressure determination is to obtain by measurement the velocity field as a function of time. From this data the flow acceleration is subsequently derived, following a Lagrangian reconstruction of imaginary fluid trajectories for structured PIV data [14]. Alternatively, actual particle trajectories are obtained from PTV data [18]. The latter have demonstrated the potential of increased accuracy in the determination of the material derivative with corresponding improvement of the pressure determination [40].

With the velocity and acceleration fields obtained, the pressure gradient is computed from the momentum Eq. (7.39). Upon spatial integration with appropriate boundary conditions, this then delivers the pressure field itself. The integration step [36] is performed solving a Poisson equation, obtained after taking the divergence of Eq. (7.39):

$$\nabla^2 p = \nabla \cdot (\nabla p) = -\rho \nabla \cdot (\mathbf{U} \cdot \nabla \mathbf{U}) \quad (7.40)$$

Note that in the final expression both the time derivative term and the viscous term have disappeared, as a consequence of $\nabla \cdot \mathbf{U} = 0$, in view of the incompressible flow assumption. Boundary conditions to be imposed on the integration domain boundaries are usually of mixed type: Dirichlet where pressure values can be prescribed (like the undisturbed pressure or calculated with Bernoulli's equation), and Neumann conditions elsewhere, taken from the local pressure gradient ∇p , as given by Eq. (7.39).

Time Averaged Pressure

As stated previously, in the case of unsteady flow the evaluation of the flow acceleration involves the temporal development of the velocity change as reflected in Eq. (7.39). As an alternative, that is in situations where time-resolved PIV measurements are not feasible, the time-mean pressure gradient can be obtained from Reynolds averaging of Eq. (7.39) [38, 39]:

$$\nabla \bar{p} = -\rho(\bar{\mathbf{U}} \cdot \nabla)\bar{\mathbf{U}} - \rho\nabla \cdot (\overline{\mathbf{U}'\mathbf{U}'}) + \mu\nabla^2\bar{\mathbf{U}} \quad (7.41)$$

Here the averaged properties are indicated by an overbar. As all terms on the right-hand side of Eq. (7.41) can be obtained from statistically averaged PIV data, the time-mean pressure can thus be estimated through appropriate integration. The Poisson equation, Eq. (7.40) may be adapted in a similar fashion [9]:

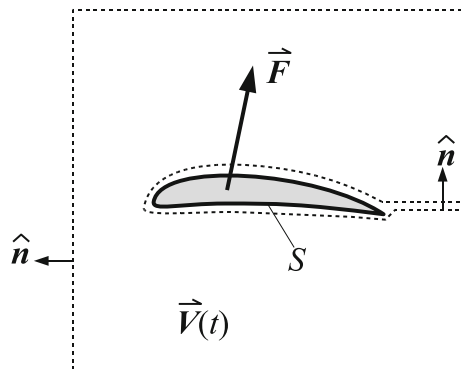
$$\nabla^2 \bar{p} = -\rho\nabla \cdot (\bar{\mathbf{U}} \cdot \nabla)\bar{\mathbf{U}} - \rho\nabla \cdot (\overline{\mathbf{U}'\mathbf{U}'}) + \mu\nabla^2\bar{\mathbf{U}} \quad (7.42)$$

The pressure determination from PIV data has also been considered for compressible flow conditions by VAN OUDHEUSDEN [39, 41] and its viability has been demonstrated in application to a two-dimensional $Ma = 2$ flow around a symmetric airfoil and to a shock-wave boundary-layer interaction at $Ma = 1.7$ [41].

Forces from PIV

Extending the exploitation of pressure determination from PIV, an integral formulation can be used to determine the loads on a body in the fluid by means of a control volume approach [16, 22, 35, 38]. This involves the acceleration inside the control volume and the momentum flux and pressure on the control-volume outer contour Fig. 7.23. Using this approach KURTULUS et al. determined the unsteady forces on a square cylinder along with the surrounding pressure fields from time-resolved 2C PIV obtained with a high speed PIV system operated at 1 kHz [13]. NOCA et al. [16] proposed alternative formulations of the control-volume approach of force estimation

Fig. 7.23 Control-volume approach for determining integral forces from two dimensional flow (after [16, 38])



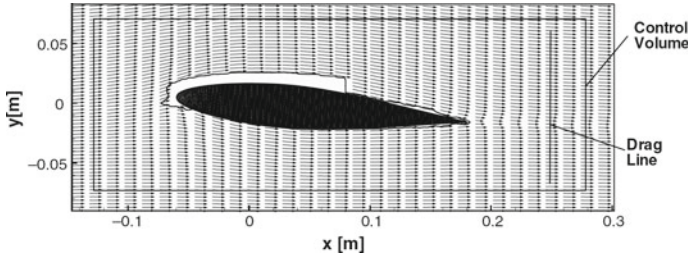


Fig. 7.24 Time averaged velocity field around a NACA airfoil, with indication of control volume and wake integration region (drag line) (reprinted from [38])

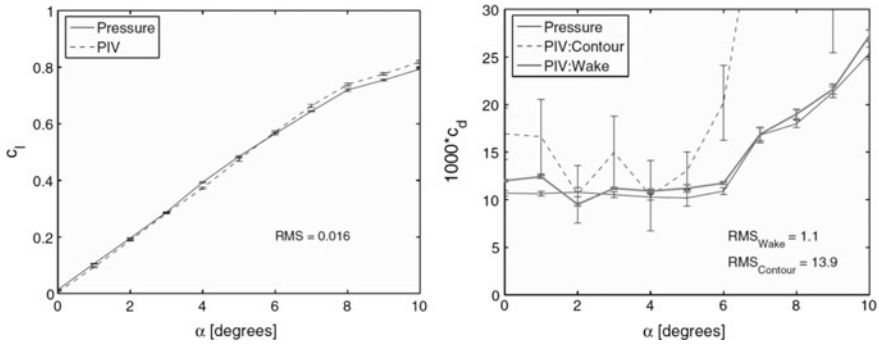


Fig. 7.25 Comparison of PIV and pressure measurements for the lift and drag of the airfoil (reprinted from [38])

from PIV data, in which the explicit dependence on the pressure had been eliminated and the integration is expressed in terms of the velocity and vorticity.

The previously described pressure and force estimation methods mostly assume two-dimensionality of the flow, as depicted in Fig. 7.23, to facilitate the implementation of the method, provided that such is justified by the geometry [35, 38].

The application to aerodynamic force measurement on an airfoil indicates that PIV based load determination is equivalent to measurements performed with conventional pressure based instrumentation (static pressure taps and Pitot wake rake) as illustrated in Fig. 7.24 with comparative results shown in Fig. 7.25.

The extension to fully three-dimensional problems is currently underway with applications attempted in the low-speed regime (see for instance Application Sect. 14.4). The further incorporation of time- and volume resolved velocity data, facilitated by recent advances in PIV hardware and processing algorithms, grants the perspective for applications beyond aerodynamics, towards aero-elasticity and aero-acoustics [19].

7.7 Vortex Detection

The velocity field obtained by PIV frequently is an intermediate result in the investigation of complex flow phenomena. Further postprocessing is required to extract important fluid mechanical properties. For validation of numerical tools and for aerodynamic studies in particular, a precise knowledge of the vortical flow is desired, which is exemplified by a number of applications provided in the later portion of this book. The following is intended to briefly outline the potential of PIV in the analysis of vortical flows.

Though there seems to be a common understanding about what a vortex looks like, it is mostly defined by empirical arguments or may be very subjective. In general, vortices are created due to conservation of angular momentum and not necessarily assume an easily detectible circular shape, especially if several vortices interact with each other. A vortex may be characterized by its location, circulation, core radius, drift velocity, peak vorticity, maximum circumferential velocity, for instance.

The velocity field generally has a tendency to hide vortices in the presence of convective flow. Streamlines, if computable (see Sect. 7.6.3), give a fairly good indication of vortical structures in the flow field as outlined in Fig. 7.26. Alternatively the vorticity field obtained from the gradient tensor already indicate the presence of vortices regardless of the frame of reference. As a finite difference from noisy data the vorticity field tends to be very noisy especially for the determination of the vortex centers. The squared vorticity field or enstrophy further enhances the visibility of the vortices but is equally susceptible to noise. A more rigorous analysis of the available vortex characterization methods is given by VOLLMERS [42] as well as SCHRAM et al. [29]. Among the available methods the rather useful λ_2 -operator shall be briefly described here.

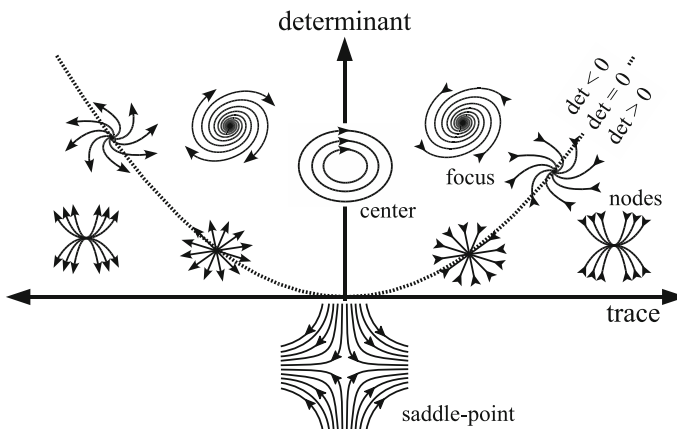


Fig. 7.26 Behavior of autonomous ordinary differential equations of two degrees of freedom in different regions dependent on trace and determinant of the velocity gradient tensor given in Eq. (7.43) (after VOLLMERS [42])

Following VOLLMERS [42] vortices appear in Fig. 7.26 for non-real eigenvalues of the gradient tensor

$$\mathcal{G} = \frac{d\mathbf{U}}{d\mathbf{X}} = \begin{bmatrix} \frac{\partial U}{\partial X} & \frac{\partial V}{\partial X} \\ \frac{\partial U}{\partial Y} & \frac{\partial V}{\partial Y} \end{bmatrix} \quad (7.43)$$

The discriminant λ_2 of non-real eigenvalues of the velocity tensor \mathcal{G} separates vortices from other patterns. It is obtained from

$$\lambda_2 = (\text{trace } \mathcal{G})^2 - 4 \det(\mathcal{G}) \quad (7.44)$$

$$= \left(\frac{\partial U}{\partial X} + \frac{\partial V}{\partial Y} \right)^2 - 4 \left(\frac{\partial U}{\partial X} \cdot \frac{\partial V}{\partial Y} - \frac{\partial U}{\partial Y} \cdot \frac{\partial V}{\partial X} \right) \quad (7.45)$$

Regions with negative values of λ_2 indicate vortices. Unlike vorticity the discriminant λ_2 generally does not identify boundary layers and shear layers as vortices. This makes it very useful for the position estimation of vortices but unfortunately does not provide information on direction of rotation. This information can be obtained by analyzing the surrounding velocity field.

As the expression Eq. (7.44) is restricted to two-dimensional interpretations of the flow, false detection may result for strongly three-dimensional flows. If the full 3C gradient tensor is available, the expression is readily extensible for three-dimensional vortex detection.

References

1. Agüí, J.C., Jiménez, J.: On the performance of particle tracking. *J. Fluid Mech.* **185**, 447–468 (1987). DOI 10.1017/S0022112087003252. URL http://journals.cambridge.org/article_S0022112087003252
2. Baur, T., Königeter, J.: PIV with high temporal resolution for the determination of local pressure reductions from coherent turbulent phenomena. In: *Third International Workshop on Particle Image Velocimetry*, Santa Barbara (USA) (1999)
3. de Kat, R., van Oudheusden, B.W.: Instantaneous planar pressure determination from PIV in turbulent flow. *Exp. Fluids* **52**(5), 1089–1106 (2012). DOI 10.1007/s00348-011-1237-5. URL <http://dx.doi.org/10.1007/s00348-011-1237-5>
4. Dieterle, L.: Entwicklung eines abbildenden Messverfahrens (PIV) zur Untersuchung von Mikrostrukturen in turbulenten Strömungen. Ph.D. thesis, Technische Universität Clausthal (1997)
5. Duncan, J., Dabiri, D., Hove, J., Gharib, M.: Universal outlier detection for particle image velocimetry (PIV) and particle tracking velocimetry (PTV) data. *Meas. Sci. Technol.* **21**(5), 057002 (2010). DOI 10.1088/0957-0233/21/5/057002. URL <http://stacks.iop.org/0957-0233/21/i=5/a=057002>
6. Etebari, A., Vlachos, P.P.: Improvements on the accuracy of derivative estimation from DPIV velocity measurements. *Exp. Fluids* **39**(6), 1040–1050 (2005). DOI 10.1007/s00348-005-0037-1. URL <http://dx.doi.org/10.1007/s00348-005-0037-1>

7. Foucaut, J.M., Stanislas, M.: Some considerations on the accuracy and frequency response of some derivative filters applied to particle image velocimetry vector fields. *Meas. Sci. Technol.* **13**(7), 1058 (2002). DOI 10.1088/0957-0233/13/7/313. URL <http://stacks.iop.org/0957-0233/13/i=7/a=313>
8. Fouras, A., Soria, J.: Accuracy of out-of-plane vorticity measurements derived from in-plane velocity field data. *Exp. Fluids* **25**(5–6), 409–430 (1998). DOI 10.1007/s003480050248. URL <http://dx.doi.org/10.1007/s003480050248>
9. Gurka, R., Liberzon, A., Hefetz, D., Rubinstein, D., Shavit, U.: Computation of pressure distribution using PIV velocity data. In: 3rd International Workshop on PIV, 16–18 September, Santa Barbara (USA), pp. 671–676 (1999)
10. Hain, R., Kähler, C.J.: Fundamentals of multiframe particle image velocimetry (PIV). *Exp. Fluids* **42**(4), 575–587 (2007). DOI 10.1007/s00348-007-0266-6. URL <http://dx.doi.org/10.1007/s00348-007-0266-6>
11. Higham, J.E., Brevis, W., Keylock, C.J.: A rapid non-iterative proper orthogonal decomposition based outlier detection and correction for PIV data. *Meas. Sci. Technol.* **27**(12), 125303 (2016). DOI 10.1088/0957-0233/27/12/125303. URL <http://stacks.iop.org/0957-0233/27/i=12/a=125303>
12. Imaichi, K., Ohmi, K.: Numerical processing of flow-visualization pictures - measurement of two-dimensional vortex flow. *J. Fluid Mech.* **129**, 283–311 (1983). DOI 10.1017/S0022112083000774. URL <http://journals.cambridge.org/article/S0022112083000774>
13. Kurtulus, D.F., Scarano, F., David, L.: Unsteady aerodynamic forces estimation on a square cylinder by TR-PIV. *Exp. Fluids* **42**(2), 185–196 (2007). DOI 10.1007/s00348-006-0228-4. URL <http://dx.doi.org/10.1007/s00348-006-0228-4>
14. Liu, X., Katz, J.: Instantaneous pressure and material acceleration measurements using a four-exposure PIV system. *Exp. Fluids* **41**(2), 227–240 (2006). DOI 10.1007/s00348-006-0152-7. URL <http://dx.doi.org/10.1007/s00348-006-0152-7>
15. Lourenco, L., Krothapalli, A.: On the accuracy of velocity and vorticity measurements with PIV. *Exp. Fluids* **18**(6), 421–428 (1995). DOI 10.1007/BF00208464. URL <http://dx.doi.org/10.1007/BF00208464>
16. Noca, F., Shiels, D., Jeon, D.: A comparison of methods for evaluating time-dependent fluid dynamic forces on bodies, using only velocity fields and their derivatives. *J. Fluids Struct.* **13**(5), 551–578 (1999). DOI 10.1006/jfifs.1999.0219. URL <http://www.sciencedirect.com/science/article/pii/S0889974699902190>
17. Nogueira, J., Lecuona, A., Rodríguez, P.A.: Data validation, false vectors correction and derived magnitudes calculation on PIV data. *Meas. Sci. Technol.* **8**(12), 1493 (1997). DOI 10.1088/0957-0233/8/12/012. URL <http://stacks.iop.org/0957-0233/8/i=12/a=012>
18. Novara, M., Scarano, F.: A particle-tracking approach for accurate material derivative measurements with tomographic PIV. *Exp. Fluids* **54**(8), 1584 (2013). DOI 10.1007/s00348-013-1584-5. URL <http://dx.doi.org/10.1007/s00348-013-1584-5>
19. Pröbsting, S., Tuinstra, M., Scarano, F.: Trailing edge noise estimation by tomographic particle image velocimetry. *J. Sound Vib.* **346**, 117–138 (2015). DOI 10.1016/j.jsv.2015.02.018. URL <http://www.sciencedirect.com/science/article/pii/S0022460X15001522>
20. Raben, S.G., Charonko, J.J., Vlachos, P.P.: Adaptive gappy proper orthogonal decomposition for particle image velocimetry data reconstruction. *Meas. Sci. Technol.* **23**(2), 025303 (2012). DOI 10.1088/0957-0233/23/2/025303. URL <http://stacks.iop.org/0957-0233/23/i=2/a=025303>
21. Raiola, M., Discetti, S., Ianiro, A.: On PIV random error minimization with optimal POD-based low-order reconstruction. *Exp. Fluids* **56**(4), 75 (2015). DOI 10.1007/s00348-015-1940-8. URL <http://dx.doi.org/10.1007/s00348-015-1940-8>
22. Rival, D.E., van Oudheusden, B.W.: Load-estimation techniques for unsteady incompressible flows. *Exp. Fluids* **58**(3), 20 (2017). DOI 10.1007/s00348-017-2304-3. URL <http://dx.doi.org/10.1007/s00348-017-2304-3>

23. Scarano, F., Moore, P.: An advection-based model to increase the temporal resolution of PIV time series. *Exp. Fluids* **52**(4), 919–933 (2012). DOI 10.1007/s00348-011-1158-3. URL <https://doi.org/10.1007/s00348-011-1158-3>
24. Schanz, D., Gesemann, S., Schröder, A.: Shake-The-Box: Lagrangian particle tracking at high particle image densities. *Exp. Fluids* **57**(5), 1–27 (2016). DOI 10.1007/s00348-016-2157-1. URL <http://dx.doi.org/10.1007/s00348-016-2157-1>
25. Schiavazzi, D., Coletti, F., Iaccarino, G., Eaton, J.K.: A matching pursuit approach to solenoidal filtering of three-dimensional velocity measurements. *J. Comput. Phys.* **263**, 206–221 (2014). DOI 10.1016/j.jcp.2013.12.049. URL <https://doi.org/10.1016/j.jcp.2013.12.049>
26. Schneiders, J.F.G., Scarano, F.: Dense velocity reconstruction from tomographic PTV with material derivatives. *Exp. Fluids* **57**(9), 139 (2016). DOI 10.1007/s00348-016-2225-6. URL <http://dx.doi.org/10.1007/s00348-016-2225-6>
27. Schneiders, J.F.G., Dwight, R.P., Scarano, F.: Time-supersampling of 3D-PIV measurements with vortex-in-cell simulation. *Exp. Fluids* **55**(3), 1692 (2014). DOI 10.1007/s00348-014-1692-x. URL <https://doi.org/10.1007/s00348-014-1692-x>
28. Schneiders, J.F.G., Scarano, F., Elsinga, G.E.: Resolving vorticity and dissipation in a turbulent boundary layer by tomographic PTV and VIC+. *Exp. Fluids* **58**(4), 27 (2017). DOI 10.1007/s00348-017-2318-x. URL <https://doi.org/10.1007/s00348-017-2318-x>
29. Schram, C., Rambaud, P., Riethmuller, M.L.: Wavelet based eddy structure eduction from a backward facing step flow investigated using particle image velocimetry. *Exp. Fluids* **36**(2), 233–245 (2004). DOI 10.1007/s00348-003-0695-9. URL <http://dx.doi.org/10.1007/s00348-003-0695-9>
30. Schröder, A.: Untersuchung der Struktur des laminaren Zylindernachlaufs mit Hilfe der Particle Image Velocimetry. Technical report, Diploma thesis, Universität Göttingen (Germany) (1996). DLR, Göttingen, Germany
31. Shinneeb, A.M., Bugg, J.D., Balachandar, R.: Variable threshold outlier identification in PIV data. *Meas. Sci. Technol.* **15**(9), 1722 (2004). DOI 10.1088/0957-0233/15/9/008. URL <http://stacks.iop.org/0957-0233/15/i=9/a=008>
32. Suzuki, T.: Reduced-order Kalman-filtered hybrid simulation combining particle tracking velocimetry and direct numerical simulation. *J. Fluid Mech.* **709**, 249–288 (2012). DOI 10.1017/jfm.2012.334. URL <https://doi.org/10.1017/jfm.2012.334>
33. Symon, S., Dovetta, N., McKeon, B.J., Sipp, D., Schmid, P.J.: Data assimilation of mean velocity from 2D PIV measurements of flow over an idealized airfoil. *Exp. Fluids* **58**(5), 61 (2017). DOI 10.1007/s00348-017-2336-8. URL <https://doi.org/10.1007/s00348-017-2336-8>
34. Taylor, J.R.: An Introduction to Error Analysis: The Study of Uncertainties in Physical Measurements, 2nd edn. University Science Books, Sausalito (1997). URL <https://archive.org/details/TaylorJ.R.IntroductionToErrorAnalysis2ed>
35. Unal, M.F., Lin, J.C., Rockwell, D.: Force prediction by PIV imaging: a momentum-based approach. *J. Fluids Struct.* **11**(8), 965–971 (1997). DOI 10.1006/jfls.1997.0111. URL <http://www.sciencedirect.com/science/article/pii/S0889974697901110>
36. van Gent, P.L., Michaelis, D., van Oudheusden, B.W., Weiss, P.É., de Kat, R., Laskari, A., Jeon, Y.J., David, L., Schanz, D., Huhn, F., Gesemann, S., Novara, M., McPhaden, C., Neeteson, N.J., Rival, D.E., Schneiders, J.F.G., Schrijer, F.F.J.: Comparative assessment of pressure field reconstructions from particle image velocimetry measurements and Lagrangian particle tracking. *Exp. Fluids* **58**(4), 33 (2017). DOI 10.1007/s00348-017-2324-z. URL <http://dx.doi.org/10.1007/s00348-017-2324-z>
37. van Oudheusden, B.W.: Principles and application of velocimetry-based planar pressure imaging in compressible flows with shocks. *Exp. Fluids* **45**(4), 657–674 (2008). DOI 10.1007/s00348-008-0546-9. URL <http://dx.doi.org/10.1007/s00348-008-0546-9>
38. van Oudheusden, B.W.: PIV-based pressure measurement. *Meas. Sci. Technol.* **24**(3), 032001 (2013). DOI 10.1088/0957-0233/24/3/032001. URL <http://stacks.iop.org/0957-0233/24/i=3/a=032001>
39. van Oudheusden, B.W., Scarano, F., Casimiri, E.W.F.: Non-intrusive load characterization of an airfoil using PIV. *Exp. Fluids* **40**(6), 988–992 (2006). DOI 10.1007/s00348-006-0149-2. URL <http://dx.doi.org/10.1007/s00348-006-0149-2>

40. van Oudheusden, B.W., Scarano, F., Roosenboom, E.W.M., Casimiri, E.W.F., Souverein, L.J.: Evaluation of integral forces and pressure fields from planar velocimetry data for incompressible and compressible flows. *Exp. Fluids* **43**(2–3), 153–162 (2007). DOI 10.1007/s00348-007-0261-y. URL <http://dx.doi.org/10.1007/s00348-007-0261-y>
41. Vlasenko, A., Steele, E.C.C., Nimmo-Smith, W.A.M.: A physics-enabled flow restoration algorithm for sparse PIV and PTV measurements. *Meas. Sci. Technol.* **26**(6), 065301 (2015). DOI 10.1088/0957-0233/26/6/065301. URL <http://stacks.iop.org/0957-0233/26/i=6/a=065301>
42. Vollmers, H.: Detection of vortices and quantitative evaluation of their main parameters from experimental velocity data. *Meas. Sci. Technol.* **12**(8), 1199 (2001). DOI 10.1088/0957-0233/12/8/329. URL <http://stacks.iop.org/0957-0233/12/i=8/a=329>
43. Wereley, S.T., Meinhart, C.D.: Second-order accurate particle image velocimetry. *Exp. Fluids* **31**(3), 258–268 (2001). DOI 10.1007/s003480100281. URL <http://dx.doi.org/10.1007/s003480100281>
44. Westerweel, J.: Digital particle image velocimetry: theory and application. Ph.D. thesis, Mechanical Maritime and Materials Engineering, Delft University of Technology (1993). URL <http://repository.tudelft.nl/islandora/object/uuid:85455914-6629-4421-8c77-27cc44e771ed/datastream/OBJ/download>
45. Westerweel, J.: Efficient detection of spurious vectors in particle image velocimetry data. *Exp. Fluids* **16**(3–4), 236–247 (1994). DOI 10.1007/BF00206543. URL <http://dx.doi.org/10.1007/BF00206543>
46. Westerweel, J.: Theoretical analysis of the measurement precision in particle image velocimetry. *Exp. Fluids* **29**(1), S003–S012 (2000). DOI 10.1007/s003480070002. URL <http://dx.doi.org/10.1007/s003480070002>
47. Westerweel, J., Scarano, F.: Universal outlier detection for PIV data. *Exp. Fluids* **39**(6), 1096–1100 (2005). DOI 10.1007/s00348-005-0016-6. URL <http://dx.doi.org/10.1007/s00348-005-0016-6>
48. Willert, C.E.: The interaction of modulated vortex pairs with a free surface. Ph.D. thesis, Department of Applied Mechanics and Engineering Sciences, University of California, San Diego (USA) (1992)

Chapter 8

Stereoscopic PIV

In spite of all its advantages, the PIV method contains some shortcomings that necessitate further developments on the basis of instrumentation. One of these disadvantages is the fact that the “classical” PIV method is only capable of recording the projection of the velocity vector into the plane of the light sheet; the out-of-plane velocity component is unknown while the in-plane components are affected by an unrecoverable error due to the perspective transformation as described in Sect. 2.5.3. For highly three-dimensional flows this can lead to substantial measurement errors of the local velocity vector. This error increases as the distance to the principal axis of the imaging optics increases. Thus it is often advantageous to select a large viewing distance in comparison to the imaged area to keep the projection error to a minimum. This is easily achieved using long focal length lenses. Nevertheless, many PIV applications require the additional knowledge of the out-of-plane velocity component.

A variety of approaches capable of recovering the complete set of velocity components have been described in the literature [11, 24]. The most straightforward, but not necessarily easily implemented, method is an additional PIV recording from a different viewing direction using a second camera. This recording approach is called stereoscopic PIV [9, 20, 21, 30, 34]. Reconstruction of the three-component velocity vector in effect relies on the perspective distortion of a displacement vector viewed from different directions.

While most stereoscopic setups employ two cameras, stereoscopic viewing can also be achieved with a single camera by placing a set of mirrors in front of the recording lens [2].

An extension of the stereo PIV system is the so called *multiplane PIV* technique. Relying on four laser pulses and four cameras, it is capable of recovering velocity data in two adjacent image planes with the same high spatial resolution available for

An overview of the Digital Content to this chapter can be found at [DC8.1].

standard PIV [15]. Thus it can be used to estimate the all quantities of the deformation tensor (Eq. (7.12)). More information on the multiplane PIV technique along with application examples can be found in Sect. 17.2.

On this page section, the emphasis will be on the recovery of a single plane of three-component velocity data using ‘only’ two cameras in a stereoscopic viewing arrangement. It has become a rather wide-spread technique for which much knowledge already has been accumulated but different implementations in terms of calibration and vector recovery exist [2, 3, 16, 19, 20, 27, 30, 31, 33, 34].

8.1 Implementation of Stereoscopic PIV

On this page the most common stereoscopic imaging approaches will be described. The adaptation of this approach to applications in liquid flows can easily be performed by changing the angles between the lens plane and sensor plane according to the refraction of the air-water interfaces. Detailed descriptions of the adaptation of stereo PIV to liquid flows are given in [20, 21, 29, 32].

Since the relative measurement uncertainty of the out-of-plane component increases as the opening angle between the two cameras with increasing observation angle. On the other hand, the larger the angle the lower the uncertainty of the in-plane components get. Therefore, the 90° configuration is often preferred because in this particular case the uncertainty of all velocity components become equal. However, if a particular velocity component is more important than others, other observation angles should be selected, see Sect. 6.3. It is also important to mention that also asymmetric recording arrangement can be used. Therefore a general description for asymmetric recording and associated calibration is provided on this page.

Figure 8.1 shows two different stereoscopic recording arrangement know as translation method and angular displacement technique. The translation method offers two advantages. First, the magnification across the field of view is constant. This implies that image deformation do no complicate the image analysis. Second, all particles will be in focus as the depth-of-focus is parallel to the main plane of the lenses. Unfortunately, the limited angular aperture restricts the distance between the lenses in a translation imaging approach (Fig. 8.1a, [14]). Designed for use with a fixed format sensor centered on the optical axis of the lens, most lenses are not only limited in their optical aperture but also characterized by a strong decrease in the modulation transfer function (MTF) towards the edges of the field of view. To adequately image small particles a good MTF at small f numbers ($f_\# < 4$) is a stringent requirement (Sect. 2.5). Since lens systems with an oblique principal axis are practically non-existent, a departure from the translation imaging method of Fig. 8.1a is unavoidable. As the best MTF is generally present near the lens principal axis, the alternative angular displacement method (Fig. 8.1b) aligns the lens with the principal viewing direction. The additional requirement for small f -numbers is associated with a very small depth of field which only can be accommodated by closing the aperture (which is often not acceptable because of the loss of signal) or addition-

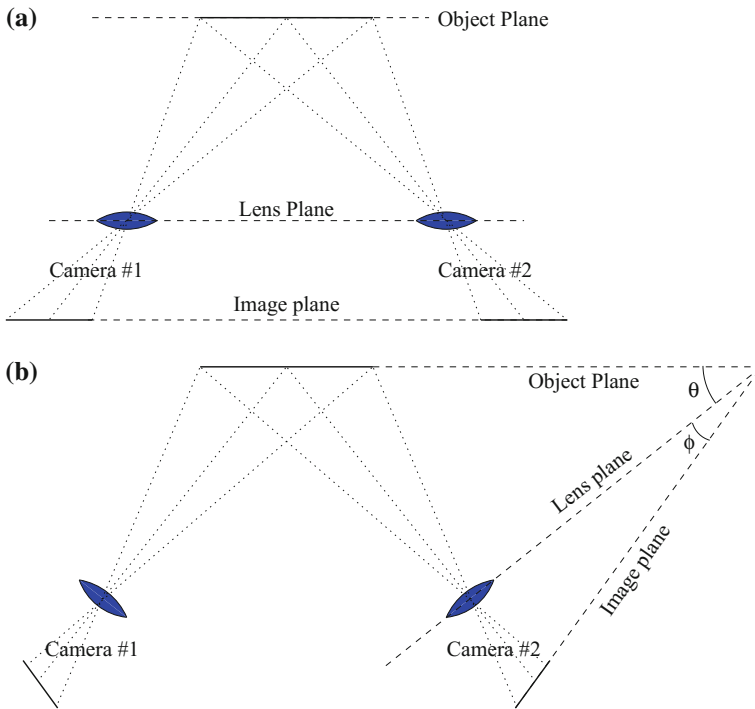


Fig. 8.1 Basic stereoscopic imaging configurations: **a** lens translation method, **b** angular lens displacement with tilted back plane (Scheimpflug condition)

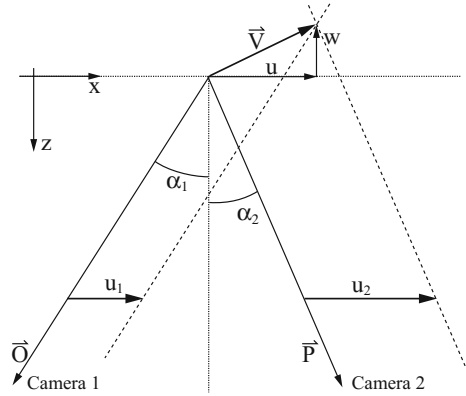
ally tilting the back plane according to the Scheimpflug criterion in which the image plane, lens plane and object plane for each of the cameras intersect in a common line [11, 21, 25]. The oblique view of the scene is associated with a perspective distortion that is further increased by the Scheimpflug imaging arrangement. In essence, the perspective distortion results in a magnification factor that is no longer constant across the field of view and requires an additional means of calibration to be described later.

On this page sections the generalized, that is nonsymmetric, description for stereoscopic PIV imaging is given first and is followed by a methodology for calibrating the perspective distortion. The feasibility of this approach is demonstrated in an experiment with an unsteady flow field, which is described in Sect. 17.1.

8.1.1 Reconstruction Geometry

This section describes the geometry necessary to reconstruct the three-dimensional displacement field from the two projected, planar displacement fields. Past descriptions of stereoscopic PIV imaging systems attempt to use a symmetric arrange-

Fig. 8.2 Stereo viewing geometry in the XZ -plane



ment [8, 20, 21, 26, 30, 33]. In the present case the two cameras may be placed in any desirable configuration provided the viewing axes are not collinear.

In Sect. 2.5.3 we determined the basic equations – 2.26 and 2.27 – for particle image displacement assuming geometric imaging:

$$x'_i - x_i = -M \left(D_X + D_Z \frac{x'_i}{z_0} \right) \quad (8.1)$$

$$y'_i - y_i = -M \left(D_Y + D_Z \frac{y'_i}{z_0} \right) \quad (8.2)$$

In the following we will use the angle α in the XZ plane between the Z axis and the ray from the tracer particle through the lens center \mathbf{O} to the recording plane as shown in Fig. 8.2. Correspondingly, β defines the angle within the YZ plane.

$$\tan \alpha = \frac{x'_i}{z_0}$$

$$\tan \beta = \frac{y'_i}{z_0}$$

The velocity components measured by the left camera are given by:

$$U_1 = -\frac{x'_i - x_i}{M \Delta t}$$

$$V_1 = -\frac{y'_i - y_i}{M \Delta t}$$

The velocity components for the right camera U_2 and V_2 can be determined accordingly. Using the above equations, the three velocity components (U , V , W) can be reconstructed from the four measured values. For $\alpha, \beta \geq 0$ we obtain:

$$U = \frac{U_1 \tan \alpha_2 + U_2 \tan \alpha_1}{\tan \alpha_1 + \tan \alpha_2} \quad (8.3)$$

$$V = \frac{V_1 \tan \beta_2 + V_2 \tan \beta_1}{\tan \beta_1 + \tan \beta_2} \quad (8.4)$$

$$W = \frac{U_1 - U_2}{\tan \alpha_1 + \tan \alpha_2} \quad (8.5)$$

$$= \frac{V_1 - V_2}{\tan \beta_1 + \tan \beta_2} \quad (8.6)$$

These formulae are general and apply to any imaging geometry. Note, that there are three unknowns and four known measured values, which results in an over-determined system that can be solved in a least-squares sense (see below). Also, the denominators can approach zero as the viewing axes become collinear in either of their two-dimensional projections. For example, in the setup described in Sect. 17.1 the cameras are approximately positioned in the same vertical position as the field of view which makes the angles β_1 , β_2 and their tangents $\tan \beta_1$ and $\tan \beta_2$ very small. Clearly, component W can only be estimated with higher accuracy using Eq.(8.5), while V has to be rewritten using Eq.(8.5) which does not include $\tan \beta_1$ and $\tan \beta_2$ in the denominator:

$$V = \frac{V_1 + V_2}{2} + \frac{W}{2} (\tan \beta_1 - \tan \beta_2) \quad (8.7)$$

$$V = \frac{V_1 + V_2}{2} + \frac{U_1 - U_2}{2} \left(\frac{\tan \beta_1 - \tan \beta_2}{\tan \alpha_1 + \tan \alpha_2} \right) \quad (8.8)$$

If $\tan \beta_1$ and $\tan \beta_2$ are very small, then V is given as the arithmetic mean of V_1 and V_2 with the out-of-plane component W having no effect.

As mentioned above the velocity components may also be solved for in a least squares sense as the system of equations is once over-determined, that is, there are three unknown Cartesian displacement components but four known displacement components:

$$\begin{bmatrix} U_1 \\ V_1 \\ U_2 \\ V_2 \end{bmatrix} = \begin{bmatrix} 1 & 0 & -\frac{O_x}{O_z} \\ 0 & 1 & -\frac{O_y}{O_z} \\ 1 & 0 & -\frac{P_x}{P_z} \\ 0 & 1 & -\frac{P_y}{P_z} \end{bmatrix} \cdot \begin{bmatrix} U \\ V \\ W \end{bmatrix} \quad (8.9)$$

$$\mathbf{U}_{\text{meas}} = \mathbf{A} \cdot \mathbf{V} \quad (8.10)$$

$$\Rightarrow \mathbf{V} = (\mathbf{A}^T \cdot \mathbf{A})^{-1} \cdot \mathbf{A}^T \cdot \mathbf{U}_{\text{meas}} \quad (8.11)$$

The residuals $\varepsilon_{\text{resid}}$ of this least squares fit can be used as a measure of quality for the three component measurement result, since they should vanish in an ideal (noise-free) measurement. In practice residuals in the range of 0.1–0.5 pixel are common.

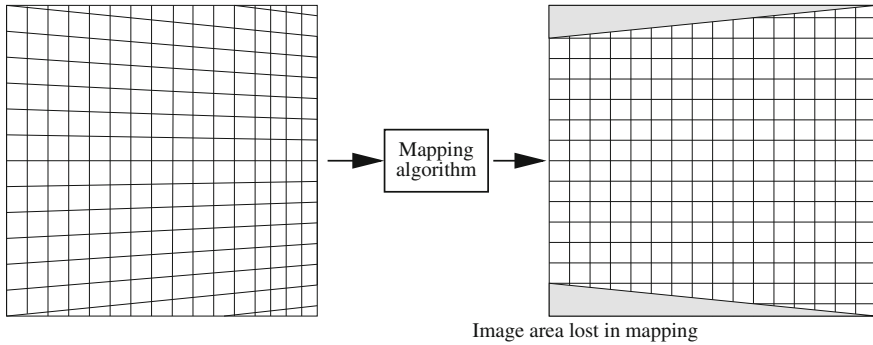


Fig. 8.3 The back-projection algorithm has to map the recorded image on the left to the reconstructed image on the right

Increased misalignment between the camera views results in significant residuals, especially for flows with high spatial variations.

To use the above reconstruction, the displacement data set must first be converted from the image plane to true displacements in the global coordinate system while taking into account all the magnification issues. Following WIENEKE [31] the literature reports three main approaches:

1. The 2C displacements for each view are computed on a regular grid in the raw image space. 3C reconstruction is performed by projecting the vector maps onto a common grid using interpolation [19].
2. The 2C displacements are computed from the raw images at positions corresponding to the desired object space coordinates [3].
3. The raw images are first mapped onto a common image space before being analyzed at coincident object positions using 2C vector processing for each view [34].

While the first approach is suited for rather fast processing time, the main drawback is that false or inaccurate vectors may result in unreliable reconstruction of the neighboring interpolated vectors. The second approach avoids the interpolation step but generally is associated with different-sized interrogation windows in object space unless elaborate processing with spatially varying, non-rectangular interrogation samples is used. The alternative, also followed here, is to first map both camera images onto a common image space as depicted in Fig. 8.3, such that subsequent PIV processing automatically makes use of common interrogation grid with constant sample size throughout. Regardless of the chosen approach, the projection onto a common grid in object space requires a priori calibration procedures which are described next.

8.1.2 Stereo Viewing Calibration

In order to reconstruct the local displacement vector the viewing direction and magnification factor for each camera must be known at each point in the respective images.

This correspondence between the image (x, y) and the object plane (X, Y) may in fact be described through geometric optics; however, it requires exact knowledge of the imaging parameters such as the lens focal length, f , the angles between the various planes, θ, ϕ (see Fig. 8.1b), the actual position of the principal plane of the lens (which is not simple to determine) and the nominal magnification factor, M_0 (the magnification along the principal optical axis):

$$X = \frac{f x \sin \phi}{M_0 \sin \theta (x \sin \phi + f M_0)}$$

$$Y = \frac{f y}{x \sin \phi + f M_0}$$

These approximate expressions, given in [33], do not incorporate nonlinearities such as lens distortions and are sensitive to small variations in each of the parameters.

A more robust approach is the second order image mapping approach employed by other researchers [22, 33]:

$$X = a_0 + a_1x + a_2y + a_3x^2 + a_4xy + a_5y^2 + \dots \tag{8.12}$$

$$Y = b_0 + b_1x + b_2y + b_3x^2 + b_4xy + b_5y^2 + \dots \tag{8.13}$$

The above equations do not constitute a mapping based on the geometry at hand. Nevertheless the twelve unknown parameters can easily be determined using a least squares approach if at least six image-object point pairs are given. The advantage of this approach is that the imaging parameters such as focal length, magnification factor, etc., never need to be determined. Also lens distortions or other image nonlinearities can be accounted for by the higher order terms.

For the reconstruction of the images, we implemented the projection equations based on perspective projection as put forth in [10, 12, 17]. Using homogeneous coordinates the perspective projection is expressed by:

$$\begin{bmatrix} w_o X \\ w_o Y \\ w_o \end{bmatrix} = \begin{bmatrix} a_{11} & a_{12} & a_{13} \\ a_{21} & a_{22} & a_{23} \\ a_{31} & a_{32} & a_{33} \end{bmatrix} \cdot \begin{bmatrix} w_i x \\ w_i y \\ w_i \end{bmatrix} \tag{8.14}$$

where w_o and w_i are constants and $a_{33} = 1$. When rewritten in standard coordinates the following two nonlinear expressions are obtained:

$$X = \frac{a_{11}x + a_{12}y + a_{13}}{a_{31}x + a_{32}y + 1} \tag{8.15}$$

$$Y = \frac{a_{21}x + a_{22}y + a_{23}}{a_{31}x + a_{32}y + 1} \tag{8.16}$$

The principal property of the perspective projection is that it maps a rectangle onto a general four-sided polygon. In other words, this mapping preserves only the straight-

ness of lines. By setting a_{31} and a_{32} equal to zero the perspective transformation Eq. (8.14) reduces to the more frequently used affine transformation which can only map a rectangle onto a parallelogram.

To account for geometric distortions due to imperfect imaging optics (i.e. pin cushion and barrel distortion) Eq. (8.15) can be extended to a higher order:

$$X = \frac{a_{11}x + a_{12}y + a_{13} + a_{14}x^2 + a_{15}y^2 + a_{16}xy}{a_{31}x + a_{32}y + a_{33} + a_{34}x^2 + a_{35}y^2 + a_{36}xy} \quad (8.17)$$

$$Y = \frac{a_{21}x + a_{22}y + a_{23} + a_{24}x^2 + a_{25}y^2 + a_{26}xy}{a_{31}x + a_{32}y + a_{33} + a_{34}x^2 + a_{35}y^2 + a_{36}xy} \quad (8.18)$$

$$a_{33} = 1$$

The determination of the unknowns in Eq. (8.15) and especially in Eq. (8.17) by means of a linear least squares method is not as simple as for the second order warping approach given in Eq. (8.12) because the equations no longer constitute linear polynomials but rather are ratios of two polynomials of the same order. Strongly deviating or erroneous point pairs cause a standard least squares method to rapidly diverge from the “true” best match. To find the best match to the eight or seventeen unknowns, a nonlinear least squares method such as the Levenberg–Marquart method [23] is required.

The Levenberg–Marquart method is implemented by first solving for the unknowns in the first order projection Eq. (8.15) and then using these as initial estimates for the solution of the higher order unknowns in Eq. (8.17).

The described projection equations can be used to either map recovered 2C displacement data or entire images onto an object space that is common to both camera views. Here the back-projection of the images is somewhat empirical because the operator needs to define a common image magnification factor for the reconstructed images (see Fig. 8.3). Due to the perspective distortion however the original raw image pixels can never be mapped at optimum sampling distances; over-sampling, under-sampling and aliasing may result. Here we suggest the use of a magnification factor that avoids loss of signal due to under-sampling. The reconstruction of the image is performed by interpolating the image intensity in the raw image using the inverse versions of the mapping functions given before. Here an adequate choice of image interpolator has direct influence on the quality of the recovered displacement data. The image interpolation methods used for the iterative image deformation PIV algorithms (see Sect. 5.3.4.4) are equally adequate here. In fact, one may combine image deformation and image back-projection in a single step [31].

8.1.3 Camera Calibration

Up to now the described calibration procedures can provide adequate mappings from image to object space, but provide no attitude information for the cameras (i.e.

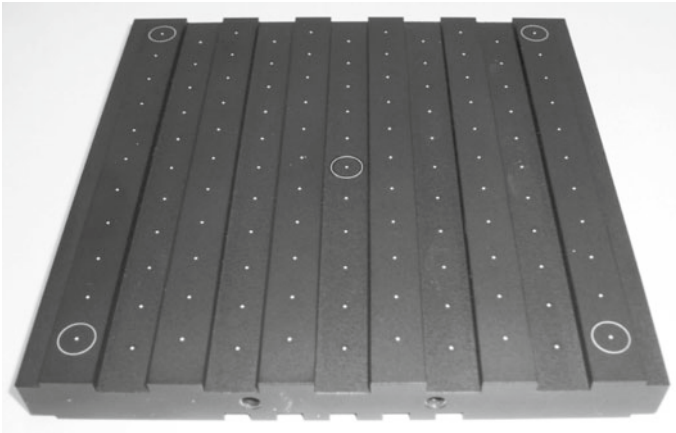


Fig. 8.4 Precision-machined dual level calibration target with dot pattern for stereo PIV calibration. Levels are separated by 2 mm, dots are equally spaced on a 10 mm grid

viewing direction) themselves that may be used to reconstruct the three-component velocity vector. The pragmatic approach is to measure the position of each camera with respect to a known point in the calibration target by means of triangulation assuming that the camera more or less abides to pinhole viewing, that is, all imaging rays pass through a single point. In practice, the location of the pinhole is located along the optical axis within the camera lens and can be easily approximated for larger observation distances.

Camera triangulation through distance measurement is not always possible especially in the presence of obstructions such as viewing windows or even air-to-water interfaces. To recover the camera positions with respect to the imaged plane, two primary calibration solutions have established themselves, one entirely empirical motivated [27], the other more or less relying on physical models [3, 28, 35]. A third approach, the so-called camera self-calibration originates from machine vision but is not described in detail here, in part because it attempts to find adequate calibration parameters for an entire volume with large depth of field – conditions that are not typical for PIV with large lens apertures imaging planar domains. Nonetheless self-calibration is usually [18] applied in tomographic PIV [5], stereoscopic PIV [7, 31] and even in μ PIV.

A common approach to calibrating a stereoscopic PIV imaging setup relies on images of planar calibration targets which are placed coincident with the light sheet plane. These calibration targets typically consist of a precise grid of markers (dots, crosses, line grid, checker board) that are easily detected with simple image processing techniques [4, 34]. A single image of planar calibration marks is then sufficient to calculate adequate mappings between image space and object space as described in the previous section, but it generally does not provide information on the camera viewing angles that are essential for reconstruction of the three-component displacement vector. This important parameter can only be calculated from a set of image-to-

object correspondence points that are not coplanar. Such a calibration data set can be rather easily generated by recording a set of images with the target slightly displaced at known positions in the direction normal to the light sheet plane. Another method is to use multi-level calibration targets that have reference markers at different heights (see Fig. 8.5).

Given the set of non-coplanar correspondence points, it is now possible to relate two-dimensional displacements on two different imaging planes to three-dimensional displacements in object space. The empirical approach mentioned earlier uses two-dimensional polynomials of second or third order to connect object volume coordinates with planar image coordinates thus simplifying the vector reconstruction in stereoscopic PIV [27]. One drawback of this approach is that the volume reconstruction makes use of a large number of polynomial coefficients not all of which are statistically relevant [31]. In fact insufficient calibration data, especially near the edges, can result in undesired oscillations in the mapping functions.

The more physically motivated camera calibration method for stereoscopic PIV originates from the field of photogrammetry and image vision, which frequently use so-called camera models to describe the imaging geometry. The simplest camera model reduces the imaging process to a pinhole configuration in which all rays passing from object to sensor must pass through a single point in space (Fig. 8.5).

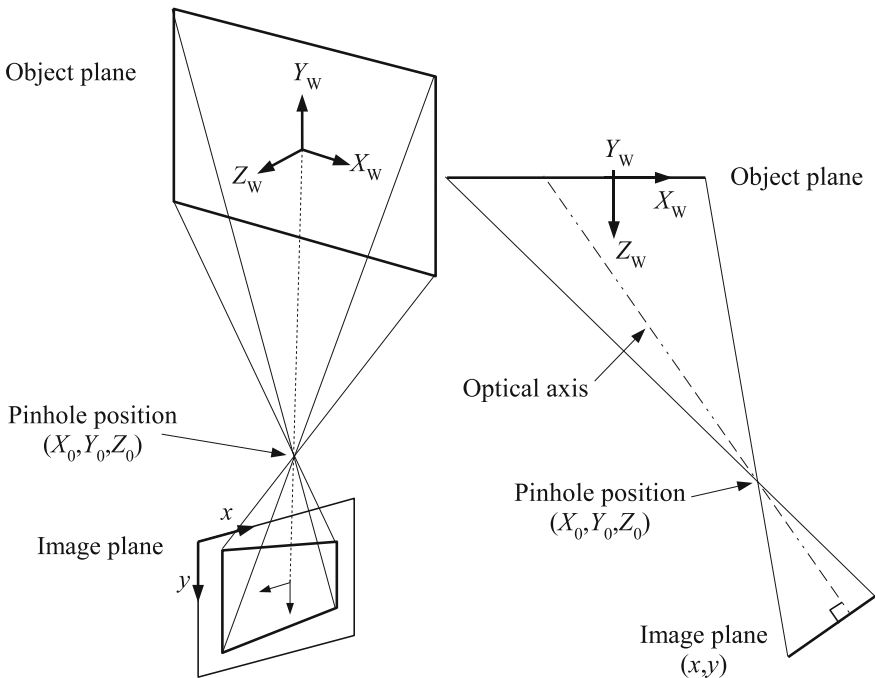


Fig. 8.5 Simple pinhole imaging model used to describe oblique camera viewing. For clarity the projection onto the XZ plane is shown on the right (reprinted from [35])

This model can be extended by additional parameters to account for radial distortions as suggested in the literature [28, 36]. The calibration procedure involves a nonlinear fit of object-space calibrated feature points to a given functional. The fitted camera parameters can thus be used to retrieve the local viewing angle for each point on the sensor and therefore is well suited for stereoscopic PIV.

A quantitative analysis of two these camera models on the background of PIV application is provided in [35]. In essence only a few parameters describing a physical imaging model are necessary to calibrate each viewing direction independently of the other. Typically 11–12 parameters are required to fully describe each view compared to a much larger number of parameters for polynomial-based reconstruction methods as proposed by SOLOFF et al. [27]. Higher order distortions can be corrected by adding additional distortion terms to the underlying models. For many practical purposes (standard lenses with narrow field of view) the local viewing angle is generally sufficiently well defined (within 0.1°) using the pinhole location estimate itself. As a consequence the image-reconstruction (back-projection) could use higher order functions to account for higher order distortions while the local viewing angle is sufficiently well estimated by a simple imaging model. Additional correction terms on the camera model were even observed to lead to erroneous results as the camera model attempted to fit the noise in the correspondence point data.

A simple camera model based on an idealized (distortion-free) imaging system, shown in Fig. 8.5, is described here. The aim is to find a mapping relating image-to-object space using correspondence points from a calibration target such that the position of the point $X_0 = (X_0, Y_0, Z_0)$ can be estimated. These correspondence points consist of image coordinates $\mathbf{x}_j = (x_j, y_j)$ with associated object coordinates $\mathbf{X}_j = (X_j, Y_j, Z_j)$. A direct linear transform (DLT) between object and image space, as first proposed in [1], yields the homogeneous equation:

$$\begin{bmatrix} x_j w_i \\ y_j w_i \\ w_i \end{bmatrix} = \begin{bmatrix} a_{11} & a_{12} & a_{13} & a_{14} \\ a_{21} & a_{22} & a_{23} & a_{24} \\ a_{31} & a_{32} & a_{33} & a_{34} \end{bmatrix} \cdot \begin{bmatrix} X_j w_o \\ Y_j w_o \\ Z_j w_o \\ w_o \end{bmatrix} \tag{8.19}$$

which is a generalized version of the projective mapping given in Eq. 8.14. The matrix $\mathbf{A} = a_{11}, \dots, a_{34}$, also called homography, has 11 degrees of freedom (3 rotations, 3 translations, 5 intrinsic parameters). The coefficients can be solved for by normalizing the weighting factors $w' = w_i/w_o$ and eliminating these resulting in the following projection equations:

$$x_j = \frac{a_{11}X_j + a_{12}Y_j + a_{13}Z_j + a_{14}}{a_{31}X_j + a_{32}Y_j + a_{33}Z_j + a_{34}} \tag{8.20}$$

$$y_j = \frac{a_{21}X_j + a_{22}Y_j + a_{23}Z_j + a_{24}}{a_{31}X_j + a_{32}Y_j + a_{33}Z_j + a_{34}} \tag{8.21}$$

$$\text{with } a_{34} = 1 \tag{8.22}$$

The coefficient a_{34} behaves as an arbitrary scaling factor for the projection matrix and should be constrained by setting $a'_{ij} = a_{ij}/a_{34}$ to prevent a trivial solution with $a_{ij} = 0$. A standard nonlinear least-squares solver such as the Levenberg–Marquardt method [23] mentioned earlier can be used to solve for a_{11}, \dots, a_{33} .

The pinhole position X_0 shown in Fig. 8.5 provides an estimate for the local viewing angle (e.g. for 3C vector reconstruction) and is located where the image coordinates \mathbf{x} vanish:

$$\begin{bmatrix} a_{11} & a_{12} & a_{13} \\ a_{21} & a_{22} & a_{23} \\ a_{31} & a_{32} & a_{33} \end{bmatrix} \cdot \begin{bmatrix} X_0 \\ Y_0 \\ Z_0 \end{bmatrix} = \begin{bmatrix} a_{14} \\ a_{24} \\ -1 \end{bmatrix} \quad (8.23)$$

The coefficient matrix \mathbf{A} can be further decomposed to extract the camera's intrinsic parameters \mathbf{I} as well as extrinsic parameters \mathbf{E} which is detailed in [6]:

$$\mathbf{A} = \mathbf{I} \cdot \mathbf{E} = \begin{bmatrix} -f_x & 0 & x_c \\ 0 & -f_y & y_c \\ 0 & 0 & 1 \end{bmatrix} \cdot \begin{bmatrix} \mathbf{r}_1^t & t_x \\ \mathbf{r}_2^t & t_y \\ \mathbf{r}_3^t & t_z \end{bmatrix} \quad (8.24)$$

Here (f_x, f_y) is the projected focal length, (x_c, y_c) the optical center on the image plane \mathbf{x} . Variables \mathbf{r}_k^t and t_k relate to rotation and translation respectively.

While the DLT assumes an idealized imaging system, real-world effects such as radial distortions are included in more advanced camera models, such as those developed by TSAI [28] and ZHANG [36].

A noteworthy aspect of model-based camera calibration is that oblique camera views may even be calibrated using a single set of coplanar calibration points (coplanar calibration, [28]). This is especially attractive in environments where the translation of a target is unfeasible due to difficult access or non-acceptable effort. In most cases the estimated camera positions are more reliable than a triangulation by hand, but requires viewing angles greater than 10° from normal. For near-normal viewing conditions the lack of perspective prevents a reliable numerical convergence of the camera models [35].

8.1.4 Disparity Correction

The previously described camera calibration provides the essential information needed for reconstruction of the 3-C vector from two separate 2-C PIV recordings obtained at the same instant but from different directions. However this reconstruction approach assumes that the calibration target is perfectly aligned with the center of the light sheet plane and that the calibration conditions stay constant during the experiment. In practice this alignment is difficult to achieve as the calibration conditions are usually not exactly identical with the measurement conditions. Small shifts of the laser light sheets, tiny vibrations of the cameras or density changes in the

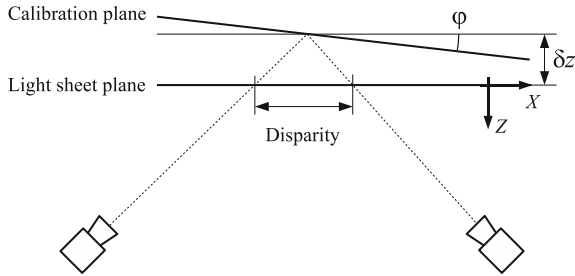


Fig. 8.6 Misalignment between calibration target and light sheet plane results in a mismatch between the actually imaged areas

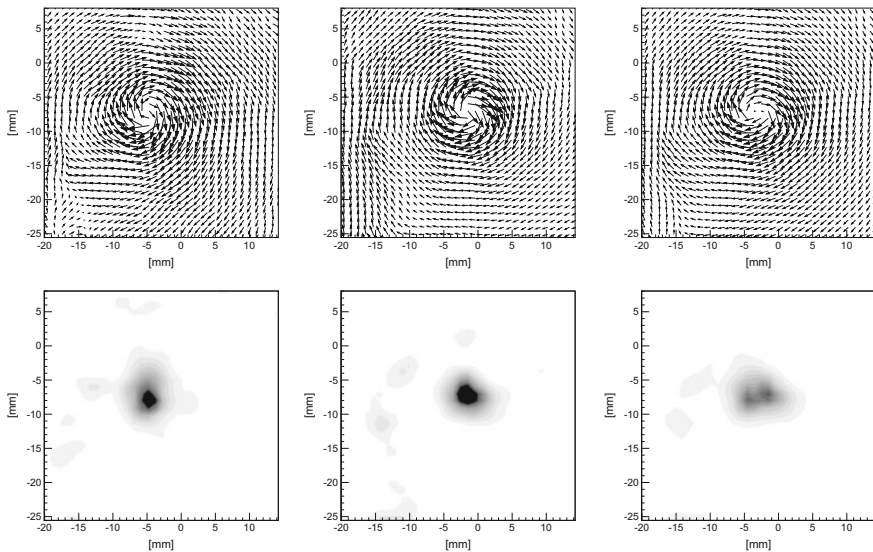


Fig. 8.7 Tip vortex flow before disparity correction; top row: left camera view, right camera view, reconstructed flow field; bottom row: corresponding maps of out-of-plane vorticity

facility are typical changes that need to be considered in practice (see Fig. 8.6, [3, 14, 31, 34]).

This misalignment of probe volumes and its correction, frequently referred to as disparity correction, is illustrated in the following example from an actual measurement. In this case, the flow field (trailing vortex) in the wake of an airfoil was mapped by stereo PIV using a pair of cameras, each with a viewing angle of about 55° off normal to the light sheet. Due to the cross-flow arrangement a light sheet thickness of 2 mm was chosen. Calibration was performed on a planar target positioned in the light sheet plane as described before. The recovered displacement field for each of the cameras as well as the 3C reconstruction is shown in Fig. 8.7. The two views exhibit a small horizontal misalignment of the vortex centers (about 3 mm), that is

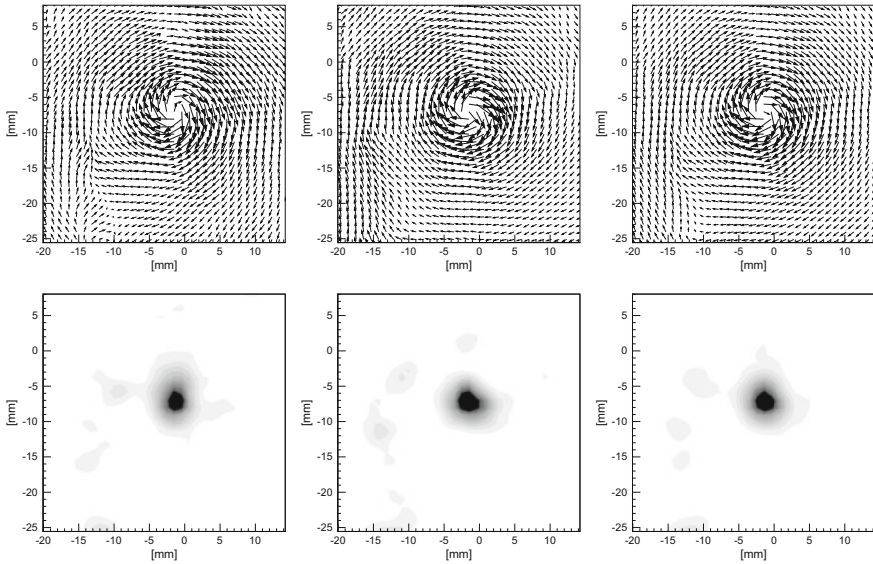


Fig. 8.8 Tip vortex flow after disparity correction (≈ 3.5 mm horizontal shift); top row: left camera view, right camera view, reconstructed flow field; bottom row: corresponding maps of out-of-plane vorticity

especially visible in the corresponding vorticity maps. The 3C reconstruction results in a vortex with an elongated horizontal shape, two maxima in the vorticity map and a significantly reduced peak vorticity.

Figure 8.8 shows the same set of data after application of a disparity correction scheme (explained later). Thereafter the vortex centers coincide and the reconstructed data shows a uniform vortex with a single round core that matches those of the individual camera views. Aside from the obvious mismatch of vortex centers, a further indicator of viewing disparity are the residuals of the vector reconstruction as described on p. 289. The misalignment results in an increase of these residuals due to the mismatch of recovered vectors between the views. In the present case a correct alignment of the views reduces the residuals to levels below 0.2 pixel (Fig. 8.9). So in theory a minimization of the residuals could be used to align the camera views with each other (provided the flow has notable variations the field of view).

In the previous example the camera view disparity was roughly 3.5 mm along the horizontal, which corresponds to an out-of-plane target placement of about 1.3 mm for a viewing geometry of $\pm 55^\circ$. Given a light sheet thickness of ≈ 2 mm, the target is only slightly offset (observation distance is about 1500 mm).

While manual alignment of flow structures or a minimization of the reconstruction residuals could be used to align the views, a much more efficient and reliable method for disparity correction procedure is described in the following. The approach relies on the actual PIV recordings from both views. These images are then back-projected according to their projection coefficients and a cross-correlation is

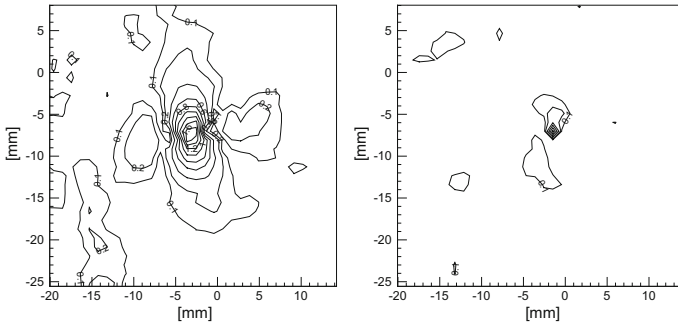
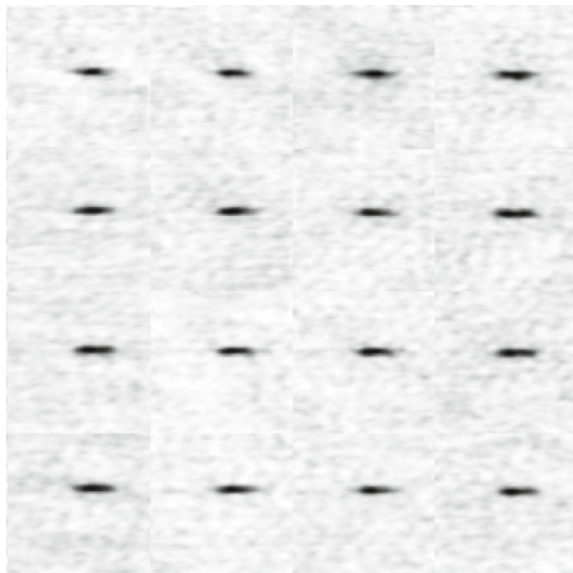


Fig. 8.9 Residuals of the 3 C vector reconstruction before (left) and after disparity correction (right). Contour levels are 0.1, 0.2, 0.4, 0.6, . . . pixel

Fig. 8.10 Image of 16 cross-correlation planes sized 64×64 pixel obtained during disparity correction of image data corresponding to Fig. 8.7. A mean offset of 30 pixel (≈ 3.5 mm) approximately centers the correlation peaks which measure about 20×4 pixel



performed between the views, that is, the first image of view *A* is correlated with the first image of view *B*. The thus recovered displacement field in fact represents the disparity of the views with respect to each other. The displacement data can now be used to correct the disparity by modifying the mapping coefficients accordingly. In practice the quality of the disparity map is improved by including the second image, or even an entire sequence of images if the cameras are stationary. In this case the average or ensemble correlation described in Sect. 5.3.2.4 should be used (Fig. 8.10).

Closer inspection of disparity maps such as Fig. 8.11 indicates that a low order two-dimensional polynomial, obtained through a least-squares fit to the data, is sufficient to describe it. Following Fig. 8.6, one displacement and two angles position the light sheet with respect to the calibration target. For optimum performance the positions

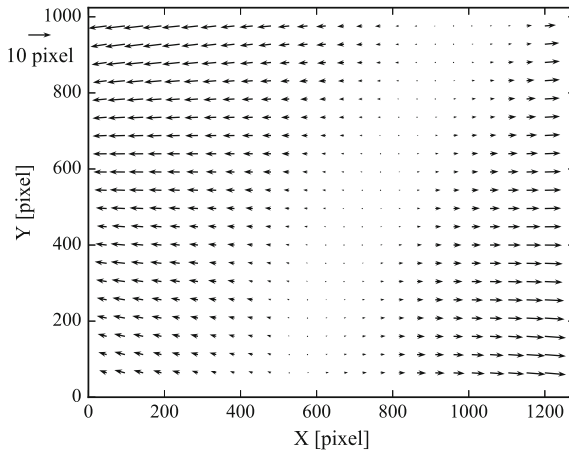


Fig. 8.11 Misalignment between the two viewing directions due to a slight offset and rotation of the calibration grid within the light sheet. A constant 8 pixel horizontal shift has already been subtracted

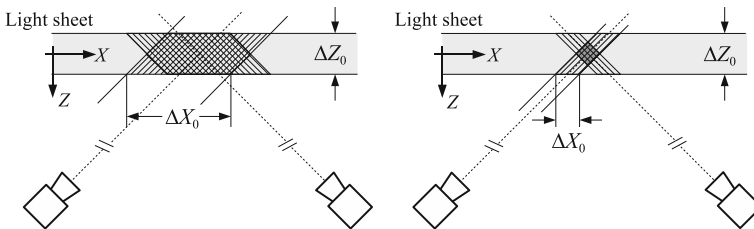


Fig. 8.12 Effective probe volume (hashed) for stereo PIV is smaller than probe volume for each individual view. Right: 3C displacement data for $\Delta X_0 < \Delta Z_0$ are questionable

of the cameras should be shifted and rotated using the recovered angles to match the coordinate system of the light sheet. However this is rarely done. Nonetheless the camera calibration described earlier can be included to iteratively recover the position of the light sheet [31].

Due to the finite thickness of the light sheet the images of the particles will never coincide between the views, even for perfect alignment. Hence, the cross-correlation peak in the disparity correction procedure will be smeared into an oblong shape (see Fig. 8.10). The major axis of this widened correlation peak coincides with the plane spanned by the two camera viewing axes. Its width is directly related to a projection of the light sheet thickness [31].

The finite thickness of the light sheet also places restrictions on the obtainable spatial resolution: the oblique viewing arrangement reduces the true probe volume to the intersection of two larger sampling rhomboids (Fig. 8.12). As the sample size decreases, the effective probe volume can decrease to questionable sizes. If a high spatial resolution is desired then either the light sheet thickness ΔZ_0 should be

reduced appropriately or a 3-D particle tracking scheme should be applied. As a rule of thumb the minimum PIV sample size should at least be the same size as the light sheet thickness: $\Delta X_0 \geq \Delta Z_0$.

8.1.5 Stereo-PIV in Liquids

The application of stereo-PIV is straightforward for the analysis of gas flows as long as compressible effects do not matter. However, if the wind tunnel is pressurized or evacuated during the experiment, the light scattered by the particles is diffracted at the interface if observed under an oblique angle. This causes two main effects. First, the calibration performed at atmospheric pressure becomes questionable as the field of view is shifted and compressed or elongated in case of density variations between the calibration and test conditions, see Fig. 8.13. Second, the imaging of the particles is deteriorated due to optical aberrations and this raises the number of spurious measurements and amplifies the uncertainty of the velocity determination. In case of gas flows these effects are only important if significant pressure and therefore density differences exist between the measurement location defined by the light sheet and the observation location determined by the camera position. However, if liquid flows are examined using stereoscopic PIV there is always a large change due to the density variation at the air/liquid interface, as illustrated in Fig. 8.13. It is evident that due to the appearance of aberrations the geometrical picture of an object-point does not possess a unique image point. This leads to optical aberrations and image deformations which lower the accuracy of the flow measurement using PIV and PTV.

Although a detailed analysis of aberrations requires the theory of diffraction in order to account for the intensity distribution, the main features become evident by using the principles of geometrical optics which identify the image by the points of intersection of the geometrical rays with the image plane. To obtain the image position z of an object located on the optical axis at Z , the law of refraction has to be applied for each ray emerging from this point. The magnitude of the refraction effect depends on the object distance Z and the index of refraction of the two media according to

Fig. 8.13 Propagation direction of light rays passing an interface between two media of different index of refraction ($n_1 > n_2$). From [13]

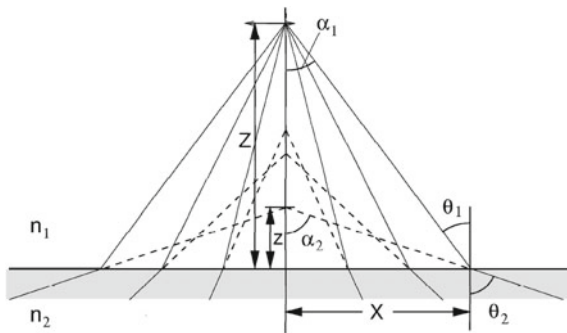


Fig. 8.13. In addition, the magnitude of the aberrations is proportional to the angle of incidence, because the variation of the intersection width z increases with increasing aperture angle. This is important for stereoscopic PIV as the observation angle must be large in order to resolve the out of plane velocity component with high accuracy, see Sect. 6.4. The limit $Z \rightarrow \infty$ is important as all rays intersect in only one point located at infinity and no aberrations occur at all. This situation can be generated by stopping the lens in a way that all rays are nearly parallel before they enter the planar interface. This possibility is frequently used in PIV but its applicability mainly depends on the output energy of the laser, on the cross-section of the light-sheet, on the scattering behavior of the particles and finally on the sensitivity of the digital camera.

To compensate the loss of light caused by closing the aperture the optical arrangement can be optimized by making use of the scattering properties of small particles. It was shown in Chap. 2 that small particles illuminated by coherent and monochromatic light scatter the light in a complex fashion determined by the theory of Mie. It follows from the Mie scattering diagram in Figs. 2.9–2.11 that the scattering intensity is rather low if the particles are observed under 90° as done in case of standard PIV. In case of stereoscopic PIV the 90° scattering configuration is illustrated in Fig. 8.14 (left). If the propagation direction of the light is changed, so that the light comes from the left hand side, the two cameras in the left figure observe particles in backward and forward scattering configuration. This will strongly increase the signal according to Mie scattering and by reducing the aperture of the lens the light might be already sufficient to avoid optical aberrations without reducing the signal-to-noise ratio too much.

The light intensity in the recording plane can be further enhanced if a pure forward scattering configuration is used as indicated in the right sketch of Fig. 8.14. In this case both cameras are on opposite sides of the light sheet and the propagation direction

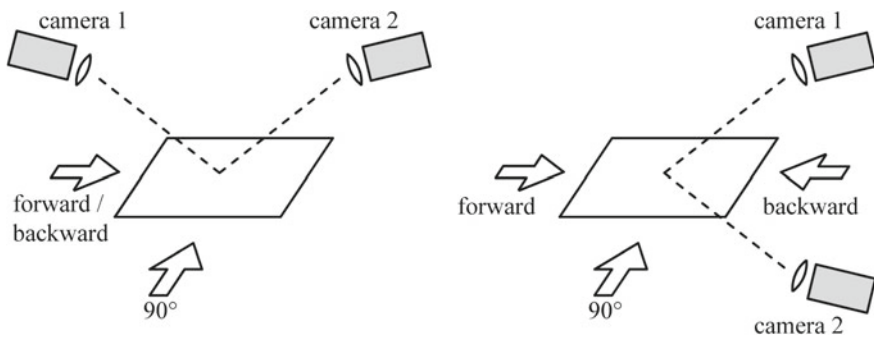


Fig. 8.14 Possible illumination and recording configurations for stereoscopic PIV. The arrows indicate various propagation directions of the light and the black dashed lines indicate the observation direction of the camera pair. As long as only the intensity of the scattered light is considered the most efficient light-sheet camera configuration is the purely forward scattering set-up, followed by the forward/backward configuration, purely backward and finally ninety degree case

of the laser must be from left to right according to the figure. However, if the light is coming from the right, the intensity in the recording plane will still be better compared to the 90° case illustrated by the third light propagating vector shown in the right figure.

Due to limited optical access, low signal or strong variations in the refractive index, closing the aperture is often not feasible or not sufficient. In this case other solutions are required in order to avoid optical aberrations without lowering the signal in the recording. As refraction effects vanish if the light passes the interface under 90°, optical elements can be used to minimize or even avoid refraction effects. In case of liquid flow analysis using stereoscopic PIV the use of prisms is a common solution to avoid optical aberrations. By using prisms the optical rays pass the interface under 90° and therefore nearly no refraction takes place. The specific prism solution can vary quite strongly in practice. For instance if a water tunnel is used as indicated in Fig. 8.15, were the water above the test section is at rest, it is possible to dip glass prisms into the water without disturbing the flow in the measurement domain.

In case of water channels without a free surface it is possible to glue water filled prisms to the side windows of the facility in order to ensure that no refraction effects appear, as displayed schematically in Fig. 8.16. In case of flow channels with complex or curved geometries such as a circular pipe as illustrated in Fig. 8.17, the curved part must be surrounded by an aquarium filled with the same liquid as the pipe. The aquarium must be shaped in a form that the laser light and the light scattered by the

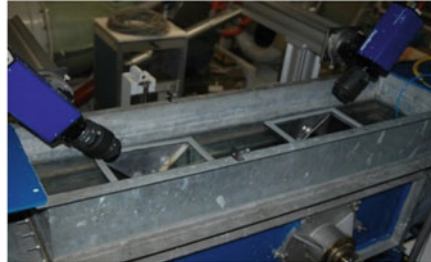
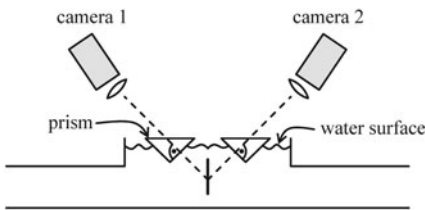
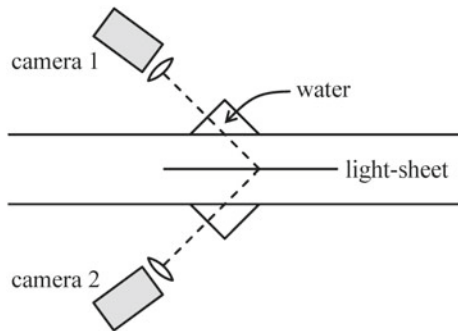


Fig. 8.15 Avoiding optical aberrations at the air-water interface by using air-filled prisms

Fig. 8.16 Avoiding optical aberrations at the air-glass-water interface by using water-filled prisms



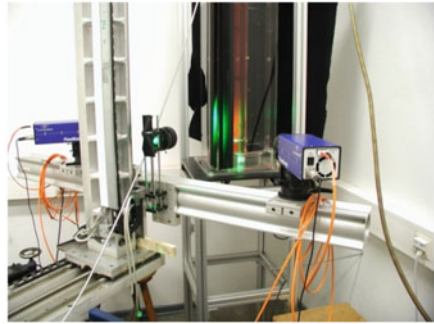
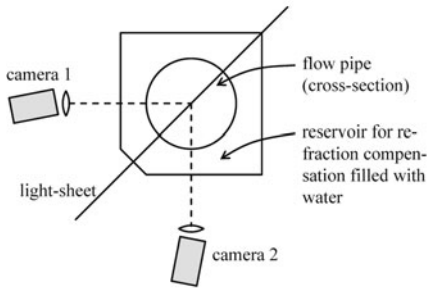


Fig. 8.17 Avoiding optical aberrations at the air-water interface by using air-filled prisms

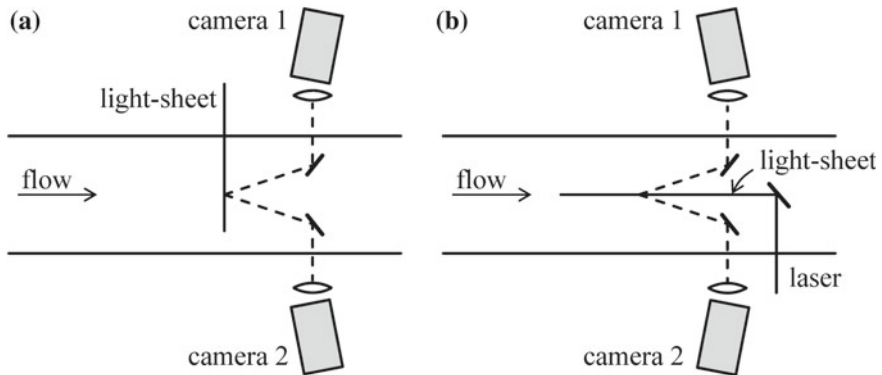


Fig. 8.18 Avoiding optical aberrations by placing the cameras at 90° to the air-glass interface illustrated for two different light-sheet configurations (a) and (b). Due to the mirror the Scheimpflug angle in the other direction

particles passes the interfaces liquid/glass/air perpendicular. In this case all unwanted refraction effects disappear and an almost perfect imaging condition can be realized which leads to particle images that are well suited for the image analysis methods typically used in PIV and PTV.

Instead of prisms, mirrors are sometimes used to avoid refraction effects, see Fig. 8.18. In this case the mirrors are placed inside the liquid and if the optical axis passes the air-liquid interface at 90° before the mirror reflects the light under a desired angle, aberrations can be avoided. If this approach is used, care must be taken with the selection of the mirrors material (silver, aluminum) because the mirror coating may vanish (erode) after some time due to ion transport in the liquid. Furthermore, the position of the mirrors must be downstream of the measurement location to avoid a disturbance of the flow at the plane of interest due to the wake flow behind the mirrors.

8.1.6 General Recommendations for Stereo PIV

- Multi-level or translated targets provide sufficiently good calibration results. Volumetric camera calibration commonly found in robot vision is not necessary and generally not possible due to the limited depth of field for large aperture lenses used for PIV.
- Calibration from a single image of a planar target is possible but should only be used if translation is not possible (i.e. due confined space).
- For optimum measurement accuracy the enclosed angle between the camera viewing axes should be close to 90° .
- The unavoidable misalignment between calibration target and light sheet plane requires disparity correction or self-calibration schemes using the actual particle images.
- Disparity correction can also be used to correct for movement of the camera(s) during the measurements (i.e. vibration).
- The minimum PIV sample size should be at least the same size as the light sheet thickness: $\Delta X_0 \geq \Delta Z_0$.
- The residuals $\varepsilon_{\text{resid}}$ of the 3C vector reconstruction serve as a quality check for the SPIV measurement and should have values in the range 0.1–0.5 pixel.
- For SPIV experiments in water the air-glass-water interface should be normal to the camera viewing axis to keep the astigmatism minimal. Oblique views are possible by attaching suitable water prisms to the test section [21, 29].
- Image reconstruction should make use of appropriate image interpolation schemes such as those reported in Sect. 5.3.4.4. For best performance iterative image deformation and image back-projection can be combined in a single step [31].
- In general it is important to invest sufficient time during the actual measurements to achieve an optimal calibration and PIV recordings. A posteriori corrections on the recorded data cannot always account for errors incurred during the measurement.

References

1. Abdel-Aziz, Y.I., Karara, H.M.: Direct linear transformation from comparator coordinates into object space coordinates in close-range photogrammetry. In: Symposium on Close-Range Photogrammetry. Falls Church, VA (U.S.A.), pp. 1–18. American Society for Photogrammetry and Remote Sensing (1971). DOI 10.14358/PERS.81.2.103. URL <https://doi.org/10.14358/PERS.81.2.103>
2. Arroyo, M.P., Greated, C.A.: Stereoscopic particle image velocimetry. Meas. Sci. Technol. 2(12), 1181 (1991). DOI 10.1088/0957-0233/2/12/012. URL <http://stacks.iop.org/0957-0233/2/i=12/a=012>
3. Coudert, S.J.M., Schon, J.P.: Back-projection algorithm with misalignment corrections for 2D3C stereoscopic PIV. Meas. Sci. Technol. 12(9), 1371 (2001). DOI 10.1088/0957-0233/12/9/301. URL <http://stacks.iop.org/0957-0233/12/i=9/a=301>
4. Ehrenfried, K.: Processing calibration-grid images using the Hough transformation. Meas. Sci. Technol. 13(7), 975 (2002). DOI 10.1088/0957-0233/13/7/303. URL <http://stacks.iop.org/0957-0233/13/i=7/a=303>

5. Elsinga, G.E., Scarano, F., Wieneke, B., van Oudheusden, B.W.: Tomographic particle image velocimetry. *Exp. Fluids* **41**(6), 933–947 (2006). DOI 10.1007/s00348-006-0212-z. URL <http://dx.doi.org/10.1007/s00348-006-0212-z>
6. Faugeras, O.D., Toscani, G.: Camera calibration for 3D computer vision. In: Proceedings of International Workshop on Machine Vision and Machine Intelligence, Tokyo, Japan (1987)
7. Fournel, T., Lavest, J.M., Coudert, S., Collange, F.: Self-calibration of PIV video-cameras in Scheimpflug condition. In: Stanislas, M., Westerweel, J., Kompenhans, J. (eds.) *Particle Image Velocimetry: Recent Improvements*, pp. 391–405. Springer, Berlin (2004). DOI 10.1007/978-3-642-18795-7_28. URL https://doi.org/10.1007/978-3-642-18795-7_28
8. Gauthier, V., Riethmuller, M.L.: Application of PIDV to complex flows: Measurement of the third component. In: *Particle Image Displacement Velocimetry*, von Karman Institute for Fluid Dynamics Lecture Series 1988-06. Von Karman Institute, Rhode-Saint-Genèse, Belgium (1988)
9. Gaydon, M., Raffel, M., Willert, C.E., Rosengarten, M., Kompenhans, J.: Hybrid stereoscopic particle image velocimetry. *Exp. Fluids* **23**(4), 331–334 (1997). DOI 10.1007/s003480050118. URL <http://dx.doi.org/10.1007/s003480050118>
10. Hartley, R., Zisserman, A.: *Multiple View Geometry in Computer Vision*, 2nd edn. Cambridge University Press, UK (2004). DOI 10.1017/CBO9780511811685. URL <https://doi.org/10.1017/CBO9780511811685>
11. Hinsch, K.D.: Three-dimensional particle velocimetry. *Meas. Sci. Technol.* **6**(6), 742 (1995). DOI 10.1088/0957-0233/6/6/012. URL <https://dx.doi.org/10.1088/0957-0233/6/6/012>
12. Jähne, B.: *Digital Image Processing and Image Formation*, 7th edn. Springer, Berlin (2018). URL <http://www.springer.com/us/book/9783642049491>
13. Kähler, C.J.: The significance of coherent flow structures for the turbulent mixing in wall-bounded flows. Ph.D. thesis, Georg-August-University zu Göttingen (Germany) (2004). URL <http://hdl.handle.net/11858/00-1735-0000-0006-B4C8-8>. DLR-FB-2004-24
14. Kähler, C.J., Kompenhans, J.: Fundamentals of multiple plane stereo particle image velocimetry. *Exp. Fluids* **29**(1), S070–S077 (2000). DOI 10.1007/s003480070009. URL <http://dx.doi.org/10.1007/s003480070009>
15. Kähler, C.J., Adrian, R.J., Willert, C.E.: Turbulent boundary layer investigations with conventional and stereoscopic particle image velocimetry. In: 9th International Symposium on Applications of Laser Techniques to Fluid Mechanics, Lisbon, Portugal (1998)
16. Kent, J.C., Eaton, A.R.: Stereo photography of neutral density He-filled bubbles for 3-D fluid motion studies in an engine cylinder. *Appl. Opt.* **21**(5), 904–912 (1982). DOI 10.1364/AO.21.000904. URL <http://ao.osa.org/abstract.cfm?URI=ao-21-5-904>
17. Klein, F.: *Elementarmathematik vom höheren Standpunkt aus*, Zweiter Band: Geometrie. Springer, Berlin (1968)
18. Lindken, R., Westerweel, J., Wieneke, B.: Stereoscopic micro particle image velocimetry. *Exp. Fluids* **41**(2), 161–171 (2006). DOI 10.1007/s00348-006-0154-5. URL <http://dx.doi.org/10.1007/s00348-006-0154-5>
19. Prasad, A.K.: Stereoscopic particle image velocimetry. *Exp. Fluids* **29**(2), 103–116 (2000). DOI 10.1007/s003480000143. URL <http://dx.doi.org/10.1007/s003480000143>
20. Prasad, A.K., Adrian, R.J.: Stereoscopic particle image velocimetry applied to liquid flows. *Exp. Fluids* **15**(1), 49–60 (1993). DOI 10.1007/BF00195595. URL <http://dx.doi.org/10.1007/BF00195595>
21. Prasad, A.K., Jensen, K.: Scheimpflug stereocamera for particle image velocimetry in liquid flows. *Appl. Opt.* **34**(30), 7092–7099 (1995). DOI 10.1364/AO.34.007092. URL <http://ao.osa.org/abstract.cfm?URI=ao-34-30-7092>
22. Pratt, W.: *Digital Image Processing: PIKS Scientific Inside*, 4th edn. Wiley-Interscience, Wiley, New York (2007). DOI 10.1002/0470097434. URL <https://doi.org/10.1002/0470097434>
23. Press, W.H., Teukolsky, S.A., Vetterling, W.T., Flannery, B.P.: *Numerical Recipes: The Art of Scientific Computing*, 3rd edn. Cambridge University Press, New York, USA (2007). URL <http://numerical.recipes/>

24. Royer, H., Stanislas, M.: Stereoscopic and holographic approaches to get the third velocity component in PIV. Particle Image Velocimetry. von Karman Institute for Fluid Dynamics Lecture Series 1996–03, pp. 11–156. Von Karman Institute, Rhode-Saint-Genèse, Belgium (1996)
25. Scheimpflug, T.: Improved method and apparatus for the systematic alteration or distortion of plane pictures and images by means of lenses and mirrors for photography and for other purposes (1904). British Patent No. 1196
26. Sinha, S.K.: Improving the accuracy and resolution of particle image or laser speckle velocimetry. *Exp. Fluids* **6**(1), 67–68 (1988). DOI 10.1007/BF00226137. URL <http://dx.doi.org/10.1007/BF00226137>
27. Soloff, S.M., Adrian, R.J., Liu, Z.C.: Distortion compensation for generalized stereoscopic particle image velocimetry. *Meas. Sci. Technol.* **8**(12), 1441 (1997). DOI 10.1088/0957-0233/8/12/008. URL <http://dx.doi.org/10.1088/0957-0233/8/12/008>
28. Tsai, R.Y.: A versatile camera calibration technique for high-accuracy 3D machine vision metrology using off-the-shelf TV cameras and lenses. *IEEE J. Robot. Autom.* **3**(4), 323–344 (1987). DOI 10.1109/JRA.1987.1087109. URL <http://dx.doi.org/10.1109/JRA.1987.1087109>
29. van Doorne, C.W.H.: Stereoscopic PIV on transition in pipe flow. Ph.D. thesis, Delft University of Technology (2004)
30. van Doorne, C.W.H., Westerweel, J.: Measurement of laminar, transitional and turbulent pipe flow using stereoscopic-PIV. *Exp. Fluids* **42**(2), 259–279 (2007). DOI 10.1007/s00348-006-0235-5. URL <http://dx.doi.org/10.1007/s00348-006-0235-5>
31. van Oord, J.: The design of a stereoscopic DPIV-system. Delft University of Technology, Delft (the Netherlands), Technical report (1997)
32. Wieneke, B.: Stereo-PIV using self-calibration on particle images. *Exp. Fluids* **39**(2), 267–280 (2005). DOI 10.1007/s00348-005-0962-z. URL <https://dx.doi.org/10.1007/s00348-005-0962-z>
33. Westerweel, J., Nieuwstadt, F.T.M.: Performance tests on 3-dimensional velocity measurements with a two-camera digital particle-image velocimeter. In: Dybbs, A., Ghorashi, B. (eds.) *Laser Anemometry - Advances and Applications 1991*, vol. 1, pp. 349–355 (1991)
34. Willert, C.E.: Stereoscopic digital particle image velocimetry for application in wind-tunnel flows. *Meas. Sci. Technol.* **8**, 1465–1479 (1997). DOI 10.1088/0957-0233/8/12/010. URL <http://stacks.iop.org/0957-0233/8/i=12/a=010>
35. Willert, C.E.: Assessment of camera models for use in planar velocimetry calibration. *Exp. Fluids* **41**(1), 135–143 (2006). DOI 10.1007/s00348-006-0165-2. URL <https://dx.doi.org/10.1007/s00348-006-0165-2>
36. Zhang, Z.: A flexible new technique for camera calibration. *IEEE Trans. Pattern Anal. Mach. Intell.* **22**(11), 1330–1334 (2000). DOI 10.1109/34.888718. URL <http://dx.doi.org/10.1109/34.888718>

Chapter 9

Techniques for 3D-PIV

9.1 Three-Component PIV Measurements in a Volume

For some studies the instantaneous velocity field in a volume of the flow (3D) is necessary to investigate the complex unsteady 3-dimensional flow behavior (e.g. vortices in wakes, the turbulent structure of boundary layers, jets and complex flow-structure interactions, etc.). Properties like velocity, vorticity and even pressure (see Sects. 7.5 and 7.6.4) are of increasing importance in both fundamental as well as industrial research. The requirements in terms of laser light intensity, cameras, evaluation algorithms and computing capacity are significantly higher than those for planar PIV. However, as discussed in this chapter, the principles and the practical rules that guide the setup of a 3D PIV experiment are established sufficiently well. As a result, a significant number of 3D PIV measurements has been realized, which demonstrates the maturity of 3D velocity measurements.

To date, several methods are available that realize the measurement of the velocity distribution in a 3D domain. Holographic PIV (HPIV) is based on the registration of the interference pattern produced by particles on high resolution photographic material [4, 37]). Registration via CCD sensors (digital holographic PIV, D-HPIV [51, 63]) allows for time-resolved measurements in a small volume. Tomographic PIV [20] achieves the information in depth of the illuminated volume via simultaneous observation with several cameras from different viewing angles. Furthermore, fast scanning of a thin light sheet (scanning PIV [12, 13]) yields time-resolved volumetric measurements in low velocity flows.

Many of these techniques are undergoing rapid development at present, their potential strongly depends on future technical developments and their characterization is beyond the scope of this book. A synthetic survey of the most common methods is given in the following section.

Multi-plane stereo PIV (details given in Sect. 17.1) requires several planes of the flow field to be illuminated simultaneously [38, 41–44, 49, 66–69]. The particle

An overview of the Digital Content to this chapter can be found at [DC9.1].

	Probe Volume [mm ³]	Time t →	Depth s ↓
(a) Stereo-PIV $f = 10$ Hz, Area = 40×40 cm ²	$5 \times 5 \times 1$		
(b) High-Speed Stereo-PIV $f = 1$ kHz, Area = 10×10 cm ²	$5 \times 5 \times 1$		
(c) Multi-plane Stereo-PIV $f = 10$ Hz, Area = 40×40 cm ² , variable Δt , Δz	$5 \times 5 \times \Delta z$		
(d) Photographic holographic PIV $f = 0$ Hz, Volume = $5 \times 5 \times 5$ cm ³	$1 \times 1 \times 1$		
(e) Digital holographic PIV $f = 10$ Hz, Volume = $1 \times 1 \times 1$ cm ³	$1 \times 1 \times 1$		
(f) Tomographic PIV $f = 10$ Hz, Volume = $6 \times 6 \times 1.5$ cm ³	$2 \times 2 \times 1$		
(g) High-speed Tomographic PIV $f = 1$ kHz, Volume = $3 \times 3 \times 1$ cm ³	$2 \times 2 \times 1$		

Fig. 9.1 Schematic overview over the present variants of the PIV method with their typical spatial and temporal resolution. The symbols represent the measurable three-component velocity vectors for each method in their spatial and temporal arrangement

images within each of such light sheets will be recorded with a separate stereo PIV system. The optical separation of these light sheets can be performed by polarization or different wavelength of the light used for illumination. This method exhibits the same properties as stereo PIV and does not allow to capture a complete volume (see Fig. 9.1c). With the information of the instantaneous velocity fields in different planes, the local determination of the full velocity gradient tensor becomes possible. Drawback of this method is the high precision required for the experimental alignment and the hardware effort. For each plane a complete stereo PIV system has to be set up together with additional elements for the required optical separation (polarization, color filters).

Another method uses fast step-wise scanning of the volume by means of a conventional light sheet arrangement [10–13]. However this method is only applicable for either the determination of mean velocity fields or for very low flow velocities (typically few cm/s, e.g. flows in water), as the different planes within the volume have to be recorded sequentially at different time instants. The measurement volume depth is limited by the depth of focus of the cameras.

Photogrammetric methods [15, 60, 80, 106, 107] capture a volume of the flow instantaneously. The complete volume is illuminated by one light pulse. The images of the tracer particles will be recorded from different camera positions. The individual particles are identified on the different recordings and their position in space is calculated by photogrammetric methods utilizing the different views. The local particle velocity is determined with particle tracking methods. In case of simple PTV algorithms, the seeding concentration in the flow needs to be limited (typically 0.001 particles/pixel) in order to be able to identify individual particles uniquely.

This results in a low spatial resolution of this method. A further problem arises from the limited depth of focus, which leads to larger unfocused particle images, which may overlap with those in focus.

Holographic PIV yields volumetric resolution without the need for particles detection [37]. The method requires a coherent light source, such as a laser. The light scattered by the particles is superimposed with light of a reference wave on the photographic recording medium. The resulting interference pattern (hologram) stores intensity and phase of the light coming from the object. The photographic medium must possess high spatial resolution in order to correctly store the interference pattern. Photographic holographic plates typically allow resolving 3000 lines per mm. Volumes of $50 \times 50 \times 50 \text{ mm}^3$ with a resolution of 1 mm^3 , corresponding to 10^6 vectors, could be successfully captured with photochemical holographic PIV (P-HPIV) [3, 4, 82]. The wet chemical processing is the main disadvantage of the method as only single recordings can be taken. After reconstruction of the hologram, the particle images are usually scanned by a CCD sensor for subsequent PIV evaluation, performed digitally by a computer.

A further approach is to use electronic sensors to record the hologram. The pixel size (typ. $3 - 5 \mu\text{m}$) is by far larger than the wavelength of light, which can be tolerated if the incident light comes with a small angle with respect to the reference illumination (“in-line”) and that the objects (particles) must be sufficiently distant from it. The reduced effective aperture is the cause of a poor depth resolution. Digital holographic PIV (D-HPIV) typically captures a volume of 1 cm^3 and allows resolving a few thousand vectors [51, 61, 63]. In holography maximum spatial resolution and observation volume strongly vary depending on the properties of the image sensors and the photographic plates, respectively (Fig. 9.1d, e). In this context digital holography becomes more and more attractive due to the fast progress made at image sensors (CCD, CMOS) at present. Further attempts to increase the signal-to-noise ratio of holography have utilized short coherence length (“light in flight”) [36]. Improvement of depth resolution can be obtained by observation from different directions [53, 100, 101, 118]. Digital holography still holds considerable potential as the pixel count of sensor arrays are continually increasing and at the same time exhibit reduced pixel sizes.

The current method of choice for capturing the instantaneous flow field with 3-D unsteady flow phenomena is represented by tomographic PIV. Figure 9.1 depicts the typical spatial and temporal resolution achieved with the different PIV measurement configurations. It must be remarked that for both stereoscopic PIV and Tomographic PIV the measurement domain can be enlarged by an order of magnitude when larger tracers are used, such as helium filled soap bubbles in air flows and coated hollow microspheres in water as discussed in Chap. 2. Given the widespread use of tomographic PIV for 3D measurements, the following part of this chapter is devoted to explain the working principle of this technique. In the same context, there have recently been rapid developments towards particle-based analysis. Therefore, the chapter concludes with some elements of 3D particle tracking velocimetry and the specific “Shake-The-Box” (STB) algorithm, which has demonstrated a high accuracy in 3D velocity measurements.

9.2 Tomographic PIV

9.2.1 General Features

The distinctive feature of tomographic PIV (often called ‘‘Tomo-PIV’’) with respect to the stereoscopic technique is that the measurement domain is modelled as a three-dimensional volume rather than a plane. In order to obtain volumetric information from its planar projections one needs to invoke the principles of tomography. A schematic diagram illustrating the steps involved in tomographic PIV is given in Fig. 9.2.

The measurement volume is produced with a typical width(height)-to-depth aspect ratio of 4:1. The illumination is obtained by expanding, or reducing the thickness of the laser light beam to the required depth of the field of view (FOV) and expanding it in the other direction. As a consequence more pulse energy is required in comparison to planar PIV experiments. A number of cameras (typically 3 to 6) is placed subtend-

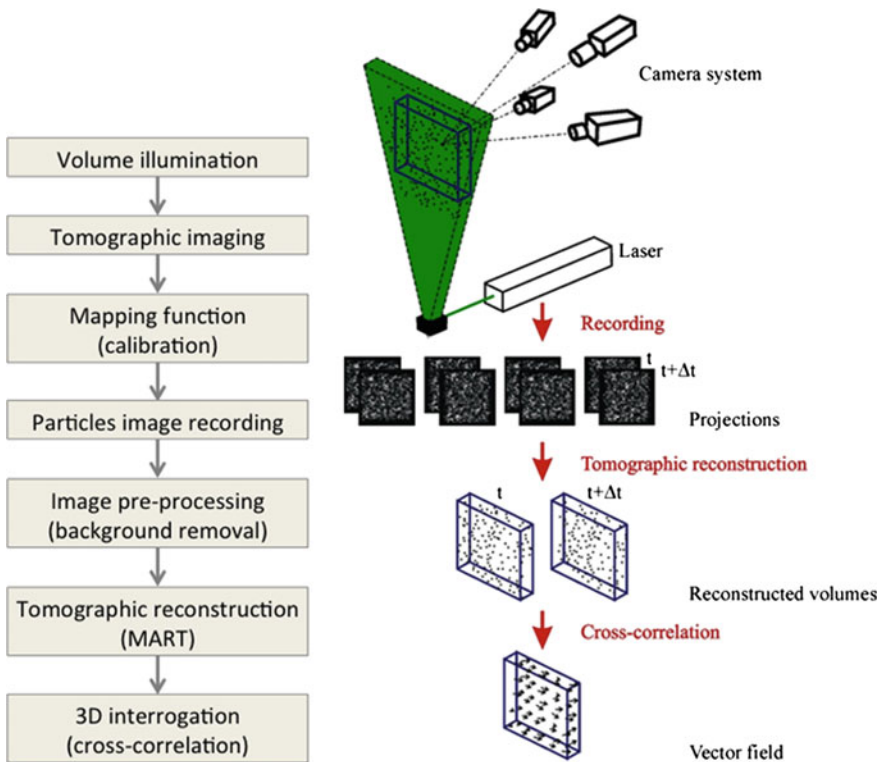


Fig. 9.2 Left: flow chart of Tomo-PIV measurement procedure. Right: schematic illustration of the technique (reproduced after ELSINGA et al. [20])

ing a solid angle to observe the illuminated region from several viewing directions. The relation between the position in three-dimensional space (X, Y, Z) and its projections onto the image planes (x_i, y_i) is obtained with a calibration procedure, similar to that of stereoscopic PIV. The light scattered by the tracers is imaged onto several cameras with the requirement that particle images are in focus. The latter requires a focal depth of the imaging system at least as large as the illumination volume thickness. The set of simultaneously recorded images from all cameras (image pairs in the common case of double-frame recordings) is the input to the tomographic reconstruction algorithm. The three-dimensional object is a discrete representation of the particles light intensity $E(X, Y, Z)$, reconstructed from its simultaneous projections $I(x_i, y_i)$ defined in the image space. This is commonly done by the iterative algebraic reconstruction method (MART among others). The analysis of the particles motion within a pair of objects is performed by three-dimensional cross-correlation.

9.2.1.1 Volume Illumination

As described in Table 9.1, the illumination source used in the majority of Tomo-PIV experiments is the same pulsed laser as in use for planar PIV measurements. Illuminating a volume is simpler than forming a plane. For instance, when an illuminated thickness of one-centimetre is required, for most Nd:YAG lasers with a comparable beam exit diameter, the optical components for volume illumination can be reduced to a minimum of one cylindrical diverging lens. When a larger thickness is required a beam expander (e.g. a pair of spherical lenses, negative followed by a positive) may be of practical use. The pulse energy needs to increase with the square of the measurement volume if light intensity is to be maintained constant. The above requirement,

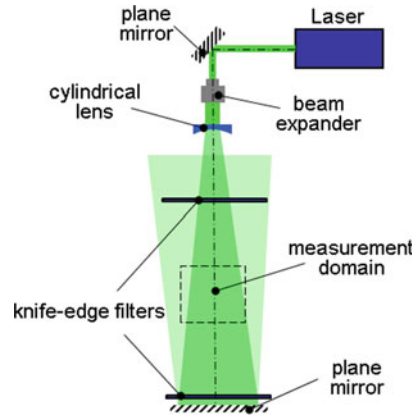
Table 9.1 Measurement volume in tomographic PIV experiments

Experiment	Medium	Tracers	Pulse energy (mJ)	Rep. rate (Hz)	Thickness (mm)	Volume (cm ³)
Cylinder wake [20]	Air	1 μm fog	200 (S) ^a	10	8	25
Cylinder wake [85]	Water	56 μm polyamide	200 (D)	10	20	200
Airfoil wake [32]	Air	1 μm fog	10 (M)	2,700	8	18
Flapping wing [79]	Water	56 μm polyamide	Computer projector	250	40	400
Flying locust [8]	Air	1 μm fog	10 (S)	1,000	4	20
Wind turbine [14]	Air	HFSB ^b	25 (S)	1,000	150	1,000
Confined thermal plume	Air	HFSB ^b	LED array	29	800	550,000

^aLight amplification: S = single-pass; D = double pass; M = multi-pass

^bHFSB = Helium Filled Soap Bubbles

Fig. 9.3 Schematic description of a double-pass illumination system

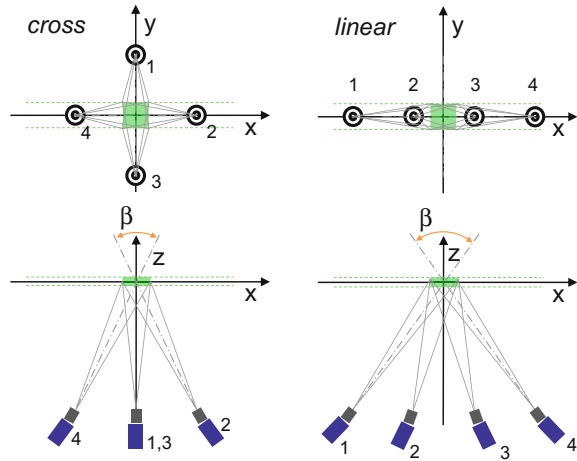


along with that of in-focus particle imaging are the most limiting factors for the scale-up of tomographic PIV experiments. The most practiced technique to increase illumination intensity for tomographic PIV is the use of mirrors for double or multiple light passes. The double pass approach [85] is the simplest and consists of placing a planar mirror along the laser light path (see Fig. 9.3). An interesting advantage of this technique is that all cameras can easily be receiving light in forward scattering direction from one of the two passes. Therefore, the effective gain, including imaging effects, of the double-pass system can be more than double the single pass. A more complex system is required for multi-pass illumination [31, 94] (see Fig. 2.53). The laser beam may be expanded to the required volume depth and sent towards a region enclosed between two highly reflective mirrors placed at a small relative angle, where its path will cover the entire region by multiple reflections (typically 10 to 20). Multiple pass illumination is mostly used for air flow experiments with high repetition rate tomographic PIV, with reported gain factor up to 7 with respect to the single pass system (see Fig. 9.4). Double and multi-pass illumination can only be applied in rather simple configurations where the mirrors can be placed aside the illuminated region.

Measurement volumes achieved in tomographic PIV experiments are summarized in Table 9.1. Typical volumes achieved in air flows are in the order of 20 cm^3 for low-rep rate systems and 10 cm^3 for kilohertz rate systems. A volume ranging from 200 to 400 cm^3 is typically achieved in water experiments. When using large neutrally-buoyant tracers (Helium filled soap bubbles, HFSB) measurement volumes from several liters up to a fraction of a cubic meter (in combination with LED array illumination) have been achieved in air flows (Table 9.1).

Knife-edge filters are often employed within the illumination systems for Tomo-PIV to sharply cut the light intensity beyond the nominal thickness of the measurement volume. Any light recorded onto the images that originate from regions outside the reconstructed volume will be included in the reconstructed object, increasing the noise in the reconstructed signal.

Fig. 9.5 Two common imaging configurations for tomographic PIV (reprinted from SCARANO [84])



of the system. Placing the cameras in a cross-like configuration has a similar effect (Fig. 9.5, left) with the advantage of an easier setting of the lens-tilt adapter (the lens plane rotates vertically or horizontally). In some cases, experiments were conducted with all cameras along a line with an arc-like system (Fig. 9.5 right), with the result that the outer cameras must be set to a large viewing angle. Placing all cameras in forward scattering direction usually requires that the object must be viewed from opposite sides, which involves a more extended optical access, similar to stereoscopic PIV. In experiments conducted in water flows the interface between the air and the wall of the container is usually made normal to the viewing direction adding optical prisms, as commonly done in stereo PIV experiments [103].

It is crucial that the particles are imaged in focus ensuring that the sensor area covered by particle images is minimized for a given amount of particles. The condition to be respected is that the focal depth δz should be larger or equal to the depth of the illuminated volume ΔZ . The equations of diffraction-limited imaging are given in Sect. 2.5.1. For the determination of the focal depth of the system, Eq. (2.16) is to be considered. Care should be taken that the Scheimpflug condition is respected between the image plane and the median plane of the illuminated volume. It is worth recalling here that the peak particle image intensity I_p is inversely proportional to the fourth power of the measurement volume depth for a chosen optical magnification. Therefore, complying with the above requirement goes rapidly at the cost of particle signal intensity.

A procedure to measure and compensate for out-of-focus conditions beyond the suggested limit of 2 pixel has been recently proposed, based on a non-uniform weighting function obtained from a calibration of the optical transfer function (OTF) [88].

9.2.1.3 Seeding Density

The concentration of particle tracers within the measurement volume ultimately determines the spatial resolution of the measurement. The number of particles within an interrogation box IB required to perform a robust cross-correlation analysis varies between 5 and 10. This is on the lower side of the requirements for planar PIV measurements because loss-of-pairs is negligible for 3D particle motion analysis. The concentration of particle tracers in the measurement domain is limited by the maximum image source density that can be accurately dealt with by the tomographic reconstruction. A four-camera system accurately reconstructs images with a seeding density up to 0.05 ppp (particles per pixel). Experiments performed with more cameras [28, 57] or with advanced algorithms for time-resolved sequences [59, 72] achieve an accurate reconstruction up to 0.2 ppp. Furthermore, the value also depends on the particle image diameter d_τ^* normalized by the pixel size and by the quality of the imaging process. Considering the fraction of image occupied by particle images (source density NS [1]) the above criteria translate to $NS < 0.5$ for a tomographic reconstruction with a standard system of four cameras and to NS approaching unity when using more cameras or advanced algorithms. In water flows, particle tracers of 10 to 100 μm are typically employed, an additional limitation to the seeding concentration comes from the increased opaqueness especially for large particle tracers. Excessive particle concentration leads to poorly controlled illumination with laser light diffusion (multi-scattering) and loss of image contrast. From experiments conducted with particles of 56 and 10 μm diameter, the limit for opacity is reached already at values of the concentration C of approximately 0.5 and 3 particles/ mm^3 respectively [64]. These effects are less important in air flows with one-micron droplets. The typical level of particles concentration that has been reached before observing decreased optical transmission is $C = 10$ to 20 particles/ mm^3 . Finally, the problem of medium opacity can be encountered in air flows when using helium filled soap bubbles (HFSB).

The design of the experiment in relation to the optimum seeding concentration is discussed below. The constraint of medium opacity is not considered here and needs to be evaluated separately. Considering an illuminated volume of dimension $V_M = L \times H \times W$ (mm^3), the total number of particles within the measurement domain is $N_P = C \times V_M$. The digital imaging resolution is $D_R = M/\Delta_{\text{pix}}$ (pixel/ mm) obtained by the ratio between optical magnification and pixel pitch. The object space is discretized in voxels: assuming a unit ratio of voxel and pixel length (in object space), the value of the digital resolution also applies to the 3D domain discretization (i.e. voxels/ mm). The particle density in the discretized object space is then expressed by particles per voxel $PPV = C/D_R^3$. The projection of the particle tracers onto the images results in the source density NS or in the number of particles per pixel ppp:

$$N_S = \text{ppp} \cdot \frac{\pi}{4} (d_\tau/\Delta_{\text{pix}})^2 = PPV \cdot W \cdot D_R \cdot \frac{\pi}{4} d_\tau^{*2}, \quad (9.1)$$

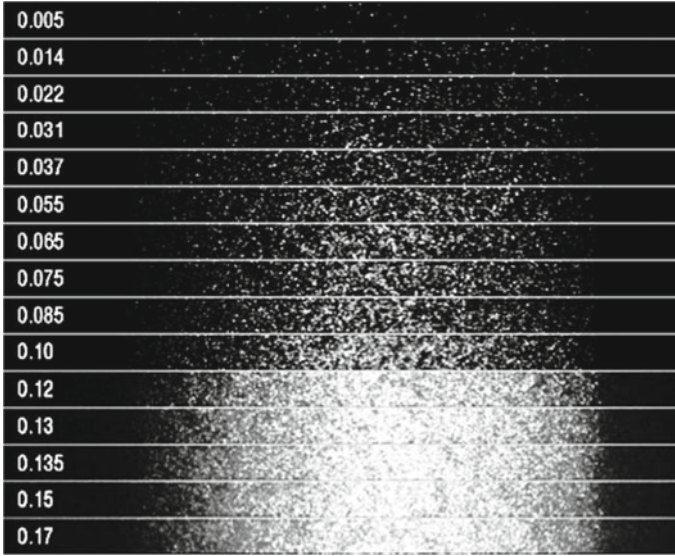


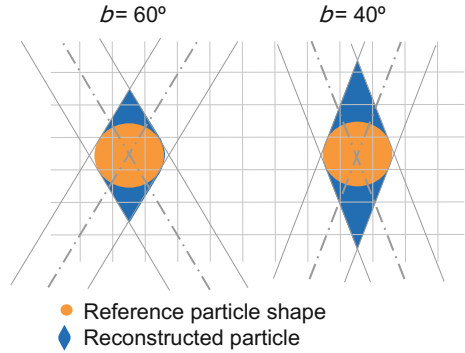
Fig. 9.6 Images of experiments at different particle concentration. The seeding density for each stripe is indicated in particles per pixel ppp (reprinted from SCARANO [84])

The relation between the particle concentration C and the source density N_S reads as:

$$C = \frac{N_S \cdot D_R^2}{W} \cdot \frac{4}{\pi d_\tau^{*2}}. \quad (9.2)$$

For a given choice of the illuminated volume and imaging conditions, the concentration is only limited by the maximum density of particle images collected on the recordings. Numerical simulations indicate that when $NS < 0.5$ an accurate reconstruction is achieved with a four-camera system. Figure 9.6 illustrates an exemplary experiment conducted in water, where the particle concentration is varied under controlled conditions [64] at constant particle image diameter ($d_\tau^* = 2$). Levels of ppp between 0.005 and 0.022, ($0.015 < NS < 0.066$) are considered too sparse for tomographic measurements, and the imaging system is used inefficiently. Increasing the seeding density up a point where the overlap between particle images remains negligible (ppp = 0.055, $NS = 0.16$) is a good indication of optimal measurement conditions. Accurate reconstruction of denser particle field is still possible slightly beyond this level (e.g. at $NS = 0.3$), however, special care must be taken in terms of image quality, calibration accuracy and using a larger number of cameras. Beyond a level of $NS \approx 0.5$ the image contrast decreases dramatically due to the loss of optical transmission in the seeded medium.

Fig. 9.7 Reconstruction error due to finite tomographic angular aperture (reprinted from SCARANO [84])

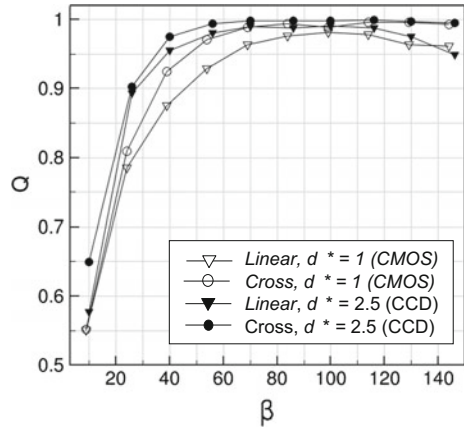


9.2.1.4 Tomographic Angular Aperture

The imaging system is typically composed of a small number of cameras N_C placed along non-collinear viewing directions that subtend a solid angle. The system angular aperture determines the ratio between the resolved element along H and L and along the depth W . A simple criterion is that the depth resolution of particle tracers depends upon the maximum planar angle β obtained within the solid angle formed by the system of cameras. The choice of a one- or two-dimensional array of cameras is often dictated by constraints on optical access or complexity of camera installation. The quality of tomographic reconstruction is maximized when the total angle β ranges between 40 and 80 degrees. For higher values of the viewing angle the reconstruction quality decreases due to the longer intersection of the lines-of-sight across the measurement volume, thus increasing the image source density. Instead, smaller values of β lead to the formation of elongated particles along the direction of the tomographic optical axis (viz. depth). This is illustrated in Fig. 9.7, where the actual particle (drawn as orange circle) is distorted approximately into a double-cone with aperture β (in light blue). Due to the three-dimensional nature of the problem, the cross configuration has a slight advantage with respect to the more practical linear arrangement (Fig. 9.8).

A condition to be avoided in the arrangement of cameras is that they are collinear. This is practically possible only when the illuminated domain is observed from opposite directions. Two viewing directions should be considered collinear when their angular separation $\Delta\theta$ leads to negligible separation between the lines of sight, compared with the back-projected particle image diameter. In practice two views may be considered non-collinear when $\Delta\theta \gg d_\tau/M/\Delta Z$. Typically, a misalignment of more than a degree is already effective in terms of ensuring non-collinear condition.

Fig. 9.8 Reconstruction quality factor Q versus system aperture angle β . Linear and cross-like configuration. Results shown for small and large particle image diameter (reprinted from SCARANO [84])



9.2.1.5 System Calibration

The tomographic reconstruction is based on the geometrical relation between the 3D physical space (viz. object space) and the image space, referred to as mapping function M [81, 114]. In 3D PIV one refers to a point in physical space as $\mathbf{P} = (X, Y, Z)$. Its projection on the image plane of the i th camera is $\mathbf{p}'_i = (x, y)$, or:

$$(x_i, y_i) = M_i(X, Y, Z). \quad (9.3)$$

Following the approach taken for stereoscopic PIV the third order polynomial and the pinhole model are the most commonly adopted choices to represent the mapping function, with a slight advantage for the former in case of unknown aberrations across the optical path (e.g. glass windows). As discussed in Sect. 8.1 the calibration function for stereoscopic measurements is obtained imaging a single- or multi-layered template at the measurement plane position. The latter is an important constraint of stereoscopic PIV calibration. Any misalignment between the calibration plane and the illuminated plane leads to rather large errors that require a correction based on the disparity vector field (see Sect. 8.1.4) [86, 114]. The calibration correction methods based on the evaluation of the disparity vector field are referred to as “self calibration” [110]. The registration error is then corrected modifying the coefficients of the polynomial fit used for the calibration. In tomographic PIV the calibration procedure does not map the position of a specific illuminated plane, but encompasses the measurement volume: a finite interval of the 3D physical space. The positive outcome is that tomographic PIV calibration does not require any alignment between the plane of the calibration target and the illuminated volume. Nonetheless, the requirements on calibration errors due to cameras misalignment after calibration are considerably stricter than those for stereoscopic PIV. The 3D particle field reconstruction by tomography requires that the lines-of-sight corresponding to particles imaged by all the cameras are intersecting precisely. Any misalignment larger than a fraction of

the particle image diameter will result in a rapid degradation of the reconstructed intensity field [20]. For instance, consider a tomographic system observing a FOV of 50 mm width from a working distance of one meter, an unwanted camera rotation in the order of 0.1 milli-radians will already introduce an unacceptable triangulation error in the order of 50 μm , corresponding to one pixel (in object space).

In realistic experimental conditions, tomographic PIV imaging systems often lack of pointing precision, due to mechanical stability of camera holders, tightness of lens-tilt adapters, thermal variations within the cameras and vibrations due to the cooling systems of the cameras or additionally from the wind tunnel. It is common to incur in misalignments of three or five pixel. In the above conditions it is imperative that the alignment between the lines-of-sight from each camera is restored by a correction procedure, or the reconstruction procedure will fail. A procedure for misalignment detection and correction for 3D measurements similar to that used in stereoscopic PIV is known as “3D self-calibration” [111], which is based on particle detection in the individual recording and their triangulation in 3D space. The correlation data

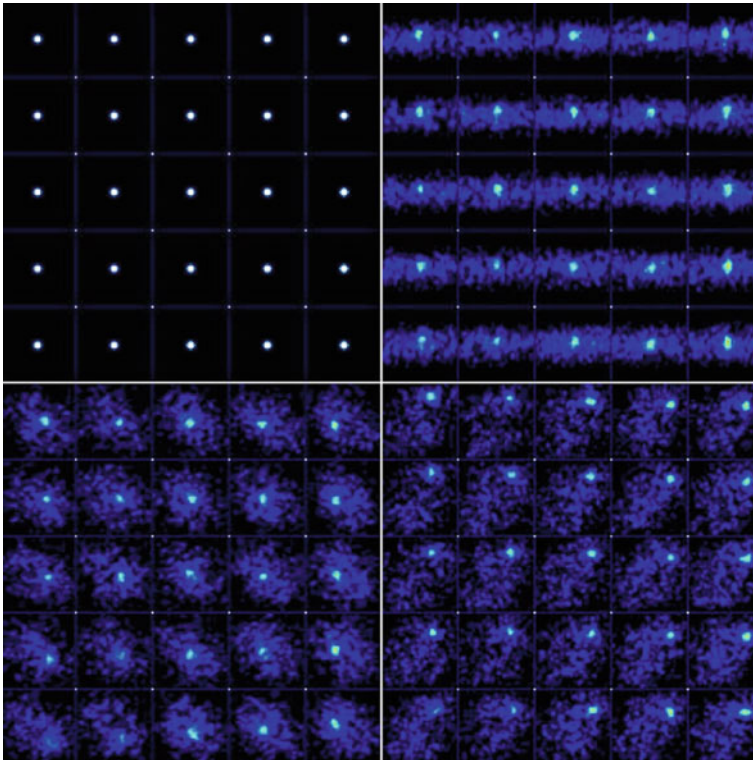


Fig. 9.9 Disparity maps for a four-camera tomographic system obtained with the 3D self-calibration technique. Camera 1 (top-left) is considered as the reference. Camera 4 (bottom-right) shows triangulation of particle images with displaced peaks, indicating a motion of the camera has occurred after calibration

is clustered over a large number of detected particles (typically in the order of 10^4) yielding the statistical estimate of the local disparity vector used to correct the mapping functions for all cameras. The above procedure is now considered the standard approach as it has been applied in several experiments detecting misalignment errors (up to several pixel) and reducing them to below 0.1 pixel (Fig. 9.9).

9.2.1.6 Image Pre-processing

Image pre-conditioning is more important in tomographic PIV than planar PIV because the reconstruction technique is sensitive to background light intensity [20]. Any light recorded by the cameras that does not originate from the measurement domain will be projected back into the reconstruction volume. An effective method for background intensity removal is a combination of pixel-wise time-history minimum subtraction and a small neighborhood (e.g. 11×11 pixel) minimum intensity subtraction. Image low-pass filtering by a Gaussian kernel of 3×3 pixel is sometimes used, mostly to mitigate residual calibration errors with increasing the particle image size. It should be retained in mind that increasing the particle image size also increases the image source density NS with detrimental effects on the reconstruction quality. Image smoothing should only be considered at low seeding density (i.e. $NS < 0.15$ or $ppp < 0.05$). For time resolved recordings, additional filtering techniques can be used that are based on spectral filtering (high-pass filter) of the images that have proven valid in planar experiments [98] (see Fig. 9.10).

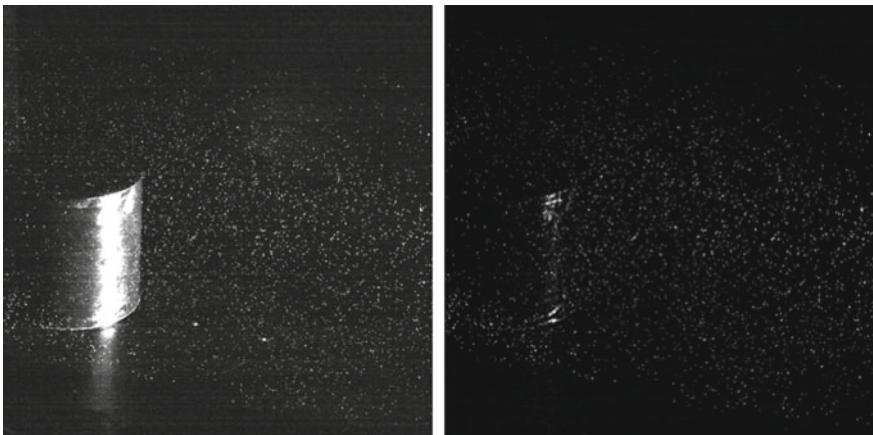


Fig. 9.10 Image recording from tomographic experiment in the wake of a cylinder obstacle. Raw image (left) after pre-processing (right) by subtracting time minimum pixel-wise (over 9 subsequent frames) and spatial sliding minimum (over a 9×9 pixel kernel)

9.2.2 3D Object Reconstruction

The novel aspect introduced with the tomographic-PIV technique is the reconstruction of the 3D field of scattering particles by optical tomography. Most early research on tomographic PIV has concentrated on the digital reconstruction techniques bringing significant advances on the side of its computational efficiency [2, 117]. The reconstruction of the 3D object from the digital images is based on the mapping function between the image planes and the physical space. The 3D intensity distribution is mathematically represented by an array of voxels discretizing the physical space of coordinates (X, Y, Z) with intensity $E(X, Y, Z)$. The projection of the volume intensity $E(X, Y, Z)$ onto the image at a position corresponding to the i th pixel position (x_i, y_i) returns the pixel intensity $I(x_i, y_i)$. This relation can be written as a linear equation in the hypothesis of linear superposition of the light intensity from all scattering particles

$$\sum_{j \in N_i} w_{i,j} E(X_j, Y_j, Z_j) = I(x_i, y_i), \tag{9.4}$$

where N_i is the number of voxels contributing to the image intensity of the i th pixel (x_i, y_i) . These voxels are intersected by the line of sight associated to (x_i, y_i) together with their close neighbours (typically within one kernel 3×3 centred on the intersected voxel). The coefficient $w_{i,j}$ weights the contribution of the j th voxel with intensity $E(X_j, Y_j, Z_j)$ to the pixel intensity $I(x_i, y_i)$. The weighting coefficient can be calculated as the fraction of volume intersection between the chosen line of sight and the considered voxel (Fig. 9.11).

The estimation of the volume intersection can be approximated assuming a conical line-of-sight intersecting spherical voxels. Because this coefficient needs to be evaluated a large number of times, it is computationally efficient to pre-calculate it and access it from a look-up-table. Different intersection models have been discussed in the literature [102]. A unit ratio between pixel projection and the voxel element is often assumed for simplicity, but algorithms that accelerate the calculations are based on voxel binning [18]. A solution approach to the problem defined by Eq. (9.4) is the subject of tomographic reconstruction algorithms. The initial comparison between the algebraic reconstruction techniques (ART) [33] and the multiplicative algebraic reconstruction techniques (MART) [35] have clearly indicated the advantages of the latter. The update equation for MART reads as:

$$E_{k+1}(X_j, Y_j, Z_j) = E_k(X_j, Y_j, Z_j) \left(\frac{I(x_i, y_i)}{\sum_{i=1}^N W_{j,i} E_k(X_j, Y_j, Z_j)} \right)^{\mu W_{i,j}} \tag{9.5}$$

where $0 \leq \mu \leq 1$ is a scalar relaxation parameter, typically set to a value of 1 for a fast convergence rate. In the MART method, the update is driven by the ratio of the pixel intensity and the corresponding object projection. The exponent ensures that only the elements in $E(X, Y, Z)$ affecting the i th pixel are updated. Furthermore the

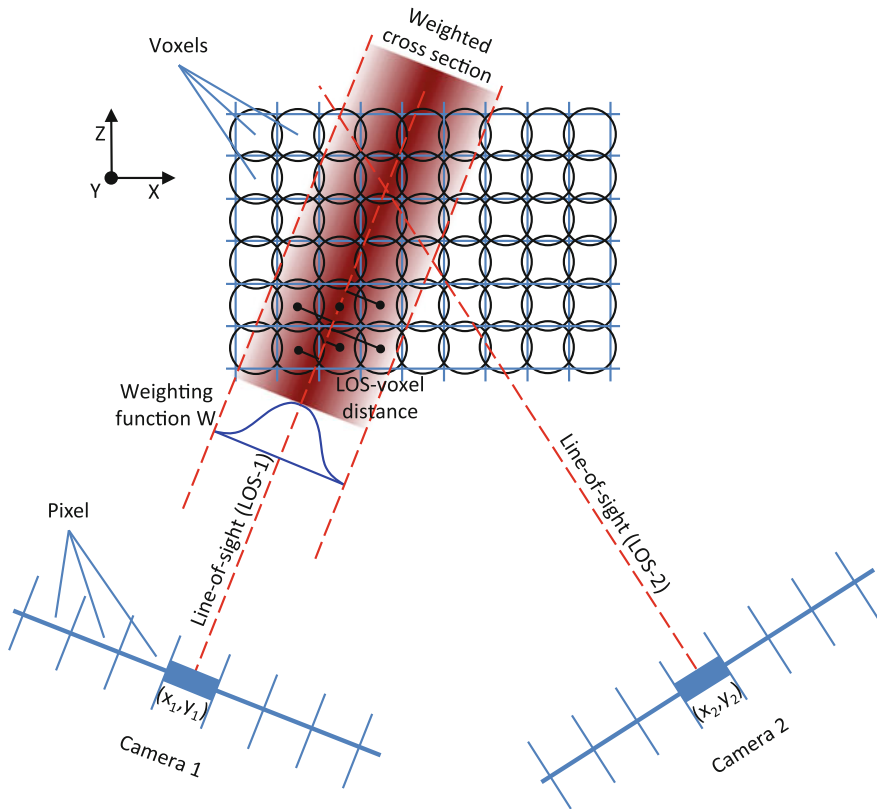


Fig. 9.11 Object discretization and imaging model used for tomographic reconstruction. The voxels falling within the shaded stripe (weighted cross section) have nonzero value of the weighting coefficient $W_{i,j}$. Spherical shape for voxels is commonly assumed that simplifies the calculation of the weighting coefficient (reprinted from SCARANO [84])

multiplicative MART scheme requires that E and I are definite positive. This detail may not be straightforward when dealing with images pre-processed with intensity subtraction. Because for ART the correction term (algebraic difference between the integrated intensity along the line of sight and the actual intensity detected on the pixel) is summed up to the current reconstructed intensity field, the method acts as an OR operator for the voxel intensity. Consequently, for any given pixel where a particle is detected, all voxels along the corresponding line-of-sight will be set to a nonzero intensity. The result is a broad dispersion of the reconstructed intensity field along all viewing directions with loss of reconstructed particle peak intensity. In contrast, the MART update is given by a multiplication of the current intensity field by a term given by the ratio between recorded intensity and integrated along the line of sight. In this case the operation approximates an AND operation and a voxel has nonzero intensity only if along all lines of sight intersecting it a particle is detected. Clearly the MART

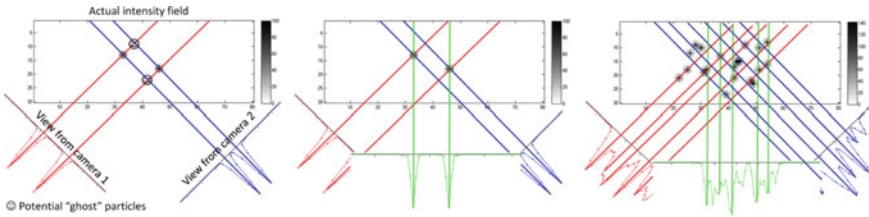


Fig. 9.12 Imaging of 3D particle field. Left: two views for two particles yield four potential reconstruction. Centre: adding a third view eliminates simultaneous spurious intersections (ghost particles). Right: seeding density not allowing particles to be imaged distinctly

method is better suited than ART for the treatment of tomographic PIV recordings. As a result, almost all tomographic experiments realized so far are based on the MART technique for 3D reconstruction. Some approaches have been also proposed, based on the intuitive concept of averaging of geometrically reprojected tomographic images [5] which can be performed in a computationally efficient way. However, the resulting intensity field is similar to that returned by a single ART iteration, which needs considerably more cameras to achieve the reconstruction accuracy of iterative MART.

Figure 9.12 illustrates the mechanism of ghost particles formation. The simplified case of a 2D object is considered: when two cameras record a set of two particles, four possible particles are the solution of the reconstruction algorithm. This problem is referred to as ghost particles [60]. Introducing a third viewing direction completely solves the ambiguity. An accurate reconstruction is still possible at higher seeding density as long as most particles are projected onto well distinct images, as shown in Fig. 9.13-centre. The solution obtained by iterative ART and MART calculation is illustrated in Fig. 9.13. The intensity reconstruction by ART exhibits peaks at intersections of the lines of sight where particles are detected. However, the object intensity initially distributed along the entire lines of sight intercepting particles is not entirely eliminated with further iterations. The object reconstruction by MART follows a similar pattern at the first iteration. The multiplicative algorithm eliminates the spurious intensity along lines of sight with the subsequent iterations. As a result a significantly higher accuracy is gained in comparison to the ART method. Nevertheless, at high seeding density, also the reconstruction obtained from MART suffers from a lower contrast due to the increased number of ghost particles, which underlines the importance of the iterative procedure that updates the object intensity. A comparison between the accuracy of the iterative MART approach to that obtained with the multiplicative line-of-sight method, a rapid, single-step evaluation by multiplication of the projected light intensity along the lines of sight [2] indicates that the single-step solution of the reconstruction problem yields an acceptable accuracy at low levels of the seeding density ($ppp < 0.02$ or $NS < 0.1$). Therefore the single-step multiplicative approaches, MFG or MLOS, are best suited as tools to accelerate the time-consuming process of iterative MART reconstruction. Their principle is that the particle distribution in the 3D object is very sparse (90% to 99% of the voxels

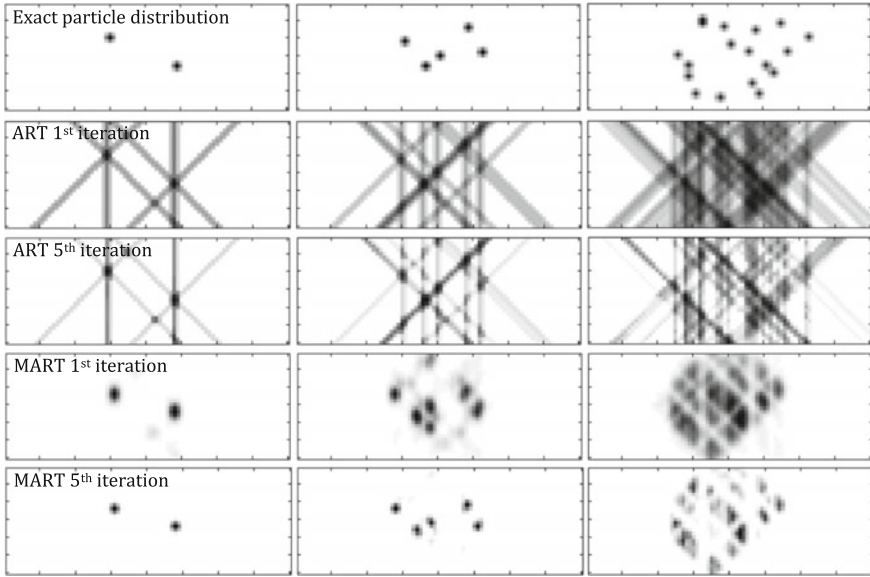


Fig. 9.13 Computer simulated particle distribution (top row) and reconstructed intensity field with 3 coplanar views. Comparison of ART and MART methods. Inverted grayscale (reprinted from SCARANO [84])

have zero intensity) and only voxels corresponding to non-zero intensity need to be updated from the second iteration further. When the seeding density is increased to the point that most particle images overlap with each other ($NS \sim 1$), even the MART iterative reconstruction approach fails as shown by the third column in Fig. 9.13.

9.2.2.1 Accuracy of Reconstruction

The quantitative analysis of field reconstruction accuracy is often performed by means of synthetically generated particle fields and their projections [2, 59, 64, 117]. The comparison between the computer-generated particle images and those reconstructed from the projection images is made by means of the normalized cross-correlation coefficient Q or the quality factor [20]

$$Q = \frac{\sum_{X,Y,Z} E_1(X, Y, Z) \cdot E_0(X, Y, Z)}{\sqrt{\sum_{X,Y,Z} E_1^2(X, Y, Z) \cdot \sum_{X,Y,Z} E_0^2(X, Y, Z)}} \quad (9.6)$$

The reconstruction quality depends upon several parameters: number of independent views (cameras) N_C , particle tracers concentration and the diameter of the particle images (C , NS , ppp , d_r^*), the angular aperture β . Experimental practice showed that additional parameters playing an important role are the accuracy of system

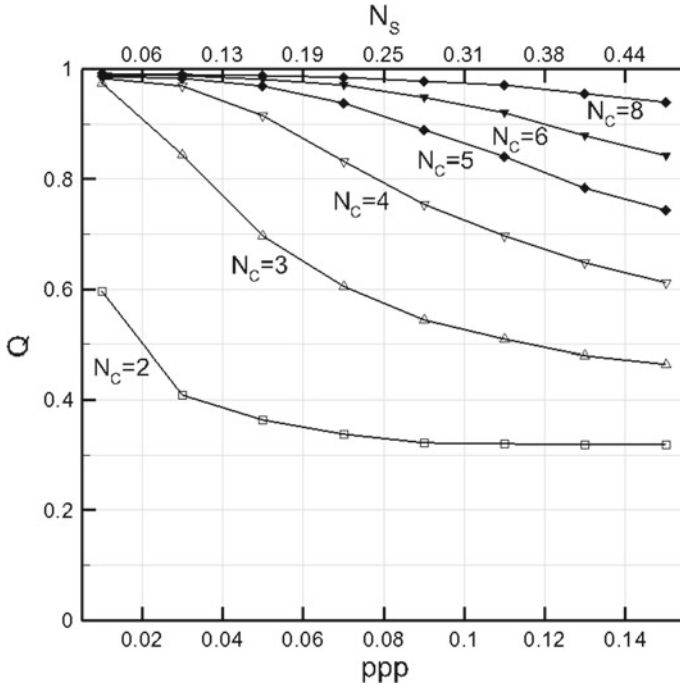


Fig. 9.14 Reconstruction quality factor Q as a function of image source density N_S or particle image number density ppp (results obtained at a fixed particle image diameter of 2 pixel). Results are parameterized as a function of the number of viewing cameras (reprinted from SCARANO [84])

calibration, the illumination intensity distribution along the depth, the image contrast and signal-to-noise ratio.

The reconstruction accuracy as a function of MART iterations increases significantly until five iterations. After that, the rate has already decreased of approximately two orders of magnitude with respect to the first update. Moreover, most experimental results show that with additional iterations the measured velocity vector field changes only within the noise level. The dependence of the reconstruction accuracy upon the seeding density (expressed in particles/pixel or ppp) is crucial as shown in Figs. 9.14 and 9.15. It is proposed that $Q > 0.75$ as acceptance criterion for the tomographic reconstruction accuracy, such that reconstruction artifacts will not affect the error level obtained in the cross-correlation analysis. A system with only two views is clearly inadequate to perform tomographic measurements even at very low seeding density. A three-camera system will work properly up to $ppp = 0.04$ (40,000 particles/megapixel), and using four cameras the recordings may include up to 90,000 particles/megapixel. Further increasing the number of cameras one may perform experiments in excess of 100,000 particles/megapixel. It should however be retained in mind that when the source density increases above 0.3 most particle images overlap with each other and the predicted high reconstruction quality levels can only be

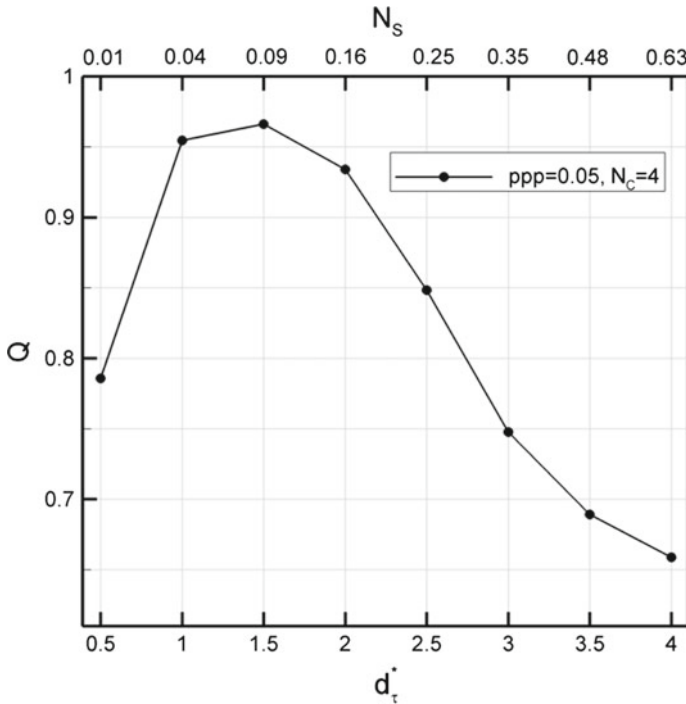


Fig. 9.15 Reconstruction quality factor Q dependence upon the particle image diameter at a given value of the particle image number density (reprinted from SCARANO [84])

achieved with recordings with high signal to noise ratio. The discussion made so far assumes a constant particle image normalized diameter $d_{\tau}^* = 3$. A further increase of the number of imaged particles can be achieved realizing experiments producing small particle images (e.g. applying a small $f_{\#}$ in conjunction with a CMOS sensor with large pixel size). The simulation results shown in Fig. 9.15 indicate that reducing the particle image diameter from 3 to 1.5 pixel for the same number of particles results in a significant increase of quality factor [84]). This is due to the reduction of source density N_s proportional to the square of the particle image diameter.

9.2.2.2 Experimental Verification of Accuracy

A few experiments report the use of more than 4 cameras [6, 28, 58]. It seems clear that increasing further the number of cameras enables measurements at high seeding density, which is consistent with the numerical predictions shown in Fig. 9.14. The evaluation of reconstruction accuracy through the quality factor is not possible in real experiments, where the exact distribution of light intensity is unknown. Therefore a simple a-posteriori method can be used to determine the reconstruction accuracy,

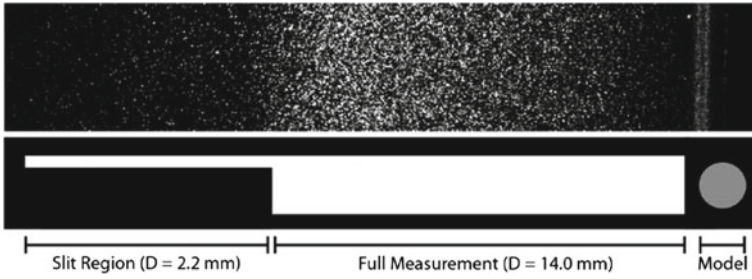


Fig. 9.16 Raw image from one camera (top) and cross section of the knife-edge filter used to produce a sharp cut of illumination. The left side of the filter (slit region) has a smaller thickness to allow a precise evaluation of seeding concentration [57]

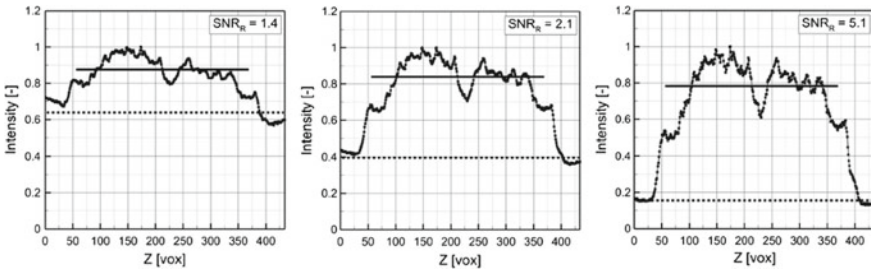


Fig. 9.17 Reconstructed intensity profile and signal-to-noise ratio using 4 (left), 6 (centre) and 12 (right) cameras. Experiments conducted in air at image density of ppp = 0.4 ($C = 18 \text{ part/mm}^3$) [57]

which returns a reconstruction signal-to-noise ratio SNR_R . The method is based on the comparison between the actual illumination intensity profile along the depth direction and that reconstructed with the tomographic algorithm. When a uniform illumination is applied with sharp edges making use of knife-edge filters, the above method reduces to the comparison between the reconstructed intensity inside the volume and that outside the illuminated volume (Figs. 9.16 and 9.17).

The calculations involved in the tomographic reconstruction are challenging for the current computer capabilities. The large number of voxels in the discretized 3D domain gives the main bottleneck of the problem. The number of voxels depends upon the sensor format and the aspect ratio (width-to-depth) of the reconstructed domain. For instance, when an experiment is conducted with 4Mpix cameras, the reconstructed domain may be formed by billions of voxels ($2,000 \times 2,000 \times 500$) to be updated at each iteration. As a result, early experiments required calculations for weeks or even months for the data processing. A major advancement has been obtained with the acceleration technique that accounts for the data sparsity of the discretized object [117]. The multiplicative first guess method (MFG) is able to rapidly identify large regions of the measurement domain where the tomographic update equation does not need to be evaluated (voxels with zero or negligible intensity). The

subsequent MART calculations yield an accuracy equivalent to that of the MART method. The large reduction in the number of active voxels (typically only 5 to 10% is updated) yields a significant acceleration of the tomographic evaluation. The multi-grid (MG) approach is another way to accelerate the calculations [19]. The method consists in reconstructing the discretized object at lower resolution (voxel binning). After having identified the regions of active voxels, the calculation is continued updating for the active voxels at higher resolution. The combination of this strategy with MFG as initialization pass yields further reductions of the computational cost. Reconstruction technique based on the concept of object refocusing (Synthetic Aperture PIV, SA-PIV [5]) have a lower computational cost. However experiments have shown that a system composed of 12 cameras would yield reconstruction accuracy comparable to that of four cameras using MART.

9.2.2.3 Multi-exposure-Methods

Object reconstruction in tomographic PIV has been tackled in a way similar to that of traditional tomography: several views are produced of a single object to be reconstructed. The reconstruction of each snapshot is regarded as a separate and independent process. PIV measurements are always conducted obtaining at least two exposures in short succession, where inside the measurement volume, the set of particles remains the same. Instead, the geometric position and relative orientation with respect to the lines of sight is slightly altered due to the particles motion. As a result, also the system of ghost particles is varied. A method that exploits the information taken at the two (or more) subsequent time instants for the tomographic

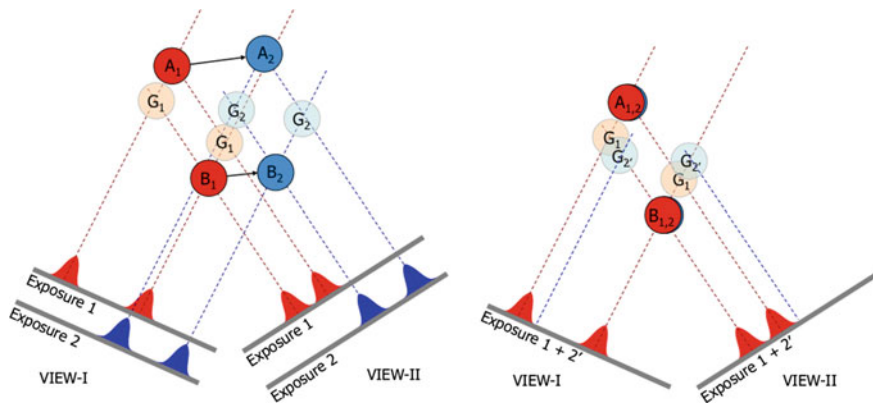


Fig. 9.18 Schematic representation of particles and their images captured along two views (left). Actual particles (A and B) and ghost particles (G) from exposure 1 (red) and 2 (blue). Intensity obtained deforming the object from the second exposure with the estimated displacement field (right)

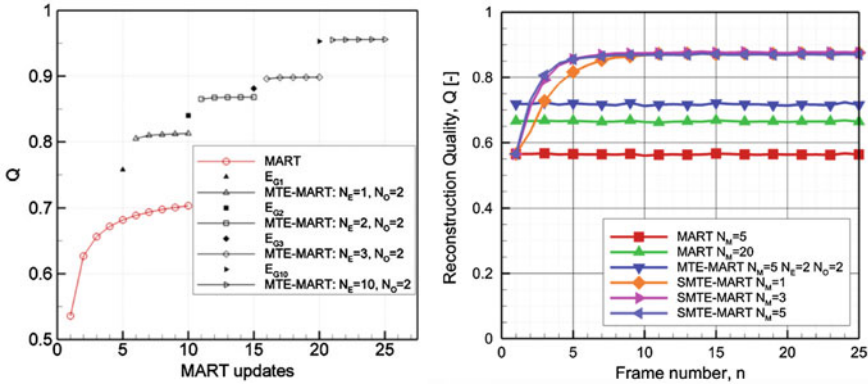


Fig. 9.19 Reconstruction quality factor from multi-exposures methods. Left: result from MTE as a function of MART updates and MTE iterations (reproduced from NOVARA et al. [72]). Right: results from SMTE as a function of sequence length (reproduced from LYNCH & SCARANO [59]). Note: results on left and right are obtained from synthetic tomo PIV images at different conditions

reconstruction of the particles field is called Motion Tracking Enhancement (MTE-MART) (Fig. 9.18).

The technique uses the object reconstruction at a given time instant to initialize the intensity field at the successive one and vice versa. The technique is based on the same principle as that of image deformation. Numerical simulations showed that for the same number of cameras, the reconstruction quality is increased and experiments can be conducted at higher seeding concentration than practised when using the MART algorithm only ($ppp > 0.1$, or $N_s > 0.5$). For instance, Fig. 9.19 illustrates how a MART reconstruction that tends to a value of $Q = 0.7$ can be enhanced up to $Q = 0.9$ by three iterations of the MTE technique. The MTE technique was proven to be effective when dealing with shear dominated flows [73]). A further enhancement is obtained when applying this concept to time series in time-marching mode (SMTE) [59]. In this case the method progressively eliminates the intensity of ghost particles and increases that of the actual particles. (Figure 9.20). An example of the difference in reconstruction accuracy between single snapshot MART reconstruction and SMTE is given in Fig. 9.21. The tomographic reconstruction from a three camera system diffuses the image intensity along the three lines of sight producing an hexagon-like intensity distribution (Fig. 9.21-left).

The sequence analysis with SMTE progressively eliminates the ghost particles intensity restoring accurately the intensity distribution from circular illumination (dashed green line). The current limit in terms of seeding density with SMTE is estimated at $ppp = 0.2$.

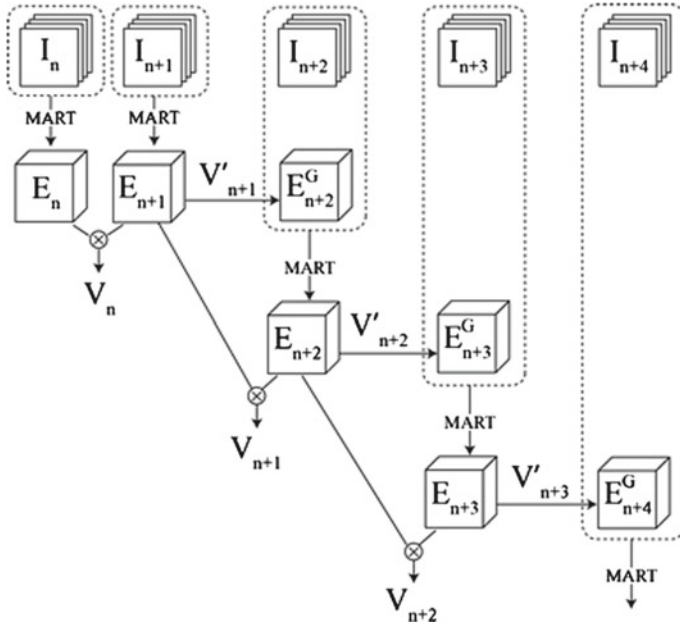


Fig. 9.20 Schematic of SMTE-MART algorithm. Images (I), reconstructed objects (E) velocity field (V) and reconstruction initial condition (EG) based on transformation of previously reconstructed objects

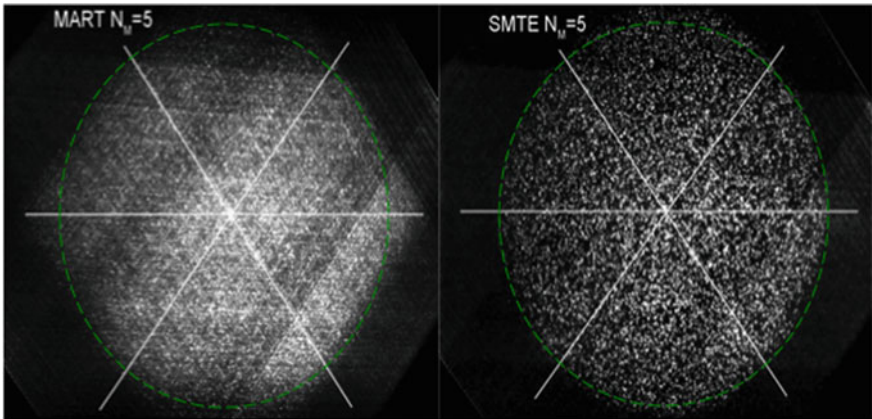


Fig. 9.21 Cross section of reconstructed intensity of particle tracers illuminated along a cylindrical domain. Tomographic imaging system composed of three cameras. Reconstruction by MART (left) and by SMTE-MART algorithm (right) Reconstruction with MART

9.2.3 3D Motion Analysis

The method used to extract the displacement from two successively acquired pictures follows that well established for planar PIV. The measurement domain is divided into several box-like interrogation volumes (IV), then for each pair of corresponding boxes, the following operations are applied:

1. *windowing* by Gaussian kernel,
2. *cross correlation* either by *FFT* technique or by direct calculation of voxel products,
3. *peak search* in the correlation domain and sub-voxel estimation by Gaussian peak fit,
4. *scaling* by optical magnification and time separation returns the local velocity.

The spatial cross-correlation operator used for the analysis of 3D data obtained from tomographic reconstruction is usually normalized by the signal covariance, yielding the normalized cross-correlation function $R(\Delta X, \Delta Y, \Delta Z)$ between the intensity field E reconstructed at time instants separated by the interval Δt :

$$R(l, m, n) = \frac{\sum_{i,j,k=1}^{l,j,k} E(i, j, k, t) \cdot E(i - l, j - m, k - n, t + \Delta t)}{\sqrt{cov(E(t)) \cdot cov(E(t + \Delta t))}} \quad (9.7)$$

where the light intensity distribution at each voxel within the interrogation box E is intended after subtraction of its mean value. The triplet (l, m, n) indicates the displacement in the discretized space of 3D shifts $(\Delta X, \Delta Y, \Delta Z)$. The parameter dominating the measurement robustness is the number of particle images pairs in the interrogation windows, although the velocity fluctuations due to unresolved flow scales within the interrogation box may rapidly degrade the measurement accuracy. The above-mentioned cross-correlation operation is typically implemented within a multi-step analysis based on multigrid window deformation, *WIDIM* [87] as also adopted in planar PIV. In the specific case of 3D data the well-known problem of the out-of-plane motion is basically eliminated and the deformation technique enables to recover most of the particle pairs between the two exposures. In exchange, the reconstructed intensity contains also spurious particles (ghost particles) that move at a velocity different from the local fluid flow and therefore increase the probability of erroneous measurements [21].

The three-dimensional form of the window deformation algorithm deals with volume 3D deformation (Volume Deformation Iterative Multigrid, *VODIM*), whereby the interrogation boxes are displaced/deformed on the basis of the velocity field estimated from the previous interrogation. The intensity field of the deformed volume at the $k + 1$ th iteration is therefore obtained from the original intensity and the predictor velocity field according to the expression:

$$E^{k+1}(X, Y, Z, t) = E(X - u_d^k/2, Y - v_d^k/2, Z - w_d^k/2, t) \quad (9.8)$$

$$E^{k+1}(X, Y, Z, t + \Delta t) = E(X + u_d^k/2, Y + v_d^k/2, Z + w_d^k/2, t + \Delta t) \quad (9.9)$$

where E is the particle pattern deformation field obtained at the k th interrogation obtained by tri-linear interpolation of the displacement field at the previous iteration. Low-pass filtering of the predictor is necessary for process stabilization [93] and consists of Gaussian smoothing or a 2nd order least-squares regression with a kernel as large as the interrogation box.

9.2.3.1 Computational Efficiency

The number of operations required to perform the interrogation of 3D objects is orders of magnitude larger than that needed in planar PIV. Three main factors are responsible for increasing the computational burden of 3D cross-correlation analysis:

1. each interrogation box counts about two orders of magnitude more elements in comparison with the planar case (e.g. $32 \times 32 \times 32$ voxels instead of 32×32 pixel). Moreover, the correlation in three dimensions further amplifies the number of operations. The calculation of cross-correlation implies 10^6 multiplications ($N^2 \times N^2$) for the 2D case compared to 10^9 operations ($N^3 \times N^3$) in 3D.
2. considering a measurement volume of $1,000 \times 1,000 \times 300$ voxels obtained from a tomographic system composed by 1 megapixel cameras, the amount of non-overlapping interrogation regions goes from 1,000 in the 2D measurement to 10,000 for the 3D case.
3. the overlap factor between interrogation regions has a more pronounced effect for 3D analysis. An overlap of 75% between interrogation boxes yields an overload of 16 times for the 2D analysis and 64 times for 3D.

As a result, the computational cost for cross-correlation analysis in tomographic PIV is 4–5 orders of magnitude higher than in planar PIV. The use of fast Fourier transform technique largely reduces the amount of computations for each interrogation box. The computational cost of FFTs required to evaluate the cross correlation is $3 \cdot 2N^2 \log(N)$ in 2D and $3 \cdot 3N^3 \log(N)$ in 3D corresponding to $2 \cdot 10^4$ and 10^6 operations respectively. Acceleration techniques follow essentially three approaches:

- (a) reducing the number of voxels in the measurement domain (sub-sampling or binning) [18],
- (b) making use of direct-correlation with small search radius (typically 2 or three voxels displacement) at advanced stages of the multi-pass interrogation,
- (c) skipping the calculation of voxel products (including 3D volume deformation) where the object intensity is zero or negligible [2].

The latter approach is very advantageous considering that the number of active voxels is typically one to two orders of magnitude less than the total. Maintaining voxel products in the computer memory makes the computational cost independent of the overlap factor.

9.2.4 4D-PIV Analysis

Similar to the case of 2D PIV, the analysis of time-resolved tomographic PIV recordings offers numerous advantages. As discussed above, the object reconstruction within a time series can be based on more than two exposures (SMTE, STB), which further enhances the accuracy of the reconstruction. The sequence of objects can be analyzed with time-sliding correlation methods. The simplest of them is the sliding-average-correlation or the *pyramid correlation* [99]. Despite their simplicity, these methods are very effective in reducing the amount of spurious vectors and the level of random noise for data acquired in continuous single-frame mode. From a time resolved experiment conducted in a submerged water jet [105], the use of four subsequent objects results in a reduction of the displacement rms error from approximately 0.12 to 0.05 voxels.

9.2.5 Media Gallery

The inspection of three-dimensional data issued from Tomographic PIV or by 3D Lagrangian Particle Tracking is a challenge due to the complexity of the flow structures in the turbulent regime. When the data relates to time-resolved measurements, the inspection of the flow requires animated illustration. A gallery in the Digital Content shows some examples of time-resolved 3D PIV measurements and related results [DC9.2].

9.3 Volumetric Particle Tracking Velocimetry

Particle tracking velocimetry (PTV) methods have a great potential to enhance the spatial resolution and the measurement accuracy compared to correlation-based approaches. If strong velocity gradients are present in the flow, PIV results are biased in 2D as well as 3D [21, 47, 52, 109]. In particular, this has strong effects on gradient based quantities such as the vorticity. To enhance the spatial resolution in order to resolve strong flow gradients, the optical magnification can be increased. However, larger magnifications lead to other problems such as a decrease in particle image density and an increase in the particle image diameter that is not ideal for spatial cross-correlation [46]. In addition, inhomogeneous seeding concentrations close to walls introduce bias errors [48]. There are a variety of single camera volumetric PTV methods, such as defocusing PTV [25, 115] and astigmatism PTV [16, 23]. The main disadvantage of these methods is that the out-of-plane component of the velocity cannot be measured with similar accuracy as the in-plane components. Furthermore, the seeding concentrations are typically rather low, since the particle depth information is derived from the shape of the defocused, and therefore large particle

images. For applications in microfluidics this is usually no drawback, since the particle image density is low due to the large magnification. However, for macroscopic flow measurements, multi-camera 3D techniques are usually better suited, provided that the optical access is available.

This section focuses on volumetric particle tracking approaches, based on multiple views of the measurement volume, where all three velocity components can be measured with similar accuracy. With the particles being imaged in focus, the particle image densities and therefore the seeding concentration can be much higher.

9.3.1 Overview of PTV Measurement Techniques

Epipolar geometry is employed to match corresponding particle images from different views of the measurement volume in the so-called 3D-PTV technique [60]. Once a particle image pair is found, the particle location is triangulated. Initially, this technique was only applied to time-resolved recordings, while it is also feasible to conduct double-frame measurements at low seeding concentrations [26, 83, 92].

Later SCHRÖDER et al. [95] used a tomographically reconstructed volume to identify individual particle locations by means of a three-dimensional fit of the intensities, and to track these sub-voxel coordinates (tomographic PTV [74]). However, due to the appearance of so-called “ghost particles” in the reconstructed volume, a time-series of images is required to be able to yield accurate tracking results [22]. To identify corresponding particle images on the other sensor, an approach combining tomography and triangulation was introduced by FUCHS et al. [24]. Here, the tomographic reconstruction is used to predict corresponding particle images and to identify multiple uses of particle images to avoid ghosts. Due to the reliable ghost elimination, this approach allows for a double-frame processing. Consequently, this technique can be applied at any flow velocity. A recently introduced approach to the group of volumetric tracking methods is the so-called “Shake-The-Box” (STB) algorithm. This time-resolved approach is described in detail in Sect. 9.4.

9.3.1.1 Particle Location Determination

3D-PTV

For the 3D-PTV method, at least two views of the measurement volume are required. To match the corresponding particle images on the different sensors, their sensor locations need to be determined first. Thus, after the image preprocessing and an intensity thresholding to detect individual particle images, a Gaussian 2D fit is used to estimate the sub-pixel particle image location. At small particle per pixel (ppp) values this might be a straightforward procedure. However, if particle images start to overlap, the detection of individual particle images is difficult and the uncertainty of the fit increases [9, 17, 65, 77].

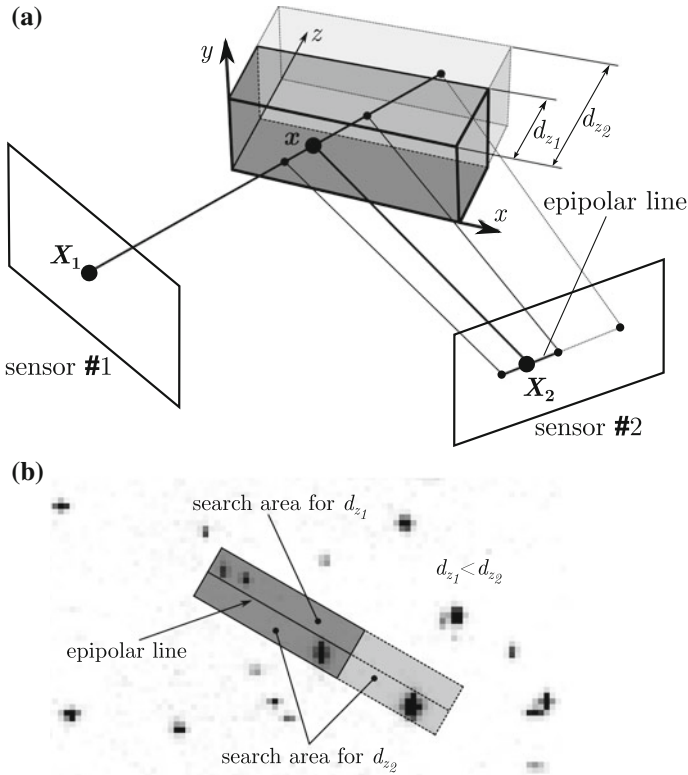


Fig. 9.22 **a** The spatial particle location x is triangulated from corresponding particle image locations X_1 and X_2 from at least two sensors. **b** The search area for corresponding particle images lies in the proximity of the epipolar line. It becomes evident that increasing the measurement depth ($d_{z1} < d_{z2}$) extends the search area over the sensor such that more ambiguities can arise

In the following, originating from a particle image on one sensor, the epipolar line on the second sensor is calculated, as illustrated in Fig. 9.22. Possible particle image matches are situated in the proximity of the epipolar line, while the extension of the search corridor increases with larger measurement depths ($d_{z1} < d_{z2}$). Obviously, multiple matches can appear such that it becomes increasingly difficult to determine the correct match with increasing particle image density. Unlike the particle image detection, the unambiguous matching procedure is a much bigger challenge. Employing more views of the volume improves the matching procedure, since ambiguities can be resolved to some extent with the additional information. However, the application of 3D-PTV is limited to ppp values below 0.01 if simple particle tracking algorithms are applied. At larger particle image densities too many ambiguities arise, not allowing for a reliable tracking procedure anymore.

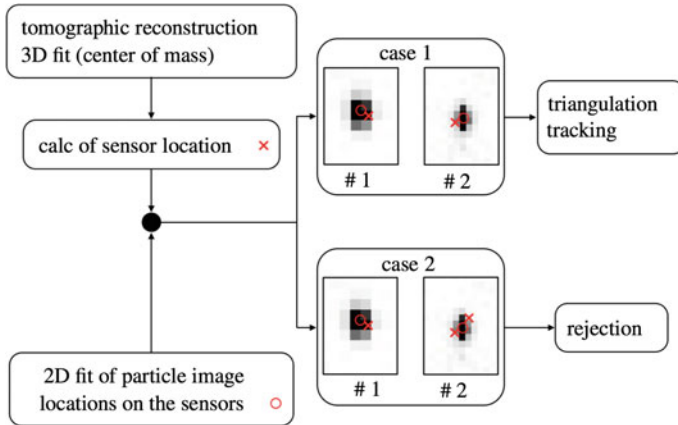


Fig. 9.23 Tomographic 3D-PTV principle: The tomographic reconstruction is used to predict the sensor locations of corresponding particle images and to detect ambiguities. Case 1 shows a unique particle image correspondence. In case 2 an ambiguity is shown, where a particle image is associated with two spatial particle coordinates

Tomographic PTV

Tomographic PTV employs a reconstruction of the measurement volume on a voxel grid. A detailed description of tomographic reconstruction techniques is given in Sect. 9.2. The reconstruction is followed by a detection of individual particles in the volume, using an intensity threshold. For the sub-voxel particle location determination, a 3D Gaussian fit is employed. Finally, the velocities are estimated from the 3D coordinates. However, it is not possible to distinguish between true particles and ghost particles based on the intensity or the size of the reconstructed particle [22]. Only the share of ghosts can be reduced by setting a size and intensity threshold, since ghosts tend to have smaller intensities and sizes. However, at the same time true particles are erased as well. Thus, a time-series of recordings is required to remove the ghost particles, as true particles yield longer trajectories than ghost particles.

Tomographic Predictor

The tomographic predictor approach takes up the ideas of 3D-PTV and optical tomography. An initial tomographic reconstruction is used to match particle images on the different camera sensors. To do so, the reconstructed volumes are binarized, following the determination of the spatial particle locations from their center of mass. These locations are mapped back to the sensor to find the actual particle image contributing to this reconstructed coordinate. If a particle image is associated with multiple reconstructed particles, it is rejected entirely and not considered for triangulation anymore. This principle is illustrated in Fig. 9.23. Thus, the tomographic reconstruction also serves as a validator to identify non-corresponding sets of particle images. Triangulating a non-corresponding set of particle images would yield a non-existent particle location.

To perform the triangulation for the particle location determination, it is necessary to find uniquely matching particle images on at least two sensors. If this is the case, the spatial particle location is determined by means of the so-called optimal triangulation method [34]. Since the tomographic predictor approach has the ability to thoroughly remove ghost particles, it is suitable for double-frame measurements. However, it has to be noted that the fraction of correct reconstructions reduces to 75% at large ppp values, yielding a maximum effective ppp, that is, the actual image information which can be utilized, of 0.05. Nonetheless, this is a significant increase compared to the previously described 3D-PTV approach.

9.3.1.2 Velocity Estimation

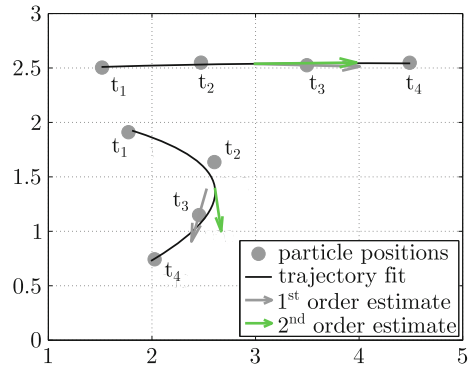
The tracking procedure is a crucial step of volumetric PTV, since it has to connect particle tracks from subsequent time steps reliably in order to derive the velocity information. At high seeding concentrations, where multiple particles lie within a range that is smaller than the actual displacements, the correct track identification becomes increasingly challenging [17].

Double-Frame Tracking

Advanced double-frame tracking algorithms analyze the motion of neighboring particles to determine the particle tracks. The simple nearest-neighbor approach quickly fails to yield reliable results, especially if the displacements are large. OHMI et al. [77] introduced a powerful double-frame tracking algorithm, iteratively updating the probabilities for single displacements by analyzing the motion of the neighbors, defined by a case sensitive search radius. Even at a ppp value of 0.06 in a planar synthetic test case [78], this algorithm could identify more than 95% of the tracks correctly. At the same time the outlier rate was below 2%. In volumes, at a constant ppp, the third spatial coordinate makes the particle track identification much easier. Other tracking approaches use an initial cross-correlation to provide a local prediction of the particle displacements [9, 54]. However, to allow for the efficient processing of large data sets and to improve the user-friendliness, FUCHS et al. [27] introduced a non-iterative tracking procedure. To identify the most probable displacement of a particle, the histogram of all possible displacements lying within the displacement limits of the 25 closest particles is analyzed. The displacement with the lowest deviation from the histogram maxima in all spatial directions is determined to be the correct displacement. This approach almost reaches the performance of the algorithm of OHMI et al. [77], while only the displacement limits need to be set by the user compared to ten additional parameters for the latter algorithm.

All these algorithms show that it is possible to apply double-frame tracking even at high seeding concentrations. However, the correct track identification becomes more reliable if temporal information is available.

Fig. 9.24 Second order velocity estimation. In particular for curved trajectories, the accuracy of the velocity estimation is increased compared to the first order estimation



Time-Resolved Tracking

The time-resolved tracking procedure starts with a double-frame initialization step. Using these initial tracks, the algorithm first projects the found displacement for the currently known trajectories in space. This procedure limits the search radius for the particle position in the third frame considerably. Now, possible particle candidates inside this search radius are evaluated, taking a global limitation for the displacement into account. For the candidate particles that fall inside the global displacement limits, the particle with the lowest relative acceleration is selected to be added to the trajectory. The major advantage of this procedure is that the algorithm inherently adapts to the flow field as the bounds for the maximal displacement will be altered locally by a certain amount of allowed acceleration.

After determining the trajectories, the velocity estimation can be based on a second order polynomial fit if at least four consecutive positions are known, as illustrated in Fig. 9.24. Taking the integral of the polynomial curve allows for a correction of the velocity estimate. In addition, the vector position is reallocated to be placed directly at the polynomial curve instead of in between the two positions as typically done in two frame representations. This method is especially suited for the correct estimation of the velocity and vector position in the case of trajectories with strong curvatures [17]. However, if only two or three successive positions are known (i.e. end of a trajectory or short trajectories), the velocity estimation is based on the classical first order displacement estimation and second order vector positioning [108]. The animation of the time resolved volumetric PTV measurements in the near wall region of a turbulent boundary layer is shown in [DC9.3].

9.3.1.3 Working Range of 3D-PTV

Selecting a suitable measurement technique for a specific experimental investigation is often difficult. If volumetric measurements are required and strong velocity gradients need to be resolved, PTV methods are an excellent choice.

Compared to the other methods, 3D-PTV certainly has the lowest information density. However, there are certainly many applications where it is difficult to provide a high seeding concentration, especially for measurements close to surfaces or in facilities with large mass flows. In these cases a costly tomographic reconstruction, like it is necessary for tomographic PTV, or the tomographic predictor approach are not efficient. Here, 3D-PTV provides accurate measurement results for mean fields allowing for a comprehensive statistical flow analysis [56].

Depending on the flow velocities and the magnification it might not be feasible to record a time-series of images. This is due to the limitations in the recording rate of the cameras and in the repetition rate of the lasers. Then, the tomographic predictor method can be employed, which is dedicated to double-pulse measurements. Since this method requires a tomographic reconstruction, it can be combined with a tomographic PIV analysis as well.

However, if the equipment is available and the flow physics allow for it, a time-series of recordings helps to increase the seeding concentration and therefore the information density of the measurement. Tomographic PTV is then feasible, especially if it is ensured that the particles stay in the measurement volume for many time steps to distinguish between ghosts and true particles. However, the recently proposed STB has proven to be more efficient in terms of its computational expense and also the maximum ppp values. Thus, STB can be considered as the replacement of time-resolved tomographic PTV. The working principle and a performance analysis of STB are outlined in the following.

9.4 Shake-The-Box Lagrangian Particle Tracking¹

3D-PTV (Particle Tracking Velocimetry), as introduced in the early nineties [60, 62, 70] relies on a triangulation procedure using epipolar lines to deduce the volumetric particle distribution on each evaluated time-step. As argued in the previous section, this procedure is well suited only for the processing of images with a low particle image density.

The Shake-The-Box (STB) method [89, 90] overcomes the limitations in particle image density for particle position based 3D methods, by heavily incorporating the temporal domain into the reconstruction process and by applying advanced triangulation algorithms. The main features of the STB framework will be introduced in the following paragraphs of this chapter and are briefly summarized here.

A first step in attaining higher particle image densities for particle tracking methods was the introduction of the Iterative Particle Reconstruction (IPR) [112], which extended the working range of single time-step particle position reconstruction, compared to standard triangulation (see Sect. 9.4.1). IPR makes heavy use of residual

¹The text on Shake-The-Box has been contributed by Daniel Schanz, Matteo Novara and Andreas Schröder. The Digital Content regarding STB as well as an extended version of this text can be found at [DC9.4].

images, created by backprojecting the triangulated particle cloud. In this step, the use of a calibrated Optical Transfer Function (OTF) [88]—describing the imaging properties of the particles—is important to avoid artificial residuals (see Sect. 9.4.2).

The Shake-The-Box algorithm (see Sect. 9.4.3) introduces temporal information into the IPR processing of each time-step, either by predicting a particle cloud for each consecutive time-step (Time-resolved STB), or by iteratively coupling the reconstruction and the tracking (Multi-Pulse STB). Trajectories of tracer particles are identified at high spatial accuracy due to a nearly complete suppression of ghost particles.

The particle trajectories are still subject to noise. To further suppress this, the paths are fitted using cubic order B-spline curves (*TrackFit*, see Sect. 9.4.5). The gained continuous functions can be derived multiple times, yielding velocity, acceleration and jolt (motivating the term “Lagrangian Particle Tracking” (LPT)).

After a full processing, the fitted particle tracks can be used freely. The locally highly accurate flow information can be used to e.g. generate high-resolution statistics of mean velocities and Reynolds stresses via ensemble averaging [97]. PDF statistics of velocity and acceleration or proximity statistics are accessible on a particle level.

Furthermore, the availability of accurate and spatially dense measurements of the flow (at each particle location) allows for regularized interpolation onto an Eulerian reference frame, using data assimilation approaches. To this end, three-dimensional grids of B-splines (*FlowFit*, see Sect. 9.4.6) [30] or Vortex-in-Cell methods [91] can be used. Opposed to correlation-based methods, the process evades spatial smoothing and allows for the introduction of regularizations – e.g. the penalization of divergence – in the resulting vector volume. Such approaches have been shown to be superior to classical low-pass filtering 3D cross-correlation methods [49, 91]. Using this scheme, derived properties – like the velocity gradient tensor or the acceleration field – can be extracted with high precision, allowing for advanced data evaluation, e.g. the extraction of pressure fields [39, 104].

9.4.1 Iterative Particle Reconstruction

The performance of particle tracking procedures heavily depends on the way, particle locations in the world reference system are determined from the projections on the several cameras.

The method of Iterative Particle Reconstruction (IPR, [112]) overcomes the limitations in particle image density for particle position based reconstruction by applying an iterative triangulation scheme, combined with an image matching procedure to correct and filter intermediate results. The flow chart of the method is given in Fig. 9.25 and will be briefly discussed in the following: The procedure starts by performing a standard triangulation on detected particle peaks on the recorded camera image. The found 3D positions will contain errors, coming from several sources: The peak detection typically suffers from an error of approx. 0.1 – 0.2 pixel, camera image noise and overlapping particle images will shift the peak positions. Depending on the particle image density, many true particles will not be found, while a significant number of ghost particles will be present. The second step of each iteration

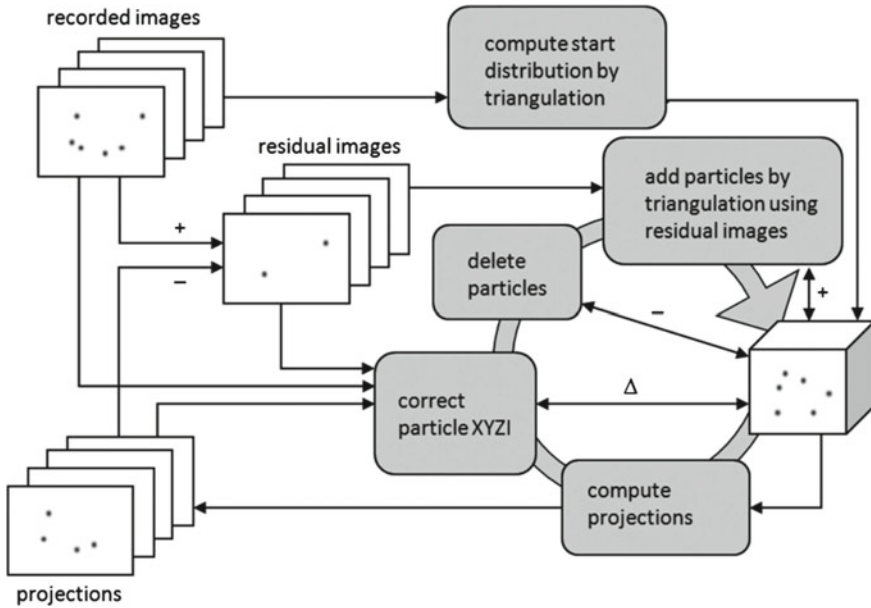


Fig. 9.25 Scheme of the IPR procedure [112]

is to correct and filter the particle cloud using image matching schemes. This step can be performed using different approaches. WIENEKE [112] iteratively calculated the gradient of the local residual of each particle by displacing (“shaking”) the particle in small steps (typically 0.1 pixel) in the volume, thus capturing the gradient of the residual and finally moving the particle in the steepest direction. JAHN [40] successfully used an analytical derivation of the residual cost function to deduce the direction and the optimal step width. After the particle was moved, a new intensity is calculated to best fit the residual images. Particles, whose intensity falls below a specified threshold, are deleted (as the intensity of ghost particles is typically lower than of real particles).

The resulting particle cloud will show higher accuracy and reduced ghost levels, compared to the originally triangulated one. From these particles, residual images are created, which are taken as source images for another iteration of the scheme (triangulation + image matching).

With each iteration, new particles are found that were previously hidden by overlapping particles and ghost particles are removed from the system, as their intensity is iteratively reduced. Figure 9.26 documents the development of the residual image and the histogram of detected true particles and ghost particles for a synthetic evaluation at 0.05 particles per pixel (ppp).

First implementations of the method [112] were able to reconstruct particle clouds with acceptable ghost levels from synthetic single-time-step images with particle image densities up to 0.05 ppp. Recently, JAHN [40] demonstrated that the use of ana-

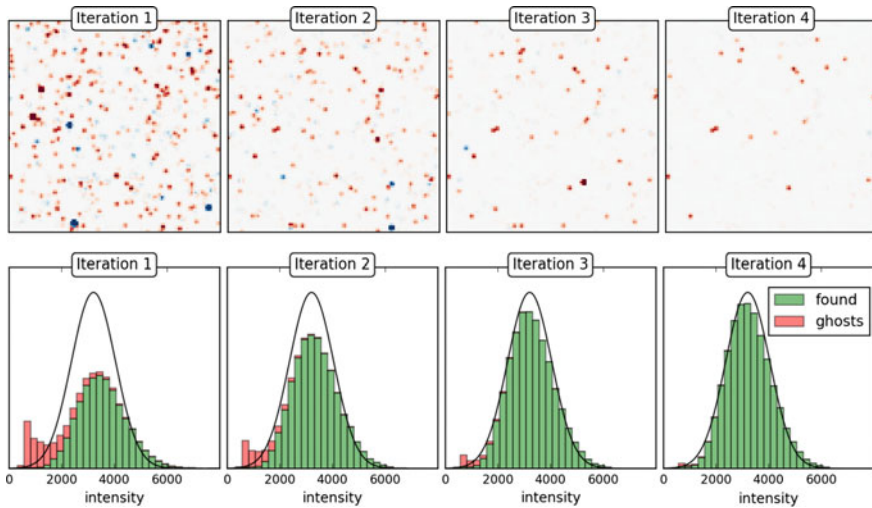


Fig. 9.26 Residual images and particle intensity distribution during convergence of the IPR algorithm, as implemented in [40]. Particle image density: 0.05 ppp with Gaussian intensity distribution. The intensity of the true particles increases, low-intensity ghost particles vanish (here shown for the first four iterations). After 7 iterations the system is fully converged

lytical image matching and advanced triangulation schemes (varying camera order) can shift this range up to 0.1 ppp.

9.4.2 Calibration of Optical Transfer Function

Reconstruction methods like IPR [112] (see previous chapter) or tomographic reconstruction using e.g. MART or SMART (see Sect. 9.2.2) [20] rely on an accurate reprojection of either 3D particle positions or non-zero voxels onto the images. An important precondition for this step is an accurate calibration of the camera lines-of-sight, which is ensured by performing a Volume-Self-Calibration [111] (see Sect. 9.2.1.5). However, not only the precise location of the projection point is important in describing the back-projected image of a particle, also the shape of the particle image is relevant. If a circular Gaussian peak shape is assumed, but the real shape is distorted, due to e.g. astigmatism, the back-projection cannot fit the recorded particle image and a residual will remain, even if the particle position is perfect. For particle-based methods, like IPR, new (false) peaks could be identified on the residual. Tomographic reconstruction will suffer from deformations in the reconstructed voxel intensities at the particles location and from energy distributed to the volume, eventually forming ghost particles. Particle distortions occur in many volumetric experiments. Due to the deep volumes that are imaged, depth-of-field cannot be neglected, especially when illumination is weak and the apertures of the lenses cannot be closed as desired.

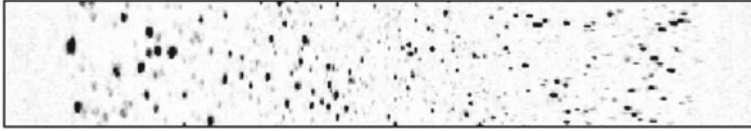


Fig. 9.27 Excerpt of camera image at $f_{\#} = 4$ for a single lightsheet in the central plane of a volumetric experiment in water. Sharp imaging in the middle of the plane; the outer regions are blurred due to depth of field and distorted due to astigmatism

Astigmatic distortions are common when viewing through interfaces with change of refractive index at non-perpendicular angles. Figure 9.27 shows a (rather extreme) example, taken at a volumetric experiment on a free jet in water [88, 105]. Only a thin sheet of 1 mm thickness in the middle of the investigate volume is illuminated, the camera is looking at the sheet at an angle of approx. 45° ; the aperture of the lens was intentionally opened to $f_{\#} = 4$, for the sake of clearer visualization. Strong out-of-focus blur and astigmatic imaging can be observed. Cameras observing the sheet at other angles will show different images of the same particles

If the imaging parameters of the particles are known, they can be incorporated into the reconstruction algorithms, thus compensating for the differences in imaging of each particle onto the different cameras. A calibration of the average imaging properties (Optical Transfer Function, OTF) [88] of particles can be performed as an add-on to the Volume-Self-Calibration (VSC). When performing VSC, the location of particles within the volume is known, as well as the position of particle images on each camera. The shape parameters for each particle image are determined (by fitting parameters of a 2D Gaussian function). Finally, the shape parameters are averaged for all particles located within a certain sub-volume for each camera individually. The result is a volumetric representation of the OTF parameters per camera, which can be directly used by the reconstruction methods. If tomographic reconstruction is used, the shape needs to be slightly adapted for the fact that here particles are represented by a cluster of voxels, not by a single point in space. Figure 9.28 outlines and illustrates the scheme.

The interrogation volume is divided into subvolumes (here $2 \times 2 \times 2$). The following steps are carried out:

1. During the volume self calibration the particles are sorted into different subvolumes.
2. For all particles the shape parameters of the particle image are determined by a 2D Gaussian peak-fit, independently for every camera.
3. The shape parameters for all particles within a certain subvolume are averaged, giving the OTF-parameter for a point-reconstruction.
4. (optional for TOMO-PIV) to account for the desired diameter of the reconstructed particle (2–3 voxel) the OTF-accounted voxel pulse spreading function is determined.
5. Organizing the found shape parameters according to the subvolume-division yields spatial maps for the OTF-calibration for every camera.

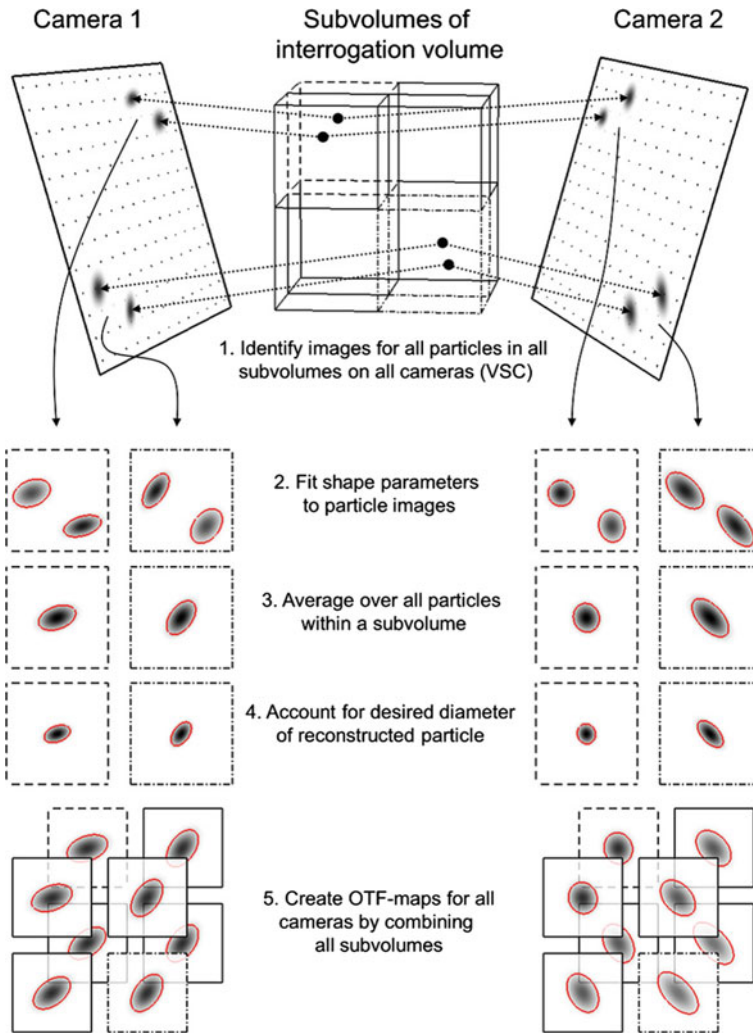


Fig. 9.28 Scheme of the OTF-calibration

The result of the OTF calibration on the experimental case shown in Fig. 9.27 is given in Fig. 9.29. 500 images at low particle image density, illuminated at three planes, were processed by the VSC procedure and the OTF was determined alongside. The interrogation volume was split into $9 \times 3 \times 3$ subvolumes, shown in Fig. 9.29 as three OTF- z -planes for the same camera as in Fig. 9.27 (out of three cameras). The effects of blurring and astigmatism are captured.

The use of a calibrated OTF showed reduced ghost levels and increased position accuracy for both TOMO-PIV [88], as well as IPR [112]. For particle based methods

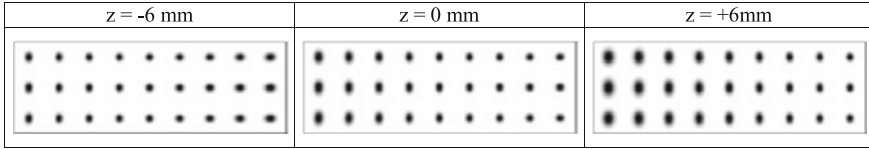


Fig. 9.29 Optical Transfer Function for the camera, which recorded Fig. 9.27. Calibrated in three z-layers of the interrogation volume, magnified by factor 2.0

the gains are more profound. Calibrating a volume-resolved OTF is recommended when applying IPR or Shake-The-Box (see next section).

9.4.3 Shake-The-Box Algorithm

Shake-The-Box is an evaluation algorithm that performs Lagrangian particle tracking on time-resolved volumetric recordings. The exploitation of the temporal domain is used to facilitate the IPR processing of each individual time-step, thus allowing for the processing of images with high particle image density. Depending on the number of consecutive frames available, different variations of the algorithm can be applied. For time-resolved sequences of recordings (see Sect. 9.4.3.1), a predictor – corrector scheme for known tracks is used to largely pre-solve the current time-step. If only few consecutive images are available the Multi-Pulse STB (see Sect. 9.4.4) applies an iterative integrated reconstruction and tracking scheme. Recently, a method to extract particle matches from double frame recordings (Two-Pulse STB) was introduced [40], which is beyond the scope of this book.

9.4.3.1 Time-Resolved Shake-The-Box

The basic concept of the STB-method relies on two (reasonable) assumptions: (1) the inclusion of the temporal domain allows for an effective way to suppress the occurrence of ghost particles as the latter have a shorter lifetime than actual particles; (2) the knowledge of a particle trajectory enables a fairly accurate estimation of the particles 3D position in the next time-step (which can be experimentally ensured by balancing the sampling rate with the Kolmogorov time scale, or the maximum expected acceleration values).

Under the assumption that the trajectories of (nearly) all particles within the system are known for a certain number of time-steps t_n , the STB-method scheme for the single time-step t_{n+1} is as follows:

1. Perform a Fit to the last k positions of all tracked particles, using a Wiener filter.
2. Predict the position of the particles in t_{n+1} by evaluating the Wiener filter coefficients

3. Shake the particles to their correct 3D positions and intensities using an image matching scheme, eliminating the error introduced by the prediction
4. Find new particles that are previously untracked on the residual images
5. Shake all particles again to correct for residual errors.
6. Remove particles either if leaving the volume or if intensity falls below a certain threshold.
7. Iterate steps 4, 5 and 6, if necessary.
8. Add new tracks for all new particles that are identified within four consecutive time-step

After such a processing of a single time-step the known particle tracks have been extended to the current time-step and new particle tracks have been added, capturing particles entering the volume. The entirety of these tracks can now be predicted for t_{n+2} and the process starts anew. This way, STB can work its way through an entire time-series, consisting of possibly thousands of images. The effort needed for every single time-step is low, as the system is largely pre-solved after the prediction-step and only minor deviations have to be corrected.

However, as the knowledge of a vast majority of particle tracks is not a given (at the beginning the method has to start from scratch), the evaluation of a dataset has to converge to such a stable solution. The progress of the algorithm can be described in three main phases: Initialization, Convergence and Converged State.

Initialization

A thorough treatment of the first images of a time-series is vital in order to quickly obtain as many reliable particle tracks as possible, allowing a sufficiently accurate prediction of the particle position in the next snapshots. Typically, the initialization is applied to the first four time-steps. Further on, the number of snapshots treated by the initialization process will be referred to as N_I .

The particle position identification is typically carried out using Iterative Particle Reconstruction. For the initialization time-steps the number of iterations is doubled with respect to the following ones.

From the reconstructed “particle candidates” (only particles that are incorporated into a track are regarded as real) of the N_I images, particle tracks have to be extracted. The default approach is to define a search radius (with a size of e.g. the maximum expected particle displacement) around each reconstructed particle and mark every particle within the next time-step as a potential match.

After all N_I images have been processed, the particles of t_1 are examined for potential matches in t_2 . These are in turn examined for matches in t_3 , until t_{N_I} is reached. That way, all potential tracks with the full length of N_I are found. In the following, a second order polynomial is fitted to the N_I particle positions of each of these track candidates and the average deviation Δ_f from this fit is determined. Track candidates above a certain threshold of Δ_f are discarded, the remaining ones are sorted in ascending order of Δ_f . Starting from the lowest Δ_f , these track candidates

are copied to the list of approved tracks. In case a particle appears in several track candidates, only the one showing the lowest Δ_f is accepted.

This approach works well for low to medium particle concentrations, but the number of false matches rises with particle concentrations. It is therefore recommended to use a predictor for the search of matching particles. Around such a predictor a significantly reduced search radius can be applied, limiting the number of false matches.

An obvious way to gain such a predictor for the first time-steps(s) is to perform a Tomo-PIV evaluation. In case the flow is at least partly predictable (e.g. a turbulent boundary layer with a roughly known velocity profile), an averaged result of previous measurements or even CFD-results can be used to derive predictors for the search of particle tracks. Also the search radius can be parameterized, using e.g. the rms-values of velocity and acceleration gained from a previous evaluation.

Convergence Phase

The N_T tracks of length N_I identified by the initialization are extended to time-step t_{N_I+1} by applying a Wiener filter [113] for extrapolation, where the filter parameters have been determined based on an estimation of the signal and noise spectra of the particle location signals. The found filter coefficients are evaluated at t_{N_I+1} and the new (temporary) positions of all tracked particles are set to these extrapolated coordinates.

The predicted particle position will be close to the real one—not more than one or two pixel off, typically only a fraction of a pixel (depending on the flow, the noise level and the temporal sampling). A mean to correct this error in particle position is to use image matching techniques, which try to (locally) minimize the residual image I_R . The same approaches as used within the IPR (see Sect. 9.4.1) can be applied.

The intensity of the predicted particle is iteratively updated. By omitting the camera showing the highest (local) intensity for the current particle, the occurrence of ghost particles can be reduced. In case the intensity falls below a specified threshold T_{int} , it is assumed that the particle was lost and the track ends.

Using the steps described above, the positions of all tracked particles are predicted and iteratively shifted to their correct position, following the gradient of the residual. Around ten shake iterations are typically sufficient to correct for the prediction errors.

Following the treatment of tracked particles, new particles can be identified on the residual images using IPR. During the convergence phase not all particle tracks have been found yet, therefore the residual images will still show a significant amount of particle images. However, the perceived particle image density will be lower compared to the original image, as particles that are already correctly tracked are removed. A light IPR processing is applied with few triangulation iterations.

After the complete processing of time-step t_{N_I+1} , a mixture of particle candidates and tracked particles is available. Using the particle candidates of time-steps t_{N_I-2} to t_{N_I+1} , additional tracks of length N_I are searched, following the scheme described

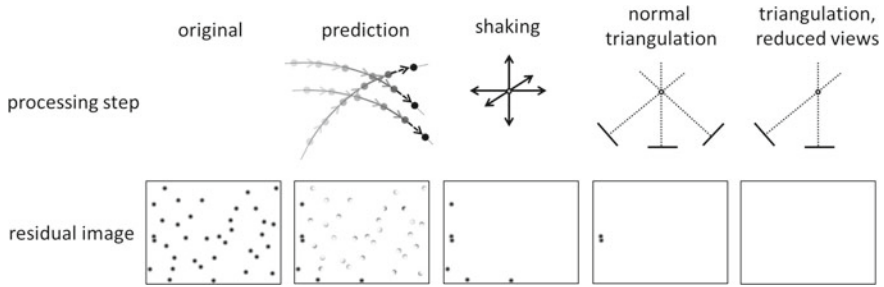


Fig. 9.30 Schematic description of the Shake-The-Box procedure for one time-step in the converged state by illustrating the effects of the different computation steps on the residual image of one single camera (out of multiple)

in the previous paragraph on the initialization. A predictor can be constructed from neighboring tracked particles.

Approved tracks of length N_I are spotted and the corresponding particles are added to the list of tracked and predicted particles. Tracks leaving the measurement domain are terminated. The algorithm continues with time-step t_{N_I+2} , which will again be easier to reconstruct. This process of finding tracks, which in turn facilitate the identification of new ones, will continue until (nearly) all true particles are tracked. At this point convergence is reached.

Converged Phase

In this stage, the vast majority of the particles is known and tracked. From here on, most tracks end only when the corresponding particles leave the measurement volume and new tracks are found when particles are newly entering the interrogation volume. The general processing remains the same as in the convergence phase.

Figure 9.30 illustrates the main steps of Shake-The-Box for a single time-step in the converged state and their impact on the residual image of a selected camera. At the beginning of the processing of this time-step, the residual image matches the recorded camera image. After predicting the positions of the tracked particles, residuals reflecting the errors occurring by the prediction are visible. New particles, entering the measurement domain from the left and the bottom appear unaltered in the residual images. After performing some iterations of shaking, the residuals of the tracked particles vanish (nearly) completely – only the new particles remain. These are then tackled by the IPR process. Due to the low effective seeding density at this point, only such particles that suffer from overlapping images remain undetected by the triangulation utilizing all cameras. Most of these situations can be resolved by successively leaving out single cameras during the triangulation, thus reducing the effects of particle overlap. The end result is a nearly completely blank residual image.

Following the example given in Fig. 9.30 it can be seen how much the prediction step – thus the inclusion of the temporal information – simplifies the problem of particle position detection. At the point where the first triangulations are performed, the perceived seeding density has drastically decreased, enabling a fast and reliable determination of the previously undetected particles.

Track Validation

Several parameters of the tracked particles are continuously checked in order to judge if the track is still valid or if the particle has been lost. First, the intensity of the particle is examined, as indicated above. Second, the track is checked for erratic behavior by fitting a function (polynomial or B-spline) of first or second order to the last four positions. In case the average deviation from this fit is larger than a predefined threshold $T_{\Delta f}$, the track is ended. Third, the surroundings of a particle is examined for neighboring particles. A basic outlier criterion is applied to decide if the current particle is not reasonably following the flow. The validation schemes can be adapted to the properties of the given flow, e.g. after gaining statistics during a preliminary evaluation.

Tracking Performance

An assessment of the tracking performance using synthetic data is available as Digital Content [DC9.5], providing updated data from the one given in [90]. It is shown that synthetic experiments at particle image densities up to 0.2 ppp can be successfully reconstructed using the STB method. The formation of ghost particles/tracks is successfully avoided, thus high accuracies are achieved.

Sections 18.2 to 18.4 demonstrate the application of time-resolved STB on various experimental data. Further details and examples can be found in [97] and [39].

9.4.4 *Shake-The-Box for multi-pulse systems: 3D Lagrangian particle tracking in high speed flows*

Due to current hardware limitations in terms of maximum acquisition frequency, long time-resolved sequences suitable for STB processing can be obtained only for relatively low flow speeds, typically limited to approximately 40 m/s. When dealing with larger flow velocities, typical of industrial and aerodynamic applications, dual-frame PIV systems are employed, where two-pulses are recorded with a short time separation of a few microseconds. Multi-pulse acquisition systems obtained by synchronizing multiple dual-frame systems in a staggered fashion enable the recording of short time resolved sequences, consisting typically of four recordings [7, 58, 96].

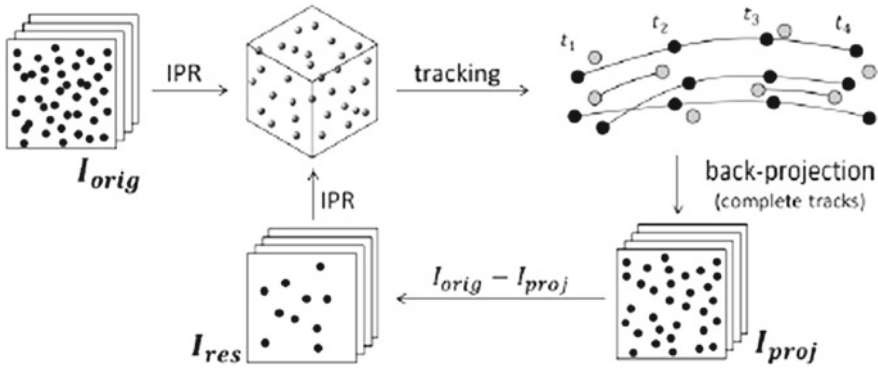


Fig. 9.31 Iterative STB processing strategy for multi-pulse sequences; t indicates the time of each of the four pulses, while *orig*, *proj* and *res* respectively refer to original, back-projected and residual images. Only particles belonging to four-pulse tracks (complete tracks—black dots) are retained and considered in the back-projection step; particles belonging to incomplete tracks (gray dots) are discarded

In order to benefit from the advantages offered by Lagrangian particle tracking (LPT) at high seeding density (accurate particle position-velocity-acceleration and highly spatially resolved ensemble statistics—see Sect. 18.5) a novel STB approach for multi-pulse sequences has been proposed by [75]. To compensate for the lack of a large number of recordings the method makes use of an iterative strategy where the sequential application of the Iterative Particle Reconstruction (IPR [112]) and predictive particle tracking (typically aided by Particle Space Correlation, PSC [76]) is used to progressively reduce the complexity of the object to be reconstructed (perceived seeding density) and increase the number of successfully retrieved particle tracks [76], Fig. 9.31.

An assessment of the multi-pulse STB method has been presented by [76]; the performances in terms of velocity and acceleration dynamic ranges (up to around 200 and 10 respectively, for real imaging conditions) suggest the suitability of multi-pulse systems in providing access to the material acceleration and to the instantaneous pressure for high-speed flows [104]. Experimental applications can be found in [75] and [29] and the investigation of a transonic jet at Mach 0.84 is described in this book in Sect. 18.5.

Details on the iterative STB strategy and on the performance assessment of multi-pulse STB can be found in the digital content available at [DC9.6].

9.4.5 Fitting Particle Positions Along the Trajectory²

A particle tracking method such as the Shake-The-Box [90] that has been described in Sect. 9.4.3 yields a temporal sequence of estimated locations for each tracked particle. Since this sequence contains measurement noise a proper noise reduction should be performed. In addition to that temporal derivatives of the position of particles are of interest: velocity and acceleration.

The *TrackFit* method, described in [30], takes such a sequence of positions and determines a cubic B-spline function for such a particle track accounting for the measurement noise as well as typical particle behaviour seen in measurements. It is based on the ideas of WIENER [113] and KALMAN [50] for its noise reduction properties but results in a continuous representation of the particle track using cubic base splines.

A simple physical model of typical tracer particle motion was derived from spectral analyses of particle location signals of real measurements, see Fig. 9.32. The measurement signal is a superposition of the real signal and measurement noise. Under the assumption that the measurement errors of particle positions are not correlated between different time steps for a particle this noise will be white and therefore spectrally flat. The signal as an amplitude spectrum is assumed to have a $1/f^3$ shape which corresponds to $1/f^6$ for the power spectral density. Noise of this kind can be thought of as the result of integrating white noise over time three times. In other words, the third order derivative of the position of a particle with respect to time (*jolt*) is assumed to be mostly white noise with a probability density peaking at zero.

The idea of the *TrackFit* method is to determine the parameters for a B-spline curve using both: the measured positions of a particle as well as the knowledge about the third order derivative (*jolt*). The *jolt* is assumed to fluctuate around zero with a certain standard deviation and the difference between the real particle track curve and the measurements is assumed to fluctuate around zero with a standard deviation due to the measurement error. Both standard deviations can be estimated based on a spectrum analysis. The standard deviation for the measurement error σ_p given in meters can be extracted from the power spectral density of higher frequencies assuming this portion of the spectrum is dominated by measurement noise. The standard deviation of the *jolt* σ_j in $\text{m} \cdot \text{s}^{-3}$ of the real particle track function according to the above simple model can be determined by the frequency f_c given in Hertz at which the assumed spectra of signal and noise cross each other (cross over frequency) and by σ_p in the following way

$$\sigma_j = \sigma_p \cdot (2\pi f_c)^3$$

because first order derivation with respect to seconds corresponds to a filter with a magnitude response of $1/(2\pi f)$ for every frequency f in Hertz. Determining the parameters for the B-spline curve is done by solving a weighted linear least squares problem which weights deviations between B-spline curve and measurement data

²The text on trajectory fitting has been contributed by Sebastian Gesemann.

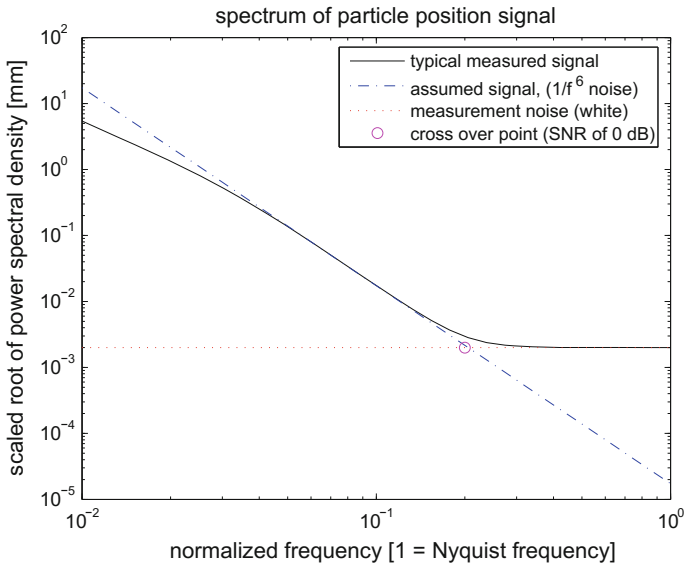


Fig. 9.32 Spectral model of signal and noise for measured particle tracks

as well as deviations of the jolt from zero inversely proportional to the respective standard deviation estimate.

It is interesting to note that the smoothing effect of this fitting method closely corresponds to the behavior of the optimal Wiener filter for the assumptions about the signal spectrum and the noise spectrum. But unlike explicit convolution in the time domain or spectral domain filtering this fitting method deals gracefully with missing data at the track boundaries and results in a continuously defined curve which can be sampled and derived at any point in time within the boundaries.

Given the estimates of the measurement noise and the process noise (jolt) it is also possible to estimate the standard deviation of the absolute errors in position, velocity and acceleration determined by this method. This can be done with the help of the pseudoinverse of the matrix of the corresponding linear equation system.

9.4.6 Data Assimilation for Interpolation to Cartesian Mesh³

After particle tracking with a method such as the Shake-The-Box [90] that has been described in Sect. 9.4.3 and smoothing the particle track with a method such as the one described in Sect. 9.4.5, velocities and accelerations are only available at the locations of the particles that are scattered within the measurement volume for a specific point in time. It is often desirable to perform a spatial interpolation onto a

³The text on Data Assimilation has been contributed by Sebastian Gesemann.

regular grid in order to identify vortices and visualise flow structures. At the same time, physically motivated regularizations can be applied to further increase the spatial resolution. Different base functions, like B-splines (as shown further on) or Vortex-in-cell methods, like *VIC+* by SCHNEIDERS et al. [91], can be applied at the grid nodes.

One such method has been introduced as *FlowFit* [30] and used in the 4th PIV Challenge 2014 [49]. The *FlowFit* method makes use of a system of evenly spaced 3D base splines and represents a velocity field as a superposition of these scaled base splines (uniform B-spline function) where the scaling factors for all base splines are computed as the solution of a cost minimization problem. To avoid any unwanted spatial smoothing the internal B-spline grid can be chosen fine enough. The B-spline grid resolution is usually chosen to result in 5 to 20 base splines for every tracked particle. This is a trade-off between the upper bound for the spatial resolution and computation time.

Of course, with many more degrees of freedom than measurement inputs, the problem of finding B-spline weights for an interpolating function is generally under-determined. In order to resolve ambiguities a form of regularization is applied that favours resulting functions that are more likely to correspond to the actual flow. One of these regularizations adds the squared Euclidean norm of a spatially high-pass filtered version of the function to the cost function – penalizing something like the overall curvature of the function. Such a regularization affects the wavenumber spectrum of the reconstructed velocity field in a way that energy is preferably distributed towards lower wavenumbers. This regularization is physically motivated since real velocity fields can be expected to have similar spectral characteristics. For a one-dimensional example for such a regularized uniform B-spline fit see Fig. 9.33. Uniform B-spline functions are easily extendable to multiple dimensions via a tensor product.

Other regularizations are possible and desirable. For velocity fields of incompressible flows the sum of squared divergences over all grid points can be included as part of the cost function to prefer interpolations that satisfy mass conservation. For acceleration fields the curl of the field can be added to the cost function to exploit the fact that the acceleration field is dominated by the pressure gradient. In both cases this results in a weighted linear least squares problem to determine the weights of the base splines. The solution can be computed using an iterative algorithm such as the conjugated gradient method.

A more sophisticated version of the *FlowFit* interpolation method performs a joint optimization of a B-spline velocity field (\mathbf{U}) and a B-spline pressure field (\bar{p}) based on estimated velocities and accelerations (\mathbf{A}) of the observed particles while accounting for mass and momentum conservation, see [30] for more details. Acceleration is derived from velocity and pressure variables using the momentum equation (9.10) and the mass conservation is handled by adding weighted squared deviations from Eqs. (9.11) and (9.12) for all grid points as part of the cost function to penalize the divergence of the velocity field assuming an incompressible flow of uniform density. The left hand side of Eq. (9.12) refers to the divergence of the temporal derivative of the velocity field which also has to be equal to zero. The use of Eq. (9.12) as part of

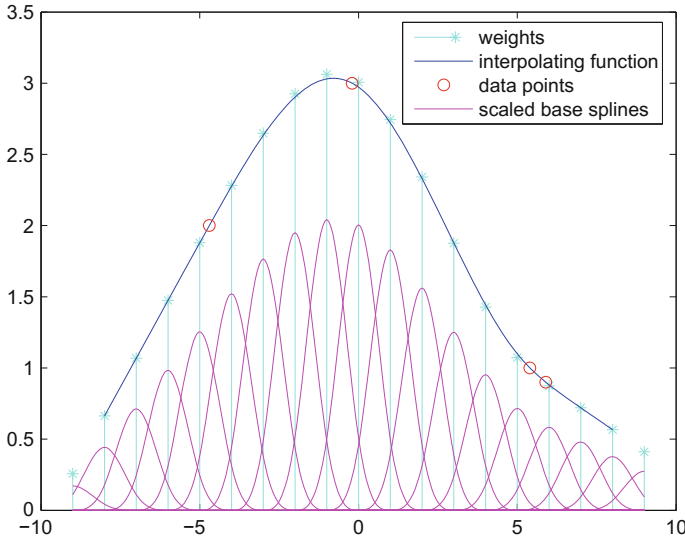


Fig. 9.33 Example for a one-dimensional uniform cubic B-spline function determined by minimising a cost function which includes deviations from the data points as well as the overall curvature

the cost function establishes a strong connection between the velocity field and the acceleration field in a way that measured accelerations will improve the velocity field reconstruction and the other way around. Due to the nonlinearity of this equation in u a different solver such as the Limited-Memory BFGS method [71] has to be used to deal with the resulting nonlinear least squares problem. It also becomes important to weight all the different terms in the cost function appropriately. Estimates of the velocity and acceleration measurement errors are needed for this in order to approximate a maximum likelihood solution and avoid amplifying measurement noise.

$$\mathbf{A} = -\nabla \bar{p} + \nu \Delta \mathbf{U} \tag{9.10}$$

$$\nabla \cdot \mathbf{U} = 0 \tag{9.11}$$

$$\Delta \bar{p} + \nabla \cdot [(\mathbf{U} \cdot \nabla) \mathbf{U}] = 0 \tag{9.12}$$

Table 9.2 summarises the different *FlowFit* variants *div0*, *div1*, *div2*, *pot* that are available. They differ in their choice of variables to compute, what input data they make use of and what the cost function accounts for. Here, HF refers to the penalization of high frequency components, U/A refers to the sum of squared velocity/acceleration deviations between measurements and B-spline curve, Div1 refers

Table 9.2 Different reconstruction variants and their properties

Variant	Input	Variables	Cost function
div0	U	U	HF + U
div1	U	U	HF + U + Div1
div2	U, A	U, \bar{p}	HF + U + A + Div1 + Div2
pot	A	\bar{p}	HF + A

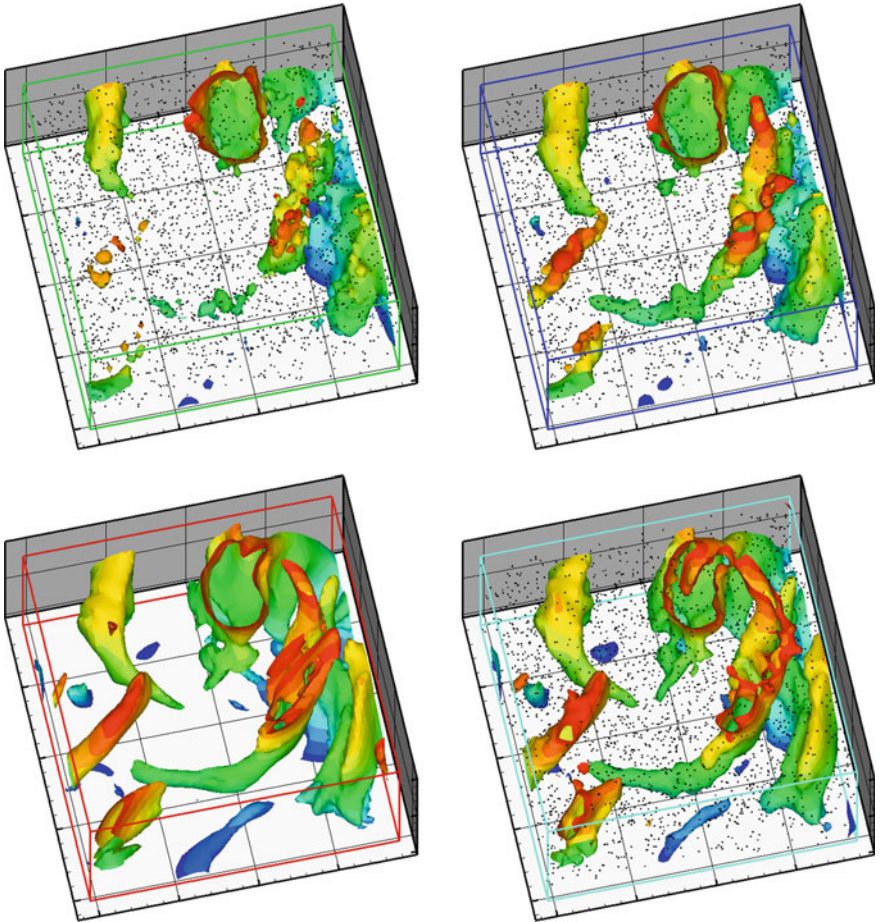


Fig. 9.34 Different reconstructions of vorticity based on 3277 simulated particles (black dots) compared to the ground truth. From top left to bottom left clockwise: div0, div1, div2, ground truth

to the divergence of the velocity field while Div2 refers to the divergence of the temporal derivative of the velocity field.

The effect of the different reconstruction variants with their regularizations can be seen in Fig. 9.34. It shows vorticity isosurfaces of velocity fields computed by different *FlowFit* variants based on simulated particles from a small sub-volume ($64 \times 64 \times 32$ DNS nodes) of the Isotropic Turbulence DNS simulation from the John Hopkins Turbulence Database [55]. The top left velocity field reconstruction (div0) is a simple B-spline fit that does not account for mass conservation and only makes use of the estimated velocities of the simulated particles. The top right reconstruction (div1) extends div0 by including a divergence penalization of the velocity field. This improves the reconstruction and recovers more of the flow structures. The bottom right reconstruction (div2) takes into account the estimated accelerations of the particles as well and jointly reconstructs the velocity field as well as the pressure field (up to an unknown offset). It is able to recover more of the flow structures and approximate the ground truth more closely.

Compared to correlation-based methods where approximately five or more particles within a correlation window are used to determine an average velocity for that correlation window, the above-mentioned interpolation methods avoid any unwanted spatial smoothing by incorporating every particle with its own velocity and position estimates as part of the cost function. In addition, physically motivated regularizations help recover smaller scale structures given a finer internal grid. The *FlowFit* interpolation methods result in a spatially continuous representation of velocity, acceleration and pressure. This makes it possible to sample the functions at any point in space within the reconstruction volume including its exact spatial derivatives which allow the computation of vorticity without numerical differentiation. For high quality visualisations these functions can be oversampled as well.

References

1. Adrian, R.J., Westerweel, J.: Particle Image Velocimetry. Cambridge Aerospace Series. Cambridge University Press, Cambridge (2011). URL <http://www.cambridge.org/de/academic/subjects/engineering/thermal-fluids-engineering/particle-image-velocimetry>
2. Atkinson, C., Soria, J.: An efficient simultaneous reconstruction technique for tomographic particle image velocimetry. *Exp. Fluids* **47**(4), 553–568 (2009). DOI 10.1007/s00348-009-0728-0. URL <http://dx.doi.org/10.1007/s00348-009-0728-0>
3. Barnhart, D.H.: Whole-field holographic measurements of three-dimensional displacement in solid and fluid mechanics. Ph.D. thesis, Loughborough University, UK (2001)
4. Barnhart, D.H., Adrian, R.J., Papen, G.C.: Phase-conjugate holographic system for high-resolution particle-image velocimetry. *Appl. Opt.* **33**(30), 7159–7170 (1994). DOI 10.1364/AO.33.007159. URL <http://ao.osa.org/abstract.cfm?URI=ao-33-30-7159>
5. Belden, J., Truscott, T.T., Axiak, M.C., Techet, A.H.: Three-dimensional synthetic aperture particle image velocimetry. *Meas. Sci. Technol.* **21**(12), 125,403 (2010). DOI 10.1088/0957-0233/21/12/125403. URL <http://stacks.iop.org/0957-0233/21/i=12/a=125403>

6. Belden, J., Ravela, S., Truscott, T.T., Techet, A.H.: Three-dimensional bubble field resolution using synthetic aperture imaging: application to a plunging jet. *Exp. Fluids* **53**(3), 839–861 (2012). DOI 10.1007/s00348-012-1322-4. URL <http://dx.doi.org/10.1007/s00348-012-1322-4>
7. Blinde, P., Lynch, K.P., Schrijer, F.F.J., van Oudheusden, B.: Determination of instantaneous pressure in a transonic base flow using four-pulse tomographic PIV, PIV15, September 14–16. Santa Barbara, California (2015)
8. Bompfrey, R.J., Henningsson, P., Michaelis, D., Hollis, D.: Tomographic particle image velocimetry of desert locust wakes: instantaneous volumes combine to reveal hidden vortex elements and rapid wake deformation. *J. R. Soc. Interface* **9**(77), 3378–3386 (2012). DOI 10.1098/rsif.2012.0418. URL <http://rsif.royalsocietypublishing.org/content/9/77/3378>
9. Brevis, W., Niño, Y., Jirka, G.H.: Integrating cross-correlation and relaxation algorithms for particle tracking velocimetry. *Exp. Fluids* **50**(1), 135–147 (2011). DOI 10.1007/s00348-010-0907-z. URL <http://dx.doi.org/10.1007/s00348-010-0907-z>
10. Brücker, C.: 3-D scanning-particle-image-velocimetry: Technique and application to a spherical cap wake flow. *Appl. Sci. Res.* **56**(2–3), 157–179 (1996). DOI 10.1007/BF02249379. URL <http://dx.doi.org/10.1007/BF02249379>
11. Brücker, C.: Spatial correlation analysis for 3-D scanning PIV: simulation and application of dual-color light-sheet scanning. In: 8th International Symposia on Applications of Laser Techniques to Fluid Mechanics, Lisbon (Portugal) (1996)
12. Brücker, C.: 3d scanning PIV applied to an air flow in a motored engine using digital high-speed video. *Meas. Sci. Technol.* **8**(12), 1480 (1997). DOI 10.1088/0957-0233/8/12/011. URL <http://stacks.iop.org/0957-0233/8/i=12/a=011>
13. Brücker, C., Hess, D., Kitzhofer, J.: Single-view volumetric PIV via high-resolution scanning, isotropic voxel restructuring and 3D least-squares matching (3D-LSM). *Meas. Sci. Technol.* **24**(2), 024,001 (2013). DOI 10.1088/0957-0233/24/2/024001. URL <http://stacks.iop.org/0957-0233/24/i=2/a=024001>
14. Caridi, G.C.A., Ragni, D., Sciacchitano, A., Scarano, F.: HFSB-seeding for large-scale tomographic PIV in wind tunnels. *Exp. Fluids* **57**(12), 190 (2016). DOI 10.1007/s00348-016-2277-7. URL <http://dx.doi.org/10.1007/s00348-016-2277-7>
15. Choi, W., Guezennec, Y., Jung, I.: Rapid evaluation of variable valve lift strategies using 3-D in-cylinder flow measurements. In: SAE 1996 Transactions - Journal of Engines, vol. 105-3, p. 960951. SAE (1996). DOI 10.4271/960951. URL <http://papers.sae.org/960951/> (SAE Technical Paper 960951)
16. Cierpka, C., Segura, R., Hain, R., Kähler, C.J.: A simple single camera 3C3D velocity measurement technique without errors due to depth of correlation and spatial averaging for microfluidics. *Meas. Sci. Technol.* **21**(4), 045,401 (2010). DOI 10.1088/0957-0233/21/4/045401. URL <http://stacks.iop.org/0957-0233/21/i=4/a=045401>
17. Cierpka, C., Lütke, B., Kähler, C.J.: Higher order multi-frame particle tracking velocimetry. *Exp. Fluids* **54**(5), 1533 (2013). DOI 10.1007/s00348-013-1533-3. URL <http://dx.doi.org/10.1007/s00348-013-1533-3>
18. Discetti, S., Astarita, T.: Fast 3D PIV with direct sparse cross-correlations. *Exp. Fluids* **53**(5), 1437–1451 (2012). DOI 10.1007/s00348-012-1370-9. URL <http://dx.doi.org/10.1007/s00348-012-1370-9>
19. Discetti, S., Astarita, T.: A fast multi-resolution approach to tomographic PIV. *Exp. Fluids* **52**(3), 765–777 (2012). DOI 10.1007/s00348-011-1119-x. URL <http://dx.doi.org/10.1007/s00348-011-1119-x>
20. Elsinga, G.E., Scarano, F., Wieneke, B., van Oudheusden, B.W.: Tomographic particle image velocimetry. *Exp. Fluids* **41**(6), 933–947 (2006). DOI 10.1007/s00348-006-0212-z. URL <http://dx.doi.org/10.1007/s00348-006-0212-z>
21. Elsinga, G.E., Westerweel, J., Scarano, F., Novara, M.: On the velocity of ghost particles and the bias errors in tomographic-PIV. *Exp. Fluids* **50**(4), 825–838 (2011). DOI 10.1007/s00348-010-0930-0. URL <http://dx.doi.org/10.1007/s00348-010-0930-0>

22. Elsinga, G.E., Tokgoz, S.: Ghost hunting—an assessment of ghost particle detection and removal methods for tomographic-PIV. *Meas. Sci. Technol.* **25**(8), 084,004 (2014). DOI 10.1088/0957-0233/25/8/084004. URL <http://stacks.iop.org/0957-0233/25/i=8/a=084004>
23. Fuchs, T., Hain, R., Kähler, C.J.: Three-dimensional location of micrometer-sized particles in macroscopic domains using astigmatic aberrations. *Opt. Lett.* **39**(5), 1298–1301 (2014). DOI 10.1364/OL.39.001298. URL <http://ol.osa.org/abstract.cfm?URI=ol-39-5-1298>
24. Fuchs, T., Hain, R., Kähler, C.J.: Double-frame 3D-PTV using a tomographic predictor. *Exp. Fluids* **57**(11), 174 (2016). DOI 10.1007/s00348-016-2247-0. URL <http://dx.doi.org/10.1007/s00348-016-2247-0>
25. Fuchs, T., Hain, R., Kähler, C.J.: In situ calibrated defocusing PTV for wall-bounded measurement volumes. *Meas. Sci. Technol.* **27**(8), 084,005 (2016). DOI 10.1088/0957-0233/27/8/084005. URL <http://stacks.iop.org/0957-0233/27/i=8/a=084005>
26. Fuchs, T., Hain, R., Kähler, C.J.: Uncertainty quantification of three-dimensional velocimetry techniques for small measurement depths. *Exp. Fluids* **57**(5), 73 (2016). DOI 10.1007/s00348-016-2161-5. URL <http://dx.doi.org/10.1007/s00348-016-2161-5>
27. Fuchs, T., Hain, R., Kähler, C.J.: Non-iterative double-frame 2D/3D particle tracking velocimetry. *Exp. Fluids* **58**(119) (2017). DOI 10.1007/s00348-017-2404-0. URL <https://doi.org/10.1007/s00348-017-2404-0>
28. Fukuchi, Y.: Influence of number of cameras and preprocessing for thick volume tomographic PIV. In: 16th International Symposium on Applications of Laser Techniques to Fluid Mechanics Lisbon, Portugal, 09–12 July (2012). URL http://lces.dem.ist.utl.pt/lxaser/lxaser2012/upload/153_paper_zxsdx.pdf
29. Geisler, R., Novara, M., Schröder, A.: Volumetric multi-pulse particle tracking measurement for separated laminar transitional flow investigations. In: 18th International Symposium on Applications of Laser Techniques to Fluid Mechanics, 4–7 July 2016, Lisbon, Portugal (2016)
30. Gesemann, S., Huhn, F., Schanz, D., Schröder, A.: From noisy particle tracks to velocity, acceleration and pressure fields using B-splines and penalties. In: 18th International Symposium on Applications of Laser and Imaging Techniques to Fluid Mechanics, Lisbon, Portugal (2016). URL http://lces.dem.ist.utl.pt/lxaser/lxaser2016/finalworks2016/papers/04.5_4_186paper.pdf
31. Ghaemi, S., Scarano, F.: Multi-pass light amplification for tomographic particle image velocimetry applications. *Meas. Sci. Technol.* **21**(12), 127,002 (2010). DOI 10.1088/0957-0233/21/12/127002. URL <http://stacks.iop.org/0957-0233/21/i=12/a=127002>
32. Ghaemi, S., Scarano, F.: Counter-hairpin vortices in the turbulent wake of a sharp trailing edge. *J. Fluid Mech.* **689**, 317–356 (2011). DOI 10.1017/jfm.2011.431. URL <http://dx.doi.org/10.1017/jfm.2011.431>
33. Gordon, R., Bender, R., Herman, G.T.: Algebraic reconstruction techniques (ART) for three-dimensional electron microscopy and X-ray photography. *J. Theor. Biol.* **29**(3), 471–481 (1970). DOI 10.1016/0022-5193(70)90109-8. URL <http://www.sciencedirect.com/science/article/pii/0022519370901098>
34. Hartley, R.I., Sturm, P.: Triangulation. *Comput. Vis. Image Underst.* **68**(2), 146–157 (1997). DOI 10.1006/cviu.1997.0547. URL <http://www.sciencedirect.com/science/article/pii/S1077314297905476>
35. Herman, G.T., Lent, A.: Iterative reconstruction algorithms. *Comput. Biol. Med.* **6**(4), 273–294 (1976). DOI 10.1016/0010-4825(76)90066-4. URL [http://dx.doi.org/10.1016/0010-4825\(76\)90066-4](http://dx.doi.org/10.1016/0010-4825(76)90066-4)
36. Herrmann, S.F., Hinsch, K.D.: Light-in-flight holographic particle image velocimetry for wind-tunnel applications. *Meas. Sci. Technol.* **15**(4), 613 (2004). DOI 10.1088/0957-0233/15/4/002. URL <http://stacks.iop.org/0957-0233/15/i=4/a=002>
37. Hinsch, K.D.: Holographic particle image velocimetry. *Meas. Sci. Technol.* **13**(7), R61 (2002). DOI 10.1088/0957-0233/13/7/201. URL <http://dx.doi.org/10.1088/0957-0233/13/7/201>
38. Hu, H., Saga, T., Kobayashi, T., Taniguchi, N., Yasuki, M.: Dual-plane stereoscopic particle image velocimetry: system set-up and its application on a lobed jet mixing flow. *Exp. Fluids* **31**(3), 277–293 (2001). DOI 10.1007/s003480100283. URL <http://dx.doi.org/10.1007/s003480100283>

39. Huhn, F., Schanz, D., Gesemann, S., Dierksheide, U., van de Meerendonk, R., Schröder, A.: Large-scale volumetric flow measurement in a pure thermal plume by dense tracking of helium-filled soap bubbles, *Exp. Fluids* **58**, 116 (2017). URL <https://doi.org/10.1007/s00348-017-2390-2>
40. Jahn, T.: Volumetric flow field measurement: an implementation of Shake-The-Box. Master Thesis, DLR Göttingen & Georg-August-Universität Göttingen, Germany (2017)
41. Kähler, C.J.: Multiplane stereo PIV - recording and evaluation methods. In: *EUROMECH 411: application of PIV to turbulence measurements*, University of Rouen (France) (2000)
42. Kähler, C.J.: Investigation of the spatio-temporal flow structure in the buffer region of a turbulent boundary layer by means of multiplane stereo PIV. *Exp. Fluids* **36**(1), 114–130 (2004). DOI 10.1007/s00348-003-0680-3. URL <http://dx.doi.org/10.1007/s00348-003-0680-3>
43. Kähler, C.J., Kompenhans, J.: Multiple plane stereo PIV – technical realization and fluid-mechanical significance. In: *3rd International Workshop on PIV*, Santa Barbara (USA) (1999)
44. Kähler, C.J., Kompenhans, J.: Fundamentals of multiple plane stereo particle image velocimetry. *Exp. Fluids* **29**(1), S070–S077 (2000). DOI 10.1007/s003480070009. URL <http://dx.doi.org/10.1007/s003480070009>
45. Kähler, C.J., Stanislas, M., Dewhirst, T., Carlier, J.: Investigation of the spatio-temporal flow structure in the log-law region of a turbulent boundary layer by means of multi-plane stereo particle image velocimetry. In: *Laser Techniques for Fluid Mechanics*, pp. 39–53. Springer, Berlin (2002). DOI 10.1007/978-3-662-08263-8_3. URL https://doi.org/10.1007/978-3-662-08263-8_3
46. Kähler, C.J., Scholz, U., Ortmanns, J.: Wall-shear-stress and near-wall turbulence measurements up to single pixel resolution by means of long-distance micro-PIV. *Exp. Fluids* **41**(2), 327–341 (2006). DOI 10.1007/s00348-006-0167-0. URL <http://dx.doi.org/10.1007/s00348-006-0167-0>
47. Kähler, C.J., Scharnowski, S., Cierpka, C.: On the resolution limit of digital particle image velocimetry. *Exp. Fluids* **52**(6), 1629–1639 (2012). DOI 10.1007/s00348-012-1280-x. URL <http://dx.doi.org/10.1007/s00348-012-1280-x>
48. Kähler, C.J., Scharnowski, S., Cierpka, C.: On the uncertainty of digital PIV and PTV near walls. *Exp. Fluids* **52**(6), 1641–1656 (2012). DOI 10.1007/s00348-012-1307-3. URL <http://dx.doi.org/10.1007/s00348-012-1307-3>
49. Kähler, C.J., Astarita, T., Vlachos, P.P., Sakakibara, J., Hain, R., Discetti, S., Foy, R., Cierpka, C.: Main results of the 4th international piv challenge. *Exp. Fluids* **57**(6), 1–71 (2016). DOI 10.1007/s00348-016-2173-1. URL <http://dx.doi.org/10.1007/s00348-016-2173-1>
50. Kalman, R.E.: A new approach to linear filtering and prediction problems. *J. Basic Eng.* **82**(1), 35–45 (1960)
51. Katz, J., Sheng, J.: Applications of holography in fluid mechanics and particle dynamics. *Annu. Rev. Fluid Mech.* **42**(1), 531–555 (2010). DOI 10.1146/annurev-fluid-121108-145508. URL <http://dx.doi.org/10.1146/annurev-fluid-121108-145508>
52. Keane, R.D., Adrian, R.J.: Theory of cross-correlation analysis of PIV images. *Appl. Sci. Res.* **49**(3), 191–215 (1992). DOI 10.1007/BF00384623. URL <http://dx.doi.org/10.1007/BF00384623>
53. Konrath, R., Schröder, W., Limberg, W.: Holographic particle image velocimetry applied to the flow within the cylinder of a four-valve internal combustion engine. *Exp. Fluids* **33**(6), 781–793 (2002). DOI 10.1007/s00348-002-0495-7. URL <http://dx.doi.org/10.1007/s00348-002-0495-7>
54. Lei, Y.C., Tien, W.H., Duncan, J., Paul, M., Ponchaut, N., Mouton, C., Dabiri, D., Rösgen, T., Hove, J.: A vision-based hybrid particle tracking velocimetry (PTV) technique using a modified cascade correlation peak-finding method. *Exp. Fluids* **53**(5), 1251–1268 (2012). DOI 10.1007/s00348-012-1357-6. URL <http://dx.doi.org/10.1007/s00348-012-1357-6>
55. Li, Y., Perlman, E., Wan, M., Yang, Y., Meneveau, C., Burns, R., Chen, S., Szalay, A., Eyink, G.: A public turbulence database cluster and applications to study Lagrangian evolution of velocity increments in turbulence. *J. Turbul.* **9**(31), 1–29 (2008). DOI 10.1080/14685240802376389. URL <http://dx.doi.org/10.1080/14685240802376389>

56. Lüthi, B., Tsinober, A., Kinzelbach, W.: Lagrangian measurement of vorticity dynamics in turbulent flow. *J. Fluid Mech.* **528**, 87–118 (2005). DOI 10.1017/S0022112004003283. URL <http://dx.doi.org/10.1017/S0022112004003283>
57. Lynch, K.P., Scarano, F.: Experimental determination of tomographic PIV accuracy by a 12-camera system. *Meas. Sci. Technol.* **25**(8), 084,003 (2014). DOI 10.1088/0957-0233/25/8/084003. URL <http://stacks.iop.org/0957-0233/25/i=8/a=084003>
58. Lynch, K.P., Scarano, F.: Material acceleration estimation by four-pulse tomo-PIV. *Meas. Sci. Technol.* **25**(8), 084005 (2014). DOI 10.1088/0957-0233/25/8/084005. URL <http://stacks.iop.org/0957-0233/25/i=8/a=084005>
59. Lynch, K.P., Scarano, F.: An efficient and accurate approach to MTE-MART for time-resolved tomographic PIV. *Exp. Fluids* **56**(3), 66 (2015). DOI 10.1007/s00348-015-1934-6. URL <http://dx.doi.org/10.1007/s00348-015-1934-6>
60. Maas, H.G., Gruen, A., Papantoniou, D.: Particle tracking velocimetry in three-dimensional flows. *Exp. Fluids* **15**(2), 133–146 (1993). DOI 10.1007/BF00190953. URL <http://dx.doi.org/10.1007/BF00190953>
61. Malek, M., Allano, D., Coëtmelec, S., Özkul, C., Lebrun, D.: Digital in-line holography for three-dimensional-two-components particle tracking velocimetry. *Meas. Sci. Technol.* **15**(4), 699 (2004). DOI 10.1088/0957-0233/15/4/012. URL <http://stacks.iop.org/0957-0233/15/i=4/a=012>
62. Malik, N.A., Dracos, T., Papantoniou, D.A.: Particle tracking velocimetry in three-dimensional flows. *Exp. Fluids* **15**(4), 279–294 (1993). DOI 10.1007/BF00223406. URL <http://dx.doi.org/10.1007/BF00223406>
63. Meng, H., Pan, G., Pu, Y., Woodward, S.H.: Holographic particle image velocimetry: from film to digital recording. *Meas. Sci. Technol.* **15**(4), 673 (2004). DOI 10.1088/0957-0233/15/4/009. URL <http://stacks.iop.org/0957-0233/15/i=4/a=009>
64. Michaelis, D., Novara, M., Scarano, F., Wieneke, B.: Comparison of volume reconstruction techniques at different particle densities. In: 15th International Symposium on Applications of Laser Techniques to Fluid Mechanics, Lisbon, Portugal (2010). URL http://ltces.dem.ist.utl.pt/lxaser/lxaser2010/upload/1708_toytpv_3.10.5.Full_1708.pdf
65. Mikheev, A.V., Zubtsov, V.M.: Enhanced particle-tracking velocimetry (EPTV) with a combined two-component pair-matching algorithm. *Meas. Sci. Technol.* **19**(8), 085,401 (2008). DOI 10.1088/0957-0233/19/8/085401. URL <http://stacks.iop.org/0957-0233/19/i=8/a=085401>
66. Mullin, J.A., Dahm, W.J.A.: Highly-resolved three-dimensional velocity measurements via dual-plane stereo particle image velocimetry (DSPIV) in turbulent flows (2002). DOI 10.2514/6.2002-290. URL <https://doi.org/10.2514/6.2002-290>
67. Mullin, J.A., Dahm, W.J.A.: Dual-plane stereo particle image velocimetry (DSPIV) for measuring velocity gradient fields at intermediate and small scales of turbulent flows. *Exp. Fluids* **38**(2), 185–196 (2005). DOI 10.1007/s00348-004-0898-8. URL <http://dx.doi.org/10.1007/s00348-004-0898-8>
68. Mullin, J.A., Dahm, W.J.A.: Dual-plane stereo particle image velocimetry measurements of velocity gradient tensor fields in turbulent shear flow. i. accuracy assessments. *Phys. Fluids* **18**(3), 035,101 (2006). DOI 10.1063/1.2166447. URL <https://doi.org/10.1063/1.2166447>
69. Mullin, J.A., Dahm, W.J.A.: Dual-plane stereo particle image velocimetry measurements of velocity gradient tensor fields in turbulent shear flow. ii. experimental results. *Phys. Fluids* **18**(3), 035,102 (2006). DOI 10.1063/1.2166448. URL <https://doi.org/10.1063/1.2166448>
70. Nishino, K., Kasagi, N., Hirata, M.: Three-dimensional particle tracking velocimetry based on automated digital image processing. *J. Fluids Eng.* **111**(4), 384–391 (1989). DOI 10.1115/1.3243657. URL <http://dx.doi.org/10.1115/1.3243657>
71. Nocedal, J.: Updating quasi-Newton matrices with limited storage. *Math. Comput.* **35**(151), 773–782 (1980). URL [http://www.ams.org/journals/mcom/1980-35-151/S0025-5718-1980-0572855-7.pdf](http://www.ams.org/journals/mcom/1980-35-151/S0025-5718-1980-0572855-7/S0025-5718-1980-0572855-7.pdf)
72. Novara, M., Batenburg, K.J., Scarano, F.: Motion tracking-enhanced MART for tomographic PIV. *Meas. Sci. Technol.* **21**(3), 035,401 (2010). DOI 10.1088/0957-0233/21/3/035401. URL <http://stacks.iop.org/0957-0233/21/i=3/a=035401>

73. Novara, M., Scarano, F.: Performances of motion tracking enhanced Tomo-PIV on turbulent shear flow. *Exp. Fluids* **52**(4), 1027–1041 (2012)
74. Novara, M., Scarano, F.: A particle-tracking approach for accurate material derivative measurements with tomographic PIV. *Exp. Fluids* **54**(8), 1584 (2013)
75. Novara, M., Schanz, D., Reuther, N., Kähler, C.J., Schröder, A.: Lagrangian 3D particle tracking in high-speed flows: Shake-The-Box for multi-pulse systems. *Exp. Fluids* **57**, 128 (2016a)
76. Novara, M., Schanz, D., Gesemann, S., Lynch, K.P., Schröder, A.: Lagrangian 3D particle tracking for multi-pulse systems: performance assessment and application of Shake-The-Box. In: 18th International Symposium on Applications of Laser Techniques to Fluid Mechanics, 4–7 July 2016, Lisbon, Portugal (2016b)
77. Ohmi, K., Li, H.Y.: Particle-tracking velocimetry with new algorithms. *Meas. Sci. Technol.* **11**(6), 603 (2000). DOI 10.1088/0957-0233/11/6/303. URL <http://stacks.iop.org/0957-0233/11/i=6/a=303>
78. Okamoto, K., Nishio, S., Saga, T., Kobayashi, T.: Standard images for particle-image velocimetry. *Meas. Sci. Technol.* **11**(6), 685 (2000). DOI 10.1088/0957-0233/11/6/311. URL <http://stacks.iop.org/0957-0233/11/i=6/a=311>
79. Percin, M., Hu, Y., van Oudheusden, B.W., Remes, B., Scarano, F.: Wing flexibility effects in clap-and-fling. *Int. J. Micro Air Veh.* **3**(4), 217–227 (2011). DOI 10.1260/1756-8293.3.4.217. URL <http://dx.doi.org/10.1260/1756-8293.3.4.217>
80. Pereira, F., Stüer, H., Graff, E.C., Gharib, M.: Two-frame 3D particle tracking. *Meas. Sci. Technol.* **17**(7), 1680 (2006). DOI 10.1088/0957-0233/17/7/006. URL <http://stacks.iop.org/0957-0233/17/i=7/a=006>
81. Prasad, A.K.: Stereoscopic particle image velocimetry. *Exp. Fluids* **29**(2), 103–116 (2000). DOI 10.1007/s003480000143. URL <http://dx.doi.org/10.1007/s003480000143>
82. Pu, Y., Meng, H.: An advanced off-axis holographic particle image velocimetry (HPIV) system. *Exp. Fluids* **29**(2), 184–197 (2000). DOI 10.1007/s003489900088. URL <http://dx.doi.org/10.1007/s003489900088>
83. Rochlitz, H., Scholz, P., Fuchs, T.: The flow field in a high aspect ratio cooling duct with and without one heated wall. *Exp. Fluids* **56**(12), 208 (2015). DOI 10.1007/s00348-015-2071-y. URL <http://dx.doi.org/10.1007/s00348-015-2071-y>
84. Scarano, F.: Tomographic PIV: principles and practice. *Meas. Sci. Technol.* **24**(1) (2012) DOI 10.1088/0957-0233/24/1/012001. URL <http://doi.org/10.1088/0957-0233/24/1/012001>
85. Scarano, F., Poelma, C.: Three-dimensional vorticity patterns of cylinder wakes. *Exp. Fluids* **47**(1), 69 (2009). DOI 10.1007/s00348-009-0629-2. URL <http://dx.doi.org/10.1007/s00348-009-0629-2>
86. Scarano, F., Riethmuller, M.L.: Advances in iterative multigrid PIV image processing. *Exp. Fluids* **29**(1), S051–S060 (2000). DOI 10.1007/s003480070007. URL <http://dx.doi.org/10.1007/s003480070007>
87. Scarano, F., David, L., Bsibsi, M., Calluad, D.: S-PIV comparative assessment: image dewarping + misalignment correction and pinhole + geometric back projection. *Exp. Fluids* **39**(2), 257–266 (2005). DOI 10.1007/s00348-005-1000-x. URL <http://dx.doi.org/10.1007/s00348-005-1000-x>
88. Schanz, D., Gesemann, S., Schröder, A., Wieneke, B., Novara, M.: Non-uniform optical transfer functions in particle imaging: calibration and application to tomographic reconstruction. *Meas. Sci. Technol.* **24**(2) (2013). DOI 10.1088/0957-0233/24/2/024009. URL <http://stacks.iop.org/0957-0233/24/i=2/a=024009>
89. Schanz, D., Schröder, A., Gesemann, S., Michaelis, D., Wieneke, B.: ‘Shake The Box’: a highly efficient and accurate tomographic particle tracking velocimetry (tomo-PTV) method using prediction of particle positions. In: PIV13; 10th International Symposium on Particle Image Velocimetry, Delft, The Netherlands, July 1–3, 2013. Delft University of Technology, Faculty of Mechanical, Maritime and Materials Engineering, and Faculty of Aerospace Engineering (2013). URL <http://repository.tudelft.nl/islandora/object/uuid:212b0c2d-3210-482f-b751-91d98d5ea43d/?collection=research>

90. Schanz, D., Gesemann, S., Schröder, A.: Shake-The-Box: Lagrangian particle tracking at high particle image densities. *Exp. Fluids* **57**(5), 1–27 (2016). DOI 10.1007/s00348-016-2157-1. URL <http://dx.doi.org/10.1007/s00348-016-2157-1>
91. Schneiders, J.F.G., Scarano, F.: Dense velocity reconstruction from tomographic PTV with material derivatives. *Exp. Fluids* **57**(9), 139 (2016). DOI 10.1007/s00348-016-2225-6. URL <http://dx.doi.org/10.1007/s00348-016-2225-6>
92. Schosser, C., Fuchs, T., Hain, R., Kähler, C.J.: Non-intrusive calibration for three-dimensional particle imaging. *Exp. Fluids* **57**(5), 69 (2016). DOI 10.1007/s00348-016-2167-z. URL <http://dx.doi.org/10.1007/s00348-016-2167-z>
93. Schrijer, F.F.J., Scarano, F.: Effect of predictor-corrector filtering on the stability and spatial resolution of iterative PIV interrogation. *Exp. Fluids* **45**(5), 927–941 (2008). DOI 10.1007/s00348-008-0511-7. URL <http://dx.doi.org/10.1007/s00348-008-0511-7>
94. Schröder, A., Geisler, R., Elsinga, G.E., Scarano, F., Dierksheide, U.: Investigation of a turbulent spot and a tripped turbulent boundary layer flow using time-resolved tomographic PIV. *Exp. Fluids* **44**(2), 305–316 (2008). DOI 10.1007/s00348-007-0403-2. URL <http://dx.doi.org/10.1007/s00348-007-0403-2>
95. Schröder, A., Geisler, R., Staack, K., Elsinga, G.E., Scarano, F., Wieneke, B., Henning, A., Poelma, C., Westerweel, J.: Eulerian and Lagrangian views of a turbulent boundary layer flow using time-resolved tomographic PIV. *Exp. Fluids* **50**(4), 1071–1091 (2011). DOI 10.1007/s00348-010-1014-x. URL <http://dx.doi.org/10.1007/s00348-010-1014-x>
96. Schröder, A., Schanz, D., Geisler, R., Willert, C., Michaelis, D.: Dual-volume and four-pulse Tomo-PIV using polarized light, 10th Symp PIV. Delft, The Netherlands (2013)
97. Schröder, A., Schanz, D., Michaelis, D., Cierpka, C., Scharnowski, S., Kähler, C.J.: Advances of PIV and 4D-PTV ‘Shake-The-Box’ for turbulent flow analysis - the flow over periodic hills. *Flow Turbul. Combust.* **95**(2), 193–209 (2015). DOI 10.1007/s10494-015-9616-2. URL <http://dx.doi.org/10.1007/s10494-015-9616-2>
98. Sciacchitano, A., Scarano, F.: Elimination of PIV light reflections via a temporal high pass filter. *Meas. Sci. Technol.* **25**(8), 084,009 (2014). DOI 10.1088/0957-0233/25/8/084009. URL <http://stacks.iop.org/0957-0233/25/i=8/a=084009>
99. Sciacchitano, A., Scarano, F., Wieneke, B.: Multi-frame pyramid correlation for time-resolved PIV. *Exp. Fluids* **53**(4), 1087–1105 (2012). DOI 10.1007/s00348-012-1345-x. URL <http://dx.doi.org/10.1007/s00348-012-1345-x>
100. Soria, J., Atkinson, C.: Towards 3C-3D digital holographic fluid velocity vector field measurement—tomographic digital holographic piv (tomo-hpiv). *Meas. Sci. Technol.* **19**(7), 074,002 (2008). DOI 10.1088/0957-0233/19/7/074002. URL <http://stacks.iop.org/0957-0233/19/i=7/a=074002>
101. Svizher, A., Cohen, J.: Holographic particle image velocimetry system for measurements of hairpin vortices in air channel flow. *Exp. Fluids* **40**(5), 708–722 (2006). DOI 10.1007/s00348-006-0108-y. URL <http://dx.doi.org/10.1007/s00348-006-0108-y>
102. Thomas, L., Tremblais, B., David, L.: Optimization of the volume reconstruction for classical tomo-PIV algorithms (MART, BIMART and SMART): synthetic and experimental studies. *Meas. Sci. Technol.* **25**(3), 035,303 (2014). DOI 10.1088/0957-0233/25/3/035303. URL <http://stacks.iop.org/0957-0233/25/i=3/a=035303>
103. van Doorne, C.W.H., Westerweel, J.: Measurement of laminar, transitional and turbulent pipe flow using stereoscopic-PIV. *Exp. Fluids* **42**(2), 259–279 (2007). DOI 10.1007/s00348-006-0235-5. URL <http://dx.doi.org/10.1007/s00348-006-0235-5>
104. van Gent, P.L., Michaelis, D., van Oudheusden, B.W., Weiss, P.É., de Kat, R., Laskari, A., Jeon, Y.J., David, L., Schanz, D., Huhn, F., Gesemann, S., Novara, M., McPhaden, C., Neeteson, N.J., Rival, D.E., Schneiders, J.F.G., Schrijer, F.F.J.: Comparative assessment of pressure field reconstructions from particle image velocimetry measurements and Lagrangian particle tracking. *Exp. Fluids* **58**(4), 33 (2017). DOI 10.1007/s00348-017-2324-z. URL <http://dx.doi.org/10.1007/s00348-017-2324-z>
105. Violato, D., Scarano, F.: Three-dimensional evolution of flow structures in transitional circular and chevron jets. *Phys. Fluids* **23**(12), 124,104 (2011). DOI 10.1063/1.3665141. URL <https://doi.org/10.1063/1.3665141>

106. Virant, M., Dracos, T.: Establishment of a videogrammetric PTV system. In: Dracos, T. (ed.) *Three-Dimensional Velocity and Vorticity Measuring and Image Analysis Techniques*. ERCOFTAC Series, vol. 4, pp. 229–254. Springer, Netherlands (1996). DOI 10.1007/978-94-015-8727-3_11. URL https://doi.org/10.1007/978-94-015-8727-3_11
107. Watanabe, Y., Hideshima, Y., Shigematsu, T., Takehara, K.: Application of three-dimensional hybrid stereoscopic particle image velocimetry to breaking waves. *Meas. Sci. Technol.* **17**(6), 1456 (2006). DOI 10.1088/0957-0233/17/6/025. URL <http://stacks.iop.org/0957-0233/17/i=6/a=025>
108. Wereley, S.T., Meinhart, C.D.: Second-order accurate particle image velocimetry. *Exp. Fluids* **31**(3), 258–268 (2001). DOI 10.1007/s003480100281. URL <http://dx.doi.org/10.1007/s003480100281>
109. Westerweel, J.: On velocity gradients in PIV interrogation. *Exp. Fluids* **44**(5), 831–842 (2008). DOI 10.1007/s00348-007-0439-3. URL <http://dx.doi.org/10.1007/s00348-007-0439-3>
110. Wieneke, B.: Stereo-PIV using self-calibration on particle images. *Exp. Fluids* **39**(2), 267–280 (2005). DOI 10.1007/s00348-005-0962-z. URL <http://dx.doi.org/10.1007/s00348-005-0962-z>
111. Wieneke, B.: Volume self-calibration for 3D particle image velocimetry. *Exp. Fluids* **45**(4), 549–556 (2008). DOI 10.1007/s00348-008-0521-5. URL <http://dx.doi.org/10.1007/s00348-008-0521-5>
112. Wieneke, B.: Iterative reconstruction of volumetric particle distribution. *Meas. Sci. Technol.* **24**(2) (2013). DOI 10.1088/0957-0233/24/2/024008. URL <http://stacks.iop.org/0957-0233/24/i=2/a=024008>
113. Wiener, N.: *Extrapolation, Interpolation, and Smoothing of Stationary Time Series*, vol. 2. MIT Press Cambridge, Cambridge (1949)
114. Willert, C.E.: Stereoscopic digital particle image velocimetry for application in wind-tunnel flows. *Meas. Sci. Technol.* **8**, 1465–1479 (1997). DOI 10.1088/0957-0233/8/12/010. URL <http://stacks.iop.org/0957-0233/8/i=12/a=010>
115. Willert, C.E., Gharib, M.: Three-dimensional particle imaging with a single camera. *Exp. Fluids* **12**(6), 353–358 (1992). DOI 10.1007/BF00193880. URL <http://dx.doi.org/10.1007/BF00193880>
116. Willert, C.E., Stasicki, B., Klinner, J., Moessner, S.: Pulsed operation of high-power light emitting diodes for imaging flow velocimetry. *Meas. Sci. Technol.* **21**(7), 075402 (2010). DOI 10.1088/0957-0233/21/7/075402. URL <http://dx.doi.org/10.1088/0957-0233/21/7/075402>
117. Worth, N.A., Nickels, T.B.: Acceleration of tomo-piv by estimating the initial volume intensity distribution. *Exp. Fluids* **45**(5), 847 (2008). DOI 10.1007/s00348-008-0504-6. URL <http://dx.doi.org/10.1007/s00348-008-0504-6>
118. Zhang, Z.: A flexible new technique for camera calibration. *IEEE Trans. Pattern Anal. Mach. Intell.* **22**(11), 1330–1334 (2000). DOI 10.1109/34.888718. URL <http://dx.doi.org/10.1109/34.888718>

Chapter 10

Micro-PIV

10.1 Introduction

In many areas of science and engineering it is important to determine the flow field at the micron scale. Industrial applications of microfabricated fluidic devices are ubiquitous in the aerospace, automotive, computer, process engineering, pharmaceutical and biomedical industries. The study of flow in these devices is usually called microfluidics.

10.1.1 Microfluidics Background

The field of microfluidics can be divided broadly into two classes: continuum and sub-continuum microfluidics [86]. In *continuum microfluidics* the device size scale is large enough that the fluid behaves as a continuum, *i.e.* by the same rules as flows at the much larger length scales we encounter in more conventional flows, such as flows over airfoils, inside pipes, etc. Non-intuitive behaviors requiring special consideration can still occur in continuum microfluidics because fluid forces scale differently as a system's size scale is reduced. For instance, inertia scales with the third power of length scale whereas shear stress scales as the second power of length scale. Consequently, many continuum microfluidic systems operate in a viscosity-dominated regime (low Reynolds number, *i.e.* $Re \ll 1$). Moreover, surface tension scales with the length scale and hence has a very big influence on microscopic systems despite having little influence on the larger flows we experience in our daily lives. The force balance on tracer particles in a continuum microflow is identical to the force balance in larger systems (see Sect. 2.1.1). One significant difference between continuum microfluidics and macroscopic flows is that the effect of random thermal vibrations in the form of Brownian motion is much more apparent and can

An overview of the Digital Content to this chapter can be found at [DC10.1].

significantly influence the PIV measurements by increasing the random noise level (see Sect. 2.1.4).

In *sub-continuum microfluidics*, the governing equations for fluid behavior change. The appropriate governing equations for sub-continuum flows are not the Navier-Stokes equations but rather one of several governing equations depending on the nature of the flow. Examples of sub-continuum microfluidics include water flowing through single-wall carbon nanotubes where preferred water molecule orientations are observed, resulting in radical fluctuations of density and viscosity over length scales of nanometers. In such cases it may be necessary to use the Boltzmann equation or molecular dynamics to predict how the water molecules interact with the carbon molecules comprising the carbon nanotube. Another example of sub-continuum microfluidics is the rarefied gas flow around a hard drive read/write head. For small Knudsen numbers ($Kn < 0.1$) the Navier-Stokes equations can be used while for larger Knudsen numbers lattice Boltzmann or Direct Simulation Monte Carlo (DSMC) methods must be used to describe the flow through a system. The dynamics of particles interacting with the fluids transporting them in sub-continuum microfluidic systems are similarly *much* more complicated than macroscopic particles (see Sect. 2.1.4). Fortunately, because sub-continuum microfluidic systems are generally very small, they are often too small to be imaged using the visible wavelengths of light that are typically used in PIV. The issue of whether the particles track the flow is no longer important when the particles cannot be seen. Consequently, this chapter will concentrate on continuum microfluidics.

In the continuum microfluidics domain, the aerospace industry is designing and using micron-scale supersonic nozzles to be used as microthrusters on micro- and nano-satellites and for flow control devices for palm-size micro-air vehicles. In the computer industry, inkjet printers, which consist of an array of nozzles with exit orifices on the order of tens of microns in diameter, account for the majority of the computer printer market [86]. In the automotive domain tiny nozzles are needed for the spray generation in engines and in the process engineering and pharmaceutical industries the homogenization of media using membranes or tiny orifices is common practice [28, 50]. The biomedical industry is currently developing and using microfabricated lab-on-chip (LoC) devices for patient diagnosis, patient monitoring, and drug delivery, but also for the trapping, separation and sorting of cells [12, 60, 83]. Examples of microfluidic devices for biomedical research include microscale flow cytometers for cancer cell detection, micromachined electrophoretic channels for DNA fractionation, and polymerase chain reaction (PCR) chambers for DNA amplification [64]. The details of the fluid motion through these small channels, coupled with nonlinear interactions between macromolecules, cells, and the surface-dominated physics of the channels create very complicated phenomena, which can be difficult to simulate numerically. In these cases an experimental approach using PIV is an ideal solution.

10.1.2 Microfluidic Diagnostics

A wide range of diagnostic techniques have been developed for experimental continuum microfluidic research. Experimenters have been particularly interested in non-contact, optical flow measurement diagnostics because they minimally disturb the flow. Some of these techniques have been designed to obtain the highest spatial resolution and velocity resolution possible, while other techniques have been designed for application in non-ideal situations where optical access is limited [59, 63], or in the presence of highly scattering media [14]. Several of the common macroscopic full-field measurement techniques have been extended to microscopic length scales. Examples of these are Scalar Image Velocimetry [23], Molecular Tagging Velocimetry [56], as well as PIV, which at small length scales has become known as micro-PIV or μ PIV. Table 10.1 lists several foundational papers in the area of non-contact, optical microflow diagnostics. This table is not meant to be complete or exhaustive but rather to give the reader a starting point for finding alternatives if μ PIV is not applicable.

Table 10.1 Non-contact High-Resolution Optical Velocimetry Techniques (after [76])

Technique	Author	Flow Tracer	Spatial Resolution (μm^3)	Observation
LDA	Tieu et al. (1995)	—	$5 \times 5 \times 10$	4–8 fringes limits velocity resolution
Optical Doppler tomography	Chen et al. (1997)	1.7 μm polystyrene beads	5×15	Can image through highly scattering media
Optical flow using video microscopy	Hitt et al. (1996)	5 μm blood cells	$20 \times 20 \times 20$	In vivo study of blood flow
Optical flow using X-ray imaging	Lanzilotto et al. (1996)	1–20 μm emulsion droplets	$\sim 20 - 40$	Can image without optical access
Uncaged fluorescent dyes	Paul et al. (1997)	Molecular dye	$100 \times 20 \times 20$	Resolution limited by molecular diffusion
Micro molecular tagging	Mohand et al. (2017)	Acetone vapor	$30 \times 30 \times 30$	Advection of gas phase phosphorescent vapor
Particle streak velocimetry	Brody et al. (1996)	0.9 μm polystyrene beads	~ 10	Particle streak velocimetry

10.2 Typical Implementation of 2D Planar μ PIV

Micro-PIV is a variant of PIV. In common with PIV, μ PIV uses an imaging system to take images of a particle population at a minimum of two time instants. The images of the particle population are divided into interrogation windows and evaluated with statistical methods to extract the mean particle image displacement within each interrogation window. Nearly all of the advanced algorithms discussed earlier in this book are applicable to μ PIV as well. In order to discuss the important differences between the PIV and μ PIV, the most common hardware implementation of μ PIV will be presented.

In μ PIV high spatial resolution is obtained by using flow-tracing particles with very small diameters (d_p about $1\ \mu\text{m}$ or smaller) so that they faithfully follow the flow and flow gradients in microfluidic devices [119], but also to ensure that they do not change a single phase flow into a flow showing multiphase effects. Furthermore, these small particles must be used in order to prevent particle-particle interactions as well as clogging events in tiny geometries. In order to image such small particles microscopes with high numerical aperture, diffraction-limited optics and high enough magnification are needed. Microscope objective lenses that are used commonly in μ PIV range from oil-immersion lenses ($M = 100$, $NA = 1.4$) to air-immersion lenses ($M = 10$, $NA = 0.1$). The light sources frequently used in μ PIV range from standard microscope light sources like Hg-arc lamps and LEDs to pulsed lasers like the Nd:YAG lasers commonly used in PIV. The same cameras commonly used in PIV are also used in μ PIV. One commonality among most μ PIV flow measurements is that optical access to the flow is typically very limited. Unlike PIV where one may have a wind tunnel with an open test section or a closed facility with sufficient glass windows and excellent optical access, optical access in the microscopic world is often limited to a single glass window through which both the illumination must be introduced and the scattered light has to be observed. In the microfluidic world, flows can be driven by pressure or gravity as in the macro world, but can also be driven by a myriad of other forces and devices not typically observed in the macro world, such as electrokinetics, surface tension, and thermal gradients. The typical arrangement and integration of these elements is shown in Fig. 10.1.

The microscopic world presents a unique set of technical challenges that must be overcome in order to perform μ PIV. These are:

- The limited optical access means that most implementations of μ PIV are volume-illuminated, even those that are 2D planar in nature (Sect. 2.4.3). Illumination is typically introduced to the flow through a planar transparent window. The light scattered or emitted by the tracer particles is collected through this same window in what is commonly called a back-scatter configuration (see e.g. Fig. 10.1). Light scattered from the window interfaces as well as from whatever boundary is confining the flow can easily overwhelm the minute scattering from the tracer particles. Consequently, fluorescent particles are typically used as flow tracers and a common microscope element called an epi-fluorescent prism cube is used to eliminate the excitation light from the scattered light (Sect. 2.2.1). Such fluorescent particles are also used in macroscopic PIV experiments performed in liquids but often prove

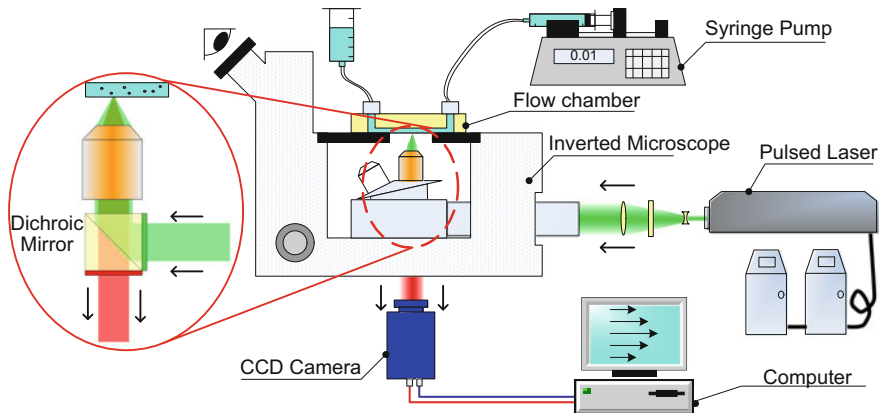


Fig. 10.1 Schematic of a common 2D, planar μ PIV system. A pulsed Nd:YAG laser is used to illuminate fluorescent flow-tracing particles and a CCD camera is used to record the particle images (after CHUANG [17])

prohibitively expensive in macroscopic applications (at least in case of particles with a narrow band size distribution) whereas in microscopic flows the quantity of particles used is minuscule.

- Even when using fluorescence, imaging particles in a volume-illuminated environment presents challenges – and opportunities. In 2D planar μ PIV, the challenge arising from the volume illumination is that all the particles along the optical axis are illuminated and they all scatter or fluoresce light back toward the objective. Since the depth of the flow is typically greater than the depth of field of the objective lens, depending on how far each particle is from the focal plane of the objective lens, it will contribute differently to the correlation function. Particles closer to the focal plane will be imaged brighter with a smaller diameter whereas particles farther from the focal plane will be dimmer and broader. The depth over which particle images contribute significantly to the correlation function has been a topic of considerable research and is called the *depth of correlation* (DOC) (Sect. 10.4.3). Another important challenge caused by the fact that the objective lens usually has a smaller depth of correlation than the flow depth is *particle visibility* (Sect. 10.4.4). The light scattered or fluoresced by out-of-focus particles may be much brighter than the light scattered or fluoresced by the in-focus particles if, for example, the depth of correlation is $2\ \mu\text{m}$ and the depth of the microchannel is $200\ \mu\text{m}$.
- The typically smaller tracer particles and slower flow velocities in microfluidic applications mean that Brownian motion is a phenomenon that cannot be ignored. In the best case it remains an unbiased source of experimental uncertainty. In certain cases, such as those with thermal gradients, it can cause particle migration independent of the flow velocity (Sect. 2.1.4).

The study of these three main differences between PIV and μ PIV is the subject of the next few sections of this chapter.

10.3 2D Planar Micro-PIV Development

Micro-PIV was a natural extension of the trend in PIV towards high spatial resolution. This progression towards ever increasing spatial resolution is illustrated in Table 10.2. Micro-PIV was born in 1998 when SANTIAGO et al. [105] demonstrated the first μ PIV system – a PIV system with a spatial resolution sufficiently large to be able to make measurements in microfluidic systems. Since then the use of the technique has grown at a tremendous rate. Santiago’s μ PIV system was demonstrated on a contrived problem, the Stokes flow around the surface irregularities on a piece of frosted glass. The flow velocity was slow, on the order of hundreds of microns per second – and a spatial resolution of $6.9 \times 6.9 \times 1.5 \mu\text{m}^3$ was reached [105]. The flow was driven by surface tension. The system used an epi-fluorescent microscope and an intensified CCD camera to record the 300 nm-diameter polystyrene flow-tracing particles carried by the water flow. The particles were illuminated using a standard microscope continuous Hg-arc lamp. The continuous Hg-arc lamp is a good choice for flows that can be damaged by high intensity illumination (e.g., flows containing living biological specimens) and where the velocity is sufficiently small that the particle motion can be effectively frozen by the CCD camera’s electronic shutter. One of the key features of an epi-fluorescent microscope is that the particles can be illuminated with short wavelength light (469 nm in this case) which they absorb and

Table 10.2 Historical Progression of 2D Planar μ PIV Techniques Toward Higher Spatial Resolution (after [76])

Technique	Author	Flow Tracer	Spatial Resolution (μm^3)	Observation
PIV	Urushihara et al. (1993)	1 μm oil droplets	$280 \times 280 \times 200$	Turbulent flows
Super-resolution PIV	Keane et al. (1995)	1 μm oil droplets	$50 \times 50 \times 200$	Particle tracking velocimetry
μ PIV	Santiago et al. (1998)	300 nm polystyrene particles	$6.9 \times 6.9 \times 1.5$	Hele-Shaw Flow
μ PIV	Meinhart et al. (1999)	200 nm polystyrene particles	$5.0 \times 1.3 \times 2.8$	Microchannel flow
μ PIV	Westerweel et al. (2004)	500 nm polystyrene particles	$0.5 \times 0.5 \times 2.0$	Silicon microchannel flow
Evanescent Wave PIV	Sadr et al. (2012)	50 nm polystyrene particles	$78 \times 28 \times 0.3$	Fused silica microchannel flow
μ PIV (SPE)	Chuang et al. (2012)	100 nm polystyrene particles	$0.13 \times 0.13 \times 1.2$	PDMS microchannel flow

fluoresce at a longer wavelength (509 nm in this case). With a suitable filter in front of the camera none of the original illumination reaches the camera, only the light fluoresced from the particles. Fluorescent particles are used in many μ PIV systems because of their effectiveness in getting rid of light scattered from the background. The μ PIV system looks very similar to that shown in Fig. 10.1 – if the pulsed laser is replaced with a continuous Hg-arc lamp and the syringe pump is removed.

KOUTSIARIS et al. [57] demonstrated a μ PIV system suitable for slow flows that used 10 μ m glass spheres as tracer particles and a low spatial resolution high-speed video system to record the particle images yielding a spatial resolution of 26.2 μ m. They measured the flow of water inside 236 μ m round glass capillaries and found agreement between the measurements and the analytical solution within the measurement uncertainty.

Subsequent applications of the μ PIV technique moved steadily toward faster flows and higher spatial resolution. In many implementations the continuous Hg-arc lamp was replaced with a pulsed laser such as the two-headed Nd:YAG lasers commonly used in macroscopic PIV (see Sect. 2.3.1). Delivering all the illuminating light in a few nanoseconds can create frozen (i.e. non-streaked) images of all but the fastest microflows (>tens of meters per second). With pulsed lasers cross-correlation analysis of singly-exposed image pairs acquired with sub-microsecond time steps between images can be performed. At macroscopic length scales this short time step would allow analysis of supersonic flows. However, because of the high magnification, the maximum velocity measurable with this time between images in the microfluidics world is reduced. MEINHART et al. [75] applied μ PIV to measure the flow field in a 30 μ m \times 300 μ m (height \times width) rectangular channel, with a flow rate of 50 μ l/h, equivalent to a centerline velocity of 10 mm/s. The experimental apparatus, shown in Fig. 10.1, images the flow with a 60 \times , $NA = 1.4$, oil-immersion lens. The 200 nm-diameter polystyrene flow-tracing particles were chosen small enough so that they faithfully followed the flow and were 150 times smaller than the smallest channel dimension. A subsequent investigation by MEINHART & ZHANG [77] of the flow inside a microfabricated inkjet printer head yielded very high speed liquid microfluidics measurements made with μ PIV. Using a slightly lower magnification (40 \times) and consequently lower spatial resolution, measurements of velocities as high as 8 m/s were made.

ZETTNER & YODA [127] were the first to report the use of an evanescent field to illuminate flow tracing particles in a microchannel near the wall. An evanescent field is the light that leaks through an interface when a light source propagating through a high-refractive-index material is totally internally reflected by a low-refractive-index medium. The evanescent field decays exponentially with distance from the interface and is typically on the order of hundreds of nanometers thick. The evanescent wave will illuminate only those particles within it, hence very near the wall. The depth of correlation issue is radically transformed because the objective lens will typically have a depth of field much greater than the evanescent wave thickness. However, the depth of correlation problem is not eliminated because the varying intensity of the evanescent wave causes particles at different distances from boundary to contribute to the correlation differently. Typical implementations of evanescent wave illumination

have required relatively large in-plane interrogation regions because of the relatively small number of particles in the immediate vicinity of the wall and the high fraction of unpaired particle images. ZETNER & YODA [127] reported spatial resolution of $40 \times 40 \times 0.38 \mu\text{m}$. Later SADR et al. [104] reported a spatial resolution of $154 \times 24 \times 0.2 \mu\text{m}$. One of the key virtues of evanescent wave PIV is minimizing the out of plane spatial resolution. Evanescent wave PIV is discussed in much more detail in Sect. 16.5.

CHUANG et al. [16] used for the evaluation single pixel ensemble correlation methods to increase the in-plane spatial resolution [44, 45]. This algorithm reorganizes how the spatial cross-correlation is calculated [15, 46, 120] and is discussed in Sect. 5.3.2.5. The out-of-plane spatial resolution is governed by the depth of correlation (Sect. 10.4.3), as it is with other volume-illuminated μPIV implementations. They used theory and Monte Carlo simulations to show that the ultimate in-plane spatial resolution of a particle-based pixelated camera with pixel sizes around $6 \mu\text{m}$ is approximately 65 nm and can be attained with particles 60 nm or smaller. They further conducted experiments in a PDMS channel using a $100\times$, $NA = 1.4$ objective. The 60 nm particles were not visible in against the background noise so the experiments were conducted using 100 nm particles. The best possible in-plane spatial resolution with these experimental parameters was approximately 130 nm . With a more sensitive camera or one with smaller pixel (such as a CMOS camera), this in-plane spatial resolution might even be reduced further. However, it must be stated that these values do not take the lowering of the resolution due to the particle image displacement into account. For more details see Chap. 6.

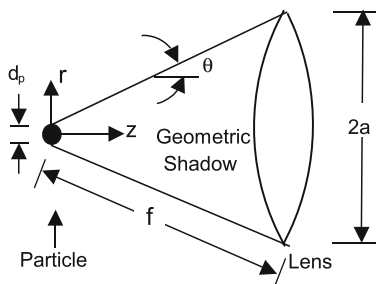
10.4 Imaging of Volume-Illuminated Small Particles in μPIV

Three fundamental problems differentiate the imaging configuration in μPIV from conventional macroscopic PIV: The particles are not considerably larger than the wavelength of the illuminating light; the illumination source is typically not a light sheet but rather an illuminated volume of the flow; and the particles are typically imaged against a background of similar particles that are out-of-focus. Addressing these three issues requires in-depth study of how the particles are imaged.

10.4.1 *Three-Dimensional Diffraction Pattern*

Following BORN & WOLF [7], the intensity distribution of the three-dimensional diffraction pattern of a point source imaged through a circular aperture of radius a can be written in terms of the dimensionless diffraction variables (u, v):

Fig. 10.2 Geometry of a particle with a diameter d_p , being imaged through a circular aperture of radius a , by a lens of focal length f (after [74])



$$I(u, v) = \left(\frac{2}{u}\right)^2 [U_1^2(u, v) + U_2^2(u, v)] I_0 \tag{10.1}$$

$$I(u, v) = \left(\frac{2}{n}\right)^2 \left\{ 1 + V_0^2(u, v) + V_1^2(u, v) - 2V_0(u, v) \cos \left[\frac{1}{2} \left(u + \frac{v^2}{u} \right) \right] - 2V_1(u, v) \sin \left[\frac{1}{2} \left(u + \frac{v^2}{u} \right) \right] \right\} I_0 \tag{10.2}$$

where $U_n(u, v)$ and $V_n(u, v)$ are called *Lommel functions*, which may be expressed as an infinite series of Bessel functions of the first kind:

$$U_n(u, v) = \sum_{s=0}^{\infty} (-1)^s \left(\frac{u}{v}\right)^{n+2s} J_{n+2s}(v) \tag{10.3}$$

$$V_n(u, v) = \sum_{s=0}^{\infty} (-1)^s \left(\frac{v}{u}\right)^{n+2s} J_{n+2s}(v).$$

The dimensionless diffraction variables are defined as:

$$u = 2\pi \frac{z}{\lambda} \left(\frac{a}{f}\right)^2 \tag{10.4}$$

$$v = 2\pi \frac{r}{\lambda} \left(\frac{a}{f}\right)$$

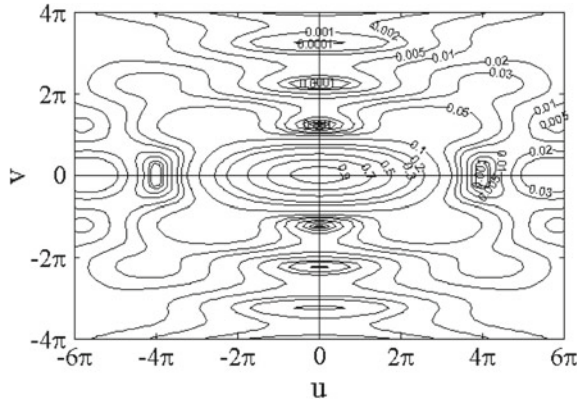
where f is the radius of the spherical wave as it approaches the aperture (which can be approximated as the focal length of the lens), λ is the wavelength of light, and r and Z are the in-plane radius and the out-of-plane coordinate, respectively, with the origin located at the point source (Fig. 10.2).

Although both, Eqs. (10.1) and (10.2) are valid in the region near the point of focus, it is computationally convenient to use Eq. (10.1) outside the geometric shadow, where $|u/v| < 1$, and to use Eq. (10.2) inside the geometric shadow, where $|u/v| > 1$ [7].

Within the focal plane, the intensity distribution reduces to the expected result

$$I(0, v) = \left[\frac{2J_1(v)}{v} \right]^2 I_0 \tag{10.5}$$

Fig. 10.3 Three-dimensional intensity distribution pattern expressed in diffraction units (u, v), following BORN & WOLF [7]. The focal point is located at the origin, the optical axis is located along $v = 0$, and the focal plane is located along $u = 0$ (after [7])



which is the Airy function for Fraunhofer diffraction through a circular aperture. Along the optical axis, the intensity distribution reduces to

$$I(u, 0) = \left[\frac{\sin u/4}{u/4} \right]^2 I_0. \tag{10.6}$$

The three-dimensional intensity distribution calculated from Eqs. (10.1) and (10.2) is shown in Fig. 10.3. The focal point is located at the origin, the optical axis is located at $v = 0$, and the focal plane is located at $u = 0$. The maximum intensity, I_0 , occurs at the focal point. Along the optical axis, the intensity distribution reduces to zero at $u = \pm 4\pi, \pm 8\pi$, while a local maximum occurs at $u = \pm 6\pi$.

10.4.2 Depth of Field

The depth of field of a standard microscope objective lens is given by INOUÉ & SPRING [41] as:

$$\delta_z = \frac{n\lambda_0}{NA^2} + \frac{ne}{NA \cdot M} \tag{10.7}$$

where n is the refractive index of the fluid between the microfluidic device and the objective lens, λ_0 is the wavelength of light in vacuum being imaged by the optical system, NA is the numerical aperture of the objective lens, M is the total magnification of the system, and e is the smallest distance that can be resolved by a detector located in the image plane of the microscope (for the case of a CCD sensor, e is the spacing between pixel). Equation (10.7) is the summation of the depths of field resulting from diffraction (first term on the right-hand side) and geometric effects (second term on the right-hand side).

The cutoff for the depth of field due to diffraction (first term on the right-hand side of Eq. (10.7) is chosen by convention to be one-quarter of the out-of-plane distance between the first two minima in the three-dimensional point spread function, that is, $u = \pm\pi$ in Fig. 10.3 and Eq. (10.1). Substituting $NA = n \sin \theta = n \cdot a/f$, and $\lambda_0 = n\lambda$ yields the first term on the right-hand side of Eq. (10.7).

If a CCD sensor is used to record particle images, the geometric term in Eq. (10.7) can be derived by projecting the CCD array into the flow field, and then, considering the out-of-plane distance, the CCD sensor can be moved before the geometric shadow of the point source occupies more than a single pixel. This derivation is valid for small light collection angles, where $\tan \theta \sim \sin \theta = NA/n$.

10.4.3 Depth of Correlation

The depth of correlation is defined as twice the distance that a particle can be positioned from the object plane so that the intensity along the optical axis is an arbitrarily specified fraction of its focused intensity, denoted by ε . Beyond this distance, the particle's intensity is sufficiently low that it will not influence the velocity measurement.

While the depth of correlation is related to the depth of field of the optical system, it is important to distinguish between them. The depth of field is defined as twice the distance from the object plane in which the object is considered unfocused in terms of image quality. In the case of volume-illuminated μ PIV, the depth of field does not define precisely the thickness of the measurement plane. The theoretical contribution of an unfocused particle to the correlation function is estimated by considering (1) the effect due to diffraction, (2) the effect due to geometric optics, and (3) the finite size of the particle. For the current discussion, the cutoff for the on-axis image intensity, ε , is assumed to be arbitrarily one-tenth of the in-focus intensity. The reason for this choice is that the correlation function varies like the intensity squared so a particle image with one-tenth the intensity of a focused image can be expected to contribute less than 1% to the correlation function.

The effect of diffraction can be evaluated by considering the intensity of the point spread function along the optical axis in Eq. (10.6). If $\varepsilon = 0.1$, then the intensity cutoff will occur at $u \approx \pm 3\pi$. Using Eq. (10.4), substituting $\delta_Z = 2Z$, and using the definition of numerical aperture, $NA \equiv n \sin \theta = n \cdot a/f$, one can estimate the depth of correlation due to *diffraction* as:

$$\delta_{Z_{\text{diff}}} = \frac{3n\lambda_0}{NA^2}. \quad (10.8)$$

The effect of geometric optics upon the depth of correlation can be estimated by considering the distance from the object plane in which the intensity along the optical axis of a particle with a diameter, d_p , decreases an amount, $\varepsilon = 0.1$, due to the spread in the geometric shadow, that is, the lens' collection cone. If the light

flux within the geometric shadow remains constant, the intensity along the optical axis will vary as $\sim z^{-2}$. From Fig. 10.3, if the geometric particle image is sufficiently resolved by the CCD array, the depth of correlation due to *geometric* optics can be written for an arbitrary value of ε as:

$$\delta_{Z_{\text{geo}}} = \frac{(1 - \sqrt{\varepsilon})d_p}{\sqrt{\varepsilon} \tan \theta} \text{ for } d_p > \frac{e}{M} \quad (10.9)$$

Following the analysis of OLSEN & ADRIAN [87, 88] and using Eq. (2.28), the effective image diameter of a particle displaced a distance Z from the objective plane can be approximated by combining the effective image diameter d_r with a geometric approximation to account for the particle image spreading due to displacement from the focal plane to yield

$$d_r = \left\{ M^2 d_p^2 + 1.49 (M + 1)^2 \lambda^2 \left[\left(\frac{n}{NA} \right)^2 - 1 \right] + \left[\frac{M D_a Z}{Z_0 + Z} \right]^2 \right\}^{\frac{1}{2}} \quad (10.10)$$

where Z_0 is the object distance and D_a is the diameter of the recording lens aperture.

The relative contribution ε of a particle displaced a distance Z from the focal plane, compared to a similar particle located at the focal plane can be expressed in terms of the ratio of the effective particle image diameters raised to the fourth power

$$\varepsilon = \left[\frac{d_r(0)}{d_r(Z_{\text{corr}})} \right]^4. \quad (10.11)$$

Approximating $D_a^2/(Z_0 + Z)^2 \approx D_a^2/Z_0^2 = 4[(n/NA)^2 - 1]^{-1}$, combining Equations (10.10) and (10.11), and solving for Z_{corr} yields an expression for the depth of correlation (DOC)

$$\delta_{Z_{\text{corr}}} = 2Z_{\text{corr}} = 2 \left\{ \left(\frac{1 - \sqrt{\varepsilon}}{\sqrt{\varepsilon}} \right) \left[\frac{d_p^2 [(n/NA)^2 - 1]}{4} + \frac{1.49(M+1)^2 \lambda^2 [(n/NA)^2 - 1]^2}{4M^2} \right] \right\}^{\frac{1}{2}}. \quad (10.12)$$

From Eq. (10.12) it is evident that the depth of correlation Z_{corr} is strongly dependent on numerical aperture NA and particle size d_p and is weakly dependent upon magnification M . Table 10.3 gives the thickness of the measurement plane, $2Z_{\text{corr}}$, for various microscope objective lenses and particle sizes. The highest out of plane resolution for these parameters is $2Z_{\text{corr}} = 0.36 \mu\text{m}$ for a $NA = 1.4$, $M = 60$ oil-immersion lens and particle sizes $d_p < 0.1 \mu\text{m}$. For these calculations, it is important to note that the effective numerical aperture of an oil-immersion lens is reduced according to Eq. (2.31) when imaging particles suspended in fluids such as water, where the refractive index is less than that of the immersion oil.

Table 10.3 Thickness of the measurement plane for typical experimental parameters, $2Z_{\text{corr}}$ [μm] [118]

M	60	40	40	20	10
NA	1.40	0.75	0.60	0.50	0.25
n	1.515	1.00	1.00	1.00	1.00
d_p [μm]	Meas. plane thickness $2Z_{\text{corr}}$ [μm]				
0.01	0.36	1.6	3.7	6.5	34
0.10	0.38	1.6	3.8	6.5	34
0.20	0.43	1.7	3.8	6.5	34
0.30	0.52	1.8	3.9	6.6	34
0.50	0.72	2.1	4.2	7.0	34
0.70	0.94	2.5	4.7	7.4	35
1.00	1.3	3.1	5.5	8.3	36
3.00	3.7	8.1	13	17	49

OLSEN & ADRIAN [88] used a small angle approximation to derive the depth of correlation $\delta_{Z_{\text{corr}}}$ as

$$\delta_{Z_{\text{corr}}} = 2 Z_{\text{corr}} = 2 \left\{ \left(\frac{1 - \sqrt{\varepsilon}}{\sqrt{\varepsilon}} \right) \left[f^{\#2} d_p^2 + \frac{5.95 (M + 1)^2 \lambda^2 f^{\#4}}{M^2} \right] \right\}^{\frac{1}{2}}, \quad (10.13)$$

where all the variables are as given above. Because it is given in terms of $f^{\#}$ instead of NA , it is only applicable for air-immersion lenses and not oil- or water-immersion lenses. This model for the depth of correlation has been indirectly experimentally confirmed for low magnification ($M \leq 20\times$) and low numerical aperture ($NA \leq 0.4$) air-immersion lenses. Particle images obtained from observing a $2\ \mu\text{m}$ particle with $M = 20\times$ and $M = 63\times$ lenses, at different distances from the focal plane, are shown in Fig. 10.4. The corresponding theoretical diameters represented by a white circle, are superimposed on each image. From a qualitative observation of the images, the theoretical diameters match the border of the particle images at $M = 20\times$ but fail for images at $M = 63\times$. It can be observed in Fig. 10.5 that for $M = 20\times$ the measured diameters follow the theoretical prediction nicely for all out-of-plane positions measured, while in the case of $M = 63\times$ the diameters grow much more slowly than expected. For a detailed discussion see [103]. It is evident from the results in Figs. 10.4 and 10.5 that at large magnification the measurement resolution in depth direction is lower than predicted by Eq. (10.13) because the intensity drop of the particle image with Z is weaker. To enhance the spatial resolution in depth direction image preprocessing can be applied as outlined in [103].

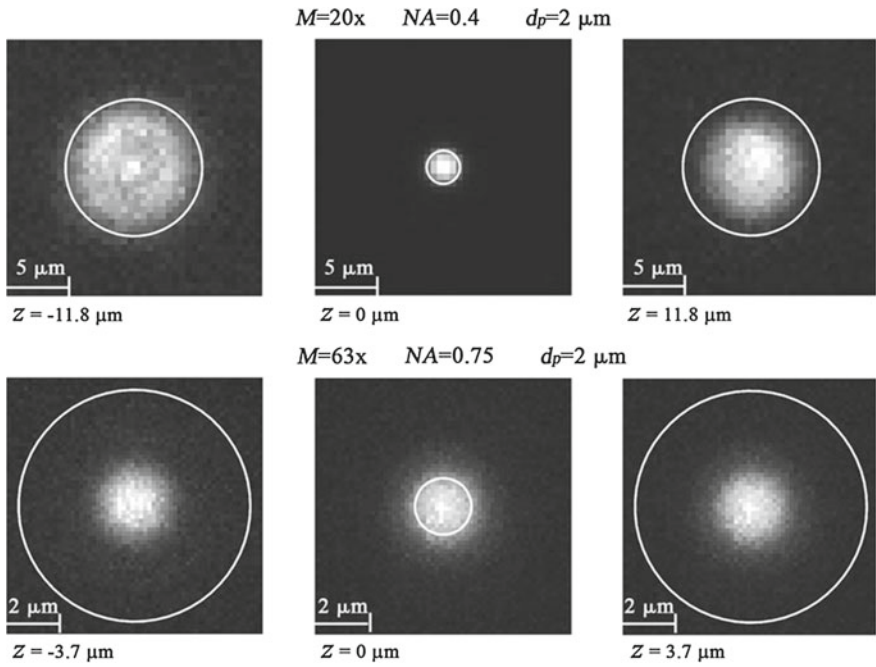


Fig. 10.4 Particle images obtained observing a $2\ \mu\text{m}$ particle with $M = 20\times$ and $M = 63\times$ lenses, at different distances from the focal plane. The corresponding theoretical diameters for each image are represented with a superimposed white circle (from [103])

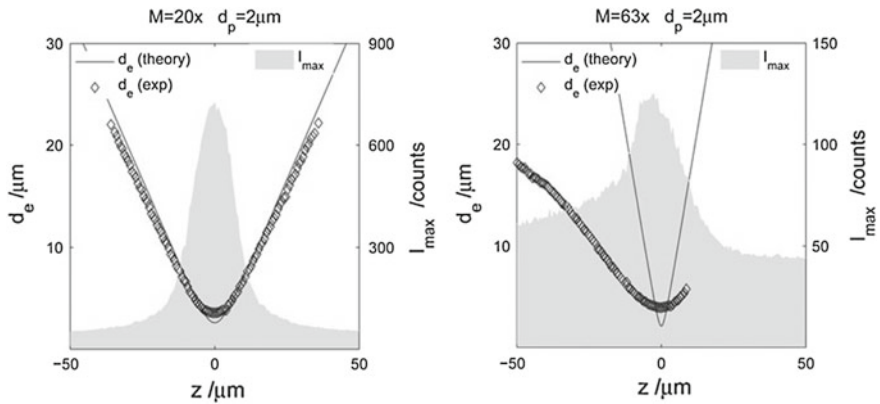


Fig. 10.5 Particle image diameters (left y-axis) and maximum particle image intensity (right y-axis) as a function of the distance Z from the focal plane ($Z = 0$), for a $2\ \mu\text{m}$ particle observed with $M = 20\times$ and $M = 63\times$ lenses (from [103])

10.4.4 Particle Visibility

One important implication of volume illumination that affects both large and small depth of focus imaging systems is that all particles in the illuminated volume will contribute to the recorded image. This implies that the particle concentrations will have to be optimized for deep flows such that the particle concentration is low enough so that the in-focus particles can be imaged against the background of out-of-focus particles yet high enough that in-plane spatial resolution is not sacrificed more than necessary.

The quality of μ PIV velocity measurements strongly depends upon the quality of the recorded particle images from which those data are calculated. Experiments using μ PIV must be designed so that focused particle images can be observed even in the presence of background light from unfocused particles and test section surfaces. The background light scattered from test section surfaces can be removed by using fluorescence techniques to filter out elastically scattered light (at the same wavelength as the illumination) while leaving the fluoresced light (at a longer wavelength) virtually unattenuated [105].

Background light fluoresced from unfocused tracer particles is not so easily removed because it occurs at the same wavelength as the signal, i.e. the focused particle images, but it can be lowered to acceptable levels by choosing proper experimental parameters. OLSEN & ADRIAN [88] present a theory to estimate particle visibility, defined as the ratio of the intensity of a focused particle image to the average intensity of the background light produced by the unfocused particles. The analysis in this section refers to the dimensions labeled on Figs. 2.51 and 2.62.

Assuming light is emitted uniformly from the particle, the light from a single particle reaching the image plane can be written as

$$J(Z) = \frac{J_p D_a^2}{16 (Z_0 + Z)^2} \quad (10.14)$$

where J_p is total light flux emitted by a single particle. We approximate the intensity of a focused particle image as Gaussian,

$$I(r) = I_0 \exp\left(\frac{-4\beta^2 r^2}{d_\tau^2}\right) \quad (10.15)$$

where the unspecified parameter β is chosen to determine the cutoff level that defines the edge of the particle image. Approximating the Airy distribution by a Gaussian distribution, with the area of the two axisymmetric functions being equal, the first zero in the Airy distribution corresponds to [2]

$$\frac{I}{I_0} = \exp(-\beta^2) \approx \exp(-3.67). \quad (10.16)$$

Integrating Eq.(10.15) over an entire particle image and equating that result to Eq.(10.14) allows I_0 to be evaluated and Eq.(10.15) to be written as

$$I(r, Z) = \frac{J_p D_a^2 \beta^2}{4\pi d_\tau^2 (Z_0 + Z)^2} \exp \frac{-4\beta^2 r^2}{d_\tau^2}. \quad (10.17)$$

Making the simplifying assumption that particles located outside a distance $|Z| > \delta/2$ from the object plane as being completely unfocused and contributing uniformly to background intensity, while particles located within a distance $|Z| < \delta/2$ as being completely focused, the total flux of background light J_B can be approximated by

$$J_B = A_v C \left\{ \int_{-a}^{-\frac{\delta}{2}} J(z) dz + \int_{\frac{\delta}{2}}^{L-a} J(z) dz \right\}, \quad (10.18)$$

where C is the number of particles per unit volume of fluid, L is the depth of the device, and A_v is the average cross sectional area contained within the field of view. Combining Eqs.(10.14) and (10.18), correcting for the effect of magnification, and assuming $Z_0 \gg \delta/2$, the intensity of the background glow can be expressed as [88]

$$I_B = \frac{C J_p L D_a^2}{16M^2 (Z_0 - a) (Z_0 - a + L)}. \quad (10.19)$$

Following OLSEN & ADRIAN [88], the *visibility* V of a focused particle can be obtained by combining Eqs.(10.10) and (10.17), dividing by Eq.(10.19), and setting $r = 0$ and $Z = 0$,

$$V = \frac{I(0, 0)}{I_B} = \frac{4M^2 \beta^2 (Z_0 - a) (Z_0 - a + L)}{\pi C L Z_0^2 \left\{ M^2 d_p^2 + 1.49 (M + 1)^2 \lambda^2 \left[\left(\frac{n}{NA} \right)^2 - 1 \right] \right\}}. \quad (10.20)$$

From this expression it is clear that for a given recording optics configuration, particle visibility V can be increased by decreasing the particle concentration C or by decreasing the test section thickness L . For a fixed particle concentration, the visibility can be increased by decreasing the particle diameter d_p or by increasing the numerical aperture NA of the recording lens. Visibility depends only weakly on magnification and object distance Z_0 .

An expression for the volume fraction V_{fr} of particles in solution that produce a specific particle visibility can be obtained by rearranging Eq.(10.20) and multiplying by the volume occupied by a spherical particle to get

$$V_{fr} = \frac{2d_p^3 M^2 \beta^2 (Z_0 - a) (Z_0 - a + L)}{3V L Z_0^2 \left\{ M^2 d_p^2 + 1.49 (M + 1)^2 \lambda^2 \left[\left(\frac{n}{NA} \right)^2 - 1 \right] \right\}}. \quad (10.21)$$

Table 10.4 Maximum volume fraction of particles V_{fr} , expressed in percent, necessary to maintain a visibility V greater than 1.5 when imaging the center of an $L = 100 \mu\text{m}$ deep device [119]

M	60	40	40	20	10
NA	1.40	0.75	0.60	0.50	0.25
n	1.515	1.00	1.00	1.00	1.00
Z_0 [mm]	0.38	0.89	3	7	10.5
d_p [μm]	Volume Fraction (%)				
0.01	2.0E-5	4.3E-6	1.9E-6	1.1E-6	1.9E-7
0.10	1.7E-2	4.2E-3	1.9E-3	1.1E-3	1.9E-4
0.20	1.1E-1	3.1E-2	1.4E-2	8.2E-3	1.5E-3
0.30	2.5E-1	9.3E-2	4.6E-2	2.7E-2	5.1E-3
0.50	6.0E-1	3.2E-1	1.8E-1	1.1E-1	2.3E-2
0.70	9.6E-1	6.4E-1	4.1E-1	2.8E-1	6.2E-2
1.00	1.5E+0	1.2E+0	8.7E-1	6.4E-1	1.7E-1
3.00	4.8E+0	4.7E+0	4.5E+0	4.2E+0	2.5E+0

Reasonably high quality velocity measurements require visibilities in excess of 1.5. Although this is an arbitrary threshold, it works well in practice. To see this formula in practice, assume that we are interested in measuring the flow at the centerline ($a = L/2$) of a microfluidic device with a characteristic depth of $L = 100 \mu\text{m}$. Table 10.4 shows for various experimental parameters the maximum volume fraction of particles that can be seeded into the fluid while maintaining a focused particle visibility greater than 1.5. Here, the object distance Z_0 is estimated by adding the working distance of the lens to the designed coverslip thickness.

MEINHART et al. [74] verified these trends with a series of imaging experiments using known particle concentrations and flow depths. The particle visibility V was estimated from a series of particle images taken of four different particle concentrations and four different device depths. A particle solution was prepared by diluting $d_p = 200 \text{ nm}$ diameter polystyrene particles in de-ionized water. Test sections were formed using two feeler gauges of known thickness sandwiched between a glass microscope slide and a coverslip. The images were recorded with an oil-immersion $M = 60\times$, $NA = 1.4$ objective lens. The remainder of the μ PIV system was as described above.

The measured visibility is shown in Table 10.5. As expected, the results indicate that, for a given particle concentration, a higher visibility is obtained by imaging a flow in a thinner device. This occurs because decreasing the thickness of the test section decreases the number of unfocused particles, while the number of focused particles remains constant. Also, increasing the particle concentration decreases the visibility, as expected. In general, thinner test sections allow higher particle concentrations to be used, which can be analyzed using smaller interrogation regions. Consequently, the seeding particle concentration must be chosen judiciously so that

Table 10.5 Experimental assessment of particle visibility as a function of depth and particle concentration [75]

Depth [μm]	Particle Concentration (by Volume)			
	0.01%	0.02%	0.04%	0.08%
25	2.2	2.1	2.0	1.9
50	1.9	1.7	1.4	1.2
125	1.5	1.4	1.2	1.1
170	1.3	1.2	1.1	1.0

the desired spatial resolution can be obtained, while maintaining adequate image quality (i.e. particle visibility Sect. 2.1.4).

10.5 3D Micro-PIV

10.5.1 Overview

While in many cases 2D planar velocity data is sufficient in μPIV experiments, there are many complicated flow situations in which knowledge of the full 3-dimensional and 3-component velocity field is required. In the recent years, more and more complex microfluidic devices such as micro-mixers, micro-bioreactors and micro-heat exchangers, among others, have been designed for life science and process engineering applications [125]. Although the Reynolds numbers for microfluidic devices are often fairly low and the state of the flow is mostly laminar, the flow can be quite complex. Difficulties arise due to complex fluid properties and flow geometries, surface phenomena such as electrokinetic or electrophoretic forces, electric or magnetic field gradients, fluid-structure interaction, etc. A comprehensive review about the manifold of physical effects on these small scales can be found in SQUIRES & QUAKE [111] and the references herein. However, for a proper and effective design of microfluidic devices or the validation of numerical flow simulations, the reliable experimental characterization of three-dimensional flows is often an important issue in microfluidics.

In the last years, different particle based imaging methods, such as confocal scanning microscopy, stereoscopic and tomographic imaging or approaches based on defocused particle images or optical aberrations have been developed and applied successfully to measure complex 3D velocity fields in microfluidic systems. The benefits and drawbacks of the most common techniques will be discussed in the following as the proper understanding of the measurement principle is essential to select the most appropriate technique for a desired measurement application. Beside the advantage of these techniques to determine volumetric flow field data they are also able to solve the depth-of-correlation problem.

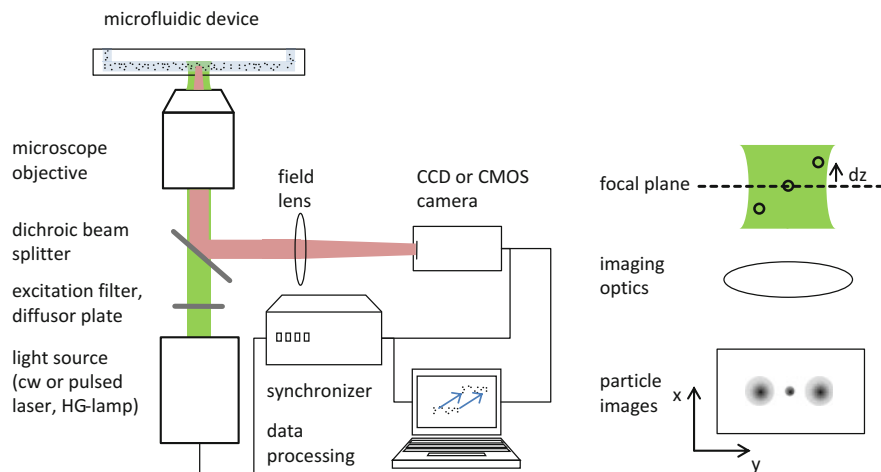


Fig. 10.6 Schematic of a typical μ PIV system (left) and principle schematic of the imaging with reversed colors (right), (from [18])

In the previous section it was outlined that in case of standard μ PIV, the transparent flow of interest is usually seeded with fluorescent tracer particles and imaged by high quality microscope objective lenses. The whole microfluidic channel is then illuminated by a laser, or another bright light source (continuous or pulsed) such as high power LEDs [32]. To homogenize the beam profile, a diffusor plate is often used. If a white light source is deployed, a filter cube is applied to only let short wavelength (green) light through. This short wavelength light is then absorbed by the tracer particles' fluorescent dye and a distribution of longer wavelength, red light is emitted. A filter is used to only let the emitted red light pass onto the camera. The major benefit of the fluorescence is that reflections from the channel walls can be removed from the images at the cost of weaker fluorescence signals. The particle images are then recorded by a digital CCD (Charge Coupled Device), CMOS (Complementary Metal Oxide Semiconductor) or intensified camera. The synchronization of the whole system is assured by the synchronizing electronics. Applying a proper calibration from image space to the real physical coordinates, the recorded images can be used to estimate the velocity of the fluid indirectly by measuring the displacement of the tracer particles, using correlation or particle tracking algorithms. One major limitation of this working principle arises from the fact that in contrast to standard PIV, where the measurement plane is defined by a laser light sheet, the measurement plane in μ PIV is determined by the depth of focus of the optical system, which can reach several micrometers as discussed in the previous section and according to [8, 55, 88, 102]. In effect, out-of-focus particles, as shown on the right side of Fig. 10.6, contribute to the cross correlation and bias the measurements in case of out-of-plane gradients due to the depth of correlation [102].

As can be seen from Eq. (10.12) and Fig. 10.4, increasing the numerical aperture NA decreases the depth of correlation (DOC). A high numerical aperture lens also resolves more details of the particle image. However, with increasing numerical aperture, the magnification usually increases as well, which is not always beneficial for the resolution in PIV [44]. In addition the field of view will be further limited and thus the dynamic spatial range decreases [1]. On the other hand, smaller particles can decrease the DOC as well according to Eq. (10.12). Unfortunately smaller particles will result in lower signal to noise ratios (SNR) thus reducing the accuracy of the method. Image preprocessing may help to enhance the spatial resolution to a certain extent [103]. However, in standard μ PIV, the velocity estimate will always be biased by the DOC and the experimenter should know the depth of correlation to determine the spatial resolution in depth direction and the introduced error due to spatial averaging according to Eq. (10.12) [88].

To overcome these limitations and to extend the velocity reconstruction to the third component is the main motivation of using 3D velocity measurement techniques in microfluidics. Recent reviews about advanced methods, including some 3D techniques and proper experimental design can be found by LEE & KIM [62], WILLIAMS et al. [122] and CIERPKA & KÄHLER [18]. The following discussion is based on the last reference.

10.5.2 *Epi-Fluorescence Scanning Microscopy*

The standard μ PIV system is able to measure the 2D2C velocity field in a microfluidic device. In principle it is possible to obtain the 3D3C information from a representation of 2C2D slices if the flow is steady. Applying the incompressible continuity equation with non slip boundary conditions at the wall ($U, V, W = 0$) the third component can be calculated by integrating $\partial U_i / \partial X_i = 0$ [10, 11]. Due to the volume illumination used for μ PIV, particles with large out-of-plane motion will remain in the images for successive illuminations. The resulting measured velocity vector will therefore be a projection of the true motion of the particles, hence decreasing the accuracy. The reconstruction of the 3D3C velocity field by scanning measurements in microflows was applied by several authors. ANGELE et al. [4] used a rotating disk with glass plates of different thickness to quickly vary the optical path, and thus the depth-wise position of the focal plane. They were able to reach a scanning speed of 100 fps in the vertical direction with their system. The dual-plane PIV concept is able to measure the third velocity component [96]. In combination with scanning μ PIV measurements, it was applied by SHINOHARA et al. [109] using a piezo actuator to move the microscope objective lens while recording, thus allowing for the reconstruction of the velocity in the whole volume. Unfortunately, the flow under investigation was unidirectional and the system was not tested in real 3D flow. BOWN et al. [9] used scanning in the depth direction to evaluate the flow in a ribbed channel geometry. The authors used the velocity data to later fit parabolic profiles and thus determine the position of the channel wall with an accuracy of $0.2 \mu\text{m}$ in the depth direction. ROSSI et al. [101]

used eight planes, each $2\ \mu\text{m}$ apart, for measurements in a micro channel with living cells on the wall. By the use of the velocity profiles in the direction of observation, the authors were able to extract the mean shear stress and the average surface topology of cells exposed to different shear strengths.

10.6 Multi Camera Approaches

10.6.1 (Scanning) Stereoscopic Imaging

Another way to obtain out-of-plane velocity is the observation from two different perspectives, see Sect. 8.1. For microscopic applications, a description of the optical setups used can be found in LEE & KIM [62]. Two different types of stereoscopic microscopes exist and are schematically shown in Fig. 10.7.

The Greenough type features two separated optics for each viewing direction and thus has a high numerical aperture and high optical resolution. However, large perspective distortions are the drawback (see Sect. 6.1). The more widely used systems for microfluidic investigations apply standard stereo microscopes and are of the common main objective (CMO) design. The benefit of these systems compared to use two different optics for each camera, is the large overlapping in-focus region for the two views. However, since the light beams are not passing through the center of the large objective lens, they are asymmetrically distorted. Nevertheless, a recent comparison of both systems for velocity field measurements showed lower uncertainties using a

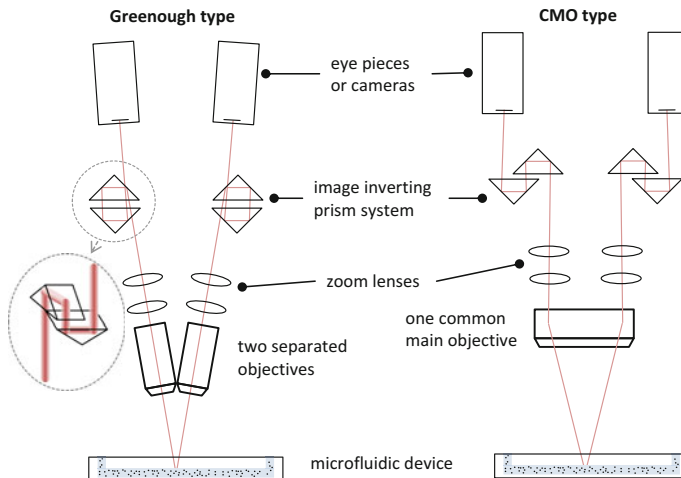


Fig. 10.7 Schematic of stereoscopic microscopes. Greenough type with two separated objectives (left) and the common main objective type (right), (from [18])

CMO system [126]. The CMO design is especially adopted for human sight and thus uses a large diameter objective lens, through which both the left and right channels view the object at small angles between both views. The optical axis of the objective is normal to the object plane, therefore there is no inherent tilt of the image at the camera sensor plane. Due to the large and costly objective lens, systems are often limited in magnification to around $20\times$. The left and right images are viewed by separated CCD cameras. Both cameras record the illuminated particles and the in-plane velocity vectors can be estimated using PIV or PTV algorithms. Since the angle of observation is known by a 3D calibration procedure, the out-of-plane velocity can be calculated in the overlapping region of both views by using the stereoscopic Equations (8.3)–(8.6). However, in a real system, the calibration is a complex procedure and suffers from distortions and aberrations induced by imperfections of the lens or by refraction between different media (e.g., glass and water of the microchannel). Especially, the small angle between the different views, typically $5 - 7^\circ$, is far from being optimal ($\geq 30^\circ$, [61]) and introduces errors in the estimation of the out-of-plane component (see Sect. 6.1). Another main problem for stereoscopic μ PIV arises from the complex calibration procedure required. Imperfections in the lens system and slight misalignment result in the misalignment of the focal planes inside the measurement volume [21]. Since the third component is reconstructed using the in-plane results with the assumption of the same focal plane, the errors for the out-of-plane velocity increase strongly, especially in regions of strong gradients. An additional inherent problem is the large depth of field for the CMO lenses and thus the large depth of correlation. It is therefore nearly impossible to get unbiased data with a stereoscopic CMO setup.

10.6.2 Tomographic Imaging

A real volumetric method is the tomographic PIV or PTV as outlined in Chap. 9. For the velocity estimation, the volume distribution of the particles is reconstructed from the images, recorded from different viewing directions. The velocity field is then calculated by either a volumetric cross-correlation or a volumetric tracking algorithm as opposed to stereoscopic approaches, where the third component is reconstructed by the in-plane velocity. Normally, four different views are required for a reconstruction with sufficient quality for most applications [25]. The reconstruction of the volumetric intensity field is a mathematically ill-posed problem and iterative algorithms have to be used (see Sect. 9.2). However, a major difficulty for the tomographic reconstruction is the appearance of so called ghost particles arising from the mathematically ill-posed problem as illustrated in Fig. 10.8. The number of ghost particles increases with the number of real particles and thus limits the seeding concentration to 0.05 particles per pixel, which is about one order of magnitude lower than for 2D PIV. Since a certain amount of particles is required in an interrogation volume, also the dynamic spatial range (DSR) of scale, defined as mean value of the ratio between the length of the whole volume and the corresponding length of an interrogation volume

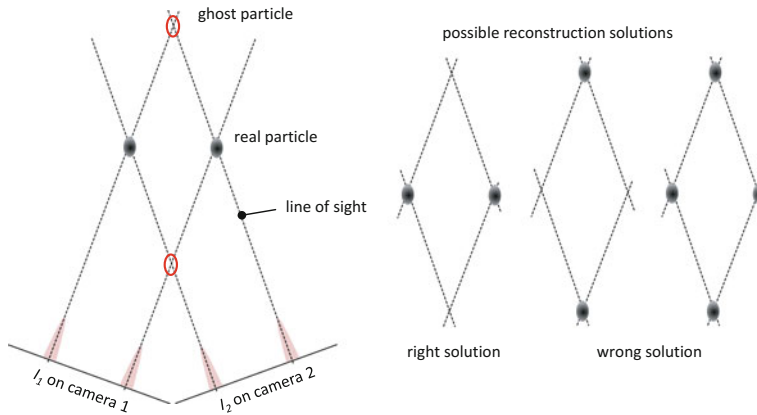


Fig. 10.8 Schematic of the tomographic imaging and the appearance of ghost particles (left) and possible solutions of the reconstruction out of the two camera images (right), (from [18])

is often low, see Chap. 6. Therefore PTV evaluation techniques are often better suited for the data analysis compared to PIV evaluation methods [18, 19, 44, 45]. The ghost particles are usually of lower intensity but will contribute to the velocity estimate. If ghost particles occur from the same set of particles in both frames, their displacement corresponds to the averaged displacement of the actual particles causing them [26]. Therefore ghost particles will always bias the velocity estimate and great care has to be taken to achieve the proper seeding concentration in tomographic PIV/PTV experiments.

Using a stereo microscope, two different views are available. An attempt to reconstruct the particle distribution in a micro volume was presented by LINDKEN et al. [68]. The velocity estimation suffered from the elongated reconstruction of the particles due to the small viewing angles of the stereoscopic setup as schematically shown in Fig. 10.7. Viewing angles of 20° were reported by KIM et al. [52], who used a self made microscope and applied four cameras to investigate the flow inside a droplet on a moving surface by means of tomographic PIV. The measurement volume was $2.5 \times 2.1 \times 0.4 \text{ mm}^3$. To decrease the amount of ghost particles, sparse seeding was used and 25 successive reconstructions of the 3D distribution of tracer particles were added to synthetically increase the seeding concentration and to allow for volumetric cross correlation. Currently this limits the technique in microfluidics to stationary flows. The authors used a continuity based approach to estimate a global uncertainty for all directions, which was reported to be 0.2 pixel.

In general, the recording of the tracer particles from multiple views and the need for a precise calibration of the two or more cameras in the common field of view is the major drawback of multi-camera techniques in microfluidics. Methods to record the 3D particle distribution in a volume with a single camera are therefore more attractive in microfluidics such as the fast point-wise scanning of the volume as outlined next.

10.7 Single Camera Approaches

10.7.1 Confocal Scanning Microscopy

In comparison to epi-fluorescent imaging, confocal scanning microscopy is an approach to dramatically increase the out-of-plane, as well as the in-plane resolution. This is achieved using point wise illumination. Point wise illumination was generated by using a lamp and an aperture at the time it was invented [79, 80]. Nowadays, focused laser beams are most often used for the illumination and the technique is often referred to as confocal laser scanning microscopy (CLSM). In Fig. 10.9, the principle schematic of a confocal laser scanning microscope is drawn. The laser light is focused by a micro lens onto the sample. The micro lenses are often arranged on a rotating disk to increase scanning speed. However, focusing at a certain time instant result in just a small part of the sample being illuminated. Another pinhole aperture (typically several microns) is used to filter light that is coming from outside the focal point. These pinholes are also equally spaced and arranged in a spiral on a spinning disk, which is called Nipkow disk after its inventor. The mechanical connection of both disks allows for an easy and precise synchronization. A photodetector or a camera can then be used to record the fluorescence intensity at the focused point. To record a whole 2D representation of the sample, data points in the XY -direction have to be scanned. The technique is widely used in biology, where the contrast of the images and the increased resolution was necessary to observe certain micro organisms. The calibration of the system can be performed in the same way as for epi-fluorescence imaging with a grid or other well suited object.

The technique was first used in microfluidics to investigate the mixing process in micro mixers [27, 42]. Conventional methods for scanning used galvanic or

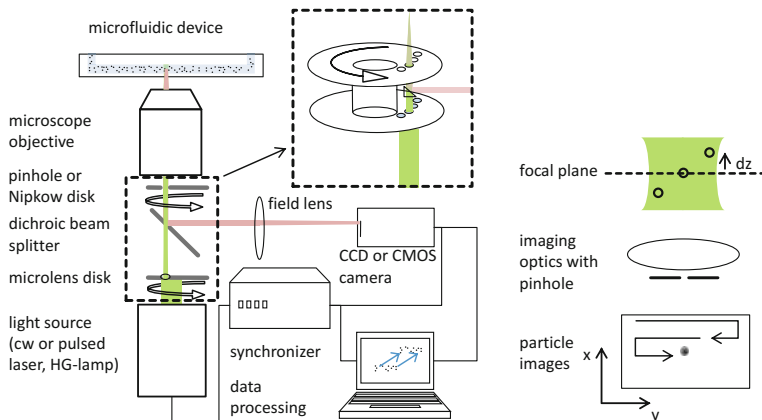
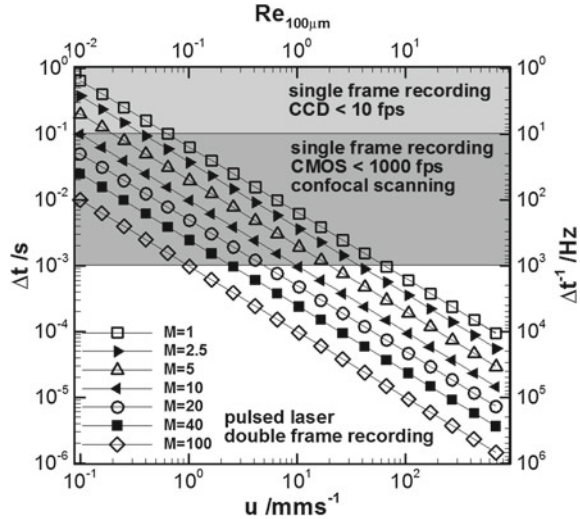


Fig. 10.9 Schematic of a confocal laser scanning μ PIV system with a spinning disk system after [66] (left) and principle schematic of the imaging with reversed colors (right), (from [18])

Fig. 10.10 Δt versus U for different magnifications, after [34]



piezoelectric mirrors to scan the probe volume. However, the scanning speed was usually limited to several frames per second. The scanning time was decreased considerably by the Nipkow disk and a rotating disk with microlenses to focus the laser. Typical full field scanning rates were 50 Hz [66], 120 Hz [91], 200 Hz [65] up to 4800 Hz [53].

The application of these techniques to velocity field measurements has the benefit that the images of particles viewed by confocal microscopy show a significant increase in signal to noise ratio. The thickness of an optical slice is in the order of 1 . . . 2 μm and light from out-of-focus particles does not decrease the image quality and thus no bias in the velocity measurement is introduced. KLEIN & POSNER [54] showed a large increase in vector yield using confocal scanning μPIV in comparison to wide field μPIV . Scanning confocal microscopy was successfully applied to microscopic flows of evaporating droplets [53], biological cell flows [65, 66], and capillary flows [91].

The limitations of the confocal microscopy are the expensive lab equipment and further more the limited temporal resolution. The minimal time distance between images is restricted by the scanning speed. In Fig. 10.10, the necessary time resolution Δt is given versus the fluid velocity U for different magnifications, similar to the analysis by HAIN et al. [34]. The graph is based on the assumption of a 10 pixel particle image displacement on the image for simplicity. The Reynolds number given on the upper horizontal axis should provide a first estimate for the user and is based on a length scale of 100 μm and the kinematic viscosity of water.

The region highlighted in light gray indicates the use of CCD cameras with a scanning rate lower than 10 Hz or a minimal time interval between two frames of 0.1 sec. It is evident from Fig. 10.10 that this kind of equipment is useful for low Reynolds number investigations ($Re = \mathcal{O}(0.01 \dots 0.1)$) and low magnifications.

Using high speed cameras and/or high speed confocal laser scanning microscopy increases the range for measurements to $Re < 5$. For higher Reynolds numbers, pulsed light sources and double frame cameras have to be applied (white region). However, with increasing scanning speed, confocal microscopy shows a great potential for further use in μ PIV/PTV, since the problems due to low SNR and depth of correlation can be avoided successfully.

10.7.2 *Techniques Based on Out-of-Focus Imaging Without Aperture*

As confocal laser scanning microscopes are very expensive 3D measurement techniques based on out-of-focus effects are more common in microfluidics. They only require standard equipment are simple to use and robust. On the right hand side of Fig. 10.6 the images for particles beyond the focal plane are drawn. It is evident, that the image diameter depends on the distance from the focal plane. A model to describe the defocussed imaging of particles in microscopes was developed by OLSEN & ADRIAN [88], see Sect. 10.4.3. They assumed a Gaussian intensity distribution for the particle images. Contributions are due to the diameter of the particle itself (geometric part), diffraction and defocusing. The diameter $d_\tau(Z)$ of a particle image can now be described as a function of the distance to the focal plane Z , with the assumption that the working distance of the lens is significantly larger than Z . This surely holds for most microscopes where the working distance of the lens is typically at least one order of magnitude larger than the channel width. The diameter is given by Eq. (10.10), see [73, 103]. However, as already shown in Figs. 10.4 and 10.5, recent experiments showed differences, especially for high NA objective lenses [55, 103]. Nevertheless, the diameter of the particle image can be correlated with its depth by a proper calibration, see BARNKOB et al. [6] for details.

One of the first applications of defocused images to determine the out-of-plane velocity was realized by STOLZ & KÖHLER [112]. They used the size of the defocused particle images to estimate the third velocity component by PTV in a 1.5 mm thick light sheet. The mean value of the velocity in the axial direction, in a laminar channel flow, was just 5% higher than the reference measurement by laser Doppler anemometry, although

the standard deviation was 10%. The same principle was also applied for macroscopic flows by MURATA & KAWAMURA [84], who reported an rms error for the out-of-plane position of the particles' position below 5% of the measurement depth.

HIRAOKA et al. [37] analyzed the three-dimensional optical transfer function of particles, to determine the three-dimensional structure of biological specimens with an epi-fluorescence microscope. For microscopic flows, a method taking advantage of the size of diffraction rings using forward scattering of light was developed by OVRYN & HOVENAC [89] and applied to a micro channel of 315 μm in depth to measure the velocity profile in the depth direction. However, for a good SNR, the particles had

a diameter of $7\ \mu\text{m}$ and showed a tendency to sink in the fluid. Only the lower part of the profile could be measured. GUERRERO et al. [30] extended the method to backward and side scatter configurations and compared experimental results with Lorentz-Mie theory. In a later study [31] the method was extended, also including Huygens-Fresnel light propagation. However, the measurement errors for the position are relatively large (up to 30 % of the volume). Recently, MORENO et al. [82] used wavelet based noise reduction and the central spot size of the interference pattern. A theoretical assessment of the method's uncertainty for 3D-PTV regarding particle and pixel size, magnification and resolution was performed by PADILLA SOSA et al. [90]. Another method to detect particle depth positions is the use of diffraction gratings [24, 116]. Evaluating the defocused particle images for different orders of diffraction, it is possible to determine the depth position. ANGARITA- JAIMES et al. [3] reported an uncertainty of $8\ \mu\text{m}$ over a depth range of 0.2 mm. The disadvantage of this technique is that three particle images are produced, thus decreasing the effective sensor size.

Another more specific approach is called Bessel beam microscopy (BBM). By placing a lens in series with an axicon in the optical path of a microscope, the diffraction-limited resolution of the base microscope can be improved according to SNOEYINK & WERELEY [110].

10.7.3 Defocused Imaging with Aperture (Three-Pinhole Technique)

The depth coding via a three-pinhole aperture is a method that applies defocused particle imaging with an optical spatial filter. This method was originally proposed for fluid flows by WILLERT & GHARIB [121] and applied for macroscopic two phase flow by PEREIRA et al. [92, 93]. A theoretical examination of the underlying optics for macroscopic applications was presented by KAJITANI & DABIRI [47, 48]. Later the particle characterization was improved by a new imaging volume definition [29].

YOON & KIM [124] successfully adopted the technique to microfluidics. The principle schematic is given in Fig. 10.11. In contrast to the original μPIV setup, shown in Fig. 10.6, an aperture mask, featuring three pinholes is introduced directly after the objective lens. Since the aperture mask would block a large amount of the laser light, usually the illumination is shifted to shine onto the sample from another axis, thus requiring transparent samples. On the right side of the same figure, the imaging of particles in the volume is schematically shown. For a complete treatment of the geometric optics using a microscope, the interested reader is referred to [124]. Recently, the calibration procedure was extended to interfaces with different index of refraction [123]. In general, an out-of-focus particle is imaged as a triplet depending on its position in the volume. In the focal plane, a single image will be detected on the sensor. Depending on whether a particle is in front or behind the focal plane, the arrangement of the triplet is mirrored, allowing for an unambiguous determination of the particles position. For the out-of-focus particles, the distance between the

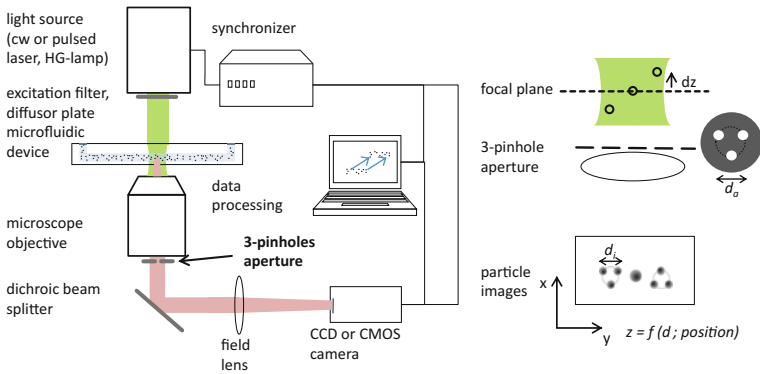


Fig. 10.11 Schematic of the three-pinhole defocusing technique (left) and principle schematic of the imaging with reversed color (right), (from [18])

edges of the imaged triplet is directly related to the distance from the focal plane. Image preprocessing must now be applied to detect corresponding spots, forming a triplet. A circumcircle (diameter d_i in Fig. 10.11) can be fitted through the single spots. Its center is related to the particles' position in the XY -plane. The diameter d_i of a triplet can be calibrated to the actual Z -position of the particle and increases linearly with distance from the focal plane for microscopic imaging. Changing the circumcircle for the aperture mask d_a will also change the slope of dd_i/dZ . The larger the diameter at the aperture d_a , the larger the slope dd_i/dZ . Thus, the measurement depth and the sensitivity and resolution of the system can easily be adopted to different requirements. Since no additional elements, such as lenses or diffraction gratings are introduced, the benefit of high quality microscope objectives with low image aberrations is preserved. Therefore the calibration for the Z -direction, holds for the entire sensor ($dd_i/dZ = \text{const.}$). Another advantage of such a system is that the error of the particle image detection algorithm is spread over three images.

The low seeding rates and the low light intensity due to the small pinholes are the major limitations of this technique. The SNR, in this respect the maximum intensity divided by the background noise is shown in Fig. 10.12 for standard imaging, the 3-pinhole method and astigmatic imaging. The pinholes had a diameter of 1.5 mm, the diameter of the circumcircle was 4 mm. The magnification was $20\times$. This were the same conditions used by YOON & KIM [124]. A glass plate with $5\ \mu\text{m}$ fluorescent particles from Microparticles GmbH was illuminated from the top by an optical fiber connected to a diode pumped cw-laser with an output power of 1 W. To reach approximately the same measurement depth, a cylindrical lens with $f = 150\ \text{mm}$ was used for the astigmatic imaging. The images were recorded with a Sensicam QE from PCO with an exposure of 10 ms to reach almost full well capacity for in-focus particles with standard imaging. The SNR for standard imaging shows the highest values of $\text{SNR} \approx 90$ at the focal plane at $Z = 0\ \mu\text{m}$ and decreased to $\text{SNR} \approx 10$ at a distance of $Z = \pm 20\ \mu\text{m}$ from the focal plane. The astigmatic imaging is a technique

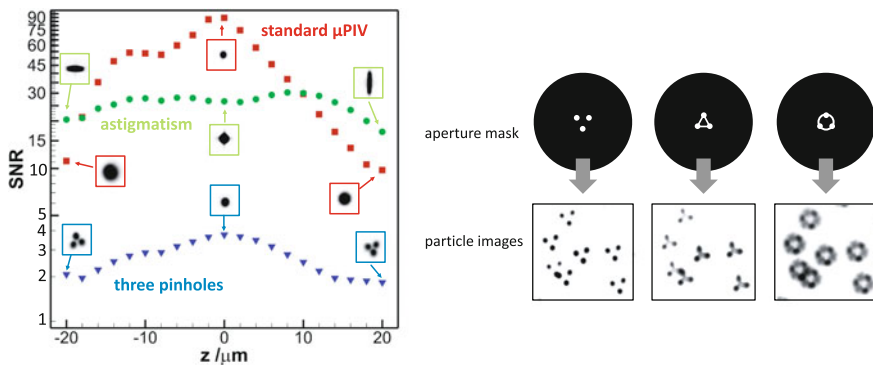


Fig. 10.12 Comparison of the signal to noise ratio (SNR) for standard imaging, the three-pinhole method and astigmatic imaging (left). Particle images for different apertures masks (right), (from [18])

that works without masking the optics and thus allows more light to reach the sensor. The principle will be explained in detail in the next section, however, the graph shows two peaks in the maximum intensity where the two distinct focal planes lie [20]. The SNR is much lower than for standard imaging and decreases from around $\text{SNR} = 30$ to $\text{SNR} = 15$ for out-of-focus imaging. Using the 3-pinhole mask, a large portion of the light is filtered out and the SNR reaches a maximum of $\text{SNR} = 4$ in the center and decreases to around $\text{SNR} = 2$ for out-of-focus regions. The results give an estimate for the image quality that can be expected for the different techniques. Applying astigmatic imaging the SNR decreases by a factor of 3 and using the pinhole aperture it decreases by a factor of more than 20 compared to standard imaging. MIN & KIM [78] used large particles ($5 \mu\text{m}$) and an image intensifier to increase the image quality. They combined the defocused PTV method in the far field with total internal reflection microscopy close to the wall and reported a decreased uncertainty for the estimation of the wall gradients.

However, if the image quality is sufficiently high, it is often difficult to determine particle images that correspond to a triplet. For this reason masks with different patterns can be used to improve this procedure. On the right hand side of Fig. 10.12 the particle images are shown for the standard mask, a mask where the pinholes are connected by lines and a mask with a circle connecting the pinholes. It is evident from the images that it is much easier for data processing to find corresponding triplets if they are somehow connected. All kinds of masks are possible. Additionally, image preprocessing correlation with a virtual mask [85] might help to reliably detect triplets. Other possibilities include, using a color camera and color filters in front of each pinhole in the aperture mask [115], or using an annular aperture [67], or the known active rotation of an off-axis aperture [99]. To the authors knowledge YOON & KIM [124] were the first using the technique to investigate the flow over a backward facing step in a volume of $768 \times 388 \times 50 \mu\text{m}^3$. From geometric optics it is evident that the center of the circumcircle does not directly correspond to the particle

position in the XY -plane. For the correction of the XY -position, a polynomial fit was used to map the final data. The calibration was done by moving a glass plate with particles in the axial, i.e., Z -direction using a translation stage. In order to take into account the change of refractive index, the same glass plates and the same fluid was used. The authors used a high speed camera at a recording rate of 1000 fps to measure time resolved particle trajectories, restricting the experiment to a Reynolds number based on the hydraulic diameter of $Re = 0.025$ (cmp. Fig. 10.10). To overcome the problems due to low SNR, relatively large particles of $3 \mu\text{m}$ were used.

To study the flow inside an evaporating water droplet, [94] applied the technique to a volume of $400 \times 300 \times 150 \mu\text{m}^3$. A high speed CCD camera (~ 250 fps), using 16 separated areas on the chip was used. Thus a background image, taking into account the different gain for all 16 areas, had to be removed. An extensive error analysis is reported. Finally, taking all sources of errors into account (calibration stage resolution, processing algorithm, pixel size), the authors reported an error lower than 3% ($3.3 \mu\text{m}$) for a depth range of $110 \mu\text{m}$. The authors were able to successfully measure the particle trajectories with flow velocities up to 1.5 mm/s (cmp. Fig. 10.10). LU et al. [69] applied the method later for in-vivo measurements of the beating heart of an embryonic zebrafish. The authors used an aperture with $d_a \approx 4$ and a pinhole size of 2 mm to image $1 \mu\text{m}$ fluorescent beads. For the recording an Ar^+ -laser was used in combination with a high-speed camera. They were able to reconstruct the movement of the ventricle by recording images of trapped particles at the wall during a full cardiac cycle. [85] measured the flow of a toroidal micro vortex in a channel with $50 \mu\text{m}$ in depth. The aperture triplet had pinholes with a diameter of 1 mm and a circumscribed circle with a diameter $d_a = 4 \text{ mm}$. The particles used had a diameter of $1 \mu\text{m}$ and were imaged with $20\times$ magnification. The author mentioned that due to the long exposure time, trails at the particle images appeared which negatively affected the accuracy. Nevertheless, using advanced image preprocessing, the errors were reported to be $2 \mu\text{m}$ for the in-plane position and $3.8 \mu\text{m}$ for the out-of-plane position. TIEN et al. [114] could improve the SNR of the technique by using a color camera and three color LED directed toward the pinhole aperture. The reported uncertainty was only 1.5% in the out-of-plane direction for a measurement range of 325 mm . Due to the slow color camera a backward facing step with a Reynolds number of only around 1 could be measured. However, this is not an inherent limitation of the procedure. The identification of particle triplets was easily possible due to the different color filters, even for increased seeding density. Recently, TIEN [113] modified the setup to use three different cameras to avoid cross-talk and overlap as observed for the color camera. However, the advantage of using only one camera becomes obsolete with such setup. Although the technique is widely used, it has the drawback that a big part of the fluorescence signal is blocked by the aperture lens. A technique that uses the whole incoming light is astigmatic imaging.

10.7.4 Imaging Based on Aberrations (Astigmatism)

Astigmatism or anamorphic imaging is a way to break the axis symmetry of an optical system thus allowing for the depth coding in 2D images. The word astigmatism is based on the Greek description for not point-shaped. An optical system that features astigmatism has two focal lines instead of a focal point and the astigmatic image of a point source is thus an ellipse. The principle is schematically shown in Fig. 10.13. The off-axis imaging of a point source can already cause astigmatism. Due to the different refraction that takes place in the horizontal and the vertical directions of a lens looked upon at an angle two focal lines perpendicular to each other are produced. The image of the point source is first a vertical line and changes gradually into a defocused circle and later to a horizontal line at the position of the second focal line. Usually, opticians try to avoid astigmatism in their optical systems. Nevertheless, it is commonly used in CD, DVD and Blue-ray players to measure with high accuracy the distance between the disk and the reader head as well as for other auto-focus systems [39]. Another approach that produces an astigmatic image aberration is utilizing a tilt angle between the measurement volume and the camera, which results in off-axis imaging [33]. This method was applied by HAIN et al. [35] to measure the velocity of particles in a macroscopic volume of $16 \times 16 \times 20 \text{ mm}^3$. Unfortunately, the appearance of the particle images did not only changed in the z -direction, but also in the xy -plane. A complex calibration procedure using a higher order polynomial fit was therefore applied by scanning light sheets with known positions. A similar approach was employed by VAN HINSBERG et al. [36] to measure the flow in a volume of $5.6 \times 4.5 \times 2.1 \text{ mm}^3$. The astigmatic aberrations were produced by an optical filter plate, placed under an angle in the light path. The particle images for a certain range of axis ratios were later artificially reconstructed and the 2D velocity vectors were then obtained by cross-correlation methods.

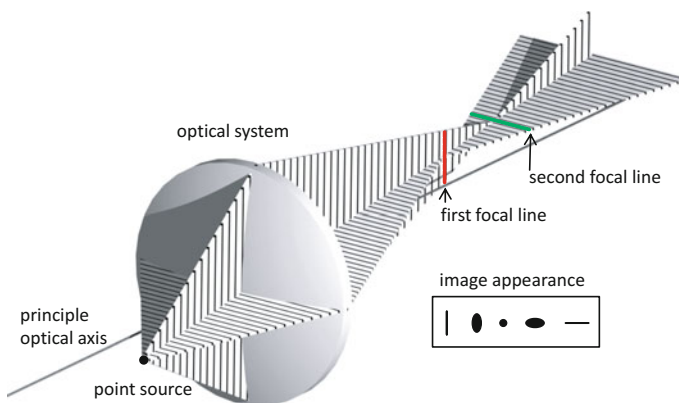


Fig. 10.13 Schematic of astigmatism caused by off-axis imaging and the appearance of the image at various distances between the two focal planes, according to [35]

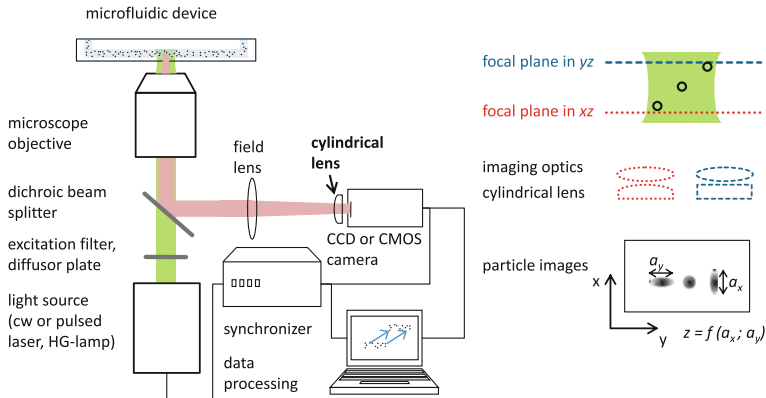


Fig. 10.14 Schematic of the astigmatism technique (left) and principle schematic of the imaging with reversed colors (right), (from [18])

Another more flexible method is the use of cylindrical lenses. KAO & VERKMAN [49] applied this technique to the measurement of the position of fluorescent particles in living cells. They used a $60\times$ oil immersion lens to image 93 nm fluorescent latex beads over a depth range of $4\ \mu\text{m}$. The implementation of this approach to a standard μPIV system is shown in Fig. 10.14. The main difference is the cylindrical lens located directly in front of the camera chip. Since no mask is used, the microfluidic device does not have to be illuminated from another direction and the SNR is improved, compared to techniques that rely on masking the optics (cmp. Fig. 10.12). On the right side of Fig. 10.14 the imaging of particles is schematically shown. The cylindrical lens has a curvature only in one direction and acts as a flat window in the other direction. Therefore, two distinct focal planes are produced, similar to Fig. 10.13. In the left (red dotted) schematic the cylindrical lens causes a shortening of the distance between the focal plane and the objective lens. Particles that are close to this focal plane show a sharp and small diameter in the x -direction a_x and a larger defocused diameter in the y -direction a_y , thus producing an oblate particle image. On the right side of the schematic (blue dashed), with the cylindrical lens rotated by 90° , results in a focal plane further away from the objective lens. a_y is now smaller than a_x , resulting in a prolate particle image. The particle image width and height can now be related to the depth position by a proper calibration [DC10.2].

TOWERS et al. [116] used a diffraction grating for multi-planar imaging as well as a cylindrical lens with a large focal length of $f = 2000\ \text{mm}$ and found astigmatism to have less uncertainty for depth wise position estimation. Furthermore, since three images are used by the method applying the diffraction grating, the field of view is limited to one third of the camera sensor and hence is less efficient. Using both techniques, an air flow with an obstacle was later investigated [3]. For the calibration, a fiber light source was moved to defined positions. The measurements were later performed in a volume of $28 \times 21 \times 28\ \text{mm}^3$ and the uncertainty in depth was estimated to be $25\ \mu\text{m}$ for the calibration. In this preliminary study some 20 vectors

were reconstructed. The difference of the axes of the ellipse ($a_x - a_y$) was used for the depth wise calibration but other calibration approaches are possible [100].

CHEN et al. [13] applied the method to a volume of $1.8 \times 1.4 \times 0.5 \text{ mm}^3$. They used a cylindrical lens with a focal length of $f_{\text{cyl}} = 500 \text{ mm}$. The distance between both focal planes was $\approx 600 \text{ }\mu\text{m}$. The channel with a $170 \text{ }\mu\text{m}$ backward facing step had a depth of $500 \text{ }\mu\text{m}$, ensuring that particles were not too close to either one of the focal planes. The uncertainty for the depth position was $2.8 \text{ }\mu\text{m}$ for the calibration images. The authors presented a theoretical estimation of the measurement depth, which is, in the first approximation $\Delta Z \approx L^2/f$, where L^2 denotes the distance from the center of the measurement volume to the first principle plane and f the focal length of the cylindrical lens. The rms value of the measured velocity was 3.3 m/s (above one third of U_∞), even though 2.8 m/s was expected from the measurement uncertainty. CIERPKA et al. [22] investigated the laminar flow in a channel with a square cross section of $500 \times 500 \text{ }\mu\text{m}^2$ at $\text{Re} = 23$. The cylindrical lens used had a focal length of $f_{\text{cyl}} = 150 \text{ mm}$. The ratio of the particle image width and height a_x/a_y was used for determining the Z -position. This limits the measurement depth to about $40 \text{ }\mu\text{m}$, making scanning of volumes necessary. The data was validated against standard μPIV measurements as well as the theoretical Poiseuille flow profile and agreed within an uncertainty of $< 6\%$ of U_∞ for a confidence interval of 20:1. Since the measurement depth using $a_x - a_y$ or a_x/a_y is limited by the two focal planes, an intrinsic calibration procedure, allowing also to use strong out-of-focus particles was developed. This procedure is based on Eq. (10.10) and takes into account all image aberrations since it is based on the particle images itself. Thus no scanning procedure is necessary. The same optical path as well as the same image preprocessing is used for calibration and measurements, decreasing the uncertainty of the measurements. Using this procedure, the measurement depth could be largely increased in addition. Figure 10.15 illustrates how the different calibration curves look like in dependency on the specific approach used. More details on the calibration as well as an experimental estimation of the measurement depth for different magnifications and focal length can be found in CIERPKA et al. [20] and ROSSI & KÄHLER [100].

Today, astigmatic particle tracking is a well established measurement technique for 3D flow analysis in microfluidics [DC10.3]. RAGAN et al. [97] applied a bent dichroic mirror in the light path of a two-photon microscope to introduce astigmatism. They were able to study the motion of kidney cells expelled to external forces in real time with 28 Hz. Quantum dots were used by HOLTZER et al. [38], observed through a cylindrical lens with a very large focal length of $f_{\text{cyl}} = 10 \text{ m}$, thus allowing for very precise measurements of small depths. The accuracy for the position measurements of the quantum dots was 43 nm for the in-plane and 130 nm for the out-of-plane position in a volume of $\approx 1 \text{ }\mu\text{m}^3$. HUANG et al. [40] used a $100\times$ oil immersion lens and a emCCD (Electron Multiplying Charge Coupled Device) to detect the position of 200 nm beads that were labeled with photo-switchable molecules. In a volume of $200 \times 200 \times 200 \text{ nm}^3$ around the focal point, the accuracy was reported to be $\leq 26 \text{ nm}$ for the in-plane, and $\leq 52 \text{ nm}$ for the out-of-plane position. MLODZIANOSKI et al. [81] compared the performance of bi-plane imaging and

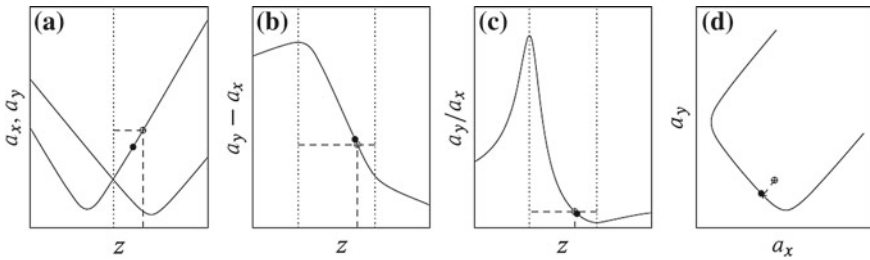


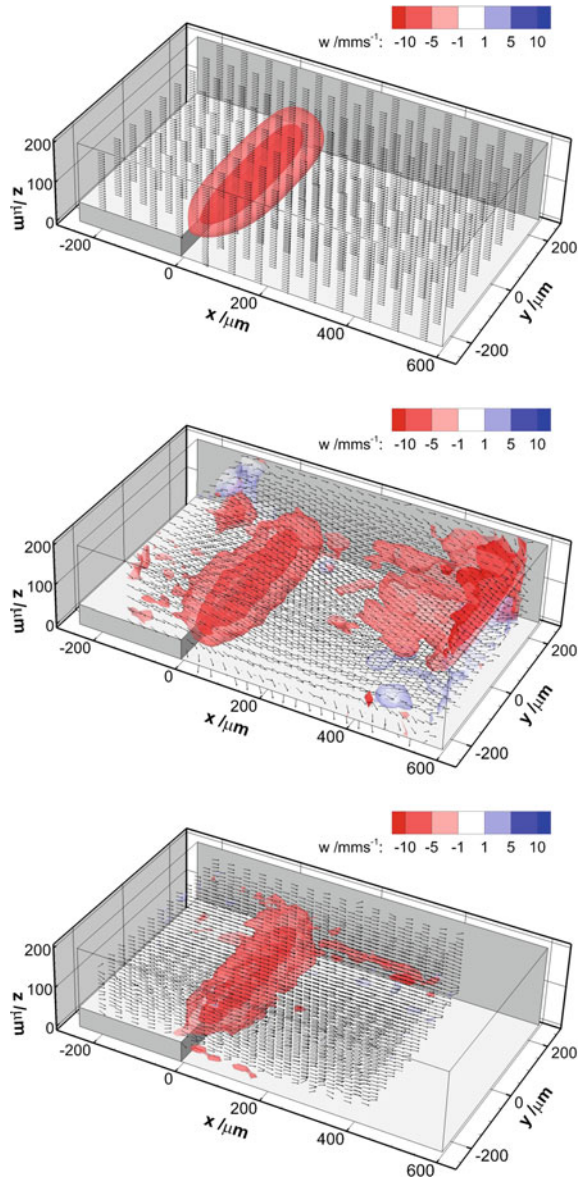
Fig. 10.15 Different calibration approaches for a typical calibration curve. The empty circle represents the measured point, the filled circle represents the true value. Z is estimated from: **a** larger diameter, **b** diameter difference, **c** diameter ratio, **d** minimal distance from the calibration curve in the $a_x a_y$ space, (from [100])

astigmatic imaging using a emCCD camera. Both techniques showed a comparable measurement accuracy. For certain biological applications with thick sample sizes, the authors found the bi-plane imaging more adaptable but also stated that for cameras with non-negligible readout noise (like standard CCD), astigmatic imaging is favorable. Recently, time resolved particle trajectories in an electro-thermally generated micro vortex could be measured in a micro volume with $50 \mu\text{m}$ in depth without traversing [58]. The three-dimensional structure of the vortex and the mechanisms of particle trapping inside the vortex were studied. The results were used to validate the numerical boundary conditions for a simulation of such a scenario.

In general, the astigmatism approach based on cylindrical lenses is very easy to apply and allows for the extension of existing 2D measurement systems to fully 3D measurements, without changing the illumination light path. The measurement depth and resolution can be changed by adopting the focal length of the cylindrical lens used, and the intrinsic calibration procedure [20] makes the technique easily applicable without special expert knowledge. Since no mask is used, the technique is optically very efficient.

The comparison between standard μPIV , stereoscopic μPIV and astigmatism μPTV showed a similar uncertainty for the in-plane velocity components [21]. In Fig. 10.16, iso-surfaces of the out-of-plane component are shown for the flow over a backward facing step. On the upper part of the figure, numerical flow simulations are shown for comparison and indicate a downward flow in the vicinity of the step. In the middle, stereoscopic measurements are presented and the region of the downward flow was well captured. Although great care was taken to align the system, the focal planes of both cameras differ by several micrometers as outlined in [21]. Thus the in-plane velocity corresponds to different regions in the volume. Since the out-of-plane components are determined from the in-plane velocity they are affected by this misalignment. The iso-surfaces downstream of the step for $X > 400 \mu\text{m}$ are caused by this effect and truly not physical. The results for the astigmatism particle tracking cannot be affected by misalignment, since just one camera is used. The downward flow region close to the step is well captured, although the size of this region is slightly

Fig. 10.16 Iso-surfaces of the out-of-plane velocity for the flow over a $50\ \mu\text{m}$ backward facing step in a channel with a cross-section of $200 \times 500\ \mu\text{m}^2$. Numerical flow simulation (top, every 10th vector shown), stereoscopic μPIV (middle, every 2nd vector shown) and astigmatism μPTV (bottom, every 2nd vector shown), (from [21])



underestimated. However, the overall comparison showed that the uncertainty of the out-of-plane component for astigmatism μPTV is almost two times lower than for stereoscopic μPIV [21].

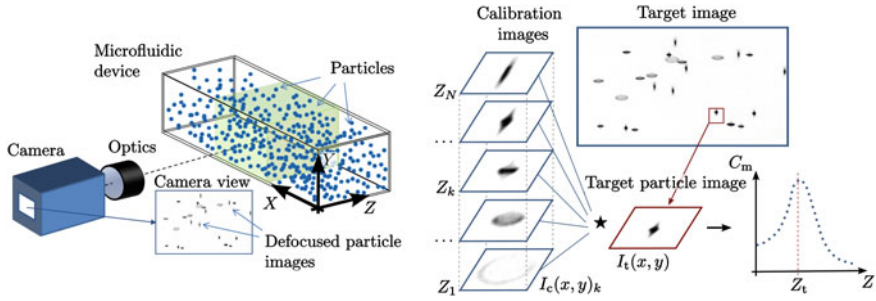


Fig. 10.17 Left: Sketch of a single-camera setup for determining the 3D particle positions via defocused particle images, where the particle images change as function of the depth coordinate. Right: GDPT working principle: a target particle image I_t is compared to a set of calibration images I_c by use of the normalized cross-correlation (\star). The out-of-plane coordinate Z_t for the target particle is found where the maximum correlation C_m is highest as a function of the out-of-plane coordinate Z , (figure adapted from [6])

10.7.5 General Defocusing Particle Tracking (GDPT)

In the last years different calibration procedures were examined and compared in detail by ROSSI & KÄHLER [100] and the calibration was extended so that arbitrary particle image deformation can be used to determine the 3D velocity field [6]. This approach is called General Defocusing Particle Tracking (GDPT). The GDPT working principle is sketched in Fig. 10.17 (right). The method is based on N_c experimental calibration images $I_c(x, y)_k$, with $k = 1, 2, \dots, N_c$, of identical tracer particles taken at different positions along the depth direction. This is for instance easily done by scanning a microscope focus while observing a particle at a fixed depth position. In a GDPT evaluation, a target image of defocused particles is searched for individual target particle images and each target particle image $I_t(x, y)$ is compared to the calibration images. I_t and I_c are compared using the normalized cross-correlation function. The correlation function gives a maximum peak in the position of best overlap with a peak amplitude C_m that rates the quality of the match (from 0 to 1). The calibration images are searched until the best matching I_c is identified to give the corresponding depth coordinate Z_k . To obtain “sub-image accuracy”, a three-point parabolic fit estimator is applied to refine the Z -position, while the in-plane particle position is determined with “sub-pixel accuracy” in analogy with conventional μ PIV analysis. Figure 10.18 shows a measurement of a channel flow in a microchannel and a comparison with numerical results. The complex variation of the particle images in this particular experiment is displayed in the top image of Fig. 10.18.

Today, the astigmatism PTV and GDPT technique is used for the analysis of complex flows in many fields [5, 51, 58, 70, 71, 83, 98, 117] [DC10.4]. Furthermore, the technique can be used for simultaneous 3D velocity and 3D temperature fields for instance by using functional particles such as thermochromic liquid crystals (TLC) [95, 106–108] or particles that are doped with a temperature sensitive dye [43, 72].

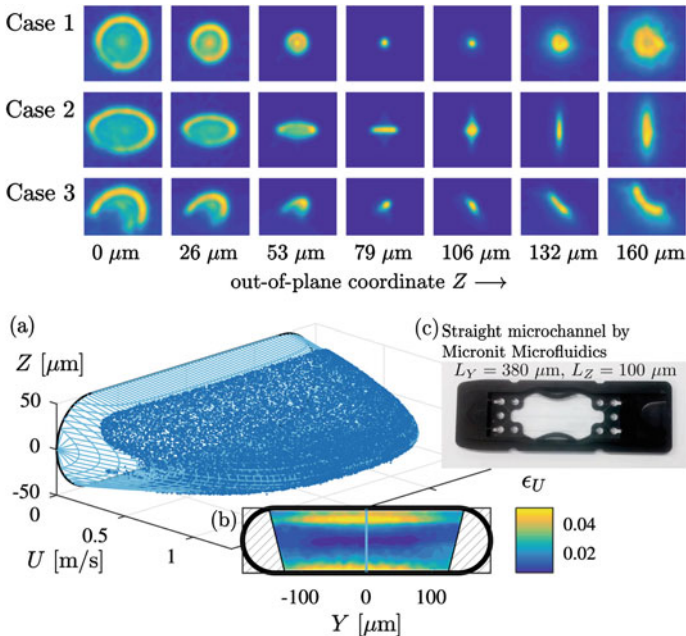


Fig. 10.18 Top: Experimental particle images as a function of the out-of-plane coordinate Z from 0 to 160 μm for the three test cases of different type of particle image shapes. Bottom: **a** Experimental velocity profile $U(Y, Z)$ for Case 1 in the channel cross-section together with the theoretical velocity profile obtained using COMSOL Multiphysics. **b** Colormap of the relative velocity error ϵ_U . **c** Isotropically-etched microchannel from Micronit Microfluidics, (figure adapted from [6])

This opens the door for broadening the application spectrum of the technique in the future.

References

1. Adrian, R.J.: Dynamic ranges of velocity and spatial resolution of particle image velocimetry. *Meas. Sci. Tech.* **8**(12), 1393–1398 (1997). DOI 10.1088/0957-0233/8/12/003. URL <https://doi.org/10.1088/0957-0233/8/12/003>
2. Adrian, R.J., Yao, C.S.: Pulsed laser technique application to liquid and gaseous flows and the scattering power of seed materials. *Appl. Opt.* **24**(1), 44–52 (1985). DOI 10.1364/AO.24.000044. URL <http://ao.osa.org/abstract.cfm?URI=ao-24-1-44>
3. Angarita-Jaimes, N., McGhee, E., Chennaoui, M., Campbell, H.I., Zhang, S., Towers, C.E., Greenaway, A.H., Towers, D.P.: Wavefront sensing for single view three-component three-dimensional flow velocimetry. *Exp. Fluids* **41**, 881–891 (2006). DOI 10.1007/s00348-009-0737-z. URL <http://dx.doi.org/10.1007/s00348-009-0737-z>
4. Angele, K.P., Suzuki, Y., Miwa, J., Kasagi, N.: Development of a high-speed scanning micro PIV system using a rotating disc. *Meas. Sci. Tech.* **17**, 1639–1646 (2006). DOI 10.1088/0957-0233/17/7/001. URL <http://stacks.iop.org/0957-0233/17/i=7/a=001>

5. Baczyzmalski, D., Weier, T., Kähler, C.J., Cierpka, C.: Near-wall measurements of the bubble- and Lorentz-force-driven convection at gas-evolving electrodes. *Exp. Fluids* **56**(8), 162 (2015). DOI 10.1007/s00348-015-2029-0. URL <http://dx.doi.org/10.1007/s00348-015-2029-0>
6. Barnkob, R., Kähler, C.J., Rossi, M.: General defocusing particle tracking. *Lab Chip* **15**, 3556–3560 (2015). DOI 10.1039/C5LC00562K. URL <http://dx.doi.org/10.1039/C5LC00562K>
7. Born, M., Wolf, E.: Principles of Optics, 7th edn. Cambridge University Press, Cambridge (1999). URL <https://www.cambridge.org/de/academic/subjects/physics/optics-optoelectronics-and-photonics/principles-optics-electromagnetic-theory-propagation-interference-and-diffraction-light-7th-edition>
8. Bourdon, C.J., Olsen, M.G., Gorby, A.D.: Validation of an analytical solution for depth of correlation in microscopic particle image velocimetry. *Meas. Sci. Tech.* **15**(2), 318–327 (2004). DOI 10.1088/0957-0233/15/2/002. URL <http://stacks.iop.org/0957-0233/15/i=2/a=002>
9. Bown, M.R., MacInnes, J.M., Allen, R.W.K.: Micro-PIV measurements and simulation in complex microchannel geometries. *Meas. Sci. Tech.* **16**(3), 619–626 (2005). DOI 10.1088/0957-2333/16/3/002. URL <http://stacks.iop.org/0957-0233/16/i=3/a=002>
10. Brücker, C.: Digital-particle-image-velocimetry (DPIV) in a scanning light-sheet: 3-D starting flow around a short cylinder. *Exp. Fluids* **19**, 255–263 (1995). DOI 10.1007/BF00196474. URL <http://dx.doi.org/10.1007/BF00196474>
11. Brücker, C.: 3d scanning PIV applied to an air flow in a motored engine using digital high-speed video. *Meas. Sci. Tech.* **8**(12), 1480 (1997). DOI 10.1088/0957-0233/8/12/011. URL <http://stacks.iop.org/0957-0233/8/i=12/a=011>
12. Bruus, H., Dual, J., Hawkes, J., Hill, M., Laurell, T., Nilsson, J., Radel, S., Sadhal, S., Wiklund, M.: Forthcoming lab on a chip tutorial series on acoustofluidics: Acoustofluidics-exploiting ultrasonic standing wave forces and acoustic streaming in microfluidic systems for cell and particle manipulation. *Lab Chip* **11**, 3579–3580 (2011). DOI 10.1039/C1LC90058G. URL <http://dx.doi.org/10.1039/C1LC90058G>
13. Chen, S., Angarita-Jaimes, N., Angarita-Jaimes, D., Pelc, B., Greenaway, A.H., Towers, C.E., Lin, D., Towers, P.D.: Wavefront sensing for three-component three-dimensional flow velocimetry in microfluidics. *Exp. Fluids* **47**, 849–863 (2009). DOI 10.1007/s00348-009-0737-z. URL <http://dx.doi.org/10.1007/s00348-009-0737-z>
14. Chen, Z., Milner, T.E., Dave, D., Nelson, J.S.: Optical Doppler tomographic imaging of fluid flow velocity in highly scattering media. *Opt. Lett.* **22**(1), 64–66 (1997). DOI 10.1364/OL.22.000064. URL <http://ol.osa.org/abstract.cfm?URL=ol-22-1-64>
15. Chuang, H.S., Gui, L., Wereley, S.T.: Study of single pixel evaluation for experimental measurements in a microchannel. In: Proceedings of the ASME International Mechanical Engineering Congress and Exposition, pp. IMECE2006–14,517. Chicago, IL (2006)
16. Chuang, H.S., Gui, L., Wereley, S.T.: Nano-resolution flow measurement based on single pixel evaluation PIV. *Microfluid. Nanofluid.* **13**(1) (2012). DOI 10.1007/s10404-012-0939-1
17. Chuang, H.S., Kumar, K., Wereley, S.T.: Optical flow characterization microparticle image velocimetry μ PIV. In: J.D. Zahn (ed.) *Methods in bioengineering: biomicrofabrication and biomicrofluidics*, chap. 12. Artech House (2009)
18. Cierpka, C., Kähler, C.J.: Particle imaging techniques for volumetric three-component (3D3C) velocity measurements in microfluidics. *J. Vis.* **15**(1), 1–31 (2012). DOI 10.1007/s12650-011-0107-9. URL <http://dx.doi.org/10.1007/s12650-011-0107-9>
19. Cierpka, C., Lütke, B., Kähler, C.J.: Higher order multi-frame particle tracking velocimetry. *Exp. Fluids* **54**(5), 1533 (2013). DOI 10.1007/s00348-013-1533-3. URL <http://dx.doi.org/10.1007/s00348-013-1533-3>
20. Cierpka, C., Rossi, M., Segura, R., Kähler, C.J.: On the calibration of astigmatism particle tracking velocimetry for microflows. *Meas. Sci. Tech.* **22**(1), 015,401 (2011). DOI 10.1088/0957-0233/22/1/015401. URL <https://doi.org/10.1088/0957-0233/22/1/015401>
21. Cierpka, C., Rossi, M., Segura, R., Mastrangelo, F., Kähler, C.J.: A comparative analysis of the uncertainty of astigmatism- μ PTV, stereo- μ PIV, and μ PIV. *Exp. Fluids* **52**(3), 605–615 (2012). DOI 10.1007/s00348-011-1075-5. URL <https://doi.org/10.1007/s00348-011-1075-5>

22. Cierpka, C., Segura, R., Hain, R., Kähler, C.J.: A simple single camera 3C3D velocity measurement technique without errors due to depth of correlation and spatial averaging for microfluidics. *Meas. Sci. Tech.* **21**(4), 045,401 (2010). DOI 10.1088/0957-0233/21/4/045401. URL <http://stacks.iop.org/0957-0233/21/i=4/a=045401>
23. Dahm, W.J.A., Su, L.K., Southerland, K.B.: A scalar imaging velocimetry technique for fully resolved four-dimensional vector velocity field measurements in turbulent flows. *Phys. Fluids A* **4**(10), 2191–2206 (1992). DOI 10.1063/1.858461. URL <http://scitation.aip.org/content/aip/journal/pofa/4/10/10.1063/1.858461>
24. Dalgarno, P.A., Dalgarno, H.I., Putoud, A., Lambert, R., Paterson, L., Logan, D.C., Towers, D.P., Warburton, R.J., Greenaway, A.H.: Multiplane imaging and three dimensional nanoscale particle tracking in biological microscopy. *Opt. Express* **18**, 877–884 (2010). DOI 10.1364/OE.18.000877. URL <http://dx.doi.org/10.1364/OE.18.000877>
25. Elsinga, G.E., Scarano, F., Wieneke, B., van Oudheusden, B.W.: Tomographic particle image velocimetry. *Exp. Fluids* **41**(6), 933–947 (2006). DOI 10.1007/s00348-006-0212-z. URL <http://dx.doi.org/10.1007/s00348-006-0212-z>
26. Elsinga, G.E., Westerweel, J., Scarano, F., Novara, M.: On the velocity of ghost particles and the bias errors in tomographic-PIV. *Exp. Fluids* **50**(4), 825–838 (2011). DOI 10.1007/s00348-010-0930-0. URL <http://dx.doi.org/10.1007/s00348-010-0930-0>
27. Gösch, M., Blom, H., Holm, J., Heino, T., Rigler, R.: Hydrodynamic flow profiling in microchannel structures by single molecule fluorescence correlation spectroscopy. *Anal. Chem.* **72**(14), 3260–3265 (2000). DOI 10.1021/ac991448p. URL <http://dx.doi.org/10.1021/ac991448p>
28. Gothsch, T., Schilcher, C., Richter, C., Beinert, S., Dietzel, A., Büttgenbach, S., Kwade, A.: High-pressure microfluidic systems (HPMS): flow and cavitation measurements in supported silicon microsystems. *Microfluid. Nanofluid.* **18**(1), 121–130 (2015). DOI 10.1007/s10404-014-1419-6. URL <http://dx.doi.org/10.1007/s10404-014-1419-6>
29. Grothe, R.L., Dabiri, D.: An improved three-dimensional characterization of defocusing digital particle image velocimetry (DDPIV) based on a new imaging volume definition. *Meas. Sci. Tech.* **19**(6), 065,402 (2008). DOI 10.1088/0957-0233/19/6/065402. URL <http://stacks.iop.org/0957-0233/19/i=6/a=065402>
30. Guerrero, J.A., Mendoza-Santoyo, F., Moreno, D., Funes-Gallanzi, M., Fernandez-Orozco, S.: Particle positioning from CCD images: experiments and comparison with the generalized Lorenz-Mie theory. *Meas. Sci. Tech.* **11**(5), 568–575 (2000). DOI 10.1088/0957-0233/11/5/318. URL <http://stacks.iop.org/0957-0233/11/i=5/a=318>
31. Guerrero-Viramontes, J.A., Moreno-Hernández, D., Mendoza-Santoyo, F., Funes-Gallanzi, M.: 3D particle positioning from CCD images using the generalized Lorenz-Mie and Huygens-Fresnel theory. *Meas. Sci. Tech.* **17**(8), 2328–2334 (2006). DOI 10.1088/0957-0233/17/8/039. URL <http://stacks.iop.org/0957-0233/17/i=8/a=039>
32. Hagsäter, S.M., Westergaard, C.H., Bruus, H., Kutter, J.P.: Investigations on LED illumination for micro-PIV including a novel front-lit configuration. *Exp. Fluids* **44**(2), 211–219 (2008). DOI 10.1007/s00348-007-0394-z. URL <http://dx.doi.org/10.1007/s00348-007-0394-z>
33. Hain, R., Kähler, C.J.: Single camera volumetric velocity measurements using optical aberrations. In: 12th International Symposium on Flow Visualization. Göttingen, Germany (2006)
34. Hain, R., Kähler, C.J.: Fundamentals of multiframe particle image velocimetry (PIV). *Exp. Fluids* **42**(4), 575–587 (2007). DOI 10.1007/s00348-007-0266-6. URL <http://dx.doi.org/10.1007/s00348-007-0266-6>
35. Hain, R., Kähler, C.J., Radespiel, R.: Principles of a volumetric velocity measurement technique based on optical aberrations In: Notes on Numerical Fluid Mechanics and Multidisciplinary Design, vol. 106, pp. 1–10. Springer, Berlin (2009). DOI 10.1007/978-3-642-01106-1_1. URL http://dx.doi.org/10.1007/978-3-642-01106-1_1
36. van Hinsberg, N.P., Roisman, I.V., Tropea, C.: Three-dimensional, three-component particle imaging using two optical aberrations and a single camera. In: 14th International Symposium on Applications of Laser Techniques to Fluid Mechanics. Lisbon, Portugal (2008). URL http://lces.dem.ist.utl.pt/lxlasers/lxlasers2008/papers/03.1_2.pdf

37. Hiraoka, Y., Sedat, J.W., Agard, D.A.: Determination of three-dimensional imaging properties of a light microscope system. Partial confocal behavior in epifluorescence microscopy. *Biophys. J.* **57**, 325–333 (1990). DOI 10.1016/S0006-3495(90)82534-0. URL <http://www.sciencedirect.com/science/article/pii/S0006349590825340>
38. Holtzer, L., Meckel, T., Schmidt, T.: Nanometric three-dimensional tracking of individual quantum dots in cells. *Appl. Phys. Lett.* **90**(5), 053,902 (2007). DOI 10.1063/1.2437066. URL <http://dx.doi.org/10.1063/1.2437066>
39. Hsu, W.Y., Lee, C.S., Chen, P.J., Chen, N.T., Chen, F.Z., Yu, Z.R., Kuo, C.H., Hwang, C.H.: Development of the fast astigmatism auto-focus microscope system. *Meas. Sci. Tech.* **20**(4), 045,902 (2009). DOI 10.1088/0957-0233/20/4/045902. URL <http://stacks.iop.org/0957-0233/20/i=4/a=045902>
40. Huang, B., Wang, W., Bates, M., Zhuang, X.: Three-dimensional super-resolution imaging by stochastic optical reconstruction microscopy. *Science* **319**, 810–813 (2008). DOI 10.1126/science.1153529. URL <http://science.sciencemag.org/content/319/5864/810>
41. Inoué, S., Spring, K.R.: *Video Microscopy: The Fundamentals*, 2nd edn. Language of Science. Springer, New York (1997)
42. Ismagilov, R.F., Stroock, A.D., Kenis, P.J.A., Whitesides, G., Stone, H.A.: Experimental and theoretical scaling laws for transverse diffusive broadening in two-phase laminar flows in microchannels. *Appl. Phys. Lett.* **76**(17), 2376–2378 (2000). DOI 10.1063/1.126351. URL <http://dx.doi.org/10.1063/1.126351>
43. Kähler, C.J.: Visualization of 3D velocity and temperature fields with micron resolution. In: 16th International Symposium on Flow Visualization, Okinawa (Japan) (2014). URL <https://athene-forschung.unibw.de/?id=108998>
44. Kähler, C.J., Scharnowski, S., Cierpka, C.: On the resolution limit of digital particle image velocimetry. *Exp. Fluids* **52**(6), 1629–1639 (2012). DOI 10.1007/s00348-012-1280-x. URL <http://dx.doi.org/10.1007/s00348-012-1280-x>
45. Kähler, C.J., Scharnowski, S., Cierpka, C.: On the uncertainty of digital PIV and PTV near walls. *Exp. Fluids* **52**(6), 1641–1656 (2012). DOI 10.1007/s00348-012-1307-3. URL <http://dx.doi.org/10.1007/s00348-012-1307-3>
46. Kähler, C.J., Scholz, U., Ortmanns, J.: Wall-shear-stress and near-wall turbulence measurements up to single pixel resolution by means of long-distance micro-PIV. *Exp. Fluids* **41**(2), 327–341 (2006). DOI 10.1007/s00348-006-0167-0. URL <http://dx.doi.org/10.1007/s00348-006-0167-0>
47. Kajitani, L., Dabiri, D.: A full three-dimensional characterization of defocusing digital particle image velocimetry. *Meas. Sci. Tech.* **16**(3), 790–804 (2005). DOI 10.1088/0957-0233/16/3/022. URL <http://stacks.iop.org/0957-0233/16/i=3/a=022>
48. Kajitani, L., Dabiri, D.: A full three-dimensional characterization of defocusing digital particle image velocimetry. *Meas. Sci. Tech.* **19**(4), 049,801 (2008). DOI 10.1088/0957-0233/19/4/049801. URL <http://stacks.iop.org/0957-0233/19/i=4/a=049801>
49. Kao, H.P., Verkman, A.S.: Tracking of single fluorescent particles in three dimensions: Use of cylindrical optics to encode particle position. *Biophys. J.* **67**, 1291–1300 (1994). DOI 10.1016/S0006-3495(94)80601-0. URL [http://dx.doi.org/10.1016/S0006-3495\(94\)80601-0](http://dx.doi.org/10.1016/S0006-3495(94)80601-0)
50. Kelemen, K., Crowther, F.E., Cierpka, C., Hecht, L.L., Kähler, C.J., Schuchmann, H.P.: Investigations on the characterization of laminar and transitional flow conditions after high pressure homogenization orifices. *Microfluid. Nanofluid.* **18**(4), 599–612 (2015). DOI 10.1007/s10404-014-1457-0. URL <http://dx.doi.org/10.1007/s10404-014-1457-0>
51. Kiebert, F., Wege, S., Massing, J., König, J., Cierpka, C., Weser, R., Schmidt, H.: 3D measurement and simulation of surface acoustic wave driven fluid motion: a comparison. *Lab Chip* (2017). DOI 10.1039/C7LC00184C. URL <http://dx.doi.org/10.1039/C7LC00184C>
52. Kim, H., Große, S., Elsinga, G., Westerweel, J.: Full 3D–3C velocity measurement inside a liquid immersion droplet. *Exp. Fluids* **51**(2), 395–405 (2011). DOI 10.1007/s00348-011-1053-y. URL <http://dx.doi.org/10.1007/s00348-011-1053-y>
53. Kinoshita, H., Kaneda, S., Fujii, T., Oshima, M.: Three-dimensional measurement and visualization of internal flow of a moving droplet using confocal micro-PIV. *Lab Chip* **7**, 338–346 (2007). DOI 10.1039/B617391H. URL <http://dx.doi.org/10.1039/B617391H>

54. Klein, S.A., Posner, J.D.: Improvement in two-frame correlations by confocal microscopy for temporally resolved micro particle imaging velocimetry. *Meas. Sci. Tech.* **21**(10), 105,409 (2010). DOI 10.1088/0957-0233/21/10/105409. URL <http://stacks.iop.org/0957-0233/21/i=10/a=105409>
55. Kloosterman, A., Poelma, C., Westerweel, J.: Flow rate estimation in large depth-of-field micro-PIV. *Exp. Fluids* **50**(6), 1587–1599 (2010). DOI 10.1007/s00348-010-1015-9. URL <http://dx.doi.org/10.1007/s00348-010-1015-9>
56. Koochesfahani, M.M., Cohn, R.K., Gendrich, C.P., Nocera, D.G.: Molecular tagging diagnostics for the study of kinematics and mixing in liquid-phase flows. In: Adrian, R.J., Durao, D., Durst, F., Heitor, M., Maeda, M., Whitelaw, J.H.(eds.) *Developments in Laser Techniques in Fluid Mechanics*, pp. 125–134. Springer Verlag, New York (1997). URL http://www.egr.msu.edu/tmual/Papers_PDF/1996_MTV_Review-Springer-Chapter.pdf
57. Koutsiaris, A.G., Mathioulakis, D.S., Tsangaris, S.: Microscope PIV for velocity-field measurement of particle suspensions flowing inside glass capillaries. *Meas. Sci. Tech.* **10**(11), 1037 (1999). DOI 10.1088/0957-0233/10/11/311. URL <http://stacks.iop.org/0957-0233/10/i=11/a=311>
58. Kumar, A., Cierpka, C., Williams, S.J., Kähler, C.J., Wereley, S.T.: 3D3C velocimetry measurements of an electrothermal microvortex using wavefront deformation PTV and a single camera. *Micro Nano* **10**, 355–365 (2011). DOI 10.1007/s10404-010-0674-4. URL <http://dx.doi.org/10.1007/s10404-010-0674-4>
59. Lanzillotto, A.M., et al.: Applications of X-ray micro-imaging, visualization and motion analysis techniques to fluidic microsystems. In: *Technical Digest of the IEEE 8th International Conference on Solid State Sensor and Actuator Workshop*, 3–6 June, Hilton Head Island, SC, pp. 123–126 (1995)
60. Laurell, T., Petersson, F., Nilsson, A.: Chip integrated strategies for acoustic separation and manipulation of cells and particles. *Chem. Soc. Rev.* **36**, 492–506 (2007). DOI 10.1039/B601326K. URL <http://dx.doi.org/10.1039/B601326K>
61. Lawson, N.J., Wu, J.: Three-dimensional particle image velocimetry: experimental error analysis of a digital angular stereoscopic system. *Meas. Sci. Tech.* **8**(12), 1455 (1997). DOI 10.1088/0957-0233/8/12/009. URL <http://stacks.iop.org/0957-0233/8/i=12/a=009>
62. Lee, S.J., Kim, S.: Measurement of Dean flow in a curved micro-tube using micro digital holographic particle tracking velocimetry. *Exp. Fluids* **46**, 255–264 (2009). DOI 10.1007/s00348-008-0555-8. URL <http://dx.doi.org/10.1007/s00348-008-0555-8>
63. Leu, T.S., Lanzillotto, A.M., Amabile, M., Wildes, R.: Analysis of fluidic and mechanical motion in MEMS by using high speed X-ray micro-imaging techniques. In: *Solid State Sensors and Actuators. TRANSDUCERS '97 Chicago*, 1997 International Conference on, vol. 1, pp. 149–150 (1997). DOI 10.1109/SENSOR.1997.613604. URL <http://dx.doi.org/10.1109/SENSOR.1997.613604>
64. Li, D.: *Encyclopedia of Microfluidics and Nanofluidics*, 2nd edn. Encyclopedia of Microfluid. Nanofluidics. Springer, New York (2015). URL <https://books.google.com/books?id=vFI5fcNFbgYC>
65. Lima, R., Wada, S., Takeda, M., Tsubota, K., Yamaguchi, T.: In vitro confocal micro-PIV measurements of blood flow in a square microchannel: The effect of the haematocrit on instantaneous velocity profiles. *J Biomech.* **40**, 2752–2757 (2007). DOI 10.1016/j.biomech.2007.01.012. URL <https://doi.org/10.1016/j.biomech.2007.01.012>
66. Lima, R., Wada, S., Tsubota, K., Yamaguchi, T.: Confocal micro-PIV measurements of three-dimensional profiles of cell suspension flow in a square microchannel. *Meas. Sci. Tech.* **17**(4), 797–808 (2006). DOI 10.1088/0957-0233/17/4/026. URL <http://stacks.iop.org/0957-0233/17/i=4/a=026>
67. Lin, D., Angarita-Jaimes, N.C., Chen, S., Greenaway, A.H., Towers, C.E., Towers, D.P.: Three-dimensional particle imaging by defocusing method with an annular aperture. *Opt. Lett.* **33**(9), 905–907 (2008). DOI 10.1364/OL.33.000905. URL <https://doi.org/10.1364/OL.33.000905>

68. Lindken, R., Westerweel, J., Wieneke, B.: Stereoscopic micro particle image velocimetry. *Exp. Fluids* **41**(2), 161–171 (2006). DOI 10.1007/s00348-006-0154-5. URL <http://dx.doi.org/10.1007/s00348-006-0154-5>
69. Lu, J., Pereira, F., Fraser, S.E., Gharib, M.: Three-dimensional real-time imaging of cardiac cell motions in living embryos. *J. Biomed. Opt.* **13**, 014006 (2008). DOI 10.1117/1.2830824. URL <http://dx.doi.org/10.1117/1.2830824>
70. Marin, A., Liepelt, R., Rossi, M., Kähler, C.J.: Surfactant-driven flow transitions in evaporating droplets. *Soft Matter* **12**, 1593–1600 (2016). DOI 10.1039/C5SM02354H. URL <http://dx.doi.org/10.1039/C5SM02354H>
71. Marin, A., Rossi, M., Rallabandi, B., Wang, C., Hilgenfeldt, S., Kähler, C.J.: Three-dimensional phenomena in microbubble acoustic streaming. *Phys. Rev. Appl.* **3**, 041,001 (2015). DOI 10.1103/PhysRevApplied.3.041001. URL <https://link.aps.org/doi/10.1103/PhysRevApplied.3.041001>
72. Massing, J., Kaden, D., Kähler, C.J., Cierpka, C.: Luminescent two-color tracer particles for simultaneous velocity and temperature measurements in microfluidics. *Meas. Sci. Tech.* **27**(11), 12 (2016). DOI 10.1088/0957-0233/27/11/115301. URL <http://stacks.iop.org/0957-0233/27/i=11/a=115301>
73. Meinhart, C.D., Wereley, S.T.: The theory of diffraction-limited resolution in microparticle image velocimetry. *Meas. Sci. Tech.* **14**(7), 1047 (2003). DOI 10.1088/0957-0233/14/7/320. URL <http://stacks.iop.org/0957-0233/14/i=7/a=320>
74. Meinhart, C.D., Wereley, S.T., Gray, M.H.B.: Volume illumination for two-dimensional particle image velocimetry. *Meas. Sci. Tech.* **11**(6), 809 (2000). DOI 10.1088/0957-0233/11/6/326. URL <http://stacks.iop.org/0957-0233/11/i=6/a=326>
75. Meinhart, C.D., Wereley, S.T., Santiago, J.G.: PIV measurements of a microchannel flow. *Exp. Fluids* **27**(5), 414–419 (1999). DOI 10.1007/s003480050366. URL <http://dx.doi.org/10.1007/s003480050366>
76. Meinhart, C.D., Wereley, S.T., Santiago, J.G.: Micron-resolution velocimetry techniques. In: Adrian, R., Durão, D., Durst, F., Heitor, M., Maeda, M., Whitelaw, J.(eds.) *Laser Techniques Applied to Fluid Mechanics*, pp. 57–70. Springer, Berlin (2000). DOI 10.1007/978-3-642-56963-0_4. URL http://dx.doi.org/10.1007/978-3-642-56963-0_4
77. Meinhart, C.D., Zhang, H.: The flow structure inside a microfabricated inkjet printer head. *J. Microelectromech. Syst.* **9**(1), 67–75 (2000). DOI 10.1109/84.825779. URL <http://dx.doi.org/10.1109/84.825779>
78. Min, Y.U., Kim, K.C.: Hybrid micro-/nano-particle image velocimetry for 3D3C multi-scale velocity field measurement in microfluidics. *Meas. Sci. Tech.* **22**, 064,001 (2011). DOI 10.1088/0957-0233/22/6/064001. URL <http://stacks.iop.org/0957-0233/22/i=6/a=064001>
79. Minsky, M.: Microscopy apparatus (1961). US Patent 3,013,467
80. Minsky, M.: Memoir on inventing the confocal scanning microscope. *Scanning* **10**(4), 128–138 (1988). DOI 10.1002/sca.4950100403. URL <http://dx.doi.org/10.1002/sca.4950100403>
81. Mlodzianoski, M.J., Juette, M.F., Beane, G.L., Bewersdorf, J.: Experimental characterization of 3D localization techniques for particle-tracking and super-resolution microscopy. *Opt. Express* **17**, 8264–8277 (2009). DOI 10.1364/OE.17.008264. URL <https://doi.org/10.1364/OE.17.008264>
82. Moreno-Hernandez, D., Bueno-ía, J.A., Guerrero-Viramontes, J.A., Mendoza-Santoyo, F.: 3D particle positioning by using the Fraunhofer criterion. *Opt. Lasers Eng.* **49**(6), 729–735 (2011). DOI 10.1016/j.optlaseng.2011.01.019. URL <http://www.sciencedirect.com/science/article/pii/S0143816611000315>
83. Muller, P.B., Rossi, M., Marín, A.G., Barnkob, R., Augustsson, P., Laurell, T., Kähler, C.J., Bruus, H.: Ultrasound-induced acoustophoretic motion of microparticles in three dimensions. *Phys. Rev. E* **88**, 023,006 (2013). DOI 10.1103/PhysRevE.88.023006. URL <https://link.aps.org/doi/10.1103/PhysRevE.88.023006>
84. Murata, S., Kawamura, M.: Particle depth measurement based on depth-from-defocus. *Opt. Laser Tech.* **31**, 95–102 (1999). DOI 10.1016/S0030-3992(99)00027-4. URL [https://doi.org/10.1016/S0030-3992\(99\)00027-4](https://doi.org/10.1016/S0030-3992(99)00027-4)

85. Nasarek, R.: Temperature field measurements with high spatial and temporal resolution using liquid crystal thermography and laser induced fluorescence. Ph.D. thesis, Technische Universität Darmstadt, Germany (2010)
86. Nguyen, N.T., Wereley, S.T.: Fundamentals and Applications of Microfluidics. Artech House integrated microsystems series. Artech House (2006). URL <https://books.google.com/books?id=ZbTCQgAACAAJ>
87. Olsen, M.G., Adrian, R.J.: Brownian motion and correlation in particle image velocimetry. *Opt. Laser Tech.* **32**(7–8), 621–627 (2000). DOI 10.1016/S0030-3992(00)00119-5. URL <http://www.sciencedirect.com/science/article/pii/S0030399200001195>. Optical methods in heat and fluid flow
88. Olsen, M.G., Adrian, R.J.: Out-of-focus effects on particle image visibility and correlation in microscopic particle image velocimetry. *Exp. Fluids* **29**(1), S166–S174 (2000). DOI 10.1007/s003480070018. URL <http://dx.doi.org/10.1007/s003480070018>
89. Ovryn, B., Hovenac, E.A.: Coherent forward scattering particle-image velocimetry: application of Poisson's spot for velocity measurements in fluids. In: *Optical Diagnostics in Fluid and Thermal Flow*, pp. 338–348. San Diego, CA, USA (1993). DOI 10.1117/12.163718. URL <http://dx.doi.org/10.1117/12.163718>
90. Padilla Sosa, P., Moreno, D., Guerrero, J.A., Funes-Gallanzi, M.: Low-magnification particle positioning for 3D velocimetry applications. *Opt. Laser Tech.* **34**(1), 59–68 (2002). DOI 10.1016/S0030-3992(01)00096-2. URL <http://www.sciencedirect.com/science/article/pii/S0030399201000962>
91. Park, J.S., Choi, C.K., Kihm, K.: Optically sliced micro-PIV using confocal laser scanning microscopy CLSM. *Exp. Fluids* **37**, 105–119 (2004). DOI 10.1007/s00348-004-0790-6. URL <http://dx.doi.org/10.1007/s00348-004-0790-6>
92. Pereira, F., Gharib, M.: Defocusing digital particle image velocimetry and three-dimensional characterization of two phase flows. *Meas. Sci. Tech.* **13**(5), 683–694 (2002). DOI 10.1088/0957-0233/13/5/305. URL <http://stacks.iop.org/0957-0233/13/i=5/a=305>
93. Pereira, F., Gharib, M., Dabiri, D., Modarress, D.: Defocusing digital particle image velocimetry: a 3-component 3-dimensional DPIV measurement technique. Application to bubbly flows. *Exp. Fluids* **29**(1), S78–S84 (2000). DOI 10.1007/s003480070010. URL <http://dx.doi.org/10.1007/s003480070010>
94. Pereira, F., Lu, J., Castaño Graff, E., Gharib, M.: Microscale 3D flow mapping with μ DDPIV. *Exp. Fluids* **42**, 589–599 (2007). DOI 10.1007/s00348-007-0267-5. URL <http://dx.doi.org/10.1007/s00348-007-0267-5>
95. Puccetti, G., Rossi, M., Morini, G.L., Kähler, C.J.: Sensitivity to shear stress of non-encapsulated thermochromic liquid crystal (TLC) particles for microfluidic applications. *Microfluid. Nanofluid.* **20**(1), 19 (2016). DOI 10.1007/s10404-015-1694-x. URL <http://dx.doi.org/10.1007/s10404-015-1694-x>
96. Raffel, M., Westerweel, J., Willert, C.E., Gharib, M., Kompenhans, J.: Analytical and experimental investigations of dual-plane particle image velocimetry. *Opt. Eng.* **35**(7), 2067–2074 (1996). DOI 10.1117/1.600695. URL <http://dx.doi.org/10.1117/1.600695>
97. Ragan, T., Huang, H., So, P., Gratton, E.: 3D particle tracking on a two-photon microscope. *J. Fluoresc.* **16**(3), 325–336 (2006). DOI 10.1007/s10895-005-0040-1. URL <http://dx.doi.org/10.1007/s10895-005-0040-1>
98. Rallabandi, B., Marin, A., Rossi, M., Kähler, C.J., Hilgenfeldt, S.: Three-dimensional streaming flow in confined geometries. *J. Fluid Mech.* **777**, 408–429 (2015). DOI 10.1017/jfm.2015.336. URL <https://doi.org/10.1017/jfm.2015.336>
99. Rohály, J., Lammerding, J., Frigerio, F., Hart, D.P.: Monocular 3-D active μ -PTV. In: 4th International Symposium on PIV. Göttingen, Germany (2001)
100. Rossi, M., Kähler, C.J.: Optimization of astigmatic particle tracking velocimeters. *Exp. Fluids* **55**(9), 1809 (2014). DOI 10.1007/s00348-014-1809-2. URL <http://dx.doi.org/10.1007/s00348-014-1809-2>
101. Rossi, M., Lindken, R., Hierck, B.P., Westerweel, J.: Tapered microfluidic chip for the study of biochemical and mechanical response of endothelial cells to shear flow at subcellular level.

- Lab Chip **9**, 1403–1411 (2009). DOI 10.1039/B822270N. URL <http://dx.doi.org/10.1039/B822270N>
102. Rossi, M., Lindken, R., Westerweel, J.: Optimization of multiplane μ PIV for wall shear stress and wall topography characterization. *Exp. Fluids* **48**, 211–223 (2010). DOI 10.1007/s00348-009-0725-3. URL <http://dx.doi.org/10.1007/s00348-009-0725-3>
 103. Rossi, M., Segura, R., Cierpka, C., Kähler, C.J.: On the effect of particle image intensity and image preprocessing on the depth of correlation in micro-PIV. *Exp. Fluids* **52**(4), 1063–1075 (2012). DOI 10.1007/s00348-011-1194-z. URL <http://dx.doi.org/10.1007/s00348-011-1194-z>
 104. Sadr, R., Anoop, K., Khader, R.: Effects of surface forces and non-uniform out-of-plane illumination on the accuracy of nPIV velocimetry. *Meas. Sci. Tech.* **23**(5), 055,303 (2012). DOI 10.1088/0957-0233/23/5/055303. URL <http://stacks.iop.org/0957-0233/23/i=5/a=055303?key=crossref.0d604a3da34abe9a910046b1125f2779>
 105. Santiago, J.G., Wereley, S.T., Meinhart, C.D., Beebe, D.J., Adrian, R.J.: A particle image velocimetry system for microfluidics. *Exp. Fluids* **25**(4), 316–319 (1998). DOI 10.1007/s003480050235. URL <http://dx.doi.org/10.1007/s003480050235>
 106. Segura, R., Cierpka, C., Rossi, M., Joseph, S., Bunjes, H., Kähler, C.J.: Non-encapsulated thermo-liquid crystals for digital particle tracking thermography/velocimetry in microfluidics. *Microfluid. Nanofluid.* **14**(3), 445–456 (2013). DOI 10.1007/s10404-012-1063-y. URL <http://dx.doi.org/10.1007/s10404-012-1063-y>
 107. Segura, R., Cierpka, C., Rossi, M., Kähler, C.J.: Thermochromic liquid crystals for particle image thermometry. In: Li, D (ed.) *Encycl. Microfluid. Nanofluid.* pp. 1–10. Springer US, Boston, MA (2013). DOI 10.1007/978-3-642-27758-0_1183-6. URL http://dx.doi.org/10.1007/978-3-642-27758-0_1183-6
 108. Segura, R., Rossi, M., Cierpka, C., Kähler, C.J.: Simultaneous three-dimensional temperature and velocity field measurements using astigmatic imaging of non-encapsulated thermo-liquid crystal (TLC) particles. *Lab Chip* **15**, 660–663 (2015). DOI 10.1039/C4LC01268B. URL <http://dx.doi.org/10.1039/C4LC01268B>
 109. Shinohara, K., Sugii, Y., Jeong, J.H., Okamoto, K.: Development of a three-dimensional scanning microparticle image velocimetry system using a piezo actuator. *Rev. Sci. Instrum.* **76**, 106109 (2005). DOI 10.1063/1.2114889. URL <http://dx.doi.org/10.1063/1.2114889>
 110. Snoeyink, C., Wereley, S.: Single-image far-field subdiffraction limit imaging with axicon. *Opt. Lett.* **38**(5), 625–627 (2013). DOI 10.1364/OL.38.000625. URL <http://ol.osa.org/abstract.cfm?URI=ol-38-5-625>
 111. Squires, T.M., Quake, S.R.: Microfluidics: Fluid physics at the nanoliter scale. *Rev. Mod. Phys.* **77**, 977–1026 (2005). DOI 10.1103/RevModPhys.77.977. URL <https://link.aps.org/doi/10.1103/RevModPhys.77.977>
 112. Stolz, W., Köhler, J.: In-plane determination of 3D-velocity vectors using particle tracking anemometry (PTA). *Exp. Fluids* **17**(1), 105–109 (1994). DOI 10.1007/BF02412811. URL <http://dx.doi.org/10.1007/BF02412811>
 113. Tien, W.H.: Development of multi-spectral three-dimensional micro particle tracking velocimetry. *Meas. Sci. Tech.* **27**(8), 084,010 (2016). DOI 10.1088/0957-0233/27/8/084010. URL <https://doi.org/10.1088/0957-0233/27/8/084010>
 114. Tien, W.H., Hove, Dabiri Danaeand, J.R., : Color-coded three-dimensional micro particle tracking velocimetry and application to micro backward-facing step flows. *Exp. Fluids* **55**(3), 1684 (2014). DOI 10.1007/s00348-014-1684-x. URL <http://dx.doi.org/10.1007/s00348-014-1684-x>
 115. Tien, W.H., Kartes, P., Yamasaki, T., Dabiri, D.: A color-coded backlighted defocusing digital particle image velocimetry system. *Exp. Fluids* **44**(6), 1015–1026 (2008). DOI 10.1007/s00348-007-0457-1. URL <http://dx.doi.org/10.1007/s00348-007-0457-1>
 116. Towers, C.E., Towers, D.P., Campbell, H.I., Zhang, S., Greenaway, A.H.: Three-dimensional particle imaging by wavefront sensing. *Opt. Lett.* **31**(9), 1220–1222 (2006). DOI 10.1364/OL.31.001220. URL <http://ol.osa.org/abstract.cfm?URI=ol-31-9-1220>

117. Volk, A., Rossi, M., Kähler, C.J., Hilgenfeldt, S., Marin, A.: Growth control of sessile microbubbles in PDMS devices. *Lab Chip* **15**, 4607–4613 (2015). DOI 10.1039/C5LC00982K. URL <http://dx.doi.org/10.1039/C5LC00982K>
118. Wereley, S.T., Meinhart, C.D.: Micron-resolution particle image velocimetry. In: Breuer, K.S. (ed.) *Microscale Diagnostic Techniques*, pp. 51–112. Springer, Berlin (2005). DOI 10.1007/3-540-26449-3_2. URL http://dx.doi.org/10.1007/3-540-26449-3_2
119. Wereley, S.T., Meinhart, C.D.: Recent advances in micro-particle image velocimetry. *Ann. Revi. Fluid Mech.* **42** (2010). doi:10.1146/annurev-fluid-121108-145427. URL <http://dx.doi.org/10.1146/annurev-fluid-121108-145427>
120. Westerweel, J., Geelhoed, P., Lindken, R.: Single-pixel resolution ensemble correlation for micro-PIV applications. *Exp. Fluids* **37**(3), 375–384 (2004). DOI 10.1007/s00348-004-0826-y. URL <http://dx.doi.org/10.1007/s00348-004-0826-y>
121. Willert, C.E., Gharib, M.: Three-dimensional particle imaging with a single camera. *Exp. Fluids* **12**(6), 353–358 (1992). DOI 10.1007/BF00193880. URL <http://dx.doi.org/10.1007/BF00193880>
122. Williams, S.J., Park, C., Wereley, S.T.: Advances and applications on microfluidic velocimetry techniques. *Micro Nano* **8**, 709–726 (2010). DOI 10.1007/s10404-010-0588-1. URL <http://dx.doi.org/10.1007/s10404-010-0588-1>
123. Yoon, S.Y., Khim, K.D., Kim, K.C.: Correlation of fluid refractive index with calibration coefficient for micro-defocusing digital particle image velocimetry. *Meas. Sci. Tech.* **22**(3), 037,001 (2011). DOI 10.1088/0957-0233/22/3/037001. URL <http://stacks.iop.org/0957-0233/22/i=3/a=037001>
124. Yoon, S.Y., Kim, K.C.: 3D particle and 3D velocity field measurement in a microvolume via the defocusing concept. *Meas. Sci. Tech.* **17**(11), 2897–2905 (2006). DOI 10.1088/0957-0233/17/11/006. URL <http://stacks.iop.org/0957-0233/17/i=11/a=006>
125. Yoshida, H.: The wide variety of possible applications of micro-thermofluid control. *Microfluid. Nanofluid.* **1**, 289–300 (2005). DOI 10.1007/s10404-004-0014-7. URL <http://dx.doi.org/10.1007/s10404-004-0014-7>
126. Yu, C.H., Yoon, J.H., Kim, H.B.: Development and validation of stereoscopic micro-PTV using match probability. *J. Mech. Sci. Tech.* **23**(3), 845–855 (2009). DOI 10.1007/s12206-008-1209-8. URL <http://dx.doi.org/10.1007/s12206-008-1209-8>
127. Zettner, C.M., Yoda, M.: Particle velocity field measurements in a near-wall flow using evanescent wave illumination. *Exp. Fluids* **34**(1), 115–121 (2003). DOI 10.1007/s00348-002-0541-5. URL <http://dx.doi.org/10.1007/s00348-002-0541-5>

Chapter 11

Applications: Boundary Layers

The following two experiments have been performed in the second half of the 1990s' in the DLR low turbulence wind tunnel (TUG), which is of an Eiffel type. Screens in the settling chamber and a high contraction ratio of 15:1 lead to a low turbulence level in the test section (cross section $0.3 \times 1.5 \text{ m}^2$). The basic turbulence level in the test section of the TUG of $Tu = 0.06\%$ (measured by means of a hot wire) allows the investigation of acoustically excited transition from laminar to turbulent flow as well as turbulent boundary layers that develop in the relatively long test section. The flow was seeded in the settling chamber upstream of the screens used to reduce the turbulence of the wind tunnel flow.

11.1 Boundary Layer Instabilities

Contributed by:

C. Kähler and J. Kompenhans

In the case of periodic flows, the conditional sampling technique can be utilized in order to record instantaneous velocity vector maps always at the same phase angle. The excitation of the periodic process and the recording sequence must be phase locked. As an example for the application of conditional sampling, the investigation of instabilities in a boundary layer will be described.

The transitional process in a boundary layer is determined by a mechanism of generation and interaction of various instabilities. Small oscillations may cause primary instability – two-dimensional waves, the Tollmien–Schlichting (TS) waves. The growth of such TS waves leads to a streamwise periodic modulation of the basic flow, which gets sensitive to three-dimensional, spanwise periodic disturbances. These disturbances are amplified and lead to a three-dimensional distortion of the TS waves

An overview of the Digital Content to applications on boundary layers can be found at [\[DC11.1\]](#).

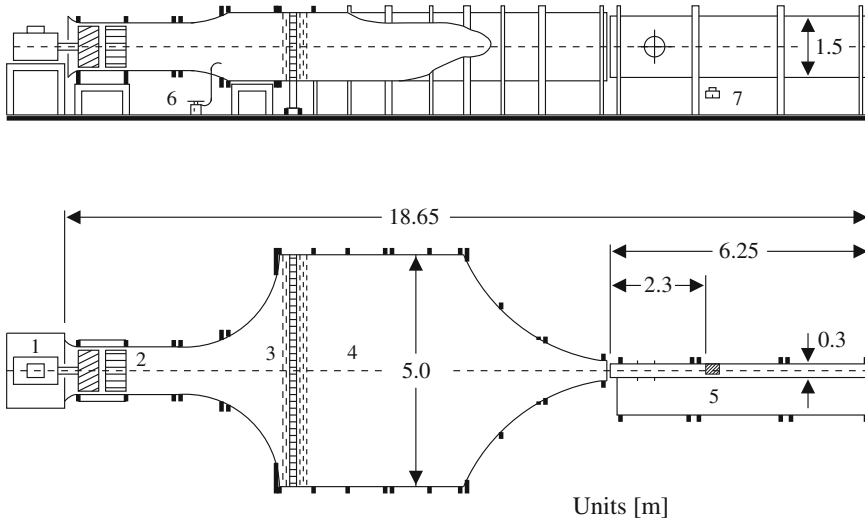


Fig. 11.1 Low turbulence wind tunnel

and farther downstream to the generation of three-dimensional Λ vortices. The extension of the knowledge about this mechanism enables the prediction and control of transition as required for applications in fluid mechanical engineering.

In order to study the behavior of instabilities, quantitative data of velocity fields with known initial conditions have been acquired in a flat plate boundary layer, in the TUG wind tunnel (see Fig. 11.1). In order to get reproducible and constant conditions for the development of the instabilities it is necessary to know the initial amplitude of the velocity fluctuations at the beginning of the observation area [34]. In the experiment of WIEGEL & FISCHER this is achieved by introducing controlled disturbances by means of a device for acoustic excitation which consists of a single spanwise slot for the controlled input of two-dimensional disturbances and 40 separate slots (positioned spanwise as well) for the input of controlled three-dimensional disturbances. The velocity at the outer edge of the boundary layer was about $U = 12$ m/s. The average free stream turbulence level was $Tu = 0.065\%$. The light sheet (thickness $\delta_z = 0.5$ mm in the observation area) was oriented parallel to the plate. Its height above the plate could be varied but was usually 0.5 mm in the experiment. The observation area was 70×70 mm². The PIV parameters used for this investigation are listed in Table 11.1.

By applying different input signals to the acoustic excitation it was possible to excite different transition types. We mention here the *fundamental type*, the *subharmonic type* and the *oblique type*. Figure 11.2 presents the phase locked field of the instantaneous velocity fluctuations ($U - U_{\text{mean}}, V$) obtained by exciting the *oblique type* for two different disturbances. The Λ -vortices exhibit in an aligned pattern. The spanwise wavelength of these Λ -vortices (here ≈ 20 mm) matches with the wavelength of the controlled input of the 3D-waves.

Table 11.1 PIV recording parameters for boundary layer instabilities

Flow geometry	Parallel to light sheet and plate
Maximum in-plane velocity	$U_{\max} \approx 12 \text{ m/s}$
Field of view	$70 \times 70 \text{ mm}^2$
Interrogation volume	$1.9 \times 1.9 \times 0.5 \text{ mm}^3 (H \times W \times D)$
Dynamic spatial range	$\text{DSR} \approx 31 : 1$
Dynamic velocity range	$\text{DVR} \approx 137 : 1$
Observation distance	$Z_0 \approx 0.6 \text{ m}$
Recording method	Dual frame/single exposure
Ambiguity removal	Frame separation (frame-straddling)
Recording medium	Full frame interline transfer CCD
Recording lens	$f = 60 \text{ mm}, f_{\#} = 2.8$
Illumination	Nd:YAG laser ^a 320 mJ/pulse
Pulse delay	$\Delta t = 80 \mu\text{s}$
Seeding material	Oil droplets ($d_p \approx 1 \mu\text{m}$)

^aFrequency doubled

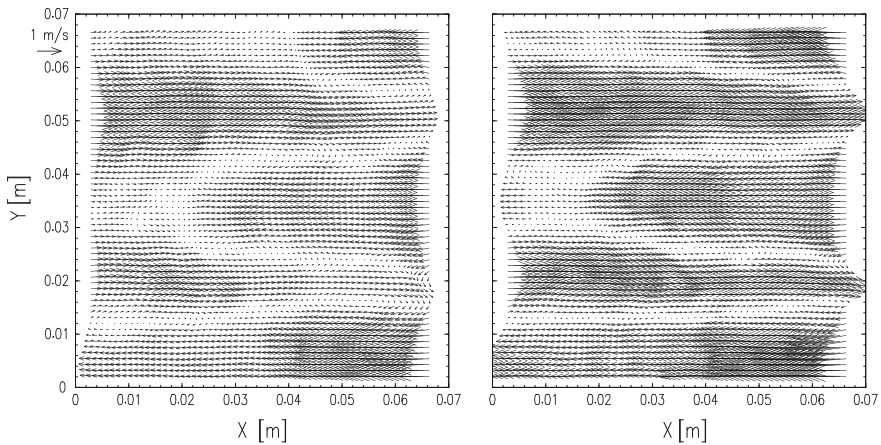


Fig. 11.2 Field of instantaneous velocity fluctuations of boundary layer instabilities above a flat plate for two different amplitudes of the input signal

The direction of the flow is from left to right. The mean velocity U_{mean} (calculated by averaging over all velocity vectors in the recording) has been subtracted from all velocity vectors in order to show the fluctuating components of the velocity vector field.

11.2 Near Wall Turbulent Boundary Layer

Contributed by:

C. Kähler and J. Kompenhans

The following PIV application performed in 1996 in a turbulent boundary layer at the wall of a flat plate illustrates two problems: obtaining PIV data close to a wall and recovering PIV data even in a flow with gradients (due to the velocity profile of the boundary layer).

In the present series of experiments the measurement position was 2.3 m downstream of a tripping region in the low-turbulence wind tunnel (see Fig. 11.1) at the DLR-Göttingen research center [17]. At this position the turbulent boundary layer thickness δ was of the order of 5 cm, of which the lower 3 cm was imaged. At free stream velocities of 10.3, 14.9 and 19.8 m/s between 90 and 100 PIV image pairs were recorded. The evaluation of the recordings were made without windows shifting and window deformation which were not available at that time. By removing a constant velocity profile of $U_{\text{ref}} = 8 \text{ m/s}$ from the PIV data set, the small scale structures in the boundary layer are highlighted as can be seen in Fig. 11.3. It is remarkable how close to the wall, the velocity data could be recovered. The PIV parameters used for this investigation are listed in Table 11.2.

In the first part of the evaluation the boundary layer profile and the RMS components of the velocity fluctuations were calculated as an average over all PIV recordings. These averaged quantities agree very well with the results from theory and pointwise velocity measurements as carried out by means of a hot wire.

Fig. 11.3 Field of instantaneous velocity fluctuations in a fully turbulent boundary layer, $(U - U_{\text{ref}}, V)$. Position of the wall at $Y = 0$

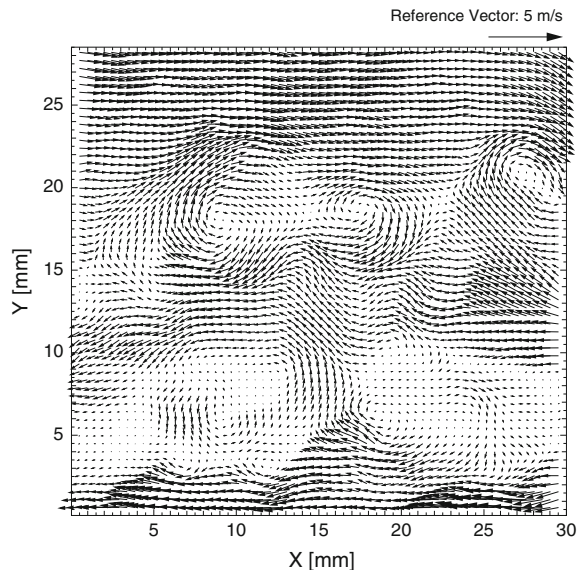
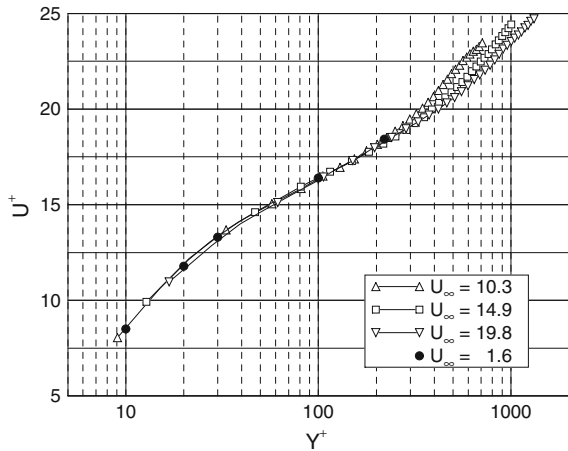


Table 11.2 PIV recording parameters for turbulent boundary layer over a flat plate with zero pressure gradient

Flow geometry	Parallel to light sheet
Maximum in-plane velocity	$U_\infty = 10.3, 14.9, 19.8$ m/s
Field of view	30×30 mm ²
Interrogation volume	$2.0 \times 2.0 \times 1.0$ mm ³ ($H \times W \times D$)
	$2.0 \times 1.0 \times 1.0$ mm ³ ($H \times W \times D$)
	$2.0 \times 0.5 \times 1.0$ mm ³ ($H \times W \times D$)
	$1.0 \times 1.0 \times 1.0$ mm ³ ($H \times W \times D$)
Dynamic spatial range	DSR $\approx 31 : 1$
Dynamic velocity range	DVR $\approx 44 : 1$
Observation distance	$Z_0 \approx 1.5$ m
Recording method	Dual frame/single exposure
Ambiguity removal	Frame separation (frame-straddling)
Recording medium	Full frame interline transfer CCD
Recording lens	$f = 180$ mm, $f_\# = 2.8$
Illumination	Nd:YAG laser ^a , 70 mJ/pulse
Pulse delay	$\Delta t = 7 - 20$ μ s
Seeding material	Oil droplets ($d_p \approx 1$ μ m)

^aFrequency doubled

Fig. 11.4 Mean velocity profiles, scaled with inner variables (averaged over 100 PIV recordings)



The nondimensional velocity profiles given in Fig. 11.4 start near the outer edge of the viscous sublayer ($Y^+ \approx 10$) and extend well into the region where the large scale structures in the boundary layer cause a departure from the logarithmic profile ($Y^+ \approx 200$).

As already mentioned, the strong velocity gradients within the interrogation areas close to the wall have mainly two effects.

First, due to the inhomogeneous displacement of paired particle images, the amplitude of the signal peak R_{D^+} is diminished. In addition, the diameter of the peak is broadened in the direction of shear. Therefore the velocity variation in the near wall region will decrease the likelihood of detection of the displacement peak.

Second, besides these experimental difficulties it has to be carefully checked whether the velocity vector assigned to the center of the interrogation window really represents the flow velocity at this location also in the presence of velocity gradients, as has been obtained by averaging over the interrogation window (see Fig. 7.19).

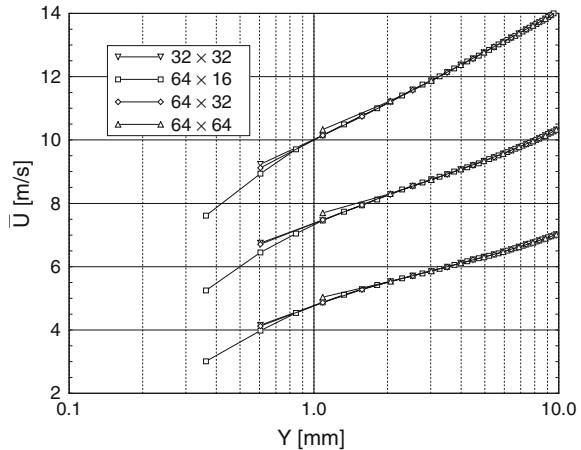
To investigate the effect of different interrogation area size on the number of outliers all PIV recordings were interrogated four times. The result can be seen in Table 11.3 (for more details see [17]). The number of outliers in the 64×32 window is smaller compared to the other cases, because the number of particles is two times larger. The fraction of outliers is only of the order of 1% in the worst case, which clearly shows the reliability of the measurement technique.

Figure 11.5 represents the semilogarithmic mean velocity profiles as a function of the distance from the wall. For wall distances $Y \geq 2$ mm the mean velocity is

Table 11.3 Number of outliers as a function of the interrogation area size, shape and free stream velocities

$\Delta x_0 \times \Delta y_0$ [pixel]	Outliers [%] [10.3 m/s]	Outliers [%] [14.9 m/s]	Outliers [%] [19.8 m/s]
32×32	1.07	1.00	1.26
64×16	0.72	0.58	1.03
64×32	0.20	0.21	0.30
64×64	0.14	0.19	0.17

Fig. 11.5 Spatial resolution effects in the near wall region (averaged over 100 PIV recordings)



independent of the size of the interrogation window for three different measurements ($U_\infty = 10.3, 14.9$ and 19.8 m/s).

However, for $0 < Y < 2$ mm the curves do not coincide due to the different averaging. The extension of the interrogation windows in the Y direction is mainly responsible for this. Rectangular windows (extending parallel to the wall) show better performance as compared to square windows.

Windows deformation techniques for PIV evaluation as available nowadays have considerably contributed to the improvement of the data quality in boundary layers and shear flows. However, it should be stressed that a test on scale sensitivity (size and shape of interrogation window) of the velocity data and the number of outliers should always be carried out in order to assess the data quality.

11.3 Boundary Layer Characterization

Contributed by:

C. Willert

The boundary layer measurements described in the following were performed in the low speed wind tunnel of the DLR in Göttingen which is of an Eiffel type with a cross section of 1×1 m². The measurements presented here intend to demonstrate the potential of PIV in obtaining statistically converged turbulence data, here in a wall-normal direction using a combination of high-speed imaging and high image magnification. By limiting the field of view in streamwise direction to only a few millimeters (≈ 200 pixel), a large number of PIV images ($\mathcal{O}(10,000)$ to $\mathcal{O}(100,000)$) can be acquired at kilohertz rates resulting in continuous sequences that enable spatio-temporal analysis of the data. The measurement technique is described in further detail in [35].

The measurement location is about 2.0 m downstream of a boundary layer tripping device (zig-zag tape) at the end of the convergent section immediately upstream of the test section. The closed circuit wind tunnel flow is seeded with atomized DEHS droplets of about $1 \mu\text{m}$ size. Illumination is provided by a cost-efficient, continuous-wave (CW) multi-diode laser that can be externally modulated at up to 100 kHz. Synchronization between high-speed camera and laser pulses is achieved using a micro-controller (ATMEL AT-MEGA2560).

Details regarding image acquisition are provided in Table 11.4. Noteworthy is the use of macro-lenses with long working distances to achieve image magnifications up to unity. For displacement retrieval the images are processed with high-aspect ratio rectangular sampling windows in order to reach a high spatial resolution in wall-normal direction (Table 11.5).

Figure 11.6 presents the mean stream-wise velocity profile scaled in viscous units using the friction velocity u_τ .

Table 11.4 PIV recording parameters for turbulent boundary layer over a flat plate

Flow geometry	Parallel to light sheet	
Illumination	Modulated CW laser, 10 W at 520 nm	
Seeding material	DEHS droplets ($d_p \approx 1 \mu\text{m}$)	
Recording method	Dual frame/single exposure	
Ambiguity removal	Frame separation (frame-straddling)	
Recording medium	High-speed CMOS	
Pixel size	10 μm	
Recording lenses	$f = 100 \text{ mm}/f_{\#}2.8$	400 mm/ $f_{\#}8.0$
Magnification	$M = 42.4$	$M = 99.8 \mu\text{m}/\text{pixel}$
	$M = 0.47$	$M = 1.10$
Observation distance	$Z_0 \approx 0.55 \text{ m}$	
Maximum in-plane velocity	$U_{\infty} \approx 10.0 \text{ m/s}, 15.0 \text{ m/s}$	
Field of view ($W \times H$)	200 \times 2016	200 \times 1008 pixel
	4.7 \times 47.6	2.0 \times 10.1 mm^2
Interrogation area ($W \times H$)	64 \times 6	64 \times 6 pixel
	1.51 \times 0.142	0.641 \times 0.060 mm^2
Acquisition rate	$f_{\text{acq}} = 2000 \text{ Hz}$	4000 Hz
Number of samples	$N_{\text{tot}} = 31\,739$	63\,464
Dynamic spatial range ^a	DSR > 300 : 1	
Dynamic velocity range ^b	DVR > 300 : 1	
Pulse delay	$\Delta t = 80 \mu\text{s}$	40 μs
Pulse width	$\tau = 20 \mu\text{s}$	15 μs

^aIn wall-normal direction^bIn stream-wise direction

$$u_{\tau} = \sqrt{\frac{\tau_w}{\rho}} = \sqrt{\nu \left. \frac{\partial u}{\partial y} \right|_0} \quad (11.1)$$

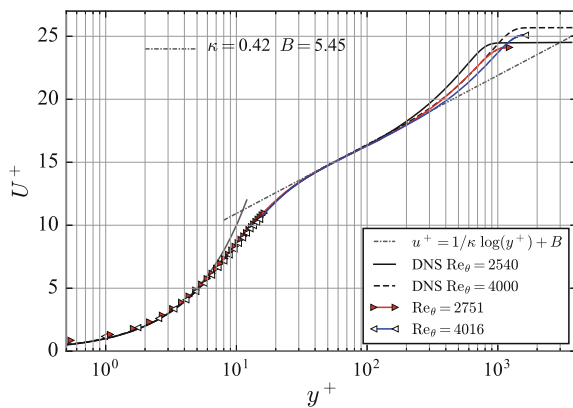
where $\partial u/\partial y|_0$ is the gradient of the stream-wise velocity right at the wall. With sufficient imaging resolution this quantity can be estimated by tracking particles in the linear region of the viscous sublayer ($y < 5^+$) [35]. Alternatively, a fit of the data to direct numerical simulations (DNS) data in the buffer layer and logarithmic region can be used for the estimation.

For the present measurements the viscous sub-layer in the immediate vicinity of the wall is well resolved and matches the expected linear trend before deviating within the buffer layer ($y^+ > 5$). Overall the velocity profile and variances, shown in Fig. 11.7, match data from DNS for a zero pressure gradient turbulent boundary layer at similar Reynolds numbers [30, 32]. Similar agreement can be observed for the skewness and flatness (kurtosis) of the streamwise velocity fluctuation shown in Fig. 11.8, with a skewness of zero and flatness of 3 corresponding to a Gaussian distribution. Just as for the streamwise fluctuation $\langle u'u' \rangle^2$ noticeable deviations are

Table 11.5 Global parameters of the turbulent boundary layer measurement

Free stream velocity	U_∞	[m/s]	10.1	15.2
Boundary layer thickness	δ_{99}	[mm]	35.7	34.7
Displacement thickness	δ^*	[mm]	5.77	5.65
Momentum thickness	θ	[mm]	4.19	4.06
Shape factor	$H_{12} = \delta^*/\theta$		1.377	1.391
Wall shear rate	$\partial u/\partial y _0$	[s] ⁻¹	11 380	23 800
Friction velocity	u_τ	[m/s]	0.418	0.605
Friction coefficient	c_f		0.00343	0.00316
Reynolds number	Re_δ		23 400	34 300
Momentum Reynolds number	Re_θ		2 750	4 020
Shear Reynolds number	Re_τ		970	1 360
Wall unit	$y^+ = \nu/u_\tau$	μm	36.8	25.4
Integral time scale	T_I	ms	3.33	2.15
BL turnover time	$T_e = \delta_{99}/U_\infty$	ms	3.53	2.28

Fig. 11.6 Mean stream-wise velocity profile scaled with inner variables (viscous scaling) for a turbulent boundary layer at $Re_\theta = 2750$ and $Re_\theta = 4020$. For better visibility symbols are only shown for $y^+ < 15$



observed in the viscous sublayer ($y^+ < 5$) which can be attributed to both the spatial filtering effect of the PIV interrogation sample and the increased noise originating from light scattering from the glass surface.

Fig. 11.7 Profiles of Reynolds stresses for a turbulent boundary layer at $Re_\theta = 2750$ and $Re_\theta = 4020$. Legend as in Fig. 11.6. For better visibility symbols are only shown for $y^+ < 15$

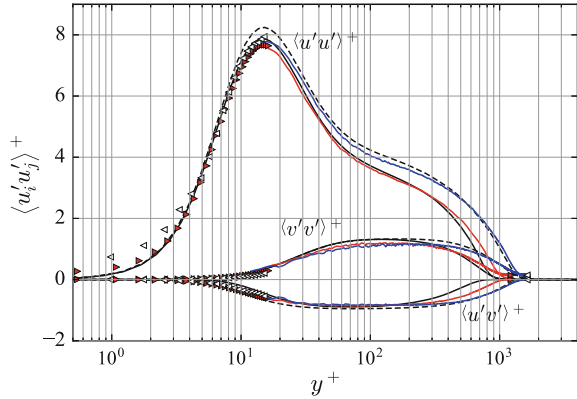
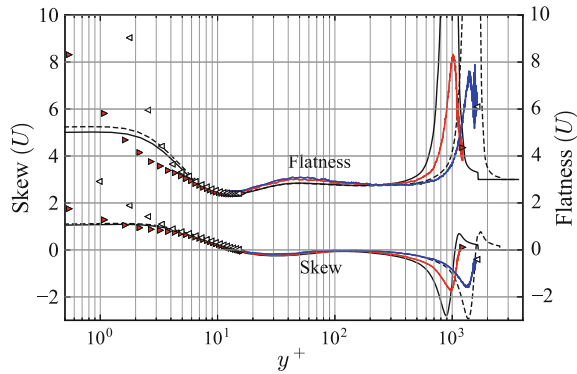


Fig. 11.8 Profiles of skewness and flatness of the stream-wise velocity for a turbulent boundary layer at $Re_\theta = 2750$ and $Re_\theta = 4020$. For better visibility symbols are only shown for $y^+ < 15$

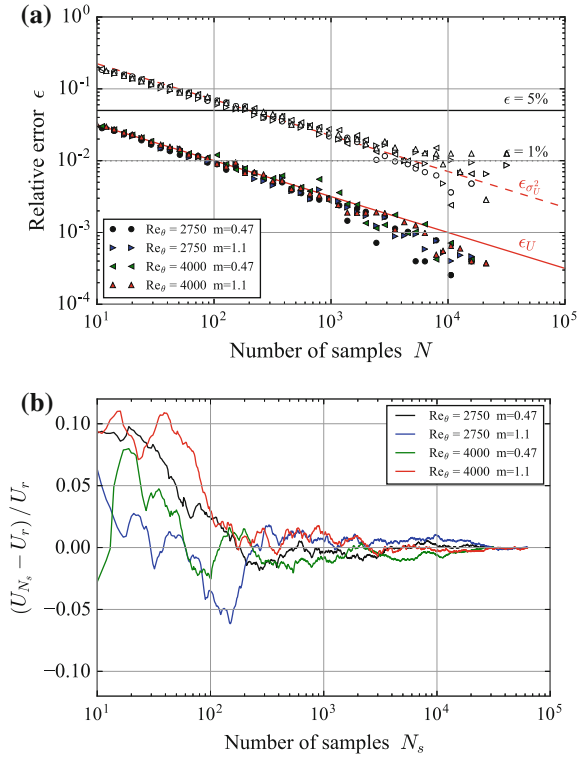


An estimate of the measurement uncertainty can be provided through the 95% confidence interval, which indicates a 95% certainty that the mean \bar{u} falls within the bounds

$$\bar{u} \pm 1.96 \sqrt{\frac{\sigma_u^2}{N}} \tag{11.2}$$

where σ_u^2 is the variance of the velocity U consisting of N independent samples [1, 2]. The convergence behavior presented in Fig. 11.9 was obtained using a bootstrapping approach (see e.g., [27]) that assumes that the mean of entire sample corresponds to the expected value of a sample of infinite length. Based on this figure the number of *independent* samples for convergence to a given uncertainty can be approximated. In this case a 1% uncertainty requires about 100 independent samples for mean and about 5000 samples for the variance. In this context it is important to observe that for time-resolved velocity data the number of independent samples N can be orders of magnitude smaller than the actual number of samples in the sequence N_{tot} , especially at increased sampling frequencies. Here the integral time scale T_I , obtained through integration of the auto-correlation of time-varying velocity $u(t)$,

Fig. 11.9 **a** relative error of mean and variance of streamwise velocity U at $y^+ = 100$ with respect to number of samples; **b** convergence behaviour of the streamwise velocity at $y^+ = 100$ for selected image sequences at two Reynolds numbers and two magnifications



can be used to estimate the effective number of independent samples in a sequence of temporal length T :

$$N_{\text{eff}} = \frac{T}{2T_I} \tag{11.3}$$

An alternative estimate for the number of independent samples can be obtained using the number of eddy turn-over times of the boundary layer flow T_e :

$$N_{\text{eff}} = \frac{T U_\infty}{T_e} \tag{11.4}$$

As presented in Table 11.6 the values of T_I and T_e are of similar magnitude suggesting that the boundary layer turn-over time is suitable for the estimation of the number of independent samples N_{eff} . The overall convergence of the measurands can be further improved proportional to $1/\sqrt{M}$ by averaging M independent sequences of equal length [27]. This is of particular relevance when computing frequency spectra from the data [26].

Table 11.6 Uncertainty estimates based on 95% confidence interval of mean and variance of the streamwise velocity at $y = 100^+$

Re_θ	Magn. m	Tot. Samples N_{tot}	Eff. samples N_{eff}	Uncert. Mean ϵ_U (%)	Uncert. Variance $\epsilon_{\sigma_U^2}$ (%)
2750	1.1	63 464	2382	0.48	3.52
4020	1.1	63 464	4087	0.39	1.74

11.4 Turbulent Boundary Layer Analysis by Means of Large-Scale PIV and Long-Range μ PTV

Contributed by:

N. Reuther and C.J. Kähler

The investigation of turbulent boundary layer flows is of great importance from both the scientific and technological point of view. In aerodynamics turbulent boundary layers are of major interest as they determine the drag of aircrafts and the separation characteristics of airfoils. In recent years the observation of very large scale coherent flow motions has achieved a lot of scientific attention because a manipulation of these so-called superstructures may help to reduce the drag and to delay flow separation. Furthermore, their existence might explain the development of a second peak in the streamwise turbulent intensity profile at high Reynolds numbers in the outer layer, observed by FERNHOLZ & FINLEY [12]. The average length of these structures is about 8 boundary layer thicknesses but they can be much longer in a non-averaged or instantaneous representation. These structures have been well described in flat plate boundary layer flows with zero pressure gradient [5, 9, 16]. However, in most practical applications the pressure gradient is of paramount importance for the aerodynamic performance.

Since turbulent boundary layers subjected to pressure gradients were barely investigated in the past, more experimental data is needed. Hence, the aim of the experiment described subsequently is to investigate the behavior of superstructures subjected to pressure gradients. Moreover, statistically averaged quantities are of great interest in terms of pressure gradient flows and high Reynolds numbers as the scaling of the universal constants and the boundary layer profile with the pressure gradient is still under scientific discussion [24, 25]. In particular, resolving the near wall flow motion to determine the wall-shear-stress adequately is highly relevant in terms of determining the friction velocity u_τ which is important for scaling these types of flows. The application of PIV to measurements of high Re_τ turbulent boundary layer flows is also challenging due to the necessity to resolve a wide range of scales.

To realize a sufficiently large turbulent boundary layer with well-defined pressure gradients a 7 m long boundary layer model, which consists of two s-shaped deflections and a 4 m long flat plate part, was installed in the atmospheric wind tunnel at the Bundeswehr University Munich (AWM). A schematic of the wind tunnel

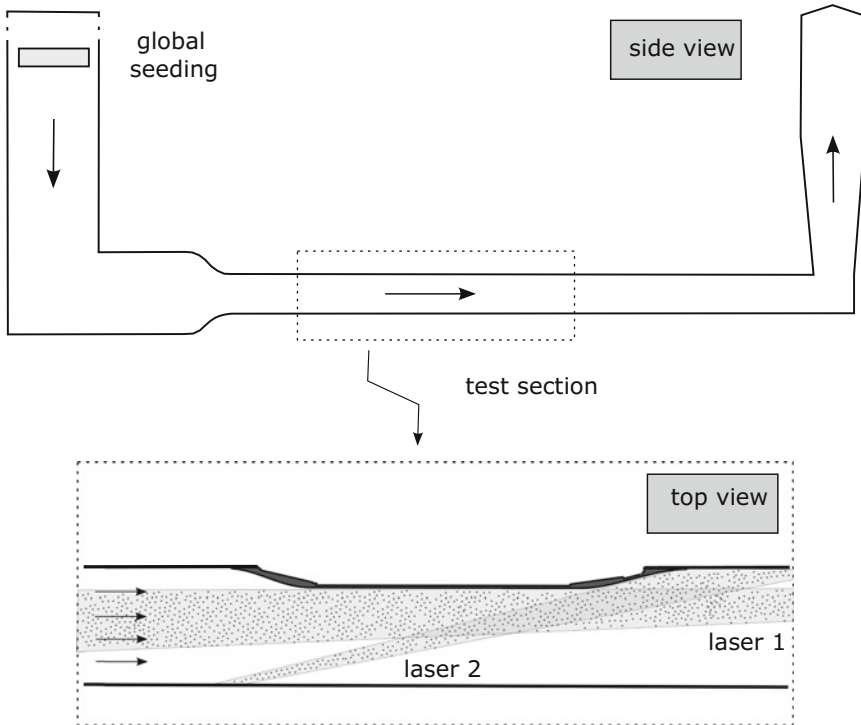


Fig. 11.10 Schematic of the atmospheric wind tunnel Munich (AWM) and the boundary layer experiment

and the boundary layer experiment, which was mounted to the side wall to avoid flow phenomena at the trailing edge affecting the measurement domain, is shown in Fig. 11.10.

Due to the size of the turbulent superstructures, large-scale PIV was used to fully resolve the total length even of the largest turbulent scales. The field of view was approximately 18 boundary layer thicknesses δ or 2.3 m in streamwise direction, respectively. In order to locally increase the resolution in the adverse pressure gradient region and to resolve the smaller scales for proper scaling, the 2D-2C PIV measurement was combined with long-range μ PTV, which is more suitable to the very near wall region where sharp velocity gradients are present [20, 21, 23]. The strong dynamic of the near wall turbulence is displayed best by means of high resolution volumetric PTV measurements, see [DC11.2], [DC11.3] and [3, 4] for details. Details about the PTV approach can be found in [8, 13, 14]. Figure 11.11 schematically shows the location of the large-scale and the long-range microscope camera. All PIV parameters used for this investigation are listed in Table 11.7. To analyze the Reynolds number sensitivity, experiments were performed at three different flow velocities.

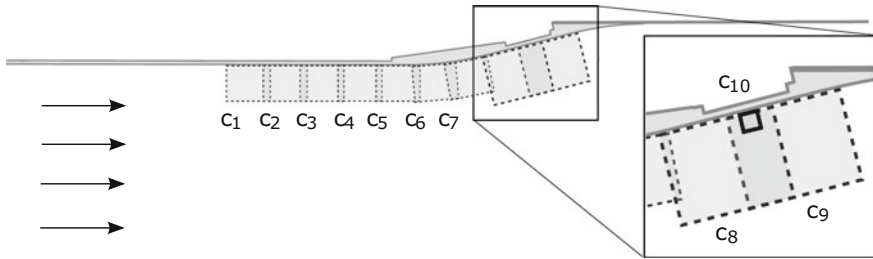


Fig. 11.11 Boundary layer experiment: dashed rectangles indicate FOV resolved by means of 9 large-scale cameras ($c_1 - c_9$) while solid rectangle indicates location of the long range microscope camera (c_{10})

Table 11.7 PIV recording parameters for the three Reynolds numbers investigated

Flow geometry	Nearly parallel to light sheet
Maximum in-plane velocity	$U_{\max} \approx 11.5 \text{ m/s}$
	$U_{\max} \approx 28.2 \text{ m/s}$
	$U_{\max} \approx 43.2 \text{ m/s}$
Field of view	$270 \times 320 \text{ mm}^2$ ($c_1 - c_7$)
	$370 \times 440 \text{ mm}^2$ ($c_8 + c_9$)
	$17 \times 20 \text{ mm}^2$ (c_{10})
Interrogation volume	$2.0 \times 2.0 \times 1 \text{ mm}^3$ ($H \times W \times D$) ($c_1 - c_7$)
	$2.7 \times 2.7 \times 1 \text{ mm}^3$ ($H \times W \times D$) ($c_8 + c_9$)
Observation distance	$Z_0 \approx 1.0 \text{ m}$
Recording method	Dual frame/single exposure
Ambiguity removal	Frame separation
Recording medium	sCMOS
Recording lens	$f = 35/50/180 \text{ mm}$ ($c_1 - c_7/c_8 + c_9/c_{10}$)
Illumination	Nd:YAG laser, 400 mJ/pulse
Pulse delay	160/70 μ s ($c_1 - c_9/c_{10}$)
	70/30 μ s
	40/20 μ s
Seeding material	Oil droplets ($d_p \approx 1 \mu\text{m}$)

To achieve a homogeneous seeding density in the test section DEHS particles, with an average size of approximately $1 \mu\text{m}$ [19], were added to the flow in the intake tower of the blow-down wind tunnel. Particularly for the high Reynolds number case multiple seeding generators were required to obtain an adequate seeding density as well for large-scale PIV as close to the wall in the adverse pressure gradient region for particle tracking. Illuminating the particles in the experiment described is challenging for two reasons. Firstly, undesirable reflections at the wall must be avoided in order to resolve the flow velocity close to the wall. This is very difficult or even impossible to realize for curved geometries as a tangential model illumination

is required to avoid reflections at metal surfaces [18, 23]. Secondly, setting up a light sheet with a constant thickness, ideally approximately 1 mm, over more than 2 m is demanding. Hence, to overcome these difficulties, two Nd:YAG lasers were used to illuminate the particles in the region of interest: One illuminating the flat plate part tangentially and one illuminating the pressure gradient region as indicated in Fig. 11.10. To prevent reflections the aluminum model was polished additionally as this allows to suppress reflections nearly totally as shown in [23]. To keep the light sheet thickness constant along the field of view, long working distances and adequate long focal length lenses are required. Moreover, ensuring a perfect overlap between the two laser sheets aligned separately is of great importance as well as avoiding vibrations of both laser sheets.

To capture the full boundary layer instantaneously, 9 sCMOS cameras, arranged side by side, were equipped with 50 mm lenses ($c_1 - c_7$) and 35 mm lenses ($c_8 + c_9$), respectively, where the boundary layer thickness increases significantly. The long-range microscope PTV camera was equipped with a 180 mm lens and two tele-converters, each with amplification of factor 2, resulting in an effective focal length of 720 mm. Usually special long-range microscopes are used for the imaging but using low cost tele-converters leads often to similar particle images, in terms of shape and intensity, than expensive long-range microscopes. Thus, individual field of views of $0.27 \times 0.32 \text{ m}^2$ (50 mm lens), $0.37 \times 0.44 \text{ m}^2$ (35 mm lens) and $0.017 \times 0.02 \text{ m}^2$ (180 mm lens/2 tele-converters), respectively, were realized based on a working distance of approximate 1 m. Since strong velocity gradients are present in case of boundary layer flows, choosing an adequate pulse delay requires special care. In this case, the flow velocity and thus the particle displacement additionally decreases in streamwise direction due to increased effect of the pressure gradient. Hence, the local particle displacement, or in other words the pulse delay, was adjusted to guarantee relatively low measurement uncertainties over the whole field of view by allowing an average particle image shift of 15 pixel in the outer flow.

Statistical averaged quantities were investigated based on 20,000 double-frame images in case of the large-scale and 30,000 double-frame images in case of long-range microscope camera, respectively. The large number of samples is required to obtain statistically converged values of higher order moments according to [22]. Single large-scale PIV recordings were evaluated by using iterative multi-pass window-correlation approaches with image deformation. The final interrogation windows size was 16×16 pixel with 50 % overlap. In contrast, the long-range microscope data was evaluated by means of state-of-art PTV algorithms which is beneficial to avoid bias errors due to a spatial averaging but also to get velocity information closer to the wall [20, 21]. Subsequently, the single vector fields of the 9 large scale FOVs were stitched by interpolating the overlapping regions in Matlab. Therefore, an accurate calibration and perfect alignment of each camera is an indispensable requirement in order to avoid aberrations and thus unpleasant transitions of the individual FOVs.

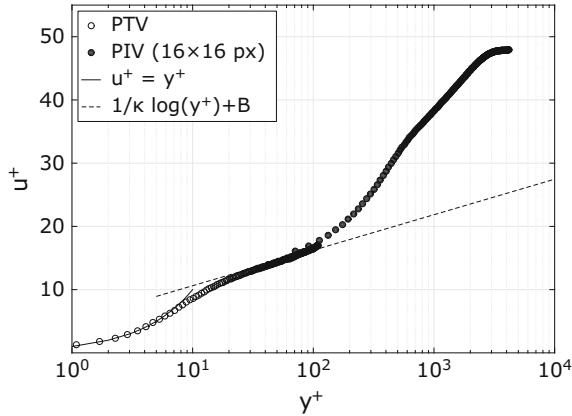


Fig. 11.12 Mean boundary layer velocity profile scaled in inner units for the low Re case ($U_\infty = 10$ m/s)

By combining both, large-scale PIV and long-range μ PTV, respectively, the inner as well as outer region of the turbulent boundary layer could be sufficiently well resolved to determine all relevant quantities for the scaling properly. The mean velocity profile scaled in inner variables is shown in Fig. 11.12. Experimental data of the large-scale PIV provides data down to $Y^+ \approx 70$ ($1/Y^+ \approx 35 \mu\text{m}$), while the long-range μ PTV resolves the inner region, in other words the viscous sublayer, the buffer and the logarithmic layer up to $Y^+ \approx 100$. Thus, there is a small region where the data obtained overlaps ($70 < Y^+ < 100$). As can be seen in Fig. 11.12, velocities obtained in this region by means of window correlation are slightly higher than the ones obtained by particle tracking. Strong velocity gradients exist particularly in the near wall region, which significantly decrease the PIV measurement accuracy as the vector assigned to the center of the interrogation window does not adequately represent the flow velocity at this location, see [21]. Hence, flow velocities obtained by means of PIV in proximity to the wall were slightly over predicted.

Figure 11.13 represents the streamwise turbulent intensity profile in the adverse pressure gradient region. Here, the turbulent intensities are slightly under predicted by using PIV due to averaging over the interrogation window. Hence, small-scale fluctuations are barely resolved by means of large-scale PIV. However, a fairly good agreement was obtained for the overlapping region. Small as well as the large-scale fluctuation were adequately resolved by combining large-scale PIV and long-range microscope PTV. In terms of turbulent boundary layer research, it is interesting to note that in the adverse pressure gradient region even at lower Reynolds numbers a second outer layer peak evolves at a similar location where FERNHOLZ & FINLEY observed a second outer layer peak for high Reynolds number zero pressure gradient flows [12]. It is assumed by some researchers that this peak is associated with the superstructures.

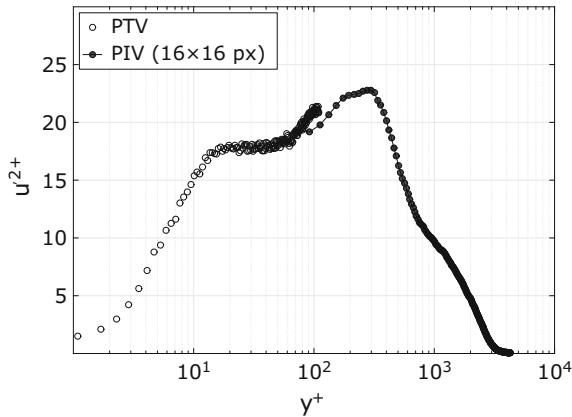


Fig. 11.13 Streamwise turbulent intensity profile scaled in inner units for the low Re case ($U_\infty = 10$ m/s)

Due to their three-dimensional nature, analyzing the coherent large-scale superstructures is challenging. However, in order to analyze their approximate streamwise extent, it is sufficient to characterize the projection of the structures in the measurement plane. Such an instantaneous projection is shown in Fig. 11.14, where instantaneous streamwise velocity fluctuations resolved by the multi-camera approach are presented. Here, the black line indicates the instantaneous turbulent/non-turbulent interface calculated based on local flow velocities [6]. This figure demonstrates the necessity of a multiple cameras approach to adequately resolve the turbulent superstructures, since the streamwise extent of an individual structure is multiple boundary layer thicknesses long. To understand the flow physics with respect to superstructures, average properties are of interest rather than characteristics of individual structures. Thus, spatial correlations of streamwise velocity fluctuations were performed for various wall-normal and streamwise locations, respectively. Results are shown in Fig. 11.15 for correlation points located in the zero- (ZPG), favorable (FPG) and adverse pressure gradient region (APG). Comparing the behavior of the average streamwise extent to the pressure gradient reveals that large-scale motions subjected to negative pressure gradients seem to gain size dependent on the pressure gradient. In contrast, motions subjected to positive pressure gradients seem to decrease in streamwise extent. As shown in [15], the shortening and lengthening of the superstructures can be linked to the decreasing and increasing edge velocity.

In summary, it can be stated that large-scale flow measurements with high spatial resolution are technically possible by installing multiple cameras side by side. However, this requires a light sheet of constant thickness along the full field of view. By using long distances between the laser and the measurement position and long focal length lenses, light sheets of a thickness of 1 mm over 2 m can be generated. To avoid wall reflections a polished model surface in combination with tangential model illumination is required. The latter cannot be done if the model is curved. However,

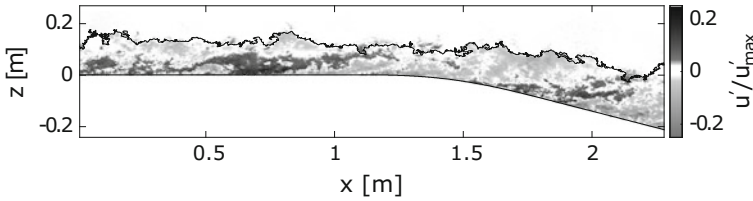


Fig. 11.14 Streamwise velocity fluctuation field of the FOV realized by means of 9 sCMOS cameras. Black line indicates instantaneous turbulent/non-turbulent interface

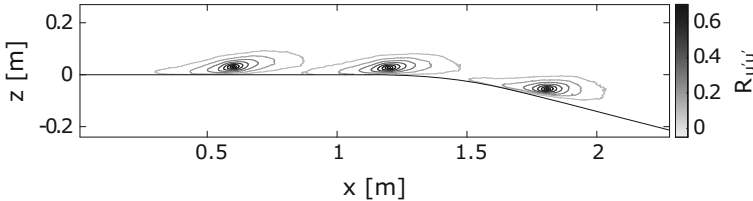


Fig. 11.15 Two-point correlation results obtained for correlation points in the ZPG, FPG and APG. Contours are plotted for 0.2–0.9 in intervals of 0.1

by combining several independent double pulse lasers whose light sheets overlap perfectly in the measurement location, it was possible to generate an almost tangential illumination along the complete region of interest with minimal wall reflections. Intensity variations due to the intensity overlap did not bias the results. Nevertheless, perfect alignment of the camera systems and accurate calibration of the single FOVs was the fundamental prerequisite for stitching individual instantaneous vector fields after PIV evaluation. Moreover, by allowing an average particle image shift of 15 pixel in the outer flow, the measurement uncertainty was minimized as much as possible. However, close to the wall the PIV results are biased due to spatial averaging effects [20]. In order to measure the friction velocity for the inner scaling of the data a long-range microscope was used for the imaging of the particles and a PTV evaluation approach to avoid bias errors due to spatial averaging and to increase the spatial resolution in proximity to the wall. Recently, the technology was used to capture the boundary layer along a model with 16 cameras simultaneously, see [15].

11.5 Shock Wave/Turbulent Boundary Layer Interaction

Contributed by:

F. Scarano, R.A. Humble, B.W. van Oudheusden

The interaction between an oblique shock wave and a turbulent boundary layer (SWTBLI) creates a series of complicated flow phenomena, such as unsteady flow separation and shock/turbulence interaction that present unique experimental challenges [10, 31, 33]. The application of PIV in the supersonic flow regime presents

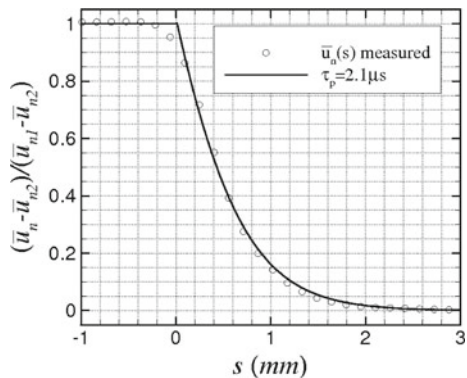
Table 11.8 PIV recording parameters for shock wave/turbulent boundary layer interaction on a flat plate (second set denotes parameters for boundary layer study.)

Flow geometry	Parallel to light sheet
Maximum in-plane velocity	$U_{\max} \approx 500 \text{ m/s}$ ($Ma = 2.1$)
Field of view	$124 \times 39 \text{ mm}^2$ ($16 \times 5 \text{ mm}^2$) ($W \times H$)
Interrogation volume	$1.9 \times 1.9 \times 1.5 \text{ mm}^3$ ($0.7 \times 0.08 \times 1.5 \text{ mm}^3$)
Dynamic spatial range	$DSR \approx 136 : 1$
Dynamic velocity range	$DVR \approx 400 : 1$
Observation distance	$z_0 \approx 600 \text{ mm}$ ($z_0 \approx 150 \text{ mm}$)
Recording method	Dual frame/single exposure
Ambiguity removal	Frame separation (frame-straddling)
Recording medium	Full frame interline transfer CCD 1376×1040 (432 active) pixel
Recording lens	$f = 60 \text{ mm}$, $f_{\#} = 8$ ($f = 105 \text{ mm}$, $f_{\#} = 8$)
Illumination	Freq. doubled Nd:YAG laser, 400 mJ/pulse at 532 nm
Pulse delay	$\Delta t = 2 \mu\text{s}$ ($0.6 \mu\text{s}$)
Seeding material	TiO_2 ($d_p \approx 400 \text{ nm}$)

the specific challenges of describing the high-speed flow in the presence of shock waves with sufficient accuracy, necessitating the quantitative evaluation of the tracer particle’s dynamic behavior [29]. The SWTBLI problem additionally requires the large velocity gradient close to the wall and the high-frequency turbulent fluctuations to be resolved. The PIV parameters used for this investigation are listed in Table 11.8.

The particle tracer relaxation time/length is a crucial parameter dictating the spatio-temporal resolution of the measurement. It is directly evaluated by measuring the particle velocity profile across a planar steady shock wave. Figure 11.16 shows the normal velocity profile against the shock-normal abscissa s , and returns a particle relaxation time of $\tau_p = 2.1 \mu\text{s}$. The corresponding frequency response is

Fig. 11.16 Normal velocity profile against shock-normal abscissa s



$f_p \approx 0.5$ MHz. The Stokes number $St = \tau_p/\tau_{flow}$ ($\tau_{flow} = \delta/U_\infty$) expresses the fidelity of particle tracers in the specific flow experiment [28]. For the present case $St = 0.06$, yielding an RMS tracking error below 1%.

The flow statistical properties are evaluated on the basis of 500 PIV recordings acquired at 10 Hz in a supersonic wind tunnel of $270(H) \times 280(W)$ mm² test section. The upstream mean boundary layer profile ($\delta_{99} = 20$ mm, $Re_\theta = 3.36 \times 10^4$) scaled with inner variables is shown in Fig. 11.17. The experimental data agree with the composite formula down to $y^+ \approx 200$. When the evaluation is carried out using high-aspect ratio interrogation windows (61×7 pixel) the wall-normal spatial resolution is improved extending the agreement to the overlap region ($y^+ \approx 80$, $y < 0.2$ mm).

The instantaneous recording depicted in Fig. 11.18 shows a non-uniform seeding particle concentration due to the density variation in the flow. The incident and reflected shock waves can be visualized by the increase in tracer particle density, whilst the boundary layer is highlighted by a comparatively lower seeding level. Laser light reflections from the wall were minimized during the experiment by illuminating almost tangent to the wall.

Fig. 11.17 Upstream mean boundary layer velocity profile

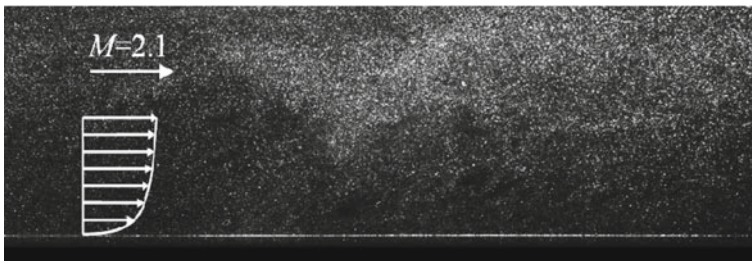
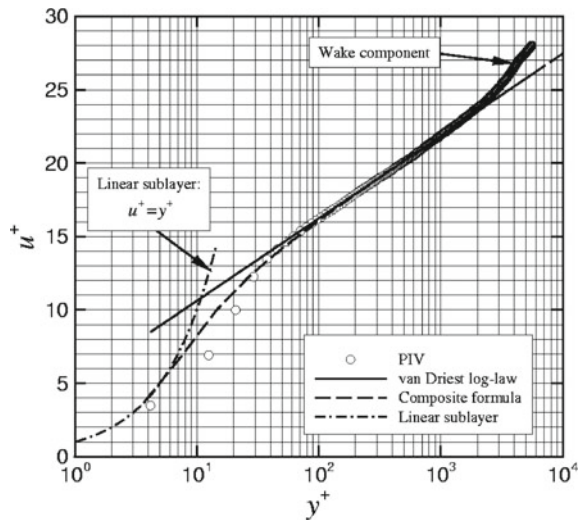


Fig. 11.18 Single PIV recording with mean velocity profile

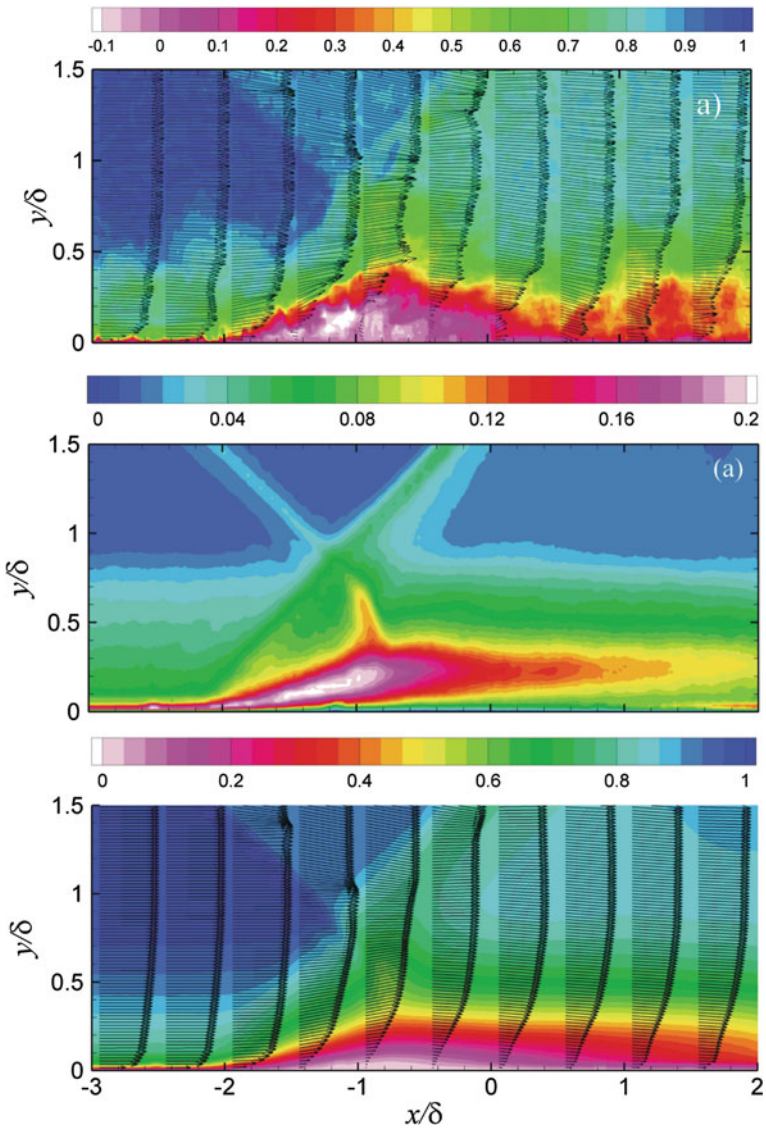


Fig. 11.19 Instantaneous stream-wise velocity distribution (top) and statistical fluctuations (middle). Mean velocity vector field (bottom)

An instantaneous stream-wise velocity distribution is shown in Fig. 11.19 (top). The incoming boundary layer has a clear intermittent nature. The global structure of the interaction is formed by the impinging shock penetrating the boundary layer, turning and weakening until it vanishes at the sonic line. The adverse pressure gradient generated by the shock causes a dilation of the subsonic layer, which causes a second compression wave system to emanate upstream of the impinging shock. The irregular shape of the separated region exhibits turbulent coherent structures, mostly originating from the separated shear layer instability. Downstream of the interaction these structures enhance the momentum mixing, which drives the boundary layer recovery.

The mean flow behavior is described by the averaged velocity field in Fig. 11.19 (middle). The incident and reflected shock waves are visible as a sharp flow deceleration and change of direction for the first, whereas the reflected shock exhibits a smoother spatial variation of the velocity due to its unsteady nature and the averaging effect. An inflection point prior to separation is visible in the boundary layer profile. However, from the mean velocity vector profiles no reverse flow can be inferred. After reattachment, the distorted boundary layer has approximately doubled its thickness and develops downstream with a relatively low rate of recovery.

The spatial distribution of the turbulence intensity magnitude $(\bar{u}^2 + \bar{v}^2)^{1/2}/U_\infty$ is depicted in Fig. 11.19 (bottom) and shows the turbulent properties of the incoming boundary layer, the increased level of fluctuations throughout the interaction region and its redevelopment downstream. The higher level of fluctuations associated to the impinging shock (approximately 4%) is typically encountered in these experimental conditions and is ascribed to the combined effect of the decreased measurement precision and to small fluctuations of the shock position. The increased level of fluctuations associated with the impinging shock penetrating the boundary layer is due to its interaction with turbulent coherent structures convected in this region. The reflected shock exhibits a clear unsteady behavior and relatively high levels of fluctuation, which in this case should not be regarded as turbulence. Two weak features downstream of the reflected shock (one parallel and the other roughly perpendicular to it) are due to optical aberration effects introduced by the inhomogeneous index of refraction field of this compressible flow [11].

References

1. Bendat, J.S., Piersol, A.G.: Random Data: Analysis and Measurement Procedures, 4th edn. Wiley, New York (2012). DOI 10.1002/9781118032428. URL <https://doi.org/10.1002/9781118032428>
2. Benedict, L.H., Gould, R.D.: Towards better uncertainty estimates for turbulence statistics. *Exp. Fluids* **22**, 129–136 (1996). DOI 10.1007/s003480050030. URL <https://doi.org/10.1007/s003480050030>
3. Bross, M., Kähler, C.J., (2016) Time-Resolved 3D-PTV Analysis of Near Wall Reverse Flow Events in APG Turbulent Boundary Layers. 18th International Symposium on Applications of Laser and Imaging Techniques to Fluid Mechanics, July 4–7, Lisbon, Portugal

4. Bross, M., Kähler, C.J., (2017) Three Dimensional Near-Wall Events in an Adverse Pressure Gradient Boundary Layer. 10th International Symposium on Turbulence and Shear Flow Phenomena (TSFP10), July 6–9, Chicago, USA
5. Buchmann, N.A., Kücükosman, Y.C., Ehrenfried, K., Kähler, C.J.: Wall pressure signature in compressible turbulent boundary layers. In: Stanislas, M., Jimenez, J., Marusic, I. (eds.) *Progress in Wall Turbulence 2*, ERCOFTAC Series, vol. 23, pp. 93–102. Springer, Cham (2015). DOI 10.1007/978-3-319-20388-1_8. URL https://doi.org/10.1007/978-3-319-20388-1_8
6. Chauhan, K., Philip, J., de Silva, C.M., Hutchins, N., Marusic, I.: The turbulent/non-turbulent interface and entrainment in a boundary layer. *J. Fluid Mech.* **742**, 119–151 (2014). DOI 10.1017/jfm.2013.641. URL <https://doi.org/10.1017/jfm.2013.641>
7. Cierpka, C., Scharnowski, S., Kähler, C.J.: Parallax correction for precise near-wall flow investigations using particle imaging. *Appl. Opt.* **52**(12), 2923–2931 (2013). DOI 10.1364/AO.52.002923. URL <https://doi.org/10.1364/AO.52.002923>
8. Cierpka, C., Lütke, B., Kähler, C.J.: Higher order multi-frame particle tracking velocimetry. *Exp. Fluids* **54**(5), 1533 (2013). DOI 10.1007/s00348-013-1533-3. URL <https://doi.org/10.1007/s00348-013-1533-3>
9. Dennis, D.J.C., Nickels, T.B.: Experimental measurement of large-scale three-dimensional structures in a turbulent boundary layer. Part 2 Long structures. *J. Fluid Mech.* **673**, 218–244 (2011). DOI 10.1017/S0022112010006336. URL <https://doi.org/10.1017/S0022112010006336>
10. Dolling, D.S.: Fifty years of shock-wave/boundary-layer interaction research: what next? *AIAA J.* **39**(8), 1517–1531 (2001). DOI 10.2514/2.1476. URL <https://doi.org/10.2514/2.1476>
11. Elsinga, G.E., van Oudheusden, B.W., Scarano, F.: Evaluation of aero-optical distortion effects in PIV. *Exp. Fluids* **39**(2), 246–256 (2005). DOI 10.1007/s00348-005-1002-8. URL <https://doi.org/10.1007/s00348-005-1002-8>
12. Fernholz, H.H., Finley, P.J.: The incompressible zero-pressure gradient turbulent boundary layer: an assessment of data. *Prog. Aerosp. Sci.* **32**, 245–311 (1996). DOI 10.1016/0376-0421(95)00007-0. URL [https://doi.org/10.1016/0376-0421\(95\)00007-0](https://doi.org/10.1016/0376-0421(95)00007-0)
13. Fuchs, T., Hain, R., Kähler, C.J. Double-frame 3D-PTV using a tomographic predictor. *Experiments in Fluids* **57**(11) (November, 2016). DOI 10.1007/s00348-016-2247-0. URL <https://doi.org/10.1007/s00348-016-2247-0>
14. Fuchs, T., Hain, R., Kähler, C.J.: Non-iterative double-frame 2D/3D particle tracking velocimetry. *Experiments in Fluids* **58**(9), 119 (August, 2017). <https://doi.org/10.1007/s00348-017-2404-0>. URL <https://doi.org/10.1007/s00348-017-2404-0>
15. Hain, R., Scharnowski, S., Reuther, N., Kähler, C.J., Schröder, A., Geisler, R., Agocs, J., Röse, A., Novara, M., Stanislas, M., Cuvier, C., Foucaut, J.M., Srinath, S., Laval, J., Willert, C., Klinner, J., Soria, J., Amili, O., Atkinson, C.: Coherent large scale structures in adverse pressure gradient turbulent boundary layers. In: 18th International Symposium on Applications of Laser Techniques to Fluid Mechanics Lisbon, Portugal, 04–07 July (2016). URL http://tces.dem.ist.utl.pt/lxaser/lxaser2016/finalworks2016/papers/03.7_5_135paper.pdf
16. Hutchins, N., Marusic, I.: Evidence of very long meandering features in the logarithmic region of turbulent boundary layers. *J. Fluid Mech.* **579**, 1–28 (2007). DOI 10.1017/S0022112006003946. URL <https://doi.org/10.1017/S0022112006003946>
17. Kähler, C.J.: Ortsaufgelöste Geschwindigkeitsmessungen in einer turbulenten Grenzschicht. Technical report, DLR, Göttingen, Germany (1997). DLR-FB-1997-32
18. Kähler, C.J.: High resolution measurements by long-range micro-PIV. VKI Lecture Series: Recent advances in Particle Image Velocimetry (2009). URL <https://store.vki.ac.be/lecture-series-monographs/measurement-techniques/recent-advances-in-particle-image-velocimetry.html>

19. Kähler, C.J., Sammler, B., Kompenhans, J.: Generation and control of tracer particles for optical flow investigations in air. *Exp. Fluids* **33**(6), 736–742 (2002). DOI 10.1007/s00348-002-0492-x. URL <https://doi.org/10.1007/s00348-002-0492-x>
20. Kähler, C.J., Scharnowski, S., Cierpka, C.: On the resolution limit of digital particle image velocimetry. *Exp. Fluids* **52**(6), 1629–1639 (2012). DOI 10.1007/s00348-012-1280-x. URL <https://doi.org/10.1007/s00348-012-1280-x>
21. Kähler, C.J., Scharnowski, S., Cierpka, C.: On the uncertainty of digital PIV and PTV near walls. *Exp. Fluids* **52**(6), 1641–1656 (2012). DOI 10.1007/s00348-012-1307-3. URL <https://doi.org/10.1007/s00348-012-1307-3>
22. Kähler, C.J., Scharnowski, S., Cierpka, C.: Highly resolved experimental results of the separated flow in a channel with streamwise periodic constrictions. *J. Fluid Mech.* **796**, 257–284 (2016). DOI 10.1017/jfm.2016.250. URL <https://doi.org/10.1017/jfm.2016.250>
23. Kähler, C.J., Scholz, U., Ortmanns, J.: Wall-shear-stress and near-wall turbulence measurements up to single pixel resolution by means of long-distance micro-PIV. *Exp. Fluids* **41**(2), 327–341 (2006). DOI 10.1007/s00348-006-0167-0. URL <https://doi.org/10.1007/s00348-006-0167-0>
24. Knopp, T., Buchmann, N.A., Schanz, D., Eisfeld, B., Cierpka, C., Hain, R., Schröder, A., Kähler, C.J.: Investigation of scaling laws in a turbulent boundary layer flow with adverse pressure gradient using PIV. *J. Turbul.* **16**(3), 250–272 (2015). DOI 10.1080/14685248.2014.943906. URL <https://doi.org/10.1080/14685248.2014.943906>
25. Knopp, T., Schanz, D., Schröder, A., Dumitru, M., Cierpka, C., Hain, R., Kähler, C.J.: Experimental investigation of the log-law for an adverse pressure gradient turbulent boundary layer flow at $Re_\theta = 10000$. *Flow Turbul. Combust.* **92**, 451–471 (2014). DOI 10.1007/s10494-013-9479-3. URL <https://doi.org/10.1007/s10494-013-9479-3>
26. Miller, J.D., Jiang, N., Slipchenko, M.N., Mance, J.G., Meyer, T.R., Roy, S., Gord, J.R.: Spatiotemporal analysis of turbulent jets enabled by 100-kHz, 100-ms burst-mode particle image velocimetry. *Exp. Fluids* **57**(12), 192 (2016). DOI 10.1007/s00348-016-2279-5. URL <https://doi.org/10.1007/s00348-016-2279-5>
27. Papageorge, M., Sutton, J.A.: Statistical processing and convergence of finite-record-length time-series measurements from turbulent flows. *Exp. Fluids* **57**(8), 1–22 (2016). DOI 10.1007/s00348-016-2211-z. URL <https://doi.org/10.1007/s00348-016-2211-z>
28. Samimy, M., Lele, S.K.: Motion of particles with inertia in a compressible free shear layer. *Phys. Fluids A* **3**(8), 1915–1923 (1991). DOI 10.1063/1.857921. URL <https://doi.org/10.1063/1.857921>
29. Scarano, F., van Oudheusden, B.W.: Planar velocity measurements of a two-dimensional compressible wake. *Exp. Fluids* **34**(3), 430–441 (2003). DOI 10.1007/s00348-002-0581-x. URL <https://doi.org/10.1007/s00348-002-0581-x>
30. Schlatter, P., Örlü, R., Li, Q., Brethouwer, G., Fransson, J.H.M., Johansson, A.V., Alfredsson, P.H., Henningson, D.S.: Turbulent boundary layers up to $Re_\theta = 2500$ studied through simulation and experiment. *Phys. Fluids* **21**(5), 051,702 (2009). DOI 10.1063/1.3139294. URL <https://doi.org/10.1063/1.3139294>
31. Schrijer, F.F.J., Scarano, F., van Oudheusden, B.W.: Application of PIV in a Mach 7 double-ramp flow. *Exp. Fluids* **41**(2), 353–363 (2006). DOI 10.1007/s00348-006-0140-y. URL <https://doi.org/10.1007/s00348-006-0140-y>
32. Sillero, J.A., Jiménez, J., Moser, R.D.: One-point statistics for turbulent wall-bounded flows at Reynolds numbers up to $\delta^+ \approx 2000$. *Phys. Fluids* **25**(10), 105,102–17 (2013). DOI 10.1063/1.4823831. URL <https://doi.org/10.1063/1.4823831>
33. Urban, W.D., Mungal, M.G.: Planar velocity measurements in compressible mixing layers. *J. Fluid Mech.* **431**, 189–222 (2001). DOI 10.1017/S0022112000003177. URL https://journals.cambridge.org/article_S0022112000003177

34. Wiegel, M., Fischer, M.: Proper orthogonal decomposition applied to PIV data for the oblique transition in a Blasius boundary layer. In: Cha, S.S., Trolinger, J.D. (eds.) *Optical Techniques in Fluid, Thermal, and Combustion Flow*, San Diego, CA, United States, vol. 2546, pp. 87–97 (1995). DOI 10.1117/12.221512. URL <https://doi.org/10.1117/12.221512>
35. Willert, C.E.: High-speed particle image velocimetry for the efficient measurement of turbulence statistics. *Exp. Fluids* **56**(1), 17 (2015). DOI 10.1007/s00348-014-1892-4. URL <https://doi.org/10.1007/s00348-014-1892-4>

Chapter 12

Applications: Transonic Flows

Common problems appearing the application of PIV at high flow velocities in wind tunnels are limited in optical access and problems of focusing the images of the tracer particles due to vibrations and density gradients in the flow [19]. Nevertheless, the instantaneous flow fields above a helicopter blade profile and in the wake of a model of a cascade blade have been investigated successfully at transonic flow velocities by means of the photographic PIV technique already two decades ago [21].

Today, PIV can be applied to transonic flows in industrial wind tunnels, such as the DNW-TWG with a cross-section of $1 \times 1 \text{ m}^2$, even on a routine basis. Modern model deformation measurement techniques allow for the determination of the exact model location and deformation under load in parallel with the measurement of the instantaneous flow fields.

The first two experiments were carried out in the DLR high-speed blow-down wind tunnel (HKG). Transonic flow velocities are obtained by sucking air from an atmospheric intake into a large vacuum tank. A quick-acting valve, located downstream of the test section, is rapidly opened to start the flow. Ambient air, which is dried before entering the test chamber, flows for a maximum of 20 s through a test section with 725 mm spanwise extension. Grids in the settling chamber and a high contraction ratio lead to a low turbulence level in the test section.

12.1 Cascade Blade with Cooling Air Ejection

Contributed by:

M. Raffel and J. Kompenhans

The aim of this investigation carried out in 1996 was to study the effect of the ejection of cooling air on the wake behind a model of a cascade blade [21]. Due to

An overview of the Digital Content to applications on transonic flows can be found at [\[DC12.1\]](#).

Table 12.1 PIV recording parameters for cascade flow

Flow geometry	$Ma = 1.27$ parallel to light sheet
Maximum in-plane velocity	$U_{\max} \approx 400$ m/s
Field of view	150×100 mm ²
Interrogation volume	$2.8 \times 2.8 \times 1$ mm ³ ($H \times W \times D$)
Dynamic spatial range	$DSR \approx 57 : 1$
Dynamic velocity range	$DVR \approx 100 : 1$
Observation distance	$z_0 \approx 1$ m
Recording method	Single frame/double exposure
Ambiguity removal	Image shifting/rotating mirror
Recording medium	35 mm film, ASA 3200, 100fps/mm
Recording lens	$f = 100$ mm, $f_{\#} = 2.8$
Illumination	Nd:YAG laser ^a 70 mJ/pulse
Pulse delay	$\Delta t = 2 - 4$ μ s
Seeding material	Oil droplets ($d_p \approx 1$ μ m)

^aFrequency doubled

a specially adapted wind tunnel wall above and below the model and an adjustable tailboard above the model, the flow field of a real turbine blade could be simulated in a realistic manner. The PIV recordings were taken with the photo-graphical PIV recording system utilizing the high-speed rotating mirror for image shifting at a time delay between the two laser pulses of 2 – 4 μ s. The PIV parameters used for this investigation are listed in Table 12.1. Figure 12.1 presents the instantaneous flow velocity field at the trailing edge of the plate (thickness 2 cm) for a cooling mass flow rate of 1.4% at a free stream Mach number of $Ma = 1.27$. Expansion waves and terminating shocks can be easily seen. No data were obtained in the area above the model as the laser light was blocked off by the model. Data drop-out was also found in the area directly downstream of the model. The reason is mainly that the size of the interrogation area could not be further decreased at evaluation due to algorithms available at that time. This would have been necessary in order to satisfactorily resolve the strong velocity gradients close to the trailing edge of the model. In addition, strong density gradients in this part of the flow field caused much broader particle images. Without ejection of cooling air, the wake behind the plate can be characterized as a vortex street. With ejection of air this is no longer true: two separate thin shear layers can be detected in the presentation of the instantaneous vorticity shown in Fig. 12.1.

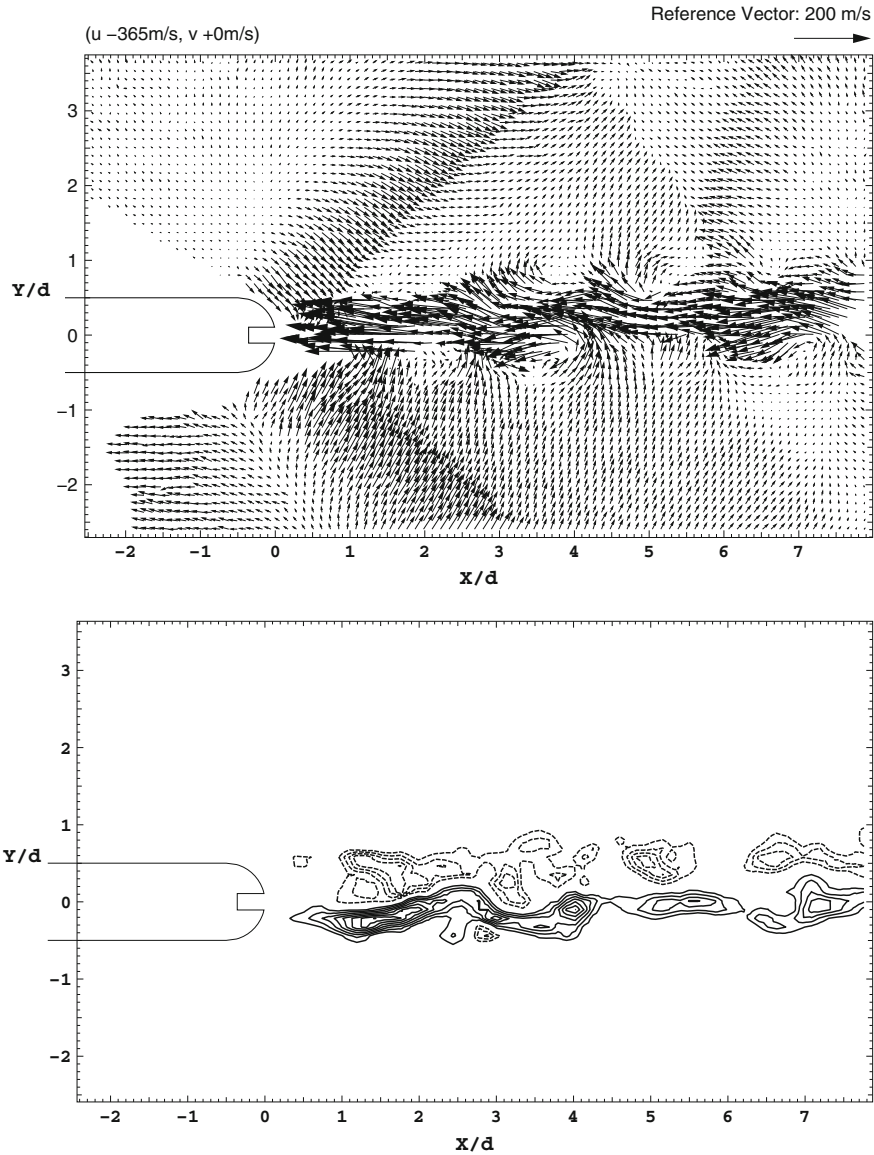


Fig. 12.1 Flow velocity (top) and vorticity field (bottom) behind a cascade blade at $Ma = 1.27$ and a cooling mass flow rate of 1.4%

12.2 Transonic Flow Above an Airfoil

Contributed by:

M. Raffel and J. Kompenhans

The application of PIV in high-speed flows yields two additional problems: the limited velocity fidelity of the tracer particles and the presence of strong velocity and density gradients.

For the proper understanding of the velocity maps it is important to know at which distance behind a shock the tracer particles will again move with the velocity of the surrounding fluid. Experience shows that a good compromise between particle following behavior and sufficiently high light scattering can be found if this distance is allowed to be of the order of one or two interrogation areas.

Strong velocity gradients in the flow will lead to a variation of the displacement of the images of the tracer particles within the interrogation area. Back in 1992, this influence could only be reduced by application of image shifting, that is by decreasing the temporal separation between the two illumination pulses and increasing the displacement between the images of the tracer particles by image shifting to the optimum for evaluation. This was especially important, when auto-correlation and optical evaluation methods were applied as in this case it is required to be able to adjust the displacement of the images of the tracer particles to the range for optimal evaluation (i.e., $\approx 200 \mu\text{m}$). The PIV parameters used for this investigation are listed in Table 12.2.

In the case of optical evaluation methods image shifting helps also to solve the problem of large variations of the displacements of the tracer particle images within

Table 12.2 PIV recording parameters for transonic flow above a NACA0012 airfoil

Flow geometry	$Ma = 0.75$ parallel to light sheet
Maximum in-plane velocity	$U_{\max} \approx 520 \text{ m/s}$
Field of view	$300 \times 200 \text{ mm}^2$
Interrogation volume	$5.6 \times 5.6 \times 1 \text{ mm}^3 (H \times W \times D)$
Dynamic spatial range	$DSR \approx 57 : 1$
Dynamic velocity range	$DVR \approx 150 : 1$
Observation distance	$z_0 \approx 1 \text{ m}$
Recording method	Single frame/double exposure
Ambiguity removal	Image shifting/rotating mirror
Recording medium	35 mm film, ASA 3200, 100 lps/mm
Recording lens	$f = 100 \text{ mm}$, $f_{\#} = 2.8$
Illumination	Nd:YAG laser ^a 70 mJ/pulse
Pulse delay	$\Delta t = 3 \mu\text{s}$
Seeding material	oil droplets ($d_p \approx 1 \mu\text{m}$)

^aFrequency doubled

the PIV recording. A successful evaluation is achieved for a range of particle image displacements of $150 \mu\text{m} \leq d_{\text{opt}} \leq 250 \mu\text{m}$. The upper and lower limits for this optimal particle image displacement is determined by the flow to be investigated and can be adapted to the optimal range of displacement on the recording medium by applying the image shifting technique, and adding an additional shift in the direction of the mean flow. Less data drop-out can be expected by this means.

Strong velocity gradients are present in flow fields containing shocks as are present in transonic flows. Figure 12.2 shows such an instantaneous flow field – above a NACA 0012 airfoil with a chord length of $C_l = 20 \text{ cm}$ – at $Ma_\infty = 0.75$ [22]. By subtracting the speed of sound from all velocity vectors the supersonic flow regime and the shock are clearly detectable. Due to the application of image shifting ($U_{\text{shift}} = 174 \text{ m/s}$) the requirement for the fluctuations to be less or equal to the diameter of the interrogation spot could be fulfilled with an optimum interrogation spot diameter of 0.7 mm even at the location of the shock. No data drop-out is found even in interrogation spots located in front and behind the shock (flow velocities from $U = 280 \text{ m/s}$ to 520 m/s). The associated parameters for the PIV recording are presented in Table 12.3.

The previous example should demonstrate, that already two decades ago the physical problems associated with the application of PIV in transonic flows could be tackled with some experimental effort even for photographic recording. To date, many of these problems have been solved in a more general way, for example using

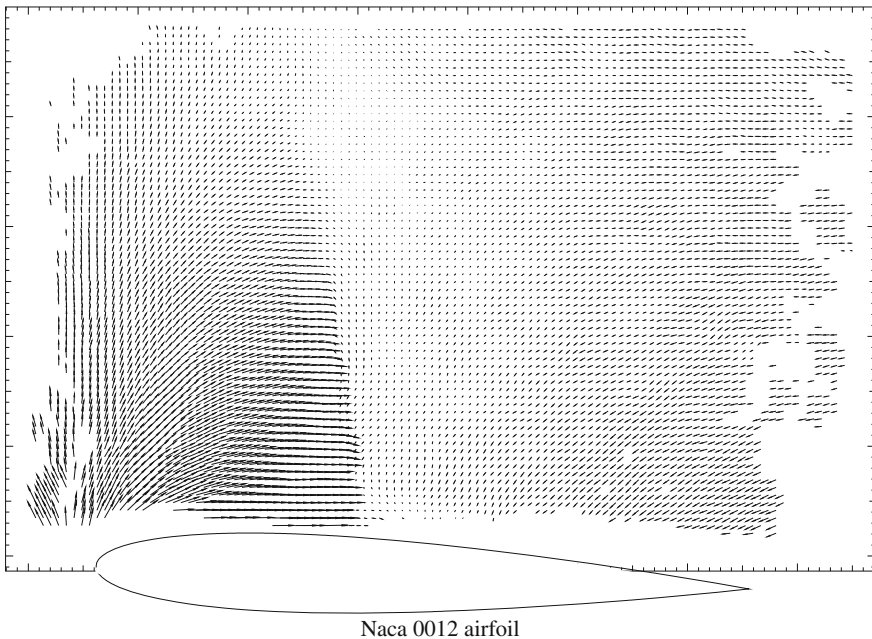


Fig. 12.2 Instantaneous flow field over a NACA 0012 airfoil at $\alpha = 5^\circ$ and $Ma_\infty = 0.75$, $U_{\text{shift}} = 174 \text{ m/s}$, $C_l = 20 \text{ cm}$

Table 12.3 Image recording parameters associated with the instantaneous flow field of Fig. 12.2

$M = 1 : 6.7$	$N \approx 15$						
	U_{\min} [m/s]	U_{\max} [m/s]	Δt [μ s]	U_{shift} [m/s]	ΔX_{shift} [μ m]	ΔX_{\min} [μ m]	ΔX_{\max} [μ m]
Without I.S.	200	520	5	0	0	149	388
With I.S.			3	174	78	167	311

frame straddling enabling pulse delays of the laser of much less than 1μ s (optimal displacement of particle images). Furthermore, sophisticated evaluation algorithms providing high local resolution even in presence of strong displacement gradients and much stronger pulse lasers providing much higher intensities allow for either larger observation areas or a smaller aperture leading to sharp particle images even in case of strong vibrations of the wind tunnel and the PIV set-up.

12.3 Transonic Flow Around a Fan Blade

Contributed by:

J. Klinner, C. Willert

In the following, two experiments are briefly described which were performed at the transonic cascade wind tunnel of the DLR in Köln (see Fig. 12.3) at $Ma_1 = 1.25$. The tunnel is a closed loop, continuously running facility featuring chord Reynolds numbers ranging from $Re = 1 \times 10^5 - 3 \times 10^6$.

The purpose of the first campaign was to study the impact of various transition control methods on shock induced separation. PIV measurements were conducted above the blade's suction side in the separation region and within the transitional separation bubble. In this environment PIV investigations have to deal with pronounced shock motion and associated unsteadiness of the separation region (see Fig. 12.4). Further experimental challenges involve buffeting of the highly loaded thin air foil as well as low seeding densities inside the upstream boundary layer and in the attached transitional separation bubble.

The second measurement campaign was focussed on the transonic velocity field around the erosion-degraded leading edge of a fan airfoil. The leading edge of a fan blade is one of the most affected parts of a turbofan since it has a high probability of high momentum, foreign particle impact such as dust in particular during take-off and landing. The intention of the study was to provide a database on velocity fields around different leading edge geometries in order to confirm numerical predicted locally increased accelerations around the leading edge. These flow accelerations in turn lead to changes of the shock system and expansion region and are believed to be partially responsible for stagnation pressure losses of the fan.

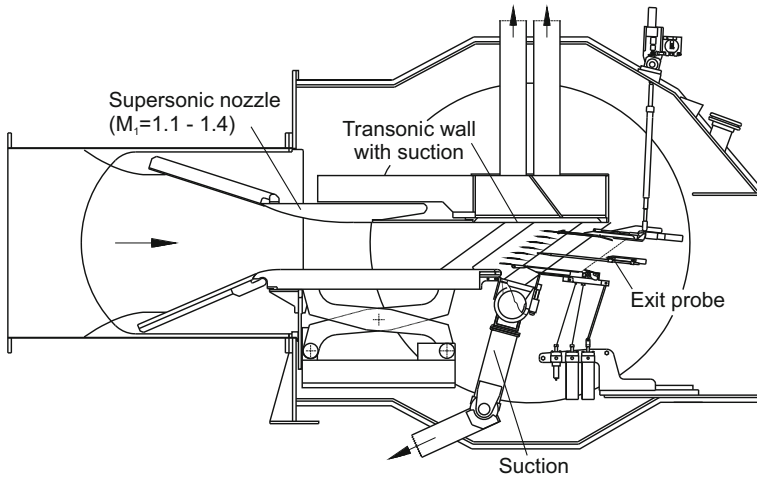


Fig. 12.3 Schematic of the transonic cascade wind tunnel at the DLR Institute of Propulsion Technology

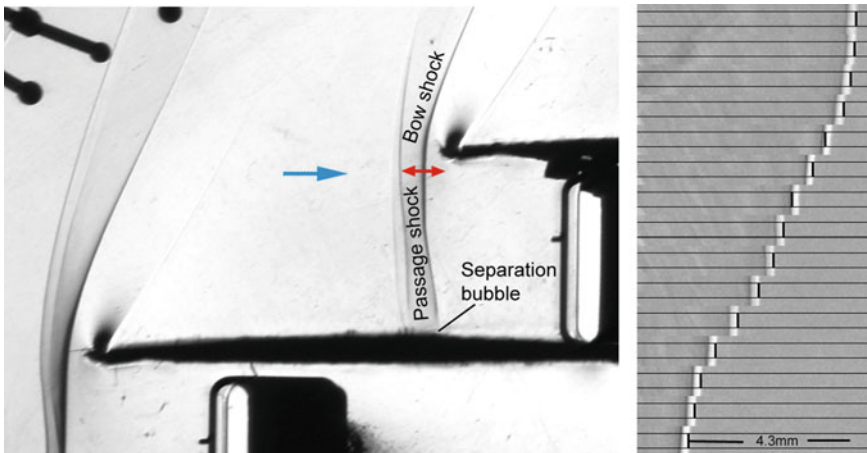


Fig. 12.4 Left: Schlieren image of the shock system in front of the leading edge near stall at $Ma_1 = 1.25$; the red arrows mark positional changes of the shock wave visualized by time resolved schlieren imaging at frame rates of 20 kHz (right)

Both experiments involved the same planar 2C PIV setup using a classical normal viewing arrangement (see Table 12.4) with the measurement plane located at midspan. Due to restrictions of optical accessibility the laser light is introduced through a light-sheet probe about 550 mm downstream from the cascade as illustrated in Fig. 12.5. The far downstream distance of the PIV light sheet probe is chosen to minimize disturbances of the flow in upstream direction. For leading edge measurements the droplet seeding consisted of an atomized paraffin-ethanol mixture that is dispersed by two Laskin type atomizers. More details regarding the light sheet

Table 12.4 PIV recording parameters for leading edge flow and for the flow in the vicinity of the transitional separation bubble

Flow geometry	Parallel to light sheet	
Maximum in-plane velocity	$U_\infty \approx 410$ m/s (Ma= 1.22)	
Re based on chord length	1.4×10^6	
Illumination	Dual Nd:YAG laser ^a , 50 mJ/pulse	
Seeding material	Paraffin droplets ($d_p \approx 0.5 \mu\text{m}$)	
Recording lenses	$f = 200$ mm $f_\# 5.6$	
Recording medium	Full frame interline transfer CCD	
Pixel size	7.4 μm	
Ambiguity removal	Frame separation (frame-straddling)	
Observation distance	$z_0 \approx 0.5$ m	
Magnification	$M = 0.66$ (11.2 μm /pixel)	
Field of view ($W \times H$)	22.9 \times 22.9	22.9 \times 7.83 mm ²
Interrogation volume ($W \times H \times D$)	0.54 \times 0.54 \times 0.5	0.54 \times 0.27 \times 0.5 mm ³
Number of samples	$N_{\text{tot}} = 2000$	10 000
Dynamic spatial range	DSR $\approx 43 : 1$	$\approx 43 : 1$
Dynamic velocity range	DVR $\approx 100 : 1$	$\approx 150 : 1$
Pulse delay	$\Delta t = 250$ ns	400 ns

^aFrequency doubled

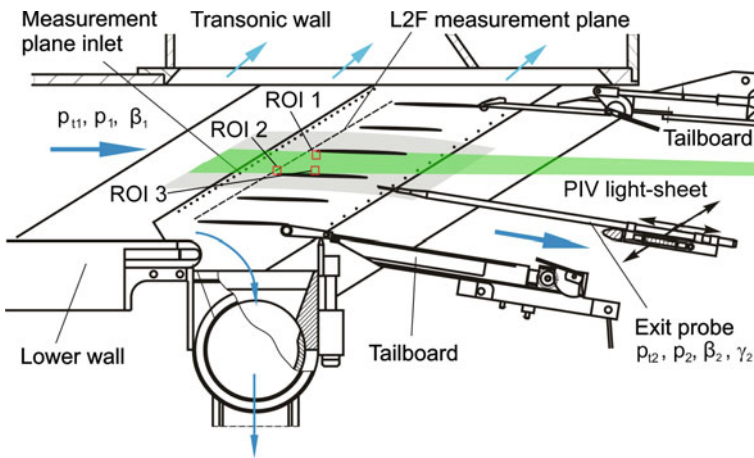


Fig. 12.5 Test section and light sheet orientation

probe and seeding procedure are described in [18]. For measurements of the separation bubble the tracer density of paraffine droplets was found to be insufficient and thus a smoke generator is used which generated tracer droplets by evaporation and re-condensation of refined mineral oil.

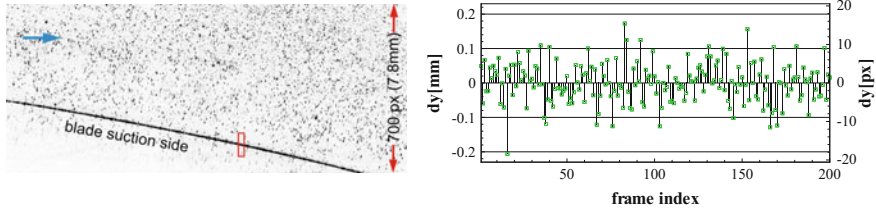


Fig. 12.6 Left: PIV raw image with rectangular region for evaluation of blade displacements; Right: vertical blade displacements over 200 frames

The unsteady aerodynamic loading of the thin blade resulted in flexure (i.e., vibrations) of up to ± 0.23 mm (± 20 pixel). Using a correlation-based tracking algorithm the relative position of the blade surface was determined for each recording and used to offset the image data to a coincident blade position prior to PIV processing. Therefore, positional blade displacements are evaluated in a small rectangular region above the blade suction side as indicated in Fig. 12.6.

At midspan, the chord-wise position of the shock-induced separation is coupled with the unsteady shock position above the suction side (for details on self-sustaining shock oscillation above transonic airfoils see [20]). Near the blade, both passage shock and separation region fluctuated by ± 5 mm ($\pm 5\%$ of chord or ± 450 pixel). In order to enable a conditional averaging with regard to the chordwise position of the separation region sequences of up to 10000 PIV samples were acquired and sorted by shock position with an axial resolution of 1 mm. For each sample the instantaneous axial shock position in each PIV sample was detected based on the maximum axial velocity gradient in a row that is located ≈ 7 mm above the blade.

Figure 12.7 presents a PIV result that was obtained by averaging of $N_{tot} = 1500$ samples at a ‘fixed’ shock position. The reverse flow within the transitional separation bubble is clearly visible. Through postprocessing the dividing streamline was obtained at zero net mass flux by direct integration of the velocity profile normal to the profile (see [10]). Through this procedure the blade-normal extension of the shock induced flow separation can be visualized. The measured flow field also indicates reattachment of the turbulent shear layer downstream of the separation bubble.

Regarding the leading edge measurements, Fig. 12.8 shows two examples for the transonic flow around different leading edge geometries near choking. The sharp leading edge (left sub-figure) exhibits a homogeneous expansion around the suction side and shows a weak lip shock on the pressure side of the blade. A small subsonic region is visible between bow shock and leading edge. For the eroded leading edge model (right sub-figure) this subsonic region shifts upstream of the leading edge and is significantly larger which as a consequence leads to higher shock losses compared to the sharp edge. In addition, the blunt leading edge exhibits differences in the expansion region downstream of the shock. The pressure side lip shock is more

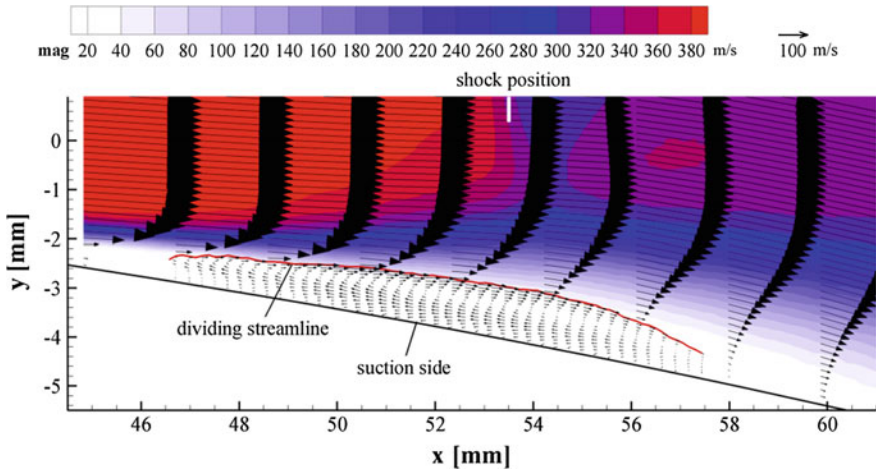


Fig. 12.7 Shock induced flow separation with reverse flow inside the transitional separation bubble for a highly loaded fan blade at $Ma_1 = 1.25$

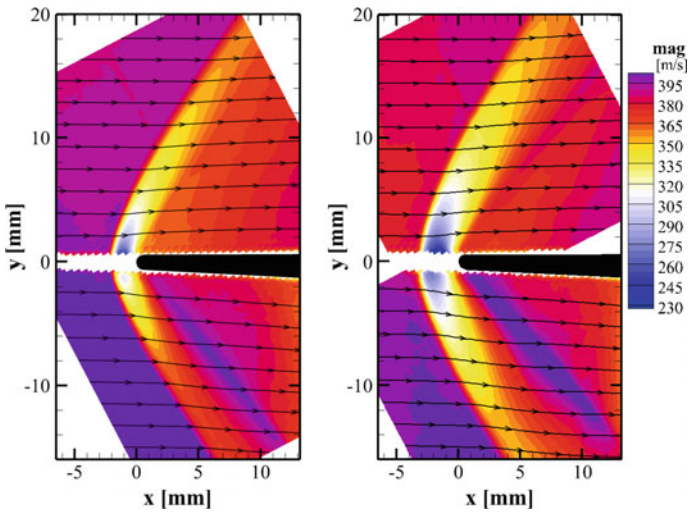


Fig. 12.8 Flow velocities around the sharp (left) and the blunt (right) leading edge near choking at $Ma_1 = 1.25$

pronounced and a further weak lip shock appears on the suction side, both caused by the higher flow acceleration around the blunt leading edge. More details on the leading edge flow around transonic fan blades at different operation conditions as well as numerical results are published in [17].

12.4 Stereo PIV Applied to a Transonic Turbine

Contributed by:

J. Woisetschläger, H. Lang and E. Göttlich

In axial rotating machinery, usually velocity data are provided in terms of axial, circumferential and radial velocity. Stereo PIV allows the calculation of these components from the in- and out-of-plane velocities recorded within the light-sheet plane. For this example of application, the schematic of the test section is given in Fig. 12.9. 24 stator blades and 36 rotor blades were used in this turbine with rotational speeds between 9600 and 10600 rpm. For this test rig air is continuously provided by a compressor station in the basement of the institute at maximum electric power of 2.8 MW with a total mass flow of 22 kg/s and a pressure ratio of 3.5 (stage). Inlet flow temperature was between 360 and 403 K. The turbine's control system (Bently Nevada) provided 12 TTL and 1 analog pulse per revolution. By combining both, a high-resolution trigger signal was available.

Optical Configuration

Most challenging about this application is the highly turbulent, high speed and unsteady flow where neither to the observation window nor the light sheet probe nor the seeding pipe are allowed to cause disturbances. High amounts of seeding have to be used and a careful calibration of the imaging geometry has to be done due to a curved observation window. The benefit of PIV to immediately obtain unsteady flow field data outweighs these difficulties. The recording parameters for this flow are given in Table 12.5. The test rig and the camera arrangement are shown in Fig. 12.10, with one camera axis being perpendicular to the light sheet and the second camera

Table 12.5 PIV recording parameters for the transonic turbine flow

Flow geometry	Three-dimensional flow through curved turbine blades with a small radial velocity component
Maximum in-plane velocity	$U_{max} \approx 450$ m/s
Field of view (both cameras)	47.5×37.5 mm ²
Interrogation volume	$1.2 \times 1.2 \times 2$ mm ³ (H×W×D)
Observation distance	260 mm
Recording method	Dual frame/single exposure
Recording medium	1280 × 1024 pixel, progressive scan interline transfer CCD (6.7 μm pixel pitch)
Recording lens	$f = 60$ mm/ $f_{\#}2.8$
Illumination	Dual cavity Nd:YAG laser* 120 mJ/pulse
Pulse delay	$\Delta t = 0.7$ μs
Seeding material	DEHS, Palas-AGF 5.0D particle generator ($d_p \approx 0.3 - 0.7$ μm)

*Frequency doubled

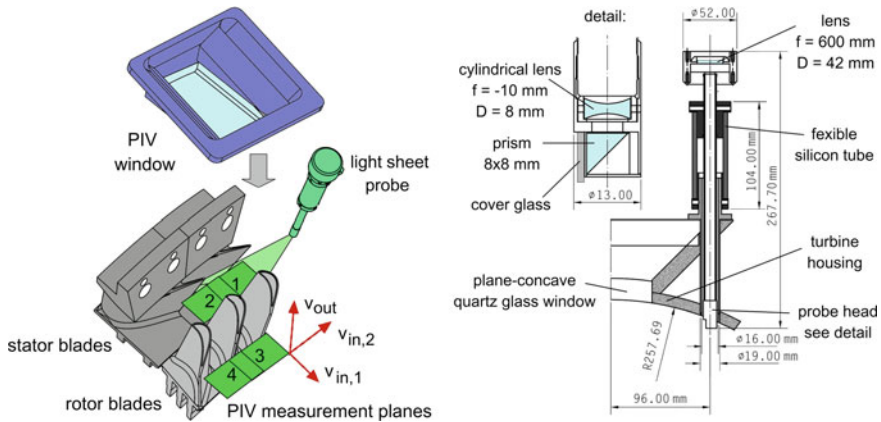


Fig. 12.9 Test section (measures in mm)

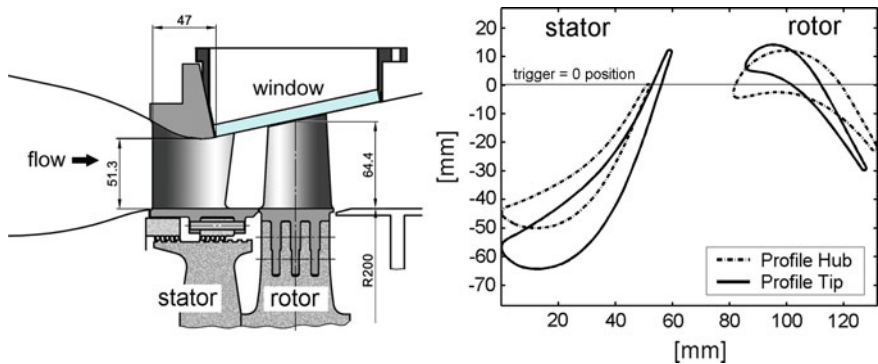


Fig. 12.10 Turbine test rig with optical setup for stereoscopic PIV with transonic flow conditions after stator and rotor

axis inclined by 27° to the first. This angle was limited by the geometry of the turbine’s casing. The cameras were mounted according to the Scheimpflug condition. Figures 12.10 and 12.11 provide details on the two light sheets used (rotor and stator planes). The stator ring was rotatable, so that a full blade pitch was accessible with two consecutive recordings. Figure 12.11 also gives details on the light sheet probe. The light sheet probe was fixed to the cameras base plate while a flexible silicon tube was used to seal the air inside the turbine. This rigid system eased focusing and calibration. The camera lenses were focused remotely controlled during test rig operation by two stepper motors. The laser light was guided through an articulated arm to the light sheet probe. A high-temperature resin was used to glue the single elements, especially the cover glass (three-component resin, R&G GmbH). This glass shielded the aligned optical prism against the fluctuating pressure caused by the flow. The light sheet was observed through a plane-concave quartz glass window (HERASIL; anti-reflection coated) with dimensions $123 \times 75 \times 15 \text{ mm}^3$ and a R264 curvature on one side.

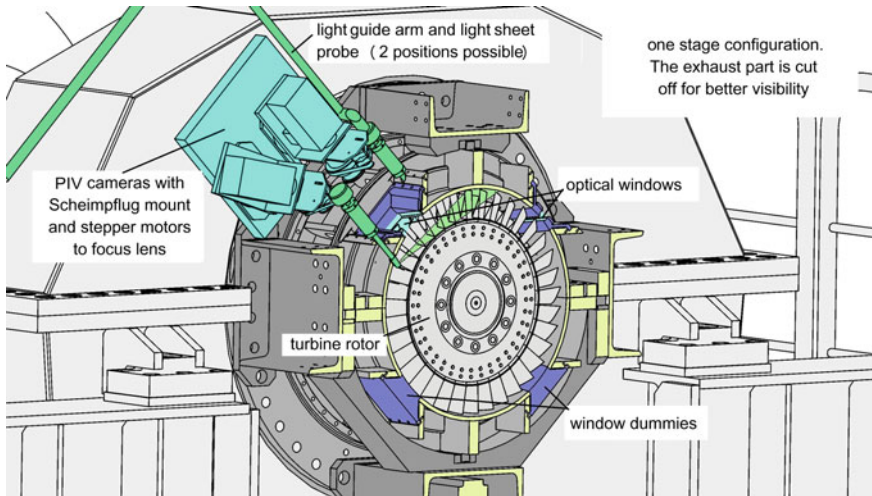


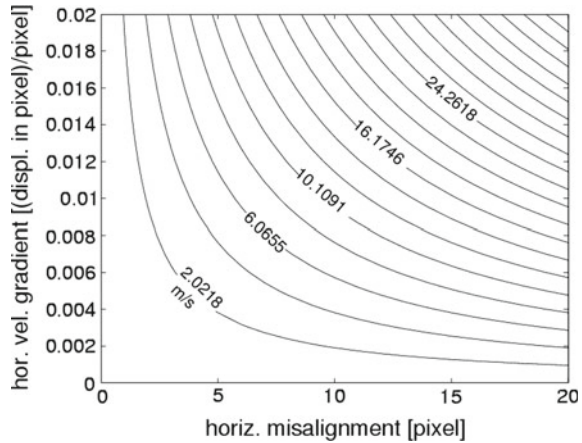
Fig. 12.11 Optical setup and light sheet probe (all measures in mm)

An aerosol generator (AGF 5.0D, PALAS GmbH) injected DEHS oil droplets approximately 500 mm upstream the stator blades through a specially formed pipe (S shape, 7 mm inner diameter). In the most upstream part of the pipe a large number of holes with 1.8 mm diameter were drilled (shower head). This part with a length of 130 mm was aligned in a tangential direction upstream the light sheet, parallel to the light sheet. With an approximate diameter of $0.7 \mu\text{m}$ these tracer particles act as low-pass filter with a cut-off frequency of approximately 80 kHz [34].

Results

Since the flow through a turbine is highly directional with only the secondary flow effects (vortex shedding, rotor interaction) being of special interest, an image shifting technique was applied in the main flow direction (up to 11 pixel). Additionally, a background image with no seeding was subtracted from each of the single recordings in order to improve the contrast of the tracer particles. In some cases a peak locking effect was observed from the images (see Sect. 6.2.2). A slight defocusing using a step motor driven device for focusing the camera lenses helped to reduce this effect. For each rotor-stator position investigated, approximately 200 recordings (dual frame) were done. Such procedure is known as ensemble-averaging. Here the ensembles are sorted by the angular position of the rotor (rotor-stator position). A cross-correlation technique with 64×64 interrogation size and 50 % overlap was then applied resulting in the single vector fields. A 2D-Gaussfit in an 3×3 pixel matrix was used for sub-pixel resolution. The single vector fields were validated using the peak height, a maximum and minimum range and a moving average filter (5×5 pixel). This filter compares mean value and standard deviation for the centre vector with the values of the surrounding vectors. If the deviation is too high the vector is rejected. Due to the high turbulence sometimes only a relatively small number of vectors were validated

Fig. 12.12 Error in the out-of-plane component in the vicinity of the shock due to a misalignment during the calibration procedure



(50%). Then, a higher number of single recordings must be used for the averaging. Additionally, the wake region is always poorly seeded, due to the fact that the vortex shedding from the trailing edge of the turbine blade contains boundary layer fluid without seeding. After averaging a number of recordings at a given phase of vortex shedding the core of the vortices will contain less validated vectors compared to the main flow. In these areas this might increase the uncertainty in the estimation of the mean value by 10% or even more compared to the rest of the field. Since the light sheet plane was observed through a curved window section a higher order approach had to be used for dewarping the two camera images [27]. After the recordings were done, the window section was fixed to the base plate of the two cameras (with the light sheet probe attached). So all parts were removed from the turbine together to enable calibration outside the turbine test rig.

Since the shock areas are most pronounced only at mid-span, focusing the particles in the shock area is less of a problem. Unfortunately, the displacement gradients happen to influence the results, especially when the calibration target is misaligned. This effect depends on the strength of the gradients and the misalignment of the two camera projections due to a misalignment of the calibration target. When backprojecting the two vector sets to the measurement plane one camera will then provide the value from upstream the shock for a given position, while the other projection provides the value from downstream the shock for the same position in the light-sheet plane. This will lead to a measurement error which can be easily recognised by a far too large out-of-plane component. This effect can be seen in Fig. 12.12.

Finally we ended up with following error estimates:

- $\pm 2 - 4$ m/s per recording (main flow section) with 10–12 pixel particle movement, 0.1 pixel uncertainty (Gauss fit) and more than 10 particles per interrogation area,
- five times less sensitivity of the out-of-plane component compared to the in-plane-component (due to only 27° between the camera axes),
- additional ± 3 m/s in the shock vicinity (5 pixel misalignment),
- after averaging ± 1 m/s statistical error (in-plane) and ± 5 m/s out-of-plane with a minimum of 100 validated vectors per interrogation area (outside the wake).

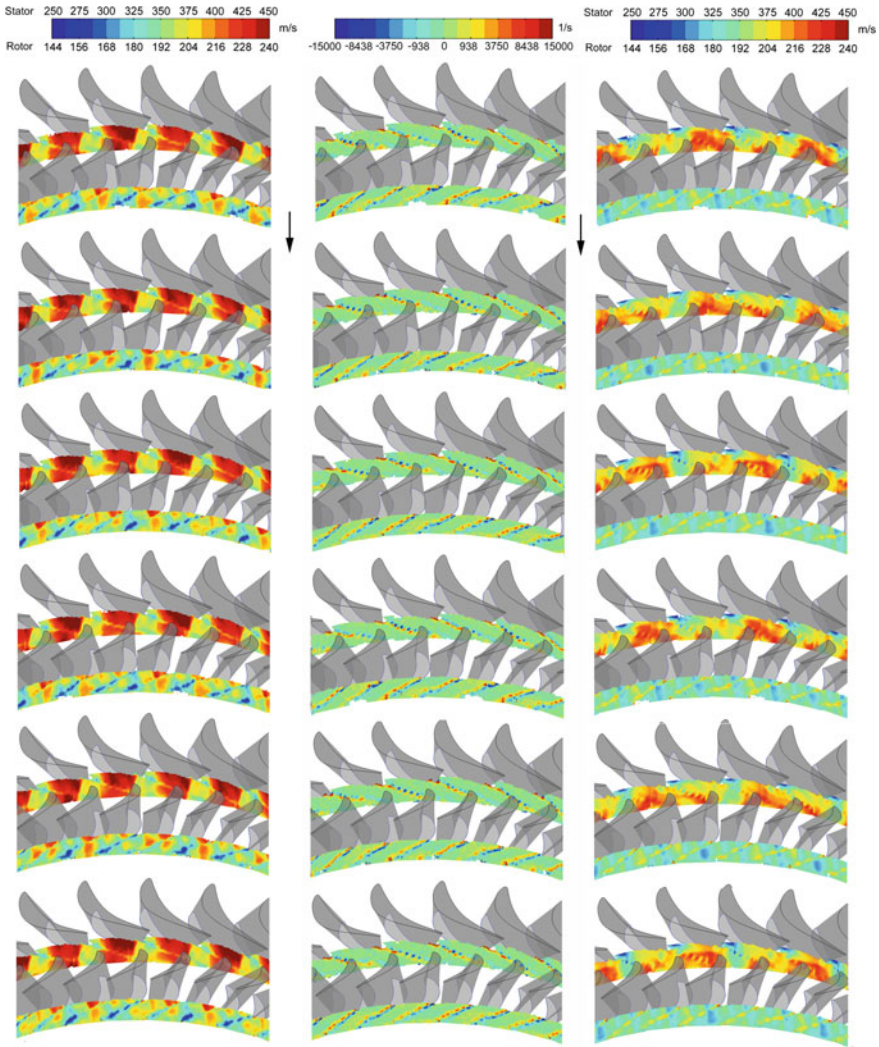


Fig. 12.13 Velocity (left), vorticity (middle) and yaw angle (right) at mid-span in a transonic turbine stage for six different rotor-stator positions at 10600 rpm [DC12.2]

In a final step the in-plane and out-of-plane components have to be transformed into axial, tangential and radial components to provide the full data set for comparison to data obtained by computational fluid dynamics. Two results for the mean velocity (all three components) and the vorticity (from the two in-plane components) are presented in Fig. 12.13 for six rotor-stator positions. When looking at the vorticity one can observe seven phases of vortex shedding during one period of blade passing. This means the vortex shedding frequency is about 40 kHz. A detailed comparison with

interferometric measurements indicated that the tracer particles used started to act as low-pass filter at about 80 kHz [34]. Therefore, only the first harmonic of the vortex movement can be found in the PIV results. While high resolution CFD methods predict kidney-shaped vortices, PIV results showed vortices of more or less circular type because of the tracer particles acting as low-pass filter. On the other hand, PIV provided the unique possibility to investigate the interaction between shocks, shock reflections, vortex shedding and wake-wake interaction in these turbulent and transonic flows. In such transonic turbine flows the stator shock is reflected by the rotor blades as seen in the yaw angle plots. These reflections trigger vortex shedding – every 7th vortex is thus enforced. It also means that rotor movement, shock reflections and vortex shedding, are in phase in such types of machinery. Thus, ensemble averaging for one rotor-stator position results in clearly defined, sharp vortices, although 200 images are averaged for each frame in Fig. 12.13. Further discussion of the results can be found in [13, 14, 33–35].

12.5 PIV Applied to a Transonic Centrifugal Compressor

Contributed by:

M. Voges and C. Willert

In the present application PIV was chosen to analyze the complex flow phenomena inside a vaned diffuser of a new generation transonic centrifugal compressor, as this planar technique is capable of detecting unsteady flow structures and to resolve even high velocity gradients as well as unsteady shock configurations previously undetectable with point-wise techniques such as laser-2-focus velocimetry (L2F) [11]. Measurements were carried out at rotational speeds between 35,000 and 50,000 rpm. The operating conditions are summarized in Table 12.6. The compressor stage was designed for a pressure ratio of 6 : 1. Due to the advanced impeller geometry the diffuser section has a conical shape with a constant passage height of 8.1 mm (Fig. 12.14).

The conical shape of the diffuser plane required specialized engineering solutions concerning the laser light delivery as well as on the imaging side. Off-the-shelf light

Table 12.6 Operating conditions for PIV investigation inside the diffuser passage

Rotational speed	35, 000 rpm	44, 000 rpm	50, 000 rpm	50, 000 rpm
Pressure ratio	2.5 : 1	4.0 : 1	5.6 : 1	5.3 : 1
Mass flow	1.4 kg/s	2.15 kg/s	2.6 kg/s	2.83 kg/s
Mean temperature	110 °C	175 °C	245–255 °C	230–235 °C
PIV pulse separation Δt	2.5 μ s	2.0 μ s	1.5 μ s	1.5 μ s

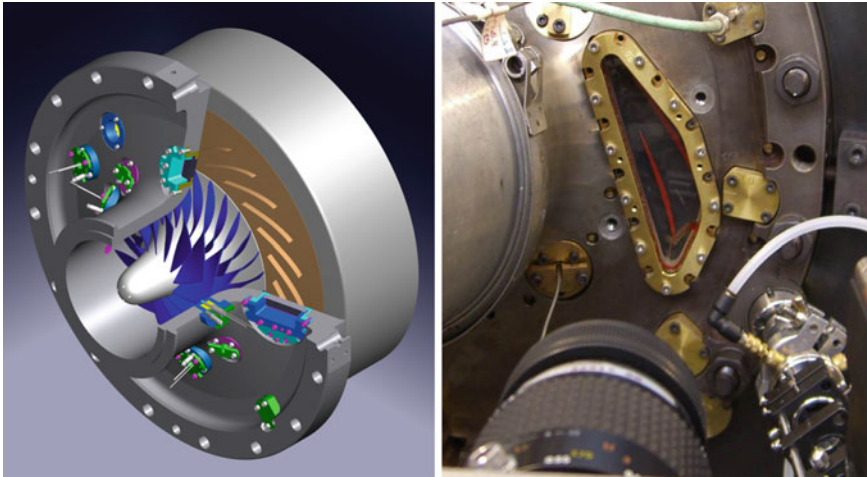


Fig. 12.14 Centrifugal compressor test rig (left); photograph of pressure casing with window and light sheet probe in lower-right corner (right)

sheet probes commonly have a 90° beam deflection and generally are not actively cooled or heat resistant. For this application a special periscope probe was specifically designed that precisely matched to the geometrical conditions of the diffuser and casing. The light sheet probe including the internal beam path is shown in Fig. 12.15. The periscope probe allowed for adjustment of the light sheet in rotational and axial position and angle relative to the chord of the vane profile. Together with the probe support in the diffuser casing it was possible to adjust the light sheet to the three vane span locations chosen for flow investigation: center plane (50% span), one plane close to the hub (19% span) and one plane close to the tip (74% span). The probe support close to the diffuser outlet was not perpendicular to the outer machine casing, but inclined to match the conical diffuser area. The free beam path inside the probe had a diameter of 6 mm. A pair of cylindrical lenses inside the probe formed the light sheet with a thickness of 1 mm and a divergence angle of about 6° . At the outlet of the periscope probe a mirror deflected the light sheet with an angle of 97° , in order to facilitate its adjustment in the diffuser vane passage. Before entering the light sheet probe the beam diameter of the PIV laser has to be reduced to pass through the periscope probe without striking the surface of the metal inner tube. Here a pair of spherical lenses was used in a telescopic set up. The periscope was also continuously purged with compressed, dry air to prevent deposition of seeding particles as well as to cool the probe with its optical components with air exiting at the open delivery end.

To provide sufficient optical access for planar PIV measurements a relatively large quartz window was needed in the diffuser casing. The prepared access port provided a camera observation area of one complete diffuser vane passage, including the impeller exit region (Fig. 12.16). A quartz window and a metal window supporting

Fig. 12.15 Setup of periscope light sheet probe

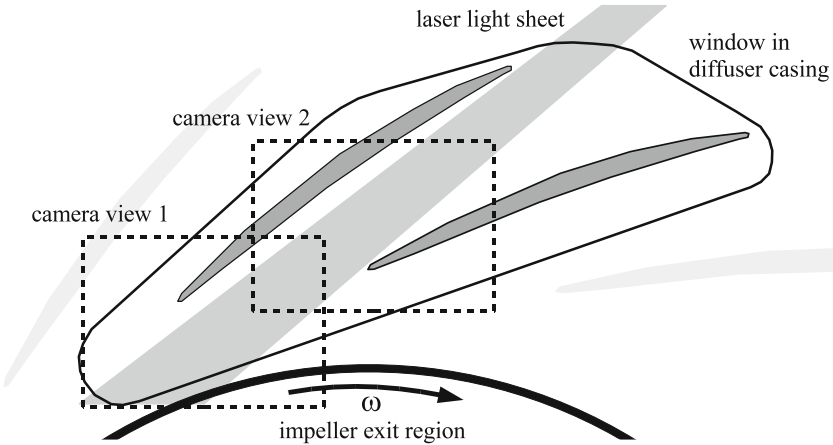
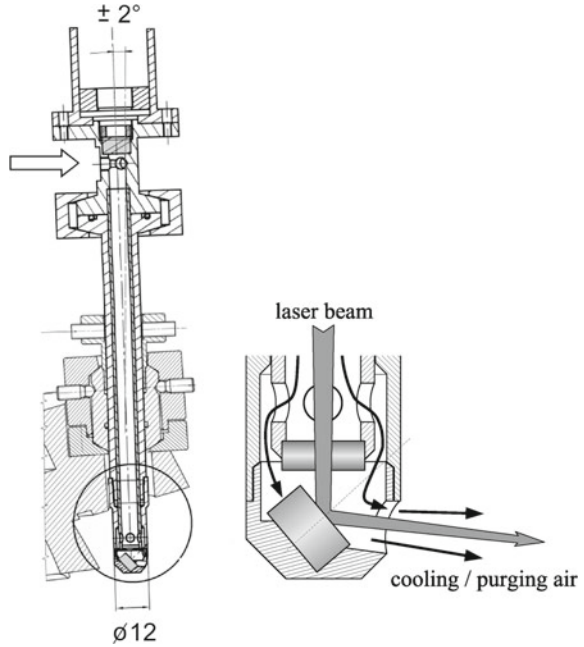
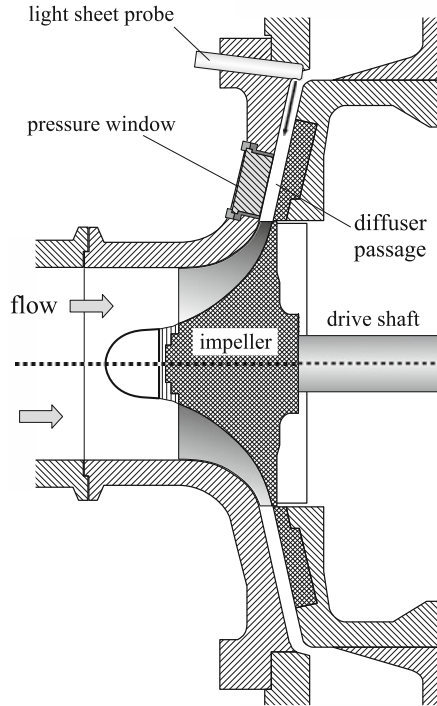


Fig. 12.16 Observation window and camera positions

brace were manufactured with considerable effort to precisely match the inner contour of the diffuser casing, thereby minimizing disturbances of the near-wall flow (Fig. 12.17). While the outer surface of the glass was flat, the inner surface was CNC-milled according to the conical diffuser shape and subsequently surface polished by hand. A bulky design of the window was necessary in order to withstand the high temperature and pressure strains during compressor operation and also reduces the

Fig. 12.17 Cross-sectional view of centrifugal compressor



likelihood of glass fracture. To reduce compressive stresses and to provide a reliable seal between the vane passages a silicone sealing was applied to the contact surface of the vanes in the window area. For flow observation both the frequency-doubled, dual-cavity Nd:YAG laser and the thermo-electrically cooled, double-shutter CCD camera (1600×1200 pixel at 14 bit/pixel) were operated at a frame rate of 15 Hz. The increased frame rate significantly reduced overall measurement time, thus reducing operating costs of the test facility. In addition facility seeding is only required for a reduced time period, which resulted in significantly decreased window contamination. The camera itself was mounted on a Scheimpflug adapter to optimize alignment of the camera optics with the laser light sheet. To further increase the camera's spatial resolution in the investigated diffuser passage the camera was traversed resulting in two camera positions, one position observing the impeller exit, the other position observing the flow downstream in the diffuser throat (Fig. 12.16). Both measurements were performed in succession for each operating condition and light sheet position respectively.

Calibration and light sheet alignment was performed by means of a target that could reproducibly positioned between the vanes of the diffuser passage. To account for refraction effects due to the thick glass window it was necessary to perform the calibration with the window installed. The target was made of a thin aluminum plate

thickness with a precise $2.0 \times 2.0 \text{ mm}^2$ dot grid applied to its surface. Adjustment of the grid within the vane passage was achieved with three small set-screws.

All of the PIV equipment was mounted on a separate rigid support in order to minimize the influence of rig vibration. An articulated laser guide arm delivered the laser light to light sheet forming shaping optics and light sheet probe which were rigidly attached to the compressor rig. Seeding particles were introduced upstream of a contraction in front of the impeller. Here a circumferential traverse supported four seeding probes with different radial positions which allowed for a nearly uniform seeding distribution across a given sector of the pipe flow. Droplet-based seeding was produced by a battery of three Laskin-nozzle generators filled with paraffin oil. Although the oil evaporation temperature is near 200°C , it should be noted that the evaporation temperature increases with increased pressures, which in part explains the fact the seeding particles remained visible in the diffuser at temperatures above 250°C . The use of solid particle seeding was also considered but deemed too risky without additional investigations. However WERNET reports successful use of solid particle seeding in previous turbomachinery investigations [30, 31].

The size of the seeding particles was limited to $0.3 - 0.8 \mu\text{m}$ through the use of an impactor downstream of the Laskin-nozzle generators. At higher temperatures during compressor operation, the smallest particles might evaporate while larger particles survive longer in the flow field, although they have reduced their size when reaching the investigated flow area. By switching off the impactor the particle size distribution in the seeded flow could be increased to $0.8 - 1.2 \mu\text{m}$. This had a significant positive effect on the PIV signal during measurements at design conditions of the compressor stage, but also did not result in window contamination.

For phase-stationary acquisition of PIV images a phase shifter was triggered by the 1/rev-trigger of the compressor. PIV image sequences of 188 images each were obtained at 16 equally spaced phase angles on one particular main-splitter-main blade passage of the impeller. While this number of images is considered to be sufficient for the calculation of phase-average velocities, it certainly is insufficient to reach convergence for the estimation of statistical quantities such as RMS values or Reynolds stresses. Here an estimated 1000 images per phase angle may have been more adequate. For this application a compromise was made between the detailed investigation of the flow phenomena occurring in the advanced compressor stage on the one hand and the precise analysis of the various parameters characterizing the diffuser flow on the other hand. Thus the limited operation time interval on the compressor rig was used to perform detailed investigation of the diffuser flow field with respect to the various operating conditions.

Evaluation of the PIV image data was performed after pre-processing with high pass filter, subtraction of background image and masking image areas without velocity information (e.g., diffuser casing, window support or shadowed areas). Transformation from the CCD sensors coordinates to physical space was performed using the calibration grid. Fortunately distortion of the particle images (blurring) as well as geometrical distortion (lensing effect) by the curved inner contour of the window was insignificant due to the proximity of the light sheet plane to the window surface. Therefore a separate nonlinear mapping procedure of the images was not required.

The PIV processing was based on an adaptive, grid refining cross-correlation scheme with continuous image deformation as described in Sect. 5.3.4.3. At the final resolution the algorithm used interrogation sample sizes of 32×32 pixel ($1.0 \times 1.0 \text{ mm}^2$) at 50% overlap (final grid size: $0.5 \times 0.5 \text{ mm}^2$) and sub-pixel peak position estimation using Whittaker reconstruction. Outlier detection employed normalized median filtering [32], followed by linear interpolation of rejected vectors. A correlation plane signal-to-noise ratio of 50 or better could be achieved; the number of spurious vectors was below 3% for all imaged planes.

The re-combination of the obtained velocity fields for both camera views could be easily performed during post-processing of the PIV data with the help of the common calibration grid, as both camera views overlap in one area. With a mean pixel shift varying from 13 pixel at 35,000 rpm up to 20 pixel at 50,000 rpm, the corresponding relative measurement error was estimated at 0.5 – 0.8% (2.7 – 3.5 m/s). Given a final size of $1.0 \times 1.0 \text{ mm}^2$ for the interrogation area results in structure passing frequencies between 600 kHz and 1.4 MHz in the measured velocity range of 300 – 700 m/s. Here the size of the particles has an important influence on the obtained velocity data. As the response time of particles about $1 \mu\text{m}$ in size is on the order of $10 \mu\text{s}$ (see Sect. 2.1.1), the particles behave like a low pass filter with a cut off frequency of 100 kHz applied to the flow. Given a blade passing frequency around 20 kHz suggests that only large scale structures are faithfully captured, while smaller scales are damped out. Here the use of sub-micron particles may be considered, but this would have the effect of a significant decrease in light scattering efficiency of the particles (Rayleigh scattering regime). In this context it should be noted that PIV is only capable of capturing a certain

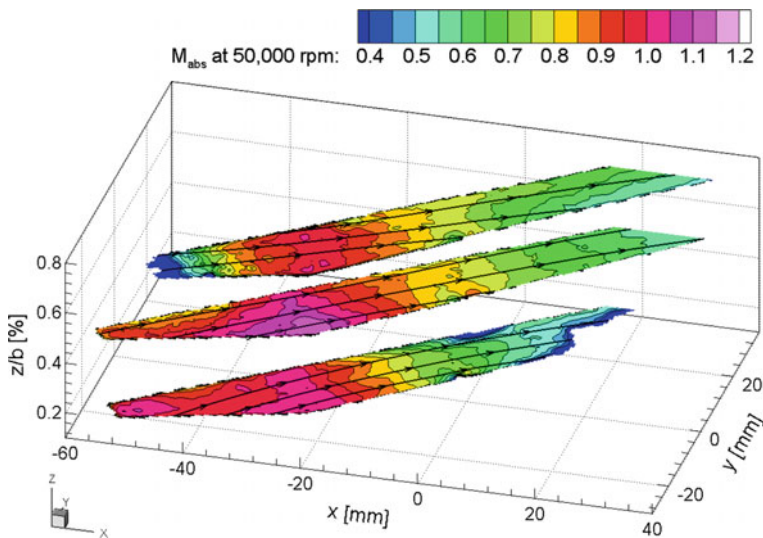


Fig. 12.18 Mach number distribution calculated from the averaged velocity fields at 19, 50 and 74% diffuser passage height (operating conditions: 50,000 rpm, mass flow = 2.6 kg/s) [DC12.3]

Fig. 12.19 Stream lines at 19% (hub) follow the deflection imposed by the diffuser vane, with the passage core flow passing straight through; at 74% (tip region) the stream lines show evidence of the tip clearance flow as the stream traces turn in the opposite direction compared to the hub flow

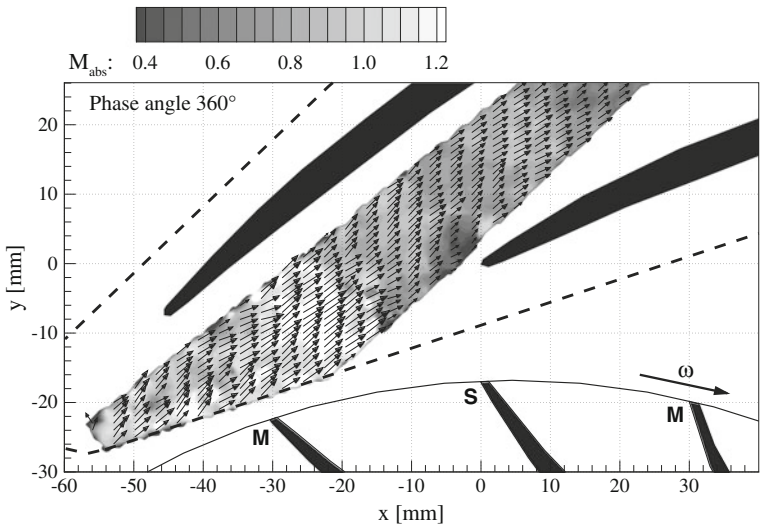
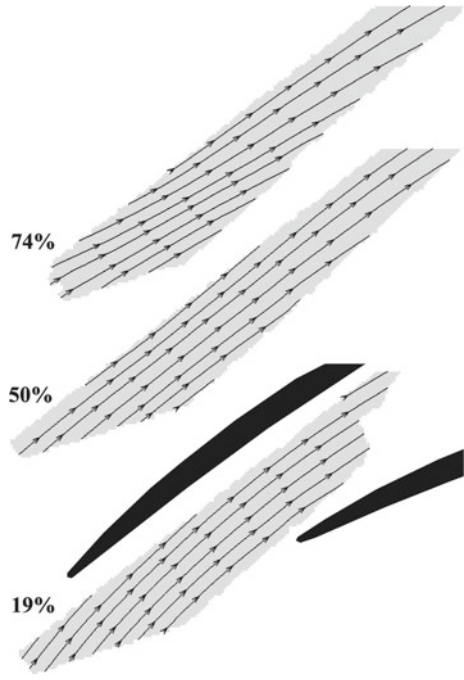


Fig. 12.20 Instantaneous Mach number distribution at 50% span, 50,000 rpm, for one phase angle, characterizing the splitter passage flow; flow patterns of preceding impeller passages are visible in the diffuser throat (1/12th of total vectors displayed) [DC12.4]

Table 12.7 PIV recording parameters for transonic centrifugal compressor

Flow geometry	$Ma = 0.4 - 1.2$ parallel to light sheet
Maximum in-plane velocity	$U_{\max} \approx 300 - 700$ m/s
Field of view	48×33 mm ²
Interrogation volume	$1 \times 1 \times 1$ mm ³ ($H \times W \times D$)
Dynamic spatial range	DSR $\approx 80 : 1$
Dynamic velocity range	DVR $\approx 200 : 1$
Observation distance	≈ 500 mm
Recording method	Dual frame/single exposure
Recording medium	1600(H) \times 1200(V) pixel ^a , progressive scan CCD
Recording lens	$f = 105$ mm, $f_{\#} = 4.0$
Illumination	Dual cavity Nd:YAG laser ^b , 120 mJ/pulse
Acquisition rate	15 Hz (188 image pairs per sequence)
Pulse delay	$\Delta t = 1.5 - 2.5$ μ s
Seeding material	Paraffin oil ($d_p \approx 0.3 \dots 1.2$ μ m)

^aOnly 1100(V) lines utilized^bFrequency doubled

portion of the spatial energy spectrum, limited by the wave numbers corresponding to the largest scales (given by the field size) and the smallest scales respectively (interrogation window size). A detailed analysis on the effect of the velocity spectrum captured with PIV on the measurement accuracy is given by FOUCAULT et al. [12].

Figures 12.18, 12.19 and 12.20 provide some samples of the experimental data obtained with PIV in the radial compressor diffuser passage (Table 12.7). A closer discussion of these PIV results, more detailed information on the compressor rig as well as further investigations using stereo PIV can be found in VOGES et al. [28].

12.6 Transonic Buffeting Measurements on a 1:60 Scale Ariane 5 Launcher Using High Speed PIV

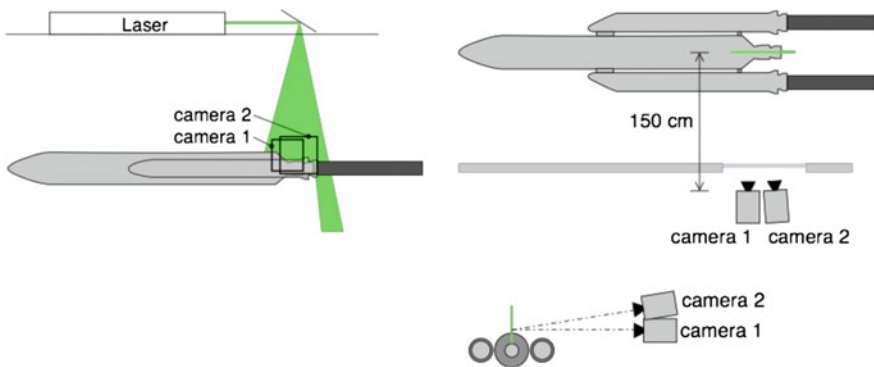
Contributed by:

F. Schrijer, A. Sciacchitano and F. Scarano

The aim of the experiments was to investigate transonic buffeting in the base region of the Ariane 5 launcher within the framework of the ESA TRP “Unsteady Subscale Force Measurements within a Launch Vehicle Base Buffeting Environment”. Measurements were performed on a 1:60 scale Ariane 5 model in the DNW-HST wind tunnel at Mach 0.5 and 0.8. Various flow control devices were added to the base of the main launcher such as a skirt and scoop and their effect on the flow field unsteadiness was inferred. In total four configurations are tested. For more information on the tested configurations, the reader is referred to [15] (Table 12.8).

Table 12.8 Experimental parameters

Flow geometry	Ma = 0.5 and 0.8 parallel to light sheet
Maximum in-plane velocity	$U_{\max} = 280$ m/s
Field of view	92×92 mm ² ; 110×100 mm ²
Interrogation volume	$3.6 \times 3.6 \times 2$ mm ³ ($H \times W \times D$)
Dynamic spatial range	DSR = 25 : 1
Dynamics velocity range	DVR = 100 : 1
Observation distance	150 cm
Recording method	Dual frame/single exposure
Recording medium	CMOS camera (Highspeed star 6)
Recording lens	$f = 200$ mm, $f_{\#} = 2$; $f = 180$ mm, $f_{\#} = 2.8$
Illumination	Nd:YLF laser
Recording frequency	$f_{\text{acq}} = 2.7$ kHz
Seeding material	DEHS

**Fig. 12.21** Experimental setup

The model is located horizontally in the wind tunnel test section and is supported by a z-sting to reduce acoustic interference. Illumination was provided by a Litron LDY303HE Nd:YLF laser which is rated at 22.5 mJ/pulse at 1 kHz. The laser is positioned on top of the test section inside the wind tunnel plenum. The light sheet forming optics is placed directly at the exit of the laser. Subsequently, the formed sheet is reflected into the test section by means of a front-coated mirror (Fig. 12.21).

The laser sheet thickness was set to approximately 2 mm and the width was 15 cm. The particle images were recorded by 2 LaVision HighSpeedStar 6 CMOS cameras having a resolution of 1024×1024 pixel. Camera 1 was equipped with a Nikkor 200 mm objective at $f_{\#} = 2$. The field of view of this camera was 92×92 mm² (optical magnification is 0.22). The second camera had a Nikkor 180 mm objective at $f_{\#} = 2.8$ and the field of view was 110×100 mm² (optical magnification is 0.19). Liquid DEHS tracer particles were used in the experiments having a typical response

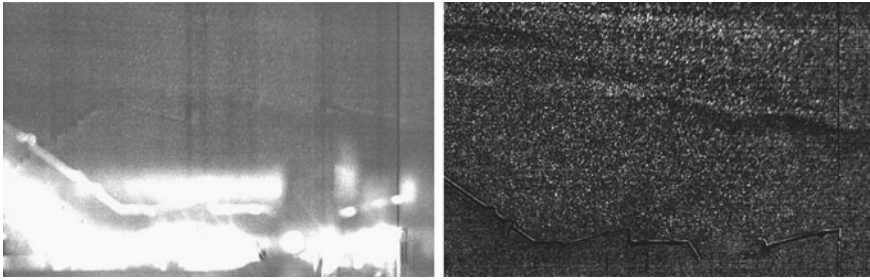


Fig. 12.22 Raw image taken by the camera 2 (left) and image after pre-processing (right)

time of $2\ \mu\text{s}$ [23]. The particle concentration was estimated to be between 1 and 5 particles/ mm^3 .

The measurement acquisition frequency was set to 2.7 kHz (maximum at full resolution). The laser pulse time separation was set to $5\ \mu\text{s}$ for Mach 0.5 and $4\ \mu\text{s}$ at Mach 0.8 in order to optimize the particle displacement between two successive PIV snapshots. At Mach 0.5, 1000 image pairs were recorded for each configuration, which resulted into a measurement duration of 370 ms. For Mach 0.8 the camera buffer was completely filled resulting in 2728 image pairs and a total measurement duration of 1010 ms.

Although the model was treated with a black marker pen, substantial image pre-processing was required in order to remove laser-light reflections coming from the model, wind tunnel walls and windows. The pre-processing algorithm is based on a pixel wise filtering in the frequency domain, which allows to separate the low frequency which is associated to the reflections from the high frequency content coming from the particles [26]. A typical result of the pre-processing algorithm is illustrated in Fig. 12.22, where it can be clearly seen that reflections present in the top image are successfully removed without compromise to the particle images.

After pre-processing, the velocity fields are obtained from the image pairs using an iterative cross-correlation based interrogation algorithm using window deformation. The software used for acquisition and processing is DaVis 7.4 by LaVision. The instantaneous velocity fields use snapshot correlation with a final window size of 32×32 pixel and 75% overlap; this choice allows sufficient spatial resolution (vector pitch of 0.72 mm in the stitched flow field) and robustness (about 8–10 particle images per window). The PIV interrogation window is elliptically shaped with aspect ratio 2:1 for a more accurate measurement of the velocity field in the shear layer. The time-averaged flow in the boundary layer is calculated by averaging the correlation signal over the entire sequence, which results in a very robust estimate of the velocity profile at high spatial resolution (window size: 16×16 pixel and vector pitch of 0.36 mm) (Fig. 12.23). After the images are processed, the results from both cameras are stitched to provide the complete flow field in the base of the model spanning a region from 1 cm upstream to 1 cm downstream of the nozzle.

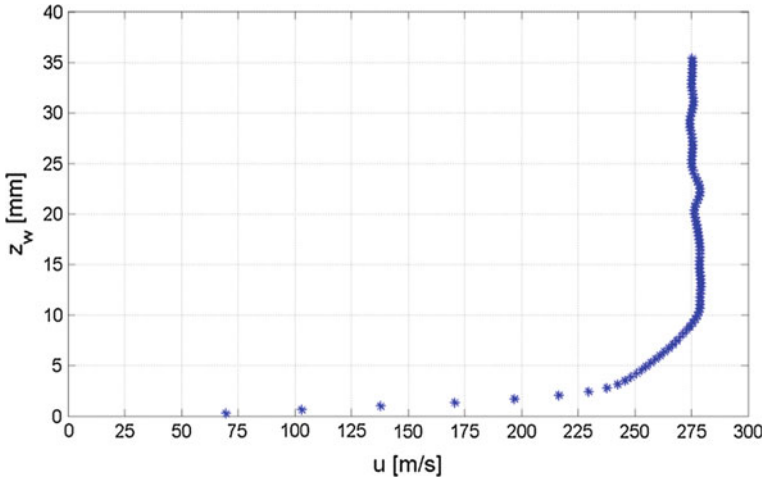


Fig. 12.23 Boundary layer profile close to shear layer separation

A typical instantaneous velocity field is depicted in Fig. 12.24, where the vectors are sub-sampled of factor 4 in the horizontal direction for clear visualization. The continuous black line in the contour delimits the back-flow regions. The main features of the flow are visible: the flow separates at the edge of the model base and reattaches on the nozzle surface at approximately $x = -10$ mm. The shear layer between the external and the base flow has unsteady behaviour and flaps in the vertical direction. Therefore, the reattachment point oscillates forth and back over the model surface.

In Fig. 12.25 the mean horizontal velocity is shown for Mach 0.8. Similar to the instantaneous snapshots the vector field as is shown is subsampled with a factor 4 in

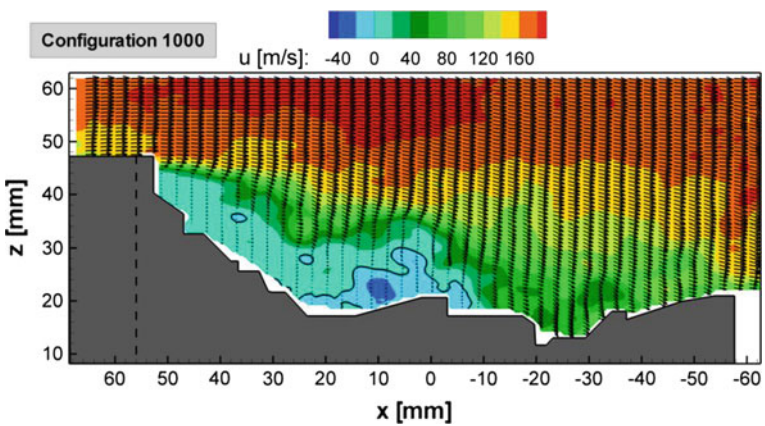


Fig. 12.24 Instantaneous flow field for Mach 0.5

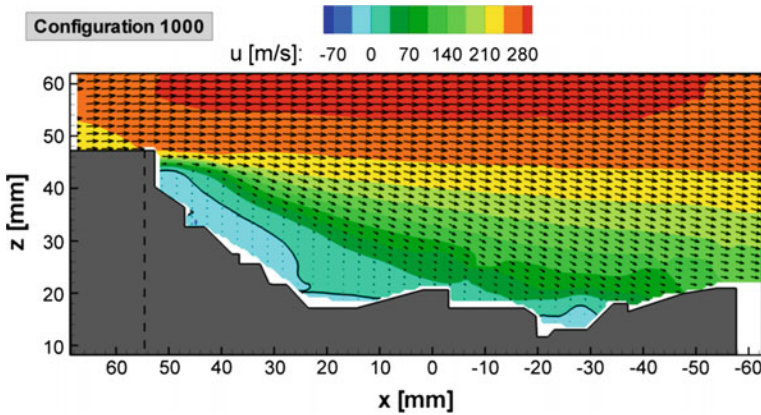


Fig. 12.25 Average flow field for Mach 0.8 (solid black line indicates the region of backflow)

horizontal and a factor 2 in vertical direction for sake of clarity. The mean velocity field also clearly shows the low velocity region between the model and the shear layer, where the velocity is below 20 m/s. The reverse-flow region (above -20 m/s) takes place close to the model surface and is relatively small. Shear layer impingement occurs on the nozzle between $x = -30$ mm and $x = -40$ mm.

The turbulence intensity herein defined as $TI = \sqrt{0.5 [(\bar{u}'/U_\infty)^2 + (\bar{v}'/U_\infty)^2]}$ is shown in Fig. 12.26 for Mach 0.8. When travelling downstream along the shear layer, the turbulence intensity increases and reaches a peak value of about 18 %.

Finally the power spectrum of the velocity is computed in a region directly above the separated shear layer, see Fig. 12.27. A peak is found at a frequency of 400 Hz, which corresponds to a Strouhal number of 0.2 which is the typical frequency at which transonic baseflow buffeting occurs.

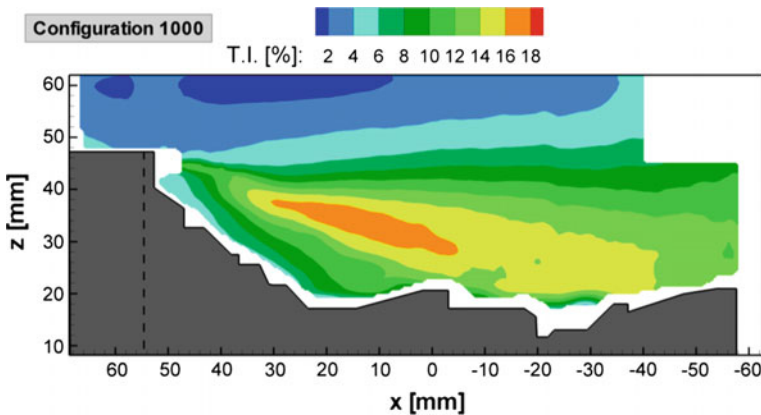


Fig. 12.26 Turbulence intensity for Mach 0.8

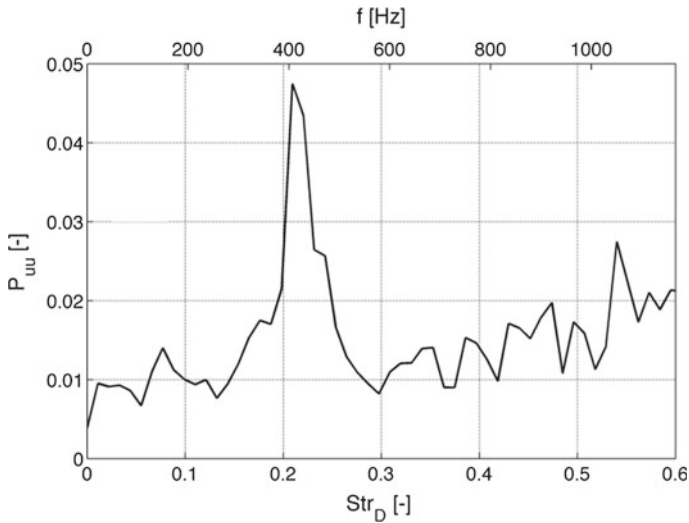


Fig. 12.27 Velocity power spectrum taken directly above the separation point

12.7 Supersonic PIV Measurements on a Space Shuttle Model

Contributed by:

J.T. Heineck, E.T. Schairer and S.M. Walker

Before the Space Shuttle could return to flight after the loss of Columbia, NASA was required to validate the computational fluid dynamics (CFD) codes that it uses to predict the trajectories of debris that may be shed from the External Tank (ET) during launch. To meet this and other requirements, NASA conducted two tests of a 3% scale model of the Shuttle ascent configuration in the NASA Ames Unitary Plan 9– by 7–foot Supersonic Wind Tunnel (9×7 SWT). In these tests, Dual Plane Particle Image Velocimetry (PIV) was used to measure the three components of velocity upstream of the Orbiter wings where debris shed from the ET would be convected downstream. The measurements were made in four cross-stream vertical planes located at different axial positions upstream of the Orbiter and above the ET. The measurements were made at two Mach numbers (1.55 and 2.5) over a range of model attitudes (Table 12.9).

An adjustable dual-plane laser projection system was required to allow the position of the second plane to be remotely moved downstream during testing operations. This was necessary because the Mach number range was too large to allow a fixed downstream separation of the first and second laser sheets. Each sheet was produced from separate laser heads, with each head providing 250 mJ per pulse. The laser heads were rotated 90° with respect to each other to allow the beams to be combined using a polarized beamsplitter cube. The beam from

Table 12.9 PIV recording parameters for supersonic flow above space shuttle external tank

Recording geometry	Light sheet swept 15° from normal to the stream
Maximum cross-plane velocity	$U_{\max} = 585 \text{ m/s}$
Maximum in-plane velocity	$V_{\max} = 130 \text{ m/s}$
Field of view	$870 \times 380 \text{ mm}^2$
Interrogation volume	$20 \times 10 \times 4 \text{ mm}^3 (H \times W \times D)$
Observation distance	1.8 m–3.2 m
Recording method	Dual frame - single exposure
Recording medium	CCD 1386×1024 pixel
Recording lens	$f = 35 \text{ mm}, f_{\#} = 2.0$ and $50 \text{ mm}, f_{\#} = 1.2$
Illumination	Two Nd:YAG laser* 250 mJ/pulse
Seeding material	Oil droplets ($d_p \approx 0.5 \mu\text{m} - 1.0 \mu\text{m}$)

*Frequency doubled

the second laser was reflected into the cube by a mirror mounted on a high-resolution translation stage. With this arrangement, the separation of the laser sheets corresponded to the readout of the translation stage controller. The plate that supported both lasers and all of the optics was carried by a linear traverse that provided one meter of displacement in the streamwise direction. This traverse permitted remote control of the streamwise locations of the measurement planes.

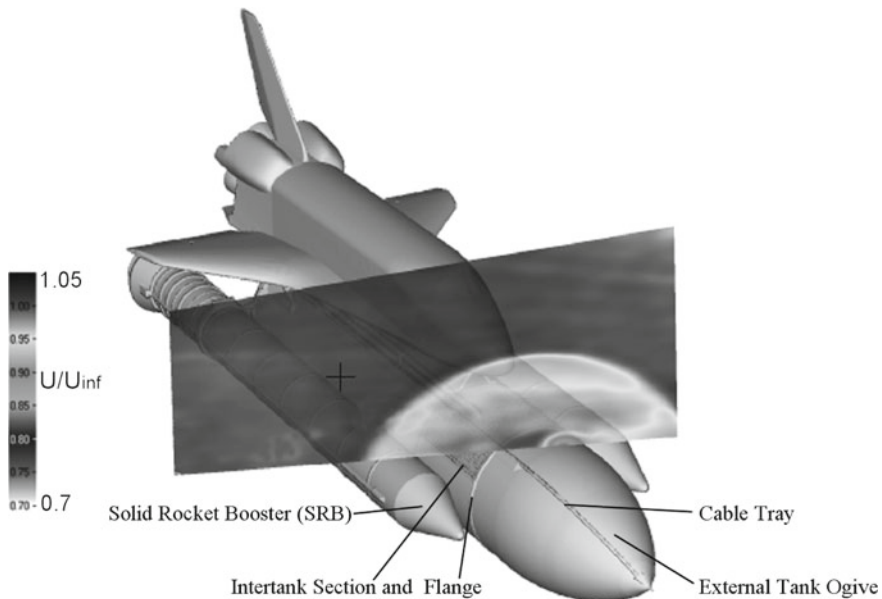


Fig. 12.28 Sample plot of normalized axial velocity in the most upstream measurement plane $Ma_{\infty} = 2.5, \alpha = 0^\circ, \beta = 0^\circ$

The high stream velocity necessitated the use of the dual plane technique. These measurements revealed a complex network of interacting shock waves and a region of turbulent, separated flow on the ET just upstream of the Orbiter-to-ET attach point (“bipod”), where foam broke loose during Columbia’s final flight. Figure 12.28 shows average axial velocities in the most upstream measurement plane for a typical case. Higher spatial-resolution measurements were made in a single vertical plane in the separated-flow region above the Intertank section of the ET. More than 7000 samples were acquired at a single test condition to allow computing turbulence statistics. Figure 12.29 shows a plot of the overall velocities measured at this position. Further details can be found in [16].

Figure 12.28 clearly shows the bow shock-wave from the nose of the External Tank (ET). The data are not laterally symmetric because the measurement plane was not perpendicular to the flow (it was yawed 15°). In addition, the cable tray on the starboard side of the ET ogive (Fig. 12.28) probably induced flow asymmetry. Figure 12.29 shows the shock wave from the flange at the upstream edge of the Intertank. As in Fig. 12.28, the measurement plane is yawed with respect to the freestream direction. The lower-speed region near the surface is a separation bubble. Turbulence statistics were derived from this dataset.

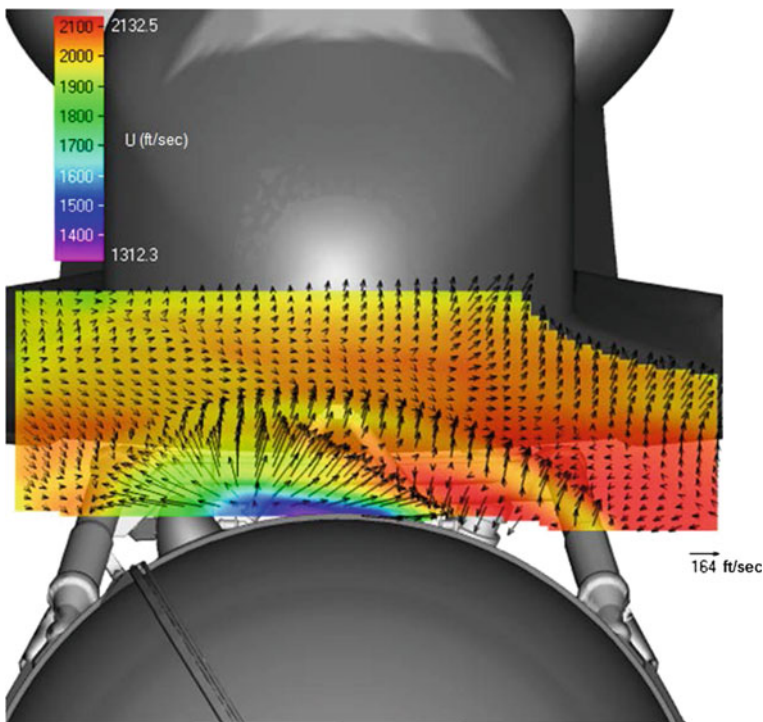


Fig. 12.29 Contours of mean axial velocity with vectors indicating mean spanwise and vertical velocities (m/s). $Ma_\infty = 2.5$, $\alpha = 0^\circ$, $\beta = 0^\circ$

12.8 PIV in a High-Speed Wind Tunnel

Contributed by:

S.J. Beresh

Introducing PIV to compressible flows raises unique challenges, but this has not prevented many users from successfully implementing PIV at supersonic and even hypersonic Mach numbers (e.g., [25]). This brief chapter is meant only to describe the author's own experience operating PIV at transonic and supersonic velocities in the Trisonic Wind Tunnel (TWT) at Sandia National Laboratories. The TWT is a blowdown-to-atmosphere facility capable of Mach 0.5 – 3.0 using a number of interchangeable test sections of typically 305 mm × 305 mm dimensions, all enclosed in a pressurized plenum (more recording parameters are listed in Table 12.10).

As is often the case when operating PIV in demanding flows, the largest challenge is satisfactorily seeding the flow. In a high-speed flow, particle lag must be minimized by using smaller particles. These scatter less light, which generally must be compensated by greater laser energy, though sometimes laser and camera arrangements may be advantageously designed to collect light in forward scatter. Moreover, most high-speed tunnels used for research are blowdown facilities, which are considerably more difficult to seed than closed-return wind tunnels because only one pass is available to achieve an adequate uniformity of the particle distribution in time and space.

Seeding in TWT is accomplished using a thermal smoke generator (Corona Vi-Count 5000) that produces a large quantity of particles typically 0.2 – 0.3 μm in diameter (peak of q_1 , see Sect. 2.1.6) from a mineral oil base. The smoke generator is contained within a pressurized tank to force the smoke through a duct into the elevated pressure of the TWT's stagnation chamber, where injector tubes distribute the particles throughout the flow. The flow conditioning section of the TWT removes disturbances induced by particle injection and assists in dispersing the particles. This method has successfully scaled up to larger facilities as well [7].

In situ measurement of particle response across the shock wave generated by a wedge has been conducted at several supersonic Mach numbers and shock angles, consistently indicating a particle diameter of 0.7–0.8 μm . This is greater than the nominal particle diameter produced by the smoke generator and is assumed to be attributed to agglomeration in the ducting. Further details on the analysis of measured particle sizes are given in Sect. 2.1.6. The particle size is expected to be identical under transonic operation of the TWT. A posteriori analysis of the velocity gradients in several transonic PIV experiments estimates Stokes numbers of no more than 0.05, which indicates negligible error due to particle lag.

Solid particles also have been effectively used in high-speed facilities (e.g., [7]). These have the advantage of dispersal as smaller agglomerated particle sizes if treated appropriately, but ordinarily have a specific gravity about four times that of oils. They also can be more difficult to clean and may pose a damage risk to some tunnel components. The liquid-based particles have proven effective and reliable in TWT for all cases save those with massively separated, low density wakes at supersonic conditions.

Table 12.10 Typical PIV recording parameters for flows in Sandia's TWT

Flow geometry	Many varied aerodynamic applications
Maximum in-plane velocity	285 m/s at Mach 0.8; 600 m/s at Mach 2.5
Field of view	From $25 \times 25 \text{ mm}^2$ to $250 \times 160 \text{ mm}^2$
Interrogation volume	From $0.5 \times 0.5 \times 1.0 \text{ mm}^3$ to $5.0 \times 5.0 \times 2.0 \text{ mm}^3$
Dynamic spatial range	Maximum $\sim 100 : 1$
Dynamic velocity range	Maximum $\sim 150 : 1$
Observation distance	$\sim 1.0 \text{ m}$
Recording method	Dual frame/single exposure
Ambiguity removal	Frame-straddling
Recording medium	Full-frame interline transfer CCD or CMOS
Recording lens	$f = 105$ or 200 mm
Illumination	Dual-cavity frequency-doubled Nd:YAG laser 300 – 400 mJ/pulse at 532 nm, 10 Hz
Pulse delay	0.5 – 4.0 μs
Seeding material	Mineral oil ($d_p = 0.7 - 0.8 \mu\text{m}$)

Additional considerations arise for high-speed flows, an example of which is aero-optical distortion [9]. An inhomogeneous refractive index due to turbulence is generally negligible at the modest compressibility of the TWT, but bulk differences in the refractive index are present at the windows. This creates a subtle but non-negligible difference in the optical path for oblique camera angles in stereoscopic PIV for wind-off versus wind-on conditions, influencing the camera registration. Self-calibration may be used to correct such errors, but is not universally effective [8]. Obviously, the greater velocities of compressible flows require briefer laser pulse separation times, but this lies well within the capabilities of modern PIV cameras. Time-resolved [DC12.5] PIV remains difficult because rapid pulse sequences are required rather than just pairs, but recently even this has become feasible in compressible flows [2]. Finally, optical access tends to be considerably more restricted in high-speed facilities, in part due to pressure requirements but also because most such facilities date from when schlieren imaging was the only optical consideration. Creating paths for the laser sheet may require a fair amount of mechanical alteration. Stereo PIV often is advantageous over two-component PIV because of its greater flexibility in camera position.

Despite these complications, and numerous other surprises that inevitably emerge during the course of an experiment, PIV has proven very capable and rewarding in compressible flows. An example is shown in Fig. 12.30, in which stereo PIV was acquired in the crossplane of a trailing vortex generated by a wall-mounted fin. The laser sheet was introduced from the bottom of the wind tunnel (left), passing through a window in the underside of the plenum then through a matching flush-mounted

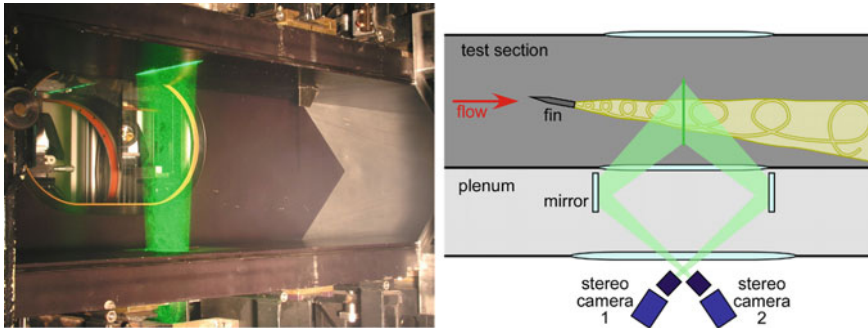


Fig. 12.30 Stereo PIV in the crossplane of a fin trailing vortex; photograph (left) and experimental sketch (right). Not to scale. Mirrors reduce the oblique camera angles [DC12.6]

window in the floor of the test section. Both cameras looked through the same window of the test section (right), viewing the laser sheet from opposite directions, because placing one camera at the other side-wall window precludes access to the test section. To accommodate the limited optical access, the laser sheet was positioned in the center of the side-wall window used for imaging, then mirrors were rigidly mounted inside the plenum to reduce the sharpness of the oblique camera angles. Wind tunnel vibrations have been found not to pose a difficulty for the mirrors at subsonic conditions, or even for supersonic conditions at modest Reynolds numbers. Camera lenses were placed on Scheimpflug mounts to obtain the necessary oblique focal plane. Four different downstream stations were surveyed not by translating the laser sheet and cameras, but instead by the much simpler process of moving the fin itself. Data were obtained using a 10 Hz laser with about 400 mJ per pulse, with pulse separation times of 1.4 μs .

Figure 12.31 shows an example of the results with the fin canted at a 10° angle of attack and a freestream Mach number of 0.8 [5]. Four measurement stations show contour plots of the out-of-plane (streamwise) velocities along with an inset that adds in-plane velocity vectors for the downstream station. The axes have been normalized by the fin chord length c and velocities by the freestream velocity U_∞ . Data such as these measure the fin trailing vortex and derived quantities such as vortex circulation, position, and size [DC12.7] may be used to explore the aerodynamic interference with a downstream control surface [5]. Mean [3] and turbulent [4] characterization [DC12.8] of the vortex provide insight into its behavior and decay as well as aid the development of predictive models.

A more complex optical arrangement was required for the example shown in Fig. 12.32. Here, a Mach 0.8 flow over a finite-width rectangular cavity was measured by a dual stereo configuration employing four cameras viewing a laser sheet aligned to the streamwise plane [2, 6]. The cavity was installed into the floor of the test section and a glass floor to the cavity allowed the laser sheet entry. Four cameras were used to obtain two stereo fields of view that together spanned the entire cavity extent. All four cameras were equipped with lenses mounted on Scheimpflug platforms viewing the imaging region using compound angles. Half-angles of 12° separated the two cameras of each stereo pair in the streamwise plane; this is sub-optimal for

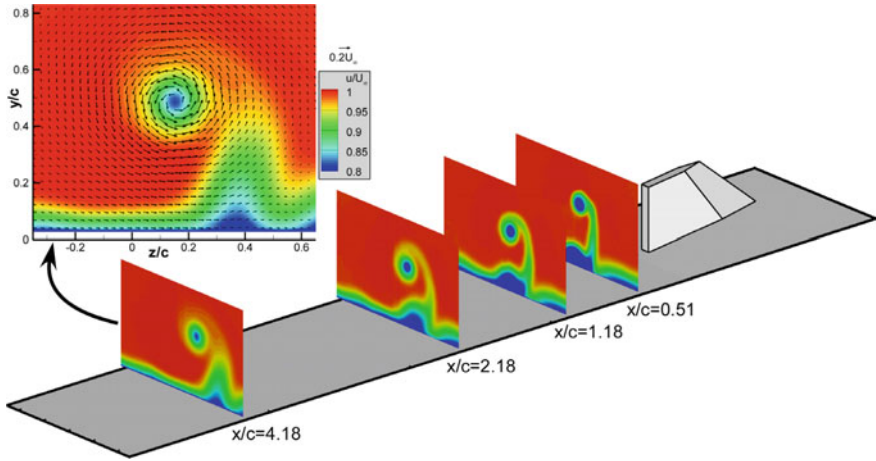


Fig. 12.31 Mean streamwise velocity field (out-of-plane) of the fin trailing vortex at Mach 0.8 [DC12.9]

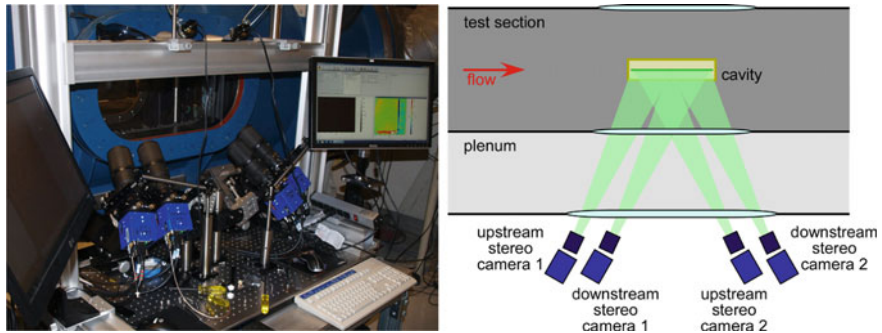


Fig. 12.32 Dual stereo PIV of transonic flow over a rectangular cavity; photograph of the camera positions (left) and experimental sketch (right). Not to scale [DC12.10]

stereoscopic measurements but a greater angle would have suffered occlusion of the field of view by the fore or aft edges of the cavity. Additionally, the cameras were tilted in the vertical plane at about 35° to provide sufficient angle to peer over the cavity side lip and view its floor. This vertical angle was made possible within the optical access restrictions of the TWT by rigidly mounting a mirror horizontally inside the plenum to reflect scattered light back down towards the cameras at a sharper angle. The mirrors are not evident in Fig. 12.32.

The camera configuration of Fig. 12.32 is a good example of the power and flexibility of stereo calibration. Cameras may be aligned as demanded by optical access restrictions and a routine calibration will provide the necessary corrections. The cameras were each placed on tilt and translation stages to facilitate a precise alignment. Calibrations were accomplished by scanning a single-plane alignment target through the volume of the laser sheet to acquire seven planes of calibration data, which were

calibrated using a polynomial fit. Self-calibration was performed to minimize camera registration error. The polynomial calibration is preferred due to its superiority for imaging through the two thick windows of the test section and plenum. While the use of a two-plane target has become commonplace in PIV experiments, the extra calibration planes provide additional fiduciary dots to improve the quality of the polynomial fit.

Although the vibration external to the wind tunnel is fairly mild, over the duration of an experiment such perturbations are sufficient to cause camera alignment to drift. Self-calibration can be used to correct such drift on a daily or even run-to-run basis, but if possible it is preferable to construct a rigid camera setup. The photograph in Fig. 12.32 shows that numerous optomechanics were used to brace both the camera bodies and the lenses. Once alignment was complete – but prior to the final stereo calibration – the braces were secured. In practice, a well-designed experiment can remain stable for many weeks if quality optomechanics are used and care is taken by personnel working nearby.

An example instantaneous velocity field is shown in Fig. 12.33. Vectors show the in-plane velocities superposed on a contour plot of the streamwise velocity component. The positions of the cavity walls coincide with the axes to locate the field of view. In the primary plot, vectors have been subsampled by a factor of four along each axis and smoothed to emphasize the large-scale turbulent structure; the inset shows the finer scale turbulence that can be measured from unaltered vectors. Figure 12.33 portrays the shear layer over the top of the cavity growing as it approaches the aft end of the cavity, while reverse velocities can be observed in the recirculation region near the cavity floor. Large-scale vortices are visible in the primary plot and the smaller scales shown in the inset demonstrate the range of features that are contained in a single measurement. Data such as these may be further analyzed for such quantities as mean and turbulent fields [2] [DC12.11] or the coherent structures associated with resonance [29].

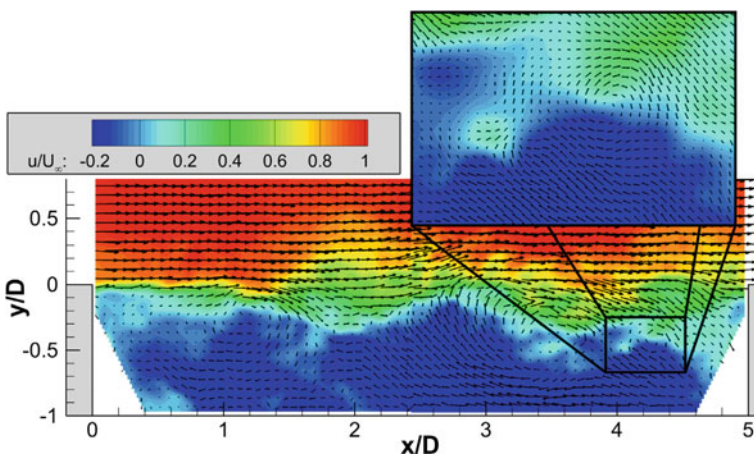


Fig. 12.33 Sample instantaneous vector field of flow over a cavity. Vectors in the primary plot are subsampled 4×4 and the inset shows all vectors in a zoomed region [DC12.12]

In addition to their value for the discovery of fluid dynamics, data such as these are used for the development and validation of predictive simulations. For example, the cavity flow data have been used to develop predictive capability for the aeroacoustic environment of stores carried in flight [1]. Other PIV data sets concerning a jet in crossflow have been used to calibrate simulations for jet interactions on maneuvering vehicles [24]. Numerous other examples may be found in which PIV is impacting the predictive tools used for modern aerospace engineering.

References

1. Arunajatesan, S., Barone, M.F., Wagner, J.L., Casper, K.M., Beresh, S.J.: Joint experimental/computational investigation into the effects of finite width on transonic cavity flow. *AIAA Pap.* **3027** (2014). DOI 10.2514/6.2014-3027. URL <https://doi.org/10.2514/6.2014-3027>
2. Beresh, S., Kearney, S., Wagner, J., Guildenbecher, D., Henfling, J., Spillers, R., Pruett, B., Jiang, N., Slipchenko, M., Mance, J., Roy, S.: Pulse-burst PIV in a high-speed wind tunnel. *Meas. Sci. Technol.* **26**(9), 095,305 (2015). DOI 10.1088/0957-0233/26/9/095305. URL <https://doi.org/10.1088/0957-0233/26/9/095305>
3. Beresh, S.J., Henfling, J.F., Spillers, R.W.: Planar velocimetry of a fin trailing vortex in subsonic compressible flow. *AIAA J.* **47**(7), 1730–1740 (2009). DOI 10.2514/1.42097. URL <https://doi.org/10.2514/1.42097>
4. Beresh, S.J., Henfling, J.F., Spillers, R.W.: Turbulence of a fin trailing vortex in subsonic compressible flow. *AIAA J.* **50**(11), 2609–2622 (2012). DOI 10.2514/1.J051904. URL <https://doi.org/10.2514/1.J051904>
5. Beresh, S.J., Smith, J.A., Henfling, J.F., Grasser, T.W., Spillers, R.W.: Interaction of a fin trailing vortex with a downstream control surface. *J. Spacecr. Rockets* **46**(2), 318–328 (2009). DOI 10.2514/1.40294. URL <https://doi.org/10.2514/1.40294>
6. Beresh, S.J., Wagner, J.L., Henfling, J.F., Spillers, R.W., Pruett, B.O.M.: Width effects in transonic flow over a rectangular cavity. *AIAA J.* **53**(12), 3831–3834 (2015)
7. Beresh, S.J., Wagner, J.L., Pruett, B., Spillers, R., McWithey, M., Gary, J., Chankaya, K.: Deployment of particle image velocimetry into the Lockheed Martin High Speed Wind Tunnel. In: 52nd Aerospace Sciences Meeting, p. 1238 (2014). DOI 10.2514/6.2014-1238. URL <https://doi.org/10.2514/6.2014-1238>
8. Beresh, S.J., Wagner, J.L., Smith, B.L.: Self-calibration performance in stereoscopic PIV acquired in a transonic wind tunnel. *Exp. Fluids* **57**(4), 1–17 (2016). DOI 10.1007/s00348-016-2131-y. URL <https://doi.org/10.1007/s00348-016-2131-y>
9. Elsinga, G.E., van Oudheusden, B.W., Scarano, F.: Evaluation of aero-optical distortion effects in PIV. *Exp. Fluids* **39**(2), 246–256 (2005). DOI 10.1007/s00348-005-1002-8. URL <https://doi.org/10.1007/s00348-005-1002-8>
10. Fitzgerald, E.J., Mueller, T.J.: Measurements in a separation bubble on an airfoil using laser velocimetry. *AIAA J.* **28**(4), 584–592 (1990). DOI 10.2514/3.10433. URL <https://doi.org/10.2514/3.10433>
11. Förster, W., Karpinsky, G., Krain, H., Röhle, I., Schodl, R.: 3-component Doppler laser-two-focus velocimetry applied to a transonic centrifugal compressor. In: *Laser Techniques for Fluid Mechanics*, pp. 55–74. Springer, Berlin (2002). DOI 10.1007/978-3-662-08263-8_4. URL https://doi.org/10.1007/978-3-662-08263-8_4
12. Foucaut, J.M., Carlier, J., Stanislas, M.: Piv optimization for the study of turbulent flow using spectral analysis. *Meas. Sci. Technol.* **15**(6), 1046 (2004). DOI 10.1088/0957-0233/15/6/003. URL <https://doi.org/10.1088/0957-0233/15/6/003>
13. Göttlich, E., Neumayer, F., Woisetschläger, J., Sanz, W., Heitmeir, F.: Investigation of stator-rotor interaction in a transonic turbine stage using laser-doppler-velocimetry and pneumatic

- probes. In: ASME Turbo Expo 2003, collocated with the 2003 International Joint Power Generation Conference, pp. 163–172. American Society of Mechanical Engineers (2003). DOI 10.1115/1.1649745. URL <https://doi.org/10.1115/1.1649745>
14. Göttlich, E., Woisetschläger, J., Pieringer, P., Hampel, B., Heitmeir, F.: Investigation of vortex shedding and wake-wake interaction in a transonic turbine stage using laser-doppler-velocimetry and particle-image-velocimetry. *J. Turbomach.* **128**(1), 178–187 (2006). DOI 10.1115/1.2103092. URL <https://doi.org/10.1115/1.2103092>
 15. Hannemann, K., Lüdeke, H., Pallegoix, J.F., Ollivier, A., Lambaré, H., Maseland, H., Geurts, E., Frey, M., Deck, S., Schrijer, F., Scarano, F., Schwane, R.: Launch vehicle base buffeting—recent experimental and numerical investigations. In: 7th European Symposium on Aerothermodynamics, Brugge, Belgium, vol. 692, p. 102 (2011)
 16. Heineck, J.T., Schairer, E.T., Walker, S.M.: Piv measurements of flow past the space shuttle ascent configuration in the nasa ames 9-by 7-foot supersonic wind tunnel. In: Proceedings of the 6th International Symposium on Particle Image Velocimetry (PIV 2005), Pasadena, CA (2005)
 17. Hergt, A., Klinner, J., Steinert, W., Grund, S., Beversdorff, M., Giebmanns, A., Schnell, R.: The effect of an eroded leading edge on the aerodynamic performance of a transonic fan blade cascade. *J. Turbomach.* **137**(2), 021,006–021,006–11 (2014). DOI 10.1115/1.4028215. URL <https://doi.org/10.1115/1.4028215>
 18. Klinner, J., Hergt, A., Willert, C.E.: Experimental investigation of the transonic flow around the leading edge of an eroded fan airfoil. *Exp. Fluids* **55**(9), 1800 (2014). DOI 10.1007/s00348-014-1800-y. URL <https://doi.org/10.1007/s00348-014-1800-y>
 19. Kompenhans, J., Raffel, M.: Application of PIV technique to transonic flows in a blow-down wind tunnel. In: Cha, S.S., Trolinger, J.D. (eds.) *Optical Techniques in Fluid, Thermal, and Combustion Flow*, San Diego, CA, United States, vol. 2005, pp. 425–436 (1993). DOI 10.1117/12.163727. URL <https://doi.org/10.1117/12.163727>
 20. Lee, B.H.K.: Self-sustained shock oscillations on airfoils at transonic speeds. *Prog. Aerosp. Sci.* **37**(2), 147–196 (2001). DOI 10.1016/S0376-0421(01)00003-3. URL <https://www.sciencedirect.com/science/article/pii/S0376042101000033>
 21. Raffel, M., Höfer, H., Kost, F., Willert, C.E., Kompenhans, J.: Experimental aspects of PIV measurements of transonic flow fields at a trailing edge model of a turbine blade. In: 8th International Symposium on Applications of Laser Techniques to Fluid Mechanics, Lisbon (Portugal) (1996)
 22. Raffel, M., Kompenhans, J.: PIV measurements of unsteady transonic flow fields above a NACA0012 airfoil. In: 5th International Conference on Laser Anemometry, Veldhoven (the Netherlands), pp. 527–535 (1993)
 23. Ragni, D., Schrijer, F., van Oudheusden, B.W., Scarano, F.: Particle tracer response across shocks measured by PIV. *Exp. Fluids* **50**(1), 53–64 (2011). DOI 10.1007/s00348-010-0892-2. URL <https://doi.org/10.1007/s00348-010-0892-2>
 24. Ray, J., Lefantzi, S., Arunajatesan, S., Dechant, L.: Bayesian parameter estimation of a $k-\epsilon$ model for accurate jet-in-crossflow simulations. *AIAA J.* pp. 1–17 (2016). DOI 10.2514/1.J054758. URL <https://doi.org/10.2514/1.J054758>
 25. Scarano, F.: Overview of PIV in supersonic flows, pp. 445–463. Springer, Berlin (2008). DOI 10.1007/978-3-540-73528-1_24. URL <https://doi.org/10.1007/978-3-540-73528-1>
 26. Sciacchitano, A., Scarano, F.: Elimination of PIV light reflections via a temporal high pass filter. *Meas. Sci. Technol.* **25**(8), 084,009 (2014). DOI 10.1088/0957-0233/25/8/084009. URL <http://stacks.iop.org/0957-0233/25/i=8/a=084009>
 27. Soloff, S.M., Adrian, R.J., Liu, Z.C.: Distortion compensation for generalized stereoscopic particle image velocimetry. *Meas. Sci. Technol.* **8**(12), 1441 (1997). DOI 10.1088/0957-0233/8/12/008. URL <https://doi.org/10.1088/0957-0233/8/12/008>
 28. Voges, M., Beversdorff, M., Willert, C., Krain, H.: Application of particle image velocimetry to a transonic centrifugal compressor. *Exp. Fluids* **43**(2–3), 371–384 (2007). DOI 10.1007/s00348-007-0279-1. URL <https://doi.org/10.1007/s00348-007-0279-1>

29. Wagner, J.L., Casper, K.M., Beresh, S.J., Arunajatesan, S., Henfling, J.F., Spillers, R.W., Pruett, B.O.: Relationship between acoustic tones and flow structure in transonic cavity flow. In: 45th AIAA Fluid Dynamics Conference (2015). DOI 10.2514/6.2015-2937. URL <https://doi.org/10.2514/6.2015-2937>
30. Wernet, M.P.: Development of digital particle imaging velocimetry for use in turbomachinery. *Exp. Fluids* **28**(2), 97–115 (2000). DOI 10.1007/s003480050015. URL <https://doi.org/10.1007/s003480050015>
31. Wernet, M.P.: A flow field investigation in the diffuser of a high-speed centrifugal compressor using digital particle imaging velocimetry. *Meas. Sci. Technol.* **11**(7), 1007 (2000). DOI 10.1088/0957-0233/11/7/316. URL <https://doi.org/10.1088/0957-0233/11/7/316>
32. Westerweel, J., Scarano, F.: Universal outlier detection for PIV data. *Exp. Fluids* **39**(6), 1096–1100 (2005). DOI 10.1007/s00348-005-0016-6. URL <https://doi.org/10.1007/s00348-005-0016-6>
33. Woisetschläger, J., Lang, H., Hampel, B., Göttlich, E., Heitmeir, F.: Influence of blade passing on the stator wake in a transonic turbine stage investigated by particle image velocimetry and laser vibrometry. *Proc. Inst. Mech. Eng. Part A: J. Power. Energy* **217**(4), 385–391 (2003). DOI 10.1243/095765003322315441. URL <https://doi.org/10.1243/095765003322315441>
34. Woisetschläger, J., Mayrhofer, N., Hampel, B., Lang, H., Sanz, W.: Laser-optical investigation of turbine wake flow. *Exp. Fluids* **34**(3), 371–378 (2003). DOI 10.1007/s00348-002-0568-7. URL <https://doi.org/10.1007/s00348-002-0568-7>
35. Woisetschläger, J., Pecnik, R., Göttlich, E., Schennach, O., Marn, A., Sanz, W., Heitmeir, F.: Experimental and numerical flow visualization in a transonic turbine. *J. Vis.* **11**(1), 95–102 (2008). DOI 10.1007/BF03181919. URL <https://doi.org/10.1007/BF03181919>

Chapter 13

Applications: Helicopter Aerodynamics

Rotor Nomenclature

a_∞	speed of sound (m)
c	chord (m/s)
C_T	rotor thrust coefficient ($C_T = T/\rho\pi\Omega^2 R^4$)
M_H	hover tip Mach number ($M_H = \Omega R/a_\infty$)
N_b	number of blades
R	blade radius (m)
r	radial distance (m)
r_c	vortex core radius (m)
T	thrust (N)
σ	solidity ($\sigma = N_b c/\pi R$)
ψ	blade azimuthal position (<i>deg</i>)
Ω	rotational rotor speed (rad/s)

13.1 Rotor Flow Investigation

Contributed by:

H. Richard, B.G. van der Wall and M. Raffel

With increasing use of civil helicopters the problem of noise radiation has become increasingly important within the last decades. Blade vortex interactions (BVI) have been identified as a major source of impulsive noise. As BVI-noise is governed by the induced velocities of tip vortices, it depends on vortex strength and miss-distance, which itself depends on vortex location, orientation, and convection speed relative to the path of the advancing blade. Blade vortex interaction can occur at different

An overview of the Digital Content to applications on helicopter aerodynamics can be found at [\[DC13.1\]](#).

locations inside the rotor plane depending on flight velocity and orientation of the blade tip path plane.

Within the last decade a large number of experimental investigations were performed in order to better understand and to model the development of rotor blade tip vortices [10, 15, 18, 19, 24, 25, 27, 28, 30, 31, 34, 36, 38]. Most of these studies were done in hovering condition, because the flow field is azimuthal axisymmetric under this condition, the vortices are convected below the rotor plane and are isolated in early stage in comparison to forward or descent flight where the vortices are entrained downstream and might interact with blade wake, other vortices and with the following blades. While earlier velocity measurements were obtained using intrusive techniques such as hot-wires, more recent flow measurements rely exclusively on optical techniques, mainly PIV [18, 37].

13.2 Wind Tunnel Measurements of Rotor Blade Vortices

Contributed by:

H. Richard, B.G. van der Wall and M. Raffel

This wind tunnel experiment has been performed in 2001 on a rotor model of 4 m diameter in the 6 m \times 8 m open test section of the Large Low-speed Facility (LLF) of the German Dutch Wind Tunnel (DNW) operated at 33 m/s. The helicopter rotor model used was a model of the MBB Bo 105 of the German Aerospace Center (DLR) Institute of Flight Systems in Braunschweig. The measurements have been performed in the frame of the HART II program [39]. The PIV parameters used for this investigation are listed in Table 13.1.

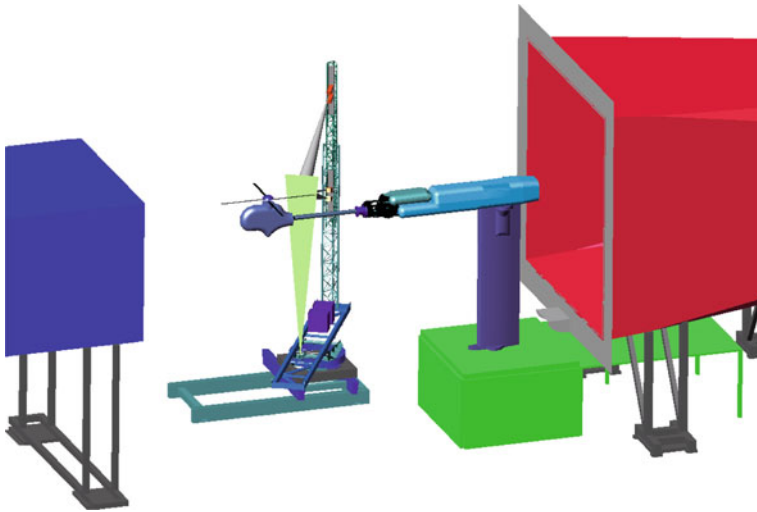
The rotor consists of four hingeless blades with 0.121 m chord length, rectangular blade planform, and -8° linear twist. The airfoil was a NACA 23012 with tabbed trailing edge. During this test, the model was mainly operated in descent flight conditions where blade vortex interaction dominates the noise radiation. The rotor rotational frequency was 17.35 Hz leading to a tip speed of 218 m/s. The PIV system consisted of five digital cameras and three double pulse Nd:YAG lasers with 2×320 mJ each, which were mounted, as sketched on Fig. 13.1, onto a common traversing system in order to keep the distance between the cameras and the light sheet constant while scanning the rotor wake. The length of the traversing system was in the order of 10 m, the height approximately 15 m. Two stereo systems were used simultaneously. One system was equipped with a 300 mm lens in order to record a small observation area: 0.15 m \times 0.13 m, centered to the blade tip vortex and the second system was equipped with a 100 mm lens resulting in a field of view of 0.45 m \times 0.38 m. The large field of view was intended for an overview of the vortex and of the surrounding flow whereas the small field of view was intended for vortex analysis.

For each position and rotor condition, 100 instantaneous PIV images were recorded. More than half a Tera Byte (650 GB) of PIV raw data had been recorded at

Table 13.1 PIV recording parameters for HART II

Flow geometry	$U_{\infty} = 70 \text{ m/s}$
Maximum in-plane velocity	$U_{\max} \approx 70 \text{ m/s}$
Field of view	$450 \times 380 \text{ mm}^2$ and $150 \times 130 \text{ mm}^2$
Interrogation volume	$3.1 \times 3.1 \times 2 \text{ mm}^3$ ($H \times W \times D$)
Dynamic spatial range	$\text{DSR} \approx 31 : 1$
Dynamic velocity range	$\text{DVR} \approx 40 : 1$
Observation distance	$z_0 \approx 5.6 \text{ m}$
Recording method	Double frame/single exposure
Ambiguity removal	Frame separation (frame-straddling)
Recording medium	Full frame interline transfer CCD (1280×1024 pixel)
Recording lens	$f = 100 \text{ mm}$ and 300 mm , $f_{\#} = 2.8$
Illumination	$3 \times \text{Nd:YAG laser}^a$ 320 mJ/pulse
Pulse delay	$\Delta t = 7 - 20 \mu\text{s}$
Seeding material	DEHS droplets ($d_p \approx 1 \mu\text{m}$)

^aFrequency doubled

**Fig. 13.1** HART II stereoscopic PIV setup

various positions on the advancing and the retreating side. 3C-PIV data from rotating tip vortices experiments are challenging from an analysis point of view. Conditional averaging is mandatory for proper analysis of vortex properties in order to take into account the model motion, vortex wander, aperiodic phenomena and other disturbing

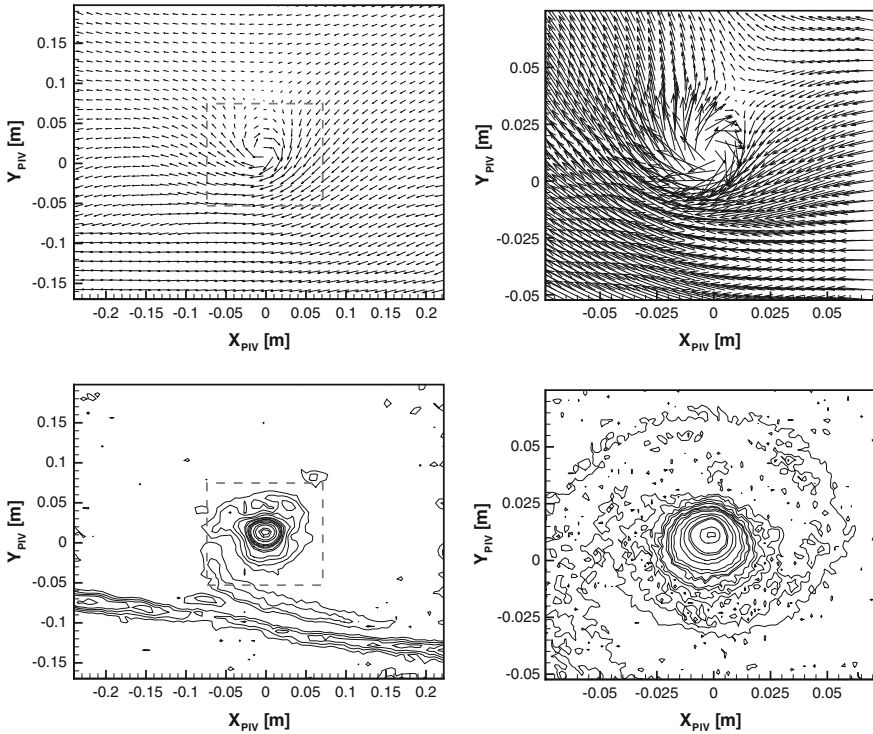


Fig. 13.2 Averaged velocity (top) and vorticity (bottom) maps of a blade tip vortex; large field of view (left) and close-up view (right)

effects. In most cases the vortices are not measured perfectly perpendicular to their axis and the measurement plane must be re-oriented into the vortex axis system. Several methods to perform such post-processing are described in [37].

Conditionally averaged velocity and vorticity maps obtained by each stereo system are displayed in Fig. 13.2. The detection of the vortex needed to perform the conditional average was done using the wavelet detection method.

The results on the left were obtained with the large field of view stereo system. The blade tip vortex is clearly visible as well as the wake of the previous blade whereas on the small field of view on the right only the vortex can be seen but with a high spatial resolution.

13.3 Measurement of Rotor Blade Vortices in Hover

Contributed by:

H. Richard, B.G. van der Wall and M. Raffel

In order to investigate the development of blade tip vortices under different rotor conditions like thrust and rotational speed, both two- and three-component PIV measurements were performed on the same 40% Mach scaled Bo105 model rotor in hover condition as has been explained earlier. The vortices were traced from their creation at the trailing edge of the blade up to half a revolution behind the blade with azimuth steps between 1° and 10° and different spatial resolutions. In addition, a sequence of three-component measurements was performed just after the vortex creation at finer azimuth steps of 0.056° in order to generate a three-dimensional volumetric data set of the blade tip vortex. The influence of the PIV image analysis parameters on the vortex parameters derived -in particular sampling window size and window overlap- has been investigated. The measurements presented are part of the HOTIS (HOVer Tip vortex Structure) project.

Within the HOTIS project velocity field measurements were conducted using two-component (2C) and three-component (3C) PIV on a four-bladed rotor in hover condition in ground effect inside the rotor preparation hall of the Institute of Flight Systems at DLR Braunschweig. The aging process of the blade tip vortex and the influence of the rotor parameters on the vortex characteristics were investigated at different vortex ages from 1° to 150° for several rotor parameters: rotation speed

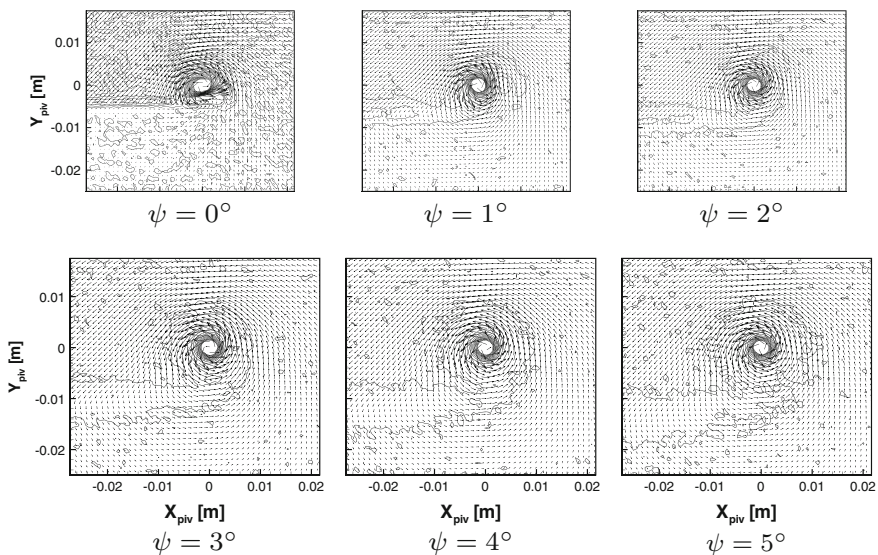


Fig. 13.3 Averaged velocity and vorticity maps of a young blade tip vortex measured with 2C-PIV

(200, 540 and 1041 rpm) and thrust (from 0 N to 3500 N). The blade tip vortex was measured with different spatial resolutions: low and very high spatial resolution in case of 2C-PIV measurements and with high spatial resolution for 3C-PIV. Figure 13.3 shows an example of the vortex development measured with the very low resolution 2C-PIV system. The spatial resolution, defined by the field of view and the size of the interrogation window, is an important parameter when looking for vortex properties such as maximum swirl velocity or core radius [37]. In addition to these measurements, 3C measurements were performed for vortex ages between 3.4° and 7° using very fine age increments of 0.056° in order to generate an averaged volumetrically resolved velocity data set of the vortex.

13.3.1 The Experimental Setup

The rotor model, which has been described in Sect. 13.2 was installed in the center of the $12\text{ m} \times 12\text{ m} \times 8\text{ m}$ rotor testing hall of DLR Braunschweig. The rotor was operated in ground effect - the hub center located 2.87 m above the ground - at different rotation speeds of 200, 540 and 1041 rpm, corresponding to tip Mach numbers of $M_H = 0.122, 0.329$ and 0.633 , and with different thrust coefficients varying from $C_T/\sigma = 0$ to 0.072 . Due to the closed hall, recirculation existed and generated an inherently unsteady flow field.

The illumination source of the PIV setup consisted of a double oscillator, frequency-doubled Nd:Yag laser (320 mJ/pulse at 532 nm) and light sheet forming optics which were bolted to the ground below the rotor. The light sheet was oriented vertically upward and parallel to the trailing edge of the rotor blade and had a waist thickness of 1–2 mm at the measurement plane and a width of around 30 cm. Three thermo-electrically cooled CCD-cameras, one regular (1280×1024 pixel) and two intensified PCO cameras (1360×1076 pixel) were used. One camera for 2C-PIV and for recording the position of the blade tip and the two other cameras in stereo

Fig. 13.4 Sketch of the PIV setup and of the rotor model

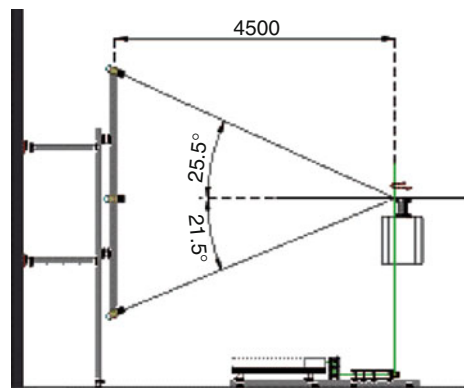
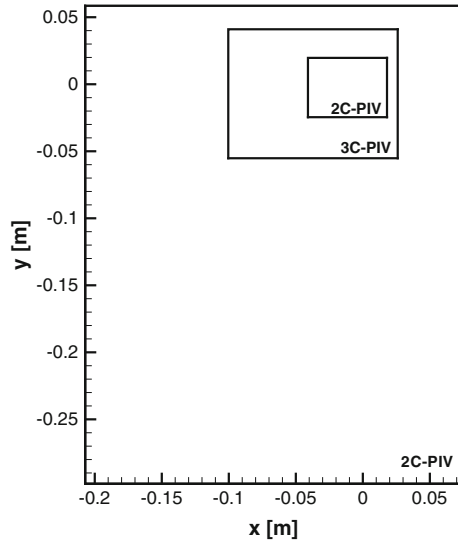


Fig. 13.5 The different fields of view



arrangement for 3C-PIV. The cameras were mounted on a support structure consisting of standard optical rails which was bolted to the wall of the testing hall. The complete PIV setup is shown on Fig. 13.4. The camera support can be seen on the left hand side of the figures. The cameras were located at 4.5 m from the rotor hub and the stereo cameras were mounted with a stereo viewing angle of 47° . Laser and camera were synchronized according to the one per revolution signal given by the reference blade of the rotor. This signal was delayed using a phase-shifter in order to measure at a desired blade azimuth angle.

Two component PIV measurements were performed using the middle camera which was first equipped with a $f = 85$ mm lens and later with a $f = 600$ mm yielding field of views of $281 \text{ mm} \times 357 \text{ mm}$ (low spatial resolution) and $58 \text{ mm} \times 45 \text{ mm}$ (high spatial resolution). The stereo system was equipped with a pair of $f = 300$ mm lenses with a common field of view of $126 \text{ mm} \times 96 \text{ mm}$.

Figure 13.5 shows the different fields of view measured during the campaign. The time delay between the two laser pulses was between 2 and $40 \mu\text{s}$ depending of the size of the field of view and of the velocity to be measured. Around 200 measurements were taken for each setting. The flow seeding was introduced to the measurement area by Laskin nozzle particle generators filled with DEHS fluid producing particles with a mean diameter below $1 \mu\text{m}$.

13.3.2 Evaluation and Analysis

Dewarping coefficients were extracted from calibration images in order to map the stereo recordings onto a common grid. A so-called disparity correction was applied as well using the actual PIV recordings in order to account for possible misalignment

between the calibration target and the light sheet plane. This correction is performed by cross-correlating simultaneously recorded images of the two views (upper and lower camera). The residual misalignment was found to be on the order of 100 pixel corresponding to a few millimeters in the object space. The resulting vector map is then used to correct the original mapping coefficients which were used to dewarp the raw PIV images prior to PIV interrogation. The images obtained during the measurement were pre-processed using high pass filter ($=3$ pixel), then binarized and finally low-pass filtered ($=0.7$ pixel) in order to increase the signal to noise ratio. A multi-grid PIV algorithm based on pyramid grid refinement and full image deformation was applied to process the image starting with large interrogation windows on a coarse grid and refining the windows and the grid with each pass. A sampling window of 64×64 pixel was used in the initial step gradually refining down to 24×24 pixel as final window size at 75% sample overlap which represent an interrogation area of $2.3 \text{ mm} \times 2.3 \text{ mm}$ for the 3C measurements and $1.05 \text{ mm} \times 1.05 \text{ mm}$ for the 2C measurements with very high resolution. Sub-pixel peak position estimation was performed by means of Whittaker reconstruction. All the processing was done using the PIVview software which makes use of the advanced algorithms presented in Sect. 5.3.4.3.

The primary aim of these measurements was to gain a better understanding of the development of the blade tip vortex, especially in its early stages of development. The velocity vector fields are used to extract vortex characteristics such as the maximum swirl velocity, the core radius or the peak of vorticity. Prior to the full processing of the PIV image, the influence of the PIV interrogation window size and overlap on these characteristics was investigated.

Sampling window size: One of the most important PIV parameters is the size of the interrogation or sampling window which, in terms of other measurement techniques, defines the probe volume. In case of vortex characteristic investigation, the decrease of window size results in an increase of maximum swirl velocity and a decrease of vortex radius [31, 37].

Sampling window overlap: Numerical investigations of the effect of correlation window overlap on vortex characteristics (maximum swirl velocity and core radius) were performed in [37] using a Vatistas model [35]. The same investigation was reproduced using a real PIV image ($\psi = 5^\circ$, $\Omega = 56.55 \text{ rad/s}$ and thrust $T = 550 \text{ N}$).

First this image was processed with 96×96 pixel and 128×128 pixel windows sizes with overlap between 2 pixel (98% overlap) to the window size value (0% overlap) in x direction whereas the overlap in y direction was kept constant at 50% of the window size. Figure 13.6 shows the maximum tangential (swirl) velocity and core radius extracted from the horizontal velocity profile (one dimensional analysis).

The curves obtained are in good agreement with the numerical simulation mentioned before. They converge to different values depending on the window size and the oscillations decrease with increasing overlap. The swirl velocity values are always equal or below the value obtained with the maximum sampling whereas the core radius oscillates around it. Maximum swirl velocity is reached when the center point of an interrogation window falls onto the maximum in the velocity profile which has an increased probability as the overlap is increased.

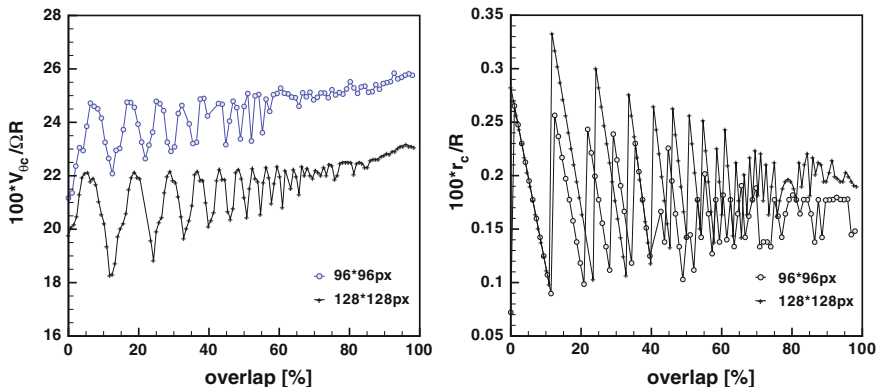


Fig. 13.6 Maximum tangential velocity and core radius versus overlap

In a second step the same image was processed using window sizes of 48, 64, 96, and 128 pixel size with overlap between 2 pixel and the window size value. The maximum swirl velocity and core radius were computed by averaging circularly the tangential velocity profile over r (two dimensional analysis), the radial distance from the vortex center. This radial averaging method is known to be more robust. The curves obtained are presented on Fig. 13.7.

The effect of the window size is still noticeable but the curves are smoother and the oscillations which were observed in Fig. 13.7 are nearly completely damped. This investigation shows that the overlap parameter can play an important role when looking for vortex characteristics and that in order to avoid random effects an overlap as large as possible should be used in order to avoid these sampling artifacts.

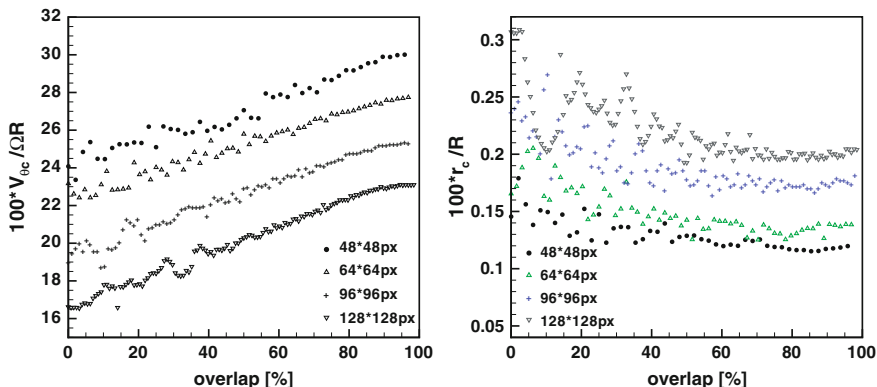


Fig. 13.7 Maximum tangential velocity and core radius versus overlap

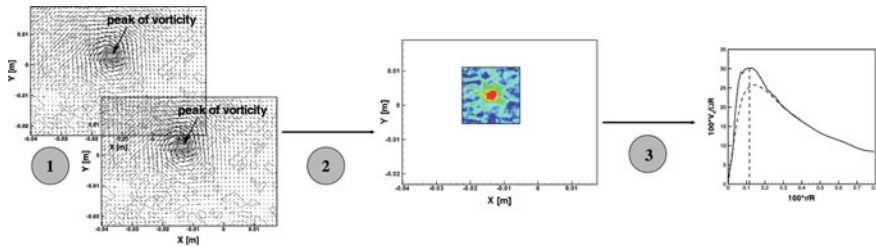


Fig. 13.8 Multi region principle for vortex flow analysis

While the minimum interrogation window size is limited by experimental parameters like seeding distribution, in-plane loss of image pairs (mainly compensated by multi-grid algorithms) and image background noise, the overlap parameters do not have such limitation. The only limitation for the use of large sample overlap is the processing time and the size of the resulting data set. In effect the processing time and the size of the resulting data set increase by a factor of 4 when the overlap is increased by 50%. The processing performed in 2004 on a Pentium IV (3.0 GHz, 1GB RAM) of a 1360×1076 pixel 2C-PIV image using multi-grid algorithm with 64×64 pixel initial window size and 24×24 pixel final window size with an overlap of 22 pixel (91% overlap) lasted 2.5 min and generated files of 14MB. Under these conditions it was not realistic to use such parameters for a large number of images: the processing of the images recorded during HOTIS campaign would require few months requiring nearly one Tera Byte to store the result. In order to overcome this problem and to be able to use larger sample overlap a new feature was implemented within the processing software which allowed using multi-region interrogation parameters based on physical properties. The procedure consisted of:

1. Processing of the PIV image using a large window size and small overlap, for example 64×64 pixel window size with 50% overlap, the vector field obtained is used to compute differential operators. In case of vortex flow: the vorticity and the λ_2 operator.
2. The vorticity or/and the λ_2 operator are used to estimate the location of the vortex center which is used to define the position of the new region of interest. This region is then processed using finer window size and larger overlap, for example 24×24 pixel window size with 90% overlap.
3. The vortex characteristics are extracted from this region (solid curve in Fig. 13.8).

In the example, Fig. 13.8, less than a sixth of the PIV image area was processed using small window size optimizing in this way the time and storage requirements.

In addition to azimuth steps of 1° to 10° , sequences of 3C measurements were performed with vortex age increments of about 0.056° for vortex ages from 3.4° to 7° for different rotor conditions. These small increments allow reconstructing a 3D volume of the vortex due to the azimuthal axisymmetry of the flow field. The resulting volume allows the computation of the two missing components of the

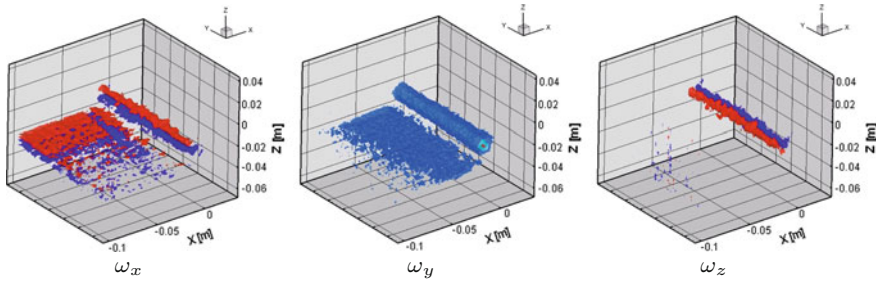


Fig. 13.9 Contour plot of the three vorticity components

vorticity vector (ω_x and ω_y), based on out-of-plane derivatives of u , v and w . The reconstruction of the volume can only be done using averaged results because every plane forming the volume was recorded at different instants of time. After conditional averaging, the orientation of each plane was corrected in order to take the step angle into account. Figure 13.9 shows the three vorticity components after merging all the 3C-PIV vector fields. The vortex tube as well as the blade wake is clearly visible on these graphs.

13.3.3 Conclusions

Helicopter model tests were performed with a 40% Mach scaled rotor of the Bo105 in a hover testing chamber and in a large low-speed wind tunnel. The blade tip vortices were traced from their creation up to half a revolution with small age increments. A parametric study of the two main PIV parameters - the correlation window size and the overlap - was done. It shows that the overlap should be as large as possible in order to avoid random effects and to improve the accuracy of the vortex characteristics which can be extracted from the result. The results show that a high spatial resolution is required in order to resolve the vortex characteristics and particularly the core radius of young vortices properly. A three-dimensional reconstruction of the blade tip vortex has been applied for vortex ages between $\psi = 3.4^\circ$ and 7° using a very fine age increment step of $\Delta\psi_v = 0.056^\circ$. The volume reconstruction allows computing all the differential quantities which can not be obtained by single plane 3C-PIV. A first post-processing and analysis shows that the vortex characteristics - swirl velocity, core radius and axial velocity - seem to be independent of the blade tip speed at least in the range measured during the tests ($0.122 \leq M_H \leq 0.633$).

13.4 Flow Diagnostics of Dynamic Stall on a Pitching Airfoil

Contributed by:

K. Mulleners and M. Raffel

Dynamic stall is a classic example of unsteady flow separation that occurs for example on helicopter or wind turbine rotor blades in response to an unsteady change of the angle of attack beyond the static stall angle. It is characterized by the formation of a large-scale dynamic stall vortex and a delayed onset of massive flow separation with respect to static stall [2, 20, 21].

Guided by the idea that an unsteady aerodynamic phenomenon such as dynamic stall is best studied in a time-resolved manner, MULLENERS & RAFFEL [22, 23] developed a novel approach to characterize dynamic stall on a pitching airfoil based on a combination of time-resolved PIV and an extensive coherent structure analysis, which is summarized here.

Experimental Setup

Stereoscopic time-resolved PIV was conducted in the vertical cross sectional plane at the mid-span location of a pitching airfoil. The PIV parameters for this investigation are listed in Table 13.2. The two-dimensional airfoil model with OA209 profile and chord length $c = 0.3$ m was placed in a uniform flow at a free stream Reynolds number $Re = 9.2 \times 10^5$ in the closed-circuit, continuous low-speed wind tunnel at DLR Göttingen. The wind tunnel had an open test section with a rectangular nozzle of $0.7 \text{ m} \times 1.0 \text{ m}$. The airfoil was subjected to a sinusoidal oscillation about its quarter

Table 13.2 Stereoscopic time-resolved PIV recording parameters for the investigation of dynamic stall on a pitching airfoil

Flow geometry	Parallel to light sheet
Free stream velocity	$U_\infty = 50 \text{ m/s}$
Field of view	$335 \times 165 \text{ mm}^2 (W \times H)$
Interrogation window	$6.4 \times 6.4 \text{ mm}^2 (W \times H)$
Recording method	Dual frame/double exposure
Ambiguity removal	Frame separation (frame-straddling)
Recording medium	High repetition rate CMOS camera 1024×1024 pixel
Acquisition frequency	1500 Hz (double images) = 3000 fps
Recording lens	$f = 85 \text{ mm}$
Illumination	Freq. doubled Nd:YLF laser 12 mJ/pulse at 527 nm
Pulse delay	$\Delta t = 30 \mu\text{s}$
Seeding material	DEHS ($d_p \approx 1 \mu\text{m}$)

chord axis with mean incidence α_0 , amplitude α_1 , and reduced frequency k . The latter is defined as $k = \pi f_{osc} c / U_\infty$, with f_{osc} the pitching frequency. Mean incidence, amplitude and reduced frequency were varied to attain different stall cases. In the current example, results are presented for a representative deep dynamic stall case with $\alpha_0 = 20^\circ$, $\alpha_1 = 8^\circ$, and $f_{osc} = 2.6 \text{ Hz}$ resulting in $k = 0.05$ and about 570 velocity snapshots per pitching cycle.

The PIV data was evaluated according to standard procedures using the multi grid algorithm with image deformation, a final interrogation window size of $32 \text{ pixel} \times 32 \text{ pixel}$, and an overlap of approximately 80%. This yields a grid spacing or physical resolution of 6 pixel or $1.2 \text{ mm} = 0.004c$.

Prior to analysis, the velocity fields were rotated into the airfoil reference system with the x -axis along the chord, the y -axis along the span and the z -axis upward perpendicular to the chord, while the origin coincides with the rotation axis, i.e., the airfoil's quarter chord axis, at model mid-span.

Coherent Structure Analysis

The coherent structure analysis methods selected to identify and characterise the salient flow features that emerge during a dynamic stall cycle include an Eulerian and a Lagrangian procedure to locate the axes of vortices and the edges of Lagrangian coherent structures respectively, and a proper orthogonal decomposition of the velocity field to extract the energetically dominant coherent flow patterns and their temporal evolution.

The Eulerian vortex detection method utilises the dimensionless scalar function Γ_2 introduced by GRAFTIEAUX et al. [4] to locate the axis of individual vortices and to determine their sense of rotation. According to its definition, Γ_2 is a dimensionless scalar function, with $-1 \leq \Gamma_2 \leq 1$. The location of possible vortex axes is indicated by the local extrema of Γ_2 and the sense of rotation is given by the sign of the extrema. The markers in Fig. 13.10 indicate the assessed vortex axes locations and the colour of the markers indicates whether these vortices are clockwise or counter-clockwise rotating.

The Lagrangian approach adopted here is the finite-time Lyapunov exponent (FTLE) method [5, 7], which is deemed robust and relatively insensitive to short-term anomalies in the velocity data and thus particularly suited to analyse experimental data [9]. The FTLE is a scalar measure for local stretching or expansion of fluid particle trajectories and maximising ridges in the FTLE field have been shown to represent structure boundaries in vortex dominated flows [6, 8, 32]. The FTLE field is calculated at a time instant t_n as

$$\text{FTLE}(x_n, t_n, T) = \frac{1}{2T} \log \sigma(x_n, t_n, T), \quad (13.1)$$

with x_n the initial vector locations for trajectories starting at t_n , and σ the coefficient of expansion for the trajectories after an integration time T . The coefficient of expansion is defined as the maximum eigenvalue λ of the Cauchy–Green tensor, which is determined from the local spatial gradient of the flow map, according to

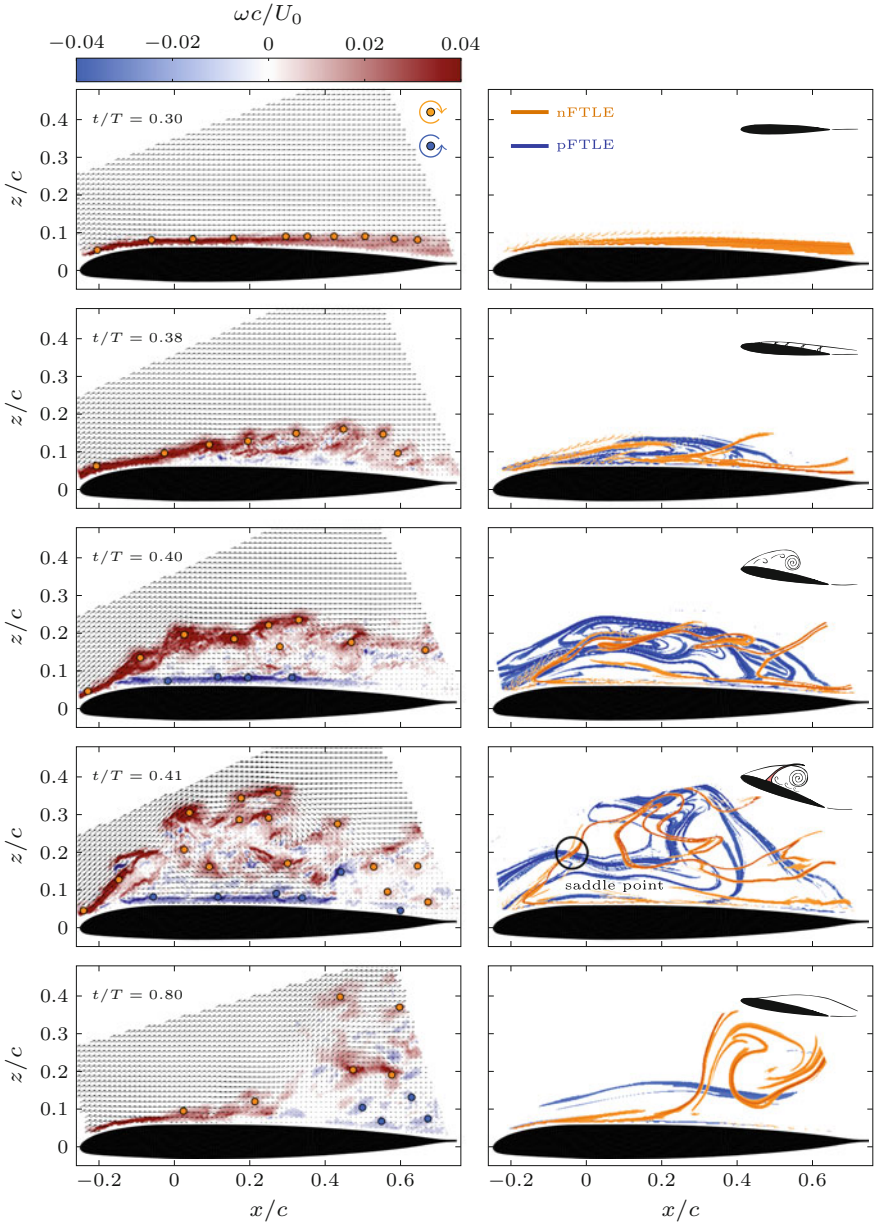


Fig. 13.10 Velocity, vorticity, and FTLE fields representing the different stages of the dynamic stall life cycle: attached flow (row 1), emergence of flow reversal and shear layer growth (row 2), shear layer roll-up (row 3), stall onset (row 4), and flow reattachment (row 5). (A colored version of the figure can be found at [DC13.2])

$$\sigma(x_n, t_n, T) = \lambda_{\max} \left(\left[\frac{\partial \chi(x_n, t_n, T)}{\partial x_n} \right]^t \left[\frac{\partial \chi(x_n, t_n, T)}{\partial x_n} \right] \right), \quad (13.2)$$

with $\chi(x_n, t_n, T)$ the flow map that maps particles with initial vector locations x_n at time t_n along their Lagrangian trajectories onto their new location after an integration time T . The superscript t indicates a matrix transposition.

The FTLE fields can be evaluated for both forward $T > 0$, and backward $T < 0$ advection and are labelled correspondingly as positive (pFTLE) and negative finite-time Lyapunov exponent (nFTLE) fields. Maximising ridges in the pFTLE and the nFTLE fields respectively indicate regions where the flow is currently experiencing local stretching or local attraction.

The presence and form of relevant FTLE ridges are indicated in the right column of Fig. 13.10. The ridges are selected as regions where the values of the FTLE are larger than 40% of the maximum of the field. In the present example, the FTLE method is applied to a low order model of the velocity field to highlight the dynamics and the topological signature of the large-scale coherent structures that dominate the flow field. The low-order model was constructed based on the first 69 modes of the proper orthogonal decomposition of the velocity field, representing 99.5% of the energy.

The third method used to extract coherent flow structures is the proper orthogonal decomposition (POD) of the velocity field. The fundamental idea of POD is to approximate the flow field by a linear combination of spatial eigenfunctions with temporal coefficients such that the original spatiotemporal flow field is approximated as accurate as possible based on an energy-weighted measure [17]. In the current example, the two-dimensional in-plane velocity field $\mathbf{u} = (u, w)$ was decomposed, according on the snapshot method introduced by SIROVICH [33], as

$$\mathbf{u}(x, z, t_n) = \sum_{i=1}^N a_i(t_n) \boldsymbol{\psi}_i(x, z), \quad (13.3)$$

where N is the number of instantaneous field realisations and t_n is the discrete time stamp. The spatial functions or modes $\boldsymbol{\psi}_i(x, z)$ can be associated with instantaneous organised flow pattern whose temporal evolution is described by the corresponding temporal mode $a_i(t)$ and whose relative contribution to the total energy is represented by the corresponding eigenvalue λ_i [17]. The eigenvalues are sorted in decreasing order such that the first modes represent the most dominant flow structures in terms of energy content.

Results

Based on the combination of time-resolved velocity field information and the results of the coherent structures analysis methods, the chronology and causality of the prominent stall events was revisited and characterised [22, 23]. By analysing the locations and interactions of the identified vortex cores, the unsteady flow development over an oscillating airfoil within a single dynamic stall life cycle was classified into five successive stages: the attached flow stage, the stall development stage, stall

onset, the stalled stage, and flow reattachment. Snapshots representative of the different stages are presented in Fig. 13.10, including the velocity and vorticity fields in the left column and the corresponding FTLE fields in the right column. The markers in the velocity field indicate the vortex cores as identified by the Eulerian vortex detection method and the timing of the snapshot is given with respect to the pitching period starting at the minimum angle of attack.

The stall development stage is the part of the DS life cycle between static and dynamic stall onset covering the unsteady separation process. The flow separation is initiated by an adverse pressure gradient and involves the formation and detachment of a shear layer from the airfoil's surface [3, 29]. With increasing angle of attack beyond static stall, an adverse pressure gradient builds up and leads to the formation of a prominent recirculation region that grows normal to the surface (Fig. 13.10 row 2). At the interface between regions of reverse and free stream flow, a shear layer develops that controls the successive stall development [11]. The primary instability of the shear layer generates small-scale vortices that interact only weakly at first. Subsequently, viscous interactions increase leading to the roll-up of the shear layer into a large-scale DS vortex (Fig. 13.10 row 3). The development of this secondary instability of the shear layer is clearly visualised by the ridges in the nFTLE field, which represent material lines that segregate the inviscid free-stream flow from the viscous flow within the shear layer. The bulging of these ridges indicates the engulfing process that accompanies the shear layer roll-up.

The primary stall vortex subsequently detaches due to vortex induced separation signalling dynamic stall onset (Fig. 13.10 row 4) [26]. The onset of dynamic stall was specified directly from the velocity field based on the third POD eigenmode (ψ_3), which represents the large-scale dynamic stall vortex (Fig. 13.11). The first and second POD mode represent a fully attached and a fully separated flow state, respectively. Time histories of the associated time development coefficients are presented in the top panel of Fig. 13.11 with the sinusoidal variation of the pitch angle in the background for reference. In the beginning of the cycle, the flow is attached, indicated by high absolute values of a_1 . Near $t/T = 0.4$, $|a_1|$ decreases while $|a_2|$ increases, indicating a transition from an attached to a separated flow state. During that transition, $|a_3|$ increases, indicating the growth of the primary stall vortex. Once the dynamic stall vortex separates from the shear layer that provides its circulation, the time coefficient drops drastically. The first local maximum of $|a_3|$ thus marks the detachment of the dynamic stall vortex and dynamic stall onset. The occurrence of dynamic stall onset can also be identified by the emergence and subsequent downstream convection of a saddle point near the leading edge. The saddle point can be recognised by the intersection of the ridges in the pFTLE and the nFTLE field [12]. Near the end of the cycle, the excess wake fluid is convected downstream and the flow reattaches from the leading edge toward the trailing edge, as indicated by the nFTLE ridges (Fig. 13.11 row 5).

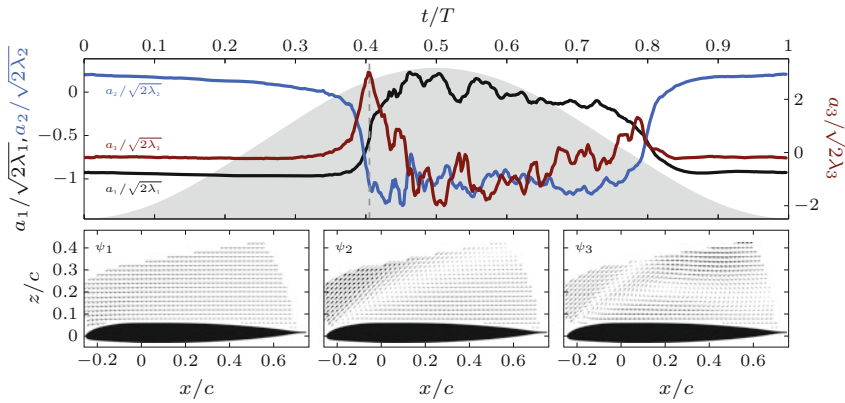


Fig. 13.11 Three most dominant POD modes representing an attached flow state (ψ_1), a separated flow state (ψ_2), and the dynamic stall vortex (ψ_3). The associated time development coefficients, normalised with the square root of twice the eigenvalue, indicate the temporal evolution of the relative contributions of the individual modes within a single pitching period T . The pitch angle history is added in the background in grey for reference. (A colored version of the figure can be found at [DC13.3])

13.5 Investigation of Laminar Separation Bubble on Helicopter Blades

Contributed by:

M. Raffel, C. Rondot, D. Favier and K. Kindler

Detailed studies of the boundary layer profile and the characteristics of the flow velocity distribution close to the leading edge of a helicopter blade profile were conducted using 2C-PIV. The relatively small scales of flow structures related to

Table 13.3 PIV recording parameters for microscale wind tunnel investigations

Flow geometry	Boundary layer on an OA209 blade tip model
Maximum in-plane velocity	$U_{\max} = 10 \text{ mm/s}$
Field of view	$1.658 \times 1.358 \text{ mm}^2$
Interrogation volume	$96 \times 96 \text{ pixel}$
Observation distance	$z_0 = 35.5 \text{ cm}$
Recording method	Double frame/single exposure
Recording medium	CCD camera, $1280 \times 1024 \text{ pixel}$
Recording lens	Mirror objective lens, $M = 4.86$, $f_{\#} = 6$
Illumination	Nd:YAG laser ^a $2 \times 200 \text{ mJ/pulse}$
Pulse delay	$\Delta t = 10 \text{ ms}$
Seeding material	Oil droplets ($d_p \simeq 1 \mu\text{m}$)

^aFrequency doubled

dynamic stall, the study in which the flow field has been measured with a relatively high spatial resolution. The feasibility of μ -PIV measurements utilizing a mirror telescope in a wind tunnel has been demonstrated successfully. The spatial resolution of approximately $50\ \mu\text{m}$ allowed for an assessment of the different turbulence models and damping coefficients for the improvement of CFD predictions (Table 13.3).

Introduction

Over the past decade, considerable progress has been made in the development of performance prediction capabilities for isolated helicopter components. Modern CFD methods deliver promising results for most attached air flows. The prediction of high-speed and high-load cases still needs more intensive experimental investigations of the unsteady viscous flow phenomena, such as the dynamic stall at the retreating side of the rotor and the complex mechanism of the stall in the vicinity of the blade tip.

Overall flow field measurements on pitching airfoils, pitching finite blade models and on rotating blades in hover chambers and wind tunnels have been successfully performed at different places. In this section we focus on measurements, which have been obtained for a steady incidence angle of 11.5° , since the flow phenomena involved are well understood and documented. This incidence angle corresponds to the point where maximum lift is obtained, shortly below the incidence angle where massive flow separation occurs. The flow around the OA209 profile for this range of Reynolds number, span wise location and incidence angle is determined by the transition of the boundary layer and the flow separation on the suction side which results in the generation of vorticity dominating the wake flow and the performance of the wing. This holds in a similar way for finite wings and 2D-airfoil profiles. For the present case of moderate Reynolds numbers and high incidence angles, laminar flow separation occurs shortly behind the leading edge and transition to turbulent flow conditions occurs immediately after separation. The resulting turbulence intensity forces a reattachment of the flow within a short distance, resulting in a significantly increased maximum lift with respect to the low Reynolds number cases. The separation together with the re-attachment forms a laminar separation bubble containing a recirculation region, which has only a few millimeter extension in chord wise direction (see Fig. 13.12). The turbulent boundary layer behind the bubble allows the flow to stay attached even at relatively high adverse pressure gradients.

Detailed investigations of the turbulence intensity, the size and the temporal development of the flow structure at the leading edge are required in order to validate CFD-codes which are under development for a more accurate prediction of the dynamic stall cases. Therefore, stereoscopic PIV and pressure measurements have been performed to quantize the overall flow features close to the tip of a rotor blade, both in steady cases and during pitching motion. Two-components PIV measurements with an observation field size of $1\ \text{mm}$ and $50\ \mu\text{m}$ resolution, have been performed further inboard in order to resolve the relevant flow features in the phase shortly before the stall onset in steady and unsteady cases. The results of the steady case have been compared with ELDV (Embedded Laser Doppler Velocimetry see [1]) and CFD data.

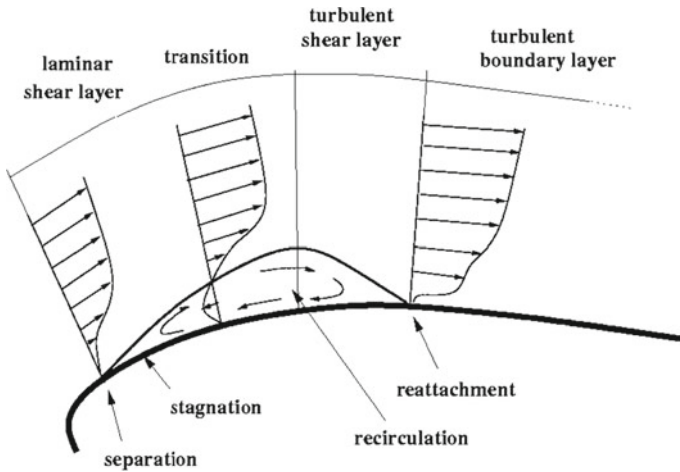


Fig. 13.12 Sketch of the separation bubble

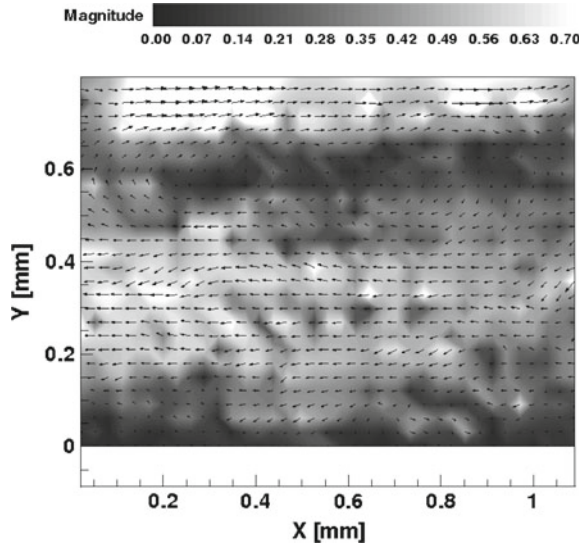
The Test Setup

The Nd:YAG laser system used had 2×200 mJ pulse energy at 532 nm and was equipped with conventional light sheet optics. The cameras had a resolution of 1280×1024 pixel.

The setup used for the PIV measurements with a very high resolution is similar to the one described in [16], but has been used under relatively rough conditions in a wind tunnel. The microscope lens used for the test was a mirror objective lens QM100 of Questar Corporation. It is optimized for working distances G , ranging from $G = 150$ mm to $G = 380$ mm. It has an aperture angle of $\omega = \arctg(D/2G)$ with D being the aperture diameter. The numerical aperture for the working distance of $G = 355$ mm, which has been chosen for the experiment, is $A = n \cdot \sin \omega = 0.083$ with n being the refractive index of air. The F-number was $f_{\#} = 1/2A = 6$ and the magnification $M = 4.86$ resulting in a calibration factor of 754 pixel/mm. The diffraction limited minimum image diameter was $d_{diff} = 2.44 f_{\#}(M+1) = 45.6 \mu\text{m}$ and the estimated depth of focus $\delta Z = 2 f_{\#} d_{diff} (M+1)/M^2 = 136 \mu\text{m}$. The light sheet thickness was $400 \mu\text{m}$. Particle image diameters observed were between 50 and $130 \mu\text{m}$ (8–20 pixel) which is similar to observations made in [13, 14]. The development of the boundary layer, the reverse flow region and the shear layer towards the outer flow can clearly be seen in the results presented in Fig. 13.13.

The experiments have been performed in the S2 Luminy wind tunnel of the Laboratoire d'Aérodynamique et de Biomécanique du Mouvement LABM of the French research center CNRS at the University of Marseille. The PIV measurements were performed close to the leading edge of an OA209 blade tip model, in a plane orthogonal to the span in a distance of approximately 200 mm.

Fig. 13.13 PIV results obtained with a mirror telescope objective at $\alpha = 11.55^\circ$, steady case. The magnitude of the velocity has been plotted by gray levels. The coordinates x and y are given in millimeters. The origin is placed on the model surface (y), 5% chord length behind the leading edge (x) (A colored version of the figure can be found at [\[DC13.4\]](#))



The majority of the μ -PIV measurement has been made at a steady incidence angle of 11.5° and has been compared with CFD and ELDV results at the same condition.

Results and Discussion

The image quality obtained with the mirror telescope objective, allows for the analysis of the unsteady flow features at a spatial resolution of $\simeq 50 \mu\text{m}$. The number of outliers is of the acceptable order of 5%. The relative accuracy, as compared to conventional PIV recordings, is slightly lower due to the fact that the particle images are approximately five times larger. However, the uncertainty due to noise is assumed to be in the order of 0.1 m/s and the wall distance of each measurement location can be determined very precisely, since the surface is visible in each recording. Therefore, the development of the boundary layer, the reverse flow region and the shear layer towards the outer flow can clearly be seen in the result Fig. 13.13.

Figure 13.14 depicts tangential velocity profiles through the laminar separation bubble obtained by CFD with SA- and SST turbulence models and by ELDV, PIV and μ PIV. It can be seen that the agreement of most of the different methods in the outer regions (20 mm and above) is relatively high ($\sim 98\%$) with respect to the free stream velocity). However, the more detailed presentation in Fig. 13.14 shows that the differences between the different experimental results as well as of the different CFD results becomes evident. The reason for the differences of the PIV and the μ -PIV results can easily be explained by the weak spatial resolution of the recordings made with the 100 mm-lens. The differences between the ELDV measurements and the μ -PIV measurements are more significant and differ not as much in the measured flow velocity, but in the size of the separation bubble in wall normal direction. One reason for this might be a small disagreement of the incidence angle adjustment of

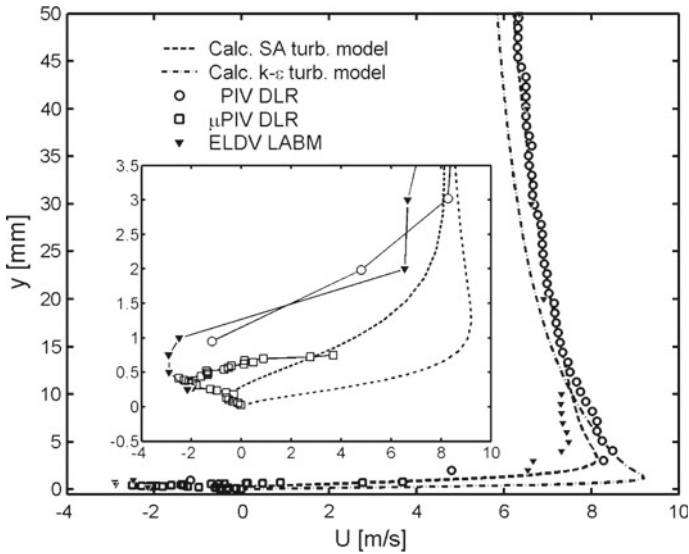


Fig. 13.14 CFD, ELDV and PIV results of the laminar separation bubble at $\alpha = 11.5^\circ$ and $x/c = 0.05$; steady case

both tests. However, the conclusion, which turbulence model resolves the flow field in the separation bubble best, can easily be drawn in favor for the SA-turbulence model.

Conclusions

Discrepancies concerning the size of the separation bubble on a helicopter blade profile have been observed as well as an acceptable agreement of the velocity magnitudes found by the different measurements. The present results can be considered to be a good data basis for the validation of numerical codes. It has been demonstrated that instantaneous velocity fields determined by PIV at high spatial resolutions can be used to choose turbulence models and numerical damping coefficients. The strength, scale, and distribution of the laminar separation bubble - measured for the first time with such a high resolution in a wind tunnel experiment - are essential for the validation of numerical simulation techniques.

References

1. Berton, E., Favier, D., Nsi Mba, M., Maresca, C., Allain, C.: Embedded LDV measurement methods applied to unsteady flow investigation. *Exp. Fluids* **30**(1), 102–110 (2001). DOI 10.1007/s003480000144. URL <https://doi.org/10.1007/s003480000144>
2. Carr, L.W.: Progress in analysis and prediction of dynamic stall. *J. Aircr.* **25**(1), 6–17 (1988). DOI 10.2514/3.45534. URL <https://doi.org/10.2514/3.45534>

3. Degani, A.T., Walker, J.D.A., Smith, F.T.: Unsteady separation past moving surfaces. *J. Fluid Mech.* **375**, 1–38 (1998). DOI 10.1017/S0022112098001839. URL <https://doi.org/10.1017/S0022112098001839>
4. Graftieaux, L., Michard, M., Grosjean, N.: Combining PIV, POD and vortex identification algorithms for the study of unsteady turbulent swirling flows. *Meas. Sci. Technol.* **1422** (2001). DOI 10.1088/0957-0233/12/9/307. URL <https://doi.org/10.1088/0957-0233/12/9/307>
5. Green, M.A., Rowley, C.W., Haller, G.: Detection of Lagrangian coherent structures in three-dimensional turbulence. *J. Fluid Mech.* **572**, 111–120 (2007). DOI 10.1017/S0022112006003648. URL <https://doi.org/10.1017/S0022112006003648>
6. Green, M.A., Rowley, C.W., Smits, A.J.: The unsteady three-dimensional wake produced by a trapezoidal pitching panel. *J. Fluid Mech.* **685**, 117–145 (2011). DOI 10.1017/jfm.2011.286. URL <https://doi.org/10.1017/jfm.2011.286>
7. Haller, G.: Finding finite-time invariant manifolds in two-dimensional velocity fields. *Chaos: an Interdiscip. J. Nonlinear Sci.* **10**(1), 99–108 (2000). DOI 10.1063/1.166479. URL <https://doi.org/10.1063/1.166479>
8. Haller, G.: Lagrangian structures and the rate of strain in a partition of two-dimensional turbulence. *Phys. Fluids* **13**(11), 3365 (2001). DOI 10.1063/1.1403336. URL <https://doi.org/10.1063/1.1403336>
9. Haller, G.: Lagrangian coherent structures from approximate velocity data. *Phys. Fluids* **14**(6), 1851 (2002). DOI 10.1063/1.1477449. URL <https://doi.org/10.1063/1.1477449>
10. Heineck, J.T., Wadcock, A.J., Yamauchi, G.K., Lourenco, L., Abrego, A.I.: Application of three-component PIV to a hovering rotor wake. In: 56th Annual Forum of the American Helicopter Society, Virginia Beach (USA) (2000). URL <https://ntrs.nasa.gov/search.jsp?R=20000094565>
11. Ho, C.M.: An alternative look at the unsteady separation phenomenon. In: Krothapalli, A., Smith, C.A. (eds.) *Recent Advances in Aerodynamics: Proceedings of an International Symposium held at Stanford University, August 22–26, 1983*, pp. 165–178. Springer, New York (1986). DOI 10.1007/978-1-4612-4972-6/_4. URL https://doi.org/10.1007/978-1-4612-4972-6/_4
12. Huang, Y., Green, M.A.: Detection and tracking of vortex phenomena using Lagrangian coherent structures. *Exp. Fluids* **56**(7), 147–158 (2015). DOI 10.1007/s00348-015-2001-z. URL <https://doi.org/10.1007/s00348-015-2001-z>
13. Kähler, C.J., Scholz, U.: Transonic jet analysis using long-distance micro-PIV. In: 12th International Symposium on Flow Visualization - ISFV 12, Göttingen, Germany (2006)
14. Kähler, C.J., Scholz, U., Ortmanns, J.: Wall-shear-stress and near-wall turbulence measurements up to single pixel resolution by means of long-distance micro-PIV. *Exp. Fluids* **41**(2), 327–341 (2006). DOI 10.1007/s00348-006-0167-0. URL <https://doi.org/10.1007/s00348-006-0167-0>
15. Kato, H., Watanabe, S., Kondo, N., Saito, S.: Application of stereoscopic PIV to helicopter rotor blade tip vortices. In: 20th Congress on Instrumentation in Aerospace Simulation Facilities, Göttingen (Germany) (2003)
16. Lindken, R., Di Silvestro, F., Westerweel, J., Nieuwstadt, F.: Turbulence measurements with μ PIV in large-scale pipe flow. In: 11th International Symposium on Applications of Laser Techniques to Fluid Mechanics (2002)
17. Lumley, J.L.: *Stochastic Tools in Turbulence*. Dover Books on Engineering, Dover Publications (1970)
18. Martin, P.B., Pugliese, J.G., Leishman, J.G., Anderson, S.L.: Stereo PIV measurements in the wake of a hovering rotor. In: 56th Annual Forum of the American Helicopter Society, Virginia Beach (USA) (2000)
19. McAlister, K.W.: Rotor wake development during the first revolution. *J. Am. Helicopter Soc.* **49**, 371–390 (2004). DOI 10.4050/JAHS.49.371. URL <https://doi.org/10.4050/JAHS.49.371>
20. McAlister, K.W., Carr, L.W., McCroskey, W.J.: Dynamic stall experiments on the NACA 0012 airfoil. Technical Report NASA Technical Paper 1100, NASA (1978)

21. McCroskey, W.J.: The phenomenon of dynamic stall. Technical Report NASA Technical Memorandum 81264, NASA (1981)
22. Mulleners, K., Raffel, M.: The onset of dynamic stall revisited. *Exp. Fluids* **52**(3), 779–793 (2012). DOI 10.1007/s00348-011-1118-y. URL <https://doi.org/10.1007/s00348-011-1118-y>
23. Mulleners, K., Raffel, M.: Dynamic stall development. *Exp. Fluids* **54**(2), 1469–1477 (2013). DOI 10.1007/s00348-013-1469-7. URL <https://doi.org/10.1007/s00348-013-1469-7>
24. Murashige, A., Kobiki, N., Tsuchihashi, A., Inagaki, K., Nakamura, H., Tsujiuchi, T., Hasegawa, Y., Yamamoto, Y., Yamakawa, E.: Second ATIC aeroacoustic model rotor test at DNW. In: 26th European Rotorcraft Forum, The Hague (the Netherlands) (2000)
25. Murashige, A., Kobiki, N., Tsuchihashi, A., Nakamura, H., Inagaki, K., Yamakawa, E.: ATIC aeroacoustic model rotor test at DNW. In: 24th European Rotorcraft Forum, Marseille (France) (1998)
26. Obabko, A.V., Cassel, K.W.: Detachment of the dynamic-stall vortex above a moving surface. *AIAA J.* **40**(9), 1811–1822 (2002). DOI 10.2514/2.1858. URL <https://doi.org/10.2514/2.1858>
27. Raffel, M., Seelhorst, U., Willert, C.E.: Vortical flow structures at a helicopter rotor model measured by LDV and PIV. *Aeronaut. J.* **102**(1014), 221 (1998). DOI 10.1017/S0001924000096391. URL <https://doi.org/10.1017/S0001924000096391>
28. Raffel, M., Höfer, H., Kost, F., Willert, C.E., Kompenhans, J.: Experimental aspects of PIV measurements of transonic flow fields at a trailing edge model of a turbine blade. In: 8th International Symposium on Applications of Laser Techniques to Fluid Mechanics, Lisbon (Portugal) (1996)
29. Reynolds, W.C., Carr, L.W.: Review of Unsteady, Driven, Separated Flows, pp. 1–46. American Institute of Aeronautics and Astronautics (1985). DOI 10.2514/6.1985-527. DOI 10.2514/6.1985-527. URL <https://doi.org/10.2514/6.1985-527>
30. Richard, H., Raffel, M.: Full-scale and model tests. In: 58th Annual Forum of the American Helicopter Society, Montreal (Canada) (2002)
31. Richard, H., van der Wall, B.G.: Detailed investigation of rotor blade tip vortex in hover condition by 2C and 3C-PIV. In: 32nd European Rotorcraft Forum, Maastricht (the Netherlands) (2006)
32. Shadden, S.C., Lekien, F., Marsden, J.E.: Definition and properties of Lagrangian coherent structures from finite-time Lyapunov exponents in two-dimensional aperiodic flows. *Phys. D: Nonlinear Phenom.* **212**(3–4), 271–304 (2005). DOI 10.1016/j.physd.2005.10.007. URL <https://doi.org/10.1016/j.physd.2005.10.007>
33. Sirovich, L.: Turbulence and the dynamics of coherent structures. *Q. Appl. Math.* **45**(3), 561–590 (1987)
34. Spletstößer, W.R., van der Wall, B.G., Junker, B., Schultz, K., Beaumier, P., Delrieux, Y., Lecante, P., Crozier, P.: The ERATO programme: Wind tunnel results and proof of design for an aeroacoustically optimized rotor. In: 25th European Rotorcraft Forum, Rome (Italy) (1999)
35. Vatistas, G.H., Kozel, V., Mih, W.C.: A simpler model for concentrated vortices. *Exp. Fluids* **11**(1), 73–76 (1991). DOI 10.1007/BF00198434. URL <https://doi.org/10.1007/BF00198434>
36. van der Wall, B.G., Junker, B., Yu, Y.H., Burley, C.L., Brooks, T.F., Tung, C., Raffel, M., Richard, H., Wagner, W., Mercker, E., Pengel, K., Holthusen, H., Beaumier, P., Delrieux, Y.: The HART II test in the LLF of the DNW - A major step towards rotor wake understanding. In: 28th European Rotorcraft Forum, Bristol (England) (2002)
37. van der Wall, B.G., Richard, H.: Analysis methodology for 3C PIV data. In: 31st European Rotorcraft Forum, Florence (Italy) (2005)
38. Yamauchi, G.K., Burley, C.L., Mercker, E., Pengel, K., Janakiram, R.: Flow measurements of an isolated model tilt rotor. In: 55th Annual Forum of the American Helicopter Society, Montreal (Canada) (1999)
39. Yu, Y.H.: The HART II test - rotor wakes and aeroacoustics with higher-harmonic pitch control (hhc) inputs - the joint German/French/Dutch/US project. In: 58th Annual Forum of the American Helicopter Society, Montreal (Canada) (2002)

Chapter 14

Applications: Aeroacoustic and Pressure Measurements

14.1 PIV Applied to Aeroacoustics

Contributed by:

A. Henning

In the research field of aeroacoustics, fluctuations in turbulent flows which are part of a sound generating process can be identified by means of the so-called causality correlation technique [5, 6, 29]. In this approach, the coefficient matrix resulting from the calculated correlation coefficients between the acoustic pressure fluctuations in the far field and velocity fluctuations in a turbulent flow field is analysed. The temporal resolution of the coefficient matrix is set by the sampling rate of the pressure signal in the far field. The spatial resolution is determined by the spatial sampling rate of the measured flow quantity (Table 14.1).

In the wind-tunnel study presented here, noise sources at the leading edge slat in a high-lift device configuration are detected by a technique, using PIV for the acquisition of the velocity field in the vicinity of the slat cove [7]. Pressure fluctuations in the far field are captured via microphone arrays located outside of the test section. PIV measurements provide instantaneous flow quantities ϕ at the position \mathbf{x} at the time t_i . Synchronously the pressure fluctuations p are recorded at positions \mathbf{y} with a sampling rate of 100 kHz. This allows the calculation of the time resolved correlation coefficient matrix $R_{\phi,p}$. The sample correlation coefficient $R_{\phi,p}(\mathbf{x}, \mathbf{y}, \tau)$ is defined as:

$$R_{\phi,p}(\mathbf{x}, \mathbf{y}, \tau) = \frac{S_{\phi,p}(\mathbf{x}, \mathbf{y}, \tau)}{\sigma_{\phi}(\mathbf{x}) \sigma_p(\mathbf{y})} = \frac{\langle \phi'(\mathbf{x}, t) p'(\mathbf{y}, t + \tau) \rangle}{\sqrt{\langle \phi'^2(\mathbf{x}, t) \rangle \langle p'^2(\mathbf{y}, t) \rangle}}, \quad (14.1)$$

with the correlation function defined as:

An overview of the Digital Content to applications on acoustic and pressure measurements can be found at [DC14.1].

Table 14.1 PIV recording parameters for aeroacoustic investigation on high-lift device

Flow geometry	Flow inside leading edge slat-cove
Maximum in-plane velocity	$U_{\max} \approx 90$ m/s
Field of view	75×48 mm ² ($W \times H$)
Interrogation volume	$1.5 \times 1.5 \times 1.0$ mm ³ ($W \times H \times D$)
Dynamic spatial range	DSR $\approx 50 : 1$
Dynamic velocity range	DVR $\approx 300 : 1$
Observation distance	$z_0 \approx 1000$ mm
Recording method	Dual frame/single exposure @5Hz
Ambiguity removal	Frame separation (frame-straddling)
Recording medium	Full frame interline transfer CCD 1600×1200 pixel
Recording lens	$f = 180$ mm $f_{\#} = 2.8$
2× Illumination	Freq. doubled Nd:YAG laser 200 mJ/pulse at 532 nm
Pulse delay	$\Delta t = 15 - 25$ μ s
Seeding material	DEHS ($d_p \approx 1000$ nm)

$$S_{\phi,p}(\mathbf{x}, \mathbf{y}, \tau) = \frac{1}{N} \sum_{n=1}^N [\phi'(\mathbf{x}, t_n) p'(\mathbf{y}, t_n + \tau)]. \quad (14.2)$$

where $\phi'(\mathbf{x}, t)$ represents the zero-mean part of a near-field quantity ϕ measured at position \mathbf{x} and time t . The variable τ is the time shift between the pressure signal and ϕ . The correlation coefficient is normalized by the root-mean-square (RMS) values of ϕ' and p' which are denoted by $\sigma_{\phi}(\mathbf{x})$ and $\sigma_p(\mathbf{y})$. The statistical significance and therewith the signal to noise ratio of the resulting coefficients increases with \sqrt{N} , but only if the PIV samples are statistically independent [30]. Therefore in most cases using a high-speed PIV system for the correlation technique will result in a large number of samples not contributing to the significance of the results. Only a low sampling rate of the PIV measurement guarantees a maximal contribution of each sample to the significance of $R_{\phi,p}$. The measurements under free field conditions presented here demonstrate the applicability of this technique, if the number of PIV samples N is chosen to be high enough ($N = 16000$ in the present case).

Experiments were conducted in the Aeroacoustic Wind Tunnel Braunschweig (AWB) of DLR, which is an open-jet closed-circuit anechoic test facility with a rectangular 0.8 m by 1.2 m nozzle exit. The AWB is equipped with acoustic wall-treatment in combination with sound absorbing turning vanes installed in the flow circuit [20]. Measurements are performed on the DLR F16 model. It is a multi element 2D high-lift airfoil with a modular design. In the work presented here a 3 elements configuration is investigated. In this experiment special slat-tracks on the suction side have been designed allowing the PIV camera to look inside the slat-cove (see Fig. 14.1). The 2D model is installed between side plates with turntables,

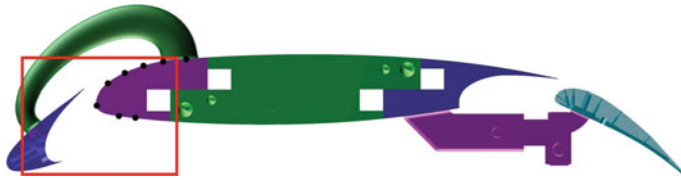


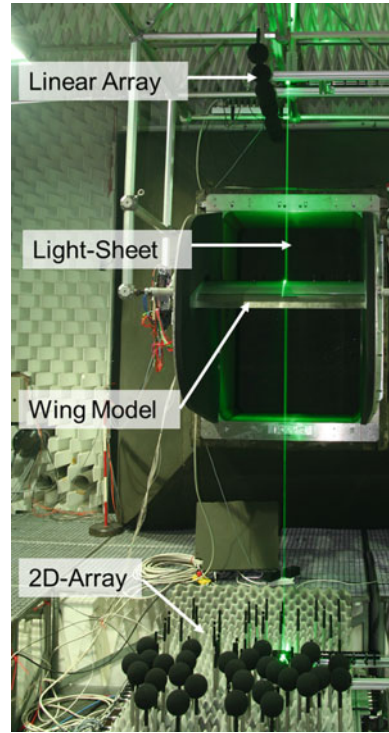
Fig. 14.1 Cross sectional view of the F16 model. The span of the airfoil is $l = 800$ mm. The box indicates the regions of interest (ROI) observed by the PIV camera. Dots are indicating the positions of the pressure probes at the mid-span

designed in extension of the nozzle. The model chord length is $c = 300$ mm (clean configuration) and the span measures 800 mm. A parametric study is performed varying the deflection-angle α , the slat -gap and -overlap as well as the flow speed U_∞ (see Table 14.2). The PIV measurements are sampled at a low frequency of 5 Hz and can be regarded as statistically independent. To avoid shadowing effects, the slat region is illuminated from the top and the bottom of the model simultaneously. The PIV-camera is installed on a mount capable to rotate around the same axis as the model, allowing to maintain the field of view in the coordinate system of the model for all different values of α . The seeding is injected from a corner of the wind tunnel upstream of the model configuration in a way that the particles have to pass the complete wind tunnel before they reach the PIV field of view. Figure 14.2 shows a picture of the experimental setup. A 2D-microphone array is located outside the flow-field below the high-lift device (pressure side). It consists of 64 microphones (M51 by LinearX). The distance between the model and the microphone membranes is approximately $-5.89c$ in the vertical y -direction. A linear microphone array is located above the model (suction-side) at a distance of approximately $3c$. It consists of 8 microphones. The microphone signals were simultaneously sampled with an A/D conversion of 16 bits at a sampling frequency of $f_s = 100$ kHz. All channels had an anti-aliasing filter at $f_u = 50$ kHz. To reduce the influence of low-frequency wind-tunnel noise on the measured signals a high-pass filter with a cut-off frequency $f_l = 500$ Hz has been applied. In order to avoid a jitter between the PIV timing and the pressure data acquisition both measurement systems are synchronized by a master clock. Wall pressure fluctuations are measured with a set of pressure probes (XQC-132A-093, manufactured by KULITE) at the mid-span of the airfoil arranged in the chordwise direction at the leading edge of the wing main-body. A second set

Table 14.2 Deflection-angle, gap and overlap values for slat (δ_s, g_s, ovl_s) and flap (δ_f, g_f, ovl_f) normalized with the model chord. Measurements have been performed at free stream velocities of $U_\infty = 40, 50$ and 60 m/s

Conf	δ_s	g_s (%)	ovl_s (%)	δ_f	g_f (%)	ovl_f (%)
Ref	27.834°	2.27	1.07	35	2.11	0.56
3eopt-2	23.299°	2.61	2.09	35.011	0.986	1.52

Fig. 14.2 Picture of the experimental setup in the Aeroacoustic Wind Tunnel Braunschweig (AWB)



of sensors is distributed in spanwise direction along the leading edge of the wing main-body. The analog signals were filtered, digitalized and recorded by the Viper data acquisition system used for the microphone signals with the same parameters.

Figure 14.3 shows the correlation results $R_{v,p}$ for the 3eopt-2 configuration at $U_\infty = 60$ m/s and $\alpha = 11^\circ$ with v being the velocity component in the vertical y -direction. Here p is the pressure fluctuation measured at a single microphone of the 2D-Array located at 90° to the flow direction at $x/c \approx 0$ (pressure side). Figure 14.3a shows the spatial distribution of the overall maximum values. One result obtained during previous applications of the technique is the fact, that regions of maximum correlation values cannot be interpreted as dominant source regions [6]. Figure 14.3b depicts the temporal evolution of the coefficient for a fixed point in space $\mathbf{x} = [x/c; y/c] = [0.064; -0.024]$; corresponding to the point where the overall maximum is located in Fig. 14.3a. Figure 14.3c shows the spatial distribution of $R_{v,p}$ for $\tau = 3.99$ ms, the point in time the coefficient is maximal in Fig. 14.3b. This value of τ does not correspond to the sound travel time from the slat cove to the position of the microphone. Analyzing the point in time when the maximal correlation values occur depending on the position in space is a key element for a deeper understanding of the sound generating process using the causality correlation technique. Figure 14.3d shows the temporal evolution of $R_{v,p}$ along a streamline

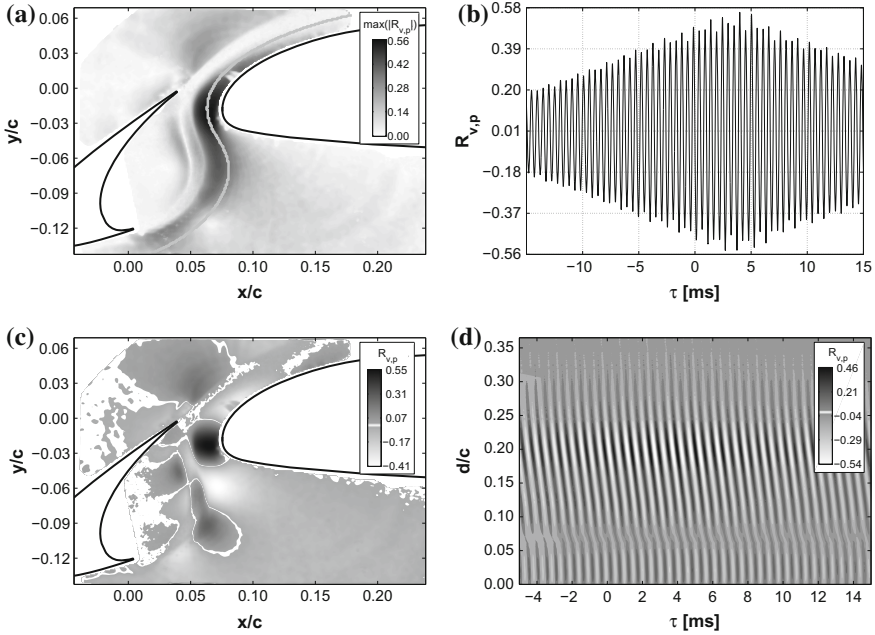


Fig. 14.3 Cross-correlation results $R_{v,p}$ with v being the velocity component in the vertical y -direction. **a** Spatial distribution of the overall maximum values. **b** Temporal evolution of $R_{v,p}$ for $\mathbf{x} = [x/c; y/c] = [0.064; -0.024]$. **c** Spatial distribution of $R_{v,p}$ for $\tau = 3.99$ ms. **d** Space-time evolution of $R_{v,p}$ along the gray line in Figure **a**

shown in Fig. 14.3a (gray line) crossing the point of the overall correlation maximum. The time delay corresponding to the sound travel time from a possible source in the flow field to the microphone is $\tau \approx 5.2$ ms. Analyzing the diagonal of maximum values in Fig. 14.3c, this corresponds to a location at the slat-cusp; the source of coherent flow structures being convected through the slat cove and being accelerated through the slat gap.

14.2 PIV in Trailing-Edge Noise Estimation

Contributed by:

D. Ragni

The application of PIV in the measurement of broadband trailing-edge noise generated by the scattering of the turbulent-flow past the trailing-edge of an airfoil [3] is quite recent. The topic is mostly relevant in the wind-turbine industry, which is exploring new add-ons installation such as serrations [16] and porous trailing-edges [9] for noise mitigation. Tomographic PIV has been used to elucidate the complex

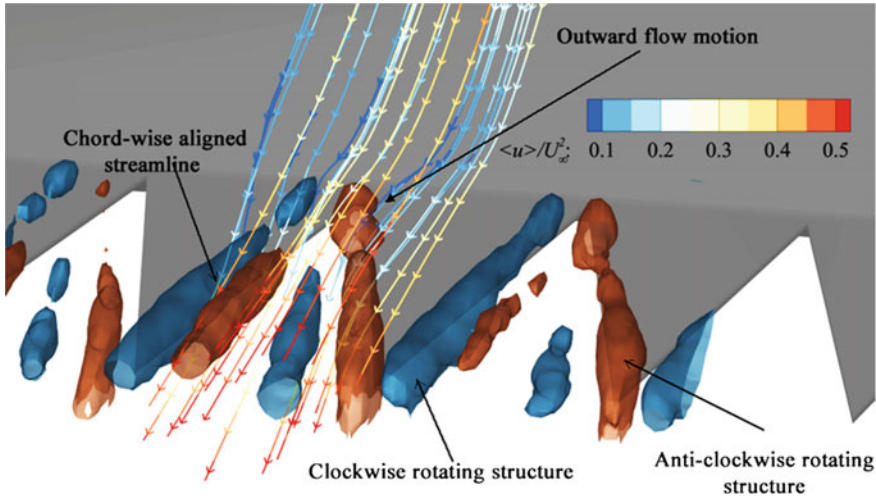


Fig. 14.4 Iso-surface of streamwise vorticity along the serration surface. Streamlines are color contoured with streamwise-velocity component. Free-stream velocity 10 m/s, serration $h/b = 4/2$ cm, NACA0018 airfoil with 20 cm chord [2]

3D flow created by those add-ons under substantial pressure gradient, as it can be seen for example in Fig. 14.4, concerning a recent application about serrated-trailing edges for noise reduction [2].

Tomographic PIV additionally allows to use the 3D velocity fields in the estimation of trailing-edge noise. Studies from diffraction theory [1] showed in fact that turbulent trailing-edge noise can be estimated from the hydrodynamic characteristics of the incoming boundary-layer on an airfoil edge. In particular the energy associated to the pressure fluctuations on the surface can be computed from tomographic PIV data by estimating:

- the unsteady surface pressure auto-spectral density Φ_{pp} ;
- the spanwise correlation length of the structures l_z ;
- the convective-velocity of the associated flow structures u_c .

By knowing the energy associated to the pressure fluctuations, the trailing edge noise estimation can be carried out through a radiation integral, as explained by [23, 27]. Although unsteady-surface pressure is typically retrieved by high repetition-rate PIV systems, recent studies are proposing a smart adaptation of Taylor's hypothesis of frozen turbulence, for the conversion of the relatively higher spatial-resolution of low-repetition-rate PIV systems into temporal information [22].

As a remarkable example, the study from [22] a tomographic PIV setup has been used to measure 3D velocity fields of a turbulent boundary-layer convecting over a straight trailing-edge of a flat plate Table 14.3. An instantaneous tomogram is presented in Fig. 14.5 together with a close-up of the flow features in the boundary layer. For a free-stream velocity of 10 m/s, 2000 images have been acquired and

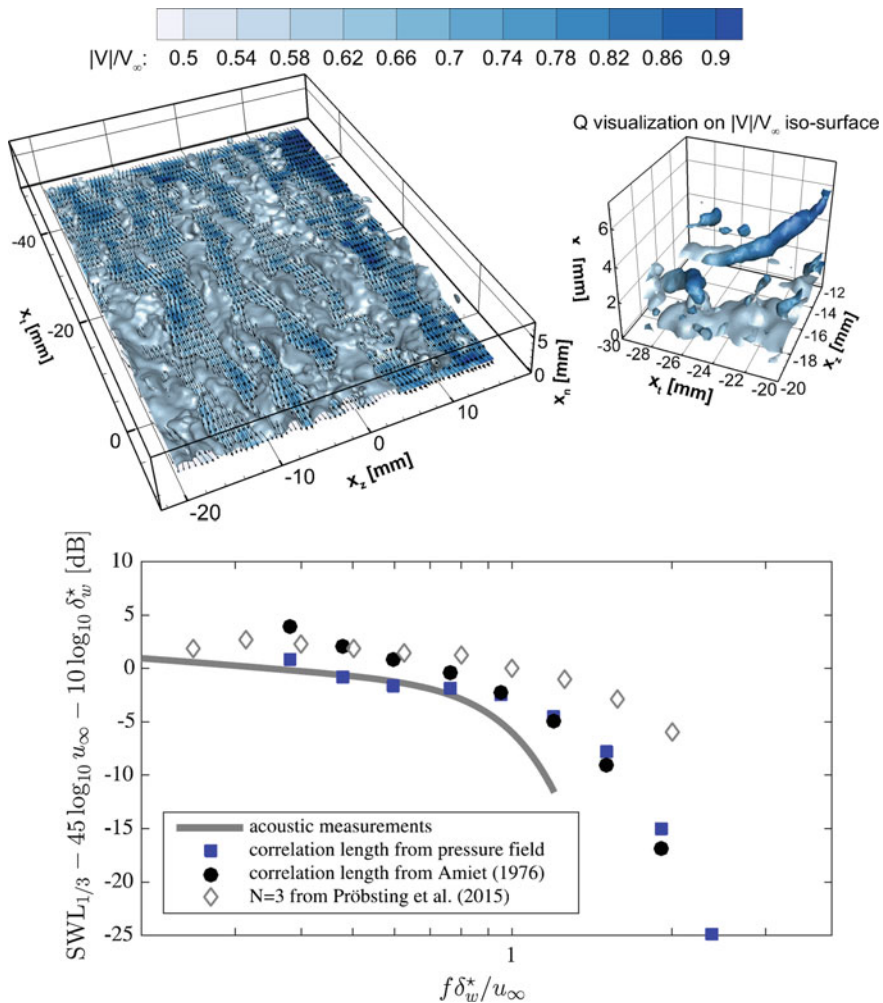


Fig. 14.5 Top: Iso-surfaces of the velocity magnitude at 0.6 of the free-stream value of a turbulent boundary-layer convecting on a straight edge ($x_t = 0$), together with contours of velocity magnitude at x_t - x_z -plane at $x_n = 0.64$ mm. Detail with additional iso-surfaces of Q on top-right. Bottom: estimation of equivalent source power level based on reconstructed pressure field and comparison with acoustic measurements [23], free-stream velocity of 10 m/s

the aforementioned statistical parameters have been computed. Estimation of the equivalent source power level based on the reconstructed pressure fields are presented in Fig. 14.5 and compared to acoustic measurement from far-field microphones and from a similar approach, but using high-speed PIV [23]. From the comparison of the resulting scaled 1/3 octave band SWL a relatively good agreement with the acoustic measurements within 4 dB is appreciated from for $f\delta_w^*/u_\infty$ lower than 7. The sharp

Table 14.3 Parameters for tomographic PIV experiment

Configuration	3D-3C
Field of view (3D)	$60 \times 30 \times 6 \text{ mm}^3$
Interrogation window (3D)	$0.5 \times 0.5 \times 0.5 \text{ mm}^3$
Spatial dynamic range (FOV)	$\text{DSR} \approx 70$
Free Stream pixel shift (FOV)	16 pixel
Magnification	$M = 0.40$
Recording method	Dual-frame
Dataset ensemble (N)	2000
Recording medium	LaVision Imager Pro LX $4870 \times 3246 \text{ pixel}^2$
Recording lens	$f = 105 \text{ mm}$ $f\# = 16$
Illumination	Freq. doubled Nd:YAG laser 200 mJ/pulse at 532 nm

drop off seen in the acoustic measurements at $f\delta_*/u_\infty = 1$ cannot be reproduced by the estimation from the high-speed data due to hardware limitations and to signal-to-noise ratio effects, which typically sets the maximum effective flow measured frequency to about 4 kHz (systems with 10 kHz acquisition frequency), just below the Nyquist value. On the other side, by employing a relatively higher resolution with a low-repetition rate PIV system, the curve of the microphone data can be better approximated. More in detail, the blue squares show the results obtained in the present study using the low repetition rate tomographic PIV system and the correlation length obtained from the pressure field. The low frequency range is limited by domain extent in streamwise direction and frequencies below $f\delta_*/u_\infty = 3$ are not obtained by the low repetition rate system too. For higher frequencies up to $f\delta_*/u_\infty = 1$ agreement within 2 dB can be easily reached.

14.3 A High-Speed PIV Study on Trailing-Edge Noise Sources

Contributed by:

A. Schröder, U. Dierksheide, M. Herr, T. Lauke

Introduction

Airframe noise is essentially due to the interaction of unsteady, mostly turbulent flow with the structure of the airplane, particularly caused by vortical flows around edges or over open cavities. A classical problem in this field is the trailing edge noise, which involves different noise generating mechanisms. Extensive investigations have been conducted on airfoil- and on flat plate trailing edges. According to [10, 15, 21] the

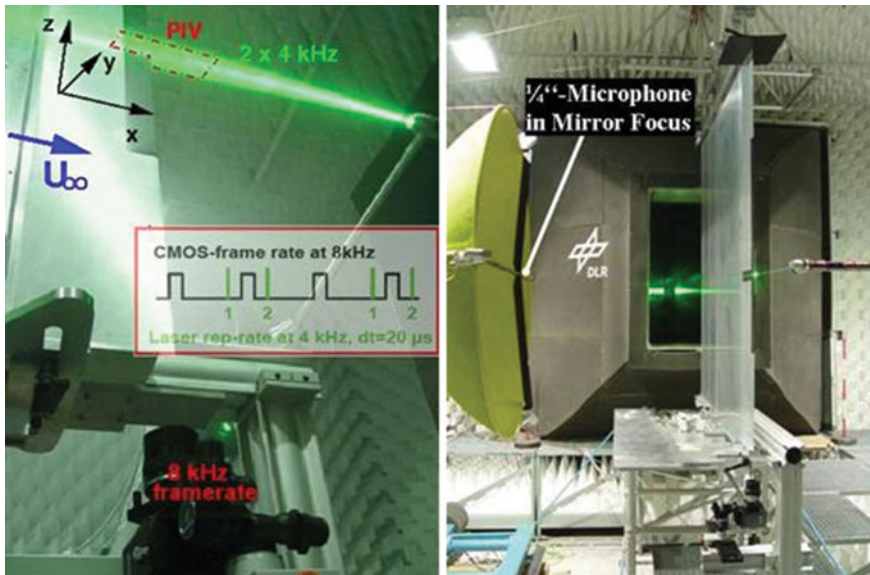


Fig. 14.6 Setup of the high-speed-PIV system at AWB (left) and the directional microphone focused at the measurement volume at the trailing-edge (right)

major noise contribution is provided by the span-wise component of vorticity, the corresponding dipole (“principal edge noise dipole”) is the sc. perturbed Lamb vector being perpendicular to the plane of the plate. A numerical simulation of trailing edge noise can be performed, based on such HS-PIV input data.

Setup, Measurements and Procedure

A flat plate (chord based $Re = 5.3 \times 10^6$ and 6.6×10^6) with profiled leading and trailing edges was mounted vertically in the Aeroacoustic Wind Tunnel Braunschweig (AWB), which is an open jet anechoic test facility (see Fig. 14.6). The flat plate boundary layer was tripped at the leading edge, reaching a thickness of $\delta = 0.03$ m on each side of the trailing edge, corresponding to free stream velocities of $U = 40$ m/s to 50 m/s and a chord length of 2 m. Towards the trailing edge the plate is slightly and symmetrically convergent (5° taper), but no flow separation occurs. Table 14.4 gives the PIV recording parameters, a full description of the experimental setup is provided in [8, 28]. The PIV measurement volume was located at the trailing edge in a x - y -plane within the turbulent boundary layer in order to track the flow structures with a spatial resolution of 256 pixel in y - and 1024 pixel (corresponding to 135 mm) in x -direction. The used high-speed PIV system consists of a New Wave Pegasus PIV, dual cavity Nd:YLF laser with an output beam wavelength of 527 nm, a pulse length of 135 ns and 2×10 mJ at 1 kHz and approximately 2×7 mJ at 4 kHz for each resonator, optics to produce a light sheet and a HighSpeedStar4 (HSS4) CMOS camera with a spatial resolution of max. 1024×1024 pixel at 2 kHz frame

Table 14.4 PIV recording parameters for high-speed PIV (HS-PIV) measurements at the trailing-edge of a flat plate

Flow geometry	Perpendicular to trailing-edge
Maximum velocity	50 m/s
Field of view	$140 \times 37 \text{ mm}^2$
Interrogation volume	$4 \times 4 \times 0.7 \text{ mm}^3$
Dynamic velocity range	0–50 m/s
Observation distance	1.2 m
Recording method	Double frame/single exposure/4 kHz
Recording medium	CMOS-camera
Recording lens	$f = 105 \text{ mm}$, $f_{\#} = 1.8$
Illumination	Nd:YLF laser, 7 mJ per pulse
Pulse delay	$\Delta t = 20 \text{ s}$
Seeding material	DEHS ($d_p \approx 1 \mu\text{m}$)

rate. In this application, a double frame rate of 4 kHz was achieved, thus yielding images at 8 kHz with a spatial resolution of 1024×256 pixel and a 10 bits gray-scale dynamics. 2.6 GB camera memory inside the camera housing allowed to capture 4096 double-images per run. The camera lens was a Nikon 105 mm with an aperture of $f_{\#} = 1.8$. The evaluation of the particle images was performed with a cross correlation scheme using standard FFT with multi-pass (four iteration steps), image deformation, interrogation window shift and a final window size of 32×32 pixel, with 75 % overlap, corresponding to a resolution down to 3 mm in both directions. The Whittaker reconstruction was used for the deformation scheme and peak detection was achieved by a three point Gaussian fit. For post-processing, a median filter was used to remove outliers. As an example, Fig. 14.7 shows an instantaneous velocity field out of a run of 4096 velocity vector fields measured in one second.

A “straight forward” method which should result in a direct calculation of the source terms and therefore a reconstruction of the whole sound field was applied: As the major vortex source term, the perturbed Lamb vector, i.e., the source term of the acoustic analogies of [10, 15, 21], was directly computed from the measured HS-PIV velocity field quantities (namely the instantaneous velocity, vorticity and the mean flow). After linear interpolation onto the body-fitted block-structured grid for the trailing edge, these source term values were fed into the subsequent computational aeroacoustic (CAA) simulations. Assuming a mean flow at rest ($Ma = 0$) the computations were performed by the DLR acoustic code PIANO (Perturbation Investigation of Aerodynamic Noise), which in this case solves the acoustic perturbation equations (Fig. 14.8).

Conclusions

The example presented is one of the first applications of highly time-resolved PIV to a classical aeroacoustic problem at industrially relevant Reynolds numbers. A new

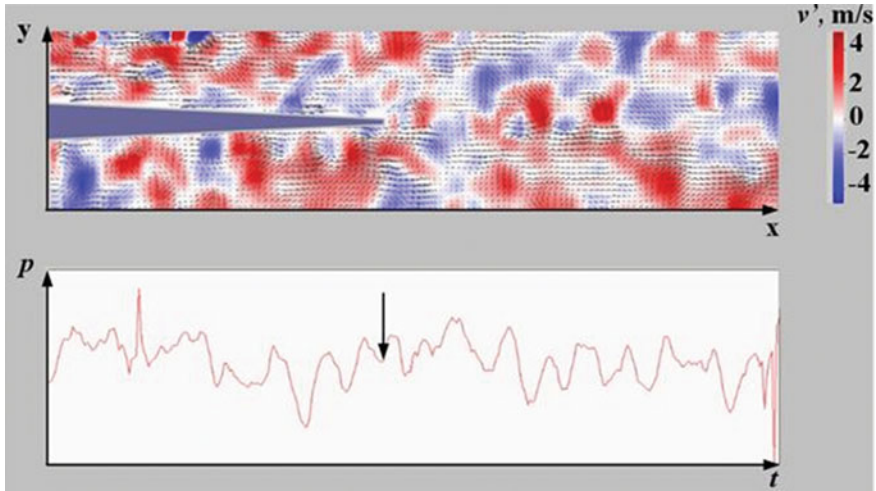


Fig. 14.7 Instantaneous velocity vector field (v' scalar field gray leveled) of a 4 kHz run in the trailing edge region (top) and the corresponding directional microphone signal (actual value at the arrow position)

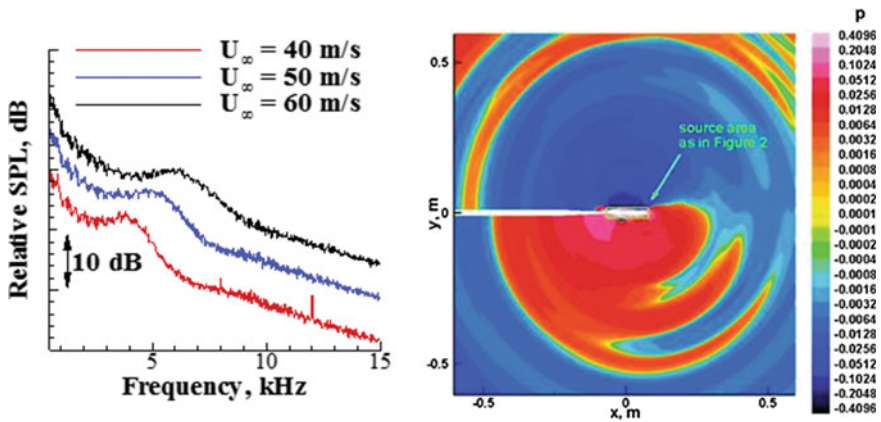


Fig. 14.8 Frequency spectra at different flow velocities measured by the directional microphone (left) and the pressure wave calculations by CAA code PIANO on the basis of HS-PIV data (right)

method for the prediction of trailing edge noise was suggested with the future aim to compute the noise field and directivity by using PIV data, namely the aeroacoustic source quantities, as input for a CAA calculation. Both high-speed PIV and acoustic experiments (for a later validation of the suggested method) were performed on a flat plate model in an aeroacoustic wind tunnel. The PIV data-set was captured at a double-frame rate of 4 kHz with a sufficiently large field of view and enough spatial resolution to resolve all main features of the sound generating flow.

Time resolved PIV allows the non-intrusive quantification of the relevant flow parameters and helps to investigate vortex- structure interactions. In terms of the aeroacoustic optimization of existing aircraft components such an “optical” detection of aeroacoustic source terms will be beneficial, since a huge amount of (at least low-speed) problems could be investigated at lower costs without the need of quiet test facilities.

14.4 Three-Dimensional Vortex and Pressure Dynamics of Revolving Wings

Contributed by:

M. Percin, R. van de Meerendonk and B.W. van Oudheusden

Flapping-wing aerodynamics, as observed in biological flyers, is a three-dimensional unsteady phenomenon, where the flow structure is further complicated by the use of low-aspect ratio wings. Accordingly, flapping wings generate three-dimensional flow structures, among which the leading edge vortex (LEV) was shown to be responsible for the enhanced force generation [4, 13]. The stability of the LEV, which ensures continuous generation of high forces, has received special attention and it has been hypothesized that spanwise pressure gradients and the associated vorticity transport [4], and the apparent rotational accelerations that are characterized by the Rossby number [11, 12] play an important role in this aspect. Clearly, to fully characterize the flow structure, experimental investigation in flapping-wing aerodynamics requires a time-resolved volumetric measurement technique which is capable of capturing three-dimensional vortical structures. In this respect, tomographic-PIV technique, the applicability of which has been explored in earlier studies [18, 19], is used in order to obtain three-dimensional velocity fields around a revolving-surging flat-plate wing model starting from rest.

The experiments were performed in an octagonal water tank (600 mm in diameter and 800 mm in height) at the Aerodynamics Laboratory of Delft University of Technology (see Fig. 14.9). The water tank is made of acrylic glass allowing full optical access for illumination and tomographic imaging. The revolving motion of the model is controlled by a driving system that is mounted vertically in the water tank and it consists of a brushed DC motor and a gearbox (gear ratio of 132:1). A water-submersible ATI Nano-17/IP68 force sensor and a servo motor are connected to the wing to measure the hydrodynamic forces and to control the angle of attack, respectively. The latter is set to 45° in the current study. Three flat plate models (viz., a rigid wing made of acrylic glass of 1 mm thickness, a moderate-flexible wing of 0.175 mm thick polyester film and a high-flexible wing of 0.125 mm thick polyester film) were tested, all sharing the same geometry of 50 mm chord length (c) and 100 mm span length (R), resulting in an aspect ratio of 2. The model was positioned at approximately $5c$ distance from the water surface, $7c$ distance from the bottom wall and $4.2c$ (wing-tip to wall) distance from the side wall to avoid wall interfer-

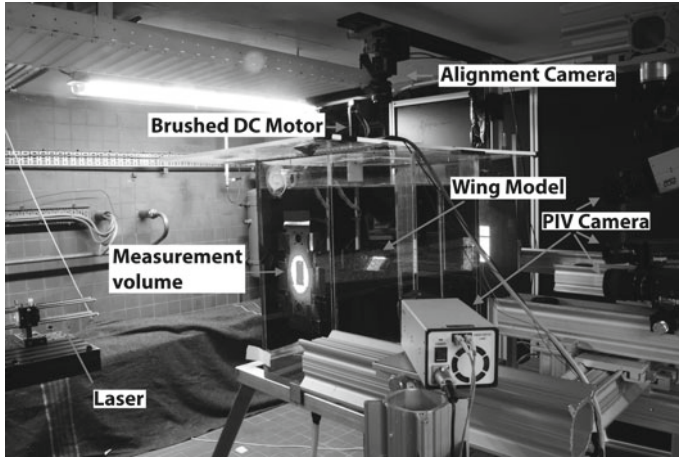


Fig. 14.9 Overview of the experimental setup

Table 14.5 PIV recording parameters for the flow around a revolving wing

Flow geometry	Flow around a revolving low-aspect-ratio flat plate
Reference velocity	$V_{ref} = 0.2$ m/s (velocity at $0.75 R$ span position)
Maximum velocity	$V_{tip} = 0.24$ m/s (wing-tip velocity)
Measurement volume (each)	$100 \times 75 \times 45$ mm ³ ($W \times H \times D$)
Illumination	Double-pulse Nd:YAG laser 200 mJ/pulse at 532 nm
Seeding material	Polyamide spherical particles of $d_p = 56$ μ m
Recording medium	4×12 bit PCO Sencicam CCD cameras 1376×1040 pixel with a pixel pitch of 6.45 μ m
Recording lens	$f = 60$ mm $f_{\#} = 16$
Observation distance	$z_0 \approx 650$ mm
Recording method	Dual frame/single exposure
Pulse delay	$\Delta t = 2.5 - 10$ ms
Interrogation volume	$3.3 \times 3.3 \times 3.3$ mm ³ ($W \times H \times D$)
Digital resolution	$D_R \approx 13.8$ voxels/mm
Particle image diameter	$d_{\tau} \approx 2.8$ pixel
Seeding density	0.035 ppp
Dynamic spatial range	DSR $\approx 30 : 1$
Dynamic velocity range	DVR $\approx 240 : 1$

ence or free-surface effects, as verified by dedicated tests. The wing model starts the motion with a constant acceleration from rest and reaches the terminal velocity (V_{ref}) of 0.2 m/s, as defined at the 75% span reference position, over one chord length of travel ($\delta^* = 1.0$). Subsequently, it continues to revolve at the constant velocity. The Reynolds number based on V_{ref} is 10,000 and the Rossby number is 1.93.

The components of the tomographic-PIV setup and recording parameters are summarized in Table 14.5. The flow field around the complete wing was captured by performing measurements in three volumes with an overlap of $0.1c$. The illuminated volume was kept at a fixed position corresponding to the volume 2 as shown in Fig. 14.10, and to change the measurement volume the complete driving system including the wing was shifted along the z direction. The resultant measurement domain is $100 \times 75 \times 125 \text{ mm}^3$ ($2c \times 1.5c \times 2.5c$) in x , y , z directions, respectively. Three cameras (Camera 1, 3 and 4) were arranged in a linear imaging configuration on the same $x - z$ plane at an aperture angle of 90° , while the fourth camera (Camera 2) was placed above the Camera 3 at an angle of 20° . The tomographic-PIV measurements were conducted in a phase-locked manner and double-frame images of tracer particles were taken at the moment when the wing is oriented normal to Camera 3. To capture a different phase, the starting position of the wing motion was changed accordingly. The PIV measurements were repeated five times for each phase of the motion and resultant vector fields are ensemble-averaged. The repeatability of the physical phenomenon, which is a necessary condition for the success

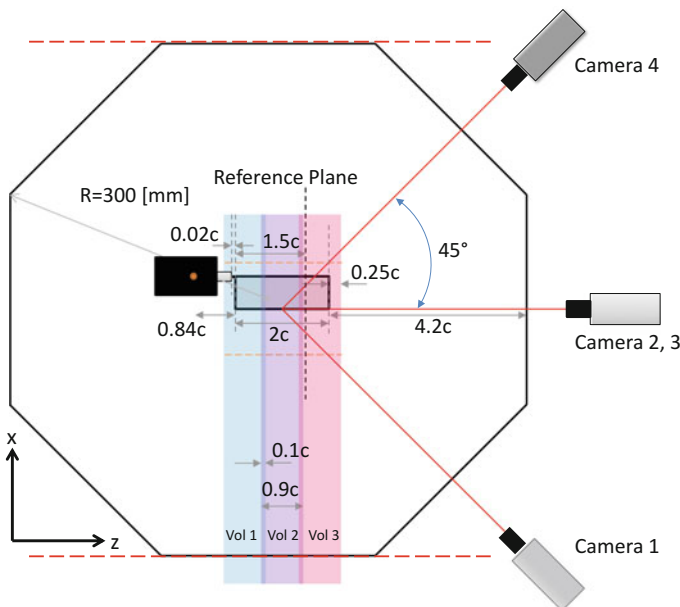


Fig. 14.10 Schematic top view of the tomographic-PIV arrangement

of this approach, was tested and verified in the previous experiments [17]. The PIV measurements were performed for the interval of $0 < \delta^* < 4$ ($\delta^* = \delta/c$, where δ is the distance travelled at $0.75R$ reference position) with temporal resolutions of $dt^* = 0.25$ and 0.5 ($dt^* = t \times V_{ref}/c$, where t is time in seconds). In addition to obtaining the flow fields, the PIV images were used for the reconstruction of the wing geometry. The wing profile at the wing tip is detected in all camera images by means of an in-house algorithm and the profile is reconstructed in the three-dimensional space by use of the mapping information acquired in the tomographic-PIV calibration. To account for the twist of the flexible wings, a number of guidance points at three other spanwise locations are triangulated and used in the reconstruction of the three-dimensional wing geometry.

Figure 14.11 illustrates three-dimensional vortical structures by means of isosurfaces of Q criterion at $\delta^* = 1, 2.5$ and 3.5 . The results for the moderate-flexible wing show the presence of a vortical system that consists of an LEV, a tip vortex (TV), a root vortex (RV), a coherent starting trailing-edge vortex (TEV) and subsequent small-scale TEVs that are connected to swirling features around the TV. During the course of the revolving motion, the LEV lifts off from the wing surface at the out-board sections of the wing, tilts toward the trailing edge and eventually bursts into smaller structures. It is noteworthy that the flow structures captured in the three different volumes are matching fairly well although the measurements were performed asynchronously, which verifies the repeatability of the physical phenomenon and justifies the ensemble-averaging measurement approach.

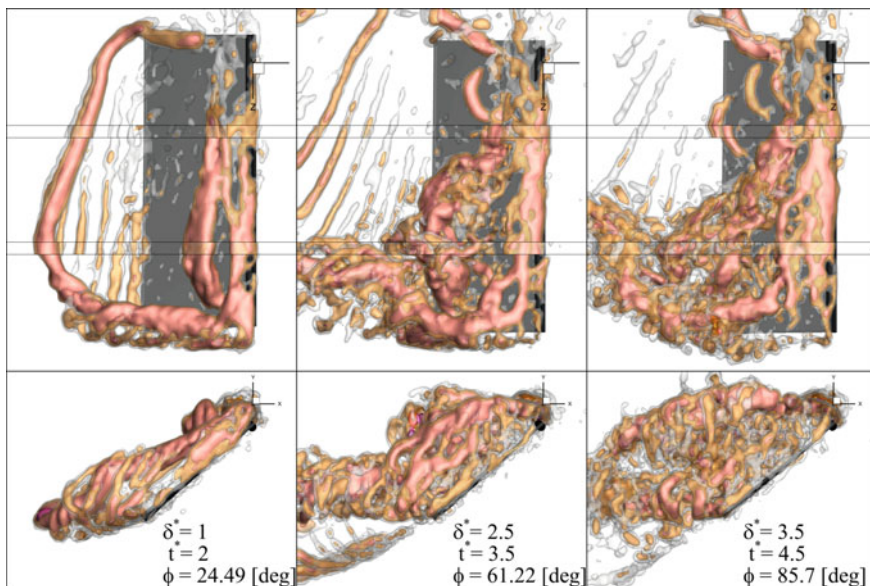


Fig. 14.11 Vortical structures for the case of the moderate-flexible wing visualized by mean of isosurfaces of Q criterion at $\delta^* = 1, 2.5$ and 3.5

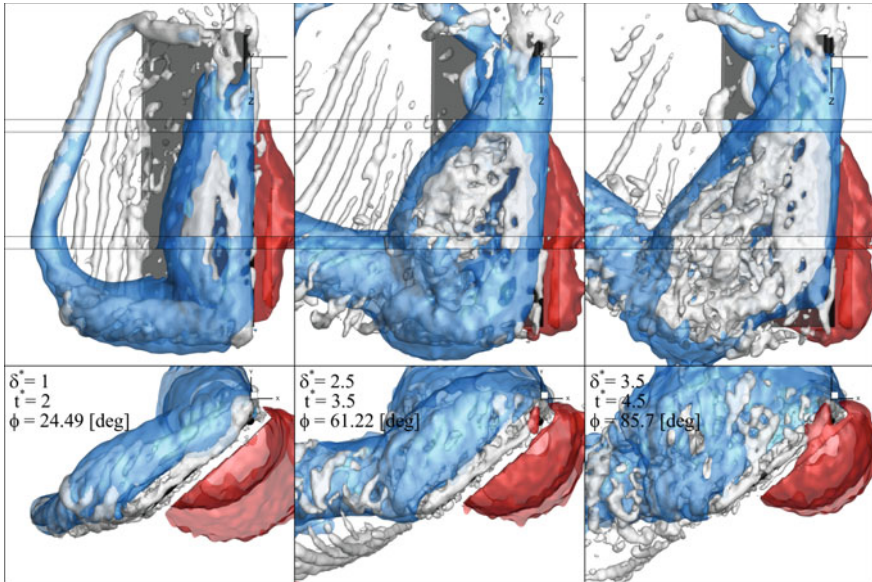


Fig. 14.12 Vortical structures and reconstructed pressure fields (blue: -13 Pa, red: 6 Pa) for the case of the moderate-flexible wing at $\delta^* = 1, 2.5$ and 3.5

The three-dimensional velocity fields were also used to reconstruct instantaneous pressure fields around the wing. A representative result is shown in Fig. 14.12, where isosurfaces of negative (blue) and positive (red) pressure are plotted together with the isosurfaces of the Q criterion. The pressure fields reveal that there is a large suction region associated to the LEV enhancing the lift generation [14].

14.5 PIV-Based Pressure and Load Determination in Transonic Aircraft Propellers

Contributed by:

D. Ragni

The increased demand of low fuel consumption and high efficiency has encouraged the use of aircraft propellers in the aeronautical field. To be competitive with turbofans and turbojets, modern aircraft propellers usually need to operate at high revolution frequencies and severe blade loading, typically determining the coexistence of high Reynolds number and compressibility effects. On the experimental side, the complexity involved in measuring at transonic speed on rotating objects has inspired the use of non-intrusive techniques such as particle image velocimetry to compute the flow pressure and the sectional loads in rotating blades. Figure 14.13 shows an

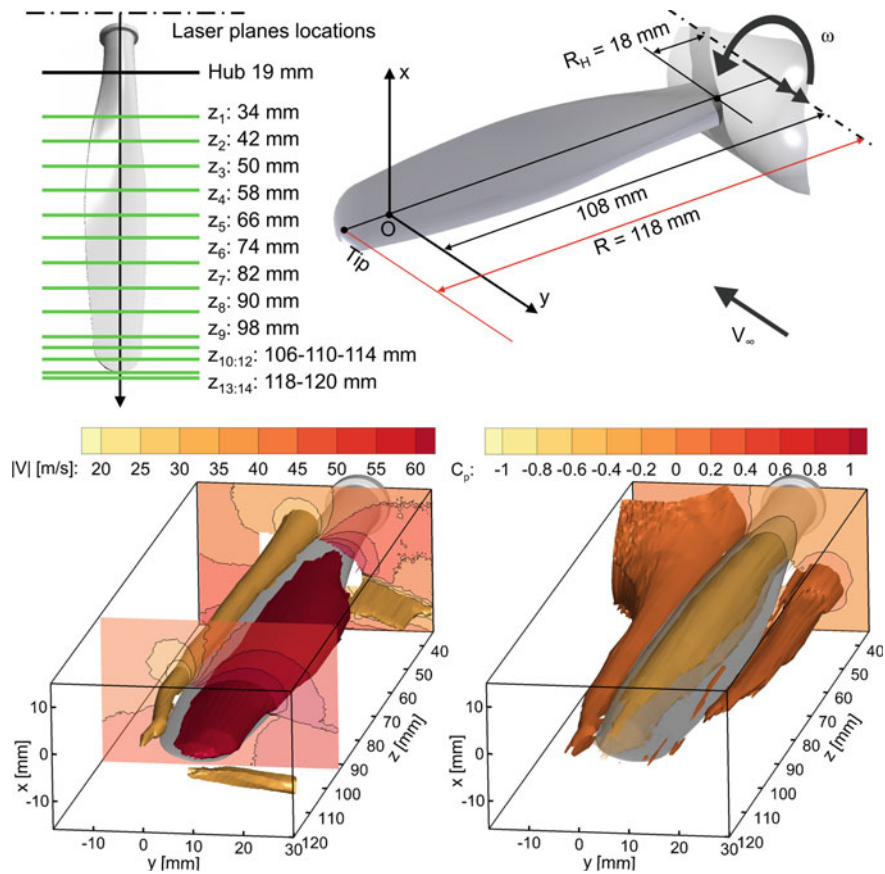


Fig. 14.13 Setup and visualization of absolute velocity and 3D pressure-coefficient of a Beaver aircraft-propeller blade operating in the transonic regime ($Re = 230,000$, $M_R(r/R = 1) = 0.71$) [25]

application from the authors in [25] following the study from the same authors in [24]. The flow field of a scaled DHC Beaver aircraft propeller running at transonic speed has been investigated by means of a multi-plane stereoscopic particle image velocimetry setup. Velocity fields, phase-locked with the blade rotational motion, are acquired across several planes perpendicular to the blade axis and merged to form a 3D measurement volume. Transonic conditions have been reached at the tip region, with a blade revolution frequency of 19,800 rpm and a relative free-stream Mach number of 0.73 at the tip. The pressure field and the surface pressure distribution are inferred from the 3D velocity data through integration of the Navier–Stokes momentum equation in differential form, allowing for the simultaneous flow visualization and the computation of sectional and total aerodynamic loads. The momentum and pressure data are further integrated by means of a contour-approach to yield the

aerodynamic sectional force components as well as the blade torsional moment. In the referenced study, a steady Reynolds averaged Navier–Stokes numerical simulation of the entire propeller model has been used for comparison to the measurement data.

The wind-tunnel has been continuously operated during the PIV images acquisition; in particular, the values of the free-stream velocity, stagnation/free-stream pressure and temperature have been averaged during the single-plane acquisition (≈ 2 min) and the data corrected for it. The flow is seeded with particles produced by a SAFEX Twin Fog generator with SAFEX Inside Nebelfluide (mixture of dyethelene-glycol and water, with 1 micron median diameter). The tracer particles are introduced directly downstream of the wind-tunnel test section and uniformly mixed during the recirculation. Laser light is provided by a Quantel CFR200 Nd-Yag laser with 200 mJ/pulse energy, illuminating the field of view through laser optics forming a laser sheet of 2 mm thickness (about 20 cm wide). Two LaVision Imager Pro LX cameras with $4,872 \times 3,248$ pixel and two Nikon lenses of 180 mm focal length at $f_{\#}8$ have been used. Sets of 150 images have been recorded in phase-lock mode at a maximum acquisition frequency of 2.5 Hz. Cameras and laser have been simultaneously traversed by two separate mechanisms, the relative position of which determined the actual field of view. The recordings are evaluated with a window deformation iterative multi-grid with window size down to 8×8 pixel at 50 % overlap (0.20 mm resolution), and subsequently averaged. In propeller applications the major sources of uncertainties are due to reflections/shadows, particle relaxation time and peak-locking. Of crucial importance is the choice of the particles [26] due to the high centrifugal forces and to the high acceleration dictated by the rotating blades. If multiple optical-access/laser sources are not available, shadows and reflections can be mitigated by illuminating the blade sections from its trailing-edge. Beside allowing for a more correct pressure-reconstruction for the load-determination (since the region lost is mostly potential flow region, so less relevant), it allows reducing reflections due to the lower effect of perspective, especially in stereoscopic configurations (Fig. 14.14).

With the present transonic propeller configuration (chord-based Reynolds larger than 200,000 and relative Mach numbers larger than 0.6) it is recommended to have digital resolutions larger than 10 pixel/mm for an accurate determination of the sectional-loads. Best prediction of surface pressure has been achieved by keeping reflection within 0.5 mm [24] (see parameters in Table 14.6). Once a full scanning of the blade is carried out, the surface pressure distribution together with the sectional loads can be obtained for the full blade Fig. 14.14.

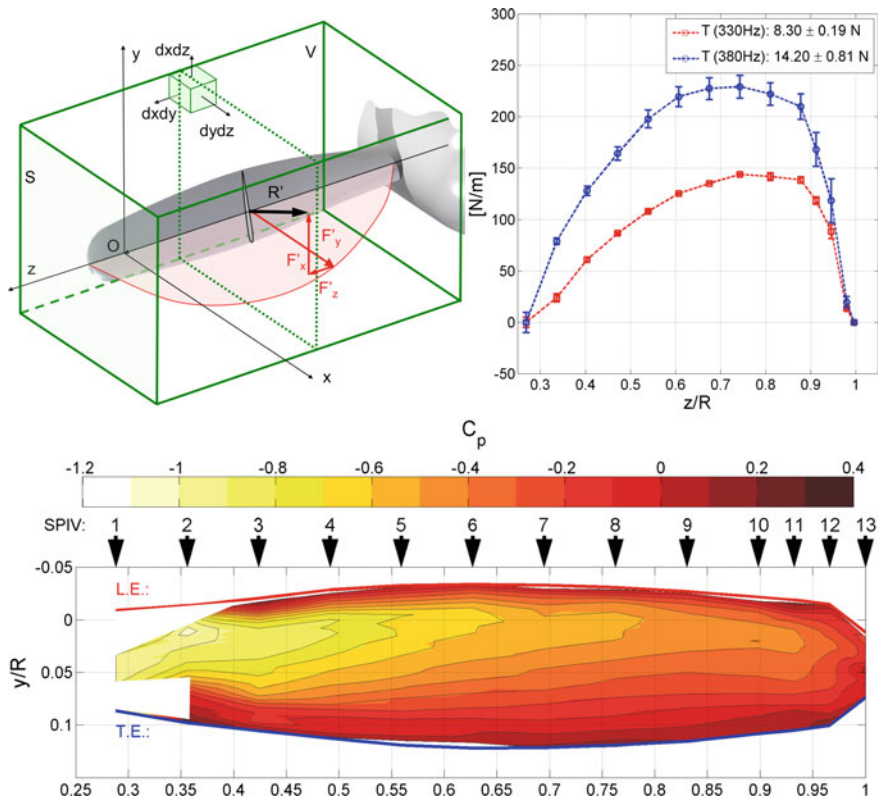


Fig. 14.14 3D sectional loads and surface-pressure distribution from PIV stereoscopic data phase-locked for a Beaver-propeller blade ($Re = 230,000$, $M_R(r/R = 1) = 0.71$) [25]

Table 14.6 PIV recording parameters for the Beaver aircraft propeller study [26]

Configuration	2D-3C
Field of view ($W \times H$)	$120 \times 80 \text{ mm}^2$
Interrogation window ($W \times H$)	$0.2 \times 0.2 \text{ mm}^2$
Free Stream pixel shift(FOV)	15 pixel
Magnification	$M = 0.31$
Recording method	dual-frame phase-locked (pl)
Dataset ensemble (N)	150–200 (pl)
Recording medium	LaVision Imager Pro LX $4870 \times 3246 \text{ pixel}^2$
Recording lens	$f = 180 \text{ mm}$ $f_{\#} = 8$
Illumination	Freq. doubled Nd:YAG laser 200 mJ/pulse at 532 nm

References

1. Amiet, R.: Noise due to turbulent flow past a trailing edge. *J. Sound Vib.* **47**(3), 387–393 (1976). DOI 10.1016/0022-460X(76)90948-2. URL [https://doi.org/10.1016/0022-460X\(76\)90948-2](https://doi.org/10.1016/0022-460X(76)90948-2)
2. Avallone, F., Arce Leon, C., Pröbsting, S., Lynch, K., Ragni, D.: Tomographic-PIV investigation of the flow over serrated trailing-edges. In: 54th AIAA Aerospace Sciences Meeting, pp. 1–14. AIAA SciTech Forum (2016). DOI 10.2514/6.2016-1012. URL <https://doi.org/10.2514/6.2016-1012>
3. Doolan, C., Moreau, D., Brooks, L.: Wind turbine noise mechanisms and some concepts for its control. *Acoust. Aust.* **40**(1), 7–13 (2012). URL https://www.acoustics.asn.au/journal/2012/2012_40_1_Doolan.pdf
4. Ellington, C.P., van den Berg, C., Willmott, A.P., Thomas, A.L.R.: Leading-edge vortices in insect flight. *Nature* **384**(6610), 626–630 (1996). DOI 10.1038/384626a0. URL <https://doi.org/10.1038/384626a0>
5. Henning, A., Kaepernick, K., Ehrenfried, K., Koop, L., Dillmann, A.: Investigation of aeroacoustic noise generation by simultaneous particle image velocimetry and microphone measurements. *Exp. Fluids* **348**, 1073–1085 (2008). DOI 10.1007/s00348-008-0528-y. URL <https://doi.org/10.1007/s00348-008-0528-y>
6. Henning, A., Koop, L., Schröder, A.: Causality correlation analysis on a cold jet by means of simultaneous particle image velocimetry and microphone measurements. *J. Sound Vib.* **332**(13), 3148–3162 (2013). DOI <https://doi.org/10.1016/j.jsv.2013.01.027>. URL <https://www.sciencedirect.com/science/article/pii/S0022460X13000758>
7. Henning, A., Wrede, B., Geisler, R.: Aeroacoustic investigation of a high-lift device by means of synchronized PIV and microphone measurements. In: 16th International Symposium on Application of Laser Techniques to Fluid Mechanics, Lisbon, Portugal (2012). URL http://lces.dem.ist.utl.pt/lxaser/lxaser2012/upload/268_paper_xvpzvq.pdf
8. Herr, M., Dobrzynski, W.: Experimental investigations in low noise trailing edge design. In: 10th AIAA/CEAS Aeroacoustics Conference, Manchester (England), 2004 (2004). DOI 10.2514/1.11101. URL <https://doi.org/10.2514/1.11101>
9. Herr, M., Dobrzynski, W.: Experimental investigations in low-noise trailing edge design. *AIAA J.* **43**(6), 1167–1175 (2005). DOI 10.2514/1.11101. URL <https://doi.org/10.2514/1.11101>
10. Howe, M.S.: A review of the theory of trailing edge noise. *J. Sound Vib.* **61**(3), 437–465 (1978). DOI 10.1016/0022-460X(78)90391-7. URL <https://www.sciencedirect.com/science/article/pii/0022460X78903917>
11. Jardin, T., David, L.: Spanwise gradients in flow speed help stabilize leading-edge vortices on revolving wings. *Phys. Rev. E* **90**(1), 013011 (2014). DOI 10.1103/PhysRevE.90.013011. URL <https://doi.org/10.1103/PhysRevE.90.013011>
12. Lentink, D., Dickinson, M.H.: Rotational accelerations stabilize leading edge vortices on revolving fly wings. *J. Exp. Biol.* **212**(16), 2705–2719 (2009). DOI 10.1242/jeb.022269. URL <https://jeb.biologists.org/content/212/16/2705>
13. Maxworthy, T.: Experiments on the Weis-Fogh mechanism of lift generation by insects in hovering flight. Part 1. dynamics of the ‘fling’. *J. Fluid Mech.* **93**(1), 47–63 (1979). DOI 10.1017/S0022112079001774. URL <https://doi.org/10.1017/S0022112079001774>
14. van de Meerendonk, R., Percin, B., van Oudheusden, B.: Three-dimensional flow and load characteristics of flexible revolving wings at low Reynolds number. In: 18th International Symposium on Applications of Laser Techniques to Fluid Mechanics, Lisbon (Portugal) (2016). URL http://lces.dem.ist.utl.pt/lxaser/lxaser2016/finalworks2016/papers/01.7_4_159paper.pdf
15. Moehring, W.: Modelling low mach number noise. In: Mueller, E.A. (ed.) *Mechanics of Sound Generation in Flows*, pp. 85–96. Springer (1979). URL <http://adsabs.harvard.edu/abs/1979msgf.proc...85M>
16. Oerlemans, S., Fisher, M., Maeder, T., Kögler, K.: Reduction of wind turbine noise using optimized airfoils and trailing-edge serrations. *AIAA J.* **47**(6), 1470–1481 (2009). DOI 10.2514/1.38888. URL <https://doi.org/10.2514/1.38888>

17. Percin, M.: Aerodynamic mechanisms of flapping flight. Ph.D. thesis, Delft University of Technology (2015). DOI 10.4233/uuid:4d535d87-d11e-4916-9143-5e6762c56152. URL <https://doi.org/10.4233/uuid:4d535d87-d11e-4916-9143-5e6762c56152>
18. Percin, M., Hu, Y., van Oudheusden, B., Scarano, F.: Wing flexibility effects in clap-and-fling. *Int. J. Micro Air Veh.* **3**(4), 217–227 (2011). DOI 10.1260/1756-8293.3.4.217. URL <https://doi.org/10.1260/1756-8293.3.4.217>
19. Percin, M., van Oudheusden, B.W.: Three-dimensional flow structures and unsteady forces on pitching and surging revolving flat plates. *Exp. Fluids* **56**(2), 47 (2015). DOI 10.1007/s00348-015-1915-9. URL <https://doi.org/10.1007/s00348-015-1915-9>
20. Pott-Pollenske, M., Delfs, J.: Enhanced capabilities of the aeroacoustic wind tunnel Braunschweig. In: 29th AIAA Aeroacoustics Conference, Vancouver, Canada, vol. 2910 (2008). DOI 10.2514/6.2008-2910. URL <https://doi.org/10.2514/6.2008-2910>
21. Powell, A.: Theory of vortex sound. *J. Acoust. Soc. Am.* **36**(1), 177–195 (1964). DOI 10.1121/1.1918931. URL <https://doi.org/10.1121/1.1918931>
22. Pröbsting, S., Schneiders, J.F., Avallone, F., Ragni, D., Scarano, F.: Trailing-edge noise diagnostics with low-repetition-rate PIV. In: 22nd AIAA/CEAS Aeroacoustics Conference, 3023 (2016). DOI 10.2514/6.2016-3023. URL <https://doi.org/10.2514/6.2016-3023>
23. Pröbsting, S., Tuinstra, M., Scarano, F.: Trailing edge noise estimation by tomographic particle image velocimetry. *J. Sound Vib.* **346**, 117–138 (2015). DOI 10.1016/j.jsv.2015.02.018. URL <https://doi.org/10.1016/j.jsv.2015.02.018>
24. Ragni, D., Ashok, A., van Oudheusden, B.W., Scarano, F.: Surface pressure and aerodynamic loads determination of a transonic airfoil based on particle image velocimetry. *Meas. Sci. Technol.* **20**(7), 074,005 (2009). DOI 10.1088/0957-0233/20/7/074005. URL <http://stacks.iop.org/0957-0233/20/i=7/a=074005>
25. Ragni, D., van Oudheusden, B.W., Scarano, F.: 3D pressure imaging of an aircraft propeller blade-tip flow by phase-locked stereoscopic PIV. *Exp. Fluids* **52**(2), 463–477 (2012). DOI 10.1007/s00348-011-1236-6. URL <https://doi.org/10.1007/s00348-011-1236-6>
26. Ragni, D., Schrijer, F., van Oudheusden, B.W., Scarano, F.: Particle tracer response across shocks measured by PIV. *Exp. Fluids* **50**(1), 53–64 (2011). DOI 10.1007/s00348-010-0892-2. URL <https://doi.org/10.1007/s00348-010-0892-2>
27. Roger, M., Moreau, S.: Back-scattering correction and further extensions of Amiet’s trailing-edge noise model. Part 1: theory. *J. Sound Vib.* **286**(3), 477–506 (2005). <https://doi.org/10.1016/j.jsv.2004.10.054>
28. Schröder, A., Herr, M., Lauke, T., Dierksheide, U.: A study on trailing edge noise sources using high speed particle image velocimetry. In: Rath, H.J., Holze, C., Heinemann, H.J., Henke, R., Hönlinger, H. (eds.) *New Results in Numerical and Experimental Fluid Mechanics V, Notes on Numerical Fluid Mechanics and Multidisciplinary Design (NNFM)*, vol. 92, pp. 373–380. Springer, Berlin (2006). DOI 10.1007/978-3-540-33287-9_46. URL https://doi.org/10.1007/978-3-540-33287-9_46
29. Siddon, T.: Noise source diagnostics using causality correlations. AGARD CP 131 on Noise Mechanism (7) (1974)
30. van der Waerden Bartel L: *Mathematische Statistik*, 3rd edn. Springer (1971)

Chapter 15

Applications: Flows at Different Temperatures

15.1 Study of Thermal Convection and Couette Flows

Contributed by:

C. Böhm, C. Willert, H. Richard

These experimental investigations of flows by means of PIV have been carried out in 1996 by DLR in cooperation with the Center of Applied Space Technology and Microgravity (ZARM), University of Bremen, in order to complete their numerical simulations and LDV measurements [3]. The experimental setup is shown in Fig. 15.1. The PIV parameters used for this investigation are listed in Table 15.1.

A fluid (silicone oils M20 and M3) seeded with $10\ \mu\text{m}$ diameter glass particles with a volumetric mass near $1.05\ \text{g/cm}^3$ and a refraction index of $n = 1.55$, is filled in the gap between two concentric spheres. The outer sphere is composed of two transparent acrylic glass hemispheres (refraction index of $n = 1.491$), with a radius of $40.0\ \text{mm}$, and the inner sphere is made out of aluminum with a radius of $26.7\ \text{mm}$. To minimize optical distortions because of the curvature of the model, the outer sphere is included in a rectangular cavity filled with silicone oil to provide a plane liquid–air interface and reduce optical refraction.

To study the thermal convection flows, the inner sphere is heated homogeneously up to $45\ ^\circ\text{C}$ whereas the outer sphere is held at constant temperature. Six temperature sensors are installed on both spheres as indicated in Fig. 15.1. A 25 Hz CCD camera with an internal shutter (40 ms between each frame) was used in combination with a continuous argon-ion laser. This was possible because of the low velocity flow studied ($\approx 0.5\ \text{cm/s}$). A 100 mm Zeiss Makro Planar objective lens was used during the flow measurements with a $f_\#$ number of 2.8. For a magnification between 1/2 and 1/4, and a f-number of $f_\# = 11$, the particle image diameters are in the range

An overview of the Digital Content to applications on different temperatures can be found at [DC15.1].

Fig. 15.1 The experimental apparatus to study the thermal convection and the Taylor flow

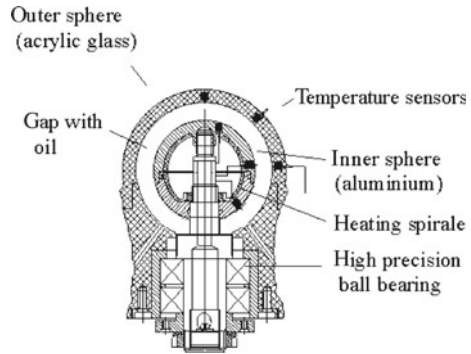


Table 15.1 PIV recording parameters for thermal convection

Flow geometry	$U_{\infty} = 0.5 \text{ cm/s}$ parallel to light sheet
Maximum in-plane velocity	$U_{\max} \approx 0.5 \text{ cm/s}$
Field of view	$50 \times 40 \text{ mm}^2$
Interrogation volume	$1.6 \times 1.6 \times 2 \text{ mm}^3$ ($H \times W \times D$)
Dynamic spatial range	$\text{DSR} \approx 24 : 1$
Dynamic velocity range	$\text{DVR} \approx 200 : 1$
Observation distance	$z_0 \approx 1.5 \text{ m}$
Recording method	Dual frame/single exposure
Ambiguity removal	Frame separation
Recording medium	Full frame interline transfer CCD ($782 \times 582 \text{ pixel}$)
Recording lens	$f = 100 \text{ mm}$ $f_{\#} = 2.8$ to 22
Illumination	Continuous argon-ion laser, 1 Watt, Internal shutter of camera
Pulse delay	$\Delta t = 40 \text{ ms}$
Seeding material	Glass particles ($d_p \approx 10 \mu\text{m}$)

between 22 and $18 \mu\text{m}$, that is to say between 2 and 3 pixel which give the lowest measurement uncertainty. For the particles utilized in this experiment, the gravitational velocity is found to be: $v_g = 2.9 \cdot 10^{-7} \text{ m/s}$ with M20 oil and $v_g = 3 \cdot 10^{-6} \text{ m/s}$ with M3 oil, which are disturbances that can be disregarded. The investigations were carried out in a meridional light sheet (Fig. 15.2) through the sphere's center.

For small ΔT between the two spheres we have the laminar convective state, and the flow structures of the PIV measurement (see Fig. 15.3) are in good agreement with the streamlines computed numerically by GARG [7]. We have an upward flow of 0.1 cm/s at the inner sphere and a downward flow of 0.05 cm/s at the outer sphere, and a ratio of 2 to 1 which has also been predicted theoretically by MACK & HARDEE

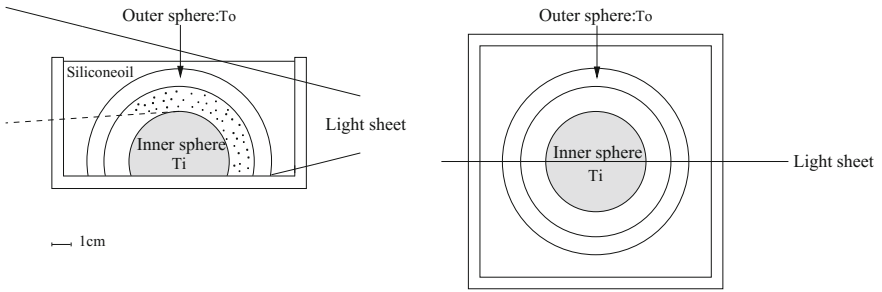


Fig. 15.2 The light sheet position

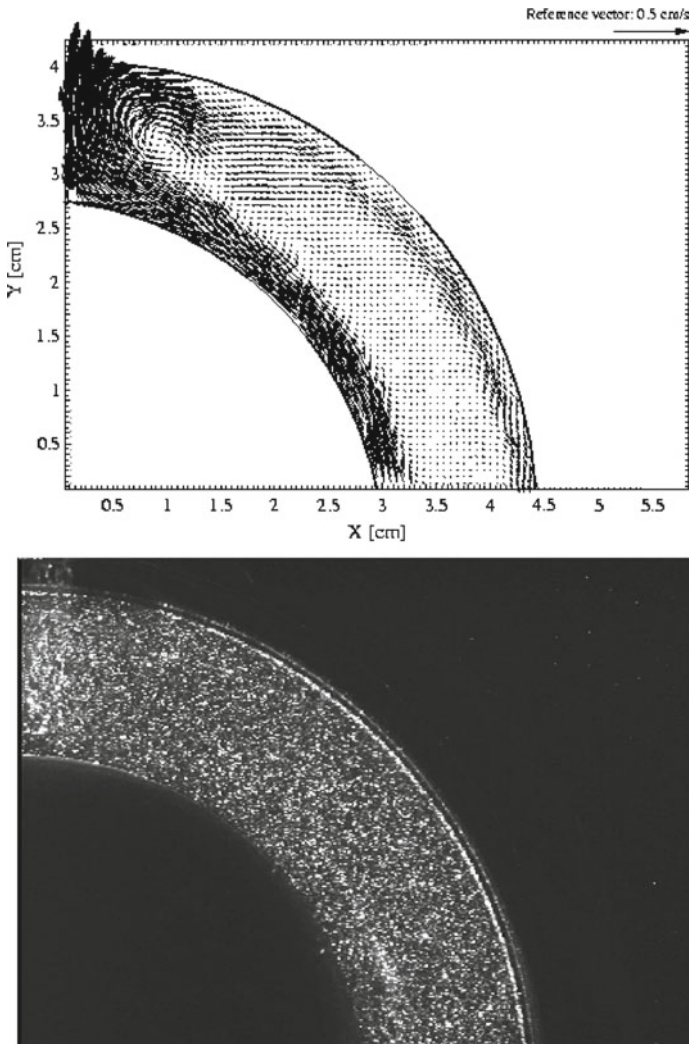


Fig. 15.3 Thermal convection velocity fields and flow picture with the two exposures

[14], and at the north pole we have a radial outward flow of 0.2 cm/s whereas in the equatorial region we have an area of zero velocity in the middle of the sphere as in the model of GARG [7].

By increasing the ΔT a time dependent pulsating ring vortex sets in at the north pole near the outer sphere (see Fig. 15.3). The maximal velocities increase up to 1 cm/s in the polar region and we have an upward flow of about 0.35 cm/s at the inner sphere and a downward flow of 0.1 cm/s at the outer sphere. The convective motion is dominant at the boundary regions and near to the pole in contrast to the vanishing velocities in a wide range of radial positions. Additionally there are small radial inward flows at the outer sphere boundary which is in agreement with the numerical simulations.

The Couette flow study required the use of another setup: the velocity being contained between 5 and 10 cm/s and therefore the previous delay used between each frame was too large. As a consequence, a pulsed Nd:YAG laser synchronized with a large format video camera was used allowing us to select appropriate pulse delays. The frame-straddling technique was employed for directional ambiguity removal. The study has been performed at 0.4 cm above the pole region (Fig. 15.4). The rotation of the inner sphere was 250 revolutions per minute for the experiment and $\Delta T = 0$. The velocity vector maps are presented in Fig. 15.5. The PIV parameters used for this investigation are listed in Table 15.2.

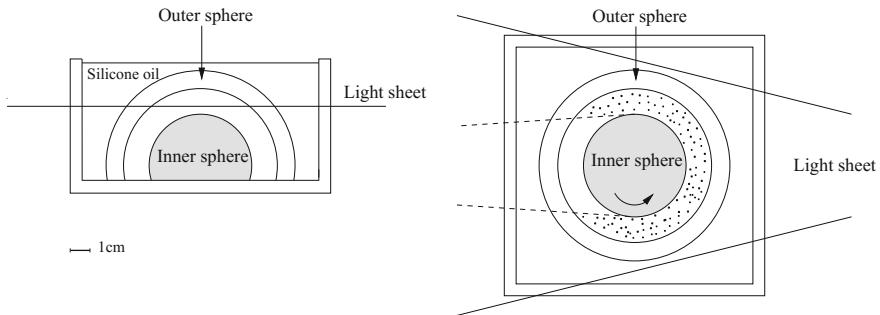


Fig. 15.4 The light sheet position: 0.4 cm up to the pole region

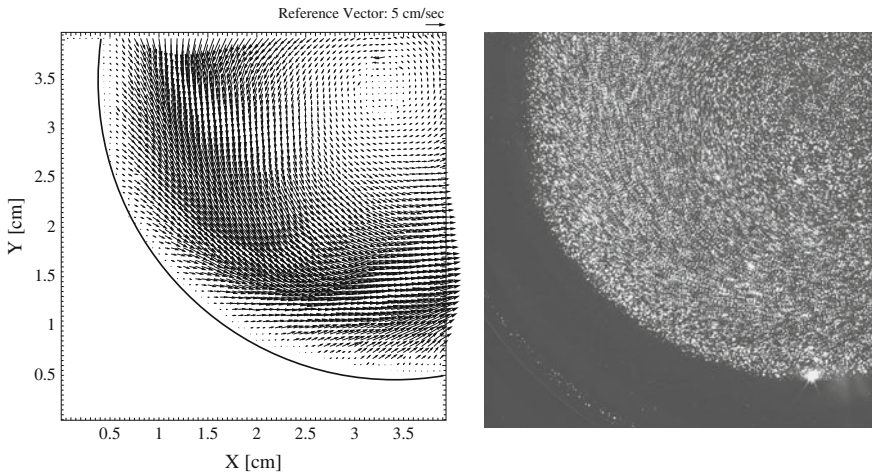


Fig. 15.5 Couette flow velocity field and picture with the two exposures

Table 15.2 PIV recording parameters for Couette flow

Flow geometry	$U_{\infty} = 10 \text{ cm/s}$ parallel to light sheet
Maximum in-plane velocity	$U_{\max} \approx 10 \text{ cm/s}$
Field of view	$50 \times 50 \text{ mm}^2$
Interrogation volume	$1.6 \times 1.6 \times 2 \text{ mm}^3 (H \times W \times D)$
Dynamic spatial range	$\text{DSR} \approx 31 : 1$
Dynamic velocity range	$\text{DVR} \approx 200 : 1$
Observation distance	$z_0 \approx 0.5 \text{ m}$
Recording method	Dual frame/single exposure
Ambiguity removal	Frame separation (frame-straddling)
Recording medium	Full frame interline transfer CCD (1008×1018 pixel)
Recording lens	$f = 60 \text{ mm}$, $f_{\#} = 2.8$ to 22
Illumination	Nd:YAG laser ^a , 70 mJ/pulse
Pulse delay	$\Delta t = 20 \text{ ms}$
Seeding material	Glass particles ($d_p \approx 10 \mu\text{m}$)

^aFrequency doubled

15.2 Combined PIT/PIV of Air Flows Using Thermo-chromic Liquid Crystals

Contributed by:

D. Schmeling, J. Bosbach and C. Wagner

Thermal convective air flows are abundant in technical applications such as heat exchangers or indoor climatisation and of great interest in fundamental studies as well. Since such flows are driven by temperature gradients, simultaneous acquisition of the instantaneous velocity and temperature fields are highly desirable. In this context, our study aims at the dynamics of thermal plumes as well as their influence on the local and global heat transfer in thermal convection. Hereto, measurements of mixed convection of air in a cuboidal sample with aspect ratio $1 \times 1 \times 5$ ($W \times H \times L$) were performed (see Fig. 15.6).

For simultaneous measurement of temperature and velocity fields, mainly two different approaches are followed: Since many decades, PIV is combined with Particle Image Thermography (PIT) for flow measurements in liquids using thermo-chromic liquid crystals (TLCs) as tracer particles (“TLC-PIV”) [8]. This approach allows for very precise measurements of small temperature differences at moderate temperatures. For a survey on this technique, the reader is referred to the recent review given by DABIRI [5]. A rather new approach comprises thermographic phosphor particles as tracer particles [1]. These are useable for larger temperature ranges, however, providing an accuracy of the order of 1 K only. For our study of mixed convection of air, we needed a very high temperature precision, and hence, adopted the TLC-PIV technique from liquids (Table 15.3).

Under illumination with white light, TLCs reveal the special behaviour to appear in different colors, depending on their temperature. More specifically, different wavelengths are reflected preferentially as a function of temperature. Further, the wavelength of the reflected light depends on the size of the particles and the viewing

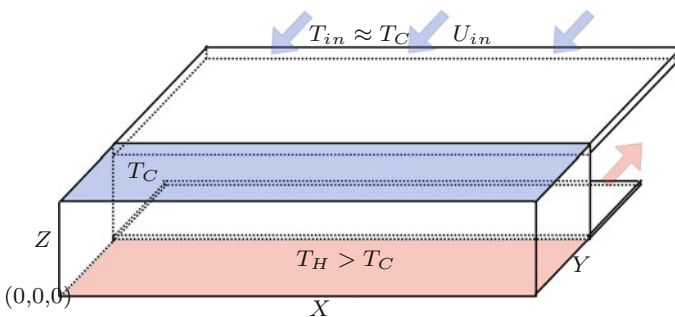


Fig. 15.6 Sketch of the mixed convection sample

Table 15.3 PIV recording parameters for turbulent thermal convection using thermochromic liquid crystals

Flow geometry	Turbulent mixed convection in a cuboidal sample with rather small out-of-plane component
Maximum in-plane velocity	$U_{\max} \approx 0.15$ m/s
Field of view	250×150 mm ² ($W \times H$)
Interrogation volume	$5.0 \times 5.0 \times 8.0$ mm ³ ($W \times H \times D$)
Dynamic spatial range	DSR $\approx 30 : 1$
Dynamic velocity range	DVR $\approx 100 : 1$
Dynamic temperature range	DTR $\approx 20 : 1$
Observation distance	$z_0 \approx 1300$ mm
Recording method	Dual frame/single exposure
Recording medium	Pixelfly qe @ 1280 \times 1024 pixel for PIV Pixelfly color @ 1280 \times 1024 pixel for PIT
Recording lens	$f = 50$ mm $f_{\#} = 1.4$
Illumination	60 white LEDs (OSRAM Platinum Dragon)
Pulse delay	$\Delta t = 8 - 16$ ms
Seeding material	Thermochromic liquid crystals (TLCs)

angle. Hence, for each experimental setup, a color-temperature calibration has to be conducted. First experiments using TLCs to visualize the temperature field have been conducted by HILLER et al. [8]. Nowadays, this technique is well established for investigations in liquids. However, its high effort, in specific for the calibration of the TLCs, makes this technique still challenging to use.

The usage of the TLCs for combined PIV/PIT in air flows is mainly restricted by the size of the TLC particles. On the one hand, the particles must be as small as possible in order to ensure good tracking of the fluid motion. On the other hand they must be large enough in order to provide a good color play. Estimations result in suitable particle diameters for air flows of the order of 10 μ m [19]. This is about one order of magnitude smaller as compared to TLC particles commonly used in liquids. Accordingly, particle generation, illumination and image filtering processes state a challenge when using TLCs as tracer particles for PIT in air flows.

We realized the particle generation using a solvent and atomization processes. The thermal and mechanical response times as well as details of the particle generation are described in SCHMELING et al. [19]. Therein, the newly developed high intensity white light source based on LEDs is described as well. The light source provides a homogeneous lightsheet with a thickness of 9 mm over a distance of 500 mm, see Fig. 15.7a. While the hue value of the color image is determined by the temperature of the TLCs [5], image filtering to increase the signal-to-noise ratio is conducted

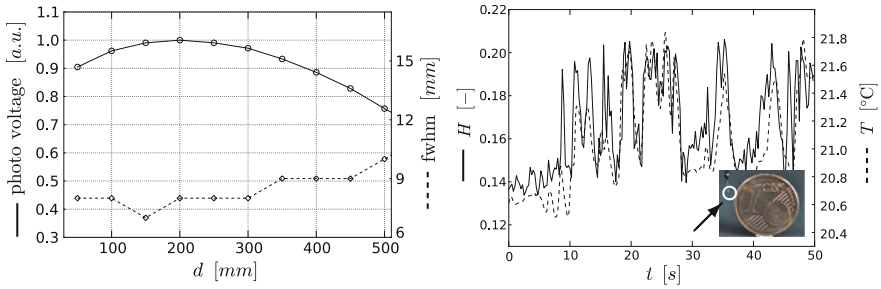


Fig. 15.7 Intensity (photo voltage) and width of the lightsheet (fwhm) as a function of the distance from the front lens (left), time series of hue (TLCs) and temperature (calibration thermistor) (right)

using the saturation and the value component. Therefore, the image is sliced into interrogation windows, in which only those pixel are taken into account, that have the n -highest V values (HSV colourspace). The hue values of these pixel are used to calculate an average hue value for the interrogation window. More details on the image filtering routine can be found in [19]. The hue-temperature calibration is usually performed at constant temperature conditions. However, in our system with continuous air exchange, such uniform and stable conditions for the temperature can not be achieved. Therefore, a dynamic calibration is applied to correlate temperature and hue values. It is based on the simultaneous recording of the temperature using a precisely calibrated, fast-reacting tiny glassbed thermistor and the hue component of the color image in its surrounding, see Fig. 15.7b. A correlation between hue signal and the recorded temperature returns the calibration function. A detailed error propagation allows to estimate an absolute and relative error of 0.19 and 0.06 K, respectively. The latter results in a dynamic range of 20 based on the investigated temperature range.

Dewarping of the b/w and the color image (see e.g., Figure 15.8a), which has to be recorded in backward reflection to improve the color play of the TLCs, as well as the superposition of the two images were conducted using well-known stereo-PIV algorithms. Standard 2C-2D PIV algorithms were used to calculate the velocity field, see Fig. 15.8b, c for details.

Figure 15.9 shows an evaluated temperature and velocity field. It represents the vertical cross section through a hot thermal plume, which was formed in the bottom thermal boundary layer and rises through the sample. Since the plume transports heat from the warm to the cold plate of the convection sample, it is of great scientific and industrial interest to get a deeper understanding of the plume dynamics. The presented figure shows the stem of the plume, where the region of warmest fluid correlates with upward motion. The top part of the plume is defined by its two side swirls. This mushroom-like shape is also name giving for this type of thermal plume. To our best knowledge the results presented in [19], are the first experimental

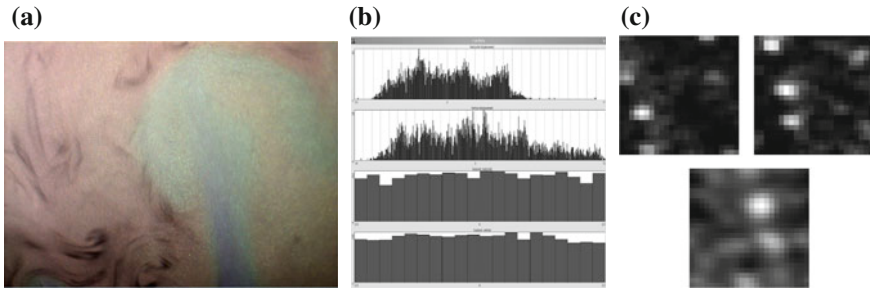


Fig. 15.8 Raw color particle image, blue particles correspond to warm, whereas red ones to cold regions (a), from top to bottom: horizontal and vertical pixel displacement as well as horizontal and vertical sub pixel displacement statistics (b), interrogation windows of frame 1 and 2 as well as correlation plane (bottom) (c) [DC15.2]

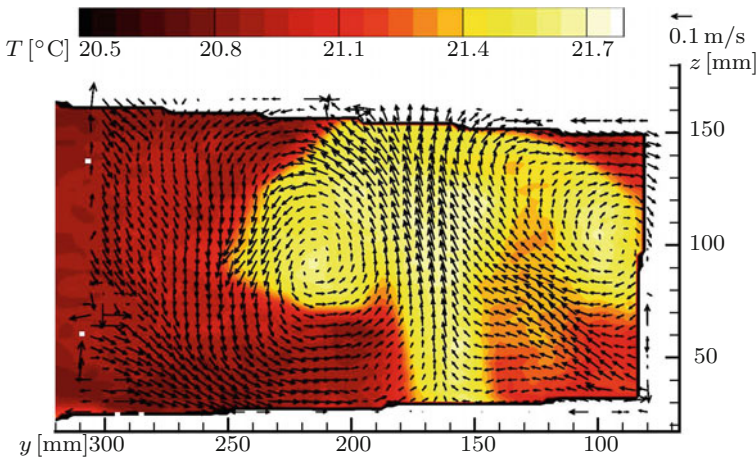


Fig. 15.9 Instantaneous temperature and velocity field, recorded at $Pr = 0.71$, $Ra = 9.0 \times 10^7$ and $Re = 0$, that is, no external pressure gradient was applied (color image and video at [DC15.3]). Every other vector is shown in each direction

measurements representing a thermal plume with such high accuracy in air. A color version of this figure as well as the time evolution, recorded at a frequency of 4 Hz, can be found online. A further application of this measurement technique can be found in [20], wherein the behaviour of line-plumes in a horizontal layer close to the bottom boundary layer of this convection sample was investigated.

As an outlook we want to emphasize recent results of SCHIEPEL et al. [18], who combined PIT using TLCs with tomographic PIV to capture all three velocity components and the temperature in a three dimensional measurement domain.

15.3 PIV for Characterisation of Plasma Actuators

Contributed by:

M. Kotsonis and S. Ghaemi

Dielectric Barrier Discharge (DBD) plasma actuators are receiving continuous attention from the flow control community due to their intrinsic features of robustness, dynamic range and efficiency [2]. The prominent flow control mechanism, enabled through these devices, is the production of a volume distributed body force in the vicinity of the actuator. The experimental measurement of such body force distribution poses considerable theoretical and practical challenges [12]. In this application example, the use of PIV is demonstrated as means to accurately extract the volume distributions of this body force from velocity fields [13].

Time-resolved PIV has been applied to characterise the flow field in the vicinity of the plasma actuator. This technique provides the required spatial and temporal resolution in order to characterise the transient behaviour of the thin wall jet induced by the actuator. A two component PIV configuration has been chosen since the large span of the actuator ensures minimal 3D effects. The two-dimensionality of the flow is also verified by hot-wire measurements.

The plasma actuator is placed flushed on the bottom of a closed Plexiglas box in order to ensure quiescent conditions. A Photron Fastcam SA1 high speed CCD camera of 1024×1024 pixel (full sensor size) is used to image the field-of-view (FOV). The experimental setup is shown in Fig. 15.10.

Image acquisition is performed at 10 KHz rate in single-frame mode. This implies a time separation of $100 \mu\text{s}$ between successive images. A Micro-Nikkor 105 mm objective is set at $f_{\#} = 4$ and is used along with extension tubes in order to achieve a magnification factor $M = 0.8$ and a FOV of $15 \times 6 \text{ mm}^2$. To achieve the high sample rate needed for these measurements, the sensor is cropped to a size of 1024×512 pixel (Table 15.4).

An important issue in PIV techniques for characterisation of plasma actuators is the use of tracer particles [16]. Although under normal conditions these techniques can be considered non-intrusive, the existence of trace particles in areas of strong

Fig. 15.10 Experimental setup

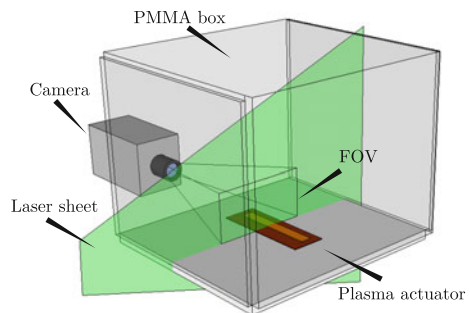


Table 15.4 PIV parameters for plasma actuator characterisation experiments

Flow geometry	Parallel to light sheet
Maximum-in-plane velocity	$U_{\max} \approx 4 \text{ m/s}$
Field-of-view	$15 \times 6 \text{ mm}^2$
Sensor resolution	$1024 \times 512 \text{ pixel}$
Pixel pitch	$20 \text{ }\mu\text{m}$
Magnification factor	0.8
Interrogation window size	$12 \times 12 \text{ pixel}$
Interrogation window overlap	75%
Final vector resolution	13 vectors per mm
Working distance	0.3 m
Recording method	Single frame
Recording rate	10 kHz
Objective focal length	105 mm with extension rings
Aperture	$f_{\#} 8$
Illumination	Nd:YLF, 30 mJ per pulse at 1 kHz, 527 nm
Pulse delay	$100 \text{ }\mu\text{s}$
Seeding material	Olive oil ($\approx 1 \text{ }\mu\text{m}$ diameter)

electric fields and ionisation typical for plasma actuators, should not be neglected. Tracer particles can dissociate, get charged due to the strong electric field. When charged, their movement is no longer governed purely by the flow field but also by the electrical conditions [4]. An additional problem can be accumulation of the tracer droplets on the wall which can influence the electrical properties of the dielectric. Based on these considerations, the air in the Plexiglas box is seeded with olive oil droplets of approximately $1 \text{ }\mu\text{m}$ diameter generated by a TSI atomiser. The olive oil is found to be sufficiently resistive to dielectric breakdown in high electric fields. The particles at the mid span of the actuator are illuminated by a light sheet of 2 mm thickness generated by a Quantronix Darwin-Duo laser system with an average output of 80 W at 3 kHz. The images are analysed using Davis 7.4 (Lavisision GmbH) by cross-correlating successive images. Final interrogation window size of $12 \times 12 \text{ pixel}$ and overlap factor of 75% are used. The interrogation windows are elongated in the flow direction using a 4:1 aspect ratio in order to obtain higher spatial resolution. The velocity vectors are returned on a grid of 13 vectors per mm.

The body force measurement technique determines the spatial distribution of the plasma induced body force from time-resolved velocity field. A snapshot sequence of the measured velocity field in the first moments after the initiation of actuation is shown in Fig. 15.11 indicating the issuing of a starting vortex and the later relaxation of the flow to a wall-tangent jet.

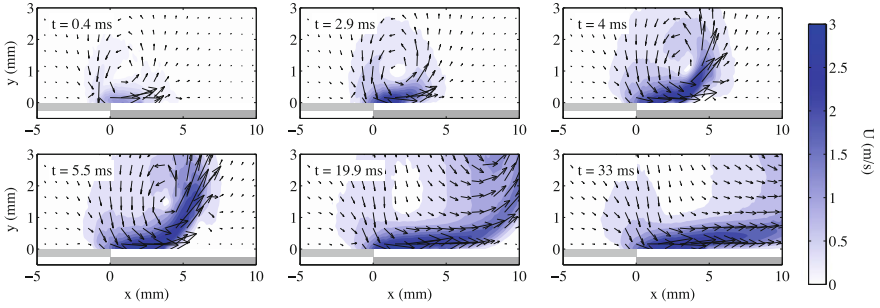


Fig. 15.11 Snapshot sequence of velocity field after initiation of actuation. The displayed time is referenced to the start of actuation. Thick grey lines indicate the position of the DBD electrodes

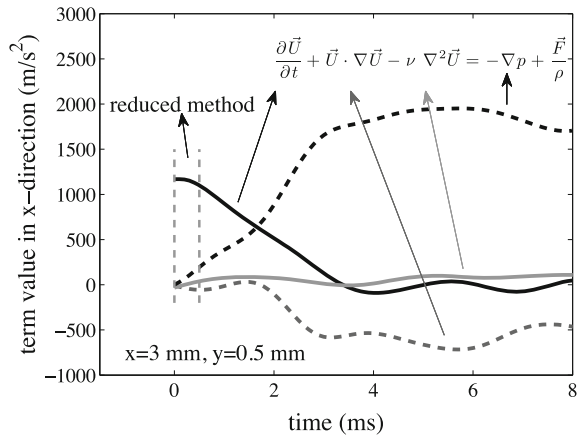
An analysis of the velocity field using the full Navier–Stokes (NS) equations can provide the body force. The 2D incompressible NS equations in the presence of body forces read as:

$$\frac{\partial U}{\partial t} + U \cdot \nabla U - \nu \nabla^2 U = -\frac{\nabla p}{\rho} + \frac{F}{\rho} \tag{15.1}$$

where U is the 2D velocity field, p is the static pressure, ν is the kinematic viscosity of the fluid and ρ is the density.

A first approach in deriving the body force (F) is to apply Eq. (15.1) only for the first moments after the actuation, assuming all other terms can be neglected due to quiescent conditions. This reduces Eq. (15.1) to what basically is Newton’s second law. This method will be referenced as the ‘*reduced method*’. The time interval for the application of the *reduced method* is indicated with dashed lines in Fig. 15.12.

Fig. 15.12 Navier Stokes term decomposition in the vicinity of the actuator ($x = 3 \text{ mm}$, $y = 0.5 \text{ mm}$) based on the *gradient method*. Dashed lines indicate the interval pertinent to the *reduced method*



A second approach involves the use of the full Navier–Stokes equations to derive the force. In this case, it is necessary to calculate all the terms involved. The acceleration, convective and viscous terms are obtained from the available spatio-temporal measurement of the velocity field. In the case of the plasma actuator, the body force and pressure terms appear as unknowns, rendering the problem under-determined. To be able to bypass the problem of one extra unknown, two major assumptions must be made: (1) the body force remains quasi steady over a large number of actuation cycles and (2) the pressure gradient prior to the actuation is zero. These allow the differentiation and back-integration of Eq. (15.1) to the final form of:

$$\int_0^t \left(\frac{\partial^2 U}{\partial t^2} + \frac{\partial(U \cdot \nabla U)}{\partial t} - \nu \frac{\partial(\nabla^2 U)}{\partial t} \right) dt = -\frac{(\nabla p)}{\rho} + A \quad (15.2)$$

In the process of integration a constant A appears which has to be defined. This is set to zero based on the quiescent flow assumption. Equation (15.2) is plugged back into Eq. (15.1) and leaves the body force term as the only unknown. Since the time gradient of the NS is used, this method will be referenced as the ‘*gradient method*’. The term decomposition based on the aforementioned assumptions is shown in Fig. 15.12 for a representative point in the vicinity of the actuator.

In contrast to conventional reaction force techniques (where the actuator is placed on a load-cell), the *reduced* and *gradient* methods have the advantage of providing spatial distribution of body force vectors instead of an integrated thrust value [12]. An example of the measured body force distribution is shown in Fig. 15.13. The results from such analysis can be valuable for validation of numerical models of plasma actuators as well as an input into flow solvers investigating flow control concepts.

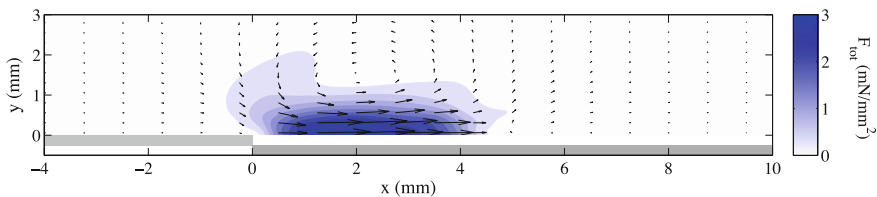


Fig. 15.13 Body force distribution calculated using the *gradient* method

15.4 PIV in Reacting Flows

Contributed by:

C. Willert, M. Schroll

Application of PIV in reacting flows is associated with a number of additional challenges not found in typical aerodynamic applications. Most importantly the seed material must withstand the high temperatures without evaporating or chemically interacting with the flow under investigation. Metal oxide powders such as silica, alumina or titanium oxide are generally well suited for this purpose due to their high melting point and availability. These powders are best introduced into the flow using fluidized bed seeders as described in Sect. 2.2.2.

Another difficulty arises due to flame luminosity which generally increases with higher pressures and higher fuel-air ratios and is mainly caused due to glowing soot. This flame luminosity can be reduced by placing a narrow-bandwidth interference filter tuned to the wavelength of the PIV laser in front of the sensor or collecting lens. Due to the rather long sensor exposure of the second image frame in modern PIV cameras, this filter may however be insufficient in the suppression of the flame luminosity. Here fast acting electro-mechanical or electro-optical shutters [9, 23] are required. Alternatively a pair of CCDs could be used, each synchronized to one of the two PIV laser pulses [25] (Table 15.5).

The pressurized single section combustion chamber, schematically shown in Fig. 15.14, can be operated at up to 20 bar with air preheating of up to 850 K at

Table 15.5 PIV recording parameters for reactive flow in pressurized combustor

Flow geometry	Swirling flow with strong out-of-plane component near nozzle
Maximum in-plane velocity	$U_{\max} \approx 70$ m/s
Field of view	70×40 mm ² ($W \times H$)
Interrogation volume	$1.7 \times 1.7 \times 1.0$ mm ³ ($W \times H \times D$)
Dynamic spatial range	DSR $\approx 40 : 1$
Dynamic velocity range	DVR $\approx 120 : 1$
Observation distance	$z_0 \approx 500$ mm
Recording method	Dual frame/single exposure
Ambiguity removal	Frame separation (frame-straddling)
Recording medium	Full frame interline transfer CCD 1280 \times 1024 pixel (770 illuminated lines)
Recording lens	$f = 55$ mm $f_{\#} = 8$
Magnification	$m = 0.129$ (51.8 μ m/pixel)
Illumination	Freq. doubled Nd:YAG laser 120 mJ/pulse at 532 nm
Pulse delay	$\Delta t = 4$ μ s
Seeding material	Si ₂ O ₃ and Al ₂ O ₃ ($d_p \approx 200 - 800$ nm)

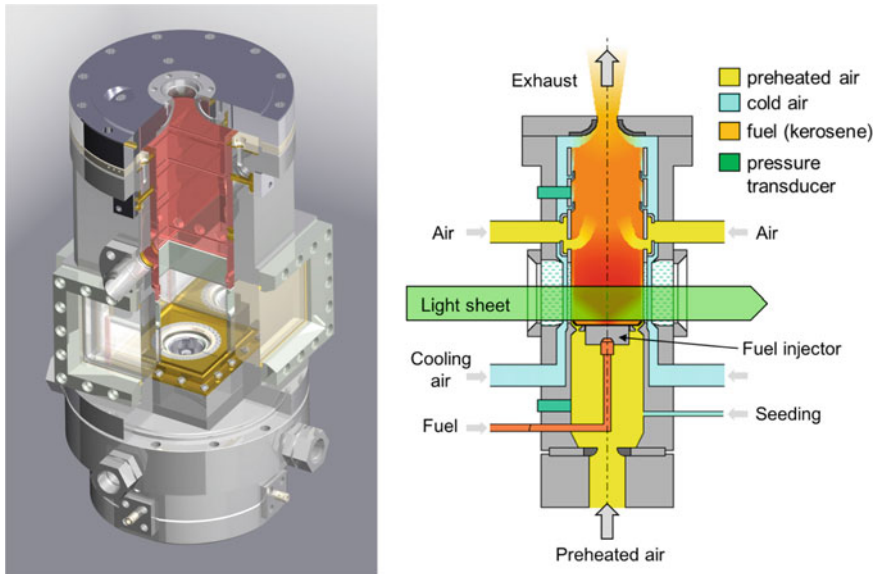


Fig. 15.14 Single sector pressurized combustion facility

mass flow rates of 1.5 kg/s. The nozzle plenum is supplied with preheated primary air downstream of a critical throttle. The primary air is split in a 2:1 ratio and guided into the double swirl nozzle and the inner window cooling slits, respectively. The pressure and mass flow in the chamber is controlled through a sonic orifice at the exit. Jets in cross-flow arrangement at a roughly mid-length position of the 250 mm long combustor provide preheated mixing air and confine the primary zone to a roughly cubic volume.

Optical access is granted from three sides through windows consisting of a thick pressure window and a thin liner window (Fig. 15.14). The gap between the windows is purged with cooling air while the inside of the liner window is film-cooled using a portion of the plenum air. For PIV the light sheet was aligned with the burner axis with the camera arranged in a classical light sheet normal viewing arrangement. By allowing the laser light sheet to pass straight through the combustor the amount of laser flare on imaging windows and walls could be kept at an acceptable level. Seeding consisting of amorphous silicon dioxide particles was introduced to the plenum upstream of the burner through a porous annular tube. As the window film-cooling is supplied directly with seeded air from the plenum, the windows are unfortunately subjected to an accelerated build-up of seeding deposits. Preferably the film-cooling air should have been separated from the main burner air. Fired with kerosene the combustor provided PIV images exhibiting strong Mie scattering off the kerosene spray as well as strong flame luminosity. A corresponding PIV result obtained at lean operating conditions with less kerosene spray is provided in Fig. 15.15. Image enhancement as shown in Fig. 15.16 was applied prior to PIV processing and reduced the influence of droplet velocities on the air flow velocity estimates by equalizing

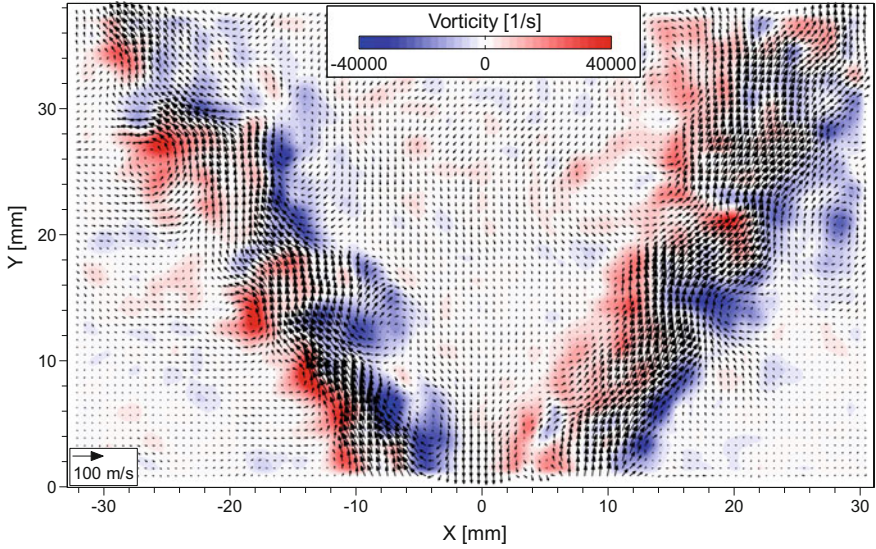


Fig. 15.15 Velocity vector map and vorticity (color-coded) obtained at 3 bar. (A colored version can be found at [DC15.4])

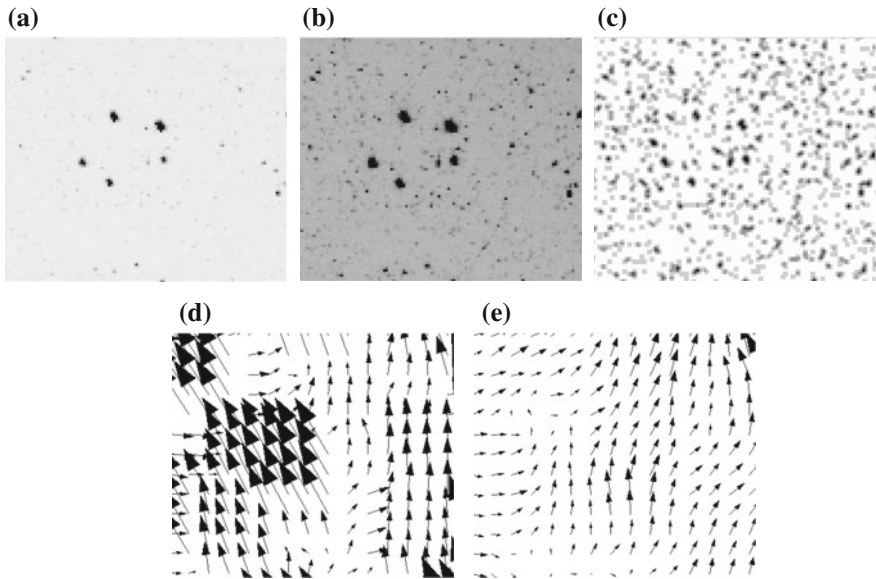


Fig. 15.16 Portion (120×100 pixel) of PIV recordings—inverted for clarity—and processed PIV data: **a** fuel droplets, **b** brightened version of **a** with seeding visible, **c** pre-processed image, **d** flow field after standard PIV analysis, **e** flow field obtained after enhancement of PIV images (from [23])

the droplet image intensities with the much weaker intensity of the seeding particles [23].

PIV in Highly Luminous Flames

Conventional PIV cameras operate in the “double shutter” mode, enabling two immediately consecutive and separately exposed frames. However, the rather long read-out time of about 10–50 ms of the first frame from a double shutter camera (see Sect. 3.1.3) has the undesired side effect that the camera sensor stays sensitive during this period, which inadvertently (over) exposes the second frame in a highly luminous environment, such as the rich primary zone of pressurized combustors. Common solutions to this problem have been the use of narrow band laser line filters and mechanical or electro-optic shutters, but were found to be insufficient in highly luminous flames. The main drawbacks of these shutters is combination of increased light attenuation, limited temporal response or limited lifetime [23].

A viable solution to this problem is a dual sensor setup as shown in Fig. 15.17. Light is collected by a single objective lens and split into two optical paths using a 50/50 non-polarizing, beam splitter cube. With each sensor only active in the sub-microsecond range over the respective, short-duration laser pulse, background light can be sufficiently suppressed to provide reliable PIV data. The common lens of the dual-sensor PIV camera allows refocusing on both sensors simultaneously and is mounted on a micro-traverse for remote operation at the test rig. However, even for a rigid assembly, the position of the sensors with respect to each other is usually not constant through the course of the measurement; even minor shift of a few microns introduced by thermal variations of the camera assembly quickly results in offsets in the pixel range—with correspondingly large bias errors in the data. Therefore, in-situ calibration images are acquired throughout the measurement to capture the time-varying offset. This can for instance be achieved by traversing a mirror into the optical path that directs the field of view onto a reference image containing a fine-grained random dot pattern, similar to that used in background-oriented schlieren (BOS, see Sect. 19.2). While this offset principally can be obtained from an simultaneously exposed particle image pair, the random dot pattern approach is preferred to prevent

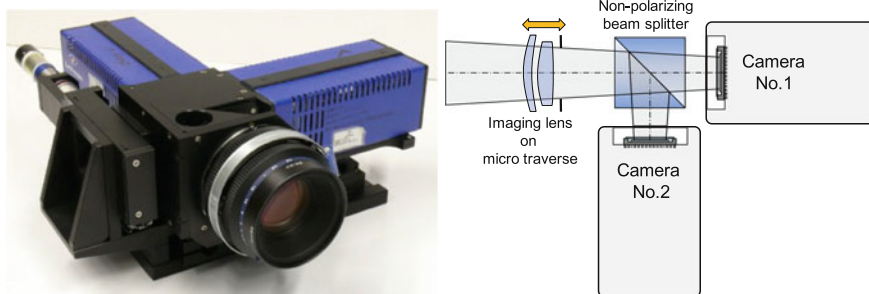


Fig. 15.17 Dual sensor PIV camera system with a common objective lens and remote focusing capability via micro-traverse

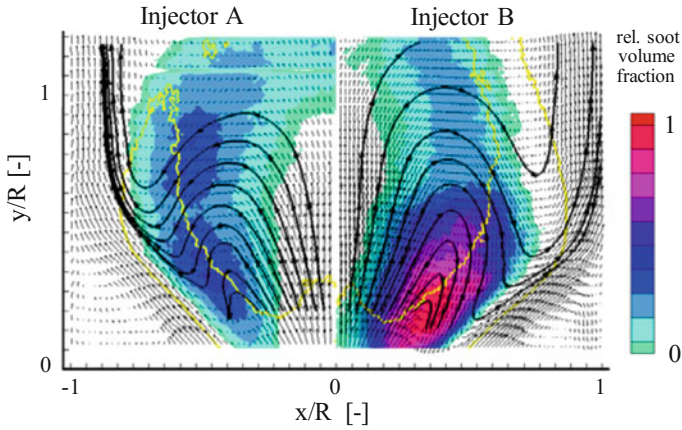


Fig. 15.18 Composite plot of velocity streamlines of the averaged PIV velocity field for two different fuel injectors overlaid with soot concentration (obtained by LII) and heat release by OH-chemiluminescence (yellow contour)

the introduction of pixel-locking effects [15]. The spatially-varying, global sensor offset pattern is then recovered via standard PIV processing and can be accurately described with a low-order polynomial fit, that is then subtracted from the actual particle displacement to yield the actual flow field data.

The acquired velocity information along with data of accompanying spectroscopic methods provides important insights into the convective transport of reactants and their products. An example is provided in Fig. 15.18 showing information on fuel placement, reaction zone and temperature field.

Application of 3C-PIV in Combustion

The application of stereo PIV in facilities of this type is not trivial even if optical access seems sufficient. Aside from the loss of common viewing area caused by the oblique views of two cameras through a common window, further problems are introduced by the reflections of laser flare from the light sheet entering the test section through an orthogonal window. Hence the most desirable arrangement is the ‘classical’ normal view of the light sheet through a window that itself is parallel to it. For stereoscopic viewing the second camera will suffer from the reflection and occlusion effects described before such that reconstructed 3C velocity data will be available in a reduced area.

One solution to the limited access problem of multi-camera PIV imaging is to combine standard 2C-PIV with Doppler global velocimetry (DGV) which has a sensitivity to the out-of-plane component [6, 17]. The so-called DGV-PIV method was applied to recover the velocity field inside the dilution zone of the single sector combustor [22]. Since the dilution zone could only be observed through two windows opposite to each other the light sheet was introduced through the top of the combustion

chamber. Traversal of the entire acquisition system allowed the recovery of time-averaged volume resolved data sets of the dilution zone at pressures of up to 10 bars [22].

In this particular application DGV and PIV were applied in succession due to technical limitations with the lasers used for illumination. Truly simultaneous DGV-PIV measurements were demonstrated for instance on a free jet experiment by WERNET [21].

15.5 Flow Field Measurements Above Wing of High-Lift Aircraft Configuration at High Reynolds Number

Contributed by:

R. Konrath

Of special interest for the optimization of high-lift systems for starting and landing transport aircraft is the flow field above the wing that is directly impacted by the flow around the nacelle/pylon and the edges of retracted slats. To suppress flow separations, streaks are placed on the nacelle to generate vortices possessing a high amount of kinetic energy at high angles of attack. It is crucial to investigate the complex interaction between the streak vortices and the boundary layer of the wing at the correct Reynolds number. Therefore, a half-wing model of a real aircraft was tested in the European Transonic Wind tunnel (ETW) by using stereoscopic PIV. The ETW is beside the National Transonic Facility (NTF) at NASA Langley worldwide the only facility capable of correctly simulating on scaled test models the flight Mach and Reynolds numbers of wide-bodied aircraft. This is achieved by using a test gas of moderately compressed (up to 450 kPa), pure nitrogen at cryogenic temperatures (down to 110 K). The 2.4 m wide and 2 m high test section of the ETW is encapsulated by a large pressure shell and the whole wind tunnel circuit is internally clad with insulation material. To make flow field investigations possible, a cryo PIV system has been developed to address issues related to the specific test conditions, such as the generation of suitable flow tracers for cryogenic flows, with due consideration of the specific requirements for an application in the ETW, as well as the provision of laser light of high pulse energy in the test section and the placement of optical components within a cryogenic environment. Furthermore, optical effects caused by gas density changes within the wind tunnel and light beam deflections or shifts have to be considered. Additionally, the extreme operational costs of such a wind tunnel make it in particular essential that a measurement system operate reliably to avoid costly tunnel access. The cooling down or warming up of the ETW takes several hours and consumes a huge amount of liquid nitrogen and electrical power. A sketch of the employed stereoscopic PIV arrangement is illustrated in Fig. 15.19. There are a number of window openings available in the test section walls. For a placement of the PIV cameras and light-sheet optics the cryo PIV system provides special optical modules consisting of heated housings, because of the cryogenic environment within

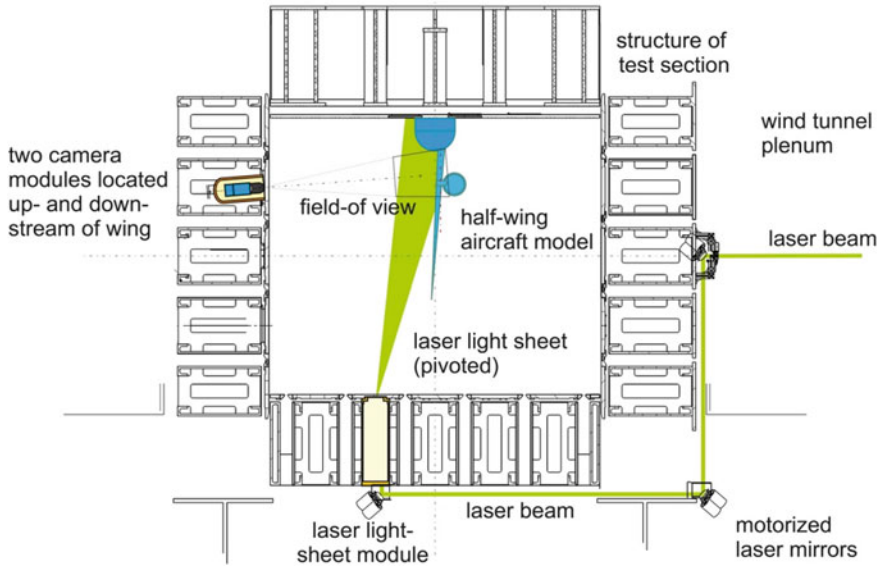


Fig. 15.19 Sketch of stereoscopic PIV arrangement at test section of ETW

the plenum. Since these modules are no longer accessible when the wind tunnel is closed for a cool-down, necessary adjustments as the lens focus or the light sheet position are remotely controllable. Furthermore, to compensate for beam position and direction deviations, a beam monitor is employed in the light sheet module which permits automatic repositioning and redirection of the laser beam using motorized mirrors. Therewith, the beam is kept on the optical axis of the light sheet forming optics while the tunnel temperature or pressure is changing. The light-sheet module also consists of optics to remotely adjust the light-sheet orientation and thickness at the measurement position. The light-sheet is formed through a window in the bottom wall such that the light hits the inboard wing section at a flat angle. Due to the limited size of the test section windows the light-sheet is pivoted to achieve different chordwise measurement positions on the wing resulting in measurement planes that are slightly tilted with respect to the cross-plane of the free stream flow. The two PIV cameras are placed behind windows in the top row of the side wall facing the suction side of the wing. The positions are chosen such that the viewing angles are close to $\pm 45^\circ$ with respect to the light-sheet. The Scheimpflug angle and axis can be quickly re-aligned using fixed servo motor settings for each light sheet position.

To avoid a damage of the internal wind tunnel insulation material, conventional PIV seeding substances cannot be used. Therefore, tiny ice crystals are generated inside the cryogenic environment with the great advantage that the water evaporates completely during a warm-up of the wind-tunnel without leaving residuals. For this

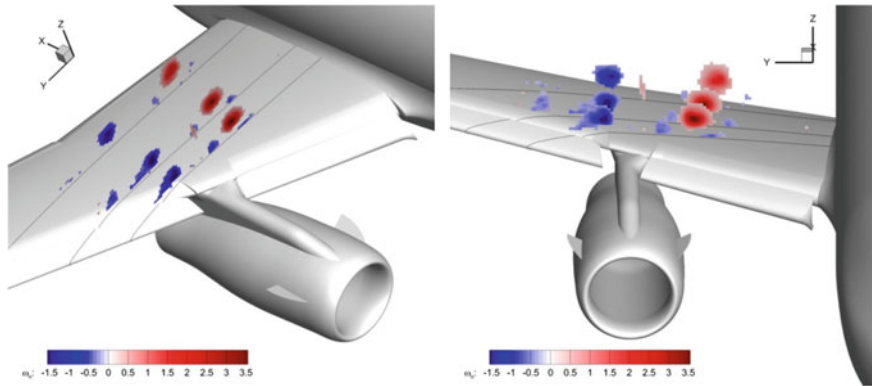


Fig. 15.20 Vorticity distributions above wing at three chord stations calculated from the measured velocity field data for $M = 0.186$, $Re = 13.3$ million and an incidence of $\alpha = 16.5^\circ$. The black lines indicate the positions of the measurement planes on the wing

purpose a very small amount of water aerosol is injected at the center line of the second throat down-stream the test section. The PIV images are evaluated using a multi-grid cross-correlation algorithm with image deformation using a final interrogation spot size of 48×48 pixel that corresponds to a spatial resolution of about 5 mm. In Fig. 15.20 the vorticity distributions are shown inside three different measurement positions above the wing which are calculated from time averaged velocity fields using 800 samples. The Mach and Reynolds number represent the design point for this landing configuration.

Different vortices can be detected above the wing and following their tracks in a streamwise direction the vortices are moving slightly inwards. Two larger counter-rotating vortices of approximately the same size and strength dominate the flow field and originate from the in- and outboard streak on the nacelle. The inboard located vortex rotates in a counter-clockwise sense and shows at all measured chord stations a circular shape. The dominant outboard vortex initially evolves close to the wing surface indicating a strong interaction with the wing flow. Smaller vortices can be tracked as well, such as a clockwise rotating vortex that occurs downstream the inner edge of the inboard slat and a secondary vortex that is probably produced by the dominant inner vortex. The velocity data can be used to evaluate the effectiveness of the streaks in regard to the suppression of flow separations on the wing for the correct Reynolds number. Further details of the recording and analysis of the velocity data are given in [10, 11] (Table 15.6).

Table 15.6 PIV parameters for measurements at cryogenic conditions on high-lift aircraft model

Flow condition	$M = 0.186$, $Re = 13.3$ million, $T_0 = 130$ K, $p_0 = 340$ kPa
Maximum in-plane velocity	ca. 20 m/s
Interrogation volume	$250 \times 400 \times 180$ mm ³ (H \times W \times D)
Dynamic spatial range	DSR $\approx 80 : 1$
Dynamic velocity range	DVR $\approx 30 : 1$
Observation distance	1.6 m and 1.9 m
Recording method	Multi frame, single exposure
Recording medium	PCO.edge, 2560×2160 pixel
Recording lens	$f = 50$ and 60 mm, $f_{\#} = 2.8$
Illumination	Nd:YAG laser*, 450 mJ/pulse @ 15 Hz
Pulse delay	$\Delta t = 22$ μ s
Seeding material	Ice crystals

*Frequency doubled

References

1. Abram, C., Fond, B., Beyrau, F.: High-precision flow temperature imaging using ZnO thermographic phosphor tracer particles. *Opt. Express* **23**(15), 19453–19468 (2015). DOI 10.1364/OE.23.019453. URL <http://www.opticsexpress.org/abstract.cfm?URI=oe-23-15-19453>
2. Benard, N., Moreau, E.: Electrical and mechanical characteristics of surface AC dielectric barrier discharge plasma actuators applied to airflow control. *Exp. Fluids* **55**(11), 1846 (2014). DOI 10.1007/s00348-014-1846-x. URL <https://doi.org/10.1007/s00348-014-1846-x>
3. Böhm, C., Wulf, P., Egbers, C., Rath, H.J.: LDV- and PIV-measurements on the dynamics in spherical Couette flow. In: *International Conference on Laser Anemometry - Advances and Applications*, Karlsruhe, (Germany) (1997)
4. Boucinha, V., Magnier, P., Weber, R., Leroy-Chesneau, A., Dong, B., Hong, D., Jousset, R.: Characterization of the ionic wind induced by a sine DBD actuator used for laminar-to-turbulent transition delay. In: *4th Flow Control Conference Seattle, Washington*, vol. AIAA 2008-4210 (2008). DOI 10.2514/6.2008-4210. URL <https://doi.org/10.2514/6.2008-4210>
5. Dabiri, D.: Digital particle image thermometry/velocimetry: a review. *Exp. Fluids* **46**(2), 191–241 (2009). DOI 10.1007/s00348-008-0590-5. URL <https://doi.org/10.1007/s00348-008-0590-5>
6. Elliott, G.S., Beutner, T.J.: Molecular filter based planar Doppler velocimetry. *Prog. Aerosp. Sci.* **35**(8), 799–845 (1999). DOI 10.1016/S0376-0421(99)00008-1. URL [https://doi.org/10.1016/S0376-0421\(99\)00008-1](https://doi.org/10.1016/S0376-0421(99)00008-1)
7. Garg, V.K.: Natural convection between concentric spheres. *Int. J. Heat Mass Transf.* **35**(8), 1935–1945 (1992). DOI 10.1016/0017-9310(92)90196-Y. URL <https://www.sciencedirect.com/science/article/pii/001793109290196Y>
8. Hiller, W., Kowalewski, T.: Simultaneous measurement of temperature and velocity fields in thermal convective flows. In: *4th International Symposium on Flow Visualization*. Paris, France (1986)

9. Honoré, D., Maurel, S., Quinqueneau: Particle image velocimetry in a semi-industrial 1 MW boiler. In: 4th International Symposium on Particle Image Velocimetry, Göttingen (Germany) (2001)
10. Konrath, R.: Tracking the nacelle vortex above aircraft wing in the ETW at real Mach-and Reynolds numbers by means of PIV. In: 53rd AIAA Aerospace Sciences Meeting, p. 1560 (2015). DOI 10.2514/6.2015-1560. URL <https://doi.org/10.2514/6.2015-1560>
11. Konrath, R., Geisler, R., Otter, D., Philipp, F., Ehlers, H., Agocs, J., Quest, J.: High-speed PIV applied to the wake of the NASA CRM model in ETW at high Re-number stall conditions for sub- and transonic speeds. In: 53rd AIAA Aerospace Sciences Meeting, p. 1095 (2015). DOI 10.2514/6.2015-1095. URL <https://doi.org/10.2514/6.2015-1095>
12. Kotsonis, M.: Diagnostics for characterisation of plasma actuators. *Meas. Sci. Technol.* **26**(9), 092,001 (2015). DOI 10.1088/0957-0233/26/9/092001. URL <http://stacks.iop.org/0957-0233/26/i=9/a=092001>
13. Kotsonis, M., Ghaemi, S., Veldhuis, L., Scarano, F.: Measurement of the body force field of plasma actuators. *J. Phys. D: Appl. Phys.* **44**(4), 045,204 (2011). DOI 10.1088/0022-3727/44/4/045204. URL <http://stacks.iop.org/0022-3727/44/i=4/a=045204>
14. Mack, L.R., Hardee, H.C.: Natural convection between concentric spheres at low Rayleigh numbers. *Int. J. Heat Mass Transf.* **11**(3), 387–396 (1968). DOI 10.1016/0017-9310(68)90083-5. URL <http://www.sciencedirect.com/science/article/pii/S0017931068900835>
15. Meier, U., Freitag, S., Heinze, J., Lange, L., Magens, E., Schroll, M., Willert, C., Hassa, C., Bagchi, I.K., Lazik, W., Whiteman, M.: Characterisation of lean burn module air blast pilot injector with laser techniques. In: ASME Turbo Expo: Power for Land, Sea, and Air, Volume 1A: Combustion, Fuels and Emissions (2013). DOI 10.1115/GT2013-94796. URL <https://doi.org/10.1115/GT2013-94796>
16. Melling, A.: Tracer particles and seeding for particle image velocimetry. *Meas. Sci. Technol.* **8**(12), 1406 (1997). DOI 10.1088/0957-0233/8/12/005. URL <https://stacks.iop.org/0957-0233/8/i=12/a=005>
17. Roehle, I.: Three-dimensional Doppler global velocimetry in the flow of a fuel spray nozzle and in the wake region of a car. *Flow Meas. Instrumen.* **7**(3–4), 287–294 (1996). DOI 10.1016/S0955-5986(97)00011-3. URL [https://doi.org/10.1016/S0955-5986\(97\)00011-3](https://doi.org/10.1016/S0955-5986(97)00011-3)
18. Schiepel, D., Schmeling, D., Wagner, C.: Simultaneous velocity and temperature measurements in turbulent Rayleigh-Bénard convection based on combined tomo-PIV and PIT. In: 18th International Symposium on Applications of Laser Techniques to Fluid Mechanics Lisbon, Portugal, 04-07 July (2016). URL http://ltces.dem.ist.utl.pt/lxaser/lxaser2016/finalworks2016/papers/01_9_5_368paper.pdf
19. Schmeling, D., Bosbach, J., Wagner, C.: Simultaneous measurement of temperature and velocity yields in convective air flows. *Measurement Science and Technology* **25**(3), 035,302 (2014). DOI 10.1088/0957-0233/25/3/035302. URL <http://stacks.iop.org/0957-0233/25/i=3/a=035302>
20. Schmeling, D., Bosbach, J., Wagner, C.: Measurements of the dynamics of thermal plumes in turbulent mixed convection based on combined PIT and PIV. *Exp. Fluids* **56**(6), 134 (2015). DOI 10.1007/s00348-015-1981-z. URL <https://doi.org/10.1007/s00348-015-1981-z>
21. Wernet, M.P.: Planar particle imaging Doppler velocimetry: a hybrid PIV/DGV technique for three-component velocity measurements. *Meas. Sci. Technol.* **15**(10), 2011 (2004). DOI 10.1088/0957-0233/15/10/011. URL <https://stacks.iop.org/0957-0233/15/i=10/a=011>
22. Willert, C.E., Hassa, C., Stockhausen, G., Jarius, M., Voges, M., Klinner, J.: Combined PIV and DGV applied to a pressurized gas turbine combustion facility. *Meas. Sci. Technol.* **17**(7), 1670 (2006). DOI 10.1088/0957-0233/17/7/005. URL <https://stacks.iop.org/0957-0233/17/i=7/a=005>
23. Willert, C.E., Jarius, M.: Planar flow field measurements in atmospheric and pressurized combustion chambers. *Exp. Fluids* **33**(6), 931–939 (2002). DOI 10.1007/s00348-002-0515-7. URL <https://doi.org/10.1007/s00348-002-0515-7>

24. Willert, C.E., Raffel, M., Stasicki, B., Kompenhans, J.: High-speed digital video camera systems and related software for application of PIV in wind tunnel flows. In: 8th International Symposium on Laser Techniques to Fluid Mechanics, Lisbon, Portugal, 8–11 July (1996)
25. Willert, C.E., Stasicki, B., Raffel, M., Kompenhans, J.: Digital video camera for application of particle image velocimetry in high-speed flows. In: Cha, S.S., Trolinger, J.D. (eds.) *Optical Techniques in Fluid, Thermal, and Combustion Flow*, San Diego, CA, United States, vol. 2546, pp. 124–134 (1995). DOI 10.1117/12.221515. URL <https://doi.org/10.1117/12.221515>

Chapter 16

Applications: Micro PIV

This section discusses various applications and techniques used in μ PIV. The applications include very high spatial resolution measurements of pressure-driven flow in a rectangular capillary and measurements in a challenging toroidal vortex. Then several techniques necessitated by the challenges of working in a microscopic domain are discussed. These include Stereo and Confocal Imaging for MicroPIV, Proper Orthogonal Reconstruction (3D data), and Hybrid experimental-numerical technique for 3D Reconstruction.

16.1 Flow in a Microchannel

Contributed by:

S.T. Wereley and C.D. Meinhart

No flow is more fundamental than the pressure driven flow in a straight channel of constant cross section. Since analytical solutions are known for most such flows, they prove invaluable for gauging the accuracy of μ PIV (Table 16.1).

16.1.1 Analytical Solution to Channel Flow

Although the solution to flow through a round capillary is the well-known parabolic profile, the analytical solution to flow through a capillary of a rectangular cross section is less well known. Since one of the goals of this section is to illustrate the accuracy of μ PIV by comparing to a known solution, it is useful here to briefly

An overview of the Digital Content to applications on micro PIV can be found at [DC16.1].

Table 16.1 PIV recording parameters for Poiseuille flow through microchannels

Flow geometry	Rectangular cross-section microchannel pressure-driven flow
Maximum velocity	10 mm/s
Field of view	$120\ \mu\text{m} \times 90\ \mu\text{m}$
Interrogation volume	$13.6\ \mu\text{m} \times 0.9\ \mu\text{m} \times 1.8\ \mu\text{m}$
Observation distance	$130\ \mu\text{m}$
Recording method	Multiframe/single exposure
Recording medium	Interline transfer CCD camera
Recording lens	Microscope objective ($60\times$, $NA = 1.4$)
Illumination	Nd:YAG laser
Time interval between images	$< 10\ \mu\text{s}$
Seeding material	Fluorescently dyed polystyrene spheres ($d_p = 200\ \text{nm}$)

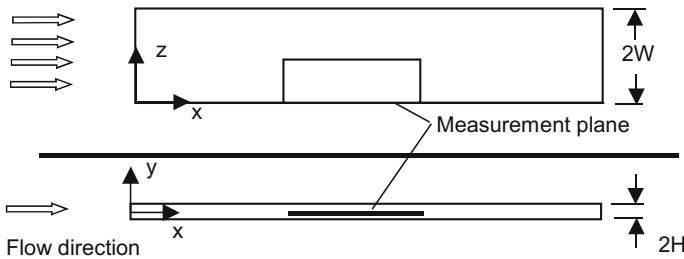


Fig. 16.1 Geometry of the microchannel. The microchannel is $2H$ high and $2W$ wide, and is assumed infinitely long in the axial direction. The measurement plane of interest is orientated in the $X - Z$ plane and includes the microchannel wall at $Z = 0$. The centerline of the channel is at $Y = 0$. The microscope objective images the test section from below, in the lower part of the figure (after [43])

discuss the analytical solution. The velocity field of flow through a rectangular duct can be calculated by solving the Stokes equation (the low Reynolds number version of the Navier–Stokes equation), with no-slip velocity boundary conditions at the wall [17] using a Fourier Series approach. Figure 16.1 shows a rectangular channel in which the width W is much greater than the height H . Sufficiently far from the wall (i.e., $Z \gg H$) the analytical solution in the Y direction (for constant Z), converges to the well-known parabolic profile for flow between infinite parallel plates. In the Z direction (for constant Y), however, the flow profile is unusual in that it has a very steep velocity gradient near the wall ($Z < H$) which reaches a constant value away from the wall ($Z \gg H$).

16.1.2 Experimental Measurements

A $30 \times 300 \mu\text{m}$ cross-section glass rectangular microchannel, fabricated by Wilmad Industries, was mounted flush to a $170 \mu\text{m}$ thick glass coverslip and a microscope slide. By carefully rotating the glass coverslip and the CCD camera, the channel was oriented to the optical plane of the microscope within 0.2° in all three angles. The orientation was confirmed optically by focusing the CCD camera on the microchannel walls. The microchannel was horizontally positioned using a high-precision $X - Y$ stage, and verified optically to within $\sim 400 \text{ nm}$ using epi-fluorescent imaging and image enhancement. The experimental arrangement is sketched in Fig. 16.1.

The flow in the glass microchannel was imaged through an inverted epi-fluorescent microscope and a Nikon Plan Apochromat oil-immersion objective lens with a magnification $M = 60$ and a numerical aperture $NA = 1.4$. The object plane was placed at approximately $7.5 \pm 1 \text{ mm}$ from the bottom of the $30 \mu\text{m}$ thick microchannel. The Plan Apochromat lens was chosen for the experiment because it is a high quality microscope objective designed with low curvature of field, low distortion, and is corrected for spherical and chromatic aberrations.

Since deionized water (refractive index $n_w = 1.33$) was used as the working fluid but the lens immersion fluid was oil (refractive index $n_i = 1.515$), the effective numerical aperture of the objective lens was limited to $NA \approx n_w/n_i = 1.23$ [24].

A filtered continuous white light source was used to align the test section with the CCD camera and to test for proper particle concentration. During the experiment, the continuous light source was replaced by the pulsed Nd:YAG laser. A Harvard Apparatus syringe pump was used to produce a 200 ml/h flow through the microchannel.

The particle-image fields were analyzed using a custom-written PIV interrogation program developed specifically for microfluidic applications. The program uses an ensemble-averaging correlation technique to estimate velocity vectors at a single measurement point by (1) cross-correlating particle-image fields from 20 instantaneous realizations, (2) ensemble averaging the cross-correlation functions, and (3) determining the peak of the ensemble-averaged correlation function. The signal-to-noise ratio is significantly increased by ensemble averaging the correlation function before peak detection, as opposed to either ensemble averaging the velocity vectors after peak detection, or ensemble averaging the particle-image field before correlation. This process is described in detail in Sect. 5.3.2.4. For the current experiment, 20 realizations were chosen because that was more than a sufficient number of realizations to give an excellent signal, even with a first interrogation window of only $120 \times 8 \text{ pixel}$.

The signal-to-noise ratio resulting from the ensemble-average correlation technique was high enough that there were no spurious velocity measurements. Consequently, no vector validation postprocessing was performed on the data after interrogation. The velocity field was smoothed using a 3×3 Gaussian kernel with a standard deviation of one grid spacing in both directions.

Figure 16.2 shows an ensemble-averaged velocity-vector field of the microchannel. The interrogation windows were chosen to be longer in the streamwise direction than in the wall-normal direction. This allowed for a sufficient number of particle

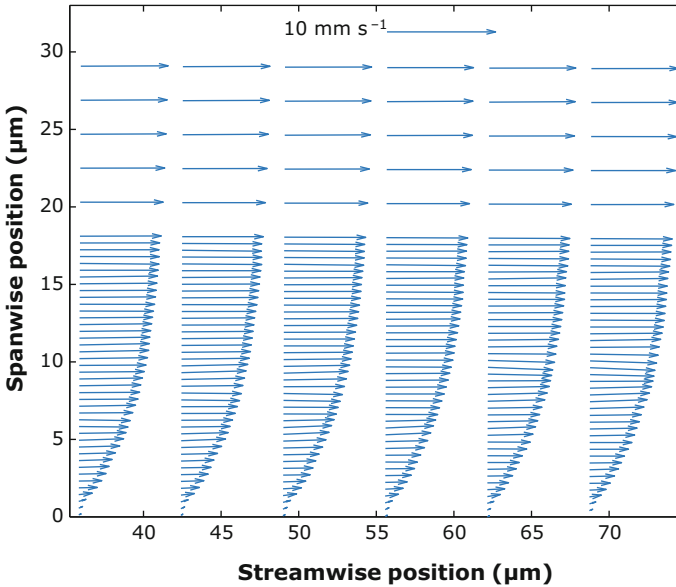


Fig. 16.2 Ensemble-averaged velocity-vector field measured in a $30\ \mu\text{m} \times 300\ \mu\text{m}$ cross-section channel. The in-plane spatial resolution, defined by the interrogation spot size of the first interrogation window, is $13.6\ \mu\text{m} \times 0.9\ \mu\text{m}$ (after [43])

images to be captured in an interrogation spot, while providing the maximum possible spatial resolution in the wall-normal direction. The spatial resolution, defined here by the size of the first interrogation window, was 120×8 pixel near the wall. This corresponds to an in-plane spatial resolution of $13.6\ \mu\text{m} \times 0.9\ \mu\text{m}$. The interrogation spots were overlapped by 50% to extract the maximum possible amount of information for the chosen interrogation region size according to the Nyquist sampling criterion. Consequently, the velocity vector spacing in the wall-normal direction was 450 nm. The streamwise velocity profile was estimated by line-averaging the measured velocity data in the streamwise direction. Figure 16.3 compares the streamwise velocity profile estimated from the PIV measurements (shown as symbols) to the analytical solution for laminar flow of a Newtonian fluid in a rectangular channel (shown as a solid curve). The agreement is within 2% of full-scale resolution. Hence, the accuracy of μPIV is at worst 2% of full-scale for these experimental conditions. The bulk flow rate of the analytical curve was determined by matching the free-stream velocity data away from the wall. The wall position of the analytical curve was determined by extrapolating the velocity profile to zero near the wall.

Since the microchannel flow was fully developed, the wall-normal component of the velocity vectors is expected to be close to zero. The average angle of inclination of the velocity field was found to be small, 0.0046 rad, suggesting that the test section was slightly rotated in the plane of the CCD array relative to a row of pixel on the array. This rotation was corrected mathematically by rotating the coordinate system of the velocity field by 0.0046 rad. The position of the wall can be determined to

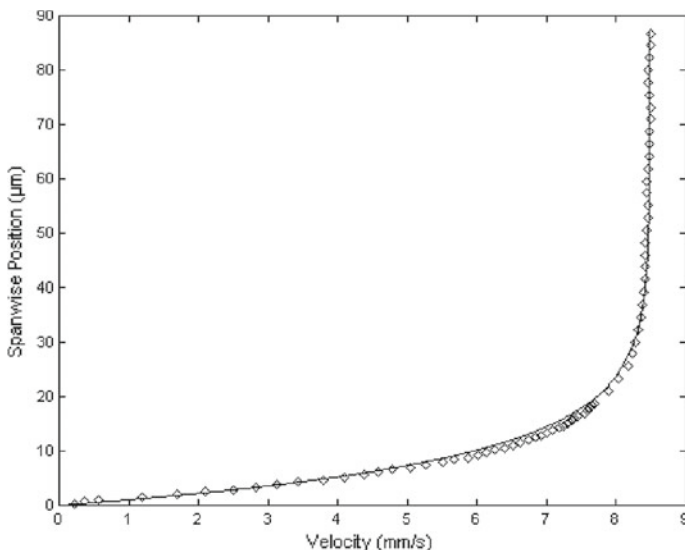


Fig. 16.3 Velocity profile measured in a nominally $30\ \mu\text{m} \times 300\ \mu\text{m}$ channel. The symbols represent the experimental PIV data while the solid curve represents the analytical solution (after [43])

within about 400 nm by direct observation of the image because of diffraction as well as the blurring of the out-of-focus parts of the wall. The precise location of the wall was more accurately determined by applying the no-slip boundary condition, which is expected to hold at these length scales for the combination of water flowing through glass, and extrapolating the velocity profile to zero at 16 different streamwise positions (Fig. 16.2). The location of the wall at every streamwise position agreed to within 8 nm of each other, suggesting that the wall is extremely flat, the optical system has little distortion, and the PIV measurements are very accurate.

Most PIV experiments have difficulty measuring velocity vectors very close to the wall. In many situations, hydrodynamic interactions between the particles and the wall prevent the particles from traveling close to the wall, or background reflections from the wall overshadow particle images. By using 200 nm diameter particles and epi-fluorescence to remove background reflections, we have been able to make accurate velocity measurements to within about 450 nm of the wall; see Fig. 16.2.

16.2 Flow in an Electrothermal Micro-Vortex

Contributed by:

S.T. Wereley and C.D. Meinhart

Electrothermal (ET) flow is the electrokinetic motion of a fluid, generated by the simultaneous application of an AC electric field and a heat source to a body of

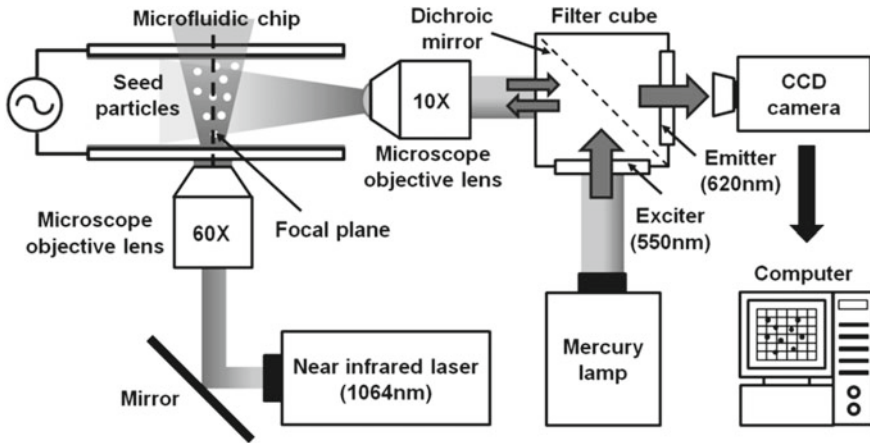


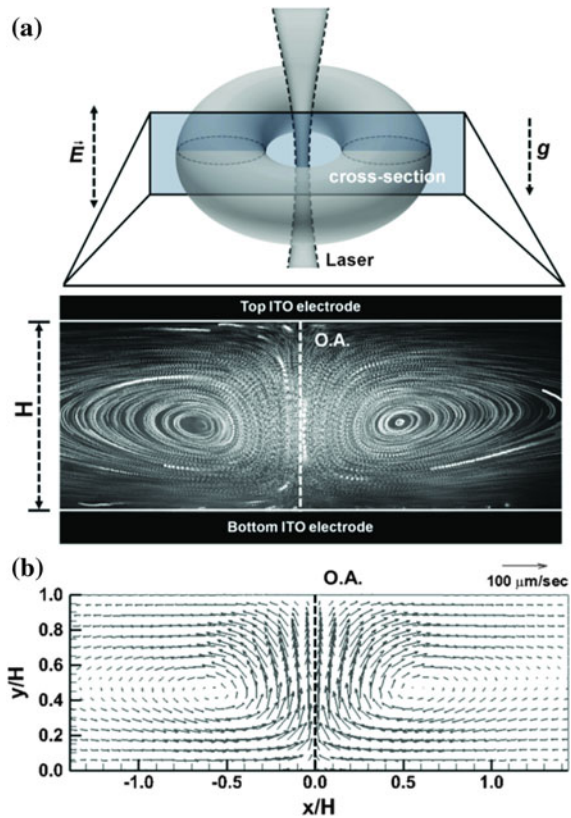
Fig. 16.4 Electrothermal flow PIV experimental apparatus featuring two orthogonal microscopes. One objective is oriented vertically for creating the temperature gradient while the second is oriented horizontally for imaging the ET flow (after [35])

fluid [46, 55]. The temperature gradient in a non-uniformly heated fluid results in a spatially varying electrical conductivity and permittivity within the fluid. These conductivity and permittivity variations interact with the applied electric field to produce an electrical body force that drives an ET flow. ET flows have many attractive properties. They can control and manipulate extremely small particles or volumes of fluid precisely and without damaging them. They are dynamic and can be switched on and off rapidly. The location, speed and spatial distribution of the flows produced can be tailored at run time rather than when the chip is manufactured as with DEP and related phenomena. ET flows have been applied widely to many research fields ranging from colloidal science to biotechnology.

KWON & WERELEY [35] carried out a set of PIV measurement experiments on ET flows to quantify their behavior. They used a microfluidic chip consisting of two indium tin oxide (ITO) parallel-plate electrodes Fig. 16.4. A light-actuated ET flow is driven by the simultaneous application of an AC electric field (10 to 60 V_{pp} and 9 kHz to 1 MHz) and laser illumination (30 to 200 mW) in deionized (DI) water in the chip. The resulting flows were directly observed and imaged from the side of the microfluidic chip, and the acquired images were analyzed by PIV. Because the non-uniform heating is provided by a laser that was concentrated by a microscope objective lens, the experimental setup requires two orthogonal microscopes.

The ET flows are directly observed and imaged from the side of the microfluidic chip through a boom-stand microscope system (Nikon) where a 10 \times objective lens (Nikon) and a digital charge-coupled device (CCD) camera (PCO Imaging Co.) are installed. For the flow visualization and PIV imaging, 3 μm red fluorescent particles (Duke Scientific) are suspended in the DI water after being washed by centrifugation at 2500 rpm for 5 min. Their excitation ($\lambda_{ex} = 550 \text{ nm}$) and emission ($\lambda_{em} = 620 \text{ nm}$)

Fig. 16.5 A schematic drawing of the ET flow is shown in **a** along with 200 superposed images which shows the streamlines of the toroidal flow while in **b** shows the PIV calculated velocity field (after [35])



are implemented using an epi-fluorescent filter cube (Nikon, USA) and a mercury-arc lamp (Lumen Dynamics Group Inc.). 200 pairs of images were acquired for most experimental conditions for the PIV analysis. The PIV analysis was performed with EDPIV [19]. The PIV evaluation used 64×64 pixel interrogation windows and a central difference image correction (CDIC) method [68] and a correlation averaging technique [43, 44] to increase signal strength in the steady-state flow.

Figure 16.4 shows the experimental configuration for flow visualization and PIV measurement of the light-actuated ET fluid motion. One novelty of these measurements with respect to other μ PIV measurements is that the imaging microscope was positioned laterally to the side of the chip rather than above or below the chip as with a conventional configuration. Consequently, the focal plane of the imaging microscope could be aligned with the optical axis (OA) of the illuminating microscope which is coincident with the line of axisymmetry of the toroidal vortex. The experimental configuration is shown in Fig. 16.5a. When the laser of 140 mW power was focused on the bottom electrode biased with $20 V_{pp}$ at 9 kHz, the fluid streamlines of the generated ET flow formed a pair of vortex rings symmetric with respect to the OA. This vortex shape occurs because of the spatial distribution of an electrical

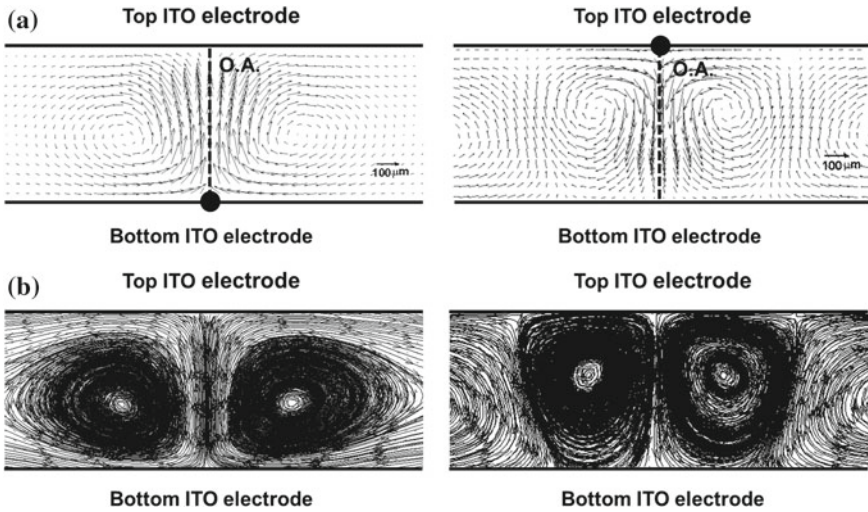


Fig. 16.6 Two electrothermal vortices showing the difference between heating the bottom electrode (a) and the top electrode (b). The location of laser heating is indicated by the large black circles in the top vector fields. The top row are the vector plots for both cases while the bottom row shows streamlines. Note that the vortices have opposite senses [35]

body force produced by the coupling of the uniform AC electric field and the non-uniform temperature field in DI water caused by the laser illumination. The focused laser creates the axisymmetric gradients of electrical conductivity and permittivity in the fluid through electrode heating. These interact with the external electrical field to produce the ET body forces. The ET body forces generate the ET vortex shown schematically in Fig. 16.5a. Figure 16.5b is an overlapping of all 200 images to show the streamlines of the ET vortex. Figure 16.5c shows a typical PIV measured velocity field of the ET vortex. The flow is axisymmetric with respect to the illuminating laser ($X/H = 0$). The flow speeds on the line connecting the two vortex centers also follow a bell curve, having a maximum value ($\sim 95 \mu\text{m/s}$) at the OA. These PIV results support the visualized toroidal flow structure quantitatively. More details about the 3D vortex topology could be gained by using the Astigmatic PTV technique, see: [34].

These experiments are performed on earth so naturally gravity is another body force that is present. The flow direction along the OA is identical to that which would be expected of natural convection induced by the heated bottom electrode. In order to discern the relative effects of buoyancy-induced natural convection and electrothermal forces, [35] experimentally investigated the ET flow created when holding all other conditions constant but varying the location of the focused laser. The applied AC electric signal and laser intensity were $30 V_{\text{pp}}$ at 20 kHz and 140 mW, respectively. The PIV measurements are shown in Fig. 16.6. When the focused laser illuminated the bottom electrode (Fig. 16.6a), the ET flow was driven inward parallel to the bottom electrode toward the OA and then upward, similar to Fig. 16.6b. When

the laser was focused on the top electrode (Fig. 16.6b), the ET flow was driven inward parallel to the top electrode and then downward at the OA. Hence the ET vortex had the opposite sense when the top electrode was illuminated. These two vortical flows have maximum velocities of $\sim 250 \mu\text{m/s}$ and $\sim 220 \mu\text{m/s}$ on the OA, respectively. The slight difference occurred because the natural convection when the bottom electrode is illuminated *reinforces* the ET flow in Fig. 16.6a but *retards* it when the top electrode is illuminated in Fig. 16.6b.

16.3 Proper Orthogonal Reconstruction of 3D Micro PIV Data

Contributed by:

S.T. Wereley and C.D. Meinhart

One common approach for reconstructing 3D velocity data from 2D planar PIV datasets is by integrating the continuity equation in the out of plane direction [69]. Here, u and v are the two in-plane components of the velocity field, which is measured on a series of parallel planes with multiple z -locations. This is especially simple for incompressible flows for which the continuity equation takes the form

$$\frac{\partial w}{\partial z} = -\frac{\partial u}{\partial x} - \frac{\partial v}{\partial y}. \quad (16.1)$$

Integrating it from some known location to some other location in the z -direction reveals the out-of-plane velocity component using the equation

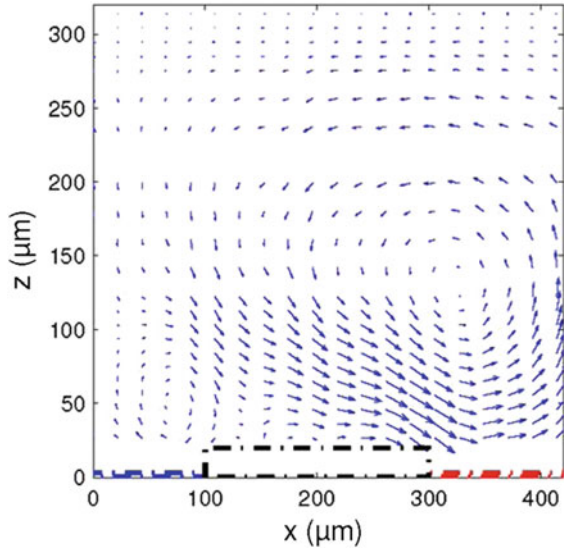
$$w(x, y, z, t) = -\int \left(\frac{\partial u}{\partial x} + \frac{\partial v}{\partial y} \right) dz + C(x, y, t). \quad (16.2)$$

Reference [29] introduced the concept for proper orthogonal reconstruction. The basic idea is to decompose the velocity field into orthogonal basis function that capture the important energy containing modes. Importantly, the decomposition can be cast to impose separation of variables, such that the basis functions $\phi_{u,k}(x, y)$ are purely a function of the in-plane coordinates x, y , while the coefficients $a_{u,k}(x, y)$ are purely a function of the out-of-plane coordinate z , such that

$$u(x, y, z) = \sum_{k=1}^n a_{u,k}(z) \phi_{u,k}(x, y). \quad (16.3)$$

This approach is quite computationally efficient as typically only about 5 modes are required to capture 99% of the energy. Separation of variables provides a convenient means for differentiation and integration.

Fig. 16.7 Proper orthogonal reconstructed velocity field [29]



$$\begin{aligned}
 w(x, y, z) = & - \sum_{k=1}^n \left[\frac{\partial \phi_{u,k}(x, y)}{\partial x} \right] \int a_{u,k}(z) dz \\
 & + \sum_{k=1}^n \left[\frac{\partial \phi_{v,k}(x, y)}{\partial y} \right] \int a_{v,k}(z) dz + C(x, y, z_0)
 \end{aligned} \tag{16.4}$$

Figure 16.7 shows an example of a reconstructed velocity field. The velocity data was obtained from multiple $x - y$ planes at several z -locations. In this experiment, the in-plane velocity field is estimated to have an uncertainty of about 1.2%, while the out-of-plane velocity uncertainty is about 3.5%.

16.4 Hybrid Experimental-Numerical Technique for 3D Reconstruction

Contributed by:

S.T. Wereley and C.D. Meinhart

In certain types of fluid mechanics problems, a hybrid experimental/computational approach may be advantageous. Optical access may constrain the experimental measurements to being able to only record 2D planes of data. Furthermore, there may also be uncertainties in fluid properties, material properties, and associated boundary conditions that may reduce the accuracy of 3D numerical simulations.

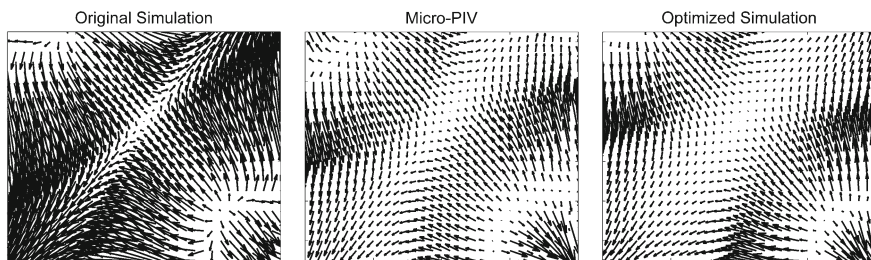


Fig. 16.8 Velocity vector field of μ PIV data (middle panel), and numerical simulation (left and right panels). The left panel shows the original simulations. The right panel shows the optimized numerical simulation. The RMS error is reduced by a factor of three in the optimized result

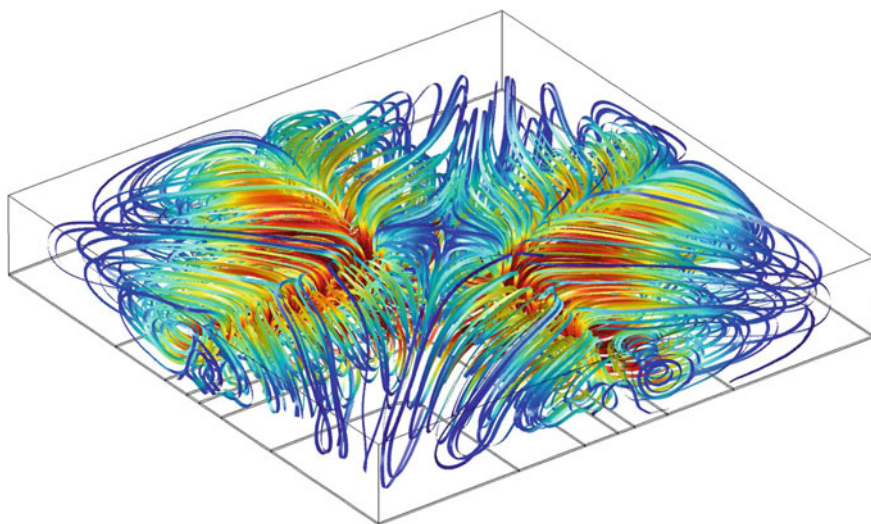


Fig. 16.9 Three-dimensional streamlines of an electrokinetic micromixer determined from the hybrid experimental/numerical approach [55]

In these types of cases, [55] proposed a hybrid experimental/numerical approach that can be used to provide a best estimate of the full 3D velocity field. In this approach accurate measurements of 2D velocity fields are obtained using μ PIV. The resulting experimental data is then compared to numerical simulation results. Due to uncertainties in the fluid properties, material properties and boundary conditions, there may exist discrepancies between the experimental and numerical simulation results. In this case, the various parameters can be adjusted (within the degree of their uncertainty) and inputted into the numerical simulation to improve the agreement between experiment and simulation. [55] used a gradient-free optimization algorithm in order to improve this agreement.

Figure 16.8 shows velocity fields from the experiment and approach reported by [55]. The left side of Fig. 16.8 shows the original simulation results, which agree

qualitatively with experimental μ PIV data (shown in the middle panel). By optimizing various experimental parameters within the ranges of uncertainty, the RMS is reduced by a factor of three, as shown in the vector field on the right panel of Fig. 16.8.

The numerical simulation represents the “best estimate” of the 3D velocity field, based upon the 2D experimental μ PIV velocity fields. Streamlines from the simulation are shown in Fig. 16.9. These streamlines illustrate the complex 3D nature of the flow, which can be used for efficient mixing at the microscale.

16.5 Particle Velocimetry Using Evanescent-Wave Illumination for Near-Wall Flows

Contributed by:

M. Yoda

Background

Measuring velocity fields near walls in microfluidic devices such as Labs on a Chip (LoC) using microscale particle-image velocimetry (μ PIV), where the entire volume of the flow is illuminated, can pose challenges. Reflections from the wall and light scattered by particles beyond the focal plane reduce the signal-to-noise ratio (SNR) of the particle images, and the spatial resolution of μ PIV may be insufficient to resolve many interfacial phenomena of interest (Table 16.2).

Particle velocimetry using evanescent-wave illumination can be used instead to measure such interfacial velocity fields. When light is incident upon a planar refractive-index fluid-solid interface between glass and water, for example, at an angle of incidence θ exceeding the critical angle θ_C ($\theta_C = \sin^{-1}(n_1/n_2) \approx 63^\circ$) for a glass-water interface where $n_1 = 1.33$ is the refractive index of water, and $n_2 \approx 1.5$

Table 16.2 MnPTV recording parameters for combined electroosmotic and Poiseuille flow through microchannels

Flow geometry	Plane parallel and adjacent to wall
Maximum velocity	1 mm/s
Field of view	130 $\mu\text{m} \times 37 \mu\text{m}$
Observation distance	<1.5 mm
Recording method	Multiframe/single exposure
Recording medium	Electron multiplying CCD (EMCCD) camera
Recording lens	Microscope objective (63 \times , $NA = 0.7$)
Illumination	Argon-ion laser (output power < 1 W)
Time interval between images	2 ms
Seeding material	Fluorescently dyed polystyrene spheres ($d_p = 250 \text{ nm}$ and 490 nm)

is the refractive index of the glass), the light will undergo total internal reflection (TIR) in the glass.

The term ‘total’ internal reflection is misleading, however, because the ‘evanescent waves’—i.e., the waves with complex wave number—will also be *transmitted* into the water, and propagate along a direction parallel to the refractive-index interface. The intensity of these inhomogeneous waves $I \propto \exp\{-z/z_p\}$ where z is the distance measured from and normal to the interface, and z_p , the (intensity-based) penetration depth, is somewhat less than the illumination wavelength in vacuum (or air) λ_0 :

$$z_p = \frac{\lambda_0}{4\pi [n_2^2 \sin^2 \theta - n_1^2]^{1/2}} \quad (16.5)$$

In general, the penetration depth is less than, but comparable in order of magnitude to, λ_0 ; for illumination at visible wavelengths, z_p is typically less than 200 nm [1].

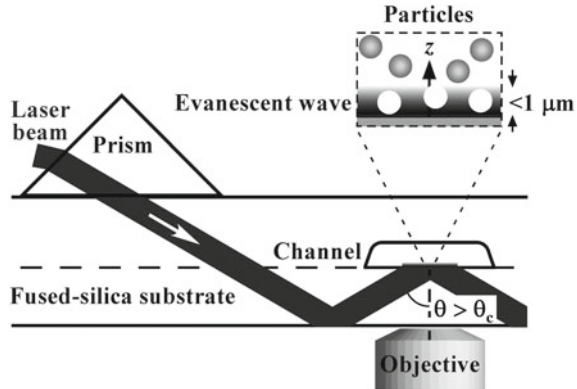
For more than a decade, evanescent waves have been used to illuminate particle tracers, including the fluorescent polystyrene (PS) spheres often used in μ PIV and visible quantum dots, to obtain the two velocity components parallel to the wall [54, 72]. Since the evanescent-wave illumination is restricted to such a small region, the tracer images have little, if any, of the additional background ‘noise’ from particles beyond the focal plane typical of volumetrically illuminated μ PIV images.

In general, the spatial resolution of the technique along the optical axis (i.e., normal to the image plane) is determined by z_p , i.e., the characteristics of the illumination and the sensitivity (characterized by the SNR, for example) of the imaging system. For a SNR of 20, the evanescent wave illuminates the region $z < 3z_p$. Hence the effective ‘thickness’ of the slice of the flow imaged by evanescent-wave particle velocimetry is usually less than 1 μ m, while that of typical μ PIV near-wall measurements, based on the depth of correlation, exceeds 2 μ m [10, 59, 69]. Evanescent-wave particle velocimetry, also known as nano-PIV (nPIV) [62] and total internal reflection velocimetry (TIRV) [26], determines velocities within about 1 μ m of the wall. Given, however, that evanescent-wave illumination is inherently limited to visualization of the interfacial (vs. bulk) flow, evanescent-wave particle velocimetry complements the capabilities of μ PIV.

The two most common methods for illuminating the flow in a LoC with evanescent-wave illumination use a microscope objective or a prism to couple the light into the flow. In objective lens-based total internal reflection microscopes (TIRM) which are commercially available from a number of manufacturers, a beam of light is refracted at an objective lens with a numerical aperture $NA > n_1$ and introduced, usually through a layer of immersion oil, into the glass wall of the LoC. The advantages of objective-based systems include ease of alignment because the illumination and imaging optical paths coincide, and images with good SNR because of the high NA of TIRM objectives. Moreover, since the flow is illuminated and imaged from below, the region above the flow is available for other types of instrumentation.

Unfortunately, using objective lens-based TIRM imposes significant limitations on the flow facility and image characteristics such as the physical field of view and exposure time. At present, commercially available TIRM objectives are limited to a single working distance, namely a 170 μ m thick (#1.5) borosilicate glass

Fig. 16.10 Prism-coupled evanescent-wave illumination of a flow seeded with fluorescent tracer particles through a fused-silica microchannel where the silica substrate is used as a waveguide



coverslip (with $n_2 = 1.518$), and magnifications of at least 60 because of difficulties in designing lower-magnification objectives with high NA . The maximum illumination intensity is limited by the maximum laser power, which is usually less than 0.5 W, that can be coupled into such objectives without damaging the objective. Finally, the evanescent-wave illumination from objective-based TIRM has a periodic, and hence non-uniform, intensity due to interference patterns caused by slight misalignment of light beams within the objective.

In prism-based evanescent-wave illumination, the light is instead coupled into the glass wall of the LoC using a prism so that $\theta > \nu_c$ (Fig. 16.10); a second prism is often then used to couple the light out of the LoC. By separating the illumination and imaging paths, this configuration gives much more flexibility because the flow can be imaged through windows of different thickness and different optical materials and the maximum illumination intensity is not limited by the limitations of the imaging system. Moreover, the region illuminated by evanescent waves can be very large when the light is coupled in to the side of a glass plate (where the plate serves as a waveguide), with dimensions of several cm [48]. However, the prism can interfere with access to the sample, and this configuration requires optical alignment of both the illumination and imaging systems.

Interestingly, the exponential decay in the evanescent-wave intensity with wall-normal distance or z can be exploited to determine the z -position of the particle, and hence the three-dimensional position of an individual particle. Because evanescent waves are generated at the fluid-solid interface, the positions of particles, when illuminated by such waves, are automatically measured with respect to the wall. Measurements of the elastic (vs. inelastic) scattering of evanescent waves created by the TIR of with linearly p -polarized light by particles of average radii $a = 680$ nm show that I_p , the intensity of the image of a particle illuminated by evanescent waves has an exponential decay with length scale z_p [20]. For particle-wall separations $h \propto z - a$ where z is the position of the particle center along the wall-normal distance (so a particle at $h = 0$ touches the wall),

$$h = z_p \ln\{I_p^0/I_p\} \quad (16.6)$$

Here, I_p^0 is the intensity of the image of a particle touching the wall (i.e., at $h = 0$).

A number of experimental studies suggest that Eq. (16.6) can be extended to inelastically scattered light from fluorescent colloidal particles, i.e., the tracers most commonly used in particle velocimetry [22, 37]. So the wall-normal, or z -position of an individual particle $z = h + a$, with h is determined using Eq. (16.6), and I_p^0 can be determined from calibration experiments, albeit with some uncertainty. Most experimental measurements of I_p^0 , typically obtained by averaging many images of particles that are adsorbed on the wall, have a standard deviation that is significantly greater than that expected from the particle polydispersity, probably because of particle-to-particle variations in fluorophore concentration and photobleaching of the fluorophore [38].

In the near-wall region, the flow is mainly parallel, or tangential, to the wall because of the no-flux boundary condition, and so the z -component of the particle velocity w is usually negligible. So the flow in this region is a shear flow where the velocity components parallel to the wall increase with z . The x - and y -locations of the center of any particle image can be determined with a resolution of ~ 0.1 pixel, using a variety of standard methods, including identifying the center of the correlation peak by cross-correlating the particle image with a Gaussian function. The particle velocity is then simply the particle displacement determined from a pair of successive images of the particle divided by the time interval between the images in the pair Δt .

Although most particle velocimetry techniques assume that the particle velocities are the flow velocities, the displacements of the colloidal particles usually used in evanescent-wave particle velocimetry (and μ PIV in many cases) are, in general not identical to the flow velocity due to several factors, which are all functions of the particle radius a , and are hence affected by particle polydispersity:

1. The particle displacements are due to both convection by the flow and Brownian fluctuations, which are significant for $a \leq 0.5 \mu\text{m}$ particles suspended in water. Given that typical Brownian fluctuation timescales are much less than 1 ns, the position of any colloidal particle is averaged over many, many such fluctuations. Unfortunately, near-wall Brownian fluctuations are anisotropic, depending upon z , and hence non-stochastic, because the wall ‘hinders’ diffusion. Indeed, several studies have used evanescent-wave techniques to measure this anisotropic Brownian diffusion both parallel to and normal to the wall [21, 31, 32]. The effects of Brownian diffusion can be minimized by using shorter exposure times τ and smaller Δt [60, 61].
2. The shear flow near the wall (due to the no-slip condition) ‘hinders’ the particle translation by inducing particle rotation, and hence reduces the particle velocity compared with the fluid velocity [23].
3. The particle velocities can overestimate the flow velocity because the particle concentration is also non-uniform near the wall. Even in a dilute colloidal suspension at rest, assuming that the tracer particles and the wall have the same sign of surface charge (usually negative), there will be a ‘particle depletion layer’ near the wall, due to repulsive particle-wall electric double layer and attractive van der Waal

interactions, as predicted by the classic Derjaguin–Landau–Verwey–Overbeek (DLVO) theory [25]. In a *flowing* suspension, there are additional, usually repulsive, ‘lift’ forces due to the pressure and voltage gradients often used to drive flows in LoC [30, 71].

4. For cross-correlation-based PIV, the non-uniform nature of evanescent-wave illumination means that particles near the wall, with smaller flow velocities, have brighter images, and hence a greater contribution, to, the cross-correlation. The actual flow velocity will therefore be greater than the particle velocity. This effect and Brownian effects can again be reduced by obtaining images with small τ and Δt [60, 61], or by using particle-tracking methods [28].

A number of approaches have been proposed to ‘extract’ flow velocities from particle velocities obtained using evanescent-wave velocimetry. Multilayer nanoparticle tracking velocimetry (MnPTV) ‘bins’ the velocity data from a sequence of images of a steady (or periodic) flow based upon the average wall-normal positions of the tracer particles over the image pair into a few layers, and reports the average velocity for each layer [37]. The z -location of this velocity is then the average of the z -positions for all the velocity samples in that layer. The technique minimizes, but does not correct for, the effects of Brownian diffusion by using small (maximum 1 ms) τ and small (comparable to τ) Δt .

Other researchers have used Brownian dynamics simulations, based for the most part on solving the Langevin equation, to determine how to estimate flow velocities from their particle velocity measurements. HUANG et al. [32] and SADR et al. [60] proposed ‘correction factors’ for velocities obtained using particle-tracking and cross-correlation-based PIV approaches, respectively, that incorporate many of these effects including Brownian effects, the lag due to shear-induced particle rotation, and the surface forces predicted by DLVO theory. Improved methods for directly estimating the near-wall particle distribution that account for the effects of polydispersity have also been proposed [66], but the method has only been tested to date on single (vs. pairs of) particle images.

A number of studies have used evanescent-wave particle velocimetry to estimate apparent slip lengths in flow over hydrophilic and hydrophobic walls [22, 36, 38]. In these studies, Poiseuille flow is driven by either a pressure gradient or syringe pump through channels with a large enough hydraulic diameter (compared with z_p) to ensure that the flow in the near-wall region illuminated by the evanescent waves is essentially shear flow with a constant shear rate $\dot{\gamma}$. The glass surfaces of the fused-silica or polydimethylsiloxane (PDMS)-glass channels were modified with an octadecyltrichlorosilane (OTS) layer to make them hydrophobic, and compared with results for otherwise identical channels with unmodified (i.e., ‘bare’) surfaces.

The earliest study by HUANG et al. [22] reported apparent slip lengths of 26 nm–57 nm for hydrophilic surfaces and 37 nm–96 nm for hydrophobic surfaces with an uncertainty of at least 30 nm. LI & Yoda [36] used MnPTV to estimate apparent slip lengths ranging from -2.3 nm to 8.0 nm with a maximum uncertainty of 22 nm for hydrophilic surfaces and from 1.8 nm to 23 nm with a maximum uncertainty of 23 nm for hydrophobic surfaces. Most recently, LI et al. [38] obtained slip lengths of 9 nm with an uncertainty of 10 nm for hydrophilic surfaces and 55 nm with an

uncertainty of 9 nm with hydrophobic surfaces. They identified photobleaching as a major factor affecting the accuracy of estimates of I_p^0 , although this may be due in part to the relatively long exposure times ($\tau = 2.5$ ms) required by their TIRM system.

Evanescent-Wave Particle Velocimetry Studies of Combined Poiseuille and Electroosmotic Flow

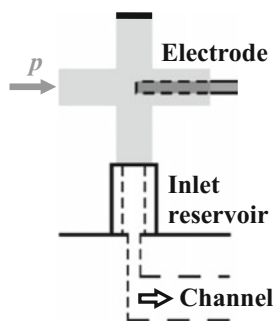
Electric fields (i.e., voltage gradients) and pressure gradients are both common ways to drive flows in microfluidic devices, and hence through microchannels. Although both electroosmotic (EO) flow driven by electric fields and Poiseuille flow driven by pressure gradients have been studied by several groups, there are relatively few studies of combined Poiseuille and EO flows driven by both voltage and pressure gradients [7, 18, 45].

Multilayer nano-particle tracking velocimetry (MnPTV) [37] was used to study combined electroosmotic (EO) and Poiseuille flows in the same direction through microchannels wet-etched into a fused-silica substrate with cross-sections of nominal depth $H = 30 \mu\text{m}$ and width $W = 300 \mu\text{m}$ driven by electric fields of magnitude $E < 10$ V/cm and pressure gradients $\Delta p/L < 1.1$ bar/m, corresponding to near-wall shear rates $\dot{\gamma} < 1200$ s⁻¹ [11]. The DC electric field was imposed using platinum electrodes sealed to four-way connectors at the upstream and downstream reservoirs; the hydrostatically generated pressure gradient was imposed through another port of the connector (Fig. 16.11).

The working fluid was a 1 mmol/l aqueous sodium tetraborate ($\text{Na}_2\text{B}_4\text{O}_7$) solution seeded at a bulk number density of $2.7 \times 10^{16} \text{ m}^{-3}$ with fluorescent carboxylated polystyrene (PS) spheres. Two different fluorescent tracer particles were used: (i) $a = (125 \pm 4.5)$ nm spheres (Invitrogen F8811) with an emission maximum at 513 nm; and (ii) $a = (245 \pm 7.5)$ nm (Invitrogen F8812) spheres with an emission maximum at 606 nm. The zeta-potentials of the particles suspended in the working fluid $\zeta_p = (-67.8 \pm 1.0)$ mV (average \pm standard deviation) for the $a = 125$ nm particles and $\zeta_p = (-49.9 \pm 0.6)$ mV for the $a = 245$ nm particles.

The evanescent-wave illumination $z_p = (110 - 120)$ nm was generated by the TIR of a continuous argon-ion laser beam (output power < 1 W) coupled into the fused-silica substrate with a fused-silica isosceles right triangle prism. The laser was

Fig. 16.11 The 4-way connector at the channel inlet



‘shuttered’ by an acousto-optic modulator (AOM) to acquire a pair of images of the particles at $\tau = 0.5$ ms and $\Delta t = 2$ ms.

The smaller particles were illuminated by the 488 nm line of the laser, and imaged through a 525 ± 25 nm bandpass filter; the larger particles were illuminated by the 514.5 nm line of the laser and imaged through a 615 nm longpass wavelength filter. The fluorescence from the particles in the center of the microchannel (to minimize the effect of the side walls) was imaged through a $M = 63$, $NA = 0.7$ microscope objective (Leica PL Fluotar L) onto an electron multiplying charge-coupled device (EMCCD) camera (Hamamatsu C9100-13). A sequence of 500 image pairs, where each 512×144 pixel images had physical dimensions of $130 \mu\text{m} \times 37 \mu\text{m}$, were recorded with a spacing between pairs of 0.2 s.

The location of the center of each particle was determined using cross-correlation with a 2D Gaussian function. After identifying and removing the images of overlapping or aggregated tracers, the displacements of the remaining particles in the plane parallel to the wall were determined simply by matching particles between the two images in the pair to their nearest neighbor

The particle-wall separation h , or the distance between the particle edge and the wall, was next determined from the particle image intensity I_p , which was defined here to be the area-averaged integral of the grayscale values in the image, and Eq. (16.6). The displacements of the $a = 125$ nm and $a = 245$ nm particles were then divided into three layers, each containing a similar number of particle samples, based on h :

1. $0 \text{ nm} \leq h \leq 100 \text{ nm}$
2. $100 \text{ nm} \leq h \leq 200 \text{ nm}$
3. $200 \text{ nm} \leq h \leq 300 \text{ nm}$

The particle velocity components parallel to the wall were then simply the particle displacement divided by Δt .

Figure 16.12 shows the flow velocities for combined EO and Poiseuille flow at an electric field magnitude $E = 8.8$ V/cm and $\dot{\gamma} = 660 \text{ s}^{-1}$ ($\Delta p/L = 0.43$ bar/m) [circles], and $\dot{\gamma} = 1150 \text{ s}^{-1}$ (1.04 bar/m) [squares]. Note that the flow velocities were estimated by subtracting the electrophoretic velocity, given by the Helmholtz–Smoluchowski relation and the measured values of ζ_p , from the measured velocities of the $a = 125$ nm (open symbols) and $a = 245$ nm (filled symbols) tracers. The z -positions of these velocity data have been corrected for the nonuniform distribution of the tracers, and the excluded volume effect where the minimum velocity of the particle (center) is that of the flow at $z = a$.

As expected, the flow velocity for this creeping flow in the near-wall region is simply the superposition of the linearly varying Poiseuille flow velocity and the uniform EO flow velocity:

$$U = \dot{\gamma}z + \mu_{eo}E \quad (16.7)$$

where μ_{eo} is the EO mobility. The slopes of the data (dashed lines) are in good agreement with the expected shear rates, and the velocity ‘offset’ due to EO flow for the range of E considered here is proportional to E .

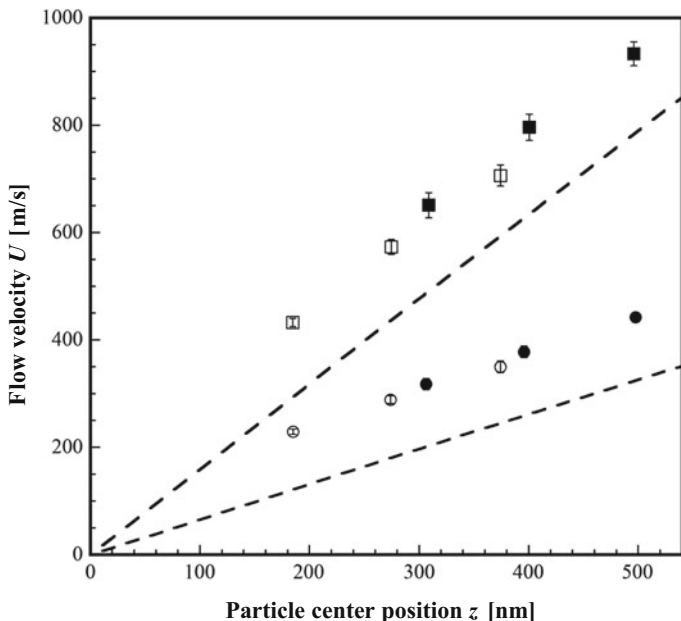


Fig. 16.12 Flow velocity profiles $U(z)$, where $h \equiv z - a$, estimated by MnPTV for combined EO flow at $E = 8.8 \text{ V/cm}$ and Poiseuille flow at $\dot{\gamma} = 660 \text{ s}^{-1}$ (circles) and 1150 s^{-1} (squares) estimated from the particle speeds using $a = 125 \text{ nm}$ (open) and $a = 245 \text{ nm}$ (filled symbols) particles. The dashed lines represent the analytical solution for Poiseuille flow at the same values of $\dot{\gamma}$, or alternatively, $\Delta p/L$. The error bars denote the standard deviations over three independent experiments [11]

16.6 Measurements of the Flow around a Growing Hydrogen Bubble Using Long-Range μ PIV and Shadowgraphy

Contributed by:

D. Baczyzmański and C. Cierpka

Introduction

The generation of hydrogen through water electrolysis and its application as an energy carrier have become increasingly important in view of the worldwide promotion of renewable energies. However, the relatively low efficiency of this process has been a major drawback for industrial applications in the past. A considerable part of the losses is related to the formation of hydrogen gas bubbles on the electrode surface, which reduces the active electrode area that would be otherwise available for the chemical reactions. Therefore, the accelerated bubble detachment from the electrode is essential to improve the performance of the process [5]. In this context, high research efforts are directed towards the application of forced convection, which can

Table 16.3 PIV recording parameters for the shear flow around a growing bubble

Flow geometry	Shear flow around a sub-millimeter sized hydrogen bubble evolving at a microelectrode
Maximum in-plane velocity	$U_{\max} \approx 35 \text{ mm/s}$
Field of view	$3 \times 3 \text{ mm}^2 / 1.3 \times 2 \text{ mm}^2 (W \times H)$
Interrogation area	$38 \times 38 \text{ }\mu\text{m}^2 / 32 \times 32 \text{ }\mu\text{m}^2 (W \times H)$
Observation distance	$Z_0 \approx 100 \text{ mm}$ and 50 mm
Recording method	Single frame
Recording medium	High speed CMOS, 2016×2016 pixel
Recording lens	Long-range microscope system
Illumination	LED: $530 - 570 \text{ nm}$, up to 250 mW
Recording frequency	500 Hz
Exposure time	$20 - 500 \text{ }\mu\text{s}$
Seeding material	polystyrene particles ($d_p = 1 \text{ }\mu\text{m}$ and $3 \text{ }\mu\text{m}$)

be conveniently generated by superimposing a magnetic field on the inherent electric field. This gives rise to Lorentz forces which act as body forces in the liquid phase surrounding the evolving bubbles [4, 67]. In order to understand the influence of the magnetohydrodynamic (MHD) flow on the bubble growth and detachment, detailed investigations of the flow around the growing bubble and its motion are necessary. In this study, single sub-millimeter sized hydrogen bubbles were generated at a microelectrode and visualized with a long-range microscope by means of shadowgraphy [3]. This allows for simultaneous measurements of the 2D flow around the bubble and its geometry using only one camera (Table 16.3).

Setup and Evaluation Techniques

The electrochemical cell consists of a small glass cuvette ($45 \times 10 \times 10 \text{ mm}^3$ [$H \times W \times D$]) with a horizontal Pt microelectrode ($100 \text{ }\mu\text{m}$ in diameter) embedded in the bottom. The cell was filled with a $1 \text{ M H}_2\text{SO}_4$ solution and placed between two NdFeB magnets, generating a homogeneous electrode-parallel magnetic field with a magnetic induction of $B = 500 \text{ mT}$ (see Fig. 16.13 left). Additional measurements were conducted at $B = 180 \text{ mT}$ by placing the cell slightly above the magnets. The electrodes were connected to a voltage-regulated power supply to generate single hydrogen bubbles at the microelectrode. The Lorentz force density $\mathbf{f}_L = \mathbf{j} \times \mathbf{B}$ around the evolving bubble acts perpendicular to the magnetic field \mathbf{B} and the electric current field \mathbf{j} , which in this case generates a wall-parallel shear flow. PIV measurements of this flow were performed by adding polystyrene tracer particles ($d_p = 3 \text{ }\mu\text{m}$) and visualizing both the particles and the bubble by means of shadowgraphy (see Fig. 16.13 right). The background illumination was provided by a green LED and was guided by a system of two mirrors in the optical path to image the main flow plane. Two 1 mm thick glass slides served as mirrors to avoid possible distortions by the magnetic coatings of conventional mirrors. A high speed camera (PCO DIMAX

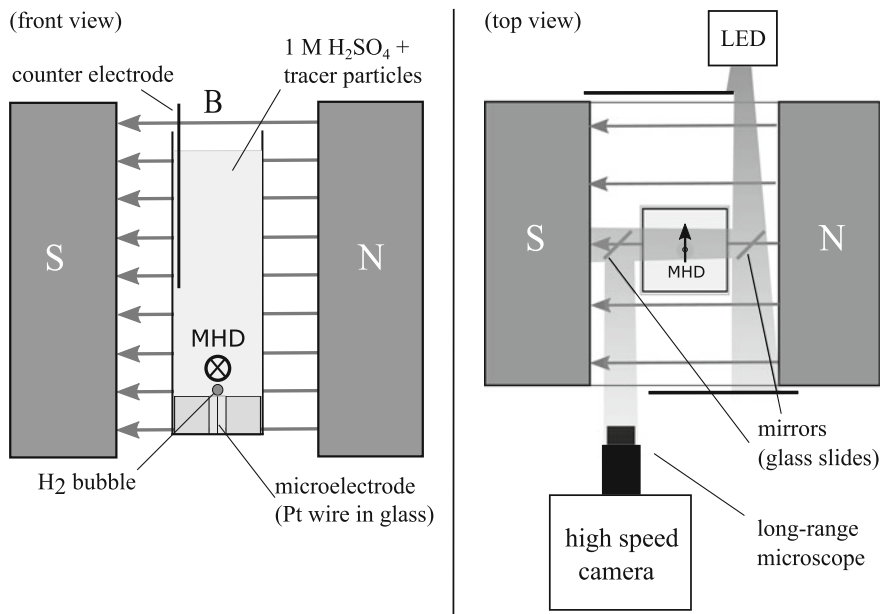


Fig. 16.13 Setup: The electrochemical cell was placed in a homogeneous magnetic field (left, front view); shadowgraphy was used to measure the 2D flow via μ PIV and to obtain the bubble geometry. The light was guided by mirrors to image the particles and the bubble in the main flow plane (right, top view)

by PCO GmbH) equipped with a long-range microscope system (K2/S by Infinity Photo-Optical Company) was used to record the shadow images at 500 Hz at a high magnification of about $M = 8.3$ with a resolution of $0.75 \text{ pixel}/\mu\text{m}$. Since the light reflection by the glass slide is low and also the reflection from its rear side is causing additional undesired shadows, a relatively low particle image density ($\approx 0.0003 \text{ ppp}$) was used to ensure a sufficient signal-to-noise-ratio. For the second set of measurements at $B = 180 \text{ mT}$, the working distance was higher which led to a slightly lower magnification of $M = 6.9$ with a resolution of $0.63 \text{ pixel}/\mu\text{m}$. However, much higher particle image densities ($\approx 0.0027 \text{ ppp}$) and smaller particle sizes ($d_p = 1 \mu\text{m}$) were possible due to the direct optical access (see Fig. 16.14 left). Moreover, only a very low illumination power and exposure time were necessary (40 mW at $20 \mu\text{s}$).

Inhomogeneities in the background illumination were removed by subtracting a background image. This way, the bubble shape and its motion can be easily obtained by segmentation of the resulting images (Fig. 16.14 left). The identified bubble images were masked out prior to the PIV evaluation to avoid a biased correlation result at the bubble surface. Additional image filters (subtraction of sliding average, intensity threshold) were then applied to remove the background noise caused by defocused particles and to reduce the effective depth of focus [12, 59]. The importance of image preprocessing, especially for imaging with large magnifications, was

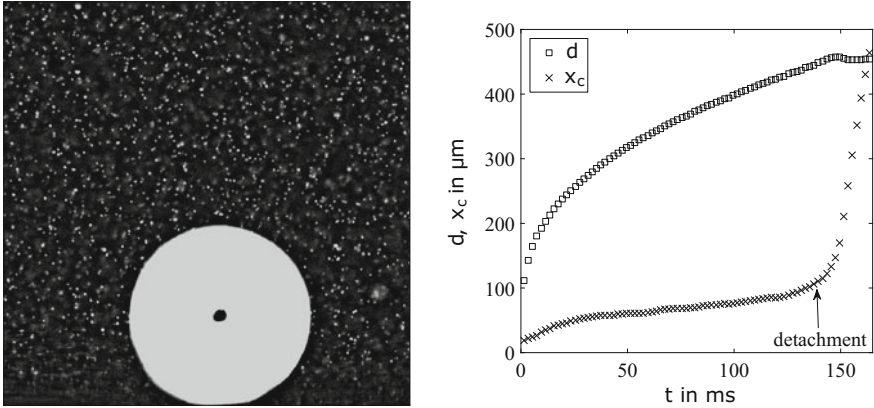


Fig. 16.14 Zoom into inverted shadowgraph image with removed background image (left). Evolution of the bubble diameter d and motion x_c parallel to the wall (right)

recently demonstrated in the International PIV Challenge [27]. The resulting measurement depth was experimentally estimated to be less than $100\ \mu\text{m}$ for a particle size of $d_p = 3\ \mu\text{m}$ and is further reduced for the measurements with $d_p = 1\ \mu\text{m}$. This is sufficiently small considering the observed bubble sizes (Fig. 16.14 right). Since the bubble evolution and detachment cycle is highly periodic [2], a phase-resolved analysis of the flow can be performed by dividing each evolution cycle ($\mathcal{O}(100\ \text{ms})$) into small phase intervals of a few milliseconds (20 phase intervals). In particular, this allows to use an ensemble-based correlation [70] in order to increase the measurement resolution at $B = 500\ \text{mT}$, where a very low seeding concentration was used. This was realized by reorganizing the PIV images according to their temporal phase and storing them into double frame images. Using approximately 500 images per phase for the ensemble correlation, interrogation window sizes of 24×24 pixel with 50% overlap were achieved, despite the low seeding concentration. For $B = 180\ \text{mT}$, the seeding concentration was sufficient for a standard PIV approach using the same final interrogation window size. In this case the results were phase-averaged (≈ 300 images per phase) during the post-processing for a higher accuracy. In addition, a time-resolved PTV algorithm was applied close to the gas-liquid interface to better resolve the Marangoni flow caused by high surface tension gradients at the foot of the bubble [13]. The obtained PTV data was phase-averaged in bins of 10×10 pixel.

Results and Discussion

The wake of the previously detached bubble is only relevant in the very first stages of the bubble growth, after which the flow around the bubble is governed by the MHD effect (see [DC16.2] for an animated view of the evolving flow). Figures 16.15 and 16.16 illustrate the induced MHD shear flow for a late phase of the bubble growth at $B = 180\ \text{mT}$ and $B = 500\ \text{mT}$, respectively (see [DC16.3] for coloured versions). In both cases the bubble is slowly sliding away from the microelectrode to the right due to the imposed drag force (see Fig. 16.14 right). As a result, the access to the electrode

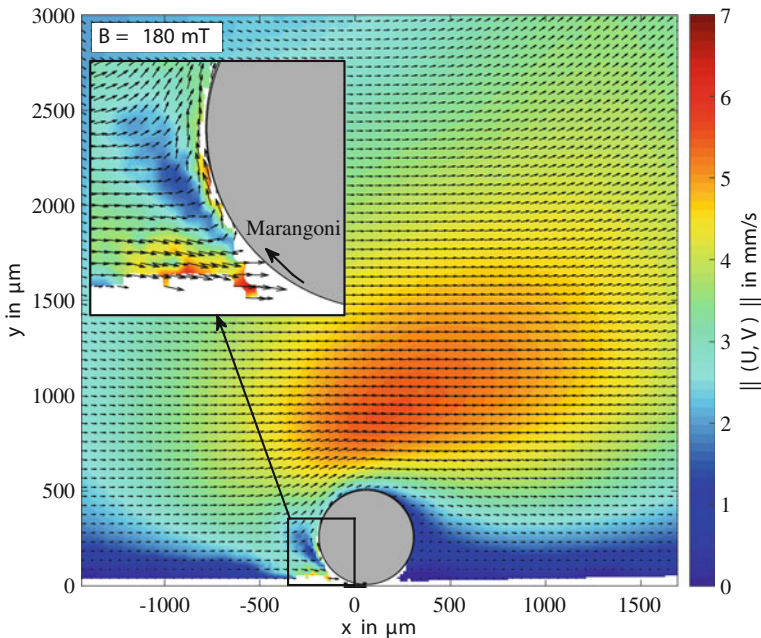
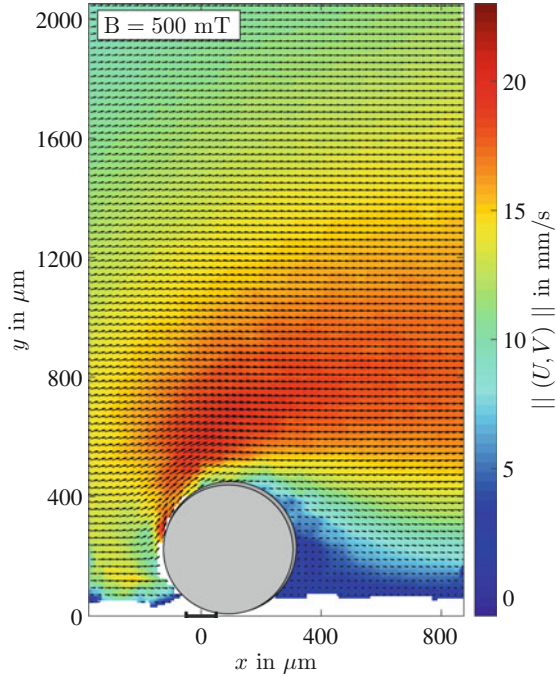


Fig. 16.15 Phase-averaged PIV velocity field for $B = 180$ mT: The Lorentz force distribution and MHD flow is asymmetric due to the motion of the bubble away from the electrode (indicated by the black line at the bottom). The Marangoni flow on the left side at the gas-liquid interface was obtained by PTV

is blocked on its right side, causing an asymmetric current field and Lorentz force distribution. The generated shear flow is following the asymmetric force distribution, which has high values on the left side of the bubble but is relatively weak on its right side, leading to a region of low momentum on that side. This imposes a strong drag force as well as a lift force which help to overcome the surface tension forces that keep the bubble attached to the wall and thus accelerate its detachment. However, the induced forces are presumably smaller when large electrodes are used as a more symmetric Lorentz force distribution can be expected.

In addition to the MHD flow, Marangoni stresses are generated at the foot of the bubble presumably due to high local concentration gradients of dissolved hydrogen or temperature gradients which give rise to surface tension gradients [39]. The Marangoni stress generates a flow with high velocity gradients directly at the gas-liquid interface as can be seen in Fig. 16.15 for $B = 180$ mT within a distance from the interface of approximately $20 \mu\text{m}$. The fluid is also accelerated toward the foot of the bubble due to conservation of mass. This is also evident at $B = 500$ mT (Fig. 16.16), although it was not possible to properly resolve the high velocity gradients directly at the interface, despite the local time-resolved PTV approach. However, a detailed investigation of the Marangoni flow is important as it might influence the bubble

Fig. 16.16 Phase-averaged (ensemble-correlation) PIV velocity field for $B = 500$ mT: The MHD flow becomes stronger with an increase of the magnetic induction (see Fig. 16.15). Although PTV was applied close to the interface, the strong velocity gradients of the Marangoni flow cannot be resolved at this magnification



growth by an enhanced mass transfer and impose an additional stabilizing force on the bubble. A further characterization of these interfacial phenomena will require an even higher magnification and a smaller measurement depth.

Conclusions

Combining shadowgraphy and long-range μ PIV allowed for a detailed study of the MHD-induced shear flow around a growing sub-millimeter sized hydrogen bubble. In these measurements the bubble shape and the tracer particles were recorded simultaneously with one camera and their respective images were subsequently separated by proper image processing of the shadow image. The presented technique is relatively simple and only requires a low illumination power and short exposure times due to the backlight illumination. For cases with limited particle image densities and low signal-to-noise ratios, a higher measurement resolution was achieved by using phase-resolved ensemble correlation PIV. Additionally, time-resolved PTV was applied to visualize the strong velocity gradients of the interfacial Marangoni flow. However, to further resolve this flow an even higher magnification is necessary.

16.7 In Vivo Blood Flow Measurements Using Micro-PIV

Contributed by:

C. Poelma

In vivo blood flow measurement provides essential insight in the role of hemodynamics during cardiovascular development. In particular, the local flow rate and wall shear stress are of great importance to understand, for instance, how flow regulates the development of vascular networks or helps form the heart [51]. Measurements using conventional (micro-)PIV are naturally limited to systems that are optically accessible and transparent. A prime example of such a system is the chicken embryo, which is a common model for human development. Measurements using PIV in this system are challenging and have demanded a number of innovations. These will also be helpful outside of this fairly niche application area.

Optical access is created by carefully exposing the embryo through removal of a part of the egg shell and membranes [50]. This allows ‘in ovo’ study of the embryo, with little influence on the development. For tracer particles, either artificial tracers or red blood cells can be used. For the former, the biocompatibility has to be ensured, e.g., by using fluorescent polystyrene particles that are coated with polyethylene glycol (PEG) [65]. After careful injection, these artificial tracer particles circulate through the entire cardiovascular system for at least several minutes. The use of the naturally occurring red blood cells would naturally be preferable, as this would make the technique less invasive. However, due to their size (approximately $8\ \mu\text{m}$ for avian blood) the spatial resolution can be an issue. Note that this holds for both in-plane and out-of-plane directions, as the depth-of-correlation can be significantly larger for red blood cells in comparison with sub-micron artificial tracers [52]. For lower magnifications, the data will be averaged (in an unpredictable manner) over a depth that may be larger than the diameter of the blood vessel under investigation. For high magnifications, red blood cells can be used without these problems [33]. In practice, blood vessel with a diameter up to $150\text{--}200\ \mu\text{m}$ can be measured. For larger diameters, the image contrast rapidly reduces as the flow becomes opaque due to the thick layer of red blood cells in the optical path. Similarly, the development of additional layers of tissue covering the vessels reduces the transparency after the first few days.

Illumination of the tracers can be achieved using conventional (high-repetition) pulsed lasers [65] using epifluorescent imaging: the light is sent, via a beam splitter, through the objective to the sample and the scattered and fluorescent light is collected by the same objective. The use of a wavelength cut-off filter before the camera ensures that only the fluorescence signal of the tracers is imaged. Recently, pulsed LEDs have been shown to be a cheap and safe alternative to lasers [33]. As micro-PIV relies on volume illumination, the LED light can simply be directed onto the embryo from the side. An additional benefit is that the incoherent nature of LED light does not cause interference issues, which can be the case for bright-field illumination using a laser. To improve the image quality and limit desiccation, the field-of-view is generally

covered using a cover glass. Imaging can be done using high-speed cameras or using conventional CCD cameras. While dependent on the magnification and application, the tracer displacements are usually so large that imaging at conventional video rates (e.g., 30 images/seconds) is not sufficient. This implies that for CCD cameras interline transfer ('double frame mode') has to be used, which in turn precludes the use of continuous light sources that are common in microscopy: the second frame will generally be overexposed due to the longer, fixed exposure length.

As the embryo floats freely on the yolk and relatively high magnifications are used (up to $25\times$), it is difficult to avoid that the field-of-view drifts over time. This is not due to movement of the embryo, which is absent at these early stages of development, but mostly due to evaporation and surface tension effects around the cover glass. It is therefore essential to perform image registration: cross-correlation of the images with the first image in the series estimates their displacement with respect to the first frame. Naturally, this can be extended to more complex corrections (e.g., rotation and stretching).

The image quality in micro-PIV, and in particular in these in vivo applications, generally demands some sort of averaging to obtain satisfactory results. As blood flow is pulsatile in nature, this requires special attention. Initially, an additional reference signal was obtained, e.g., using an ultrasonic flow meter [65]. This signal was then used to sort the PIV data in appropriate phase 'bins'. A simplified procedure is to estimate the cardiac phase from the data itself. To do so, any signal can be used that has a unique relation to the cardiac phase. The most straightforward is to determine the mean instantaneous flow, using a very large interrogation area [53]. However, many other options exist if needed, e.g., mean signal-to-noise ratio or the mean image intensity. Using this signal a phase is assigned to each image pair; note that this is only feasible if the acquisition rate is sufficiently high – in practice 5 to 10 points within each cardiac cycle is sufficient to redistribute the data into up to 10 phase 'bins'. Phase-averaging of the correlation results within each bin gives a significant improvement of the signal-to-noise ratio. Generally, 10 to 50 image pairs are used to obtain the mean velocity field within each phase bin [65]. Using more pairs generally does not lead to further improvement and biological changes (e.g., a variation in heart rate) may start to become an issue. If there is a significant temporal variation in the displacement throughout the cardiac cycle, it should be avoided to perform correlation averaging of the entire data set, i.e., without sorting. This process will likely not give the true temporal mean [33]. Note that this issue does occur when the *vector* fields are averaged.

In general, the cardiovascular flow patterns are quasi-stationary. This implies that larger regions can be studied by subsequent measurements. This can be in-plane ('stitching') or out-of-plane ('stacking'). For the former, image registration of overlapping border regions can assist in matching the domains [33]. For stacking, a standard approach is to use a computer-controlled piezo-stepper or an automated microscope translation stage. By translating the focal plane, in increments that match the depth-of-correlation, a complete volumetric velocity field can be obtained [53]. The missing out-of-plane velocity component can be estimated using the continuity equation [50]. The end result can therefore be a phase-reconstructed, volumetric

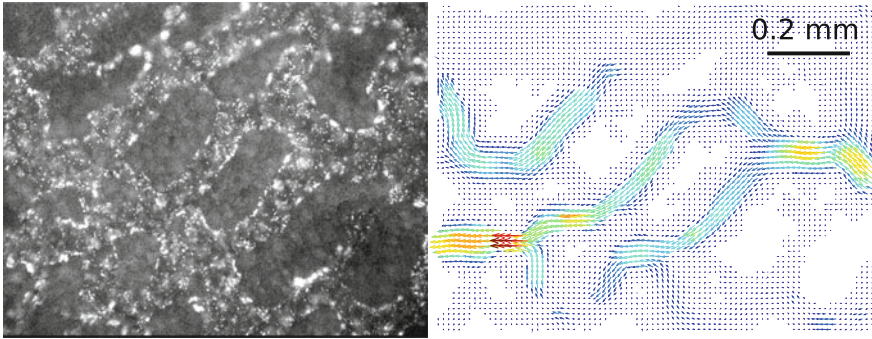


Fig. 16.17 Single raw image ($M = 6\times$, 2×2 binning) showing $1\ \mu\text{m}$ fluorescent tracer particles. The right-hand side shows the corresponding vector field, using a final interrogation area size of 16×16 pixel with 50% overlap; this results in a vector spacing of approximately $15\ \mu\text{m}$

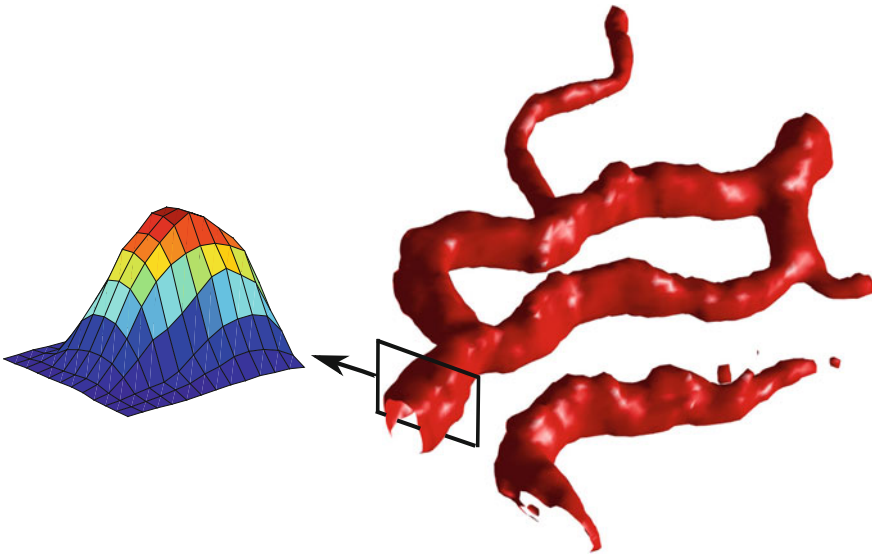


Fig. 16.18 3D reconstruction of the walls of the blood vessels. This result was obtained by stacking 20 planes, similar to the one shown in the previous figure, separated by $12\ \mu\text{m}$. The walls are visualized using an isosurface of $1/10$ of the maximum velocity magnitude. For reference, the maximum velocity of the cross-section is $2\ \text{mm/s}$. This result represents the systolic phase of the cardiac cycle

velocity measurement of all three velocity components of blood flow. This is a sound basis to start determining e.g., the wall shear stress distribution and other relevant hemodynamic parameters.

An example of an in vivo blood flow measurement is shown in Figs. 16.17 and 16.18. These figures show a typical raw image, the corresponding vector field and a

Table 16.4 PIV recording parameters for in vivo blood flow measurement

Flow geometry	Vitelline network (extra-embryonic blood vessels) of a chicken embryo
Maximum in-plane velocity	$U_{\max} \approx 2 - 3 \text{ mm/s}$
Field of view	$1.5 \times 1.1 \text{ mm}^2 (W \times H)$
Interrogation volume	$30 \times 30 \times 12 \text{ }\mu\text{m}^3 (W \times H \times D)$
Dynamic spatial range	$\text{DSR} \approx 50 : 1$
Dynamic velocity range	$\text{DVR} \approx 33 : 1$
Observation distance	$Z_0 \approx 55 \text{ mm}$
Recording method	Dual frame/single exposure
Ambiguity removal	Frame separation (frame-straddling)
Recording medium	Full frame interline transfer CCD $1376 \times 1040 \text{ pixel}$ (with 2×2 binning)
Recording lens	Leica FluoCombi III ($5\times$), Planapo $1\times$, variable zoom
Illumination	Nd:YLF laser $< 10 \text{ mJ/pulse}$ at 527 nm
Pulse delay	$\Delta t = 3000 - 5000 \text{ }\mu\text{s}$
Seeding material	$1 \text{ }\mu\text{m}$ polystyrene spheres containing Rhodamine 6G

three-dimensional reconstruction of some blood vessels. A step-by-step description of the procedures and technical details are given in POELMA et al. (2008) [53]. Table 16.4 summarizes some key parameters.

16.8 Reconstruction of Fluid Interfaces using 3D Astigmatic Particle Tracking Velocimetry

Contributed by:

M. Rossi and C.J. Kähler

In many microfluidic and lab-on-a-chip applications it is often necessary to mix different liquids on a small scale after they merged in a channel. However, as no turbulent mixing takes place in microfluidics the passive mixing is rather slow as only molecular diffusion mixes the fluids at the interfacial area between the two fluids [49, 63]. In order to enhance the molecular mixing, the interface between the different fluids can be enlarged by means of secondary vortices which are created in bended channels, as illustrated in Fig. 16.19, see also [64]. The quantitative characterization of the topology of this interface plays a critical role in the design and optimization of microfluidic devices.

One common experimental approach to assess the fluid mixing is by using dye visualization, as shown in the lower image of Fig. 16.19. However, these methods

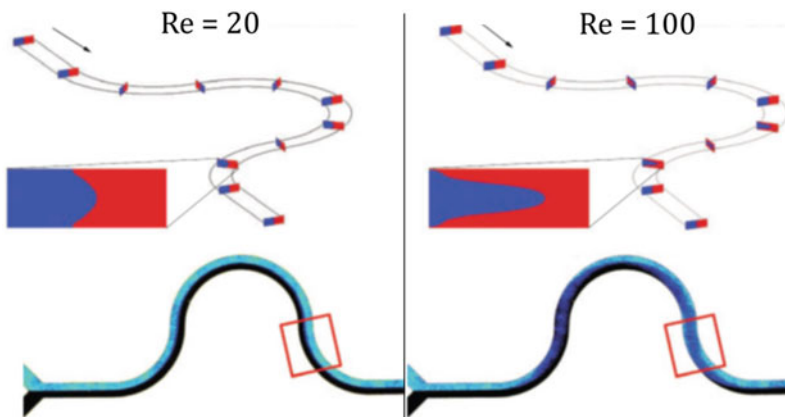


Fig. 16.19 CFD simulation (top) and dye visualization (bottom) of the contact interface between two fluids in a curved microfluidic mixer for $Re = 20$ and $Re = 100$. In areas with a highly bended interface, the dye visualization shows homogeneous mixing as a consequence of averaging over the optical axis (figure adapted from [42])

generally give an averaged concentration value over the optical axis, and do not provide adequate information about the mixing or the complex topologies of the interface between the two fluids. This can be observed in Fig. 16.19 for the case of a curved microfluidic mixer. Here the contact area is bended by the presence of two symmetric Dean vortices established as a consequence of the curvature of the microchannel [42]. In areas with a highly bended interface (red square in lower right image), the dye visualization shows homogeneous mixing but this is an artifact due to averaging along the optical axis. This is evident because after the full bend is passed the two streams are again fully separated which indicates that no significant mixing took place.

Scanning confocal microscopy can be used to overcome this problem, however it requires a significantly more costly equipment and it is always limited to stationary or quasi-stationary flows, see Sect. 10.7.1. An additional problem connected with dye visualization, is the relatively fast diffusion rate of the molecular dye that often results in a smeared interface between the two fluids as shown in Fig. 16.20.

To overcome the aforementioned disadvantages 3D Astigmatic Particle Tracking Velocimetry (APTIV) is a well suited technique to measure the topology of fluid interfaces along with the velocity of the fluid [42, 56]. The working principle is fairly simple as only one single optical view and a single camera is required to resolve the 3D flow information, see Sec. 10.7.4 for details or [15, 58]. First, tracer particles are introduced in one of the two fluids and their position is measured using the 3D Astigmatic PTV method. If the tracer particles are randomly distributed inside the volume and do not cross the interface (non-Brownian particles), the interface topology can be measured as the bounding surface of the cloud of points corresponding to the particle positions as illustrated in Fig. 16.21.

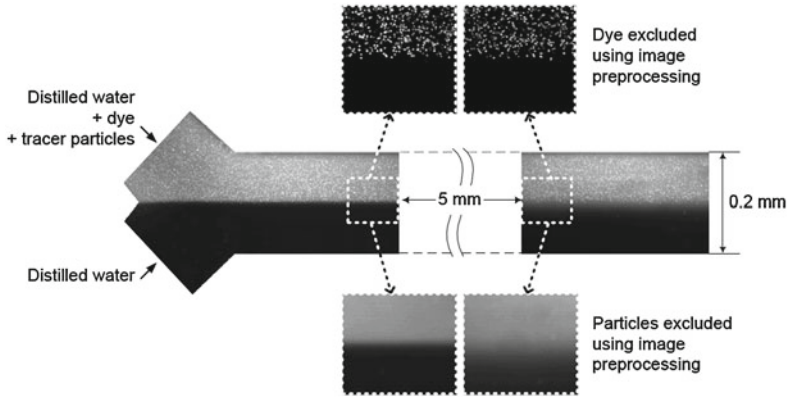
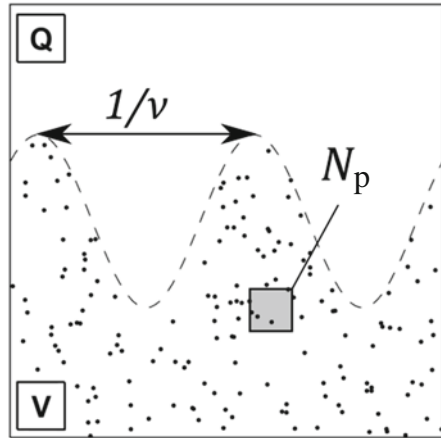


Fig. 16.20 Effect of different diffusion time scales of tracer particles ($2\ \mu\text{m}$ spheres, $D = 2 \cdot 10^{-13}\text{m}^2/\text{s}$) and molecular dye (Rhodamine B, $D = 4 \cdot 10^{-10}\text{m}^2/\text{s}$). A constant flow at $\text{Re} = 20$ was established in a straight Y-shaped micro-channel. 5 mm downstream of the junction, a blurred interface is present when looking at the dye, while no difference can be observed in the tracer particles' distribution (figure adapted from [56])

Fig. 16.21 Schematic of the measurement principle. Given two fluid regions V and Q, V is seeded with a homogeneous random distribution of tracer particles. The topology of the interface between Q and V can be inferred from the boundary of the cloud of measured particle positions. Important parameters for the reconstruction are the number of particles per unit volume N_p and the size of the structures to be resolved, given in terms of the spatial frequency ν (figure adapted from [56])



This approach allows an instantaneous 3D measurement of the interface topology and is, in most cases, insensitive to diffusion (tracer particles have a diffusion coefficient several orders of magnitude smaller than molecular dyes). The main disadvantage is obviously related to the fact that a continuum is represented by a discrete cloud of randomly distributed points, thus the interface reconstruction is not straightforward and can be problematic especially for low particle concentrations. However, for stationary flows the particle density can be indefinitely increased by repeating the number of recordings. Furthermore, in most of the applications, the interface will

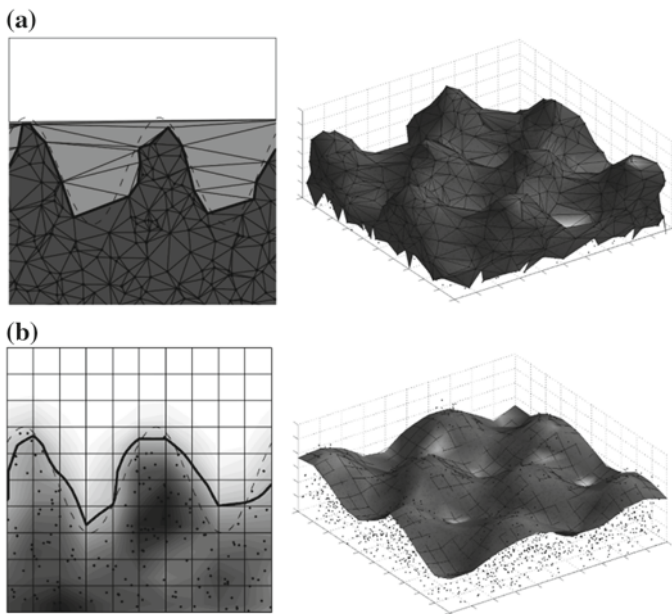


Fig. 16.22 (a) Reconstruction approach using Delaunay triangulation. (b) Reconstruction approach using numerical diffusion. On the right respective results obtained on synthetic data (figure adapted from [56])

be rather simple in geometry such that a reliable topological estimation is usually possible by means of a low number of particles. Different strategies can be used to retrieve the interface from the cloud of measured particle positions. Here the two methods described in [56] are reported.

The first approach, represented in Fig. 16.22(a), uses a Delaunay triangulation to connect the cloud of points and an erosion algorithm to reveal the structures. The erosion criterion is based on the size of the triangles (or tetrahedrons in the 3D case), assuming that given a homogeneous distribution of particles, the size of triangles will be bigger in regions where no particles exist. Implementations of this approach are commonly present in many software or programming languages (e.g. the function *boundary* in Matlab).

The second approach, represented in Fig. 16.22(b), relies on an artificial scalar concentration function defined as:

$$F(\mathbf{X}) = \sum_i^N \frac{1}{\sqrt{2\pi}\sigma^2} \exp\left(-\frac{(\mathbf{X} - \mathbf{P}_i)(\mathbf{X} - \mathbf{P}_i)}{2\sigma^2}\right) \tag{16.8}$$

where \mathbf{X} is the position vector, \mathbf{P}_i is the position vector of the i th particle and σ is an arbitrary numerical diffusion coefficient. Regions in which F falls below a certain threshold value κ are considered regions with no particles. The interface can then be

obtained as the iso-surface with $F = \kappa$. More details about the implementation of the method and optimization of σ and κ can be found in [56].

The accuracy and resolution of the reconstruction is strictly related to the average number of particles per unit volume N_p , also expressed in terms of average distance between particles $\lambda = N_p^{-1/3}$. In order to give a quantitative estimation of the reconstruction accuracy, it is useful to introduce an average reconstruction error defined as the average distance between the estimated interface and the actual interface. This error also provides an indication of the nest structures that can be resolved: for instance if the error is 10 μm , structures smaller than 10 μm will be indistinguishable from fluctuations due to the error. Numerical simulations have been used in [56] to investigate the relationship between particle concentration (expressed in terms of average distance λ) and the smallest structure that could be resolved (expressed in terms of a spatial frequency ν). Assuming as a general criterion that a structure must be 2 times larger than the error in order to be resolved, the simulations showed that $\lambda \cdot \nu \leq 0.1$. This means for instance that if λ is 1 μm only features larger than 10 μm can be resolved (thus with a spatial frequency $\nu < 0.1 \mu\text{m}^{-1}$). These results were in general valid for both the reconstruction algorithms.

In Fig. 17.5 the reconstructions of the contact area between two fluids in the microfluidic mixer shown in Fig. 16.19 are presented. The reconstruction was performed in the area highlighted by the red rectangle for $\text{Re} = 20$ and $\text{Re} = 100$. The 3D measurements were performed using Astigmatic Particle Tracking Velocimetry [15, 58] using polystyrene spheres with a diameter of 2 μm as tracer particles. The optics consists of a microscope objective with a magnification $M = 20$ coupled to a cylindrical lens with focal lens $f = 100 \text{ mm}$. The interface was reconstructed from approximately 20,000 points obtained from 1,000 images. More details about the experimental setup can be found in [42]. The measurements show nicely how the bending of the interface increases with the ow rate and consequently the magnitude of the Dean vortices.

In addition to the interface, the velocity of the particles is also obtained by using the 3D Astigmatic Particle Tracking Velocimetry. Therefore, a very detailed analysis of the flow is possible, as the strength of the Dean vortices can be measured as well. An example is shown in Fig. 16.23 for the case of microfluidic fuel cells (MFC). MFCs use the principle of co-laminar flows in microfluidics to bring together the fuel and oxidant fluid without using proton exchange membranes [16]. A mixing between fuel and oxidant in this case is not desired therefore APTV can be nicely used to check that the interface remains flat when curved channels are used (in this case the interface should lie at the symmetry plane of the Dean vortices). This is indeed shown in Fig. 16.24 where the interface between fuel and oxidant of a MFC with straight and curved channel was measured [57]. The effect of Dean vortices on the curved channel is evident by looking at the slight displacement of the maximum axial velocity (due to the centrifugal force) and at the transversal velocity which reaches a maximum value of 6% the average axial velocity. The 3D velocity field was measured with APTV only in the region seeded with tracer particles. To

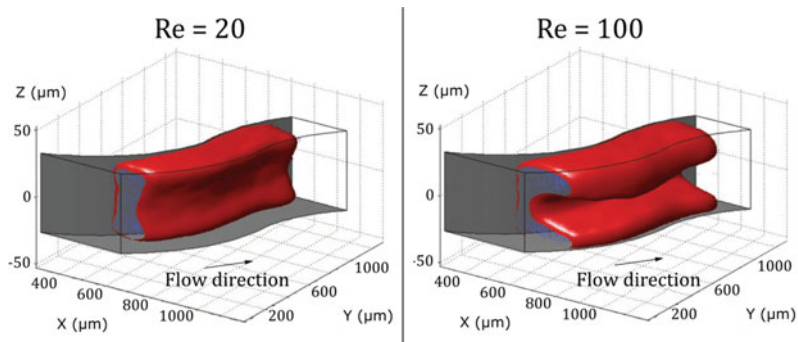


Fig. 16.23 Reconstruction of the contact interface between two fluids in the curved micromixer shown in Fig. 16.19. The reconstruction was performed in the area highlighted by the red rectangle in Fig. 16.19 for $Re = 20$ (left) and $Re = 100$ (right). The reconstructed interface shows a good agreement with the numerical simulations (figure adapted from [42])

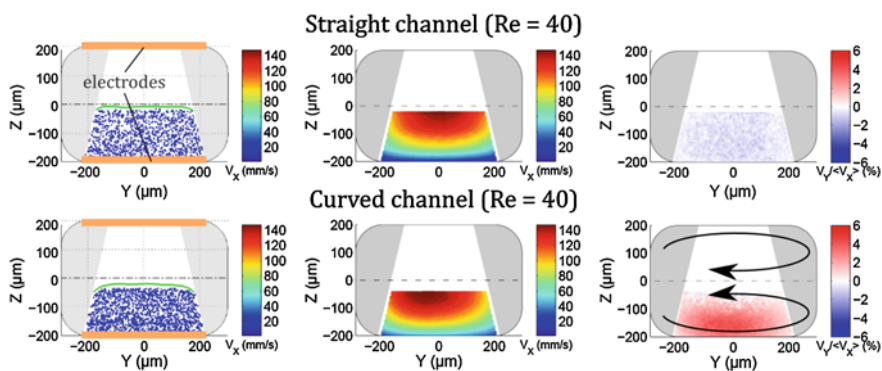


Fig. 16.24 Reconstruction of the contact interface between fuel and oxidant in microfluidic fuel cells (left), axial velocity (center) and transversal velocity (right). The transversal velocity magnitude was normalized over the average axial velocity. The gray areas represent regions where the measurement was not possible due to distortion of the channel borders. Data are reported for microfluidic fuel cells with a straight (top) and curved (bottom) channel

get the velocity information in the other half of the channel the experiment can be repeated easily after seeding the other half of the channel flow. Other applications and extensions of the APTV technique can be found in [6, 9, 14, 34, 40, 41, 47, 57].

References

1. Axelrod, D., Burghardt, T.P., Thompson, N.L.: Total internal reflection fluorescence. *Annu. Rev. Biophys. Bioeng.* **13**(1), 247–268 (1984). DOI 10.1146/annurev.bb.13.060184.001335. URL <https://doi.org/10.1146/annurev.bb.13.060184.001335>
2. Baczymalski, D., Karnbach, F., Yang, X., Mutschke, G., Uhlemann, M., Eckert, K., Cierpka, C.: On the electrolyte convection around a hydrogen bubble evolving at a microelectrode under the influence of a magnetic field. *J. Electrochem. Soc.* **163**(9), E248–E257 (2016). DOI 10.1149/2.0381609jes. URL <https://jes.ecsdl.org/content/163/9/E248.abstract>
3. Baczymalski, D., Karnbach, F., Mutschke, G., Yang, X., Eckert, K., Uhlemann, M., Cierpka, C.: Growth and detachment of single hydrogen bubbles in a magnetohydrodynamic shear flow. *Phys. Rev. Fluids* **2**(9), 093701 (2017). American Physical Society. DOI 10.1103/PhysRevFluids.2.093701, URL <https://link.aps.org/doi/10.1103/PhysRevFluids.2.093701>
4. Baczymalski, D., Weier, T., Kähler, C.J., Cierpka, C.: Near-wall measurements of the bubble- and Lorentz-force-driven convection at gas-evolving electrodes. *Exp. Fluids* **56**(8), 1–13 (2015). DOI 10.1007/s00348-015-2029-0. URL <https://doi.org/10.1007/s00348-015-2029-0>
5. Balzer, R., Vogt, H.: Effect of electrolyte flow on the bubble coverage of vertical gas-evolving electrodes. *J. Electrochem. Soc.* **150**(1), E11–E16 (2003). DOI 10.1149/1.1524185. URL <https://jes.ecsdl.org/content/150/1/E11.abstract>
6. Barnkob, R., Nama, N., Ren, L., Huang, T.J., Costanzo, F., Kähler, C.J.: Acoustically driven fluid and particle motion in confined and leaky systems. *Phys. Rev. Appl.* **9**(1), 014027 (2018)
7. Barz, D.P., Zadeh, H.F., Ehrhard, P.: Measurements and simulations of time-dependent flow fields within an electrokinetic micromixer. *J. Fluid Mech.* **676**, 265–293 (2011). DOI 10.1017/jfm.2011.44. URL <https://doi.org/10.1017/jfm.2011.44>
8. Bendat, J.S., Piersol, A.G.: *Random Data: Analysis and Measurement Procedures*, 4th edn. Wiley, New York (2012). DOI 10.1002/9781118032428. URL <https://doi.org/10.1002/9781118032428>
9. Bolaños-Jiménez, R., Rossi, M., Rivas, D.F., Kähler, C.J., Marin, A.: Streaming flow by oscillating bubbles: quantitative diagnostics via particle tracking velocimetry. *J. Fluid Mech.* **820**, 529–548 (2017)
10. Bourdon, C.J., Olsen, M.G., Gorby, A.D.: The depth of correlation in micro-PIV for high numerical aperture and immersion objectives. *J. Fluids Eng.* **128**(4), 883–886 (2006). DOI 10.1115/1.2201649. URL <https://doi.org/10.1115/1.2201649>
11. Cevheri, N., Yoda, M.: Evanescent-wave particle velocimetry studies of combined electroosmotic and Poiseuille flow. In: *Proceedings of the 10th International Symposium on Particle Image Velocimetry (PIV13)*. Delft University of Technology, Faculty of Mechanical, Maritime and Materials Engineering, and Faculty of Aerospace Engineering (2013). DOI 10.1115/MNHMT2012-75274. URL <https://doi.org/10.1115/MNHMT2012-75274>
12. Cierpka, C., Kähler, C.J.: Particle imaging techniques for volumetric three-component (3D3C) velocity measurements in microfluidics. *J. Vis.* **15**(1), 1–31 (2012). DOI 10.1007/s12650-011-0107-9. URL <https://doi.org/10.1007/s12650-011-0107-9>
13. Cierpka, C., Lütke, B., Kähler, C.J.: Higher order multi-frame particle tracking velocimetry. *Exp. Fluids* **54**(5), 1533 (2013). DOI 10.1007/s00348-013-1533-3. URL <https://doi.org/10.1007/s00348-013-1533-3>
14. Cierpka, C., Rossi, M., Segura, R., Mastrangelo, F., Kähler, C. J.: A comparative analysis of the uncertainty of astigmatism- μ PTV, stereo- μ PIV, and μ PIV. *Exp. Fluids* **52**(3), 605–615 (2012)
15. Cierpka, C., Segura, R., Hain, R., Kähler, C.J.: A simple single camera 3C3D velocity measurement technique without errors due to depth of correlation and spatial averaging for microfluidics. *Meas. Sci. Technol.* **21**(4), 045401 (2010)

16. Choban, E.R., Markoski, L.J., Wieckowski, A., Kenis, P.J.A.: Microfluidic fuel cell based on laminar flow. *J. Power Sources* **128**(1), 54–60 (2004)
17. Deen, W.: *Analysis of Transport Phenomena*, Topics in Chemical Engineering, 2nd edn. Oxford University Press, New York (2012). URL <https://global.oup.com/academic/product/analysis-of-transport-phenomena-9780199740253?cc=de&lang=en&>
18. Dutta, P., Beskok, A.: Analytical solution of combined electroosmotic/pressure driven flows in two-dimensional straight channels: Finite Debye layer effects. *Anal. Chem.* **73**(9), 1979–1986 (2001)
19. Gui, L., Merzkirch, W.: Generating arbitrarily sized interrogation windows for correlation-based analysis of particle image velocimetry recordings. *Exp. Fluids* **24**(1), 66–69 (1998)
20. Hertlein, C., Riefler, N., Eremina, E., Wriedt, T., Eremin, Y., Helden, L., Bechinger, C.: Experimental verification of an exact evanescent light scattering model for TIRM. *Langmuir* **24**(1), 1–4 (2008). DOI 10.1021/la703322d. URL <https://doi.org/10.1021/la703322d>
21. Huang, P., Breuer, K.S.: Direct measurement of anisotropic near-wall hindered diffusion using total internal reflection velocimetry. *Phys. Rev. E* **76**(4), 046,307 (2007). DOI 10.1103/PhysRevE.76.046307. URL <https://doi.org/10.1103/PhysRevE.76.046307>
22. Huang, P., Guasto, J.S., Breuer, K.S.: Direct measurement of slip velocities using three-dimensional total internal reflection velocimetry. *J. Fluid Mech.* **566**, 447–464 (2006). DOI 10.1115/IMECE2005-79938. URL <https://doi.org/10.1115/IMECE2005-79938>
23. Huang, P., Guasto, J.S., Breuer, K.S.: The effects of hindered mobility and depletion of particles in near-wall shear flows and the implications for nanovelocimetry. *J. Fluid Mech.* **637**, 241–265 (2009). DOI 10.1017/S0022112009990656. URL <https://doi.org/10.1017/S0022112009990656>
24. Inoué, S., Spring, K.R.: *Video Microscopy: The Fundamentals*, 2nd edn. Language of Science. Springer, New York (1997)
25. Israelachvili, J.N.: *Intermolecular and Surface Forces*. Academic Press (1992). URL <http://www.sciencedirect.com/science/book/9780123751829>
26. Jin, S., Huang, P., Park, J., Yoo, J.Y., Breuer, K.S.: Near-surface velocimetry using evanescent wave illumination. *Exp. Fluids* **37**(6), 825–833 (2004). DOI 10.1007/s00348-004-0870-7. URL <https://doi.org/10.1007/s00348-004-0870-7>
27. Kähler, C.J., Astarita, T., Vlachos, P.P., Sakakibara, J., Hain, R., Discetti, S., La Foy, R., Cierpka, C.: Main results of the 4th International PIV Challenge. *Exp. Fluids* **57**(6), 97 (2016). DOI 10.1007/s00348-016-2173-1. URL <https://doi.org/10.1007/s00348-016-2173-1>
28. Kähler, C.J., Scharnowski, S., Cierpka, C.: On the uncertainty of digital PIV and PTV near walls. *Exp. Fluids* **52**(6), 1641–1656 (2012). DOI 10.1007/s00348-012-1307-3. URL <http://dx.doi.org/10.1007/s00348-012-1307-3>
29. Kauffmann, P., Loire, S., Mezic, I., Meinhart, C.: Proper orthogonal decomposition based 3d micropiv: application to electrothermal flow study. In: PIV13; 10th International Symposium on Particle Image Velocimetry, Delft, The Netherlands, July 1-3, 2013. Delft University of Technology, Faculty of Mechanical, Maritime and Materials Engineering, and Faculty of Aerospace Engineering (2013)
30. Kazoe, Y., Yoda, M.: Experimental study of the effect of external electric fields on interfacial dynamics of colloidal particles. *Langmuir* **27**(18), 11481–11488 (2011). DOI 10.1021/la202056b. URL <https://doi.org/10.1021/la202056b>
31. Kazoe, Y., Yoda, M.: Measurements of the near-wall hindered diffusion of colloidal particles in the presence of an electric field. *Appl. Phys. Lett.* **99**(12), 124,104 (2011). DOI 10.1063/1.3643136. URL <https://doi.org/10.1063/1.3643136>
32. Kihm, K., Banerjee, A., Choi, C., Takagi, T.: Near-wall hindered Brownian diffusion of nanoparticles examined by three-dimensional ratiometric total internal reflection fluorescence microscopy (3D RTIRFM). *Exp. Fluids* **37**(6), 811–824 (2004). DOI 10.1007/s00348-004-0865-4. URL <https://doi.org/10.1007/s00348-004-0865-4>

33. Kloosterman, A., Hierck, B., Westerweel, J., Poelma, C.: Quantification of blood flow and topology in developing vascular networks. *PLoS One* **9**(5), e96,856 (2014). DOI 10.1371/journal.pone.0096856. URL <https://doi.org/10.1371/journal.pone.0096856>
34. Kumar, A., Cierpka, C., Williams, S.J., Kähler, C.J., Wereley, S.T.: 3D3C velocimetry measurements of an electrothermal microvortex using wavefront deformation PTV and a single camera. *Microfluidics and Nanofluidics*. **10**(2), 355–365 (2011)
35. Kwon, J.S., Wereley, S.T.: Light-actuated electrothermal microfluidic motion: experimental investigation and physical interpretation. *Microfluid. Nanofluidics* **19**(3), 609–619 (2015)
36. Li, H., Yoda, M.: An experimental study of slip considering the effects of non-uniform colloidal tracer distributions. *J. Fluid Mech.* **662**, 269–287 (2010). DOI 10.1017/S0022112010003198. URL <https://doi.org/10.1017/S0022112010003198>
37. Li, H.F., Yoda, M.: Multilayer nano-particle image velocimetry (MnPIV) in microscale Poiseuille flows. *Meas. Sci. Technol.* **19**(7), 075,402 (2008). DOI 10.1088/0957-0233/19/7/075402. URL <https://doi.org/10.1088/0957-0233/19/7/075402>
38. Li, Z., Déramo, L., Lee, C., Monti, F., Yonger, M., Tabeling, P., Chollet, B., Bresson, B., Tran, Y.: Near-wall nanovelocimetry based on total internal reflection fluorescence with continuous tracking. *J. Fluid Mech.* **766**, 147–171 (2015). DOI 10.1017/jfm.2015.12. URL <https://doi.org/10.1017/jfm.2015.12>
39. Lubetkin, S.: The motion of electrolytic gas bubbles near electrodes. *Electrochimica Acta* **48**(4), 357–375 (2002). DOI 10.1016/S0013-4686(02)00682-5. URL <https://www.sciencedirect.com/science/article/pii/S0013468602006825>
40. Marin, A., Liepelt, R., Rossi, M., Kähler, C. J.: Surfactant-driven flow transitions in evaporating droplets. *Soft Matter* **12**(5), 1593–1600 (2016)
41. Marin, A., Rossi, M., Rallabandi, B., Wang, C., Hilgenfeldt, S., Kähler, C. J.: Three-dimensional phenomena in microbubble acoustic streaming. *Phys. Rev. Appl.* **3**(4), 041001 (2015)
42. Mastrangelo, F., Rossi, M., Cierpka, C., Kähler, C.J., Pennella, F., Rasponi, M., Piraino, F., Redaelli, A., Morbiducci, U.: Reconstruction of the interface between two fluids in microfluidic-mixers using astigmatic particle imaging, 2nd European Conference in Microfluidics, Toulouse, France, December 8–10 (2010)
43. Meinhart, C.D., Wereley, S.T., Santiago, J.G.: PIV measurements of a microchannel flow. *Exp. Fluids* **27**(5), 414–419 (1999). DOI 10.1007/s003480050366. URL <https://doi.org/10.1007/s003480050366>
44. Meinhart, C.D., Wereley, S.T., Santiago, J.G.: A PIV algorithm for estimating time-averaged velocity fields. *J. Fluids Eng.* **122**(2), 285–289 (2000). DOI 10.1115/1.483256. URL <https://doi.org/10.1115/1.483256>
45. Monazami, R., Manzari, M.T.: Analysis of combined pressure-driven electroosmotic flow through square microchannels. *Microfluid. Nanofluidics* **3**(1), 123–126 (2007). DOI 10.1007/s10404-005-0065-4. URL <https://doi.org/10.1007/s10404-005-0065-4>
46. Morgan, H., Green, N.G.: AC electrokinetics. Research Studies Press, (2003)
47. Muller, P. B., Rossi, M., Marin, A., Barnkob, R., Augustsson, P., Laurell, T., Kähler, C.J., Bruus, H.: Ultrasound-induced acoustophoretic motion of microparticles in three dimensions. *Phys. Rev. E* **88**(2), 023006 (2013)
48. Needham, J.A., Sharp, J.S.: Watch your step! A frustrated total internal reflection approach to forensic footwear imaging. *Sci. Rep.* **6** (2016). DOI 10.1038/srep21290. URL <https://doi.org/10.1038/srep21290>
49. Nguyen, N.T., Wu, Z.G.: Micromixers—a review. *J. Micromech. Microeng.* **15**(2), R1–R16 (2004)
50. Poelma, C., Van der Heiden, K., Hierck, B.P., Poelmann, R.E., Westerweel, J.: Measurements of the wall shear stress distribution in the outflow tract of an embryonic chicken heart. *J. R. Soc. Interface* **7**(42), 91–103 (2010). DOI 10.1098/rsif.2009.0063. URL <https://doi.org/10.1098/rsif.2009.0063>

51. Poelma, C., Hierck, B.P.: Hemodynamics in the developing cardiovascular system. In: Becker, S., Kuznetsov, A. (eds.) *Heat Transfer and Fluid Flow in Biological Processes*, pp. 371–405. Academic Press (2015). DOI 10.1016/B978-0-12-408077-5.00013-4. URL <https://doi.org/10.1016/B978-0-12-408077-5.00013-4>
52. Poelma, C., Kloosterman, A., Hierck, B.P., Westerweel, J.: Accurate blood flow measurements: are artificial tracers necessary? *PloS One* **7**(9), e45,247 (2012). DOI 10.1371/journal.pone.0045247. URL <https://doi.org/10.1371/journal.pone.0045247>
53. Poelma, C., Vennemann, P., Lindken, R., Westerweel, J.: In vivo blood flow and wall shear stress measurements in the vitelline network. *Exp. Fluids* **45**(4), 703–713 (2008). DOI 10.1007/s00348-008-0476-6. URL <https://doi.org/10.1007/s00348-008-0476-6>
54. Pouya, S., Koochesfahani, M., Snee, P., Bawendi, M., Nocera, D.: Single quantum dot (QD) imaging of fluid flow near surfaces. *Exp. Fluids* **39**(4), 784–786 (2005). DOI 10.1007/s00348-005-0004-x. URL <https://doi.org/10.1007/s00348-005-0004-x>
55. Ramos, A., Morgan, H., Green, N.G., Castellanos, A.: Ac electrokinetics: a review of forces in microelectrode structures. *J. Phys. D: Appl. Phys.* **31**(18), 2338 (1998)
56. Rossi, M., Cierpka, C., Segura, R., Kähler, C.J.: Volumetric reconstruction of the 3D boundary of stream tubes with general topology using tracer particles. *Meas. Sci. Technol.* **22**(10), 105405 (2011)
57. Rossi, M., Kähler, C.J.: Experimental characterization of the effect of Dean vortices on microfluidic fuel cells, 4th European Conference in Microfluidics, Limerick, Ireland, December 10–12 (2014)
58. Rossi, M., Kähler, C.J.: Optimization of astigmatic particle tracking velocimeters. *Exp. Fluids* **55**(9), 1–13 (2014)
59. Rossi, M., Segura, R., Cierpka, C., Kähler, C.J.: On the effect of particle image intensity and image preprocessing on the depth of correlation in micro-PIV. *Exp. Fluids* **52**(4), 1063–1075 (2012). DOI 10.1007/s00348-011-1194-z. URL <https://doi.org/10.1007/s00348-011-1194-z>
60. Sadr, R., Anoop, K., Khader, R.: Effects of surface forces and non-uniform out-of-plane illumination on the accuracy of nPIV velocimetry. *Meas. Sci. Technol.* **23**(5), 055,303 (2012). DOI 10.1088/0957-0233/23/5/055303. URL <http://stacks.iop.org/0957-0233/23/i=5/a=055303?key=crossref.0d604a3da34abe9a910046b1125f2779>
61. Sadr, R., Hohenegger, C., Li, H., Mucha, P.J., Yoda, M.: Diffusion-induced bias in near-wall velocimetry. *J. Fluid Mech.* **577**, 443–456 (2007). DOI 10.1007/s00348-008-0491-7. URL <https://doi.org/10.1007/s00348-008-0491-7>
62. Sadr, R., Yoda, M., Zheng, Z., Conlisk, A.T.: An experimental study of electro-osmotic flow in rectangular microchannels. *J. Fluid Mech.* **506**, 357–367 (2004). DOI 10.1017/S0022112004008626. URL <https://doi.org/10.1017/S0022112004008626>
63. Squires, T.M., Quake, S.R.: Microfluidics: fluid physics at the nanoliter scale. *Rev. Mod. Phys.* **77**(3), 977–1026 (2005)
64. Stroock, A.D., Dertinger, S.K., Ajdari, A., Mezić, I., Stone, H.A., Whitesides, G.M.: Chaotic mixer for microchannels. *Science* **295**(5555), 647–651 (2002)
65. Vennemann, P., Kiger, K., Lindken, R., Groenendijk, B.C.W., Stekelenburg-de Vos, S., ten Hagen, T.L.M., Ursem, N.T.C., Poelmann, R.E., Westerweel, J., Hierck, B.P.: In vivo micro particle image velocimetry measurements of blood-plasma in the embryonic avian heart. *J. Biomech.* **39**(7), 1191–1200 (2006). DOI 10.1016/j.jbiomech.2005.03.015. URL <https://doi.org/10.1016/j.jbiomech.2005.03.015>
66. Wang, W., Huang, P.: Hybrid algorithm for extracting accurate tracer position distribution in evanescent wave nano-velocimetry. *Exp. Fluids* **57**(2), 1–8 (2016). DOI 10.1007/s00348-016-2116-x. URL <https://doi.org/10.1007/s00348-016-2116-x>
67. Weier, T., Landgraf, S.: The two-phase flow at gas-evolving electrodes: Bubble-driven and Lorentz-force-driven convection. *Eur. Phys. J. Spec. Top.* **220**(1), 313–322 (2013). DOI 10.1140/epjst/e2013-01816-1. URL <https://doi.org/10.1140/epjst/e2013-01816-1>

68. Wereley, S.T., Gui, L., Meinhart, C.D.: Advanced algorithms for microscale particle image velocimetry. *AIAA J.* **40**(6), 1047–1055 (2002). DOI 10.2514/2.1786. URL <https://arc.aiaa.org/doi/abs/10.2514/2.1786>
69. Wereley, S.T., Meinhart, C.D.: Recent advances in micro-particle image velocimetry. *Annu. Rev. Fluid Mech.* **42** (2010). DOI 10.1146/annurev-fluid-121108-145427. URL <https://doi.org/10.1146/annurev-fluid-121108-145427>
70. Westerweel, J., Geelhoed, P., Lindken, R.: Single-pixel resolution ensemble correlation for micro-PIV applications. *Exp. Fluids* **37**(3), 375–384 (2004). DOI 10.1007/s00348-004-0826-y. URL <https://doi.org/10.1007/s00348-004-0826-y>
71. Yoda, M., Cevheri, N.: Using shear and DC electric fields to manipulate and self-assemble dielectric particles on microchannel walls. In: *Journal of Nanotechnology in Engineering and Medicine*, pp. V007T09A012–V007T09A012. American Society of Mechanical Engineers (2014). DOI 10.1115/IMECE2014-37547. URL <https://doi.org/10.1115/IMECE2014-37547>
72. Zettner, C.M., Yoda, M.: Particle velocity field measurements in a near-wall flow using evanescent wave illumination. *Exp. Fluids* **34**(1), 115–121 (2003). DOI 10.1007/s00348-002-0541-5. URL <https://doi.org/10.1007/s00348-002-0541-5>

Chapter 17

Applications: Stereo PIV and Multiplane Stereo PIV

17.1 Stereo PIV Applied to a Vortex Ring Flow

Contributed by:

C. Willert

The various methods of image reconstruction and calibration as described in Sect. 8.1 were applied in the measurement of the unsteady vortex ring flow field in 1995. Figure 17.1 outlines a vortex ring generator having a simple construction with very reproducible flow characteristics. The vortex ring is generated by discharging a bank of electrolytic capacitors (60 000 μF) through a pair of loudspeakers which are mounted facing inward on to two sides of a wooden box. By forcing the loudspeaker membranes inward, air is impulsively forced out of a cylindrical, sharpened nozzle (inner diameter = 34.7 mm) on the top of the box. The shear layer formed at the tip of the nozzle then rolls up into a vortex ring and separates from the nozzle as the membranes move back to their equilibrium positions due to the decay in supply voltage. As long as the charging voltage is kept constant, the formation of the vortex ring will be very reproducible. The generator also has a seeding pipe with a check valve allowing the interior of the box and ultimately the core of the vortex ring to be seeded.

Imaging Configuration and Hardware

A noteworthy feature of the imaging configuration outlined in Fig. 17.2—which has also been used for the error estimation given in Sect. 8.1—is that the cameras are positioned on both sides of the light sheet. This arrangement allows both cameras to make use of the much higher forward scattering properties of the small (1 μm) oil droplets used for seeding. The principal viewing axes are both around 35° from the light sheet normal such that the combined opening angle is approximately 70° near the center of the image.

An overview of the Digital Content to applications on stereo PIV can be found at [DC17.1].

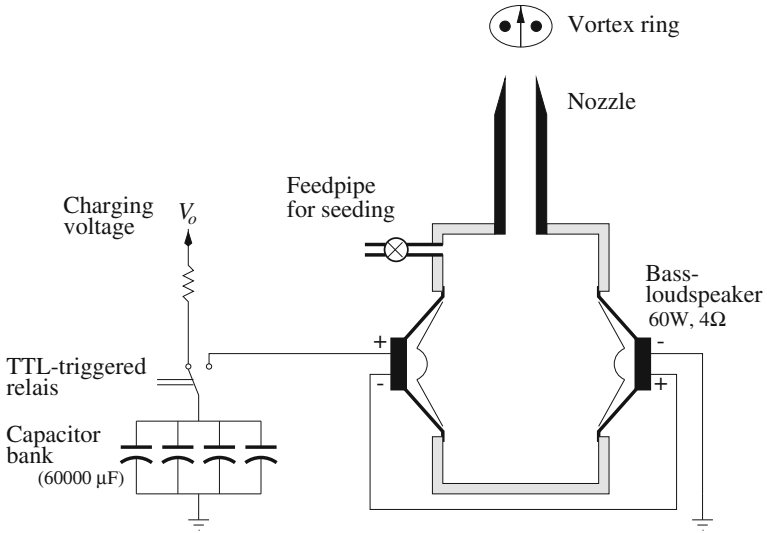


Fig. 17.1 Schematic of the vortex ring generator used to obtain an unsteady, yet reproducible flow field

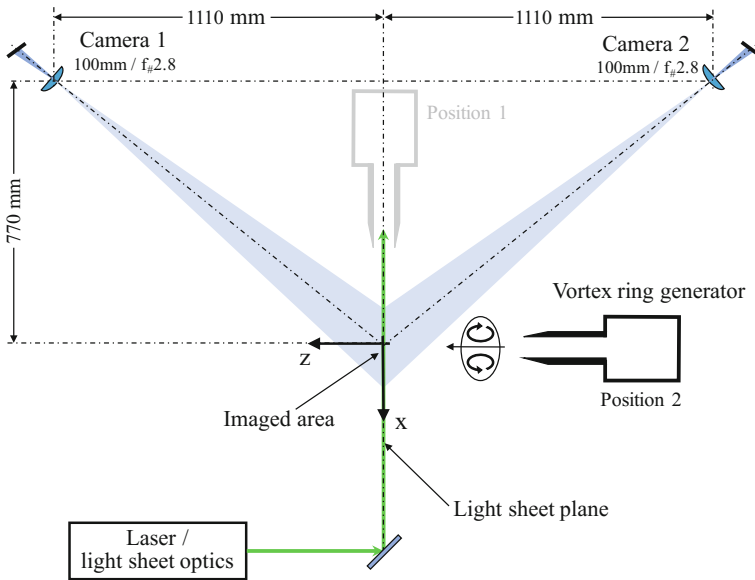
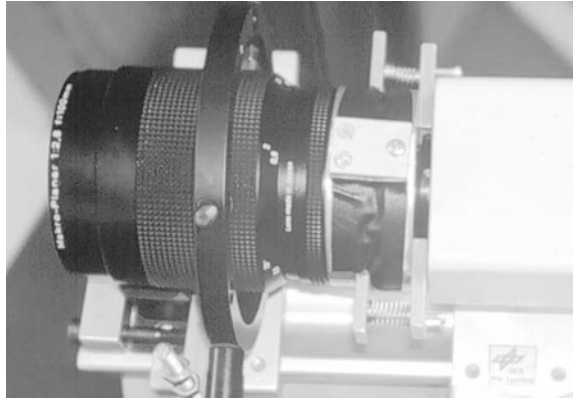


Fig. 17.2 Stereoscopic imaging configuration in forward scattering mode for both cameras

Fig. 17.3 A specially built tilt-adapter between the lens and the sensor allows adjustment according to the Scheimpflug criterion



A pair of 100 mm, $f_{\#}$ 2.8 objective lenses constitute the recording optics and are connected to the CCD cameras using specially built tilt-adapters (see Fig. 17.3). Using a pair of set screws on each of the adapters, the angle between the lens and the sensor (image plane) can be easily and precisely adjusted to meet the Scheimpflug imaging criterion (see Sect. 8.1). A live display of the particle images at large f -numbers permits an accurate adjustment within minutes. These first prototype Scheimpflug adapters had the disadvantage that the field of view changed when the Scheimpflug angle was adjusted. The following generation of adapters – now commonly available – keep the lens fixed on the desired field of view while the sensor plane (CCD) is rotated within the plane of focus (Table 17.1).

In the imaging arrangement shown in Fig. 17.2 the Scheimpflug angle (ϕ in Fig. 8.1b) was measured to be approximately 2.7° . The field of view covered about 145 mm horizontally by 115 mm vertically across the center of the image. The edge loss due to the Scheimpflug imaging arrangement was about 5 mm vertical from side to side, but since both cameras were positioned nearly symmetrically, the field of view could be matched very well, thereby allowing three-dimensional PIV measurements across the entire sensor area. This is an advantage over the “classical” stereoscopic arrangement in which both cameras view from the same side of the light sheet because the non-overlapping areas are of no use in the three-dimensional reconstruction.

The cameras used for this experiment are based on a full frame interline transfer CCD sensor with a 1008 H by 1018 V pixel resolution. The light sheet was generated by a frequency doubled, double oscillator Nd:YAG laser with more than 300 mJ per pulse. Synchronization between the cameras and the laser was achieved by means of a multiple channel sequencer. Since one of the cameras was not capable of operating in a triggered mode it provided the master timing of the entire PIV recording system. The second was operated in an asynchronously triggered mode. Two separate personal computers with interface cards captured the image pairs from the cameras at a common image pair rate of 5 Hz. (In principle the use of a common PC for both cameras would have also been possible.) One of the computers provided the trigger

Table 17.1 PIV recording parameters for vortex ring

Flow geometry	Flow with strong out-of-plane component
Maximum in-plane velocity	$U_{\max} \approx 3 \text{ m/s}$
Field of view	$145 \times 115 \text{ mm}^2 (W \times H)$
Interrogation volume	$3.8 \times 3.8 \times 2.5 \text{ mm}^3 (W \times H \times D)$
Dynamic spatial range	$\text{DSR} \approx 50 : 1$
Dynamic velocity range	$\text{DVR} \approx 100 : 1$
Observation distance	$Z_0 \approx 1500 \text{ mm}$
Recording method	Dual frame/single exposure
Ambiguity removal	Frame separation (frame-straddling)
Recording medium	Full frame interline transfer CCD 1008 × 1018 pixel
Recording lens	$f = 100 \text{ mm}$, $f_{\#} = 2.8$
Magnification	$m \approx 0.08 (11.8 \mu\text{m}/\text{pixel})$
Illumination	Freq. doubled Nd:YAG laser 300 mJ/pulse at 532 nm
Pulse delay	$\Delta t = 200 \dots 500 \mu\text{s}$
Seeding material	Oil droplets ($d_p \approx 1 \mu\text{m}$)

pulse for the vortex generator as soon as the image acquisition was started. By adding a time delay (or by moving the vortex generator back and forth) the position of the vortex ring within the PIV recording could be adjusted.

The light sheet thickness was set at approximately 2.5 mm, while the pulse delay was varied within $300 \leq \Delta t \leq 500 \mu\text{s}$ with the vortex ring propagating in-line with the light sheet (position 1 in Fig. 17.2), and $\Delta t = 200 \mu\text{s}$ while propagating normal to the light sheet (position 2 in Fig. 17.2). With maximum velocities of 3.5 m/s this translated to maximum particle displacements of 0.7 mm for the vortex ring passage normal to the light sheet. Effectively, the loss of pairs was kept to less than 30% thereby ensuring a high data yield even in regions of high out-of-plane motion. The f -number was set to $f_{\#} = 2.8$.

Experimental Results

Initially the nozzle of the vortex ring generator was placed collinearly with the light sheet to provide cross-sectional cuts through the vortex ring (Fig. 17.4). This provided reference data as well as information on the ring's circulation and stability. In the second configuration, that is, position 2 in Fig. 17.2, the generator was placed normal to the light sheet. Figure 17.5 shows a pair of two-component velocity fields prior to their combination into a three-component data set. The stereoscopic view is clearly visible. Stereoscopic reconstruction using Eqs. (8.3), (8.5) and (8.8) then produces the desired three-component data set of Fig. 17.6.

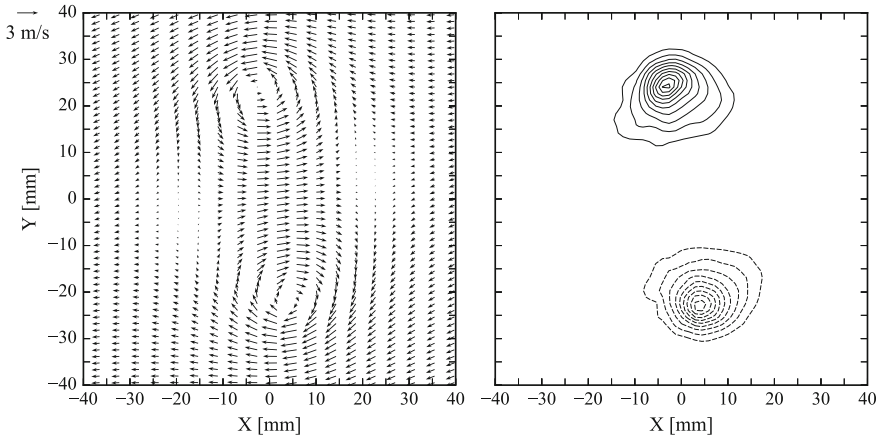


Fig. 17.4 PIV velocity (left) and vorticity data (right) in the symmetry plane of the vortex ring. To enhance the visibility of the flow’s features a velocity of $U = 1.25$ m/s, $V = 0.25$ m/s has been removed and only every third vector is shown horizontally. The propagation of the ring is left to right and slightly upward (the nozzle was inclined with the horizontal). The vorticity contours are spaced in intervals of 100 s⁻¹ excluding 0

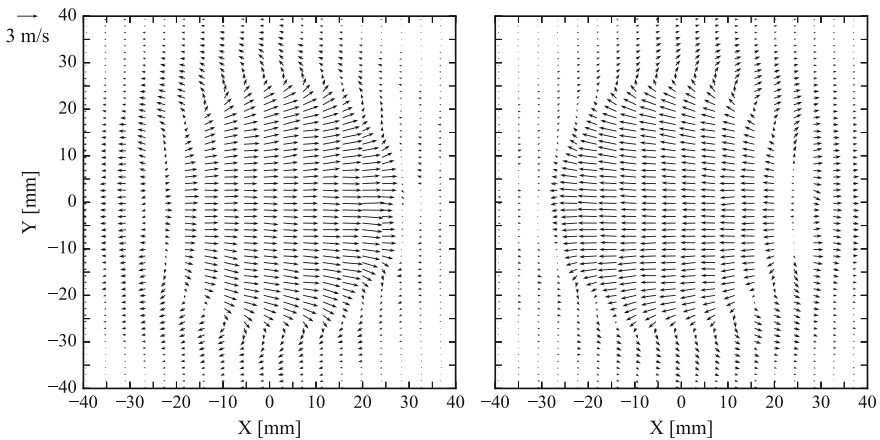


Fig. 17.5 Two-component PIV velocity data of the vortex ring while passing through the light sheet as viewed by camera 1 (left) and camera 2 (right); only every third vector is shown horizontally

In terms of processing, the image back projection was chosen such that the magnification factor was constant at 8.5 pixel mm⁻¹ in all images after reconstruction. The final image size of 1280 horizontal by 1024 vertical pixel is about 25% larger than the original images. An interrogation area of 32×32 pixel with an overlap (oversampling) of 66% was chosen. In physical space the interrogation window covers 3.8×3.8 mm² while the grid spacing is 1.4×1.4 mm². A priori image contrast enhancement – either by adaptive background subtraction using a 7×7 pixel kernel

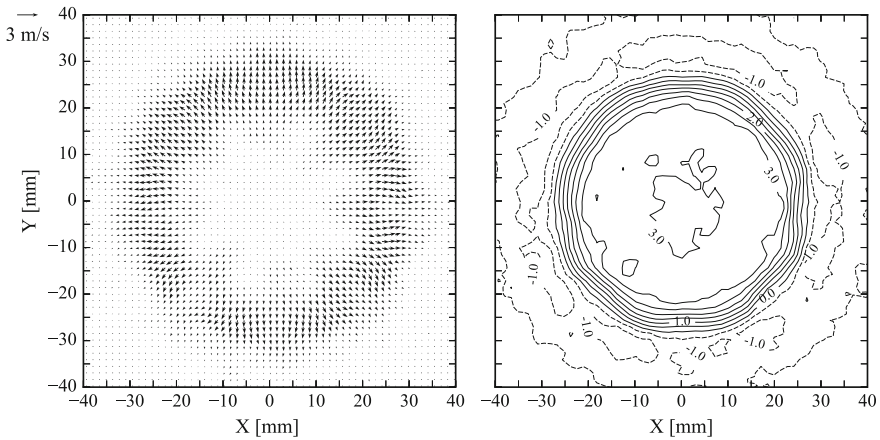


Fig. 17.6 Reconstructed three-component PIV velocity data obtained by combining the data sets shown in Fig. 17.5. The out-of-plane velocity component w is shown as a contour plot on the right (contour level intervals of 0.5 m/s)

highpass filter or local normalization (see Sect. 5.3.2.1) – significantly improved the data yield by bringing most particle images to the same intensity level. Due this preprocessing operation the data sets are essentially without outliers and in principle could be processed with even smaller sampling windows allowing the spatial resolution to be further increased.

17.2 Multiplane Stereo PIV

Contributed by:

C.J. Kähler

Introduction

Particle Image Velocimetry (PIV) has become a widely applied technique whenever the spatial distribution of the velocity together with its derivatives helps to understand the physics of the flow. However, quite often the distribution of the velocity within one single plane, captured at one instant in time, does not yield the information required to answer fluid-mechanical questions. To overcome these limitations a stereoscopic PIV based technique has been developed, which is well suited to determine many fluid-mechanical quantities with high accuracy and spatial resolution at any flow velocity [6, 9, 11, 12]. This technique is reliable, robust and easy to handle. Furthermore it is based on standard PIV equipment and evaluation procedures so that available PIV systems can be easily extended.

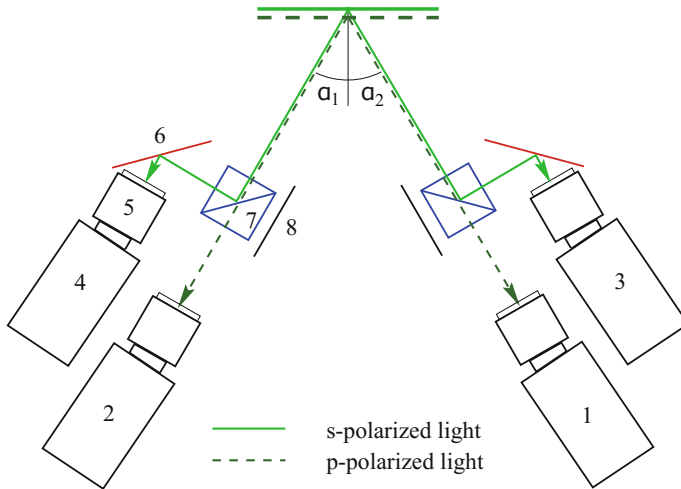


Fig. 17.7 Schematic setup of the recording system. 1-4 digital cameras, 5 lens, 6 mirror, 7 polarizing beam-splitter cube with dielectric coating between the two right-angle prisms, 8 absorbing material, α opening angle

The multiplane stereo PIV system, developed for applications in air flows in particular, consists of a four-pulse laser system delivering orthogonally polarized light, two pairs of high resolution progressive scan CCD cameras in an angular imaging configuration with Scheimpflug correction, two high reflectivity mirrors and a pair of polarizing beam-splitter cubes according to Fig. 17.7.

After the illumination of the tracer particles with orthogonally linearly polarized light, the polarizing beam-splitter cube (7) separates the incident wave-front scattered from the particles into two parts according to the state of polarization. The separation based on polarization works perfectly as long as the radius of the spherical particles is comparable to the wavelength of the laser light (see also Sect. 2.1 and [7, 13] for the generation of appropriate particles) and the observation direction is properly aligned relative to the direction of the polarization vector. In the case that these requirements cannot be fulfilled a frequency based multiplane stereo PIV approach can be applied but in this case the laser system has to be modified to generate the required frequency shift [15].

For the illumination of the tracer particles the beams of four independent laser-oscillators need to be combined in such a way that the linearly polarized light sheets can be positioned independently with respect to each other. This can be easily and precisely done by means of the four pulse system shown in Fig. 17.8.

The appropriate method of adjusting the displacement between the orthogonally polarized light-sheets depends on the desired distance [8, 9]. Small separations between the orthogonally polarized light-sheet pairs (up to a few millimeters) can be generated by a simple rotation of mirror 8c in the re-combination optics around the axis perpendicular to the laser-beam plane [12]. For a wider range of light-sheet

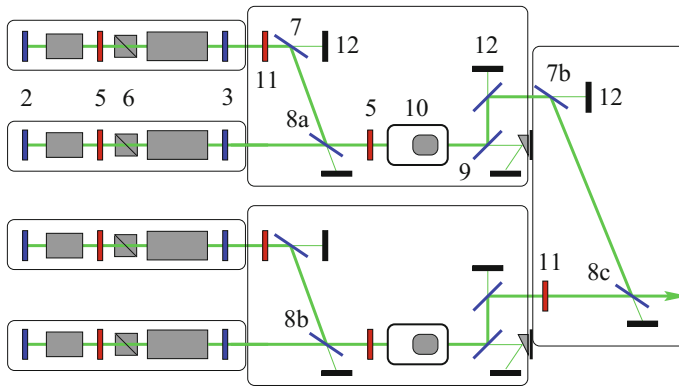


Fig. 17.8 Four-pulse laser system. 1 Pump cavity, 2 Full reflective mirror, 3 Partially transmitting mirror, 4 Pockels cell, 5 $\lambda/4$ retardation plate, 6 Glan-Laser polarizer, 7 Mirror, 8 Dielectric polarizer, 9 Dichroic mirror, 10 Frequency doubler crystal with phase angle adjustment, 11 $\lambda/2$ retardation plate, 12 Beam dump

spacings (up to a few cm) and independent positioning of both beam-pairs, it is useful to remove mirror 7b along with the beam dump (12) such that two spatially separated laser beams with orthogonally polarized radiation emerge. Using two separate light-sheet-optics (one for each polarization) each with a 45° mirror behind the last lens, all positions are possible by moving the mirrors [8]. Once calibrated, the actual position of each pair of light-sheets is determined with a micrometer scale.

The multiple plane stereo system is well suited to determine different fluid-mechanical quantities without perspective error simply by changing the time sequence or light sheet position. For constant pulse separation ($\Delta t = t_2 - t_1 = t_3 - t_2 = t_4 - t_3$) and overlapping light sheets (see Fig. 17.9), a time sequence of three velocity fields can be measured at any flow velocity by cross-correlating the first acquired gray-level distribution with the second, the second with the third and the third with the gray-level distribution from the last illumination. In this mode it is also possible to increase the accuracy of the velocity measurement by using the Multiframe PIV evaluation approach outlined in Sect. 5.3 and [3]. By increasing the time delay between the second and third illumination ($\Delta t = t_2 - t_1 = t_4 - t_3 < t_3 - t_2$) the first order estimation of the acceleration field in its Lagrangian and Eulerian form can be calculated to study the dynamic behavior and the interaction processes of moving flow structures [5]. For large time delays between a pair of images being acquired ($\Delta t = t_2 - t_1 = t_4 - t_3 \ll t_3 - t_2$), time correlations can be measured for instance [8].

When the light sheet pairs with equal polarization are spatially separated, as indicated in Fig. 17.10, further important information about the flow field can be achieved. For small separations or partially overlapping light-sheets, the spatial distribution of all three vorticity vector components can be measured when the orthogonally polarized light-pulses are fired simultaneously ($t_1 = t_3$ and $t_2 = t_4$). In addition, all

Fig. 17.9 Timing diagram for the temporally separated determination of all three velocity components. Different shading of the light-sheet profile indicates different states of polarization

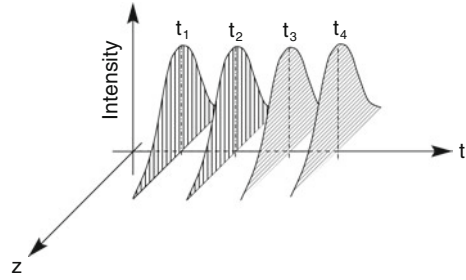
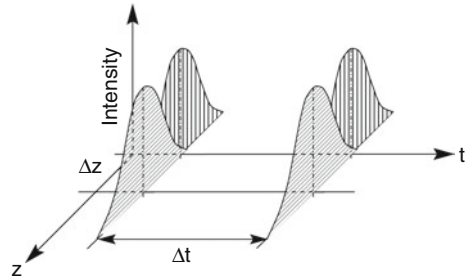


Fig. 17.10 Timing diagram for the simultaneous determination of all three velocity components in spatially separated planes



components of the velocity gradient tensor can be estimated along with the invariants of this tensor [9, 16]. This allows vortex identification to be made more reliably in combination with topological flow analysis. By increasing the distance between the light sheet pairs, the spatial correlation tensor at different locations within the flow field can be measured [14]. Furthermore the orientation of a vortex crossing the planes can be determined precisely which is of major importance for aircraft wake-vortex investigations for example. Time-correlations can also be deduced from the data by varying the time between the horizontally and vertically polarized light sheet pairs [8].

Application

To demonstrate the capabilities of the technique a flat-plate boundary layer flow was examined in stream-wise span-wise planes located at $y^+ = 10$, $y^+ = 20$ and $y^+ = 30$. The experimental investigation was performed 18 m behind the leading edge of the flat plate placed in the temperature-stabilized closed circuit wind tunnel at the Laboratoire de Mécanique de Lille (LML), see [2] for details. The flow and recording parameter are listed in Table 17.2.

For phenomena associated with the production of turbulence, the cross correlation between the fluctuating stream-wise u and the wall-normal v velocity components, measured simultaneously at different y^+ -locations, is very important, as R_{vu} reflects the size and shape of the coherent flow structures being responsible for the transport of relatively low-momentum fluid outwards into higher speed regions and for the movement of high-momentum fluid toward the wall and into lower speed regions.

Table 17.2 Relevant parameters for the characterization of the experiment performed 18 m behind the leading edge of the flat plate in the xz -plane (stream-wise span-wise) of the turbulent boundary layer flow

Re_θ	7800	[1]
Re_δ	74000	[1]
Re_x	3.6×10^6	[1]
U_∞	3	[m/s]
u_τ	0.121	[m/s]
δ	0.37	[m]
δ^+	3000	[1]
$t^+ = tu_\tau^2/\nu$		[1]
Field of view	67×35	[mm ²]
Field of view	0.18×0.09	[δ^2]
Field of view	544×284	[$\Delta x^+ \Delta z^+$]
Spatial resolution	$1.42 \times 0.6 \times 1.42$	[mm ³]
Spatial resolution	$11.5 \times 5.0 \times 11.5$	[$\Delta x^+ \Delta y^+ \Delta z^+$]
Pulse separation Δt	200	[μ s]
Dynamic range at $y^+ = 10$	1.00 to 9.330	[pixel]
Dynamic range at $y^+ = 20$	1.37 to 11.74	[pixel]
Dynamic range at $y^+ = 30$	2.61 to 11.84	[pixel]
Vectors per sample	7936	
Number of samples	4410	

Figure 17.11 displays the statistical relation between the fluctuating velocity components. The top row shows the cross-correlation $R_{v(y^+=20)u(y^+=10)}$ (left) and $R_{u(y^+=20)v(y^+=10)}$ (right). It can be stated from the negative sign of the correlation, indicated by the dashed lines, that the ejection and sweeps must be the predominant processes and the different size, shape and intensity of the functions ($R_{v(y^+=20)u(y^+=10)} > R_{u(y^+=20)v(y^+=10)}$) imply the dominance of ejection at these wall locations. In addition, it can be estimated from the location of the maximum in the upper left graph that the low momentum region appears as a shear layer in the y -direction while the strong positive side peaks in the same figure indicate that the outflow of low-momentum fluid is associated with a secondary motion. The center row of Fig. 17.11 reveals the same functions but measured at $y^+ = 20$ and $y^+ = 30$ e.g. $R_{v(y^+=30)u(y^+=20)}$ (left) and $R_{u(y^+=30)v(y^+=20)}$ (right). The bottom row of Fig. 17.11 yields the conditional cross-correlation $R_{v(y^+=20)u(y^+=10)}$ with $u > 0$ (left) and $R_{v(y^+=30)u(y^+=20)}$ with $u > 0$ (right). Especially the amplitude of R_{vu} in the lower right plot should be noted. To estimate the convection velocity of the various coherent flow structures, and further dynamical aspects which are not accessible by using standard stereoscopic PIV techniques, space-time correlations were measured in addition. See [8–10] for details.

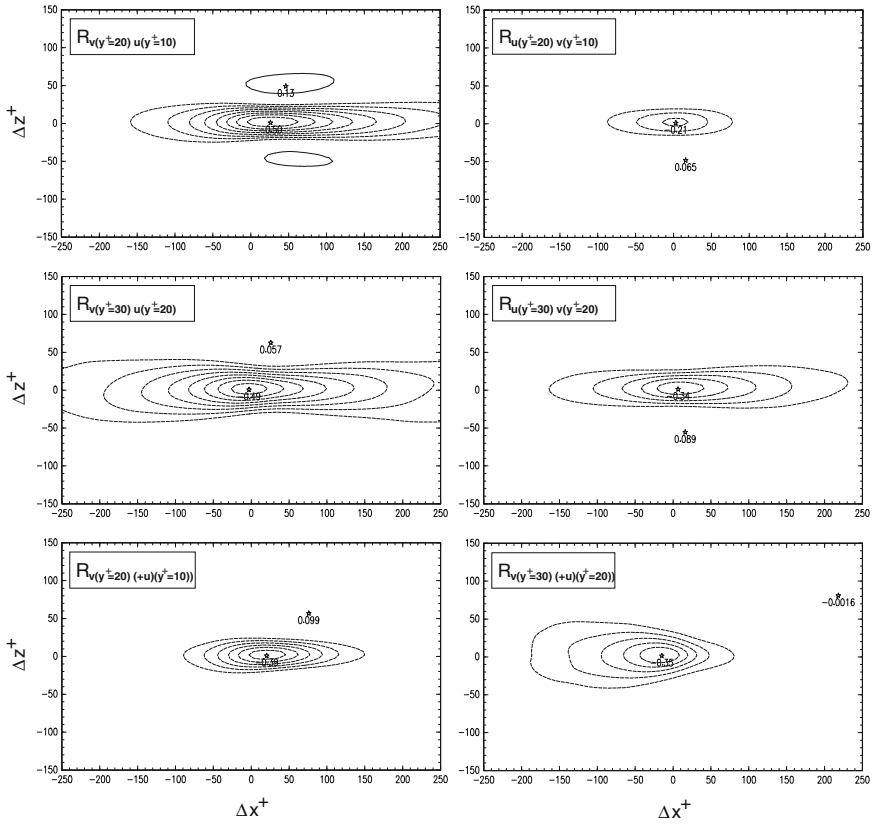


Fig. 17.11 Two-dimensional spatial cross-correlation function of fluctuating stream-wise (u) with wall-normal (v) velocity components measured at $Re_{\theta} = 7800$. *Top:* $R_{v(y^{\pm}20)u(y^{\pm}10)}$ (left) and $R_{u(y^{\pm}20)v(y^{\pm}10)}$ (right). *Center:* $R_{v(y^{\pm}30)u(y^{\pm}20)}$ (left) and $R_{u(y^{\pm}30)v(y^{\pm}20)}$ (right). *Bottom:* $R_{v(y^{\pm}20)u(y^{\pm}10)}$ with $u > 0$ (left) and $R_{v(y^{\pm}30)u(y^{\pm}20)}$ with $u > 0$ (right)

Conclusion

The Multiplane Stereo PIV system is very reliable, robust and well suited for all kinds of applications, purely scientific as well as for industrially motivated investigations in large wind tunnels where acquisition time, optical access and observation distances are constrained. Furthermore, it is based on the conventional PIV equipment and the familiar evaluation procedure so that available PIV systems can easily be expanded. The advantage of this measurement system with respect to other imaging techniques lies in its ability to determine a variety of fundamentally important fluid-mechanical quantities with high accuracy (no perspective error), simply by changing the time sequence or light sheet position. Further applications of the Multiplane Stereo PIV (sometimes named Dualplane Stereo PIV) can be found in [1, 4, 16].

References

1. Braud, C., Heitz, D., Braud, P., Arroyo, G., Delville, J.: Analysis of the wake-mixing-layer interaction using multiple plane PIV and 3D classical POD. *Exp. Fluids* **37**(1), 95–104 (2004). DOI [10.1007/s00348-004-0789-z](https://doi.org/10.1007/s00348-004-0789-z). URL <https://doi.org/10.1007/s00348-004-0789-z>
2. Carlier, J., Stanislas, M.: Experimental study of eddy structures in a turbulent boundary layer using particle image velocimetry. *J. Fluid Mech.* **535**, 143–188 (2005). DOI [10.1017/S0022112005004751](https://doi.org/10.1017/S0022112005004751). URL <https://doi.org/10.1017/S0022112005004751>
3. Hain, R., Kähler, C.J.: Fundamentals of multiframe particle image velocimetry (PIV). *Exp. Fluids* **42**(4), 575–587 (2007). DOI [10.1007/s00348-007-0266-6](https://doi.org/10.1007/s00348-007-0266-6). URL <https://doi.org/10.1007/s00348-007-0266-6>
4. Hu, H., Saga, T., Kobayashi, T., Taniguchi, N., Yasuki, M.: Dual-plane stereoscopic particle image velocimetry: system set-up and its application on a lobed jet mixing flow. *Exp. Fluids* **31**(3), 277–293 (2001). DOI [10.1007/s003480100283](https://doi.org/10.1007/s003480100283). URL <https://doi.org/10.1007/s003480100283>
5. Jakobsen, M.L., Dewhurst, T.P., Greated, C.A.: Particle image velocimetry for predictions of acceleration fields and force within fluid flows. *Meas. Sci. Technol.* **8**(12), 1502 (1997). DOI [10.1088/0957-0233/8/12/013](https://stacks.iop.org/0957-0233/8/i=12/a=013). URL <https://stacks.iop.org/0957-0233/8/i=12/a=013>
6. Kähler, C.J.: Multiplane stereo PIV—recording and evaluation methods. In: *EUROMECH 411: Application of PIV to turbulence measurements*, University of Rouen (France) (2000)
7. Kähler, C.J.: General design and operating rules for seeding atomisers. In: *5th International Symposium on Particle Image Velocimetry*, Busan (Korea) (2003)
8. Kähler, C.J.: Investigation of the spatio-temporal flow structure in the buffer region of a turbulent boundary layer by means of multiplane stereo PIV. *Exp. Fluids* **36**(1), 114–130 (2004). DOI [10.1007/s00348-003-0680-3](https://doi.org/10.1007/s00348-003-0680-3). URL <https://doi.org/10.1007/s00348-003-0680-3>
9. Kähler, C.J.: The significance of coherent flow structures for the turbulent mixing in wall-bounded flows. Ph.D. thesis, Georg-August-University zu Göttingen (Germany) (2004). URL <http://hdl.handle.net/11858/00-1735-0000-0006-B4C8-8>. DLR-FB-2004-24
10. Kähler, C.J.: The significance of turbulent eddies for the mixing in boundary layers. In: *IUTAM Symposium “One Hundred Years of Boundary Layer Research”*, Göttingen (Germany) (2004)
11. Kähler, C.J., Kompenhans, J.: Multiple plane stereo PIV – technical realization and fluid-mechanical significance. In: *3rd International Workshop on PIV*, Santa Barbara (USA) (1999)
12. Kähler, C.J., Kompenhans, J.: Fundamentals of multiple plane stereo particle image velocimetry. *Exp. Fluids* **29**(1), S070–S077 (2000). DOI [10.1007/s003480070009](https://doi.org/10.1007/s003480070009). URL <https://doi.org/10.1007/s003480070009>
13. Kähler, C.J., Sammler, B., Kompenhans, J.: Generation and control of tracer particles for optical flow investigations in air. *Exp. Fluids* **33**(6), 736–742 (2002). DOI [10.1007/s00348-002-0492-x](https://doi.org/10.1007/s00348-002-0492-x). URL <https://doi.org/10.1007/s00348-002-0492-x>
14. Kähler, C.J., Stanislas, M., Dewhurst, T., Carlier, J.: Investigation of the spatio-temporal flow structure in the log-law region of a turbulent boundary layer by means of multi-plane stereo particle image velocimetry. In: *Laser Techniques for Fluid Mechanics*, pp. 39–53. Springer, Berlin (2002). DOI [10.1007/978-3-662-08263-8_3](https://doi.org/10.1007/978-3-662-08263-8_3). URL https://doi.org/10.1007/978-3-662-08263-8_3
15. Mullin, J.A., Dahm, W.J.A.: Direct experimental measurements of velocity gradient fields in turbulent flows via high-resolution frequency-based dual-plane stereo PIV (DSPIV). In: *12th International Symposium on the Applications of Laser Techniques to Fluid Mechanics*, Lisbon (Portugal) (2004). URL http://lces.dem.ist.utl.pt/lxaser/lxaser2004/pdf/paper_16_1.pdf
16. Mullin, J.A., Dahm, W.J.A.: Dual-plane stereo particle image velocimetry (DSPIV) for measuring velocity gradient fields at intermediate and small scales of turbulent flows. *Exp. Fluids* **38**(2), 185–196 (2005). DOI [10.1007/s00348-004-0898-8](https://doi.org/10.1007/s00348-004-0898-8). URL <https://doi.org/10.1007/s00348-004-0898-8>

Chapter 18

Applications: Volumetric Flow Measurements

18.1 Vorticity Dynamics of Jets with Tomographic PIV

Contributed by:

F. Scarano and D. Violato

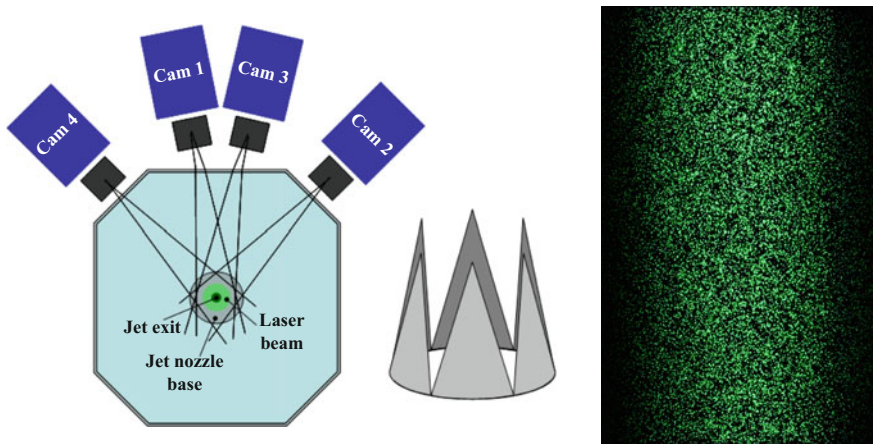
The transition to turbulence in circular jets is a complex three-dimensional process that requires the use of 3D-PIV and temporal resolution for the full understanding the dynamical behavior of coherent vortices. Jets are used in a multitude of engineering systems and their study often regards the process heat and mass transfer. Also jet noise is of relevance especially in the high-speed flow regime. In this experiment, a high-speed Tomographic PIV system is setup to study the early stages of transition in a circular jet issued from a contoured nozzle [40] with the ultimate objective of determining the relation between the dynamics of coherent structures and the noise production [41]. The temporal resolution of the measurement is necessary to capture instantaneous velocity and vorticity field. The measurement of temporal derivatives gives access to the noise source term integrand according to Powell's acoustic analogy (Table 18.1).

Realizing and optimizing a tomographic PIV experiment requires solving a number of additional constraints with respect to planar PIV experiments, which are mostly related to tomographic imaging, system calibration, seeding concentration and volume illumination. In the following a brief description is given of the design of the measurement system. The cylindrical laser illumination is realized transmitting the expanded beam from above, which avoids the setting of the Scheimpflug condition. The cameras are placed subtending an arc of 90° aperture (Fig. 18.1). With the chosen tracers any concentration exceeding 1 particle/mm^3 would result into opaque medium for illumination and imaging. The imaged seeding density attains a maximum on the jet axis (0.04 ppp) and decreases gradually towards the edge of the

An overview of the Digital Content to applications on boundary layers can be found at [\[DC18.1\]](#).

Table 18.1 Experimental parameters for Tomographic PIV measurements of circular and chevron jets

Flow geometry (working fluid)	Circular jet (water)
Maximum velocity	$U_{\text{exit}} \approx 0.45 \text{ m/s}$
Field of view (3D domain)	$50 \times 30 \text{ mm}^2$ ($50 \times 30 \times 30 \text{ mm}^3$)
Number of cameras	4
Interrogation volume	$2 \times 2 \times 2 \text{ mm}^3$
Dynamic spatial range	$\text{DSR} \approx 50 : 1$
Dynamic velocity range	$\text{DVR} \approx 100 : 1$
Observation distance	$z_0 = 40 \text{ cm}$
Recording method	Single frame (continuous)
Recording device	CMOS 1024×1024 (650 active) pixel
Recording lens	$f = 105 \text{ mm}$, $f_{\#} = 22$
Illumination	Nd:YLF laser, $50 \text{ mJ/pulse @ 1 kHz}$
Recording frequency	1.0 kHz
Seeding material	Polyamide ($d_p \approx 56 \mu\text{m}$, $\rho = 10^3 \text{ kg/m}^3$)
Seeding concentration	0.5 particles/ mm^3
Imaged seeding density	0.04 particles/pixel

**Fig. 18.1** Left: schematic top-view of the illuminated region and imaging configuration. Middle: detail of chevron nozzle geometry. Right: single-exposure image from one of the cameras (650×1024 pixel) after background reduction and peak intensity normalization

illuminated domain. System calibration needs to be performed submerging the target into the water tank and translating it over three positions spaced of 10 mm each. The volume self-calibration reduces residual errors from 0.5 pixel to less than 0.05 pixel (Table 18.2).

Table 18.2 Data analysis parameters

Data processing	Tomographic PIV
Image pre-processing	Subtraction of pixel minimum over 21 frames
Digital imaging resolution	20 pixel/mm(pixel/voxel = 1)
Particles displacement	9 voxels (at jet exit)
3D calibration	3rd order polynomial at 3 planes
Calibration correction	Volume Self-Calibration
Volume discretization	$670 \times 1060 \times 520$ voxels
Reconstruction technique	SMART (5 iterations)
Volume interrogation	VODIM ($80^3 - 60^3 - 40^3$)
Vector grid	$60 \times 100 \times 48$ (overlap factor 75 %)
Multi-framing	Sliding Average Correlation (4 frames)
Data filtering	2nd order polynomial fit (kernel $5 \times 5 \times 5$)
Spatial and temporal derivatives	From 2nd order polynomial fit coefficients

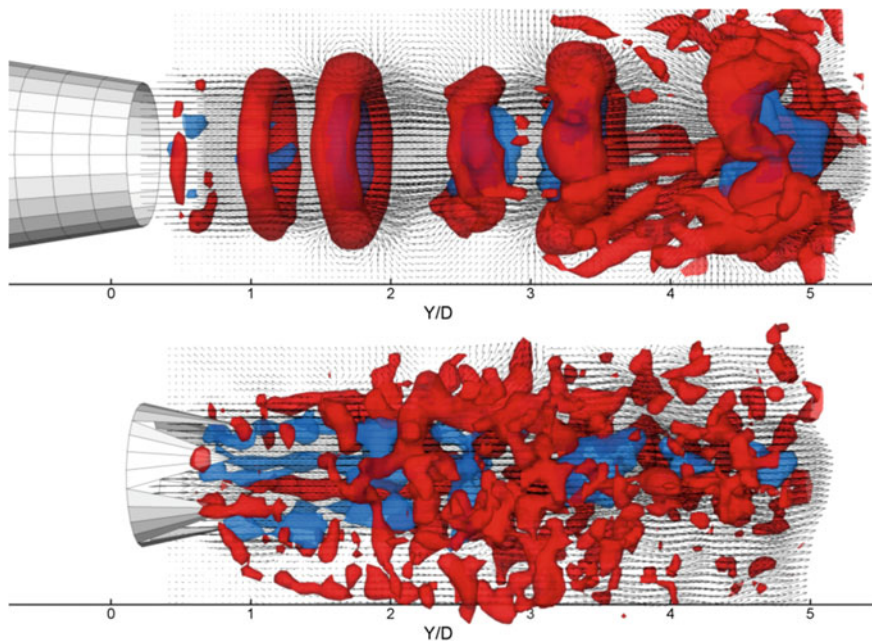


Fig. 18.2 Velocity (blue) and vortex (Q-criterion) visualization of the instantaneous flow out of a circular (top) and 6-chevron exit (A colored version of the figure can be found at [DC18.2])

The circular jet flow exhibits a regular axi-symmetric shedding of vortices due to Kelvin–Helmholtz instability of the shear layer. The shedding occurs within the first diameter ($y/D < 1$) at a frequency of approximately 29 Hz, corresponding to a Strouhal number $Sr = 0.67$, based on the jet exit velocity V_{exit} and diameter D .

Further downstream ($2 < y/D < 3$) adjacent vortices undergo pairing ($Sr = 0.33$), where the trailing vortex ring accelerates under the induced flow from the leading one. Their separation distance decreases and the trailing vortex reduces its radius and peak vorticity (negative stretching) and engulfed inside the leading one (leap-frogging). The pairing is associated to a rapid growth of azimuthal waves, typically 4 to 6 [18]. At $y/D > 4$ a second pairing is occasionally observed ($Sr = 0.16$). The vortices undergo rapid distortion, with azimuthal waves growing under the effect of rapid stretching of the vortex filament. The effect produces vortex pairs aligned along axial planes at an angle of 30 to 40°, with the upper end pointing towards the jet axis. The flow pattern temporal evolution for the jet with chevron exit differs profoundly from the circular case, due to the effect of the shear layer manipulation at the exit (non uniform curvature) (Fig.18.2).

Although exit conditions such as the shear layer thickness and peak vorticity are not significantly changed with respect to the circular exit, the dynamical evolution of the disturbances differs from the Kelvin–Helmholtz rollers growth and pairing. No axi-symmetric structure is observed and the azimuthal coherence is broken into the individual cells formed between chevrons. Also, no significant phase coherence is retrieved between structures formed in neighboring cells. The transition pattern appears to be formed directly by three-dimensional patches and filaments of vorticity shed locally from the shear layer and growing up to $y/D = 2$. The most recurrent structure is a C-shaped vortex element which resembles the V-shape of the chevrons top view, however with a smooth apex region towards the jet axis. As a result the isotropic regime is reached earlier than the circular exit case. Axial velocity fluctuations are still present in this case but not as pronounced, justifying the lowered acoustic emissions in the low-frequency range associated to the phenomenon of core breakup.

18.2 Near-Wall Turbulence Characterization in a Turbulent Boundary Layer Using Shake-The-Box

Contributed by:

A. Schröder, D. Schanz, R. Geisler and S. Gesemann

A large portion of aerodynamic drag is produced by turbulent flow structures in the near-wall region which have significant influence on the amplitude and direction of wall-shear stress events acting on the surface. Furthermore, the impact of streaky (very) large-scale motions (VLSM) present in the logarithmic region of a turbulent boundary layer (TBL) onto the near-wall region has been high-lighted in recent years [21]. Local back-flow close to the wall and thus negative wall-shear stress is a rare phenomenon in zero pressure gradient (ZPG)-TBL and is caused by spanwise vorticity [17], but so far only limited experimental data are available, which cannot directly support studies on the related role of coherent structures. Thus it is of great importance to enhance the understanding of the physics of near-wall turbulence,

Table 18.3 Experimental parameters for turbulent boundary layer investigation

Flow geometry	Zero pressure gradient turbulent boundary layer ($Re_\theta = 2,770$)
Measurement volume	Wall-parallel volume, $(x, y, z) = (16, 1.4, 16)$ mm
Dynamic spatial range	DSR $\sim 160 : 1$ (for instantaneous <i>FlowFit</i> results) $\sim 5,300 : 1$ (for 1-point statistics)
Dynamic velocity range	DVR $\sim 500 : 1$
Observation distance	45 cm
Recording medium	4 PCO.Dimax CMOS Cameras (4 MP each)
Recording lens	100 mm Carl Zeiss Yashica Contax $f_\# = 11$
Illumination	Darwin Duo at 15,834 kHz
Recording frequency	15,834 Hz
Seeding material	DEHS droplets ($\sim 1 \mu\text{m}$ diameter)

especially for the dynamics of extreme wall-shear stress events and related sweep-streak interactions, both from a fundamental and an engineering point of view. Due to strong wall-normal velocity gradients in the immediate wall region of a TBL a tomographic PIV [27] approach would fail in delivering the desired quantities due to the low-pass filtering effect of correlation windows (see e.g., Sect. 5.3.4.5). Therefore, the novel Lagrangian particle tracking method Shake-The-Box (STB) [31] (see Sect. 9.4.3) has been applied to a ZPG-TBL in order to gain time-resolved and volumetric velocity measurements including both components of the wall-shear stresses (Table 18.3).

The experiments were conducted in the 1m- wind tunnel facility at DLR Göttingen with a cross-section of $740 \times 1,000 \text{ mm}^2$ and a test section length of 3,000 mm at $U_\infty = 10 \text{ m/s}$. The boundary layer was tripped by sandpaper stripes and zig-zag bands right after the contraction section and its thickness at the measurement volume was estimated at $\delta = 43.2 \text{ mm}$, which corresponds to a Reynolds number of $Re_\theta = 2,770$ or $Re_\tau = 930$. DEHS particles with a mean diameter of $\sim 1 \mu\text{m}$ were generated by Laskin nozzles and introduced into the circuit wind tunnel enabling a homogeneous distribution with adaptable seeding densities within the measurement volume. Illumination was realized using a Quantronix DarwinDuo Nd:YLF high-repetition laser with $\sim 4 \text{ mJ}$ energy per pulse at a repetition frequency of 15.873 kHz (two cavities operating at 7.937 kHz). With a reduced resolution of 528×420 pixel four PCO dimax-S4 arranged in an in-line camera set-up below the wind tunnel see Fig. 18.3 the high frame rate imaging of the illuminated particles in the measurement volume was realized (further details [35]). The STB measurement domain consists of a wall-bounded volume covering a stream- and spanwise area of 430×430 viscous units ($l^+ = \nu/u_\tau$) and a wall-normal extension of 32 viscous units starting at the wall. A comprehensive set of relatively dense Lagrangian track data was reconstructed from two time resolved sequences of 115,000 time steps each. The data enables an accurate and very high resolution measurement of the mean-velocity- and Reynolds stress- profiles averaged in bins sized by a fraction of a viscous unit

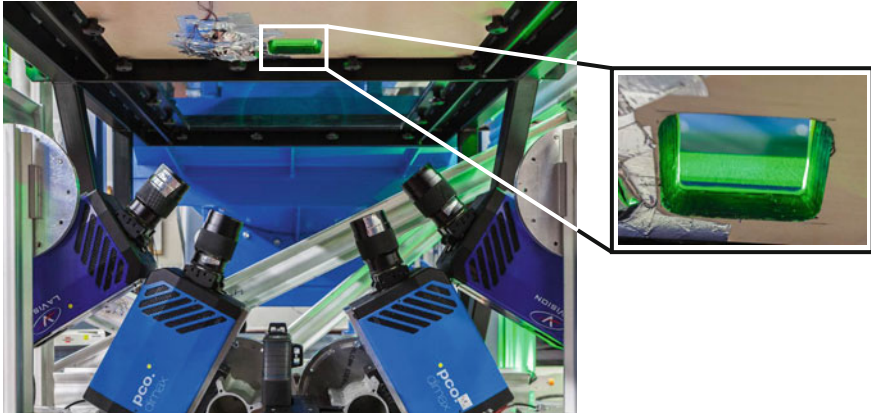


Fig. 18.3 In-line camera STB set-up with four PCO Dimax-S4 cameras operating at 15.873 kHz viewing through a glass insert of the wall onto a wall parallel light volume [35]

and of both components of the instantaneous wall shear stress (τ_{ω}^+). Furthermore, an interpolation algorithm regularized by the incompressible NS-equation named *FlowFit* [5] (see Sect. 9.4.5) has been developed in order to calculate the corresponding time-resolved 3D velocity vector volumes and gradient tensor on a regular grid using the time series of irregularly distributed Lagrangian track data. With the present data coherent structures and their dynamics close to the wall can be investigated together with their role for various (extreme) wall shear stress and sweep-streak interaction ejection events.

An STB evaluation of the gained series of particle images has been applied to the thin wall-parallel volume in order to characterize near-wall turbulence and its spatial and temporal structures at a significant Reynolds number in air flow at very high spatial resolution. The coordinate x refers to the streamwise direction while y and z respectively represent the wall-normal and spanwise directions. A friction velocity of $u_{\tau} = 0.4042$ m/s was measured by a linear fitting along the statistically converged STB bin-averaged mean u -velocity profile between $y^+ = 2$ and $y^+ = 4.5$. From $\sim 230,000$ time steps corresponding to 4,093 boundary layer turn over times U/δ or ~ 140 eddy turn over times u_{τ}/δ statistics of the near-wall mean velocity profile, together with all Reynolds stresses respectively skin friction velocity components, were then calculated from the volumetric Lagrangian track results. The exact wall position was extracted from spatially highly resolved mean velocity profiles using bin averaging of the STB tracks in bin sizes of $1/13^{th} l^+$ at four sub-volume locations and extrapolating the linear profile between $2 < y^+ < 4.5$ to zero u -velocity. After estimation of the wall position span- and streamwise symmetry in a statistical sense for the relatively small volume can be assumed, so that wall normal 1D-profiles with a very high spatial resolution can be extracted. The averaging process corresponds to 14.49 s integration time at 15.873 kHz frame rate using $\sim 8 \cdot 10^8$ data points. An example of measured instantaneous velocity vectors distributed irregularly within the

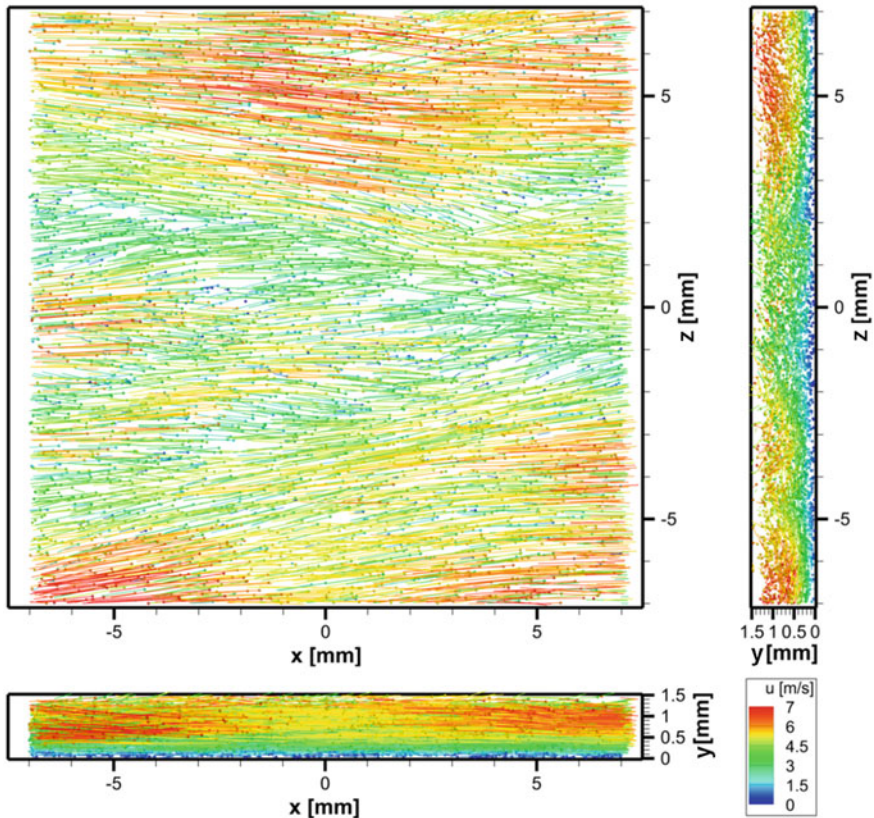


Fig. 18.4 Particle tracks in a near wall volume. (Left) Full field of view, 19 time-steps overlaid; (Right) detail view, 100 time-steps overlaid [DC18.3]

wall-parallel volume of approximately $16 \times 1.4 \times 16 \text{ mm}^3$ according to $430 \times 36 \times 430$ viscous units (l^+)³ in x -, y - and z -directions evaluated by STB is shown in Fig. 18.4. The velocity vectors are color coded by the u -velocity component and based on the application of an optimal temporal Wiener filter in the order of a few Kolmogorov time scales η . Within Fig. 18.4 the three projections of $\sim 5,700$ instantaneous velocity vectors onto the respective side planes of the measurement volume are displayed. The components of the Reynolds stresses (illustrated in Fig. 18.5 top) disclose a very good agreement between the STB bin-average results of the $\langle u'u' \rangle^+$, $\langle v'v' \rangle^+$, the covariance $\langle u'v' \rangle^+$ profiles and the respective DNS [30] data down to sub-viscous units in the near wall region. In Fig. 18.5 (bottom) a view in x -direction through a selected volume shows the interaction of a large amplitude sweep-event (negative v -velocity) with a low speed streak (low iso-contour values of u). As a result the high-momentum fluid is partly deflected while interacting with the low-momentum region causing a strong ejection (red positive v -velocity). Another effect of the depicted

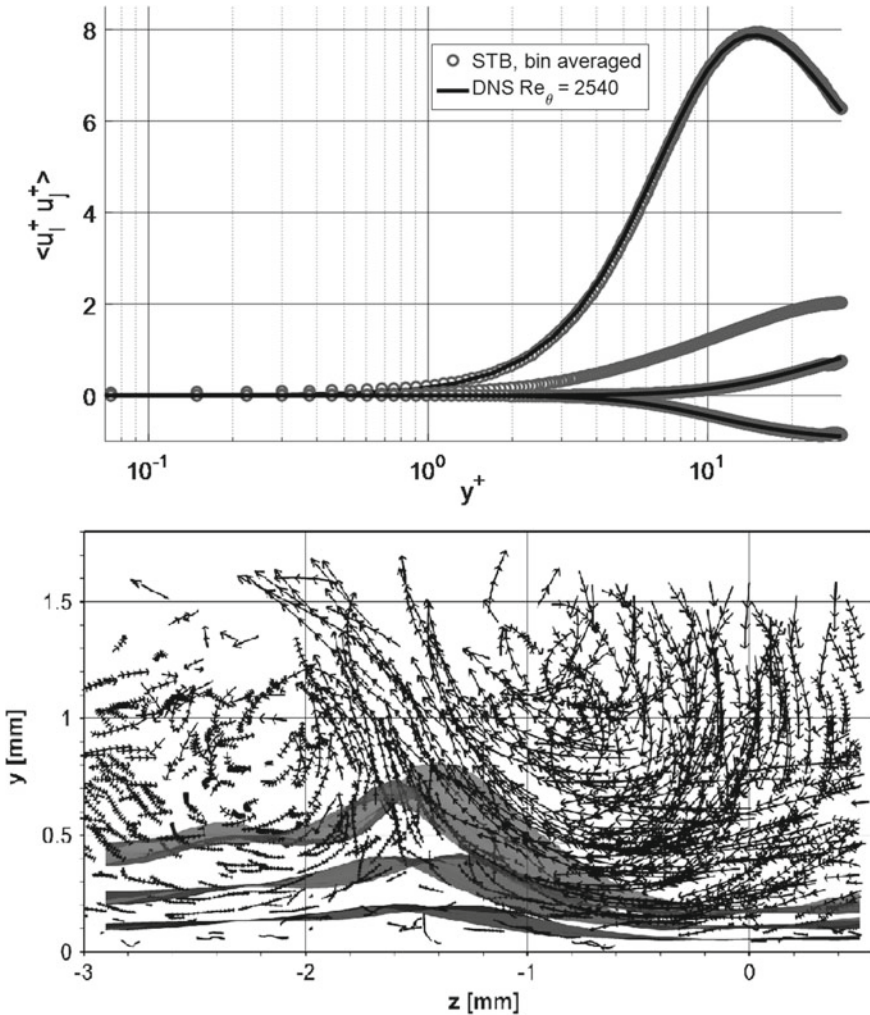


Fig. 18.5 Top: Profiles of the velocity variances the top curve represents $\langle u'u' \rangle^+$, middle curves set $\langle w'w' \rangle^+$ (upper) and $\langle v'v' \rangle^+$ (lower), bottom curve set $\langle u'v' \rangle^+$. STB: circles with $1/13^{th}$ l^+ spatial resolution and black lines from DNS data at $Re_\theta = 2540$ ([30]). Bottom: View along x -direction of some tracks in a strong sweep-streak interaction with iso-contour surfaces of low u -velocity values and tracks [DC18.4]

high v -velocity event is a high wall-shear stress value for both components below the strong sweep event (\sim around $z = 0$ mm) and relatively low ones around $z = -1.5$ mm. An animation of the particle movement over 2000 frames from different viewing angles is available as digital content [DC18.5].

In Fig. 18.6 an instantaneous local back-flow event close to the wall resulting in negative wall-shear stress (see PDF on left) is illustrated. In Fig. 18.6 (right) one

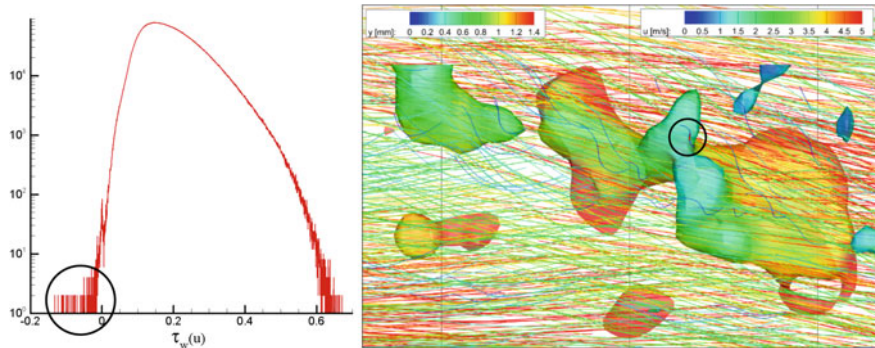


Fig. 18.6 Left: PDF of the instantaneous wall-shear stress for the streamwise velocity component showing few negative events (local back-flow) marked by black circle. Right: Lagrangian tracks (color coded by u -velocity) and iso-contour surfaces of a Q -value at middle time instant (color coded by wall-normal distance y) around a local backflow event (located at black circle) in a view from below the wall (A colored version of the figure can be found at [DC18.6])

can identify a track with negative u -velocity (black circle) within the viscous sub-layer. The track is located below a vortical structure with spanwise vorticity in close proximity to the wall (blue color of iso-surface indicate low y -values) which induce a backflow through the corresponding pressure influence onto the fluid parcel at the wall.

Many vortical structures which are passing by in the buffer layer or even above at relatively high convection velocity induce an undulating or spiraling movement of the particles in the viscous sub-layer. In general so far no measurement technique is known to the authors enabling a more accurate and higher resolution profile of all components of the (mean) velocity vector and the full Reynolds stress tensor for such small viscous unit sizes without intrusiveness and band pass filtering effects within short measurement times. The use of PTV measurement tools for obtaining accurate profile measurements close to walls is motivated by the assessment performed by KÄHLER et al. [15] in particular the additional possibility to measure the full temporal frequency range of all 3D velocity vectors along with both components of the wall-shear stress fluctuation vectors at many points simultaneously in a relatively large volume resp. area at the wall with a high spatial resolution and without band pass filtering effects is a unique feature of the STB method.

STB together with Navier–Stokes-regularized interpolation schemes, like *Flow-Fit*, which optimizes the spatial resolution of the respective interpolated time-resolved velocity, velocity gradient and pressure field, increase the capabilities for accurate and combined Lagrangian and Eulerian views into turbulent (shear) flows based on time-series of particle images from few projections.

18.3 Large-Scale Volumetric Flow Measurement of a Thermal Plume Using Lagrangian Particle Tracking (Shake-The-Box)

Contributed by:

D. Schanz, F. Huhn and A. Schröder

Time resolved volumetric flow measurements, using methods like 3D PTV [19, 20], Shake-The-Box [31] or Tomographic PIV [8] are typically restricted to relatively small volume sizes in the order of 200 cm^3 [28]. This limitation stems from the small size of the used seeding material, which is required for them to accurately follow the flow ($\sim 1\text{ }\mu\text{m}$ in air, $10 - 50\text{ }\mu\text{m}$ in water). However, neutrally buoyant helium-filled soap bubbles (HFSBs) can be of larger size, while still accurately following the flow [23, 28]. Recently, a feasibility study demonstrated that HFSBs can be used in wind tunnels as well [28].

Here, we discuss a time-resolved flow measurement on a thermal plume, using HFSBs ($300\text{ }\mu\text{m}$ diameter), which are illuminated by an extensive LED array. This way, a large measurement volume of 550 liters could be realized. The experiment was performed in a cylindrical convection chamber with a height of 2000 mm and a diameter of 1800 mm (see Fig. 18.7, left). The back wall is blackened aluminum, the front is acrylic glass of 1 mm thickness. LED illumination enters through a window in the ceiling, covered with a circular passe-partout (750 mm diameter). The convective flow is forced by a 1500 W electric hotplate (188 mm diameter), placed a few centimeters below the measurement volume. It is covered by a circular 250 mm diameter aluminum plate as heat reservoir to keep the temperature constant over time. See further details in [33] (Table 18.4).

The HFSBs are produced by a bubble generator prototype of LaVision, based on the nozzle design presented by BOSBACH et al. [1]. The measurement volume is illuminated by a LED array consisting of 7 collimated LED spotlights (Treble-Light, Power LED 20000) with an opening angle of 9° and 18,000 lm luminous flux at 170 W power input each. The LEDs are pulsed with a period of 3 ms at 29 Hz (10 % duty cycle). The five cameras (pco.edge 5.5 sCMOS, PCO, 2560×2160 pixel) are placed on a circle around the convection chamber such that the cameras look perpendicularly through the front window. The temperature difference between the air directly over the hot plate and the surrounding air was approximately 8° . 500 images were recorded at a frequency of 29 Hz. Image preprocessing consisted of subtracting the smoothed minimum gray level distribution and a constant of 50 counts.

For the 3D calibration of the cameras, a planar calibration target was set into the convection chamber and shifted to three positions, each 200 mm apart. Volume-Self-Calibration [42] and calibration of the Optical Transfer Function (OTF) [32] were conducted on images showing a low density of particle images. The attained image quality was very good due to the reflection of light on the bubble surface

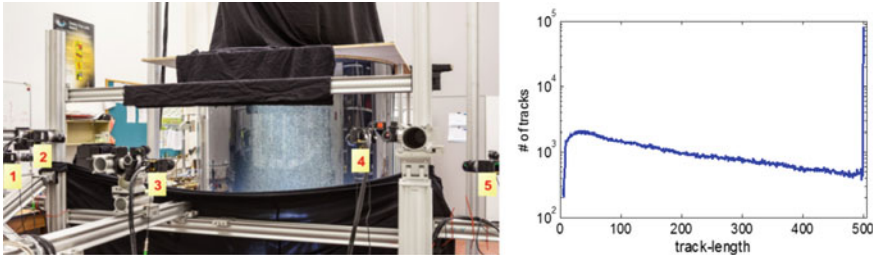


Fig. 18.7 (Left) Photograph of the convective cell with illuminated bubbles inside and the camera system (cameras labeled 1-5); (right) track-length statistics after two passes of STB

Table 18.4 Experimental parameters for thermal plume investigation

Flow geometry	Thermal plume within cylindrical chamber ($h = 2000$ mm; $d = 1800$ mm)
Measurement volume	Cylindrical volume, $h = 1100$ mm; $d = 800$ mm
Dynamic spatial range	DSR $\sim 160 : 1$ (for instantaneous <i>FlowFit</i> results, derived from the resolution of the B-spline system) DSR $\sim 30,000 : 1$ (for 1-point statistics, derived from particle position accuracy)
Dynamic velocity range	DVR $\sim 875 : 1$
Observation distance	2250 mm
Recording medium	5 pco.edge sCMOS Cameras (5.5 MP each)
Recording lens	35 mm Carl Zeiss Yashica Contax $f_{\#} = 11$
Illumination	LED array at the top of the chamber
Recording frequency	29 Hz
Seeding material	Helium filled soap bubbles ($300 \mu\text{m}$ diameter)

(instead of scattering), the homogeneous illumination and the monodisperse bubble size. Therefore, for this experiment a relatively high particle image density of approx. 0.08 ppp could be realized. Shake-The-Box particle tracking [31] (see Sect. 9.4.3) was applied to the time-series using the following parameters per time-step: The number of triangulation iterations was set to 2 (allowed triangulation error: 1.0 pixel), followed by one triangulation iteration using a reduced set of cameras. Each of these was followed by five shake-iterations ($n_1 = 2$, $n_2 = 1$, $m = 5$, $\varepsilon = 1.0$; see [31, 43]). This way, approximately 275,000 particles could be simultaneously tracked. Figure 18.7 (right) shows that over 81,000 particles were tracked over the whole time-series. These are particles slowly moving in the entrainment region. The rest of the track lengths are evenly distributed, reflecting that particles are transported

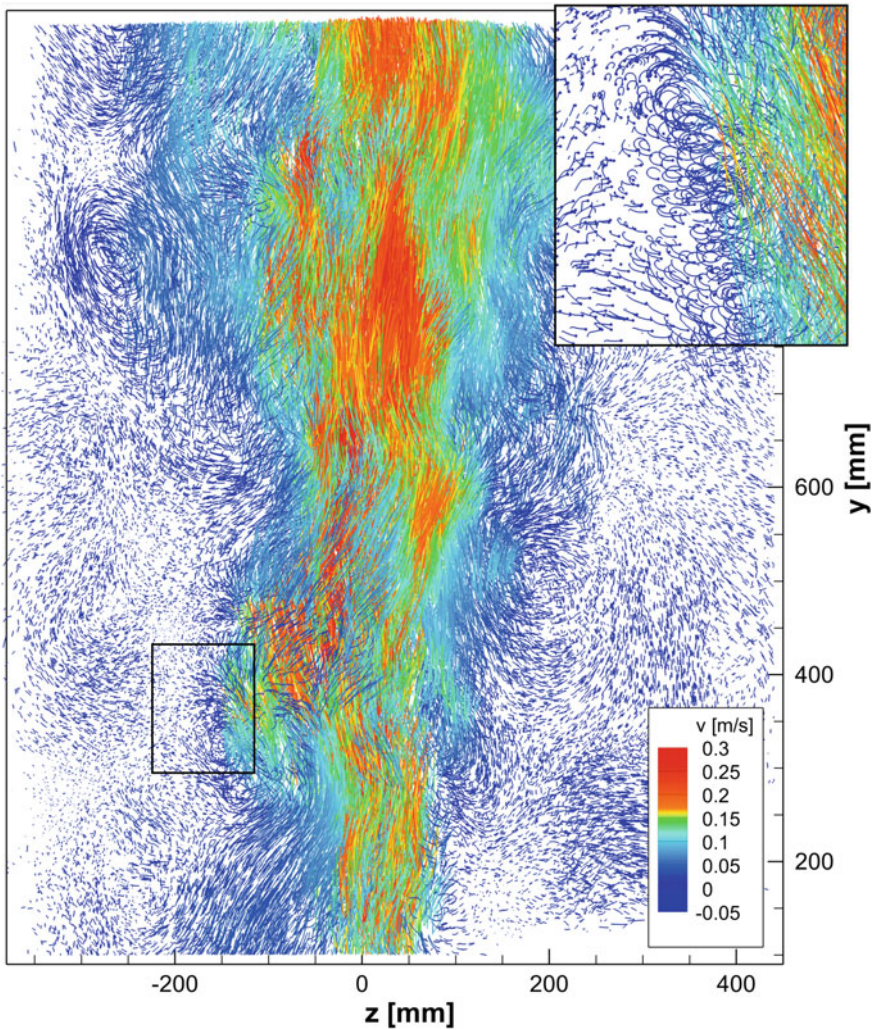


Fig. 18.8 Particle tracks in a 100 mm slice in the center of the volume, 11 time-steps overlaid; Detail view of marked area: Slice of 40 mm thickness, 41 time-steps overlaid

into and out of the volume at different speeds. Following the STB procedure, the particle tracks are temporally filtered [5] (see Sect. 9.4.4). Velocity and acceleration are calculated as temporal derivatives. After filtering, a particle position accuracy of approx. $36 \mu\text{m}$ (0.086 pixel) and a velocity error of approx. 0.0004 m/s is estimated from the spatial spectrum of the tracks which corresponds to a DVR of $\sim 875 : 1$.

Figure 18.8 shows such tracking results within a sheet in the center of the volume (slices of 100 mm out of 800 mm, parallel to the x -axis). The overview reveals the convective flow, which induces vortices of different magnitude in the shear layers.

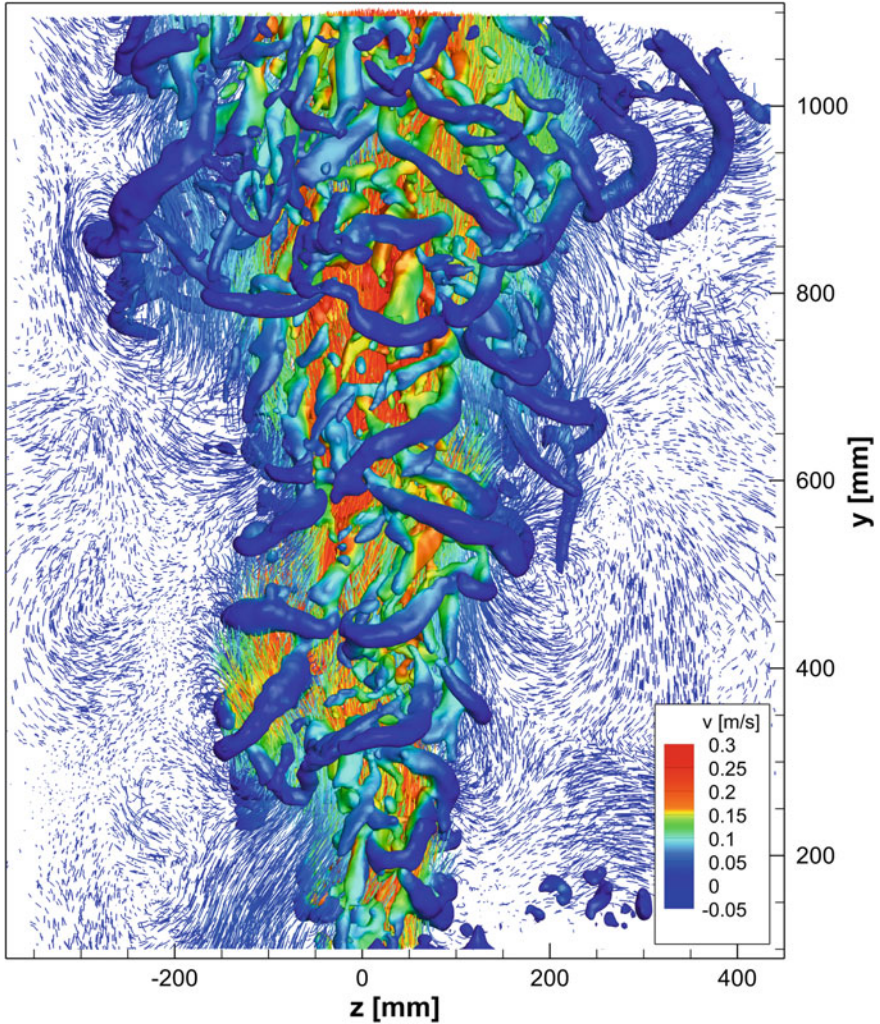


Fig. 18.9 Isosurfaces of Q -criterion $Q = 2/s^2$, color-coded by streamwise velocity. Particle tracks (11 time-steps) shown in a slice of 50 mm thickness

A large region of slowly moving particles surrounds the rising thermal plume. Due to the confining boundaries of the convection cell, outside of the thermal plume, the flow is slightly directed downwards on average. The maximum velocity value within the dataset is approx. 0.35 m/s, corresponding to a particle shift of over 30 pixel. The detailed view shows an example of the spiraling motions of the particles, induced by pressure fluctuations from passing vortices.

FlowFit [5] (see Sect. 9.4.5) was applied to each of the 500 time-steps, interpolating the velocities of the respective tracked particles onto a Cartesian grid. The B-spline system is set up, such that on average ten B-spline cells are present for every particle (0.1 particles per cell), leading to a spacing of approx. 8 mm between the cells. The resulting continuous function is closely sampled on a grid with 3 mm spacing, ultimately leading to vector volumes of $266 \times 333 \times 266$ vectors. An example of the results gained by *FlowFit* is given in Fig. 18.9, showing iso-surfaces of Q-criterion. The full amount and extent of the thermal flow structures becomes apparent. Long, undisturbed vortices are identified in the shear layers surrounding the center of the plume. The central structures are smaller, but show equal strength. When looking at a time-series of such images a high temporal coherence is noticeable. A movie showing such a time-series with Isosurfaces of Q-criterion and particle tracks is available as digital content [DC18.7]. The Q-criterion is derived from the velocity gradient tensor. As such, the temporal coherence is a clear indication that the Lagrangian Particle Tracking (LPT) measurement at high seeding density in combination with the *FlowFit* interpolation strategy is able to recover the vast majority of the present flow structures. The high quality of the tracking process translates directly into the quality of the Eulerian velocity representation.

With a comparable experimental setup, using six high-speed cameras, the three-dimensional flow around a 1 cm^3 glass cube was investigated in the hydrodynamic low-speed water tunnel at ONERA Lille. Both laminar and turbulent in-flow conditions were realized. The Shake-The-Box evaluation was able to track up to 70.000 particles instantaneously, *FlowFit* was applied with a spatial resolution of 0.05 particles per cell.

The cover of this book shows an exemplary instantaneous result from this experiment at a free stream velocity of 0.2 m/s and laminar inflow condition. Shown are isosurfaces of Q-criterion ($Q = 3000/\text{s}^2$) and a vector plane 1.4 mm above the wall. The front of the cube is surrounded by two easily identifiable horseshoe vortices, the wake of the cube is visible as a clearly confined turbulent region with vortical structures of various sizes, which are created in the shear layers surrounding the cube.

18.4 Lagrangian Particle Tracking in a Large-Scale Impinging Jet Using Shake-The-Box

Contributed by:

F. Huhn, D. Schanz, P. Manovski and A. Schröder

The results presented in Sect. 18.3 demonstrate that combining helium-filled soap bubbles (HFSBs) as tracer particles with LED illumination allows for accurate particle tracking in large volumes using Shake-The-Box (STB) [31], see Sect. 9.4.3. Another experiment was created within the same cylindrical chamber, extending the concept to flows of higher speed. High-speed cameras were combined with arrays

Table 18.5 Experimental parameters for impinging jet investigation

Flow geometry	Air jet generated by fan of 110 mm within cylindrical chamber ($h = 2000$ mm; $d = 1800$ mm)
Measurement volume	$450 \times 530 \times 200$ mm ³ @ 1.25 kHz
	$180 \times 530 \times 140$ mm ³ @ 3.9 kHz
Dynamic spatial range	DSR $\sim 155 : 1$ for instantaneous <i>FlowFit</i> results
	DSR $\sim 35,000 : 1$ ($v_J = 1$ m/s) for 1-point statistics
	DSR $\sim 18,600 : 1$ ($v_J = 16$ m/s) for 1-point statistics
Dynamic velocity range	DVR $\sim 550 : 1$ ($v_J = 1$ m/s); $\sim 230 : 1$ ($v_J = 16$ m/s)
Observation distance	1400 mm
Recording medium	6 PCO dimax CMOS Cameras (4 MP each)
Recording lenses	50 mm Carl Zeiss Yashica Contax $f_{\#} = 11$
Illumination	Two high-power LED arrays on top of the impinging plate
Frame rate	1.25 kHz ($v_J = 1$ m/s); 3.9 kHz ($v_J = 16$ m/s)
Seeding material	Helium filled soap bubbles (300 μ m; 500 μ m diameter)

of high-power LEDs, being able to emit enough light within the short pulse widths required at flow velocities up to 16 m/s. The resulting tracks are used to reconstruct pressure fields, which are compared to the signal of wall mounted microphones.

For this experiment, an air jet generated by a fan (PHYWE - 02742-93, upper and lower screen removed) with a nozzle exit diameter of $D = 110$ mm and a variable exit velocity impacts a flat acrylic glass plate at a distance of $H = 550$ mm, ($H/D = 5$), and at an angle of $\Theta = 90^\circ$. The interior of the chamber is seeded with HFSBs [1, 28] with diameters ranging from ~ 300 μ m to ~ 500 μ m, depending on the supplied air pressure applied on the generator (LaVision HFSB generator). The measurement volume, extending from the wall to the fan nozzle exit (530 mm in streamwise direction) is imaged by six high-speed cameras (PCO dimax), which record particle images at different frame rates, depending on the flow velocity (cases of 1 m/s at 1.25 kHz and 16 m/s at 3.9 kHz are presented here). Table 18.5 gives an overview on the imaging parameters for both cases.

The cameras are positioned in an in-line configuration and oriented in a way that their lines-of-sight are tangential to the flat plate. See Fig. 18.10 for images of the setup. The HFSBs are illuminated by two different pulsed LED arrays from above (through the acrylic glass plate). The central jet core is illuminated by a circular array of 150 high power LEDs, operated at 20 A (prototype from LaVision GmbH, Göttingen). Two HARDsoft arrays of 42 LEDs each (operated at 90 A) illuminate an area of approximately 200 mm in depth and 450 mm in radial direction along the glass plate. Both LED arrays are equipped with collimating lenses on top of each single LED. They are operated at 10 % duty cycle.

In order to restrict the particle shifts to no more than approximately 20 pixel for the different jet velocities v_J , the acquisition rate was increased accordingly. The usable resolution of the cameras decreases with the increasing acquisition frequency, therefore reducing the commonly imaged volume. At full resolution (up to jet exit

velocities of approximately 5 m/s), a volume of 47 liter could be reconstructed. At the highest repetition rate (3.9 kHz), the common measurement volume was 13 liter. In order to ensure sharp particle imaging, avoiding temporal streaking, the pulse width – and therefore the available light – was reduced accordingly (80 μs at 1.25 kHz and 27 μs at 3.9 kHz). For the shortest pulse widths the bubble size was increased from 300 μm to 500 μm to increase the amount of reflected light.

Following a geometrical calibration (2D target, imaged at two different z-positions), Volume-Self-Calibration [42] and calibration of the Optical Transfer Function (OTF) [32] were conducted on images with a low particle image density.

The following STB parameters were applied to all datasets: The number of triangulation iterations was set to 1, followed by one triangulation iteration using a reduced set of cameras. Each of these was followed by five shake-iterations. The allowed triangulation error was set to 1.0 pixel ($n_1 = 1, n_2 = 1, m = 5, \varepsilon = 1.0$; see [28, 31]). The search radius for new tracks was chosen according to the expected particle shift. As soon as enough tracks were present to serve as predictor for the track identification, a constant search radius of 4 pixel around the predictor point was used. Outliers were identified using a neighborhood criterion (velocity difference larger than 8 times the RMS). All cases quickly converged to a stable solution; from there on, the algorithm could quickly work through the time-series, as only a relatively small number of particles needed to be triangulated (typically 1,000–3,000). As a reference, for the 3.9 kHz-case 2,500 images could be processed with two passes of the STB algorithm overnight on a 20-core computer workstation.

At a recording frequency of 1.25 kHz, using the full camera resolution, large numbers of bubbles (up to 190,000; particle image density: 0.065 ppp) could be successfully tracked. Decreasing the pulse width leads to decreased signal-to-noise ratio, however, even at 3.9 kHz and a pulse-width of 27 μs , the image quality allows for

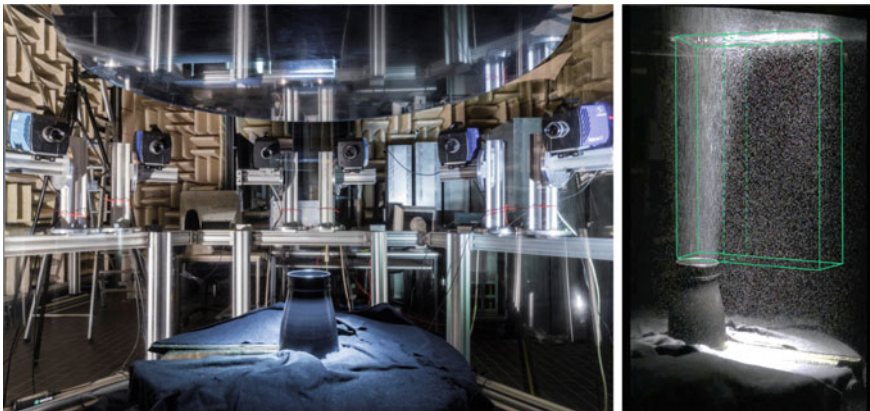


Fig. 18.10 Photographs of the impinging jet experiment. (Left) Nozzle as viewed by the cameras; (right) nozzle in operation. Solid lines indicate the measurement volume at 1.25 kHz, dashed lines at 3.9 kHz

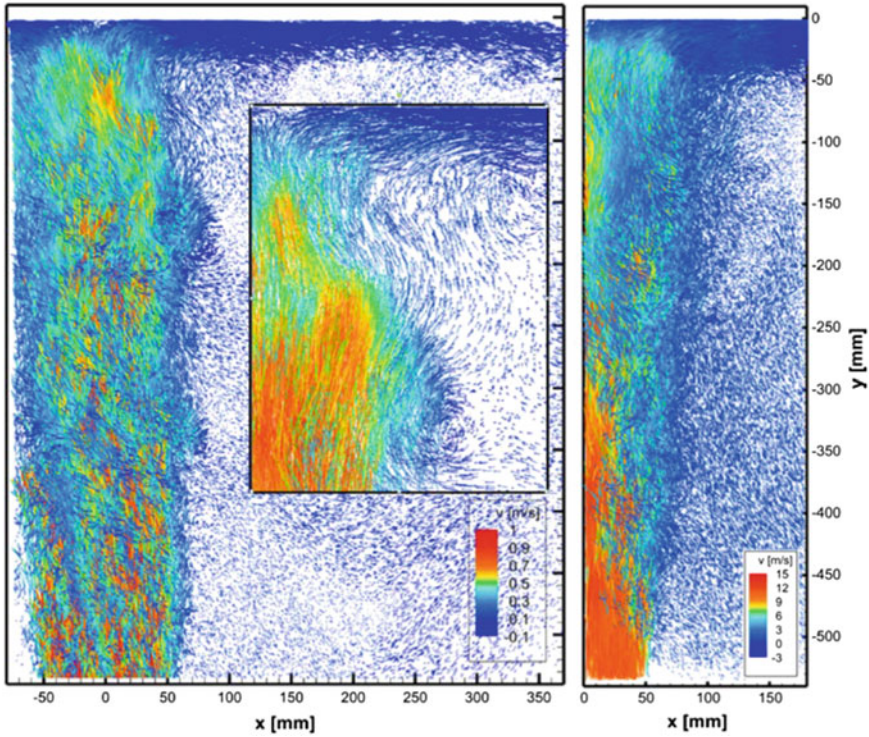


Fig. 18.11 Results from STB evaluations for the two jet flow velocities ($v_J = 1$ m/s, left and $v_J = 16$ m/s, right). Velocity vectors of particles for nine successive time-steps, color-coded by y-velocity. Detail view for 1 m/s shows a slice of 20 mm thickness from the middle of the volume at the impinging point (A colored version of the figure can be found at [DC18.8])

a reliable tracking of around 40,000 particles at seeding densities of 0.045 ppp. The particle tracks are temporally filtered [5] (see Sect. 9.4.4). Particle position accuracies of approx. $9 \mu\text{m}$ (1 m/s) and $28 \mu\text{m}$ (16 m/s) and velocity errors of approx. 0.0018 m/s (at 1 m/s) and 0.07 m/s (at 16 m/s) are estimated from the wavenumber spectrum of the tracks.

Figure 18.11 shows exemplary snapshots from the tracked particles at both jet velocities. It can be seen that for both cases the tracking system was able to reliably extract bubble trajectories at high numbers. Visual inspection shows no traces of spuriously tracked particles. The detail view of the impinging region suggests the presence of flow structures of various sizes and magnitudes. Time-resolved movies of the particle trajectories can be found as digital content for both jet velocities [DC18.9].

For an improved identification of the flow structures, the interpolation scheme *FlowFit* [5] (see Sect. 9.4.5) was applied to the tracking results. The full non-linear Navier–Stokes regularization of *FlowFit* (deploying the measured Lagrangian accel-

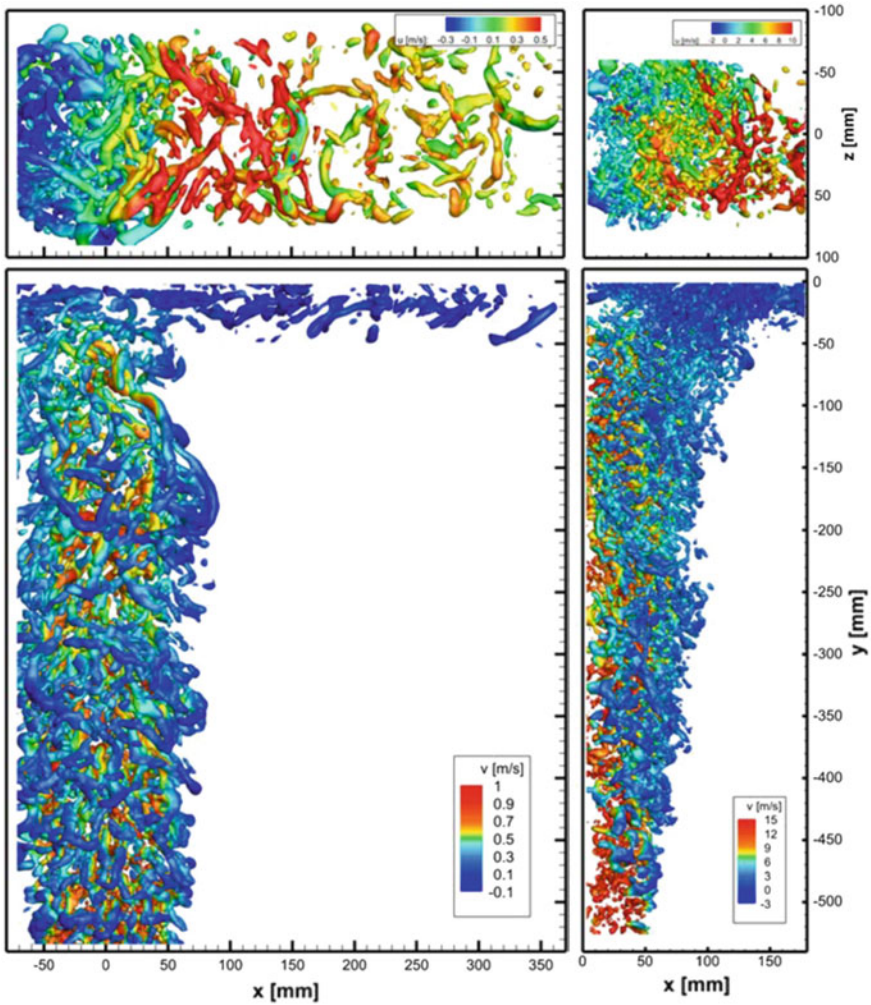


Fig. 18.12 Results from the application of *FlowFit* to the STB tracking results for jet velocities of 1 m/s (left) and 16 m/s (right). Shown are instantaneous isosurface of Q-criterion ($Q = 500/s^2$ at $v_j = 1$ m/s and $Q = 150,000/s^2$ at $v_j = 16$ m/s). Views from above the impinging plate (top, colour coded by x -velocity) and from the side (bottom, colour coded by y -velocity) are provided (A colored version of the figure can be found at [DC18.10])

eration) can be used in this case. A closely spaced system of Cubic B-splines is setup (around 0.04 particles per cell, resulting in $127 \times 155 \times 55$ independent cells for the full field-of-view). The obtained continuous function is closely sampled on a grid with 1 mm spacing, resulting in velocity volumes of 540 points in the streamwise direction and varying width and depth, depending on the case.

Figure 18.12 shows *FlowFit* results for a single time-step at 1 m/s and 16 m/s. For the low velocity, a multitude of flow structures can be identified using the Q-criterion.

The flow coming from the fan is in a turbulent state due to fan-stator interactions and the fan wake, however, typical large, elongated vortices can be observed in the jet shear layer. At the high velocity, the structures become much stronger (note the isosurface threshold) and the turbulence increases. Still, the *FlowFit* method is able to extract temporally coherent large structures from the STB tracks. The smallest scales, in contrast, cannot be fully resolved in this high Re-number turbulent case. Time-resolved movies of the particle trajectories can be found as digital content for both jet velocities [DC18.11].

While for this velocity the interpolated result might not resolve all scales, the particle tracks still contain all velocity and acceleration information based on individual bubbles (approximate fluid elements). Particle statistics (e.g., velocity and acceleration PDFs, bin ensemble averaging, two-point-correlations) are in principle free of

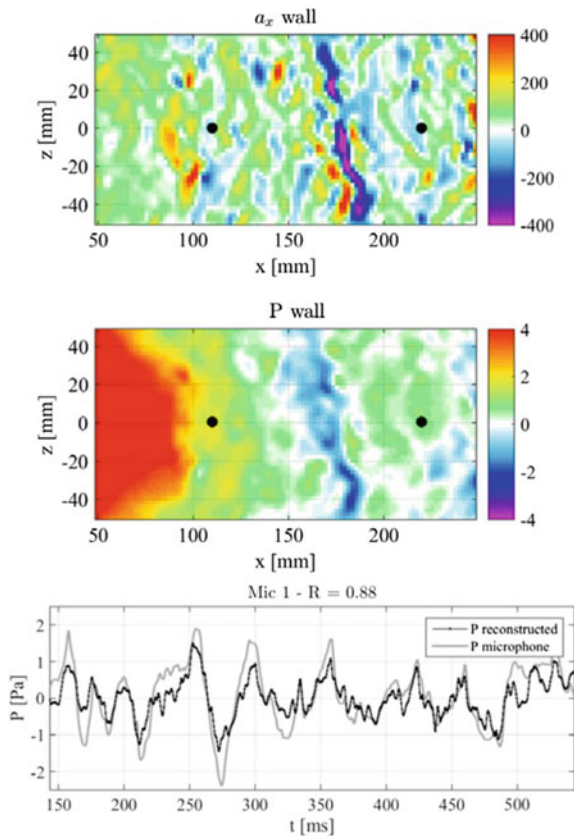


Fig. 18.13 (top) Instantaneous volumetric acceleration field at the wall, a_x -component [m/s^2] at $v_J = 5$ m/s. (center) Resulting pressure field [Pa] on the wall with microphone positions (black dots, real size). (bottom) Time series of pressure fluctuations as given by the left microphone at $x = 11$ mm and the pressure reconstruction at the same location

any systematic bias or low-pass filter effects, as long as the temporal resolution is high enough to resolve the high-frequency accelerations.

Lagrangian particle tracking allows to measure the material acceleration of the seeding particles, thus providing a way to determine the volumetric pressure field in various ways [12, 38]. As a common approach of all of these methods, the momentum equation relates the acceleration and the pressure gradient field. Here, the *FlowFit* [5] with complete Navier–Stokes regularization was used to reconstruct pressure in the volume up to the wall. For validation, two reference microphones (diameter 1/4", G.R.A.S. Type 40BF) were flush mounted on the impinging plate. Figure 18.13 (top) shows an instantaneous acceleration field at the wall for a case with $v_J = 5$ m/s (frame rate 2.0 kHz). The resulting relative pressure field is given in the figure below. Elongated pressure minima induced by passing vortices can be seen. The pressure integration constant (additive pressure offset) is set to be zero in a quiescent flow region far from the jet. The position of the microphones is given by black circles. Figure 18.13 (bottom) shows the pressure time series from the left microphone located at 11 mm from the center of the jet and the pressure at the same location as given by the measured flow field. Both time series were filtered by a Butterworth band pass filter with range 4–100 Hz in order to reduce the influence of fan noise. A high correlation coefficient of $R = 0.88$ is computed for the two signals based on 800 time steps. This validation of the volumetric pressure reconstruction documents the high local accuracy of the derived acceleration values from the large-scale measurement.

18.5 3D Lagrangian Particle Tracking of a High-Subsonic Jet Using Four-Pulse Shake-The-Box

Contributed by:

**P. Manovski, M. Novara, N.K. Depuru-Mohan,
R. Geisler, D. Schanz, J. Agocs and A. Schröder**

Synchronized 3D Lagrangian Particle Tracking (LPT) and microphone array measurements were performed on a high-subsonic jet flow at Mach 0.84 generated by a round nozzle. The Shake-The-Box (STB) technique for multi-pulse data was employed to reconstruct particle tracks along the four-pulse sequences providing highly resolved accurate flow velocity and material acceleration data. The following section describes the flow measurement only. A description of the experimental methodology is given followed by instantaneous and averaged flow results.

Experimental Setup

The experiment was carried out in the anechoic Aeroacoustics Test Facility at the German Aerospace Center (DLR) Göttingen. The jet flows issued by a round nozzle with an inner diameter (D_j) of 15 mm were investigated. The nozzle geometries, including the inner contour which follows a seventh order polynomial, are described in [22]. The ratio of stagnation pressure in the nozzle to the ambient pressure (NPR)

Table 18.6 Experimental parameters for the high-subsonic jet investigation

Flow conditions	$Ma = 0.84, Re_{D_j} \approx 3 \cdot 10^5$
Jet exit axial velocity	290.3 m/s
Pressure ratio (NPR)	1.71
Temperature ratio (NTR)	0.98
Measurement volume	$90 \times 70 \times 10 \text{ mm}^3 (x, y, z)$
Measurement domain	$0.1 \cdot D_j$ to $4.7 \cdot D_j$
Dynamic spatial range	$DSR \approx 200 : 1$ (for instantaneous <i>FlowFit</i> results)
	$DSR \approx 10,000 : 1$ (for one-point statistics)
Dynamic velocity range	$DVR \approx 400 : 1$
Observation distance	$Z_0 \approx 900 \text{ mm}$
Recording method	Dual frame/single exposure
Recording medium	8 PCO.edge sCMOS 2560×2160 pixel
Recording lens	$f = 180 \text{ mm}$, $f_{\#} = 11$ and $f = 200 \text{ mm}$, $f_{\#} = 11$
Illumination	2 Nd:YAG laser 200 mJ/pulse
Pulse delay 1-2 and 3-4	$1.25 \mu\text{s}$
Pulse delay 2-3	$3.75 \mu\text{s}$
Seeding material	DEHS droplets ($d_p \approx 1 \mu\text{m}$)

was 1.71 and the ratio of the stagnation temperature in the nozzle to the ambient temperature (NTR) was 0.98. The experimental parameters are summarized in Table 18.6.

A multi-pulse setup obtained by the combination of two dual-frame acquisition systems was used to record tracer particle images within a volume of $90 \times 70 \times 10 \text{ mm}^3$ along the jet axial (x), radial (y) and out-of-plane (z) directions, respectively. The multi-pulse acquisition strategy described by SCHRÖDER et al [36] and NOVARA et al [26] is applied here, where the use of two different states of polarization for the illumination sources is used to separate the pulses on the camera images.

Illumination is provided by two dual-cavity Quantel Evergreen Nd:YAG lasers (200 mJ pulse energy at 10 Hz) emitting horizontally and vertically polarized light respectively to produce short four-pulses bursts. The timing scheme of the two lasers is arranged to realize a four-pulse sequence, where the time separation between pulses 1 and 2, and that between pulses 3 and 4, is $\tau = 1.25 \mu\text{s}$ and a longer time interval of $\tau = 3.75 \mu\text{s}$ separates pulses 2 and 3.

The two imaging systems consisting each of four sCMOS PCO-Edge cameras, equipped with polarization filters to separate the four pulses onto the image sensor, are shown in Fig. 18.14. One imaging system (odd camera numbers in Fig. 18.14) records pulses 1 and 2 and the other (even camera numbers) pulses 3 and 4. The sensor size is 2560×2160 pixel with $6.5 \mu\text{m}$ pixel size. Cameras, in Scheimpflug condition, are equipped with objective lenses having focal lengths of $f = 200 \text{ mm}$ and

180 mm; the f-number ($f_{\#}$) was set to 11. The digital resolution was approximately 33.6 pixel/mm.

As a consequence of the uneven spacing of the pulses, the maximum displacement of particle tracers is approximately 12 pixel and 37 pixel for the shorter and longer time interval respectively, resulting in a maximum of approximately 61 pixel total particle shift. The motivation for the chosen pulse separation is to increase the velocity and acceleration dynamic ranges of the measurement.

A Laskin nozzle with a separate impactor was used to provide seeding of Di-Ethyl-Hexyl-Sebacat (DEHS) with a nominal particle diameter of 1 μm . The seeding was introduced upstream of the nozzle and the ambient air was also seeded enabling a homogenous distribution across the measurement volume. The symmetric camera setup ensures similar image quality between the two acquisition systems. The seeding concentration adopted for the experiment resulted in a particle image density of approximately 0.025 – 0.05 ppp (particles per pixel).

The 3D imaging systems are calibrated using a LaVision Type-11 two-plane target; volume self-calibration [42] is used to compensate for calibration errors and to obtain the Optical Transfer Function (OTF) of the particle images [32]. For each measurement configuration, a total of up to 60,000 four-pulse sequences were recorded at a sampling frequency of 10 Hz. Synchronously, the far-field acoustic pressure fluctuations were recorded by a microphone array consisting of 17 microphones with the aim of determining the causality correlation between the near-field flow quantities and the far-field acoustic quantities [10, 22].

Lagrangian Particle Tracking with Shake-The-Box

An adapted version of the Shake-The-Box 3D LPT algorithm, initially proposed by SCHANZ et al. [31] for time-resolved recordings, is applied here to four-pulse sequences recorded by the multi-pulse acquisition system (see Sect. 9.4.4) [26].

The iterative STB processing strategy is employed to compensate for the lack of a long observation time. The number of STB iterations, as well as the reconstruction and tracking parameters, is chosen based on the image quality, seeding density and pulse separation arrangement. The STB technique delivers four-pulse long particle tracks; together with the usage of two independent imaging systems [4], this ensures that spurious ghost particles arising from the reconstruction process, typically not coherent with the flow motion, are discarded [9].

The position of the tracers along the time sequence is fitted by means of a system of cubic b-splines as proposed by GESEMANN et al. [5]; velocity and material acceleration are evaluated analytically from the fit.

For the present investigation three STB iterations have been performed for each four-pulse recording sequence. The Iterative Particle Reconstruction technique (IPR, [43]) and the particle tracking parameters are summarized in Table 18.7, where N_c indicates the number of cameras within each imaging system. A detailed description of the reconstruction and tracking strategy and parameters can be found in [25, 26, 43].

With reference to Fig. 18.14-top-right the particle matching procedure employed for the tracking phase is divided into two stages. At first, two-pulse tracks between

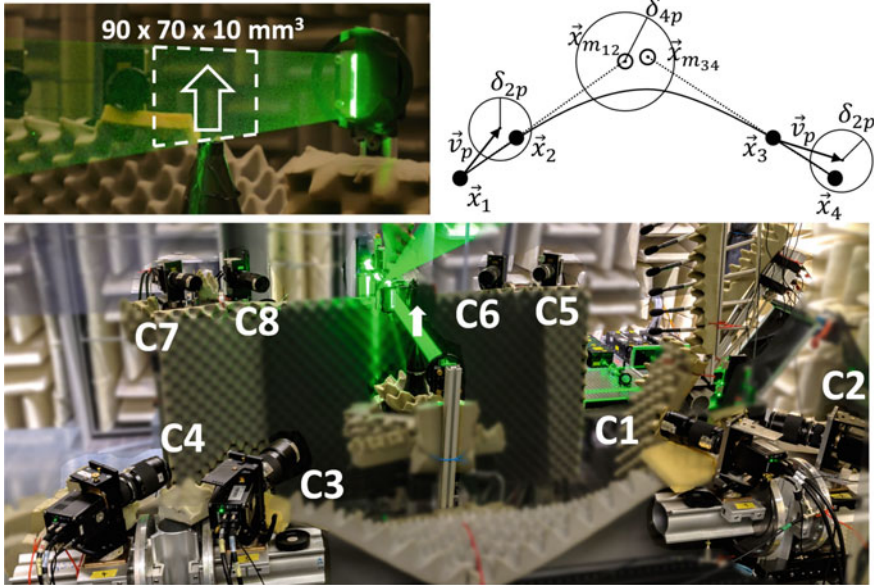


Fig. 18.14 Jet flow direction, laser light sheet and measurement volume (top-left). In-line camera STB set-up with two imaging systems each with four PCO.edge sCMOS cameras separated by two states of polarization (indicated by the odd and even camera numbers) (bottom). Particle tracking strategy for uneven pulse separation (top-right); \mathbf{x}_i indicates the position of the particles along the four-pulse sequence

pulses 1 – 2 and 3 – 4 are identified; around each particle in the first time step (pulse 1 and 3 respectively) a radius is established to define a search area where matching particles from the second step (pulse 2 and 4) are identified. This step is aided by the use of instantaneous velocity predictors obtained by means of Particle Space Correlation (PSC, [26]) performed between IPR reconstructed particle fields (\mathbf{v}_p in Fig. 18.14-top-right). The use of such a predictor allows for the reduction of the search radius thereby improving the identification of valid particle tracks [24].

The second stage of the tracking process is to obtain four-pulse tracks by connecting two-pulse tracks that have been identified. This is done by determining the position of the particles at the mid-point of the four-pulse sequence by extrapolating the two-pulse tracks from pulses 1-2 forward and 4-3 backward in time respectively ($\mathbf{x}_{m_{12}}$) and ($\mathbf{x}_{m_{34}}$) in Fig. 18.14-top-right). A search radius δ_{4p} is established to define the area within which the predicted mid-points need to be found for the two-pulse tracks belonging to pulses 1 – 2 and 3 – 4 to be connected into four-pulse tracks.

The search radii δ_{2p} and δ_{4p} are referred to as global radii; and their value is kept constant across the measurement domain and does not depend on local flow features. If an estimate of the velocity fluctuation components is available, the global search radii can be locally adapted according to the standard deviation of the velocity to obtain the local radii:

$$\delta_{2p}^* = \delta_{2p} + f_{\sigma,2p} \cdot \sigma \quad (18.1)$$

$$\delta_{4p}^* = \delta_{4p} + f_{\sigma,4p} \cdot \sigma \quad (18.2)$$

where σ indicates the standard deviation of the velocity in pixel and $f_{\sigma,2p}$ and $f_{\sigma,4p}$ are positive multiplicative factors that can be freely adjusted. Adaptive search radii result in an increase of the search area in regions where high flow dynamics are expected, therefore allowing the capture of high acceleration events; conversely, the search area is reduced in the calm region outside the jet, where an average velocity predictor is accurate enough to aid the particle matching procedure.

For the results presented here, an initial evaluation of 4,000 four-pulse sequences was performed aided by instantaneous predictor fields from PSC; as no information on the flow statistics was available, both $f_{\sigma,2p}$ and $f_{\sigma,4p}$ were initially set to zero. Whereas the global search radii were respectively increased after each STB iteration ($\delta_{2p} = 2, 3, 4$ pixel and $\delta_{4p} = 4, 5, 6$ pixel) taking advantage of the progressive reduction in the residual image density [26] and allowing for the identification of previously unidentified particle tracks.

Ensemble averaging of the instantaneous tracks obtained from this initial evaluation (based on a subset of snapshots) was then performed as proposed in [37] and [25] to obtain an estimate of the flow statistics.

The converged mean velocity is then used as a high fidelity predictor for the actual STB evaluation of the complete recording sequence of 60,000 samples. The global search radii were reduced (see Table 18.7) and locally adapted according to the velocity fluctuations magnitude as shown in equation 1. The adaptation factors ($f_{\sigma,2p}$ and $f_{\sigma,4p}$) were progressively increased at each STB iteration ensuring that by the final pass events exceeding four times the local expected displacement deviation were captured.

Table 18.7 STB processing parameters for the evaluation of the complete sequence of 60,000 recordings

	Iteration 1	Iteration 2	Iteration 3
Triangulations with N_c	3	3	3
Triangulations with N_{c-1}	2	2	2
Shake iterations (IPR)	4	4	4
Shake width [pixel]	0.1	0.1	0.1
Allowed triangulation error [pixel]	1.2	1.2	1.2
Particle peak intensity threshold [counts]	55	55	55
Particle peaks used for triangulation η [%]	100	100	100
Global search radius 2-pulse tracks δ_{2p} [pixel]	0.3	0.3	0.3
Search radius 2-pulse mult. factor $f_{\sigma,2p}$	2	3	4
Global search radius 4-pulse tracks δ_{4p} [pixel]	0.6	0.6	0.6
Search radius 4-pulse mult. factor $f_{\sigma,4p}$	3	3.5	6

As a result, an average of 30,000 – 90,000 tracks, depending on the seeding density and individual camera image quality (due to the interdependency of scattering direction and polarization), could be successfully reconstructed for each instantaneous four-pulse recording sequence. It should be noted that the number of tracks refers to complete four-pulse tracks only; particles entering or leaving the investigated domain are not considered for sake of robustness of the measurement.

The ensemble averaging of the full time series allows for the evaluation of sub-pixel spatially resolved flow statistics.

Results

A subset of the available experimental results is presented here, relating to the round jet case at Mach 0.84. Individual particles were tracked along the four-pulse sequences. The particle position, velocity and acceleration were evaluated analytically from a fit of the particle locations based on cubic b-splines [5]. The measurement of the material acceleration can be used to determine the instantaneous 3D pressure field by means of the momentum equation [5, 12, 39].

Figure 18.15-left shows instantaneous four-pulse tracks color-coded by the axial flow velocity component; due to the relatively low seeding density used for this specific recording configuration, the number of tracked particles is approximately 35,000. The scattered measurement points obtained from the tracking approach were interpolated onto a regular grid for the visualization of instantaneous flow structures via the *FlowFit* technique [5]. Figure 18.15-right shows Q-criterion iso-surfaces color-coded by the axial velocity component; as expected, the main vortical structures are found within the shear layer region.

The large sequence of 60,000 recordings and using the axial symmetry of the flow field enabled ensemble averaging with a bin size of down to 0.75 pixel ($\sim 23 \mu\text{m}$ or $0.0015 \cdot D_j$) in the radial direction and thus providing sub-pixel resolution statistical quantities of the jet flow (mean, turbulence intensities, Reynolds stresses etc.).

In Fig. 18.16 radial profiles of the average normalized axial velocity component (u/U_j) and axial turbulence intensity (u'/U_j) at axial stations $x/D_j = 0.2, 1, 4$ are presented. Results obtained from the present investigation (closed circles in Fig. 18.16) are compared with the NASA consensus dataset from BRIDGES & WERNET [2] ($\text{Ma} = 0.9$, $NPR = 1.86$, $NTR = 0.835$, $Re_{D_j} \approx 10^6$). The consensus data for this condition is obtained by weighted averages from six historical PIV datasets exploiting the axial symmetry. Despite different test conditions for the two data sets, the consensus dataset provides a good reference for comparison. At $4 \cdot D_j$ the profiles of axial velocity compare well, whereas for the turbulence intensity the current STB results show slightly larger turbulence intensity and a thicker shear layer. At $1 \cdot D_j$ the benefit of the particle tracking approach over PIV (where the finite size of the cross-correlation windows results in a modulation of the signal [14]) is highlighted by the STB's capability of capturing the thin shear layer and the steep velocity gradients; the step profile of the axial velocity component is well resolved. The size of a typical PIV correlation window of 32 pixels is indicated in Fig. 18.16 as a reference. The turbulence intensity profiles are also well resolved and show greater intensity compared with [2]; again this can be attributed to the higher

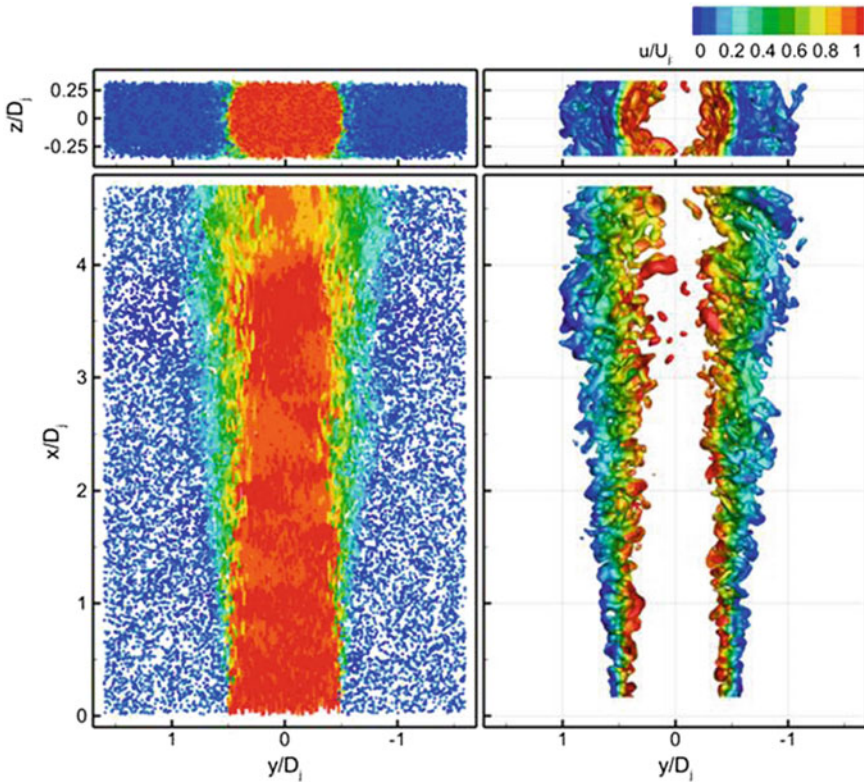


Fig. 18.15 Instantaneous STB results of flow from a round nozzle at $Ma = 0.84$. Four-pulse particle tracks color-coded by the normalized axial velocity component u/U_j (left). Instantaneous Q-criterion iso-surfaces color-coded by the normalized axial velocity component (right) (A colored version of the figure can be found at [DC18.12])

spatial resolution and accuracy of the Lagrangian particle tracking method where no spatial filtering effect is introduced.

The current experimental setup and the use of the STB technique allowed measurement close to the jet exit; the profiles of axial velocity and turbulence intensity at $0.2 \cdot D_j$ are shown in Fig. 18.16-f. At this location the shear layer is extremely thin; nevertheless, it appears to be well resolved with the STB technique and with the axial turbulence intensity showing a steep delta profile in the shear layer. To date, such highly resolved 3D flow data near the jet exit has not been achieved.

Furthermore the STB Lagrangian particle tracking approach can extract the material acceleration from individual tracked particles. Profiles of the average axial and radial acceleration components are shown in Fig. 18.16-b and c, respectively (closed circles) and show very high axial accelerations in the shear layer at the jet exit and the development of the thickening shear layer along the axial direction. In the case of 0.75 pixel radial bins 2,000 to 5,000 particles per bin were obtained, whereas

8 pixel radial bins resulted in particle numbers of around 20,000 to 50,000 per bin. For the results shown Fig. 18.16 the bin size has been selected to resolve the local flow features and to ensure statistical convergence.

In the current investigation, the shear layer was the area of focus concerning the turbulent characterization. Synchronization of the flow measurements with the far field pressure recordings enables the application of the causality correlation technique to identify sources of sound as done by HENNING et al. [11]. This will allow highly resolved velocity and acceleration results in the near field to be cross-correlated with the far-field microphone pressure measurements to determine the acoustic propagation paths and to identify noise generation mechanisms.

18.6 Flow over a Full-Scale Cyclist Model by Tomographic PTV

Contributed by:

**A. Sciacchitano, W. Terra, J.F.G. Schneiders, C. Jux,
Y. Shah and F. Scarano**

Cycling aerodynamics is a subclass of bluff-body aerodynamics that has received large attention in the recent years due to the wide variety of flows and fluid mechanisms involved [3]. The flow around a cyclist is highly unsteady and three-dimensional, and even small variations in the rider's posture may yield large changes in the flow structure and ultimately in the aerodynamic drag [3, 7]. The latter contributes to over 90% of the total resistance the cyclist has to overcome at racing speed [6, 16]. Understanding the topology of the flow structure is essential for minimization of the aerodynamic drag and enhancement of the rider's performance. In this experiment, the flow around a full-scale cyclist model and in its near wake is investigated by large-scale tomographic PTV. The use of helium-filled soap bubbles (HFSB) as flow tracers is essential to conduct measurements in a volume of the order of the cubic meter. Their higher light scattering cross-section compared to micrometric tracers [1], and their good tracing fidelity (average relaxation time below 20 μ s according to SCARANO et al. [28]) allow accurate flow measurements over human-size models.

The experiments are conducted in the Open Jet Facility (OJF) of the Aerodynamic Laboratories of Delft University of Technology. The OJF is a close-loop open-test-section wind tunnel with maximum free-stream velocity of 35 m/s and turbulence intensity of 0.5%. A full-scale cyclist replica of the 2017 Giro d'Italia winner Tom Dumoulin is mounted on a Giant Trinity Advanced Pro bicycle frame (2017 model) equipped with a Shimano Dura Ace 9070 group set, Shimano 9000 C75 front wheel and a Pro Extreme Wide disc wheel with Vittoria Corsa 25 mm tubulars. The free-stream velocity is set to 14 m/s, which is a typical racing speed during time-trial. Two different experiments are conducted, as illustrated in Fig. 18.17. In the first experimental setup (wake plane measurement), measurements are carried out in a 5 cm thick vertical plane located 80 cm downstream of the model's back. Three FastCAM SA1

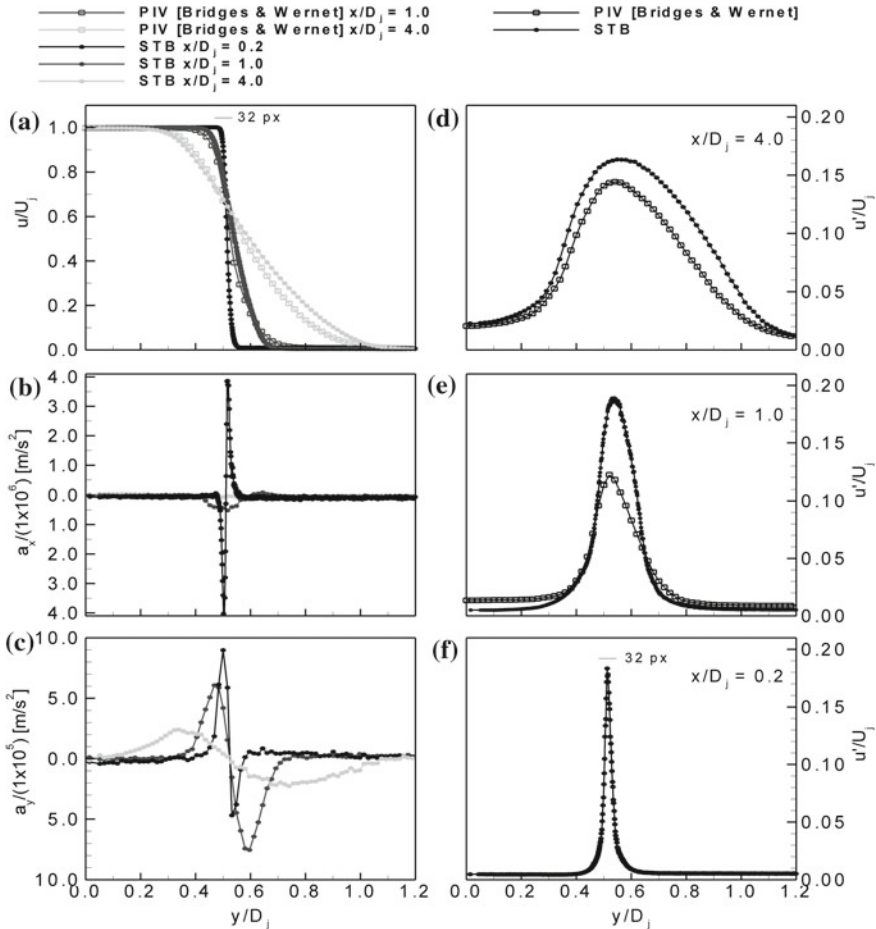


Fig. 18.16 STB results for $Ma = 0.84$ jet. **a** Radial profiles of average normalized axial velocity component (u/U_j); **b** average axial acceleration ($a_x/(1 \cdot 10^6)$); **c** average radial acceleration ($a_y/(1 \cdot 10^5)$). Axial turbulence intensity (u'/U_j) at stations $x/D_j = 4$ (**d**), $x/D_j = 1$ (**e**) and $x/D_j = 0.2$ (**f**). The consensus dataset from BRIDGES & WERNET [2], available for stations $x/D_j = 4, 1$ is plotted for $Ma = 0.9$ (hollow squares). The size of a 32 pixel wide correlation window is given as a reference

cameras record an area of $1.0 \times 1.6 \text{ m}^2$ in the wake of the mannequin. The cameras are positioned about 4 m behind the model, separated by 2.8 m in spanwise direction. The illumination is provided by a Continuum Mesa PIV Nd:YAG laser. The second experimental setup (Robotic PIV measurement) makes use of a coaxial volumetric velocimetry system (CVV, [34]), a compact measurement device composed by four high speed cameras at small tomographic aperture and an optical fiber connected to the laser head (Quantronix Darwin Duo Nd:YLF laser). The velocimeter is mounted onto an UR5 robotic arm, which enables the motion with six degrees of freedom

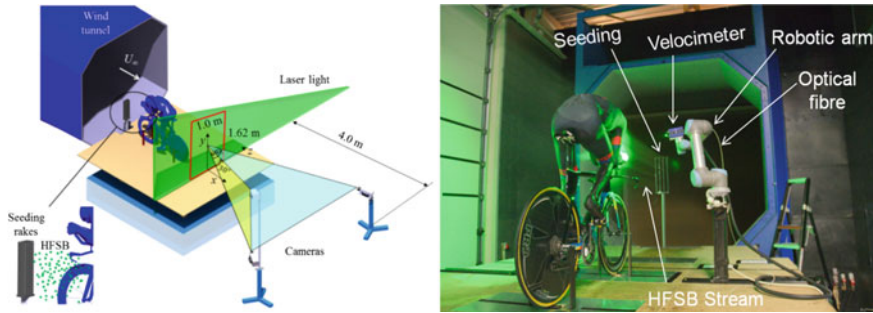


Fig. 18.17 Schematic representation of the setup of the experiment. Left: wake-plane measurement; right: robotic PIV measurement

(three translations and three rotations) with a maximum reach radius of 85 cm. The CVV system allows measurements in sub-volumes of about $25 \times 25 \times 25 \text{ cm}^3$. By moving the velocimeter at different locations relative to the cyclist model, the entire measurement volume of 2 m^3 is scanned, which comprises 450 measurement sub-volumes all around the cyclist [13]. Notice that, since the relative position among the cameras is fixed, all the measurements are conducted using just one camera calibration. In both experiments, the flow is seeded with HFSB tracers introduced into the flow by a 4-wing seeding rake. Each wing has a chord of 10 cm and a span of 50 cm and comprises 20 bubble generators spaced by 2.5 cm. The spacing between two adjacent wings is 5 cm. Each of the 80 bubble generators produces 30,000 bubbles/second, yielding a total bubble production rate of 2.4 million tracers per second. The bubble generators are fed with pressurized air, helium and soap, whose flow rates are controlled by a fluid supply unit provided by LaVision GmbH. The seeding concentration at 14 m/s is about 1.5 tracers/cm³ in a seeded streamtube of $50 \times 15 \text{ cm}^2$ cross-section. To seed the entire measurement domain, the seeding rake is translated at 16 different locations along the spanwise and vertical directions. Further details of the experimental parameters are reported in Table 18.8.

The raw particle image recordings are preprocessed by minimum intensity subtraction (wake plane measurement) and with a temporal high-pass filter (robotic PIV measurement; [29]) to eliminate most background reflections. The preprocessed images are analyzed with the Shake-the-Box algorithm [31], yielding Lagrangian particle tracks with instantaneous velocity vectors at the scattered particle locations. Particle tracks are retrieved by fitting a second order polynomial over 11 successive positions of each tracer along its trajectory. The scattered velocity data provided by the Shake-the-Box algorithm is mapped onto the global reference frame, composed by a Cartesian grid with 20 mm and 5 mm spacing for the two experiments, respectively. Each grid point is the center of a cubic cell of edge l_v (equal to 80 mm and 20 mm for the two experimental setup, respectively). The velocity of all tracers falling within a cubic cell forms the ensemble of the given cell, from which the time-averaged velocity is computed. The cell size is determined with the criterion that at

Table 18.8 Experimental parameters for the two experimental setup

	Wake plane measurement	Robotic PIV measurement
Free-stream velocity	14 m/s	14 m/s
Reynolds number (based on torso length 60 cm)	5.6×10^5	5.6×10^5
Measurement volume	$100 \times 160 \times 5 \text{ cm}^3$	$200 \times 160 \times 70 \text{ cm}^3$
Measurement sub-volumes	$60 \times 20 \times 5 \text{ cm}^3$	$25 \times 25 \times 25 \text{ cm}^3$
Number of sub-volumes	16	450
Imaging system	3× FastCam SA1 cameras (CMOS, 1024×1024 pixel, 5.4 kHz)	4× Minishaker cameras (CMOS, 832×632 pixel, 511 Hz)
Focal length	50 mm	4 mm
f-number	4	8
Optical magnification	0.013	0.014
Digital image resolution	1.6 mm/pixel	0.3 mm/pixel
Illumination system	Continuum Mesa PIV 532-120-M Nd:YAG laser ($2 \times 18 \text{ mJ}$ at 1 kHz)	Quantronix Darwin 527-80-M Nd:YLF laser ($2 \times 25 \text{ mJ}$ at 1 kHz)
Recording frequency	4 kHz within the burst 10 Hz between bursts	758 Hz
Number of samples	480 bursts	5,000
(per sub volume)	11 samples per burst	
Seeding particles	HFSB	HFSB
Seeding concentration	1.5 tracers/cm^3	1.5 tracers/cm^3
Imaged seeding density	0.1 particles per pixel	0.05 particles per pixel
Data analysis method	Lagrangian particle tracking (Shake-the-Box algorithm)	Lagrangian particle tracking (Shake-the-Box algorithm)
Interrogation bin size for statistical analysis	$80 \times 80 \times 80 \text{ mm}^3$	$20 \times 20 \times 20 \text{ mm}^3$
Vector pitch	20 mm	5 mm
Dynamic spatial range	30	100
Dynamic velocity range	50	30

least 10 valid data should be comprised in the ensemble. Combining the information from N_V sub-volumes ($N_V = 16$ for the wake plane measurement; $N_V = 450$ for the robotic PIV experiment), the velocity field in the entire measurement domain ($100 \times 160 \times 5 \text{ cm}^3$ and $200 \times 160 \times 70 \text{ cm}^3$, respectively) is retrieved. For the given settings, the measurement spatial dynamic range (DSR) is estimated as the ratio between the domain larger size and the cell size l_v , and it equals 20 and 100 for the two experimental setup, respectively. The dynamic velocity range (DVR) is estimated as the ratio between maximum and minimum measured tracers velocity and is equal to approximately 50.

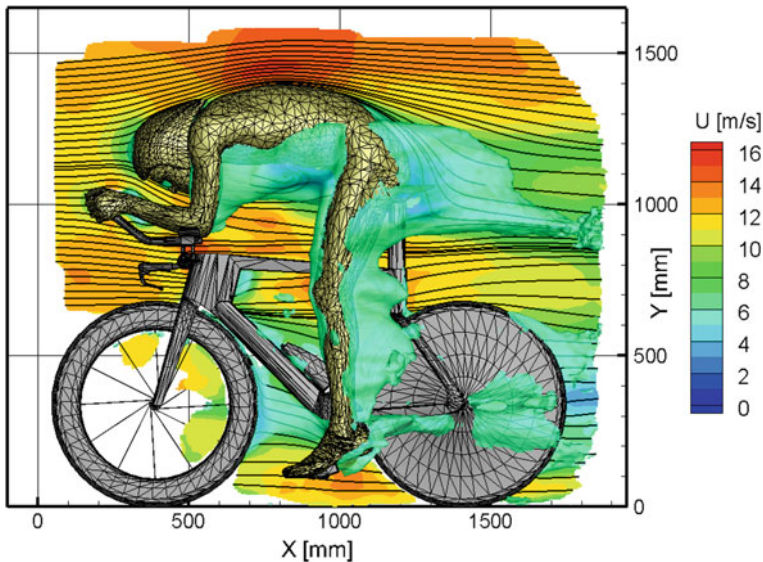


Fig. 18.18 Time-averaged velocity field visualized by a contour of streamwise velocity in the median plane ($z = 0$ mm) including surface streamlines; the iso-surface of streamwise velocity at $U = 7$ m/s is also shown

Figure 18.18 illustrates the time-averaged velocity field of the flow around the cyclist in the median xy plane ($z = 0$ mm), revealing the flow organization at largest scale. A first stagnation region is encountered at the rider's helmet. The flow accelerates along the helmet and the upper curved back, reaching a maximum at approximately half the torso length. Further downstream, the flow decelerates due to the adverse pressure gradient. The boundary layer undergoes separation at the lower back, producing a separated region of relatively small extent. The latter is terminated by a saddle point where streamlines converge right below the bicycle saddle. A secondary stagnation at the front of the rider is identified in front of the hands, which have a relatively close position optimized for time-trial. After stagnating, the flow accelerates around the arms and in the structure between the steering and the upper edge of the fork. The analysis of velocity contours and streamlines does not allow the evaluation of flow features away from the median plane and of the three-dimensional structures. For this purpose, the 3D iso-surface of streamwise velocity $U = 7$ m/s ($0.5U_\infty$) aids the interpretation of the flow. A large region of decelerated flow is comprised between the chest, the elbows and the pelvis. The latter further develops sidewise enveloping the hip of the stretched leg. Stagnation is visible upstream of the leg; the wake region is slightly more pronounced in the calf region than at the ankle, which has comparatively lower cross section. The wake from the leg connects in a three-dimensional topology to the separated region at the rider's low back. Finally, some more pronounced regions of velocity deficit with streamwise elongation are observed at the foot heel, indicating the presence of streamwise vortices. The visible deceleration closer to the back wheel may be partly accentuated by the presence of the

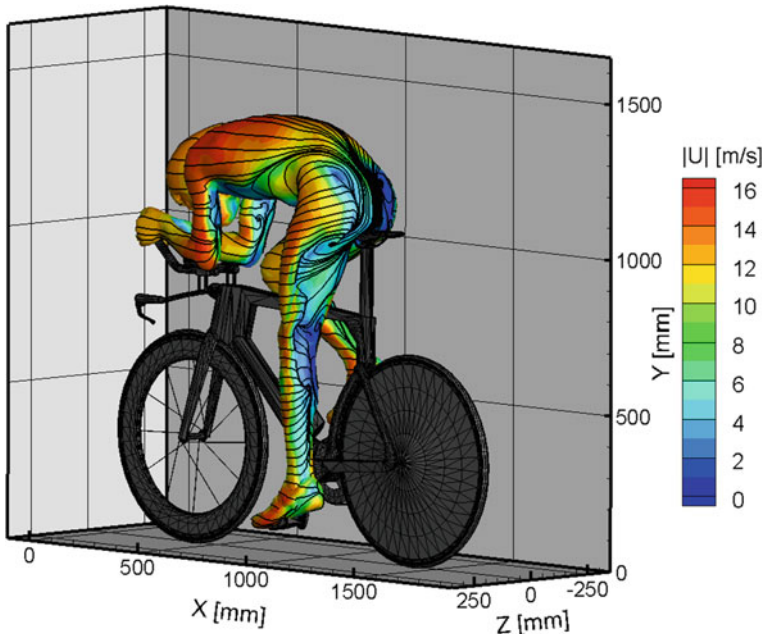


Fig. 18.19 Velocity magnitude contour at 5 mm distance from the cyclist's body. Skin friction lines evaluated over the dilated surface

necessary structure to support the model in the wind tunnel. The two (non-rotating) wheels exhibit a similar wake. The wake of the front wheel is centred at the most downstream point, whereas the back wheel has its wake in a slightly upper position.

The availability of velocity data in the vicinity of the cyclist's solid surface enables to estimate the topology of the skin friction lines (Fig. 18.19). The latter are notably difficult to detect with PIV over curved surfaces due to the challenges of following the 3D surface contour with the illumination and of minimizing the laser light reflections at the solid surface. The 3D streamlines pattern on the dilated surface (near-surface skin friction lines) is inspected to detect the relevant topological features at the surface. The velocity magnitude along the streamlines provides additional information on the flow stagnation, acceleration and separation. The flow on the rider's back appears to separate only at the sides of the low back region. The air captured in the chest region exits sideways along the lower torso and streams towards the center of the lower back. On the straight leg side, the separation occurs only at the gluteus and at the upper part of the calf, as indicated by the interruption of skin friction lines from the side of the upper leg. Conversely, no separation is detected in the lower leg towards the ankle. Flow acceleration around both upper arms and flow separation in their back is also evident. The velocity contour in the wake plane 80 cm downstream of the rider's back (Fig. 18.20 - left) evidences the presence of a significant momentum deficit downstream of the model. The momentum deficit is the largest behind the thigh of the stretched-leg and behind the rear wheel. A strong downwash is produced

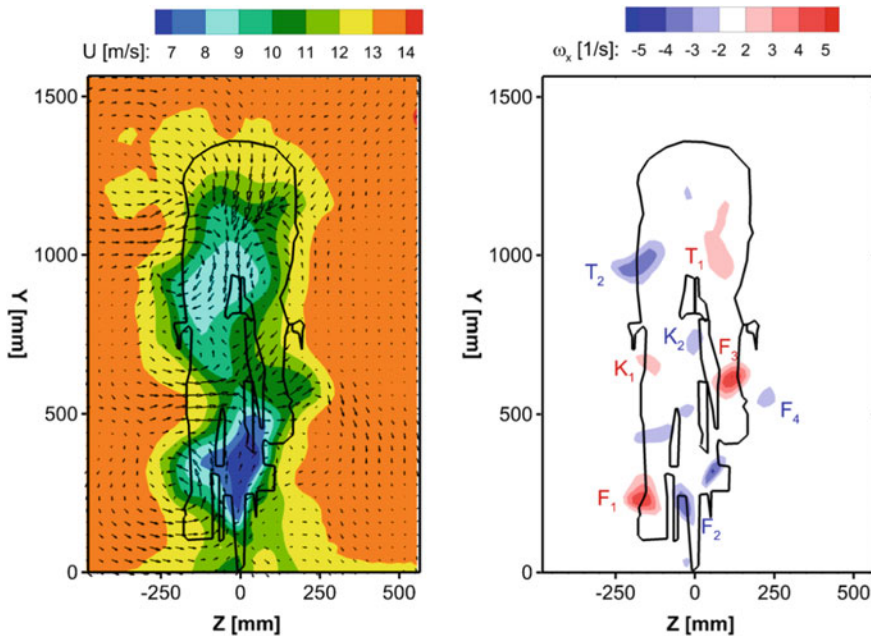


Fig. 18.20 Time-averaged velocity field with velocity vectors (left) and streamwise vorticity component (right) at the wake plane 80 cm downstream of the rider's back

by the upper curved back of the rider, as also found by CROUCH et al. [3]. A velocity deficit is noticed also in proximity of the ground due to the interaction of the model's wake with the stationary floor. A complex system of streamwise vortices takes place below the rider's torso (Fig. 18.20 - right). Two counter-rotating vortices ($T_1 - T_2$) emanate from the inner thighs and contribute to the downwash in between them, as also reported by CROUCH et al. [3]. Two pairs of counter-rotating vortices are produced also by the feet ($F_1 - F_2$ for the stretched leg; $F_3 - F_4$ for the bent leg), which is consistent with the RANS simulations of GRIFFITH et al. [7]. Further streamwise vortices emanate from the knee (K_1 and K_2) of the stretched leg. As thoroughly discussed in the works of CROUCH et al. [3] and GRIFFITH et al. [7], change in the strength and distribution of those vortices at different angles of the crank cycle is the dominant mechanism affecting the unsteady variations of the cyclist's aerodynamic drag.

References

1. Bosbach, J., Kühn, M., Wagner, C.: Large scale particle image velocimetry with helium-filled soap bubbles. *Exp. Fluids* **46**(3), 539–547 (2009). DOI 10.1007/s00348-008-0579-0. URL <https://doi.org/10.1007/s00348-008-0579-0>

2. Bridges, J., Wernet, M.P.: The NASA subsonic jet particle image velocimetry (PIV) dataset. NASA/TM-2011-216807 (2011). URL http://turbmodels.larc.nasa.gov/jetsubsonic_val.html
3. Crouch, T.N., Burton, D., Brown, N.A.T., Thompson, M.C., Sheridan, J.: Flow topology in the wake of a cyclist and its effect on aerodynamic drag. *J. Fluid Mech.* **748**, 5–35 (2014). DOI 10.1017/jfm.2013.678. URL <https://doi.org/10.1017/jfm.2013.678>
4. Discetti, S., Ianiro, A., Astarita, T., Cardone, G.: On a novel flow cost high accuracy experimental setup for tomographic particle image velocimetry. *Meas. Sci Technol.* **24**(075302) (2013). DOI 10.1088/0957-0233/24/7/075302. URL <http://stacks.iop.org/0957-0233/24/i=7/a=075302>
5. Gesemann, S., Huhn, F., Schanz, D., Schröder, A.: From noisy particle tracks to velocity, acceleration and pressure fields using B-splines and penalties. In: 18th International Symposium on Applications of Laser and Imaging Techniques to Fluid Mechanics, Lisbon, Portugal (2016). URL http://lctes.dem.ist.utl.pt/lxaser/lxaser2016/finalworks2016/papers/04.5_4_186paper.pdf
6. Gibertini, G., Grassi, D.: Cycling aerodynamics. In: Nørstrud, H.N. (ed.) *Sport Aerodynamics*, pp. 23–47. Springer Vienna, Vienna (2008). DOI 10.1007/978-3-211-89297-8_3. URL https://doi.org/10.1007/978-3-211-89297-8_3
7. Griffith, M.D., Crouch, T., Thompson, M.C., Burton, D., Sheridan, J., Brown, N.A.T.: Computational fluid dynamics study of the effect of leg position on cyclist aerodynamic drag. *J. Fluids Eng.* **136**(10), 101105: American Society of Mechanical Engineers. DOI (2014). DOI 10.1115/1.4027428. URL <https://doi.org/10.1115/1.4027428>
8. Elsinga, G.E., Scarano, F., Wieneke, B., van Oudheusden, B.W.: Tomographic particle image velocimetry. *Exp. Fluids* **41**(6), 933–947 (2006). DOI 10.1007/s00348-006-0212-z. URL <https://doi.org/10.1007/s00348-006-0212-z>
9. Elsinga, G.E., Westerweel, J., Scarano, F., Novara, M.: On the velocity of ghost particles and the bias errors in tomographic-PIV. *Experiments in Fluids* **50**(4), 825–838 (2011). DOI 10.1007/s00348-010-0930-0. URL <https://doi.org/10.1007/s00348-010-0930-0>
10. Henning, A., Koop, L., Schröder, A.: Causality correlation analysis on a cold jet by means of simultaneous particle image velocimetry and microphone measurements. *J. Sound Vib.* **332**(13), 3148–3162 (2013). DOI 10.1016/j.jsv.2013.01.027. URL <http://www.sciencedirect.com/science/article/pii/S0022460X13000758>
11. Henning, A., Wrede, B., Schröder, A.: About the ambiguity of noise source localization based on the causality correlation technique. In: 17th International Symposium on Applications of Laser and Imaging Techniques to Fluid Mechanics, Lisbon, Portugal (2014). URL http://lctes.dem.ist.utl.pt/lxaser/lxaser2014/finalworks2014/papers/02.3_3_319paper.pdf
12. Huhn, F., Schanz, D., Gesemann, S., Schröder, A.: Pressure reconstruction from lagrangian particle tracking with FFT integration. In: 18th International Symposium on Applications of Laser and Imaging Techniques to Fluid Mechanics, Lisbon, Portugal (2016)
13. Jux, C., Sciacchitano, A., Schneiders, J.F.G., Scarano, F.: Full-scale cyclist aerodynamics by coaxial volumetric velocimetry. 12th International Symposium on PIV, Busan, Korea (2017)
14. Kähler, C.J., Kompenhans, J.: Fundamentals of multiple plane stereo particle image velocimetry. *Exp. Fluids* **29**(1), S070–S077 (2000)
15. Kähler, C.J., Scharnowski, S., Cierpka, C.: On the uncertainty of digital PIV and PTV near walls. *Exp. Fluids* **52**(6), 1641–1656 (2012). DOI 10.1007/s00348-012-1307-3. URL <https://doi.org/10.1007/s00348-012-1307-3>
16. Kyle, C.R., Burke, Edmund Improving, the racing bicycle. *Mech. Eng.* **106**(9), 34–45, American Society of Mechanical Engineers 345 E 47TH ST, p. 10017. New York (1984)
17. Lenaers, P., Li, Q., Brethouwer, G., Schlatter, P., Örlü, R.: Negative streamwise velocities and other rare events near the wall in turbulent flows. *J. Phys. Conference Ser.* **318**, 022013, IOP Publishing (2011). DOI 10.1088/1742-6596/318/2/022013. URL <http://stacks.iop.org/1742-6596/318/i=2/a=022013>
18. Liepmann, D., Gharib, M.: The role of streamwise vorticity in the near-field entrainment of round jets. *J. Fluid Mech.* **245**, 643–668 (1992). DOI 10.1017/S0022112092000612. URL <https://doi.org/10.1017/S0022112092000612>

19. Maas, H.G., Gruen, A., Papantoniou, D.: Particle tracking velocimetry in three-dimensional flows. *Exp. Fluids* **15**(2), 133–146 (1993). DOI 10.1007/BF00190953. <https://doi.org/10.1007/BF00190953>
20. Malik, N.A., Dracos, T., Papantoniou, D.A.: Particle tracking velocimetry in three-dimensional flows. *Exp. Fluids* **15**(4), 279–294 (1993). DOI 10.1007/BF00223406. URL <https://doi.org/10.1007/BF00223406>
21. Mathis, R., Marusic, I., Chernyshenko, S.I., Hutchins, N.: Estimating wall-shearstress fluctuations given an outer region input. *J. Fluid Mech.* **715**, 163–180 (2013). DOI 10.1017/jfm.2012.508. URL <https://doi.org/10.1017/jfm.2012.508>
22. Miguel, E., Henning, A.: Analysis of simultaneous measurement of acoustic pressure in the far-field and density gradient in the near-field in a cold jet. In: 19th AIAA/CEAS Aeroacoustics Conference, Berlin, Germany, pp. 2013–2034 (2013). DOI 10.2514/6.2013-2034. URL <https://doi.org/10.2514/6.2013-2034>
23. Melling, A.: Tracer particles and seeding for particle image velocimetry. *Meas. Sci. Technol.* **8**(12), 1406 (1997). DOI 10.1088/0957-0233/8/12/005. URL <http://stacks.iop.org/0957-0233/8/i=12/a=005>
24. Novara, M., Scarano, F.: A particle-tracking approach for accurate material derivative measurements with tomographic PIV. *Exp. Fluids* **54**(8), 1–12 (2013). DOI 10.1007/s00348-013-1584-5. URL <https://doi.org/10.1007/s00348-013-1584-5>
25. Novara, M., Schanz, D., Gesemann, S., Lynch, K., Schröder, A.: Lagrangian 3D particle tracking for multi-pulse systems: performance assessment and application of Shake-The-Box. In: 18th International Symposium on Applications of Laser and Imaging Techniques to Fluid Mechanics, Lisbon, Portugal (2016). URL http://lces.dem.ist.utl.pt/1xlaser/1xlaser2016/finalworks2016/papers/04.5_1_126paper.pdf
26. Novara, M., Schanz, D., Reuther, N., Kähler, C.J., Schröder, A.: Lagrangian 3D particle tracking in high-speed flows: Shake-The-Box for multi-pulse systems. *Exp. Fluids* **57**(8), 128 (2016). DOI 10.1007/s00348-016-2216-7. URL <https://doi.org/10.1007/s00348-016-2216-7>
27. Scarano, F.: Tomographic PIV: principles and practice. *Meas. Sci. Technol.* **24**(1), 012001 (2013). DOI 10.1088/0957-0233/24/1/012001. URL <https://doi.org/10.1088/0957-0233/24/1/012001>
28. Scarano, F., Ghaemi, S., Caridi, G.C.A., Bosbach, J., Dierksheide, U., Sciacchitano, A.: On the use of helium-filled soap bubbles for large-scale tomographic PIV in wind tunnel experiments. *Exp. Fluids* **56**(2), 42 (2015). DOI 10.1007/s00348-015-1909-7. URL <https://doi.org/10.1007/s00348-015-1909-7>
29. Sciacchitano, A., Scarano, F.: Elimination of PIV light reflections via a temporal high pass filter. *Meas. Sci. Technol.* **25**(8), 084,009 (2014). DOI 10.1007/s00348-012-1345-x. URL <https://doi.org/10.1007/s00348-012-1345-x>
30. Schlatter, P., Örlü, R.: Assessment of direct numerical simulation data of turbulent boundary layers. *J. Fluid Mech.* **659**, 116–126 (2010). DOI 10.1017/S0022112010003113. URL <https://doi.org/10.1017/S0022112010003113>
31. Schanz, D., Gesemann, S., Schröder, A.: Shake-The-Box: Lagrangian particle tracking at high particle image densities. *Exp. Fluids* **57**(5), 1–27 (2016). DOI 10.1007/s00348-016-2157-1. URL <https://doi.org/10.1007/s00348-016-2157-1>
32. Schanz, D., Gesemann, S., Schröder, A., Wieneke, B., Novara, M.: Non-uniform optical transfer functions in particle imaging: calibration and application to tomographic reconstruction. *Meas. Sci. Technol.* **24**(2) (2013). DOI 10.1088/0957-0233/24/2/024009. URL <http://stacks.iop.org/0957-0233/24/i=2/a=024009>
33. Schanz, D., Huhn, F., Gesemann, S., Dierksheide, U., van de Meerendonk, R., Manovski, P., Schröder, A.: Towards high-resolution 3D flow field measurements at the cubic meter scale. In: 18th International Symposium on Applications Laser Techniques to Fluid Mechanics, Lisbon, Portugal (2016). URL <http://elib.dlr.de/101290/>
34. Schneiders, J.F.G., Scarano, F., Jux, C., Sciacchitano, A.: Coaxial volumetric velocimetry. 12th International Symposium on PIV, Busan, Korea (2017)

35. Schröder, A., Schanz, D., Geisler, R., Gesemann, S., Willert, C.E.: Near-wall turbulence characterization using 4D-PTV “Shake-The-Box”. In: 11th International Symposium on Particle Image Velocimetry - PIV2015. Santa Barbara, CA, USA (2015)
36. Schröder, A., Schanz, D., Geisler, R., Willert, C.E., Michaelis, D.: Dual-volume and four-pulse tomo PIV using polarized laser light. In: PIV13; 10th International Symposium on Particle Image Velocimetry, Delft University of Technology, Faculty of Mechanical, Maritime and Materials Engineering, and Faculty of Aerospace Engineering, Delft, The Netherlands (2013). URL <http://repository.tudelft.nl/islandora/object/uuid%3A5ee95ec8-02aa-47dd-98a9-ecb4cffe23a?collection=research>
37. Schröder, A., Schanz, D., Michaelis, D., Cierpka, C., Scharnowski, S., Kähler, C.J.: Advances of PIV and 4D-PTV ‘Shake-The-Box’ for turbulent flow analysis—the flow over periodic hills. *Flow, Turbul. Combust.* **95**(2), 193–209 (2015). DOI 10.1007/s10494-015-9616-2. URL <https://doi.org/10.1007/s10494-015-9616-2>
38. van Gent, P.L., Michaelis, D., van Oudheusden, B.W., Weiss, P.É., de Kat, R., Laskari, A., Jeon, Y.J., David, L., Schanz, D., Huhn, F., Gesemann, S., Novara, M., McPhaden, C., Neeteson, N.J., Rival, D.E., Schneiders, J.F.G., Schrijer, F.F.J.: Comparative assessment of pressure field reconstructions from particle image velocimetry measurements and Lagrangian particle tracking. *Exp. Fluids* **58**(4), 33 (2017). DOI 10.1007/s00348-017-2324-z. URL <https://doi.org/10.1007/s00348-017-2324-z>
39. van Oudheusden, B.W.: PIV-based pressure measurement. *Meas. Sci. Technol.* **24**(3), 032001 (2013). DOI 10.1088/0957-0233/24/3/032001. URL <http://stacks.iop.org/0957-0233/24/i=3/a=032001>
40. Violato, D., Scarano, F.: Three-dimensional evolution of flow structures in transitional circular and chevron jets. *Phys. Fluids* **23**(12), 124104 (2011). DOI 10.1063/1.3665141. URL <https://doi.org/10.1063/1.3665141>
41. Violato, D., Scarano, F.: Three-dimensional vortex analysis and aeroacoustic source characterization of jet core breakdown. *Phys. Fluids* **25**(015112), 1 (2013). DOI 10.1063/1.4773444. URL <https://doi.org/10.1063/1.4773444>
42. Wieneke, B.: Volume self-calibration for 3D particle image velocimetry. *Exp. Fluids* **45**(4), 549–556 (2008). DOI 10.1007/s00348-008-0521-5. URL <https://doi.org/10.1007/s00348-008-0521-5>
43. Wieneke, B.: Iterative reconstruction of volumetric particle distribution. *Meas. Sci. Technol.* **24**(2) (2013). DOI 10.1088/0957-0233/24/2/024008. URL <http://stacks.iop.org/0957-0233/24/i=2/a=024008>

Chapter 19

Related Techniques

As noted in Sect. 1.3, PIV developed from Laser Speckle Interferometry. Therefore, one of the early names for this technique was ‘Laser Speckle Velocimetry’ before ‘Particle Image Velocimetry’ was established. The Laser Speckle Interferometry (or Laser Speckle Photography) was mainly developed for the determination of displacement and strain in engineering structures. The laser speckles are created due to random interference of scattered light from an optically rough surface illuminated by coherent light. In a pioneering publication BURCH & TOKARSKI [5] showed that, when two such speckle patterns of an object, recorded with and without displacement, are optically transformed, fringes representing the local displacement can be obtained. These fringes where the visible squared intensities of the Fourier Transform of the speckle patterns, which is the power spectrum. An inverse Fourier Transform yields the correlation function of the original image. The method – today conducted purely digitally - is still the basis for nearly all modern “relatives” of speckle photography.

In contrast to PIV, where lasers are still most commonly used due to their ability to generate thin and intense light sheets, speckle deformation measurements nowadays favor white light illumination. White light speckles instead of laser speckles offer two major advantages: Since laser speckle fields tend to change their appearance when the displacement to be measured exceeds a certain range, the image pairs might de-correlate and the evaluation becomes increasingly difficult. Secondly, the illumination of large and highly three-dimensional objects requires small recording apertures and, as a result of that, powerful and expensive lasers for illumination. Therefore, white light illumination is more frequently used since the 1980s. For this method a speckle pattern, which simply is a random dot pattern sprayed, painted or projected on a background, is generated. The dots should have the highest possible contrast and a spatial frequency that is as high as possible and as small as necessary to be imaged with sufficient contrast. Retroreflective paint, consisting of small

An overview of the Digital Content to this chapter can be found at [\[DC19.1\]](#).

suspended glass beads for example was used by ASUNDI & CHIANG [1] for contrast enhancement. The technique of pattern projection for wind tunnel model deformation measurements has successfully been used by VAN DER DRAAI et al. [11]. Multi-camera systems can be used in order to resolve complex object shapes for the analysis of their topology. The use of pulsed white light sources allows for the observation of moving surfaces. The list of references at the end of the book contains some of the numerous publications on such deformation measurement techniques. The continuous development of digital methods in image recording and processing has led to new names for this type of geometry, shape and deformation identification. From all the various names like Image Pattern Correlation Technique (IPCT) or Electronic Speckle Interferometry (ESI), the Digital Image Correlation (DIC) apparently became the most common one name within the past decades [7, 21, 33]. Therefore, we decided to use the name DIC deformation measurement in the remainder of the book. DIC imaging systems and software packages have become common engineering tools and can be purchased.

However, not only deformations can easily be measured by means of acquisition and evaluation systems similar to PIV, but also density gradients in transparent media. This approach has probably been known since a long time, but it has not drawn much attention until a few years ago. The technique has been referred to as synthetic schlieren [8], and background-oriented schlieren (BOS) [24] by the different authors. In contrast to the conventional schlieren methods the BOS technique does not require any complex optical devices for illumination. The only optical part needed is an objective lens mounted for instance on a video camera. The camera is focused on a random dot pattern in the background, which generates an image quite similar to a particle image or speckle pattern shown as in Fig. 19.4. For this reason we refer to this approach as background-oriented. Compared to conventional schlieren techniques this procedure results in significantly reduced efforts during its application. However, the optical paths over which the density effects are integrated, are divergent with respect to each other. This can result in a clear disadvantage when large viewing angles have to be used, but is of little influence for recording distances of more than 10 meters used for the tests to be described in Sect. 19.2. In an extension towards background-oriented optical tomography (BOOT), which was proposed by RAFFEL et al. [23], the divergence of the optical paths can be compensated by the evaluation algorithms [12, 14].

Both, the measurement of density gradients in a flow and the detection of the deformation and position of a model in the flow are frequently of interest and can be obtained easily based on PIV imaging hard- and software.

19.1 Deformation Measurement by Digital Image Correlation (DIC)

One of the main motivations for measurements in fluid dynamics is the determination of forces and moments on structures resulting from their interaction with

the fluid. Those fluid dynamic forces frequently lead to model deformations and displacements of parts of the setup. Since scaling and shape factors are important experimental parameters, the shape and position of a model have to be monitored repeatedly during the test. Point-wise methods are commonly used for this purpose but are sometimes quite laborious and could miss critical regions. Whole field optical methods can be used for the non-intrusive measurement of model deformations and displacements. The Moiré Interferometry is one such techniques, which allows obtaining highly accurate results over large fields at once. The disadvantages of the Moiré techniques are their experimental complexity and the fact that the evaluation software, like in many other cases of interferometry, can not always be run fully automatically. Therefore, starting in the 1970s correlation based procedures for deformation, displacement, and strain analysis have been developed and applied more and more frequently [6, 29].

19.1.1 Deformation Measurement in a High-Pressure Facility

Due to the high costs and a limited feasibility of complex laser measurements at full-scale test conditions, most experimental studies on the aerodynamics of high-speed trains are conducted on sub-scales in wind tunnel facilities. However, in most cases the Reynolds and Mach numbers of the model investigations do not match the full-scale vehicle at the same time. Most modern low-speed wind tunnels reach appropriate Mach numbers of $0.1 < Ma < 0.3$. However, if the relative air speed is approximately the same for both the model and the full-scale train, the Reynolds number in the wind tunnel will obviously be much smaller than that of the full-scale vehicle. For aerodynamically well-designed configurations, the resulting mismatch in Reynolds number leads to a certain discrepancy of measured drag and moment values. This brings facilities into play, which are specialized for high Reynolds number investigations like high-pressure facilities. Those facilities allow for the realization of the relevant Mach and Reynolds numbers at reduced scales. Since loads on the model increases with increasing pressure, model deformations and deflections have to be monitored carefully during tests.

The high-pressure wind tunnel of DNW (HDG), shown in Fig. 19.1, is a closed circuit low-speed wind tunnel, which can be pressurized up to 100 bar. The dimensions of the test section are $0.6 \times 0.6 \text{ m}^2$ with a length of 1 m. 1 : 50 and 1 : 66 models are usually used in order to realize a blockage ratio below 10%. With the maximum speed of 35 m/s and a maximum pressure of 100 bar the achieved Reynolds number is of the same order of magnitude as the full-scale one (e.g. $Re = O[10^7]$). The flow remains incompressible over the whole range of Reynolds numbers.

The model of the lead car and the first part of the trailer of a train shown in Fig. 19.2, are designed to carry a six-component internal balance. The strain gage balance is relatively compact and measures forces up to approximately 1000 N. All

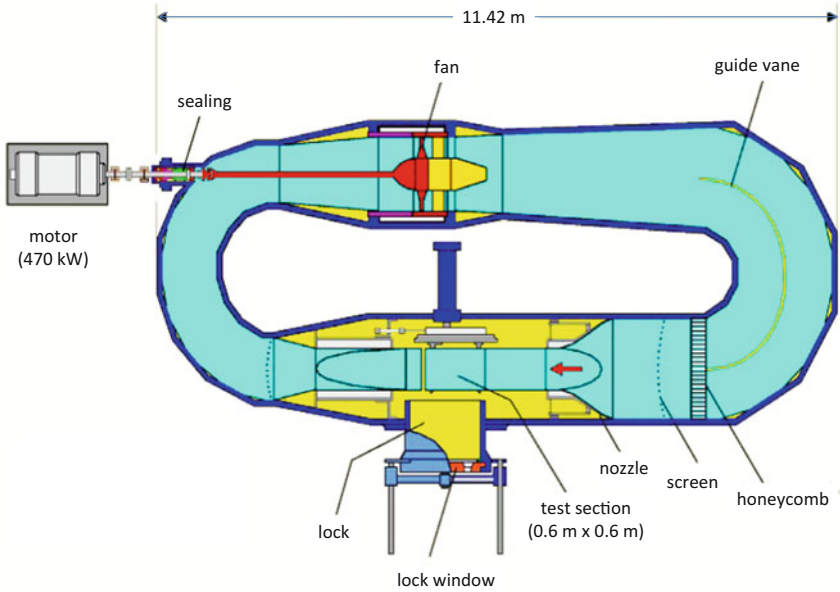
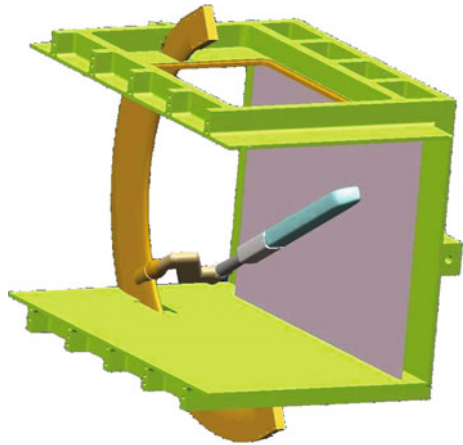


Fig. 19.1 Sketch of the high pressure wind tunnel (HDG) of DNW

Fig. 19.2 Sketch of the train model configuration in the test section of the HDG



components of force and moment are available and have been measured for a range of yaw angles between $-30^\circ < \beta < +30^\circ$ during these tests. The lead vehicle and the trailer were mounted sideways onto the sting.

Digital Image Correlation (DIC) has been applied to generic high-speed train models in order to measure model deflections and model deformations due to wind

load. The stiffness of models in high-pressure wind tunnels is generally more critical since their dimensions are smaller and the wind loads are higher as compared to conventional wind tunnels. As mentioned previously, DIC is basically an image processing technique that calculates the displacement of a random dot pattern – which is somehow attached or projected onto the object under investigation – by using correlation techniques. Today, the digital correlation algorithms used for DIC, BOS and PIV are robust and offer small relative errors below 0.1%. In the case of the model deformation measurements presented here, DIC allows for the determination of small deformations with standard deviations of approximately 0.1 pixel of the CCD-sensor used. This corresponds to a 0.01 mm accuracy for this measurement of the position of the train model in the HDG wind tunnel. The model – on which a random dot pattern of black ink has been painted – was mounted on a sting and equipped with an internal six component balance (Fig. 19.2). An additional ground plate was mounted in order to cut off the wind tunnel boundary layer and to ensure well-defined boundary conditions. The plate was parallelized to the wind tunnel floor by measuring the pressure distribution in the center (at yawing angles of $\beta = 0^\circ$). Force measurements were performed in the high-pressure wind tunnel and the DIC technique was applied in order to correct the yawing angle. It can easily be seen in Fig. 19.3, that in spite of the very stiff sting and support, the yawing angle of the model was significantly changing depending on the free stream velocity (e.g. $\pm 1.3^\circ$ at 20 m/s).

Figure 19.3 shows an example of instantaneous pattern correlations on the left hand side. One hundred vector fields were used to process the mean angle shown on the right of Fig. 19.3. It can be seen that the displacement increases linearly due to sting bending. Additional model deformations, which would result in more complex displacement patterns, were not observed. In the way the DIC technique was applied here, only deformations in the $x - z$ -plane could be determined. However, generally this technique is well-suited for three-dimensional measurements if two or more cameras are used [15, 17, 25].

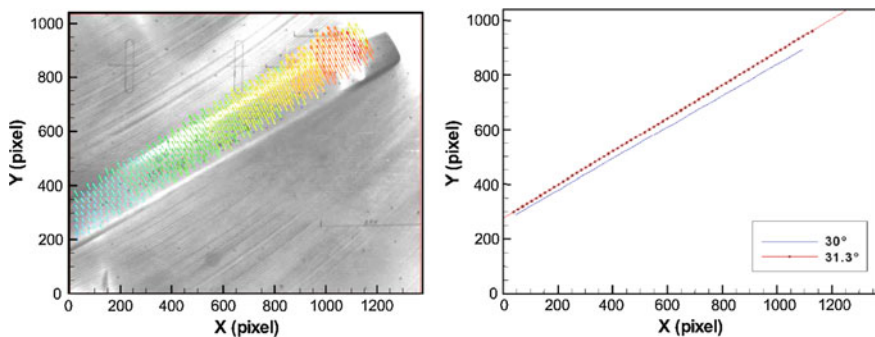


Fig. 19.3 Instantaneous DIC result, showing the local displacement vectors, the measured positions of the random dots at $\alpha = 30^\circ$ reference recording (straight line) and the positions measured under wind load at $P_0 = 30$ bar and $U_\infty = 20$ m/s (dotted line) (right)

19.2 Background-Oriented Schlieren Technique (BOS)

19.2.1 Introduction

Optical density visualization techniques such as schlieren photography, shadowgraphy or interferometry are well known and have been used world wide for many decades. The techniques are sensitive to changes of the refractive index caused by the variations in the fluid density. Even though some researchers have performed large-field and focusing schlieren photography and shadowgraphy in the great outdoors e.g. [2, 27, 31]), most of these techniques are confined to laboratories or to wind tunnels and they are less suitable for large- or full-scale applications. Nevertheless, full-scale measurements are desirable if the flow is strongly dependent on Mach and Reynolds numbers. The next section describes the theory of a technique which determines density gradients without using any sophisticated optical equipment. Practical aspects of the technique are addressed by the description of its application to a helicopter in hovering flight and to the transonic flow behind a cylinder. More examples can be found in a review article by RAFFEL [22].

19.2.2 Principle of the BOS Technique

The background-oriented schlieren technique is based on the relation between the refractive index of a gas, n , and the density, ρ , given by the Gladstone-Dale equation, $(n - 1)/\rho = \text{const.}$ It can best be compared with laser speckle density photography as described by DEBRUS et al. [9] and KÖPF et al. [16] and in improved versions by WERNEKINCK & MERZKIRCH [32] and VIKTIN & MERZKIRCH [30]. Like interferometry, the laser speckle density photography relies on an expanded parallel laser beam, which crosses through a transonic flow field or – in more general terms – through an object of varying refractive index (i.e. a phase object). However, in contrast to interferometry, laser speckle patterns are generated instead of interference fringes. Since white light based techniques for the determination of fluid density gradients are frequently called schlieren¹ techniques [19, 20], the technique described in this chapter will be referred to as the background-oriented schlieren technique. Compared to the optical techniques mentioned above, the BOS method simplifies the recording. The speckle pattern, usually generated by the expanded laser beam and ground glass, is replaced by a random dot pattern on a surface in the background of the test volume. This pattern has to have a high spatial frequency that can be imaged with high contrast.

Usually, the recording has to be performed as follows: first a reference image is generated by recording the background pattern observed through air at rest in advance or subsequent to the experiment. In the second step, an additional exposure through

¹The German word “Schliere” designates a local optical inhomogeneity in a transparent medium.

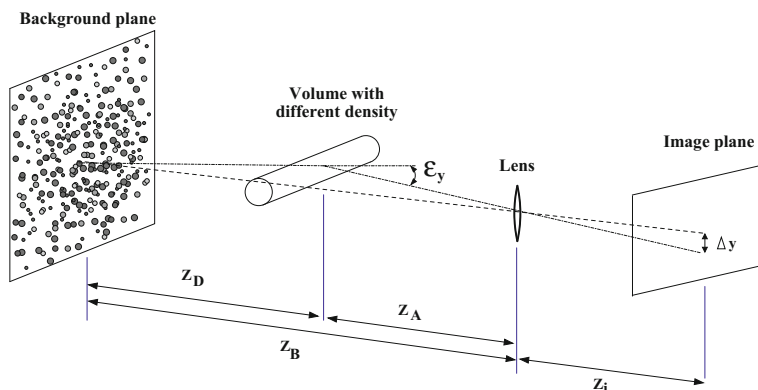


Fig. 19.4 Sketch of a BOS setup

the flow under investigation (i.e. during the wind tunnel run) leads to a displaced image of the background pattern. The resulting images of both exposures can then be evaluated by correlation methods. Without any further effort existing evaluation algorithms, which have been developed and optimized for example for particle image velocimetry (or other forms of speckle photography) can then be used to determine speckle displacements. As stated previously, the deflection of a single beam contains information about the spatial gradient of the refractive index integrated along the line of sight (see Fig. 19.4). Details on the theory of ray tracing through gradient-index media could be found in [10, 28].

The idea of the BOS method is to simplify the optical arrangement by replacing the laser speckle with a random dot pattern, which may simply consist of ink or paint droplets, splashed onto a background surface (see Fig. 19.4). The background pattern may also be generated by a print of a single exposed image of tracer particles.

Assuming paraxial recording and small deflection angles, a formula for the image displacement Δy can be derived, which is valid for density speckle photography as well as for the BOS technique.

$$\Delta y = Z_D M \varepsilon_y \tag{19.1}$$

with the magnification factor of the background, $M = Z_i / Z_B$, the distance between the dot pattern and the density gradient, Z_D , and

$$\varepsilon_y = \frac{1}{n} \int \frac{\partial n}{\partial y} dz \tag{19.2}$$

The image displacement Δy can thus be rewritten as

$$\Delta y = f \left(\frac{Z_D}{Z_D + Z_A - f} \right) \tag{19.3}$$

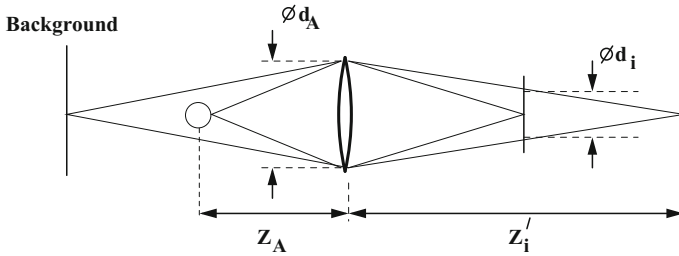


Fig. 19.5 BOS focusing position and image blur

with Z_A being the distance from the lens to the object and the focal length of the lens, f . Since the imaging system has to be focused onto the background; we note:

$$\frac{1}{f} = \frac{1}{Z_i} + \frac{1}{Z_B} \tag{19.4}$$

Equation (19.4) shows that a large image displacement can be obtained for a large Z_D and small Z_A . The maximum image displacement for Z_D approaches $\Delta y = f \cdot \varepsilon_y$. On the other hand certain constraints in the decrease of Z_A have to be fulfilled in order to image the flow field sufficiently sharply. The optical system has to be focused on the background in order to obtain maximum contrast at high spatial frequencies for later interrogation, and Eq. (19.4) applies. On the other hand, the sharp imaging of the density gradients would be best at Z_i with

$$\frac{1}{f} = \frac{1}{Z'_i} + \frac{1}{Z_A} \tag{19.5}$$

By introducing the aperture diameter d_A and the magnification of the density gradient imaging $M' = Z_i/Z_A$ a formula for the blur d_i (see also Fig. 19.5) of a point at Z_A reads:

$$d_i = d_A \left(1 - \frac{1}{f} \left(Z_i - \frac{f}{Z_A} \right) \right) . \tag{19.6}$$

Since correlation techniques average over the interrogation window area, the image blur d_i does not lead to a significant loss of information, as long as d_i is considerably smaller than the interrogation window size.

19.2.3 Application of the BOS to Compressible Vortices

19.2.3.1 Rotor Tip Vortices

The background-oriented schlieren technique was successfully applied to study different types of flows [3, 8]. In this section two experiments are presented: A helicopter blade tip vortex investigation and an investigation of the wake behind a cylinder.²

A first demonstration of the feasibility of BOS for large-scale aerodynamic investigations was given by RAFFEL et al. [24]. In this initial test, part of the rotor tip vortex system of a Eurocopter BK117 was visualized with the BOS technique. However, the analysis of typical vortex-related effects, e.g. blade vortex interaction (BVI) phenomena, requires quantitative data such as the blade tip vortex positions relative to the rotor system.

The first 3D reconstruction of an entire blade tip vortex system of a full-scale helicopter was demonstrated by BAUKNECHT et al. [3], who performed a large-scale flight test with a BO105 helicopter and a multi-camera BOS setup in an open-pit mine. The BOS setup consisted of ten digital consumer cameras that were positioned around the free-flying helicopter in front of scree-covered slopes. These natural backgrounds were illuminated by the sun and provided fine structures with sufficient contrast for the BOS evaluation. The distance between the background and the cameras was 230–300 m and the camera setup covered a horizontal angle of 80° around the helicopter. The Nikon D7100 digital single-lens reflex cameras featured CMOS image sensors with a resolution of 6000 × 4000 pixel, suitable for full-scale vortex measurements. The cameras were equipped with Nikkor 55–300 mm zoom lenses and simultaneously triggered with a cable-based triggering system. The exposure time was set to 1 ms, ISO values to 400, and aperture adapted to the natural illumination between $f/5.6$ and $f/11$.

Figure 19.6 shows an example of an image pair, consisting of an undisturbed reference image (Fig. 19.6a) and a measurement image of the helicopter (Fig. 19.6b). The measurement image was mapped onto the reference images using a de-warping algorithm based on the displacements in the corners of the image pair, as determined by cross-correlation. The apparent background displacements between the image pair were evaluated using sectional cross-correlation. A multi-grid evaluation scheme with a final window size of 16 × 16 pixel and an overlap of 75% (corresponding to a vector spacing of 1 cm in the rotor plane) was selected to resolve the small vortex-induced displacements (u, v) in the horizontal (x) and vertical (y) direction, respectively. In the resulting displacement field, the displacement vectors point towards regions of low density, i.e. the vortex cores. Vortices with peak-to-peak displacements of $\Delta v = 0.15 - 1.5$ pixel and projected diameters of 4–6 pixel were detected in this study. Robust indicators for the center position of the vortices are given by the spatial gradients du/dx and dv/dy . These indicators emphasize the vortices due to their high spatial gradients compared to the gradual changes in the

²The text on blade tip vortex investigation has been contributed by André Bauknecht.

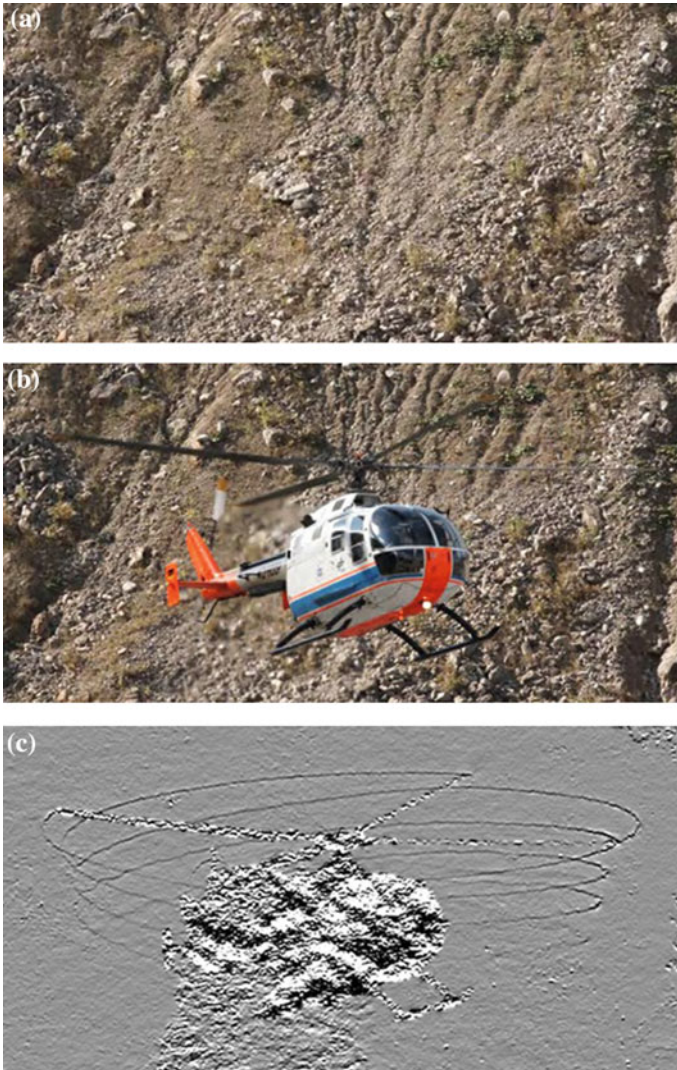
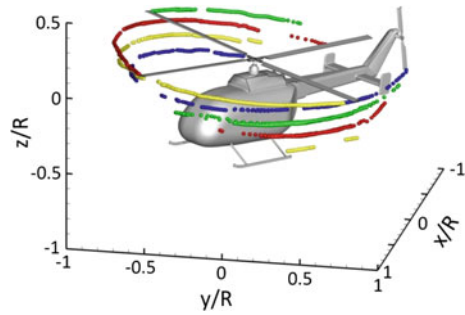


Fig. 19.6 Cutouts of measurement pictures depicting **a** the undisturbed reference image and **b** measurement image with the helicopter, after [3]. The result of a cross-correlation between the two images is shown in **c** in form of the vertical displacement gradient field, visualizing the blade tip vortex system and the engine exhaust gases [DC19.2]

surrounding flow field, see Fig. 19.6c. The evaluated image shows the vortex system of the BO105 during an ascending flight maneuver. The vortices are visible as dark helically curved lines in front of the gray background. The positions of the helicopter and its rotor blades are indicated by de-correlated regions. Below and behind the helicopter, a noisy area marks the exhaust gases of the two engines.

Fig. 19.7 Reconstruction of the blade tip vortex system of the BO105 helicopter during ascending maneuvering flight, after [3] [DC19.3]



The projected vortex locations, shown e.g. in Fig. 19.6c, were extracted from all simultaneously acquired measurement images and digitized using a semi-automatic detection routine. The camera setup was iteratively calibrated based on a random point cloud inside the measurement volume. Point correspondence between vortex segments from different cameras was established by epipolar geometry [13]. Based on the projected 2D vortex positions and points on the helicopter, the positions of the helicopter, rotor blades, and the corresponding vortex system were reconstructed in 3D space by stereo-photogrammetry.

An example for the reconstructed vortex system of the BO105 during an ascending flight maneuver is depicted in Fig. 19.7. The plot depicts a 3D computer model of the helicopter positioned according to reconstructed points on the fuselage and rotor blades of the real helicopter. Individual points were reconstructed on the vortex segments and indicate the positions and trajectories of the tip vortices. The data set allows for the extraction of geometrical vortex properties that are important for the investigation of BVI on helicopters undergoing dynamic flight maneuvers. These results demonstrate the potential of the multi-camera BOS method for the investigation of rotorcraft aerodynamics and BVI effects.

19.2.3.2 Cylinder Wake Flows

The experiment described next was set up in order to study compressible vortex flows involved in the blade vortex interaction (BVI) phenomena of helicopter rotors in more detail. Therefore, the vortex shedding on a cylinder with a diameter of $d = 25$ mm in a transonic wind tunnel – the VAG of DLR in Göttingen – has been investigated by simultaneous velocity and density gradient measurements at different free-stream Mach numbers.³ This information was complemented by additional measurements of the unsteady pressure fluctuations at different locations along the wind tunnel walls. These data enable a more detailed analysis of compressible vortices than successive measurements of single quantities. In addition, a detailed description of compressible vortices plays a key role in numerical simulations, which aim at further

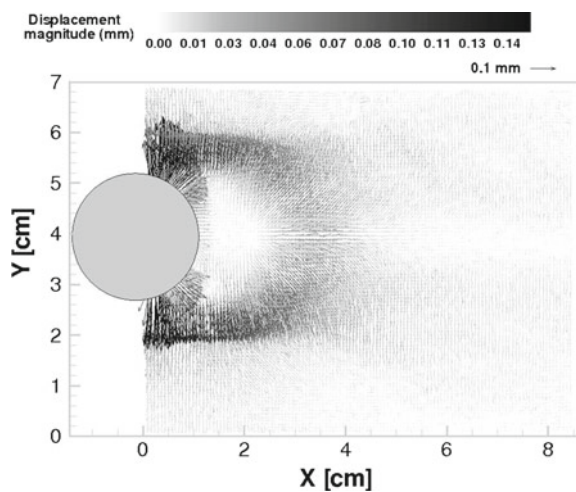
³The text on cylinder wake flows has been contributed by Hugoes Richard.

improvements in the prediction of helicopter noise emissions. The measurement of the velocity induced by the vortex is needed, since the amplitude of the pressure fluctuations which are emitted from the interaction of the vortex with a blade is proportional to the circulation, Γ , of the vortex. In the past, the velocity information has been derived by simultaneous pressure and density measurements (see e.g. [18]). Therefore, one had to assume the vortex to move at a constant convection velocity, that it is symmetric with respect to its axis and that the vortex can be described by a solution of the stationary Euler equations, that is, disregarding the effects of dissipation. Even if those assumptions were justified, they definitely limit the accuracy of the experimental results. Furthermore, the spatio-temporal derivatives of the pressure signal, which have to be computed in order to derive the induced velocities, amplify the noise and uncertainty of the data.

The situation can be improved by simultaneous measurements of pressure, density and velocity fields. The setup needed for the BOS measurements was composed of one camera looking through the test section and a light source, which illuminates a background paper containing a dot pattern (Fig. 19.4). The dot pattern was generated by printing a single exposure PIV recording on a laser printer. The size of the dots was approximately 1 mm and the size of the interrogation window backprojected into the observation area was 25 mm² on average.

Two different light sources were used: a continuous white light and a stroboscope light synchronized with the camera. The results which are shown first represent the averaged density field and were obtained with continuous light. Figure 19.8 shows displacement fields using continuous light at $Ma = 0.79$. The region of the shear layers above and below the cylinder can clearly be detected on the density gradient field for a Reynolds number of $Re = 335000$. Intermittent compression shock waves (expected at $Ma = 0.6 \dots 0.8$), however, could not be observed due to smearing effects of long exposures. However, the strong density gradients and the expected

Fig. 19.8 Density gradients obtained with a long exposure time at $Ma = 0.79$



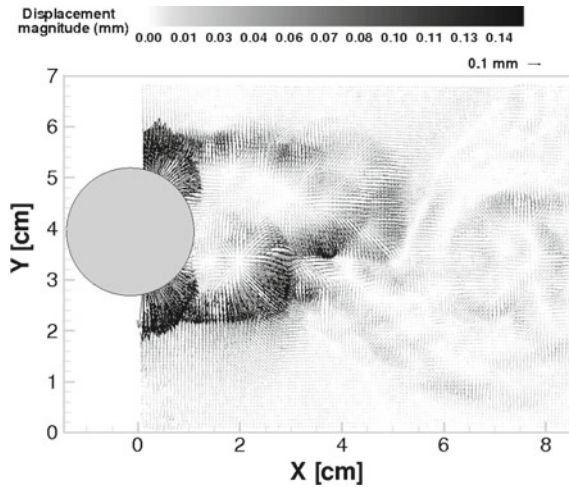


Fig. 19.9 Density gradients obtained with a short exposure time at $Ma = 0.79$

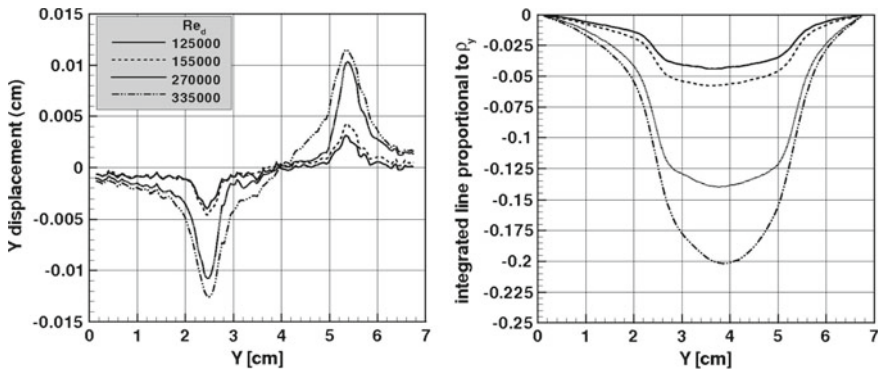


Fig. 19.10 BOS density gradient distributions (left) and their integration to density distributions (right)

decrease of density behind the cylinder can clearly be seen at this Reynolds number (cp. Fig. 19.10). The unsteadiness of the vortex wake for this set of parameters becomes visible when comparing averaged and instantaneous results (Figs. 19.8 and 19.9). This demonstrates the need of instantaneous measurements and made simultaneous velocity and density gradient fields desirable, which will be described further below.

The displacement field can be integrated in order to obtain a distribution which is proportional to the density distribution assuming a two-dimensional flow field. Two integration methods can be used: either by solution of the Poisson equation [26] or by line integration. The second method which is the simplest to implement, has the disadvantage of producing line noise. Figure 19.10 shows the line extracted (left hand

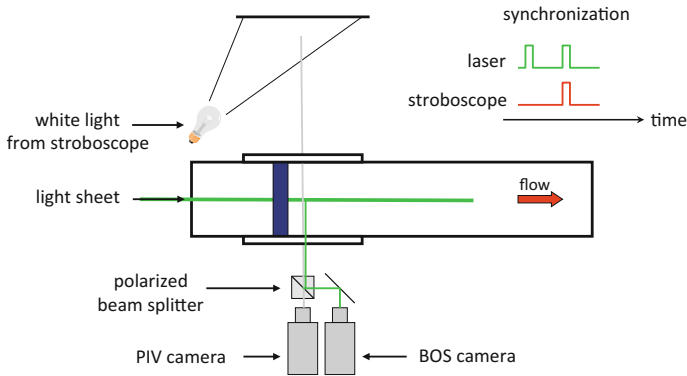


Fig. 19.11 Optical setup for simultaneous PIV and BOS measurements

side) from the time averaged displacement fields for different Reynolds numbers at $x = 1.5$ cm and the result after integration (right hand side). It can be seen that the displacement increases while the density decreases with Reynolds number and shows an almost perfect symmetry in relation to the center of the cylinder with a lowest density for $y = 4$ cm. The cylinder diameter has been chosen in order to restrict the ratio between cylinder diameter, d , and its span, s , to $d/s = 1/4$. As can be seen by comparing averaged and instantaneous results (Figs. 19.8 and 19.9), the vortex wake for this set of parameters is highly unsteady. This demonstrates the need for instantaneous measurements and makes simultaneous velocity and density gradient fields desirable. The advantage of the BOS technique is that it can very easily be coupled with PIV.

Figure 19.11 shows the setup needed to perform BOS and PIV measurements at the same time, which allows for obtaining simultaneous velocity and density data. It is composed of two cameras, one used for PIV and the other for BOS. Both cameras have the same field of view and are looking through a polarized beam splitter, which blocks the light from the laser sheet for the BOS camera. The PIV camera was focused on the laser light sheet plane, whereas the BOS camera was focused onto the background dot pattern. The stroboscope light was synchronized with the second pulse of the laser. The background of the second image is therefore brighter than the first, but the quality of the correlation data was not significantly reduced.

Figure 19.12 shows a zoom of a region where a vortex is visible: in the BOS result, the vectors are diverging from the center of the vortex, which corresponds to an area of lower density.

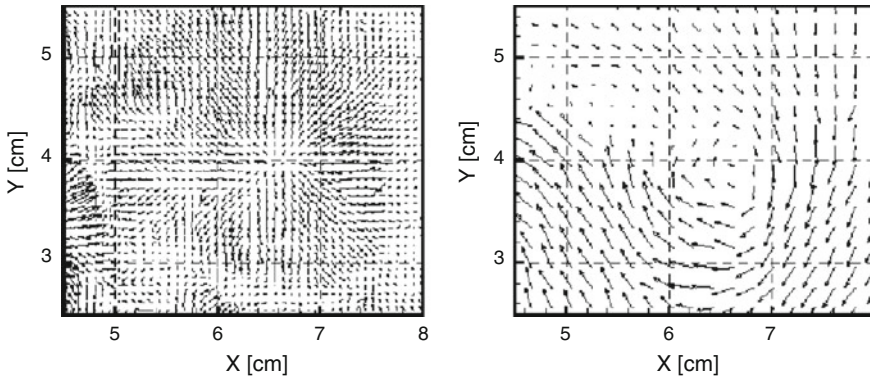


Fig. 19.12 Sample result of simultaneous BOS (left) and PIV (right) data of a cylinder wake flow

19.2.4 Conclusions

The measurements demonstrate the feasibility of the BOS technique for different applications – even large-scale ones – by visualizing the blade tip vortices of a helicopter in flight. In spite of the difficult experimental conditions density gradient data were obtained, which allows for the visualization of density fields with a high spatial resolution. Compared to previous measurements, the time needed for the setup and for data acquisition can be considerably decreased. However, quantitative position measurements of fully three-dimensional density fields, like the tip vortex system of a helicopter rotor, require multiple camera perspectives, as a single camera system is only capable of measuring two components of the spatial density gradient integrated along the optical path. In the presented rotor experiment, simultaneous image recording with a calibrated multi-camera BOS setup was applied to spatially reconstruct the vortex system of a free-flying helicopter for the first time. The resulting data set allowed for the extraction of geometry parameters such as the location of the vortex relative to the rotor plane and the orientation of the vortex axis in space, which are important for the study of BVI and other vortex interaction phenomena.

After having demonstrated the feasibility of the concept by its application to a technologically relevant but fluid mechanically complex problem, more detailed studies of vortices behind a cylinder were performed in order to reduce the complexity of the vortical structures under investigation and to perform simultaneous velocity measurements. Those measurements will allow a more accurate modeling of vortices in future aero-acoustic prediction codes for helicopters. Furthermore, BOS renders full-scale in-flight rotor tip vortex morphology studies possible by relying on fairly simple sensor units in combination with natural formation backgrounds [4]. Moreover, tomographic BOS data evaluation enables airborne vortex core density estimations [14].

References

1. Asundi, A., Chiang, F.P.: Theory and applications of the white light speckle method for strain analysis. *Opt. Eng.* **21**(4), 214570 (1982). DOI 10.1117/12.7972953. URL <http://doi.org/10.1117/12.7972953>
2. Bagai, A., Leishman, J.G.: Flow visualization of compressible vortex structures using density gradient techniques. *Exp. Fluids* **15**(6), 431–442 (1993). DOI 10.1007/BF00191786. URL <https://doi.org/10.1007/BF00191786>
3. Bauknecht, A., Ewers, B., Wolf, C., Leopold, F., Yin, J., Raffel, M.: Three-dimensional reconstruction of helicopter blade-tip vortices using a multi-camera bos system. *Exp. Fluids* **56**(1), 1–13 (2014). DOI 10.1007/s00348-014-1866-6
4. Bauknecht, A., Merz, C.B., Raffel, M.: Airborne visualization of helicopter blade tip vortices. *J. Vis.* **20**(1), 139–150 (2016). DOI 10.1007/s12650-016-0389-z. URL <http://link.springer.com/10.1007/s12650-016-0389-z>
5. Burch, J.M., Tokarski, J.M.J.: Production of multiple beam fringes from photographic scatterers. *Opt. Acta: Int. J. Opt.* **15**(2), 101–111 (1968). DOI 10.1080/713818071. URL <https://www.tandfonline.com/10.1080/713818071>
6. Chu, T.C., Ranson, W.F., Sutton, M.A.: Applications of digital-image-correlation techniques to experimental mechanics. *Exp. Mech.* **25**(3), 232–244 (1985). DOI 10.1007/BF02325092. URL <https://doi.org/10.1007/BF02325092>
7. Daly, S.H.: Digital image correlation in experimental mechanics for aerospace materials and structures. *Encycl. Aerosp. Eng.* (2010). DOI 10.1002/9780470686652.eae542. URL <https://doi.org/10.1002/9780470686652.eae542>
8. Dalziel, S.B., Hughes, G.O., Sutherland, B.R.: Whole-field density measurements by 'synthetic schlieren'. *Exp. Fluids* **28**(4), 322–335 (2000). DOI 10.1007/s003480050391. URL <https://doi.org/10.1007/s003480050391>
9. Debrus, S., Françon, M., Grover, C.P., May, M., Roblin, M.L.: Ground glass differential interferometer. *Appl. Opti.* **11**(4), 853–857 (1972). DOI 10.1364/AO.11.000853. URL <http://ao.osa.org/abstract.cfm?URI=ao-11-4-853>
10. Dorić, S.: Ray tracing through gradient-index media: recent improvements. *Appl. Opt.* **29**(28), 4026–4029 (1990). DOI 10.1364/AO.29.004026. URL <https://doi.org/10.1364/AO.29.004026>
11. van der Draai, R.K., van Schinkel, R.P.M., Telesca, A.: A new approach to measuring model deflection. In: 18th International Congress on Instrumentation in Aerospace Simulation Facilities, 1999. ICIASF 99, pp. 33/1–33/7 (1999). DOI 10.1109/ICIASF.1999.827173. URL <https://doi.org/10.1109/ICIASF.1999.827173>
12. Goldhahn, E., Seume, J.: The background oriented schlieren technique: sensitivity, accuracy, resolution and application to a three-dimensional density field. *Exp. Fluids* **43**(2–3), 241–249 (2007). DOI 10.1007/s00348-007-0331-1. URL <https://doi.org/10.1007/s00348-007-0331-1>
13. Hartley, R., Zisserman, A.: *Multiple View Geometry in Computer Vision*, 2nd edn. Cambridge University Press, UK (2004). DOI 10.1017/CBO9780511811685. URL <https://doi.org/10.1017/CBO9780511811685>
14. Kindler, K., Goldhahn, E., Leopold, F.: Recent developments in background oriented Schlieren methods for rotor blade tip vortex measurements. *Exp. Fluids* **43**(2–3), 233–240 (2007). DOI 10.1007/s00348-007-0328-9. URL <https://doi.org/10.1007/s00348-007-0328-9>
15. Kirmse, T.: Recalibration of a stereoscopic camera system for in-flight wing deformation measurements. *Meas. Sci. Technol.* **27**(5), 054,001 (2016). DOI 10.1088/0957-0233/27/5/054001. URL <http://stacks.iop.org/0957-0233/27/i=5/a=054001>
16. Köpf, U.: Application of speckling for measuring the deflection of laser light by phase objects. *Optic. Commun.* **5**(5), 347–350 (1972). DOI 10.1016/0030-4018(72)90030-2. URL <http://www.sciencedirect.com/science/article/pii/0030401872900302>
17. Li, L.G., Liang, J., Guo, X., Guo, C., Hu, H., Tang, Z.Z.: Full-field wing deformation measurement scheme for in-flight cantilever monoplane based on 3D digital image correlation. *Meas. Sci. Technol.* **25**(6), 065–202 (2014). DOI 10.1088/0957-0233/25/6/065202. URL <https://doi.org/10.1088/0957-0233/25/6/065202>

18. Mandella, M., Bershader, D.: Quantitative study of the compressible vortex: Generation, structure and interaction with airfoils. In: 25th AIAA Aerospace Sciences Meeting (1987). DOI 10.2514/6.1987-328. URL <http://doi.org/10.2514/6.1987-328>. AIAA Paper 87-328
19. Merzkirch, W.: Flow Visualization, 1st edn. Academic Press, New York (1974)
20. Merzkirch, W.: Flow Visualization, 2nd edn. Academic Press, New York (1987). URL <http://www.sciencedirect.com/science/book/9780124913516>
21. Pan, B., Qian, K., Xie, H., Asundi, A.: Two-dimensional digital image correlation for in-plane displacement and strain measurement: a review. Meas. Sci. Technol. **20**(6), 17 (2009). DOI 10.1088/0957-0233/20/6/062001. URL <http://stacks.iop.org/0957-0233/20/i=6/a=062001>
22. Raffel, M.: Background-oriented schlieren (BOS) techniques. Exp. Fluids **56**(3), 1–17 (2015). DOI 10.1007/s00348-015-1927-5. URL <https://doi.org/10.1007/s00348-015-1927-5>
23. Raffel, M., Richard, H., Meier, G.E.A.: On the applicability of background oriented optical tomography for large scale aerodynamic investigations. Exp. Fluids **28**(5), 477–481 (2000). DOI 10.1007/s003480050408. URL <https://doi.org/10.1007/s003480050408>
24. Raffel, M., Tung, C., Richard, H., Yu, Y., Meier, G.E.A.: Background oriented stereoscopic schlieren (boss) for full scale helicopter vortex characterization. In: 9th International Symposium on Flow Visualization, pp. 23–24 (2000)
25. Rastogi, P.K.: Digital Speckle Pattern Interferometry and Related Techniques, vol. 1. Wiley, New York (2000)
26. Richard, H., Raffel, M.: Principle and applications of the background oriented schlieren (BOS) method. Meas. Sci. Technol. **12**(9), 1576 (2001). DOI 10.1088/0957-0233/12/9/325. URL <http://stacks.iop.org/0957-0233/12/i=9/a=325>
27. Settles, G.S.: Schlieren and shadowgraph imaging in the great outdoors. In: PSFVIP-2 Schlieren and Shadowgraph Techniques; Visualizing Phenomena in Transparent Media, Honolulu (USA) (1999)
28. Sharma, A., Kumar, D.V., Ghatak, A.K.: Tracing rays through graded-index media: a new method. Appl. Opt. **21**(6), 984–987 (1982). DOI 10.1364/AO.21.000984. URL <http://ao.osa.org/abstract.cfm?URI=ao-21-6-984>
29. Sutton, M.A., Wolters, W.J., Peters, W.H., Ranson, W.F., McNeill, S.R.: Determination of displacements using an improved digital correlation method. Image Vis. Comput. **1**(3), 133–139 (1983). DOI 10.1016/0262-8856(83)90064-1. URL [https://doi.org/10.1016/0262-8856\(83\)90064-1](https://doi.org/10.1016/0262-8856(83)90064-1)
30. Viktin, D., Merzkirch, W.: Speckle-photographic measurements of unsteady flow processes using a highspeed CCD camera. In: 8th International Symposium on Flow Visualization, Sorrento (1998)
31. Weinstein, L.M.: Large field schlieren visualization – from wind tunnels to flight. J. Vis. **2**(3), 321–329 (2000). URL <http://ci.nii.ac.jp/naid/10004572903/en/>
32. Wernekinck, U., Merzkirch, W.: Speckle photography of spatially extended refractive-index fields. Appl. Opt. **26**(1), 31–32 (1987). DOI 10.1364/AO.26.000031. URL <http://ao.osa.org/abstract.cfm?URI=ao-26-1-31>
33. Withers, P.J.: Strain measurement by digital image correlation. Strain **44**(6), 421–422 (2008). DOI 10.1111/j.1475-1305.2008.00556.x. URL <https://doi.org/10.1111/j.1475-1305.2008.00556.x>

Appendix A

Suggested Text Books

The reader interested in a deeper treatment of the fundamentals of the topic covered in the book we recommend the following text books:

Optics

- Principles of Optics* by BORN & WOLF [4]
Fundamentals of Photonics by SALEH & TEICH [18]
Coherent Optics - Fundamentals and Applications by LAUTERBORN & KURZ [12]
Introduction to Fourier Optics by GOODMAN [9]
The New Physical Optics Notebook: Tutorials In Fourier Optics by REYNOLDS, DEVELIS, PARRENT & THOMPSON [17]

Imaging and Cameras

- Multiple View Geometry in Computer Vision* by HARTLEY & ZISSERMAN [10]

Numerical Techniques

- Numerical Recipes: The Art of Scientific Computing* by PRESS, TEUKOLSKY, VETTERLING & FLANNERY [16]

Signal Processing and Statistics

- The Scientist and Engineer's Guide to Digital Signal Processing* by SMITH [21]
Random Data: Analysis and Measurement Procedures by BENDAT & PIERSOL [3]
Probability, Random Variables and Stochastic Processes by PAPOULIS & PILLAI [14]
The Fourier Transform and Its Applications by BRACEWELL [5]
The Fast Fourier Transform by BRIGHAM [6]

Digital Image Processing

- Digital Image Processing* by GONZALEZ & WOODS [8]
Digital Image Processing and Image Formation by JÄHNE [11]
Digital Image Processing: PIKS Scientific Inside by PRATT [15]

Fluid Mechanics

- An Introduction to Fluid Dynamics* by BATCHELOR [2]
Fluid Mechanics by WHITE [23]
Analysis of Transport Phenomena: Topics in Chemical Engineering by DEEN [7]

Experimental Techniques

Springer Handbook of Experimental Fluid Mechanics by TROPEA, YARIN, & FOSS [22]

Flow Visualization

Flow Visualization by MERZKIRCH [13]

Additional Books on Particle Image Velocimetry

Particle Image Velocimetry by ADRIAN & WESTERWEEL [1]

Particle Image Velocimetry: New Developments and Recent Applications by SCHRÖDER & WILLERT [20]

Recent Advances in Particle Image Velocimetry: VKI Lecture Series on Particle Image Velocimetry by SCARANO & RIETHMULLER [19]

References

1. Adrian, R.J., Westerweel, J.: Particle Image Velocimetry. Cambridge Aerospace Series. Cambridge University Press (2011). URL <http://www.cambridge.org/de/academic/subjects/engineering/thermal-fluids-engineering/particle-image-velocimetry>
2. Batchelor, G.K.: An Introduction to Fluid Dynamics. Cambridge Mathematical Library. Cambridge University Press (2000). DOI 10.1017/CBO9780511800955. URL <http://doi.org/10.1017/CBO9780511800955>
3. Bendat, J.S., Piersol, A.G.: Random Data: Analysis and Measurement Procedures, 4th edn. John Wiley & Sons, Inc. (2012). DOI 10.1002/9781118032428. URL <http://doi.org/10.1002/9781118032428>
4. Born, M., Wolf, E.: Principles of Optics, 7th edn. Cambridge University Press, Cambridge (1999). URL <https://www.cambridge.org/de/academic/subjects/physics/optics-optoelectronics-and-photonics/principles-optics-electromagnetic-theory-propagation-interference-and-diffraction-light-7th-edition>
5. Bracewell, R.N.: The Fourier Transform and Its Applications, 3rd edn. Electrical Engineering Series. McGraw Hill (1999)
6. Brigham, E.O.: The Fast Fourier Transform. Prentice-Hall Signal Processing Series. Prentice-Hall, Englewood Cliffs, New Jersey (1974)
7. Deen, W.: Analysis of Transport Phenomena, Topics in Chemical Engineering, 2nd edn. Oxford University Press, New York (2012). URL <https://global.oup.com/academic/product/analysis-of-transport-phenomena-9780199740253?cc=de&lang=en&>
8. Gonzalez, R.C., Woods, R.E.: Digital Image Processing, 4th edn. Pearson (2018). URL http://www.imageprocessingplace.com/DIP-4E/dip4e_main_page.htm
9. Goodman, J.W.: Introduction to Fourier Optics, 4th edn. Macmillan Learning (2017). URL <http://www.macmillanlearning.com/Catalog/product/introductiontofourieroptics-fourthedition-goodman>
10. Hartley, R., Zisserman, A.: Multiple View Geometry in Computer Vision, 2nd edn. Cambridge University Press, UK (2004). DOI 10.1017/CBO9780511811685. URL <http://doi.org/10.1017/CBO9780511811685>
11. Jähne, B.: Digital Image Processing and Image Formation, 7th edn. Springer-Verlag, Berlin Heidelberg (2018). URL <http://www.springer.com/us/book/9783642049491>
12. Lauterborn, W., Kurz, T.: Coherent Optics - Fundamentals and Applications, 2nd edn. Springer Verlag, Berlin (2003). DOI 10.1007/978-3-662-05273-0. URL <http://doi.org/10.1007/978-3-662-05273-0>
13. Merzkirch, W.: Flow Visualization, 2nd edn. Academic Press, New York (1987). URL <http://www.sciencedirect.com/science/book/9780124913516>
14. Papoulis, A., Pillai, S.U.: Probability, Random Variables, and Stochastic Processes, 4th edn. McGraw-Hill Education Ltd., New York (2002). URL <http://www.mhhe.com/engcs/electrical/papoulis/>

15. Pratt, W.: Digital Image Processing: PIKS Scientific Inside, 4th edn. Wiley-Interscience, John Wiley & Sons, New York (2007). DOI 10.1002/0470097434. URL <http://doi.org/10.1002/0470097434>
16. Press, W.H., Teukolsky, S.A., Vetterling, W.T., Flannery, B.P.: Numerical Recipes: The Art of Scientific Computing, 3rd edn. Cambridge University Press, New York, NY, USA (2007). URL <http://numerical.recipes/>
17. Reynolds, G.O., DeVelis, J.B., Parrent, G.B., Thompson, B.J.: The New Physical Optics Notebook: Tutorials In Fourier Optics. Optical Engineering Press, Bellingham, Wash., USA (1989). DOI 10.1117/3.2303. URL <https://doi.org/10.1117/3.2303>
18. Saleh, B.E.A., Teich, M.C.: Fundamentals of Photonics, 2nd edn. Pure and Applied Physics. John Wiley & Sons, Inc. (2007). DOI 10.1002/0471213748. URL <http://doi.org/10.1002/0471213748>
19. Scarano, F., Riethmuller, M. (eds.): Recent advances in particle image velocimetry. von Karman Institute for Fluid Dynamics Lecture Series, VKI LS 2009-01. Von Karman Institute, Rhode-Saint-Genève, Belgium (2009). URL <https://store.vki.ac.be/lecture-series-monographs/measurement-techniques/recent-advances-in-particle-image-velocimetry.html>
20. Schröder, A., Willert, C.E. (eds.): Particle Image Velocimetry: New Developments and Recent Applications, *Topics in Applied Physics*, vol. 112. Springer-Verlag Berlin Heidelberg (2008). DOI 10.1007/978-3-540-73528-1. URL <http://doi.org/10.1007/978-3-540-73528-1>
21. Smith, S.W.: The Scientist and Engineer's Guide to Digital Signal Processing (1997). URL <http://www.dspguide.com/>
22. Tropea, C., Yarin, A.L., Foss, J.F.: Springer Handbook of Experimental Fluid Mechanics. Springer Berlin Heidelberg (2007). DOI 10.1007/978-3-540-30299-5. URL <http://doi.org/10.1007/978-3-540-30299-5>
23. White, F.: Fluid Mechanics, 8th edn. McGraw-Hill Series in Mechanical Engineering. McGraw Hill (2016). URL <http://www.mheducation.com/highered/product/fluid-mechanics-white/M0073398276.html>

Appendix B

Mathematical Appendix

B.1 Convolution with the Dirac Delta Distribution

For a real function f of the variable \mathbf{x} , and a given vector \mathbf{x}_i , we have:

$$f(\mathbf{x} - \mathbf{x}_i) = f(\mathbf{x}) * \delta(\mathbf{x} - \mathbf{x}_i)$$

where $*$ denotes convolution and δ the Dirac delta function.

B.2 Particle Images

For infinite small geometric particle images the particle image intensity distribution (intensity profile) is given by the point spread function $\tau(\mathbf{x})$, which has been assumed to have a Gaussian shape [1]:

$$\tau(\mathbf{x}) = K \exp\left(-\frac{8|\mathbf{x}|^2}{d_\tau^2}\right)$$

with

$$K = \frac{8\tau_0}{\pi d_\tau^2}. \tag{B.1}$$

B.3 Convolution of Gaussian Image Intensity Distributions

If we assume Gaussian image intensity distributions as given in Eq. (B.1) the product of two displaced images yields:

$$\tau(\mathbf{x} - \mathbf{x}_i) \tau(\mathbf{x} - \mathbf{x}_i + \mathbf{s}) = K^2 \exp\left[-8(|\mathbf{x} - \mathbf{x}_i|^2 + |\mathbf{x} - \mathbf{x}_i + \mathbf{s}|^2)/d_\tau^2\right].$$

For two vectors \mathbf{a} and \mathbf{b} , it can be shown that:

$$|\mathbf{a}|^2 + |\mathbf{a} + \mathbf{b}|^2 = |\mathbf{b}|^2/2 + 2|\mathbf{a} + \mathbf{b}/2|^2 .$$

Hence:

$$\begin{aligned} \int_{a_1} \tau(\mathbf{x} - \mathbf{x}_i) \tau(\mathbf{x} - \mathbf{x}_i + \mathbf{s}) d\mathbf{x} &= \exp\left(-\frac{4|\mathbf{s}|^2}{d_\tau^2}\right) \\ &\times \int_{a_1} K^2 \exp(-16|\mathbf{x} - \mathbf{x}_i + \mathbf{s}/2|^2/d_\tau^2) d\mathbf{x} \\ &= \exp\left(-\frac{8|\mathbf{s}|^2}{(\sqrt{2}d_\tau)^2}\right) \\ &\times \int_{a_1} \tau^2(\mathbf{x} - \mathbf{x}_i + \mathbf{s}/2) d\mathbf{x} . \end{aligned}$$

B.4 Expected Value

We defined $f_1(\mathbf{X}) = V_0(\mathbf{X})V_0(\mathbf{X} + \mathbf{D})$ in Equation (4.8). Here we will determine

$$E \left\{ \sum_{i=1}^N f_1(\mathbf{X}_i) \right\} .$$

The sum must be considered as a function of N random variables $\mathbf{X}_1, \mathbf{X}_2, \dots, \mathbf{X}_N$. Hence:

$$\begin{aligned} E \left\{ \sum_{i=1}^N f_1(\mathbf{X}_i) \right\} &= \sum_{i=1}^N E \{f_1(\mathbf{X}_i)\} = \sum_{i=1}^N \frac{1}{V_F} \int f_1(\mathbf{X}_i) d\mathbf{X}_i \\ \Rightarrow E \left\{ \sum_{i=1}^N f_1(\mathbf{X}_i) \right\} &= \frac{N}{V_F} \int_{V_F} f_1(\mathbf{X}) d\mathbf{X} . \end{aligned}$$

Reference

1. Keane, R.D., Adrian, R.J.: Theory of cross-correlation analysis of PIV images. Applied Scientific Research **49**(3), 191–215 (1992). DOI 10.1007/BF00384623, URL <https://doi.org/10.1007/BF00384623>

Appendix C

List of Symbols and Acronyms

a	aperture radius
a_I	interrogation area
\mathbf{a}	local acceleration vector
A	area
A_{crit}	critical area
C_I	spatial auto-covariance
C_{II}	spatial cross-covariance
C_R	constant factor of the correlation function
C_S	scattering cross section
c_I	spatial correlation coefficient
c_{II}	spatial cross-correlation coefficient
c_1, c_2	constant factors for outlier detection
D	diffusion coefficient
\mathbf{D}	particle displacement between the two light pulses
D_I	interrogation area
D_a	aperture diameter
D_{max}	maximum particle displacement
D_{Photo}	photographic emulsion density
\mathbf{d}	particle image displacement
\bar{d}	mean value of measured image displacement
d'	approximation of the image diameter
d_{diff}	diffraction limited imaging diameter
d_{max}	maximum particle image displacement
d_{min}	minimum particle image displacement
d_{opt}	optimum particle image displacement
d_p	particle diameter
d_r	difference between real and ideal particle image diameter
d_s	diameter of the Airy pattern
d_{shift}	particle image displacement due to the rotating mirror system
d_B	blur circle diameter
d_τ	particle image diameter

$d_{\tau x}, d_{\tau y}$	correlation peak widths along x and y respectively
d_{τ}^*	normalized particle image diameter
E	exposure during recording
$E\{\}$	expected value
E_1, E_2	energy states of an atom
e	resolution limit of a microscope
F_1	in-plane loss of correlation
F_0	out-of-plane loss of correlation
f	lens focal length
$f_{\#}$	lens f -number
$f(x)$	function
\mathbf{F}	body forces
\mathbf{g}	acceleration due to gravity
$g(x, y)$	gray value distribution
h	Planck's constant
\mathbf{H}	system transfer function
I	image intensity field of the first exposure
I_{median}	grayscale median image intensity
I'	image intensity field of the second exposure
I_0	laser intensity, incident on a particle
$I_0(Z)$	light sheet intensity profile in the Z direction
I_p	peak particle image intensity
I_z	maximum intensity of the light sheet
I^+	correlation of the intensity field with itself
\hat{I}, \hat{I}'	Fourier transforms of I and I'
J_B	light flux
J_n	Bessel function of first kind
k_{smooth}	filter kernel width
K	Boltzmann's constant
Kn_p	particle Knudsen number
l_w	imaging depth
lps	line pairs
M^2	spatial mode
M	magnification factor
M_0	magnification along the principal optical axis
Ma	Mach number
$\tilde{M}_{\text{TF}}(r')$	modulation transfer at a certain spatial frequency (r')
N	total number
m_p	particle mass
N	total number
N_p	number of individual particle images
N_l	length of tracks
N_0	number of overlapping particle images
NA	numerical aperture
\mathcal{N}	particle image density (per unit area)

\mathcal{N}_I	number of particle images per interrogation window
n_{exp}	number of exposures per recording
NS	source density (for volume PIV)
n	refractive index
n_0	refractive index of glass
n_w	refractive index of water
Pr	Prandtl number
P_S	total scattered power
q	normalized diameter
q_1	particle size distribution of length
q_2	particle size distribution of area
q_3	particle size distribution of volume
QE	quantum efficiency
QL	number of quantization levels
r	spatial frequency, radius
r'	characteristic value of the spatial frequency
r_x, r_y	spatial frequencies in orthogonal directions
R_{12}	probability of correct particle pairing
Ra	Rayleigh number
Re	Reynolds number
R_C	mean background correlation
R_D	displacement correlation peak
R_{D^+}	positive displacement correlation peak
R_{D^-}	negative displacement correlation peak
R_F	noise term due to random particle correlations
R_I	spatial auto-correlation
R_{II}	spatial cross-correlation
R_P	particle image self-correlation peak
R_τ	correlation of a particle image
s	separation vector in the correlation plane
s_D	displacement vector in the correlation plane
Stk	Stokes number
T_a	absolute temperature
$T(x, y)$	local varying intensity transmittance of photographic emulsion
t	time of the first exposure
t'	time of the second exposure
t''	time of the third exposure
t_{exp}	exposure time
t_e	frame transfer time
t_f	pulse length
Δt	exposure time delay
Δt_{min}	minimum time delay
$\Delta t_{\text{row-shift}}$	charge transfer time of a single row in a CCD sensor
$\Delta t_{\text{transfer}}$	charge transfer time in a CCD sensor
U, V	in-plane components of the velocity \mathbf{U}

\bar{U}	mean flow velocity in streamwise direction
\mathbf{U}	flow velocity vector
\mathbf{U}_g	gravitationally induced velocity
U_{\max}	maximum flow velocity in streamwise direction
U_{mean}	mean flow velocity in streamwise direction
U_{\min}	minimum flow velocity in streamwise direction
$U_n(u, v)$	Lommel function
\mathbf{U}_p	velocity of the particle
\mathbf{U}_s	velocity lag
U_{shift}	shift velocity
U_τ	friction velocity, $\sqrt{\tau_w/\rho}$
U_∞	free stream velocity
u, v	dimensionless diffraction variables
$V_0(\mathbf{x}_i)$	intensity transfer function for individual particle images
V_F	fluid volume that has been seeded with particles
V_I	interrogation volume in the flow
V_{fr}	volume fraction of particles
$V_n(u, v)$	Lommel function
v_I	interrogation area (image plane)
W	out-of-plane component of the velocity \mathbf{U}
$W_0(X, Y)$	interrogation window function back projected into the light sheet
X, Y, Z	flow field coordinate system
X_m	distance between rotating mirror and optical axis
\mathbf{X}_p	particle position within flow field
$\mathbf{X}_v, \mathbf{X}'_v$	point in the virtual light sheet plane
x, y, z	image plane coordinate system
x^*, y^*, z^*	mirror coordinate system
\mathbf{x}	point in the image plane, $\mathbf{x} = \mathbf{x}(x, y)$
$\mathbf{x}_0, \mathbf{y}_0, \mathbf{z}_0$	position of the center of the interrogation window
$\Delta x_0, \Delta y_0$	interrogation area dimensions
$\Delta X_0, \Delta Y_0$	horizontal, vertical interrogation area dimensions within light sheet
$\Delta x_{\text{step}}, \Delta y_{\text{step}}$	distance between two interrogation areas
ΔZ	depth of (illumination) volume
$\Delta X, \Delta Y$	grid spacing in object plane
Z_0	distance between object plane and lens plane
Z_m	distance between object plane and mirror axis
z_0	distance between image plane and lens plane
Z_{corr}	depth of correlation
ΔZ_0	light sheet thickness

Greek Symbols

$\delta(\mathbf{x})$	Dirac delta function at position \mathbf{x}
δ_X	measurement error
δ_Z	depth of focus
$\delta_{Z_{\text{corr}}}$	depth of correlation
$\delta_{Z_{\text{diff}}}$	depth of correlation due to geometrical optics
$\delta_{Z_{\text{geo}}}$	depth of correlation due to diffraction
Δ_{pix}	sensor pixel size
ε	cutoff of image intensity
ε_{tot}	total displacement error
$\varepsilon_{\text{bias}}$	displacement bias error
ε_{sys}	systematic error
$\varepsilon_{\text{resid}}$	residual (nonsystematic) error
$\varepsilon_{\text{resid}}$	residuals from stereo PIV vector reconstruction
ϵ_{thresh}	threshold for outlier detection
ϵ_U	velocity measurement uncertainty
γ	photographic gamma
$\mathbf{\Gamma}$	state of the ensemble
λ	wavelength of light
λ_0	vacuum wavelength of light
λ_{unst}	spatial wavelength
μ	dynamic viscosity
μ_I	spatial average of I
ν	kinematic viscosity, μ/ρ
ω_m	angular velocity of the rotating mirror
ρ	fluid density
ρ_m	spatial resolution limit during recording
ρ_p	particle density
σ	width parameter of Gaussian bell curve
σ	standard deviation
σ_I	spatial variance of I
θ	half angle subtended by the aperture
$\tau(\mathbf{x})$	point spread function of imaging lens
τ_f	characteristic time scale in the flow
τ_p	response time
τ_s	relaxation time
ω	vorticity vector
$\omega_x, \omega_y, \omega_z$	vorticity components
Ω	solid angle

Abbreviations and Acronyms

Mod	image modulation
pixel	picture element
ppp	particles per pixel

rms	root mean square
Tu	turbulence level in a flow
APS	active pixel sensor
Ar ⁺ laser	Argon-ion laser
ART	algebraic reconstruction techniques
BOS	background-oriented schlieren
CBC	correlation-based correction [4, 3]
CCD	charge coupled device
CCIR	video transmission standard
CIV	correlation image velocimetry
CLSM	confocal laser scanning microscopy
CMO	common main objective
CMOS	complementary metal-oxide-semiconductor
CW	continuous wave
DEHS	di-ethyl-hexyl-sebacate (liquid for droplet seeding CAS-No.122-62-3)
DGV	Doppler global velocimetry
DIC	digital image correlation
DLT	direct linear transform
DMD	dynamical mode decomposition
DOC	depth of correlation
DOE	diffractive optical elements
DPIT	digital particle image thermometry [2]
DPIV	digital particle image velocimetry
DSPIV	digital stereo particle image velocimetry
DAR	dynamic acceleration range
DSR	dynamic spatial range [1]
DVR	dynamic velocity range [1]
emCCD	electron multiplication CCD
FFT	fast Fourier transform
FOV	field of view
FPN	fixed pattern noise
FT	Fourier transform
FTC	fluid trajectory correlation
FTEE	fluid trajectory ensemble evaluation
He-Ne laser	Helium-Neon laser
HFSB	Helium filled soap bubbles
HPIV	holographic particle image velocimetry
IB	interrogation box
IPCT	image pattern correlation technique
IPR	iterative particle reconstruction [8]
LDA, LDV	laser Doppler anemometry, - velocimetry
LED	light emitting diode
LFC	local field correction [5]
LID	low image density

LPT	Lagrangian particle tracking
LSCM	laser scanning confocal microscope
LSV	laser speckle velocimetry
LTA, L2F	laser transit anemometry, laser-2-focus anemometry
MART	multiplicative algebraic reconstruction techniques
MFG	multiplicative first guess method
MG	multi-grid
MTE	Motion Tracking Enhancement
MTF	modulation transfer function
MOSFET	metal-oxide-semiconductor field-effect transistor
MQD	minimum quadratic differences
Nd:YAG laser	Neodym-YAG laser
Nd:YLF laser	Neodym-YLF laser
NIT	non-iterative tracking method
NTSC	National Television System Committee (refers to a video standard)
OTF	optical transfer function
pdf	probability density function
PAL	phase alternating line (video standard)
PCA	principal component analysis
PIDV	particle image displacement velocimetry (early name for PIV)
PIV	particle image velocimetry
μ PIV	micro particle image velocimetry
PPV	particles per voxel
PTF	phase transfer function
PTV	particle tracking velocimetry
PDV	planar Doppler velocimetry (= DGV)
POD	proper orthogonal decomposition
ROI	region of interest
QE	quantum efficiency
sCMOS	scientific CMOS
SHG	second harmonic generator
SLR	single-lens reflex
SNR	signal-to-noise ratio
SPIV	stereo particle image velocimetry
SPOF	symmetric phase-only filtering [7]
STB	“shake the box” (3-D particle tracking)[6]
TEM	transverse electric mode
TLC	thermochromic liquid crystals
TR-PIV	time-resolved particle image velocimetry
VIC	Vortex-in-cell
VLSI	very large scale integration
VSC	volume-self-calibration

References

1. Adrian, R.J.: Dynamic ranges of velocity and spatial resolution of particle image velocimetry. *Measurement Science and Technology* **8**(12), 1393–1398 (1997). DOI 10.1088/0957-0233/8/12/003, URL <http://doi.org/10.1088/0957-0233/8/12/003>
2. Dabiri, D.: Digital particle image thermometry/velocimetry: a review. *Experiments in Fluids* **46**(2), 191–241 (2009). DOI 10.1007/s00348-008-0590-5, URL <http://doi.org/10.1007/s00348-008-0590-5>
3. Hart, D.P.: PIV error correction. *Experiments in Fluids* **29**(1), 13–22 (2000). DOI 10.1007/s003480050421, URL <http://doi.org/10.1007/s003480050421>
4. Hart, D.P.: Super-resolution piv by recursive local-correlation. *Journal of Visualization* **3**(2), 187–194 (2000). DOI 10.1007/BF03182411, URL <http://doi.org/10.1007/BF03182411>
5. Nogueira, J., Lecuona, A., Rodríguez, P.A.: Identification of a new source of peak locking, analysis and its removal in conventional and super-resolution piv techniques. *Experiments in Fluids* **30**(3), 309–316 (2001). DOI 10.1007/s003480000179, URL <http://doi.org/10.1007/s003480000179>
6. Schanz, D., Gesemann, S., Schröder, A.: Shake-The-Box: Lagrangian particle tracking at high particle image densities. *Experiments in Fluids* **57**(5), 1–27 (2016). DOI 10.1007/s00348-016-2157-1, URL <http://doi.org/10.1007/s00348-016-2157-1>
7. Wernet, M.P.: Symmetric phase only filtering: a new paradigm for DPIV data processing. *Measurement Science and Technology* **16**(3), 601 (2005). DOI 10.1088/0957-0233/16/3/001, URL <http://doi.org/10.1088/0957-0233/16/3/001>
8. Wieneke, B.: Iterative reconstruction of volumetric particle distribution. *Measurement Science and Technology* **24**(2) (2013). DOI 10.1088/0957-0233/24/2/024008, URL <http://doi.org/10.1088/0957-0233/24/2/024008>

Index

A

Absorption, 61
Airy disk, 84
Airy function, 131
Aliasing
 displacement, 156
Astigmatism particle tracking, 397
Auto-correlation, 134, 167
Axial modes, 63

B

Backward scatter, 44
Bandpass filter, 158
Bessel function, 131
Bias error, 156
Binary image, 158
Brownian motion, 40
B-splines, 176

C

Camera
 high speed, 123
Camera calibration, 292
Camera model, 294
 coplanar calibration, 296
Capillary, 373, 547
CCD, 99
 back-thinned, 100
 dynamic range, 106
 linearity, 106
 microlens array, 101
 read noise, 105
 responsivity, 105
Center differences, 263
Central peak, 135

Centroid, 182
Channel flow, 547
Charge coupled device, 99
Charge Coupled Device (CCD)
 frame-transfer, 118
 full-frame, 116
 interline-transfer, 119
 progressive scan, 119
Chauvenet's criterion
 see data validation
 Z-score test, 251
Circulation, 271
Clocking, 370
CMOS, 99
CMOS sensor
 high speed, 123
Confidence interval, 422
Confocal scanning microscope, 99
Confocal scanning microscopy, 390
Continuum microfluidics, 367
Convergence, 419
Convolution of the geometric image, 131
Convolution of the mean intensity, 134
Coplanar calibration, 296
Correlation
 circular, 156
Correlation averaging, 161
Correlation peak
 aliased, 169
Correlation theorem, 154
Correlation-Based Correction (CBC), 161
Cross-correlation
 circular, 156
 discrete, 152
 linear, 152
 periodic, 156
Cross-correlation coefficient, 157

Cross-correlation function, 137

D

Dark current, 104

Dark current noise, 104

Data validation

dynamic mean value operator, 253

global histogram operator, 251

gradient filter, 249

mediantest, 249

minimum correlation filter, 255

normalized median test, 249

peak height ratio filter, 255

reconstruction residuals, 253, 289

signal-to-noise filter, 255

Z-score test, 251

Deconvolution, 152

Depth of correlation, 82, 377

Depth of field, 376

DGV-PIV, 540

Differential estimate

and curvature, 270

and interrogation window size, 270

and oversampling, 269

spatial resolution, 270

uncertainty, 269

Differential estimation, 262

Differentiation

flow field, 260

Diffraction, 374

Diffraction limited imaging, 84, 87

Displacement estimation

bias error, 156

one-quarter rule, 156

Doppler global velocimetry, 540

DVR, 208

Dynamic Spatial Range (DSR) , 208, 388

E

Energy level diagram, 61

Energy states, 61

Ensemble correlation, 161

Ensemble correlation, correlation averaging,
549

Enstrophy, 279

Epi-fluorescence, 386

Error propagation, 211

Etendue, 73

F

FFT, see Fourier transform, 155

Fiber bundle, 80

Fiber optics, 80

acceptance angle, 74

fiber bundle, 80

illumination, 80

Fill factor, 100

Finite differences, 262

least-squares approximation, 263

Fixed pattern noise (FPN), 105

Flatness, 420

Flow field differentiation, 260

Fluctuating noise, 134

Fluidized bed, 56

Forward differences, 263

Forward scatter, 44

Fourier transform

data windowing, 156

digital, 149

fast, 149, 155

output format, 186

symmetry properties, 155

Frame straddling, 118, 120

Fraunhofer diffraction, 84

Fullwell capacity, 100

G

General defocusing particle tracking, 402

Ghost particles, 388, 389

H

High-pass filter, 158

High-speed video, 373

Histogram stretching, 159

I

Image

intensity field, 131

Image blooming, 100

Image deformation, 172

Image enhancement, 158

high-pass filter, 158

histogram stretching, 159

intensity capping, 159

local normalization, 159

low-pass filter, 159

min/max filter, 159

POD-based, 159

thresholding, 158

Image interpolation, 176

Image modulation, 89

Inkjet, 373

- Integration
 - circulation, 271
 - mass flow, 272
- Intensity capping, 159
- Interpolation
 - B-splines, 176
 - shifted-linear, 177
 - sinc-based, 177
 - Whittaker reconstruction, 177
- Interrogation
 - areas, 129
 - multiple pass, 170
 - volumes, 129
 - windows, 129
- Interrogation window
 - and differential estimation, 270
 - offset, 169, 270

- K**
- Knudsen number, 41

- L**
- Lagrangian invariant, 73
- λ_2 operator, 280
- Laser, 60
- Laskin nozzle, 52
- LED, 73, 529
- LED array, 83
- Lens aberrations, 88
- LFC, 180
- Light scattering, 42
- Light sheet, 78
- Local normalization, 159
- Lommel functions, 375
- Loss of pairs
 - minimization, 169
- Low-pass filter, 159

- M**
- Measurement error, 209
- Measurement volume, 130
- Median test, *see* data validation
- Microchannel, 549
- Microfabricated, 367
- Microfluidic, 367, 369
- Microlens, 120
- Minimum image diameter, 86
- Min/max filter, 159
- Modulation transfer functions, 131
- Molecular tagging velocimetry, 369
- Monte Carlo simulation, 216

- Multiplane stereo PIV, 262, 590
- Multiple peak detection, 185
- Multiscattering, 45

- N**
- Navier–Stokes equation, 259, 548
- Normal strain, 261
- Nyquist theorem, 156

- O**
- One-quarter rule, 156
- 1/4 rule, 156
- Optical flow, 181
- Outliers, 245
- Oversampling
 - error due to, 269

- P**
- Particle image
 - numerically generated, 216
 - optimum diameter, 218
 - optimum displacement, 224
- Particle image diameter, 86
- Particle Image Thermography (PIT), 528
- Particle path curvature, 270
- Particle visibility, 381
- Peak detection, 182
- Peak fit
 - centroid, 182
 - Gauss fit, 183
 - three-point fit, 183
 - 2D Gaussian, 183
 - Whittaker reconstruction, 184
- Peak locking effect, 219
- Perspective
 - projection, 91
- Phase-only filtering, 160
- Photoelectric effect, 100
- Pinhole camera model, 294
- Pixel locking, 219
- Point spread function, 84, 131
- Poisson equation, 274, 276
- Population inversion, 62
- Potential well, 100
- Pressure driven flow, 547
- Pressure estimation, 275
- Pressure field, 275
- Proper orthogonal decomposition, 248
- Pump mechanism, 63

Q

Quantum efficiency, 105

R

Random error, 210
 Rayleigh criterion, 88
 Resolution limit, 88
 Response time, 34
 Richardson extrapolation, 263, 267

S

Scalar image velocimetry, 369
 Scanning PIV, 386
 Scheimpflug condition, 287
 SCMOS camera, 122
 SCMOS sensor, 102
 Seeding
 cyclone, 55
 fluidized bed, 56
 generator, 52, 56
 laskin nozzle, 52
 particles, 51, 68
 Self correlation peak, 134
 Separation vector, 134
 Shear strain
 estimation, 266
 in-plane, 261
 Sine wave test, 180
 Skewness, 420
 Slide scanner, 167
 Spatial resolution
 increasing, 171
 Spectral filtering, 160
 Spontaneous emission, 61
 Standard deviation, 210
 Statistical convergence, 419
 Stereo microscope, 387
 Stereo PIV, 585
 camera calibration, 292
 camera misalignment, 296
 multiplane, 262, 590
 reconstruction residuals, 290
 self-calibration, 293
 Stereoscopic micro PIV, 387
 Stereoscopic PIV, 285
 Stimulated emission, 62
 Stokes theorem, 265
 Strain
 out-of-plane, 261
 Strain tensor, 261

Streamline curvature, 231

Sub-continuum microfluidics, 368

T

Thermochromic Liquid Crystal (TLC), 528
 Three-pinhole technique, 393
 Three-point estimators, 183
 TLC-PIV, 528
 Tomographic micro PIV, 388
 Tomographic PIV, 312
 Transfer function, 131
 Translation imaging, 286
 Transverse mode, 63

U

Uncertainty
 differential estimate, 269
 velocity, 269
 Uncertainty quantification, 211

V

Validation, *see* data validation
 Velocity differentials, 263
 Velocity gradient tensor, 260
 Velocity lag, 34
 Visibility of a particle, 132
 Volume illumination, 381
 Vortex detection, 279
 Vorticity
 estimation, 265
 out-of-plane, 261
 spatial resolution, 270
 uncertainty, 264, 266
 Vorticity equation, 259
 Vorticity vector, 261

W

We have a duplication of material in Ch.10
 on micro-PIV, 93
 Whittaker reconstruction, 177, 184

Y

Young's fringes, 148

Z

Zero padding, 156